CROSS-BORDER CORRELATION OF THE DAMARA BELT IN NAMIBIA AND EQUIVALENT LITHOLOGIES IN NORTHWESTERN BOTSWANA FROM POTENTIAL FIELD AND MAGNETOTELLURIC INTERPRETATIONS

William Rankin

School of Geosciences, University of the Witwatersrand, Johannesburg

2015

A dissertation submitted to the Faculty of Science, University of Witwatersrand in the fulfilment of the requirements for the degree of Master of Science

Declaration

I declare that this dissertation is my own, unaided work. It is being submitted for the Degree of Master of Science at the University of the Witwatersrand, Johannesburg. It has not been submitted before for any degree or examination at any other University.

____

William Rankin

20th day of March 2015 at Johannesburg.

Abstract

Northwest Botswana holds a key position for the correlation of the Pan-African mobile belts of southern Africa (i.e. the Damara-Zambezi-Lufilian Orogeny). Phanerozoic cover (Kalahari Group) precludes direct correlation between Proterozoic lithologies of the Damara Belt and thick metasedimentary sequences of northwest Botswana. A combination of new geological and geophysical field observations, interpretation of 50 m resolution aeromagnetic data, and 2.2 km resolution gravity data of Namibia and Botswana, have led to the development of a new sub-Kalahari geological map of the Damara Belt and northwest Botswana. The interpretation of potential field and magnetotelluric (MT) data complemented with both new and published geological data, has improved the identification of the northern and southern margins of the Damara Belt and northwest Botswana, and tectonostratigraphic zones within them. In addition, these correlations have established that the northern margin of the Kalahari Craton on geological maps extends further north than previously noted.

The northeast trending Damara Belt is confidently traced into northwest Botswana (Ngamiland) to ~19.5°S, 22.0°E. At this location, in map view, aeromagnetically interpreted structures follow a radial distribution from northwest-striking in the west to northeast-striking in the east. The lithostratigraphic units to the north of this location cannot be confidently correlated with lithostratigraphic units of the Damara Belt. Instead, these units are better correlated with lithostratigraphic units in southern Angola and/or Zambia. The southeastern margin of the Damara Belt is in tectonic contact with the northern margin of the Ghanzi-Chobe Belt as identified in the aeromagnetic images. The Ghanzi-Chobe Belt is correlated with the Sinclair Supergroup in the Rehoboth Subprovince in Namibia. The basal Kgwebe volcanics are correlated with the Oorlogsende Porphyry Member and Langberg Formation and the unconformably overlying metasediments of the Ghanzi Group are correlated with the metasediments of the Tsumis Group. The correlations are based on similar aeromagnetic signatures, lithologies, mineralisation and age dates constrained by carbon isotope chemostratigraphy.

Physical property measurements were collected on Meso- to Neoproterozoic lithologies of the Damara Belt, northwest Botswana and Zambia. The measurements included hand held magnetic susceptibility measurements on 303 samples and density measurements on 174 samples. The measurements provide one of the largest physical property databases for Namibia, Botswana and Zambia. In general, the sedimentary units have the lowest magnetic susceptibility values of ~0.207 x 10^{-3} SI units, respectively. The exceptions are the iron formation and diamictite of the Chuos Formation and conglomerate of the Naauwpoort Formation of 15.2 x 10^{-3} SI units. The iron

formation ranges in magnetic susceptibility from 3.34 x 10^{-3} SI units to 92.0 x 10^{-3} SI units and the diamictite has a magnetic susceptibility of 7.68 x 10^{-3} SI units. The igneous lithologies have a density and magnetic susceptibility range from 2.58 $g.cm^{-3}$ to 3.26 $g.cm^{-3}$ and 0.001 x 10^{-3} SI units to 11.6 x 10^{-3} SI units, respectively. The lower values are associated with pegmatites and rhyolites and the higher values are associated with mafic lithologies and magnetite bearing granites (Omangambo, Salem, Sorris-Sorris and Red Granites). The metamorphic lithologies have the widest range of density and magnetic susceptibility values, between 2.61 $g.cm^{-3}$ and 3.37 $g.cm^{-3}$, and -0.299 x 10^{-3} SI units and 49.5 x 10^{-3} SI units, respectively. The lower values are associated with low grade metamorphic facies of sedimentary origin, and the higher values are associated with high-grade metamorphic facies of an igneous origin.

The first upper crustal-scale interpretation of the Southern African MagnetoTelluric EXperiment (SAMTEX) was developed. The results were derived from 1D Occam inversion models, at depth intervals of 1 – 5 km, 1 – 15 km and 1 – 35 km. The MT data were acquired across the semi-parallel, north-south striking DMB, NEN and OKA-CAM profiles in the vicinity of the Namibia – Botswana border between 2006 and 2009. Beneath the MT profiles are two zones of enhanced conductivity, a northern and southern zone. The enhanced conductivity of the northern zone (> 100 Ωm) is associated with individual geological bodies. The southern zone forms an elongated belt of enhanced conductivity (> 300 Ωm) at a depth of less than 5 km. This zone of enhanced conductivity is associated with Proterozoic plate boundaries and subduction zones.

Three ~350 km long, north-south trending magnetic profiles were 2D forward modelled to investigate the proposed northward subduction of oceanic crust and subsequently a portion of the Kalahari Plate beneath the Congo Craton. Additionally, the folding pattern of the Ghanzi-Chobe Belt was developed. The interpretation of the magnetic models suggests a northward subduction is a possible cause for the evolution of the Damara Orogen with the regionally east-west striking negative aeromagnetic anomaly, in northern Namibia, being caused by a thick package (~12 km to 20 km) of metasediments with a modelled magnetic susceptibility of 0. 829 x 10^{-3} SI units.

The Damara Orogen has passed through the subduction-collisional transition but did not evolve into a large-hot orogen. Evidence suggests that the Damara Orogen has gone through the transition of subduction of oceanic crust to terrane accretion (speculated to be represented by the Deep-Level Southern Zone and Chihabadum Complex) and continental collision. However, the doubly vergent wedges did not evolve into an orogenic plateau completing the transition from a small-cold orogen to a large-hot orogen. This is similarly observed in the Alps Orogeny.

Publications

In the course of this study, the candidate was involved in two publications and one peer reviewed abstract.

- Naydenov, K.V., Lehmann, J., Saalman, K., Milani, L., Kinnaird, J.A., Charlesworth, G., Frei, D., and Rankin, W. 2014. New constraints on the Pan-African Orogeny in Central Zambia: A structural and geochronological study of the Hook Batholith and the Mwembeshi Zone. *Tectonophysics*, **637**, 80 – 105.

The candidate initially observed the continuation of the Hook Batholith beneath the sedimentary cover. The candidate processed the aeromagnetic data and wrote a portion of the text on the image processing (Appendix 1).

- Lehmann, J., Master, S., Rankin, W., Milani, L., Kinnaird, J.A., Naydenov, K.V., Saalmann, and Kumar, M. submitted. New correlations and tectonic setting of the Kalahari Copper Belt in Namibia and Botswana. *Ore Geology Reviews*.

The candidate processed the aeromagnetic data and wrote a portion of the text and was involved in the discussions on the correlation of the Ghanzi-Chobe Belt with Mesoproterozoic lithologies in the Rehoboth Subprovince, Namibia (Appendix 2).

- Rankin, W., Webb, S.J., Kiyan, D., Kinnaird, J.A., Jones, A.G., and Evans, R.L. 2013. Geophysical modelling of the Damara (Namibia) and Lufilian/Katangan (Zambia) Belts. *13th SAGA Biennial Technical Meeting and Exhibition*, short paper, 4 pp.

In this peer-reviewed paper, the candidate processed the aeromagnetic and magnetotelluric data and wrote the text (Appendix 3).

Acknowledgements

First and foremost, I would like to express gratitude to Prof. Judith Kinnaird for supervising this research project and setting up an interesting and challenging research project with Rio Tinto Exploration. A special thanks to Prof. Guy Charlesworth for his guidance, supervision and willingness to review work and answer questions. Thank you to Dr. Susan Webb for your guidance and supervision. Special thanks to Manish Kumar and John Hart from Rio Tinto for their guidance in processing and interpretation of the potential field data sets.

Acknowledgments are owed to Rio Tinto Exploration, Post Graduate Merit Award for providing funding for 2012 and 2013. Thanks to the Geological Society of South Africa for partially financing the trip to Dublin Institute of Advanced Studies (DIAS), Dublin, Ireland.

Thanks to Rio Tinto Exploration for providing the initial geophysical and geological data sets and the Geological Surveys of Namibia and Botswana for providing the high-resolution (50 m) aeromagnetic data sets.

Thank you to Oasis Montaj, Geosoft, for the extension of various GX licences including GM-SYS and grid knitting.

I am grateful to Tsodilo Resources Ltd. and Hana Mining for allowing me access to drillcore in Botswana.

A special thank you must be said to Dr. Jérémie Lehmann for his support and guidance throughout the duration of the study.

I owe gratitude to my colleagues at DIAS and South Africa:-

DIAS: Dugyu Kiyan, Prof. Alan Jones, Dr. Mark Muller, and Robert Delhaye whom allowed me access to the SAMTEX data and who advised me in the processing and interpretation of the magnetotelluric data sets.

South Africa: to the postdoctoral fellows part of the project, Dr. Kalin Naydenov and Dr. Lorenzo Milani for all your insight and advice. To Dr. Asinne Tshibubudze, and Dr. Zubair Jinnah for all your insight and advice.

Obone Sepato, Cameron Penn-Clarke, Russell Johnson, Luke Peters, Sally Ann-Lee, Ryan McIntosh, Dr. Luisa Ashworth, Stephanie Schieber-Enslin, and Dr. Natalie Deseta for all the support and advice over the course of this project.

I would like to thank my family for their love, support, and encouragement; mom and dad, thank you for believing in me and for thinking that what I do is interesting even though it does not make a lot of sense to you.

Lastly, and most importantly, Megan Hunter, for her unending understanding and empathy through the tough times.

Table of contents

List of figures

List of tables

Chapter 1

Introduction

1.1. Background

This study is part of a larger research project set-up between Rio Tinto Exploration and researchers in EGRI (Economic Geology Research Institute) at the University of the Witwatersrand under the direction of EGRI's director Professor Judith Kinnaird. This was a multidisciplinary project which involved the incorporation of structural geology, petrology and geophysical data. The project investigated the proposed link between the mineralisation of the Pan-African Damara Orogen through Namibia, Botswana and into Zambia. This study reports the findings of the geophysical aspect of the project with a focus on the continuation of the Damara Belt into northwest Botswana.

1.2. Pan-African Orogeny

According to Roger and Santosh (2003), there have been three supercontinents in Earth's history; Columbia (~1 800 to 1 500 Ma), Rodinia (~1 100 to 800 Ma) and Gondwana (~600 to 500 Ma) (Figure 1.1), the last of which merged with Laurasia to form Pangea at 250 Ma.

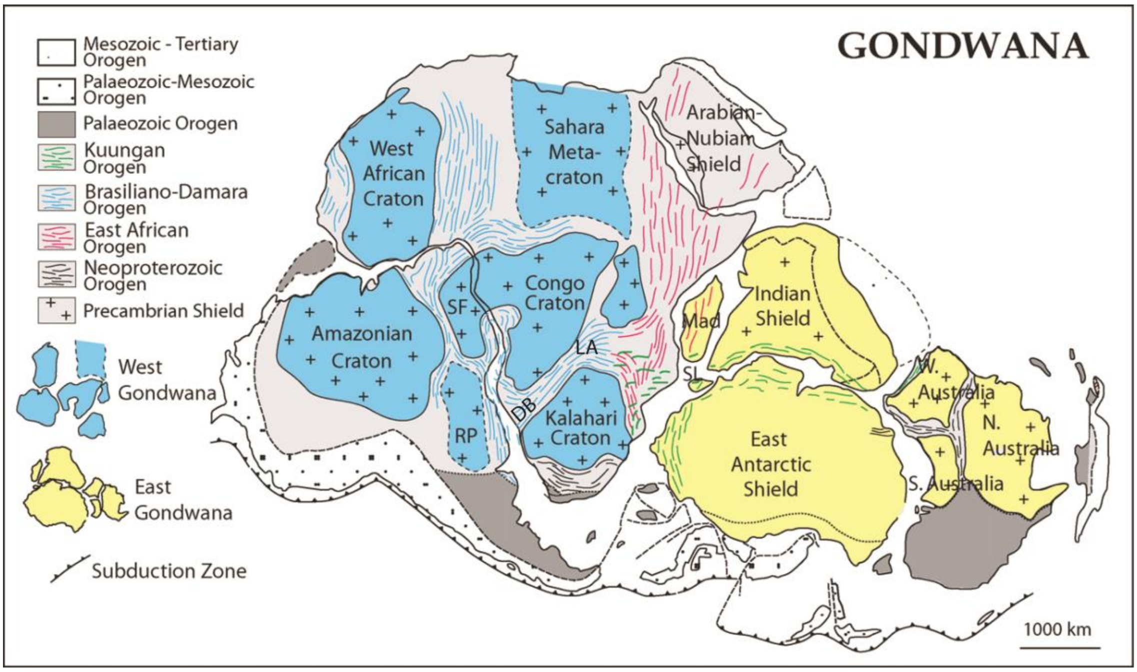

Figure 1.1: The traditionally accepted reconstruction of Gondwana displaying the Neoproterozoic and younger orogenic belts separating the various cratonic blocks (after Gray *et al*., 2008; Malone *et al*., 2008). DB represents the Damara Belt and LA represents the Lufilian Arc.

Of interest to this study, is the rifting of Rodinia that led to the formation of the Adamastor (Hartnady *et al*., 1985) and Khomas Oceans, and the closure of these oceans to form West Gondwana. The Pan-African Damara Orogen of Namibia reflects part of the suture of West Gondwana that formed at a collisional triple junction between the Río de la Plata, Kalahari and Congo Cratons (Hoffman *et al*., 1994; Gray *et al*., 2008).

The Adamastor Ocean formed between the rifting of Africa (Kalahari and Congo Cratons) and South America (Río de la Plata Craton) (Figure 1.2) (Roger *et al*., 1995; Wilson *et al*., 1997). The Khomas Ocean formed as a northeast-southwest trending "branch" of the Adamastor Ocean between the Kalahari and Congo Cratons i.e. Damara Belt (Figure 1.2) (e.g. Miller, 1983a; 2008; Kukla and Stanistreet, 1991; Wilson *et al*., 1997; Gray *et al*., 2008).

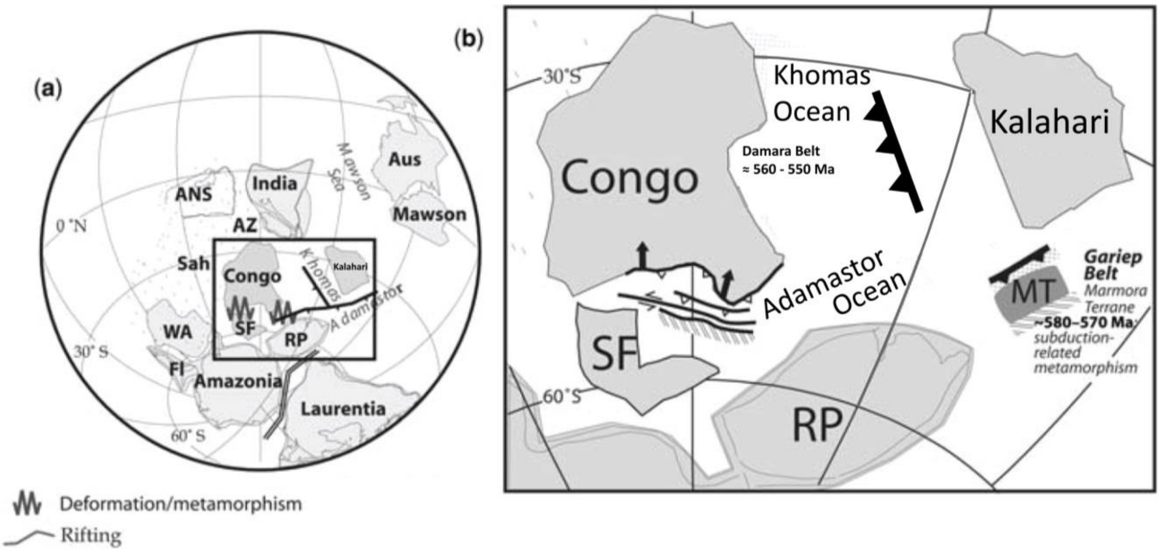

Figure 1.2: Global reconstruction of continents at ~580 Ma to 550 Ma (a) with enlargement (b) of the palaeogeographic locations of the Congo, Kalahari, São Francisco (SF) and Río de la Plata (RP) Cratons. The Marmora Terrane (MT) of the Gariep Belt and the Khomas and Adamastor Oceans before the development of the Pan-African/Brasiliano Orogenic system (after Gray *et al*., 2008). Traces of subduction zones are shown as barbed lines drawn on the upper plate side and designate the subduction zone dip.

The width and timing of closure of the Adamastor and Khomas Oceans are highly disputed (Wilson *et al*., 1997; Gray *et al*., 2008). The Khomas Ocean has been proposed by Stanistreet *et al*. (1991) to have closed before the southern part of the Adamastor Ocean (Figure 1.2). However, using sedimentological evidence Prave (1996) argued the opposite. The closure of the Adamastor Ocean is generally accepted as being diachronous, closing initially in the north and migrating southwards in a "zip closure" action and finally suturing along the Damara Belt (Stanistreet *et al*., 1991; Maloof, 2000; Gray *et al*., 2008). Geochronology and thermochronology studies for the Damara Orogen (Goscombe *et al*., 2005; Gray *et al*., 2006), linked with existing data for the Gariep

Belt (Jasper *et al*., 1995) and for the Damara Belt (Kukla, 1993), supports first closure of the northern part of the Adamastor Ocean followed by the southern part and finally the closure of the Khomas Ocean suturing along the Damara Orogen.

The exact dimensions of the Khomas Ocean are not known (Gray *et al*., 2008). Miller (1983a), Porada (1989) and Frimmel *et al*. (2011) interpret it as a narrow ocean basin, similar to the present day Red Sea, which terminated in the northwest (i.e. never cross-cutting the southern African continent). This is supported by Sr-Nd isotopic data for the Damara Belt that suggests that granitoids were primarily produced by remobilisation of older crust (McDermott *et al*., 1989) rather than containing a significant juvenile component, as would be expected in a long-lived volcanic arc setting related to closure of a major ocean basin (Wilson *et al*., 1997). Hoffman *et al*. (1994) interpreted the rift-drift in the Damara Belt occurred at ~750 Ma, although the rift history may extend as far back as 800 Ma (Jacobs *et al*., 2008). Possible seafloor spreading in the Khomas Ocean (Damara Belt) occurred until ~609 Ma (Nagel, 1999). A reversal in plate motion at ~530 Ma to 500 Ma (Gray *et al*., 2008) initiated the subduction of the Kalahari Plate beneath the Congo Craton (Miller, 2008; Frimmel *et al*., 2011). Deformation subsequently continued until ~480 Ma to 460 Ma (Miller, 1983a).

Barnes and Sawyer (1980) and Kukla (1992) proposed northward subduction of the Kalahari Plate beneath the Congo Craton for the closure of the Khomas Ocean (Figure 1.3). This was later supported by palaeomagnetic data of Meert *et al*. (1994), using comparative kinematic studies of the Southern Zone schists with the Otago Schist Belt of New Zealand, and geochemical studies on the primitive diorite and syenite, which are part of the early magmatic history of the Central Zone (Figure 1.3) (Gray *et al*., 2008). The original position of the Kalahari and Congo Cratons is still not known because of the limited number of high quality palaeomagnetic poles for the Kalahari and Congo Cratons between ~750 Ma and 550 Ma (Gray *et al*., 2008) and the lack of outcropping geology because of the obscuring Kalahari cover.

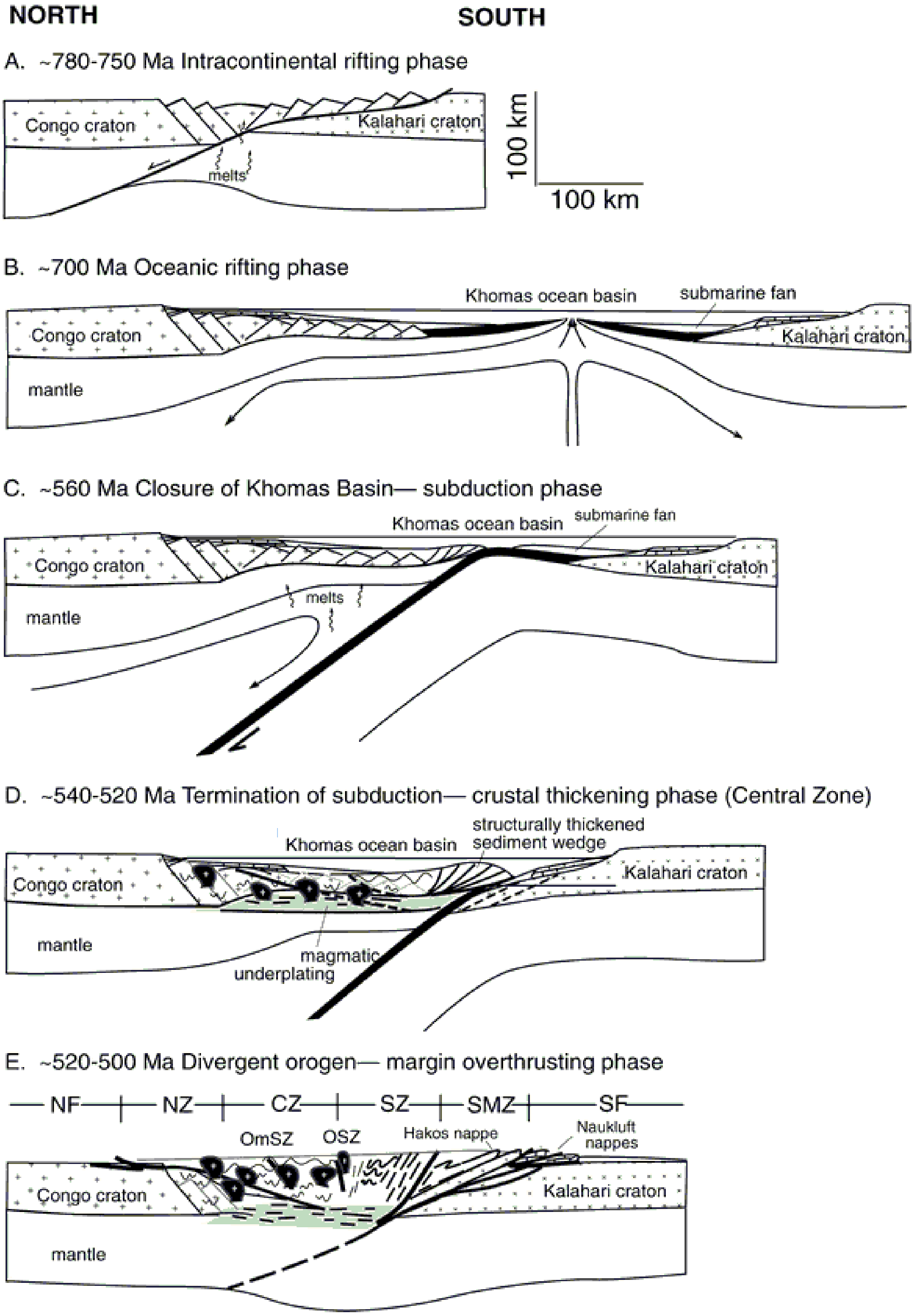

Figure 1.3: The tectonic evolution of the Damara Orogen showing the generally accepted northward subduction of the Khomas Ocean and eventual collision of the Congo and Kalahari Cratons (after Gray *et al.*, 2007). The tectonostratigraphic zones of the Damara Belt are labelled as Northern Foreland (NF), Northern Zone (NZ), Central Zone (CZ), Southern Zone (SZ), Southern Margin Zone (SMZ) and Southern Foreland (SF) and OmSZ is the Omaruru shear zone and OSZ is the Okahandja shear zone.

1.3. Geophysical data

As the direct correlation between the Meso- to Neoproterozoic lithologies of Namibia and Botswana are obscured by Kalahari sediments, aeromagnetic data effectively penetrates the non-magnetic sedimentary cover and traces the magnetic foliation of the underlying lithologies (Cordell and Grauch, 1985). Aeromagnetic data detects changes in the Earth's magnetic field resulting from magnetic properties of the rocks. The magnetic susceptibility of rocks is extremely variable depending on the lithology and mineral composition. Common causes of magnetic anomalies result from structural disturbances such as faults and dykes or from alteration and mineralisation. The aeromagnetic data is used to determine the possible southern and northern extents of the Congo and Kalahari Cratons, respectively, and the details of the intervening Damara Belt. Mobile belts are characterised by a noisier, higher amplitude aeromagnetic signal that has a magnetic fabric compared to the smoother, mid-amplitude signal of the cratonic areas which commonly lack a strong fabric (Eberle *et al*., 1996, 2002). This criteria is used to determine the correlation of the Damara Supergroup strata with strata in northwest Botswana.

The initial potential field data and the majority of the geological maps were supplied by Rio Tinto Exploration. The Namibian Geological Survey supplied the 50 m resolution aeromagnetic grids for Namibia (Chapter 3). The magnetotelluric (MT) data used was collected by the South African MagnetoTelluric EXperiment (SAMTEX) between 2006 and 2009 and the borehole data used in this study was supplied by Tsodilo Resources Ltd., a mining operation situated in Ngamiland (northwest Botswana).

Although aeromagnetic data is used to efficiently map lithological and structural features, interpretation is affected by anomaly superposition and source ambiguity. To limit ambiguity, the correlation between aeromagnetic and gravity anomalies was investigated. Variations in the physical properties and lithologies are commonly caused by 1) variations in bulk mineralogy, which controls specific density and therefore, gravity anomalies, and 2) minor mineral content, especially magnetite, which is the main cause of aeromagnetic anomalies (Lucius and von Frese, 1988). Direct or inverse correlation of the gravity and aeromagnetic anomalies, or lack thereof, can yield significant constraints on the interpretation of the potential field data. For example magnetite will have a high amplitude magnetic signal and a high Bouguer gravity signal compared to hematite which will have a low to moderate magnetic amplitude but an equally high Bouguer gravity signal.

To constrain the spatial extent of the mobile belts and cratonic margins, MT data was processed and interpreted for crustal features in the vicinity of the Namibia – Botswana border. Van Zijl and de Beer (1983) indicated that cratonic blocks are associated with high resistivity values of greater than 30 000 Ωm compared to the more conductive mobile belts of 1 000 Ωm to 10 000 Ωm. MT is an electrical technique that measures resistivity changes in the crust and mantle. The MT work presented in this study investigates the resistivity change beneath the DMD, NEN, and OKA-CAM, one-dimensional (1D) profiles (Figure 1.4). De Beer *et al*. (1975) mapped a regional zone of enhanced conductivity that was traced from Namibia, through Botswana to the Zambian border. Since then, there have been other geoelectrical studies across this conductive zone in an attempt to constrain the continuity, depth and cause of conductivity (e.g. de Beer *et al*., 1982; van Zijl and de Beer, 1983; Ritter *et al*., 2003; Khoza *et al*., 2013).

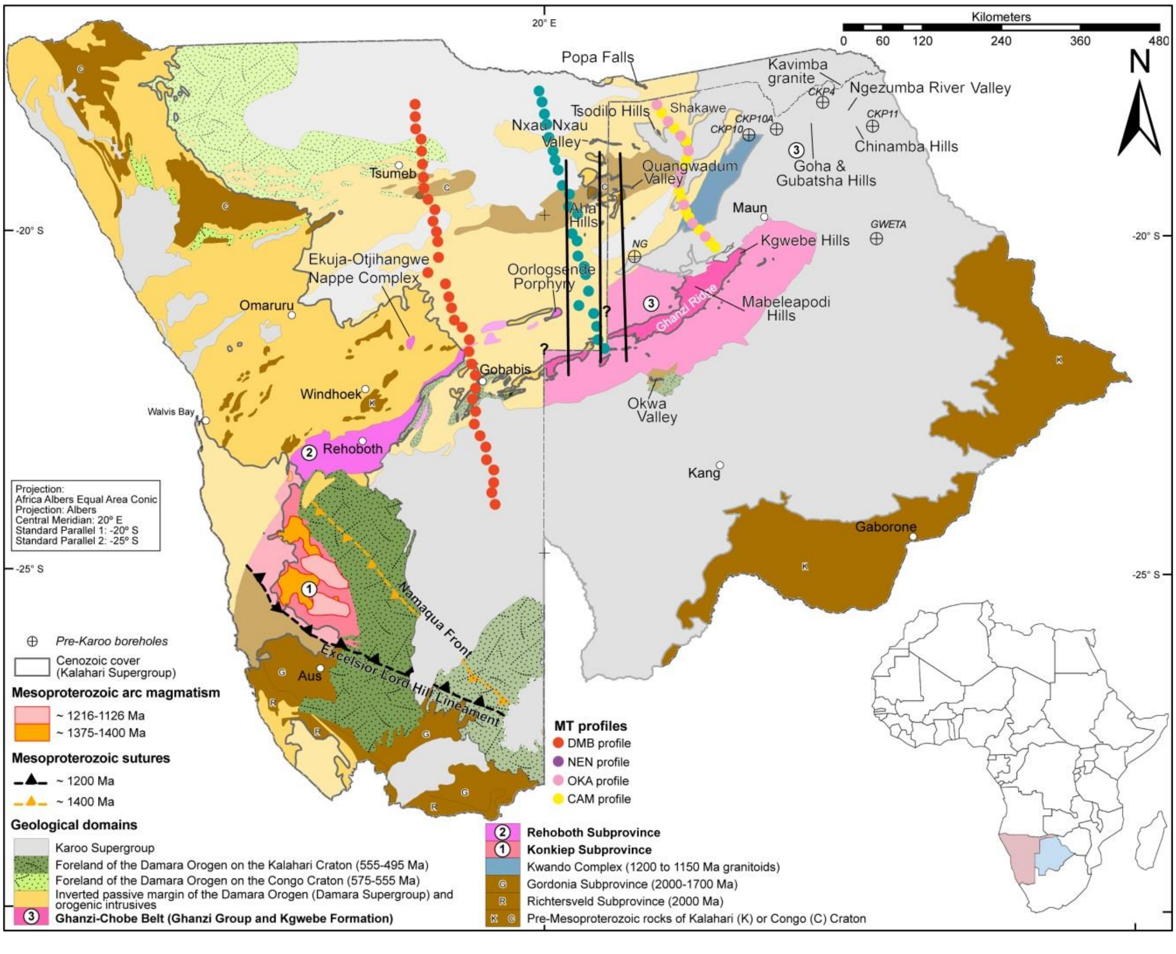

Figure 1.4: Simplified geological map of the main geological domains of Namibia and Botswana. The Cenozoic cover is shown as a slightly opaque layer over pre-Cenozoic domains (modified after Lehmann *et al*., submitted). Locations of boreholes that intersect pre-Karoo lithologies are shown as circles with crosses and location of MT profiles are shown as solid circles. Note the lack of correlation between the Mesoproterozoic Ghanzi-Chobe Belt and the Neoproterozoic Damaran sediments (1 000 Ma to 542 Ma). The insert represents the African continent with the location of Namibia (pink) and Botswana (blue).

Three approximately north-south, 340 km long 2D magnetic profiles were modelled in the vicinity of the Namibia – Botswana border (Figure 1.4) to verify the proposed northward dipping palaeo-subduction zone (e.g. Barnes and Sawyer, 1980; Kukla, 1992; Frimmel *et al*., 2011) and folding pattern of the Ghanzi-Chobe Belt.

1.4. Problem statement

Previous geological studies on the extension of the Damara Belt into northwest Botswana have been largely restricted to stratigraphic correlations based on similar lithological sequences or geochronological signatures which support correlations in a time-span of ~350 Myr to 400 Myr (Porada, 1989; Maiden and Borg, 2011). There are limited, cross-border geophysical correlations between Namibia and Botswana. This is surprising given that the majority of western Namibia and ~80% of Botswana are covered by Kalahari sediments (locally up to 300 m thick) (Haddon and McCarthy, 2005).

In Botswana, direct observation of the geology is limited to isolated pre-Karoo inliers and boreholes because of extensive Kalahari and Karoo cover. Interpretation of aeromagnetic data and these limited inliers have allowed for the geology to be extrapolated beneath the Kalahari cover which resulted in the publication of the 1:1 000 000 pre-Kalahari geological map of Botswana (Key and Ayres, 2000). This was subsequently integrated in the 1:2 500 000 sub-Kalahari geological map of southern Africa (Haddon, 2001). However, a sub-Kalahari map for Namibia has not been published and the correlation with Botswana relies on the 1:2 500 000 sub-Kalahari geological map of Haddon (2001). This map indicates that Meso- to Neoproterozoic metavolcanic and metasedimentary successions of the Ghanzi-Chobe Belt are correlated with the Neoproterozoic Southern Foreland of the Damara Orogen (Figure 1.4).

This study utilizes both geological (mapping and borehole correlations, and existing chemostratigraphy, and zircon ages) and geophysical (aeromagnetic, gravity, physical properties and MT) data sets to propose new cross-border correlations between the Meso- to Neoproterozoic rocks of Namibia and Botswana. The spatial continuity of covered lithostratigraphic domains across the border was inferred using processed 50 m aeromagnetic maps and 2.2 km Bouguer gravity maps. The crustal structure of the enhanced conductive zone of de Beer *et al*. (1975) and the transition from the cratonic blocks to mobile belts are investigated by the interpretation of 1D MT models.

1.5. Project aims

The aim of this research is to use a combination of potential field, MT and geological data sets to create a new sub-Kalahari geological map of the Damara Belt and equivalent metasedimentary sequences in northwest Botswana. This will lead to an improved resolution of the tectonostratigraphic zones of the Damara Belt of Miller (2008) and Corner (2008) and northwest Botswana of Carney *et al*. (1994). On completion of the sub-Kalahari map, 2D magnetic forward modelling will be carried out to locate and verify the proposed northward dipping palaeo-subduction zone between the Kalahari and Congo Cratons, which has not been confidently defined because of the lack of oceanic crust and high-grade metamorphic lithologies (e.g. eclogite) in central Namibia and northwest Botswana. Additionally, the regional conductor interpreted by de Beer *et al*. (1976; 1982), van Zijl and de Beer (1983), and recently Khoza *et al*. (2013), cross-cuts the tectonostratigraphic zone. This study investigates this regional conductor by crustal interpretation of MT data and better resolves the conductor so that it does not cross-cut geological boundaries.

Chapter 2

Regional geological and geophysical studies and previous cross-border correlations between Namibia and Botswana

2.1. The Rehoboth Subprovince

The Rehoboth Subprovince (Figure 2.1) forms a major component of the northwestern margin of the Kalahari Craton. It grew during prolonged crustal accretion during the Palaeoproterozoic (Hartnady *et al*., 1985; van Schijndel *et al*., 2013). This nucleus was extended by Mesoproterozoic crust and became a larger unit of the Kalahari Craton (Jacobs *et al*., 2008). The lithologies of the Rehoboth Subprovince are divided into the Rehoboth Group and Sinclair Supergroup and associated intrusive rocks (Becker and Schalk, 2008; van Schijndel *et al*., 2011).

The oldest Mesoproterozoic lithologies in the Rehoboth Subprovince are the metasedimentary sequences of the Billstein Formation (van Schijndel *et al*., 2011). The Billstein Formation has a maximum depositional age, represented by the youngest detrital zircon, of 1 770 Ma (van Schijndel *et al*., 2011). The minimum age is determined by the cross-cutting dykes dated at 1 210 ± 8 Ma (Ziegler and Stoessel, 1993). The Billstein Formation lacks the typical Palaeoproterozoic fabric and lies unconformably on the Rehoboth Group (Becker and Schalk, 2008).

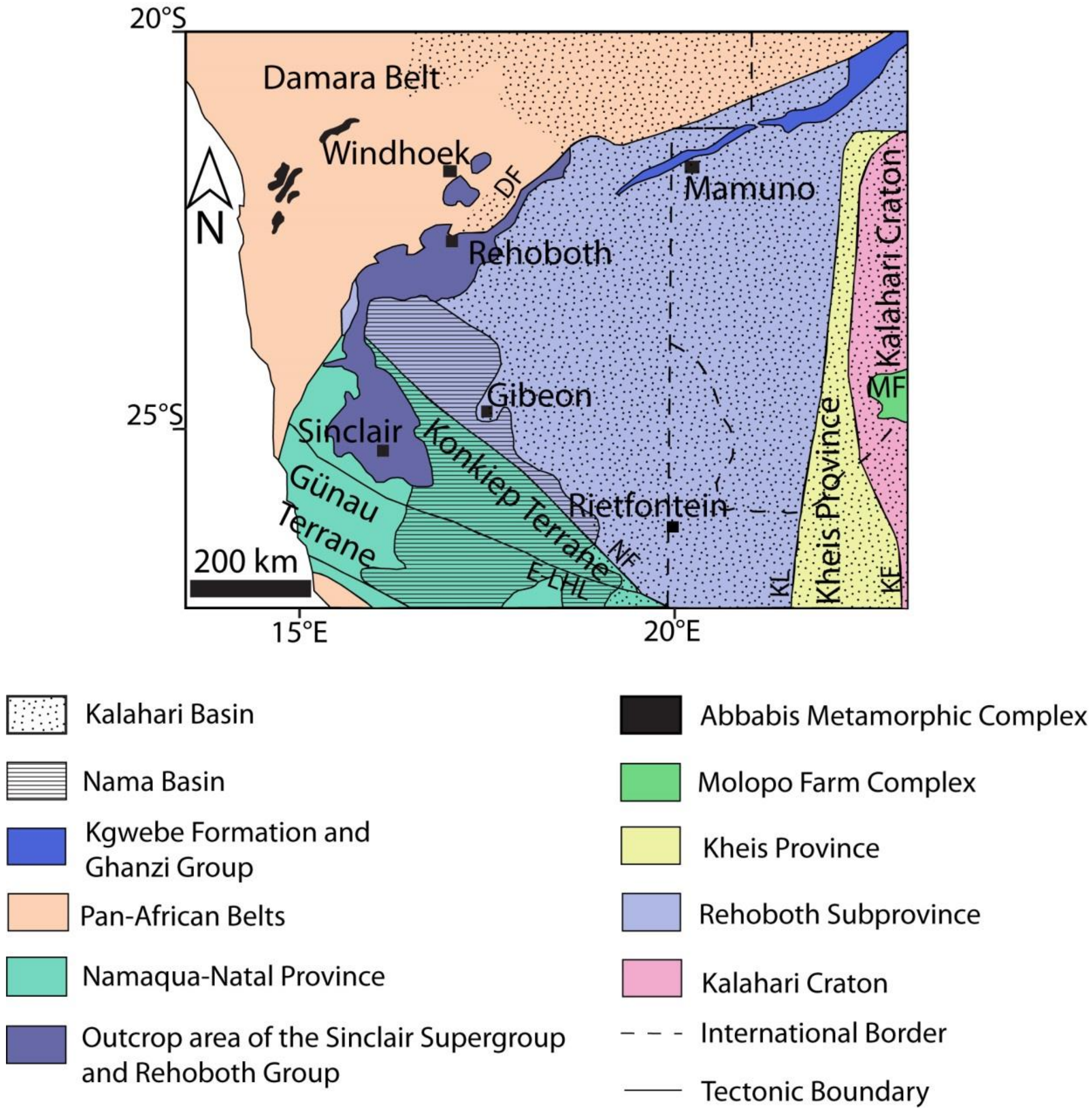

Figure 2.1: Tectonic framework of Namibia and the distribution of the Palaeoproterozoic Rehoboth Group, Mesoproterozoic Sinclair Supergroup and younger sedimentary cover (modified after van Schijndel *et al*., 2013, Becker *et al*., 2006). The Kalahari Basin outline is after Haddon and McCarthy (2005). The Nama Basin is after van Schijndel *et al*. (2013). DF is the Damara Front; E-LHL is the Excelsior-Lord Hill Lineament; KF is the Kheis Front; KL is the Kalahari Line; MF is the Molopo Farms Complex and NF is the Nama Front.

2.1.1. Sinclair Supergroup

Unconformably overlying the Billstein Formation are the volcanic and sedimentary arc sequences of the Sinclair Supergroup bracketed between ~1 400 Ma to 1 000 Ma (Becker and Schalk, 2008). It is divided into the Nauzerus and Tsumis Groups (Figure 2.2) (van Schijndel *et al*., 2011). During the Pan-African Orogeny, the Sinclair Supergroup was deformed and metamorphosed to greenschist facies (Borg and Maiden, 1987; Becker *et al*., 2006). In the Rehoboth Subprovince, Damaran lithologies are thrust over the rocks of the Sinclair Supergroup (Hoffmann, 1989) or tectonically interleaved as observed at the Oamites Cu-Ag mine (Schneider and Seeger, 1992).

Nauzerus Group, Sinclair Supergroup

The Nauzerus Group is characterised by four cycles of volcano-sedimentary deposition between 1 230 Ma to 1 100 Ma with volcanism and sedimentation being associated with graben development (Becker and Schalk, 2008). The first cycle of felsic volcanism is marked by the interfingering of the Nückopf and Grauwater Formations at ~1 230 Ma (Figure 2.2). The Nückopf Formation is a siliciclastic, clast-support polymictic conglomerate that overlies Palaeoproterozoic basement and grades to quartzite interbedded with metapelite (Becker and Schalk, 2008). Intraformational distal felsic rocks and mafic volcanic rocks confirm bimodal volcanic activity immediately after emplacement. The felsic rocks are peralkaline, suggesting an I-type origin with volcanic arc or within-plate affinities according to the Rb-Nb-Y tectonic discrimination method (Becker and Schalk, 2008). The emplacement age of this formation is constrained by U-Pb zircon crystallisation ages from intraformational rhyolites of 1 226 ± 10 Ma (Schneider *et al*., 2004), 1 232 ± 35 Ma (Burger and Coertze, 1978) and a SHRIMP zircon crystallisation age of 1 226 ± 11 Ma (Becker and Schalk, 2008). The stratigraphically younger Grauwater Formation consists of siliciclastic sedimentary rocks with minor basal volcanic rocks. The basal agglomerate-conglomerate either interfingers with and overlies felsic volcanic rocks of the Nückopf Formation or transgresses the Palaeoproterozoic basement (Figure 2.2) (Becker *et al*., 2005).

The Nückopf and Grauwater supercrustal rocks were intruded by coeval plutons of the Gamsberg Granitic Suite (Figure 2.2) (Becker and Schalk, 2008). The Gamsberg Granitic Suite consists of monzogranite to granodiorite. The granodiorites lack Palaeoproterozoic tectonic foliation and locally cut the monzogranites (Becker and Schalk, 2008). The gneisses of the Gamsberg Granitic Suite are suggested to have formed in a volcanic arc setting that was enriched by subduction-generated mantle (Becker and Schalk, 2008). The multiple granite suites within the complex provide a wide U-Pb zircon age from 1 207 ± 15 Ma, for a coarse-grained orthogneiss (Pfurr *et al*., 1991) to 926 ± 21 Ma for an aplite (Becker and Schalk, 2008). Other published U-Pb zircon ages are 1 178 ± 20 Ma, 1 064 ± 20 Ma (Burger and Coertze, 1975), 1 110 ± 30 Ma, 1076 ± 25 Ma (Burger and Coertze, 1978), 1 102 ± 7 Ma (Pfurr *et al*., 1991), and 1 079 $^{+63}/_{-41}$ Ma, 1095 $^{+121}/_{-21}$ Ma (Nagel, 1999).

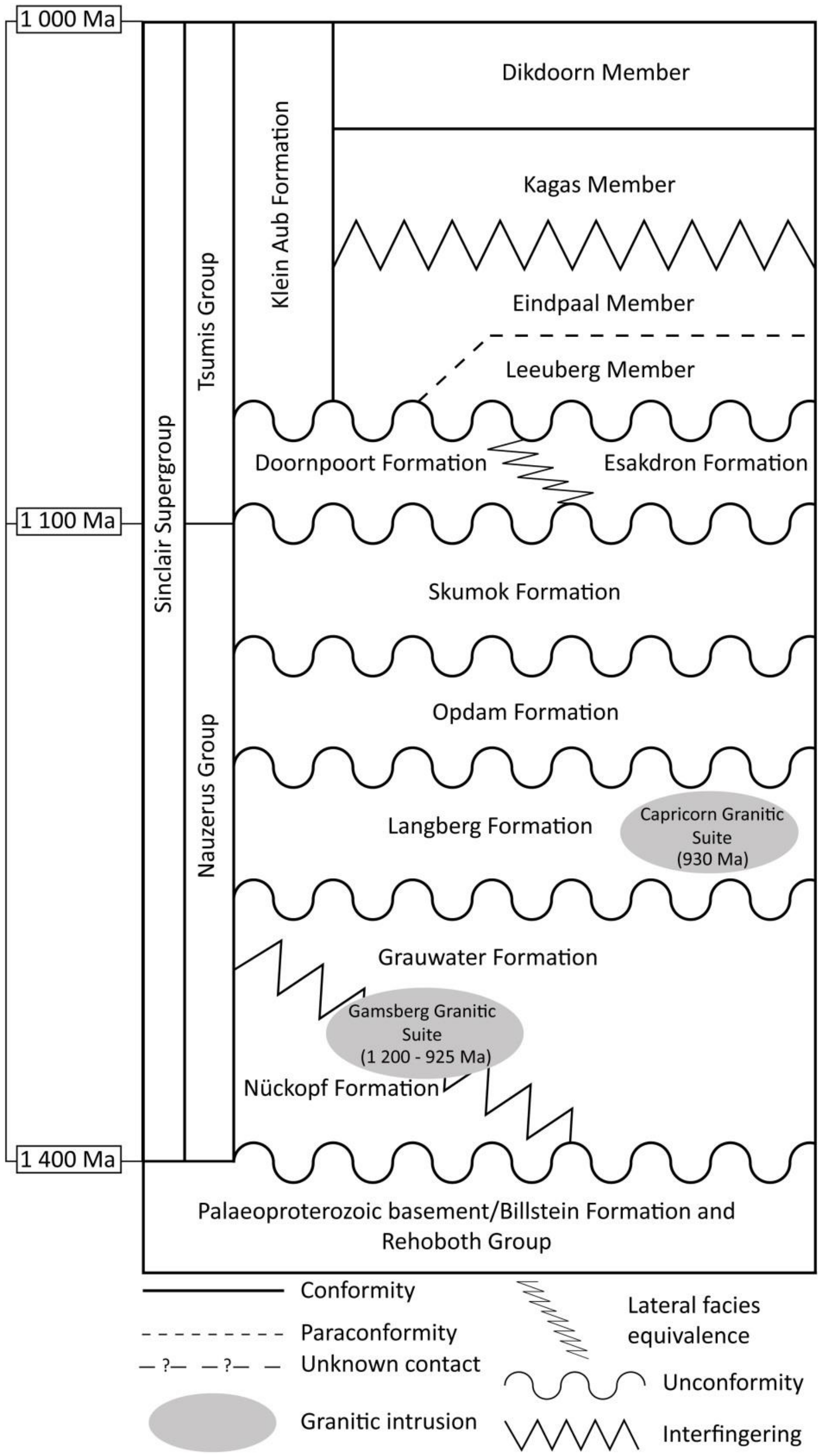

Figure 2.2: Simplified stratigraphic column of the Rehoboth Subprovince with approximate age dates (modified after, Becker *et al*., 2005; Becker and Schalk, 2008; van Schijndel *et al*., 2011). Detailed descriptions of the lithologies and age dates are in the text.

The overlying Langberg Formation is metamorphosed to lower greenschist facies and is strongly deformed (van Schijndel *et al*., 2011) consisting of a poorly sorted matrix supported basal conglomerate (van Schijndel *et al*., 2011) lying in contact with the Billstein Formation (Becker and

Schalk, 2008). The conglomerate hosts quartzite pebbles of the Billstein Formation indicating that the Billstein Formation was already lithified during the deposition of the Langberg Formation (Becker *et al*., 2005). Higher up in the formation, a succession of felsic volcanic rocks interbedded with pebbly, immature arenites occurs, indicating contemporaneous volcanism and sedimentation with quartzite and schist occurring at the top of the formation (Becker *et al*., 2005). The composition of the felsic volcanics, according to tectonic discrimination diagrams, are rhyolitic to rarely dacitic and fall in the fields of volcanic arc, within-plate and post-collisional affinities (Becker and Schalk, 2008). SHRIMP U-Pb zircon obtained from rhyolites yielded an age of 1 100 ± 5 Ma (Becker and Schalk, 2008), confirming an earlier U-Pb multigrain zircon age of 1 083 ± 30 Ma obtained from the same lithology by Burger and Coertze (1978). A SHRIMP U-Pb zircon age obtained from a rhyolitic flow yielded 1 090 ± 15 Ma (Becker *et al*., 2005). Detrital zircon analysis reveals a minor grouping of six zircon grains with an age range of 2 030 Ma to 1 750 Ma that reflects the major peaks seen in the detrital zircons from the quartzite of the Billstein Formation. All the other zircon grains plot on a broad 1 325 Ma to 1 080 Ma composite peak which corresponds in age with the Namaqua-Natal Orogenic cycle (van Schijndel *et al*., 2011). The four youngest detrital grains in this sample have an average ^{207}Pb-^{206}Pb age of 1 103 ± 24 Ma (van Schijndel *et al*., 2011).

The Langberg Formation was intruded by plutons of the Capricorn Granitic Suite (Figure 2.2) (Becker and Schalk, 2008). The Capricorn Granite Suite forms small circular to dyke-like bodies consisting of granite and probably late-stage Mesoproterozoic intrusions (Becker and Schalk, 2008). Analysis of two U-Pb multigrain zircons yielded ages of 932 ± 50 Ma and 930 ± 70 Ma (Hugo and Schalk, 1974; Burger and Coertze, 1975), which was interpreted to provide a minimum emplacement age. However, the transitional contact with the Langberg Formation suggests a cogenetic relationship between these two units, implying an age between 1 100 Ma to 1 090 Ma (Becker and Schalk, 2008), which coincides with another U-Pb multigrain zircon age of 1 104 ± 20 Ma (Burger and Coertze, 1975).

Overlying the Langberg Formation, with either an unconformable or tectonic contact, (Figure 2.2) or unconformably transgressing the Billstein Formation, is the more mafic-rich Opdam Formation (Becker and Schalk, 2008). The basal clastic sequence comprises quartzite, conglomerate, and slate, overlain by a basaltic package that is interbedded with quartzite (locally magnetite-bearing), conglomerate and phyllite. Locally, low-grade copper mineralisation occurs in the phyllites. Stratigraphically higher in the formation, there is a conglomerate layer with a paraconformable sedimentary contact over the metabasalts (Becker and Schalk, 2008). The conglomerate contains no basaltic clasts and grades into quartzite and is overlain by slate, conglomerate and subordinate basaltic lava (Becker and Schalk, 2008). The top of the formation comprises finely banded quartzite, slate, calcareous phyllite including lenses of conglomerate, limestone and subordinate metabasite lava and feldspar-porphyry. The Opdam Formation basalts have a tholeiitic composition influenced by subduction-related mantle enrichment in their sources (Becker and Schalk, 2008 and references therein).

The Skumok Formation marks the top of the Nauzerus Group. It is dominated by continental red-bed sediments and quartzite interbedded with felsic volcanic rocks in the upper part (Becker and Schalk, 2008). The breccia at the base of this formation unconformably overlies the Opdam and Langberg Formations. The Skumok Formation attests to a limited resurgence of felsic volcanism at the end of Nauzerus times (Becker and Schalk, 2008).

Tsumis Group, Sinclair Supergroup

The Tsumis Group comprises the Doornpoort, Eskadron, and Klein Aub Formations (Figure 2.2). All postdate the regional-scale Mesoproterozoic igneous activity in the Rehoboth Subprovince and were deposited during a period of regional uplift (Becker and Schalk, 2008). The basal portion of the Doornpoort Formation contains conglomerates which are in lateral variation with sedimentary breccia horizons and local basalts (Borg, 1988). The clasts vary from quartz-feldspar porphyry and granite to amphibolite. The rest of the formation is a succession of clastic rocks consisting of quartzite intercalated with slate (Becker and Schalk, 2008). To the north, rocks resembling the Doornpoort Formation are present however there is an abundance of cupriferous shale and limestone at the base of the succession, which has led to them being termed the Eskadron Formation (Miller, 2008).

The Doornpoort Formation is overlain by a basal clast-supported conglomerate of the Leeuberg Member (Klein Aub Formation) (Figure 2.2). Clasts consist of granite porphyry and quartzite derived from the underlying Doornpoort Formation in an arkosic matrix (Becker and Schalk, 2008). The succession grades to quartzite and interbedded slate. A conglomerate unit of the Eindpaal Member, similar to the basal conglomerate of the Leeuberg Member, paraconformably overlies the quartzitic unit of the Leeuberg Member in the east and transgresses upon the Doornpoort Formation in the west (Becker and Schalk, 2008). The overlying Kagas Member consists of a uniform quartzite and shale package (Maiden and Borg, 2011). Slightly calcareous quartzites are present at the base and grade to silty argillites containing beds of fine-grained sandstone, limestone and marl. At Klein Aub, these argillaceous sandstones are interbedded with siltstone and mudstone and host Cu-Ag deposits (Borg and Maiden, 1986). The top of the Klein Aub Formation is the Dikdoorn Member (Figure 2.2) consisting of slightly carbonaceous quartzite with local conglomeratic interbeds (Becker and Schalk, 2008).

2.2. Introduction to the Damara Orogen

The Damara Belt is part of a network of orogenic Neoproterozoic mobile belts (1 000 Ma to 542 Ma) that cross-cut the present day African continent (Kennedy, 1964; Miller, 2008). The mobile belts represent suture zones between continental fragments, which amalgamated during the Pan-African Orogeny to form Gondwana (Kennedy, 1964; Martin and Porada, 1977; Unrug, 1996; Frimmel *et al*., 2011). The Damara Orogeny developed as a result of successive phases of spreading, rifting, subduction and continental collision between the Kalahari, Congo and Río de la Plata Cratons, which occurred between ~850 Ma to 460 Ma (Stanistreet *et al*., 1991; Prave, 1996; Goscombe *et al*., 2003; Gray *et al*., 2008; Miller, 2008; Frimmel *et al*., 2011).

The Damara Orogen consists of three belts. The approximately north-northwest trending Kaoko Belt situated along the western coastline of Namibia into Angola and the Democratic Republic of the Congo, where it is known as the West Congo Belt (Figure 2.3) (Alkmim *et al*., 2006; Frimmel *et al*., 2011). It is correlated with the Gariep Belt located in the Northern Cape Province of South Africa, and the Riberia and Dom Feliciano Belts of South America (Alkmim *et al*., 2006; Gray *et al*., 2008; Frimmel *et al*., 2011). These coastal belts and correlatives in South America represent the suture between the African Cratons (Congo and Kalahari Cratons) and the Río de la Plata Craton (Figure 2.3) during the closure of the Adamastor Ocean (Porada, 1979; Porada *et al*., 1983; Prave, 1996; Gray *et al*., 2006, 2008). The northeast trending Damara Belt formed from the northward subduction of the Khomas Ocean and subsequently the Kalahari Plate beneath the Congo Craton resulting in continent-continent collision (Barnes and Sawyer, 1980; Becker *et al*., 2006). The collision of the Kalahari and Congo Cratons formed a doubly-vergent orogen with thrusting and nappe transportation in a southerly direction onto the Kalahari Craton and north directed thrusting and folding on the Congo Craton (Gray *et al*., 2008).

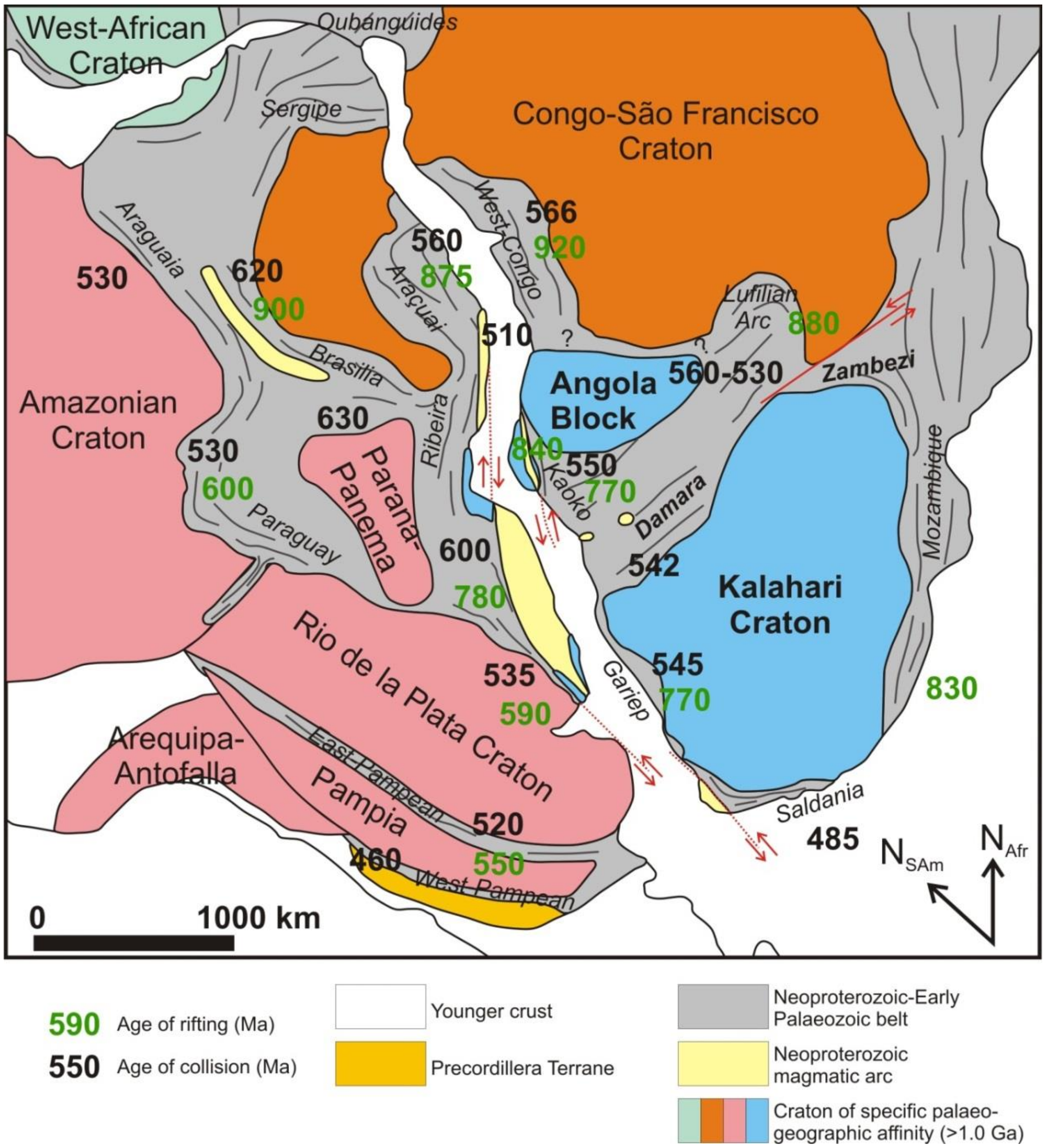

Figure 2.3: Location of Neoproterozoic fold belts and magmatic arcs between various cratonic blocks of southwest Gondwana (after Frimmel *et al*., 2011). The ages of rifting (green) and continental collision (black) are shown.

The Damara Orogen is divided into a number of sub-parallel tectonostratigraphic zones according to the various metamorphic, magmatic, structural environments, stratigraphic successions and geophysical signatures (Miller, 2008; Corner, 2008). The boundaries of these zones are delineated by regional lineaments, which produce significant aeromagnetic anomalies (Frimmel *et al*., 2011). These tectonostratigraphic zones, from south to north are the Southern Foreland, Southern Margin Zone, Southern Zone, Okahandja Lineament Zone, Deep-Level Southern Zone, Central Zone, which is subdivided into the southern and northern Central Zones, Northern Zone, Northern Margin Zone and Northern Platform (Figure 2.4) (Miller, 2008; Corner, 2008).

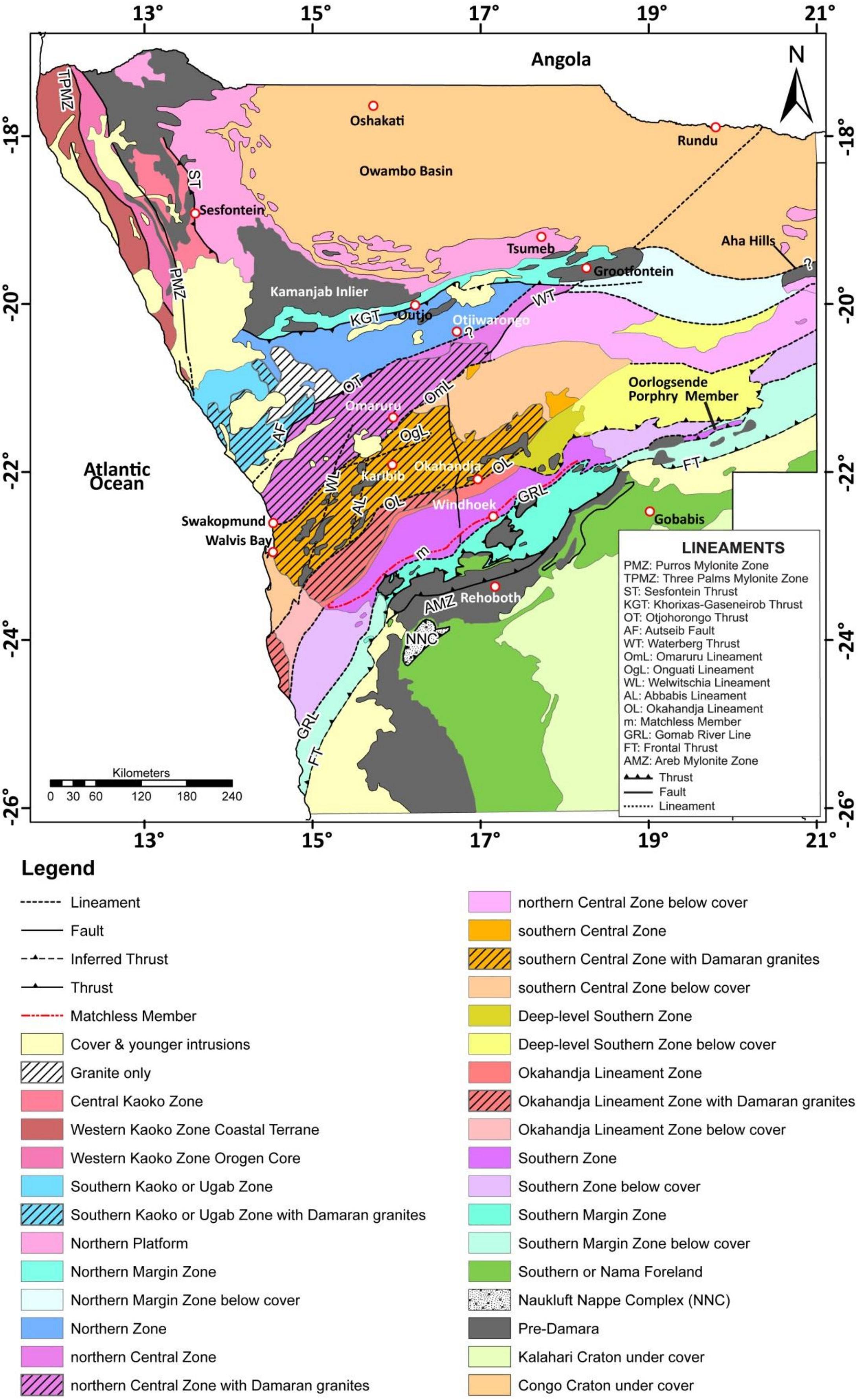

Figure 2.4: Tectonostratigraphic zones of the Damara Orogen (after Miller, 2008; Corner, 2008).

2.2.1. Depositional history of the Damara Belt

The Damara Belt consists of metasedimentary lithologies of the Damara Supergroup, which were deposited unconformably on pre-Damaran basement (Miller, 2008). The lithologies of the Damara Belt are composed of several major stratigraphic units representing continental rifting, passive margin, deep water and shelf environments (Gray *et al*., 2008).

The basal stratigraphic unit is the Nosib Group (Figure 2.5) composed of quartzite, arenite, and conglomerate (Goscombe *et al*., 2004; Gray *et al*., 2008). Sedimentation was initiated by two parallel, northeast-trending former rift grabens (Frimmel *et al*., 2011). The beginning of rift sedimentation is not constrained (Frimmel *et al*., 2011) but rift-related magmatism estimates that the northern graben (failed rift) has an upper limiting age of ~750 Ma (Hoffman *et al*., 1998; Prave, 1996; Goscombe and Gray, 2008), while the southern rift (evolved into the Khomas Ocean) is as young as ~650 Ma (Goscombe and Gray, 2008).

The deposition of the Nosib Group was followed by the Otavi (turbiditic carbonate), Swakop (lower carbonate and upper siliciclastic), Hakos (siliciclastic) and Witvlei (carbonate and siliciclastic) Groups (Figure 2.5) (Goscombe *et al*., 2004; Gray *et al*., 2008; Frimmel *et al*., 2011; Foster *et al*., 2014). Within these groups are glaciomarine diamictites intercalated with iron formations and quartzites characteristic of the Neoproterozoic Sturtian “Snowball Earth” event dated between ~750 Ma to 710 Ma (Bühn *et al*., 1992; Hoffman *et al*., 1996; Halverson *et al*., 2005, 2010).

Subsequent deposition of post-glacial cap carbonates (e.g. Rasthof, Berg Aukas, and Arandis Formations) (Figure 2.5) and accumulation of more shelf carbonates took place over a period of ~110 Myr until a major sea-level drop marking the second major glaciation (Frimmel *et al*., 2011). The Marinoan glaciation occurred at ~635 Ma (Hoffman *et al*., 2004) and deposited the Ghaub and Noas Formations in the upper parts of the Otavi, Swakop, and Hakos Groups. The deposition of the diamictites was coupled with siliciclastic successions and tholeiitic magmatism. This was followed by large-scale subsidence between the Northern Zone and Southern Zone, and the subsequent accumulation of a thick succession of turbiditic greywackes (Kuiseb Formation) (Figure 2.5) (Goscombe *et al*., 2004; Goscombe and Gray, 2008; Gray *et al*., 2008). In the Northern Zone, these greywackes reach up to 10 km in thickness and mark the end of the spreading phase (Miller *et al*., 2009a; Frimmel *et al*., 2011).

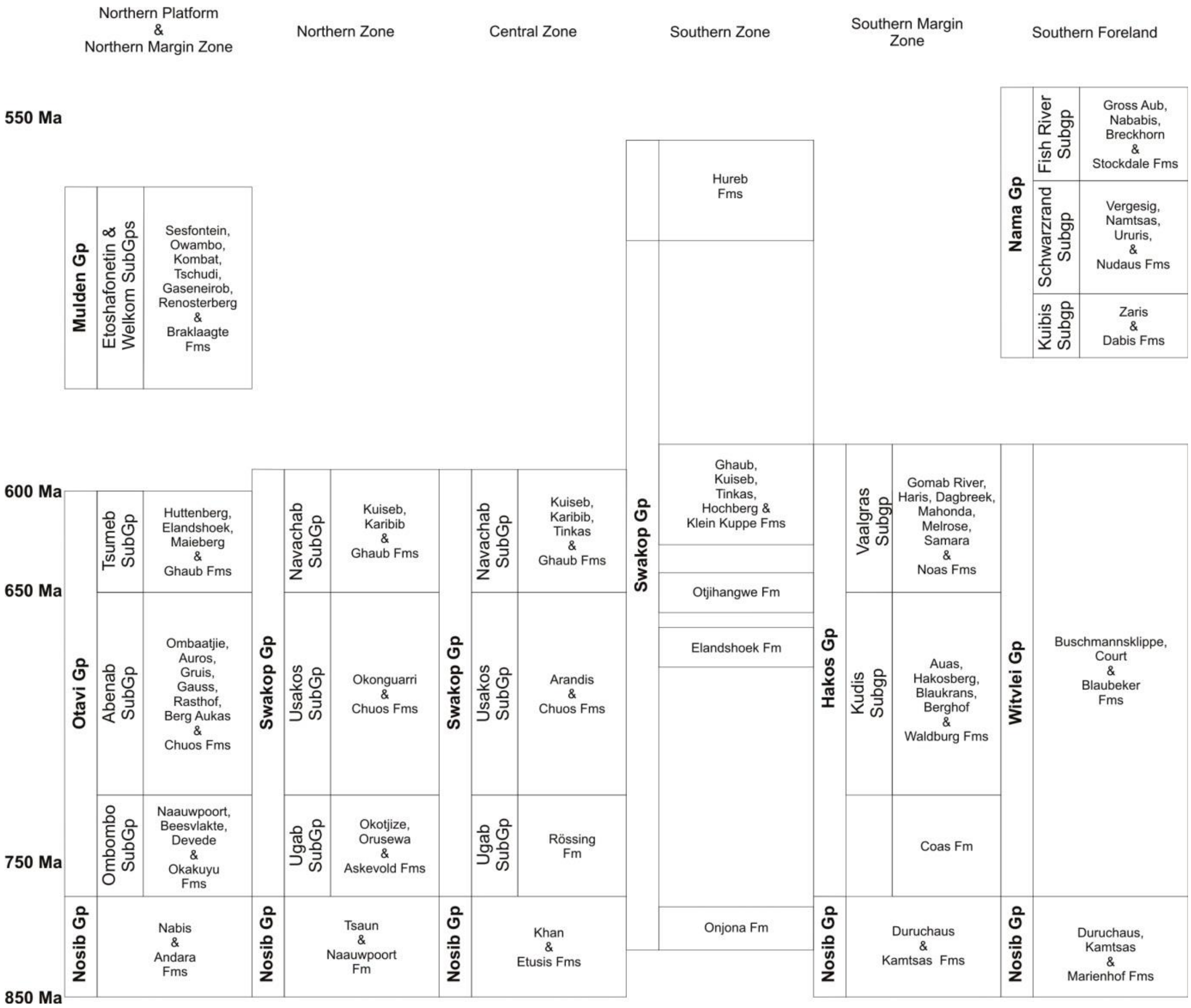

Figure 2.5: Stratigraphy and lithostratigraphic correlations across the Damara Orogen with approximate deposition ages for the Damara Supergroup. Thicknesses are not to scale. Note the post-600 Ma deposition ages of the Mulden and Nama Groups, which corresponds with the initiation of continental collision (modified after SACS, 1980, de Kock, 2001, Miller, 2008 and Longridge, 2012).

There is no evidence of progressive deepening and subsequent continental rupture in the northern graben (Frimmel *et al*., 2011). However, these processes have been noted in the Khomas Ocean in the form of Besshi-type Matchless Member, a 350 km-long narrow belt of metabasic lithologies with MORB or plume-type geochemical affinity and Cu-Fe sulphide deposits and associated metagabbro and serpentinite bodies (Barnes and Sawyer, 1980; Breitkopf and Maiden, 1988; Häussinger *et al*., 1993; Killick, 2000; Frimmel *et al*., 2011). This active mid-ocean ridge occurs at the base of, and was covered by the Kuiseb Formation (Southern Zone) but the presence of pillow lavas and cupreous pyrite deposits in the Matchless Member indicate that submarine volcanism and volcanogenic exhalative processes were active at the time (Barnes and Sawyer, 1980; Breitkopf and Maiden, 1986; Häussinger *et al*., 1993; Frimmel *et al*., 2011).

A reversal of plate motion initiated the subduction of the oceanic crust of the Khomas Ocean beneath the Congo Craton (Barnes and Sawyer, 1980; Kukla, 1992). The exact timing of this event is not known but is bracketed between 580 Ma and 545 Ma, by age dates of mafic (diorite) magnetism of the Goas Suite and related volcanics (Milani *et al*., 2014). With the uplift and erosion of the active continental margin, the arc-trench molasses successions (carbonate, shale, sandstone and greywacke) of the Mulden Group (580 Ma to 541 Ma) (Hoffmann *et al*., 2004; Gray *et al*., 2006, 2007), and the foreland orogenic flysch and molasses successions (carbonate, shale and sandstone) of the Nama Group (Figure 2.5) were deposited in the closing Khomas Ocean (Stanistreet *et al*., 1991; Germs *et al*., 2009).

2.3. Pre-Damaran geology

2.3.1. Abbabis Complex

The Abbabis Complex forms the cores of multiple anticlines surrounded by Damara Supergroup metasedimentary lithologies of the southern Central Zone (Figure 2.1). The Abbabis Complex consists of basal metapelite, gneiss, meta-arkose, subordinate marble, calc-silicate rock and meta-conglomerate of the Tsawisis Formation (Brandt, 1987). The Tsawisis Formation is overlain by the Noab Formation consisting of metapelite, amphibolite, quartzite, marble, calc-silicate and metavolcanic rock (Sawyer, 1981). These supercrustal lithologies are intruded by amphibolites and gneisses of the Narubis Granitoid Complex (Smith, 1965; Brandt, 1987).

The first isotope age for the Abbabis Complex was presented by Jacob *et al*. (1978). They obtained a discordia age of 1 925 $^{+330}/_{-280}$ Ma for highly discordant zircons from biotite-muscovite tonalite and gneissic granite. The gneissic granite yielded a lone age of 1 980 ± 30 Ma. Two zircon analyses from the Abbabis gneisses, near the mouth of the Khan River, yielded ^{207}Pb-^{206}Pb ages of 2 014 ± 39 Ma and 2 093 ± 51 Ma, whilst single zircon grain data fit regression lines which intersect the concordia at 1 038 ± 58 Ma, 1 102 ± 44 Ma and 1 239 ± 88 Ma (Kröner *et al*., 1991). In the Ida Domes area, Tack *et al*. (2002) obtained a U-Pb single zircon age of 2 038 ± 5 Ma for an augen-gneiss sample and inherited cores of zircon grains in the Damaran granites, which yielded ages of 1 820 Ma, 1 870 Ma, 2 090 Ma and 2 700 Ma. In the same area, Longridge (2012) obtained U-Pb zircon ages of 2 056 $^{+11}/_{-10}$ Ma, 2 044 $^{+32}/_{-27}$ Ma and 2 044 $^{+17}/_{-14}$ Ma for three granitoids. The discrepancy between the two ages (~2.0 Ga and 1Ga) may be attributed to either a 1 Ga Kibaran overprint on the older 2.0 Ga Eburean basement of the Congo Craton (Rainaud *et al*., 2005a; Longridge, 2012) or to the presence of an extension of the Rehoboth Subprovince (Kröner *et al*., 1991). Hawkesworth and Marlow (1983) showed that granites generated during the Damaran metamorphism have Nd modal ages which cluster around 2.0 Ga to 2.5 Ga, which provides strong support for the Abbabis Complex being Palaeoproterozoic in age.

2.3.2. Grootfontein Complex

The Grootfontein Complex is the least studied metamorphic complex in Namibia because of its poor exposure. It forms the cores of four elongated anticlines in the Grootfontein – Tsumeb – Otavi area (Figure 2.4) (Corner, 2008). In the Grootfontein area, the complex consists of three main units; 1) well foliated gneisses, amphibolites and metasedimentary rocks, 2) gabbro and 3) granite. The gneiss is intruded by the gabbro and granite and the granite may also intrude the gabbro (Sanz, 2005). The Grootfontein Complex is cut by pre-Damaran amphibolite dykes. The oldest lithologies of the Grootfontein Complex are the gneisses and schists. The gabbros, which do not outcrop, are well defined in aeromagnetic data as a 62 km long and between 1 km and 6 km wide anomaly, extending east-northeast from Grootfontein town (Miller, 2008). The youngest lithology in the Grootfontein Complex is the granites, which are highly variable in texture, grain size and composition with the possibility of several different granites being present (Miller, 2008). SHRIMP dating on a granitic gneiss sample obtained ~25 km west of the Namibian-Botswana border yielded an age of 2 022 ± 15 Ma (Hoal *et al*., 2000). LA-ICPMS dating on a fine-grained, porphyritic, biotite granite yielded a U-Pb age of 1 939 ± 64 Ma with xenocrystic zircons dated at 2 544 ± 78 Ma (Sanz, 2005).

2.4. Tectonostratigraphic zones of the Damara Belt

2.4.1. Southern Foreland

The Southern Foreland is separated from the Southern Margin Zone to the north by the northeast-southwest trending Frontal Thrust (Figure 2.4). To the south of the Frontal Thrust is the east-northeast trending Areb Mylonite Zone, which is 15 km to 20 km thick containing sub-parallel shear zones and thrusts with pre-Damara basement (Figure 2.4) (Miller, 2008). In the Southern Foreland, Damaran lithologies of the Nosib, Witvlei and Nama Groups rest on Palaeoproterozoic basement (Figure 2.6) and are locally overlain by it because of thrusting (Hall *et al*., 2013).

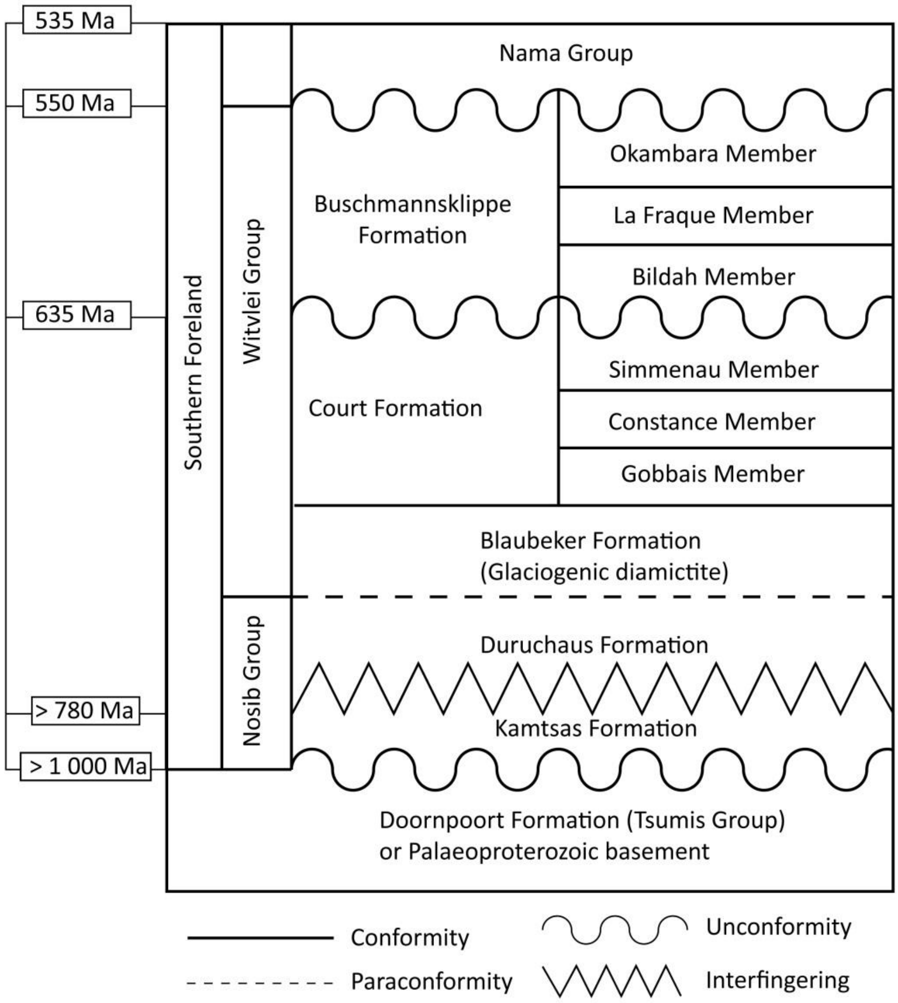

Figure 2.6: Simplified stratigraphic column of the Southern Foreland with approximate age dates (modified after, Hegenberger, 1993; Miller, 2008; Prave *et al*., 2011). Detailed descriptions of the lithologies and age dates are in the text.

The Nosib Group in both the Southern Foreland and Southern Margin Zone is composed of the arkosic Kamtsas Formation and the pelitic Duruchaus Formation (Winker, 2013). The Kamtsas Formation represents the base of the Damara Supergroup and is marked by a regional unconformity resting on either Palaeoproterozoic basement or Doornpoort Formation (Tsumis Group) (Figure 2.6) (Miller, 2008). The Kamtsas Formation extends from the platform areas in the south, into the graben where it is intercalated with and overlain by the Duruchaus Formation (Winker, 2013).

The Kamtsas Formation is a succession of feldspathic quartzite with a local basal conglomerate unit, containing clasts derived from the Rehoboth Group (Porada and Behr, 1988). The Duruchaus Formation consists of metapelite, siltstone, sandstone and conglomerate with layers of limestone and subordinate intercalations of coarser-grained Kamtsas-type sandstone and conglomerate folded into broad upright anticlines and synclines. In the Duruchaus Formation, copper mineralisation occurs between the siltstone and carbonate layers (Miller, 2008).

The Witvlei Group forms a rim around the Nama Group rocks and is unconformably to para-conformably overlain by them (Figure 2.6). The Witvlei Group comprises the Blaubeker, Court and Buschmannsklippe Formations (Figure 2.6) (Prave *et al*., 2011). The Blaubeker Formation paraconformably overlies the quartzite of the Kamtsas Formation and is a diamictite that is correlated with the Chuos Formation (Figure 2.6) (Hoffmann, 1989). The Blaubeker Formation consists of quartzite to clast-supported conglomerate with clasts of the Doornpoort and Kamtsas quartzites overlain by diamictite (Miller, 2008).

The base of the Court Formation is marked by a cap carbonate of the Sturtian glaciation (Blaubeker/Chuos Formations) which represents the base of the Gobabis Member (Figure 2.6) (Prave *et al*., 2011). The remainder of the Gobabis Member consists of alternating laminated limestone, which either grades or interleaves into a carbonate sequence (Miller, 2008). Overlying the Gobabis Member is the Constance Member (Figure 2.6) consisting of sandy shale, mudstone and siltstone with layers of dolostone (Miller, 2008). The feldspathic quartzite of the Simmenau Member marks the top of the Court Formation (Figure 2.6) (Hegenberger, 1993).

The basal unit of the Buschmannsklippe Formation is the Bildah Member (Figure 2.6) consisting of dolostone intercalated with sandy and pebbly horizons (Hegenberger, 1993). There is a regional unconformity at the base of the Bildah Member that oversteps the underlying Court Formation to rest unconformably on older Neoproterozoic rocks (Prave *et al*., 2011). Although there are no glaciogenic diamictites in the Buschmannsklippe Formation, the Bildah Member shares many similarities with the Keilberg Member, the cap carbonate of the Ghaub Formation (Otavi Group) (Miller, 2008). Overlying the Bildah Member is the La Fraque Member, (Figure 2.6) consisting of calcareous marly shale, sandstone and siltstone (Prave *et al*., 2011). The overlying Okambara Member consists of basal limestone and dolostone overlain clastic lithologies (Hegenberger, 1993). The top of the Witvlei Group is marked by a regional unconformity at the base of the Nama Group (Figure 2.6) (Hegenberger, 1993).

The Nama Group was deposited in the Nama Basin, which extends from central Namibia southwards into northwestern South Africa (Grotzinger and Miller, 2008). The Nama Group is divided into the basal Kuibis, Schwarzrand, and upper Fish River Subgroups (Figure 2.5) (Germs, 1983; Stanistreet *et al*., 1991). The clastic sedimentary lithologies of the Kuibis Subgroup are quartzite while those in the Schwarzrand Subgroup are predominantly less quartzitic. The Fish

River Subgroup lacks major carbonate beds and is dominated by feldspar-bearing siliciclastic rocks (Blanco *et al*., 2011). U-Pb dating of interleaving volcanic ash beds has been used to constrain the depositional age of the Kuibis and Schwarzrand Subgroups to between 550 Ma and 539 Ma (Grotzinger *et al*., 1995), whilst the upper portion of the Nama Group is estimated at pre-535 Ma because of a K/Ar age of 535 Ma from micas extracted from the Fish River Subgroup (Grotzinger and Miller, 2008).

2.4.2. Southern Margin Zone

The Southern Margin Zone is characterised by high pressure, low temperature (~600°C at ~10 kbar) kyanite metamorphism (Kasch, 1983; Jung *et al*., 2000). This zone is bounded by the Frontal Thrust in the south and the northeast-southwest trending Gomab River Line in the north (Figure 2.4) (Miller, 2008). This zone consists of pre-Damaran gneissic basement, basal Nosib Group, lithological varying units of the Hakos Group, and lower sequences of the Swakop Group (Miller, 1983a; Corner, 2008).

The Nosib Group in this zone is similar to that of the Southern Foreland except for the Duruchaus Formation. Firstly, it is more widespread in the Southern Margin Zone, and secondly, the correlation of the Duruchaus Formation in the Southern Foreland and Southern Margin Zone is difficult, as in the Southern Margin Zone, it outcrops within thrust sheets comprising phyllites, sandy siltstone and phyllitic sandstone which have undergone greenschist metamorphism to form mica schists (Behr *et al*., 1983; Sun, 2002; Frimmel and Miller, 2009). The Duruchaus Formation grades and interfingers with the carbonate dominant Coas Formation (Figure 2.7) (Miller, 2008). In tectonic contact or unconformably overlying either pre-Damara or Nosib Group rocks is the Hakos Group (Figure 2.7), which is correlated with the Swakop and Otavi Groups to the north and the Witvlei Group to the southeast (Miller, 2008). The Hakos Group is divided into the Kudis and Vaalgras Subgroups (Figure 2.7). The most characteristic units in the Kudis Subgroup are the graphitic schists of the Baulkrans Formation, which at basal levels interfinger with the Berghof and Waldurg Formations and towards the top of the subgroup with the Hakosberg and Auas Formations (Figure 2.7). The Berghof Formation consists of conglomerate and diamictite, which is suggested to be the lateral equivalent of the Chuos Formation (Miller, 2008). The Waldurg Formation consists of graphitic, dolomitic marble with internal layers of conglomerate. The Baulkrans Formation consists of graphite-rich schist and quartz-mica schist (Miller, 2008). The Hakosberg Formation consists of quartzite with interbeds of graphitic schist and local quartzite.

The Auas Formation is in a similar stratigraphic position to the Hakosberg Formation and contains quartzite (Figure 2.7) (Miller, 2008).

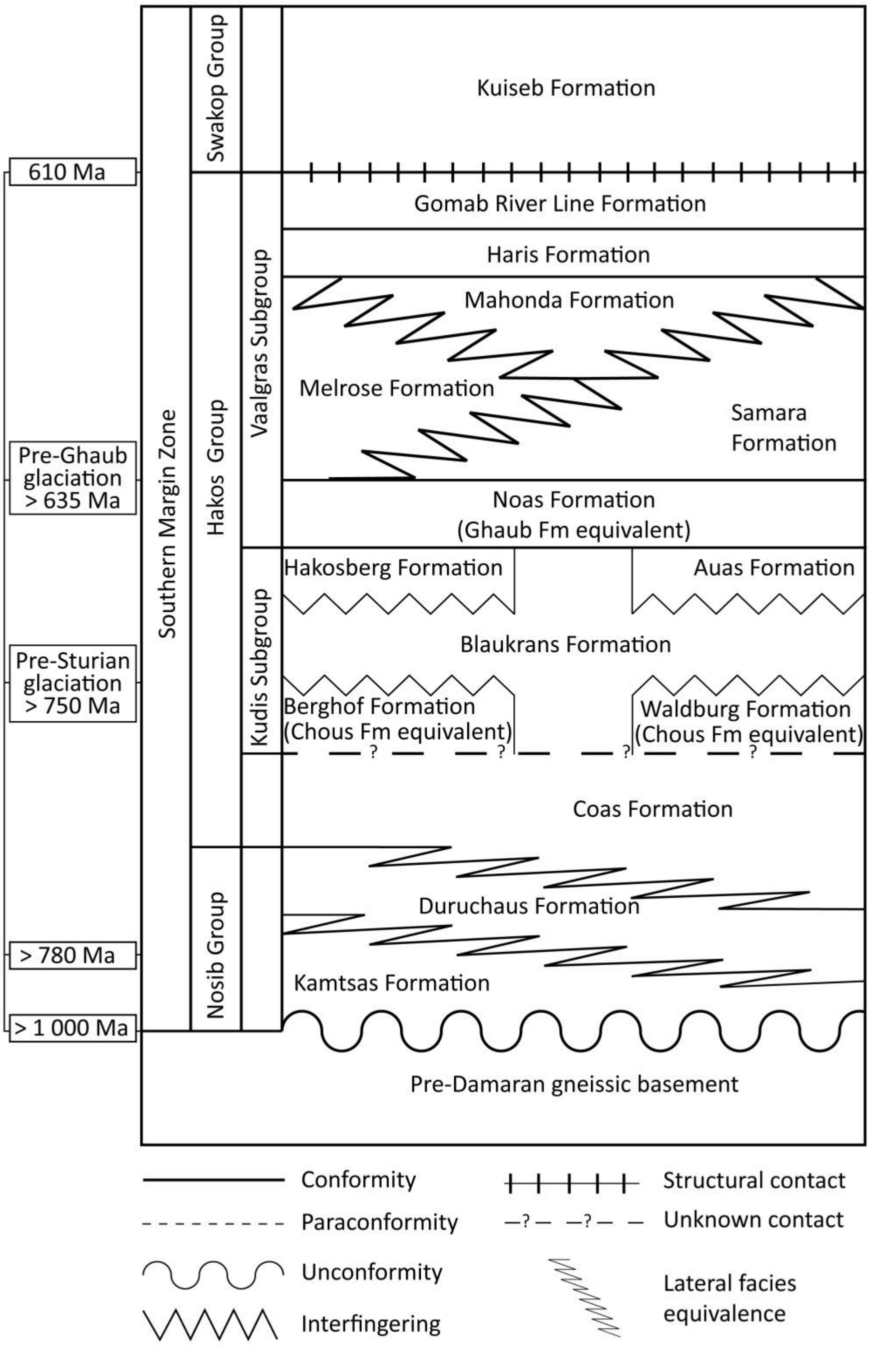

Figure 2.7: Simplified stratigraphic column of the Southern Margin Zone with approximate age dates (modified after, Hoffmann, 1989; Miller, 2008; Kaufman *et al*., 2009). Detailed descriptions of the lithologies and age dates are in the text.

The Khomas Subgroup has been re-named by Hoffmann (1983) to the Vaalgras Subgroup and is interpreted as the conjugated passive margin of the Congo Craton on the southern side of the Khomas Ocean (Miller *et al*., 2009b). The Vaalgras Subgroup consists of the glaciogenic Naos

Formation (Kaufman *et al*., 2009), previously the Chuos Formation (Martin, 1965; Miller, 1983a), Samara, Melrose, Mahonda, Haris and Gomab River Formations, which are structurally overlain by the Kuiseb Formation (Figure 2.7) (Miller, 2008). The distinguishing feature between the Vaalgras Subgroup and the underlying Kudis Subgroup is the concordant ortho-amphibolites present in the formations of the Vaalgras Subgroup (Miller, 2008). The age of the Naos Formation is unknown but is correlated with the Ghaub Formation to the north (Kaufman *et al*., 2009). The Naos Formation ranges from metadiamictite with occasional clasts of quartzite and granite interbedded with metavolcanic amphibolite, mica schist, amphibolite-chlorite schist and quartzite (Hoffmann, 1983; Kaufman *et al*., 2009). The composition of these amphibolites resembles continental, within-plate tholeiites with no primary igneous structures being observed (Miller, 1983b; Miller, 2008). Locally associated with the amphibolite are layers of laminated, iron formations composed of magnetite and hematite-rich layers (Breitkopf, 1988) and concordant lenses of chlorite-tremolite and talc schist locally containing cores of serpentinite (Hoffmann, 1983). Barnes (1982) suggests that the serpentinite has the same source as the serpentinite bodies located within the Southern Zone.

The overlying Samara Formation has a local basal conglomerate that oversteps the older units and lies unconformably on pre-Damara basement (Miller, 2008). The most complete and typical section of the Samara Formation is divided into several units of either dolomitic or quartzitic composition (Hoffmann, 1989). The Melrose Formation overlies the Naos Formation and interfingers with the Samara Formation (Figure 2.7) (Miller, 2008). It consists of garnet-chlorite schist, quartzite, calcareous schist and marble which locally interfingers with basal quartzite, amphibolite, marble and schist of the overlying Mahonda Formation (Figure 2.7). The Mahonda Formation is conformably overlain by a sharp contact with the Haris Formation (Figure 2.7), which is characterised by mica schist and calcareous schist and minor marble, amphibolite and quartzite (Miller, 2008). The Gomab River Formation (Figure 2.7) is restricted to the northern boundary of the Southern Margin Zone (Miller, 2008). It occurs as amphibolite schist with minor mica schist and marble and a rhyolite termed the Hartelust Rhyolite Member (Miller, 1983b; Miller, 2008) with a lower intercept age of $609\ ^{+8}/_{-15}$ Ma determined by a discordant zircon (Nagel, 1999).

2.4.3. Southern Zone

This zone is dominated by high pressure, low temperature kyanite metamorphism (Kasch, 1983; Jung *et al*., 2000). It is bounded by the Gomab River Line, a stratigraphic/structural contact, in the south and the Okahandja Lineament, a geophysical lineament in the north (Figure 2.4) (Kukla, 1992; Corner, 2008). The Gomab River Line represents a contact between the top of the Gomab River Formation and the overlying schists of the Kuiseb Formation (Figure 2.8) (Barnes and Sawyer, 1980). The majority of this zone comprises Kuiseb schists, which are overlain by the locally developed, syn-tectonic, arc trench metagreywackes of the Hureb Formation (Miller, 2008). Exposures in the southern portion of this zone include the Kuiseb Formation, Matchless Member and a few scattered ultramafic rocks. In the northern portion of this zone, the schists interfinger with calc-silicate and marble units of the Tinkas and Ghaub Formations (Miller *et al.*, 2009b).

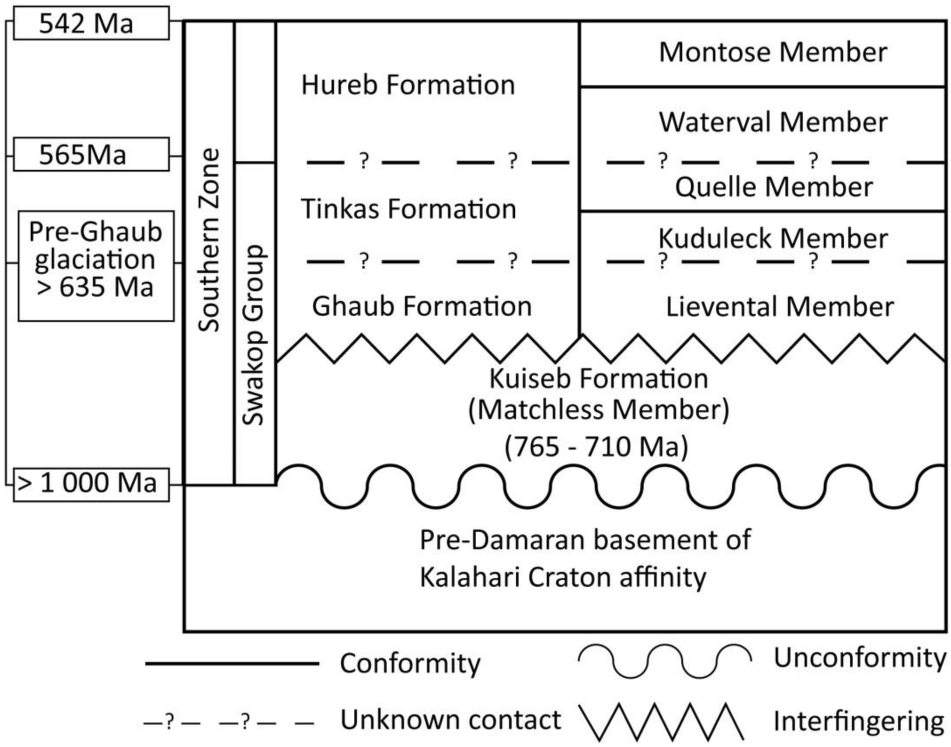

Figure 2.8: Simplified stratigraphic column of the Southern Zone with approximate age dates (modified after, Kukla and Stanistreet, 1991; Miller *et al.*, 2009b; Germs *et al.*, 2009). Detailed descriptions of the lithologies and age dates are in the text.

The Matchless Member is an ~350 km long and 3 km wide, northeast trending linear feature (Figure 2.4) (Barnes and Sawyer, 1980; Häussinger *et al.*, 1993; Killick, 2000; Miller *et al.*, 2009b) comprising two closely spaced, never more than 500 m thick, deformed amphibolite sheets. The chemical composition of the amphibolites is mid-ocean ridge basalts (MORB), which suggests a rift environment with minor continental flood basalts (Barnes and Sawyer, 1980). The Matchless Member is hosted in Kuiseb schists and formed above a sediment-covered mid-ocean ridge in the Khomas Ocean (Breitkopf and Maiden, 1986; Frimmel *et al.*, 2011). Meta-gabbros occur to the south of the Matchless Member, mainly at the contact between the amphibolite and metasediments (Kukla, 1992; Dill *et al*., 2002). Associated with the Matchless Member are magnetic quartzite markers (Dill *et al*., 2002; Corner, 2008). To the south a number of spatially separated serpentinite bodies, emplaced along thrusts in a variety of country rocks, including pre-Damaran basement (Barnes and Sawyer, 1980). The serpentinite bodies are suggested to be derived from mantle harzburgite (Barnes, 1982). The Southern Zone is the only zone where continental breakup and the development of ocean floor spreading are recorded (Miller, 2008). There are no reliable ages for the Matchless Member, with Hawkesworth *et al*. (1981) obtaining a Rb-Sr age of 765 ± 37 Ma, which they tentatively suggest as the minimum emplacement age. Nagel (1999) obtained a Sm-Nd isochron age of 711 ± 35 Ma. The Kuiseb Formation schists, which are one of the youngest formations of the Damara Orogen constrain the maximum emplacement age to ~635 Ma (Frimmel *et al*., 2011). Associated with the Matchless Member are several economic massive Cu-Fe sulphide ore bodies and prospects such as Hope, Gorob, Ongombo, Kupferberg, Matchless and Otjihase (Breitkopf and Maiden, 1986; Killick, 2000; Miller *et al*., 2009b). These massive ore deposits are speculated to have formed as part of a hydrothermal system during oceanic spreading (Killick, 1983).

The Hureb Formation is a forearc-trench sequence of calcareous schist, graphitic biotite schist and semi-pelitic schist (Waterval Member) and deep-water metapelites and metagreywackes (Montose Member) deposited on top of the greywackes of the Kuiseb Formation (de Kock, 1992; Kukla and Stanistreet, 1991). The deposition of the Hureb Formation is bracketed between 565 Ma and 542 Ma (Germs *et al*., 2009). The Hureb Formation should not have a formal stratigraphic status, as a basal contact has not been mapped (Miller, 2008).

South of the Okahandja Lineament (Figure 2.4), the Lievental Member (Ghaub Formation) (Figure 2.8) contains metabasalts that are interbedded with basal Kuiseb schists. Geochemistry of the metabasalts reflects a continental, within-plate, alkaline to tholeiitic composition (Miller *et al*., 2009b). The Lievental Member forms two metabasaltic layers locally split by the Kuiseb Formation, which rests directly on quartzites of the Etusis Formation and is overlain by the Tinkas Formation (Miller, 2008). The Tinkas Formation is developed in the Okahandja Lineament Zone and the northern portion of the Southern Zone and is divided into the Kuduleck Member (turbidites with a high percentage of carbonates interbedded with schists) and Quelle Member (distal siliciclastic and marly turbidites that have been metamorphosed to sequences of calc-silicate and schist layers) (Figure 2.8) (Miller, 2008).

2.4.4. Deep-Level Southern Zone

The Deep-Level Southern Zone is situated northeast of the Okahandja-Windhoek area (Figure 2.4). It is divided into two domains based on its aeromagnetic signal (Figure 2.4) (Corner, 2008). The first domain, ~120 km northeast of Windhoek contains the Ekuja-Otjihanwe Nappe Complex (Figure 1.4) comprising gneisses overlain by amphibolite (Steven *et al*., 2000). SHRIMP U-Pb zircon age dating on amphibolite, biotite gneiss, hornblende schist and tonalite samples yielded ages of 1 115 ± 13 Ma, 1 084 ± 7 Ma, 1 081 ± 10 Ma and 1 063 ± 9 Ma respectively (Steven *et al*., 2000). These ages and lithologies correlate with the Mesoproterozoic rocks to the south, in the Rehoboth Subprovince. However, the lower Swakop Group units present in the area are difficult to correlate with units in the surrounding zones.

2.4.5. Okahandja Lineament Zone

The Okahandja Lineament Zone is a narrow zone, which coincides with a distinct change in stratigraphy, structural style and metamorphic grade (Figure 2.4) (Sawyer, 1981; Miller, 2008) because of the 25 km (Corner, 1983) of uplift of the Central Zone relative to the Southern Zone (Miller, 1979). To the south of the Okahandja Lineament, the Nosib Group and lower portion of the Swakop Group are regularly absent compared to the north where the lower Damara Supergroup rocks are often well-developed (Kasch, 1988). Towards the southern margin of the southern Central Zone and developing passive margin of the Congo Craton, the *in-situ* carbonates of the Karibib shelf grade into the Karibib-derived debris and turbidite apron of the Tinkas Formation, which straddles the Okahandja Lineament (Miller, 2008). On the ground, the Okahandja Lineament Zone is not a definable feature and is usually included into the Southern Zone for simplicity (Miller, 2008).

2.4.6. Central Zone

This zone is characterised by high-temperature, low-pressure Pan-African metamorphism, reaching granulite facies metamorphism in the west (Basson and Greenway, 2004). The Central Zone is bounded by the Okahandja Lineament in the south and by the Autseib Fault in the north (Figure 2.4). The northeast trending Omaruru Lineament divides this zone into a southern Central Zone and a northern Central Zone (Figure 2.4). Both these zones are characterised by domal structures with an overall northeast elongation and numerous syn- to post-tectonic granitic plutons (Oliver, 1994).

Southern Central Zone

The Okahandja Lineament is thought to represent the southern edge of the Congo Craton or the Angolan Microcraton (Miller, 2008). The southern Central Zone pinches out eastwards where the Omaruru Lineament intersects the Okahandja Lineament at ~18°50'E (Figure 2.4) (Corner, 2008).

The sediments of the Nosib Group lie unconformably on the Abbabis Complex and can be subdivided into the older Etusis Formation and younger Khan Formation (Figure 2.9) (Smith, 1965; Kisters, 2005). Both formations yield modal ages of ~2.0 Ga, which corresponds to their source material, the underlying Abbabis Complex (Hawkesworth and Marlow, 1983; Miller, 2008). Ages from volcanic units within the Nosib Group suggest sedimentation occurred at ~750 Ma (Hoffman *et al*., 1996). The Etusis Formation consists of a basal conglomerate layer containing pebbles of the underlying Abbabis Complex (Miller, 2008), quartzite, quartzo-feldspathic gneiss (arkose) (Sawyer, 1981), which underlies and interfingers with feldspathic quartzite, quartz-biotite schist and gneiss of the Khan Formation (Figure 2.9) (Jacob, 1974; Sawyer, 1981). Unconformably overlying the Khan Formation is the Rössing Formation (Ugab Subgroup) (Figure 2.9) restricted to the northwestern half of the southern Central Zone consisting of interbedded dolomitic marble, pyritic quartzite and calc-silicate rocks (Longridge *et al*., 2011).

The glaciomarine sedimentary rocks of the Chuos Formation (Usakos Subgroup) (Stanistreet *et al*., 1991) rest in places directly on basement or Etusis and Khan Formation rocks (Figure 2.9). The lithology of the Chuos Formation is highly variable with massive tillite-like layers (i.e. glacial diamictites with a schistose matrix), iron formations, quartzites with minor, marbles and pelitic units (Hoffmann *et al*., 2004) and is associated with the world-wide Sturtian glaciation (Hoffman, 2005; Halverson *et al*., 2005).

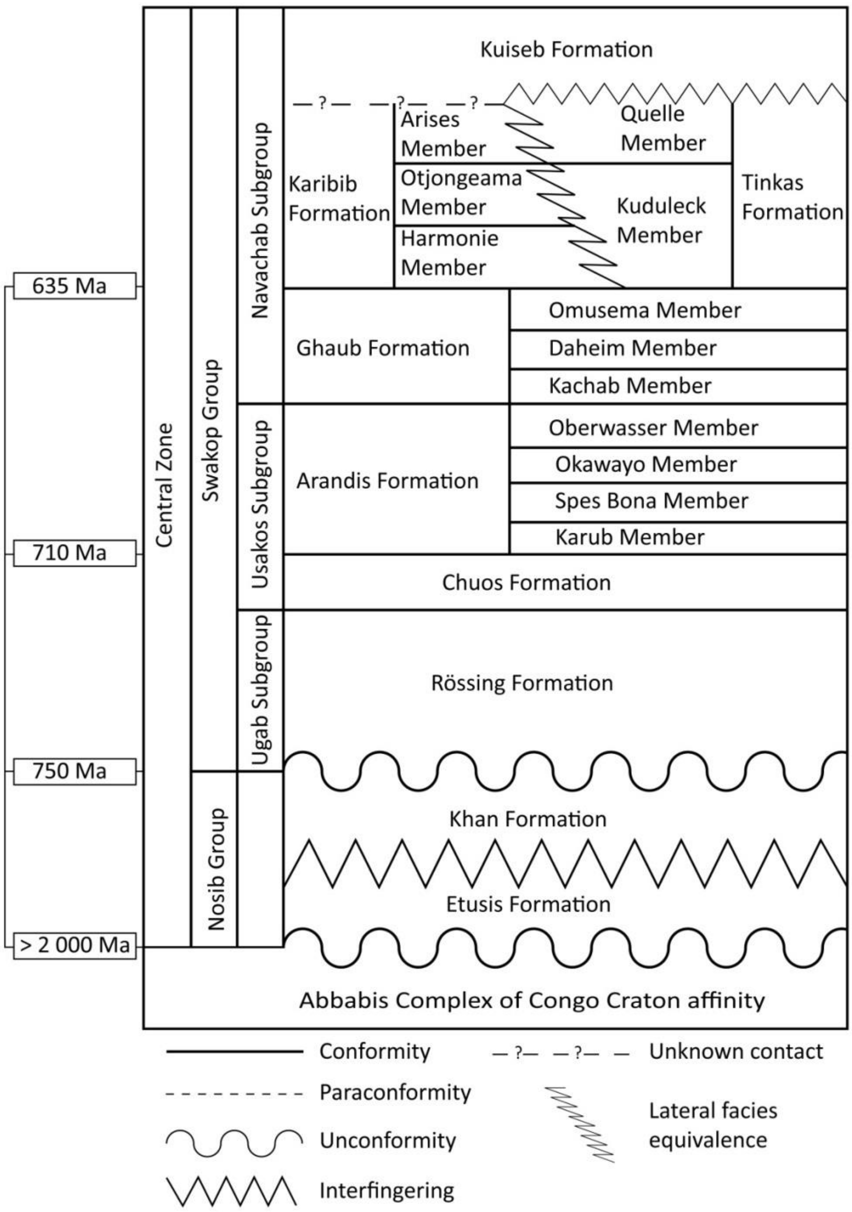

Figure 2.9: Simplified stratigraphic column of the Central Zone with approximate age dates (modified after, Badenhorst, 1992; Hoffmann *et al*., 2004; Longridge *et al*., 2011). Detailed descriptions of the lithologies and age dates are in the text.

The Arandis Formation (Usakos Subgroup) consists of calc-silicate, schist, metagreywacke, and carbonate, which forms the cap carbonate to the Chuos Formation (Figure 2.9) (Lehtonen *et al*., 1995). It can be divided into the basal Karub Member (a discontinuous marble unit interbedded with calc-silicate rock and schist layers), Spes Bona Member (intercalated calc-silicate rock, metagreywacke and biotite schist with minor marble, pyroclastic and crystal tuff layers), Okawayo Member (turbidite interbedded marbles, calc-silicate, and biotite schist), and the uppermost Oberwasser Member (quartz-biotite schist and feldspathic biotite schist with minor calc-silicate layers) (Figure 2.9) (Badenhorst, 1992; Lehtonen *et al*., 1995; Kisters, 2005; Dziggel *et al*., 2009).

Maloof (2000) correlates the Karub Member with the Rasthof Formation (cap carbonate of the Chuos Formation, Northern Zone) (Section 2.4.7).

The Navachab Subgroup consists of the Ghaub, Karibib and Kuiseb Formations (Figure 2.9). The Ghaub Formation is associated with the world-wide Marinoan glacial event from a U-Pb zircon age of 635.5 ± 1.2 Ma from an intraglacial tuff bed from the Central Zone (Hoffmann *et al*., 2004). It comprises diamictite, and graded shale and siltstone containing dropstones, conformably overlying the Oberwasser Member (Figure 2.9) (Sawyer, 1981; Hoffmann *et al*., 2004). The Ghaub Formation is divided into the Kachab Member (dropstone-bearing siliciclastic rocks) (Badenhorst, 1992), Daheim Member (metamorphosed, alkaline, basic, pillow lavas and pyroclastic rocks, which are interbedded with Kachab Member metasediments), and Omusema Member (metamorphosed succession of continental, within-plate, alkaline to tholeiitic basalts deposited subaqueously on or near the Okahandja Lineament) (Kisters, 2005; Dziggel *et al*., 2009). Sawyer (1981) mentions ferruginous quartzite and iron formation at the base of the diamictite throughout the southern Central Zone (south of 23°S).The alkali composition of the metabasaltic rocks of the Daheim Member is that of continental alkali basalt suggesting that despite the deep-water environment of deposition, eruption on the margin of a deep, submerged basin located at or near the southern passive continental margin of the Congo Craton occurred (Miller, 2008).

The Karibib Formation consists of an interbedded succession of dolostone, breccia and calc-silicate layers, schists and meta-greywackes interbedded with the marble (de Kock, 2001; Kisters, 2005). Locally, the marble unit oversteps the underlying Omusema-equivalent amphibole schist and lies directly on the Abbabis basement (Miller, 2008).

Towards the southeast margin of the southern Central Zone, the lateral equivalents of the Karibib marbles are the Tinkas Formation turbidites (Figure 2.9) (Jacob, 1974). The Tinkas Formation overlies and oversteps the Ghaub diamictites onto Nosib Group rocks and pre-Damaran basement, in what is interpreted as the eroded rift shoulder of the southern Central Zone (Miller, 2008). The Kuduleck Member (Tinkas Formation) overlies and interfingers with marbles of the Karibib Formation (Figure 2.9) and includes layers of the basal Kuiseb schists. The Quelle Member (Tinkas Formation) interfingers with the Kuiseb schists (Figure 2.9) (Miller, 2008).

northern Central Zone

The Omaruru Lineament (Figure 2.4) is marked by the presence of Nosib-cored domes and elongated granite bodies (Miller, 2008). Southeast of Otjiwarongo, the Omaruru Lineament becomes the Waterberg Thrust (Corner, 2008), a northeast branch, along which post-Karoo displacement have been recorded (Figure 2.4) (Raab *et al*., 2002; Trumbull *et al*., 2004). The northern margin of the northern Central Zone borders the Autseib Fault, which continues east of the Otjohorongo Thrust; the latter being reactivated by up to 2 km of vertical northward-directed post-Karoo movement (Raab *et al*., 2002) The Otjohorongo Thrust terminates against the Khorixas-Gaseneirob Thrust (Figure 2.4) (Corner, 2008).

In the northern Central Zone, the equivalent unit to the southern Central Zones Kachab Member (Ghaub Formation) is probably the upper Oberwasser Formation (Badenhorst, 1992), which consists of layers of calc-silicate rock, biotite schist and marble (Kisters, 2005; Dziggel *et al*., 2009). The basal member of the overlying Karibib Formation (cap carbonate) is a discontinuous dolomitic marble layer (Miller, 2008).

Klein (1980) divided the Karibib Formation into a basal Harmonie Member (basal marble unit above the Ghaub Formation, and calc-silicate and calcitic marble with disseminated calc-silicate minerals), Otjongeama Member (dolomitic marble, calcitic marble with minor interbedded calc-silicate and biotite schist layers) and an upper Arises Member (very coarse-grained, almost pure calcitic marble with a characteristic occurrence of disseminated graphite and chert layers interbedded with the overlying Kuiseb schists) (Figure 2.9).

2.4.7. Northern Zone

The Northern Zone has been thrust northwards onto pre-Damara, Otavi and Mulden Group lithologies along the Khorixas-Gaseneirob Thrust (Figure 2.4). The eastern continuation of this thrust has not been accurately located but is likely to be the east-west trending fault separating the Nosib Group rocks, to the south, from the steeply inclined and thrust-faulted Otavi Group rocks, to the north, forming the Otavi Valley Syncline (Figure 2.10) (Miller, 2008). The zone has been regionally metamorphosed to greenschist facies, and thermally metamorphosed to mid-amphibolite facies associated with the intrusion of the Salem Granites (Macey and Harris, 2006). The southern margin of the Northern Zone is represented by the Autseib Fault and the Otjohorongo Thrust (Figure 2.4). Towards the west, the Northern Zone is intruded by the large Omangambo Pluton (Figure 2.11) which forms the boundary between the Northern Zone and the Southern Kaoko Zone (Gray *et al*., 2006).

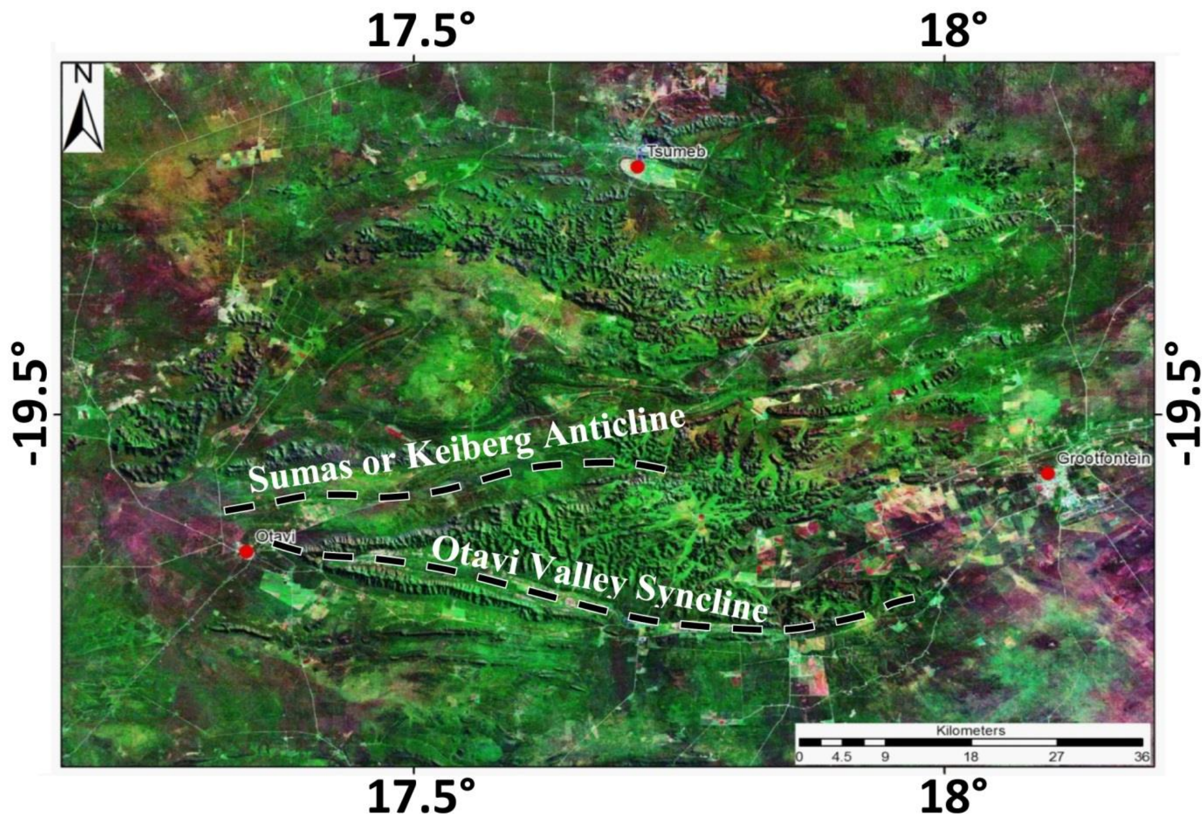

Figure 2.10: Landsat 7 satellite image of the Otavi Mountain Land area, Namibia, with the geographic position of the folds discussed in the text. Band 7 (mid-infrared light) is displayed as red, band 4 (near-infrared light) is displayed as green, and band 2 (visible green light) is displayed as blue (locations after Miller, 2008).

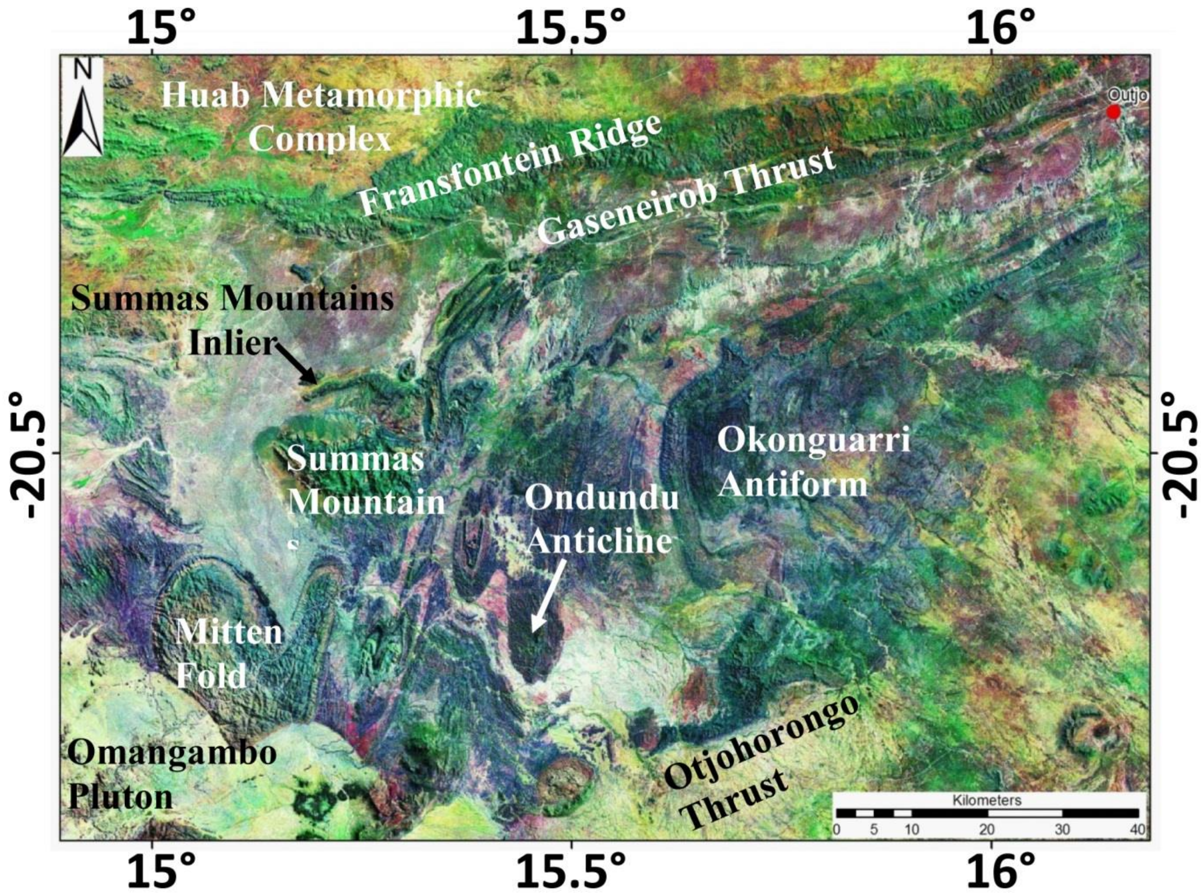

Figure 2.11: Landsat 7 satellite image showing the geographic position of geological structures discussed in the text. Band 7 (mid-infrared light) is displayed as red, band 4 (near-infrared light) is displayed as green, and band 2 (visible green light) is displayed as blue (locations after Miller, 2008).

The Nosib, Swakop and Mulden Groups are all separated by angular unconformities (Miller, 2008). The Mulden Group is not in a passive margin-related sequence and is described in Section 2.4.9. The Nosib Group consists of arkosic quartzite west and north of Otjiwarongo, possibly the volcanic rocks of the Naauwpoort Formation, and gneissic arkosic quartzite and amphibolite containing garnet and cordierite of the Tsaun Formations (Figure 2.12).

The Naauwpoort Formation and its correlatives crop out in five inliers within the Northern Zone; Welwitschia Inlier, Summas Mountains Inlier, Mitten Fold, Ais Dome and Summas Mountains (Figure 2.11). The most complete section of the Naauwpoort Formation consists of a basal conglomerate layer, which rests nonconformably on the basement and is entirely basement-derived (Kamona and Günzel, 2007) and an upper volcanic member, comprising basaltic and rhyolitic flows forming a bimodal sequence (Hoffman and Halverson, 2008; McGee *et al*., 2012). The Naauwpoort Formation is highly variable either missing the clastic or volcanic members (McGee *et al*., 2012). The age of the Naauwpoort Formation is constrained by a ^{207}Pb-^{206}Pb zircon weighted mean age 756 ± 2 Ma for the Oas Syenite (Hoffman *et al*., 1996). In the Summas

Mountains (Figure 2.11), a rhyolite flow and ash-flow tuff samples yielded ^{207}Pb-^{206}Pb zircon ages of 746 ± 2 Ma and 747 ± 2 Ma, respectively (Hoffman *et al*., 1996).

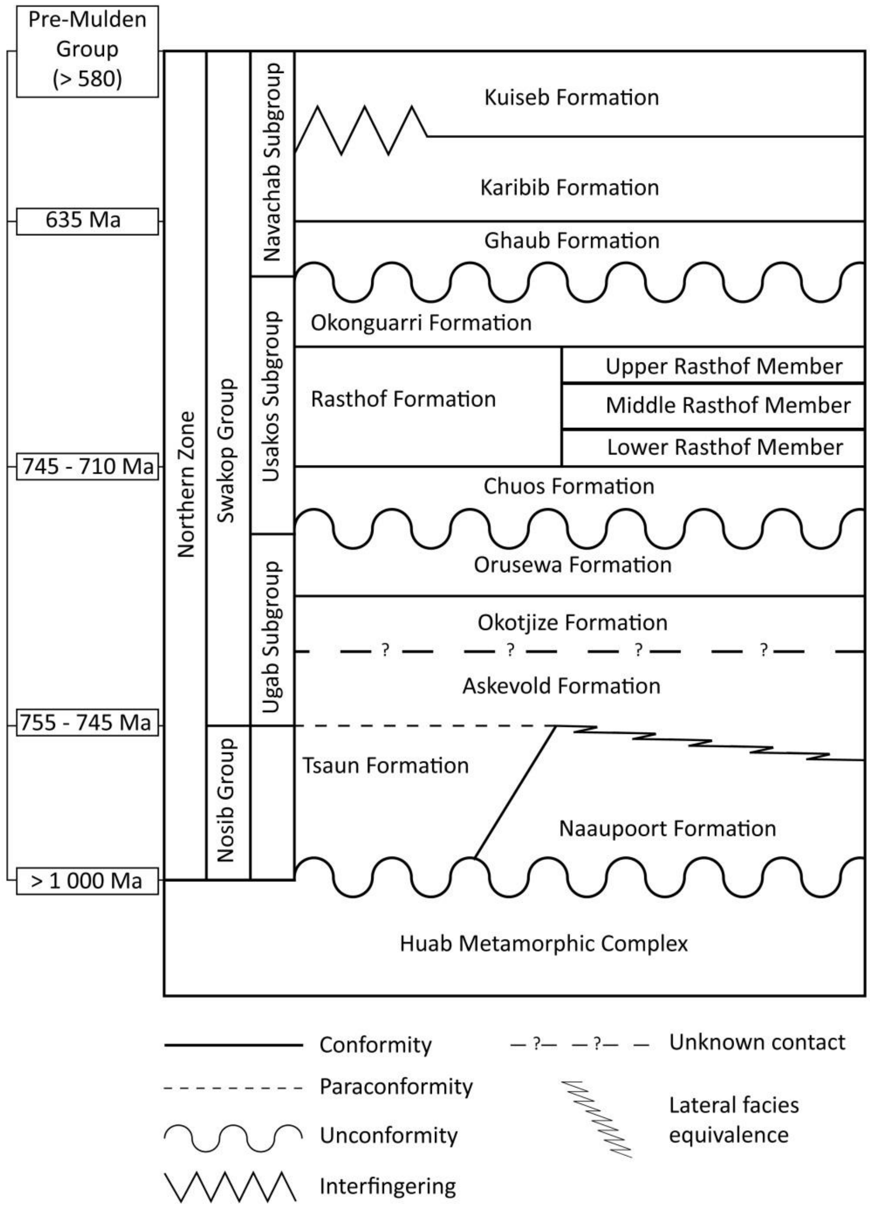

Figure 2.12: Simplified stratigraphic column of the Northern Zone with approximate age dates (modified after, Hoffman *et al*., 1996; Hoffman and Halverson, 2008; McGee *et al*., 2012). Detailed descriptions of the lithologies and age dates are in the text.

On the eastern margin of the Summas Mountains (Figure 2.11) the Naauwpoort Formation is interbedded with the Ugab Subgroup and unconformably overlies the gneisses of the Huab Metamorphic Complex (Figure 2.11) whilst, on the northern margin it is interbedded with the Ombombo Subgroup (Figure 2.12) (Clifford, 2008). The Upper Naauwpoort Formation lithologies form layers within either the Chuos or Okatjize Formations and from the age dates of Hoffman *et* *al*. (1996), the Upper Naauwpoort Formation is older than the Chuos diamictite (Hoffman and Halverson, 2008).

The Ugab Subgroup is a marine, shallow-water, mixed carbonate-clastic sequence, which grades from on-shore facies in the north to off-shore facies in the south comprises the Askevold, Okotjize and Orusewa Formations (Hoffman, 2011). Southeast of Otavi, the Askevold Formation, consisting of agglomerate with lesser amounts of schistose lithologies, basic lava and chloritised schist, which could possibly be metamorphosed basic tuffs, is correlated with the Naauwpoort Formation (Miller, 2008). The Okotjize Formation comprises iron formation intercalated with dolostone and ferruginous quartzite (Hoffman and Halverson, 2008). Conformably overlying the Okotjize Formation is the Orusewa Formation containing schists overlain by quartzites, which directly underlies the Chuos Formation (Figure 2.12) (Hoffman and Halverson, 2008).

The overlying Usakos Subgroup is divided into the Chuos, Rasthof and Okonguarri Formations (Figure 2.12) (Hoffmann *et al*., 2004; Church and Winker, 2013). The basal Chuos Formation forms a sharp erosional contact with the underlying lithologies (Hoffmann *et al*., 2004; McGee *et al*., 2012). The Chuos Formation consists of a matrix-supported glacial diamictite containing clasts of amphibolite, Naauwpoort ignimbrite, gneiss, granite, schist and carbonate and iron formations, which are regionally widespread but are thin and discontinuous (Hoffmann *et al*., 2004; Hurtgen *et al*., 2006).

The Chuos Formation is sharply overlain by carbonates of the Rasthof Formation (Le Heron *et al*., 2013). The thick cap carbonates can be divided into a continuous layer of limestone termed the Lower Rasthof Member, overlain by argillite, with a dolostone turbidite layer of the Middle Rasthof Member, and deep-water carbonates (cherty dolostone interbedded with limestone) and shales, of the Upper Rasthof Member (Figure 2.12) (Le Ber *et al*., 2013). The Upper Rasthof Member erodes the two lower members and Chuos Formation to lie directly on Naauwpoort Formation (Hoffman and Halverson, 2008).

Overlying the Upper Rasthof Member is a succession of quartz-biotite schist, siliciclastic-carbonate turbidite and pelite of the Okonguarri Formation (Hoffmann *et al*., 2004; Church and Winker, 2013). The Okonguarri Formation is wedged between outcrops of Chuos Formation (below) and Ghaub Formation (above) (Figure 2.12) (Miller, 2008) and is tentatively correlated with the Gruis Formation (Northern Platform) by Hoffman and Halverson (2008).

The overlying Ghaub Formation (Navachab Subgroup) comprises carbonate-clast diamictite, overlain by dropstone-bearing, bedded shale and siltstone (Clifford, 2008). Overlying the Ghaub

Formation is a thick package of dolomitic limestone with subordinate marble, dolostone and metapelite of the Karibib Formation (i.e. cap carbonate unit) (Figure 2.12) (Hoffman and Halverson, 2008; Longridge *et al*., 2011). The lateral equivalent of the basal dolostones of the Karibib Formation is the Keilberg Member (Otavi Group) and the overlying limestone is the limestone of the Maieberg Formation (Otavi Group) (Domack and Hoffman, 2011).

The uppermost formation of the Navachab Subgroup is the Kuiseb Formation (Figure 2.12) (Smith, 1965; Jacob, 1974; Longridge *et al*., 2011). The pre-tectonic schists of the Kuiseb Formation conformably overlie the marbles of the Karibib Formation and locally interfingers with it (Figure 2.12) (Miller, 2008). The Kuiseb Formation consists of basal metagreywacke, exposed in the Ondudu Anticline (Figure 2.11), a middle unit consisting of marly metapelite with layers of metagreywacke and an upper unit consisting of coarser-grained meta-greywacke with several laterally continuous quartzite layers near the top (Miller, 2008).

2.4.8. Northern Margin Zone

The Northern Margin Zone is a narrow zone situated between the Northern Platform and the Northern Zone (Figure 2.4). The Northern Margin Zone consists of a varied group of lithologies including the deep-water facies carbonates of the Otavi Group which contrasts with the shallow-water rocks of the Northern Platform (Goscombe *et al*., 2004; McGee, 2012). These differentiating features developed during the deposition of the Rasthof Formation and terminated with the Gruis Formation deposits. Thereafter, the Northern Margin Zone remained in a deep-water environment until the end of the deposition of the Otavi Group (Miller, 2008).

The Otavi Group is divided into the Ombombo, Abenab, and Tsumeb Subgroups (Figure 2.13) (Hoffmann and Prave, 1996). Unconformably overlying basement granitoids is the basal unit of the Naauwpoort Formation (Figure 2.13) (Hoffman and Halverson, 2008). It is composed of a coarsening upward breccia that contains entirely basement clasts. This breccia is interpreted as the lower clastic member of the Naauwpoort Formation because it is overlain by the Abenab Subgroup and lacks the significant carbonate component of the Ugab Subgroup (McGee *et al*. 2012). A pegmatite cross-cutting the basal breccia has yielded a mean weighted average $^{206}Pb/^{238}U$ age of 763 ± 5 Ma indicating that initial sedimentation began prior to 763 Ma (McGee *et al*. 2012). This basal unit is overlain by a sequence of silty mudstones with numerous thin beds of graded micaceous sandstone and conglomerate (Hoffman and Halverson, 2008).

The Naauwpoort Formation is disconformably and unconformably overlain by the discontinuous Chuos Formation (base of the Abenab Subgroup) (Figure 2.13) consisting of a basal, dolomitic-chert-quartz-granitoid, stratified diamictite overlain by massive, basement-derived (granitoid-quartz) diamictite with a locally ferruginous matrix (Le Ber *et al*., 2013; Le Heron *et al*., 2013). The Chuos Formation is conformably overlain by the post-glacial cap carbonate Rasthof Formation (Figure 2.13) comprising a lower unit of rhythmite and sediment gravity flows and an upper unit of sublittoral dolomitic microbialaminite containing roll-up structures characteristic of the Lower Rasthof Member (Hoffman and Halverson, 2008; Pruss *et al*., 2010).

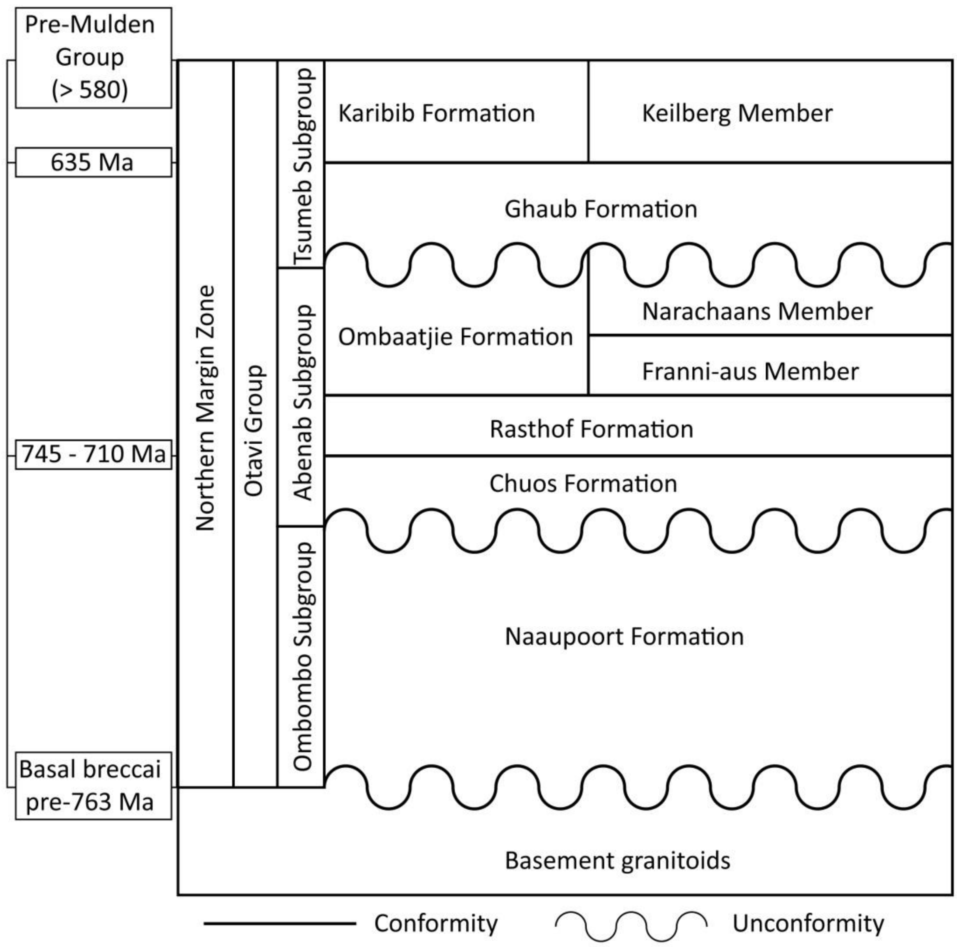

Figure 2.13: Simplified stratigraphic column of the Northern Margin Zone with approximate age dates (modified after, Hoffmann and Prave, 1996; Domack and Hoffman, 2011; Le Ber *et al*., 2013; Le Heron *et al*., 2013). Detailed descriptions of the lithologies and age dates are in the text.

The Rasthof Formation is truncated sharply by a limestone-clast rich, debris-flow complex associated with the Franni-aus Member (Ombaatjie Formation) (Figure 2.13) (Domack and Hoffman, 2011). The subaerial outcrop defining the top of the Rasthof Formation in the Northern Platform does not occur in foreslope sections and it is possible that strata included in the Rasthof Formation in the western portion of the ridge include age equivalents of the Ombaatjie and Gruis

Formations (Northern Platform) (Section 2.4.9) (Hoffman and Halverson, 2008). The upper member of the Ombaatjie Formation is the Narachaams Member (Figure 2.13) consisting of fine-grained siliciclastics (Domack and Hoffman, 2011).

The Ombaatjie Formation is overlain by the Ghaub Formation (basal unit of the Tsumeb Subgroup) (Figure 2.13) (Clifford, 2008). The Ghaub Formation comprises carbonate-clast dominated glaciomarine diamictite with clasts of basement granitoid and Rasthof dolostone (Hoffmann *et al*., 2004; Hoffman, 2011). The Ghaub Formation is sharply overlain by the cap carbonate dolostone of the Keilberg Member (base of the Karibib Formation) (Figure 2.13) (Halverson *et al*., 2002; Domack and Hoffman, 2011). The top of the Karibib Formation consists of marly turbiditic dolostone and associated debris-flows (Hoffman and Halverson, 2008).

2.4.9. Northern Platform

The Northern Platform covers the extent of the shallow-water, platform facies rocks of the Otavi Group. It extends from the Sesfontein Thrust in the west to the Nosib Anticline in the Otavi Mountain Land in the east (Miller, 2008). The Northern Platform contains the Nosib, Otavi and Mulden Groups (Kamona and Günzel, 2007). The Otavi Group is further divided in the Ombombo, Abenab and Tsumeb Subgroups, (Figure 2.14). The latter two are floored by glaciogenic diamictite formations (Hoffman and Prave, 1996; Hurtgen *et al*., 2006; Le Ber *et al*., 2013). The metamorphic grade of the Northern Platform is generally low but white micas in the Mulden Group, north of Kamanjab Inlier (Figure 2.4) record Damaran metamorphic ages (Miller, 2008).

The basal Nosib Group unconformably overlies granitic and gneissic basement and consists of the Nabis and Andara Formations (Figure 2.14), which are exposed in the central parts of the Otavi Mountain Land (Figure 2.10) (Kamona and Günzel, 2007; Master, 2013). The Nabis Formation consists of a basal conglomerate overlain by feldspathic, fluviatile sandstone (McGee, 2012). The Andara Formation occurs in the Caprivi Strip consisting of poorly sorted, coarse-grained, feldspar-free quartzite (Master, 2013).

The overlying mixed siliciclastic-carbonate dominate Ombombo Subgroup is divided into the Beesvlakte, Devede and Okakuyu Formations (Figure 2.14) (Hurtgen *et al*., 2006). The Beesvlakte Formation consists of argillite and strongly tectonised sericite dolostone. The lower half of the Devede Formation consists of strongly cyclic dolostone with coarse clastic wedges while the upper half has stromatolite biostrome (*Tungussia*). An ash bed in the Devede Formation has yielded a U-Pb zircon age of 760 ± 1 Ma, which is used to constrain the depositional age of the Ombombo Subgroup (Hoffman *et al*., 1996; Halverson *et al*., 2005; Konopásek *et al*., 2008; McGee *et al*., 2012). The Okakuyu Formation is dominated by fluvial and deltaic clasts composed of dolostone, chert and basement detritus (Le Heron *et al*., 2013).

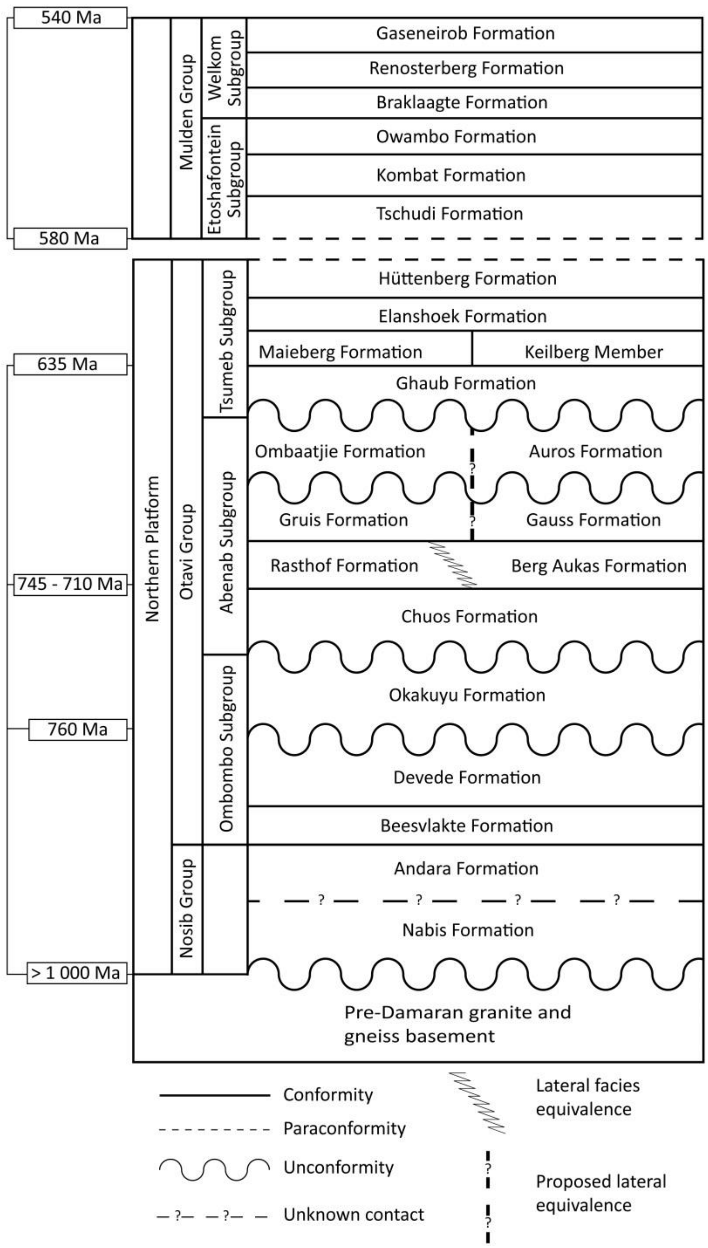

Figure 2.14: Simplified stratigraphic column of the Northern Platform with approximate age dates (modified after, Halverson *et al*., 2002; Hoffmann *et al*., 2004; Germs *et al*., 2009; Le Ber *et al*., 2013). Detailed descriptions of the lithologies and age dates are in the text.

The Abenab Subgroup is divided into Chuos, Rastof/Berg Aukas, Gruis, Ombaatjie, Auros, and Gauss Formations (Figure 2.14) (Hoffmann *et al*., 2004; Le Ber *et al*., 2013). The basal Chuos Formation occurs in the central and western Otavi Mountain Land (Figure 2.10) consisting of diamictite, usually ferruginous, containing interbedded lenses of magnetic, laminated shale, iron formation, and arkose, and commonly has granite and gneiss clasts derived from the unconformably underlying Nosib and pre-Damara basement (Kamona and Günzel, 2007). The cap carbonate of the Chuos Formation is the Rastof Formation (in the vicinity of the Kamanjab Inlier, Figure 2.4) and Berg Aukas Formation (in the vicinity of the Otavi Mountain Land) (Figure 2.14).

The Berg Aukas Formation was deposited during the massive flooding following the Sturtian glaciation event and consists of basal laminated and banded dolostone and limestone and local lenses of conglomerate and arkose containing Mississippi Valley-type (MVT) Zn-Pb-Cu-V mineralisation (Chetty and Frimmel, 2000; Schneider *et al*., 2008; Mapani *et al*., 2010). Locally, the Berg Aukas Formation has a sharp basal contact that transgresses from the Ombombo Subgroup, Chuos Formation and Nosib Group to basement (Hoffman and Halverson, 2008). The overlying Gruis Formation comprise cycles of quartz arenite, limestone, medium-bedded to massive dolostone (Halverson *et al*., 2002; Domack and Hoffman, 2011). The overlying Ombaatjie Formation consists of limestone overlain by weakly brecciated and silicified dolostone (Hurtgen *et al*., 2002; Halverson *et al*., 2002). Conformably overlying the Berg Aukos Formation is the Gauss Formation (Figure 2.14) consisting of a basal dolostone interbedded with conglomerate containing dolostone fragments overlain by varied massive dolostone sequence of grainstone and mudstone (Kamona and Günzel, 2007; Hoffman and Halverson, 2008). The overlying Auros Formation is characterised by three or four shallowing upward cycles consisting of calcareous shale horizons interbedded with and overlain by interbedded limestone and massive dolostone layers (Kamona and Günzel, 2007).

Unconformably overlying the Abenab Subgroup is the Tsumeb Subgroup consisting of Ghaub, Maieberg, Elanshoek and Hüttenberg Formations (Figure 2.14) (Chetty and Frimmel, 2000; Hoffmann *et al*., 2004). The basal Ghaub Formation consists of shale, dolostone, sandstone, diamictite, and conglomerate with clasts of limestone, dolostone, quartzite, granite, gneiss and chert derived from the underlying Abenab Subgroup, Nosib Group and pre-Damaran basement in a fine-grained dolostone, calcite and pyrite matrix (Kamona and Günzel, 2007). Sharply overlying the Ghaub Formation is the, cap carbonate, Kielberg Member (base of the Maieberg Formation) (Figure 2.14) (Clifford, 2008). Where the Ghaub Formation is absent, the Keilberg Member lies disconformably on pre-glacial strata (Hoffman, 2011). The Keilberg Member comprises dolostone and limestone containing disseminated sulphides (pyrite, pyrrhotite and marcasite), overlain by banded limestone with shaly intercalation grading to dolostone grainstone (Hurtgen *et al*., 2006; Kamona and Günzel, 2007).

The Elandshoek Formation conformably overlies the Maieberg Formation (Figure 2.14). The Elandshoek Formation consists of three dolostone units; a lower massive grainstone, middle dolostone with oolitic and chert interbeds, and an upper monotonous cycle of dolomitic mudstone capped by boundstone (Kamona and Günzel, 2007). Conformably overlying the Elandshoek Formation is the Hüttenberg Formation (Figure 2.14) consisting of a basal dolostone overlain by dolostone containing minor chert and shale and dolomitic grainstone layers (Hurtgen *et al*., 2006; Kamona and Günzel, 2007). The base of the Hüttenberg Formation resembles a major flooding surface corresponding with a step-like increase in $\delta^{13}C$ (Halverson *et al*., 2002). The positive carbon isotope excursion to ~8 per mil in the lower Hüttenberg Formation can also be recognised in the Karibib Formation on the Fransfontein Ridge (Figure 2.11) and serves as a basis for correlating the platformal and slope-facies (Hoffman and Halverson, 2008).

The Kaoko Belt-derived molasse Mulden Group accumulated in the Owambo Basin as well as in individual, and syncline basins (Miller, 2008). It was deposited on the Northern Margin Zone and Northern Platform above the Damara Supergroup with a major erosional para-to disconformable contact (Germs *et al*., 2009) or only a paraconformable contact (Figure 2.14) (Hoffman and Halverson, 2008). $^{40}Ar/^{39}Ar$ thermochronological data constrains the deposition age of the Mulden Group between ~580 Ma to 541 Ma by (Gray *et al*., 2006). The Mulden Group is divided into the Etoshafontein and Welkom Subgroups (Figure 2.14) (Germs *et al*., 2009). The Etoshafontein Subgroup consists of the basal Tschudi (conglomerate, arkose, and argillite), Kombat (shale with dolomitic lenses), and Owambo Formations (shale, marl, sandstone and siltstone) (Figure 2.14) (Germs *et al*., 2009). The Welkom Subgroup comprises the basal Braklaagte (basal conglomerate, overlain by phyllite and greywacke), overlying Renosterberg (feldspathic quartzite, which grades into arkose, greywacke and shale), and the Gaseneirob Formations (bedded to laminated, greywacke and shale) (Figure 2.14) (Germs *et al*., 2009).

2.5. Botswana

2.5.1. Introduction

The tectonostratigraphic zones of the Damara Belt have not been confidently traced eastwards into Botswana because of the increase in Phanerozoic cover. Central and northern Botswana are divided into three tectonostratigraphic zones, which have been correlated with the tectonostratigraphic zones of the Damara Belt by Carney *et al*. (1994).

2.5.2. Ghanzi-Chobe Zone

The Ghanzi-Chobe Zone has one of the most distinct aeromagnetic signals consisting of northeast-southwest trending folds. Structural styles of the Ghanzi-Chobe Zone are similar to the Southern Foreland, which comprise southeast vergent open to tight folds (Carney *et al.*, 1994). In Botswana, the limits of the Ghanzi-Chobe Zone are the Tsau Fault to the southeast (not to be confused with the Cenozoic Tsau Fault situated in the Okavango Rift Zone) and the Roibok Group and Kwando Complex to the northwest (Figure 2.15) (Carney *et al.*, 1994).

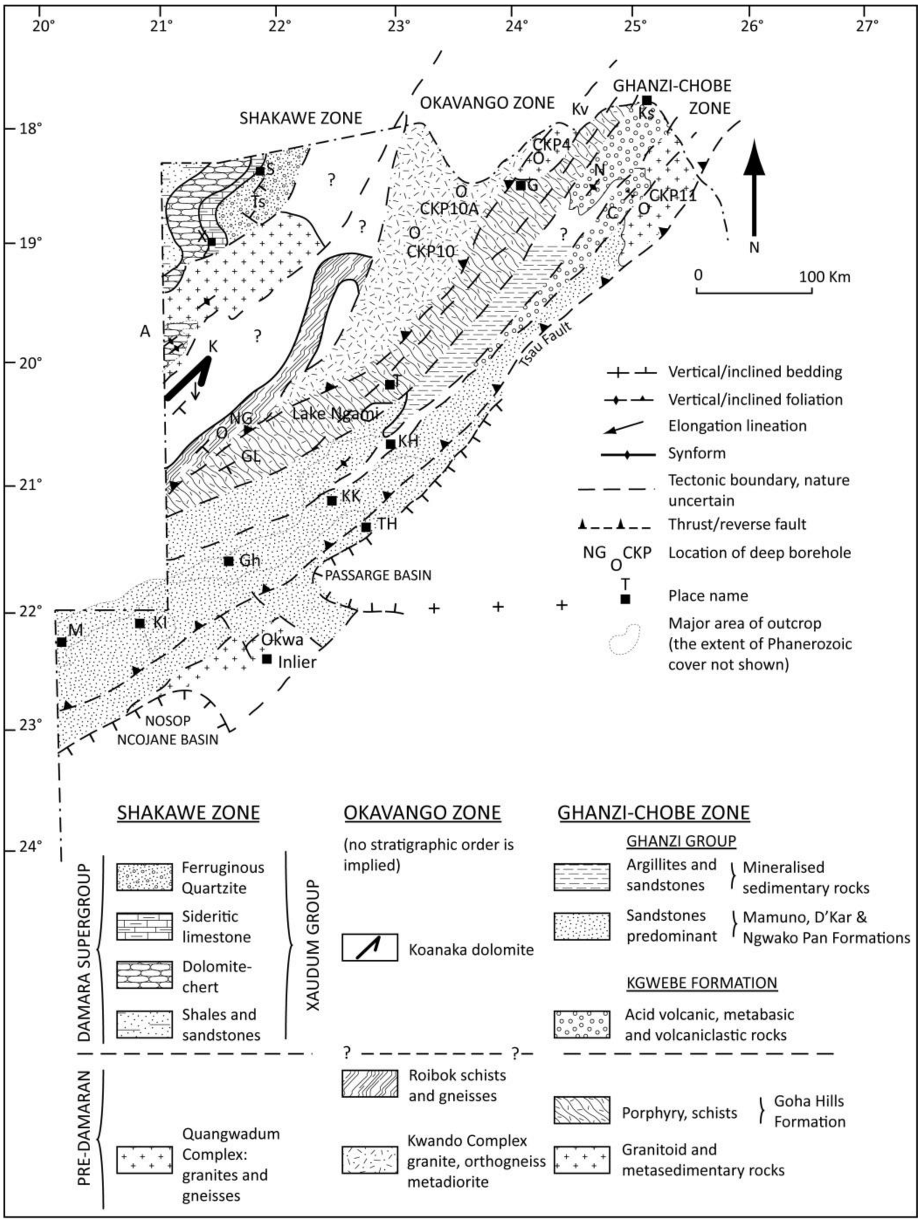

Figure 2.15: The tectonostratigraphic zones of central and northern Botswana (modified after Carney *et al.*, 1994). Where A = Aha Hills, C = Chinamba Hills, G = Goha and Gubatsha Hills, Gh = Ghanzi, GL = Groote Langte, K = Kihabe Hills, Kf = Kalkfontein, KH = Kgwebe Hills, KK = Kuke, Ks = Kasane, Kv = Kavimba, N = Ngezumba, S = Shakawe, T = Toteng, TH = Tsau Hills, Ts = Tsodilo Hills and X = Xaudum Valley.

Ghanzi-Chobe Belt

The Ghanzi-Chobe Belt forms a 500 km long and 100 km wide portion of the Kalahari Copperbelt in western and northern Botswana consisting of volcano-sedimentary lithologies (Borg and Maiden, 1989; Modie, 2000; Jones *et al*., 2009; Maiden and Borg, 2011). The line of near-surface to exposed lithologies extends northeast from Mamuno, near the Namibian border, to northern Botswana near the border with Zambia and Zimbabwe (Figure 2.16) (Modie, 2000; Hall, 2013). The Ghanzi Ridge is defined by the exposed area between Mamuno and Lake Ngami (Figure 2.15). The northwest extension of the Ghanzi-Chobe Belt is represented by exposures in the Goha and Chinamba Hills area (Figure 2.16) (Modie, 2000; Key and Ayres, 2000; Singletary *et al*., 2003). The geological history of the Ghanzi-Chobe Belt is poorly constrained because of the Phanerozoic cover (Modie, 2000). The belt has mainly been delineated by airborne geophysical techniques augmented by known geological data obtained from the limited outcrop or from exploration boreholes (Carney *et al*., 1994).

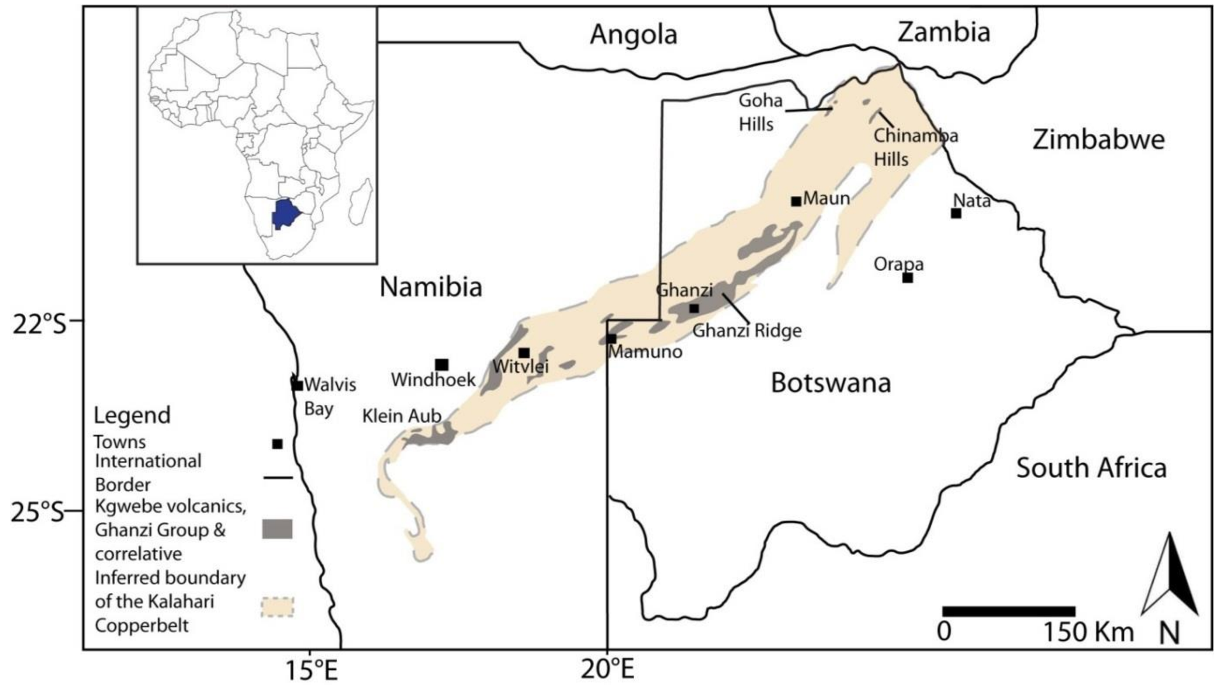

Figure 2.16: Inferred extent of the Kalahari Copper Belt from Namibia into northern Botswana with the location of outcrops shown in grey (modified from Borg and Maiden, 1989; Modie, 2000; Maiden and Borg, 2011; Hall, 2013). Insert is of Africa showing the location of Botswana (blue infill).

Geological setting

The Ghanzi-Chobe Belt was deformed during the Late Neoproterozoic to Early Palaeozoic Pan-African Damaran-Zambezi-Lufilian Orogeny (Borg and Maiden, 1989; Porada, 1989). The belt forms part of the northwestern margin of the Kalahari Craton (Jacobs *et al*., 2008) that was deposited in a rift basin (Borg, 1988). Exposures of the Kgwebe Formation at Mabeleapodi Hills (Figure 2.17) yield a U-Pb zircon age of 1 106 ± 2 Ma (Schwartz *et al*., 1995). This age was interpreted as the crystallisation age of the Kgwebe Formation (Schwartz *et al*., 1995). This age is older than previously determined from twelve samples in the same area, which gave a Rb-Sr whole rock errorochron age of 821 ± 43 Ma (Key and Rundle, 1981). The latter age is believed to represent a minimum age with the scatter in the data points thought to be caused by a metamorphic resetting event at 650 Ma to 700 Ma (Key and Rundle, 1981). The Ghanzi-Chobe sequence is interpreted to have started accumulating during the Mesoproterozoic, beginning with volcanism at ~1.1 Ga (Modie, 2000). The rift system was believed to be younging to the northeast (Borg, 1988) based on younger Rb-Sr whole rock age dates of 821 ± 43 Ma and 981 ± 43 Ma sampled from the Mabeleapodi and Goha Hills porphyries, respectively (Figure 2.17) (Key and Rundle, 1981). The latest age date of 1 106 ± 2 Ma, however, suggests differently. Hoal (1993) argued against the lateral younging to the northeast based on discrepancies in age constraints and the limited outcrop in which the age range is observed.

Models of the initial stages of rifting of the Ghanzi-Chobe Belt have changed between orogenic and anorogenic settings. One of the earliest tectonic models proposed was that the Ghanzi-Chobe Belt formed part of a laterally extensive magmatic arc (Watters, 1977). Borg (1988) proposed a thermally-initiated rifting model associated with a mantle plume. Modie (2000) favoured an anorogenic setting for the tectonic evolution of the belt, involving a thermally induced rift system because of the lack of field evidence representing an active continental margin. The tectonic setting of the Ghanzi-Chobe Belt has been modelled through geochemical interpretations of basal Kgwebe volcanics and similar rocks in Namibia. The interpretations suggest that the Ghanzi-Chobe Belt is associated with the collision along the Namaqua-Natal Belt (Kampunzu *et al*., 1998) with the open to tight folds forming during tectonic deformation at ~650 Ma (Key and Rundle, 1981).

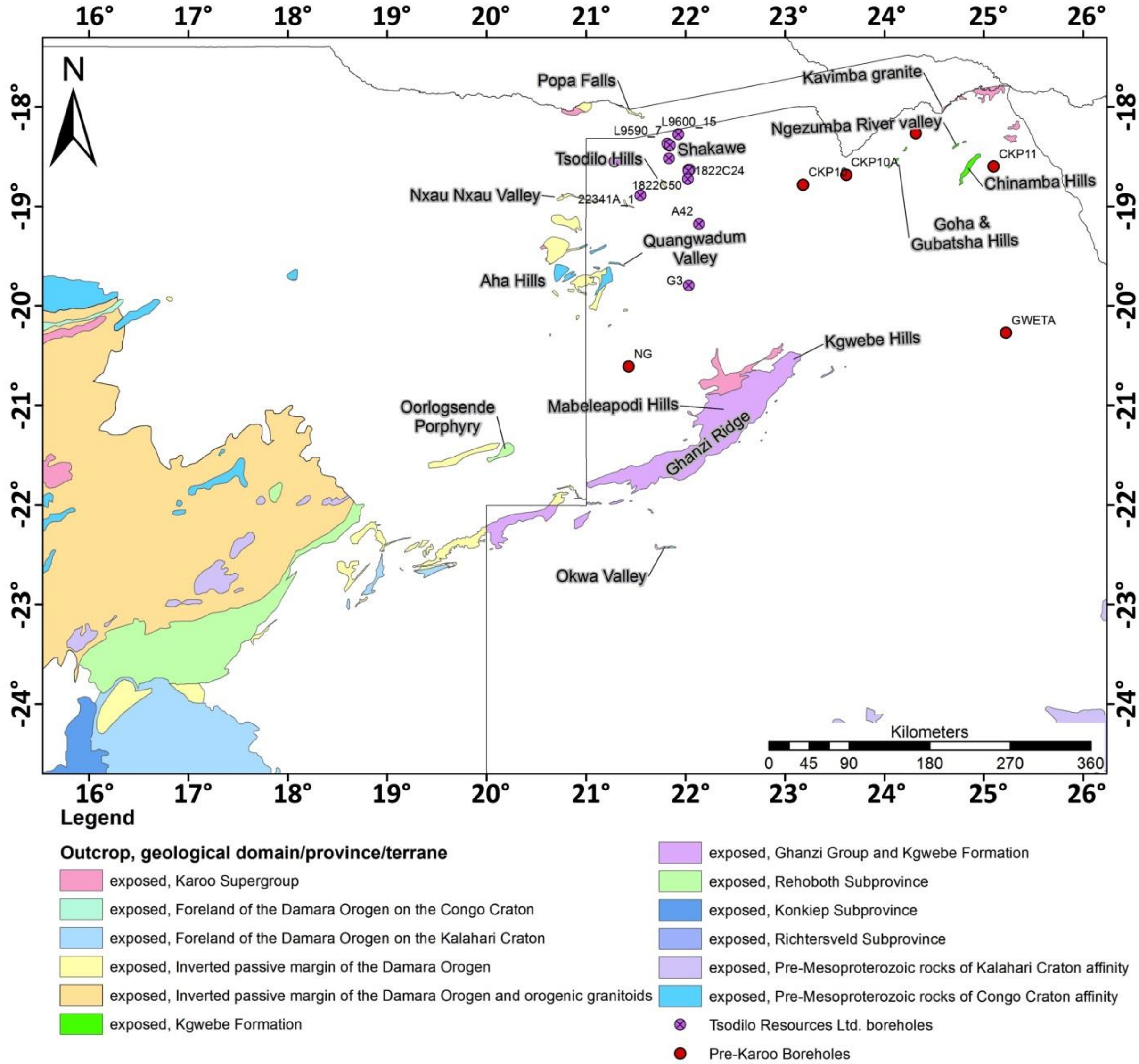

Figure 2.17: Outcrop geology of Botswana and Namibia (after Modie, 2000; Singletary *et al*., 2003; Miller, 2008).

Stratigraphy

Kgwebe Formation

The lowest structural unit of the Ghanzi-Chobe Belt is the Kgwebe Formation (Figure 2.18), which occurs within the cores of elongated northwest trending anticlines juxtaposed to the outward steeply dipping beds of the Ghanzi Group (Carney *et al*., 1994). The Kgwebe Formation has been metamorphosed to lower greenschist facies during the Damara Orogen (Schwartz *et al*., 1995). The formation is composed of magnetite-bearing porphyritic rhyolites and dacites, pyroclastic flow deposits, ignimbrites (Kampunzu *et al*., 1998; Modie, 2000). These volcanics are intercalated with minor tuffaceous sedimentary rocks, sandstones, grit, and conglomerates containing clasts of porphyries and basalts (Figure 2.18) (Carney *et al*., 1994; Modie, 1996). The geochemical analysis of the bimodal volcanic suites of the Kgwebe Formation represents within-plate low Ti-P continental tholeiites and post-orogenic within-plate high-K rhyolites (Kampunzu *et al*., 1998). The enrichment of mobile elements (K, Ba, Sr) and low Ce/Pb ratios and field relations of the mafic rocks suggests that they were enriched by a previous subduction event (Kampunzu *et al*., 1998). The rhyolitic composition suggests that they cannot be derived from melting of sediments or subducting slab but favours melting of Mesoproterozoic calcalkaline lower crust during a late orogenic collision related extensional collapse (Kampunzu *et al*., 1998).

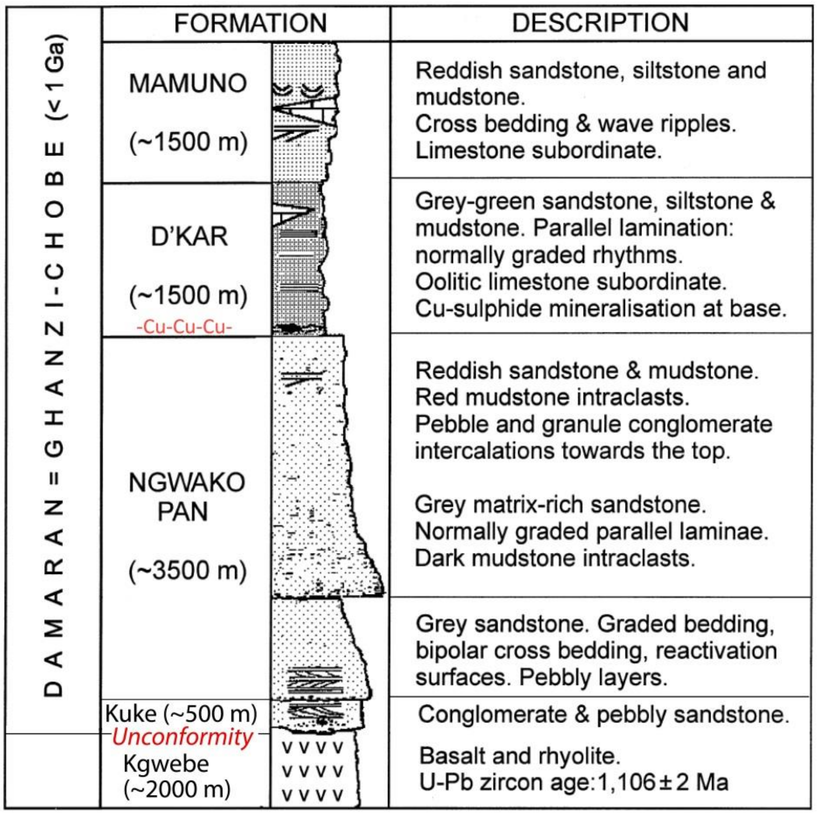

Figure 2.18: Generalised lithostratigraphic column of the Kgwebe Formation and overlying Ghanzi Group (modified after Kampunzu *et al*., 1998).

To the northeast in the Goha and Chinamba Hills area (Figure 2.17), are basal felsic volcanics informally referred to as the Goha Hills Formation, which represent the proposed continuation of the Kgwebe Formation (Modie, 2000). The Goha Hills Formation contains massive feldspar porphyry with subordinate pyroclastic flow deposits (Modie, 2000), which outcrop in the cores of tight fold structures (Carney *et al*., 1994). The Goha Hills Formation are suggested to be the lateral equivalents to the Kgwebe Formation based on SHRIMP-date of 1 106.2 ± 3.6 Ma (Singletary *et al*., 2003).

The Ghanzi Group

The Ghanzi Group unconformably overlies the Kgwebe Formation (Figure 2.18). The Ghanzi Group consists of siliciclastic sedimentary rocks with subordinate carbonate beds, and has a lateral variation in thickness from ~13 500 m in the Mamuno area to slightly over 5 000 m south of Lake Ngami (Figure 2.15) (Modie, 2000). The original stratigraphic nomenclature of the Ghanzi Group is derived from the studies of Borg and Maiden (1989) and Modie (1996), who divided the Ghanzi Group into the Lower and Upper D'Kar Formations, overlain by the Jakkalsputs Formation. Kampunzu *et al*. (1998) and Modie (2000) modified this stratigraphic nomenclature, to include a basal Kuke Formation, which is unconformably overlain by the Kgwebe Formation, followed by the Ngwako Pan Formation (previously Lower D'Kar Formation), D'Kar Formation (Previously Upper D'Kar Formation) and Mamuno Formation (previously Jakkalsputs Formation) (Figure 2.18).

The informally referred to Kuke Formation is the basal unit of the Ghanzi Group comprising of medium-grained quartz arenites with mudstone intraclasts and conglomerates (Figure 2.18) (Modie, 2000). It was previously assigned to the Kgwebe Formation (Modie, 1996; Kampunzu *et al*., 1998) or to the base of the Ngwako Pan Formation (Kampunzu *et al*., 2000). The Kuke Formation unconformably overlies the Kgwebe Formation and contains fragments of it (Kampunzu *et al*., 2000).

The Kuke Formation is overlain by the Ngwako Pan Formation, which varies in thickness from ~2 000 m in the Ghanzi Ridge area (Modie, 2000) to 3 500 m in the Hana Mining licence area, northeast of the Ghanzi Ridge (Figure 2.17) (Kampunzu *et al*., 2000; Pretorius and Park, 2011). The basal part is composed of poorly sorted, mudstone matrix grey sandstone overlain by better sorted red sandstones and arkoses, which are locally interbedded with pebbly layers and granulestones (Modie, 1996).

The D'Kar Formation conformably overlies the Ngwako Pan Formation (Figure 2.18) (Modie, 2000, Kampunzu *et al*., 2000). It comprises parallel laminated grey-green siltstones and mudstones interbedded with sandstones (Modie, 1996; Modie, 2000). At the base of the formation, locally oolitic, discontinuous, limestone units and marls occur (Master, 2010). The formation is dominated by chemically reduced facies rocks, which are characterised by an abundance of disseminated chalcopyrite, bornite, chalcocite, pyrite, pyrrhotite, malachite, azurite, and organic rich shales, sometimes rich enough in carbon to be termed black shales (Modie, 2010; Master, 2010; Hendjala, 2011).

The uppermost unit is the Mamuno Formation, which conformably overlies the D'Kar Formation (Figure 2.18) (Modie, 2000, Kampunzu *et al*., 2000). The formation consists of well-sorted, arkosic sandstone, interbedded with siltstone, limestone and mudstone (Modie, 1996). In northeast Botswana, the rocks of the Goha Hills Formation are overlain by limited exposures of carbonate-bearing siliciclastic sedimentary rocks of the informally referred to Chinamba Hills Formation (Key and Ayres, 2000). These rocks are composed of fine-grained sandstone, which are lithologically similar to and correlated with the Mamuno Formation (Carney *et al*., 1994; Key and Ayres, 2000).

Age constraints on the Ghanzi-Chobe Supergroup

Determining the depositional age of the Ghanzi Group through conventional age dating techniques is challenging because of the lack of intra-formational volcanic rocks. However, the application of chemostratigraphy has provided a way of dating carbon isotopes in marine carbonates. Chemostratigraphy is the study of stratigraphic variations in sediment chemical compositions (Halverson *et al*., 2005). These studies investigate the chemical constitutes that are proxies for seawater chemistry or environmental conditions at the time as, or shortly after deposition of the sediments (Halverson *et al*., 2010). Stable isotopes are known to experience low temperature mass fractionation, and are thus suitable proxies for seawater chemistry, especially during the Neoproterozoic (Frimmel, 2010). At least two global glaciation events are known in the Earth's history. As Earth's carbon cycle is affected by these glaciation events the marine sedimentary units, which are precipitated during the time of glaciation, exhibit major variations in their $\delta^{13}C$ forming both negative and positive anomalies (Halverson *et al*., 2010). $\delta^{13}C$ denotes the isotopic ratio of carbon 13 to carbon 12 within a globally accepted standard, for this case, the Vienna Pee Dee Belemnite (V-PDB) as outlined by Craig (1953). These large fluctuations and reproducibility in carbon isotope composition in Neoproterozoic oceans was first documented by Knoll *et al*. (1986). Noting that these fluctuations track global ice ages Knoll and Walter (1992) predicted the usefulness of using carbon isotopes as a chronostratigraphic correlation tool for unaltered Neoproterozoic carbonates.

Halverson *et al*. (2005) compiled a $\delta^{13}C$ database incorporating most of the Neoproterozoic, which included both historical data and data collected by the authors from Svalbard, Namibia and Oman. Interpretation of this compilation of data led Halverson *et al*. (2005) to suggest that there were three Neoproterozoic global glacial events, which is in agreement with the studies of Knoll (2000), Hoffman and Schrag (2002) i.e. the Sturtian (710 Ma) (Hoffman *et al*., 1998), Marinoan

(635.5 ± 1.2 Ma) (Hoffmann *et al*., 2004) and Gaskiers (speculated at being Neoproterozoic, post-Marinoan but exact age is not known, Halverson *et al*. 2005 and 2010) glaciations. Halverson *et al*. (2005) discovered the global Bitter Spring negative carbon isotope anomaly which is between 802 ± 10 Ma and 777 ± 7 Ma. Chemostratigraphy dating on several basal carbonate samples of the D'Kar Formation by Master (2010) yielded $\delta^{13}C$ values ranging from -7.33 to + 3.36 permil (‰) V-PDB. The overall age of the Ghanzi Group is bracketed between 1 047 ± 24 Ma (youngest detrital zircons; Kampunzu *et al*., 2000) and 550 Ma (age of metamorphism), but is most likely older than 750 Ma because of the lack of glacial strata (Master *et al*., 2012). This allows for the proposed dates of the Kuke and Ngwako Pan Formations to be between 1 050 Ma and 800 Ma, while the upper portion of the D'Kar and lower part of the Mamuno Formations to lie between 780 Ma and 750 Ma (Master *et al*., 2012).

2.5.3. Okavango Zone

The Okavango Zone in northwest of Botswana (Figure 2.15) consists of the Roibok and Kihabe/Koanaka Groups, and Kwando Complex (the nomenclature, Koanaka Group is more common in the literature compared to Kihabe Group, and as they both describe the same outcrop area, this study uses the term Koanaka Group). The Roibok Group and Kwando Complex have been intersected by the NG and CKP10 boreholes respectively, while the Koanaka Group is known from exposures in the Kihabe Hills area (Figure 2.19) (Carney *et al*., 1994; Singletary *et al*., 2003). The limited exposures display northwest verging folds. This implies an opposite transport direction to the Ghanzi-Chobe Zone (Figure 2.15). The zone is tectonically bounded by the Pleistocene Okavango Rift, which resulted in Proterozoic rocks in the northeastern part of the zone overlying younger rocks at a depth of 365 m (interpreted from borehole CKP-10A) (Carney *et al*., 1994). The southeastern limit was considered to be equivalent to the Areb Mylonite Zone, in Namibia (Lüdkte *et al*., 1986, in Carney *et al*., 1994). This zone was proposed to correlate in part with the Southern Zone of the Damara Belt, and its northwestern margin might contain the eastward continuation of the Okahandja Lineament Zone (Carney *et al*., 1994).

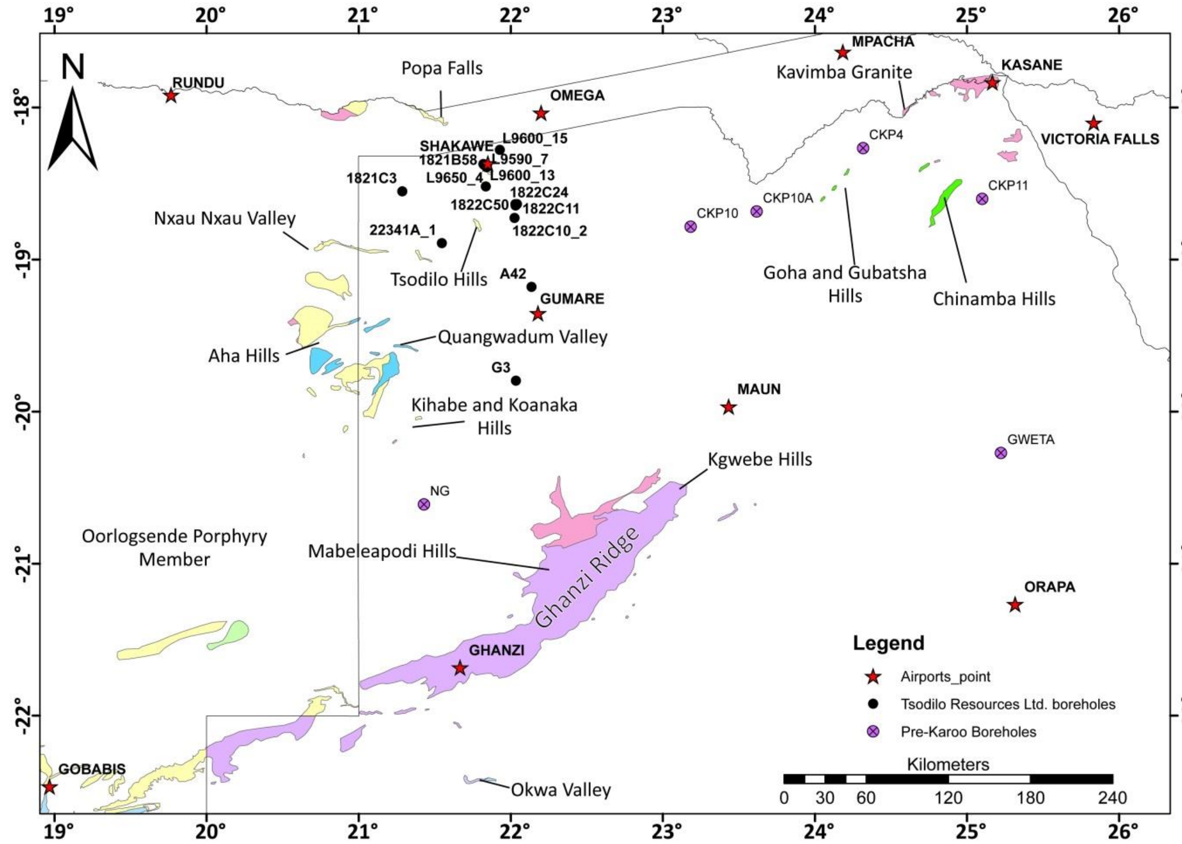

Figure 2.19: Location of outcrops and pre-Karoo research boreholes (purple circle with cross) (after Carney *et al*., 1994; Singletary *et al*., 2003) and Tsodilo Resources Ltd. boreholes used in this study (black circles). Towns and villages (red stars) are shown as a point of reference. See Figure 2.17 for legend.

Roibok Group

The Roibok Group is an unexposed terrain in the northwest of Botswana (Figure 2.15) with its geological information known from several closely spaced NG boreholes (Figure 2.19) (Singletary *et al*., 2003). Beneath the Kalahari beds, metamorphic rocks were intersected in the boreholes, which Lüdkte *et al*. (1986, in Carney *et al*., 1994) believed to be prominent magnetic markers. Paragneiss was intersected with foliation dipping to the southeast and isoclinal northwest verging folds (Carney *et al*., 1994). At a depth of 110 m, the lithologies are more mafic-rich, with abundant euhedral garnet porphyroblasts (Singletary *et al*., 2003). At greater depths, the deformation is more mylonitic (Carney *et al*., 1994). Beneath this breccia are strongly layered mylonites, which contain traces of chrysocolla (hydrated copper silicate) (Lüdtke *et al*., 1986, in Carney *et al*., 1994). In borehole NG 2, basement was intersected at 26 m, and from 102 m to 156 m, the core consists of biotite amphibolite interlayered with biotite-hornblende schist (Singletary *et al*., 2003). The bottom of the NG 3 core (45 m to 153 m) displays a well-foliated, fine-to medium-grained amphibolite (Carney *et al*., 1994). In the NG 5 core, at a depth of 98 m to 150 m, biotite-hornblende-plagioclase schists are interleaved with concordant lenses of a coarse-grained biotite granitoid, which appears to be *in-situ* (Carney *et al*., 1994).

Lüdkte *et al*. (1986, in Carney *et al*., 1994) recognised three types of amphibolite; massive amphibolite, massive garnet amphibolite and foliated epidote-plagioclase-(biotite) amphibolite. Along fracture planes, amphibolite is replaced by chlorite and garnets are chloritised and partly replaced by epidote. Chemical analyses showed that these amphibolites contain 45% to 53% silica (Lüdkte *et al*., 1986; in Carney *et al*., 1994). The majority of the amphibolites were classified as subalkaline and iron-rich with a tholeiitic trend indicated on the AFM triangular plot and Jensen Diagram. A spread of compositions between ocean floor and low-K tholeiitic basalt types are shown on trace element plots (Carney *et al*., 1994). Lüdkte (1986, in Carney *et al*., 1994) concluded that the Roibok amphibolites may represent basaltic protoliths of ocean floor or primitive island arc tholeiite affinity.

^{207}Pb-^{206}Pb dating on twelve zircons from the drill core of NG 2 plotted near the concordia with an age range of 718.8 ± 3.8 Ma to 659 ± 10.6 Ma (Singletary *et al*., 2003). The four oldest zircons yielded a ^{207}Pb-^{206}Pb weighted mean age of 716.8 ± 2.2 Ma representing the igneous crystallisation age (Singletary *et al*., 2003). Sm-Nd isotropic signatures indicate derivation from a Neoproterozoic crust with a short residence time (ε_{Nd} = -3.1 and a T_{dm} age = 845 Ma; Singletary *et al*., 2003). Tsodilo Resources Ltd. drilled borehole G3 into an aeromagnetic high anomaly situated less than 900 m (horizontal distance) from the Roibok Group (Figure 2.19). G3 intersected a foliated pink granite-gneiss. Singletary *et al*. (2003) is uncertain about the tectonic significance of the Roibok Group but suggests that the granites were emplaced during early stages of rifting of the basin in which the Damaran Sequences accumulated.

Kwando Complex

The Kwando Complex is an unexposed gneiss-granitoid unit with its inferred distribution in the northeastern part of the Okavango Zone (Figure 2.15) based on the interpretation of aeromagnetic data (Carney *et al*., 1994). Two boreholes, CKP-10 and CKP-10A, have been drilled into this domain to intersect positive aeromagnetic anomalies whose source rocks are not necessarily typical of the Kwando Complex as a whole (Figure 2.19) (Singletary *et al*., 2003). CKP-10 intersected granitic gneiss with amphibolite layers grading downwards into hornblende-biotite feldspar gneiss at a depth of 218 m (Carney *et al*., 1994). Further downhole, the rock is a migmatite composed of interlayers of biotite-gneiss and feldspathic coarse-grained leucosome, which grades to granitic orthogneiss at 300 m (Carney *et al*., 1994). The rock grades downwards to a meta-diorite (Carney *et al*., 1994). Singletary *et al*. (2003) dated nine zircons from the typical granite-gneiss and foliated granite with the same mineralogy. All zircons dated by SHRIMP were discordant. Three zircons yielded an age close to 1 150 Ma with the oldest zircon age being 1 204 ± 2.9 Ma (Singletary *et al*., 2003). From these age dates Singletary *et al*. (2003) suggest that granite emplacement in the Kwando Complex occurred during the Mesoproterozoic at 1.20 Ga to 1.15 Ga. Sm-Nd isotropic analysis, at 1 150 Ma, produced an initial ε_{Nd} value of +2.2 and a T_{dm} model age of 1 295 Ma. These data and the age data suggest that the granite protolith to gneiss was derived from a source with a short crustal residence time (Singletary *et al*., 2003).

Borehole CKP-10A (Figure 2.19), at a depth of 365 m, intersected a heterogeneous rock, which is locally coarse-grained with a metagabbroic characteristic (Carney *et al*., 1994). At a depth of 374 m, a low-grade, weakly metamorphosed gabbro to diorite was intersected, which continues to a depth of 439 m (Singletary *et al*., 2003). Singletary *et al*. (2003) analysed one baddeleyite (zirconium oxide mineral) and seven zircons. Analysis of one zircon grain and the baddeleyite grain have a concordant relationship and along with another zircon grain yielded a ^{207}Pb-^{206}Pb weighted mean age of 1 107 ± 0.8 Ma, which was interpreted as the crystallisation age of the intrusion (Singletary *et al*., 2003). Singletary *et al*. (2003) suggests that the metagabbro to dolerite was emplaced after the amphibolite-grade deformation event recorded in the granitic gneiss and that the metagabbro to dolerite represents the younger limit of the primary orogenic event in the Kwando Complex. The similar crystallisation ages for the metagabbro to dolerite and the granite within the Northwest Botswana Rift to the east suggest that the metagabbro is part of a regional magmatic event (Singletary *et al*., 2003).

Koanaka Group

The Koanaka Group lies in the northern part of the Okavango Zone and consists of dolostone and chert that are locally exposed in a series of low hills (Kihabe and Koanaka Hills) (Figure 2.19) (Carney *et al*., 1994) as well as metapelite and possible paragneiss (Key and Ayres, 2000). According to Wright (1958e, in Carney *et al*., 1994) the main lithologies of the Koanaka Group are massive, recrystallised dolostone, which include ankerite, siderite and sericite (defining bedding) or talc as accessory minerals. Vermaak (1962, in Carney *et al*., 1994) also observed tremolite, wollastonite and garnet. Field and outcrop observations suggest that the dolostone has been folded into isoclinal northwest verging structures (Vermaak, 1962, in Carney *et al*., 1994). The lithostratigraphic affinity of the Koanaka Group is ambiguous, as it appears different to the dolomitic chert units of the Aha Hills Formation, to the north and it crops out in a considerably more deformed part of the orogen (Carney *et al*., 1994).

2.5.4. Shakawe Zone

The Shakawe Zone is the northern most tectonostratigraphic zone in Botswana (Figure 2.15) with lithologies, structures and styles of mineralisation correlating with the Northern Platform (Carney *et al*., 1994). The zone consists of five main geological units; the Quangwadum and Chihabadum Complexes, Aha Hills Formation, Tsodilo Hills and Xaudum Groups. The literature of this zone is complicated with the Aha Hills Formation, Tsodilo Hills and Xaudum Groups being grouped into either the Xaudum Group or Tsodilo Hills Group. For the purpose of this study these units are considered separately with the lithologies described in the literature from outcrops assigned to the respective unit.

Quangwadum Complex

On the northern margin of the Aha Hills, in the Quangwadum Valley (Figure 2.17), granitoids outcrop for 15 km (Carney *et al*., 1994; Singletary *et al*., 2003). On the eastern end of the outcrop are porphyritic granites (Key and Ayres, 2000). Other lithologies in the area include talc-quartz schist, which occurs a short distance downstream from the Quangwa village, and banded biotite-quartz gneiss on the northern slopes of the Aha Hills (Wright, 1958b, in Carney *et al*., 1994). The western extent of the outcrop consists of biotite- muscovite- bearing granite, which also occurs as dykes cutting the porphyritic granite and augen gneiss (Singletary *et al*., 2003). There is evidence for two deformation events preserved within the talc-quartz schists (Wright, 1958b, in Carney *et al*., 1994). The first fabric is the main subvertical, northeast-southwest schistosity, which is cut by an east-northeast spaced cleavage, which may be axial planar to the prominent direction of folding in the dolostones in the Aha Hills (Figure 2.17) (Wright, 1958b, in Carney *et al*., 1994).

The best estimate of the crystallisation age was provided by a ^{207}Pb-^{206}Pb zircon age of 2 050.5 ± 0.6 Ma for an augen-gneiss sample with a corresponding ε_{Nd} value of -3.5 and T_{dm} model age of 2 551 Ma (Singletary *et al*., 2003). These data indicate that Archaean crustal components were involved in the petrogenesis of the granite protolith to the gneiss (Singletary *et al*., 2003). A porphyritic granite sample was dated and the discordia showed an upper intercept of 1 022.3 ± 1.3 Ma, which was interpreted as the igneous crystallisation age (Singletary *et al*., 2003). Only a discordant zircon analysis was obtained from the biotite-muscovite granite. The most concordant analysis, led Singletary *et al*. (2003) to propose that the crystallisation age of the fine-grained granite is 1.02 Ga to 1.00 Ga. The tectonic setting of these fine-grained granites is unknown but Singletary *et al*. (2003) suggests that they are younger and unrelated to the regional Mesoproterozoic magmatic event recorded in Botswana and Zambia. $^{40}Ar/^{39}Ar$ muscovite age of 533.3 ± 2.3 Ma for one of the shear zones in the Quangwadum Complex was interpreted to represent an overprinting of basement during Damaran Orogenesis (Singletary *et al*., 2003).

Chihabadum Complex

The Chihabadum Complex is unexposed and from its aeromagnetic signature Key and Ayres (2000) interpreted it to be comprised of igneous to meta-igneous rocks; there are no drill core samples from this unit (Singletary *et al*., 2003).

Aha Hills Formation

The Aha Hills Formation is exposed in the Aha Hills area (Figure 2.19) and consists of chert-rich limestones and dolostones (Key and Ayres, 2000). On a sheared contact the sandy, limestone, magnesian and calcareous limestones unconformably overlie the Quangwadum Complex (Carney *et al*., 1994). Several beds of phyllite, algal mats, stromatolitic units and layers of black chert also form intercalations (Carney *et al*., 1994). The Aha Hills Formation consists of a mineralised basal sedimentary sequence of dolostones, shales, ferruginous sandstones and phyllites locally, containing pyrite and graphite (Loxton Hunting and Associates, 1981; in Carney *et al*., 1994). In the Aha Hills, fold trends are orientated at 070°E of north, as determined from the interpretation of Landsat 1 imagery (Hutchins *et al*., 1976).

Tsodilo Hills Group

The Tsodilo Hills Group is exposed in small outcrops in the Tsodilo Hills and Shakawe area (Figure 2.19). In the Tsodilo Hills area the Tsodilo Hills Group is composed of rocks metamorphosed to kyanite-grade including, quartz-muscovite-kyanite schist, meta-conglomerate, quartz-mica schist with minor metapelite, meta-sandstone, ferruginous quartzite and iron formation (Carney *et al*., 1994; Key and Ayres, 2000; Wendorff, 2005). Exposures in the Tsodilo Hills define a northwest-southeast striking belt with lithological layering heavily deformed by tight, mesoscopic folds with northeast dipping axial surfaces (Wendorff, 2005). In the Shakawe area the Tsodilo Hills Group is represented by ferruginous quartzite and biotite gneiss, which are tightly folded (Key and Ayres, 2000). An iron formation, exposed in a quarry at Shakawe contains thin layers of recrystallised quartzite as well as garnet-mica schist, suggesting that it is of similar metamorphic grade to the quartz-rich rocks outcropping in the Tsodilo Hills (Singletary *et al*., 2003). The abundance of iron formations in this group helps to define the pronounced north to northwest subsurface structural trend observed in the aeromagnetic maps (Singletary *et al*., 2003).

The depositional age of the Tsodilo Hills Group is constrained by a $^{40}Ar/^{39}Ar$ muscovite deformation age of 490 ± 2.3 Ma (Singletary *et al*., 2003). SHRIMP analysis on 250 detrital zircons collected from four kyanite- muscovite quartzite samples of the Tsodilo Hills Group included 235 concordant to near concordant zircons with the main population (152) yielding an approximate age of 2.09 Ga to 1.92 Ga (Mapeo *et al*., 2008). These age data indicate that the younger depositional age of the Tsodilo Hills Group is ~1 959 Ma (Mapeo *et al*., 2008). Four granitoid gneiss samples yielded a total of 76 zircons of which 10 were less than 10% discordant (Mapeo *et al*., 2008). The age dates constrain the emplacement and deformation of the granitoids at ~2.07 Ga to 1.96 Ga (Mapeo *et al*., 2008). Mapeo *et al*. (2008) suggests that the potential source of the siliciclastic metasedimentary rocks of the Tsodilo Hills Group is these granitoid gneisses.

Xaudum Group

The Xaudum Group consists of metasedimentary rocks dominantly exposed along the Nxau Nxau Valley and Xaudum Valley (Carney *et al*., 1994) with limited exposures of cleaved argillites at Popa Falls in the Caprivi Strip (Figure 2.19) (Miller and Schalk, 1980). The exposed rocks in the westernmost portion of the Xaudum Valley (Figure 2.15) contain a variety of metasedimentary rocks including, shales and sandstones which structurally comprise the lower-most portion of the Xaudum Group (Carney *et al*., 1994). Wright (1957; in Carney *et al*., 1994) describes these rocks as quartzite with sandstone compared to the description of shale and dolostone in the same succession (Lemaire, 1971; in Carney *et al*., 1994). Overlying this mixed package are chert bearing dolostones, similar to those found in the Aha Hills. At the base of this assemblage, Wright (1957, in Carney *et al*., 1994), describes alterations between cherty limestones and calcareous siltstones with sandstone bands. Carney *et al*. (1994) describes an intraformational conglomerate that contains lenticular clasts of silicified limestone. Lemaire (1971, in Carney *et al*., 1994) also identified talc-schist layers and wollastonite. East of the Xaudum Village, Lemaire (1971, in Carney *et al*., 1994) observed sideritic limestone, which appears to cap the dolomitic-chert unit, exposed further westwards (Figure 2.19). In the Xaudum Valley these metasediments are folded to define tight north-northeast trending dome and basin structures visible on the aeromagnetic maps (Carney *et al*., 1994). In the Nxau Nxau Valley (Figure 2.19), exposures consist of marbles and associated siltstones and further to the northwest, near the Namibian border, in a hand-dug well for water, coarse-grained siliciclastic rocks have been exposed (Singletary *et al*., 2003).

Approximately 65 km north of the Xaudum Valley, within an area of subcrop, between the Xaudum Valley and Popa Falls (Figure 2.19), Mapeo *et al*. (2000) observed samples, in pits dug for water, of immature conglomeratic and arkosic sandstone associated with mature sandstone, siltstone and shale. Mapeo *et al*. (2000) analysed 13 detrital zircons from an immature coarse-grained sandstone sample and reported the youngest concordant ^{207}Pb- ^{206}Pb weighted mean age of 1 019 ± 7 Ma. From this Mapeo *et al*. (2000) interpreted that the depositional age for the Xaudum Group is between 530 Ma and 1 020 Ma. Two data outliers yielded ^{207}Pb-^{206}Pb ages of 2 055 ± 14 and 2 043 ± 16 (Mapeo *et al*., 2000). These age dates fall within the age error of the Quangwadum Complex dated by Singletary *et al*. (2003) suggesting that the Quangwadum Complex may be the source of the detrital zircons.

2.6. Regional geophysical studies of Namibia and Botswana

The following sections discuss the regional aeromagnetic, gravity and electrical surveys conducted in Namibia and Botswana. The local geophysical surveys are discussed in the subsequent chapters.

2.6.1. Namibia

Regional geophysical surveys have been conducted in Namibia since 1962 (Eberle *et al*., 2002). Preliminary regional interpretations of the aeromagnetic data sets include work by Corner (1982; 1983; 2000) and Eberle *et al*. (1996; 2002). From the interpretation of aeromagnetic and gravity data, Corner (2000; 2008) defined numerous regional geophysical lineaments, the margins of the

Congo and Kalahari Cratons, and the eastward continuation of the tectonostratigraphic zones of the Damara Belt (Figure 2.20, Table 2.1).

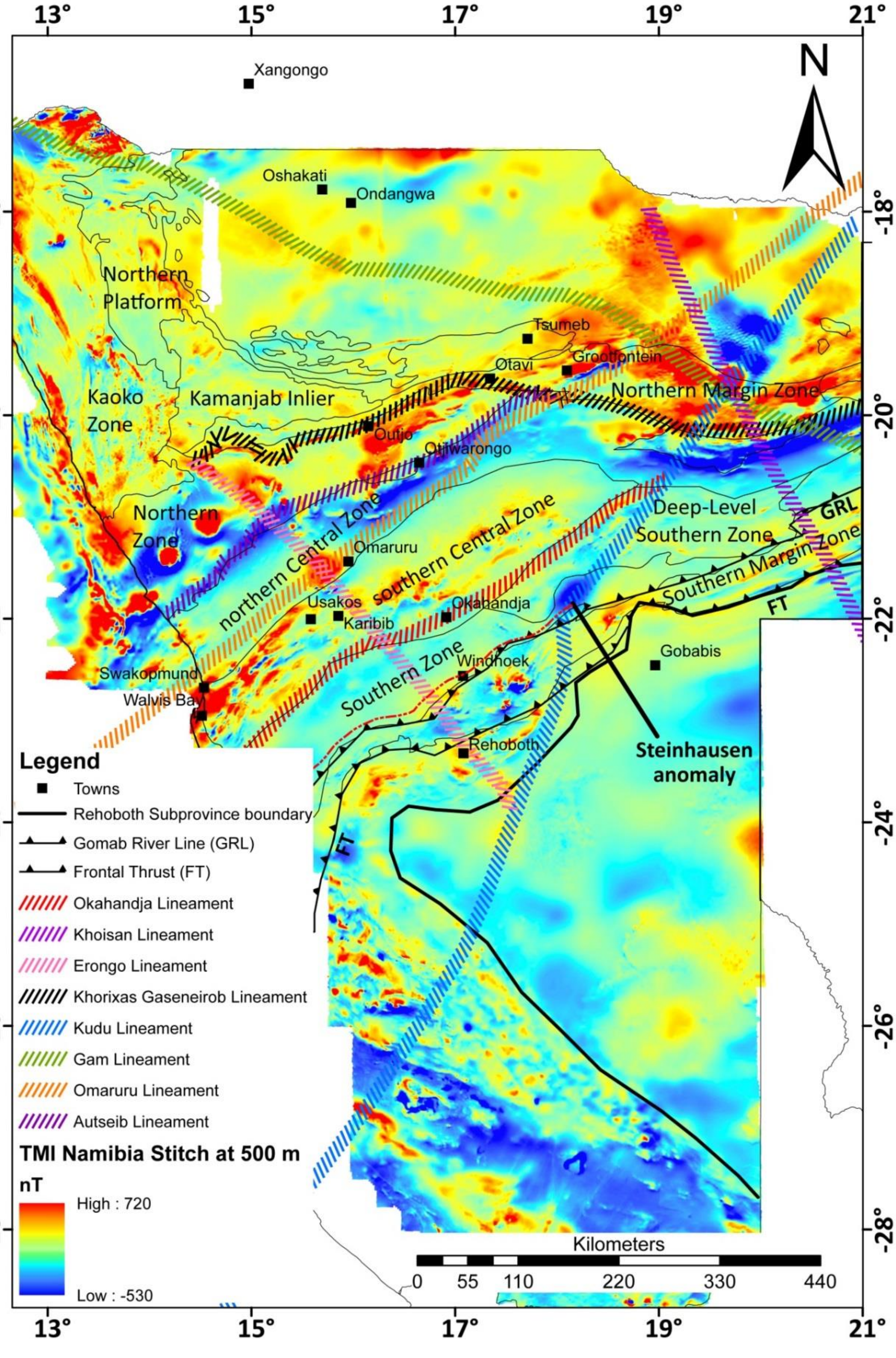

Figure 2.20: Selected structural features and geophysical lineaments overlain on the Total Magnetic Intensity map of Namibia (after Corner, 2008). The eastern segment of the Frontal Fault has been moved ~50 km further north than previously mapped (Corner, pers. comm., 2013).

Table 2.1: North to south summary of the geophysical lineaments in the Damara Belt as referred to in Figure 2.20 (after Corner, 2000, 2008).

Lineament	Major features within the swath of the Lineament
Gam	A NNW striking dyke that also forms the position of a belt of basalts within the Owambo Basin (Figure 2.4) suggesting a Karoo age.
Khorixas-Gaseneirob	Delineates a major structural boundary or transition zone between the Northern Zone and Northern Margin Zone (Figure 2.4).
Autseib	Marks the boundary between the Central Zone and the Northern Zone (Figure 2.4). Includes the geologically mapped Autseib Fault and Otjihorongo Thrust to the northeast. It delineates a prominent magnetically low, long-wavelength feature that strikes northeast from north of Henties Bay, passing south of Uis, through Otjiwarongo, and eastwards into northwest Botswana where it terminates. In the west, this magnetic anomaly correlates with the Autseib Lineament and continues eastward along the Khorixas-Gaseneirob Lineament east of Grootfontein. Geophysical evidence suggests that the Autseib Lineament results from the relative uplift of magnetically anomalous lower Nosib Group rocks to the northwest resulting in a change of the magnetic signal.
Waterberg Fault/Omaruru Lineament (WF/OL)	Boundary between the magnetically anomalous southern Central Zone and the magnetically quiet northern Central Zone (Figure 2.4). The Omaruru Lineament continues northeastward as the Waterberg Fault and south-westward (offshore) as the Walvis Fracture Zone. For simplicity this study has termed these lineaments as the Waterberg Fault/Omaruru Lineament.
Okahandja	Boundary between the Southern Zone and the southern Central Zone (Figure 2.4) evident in both geological mapping and aeromagnetic interpretation. In the west, there is major down-faulting to the southeast exposing the magnetically anomalous rocks of the southern Central Zone in the northwest. In the east, uplift occurs exposing possible pre-Damara sequences.
Kudu	The swath of the Kudu Lineament is associated with a series of NNE trending faults with Pre-Damaran rocks of the Deep-Level Southern Zone centred on the swath of the lineament (Figure 2.4). This observation and the narrowing of the Damara Belt considerably to the east of this lineament is likely to be the reason that either the Okahandja Lineament or the Matchless Member has been clearly identified geologically or in the aeromagnetic data east of this lineament. The Kudu Lineament is interpreted to cut the Damara trend, implying that it is younger than the Damara Orogen.
Erongo	Identified in the aeromagnetic data by using a modification of the analytic signal which includes the effect of deeper sources. Therefore, it is suggested to be a deep feature possibly being part of a flexure or regional open fold axis. Intrusions occur on its intersection with the Okahandja Lineament and WF/OL (Figure 2.4).
Khoisan	Associated with NNW trending faults in the southern portion of the Omatako Ring Structure (Figure 2.4). The lineament continues into Botswana where it faults the Kalahari Suture Zone.

From regional aeromagnetic data sets, Eberle *et al*. (1996) describes the magnetic signal of the cratonic regions and the Damara Belt. Accompanying these interpretations is a magnetic lineament map delineating near surface lineaments and structures (Figure 2.21). The cratonic regions are defined by extended, mid-amplitude magnetic anomalies resulting from deep-seated sources. The depth to the magnetic basement on the Botswana side is from 5 km to 10 km, while the Namibian portion of the Kalahari Craton is at a depth of 14 km to 18 km (Eberle *et al*., 1996). The overall magnetic signature of the Damara Belt can be described as consisting of strongly linear magnetic and non-magnetic zones. Each of the tectonostratigraphic zones of the Damara Belt has its own distinct magnetic signal (Eberle *et al*., 1996; Corner, 2008). The magnetic characteristics of the Rehoboth Subprovince and Damara Belt are briefly discussed below;

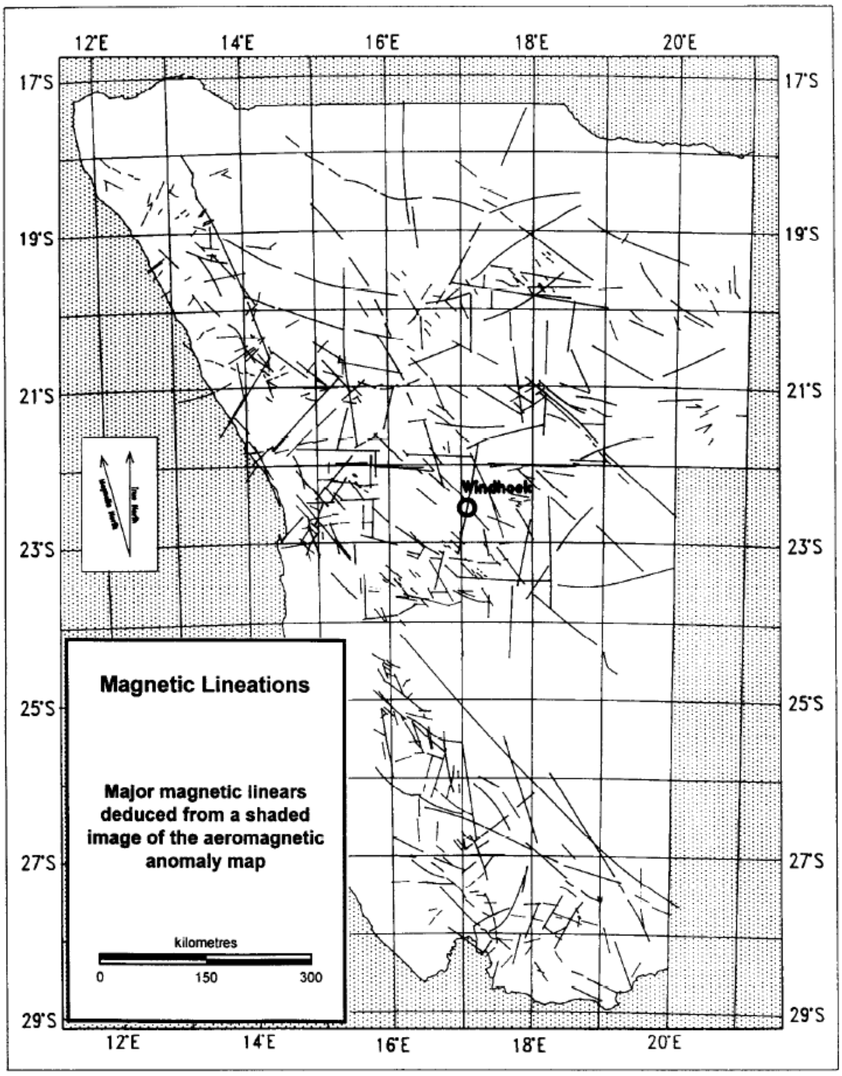

Figure 2.21: Major magnetic lineations of Namibia interpreted by Eberle *et al*. (1996).

The Sinclair Supergroup and associated intrusions in the southwest of Namibia (Figure 2.1) have a curvi-linear, high amplitude magnetic signal caused by the volcanic lithologies (Corner, 2008).

The Southern Margin Zone (Figure 2.20) comprises two magnetic subzones each with a superimposed magnetic pattern. The southern subzone is less deformed than the northern subzone and contains pre-Damaran basement rocks of the Sinclair Supergroup that results in circular shapes that have high magnetic amplitude (Eberle *et al*., 1996; Corner, 2008). The Southern Margin Zone is clearly identified in the aeromagnetic data by the contrast between the noisy, high magnetic amplitude of the zone compared to the smooth, low to moderate amplitudes of the Southern Zone (Corner, 2008). A magnetic fabric is also evident in the diamictites of the Berghof and Waldburg Formations and to a lesser extent in the Nosib Group metasediments (Corner, 2008).

As a result of the thick package of Kuiseb schists, the Southern Zone is magnetically quiet with a few exceptions aligned parallel to the general geological strike (Figure 2.20) (Eberle *et al*., 1996; Corner, 2000). Local exceptions are the magnetic schist units and quartzites associated with the Matchless Member. Approximately 30 km north of the Matchless Member, similarly shaped magnetic anomalies occur, which Eberle *et al*. (1996) interpreted as graphitic units within the Kuiseb schist.

In the Steinhausen area and northeast thereof, the magnetic signal of the Southern Zone and southern Central Zone changes dramatically (Figure 2.20) (Corner, 2008). In the Deep-Level Southern Zone (Figure 2.20) the schists of the Kuiseb Formation have high magnetic amplitude and other magnetic rocks include gabbro and epidosite (Corner, 2008). Gabbro has been reported in several boreholes and outcrops in exploration reports (Corner, 2008). To the north, there is an east-west trending belt of high magnetic amplitude anomalies that cross-cut the Southern Zone and southern Central Zone (Figure 2.20) (Corner, 2008). The high magnetic amplitude correlates with Fe-Mn reefs and drilled magnetic quartzites (Corner, 2008). The inclusion of these strata in the Damara Supergroup has been questioned by Hoffman (1989) and is suggested to form part of the pre-Damara basement.

The high amplitude magnetic signatures of the southern Central Zone (Figure 2.20) are associated with the Nosib Group, Chuos diamictites (lower Swakop Group) and the Meso- and Palaeo-proterozoic basement (Corner, 2008). The magnetic units are exposed in domal and anticlinal structures with a northeast trend. The magnetically inert carbonates and schists of the lower Swakop Group are preserved in the intervening synclines (Corner, 2008). On a regional scale the amplitudes of these anomalies decrease continuously to the east along the geological strike of the Damara Belt (Eberle *et al*., 1996). Locally, the granite phases are magnetic, particularly if they form part of the Nosib Group and basement (Corner, 2008). In the western portion of this zone the high-grade metamorphic lithologies of the Etusis and Khan Formations (Nosib Group), as well as in their granitic derivatives, are strongly magnetic with high magnetic amplitude anomalies retaining the Damaran remanence (Corner 2008).

A thick succession of magnetically inert Karibib carbonates and Kuiseb schists are preserved in the northern Central Zone, which gives an overall quiet magnetic signal (Figure 2.20) (Corner, 2008). The majority of the northern Central Zone (Figure 2.4) granites are magnetically inert. However, locally the granites are magnetic, which provides a magnetic fabric for the northern Central Zone (Figure 2.20) (Corner, 2008).

The transition from the northern Central Zone to the Northern Zone is characterised by a strong negative, deep-seated magnetic anomaly, which trends in an east-northeast direction from the Namibian coast in the west towards the Botswana border (Figure 2.20) (Eberle *et al*., 1996). Eberle *et al*. (1996) proposes that this remanent magnetic feature is possibly a failed rift or subduction zone beneath the Congo Craton. Corner (2008) interprets this magnetic low as the Autseib Lineament (Figure 2.20, Table 2.1) and in part the Autseib Fault.

The Northern Zone has a high magnetic signal (Figure 2.20) which is enhanced by field contributions from the deep-seated negative magnetic feature, to the south, as well as from extensive magnetic massifs directly beneath (Eberle *et al*., 1996). If these massifs are not obducted mafic volcanics of the Askevold Formation, possibly oceanic crust, they can be assumed to originate from the shallower iron formations of the Chuos Formation (Eberle *et al*., 1996).

The Northern Margin Zone has an unusual magnetic signal (Figure 2.20) produced by the phyllites and quartzites of the Mulden Group, which are usually non-magnetic, however, they display high amplitude remanent magnetisation, which Corner (2008) interprets as secondary magnetisation caused by pyrrhotite mineralisation that developed through hydrothermal activities along the Khorixas-Gaseneirob Lineament (Figure 2.20**,** Table 2.1) (Corner, 2008).

The magnetic data of the Northern Platform displays predominant east-west trending anticlinal structures (Figure 2.20) (Corner, 2008). These structures separate vast magnetically inert Mulden Group rocks, preserved in the synclines, from the higher amplitude magnetic signal associated with exposed or shallow diamictites and possible volcanics associated with the lower Damaran sequences within the antiforms (Corner, 2008).

2.6.2. Botswana

Geophysical exploration in Botswana grew in the 1950s to early 1980s and was directed to the discovery of groundwater, using mostly electrical resistivity techniques (Hutchins and Reeves, 1980). Mineral exploration surged in the 1960s and brought with it the introduction of other ground geophysical techniques first by the Botswana government then by exploration companies. These studies were conducted locally in areas of geochemical anomalies and ancient mineral workings (Hutchins and Reeves, 1980).

The existence of the Kunyere, Thamelakane and Mababe Faults of the Okavango Rift Zone were confirmed during a 1970 to 1971 gravity survey in the Ngamiland district (Hutchins and Reeves, 1980). These faults are characterised by an increase in seismic activity and are associated with seismic activity observed in Zambia (Hutchins *et al.*, 1976; Hutchins and Reeves, 1980). The first national gravity survey of Botswana was completed in 1973, tying-in with the Ngamiland gravity survey (Hutchins and Reeves, 1980). Preliminary interpretations on the resulting Bouguer anomaly map showed the existence of a gravity gradient that followed much of the length of the northeast-southwest seismicity axis across the central Kalahari, which divided the Bouguer gravity map into two distinctly different areas (Hutchins and Reeves, 1980). To the southeast of the seismicity axis or Makgadikgadi Line (Figure 2.22 and 2.23), the gravity field is mainly featureless, lacking steep gradients and local anomalies, while to the northwest, there are numerous large alternating gravity anomalies elongated in a dominant northeast-southwest direction (Hutchins and Reeves, 1980). The Makgadikgadi line was suggested to represent a tectonic front between the more recently tectonised rocks in the northwest from the stable cratonic regions of southern and eastern Botswana (Figure 2.22) (Hutchins and Reeves, 1980).

A second, more prominent, gravity lineament can be traced northwards from Tshabong to the Ghanzi Ridge where it is overwhelmed by the northeasterly supposed Damara trend (Reeves and Hutchins, 1975). This north-south trend is a continuation of both positive and negative anomalies that is recognised in the gravity data of the Northern Cape Province of South Africa and has been termed the Kalahari Line (Figure 2.22).

A preliminary interpretation of the regional tectonic setting of southern Africa is provided by Reeves' (1976, in Reeves and Hutchins, 1982) Bouguer anomaly map, which merged gravity data from South Africa, Namibia, Botswana and Zambia. Although the interpretation is based on a broad scale, it is one of the few that uses geophysical data to propose geological boundaries. Key features to note are the proposed connection of the Irumide Belt and the Ghanzi-Chobe Belt and the continuation and delineation of, the northwestern margin of the Damara Belt (Figure 2.22).

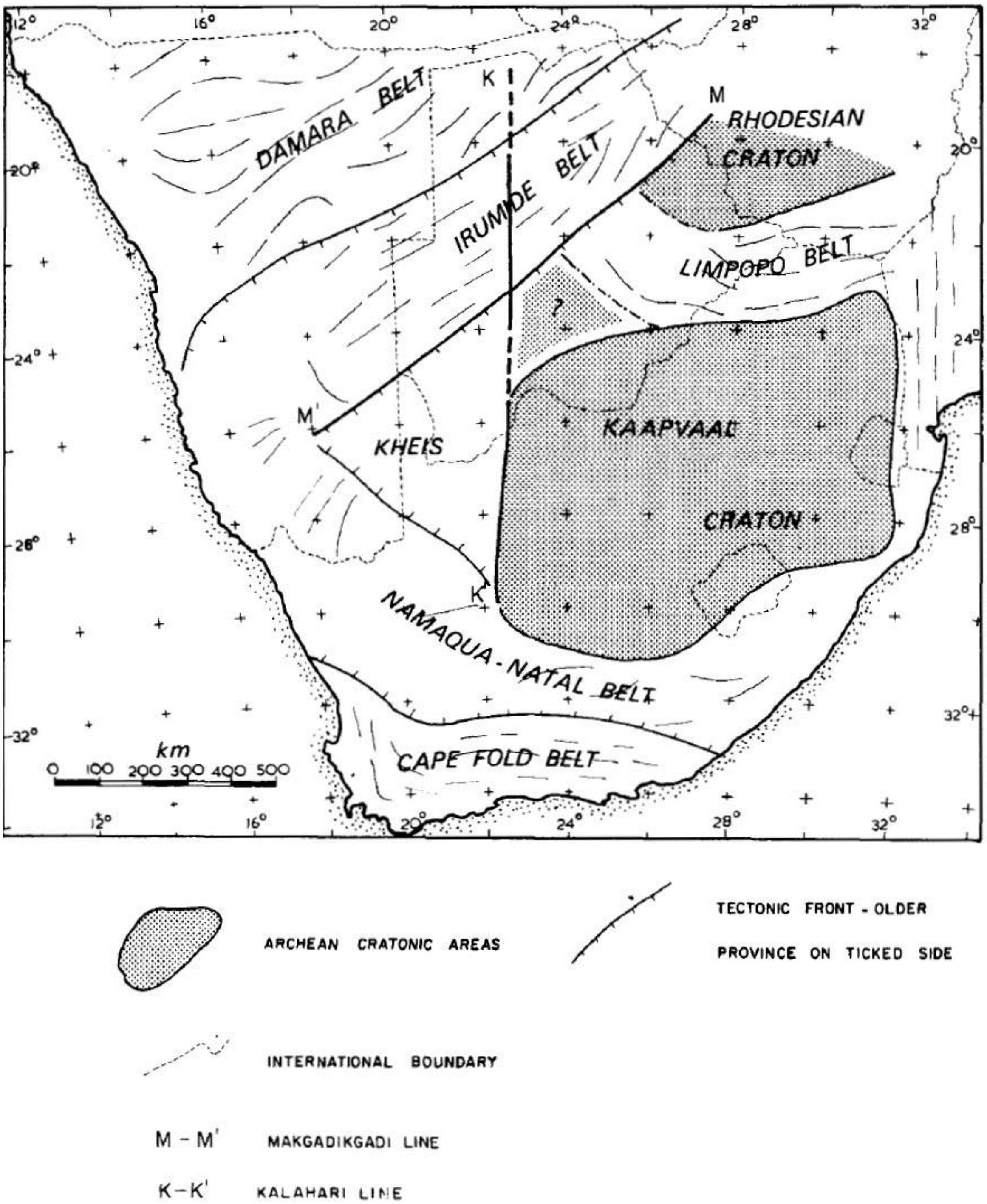

Figure 2.22: Gravitational interpretation of tectono-metamorphic provinces of southern Africa (after Hutchins and Reeves, 1980; Reeves and Hutchins, 1982). M-M' = Makgadikgadi Line, K-K' = Kalahari Line.

In 1975 a reconnaissance aeromagnetic survey of the Kalahari region commenced (Reeves and Hutchins, 1982). This aeromagnetic survey revealed that Botswana can be divided into a number of distinct domains with both the Kalahari and Makgadikgadi Lines appearing as major features

(Figure 2.23) (Hutchins and Reeves, 1980; Reeves and Hutchins, 1982). As this study is concerned with northern Botswana, regions D, G, B_1, B_2, and B_3in Figure 2.23 are discussed below.

Region D in the northwest of Botswana (Figure 2.23) is suggested to consist of a shallow gneissic basement in contact with what is assumed to be fairly thick, non-magnetic Damara sediments (Hutchins and Reeves, 1980). Region G in the northeast of Botswana (Figure 2.23) is interpreted as the Ghanzi-Chobe Belt, extending in an arc-shape from the Namibian border, in the west, to the Zambian border in the north (Reeves and Hutchins, 1982). The magnetic units in this region are suggested to be the Kgwebe Formation, exposed locally, and magnetite-rich folded sediments of the Ghanzi Group (Hutchins and Reeves, 1980; Reeves, 1985). West of the Kalahari Line and between the Makgadikgadi Line and the Ghanzi-Chobe Belt, the basement appears to be highly magnetic and deeply buried (regions B_1, B_3; Figure 2.23). The non-magnetic cover in this area can be up to 15 km thick (Hutchins and Reeves, 1980). In region B_1 in the west of Botswana (Figure 2.23) the majority of the cover is assumed to be Nama and Karoo sediments, although in B_3, non-magnetic equivalents of the Late-Precambrian sedimentary units exposed on the Ghanzi Ridge, may also contribute to the sedimentary pile (Hutchins and Reeves, 1980). Region B_2 is an area of shallow basement lithologies, which has been correlated with local exposures of granitic and gneissic units outcropping in the Okwa Valley, ~100 km south of Ghanzi (Figure 2.19) (Hutchins and Reeves, 1980).

A major post-Karoo tectonic feature is the magnetically prominent Okavango Dyke Swarm (DS in Figure 2.23). The dyke swarm consists of dolerite dykes, which traverse Botswana with a strike of 110°E and converges to the west (Hutchins and Reeves, 1980). The dyke swarm has been interpreted as the third arm of a triple junction, which is centred in the lower Limpopo Valley with the other two arms developed into spreading axes which led to the departure of another Gondwana fragment from what is now the Mozambique coast (Hutchins and Reeves, 1980; Reeves and Hutchins, 1982).

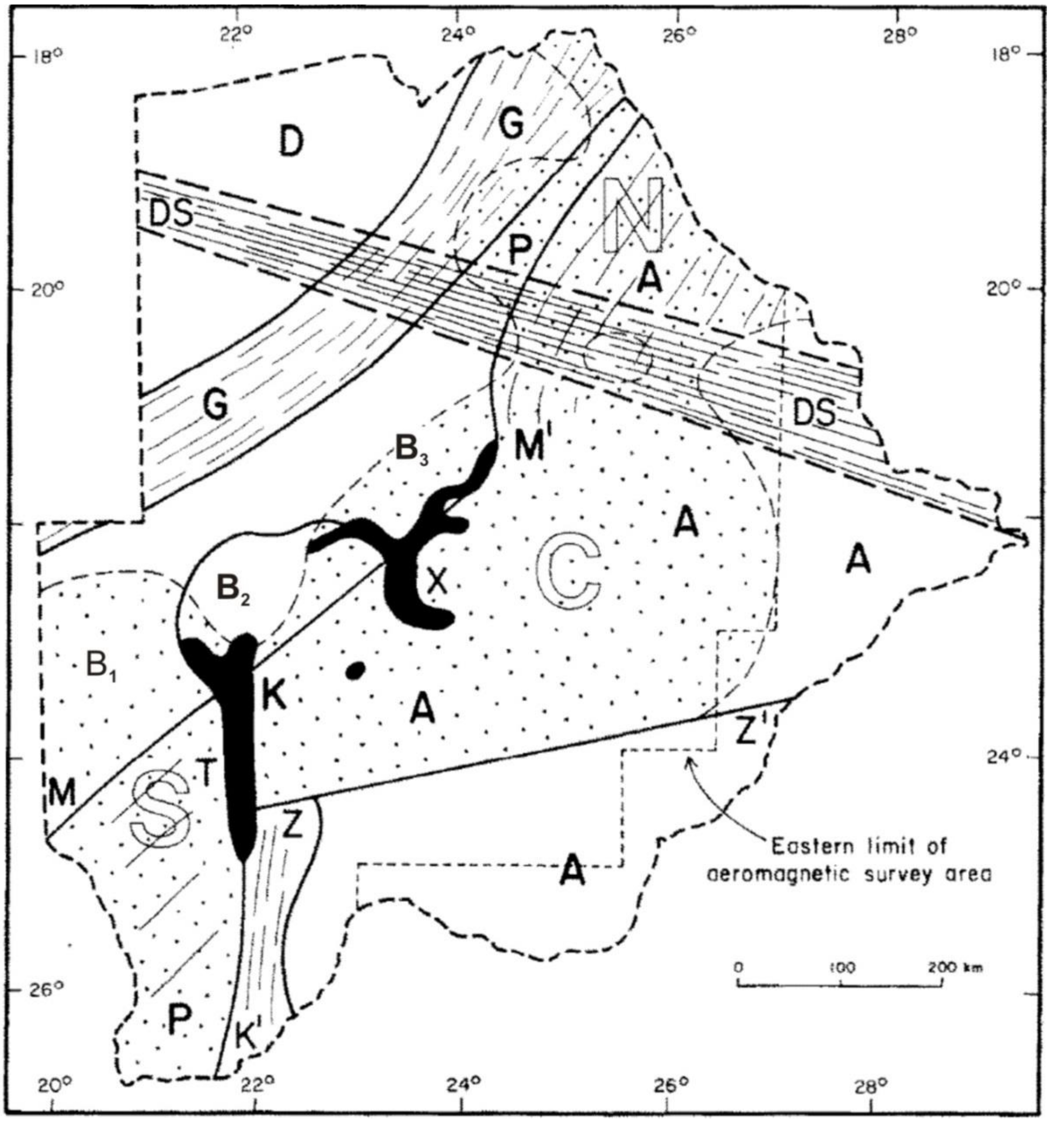

Figure 2.23: Outline interpretation of the regional aeromagnetic data (after Hutchins and Reeves, 1980; Reeves and Hutchins, 1982). Precambrian basement (solid letters): A, Archaean rocks of Kaapvaal-Limpopo-Zimbabwe affinity; P, deep Proterozoic-Palaeozoic basins. Region D is the proposed continuation of the Damara Belt, region G is the spatial extent of the Ghanzi-Chobe belt, region B_1 is the Ncojane basin, region B_2 is the Okwa basement, and region B_3 is the Passarge Basin. Solid lines represent basement lineaments; M-M' is the Makgadikgadi Line; K-K' is the Kalahari Line; Z-Z' is the Zoetfontein Fault. A Karoo feature is the Okavango Dyke Swarm (DS).

The importance of the Ghanzi-Chobe Belt relative to the Pan-African Orogeny and the mineral potential has been investigated in local studies conducted across the belt. One of the earliest studies of the Ghanzi-Chobe Belt was carried out by Reeves (1985) who identified that the belt extends from the Namibia-Botswana border, in the southeast to the Botswana-Zambia border, in the northeast by tracing the aeromagnetic highs of the Kgwebe and D'Kar Formations. Borg (1988), investigated the geophysical signature of the various basins associated with the Ghanzi-Chobe Belt (from southeast to northwest, Koras, Koras Sinclair Link, Sinclair, Klein Aub, Witvlei, Lake N'Gami, Chinamba Hills and Goha Hills). Borg (1988) showed that these basins are associated with a number of elongated Bouguer gravity high anomalies, which are flanked by negative gravity anomalies. Borg (1988) suggested that the gravity high anomalies are caused by dense basaltic lava while the gravity lows are caused by an increased thickness in sedimentary cover.

2.6.3. Previous geoelectrical studies

In 1972, a 25 three-component magnetometer study of western Zimbabwe, Botswana and Namibia discovered a conductive zone, which runs northeast–southwest from northeastern Botswana, south of the Okavango Delta, where it bends westwards into Namibia (Figure 2.24) (de Beer *et al*., 1975; 1976). De Beer *et al*. (1975) interpreted that the Botswana portion of the conductive zone is associated with fault patterns. De Beer *et al*. (1976) estimated that the conductor is at a depth of between 50 km and 125 km favouring a depth closer to the shallower limit from the examination of induction effects. The conductor was suggested to be the southwestward extension of the Zambezi Belt (Figure 2.24) (de Beer *et al*., 1976).

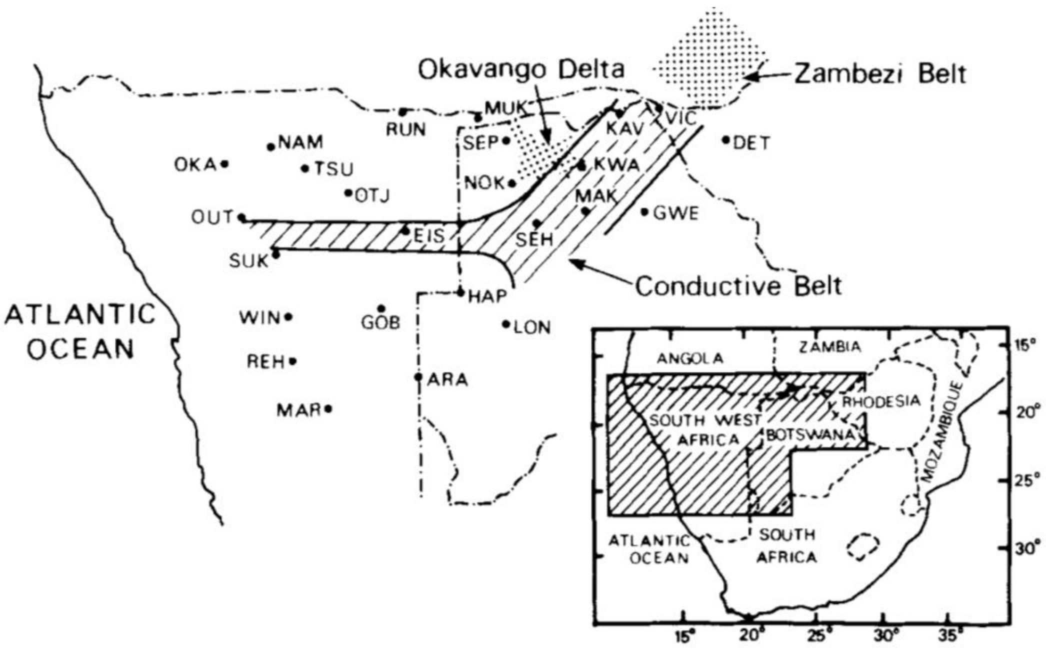

Figure 2.24: Location of the 25 three-component magnetometer array in the 1972 survey that operated in Zimbabwe (formerly Rhodesia), Botswana and Namibia (formerly South West Africa). The shaded extent is the surface outline of the conductive zone (after de Beer *et al*., 1976).

Van Zijl (1977) conducted an ultra-deep (maximum electrode spacing of 1 000 km) and deep (maximum electrode spacing of 40 km) Schlumberger soundings to study the resistivity structure of the southern African crust and mantle. The geoelectric results divided the crust and upper mantle into a generalised five zoned model (Figure 2.25) (van Zijl, 1977). Zone 1 is characterised as highly resistive, extending from 5 km to 10 km depth, with resistivity values ranging from 30 000 Ωm to 400 000 Ωm, averaging 100 000 Ωm associated with large masses of non-fractured granitic Archaean cratons (Kaapvaal and Zimbabwe Cratons) (van Zijl, 1977). Zone 2, comprising the Damara, Limpopo and Namaqua Belts is characterised by thick crust with intermediate resistivity values ranging between 2 000 Ωm to 10 000 Ωm, averaging 5 000 Ωm (Figure 2.25) (van Zijl, 1977). Van Zijl (1977) deduced that the mobile belts (Zone 2) continue laterally beneath the cratons (Zone 1) extending to a depth of 25 km to 30 km (Figure 2.25). The lower resistivity values are associated with deformed metamorphic rocks in a mobile belt with the presence of fluid-filled fractures (van Zijl, 1977; Gough, 1986; Corner, 1998). Zone 3 is a conductive layer at a depth range of 25 km to 40 km and is present in both cratonic and mobile belt areas (Figure 2.25) (van Zijl, 1977). Its resistivity is generally below 100 Ωm but is estimated at 50 Ωm and is interpreted as being caused by serpentinised ultramafic rocks (van Zijl, 1977). The thickness of Zone 3 increases in mobile belt areas in comparison to the cratonic regions (van Zijl, 1977). A highly resistive, dry zone marks the top of Zone 4 which gradually merges into the conductive Zone 5, as temperature increases with depth so electrical conductivity increases (Figure 2.25) (van Zijl, 1977).

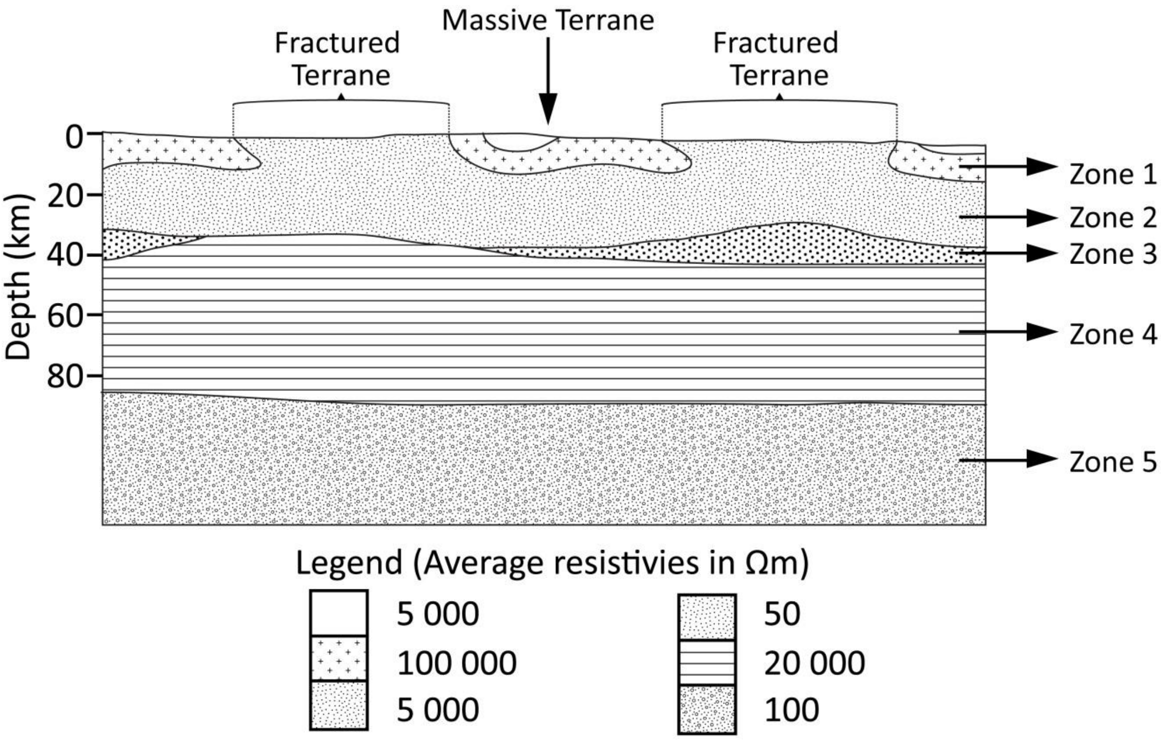

Figure 2.25: Schematic model of the crust and upper mantle based on previous electrical sounding interpretations (after van Zijl and de Beer, 1983).

To constrain the westward extent of the conductor in Namibia, de Beer *et al*. (1982) undertook a survey consisting of a 27 three-component magnetometer study, two ultra-deep Schlumberger soundings (electrode spacing greater than 200 km), one deep Schlumberger sounding (electrode spacing of 123 km) and 17 Schlumberger soundings (electrode spacing of 40 km) (Figure 2.26). De Beer *et al*. (1982) discovered that the conductor is 100 km wide, shallower than 45 km, and does not follow the east-west trend suggested earlier by de Beer *et al*. (1976) but rather bends southwards following the structural trends of the Swakop Group (Figure 2.26). In Namibia the southern boundary of the zone parallels the Waterberg/Omaruru Fault (Figure 2.4). The Schlumberger soundings showed that the conductive zone is as shallow as 3 km. The conductive zone has a resistivity of less than 20 Ωm, which is much lower in comparison to lithologies at a similar depth in the upper crust (de Beer *et al*., 1982). Rocks north of conductor have resistivities of more than 20 000 Ωm and the Damaran rocks south of the conductor have resistivities of more than 5 000 Ωm (de Beer *et al*. 1982). As more than fourteen post-Karoo alkaline intrusions are situated along the conductive zone, de Beer *et al*., (1982) concluded that the conductive zone marks a zone of weakness in the lithosphere that links the Damara Belt to the Zambezi Belt.

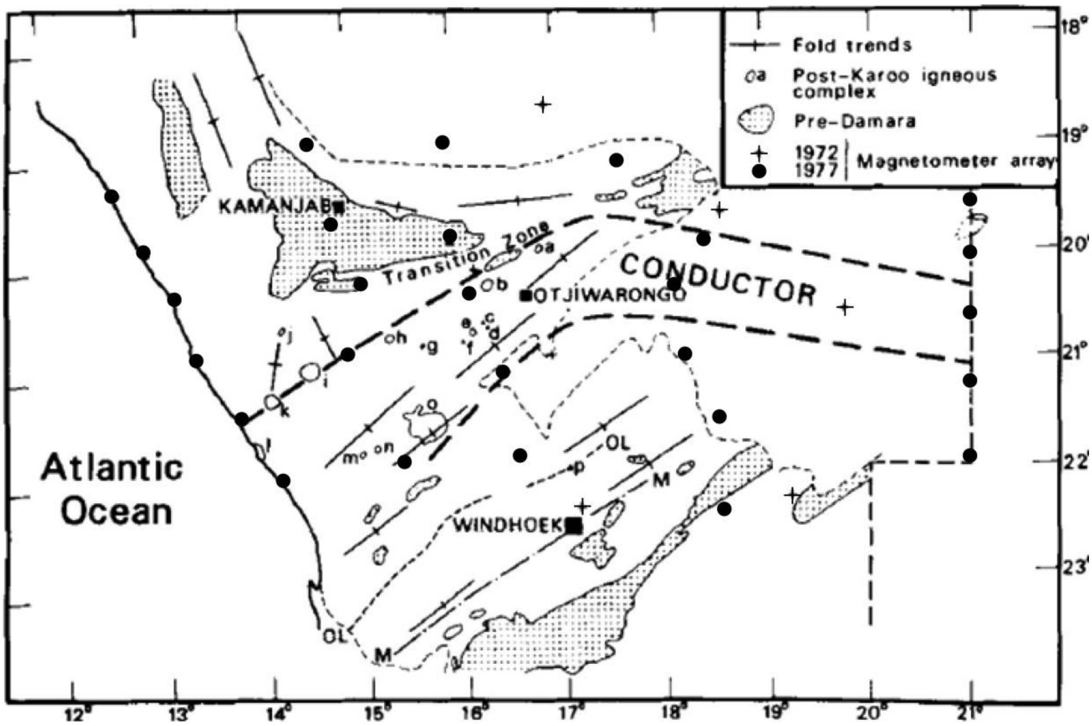

Figure 2.26: The surface outline of the conductor in relation to the 1972 magnetometer array (crosses), 1977 magnetometer array (dots), and geology and main fold trends of the Damara (modified after de Beer *et al*., 1982). The alkaline complexes are: (a) Okorusu; (b) Paresis; (c) Etaneno; (d) Ondurakorume; (e) Kalkfeld; (f) Osongombo; (g) Otjohorongo; (h) Okenyenyal; (i) Brandberg; (j) Doros; (k) Messum (l) Cape Cross; (m) Klein Spitzkop; (n) Gross Spitzkop; (o) Erongo and (p) Otjisazu. The locations of the Matchless Amphibolite Belt (m); Okahandja Lineament (OL) and the boundary between the Northern and Central Zone of the Damara Belt (N-CZ) are displayed.

Van Zijl and de Beer (1983) presented the geoelectrical results acquired from electrical sounding and magnetovariational studies conducted by the Geophysical Division of the National Physical Research Laboratory of the Council for Scientific and Industrial Research. Van Zijl and de Beer (1983) concluded that the Damara Belt is characterised by moderate resistivities of 1 000 Ωm to 10 000 Ωm, typical of Zone 2 described by van Zijl (1977) (Figure 2.25). Van Zijl and de Beer (1983) confirmed the existence of the prominent northeast trending conductor (less than 20 Ωm) in the Central Zone at a depth of 3 km to 10 km with a minimum thickness of 20 km, and 160 km wide with steeply dipping boundaries. Van Zijl and de Beer (1983) favour a lateral connection with the conductive body of Van Zijl (1977), at a depth of at least 20 km. This connection was traced by van Zijl and de Beer (1983) beyond the borders of the Damara Orogen, as in van Zijl's (1977) study, where Zone 3 was found to continue across the Limpopo Belt and into the cratonic regions. This suggests that the origin of the southern African subcontinent may have formed by a common and fundamental process and that Zone 3 marks the lower isotherm boundary where serpentine reverts back to olivine (van Zijl and de Beer, 1983). According to van Zijl and de Beer (1983) as the conductor lies within the mobile belts, it confirms that these regions are weak portions of the crust. The conductivity is interpreted to be serpentinised ultramafic material that may be derived from either ophiolitic material emplaced by subduction or shallow emplacement of asthenosphere material in a weak zone. However saline fluids in fractures are also possible (van Zijl and de Beer, 1983). The large amount of water required to create the vast amount of serpentinite responsible for producing the observed conductivity values is improbable and the alignment of a large amount of Karoo intrusions indicates a possible zone of weakness in the crust. This conductive zone most likely delineates the structural boundary between the Congo and Kalahari Cratons (van Zijl and de Beer, 1983).

To better resolve crustal features of the conductive zone, Ritter *et al*. (2003) and Weckmann *et al*. (2003) in 1998 – 1999, carried out a two part MT survey across the Damara Belt, Autseib Fault and Waterberg Fault/Omaruru Lineament (WF/OL) (Figure 2.27). The MT profile was ~200 km long consisting of 107 sites at a station spacing of 4 km to 12 km and a local 3D array of 60 sites at a spacing of 500 m to 2 km. An additional aim of the survey was to determine the geometry and connection of the Autseib Fault and WF/OL at depth. Ritter *et al*. (2003) interpreted the Autseib Fault and WF/OL as two sub-vertical zones of enhanced conductivity that penetrate the crust and dip at ~65° south. These conductive zones are bounded by narrow, high-angle shear zones corresponding to major basement features, which could not be resolved in the earlier surveys of de Beer *et al*. (1975; 1976; 1982) and van Zijl and de Beer (1983). Ritter *et al*. (2003) proposed that the conductivity is caused by graphite derived from graphite-bearing marbles situated in the area with fossilised shear zones. The geometry of the two fault zones suggests that they end in a common detachment, which is consistent with geodynamic models of collisional orogeny, where major thrusts form a connected fault system fixed in a subduction zone (Ritter *et al*., 2003).

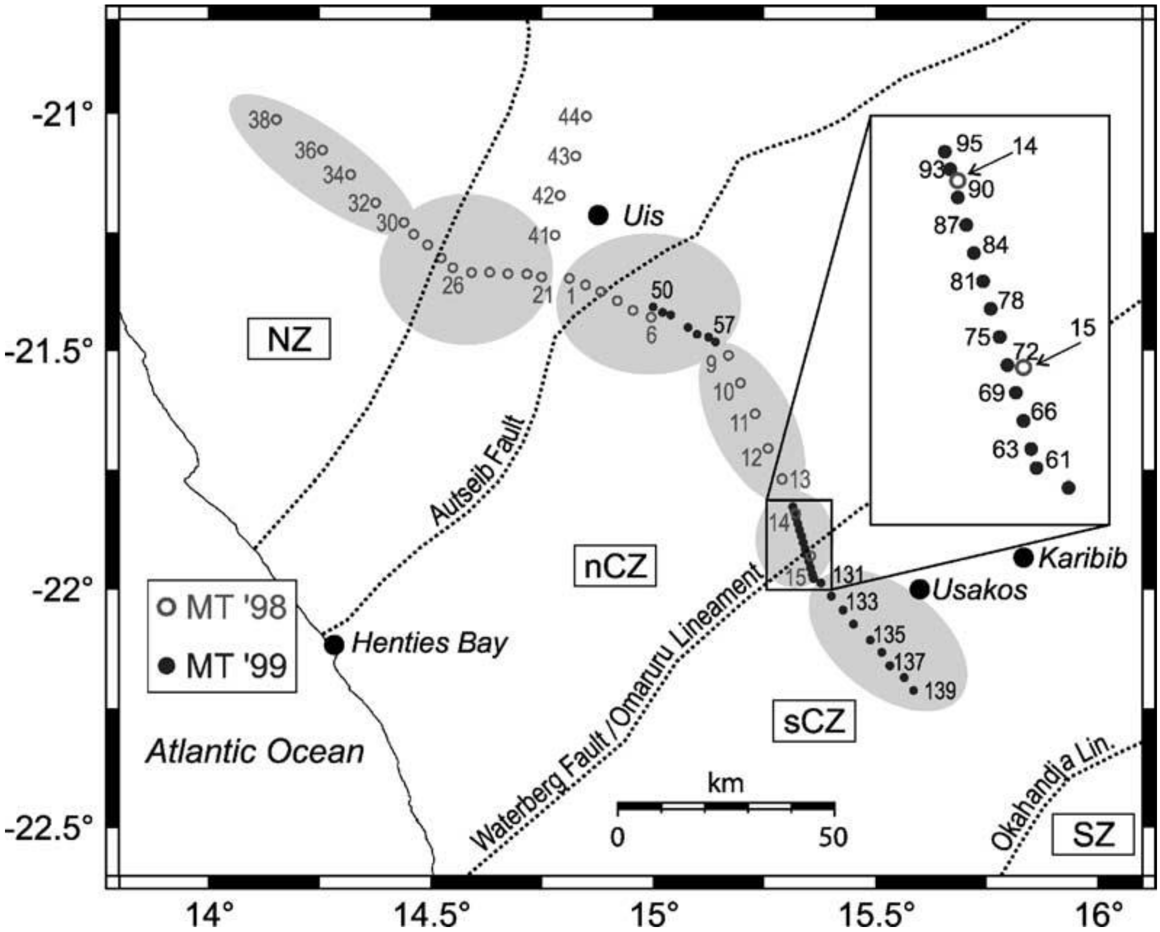

Figure 2.27: Location of the 54 MT stations in western Namibia during 1998 (open circles) and 1999 (solid circles) used in the survey (after Ritter *et al*., 2003). Boundaries of the Northern Zone (NZ), north Central Zone (nCZ) and south Central Zone (sCZ) of the Damara Belt are also shown.

MT surveys across southern Africa have also been conducted by the SAMTEX team. Muller *et al*. (2009) were the first to model and interpret the lithospheric structure of the Damara Belt, Rehoboth Terrane and Ghanzi-Chobe Belt, beneath the KIM-NAM profile (Figure 2.28). The KIM-NAM profile is ~1 400 km long, 2D MT profile which consists of 69 stations at a spacing of ~20 km (Figure 2.28). Interpretation of two independent 2D inversion models was completed; one decomposed to a geoelectric strike direction of 25°E of north for the Rehoboth Terrane and one at 45° E of north for the Damara Belt/Ghanzi-Chobe Belt. Muller *et al*. (2009) concluded that the Rehoboth Terrane has a resistivity of ~1 000 Ωm with a thickness of 180 ± 20 km while the Damara Belt/Ghanzi-Chobe Belt has a resistivity of ~500 Ωm and a thickness of 160 ± 20 km.

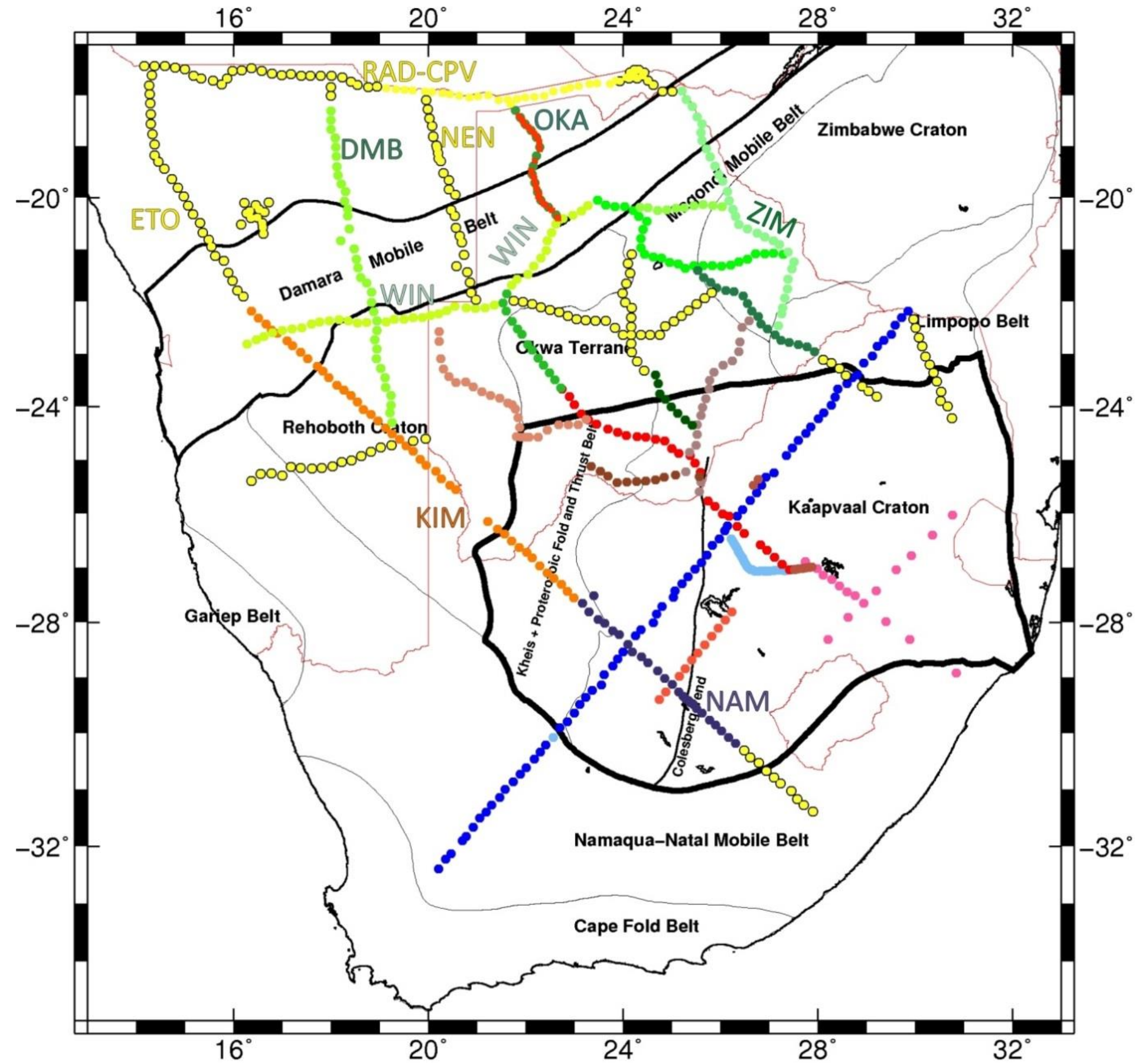

Figure 2.28: The Location of the MT stations of the SAMTEX project shown as circles with the profiles discussed in the text labelled (modified after Muller, *et al*., 2009; Meinsopust *et al*., 2011; Khoza *et al*., 2013). Background map is of tectonic provinces (black lines) and international boundaries (brown lines).

An investigation of the northeastern extent of the Ghanzi-Chobe Belt was carried out on the ZIM profile (Figure 2.28) (Miensopust *et al*., 2011). *Strike* analysis of the profile revealed that the geoelectric strike varied with depth and along the profile. The stations above the Okavango Dyke Swarm had a geoelectric strike angle of 55°E of north, while the remainder of the stations had a geoelectric strike of 35°E of north for the crust (Miensopust *et al*., 2011). Two middle to lower crustal conductors were interpreted, as similarly described by de Beer *et al*. (1982). Miensopust *et al*. (2011) explains that the sampling of the lower crustal conductor using the MT technique are too sparse to conclude if the conductor observed beneath the ZIM profile (Figure 2.28) is the continuation of the conductor in the Damara Belt observed by de Beer *et al*. (1982) and Ritter *et al*. (2003).

Khoza *et al*. (2013) constrains the geometry and the southern extent of the Congo Craton beneath the ETO-KIM, DMB, NEN, OKA, WIN and RAD-CPV profiles (Figure 2.28). The main profile for their study was the ETO-KIM profile, an extension to the KIM-NAM profile investigated by Muller *et al*. (2009). The study was designed to compare the results of the two profiles and provide insight into the variation in structure and thickness from Proterozoic to Archaean terranes by 2D and 3D MT inversion modelling. Khoza *et al*. (2013) decomposed the ETO-KIM profile to 50°E of north. From interpretation of the 3D crustal model, Khoza *et al*. (2013) correlates the middle to lower crustal conductor with the Central Zone (Damara Belt) with the cause of enhanced conductivity being attributed graphite situated along deep-seated shear zones and sulphide mineralisation in the upper crust. The MT modelling revealed that the southern border of the Kamanjab Inlier, defined by resistivity values of over 10 000 Ωm, can be extended further south to beneath stations ETO009/ETO010 compared to previous geological mapping which placed the southern margin beneath stations ETO011/ETO012 (Figure 2.28).

1D inversion modelling of the DMB (Figure 2.29), GIB, and KIM profiles by Muller (*pers. comm*., 2013) aimed at mapping the extent, depth and possibly the thickness of the Karoo Supergroup. Muller (*pers. comm*., 2013) associated the upper resistivity values of ~100 Ωm with dry Kalahari sediments. The base of the Kalahari sediments was defined by a discontinuous conductive layer of ~1 Ωm to 15 Ωm associated with a Kalahari aquifer (Figure 2.29) (Muller, *pers. comm*., 2013). The top of the Karoo sediments was estimated at a depth of ~300 m beneath the Kalahari sediments as a more resistive layer of between 20 Ωm and 55 Ωm (Figure 2.29) (Muller, *pers. comm*., 2013). The Lower Karoo sediments are interpreted as a conductive layer of ~5 Ωm at a depth of ~400 m (Muller, *pers. comm*., 2013). All these layers dip gently to the south (Figure 2.29) (Muller, *pers. comm*., 2013).

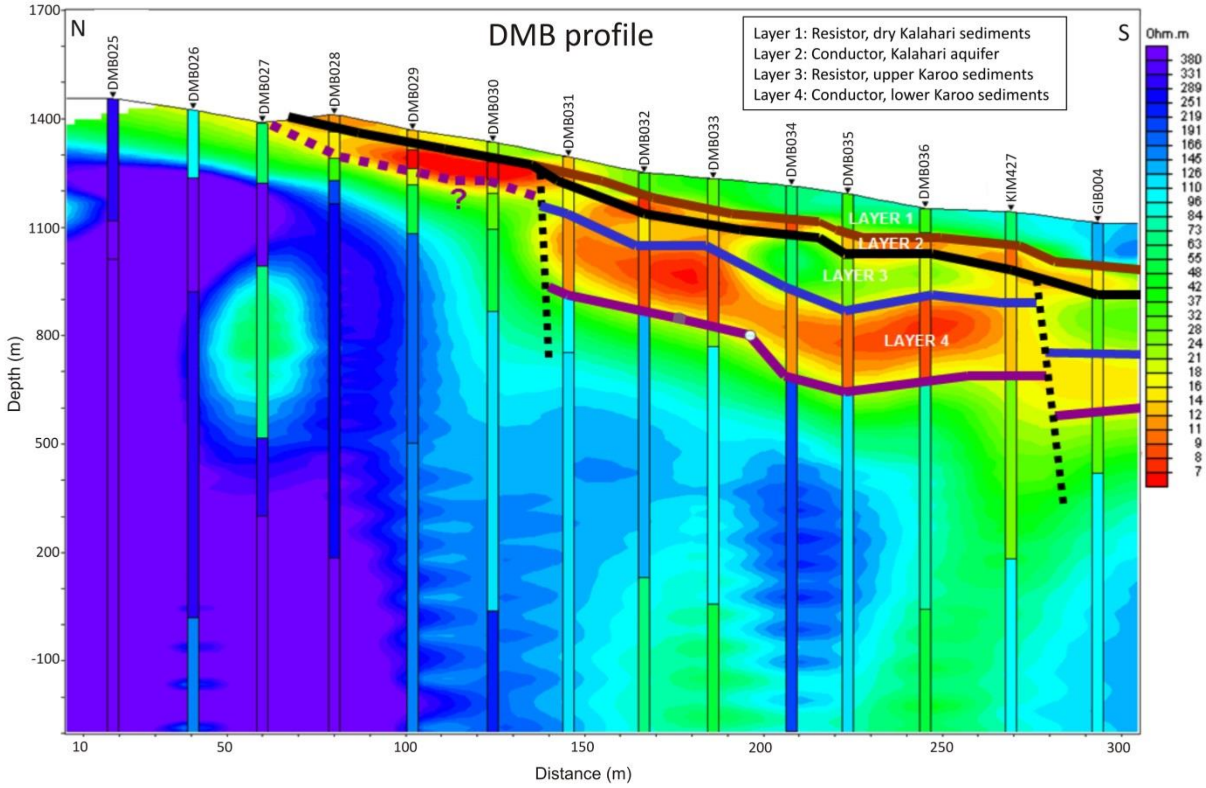

Figure 2.29: Shallow MT 1D inversion interpretation of the DMB profile (after Muller, unpublished data). Four layers are identified in the upper crust along with small scale faulting.

2.7. Previous cross-border correlation studies between the Damara Belt and northwest Botswana

This section discusses the previous geological and geophysical cross-border correlation studies between Namibia and Botswana.

Loxton Hunting and Associates (1981; in Carney *et al*., 1994) correlated the Quangwadum Complex with pre-Damaran basement by comparing the geology of the Aha Hills area with the Otavi Mountain Land area. Tracing the aeromagnetic signal of the Quangwadum Complex into Namibia Key and Ayres (2000) correlates it with Palaeoproterozoic lithologies.

Carney *et al*. (1994) suggests that the Central Zone of the Damara Belt pinches out at ~18°E, 21°S (Figure 2.30). From the interpretation of potential field data, Kgotlhang *et al*. (submitted) agrees with this suggestion and as a result the Southern and Central Zones merge into a single tectonostratigraphic zone before the Botswana border (Figure 2.31) (Kgotlhang *et al*., submitted).

Kgotlhang *et al*. (submitted) correlates the Aha Hills Formation, Koanaka and Tsodilo Hills Groups with the Swakop Group from the southern part of the Damara Belt (Figure 2.31). The iron formations of the Tsodilo Hills Group are correlated with the Chuos Formation, the quartzite, dolostone and muscovite-biotite schist units are correlated with the Kuiseb Formation and the Xaudum Group is correlated with the Otavi Group carbonate (Kgotlhang *et al*., submitted). The argument for correlating the schist units with the Kuiseb Formation is based on the assumption that the Roibok Group is the continuation of the Matchless Member (Kgotlhang *et al*., submitted). Carney *et al*. (1994) suggests that the lithologies, structures and mineralisation of the Shakawe Zone rocks correlate better with rocks of the Otavi area, in the Northern Platform (Figure 2.30). The interpretation was based on the Central Zone being characterised by strongly deformed and metamorphosed Damara lithologies with locally remobilised granitic basement and that the chert-dolostone lithologies of the Aha Hills Formation are similar to those in the Otavi Group (Carney *et al*., 1994). Stalker (1983 in Carney *et al*., 1994) compared the lithologies of the Aha Hills Formation with the Abenab Subgroup in the Tsumeb area with a focus on similar styles of Pb-Zn mineralisation. From the geological map of Namibia, Nosib Group rocks have been mapped immediately to the west of the Xaudum Valley (Miller and Schalk, 1980). Singletary *et al*. (2003) similarly notes lithological similarities between the Xaudum Group and the Nosib Group. Structural analysis from aerial photographs and ground truthing, revealed that there is a similarity between structures in the Aha Hills area and in the Northern Zone or Northern Platform (Carney *et al*., 1994). These structures include east-northeast trending upright folds and northeast trending isoclinal folds.

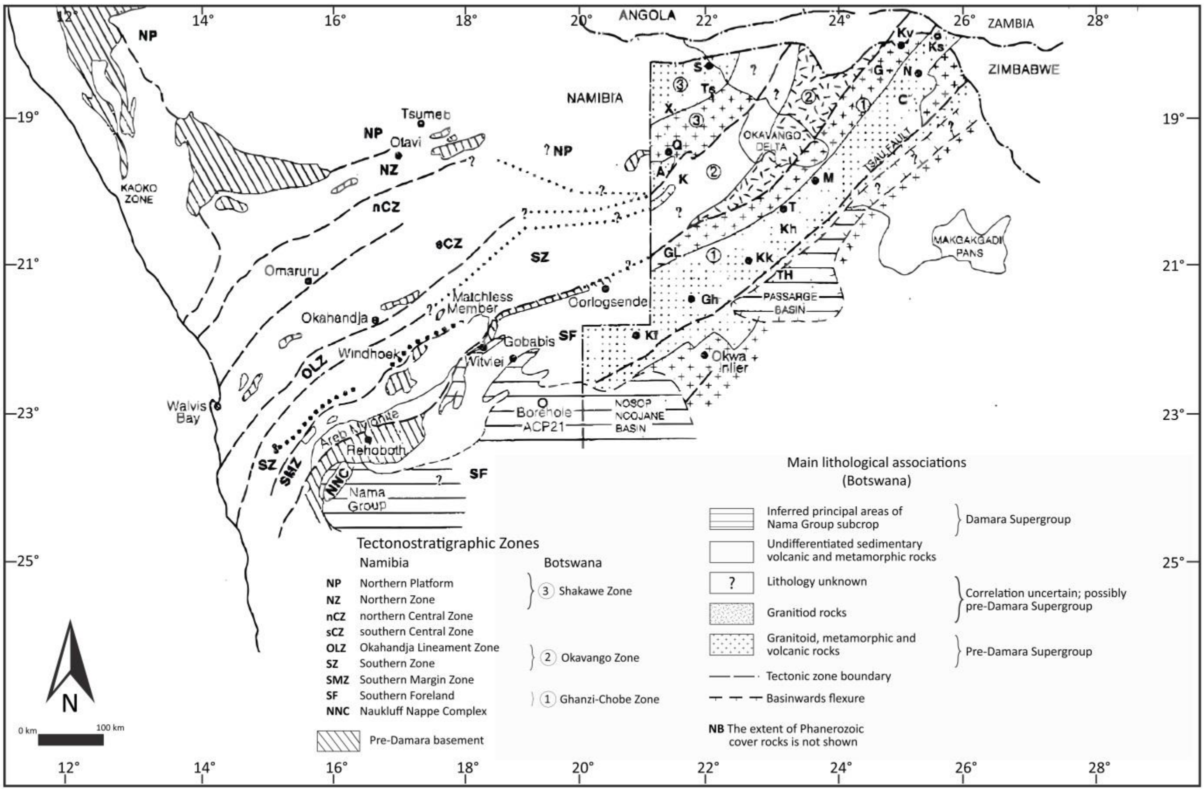

Figure 2.30: Proposed correlation between the tectonostratigraphic zones of Namibia (west) and Botswana (east) (after Carney *et al*., 1994). Where A = Aha Hills, C = Chinamba Hills, G = Goha and Gubatsha Hills, Gh = Ghanzi, GL = Groote Langte, K = Kihabe Hills, Kf = Kalkfontein, Kh = Kgwebe Hills, KK = Kuke, Ks = Kasane, Kv = Kavimba, M = Maun, N = Ngezumba, Q = Quangwadum Valley, S = Shakawe, T = Toteng, TH = Tsau Hills, Ts = Tsodilo Hills and X = Xaudum Valley.

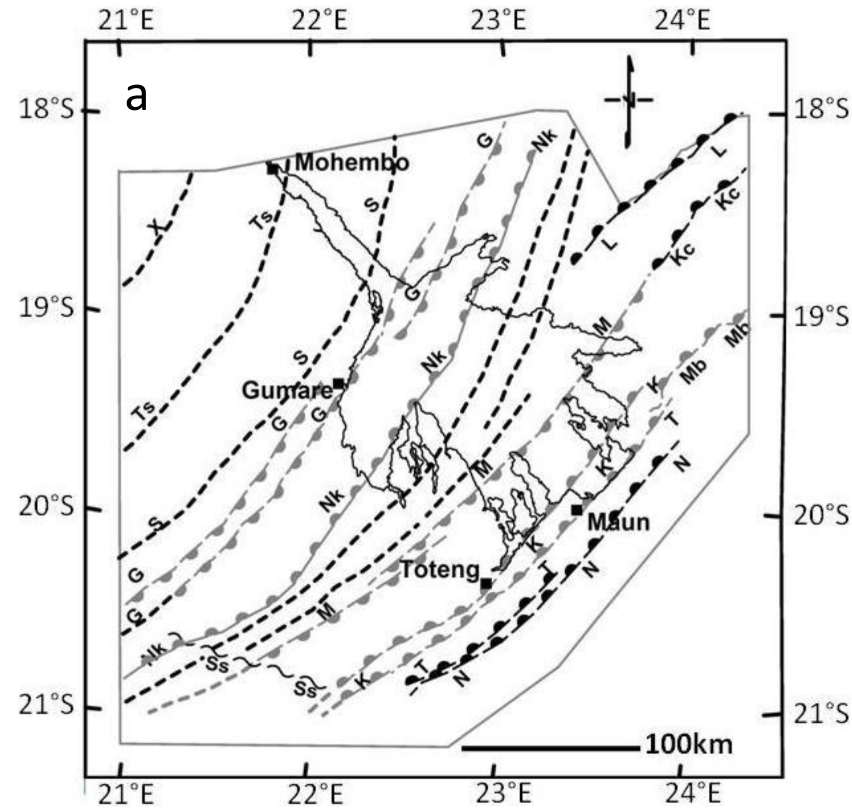

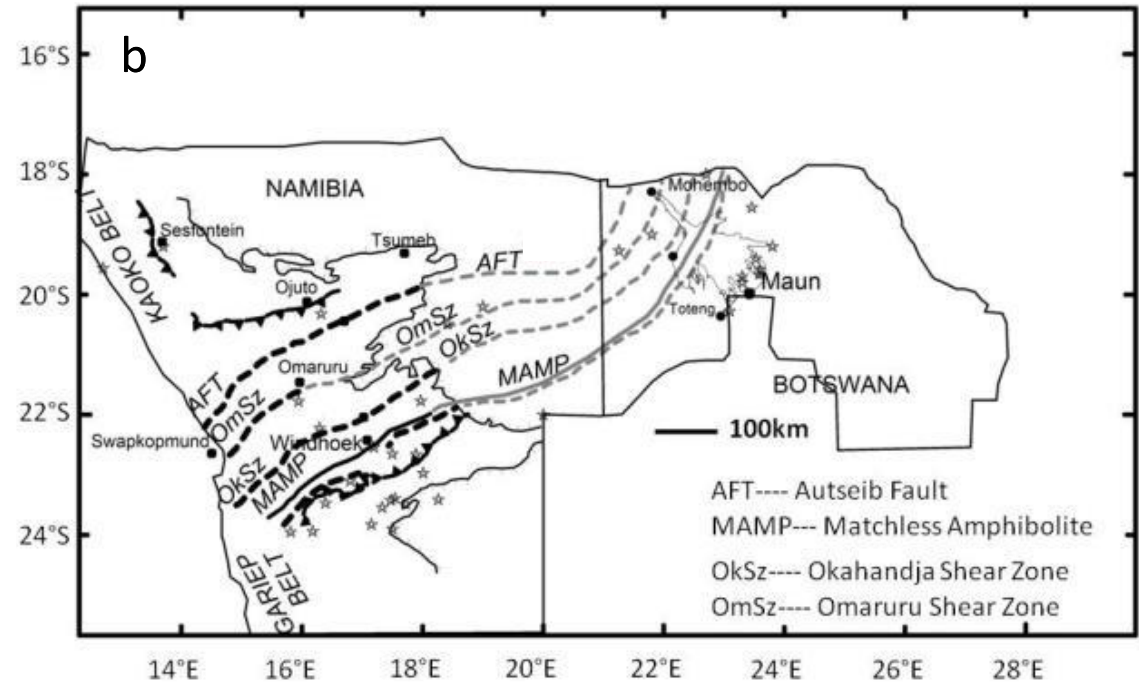

Figure 2.31: Correlation of regional lineaments between Namibia and Botswana: a) Regional lineament map of northwestern Botswana interpreted from both magnetic and gravity data sets (Kgotlhang *et al*., submitted). Grey coloured faults mark the main faults of the two grabens that define the Okavango Rift Zone. The dip of the faults is inferred from magnetic and digital elevation models. Terms of lineaments are as follows; G = Gumare, K = Kunyere, Kc = Kachikau, L = Lenyanti, M = Moremi, Mb = Mababe, N = Nare, Nk = Nokaneng, S = Sebopa, Ss = Sekaka Shear, T = Thamalakane, Ts = Tsodilo and X = Xaudum. b) Regional continuation of lineaments of the Damara Belt into Botswana (Kgotlhang *et al*., submitted). Grey stars represent seismic events.

The Chuos Formation is present in various tectonostratigraphic zones of the Damara Belt (Barnes and Sawyer, 1980) (Figure 2.5). This has led to many debates on which tectonostratigraphic zone correlates with the iron formation of the Tsodilo Hills Group. Since the Roibok Group is traditionally accepted as the continuation of the Matchless Member, the literature is dominated by the iron formations of the Chuos Formation of the Southern Zone correlating with the iron formations of the Tsodilo Hills Group. Bühn *et al*. (1992) correlated the Chuos Formation of the Central Zone with the Tsodilo Hills Group because of the abundance of iron formation and ferruginous quartzite present in both zones (Figure 2.30). The depositional age of the Chuos diamictite is suggested to be 746 ± 2 Ma (Hoffman *et al*., 1996) while the only depositional age of the Tsodilo Hills Group is bracketed between 1 959 Ma to 490 Ma (Singletary *et al*., 2003; Mapeo *et al*., 2008).

Kgotlhang *et al*. (submitted) delineates a number of geophysical lineaments in Botswana, which are correlated with geophysical lineaments in Namibia (Figure 2.31). The major lineaments that were extrapolated across the political border are the Sepopa Lineament (the southern extent of the Congo Craton), equivalent to the Okahandja Lineament, the Tsodilo Lineament equating to the WF/OL, Xaudum Lineament, equating to the Autseib Fault, while the Roibok Group is the continuation of the Matchless Member (Figure 2.31). Kgotlhang *et al*. (submitted) suggests that the zone between the Sepopa Lineament and Gumare Lineament marks the suture between the Kalahari and Congo Cratons (Figure 2.31).

Carney *et al*. (1994) proposed that the Okavango Zone correlates partly with the Southern Zone and its northwestern boundary with the Okahandja Lineament Zone (Figure 2.30). However, structures that define the Okavango Zone's southeastern margin are considered to be equivalent with the Areb Mylonite Zone (Lüdkte *et al*., 1986; in Carney *et al*., 1994). The continuation of the Areb Mylonite Zone was based on similar highly deformed and metamorphosed rocks found in the vicinity of the Areb Mylonite Zone and the southern boundary of the Okavango Zone (Lüdkte *et al*., 1986; in Carney *et al*., 1994). This implies that the Southern Margin Zone pinches out at ~19°E, 22°S (Figure 2.30).

The Koanaka Group has been correlated with either the Karibib or Chuos Formations (Vaalgras Subgroup) because of the abundant dolostone and calc-silicate rocks found in these formations (Figure 2.30) (Carney *et al*., 1994). In addition, the outcrops of the Koanaka dolostone have been correlated with the Vaalgras Subgroup on the geological map of Namibia by Miller and Schalk (1980).

One of the earliest correlations between the Matchless Member and Roibok Group was suggested by Reeves (1978a) from the interpretation of aeromagnetic data. Reeves (1978a) noticed that the Roibok Group lay along the geological strike with the Matchless Member (Figure 2.32). Lüdkte *et al*. (1986, Singletary *et al*., 2003) compared the composition of the amphibolites in both the Matchless Member and Roibok Group. Lüdkte *et al*. (1986, in Singletary *et al*. 2003) concluded that the amphibolites of the Matchless Member correlate with the amphibolites of the Roibok Group and that they represent a primitive island arc tholeiite or basaltic protoliths of ocean floor affinity (Figure 2.32). However, correlating the Roibok Group with the Matchless Member, which is in contact with the Kuiseb schists, presents two lines of evidence suggesting that there was a lateral change in thermal and structural history in the Damara Belt in the vicinity of the Namibia – Botswana border (Carney *et al*., 1994). The first would relate to the occurrence of migmatitic and gneissic layers that are present in the Roibok Group and not in the Matchless Member, which suggests a southeast displacement of Pan-African geotherms in Botswana relative to Windhoek (Carney *et al*., 1994). The second relates to the tectonic position of the Roibok Group being in contact with the Ghanzi-Chobe Belt; this contact indicates that the equivalent lithologies of the Southern Margin Zone do not occur in Botswana (Carney *et al*., 1994). An alternative view proposed by Carney *et al*. (1994) is that the Roibok Group correlates with pre-Damaran lithologies and that the resemblance with the Matchless Member is a coincidence. This led Carney *et al*. (1994) to favour a correlation of the southeastern margin of the Roibok Group with the Areb Mylonite Zone based on the migmatitic texture of the Roibok Group. De Wit (*pers. comm*., 2012) suggests that the Xaudum Magnetic High, located in the Shakawe Zone, is the northern continuation of the Matchless Member (Figure 2.32). However, metaturbidites and meta-pillow-mafic lithologies have not been intersected in the boreholes drilled by Tsodilo Resources Ltd., which is the signature of the Matchless Member.

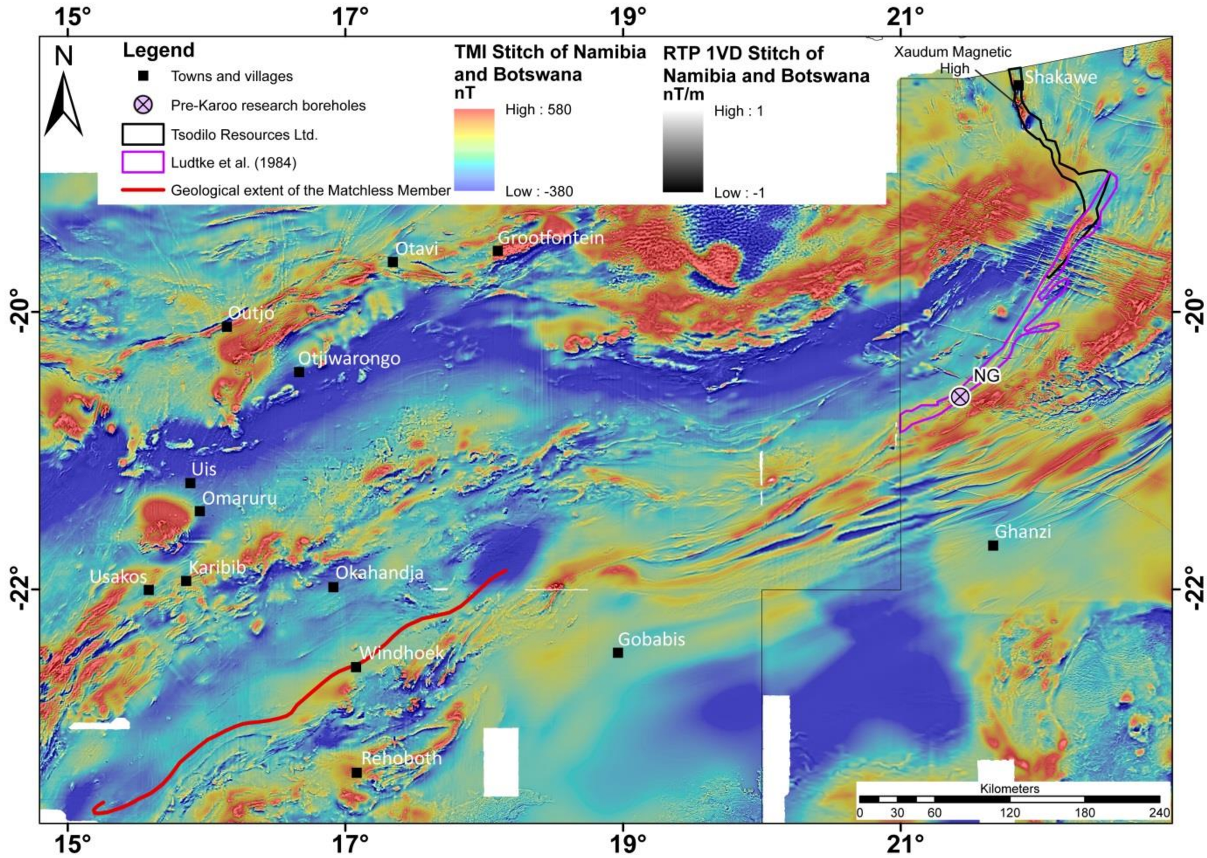

Figure 2.32: The continuation of the Matchless Member (red line) into Botswana relative to the extent of the Matchless Member proposed by Lüdkte *et al*. (1986) (purple outline) based on NG drill core information (purple circle with black cross) and Tsodilo Resources Ltd.'s proposed extent (black outline) based on their drill core of the Xaudum Magnetic High. Background image is a 50% transparent colour scale Total Magnetic Intensity stitched image of Namibia and Botswana overlain on the RTP 1VD greyscale stitched image of Namibia and Botswana.

The Ghanzi-Chobe Belt is suggested to be the continuation of the Southern Foreland based on similar structural styles (Carney *et al*., 1994). Investigations of rock exposures found in the vicinity of the Klein Aub, Dordabis and Witvlei and Sinclair Basins (Borg, 1987, 1988; Borg and Maiden, 1987; 1989; Maiden and Borg, 2011) have allowed the Ghanzi-Chobe Belt to be correlated with the Doornpoort, Klein Aub and Eskadron Formations in Namibia based on lithological and/or geochronological similarities and the occurrence of strata-bound copper sulphide mineralisation. This includes a metavolcanic basement overlain by an upward-fining clastic sequence (Borg, 1988). The various attempts at linking the rocks of the Ghanzi-Chobe Belt with rocks in Namibia include the correlation of the Kgwebe Formation with the volcanic rocks of the Sinclair Supergroup (Schwartz *et al*., 1995; Kampunzu *et al*., 1998), whereas the Ghanzi Group is either correlated with the Nosib Group (Schwartz *et al*., 1995; Kampunzu *et al*., 1998; Ramokate *et al*., 2000; Haddon, 2001) or with the Tsumis Group (Sinclair Supergroup) (Borg and Maiden, 1987).

The U-Pb single zircon age of 1 106 ± 2 Ma for the Kgwebe Formation by Schwartz *et al*. (1995) falls within error of Hegenberger and Burger's (1985) U-Pb zircon age obtained from a porphyritic rhyolite of the Oorlogsende Porphyry Member of 1 094 $^{+18}/_{-20}$. The Oorlogsende Porphyry Member is situated in a narrow belt of isolated outcrops that connects the Ghanzi-Chobe sequences with its correlatives in Namibia (Figure 2.19). The 1 106 ± 2 Ma age of the Kgwebe Formation correlates with U-Pb zircon ages from the Nückopf Porphyry in Namibia of between 1 010 Ma and 1 172 Ma (Schwartz *et al*., 1995). The correlation of the Ghanzi Group with lithologies in Namibia is based on; 1) similar occurrences of stratabound copper sulphide mineralisation are found in the basins of southern Namibia and the Ghanzi-Chobe sequence (Borg and Maiden, 1987; Borg, 1988). 2) Lithological similarities discussed by Borg and Maiden (1987), Borg (1987, 1988), Schwartz *et al*. (1995); Modie (1996), and Kampunzu *et al*. (1998). 3) There are no recorded glacial deposits in the Ghanzi Group and thus the exposed sequence must be younger than the Blaubeker Formation (Schwartz *et al*., 1995).

2.8. Summary

This chapter summarised the outcrop geology, regional geophysical studies and previous cross-border correlations between the Damara Belt and northwest Botswana. The stratigraphic and geophysical review discussed above has highlighted a number of geological units in Namibia and Botswana that can be used as magnetic marker horizons in the cross-border correlation between the two countries. The redox boundary between the Ngwako Pan and D'Kar Formations contain disseminated magnetite and pyrrhotite grains, which are used to trace the continuation of the Ghanzi-Chobe Belt into Namibia. The iron formations and diamictites of the Chuos Formation (Namibia) and iron formations of the Tsodilo Hills Group (Botswana) are associated with positive, linear magnetic signals. Other units associated with a positive magnetic signal are the Palaeoproterozoic basement, Nosib Group, Matchless Member and Roibok Group. The low negative magnetic signals of the Kuiseb Formation and Koanaka Group can also be used to propose cross-border correlations.

Enhanced zones of conductivity are expected in the graphitic Baulkrans Formation (Kudis Subgroup), Hureb Formation, Arises Member (Karibib Formation), Kuiseb Formation and the mineralised Berg Aukas Formation, Mulden Group, Opdam Formation, Duruchaus Formation, Matchless Member, Aha Hills Formation and Ghanzi Group. The Palaeoproterozoic basement is associated with high resistivity values of > 5 000 Ωm. These properties of the lithologies are used to constrain the lateral extent along strike beneath the three MT profiles investigated in this study.

Previous cross-border correlations have focused on either geological or geophysical interpretations resulting in numerous proposed correlations for a single geological domain. The proceeding chapter discusses the available geological data (digital maps of Pryer *et al*., 1997 and Key and Ayres, 2000) and the survey design of the geophysical data used in this study.

Chapter 3

Available data sets

3.1. Introduction

The data sets used to constrain the sub-surface geological map of Namibia and Botswana are potential field (aeromagnetic and gravity), magnetotelluric (MT), physical property and geological data sets. The initial aeromagnetic grids were supplied by Rio Tinto as regional gridded data at grid cell sizes of 50 m (referred to in this study as high resolution), 200 m, 250 m, 500 m and 750 m and a gravity grid of Namibia, Botswana, Zimbabwe and Zambia at a grid cell size of 5 km. The MT data were acquired by the South African MagnetoTelluric EXperiment (SAMTEX). Geological and topographic maps in both hardcopy and digital format were used for Namibia and Botswana along with a geochronology database of published age dates from the literature and new age dates from this project.

3.2. Aeromagnetic data

Aeromagnetic data have long been used in exploration as an aid in mapping and understanding economic mineral deposits (Grant, 1985; Anderson *et al*., 2013). Aeromagnetic data is relatively cheap and quick to acquire compared to other geophysical data sets. The high-resolution of the aeromagnetic data (compared with the gravity data) and the fact that magnetic anomalies and lineaments are often associated with ore deposits, has led to the aeromagnetic data being the most important geophysical data set used for this project.

Namibia, Botswana and Zambia, each have their own regional-scale aeromagnetic surveys that were flown according to the country's specifications at the time of collection. The individual survey blocks were merged into a single, continuous regional aeromagnetic grid of the respective countries by private companies and/or the respective geological surveys.

3.2.1. Namibia

The regional aeromagnetic datasets covering Namibia at a resolution of 200 m, 250 m and 500 m were compiled by the Geological Survey of Namibia (GSN) with co-operation from the German

Federal Institute of Geoscience (BGR). The surveys were flown between 1962 and 1992 and consist of ~700 000 line km in 41 survey blocks (Eberle *et al*., 1996). The survey blocks were flown perpendicular to the general strike of the geology in a specific block, at a flight height of 100 m to 150 m and with line and tie-line spacing of 1 km and 10 km, respectively (Eberle *et al*., 1996; Corner, 2000). The purpose of the survey was to collect data of the whole country at a single elevation of 100 m terrain clearance at the same magnetic time period (Eberle *et al*., 1996). To reliably determine the temporal variations in the Earth's magnetic field in time and location, the International Geomagnetic Reference Field (IGRF) had to be determined. As there are only three IGRF stations in southern Africa, Eberle *et al*. (1996) used regional models based on repeat measurements taken once every five years from a station network covering southwest Africa provided by the Hermanus Magnetic Observatory. As the majority of the surveys were flown at a constant elevation and barometric altitude readings were not stored on archive tapes, the digital terrain model (DTM) with a grid cell size of 200 m was used to constrain the vertical gradient of the Total Magnetic Intensity (TMI) map as locally, the terrain in Namibia varied from sea-level to ~2 500 m over a distance of 100 km (Eberle *et al*., 1996).

Higher resolution data collection in Namibia started in 1994 and is still ongoing. All surveys were flown by consultant companies using a fixed wing aircraft and Caesium vapour magnetometer. The line spacing was 200 m (except for the Gam and Bushmanland surveys which were 250 m) with an average flight height of 80 m and tie line spacing of 2 500 m. Most of the surveys were flown in a north-south direction with a sampling rate of between 0.05 s to 0.1 s. Before merging the data the appropriate IGRF was removed from each survey block by the contractor (Table 3.1). The high-resolution survey blocks used in this study (Figure 3.1) were supplied by the GSN.

Table 3.1: List of the dates of the surveys, the year of the IGRF removed and the contractor. The location of the survey blocks are shown in Figure 3.1.

Survey block	Name of survey block	Year of survey	Year of IGRF removal	Contractor
1	Caprivi	2009	2005 Model	GPX Surveys
2	Gam	1994	1990 Model	N/A
3	Bushmanland	1994	1990 Model	N/A
4	Rietfontein	2001	2000 Model	Tesla 10
5	Aminuis	2002	2000 Model	Tesla 10
6	Kalahari	2007/2008	2000 Model	GPX Surveys
7	Kuiseb	2005/2006	2000 Model	GPX Surveys
8	Rehoboth	1999	1995 Model	Geodass Survey
9	Hakos	1994/1995	1990 Model	World Geoscience
10	Steinhausen	2001	2000 Model	Tesla 10
11	Hochfeld	1994/1995	1990 Model	World Geoscience
12	Okahandja	2003	2000 Model	GPX Surveys
13	Erongo	1994/1995	1990 Model	World Geoscience
14	Ugab	2007	2005 Model	N/A
15	Khorixas	1997	1995 Model	Geodass Survey
16	Grootfontein	1999/2000	1995 Model	World Geoscience
17	Otavi	2007/2008	2000 Model	GPX Surveys

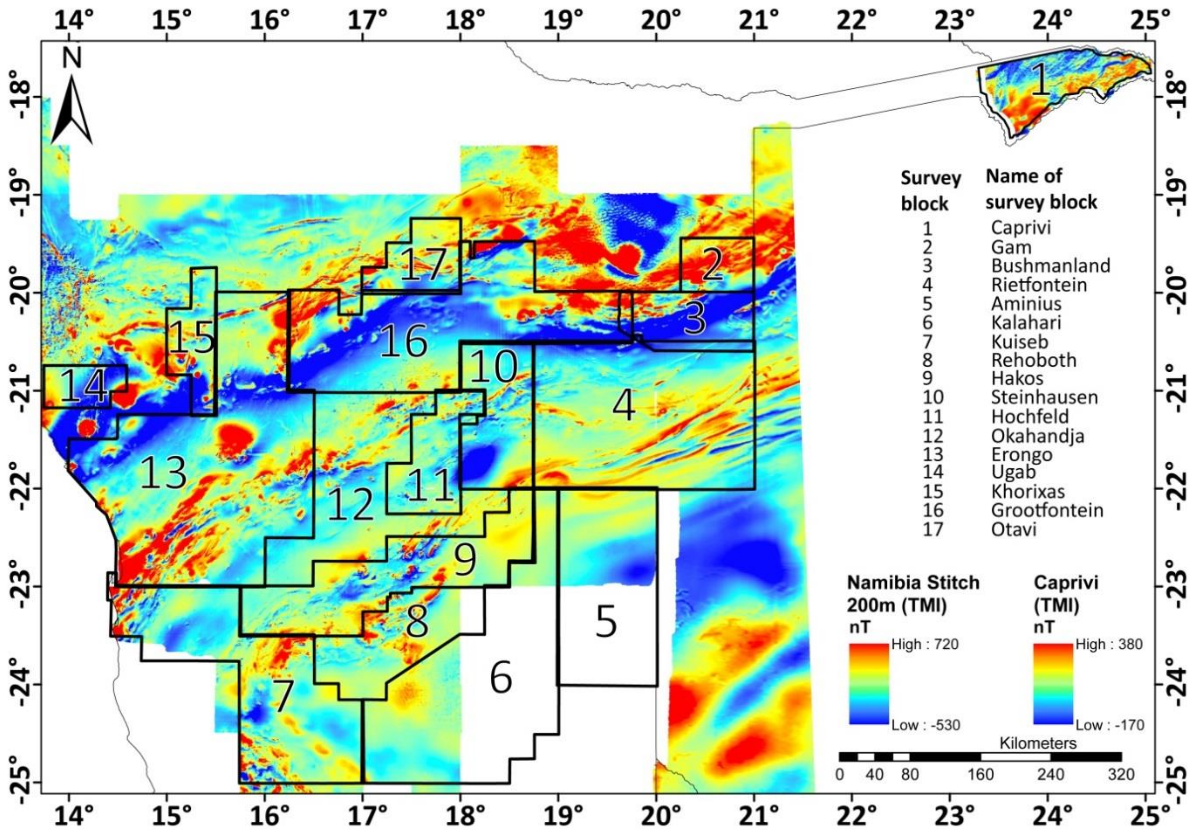

Figure 3.1: Spatial extent of the 17 high-resolution (50 m) aeromagnetic grids provided by the GSN overlain on the TMI map of Namibia gridded at 200 m and Caprivi gridded at 50 m, with the IGRF at the time of data acquisition subtracted prior to merging of the surveys.

3.2.2. Botswana

Since 1993, the Geological Survey of Botswana has collected high-resolution aeromagnetic data. These surveys have been contracted out to private airborne survey companies. Fifteen high-resolution aeromagnetic surveys cover ~90% of Botswana, of which the six used in this study are outlined in purple on Figure 3.2. All surveys were flown with a fixed wing aircraft at a line spacing of 250 m with an average tie line spacing of 1 250 m at an average flight height of 80 m. A Scintrex CS 2 was used with a sampling rate of 0.1 s. The surveys were flown perpendicular to the dominant geological strike. The IGRF of each survey was removed prior to stitching by the Geological Survey of Botswana (Table 3.2).

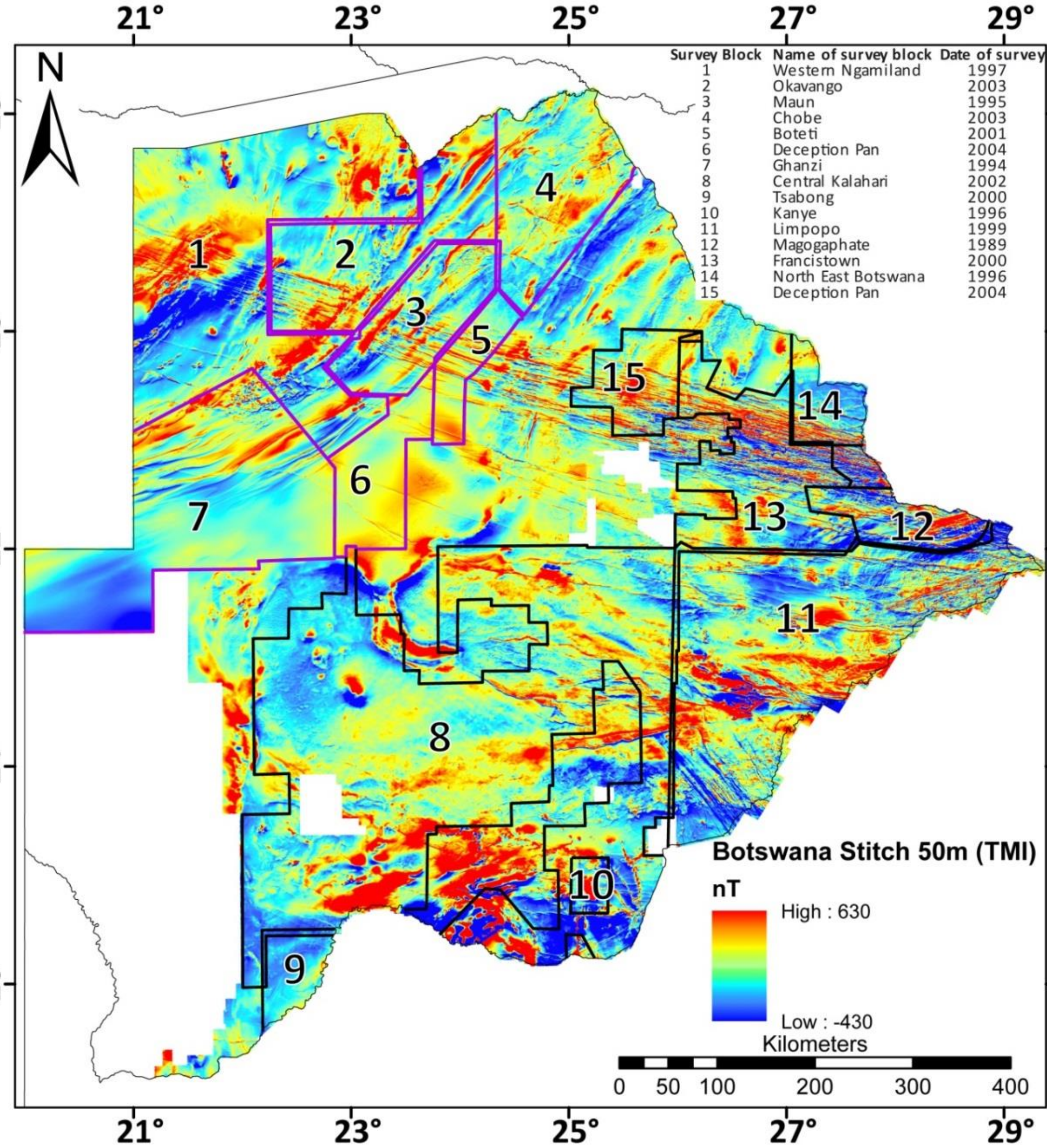

Figure 3.2: Spatial extent of the 15 high-resolution aeromagnetic surveys conducted over Botswana with the six used in this study outlined in purple overlain on the TMI map of Botswana at a grid cell size of 50 m with the IGRF at the time of data acquisition subtracted.

Table 3.2: List of the dates of the surveys, the year of the IGRF removed and the contractor. The location of the survey blocks are shown in Figure 3.2.

Survey block	Name of survey block	Year of survey	Year of IGRF removal	Contractor
1	Western Ngamiland	1997	1995 Modal	CGG
2	Okavango Survey	2002/2003	2000 Modal	Sefofane Geophysics
3	Maun	1995	1990 Modal	Aerodata Botswana
4	Chobe	2003	2000 Modal	Fugro Airborne
5	Boleti	2001	2000 Modal	Fugro Airborne
6	Deception Pan	2004	2000 Modal	Fugro Airborne
7	Ghanzi	1994	1990 Modal	Poseidon Geophysics

3.2.3. Zambia

The digital aeromagnetic data available for Zambia were derived from a compilation of various digitised contour maps of the country-wide aeromagnetic survey undertaken by the Geological Survey of Zambia between 1967 and 1982 (Saviaro, 1980; Katongo *et al*., 2002). Therefore, the data are not up to present-day standards but still provide useful information for a first pass geological interpretation. Aeromagnetic data were collected with a fluxgate magnetometer at a line spacing of between 800 m and 2 000 m at a mean flight height of 150 m (Katongo *et al*., 2002). Manually contoured magnetic intensity maps, at a scale of 1:50 000, were produced from the data (Isaacs, 1968). These contoured maps, along with data collected from later surveys were digitised, with the help of the Council of Geosciences of South Africa, and merged to produce the regional 250 m grid cell size digital map of Zambia (Figure 3.3) (Katongo *et al*., 2002).

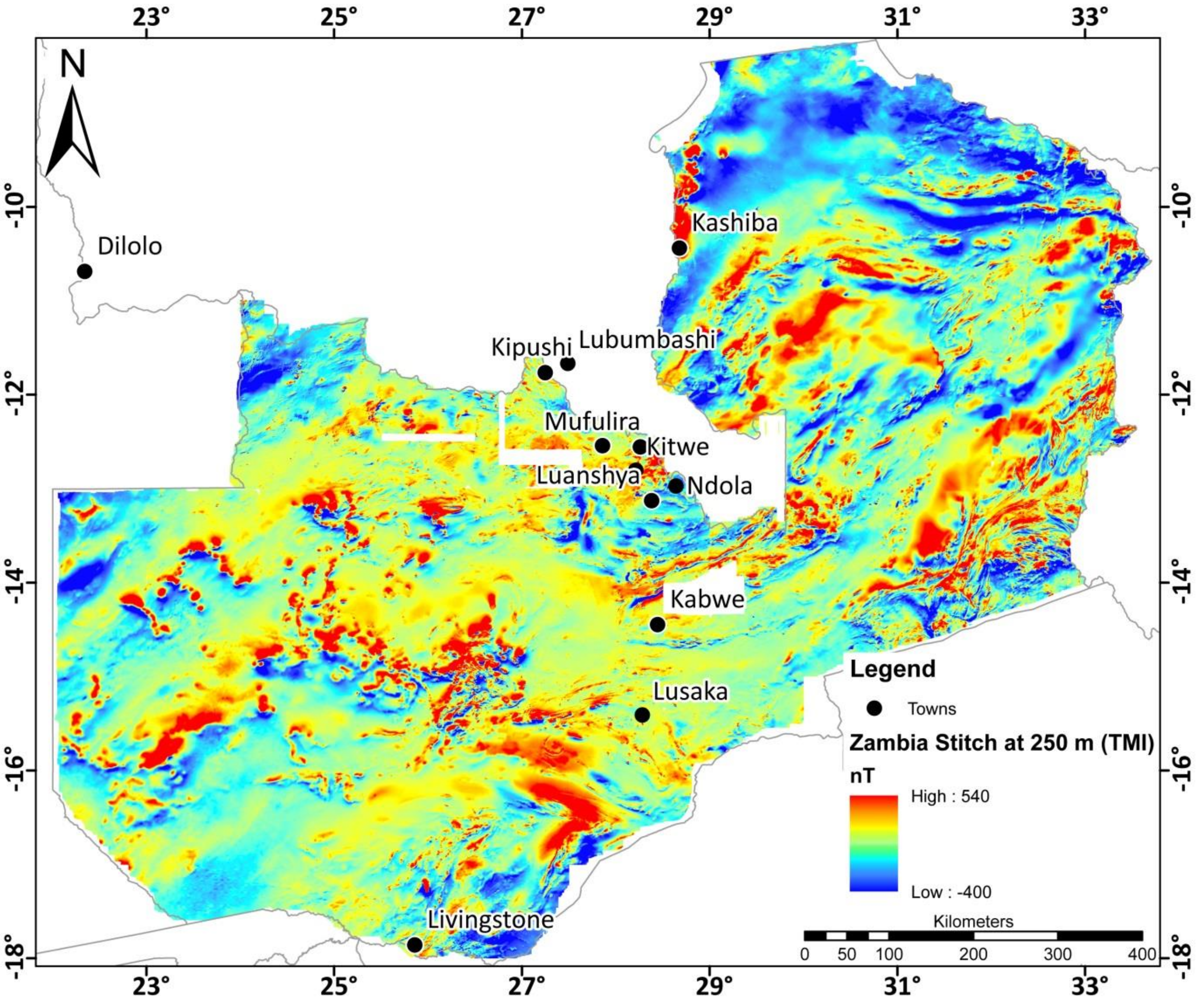

Figure 3.3: TMI map of Zambia gridded at 250 m with the IGRF at the time of data acquisition subtracted. The locations of the main towns are shown as black circles.

3.3. Gravity data

Gravity surveys are also relatively inexpensive to collect and are widely used for the detection of ore deposits, and regional and local mapping (Dentith and Mudge, 2014). The gravity data is used to compliment the regional aeromagnetic interpretations and to note any correlations or anti-correlations in the two data sets to try and determine the underlying lithologies.

Namibia, Botswana and Zambia, each have their own regional-scale gravity surveys that were acquired according to the country's specifications at the time of collection. Botswana currently has the best gravity cover with a station spacing of ~7 km to 8 km, compared with Namibia and Zambia of 15 km and 20 km, respectively.

3.3.1. Namibia

The early countrywide gravity data of Namibia was acquired by Kleywegt in the early 1960s as part of his Ph.D. thesis (Figure 3.4). The survey consisted of very coarse station spacing along roads, using barometric altimeters to constrain the elevation resulting in errors of between 2 mGal to 5 mGal (Corner, *pers. comm.*, 2013). In 1975, the gravity data for the Dordabis area were collected by Corner (1977) using a Canadian CG-2 with an accuracy of 0.02 mGal, with a Short and Mason aneroid barometer used during the winter months to measure the elevation. During the summer months because of temperature variations a System Paulin (Palab) type barometer calibrated in centimetres of mercury and metres was used to measure elevation (Corner, 1977). The survey consisted of ~600 gravity stations recorded along main, secondary and tertiary roads, at a station spacing of between 1.6 km and 3.2 km. The fork in the roads at the settlement of Dordabis was used as the base station (Corner, 1977). In addition, eight stations were used as sub-base stations (check points) which yielded a maximum error of ~1.5 mGal at any station. Using a Scintrex CG-2 (accuracy of 0.02 mGal), Corner (1982) conducted three gravity profiles across the Rössing Dome, Ida Dome and Tsaun Dome. Measurements were collected along the centre of river beds with elevation (accurate to ~5 cm) and distance measured by theodolite and staff, with intervals between stations averaging 300 m (Corner, 1982). The “leap-frog” method was used to check readings i.e. an arbitrary base station was established for each traverse and after 45 minutes of surveying the gravimeter was re-read at one of the previous stations, usually 1 km back along the traverse. The maximum error associated with each station is ~0.1 mGal when considering errors in height, gravimeter drift, station location and topography (Corner, 1982).

The GSN has continued to upgrade the regional gravity coverage of Namibia and in 1997, four absolute gravity stations located at Arandis, Tsumeb, Keetmanshoop and Windhoek were established with the aid of the National Imagery and Mapping Agency (NIMA) of the United States of America (Geol. Surv., 1998). In addition to this, 21 secondary gravity reference stations were established in the northern and central parts of Namibia using Scintrex CG-3 and La Coste Romberg gravity meters on loan from NIMA (Geol. Surv., 1998). In co-operation with Rhodes University and financed by the Minerals Development Fund, seven hundred new gravity stations were established in 1999 to study the Goas Complex in the Karibib area (Geol. Surv., 2000). By 2000 the national gravity database consisted of ~13 000 data points with the majority of these data points having been collected along main roads (Geol. Surv., 2001). In that year the systematic regional coverage on selected map sheet areas at a scale of 1:250 000 on the Rehoboth sheet 2316 was also started (Geol. Surv., 2001). During this field season, ~140 point gravity observations were made using La Coste Romberg gravity meter and a Differential GPS (DGPS) system to measure elevation to sub-decimeter accuracy (Geol. Surv., 2001). In 2000, 108 gravity measurements were collected in the Tsumeb and Grootfontein areas, including linear profiles and randomly located observation points across the *Grootfontein Complex* (Geol. Surv., 2001). The regional gravity station spacing in the Rehoboth was increased to one station per 16 km^2 with the establishment of more than 200 new gravity stations in 2002 (Geol. Surv., 2003a). In addition, 210 gravity measurements were collected along an 11 km profile ~5 km west of Rehoboth (Geol. Surv., 2003a). In 2004, 44 new first order gravity base stations were established in northern and central Namibia using Scintrex CG-3 and La Coste Romberg gravity meters and a Trimble DGPS system to measure elevation (Geol. Surv., 2003b). These new gravity measurements were tied to the absolute gravity base stations at Windhoek, Tsumeb and Arandis and improved the gravity coverage of Namibia, so that any region in Namibia was within a 150 km of a gravity base station (Geol. Surv., 2003b).

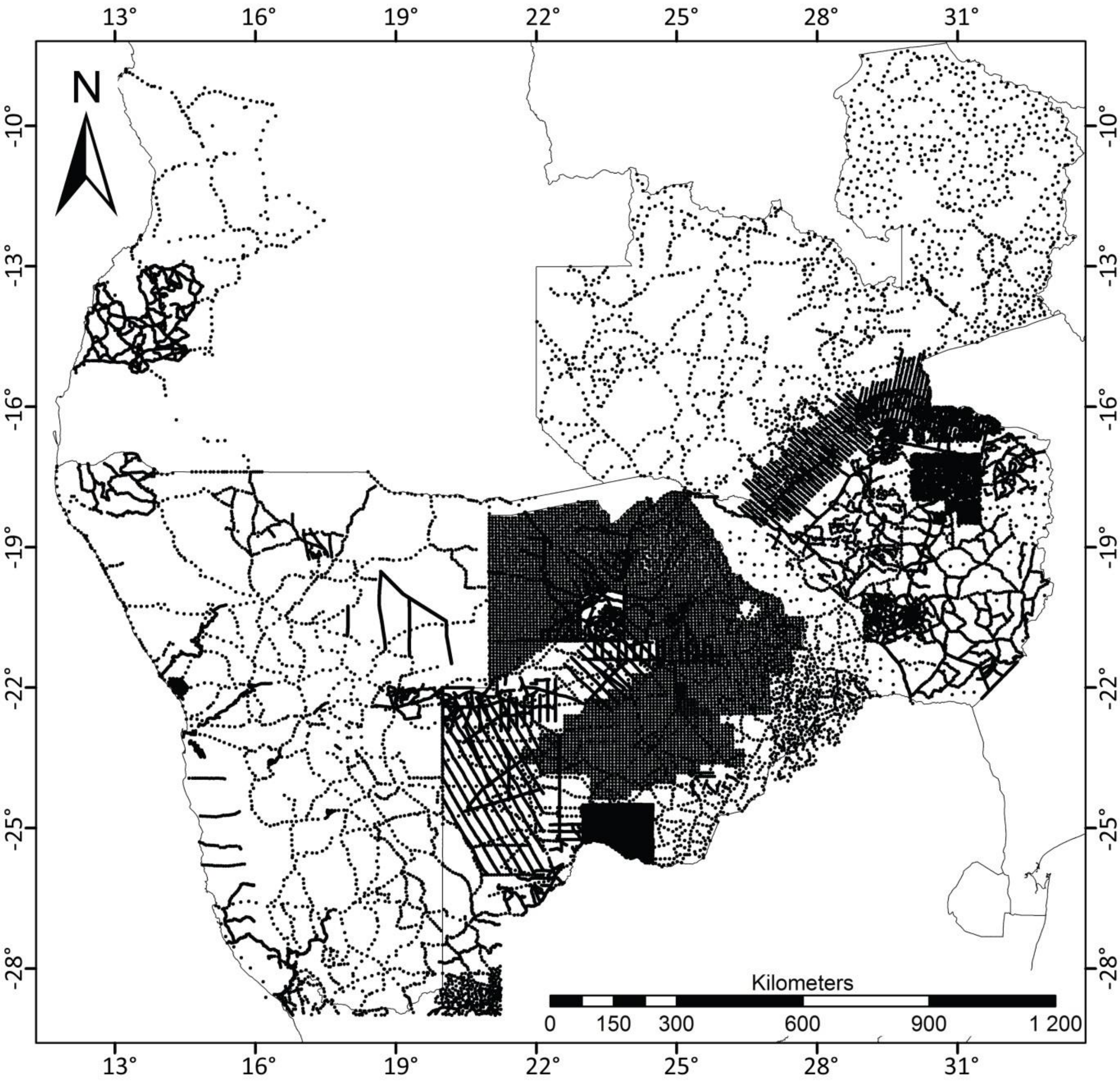

Figure 3.4: Location of gravity stations indicated by points and line traverses of Namibia, Botswana, Zimbabwe, Zambia and central western Angola.

3.3.2. Botswana

During 1970-1971 a gravity survey consisting of ~1 500 stations was conducted in the Ngamiland district, northwest Botswana. A nationwide gravity survey followed in 1972 when funds became available through the British Government's Overseas Development Ministry (Figure 3.4) (Hutchins and Reeves, 1980). The first phase of the project established a network of 23 gravity base stations. Two LaCoste and Romberg gravity meters were flown by light aircrafts between the stations and the International Gravity Standardization Net 1971 (IGSN 71) bases were located at Cape Town, Johannesburg, Livingstone, and Nairobi. Each network station had an accuracy of ~1 km in latitude, ~5 m in elevation and the total gravity values were accurate to 0.3 mGal (Carruthers and Reeves, 1974). The error was reduced by a factor of 0.05 mGal when the drift correction was applied to observations where possible (Carruthers and Reeves, 1974).

The second phase was completed during 1972 - 1973 (Reeves and Hutchins, 1976) and involved establishing 1 854 gravity stations and the tying-in of 277 gravity stations from the Ngamiland Survey. The survey was mainly truck-borne with measurements at 10 km intervals along roads, tracks and exploration cut-lines. A helicopter was used to establish 300 stations in the inaccessible central and southwest regions of Botswana (Hutchins and Reeves, 1980). This equated to a country wide coverage of 37 gravity stations per 100 km^2 (Yawsangratt, 2002). Each network station had an accuracy of ~1 km in latitude, ~5 m in elevation and the total gravity values were accurate to 0.05 mGal (Yawsangratt, 2002).

During 1998 - 1999 a gravity survey was carried out in northern Botswana to increase the data resolution of the 1972 - 1973 gravity survey (Figure 3.4) (Yawsangratt, 2002). The survey was completed by Poseidon Geophysics (Pty) Limited on behalf of the Geological Survey Department, Ministry of Minerals, Energy and Water Affairs, Republic of Botswana. A total of 4 003 gravity stations at a spacing of 7.5 km were established with an improved accuracy in latitude and elevation of ~10 m and 0.15 m respectively, and a gravity accuracy of 0.03 mGal for northern Botswana (Yawsangratt, 2002). The gravity measurements were recorded with a Scintrex CG-3 flown by light aircrafts (helicopter and light fixed wing aircraft) (Yawsangratt, 2002).

3.3.3. Zambia

The Geological Survey of Zambia, in collaboration with the University of Zambia and the University of Michigan, carried out a nationwide reconnaissance gravity survey of Zambia from 1971 to 1975 (Cowan and Pollack, 1977). The survey consisted of over 2 700 gravity stations established along primary and secondary roads at ~10 km to 15 km station spacing, equating to one gravity station per 400 km^2 (Figure 3.4) (Cowan and Pollack, 1977). All stations were referenced to the established East African primary net (Masson Smith and Andrew, 1962). The 1930 International Gravity Formula and a density of 2.67 $g.cm^{-3}$ were used to calculate the free-air and simple Bouguer anomalies. Topographic contour maps were used for approximately one-third of the elevation corrections with the elevations of the remaining stations being determined with aneroid barometers, which yielded a mean error of ~2 mGal (Cowan and Pollack, 1977).

The Bouguer gravity anomaly map of the countries was merged and gridded at a grid cell size of 5 km using the minimum curvature technique (Briggs, 1974) to produce a southern African Bouguer anomaly map (Figure 3.5).

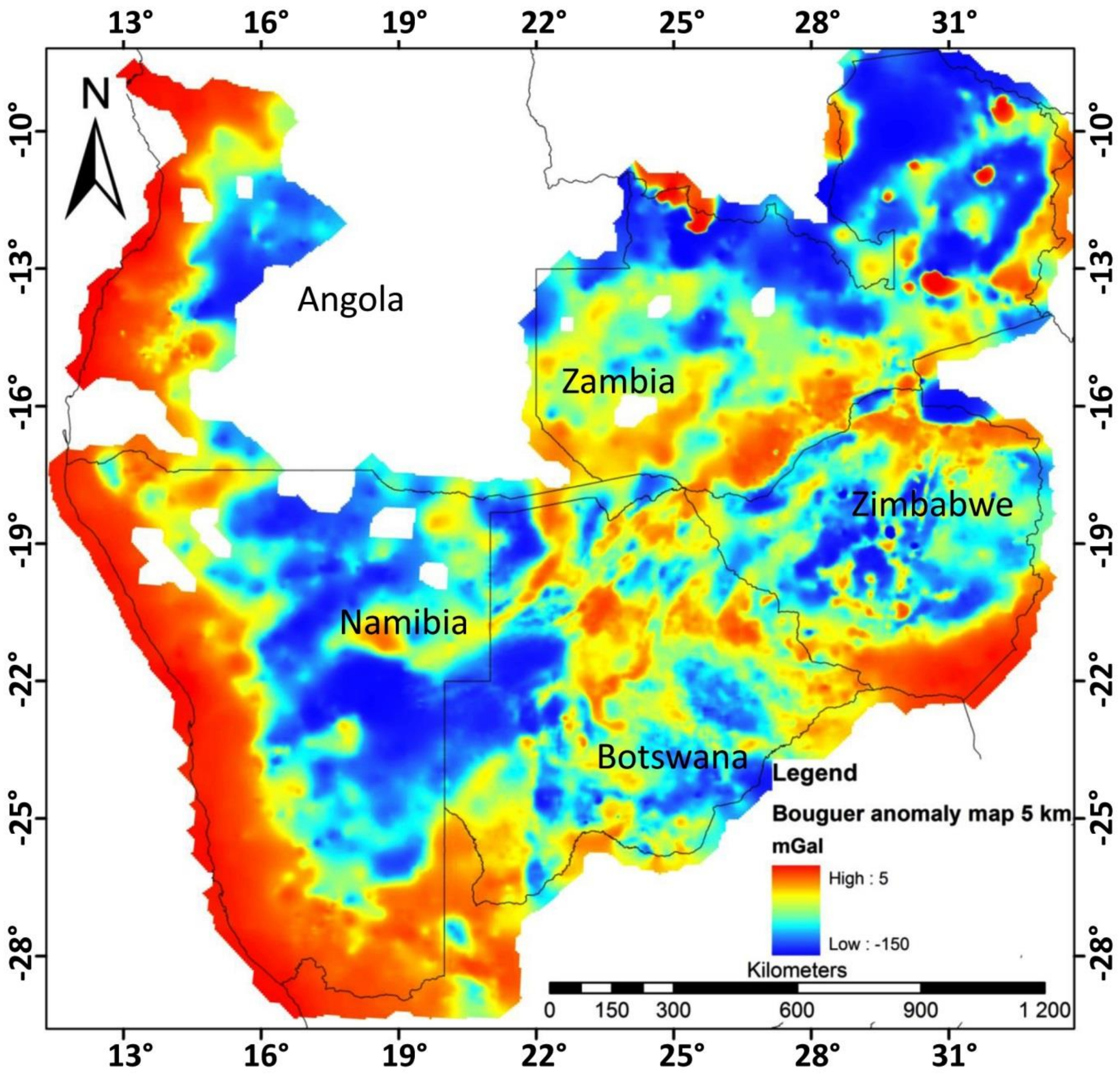

Figure 3.5: Bouguer anomaly map of Namibia, Botswana, Zimbabwe, Zambia and part of Angola, gridded at 5 km.

3.4. Summary of aeromagnetic and gravity data grids

The aeromagnetic and gravity grids used in this study are summarised in Table 3.3 with the location of the aeromagnetic grid shown in Figure 3.1 and 3.2. The country names are in bold with the respective name of the aeromagnetic survey blocks beneath them. The grid cell size of the survey block is highlighted.

Table 3.3: Summary of the resolution of the aeromagnetic and gravity grids used in this study. The yellow blocks indicate grids provided by Rio Tinto Exploration while the green blocks were provided by the Namibian Geological Survey. The location of the grids is shown in Figure 3.1 and 3.2.

Area	Aeromagnetic grid cell size (m)							Gravity cell size (km)				
	50	75	125	200	250	500	750	2.1	2.2	2.8	5	6.7
Namibia												
Caprivi												
Erongo												
Stitch of Gam-Bushmanland												
Kalahari												
Aminuis												
Hakos												
Hochfeld												
Okahandja												
Rehoboth												
Rietfontein												
Steinhausen												
Grootfontein												
Otavi												
Khorixas												
Kuiseb												
Ugab												
Zambia												
Botswana												
Ghanzi												
Western												
Maun												
Deception Pan												
Okavango												
Chinamba												
Zimbabwe												
Regional (Namibia, Botswana, Zambia and Zimbabwe)												

3.5. Magnetotelluric data

The MT data used in this project was acquired by the SAMTEX team, which was established in 2003. The SAMTEX database consists of ~780 MT stations deployed across South Africa, Namibia and Botswana (Figure 3.6). The project was designed to image lithospheric and mantle structures which would lead to a better understanding of the tectonic evolution and relationship of the various cratons and mobile belts of southern Africa by having the MT profiles perpendicularly cross-cut known geological terranes. One month was spent at the Dublin Institute of Advanced Studies (DIAS), investigating three approximately north-south, sub-parallel profiles; namely DMB, NEN and OKA-CAM profiles (Figure 3.6). The DMB, NEN and OKA profiles were acquired in 2006 during the third phase of the SAMTEX project with each profile having a station spacing of 20 km (Khoza *et al*., 2013). In 2009, the fourth phase of the SAMTEX project, additional stations of the CAM profile were interspersed with the OKA profile, improving the station spacing on the OKA-CAM profile to ~5 km.

The westernmost profile, the DMB profile, is ~680 km long consisting of 35 broad-band MT (BBMT) (Figure 3.6) stations. Approximately 220 km to the east is the central NEN profile, which is ~440 km long and is composed of 23 BBMT stations (Figure 3.6). The ~260 km long OKA-CAM profile is the easternmost profile, ~190 km to the east of the NEN profile, consisting of 47 BBMT stations. The BBMT sites used Phoenix Geophysics equipment, namely MTU-5 and MTU-5A recording units and MTC-50 induction coils, which recorded time series data for 2 to 3 days in the period range of ~0.002 s to 10 000 s (Jones *et al*., 2007; Khoza *et al*., 2013). However, the longest usable recorded periods for the SAMTEX project are a few 1 000 s because of the short acquisition period of 2-3 days. At each BBMT station, time variations in the horizontal electric and magnetic field was measured. Difficult terrane disallowed for the vertical magnetic field component (H_z) to be measured at every station, therefore only 6 stations along the DMB profile, 5 stations along the NEN profile and 7 stations along the OKA-CAM profile recorded H_z (Khoza *et al*., 2013).

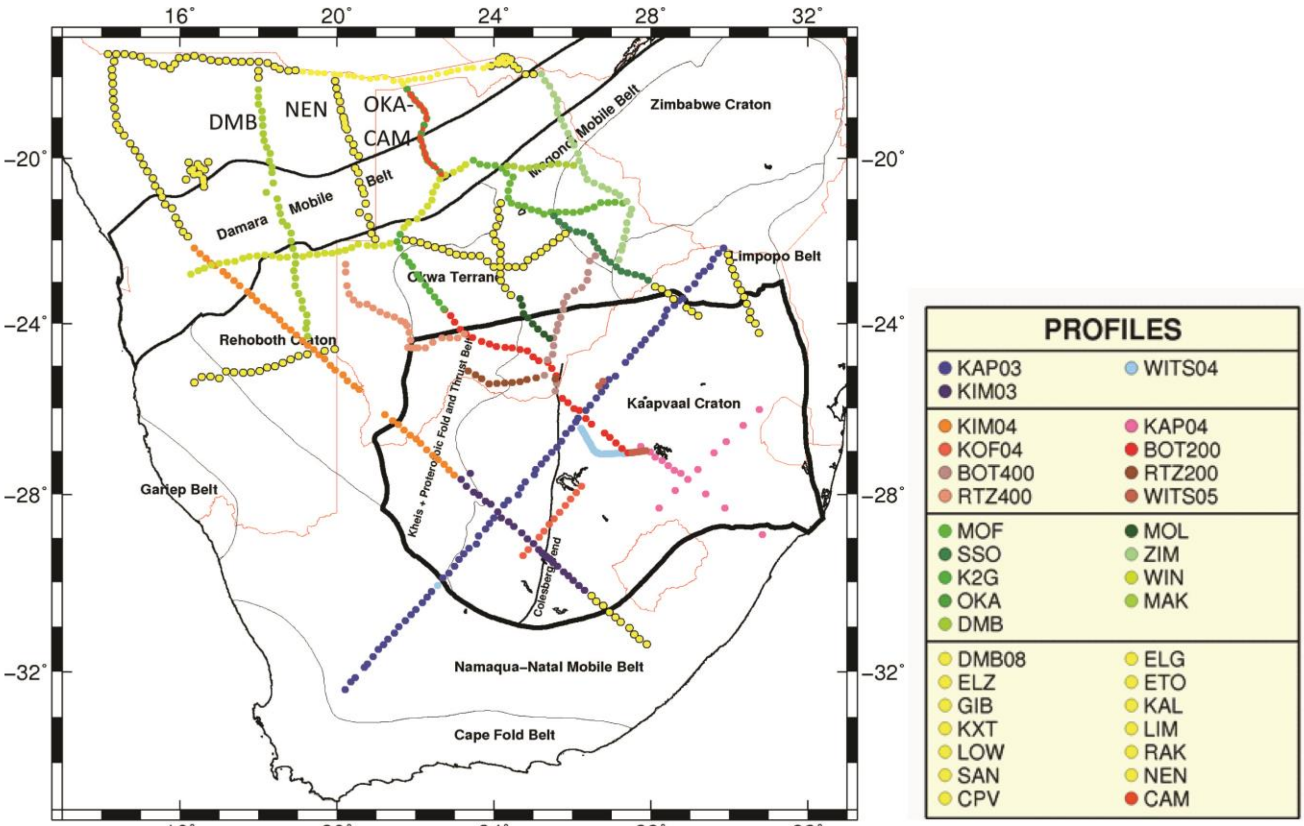

Figure 3.6: Locations of the MT stations of the SAMTEX project are shown as circles with the DMB, NEN and OKA-CAM profiles on a background map of tectonic provinces (black lines) and country boundaries (brown lines; location of MT stations, after Meinsopust *et al*., 2011; Khoza *et al*., 2013).

3.6. Physical properties

Physical property (magnetic susceptibility and specific density) data are sparse in eastern Namibia, northern Botswana and western Zambia because of the extensive sand cover and lack of scientific boreholes and down-hole geophysical studies. The Council for Geoscience of South Africa has compiled physical property measurements for South Africa (Maré *et al*., 2002) with a similar compilation by McMullan *et al*. (1995) for Botswana (summarised in Table 3.4). Physical property data have been collected by Walker *et al*. (2010) in the Molopo Farms Complex of southern Botswana.

Table 3.4: Specific density range and average values for rocks in Botswana (after McMullan *et al.*, 1995). N is the number of samples measured.

Geological unit	Density range ($g.cm^{-3}$)	Average density ($g.cm^{-3}$)	Standard deviation	N
Kalahari beds	1.82 - 2.53	2.26	0.27	10
Dolerite dyke	2.75 - 2.88	-	-	2
Karoo clastic sediments	1.90 - 2.64	2.40	0.19	203
Karoo basalts	2.23 - 2.86	2.62	0.14	76
Ghanzi Group	2.57 - 2.69	2.64	0.054	54
Kgwebe porphyry	2.63 - 3.02	2.76	0.18	11
Precambrian metamafics	2.71 - 3.08	-	-	5
Precambrian gneiss	2.64 - 2.65	-	-	3
Proterozoic basement	2.48 - 2.93	2.72	0.11	19
Archaean basement	2.54 - 3.14	-	-	280

During two one month field seasons hand-held susceptibility measurements were collected on outcrop and borehole samples from Namibia, Botswana and Zambia. Specific density measurements were also collected on selected samples that were brought back to the University of the Witwatersrand. These measurements constrain the interpretation of the aeromagnetic and gravity data as several lithologies can be identified from their physical properties. However, for a complete database more work needs to be carried out as these measurements are very sparse. The location, results and interpretation of the measurements are discussed in Chapter 5.

3.7. Topographic data

The main source of the topographic data used in this study was Shuttle Radar Topography Mission (SRTM) data obtained from the Geosoft DAP Server (Figure 3.7). The SRTM data is gridded at a cell size of 90 m. The primary use of the SRTM data was to determine elevation, which was used in the 2D magnetic forward models and the Euler deconvolution calculations (discussed further in Chapter 8) i.e. to determine the depth of a magnetic source.

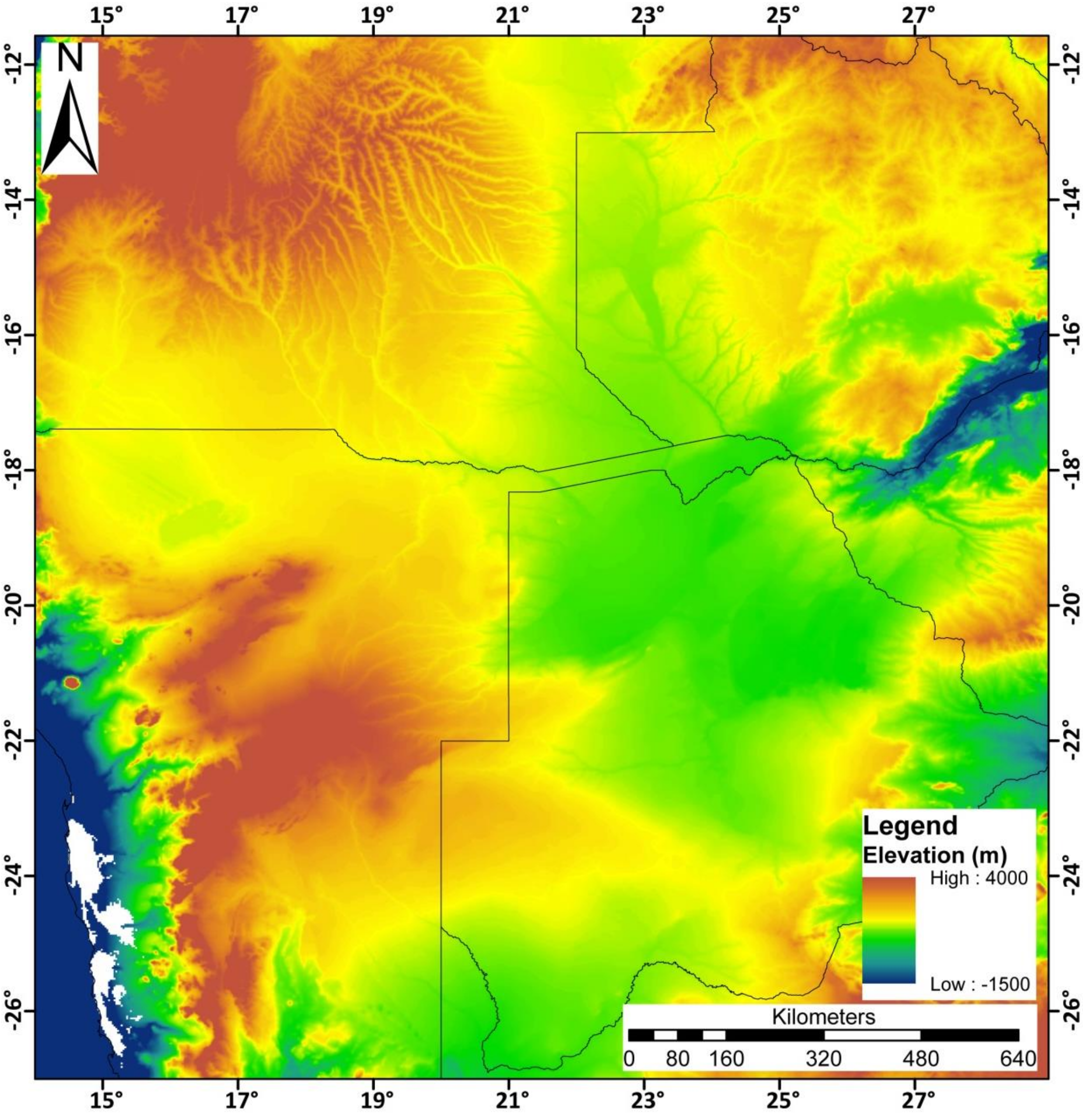

Figure 3.7: SRTM model of southern Africa gridded at a cell size of 90 m, from the Geosoft DAP Server.

3.8. Digital geological maps

Three digital geological maps were used as a first pass interpretation of the geophysical data. These included a regional 1:1 000 000 map of Botswana interpreted by Key and Ayres (2000), a 1:250 000 map of Ngamiland by Pryer *et al*. (1997) and a 1:250 000 map of western Namibia, which is a compilation of geological data from 1:50 000 and 1:100 000 manuscript maps or from provisional 1:250 000 maps held by the Geological Survey of Namibia.

3.8.1. Mapping discrepancies between the 1:250 000 and 1:1 000 000 geological maps of Botswana

The geology of the sub-Kalahari in Botswana has been previously interpreted by Pryer *et al*. (1997), where they mapped Ngamiland at a 1:250 000 scale, and a later interpretation of the whole of Botswana on a 1:1 000 000 scale by Key and Ayres (2000). As most of the geology is covered by Kalahari Group sediments and research boreholes are limited, the main technique in mapping the sub-surface geology is through aeromagnetic interpretation and hence, discrepancies in the interpretation of the magnetic signal by different researchers are common. Both studies agree roughly on the location and extent of the Quangwadum Complex (Figure 3.8a, b). Therefore, this is used as the reference point for discussing the discrepancies.

Metasedimentary rocks north and northeast of the Quangwadum Complex: The Tsodilo Hills and Xaudum Groups

Northwest Botswana is composed of metasedimentary rocks of the Xaudum Group, according to Pryer *et al*. (1997) (Figure 3.8a), or a combination of Xaudum and Tsodilo Hills Group, according to Key and Ayres (2000) (Figure 3.10b).

Pryer *et al*. (1997) divided the Xaudum Group into four sub-groups (Figure 3.8a) based on lithologies determined from the aeromagnetic signal. The main lithologies identified are “carbonates, shales and sandstones” or “ferruginous quartzite”. Within the ferruginous quartzites Pryer *et al*. (1997) interpreted linear magnetic high anomalies to be “ironstone (Chuos equivalent)”. The final group includes areas of “negative magnetic signal” with no rock type associated to the group. The distinction between the Tsodilo Hills and Xaudum Group by Key and Ayres (2000) is both geophysical and lithological. The Tsodilo Hills Group is described by areas of “ferruginous and micaceous quartzite, quartz-mica-schist, metamorphosed conglomerate, minor shale, phyllite, sandstone and ironstone”, and “areas with negative magnetic signature shown to highlight structure” (Figure 3.8b). The Xaudum Group is described by “assorted metasedimentary (siliciclastic and carbonate) rocks including prominent ironstone” (Figure 3.8b). These are important discrepancies between the two surveys. However, there is a general correspondence between specific groups i.e. the lithologies of the Tsodilo Hills Group described by Key and Ayres (2000) correlates with the “ferruginous quartzite” of the Xaudum Group mapped by Pryer *et al*. (1997) (Figure 3.8a, b). The Tsodilo Hills Group described by Key and Ayres (2000) as “areas with negative magnetic signature shown to highlight structure” correlates with Pryer *et al*. (1997)

“negative magnetic signal” of the Xaudum Group (Figure 3.8a, b). The Xaudum Group description of “assorted metasedimentary (siliciclastic and carbonate) rocks including prominent ironstone” by Key and Ayres (2000) correlates with “carbonates, shales, and sandstone” mapped by Pryer *et al*. (1997) (Figure 3.8a, b).

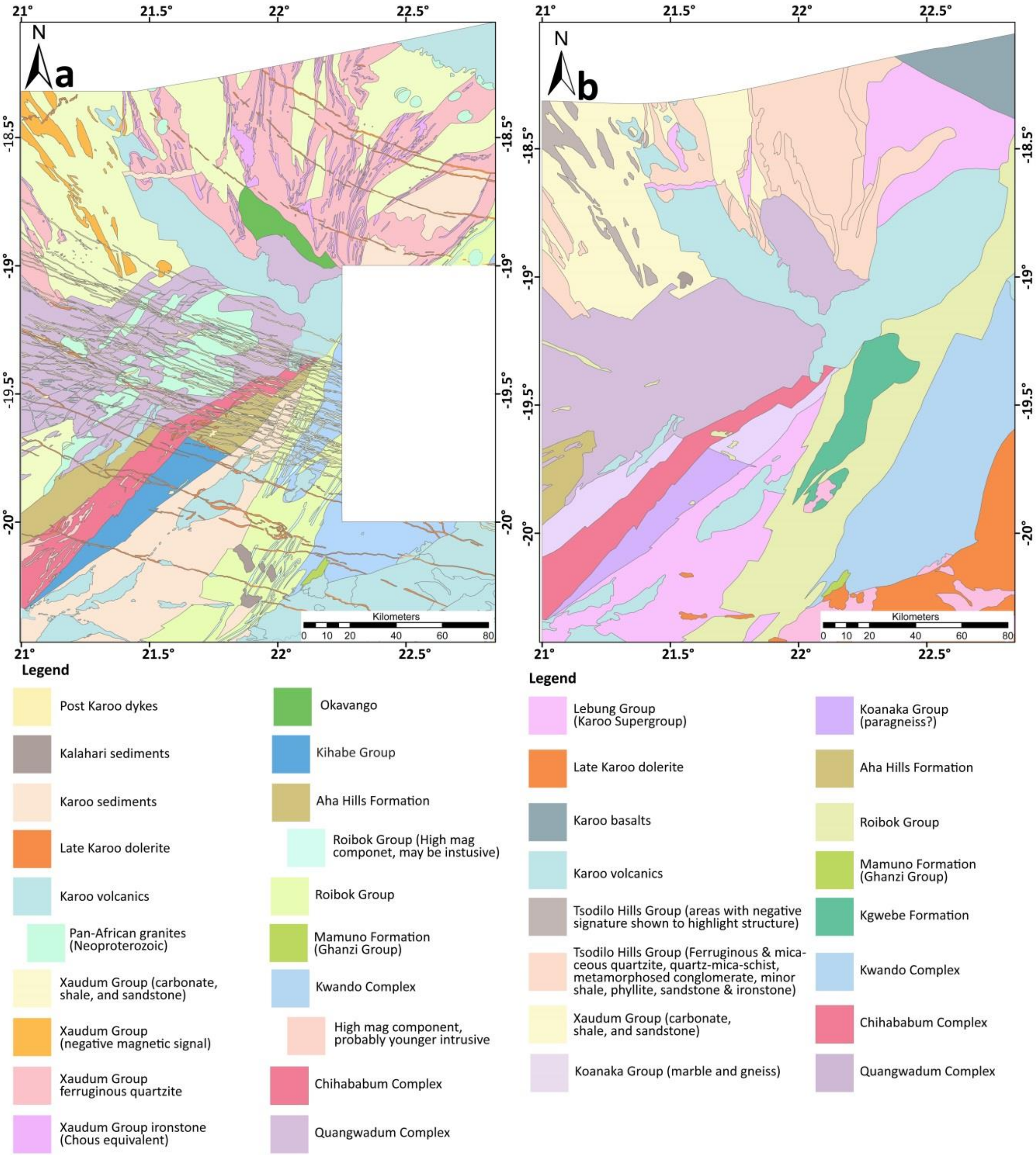

Figure 3.8: Comparison of the Sub-Kalahari geological maps of a) Pryer *et al*. (1997) and b) Key and Ayres (2000). Note the spatial correspondence between the Tsodilo Hills Group of Key and Ayres (2000) with the “ferruginous quartzite” of the Xaudum Group of Pryer *et al*. (1997), the Tsodilo Hills Group of Key and Ayres (2000) as “areas with negative magnetic signature shown to highlight structure” with Pryer *et al*. (1997) “negative magnetic signal” of the Xaudum Group, and the “assorted metasedimentary (siliciclastic and carbonate) rocks including prominent ironstone” of the Xaudum Group of Key and Ayres (2000) correlates with “carbonates, shales, and sandstone” of Pryer *et al*. (1997).

Metasedimentary rocks south of the Quangwadum Complex: Aha Hills Formation, Xaudum Group, Koanaka Group, Chihabadum Complex and Kihabe Group

The lithologies in this area are mainly carbonates and according to the mapping of Pryer *et al*. (1997) and Key and Ayres (2000) they have a similar location and extent but differ in detailed lithological descriptions and nomenclature (Figure 3.8a, b).

According to the mapping of Key and Ayres (2000), from north to south, these units are; the Aha Hills Formation consisting of “dolomitic marble and chert”, Koanaka Group consisting of “paragneiss?”, Chihabadum Complex consisting of “igneous and meta-igneous rocks” and Koanaka Group consisting of “dolomitic marble and poorly exposed granitic gneiss” (Figure 3.8b). According to the mapping of Pryer *et al*. (1997), however, from north to south these units are; Xaudum Group described as being “carbonates, shales and sandstone”, Aha Hills Formation having a low susceptibility and comprising “possible paragneiss”, Chihabadum Complex with no lithological description except for the identified magnetic high amplitude anomalies situated in the complex “high magnetic component, probably younger intrusions” and Kihabe Group with no lithological description (Figure 3.8a).

Due to the lithological differences between these two maps, the correlation between certain units in Namibia and Botswana is very speculative. To resolve these mapping discrepancies, this study correlates lithologies according to their aeromagnetic and gravity signal, lithological descriptions in the literature, and geochronology. The nomenclature used in this study follows that of Key and Ayres (2000).

3.9. Geochronology

The geochronology database comprises ~1 300 data points, including isotopic studies from the late seventies and early eighties, to recent papers published in 2013. Age dates cover the time-span from the Ordovician to the Neo-Mesoarchaean. Location of the available age dates, which include dates from outcrop and borehole samples are shown in Figure 3.9. The majority of these data are from conventional Isotope Dilution Thermal Ionization Mass Spectrometry (ID-TIMS) and spot Laser Ablation Induced Coupled Plasma Mass Spectrometry (LA-ICP-MS) or Sensitive High Resolution Ion Microprobe (SHRIMP) geochronology results from U-Th-Pb isotope system studies. Other dating techniques in the database include $^{40}Ar/^{39}Ar$ thermo-chronology, minor Sm-Nd, Lu-Hf and Rb-Sr and several Re-Os data sets. Zircon grains are the most commonly used mineral to date the Pan-African Orogeny; whilst monazite and garnet analyses provide information about metamorphic events.

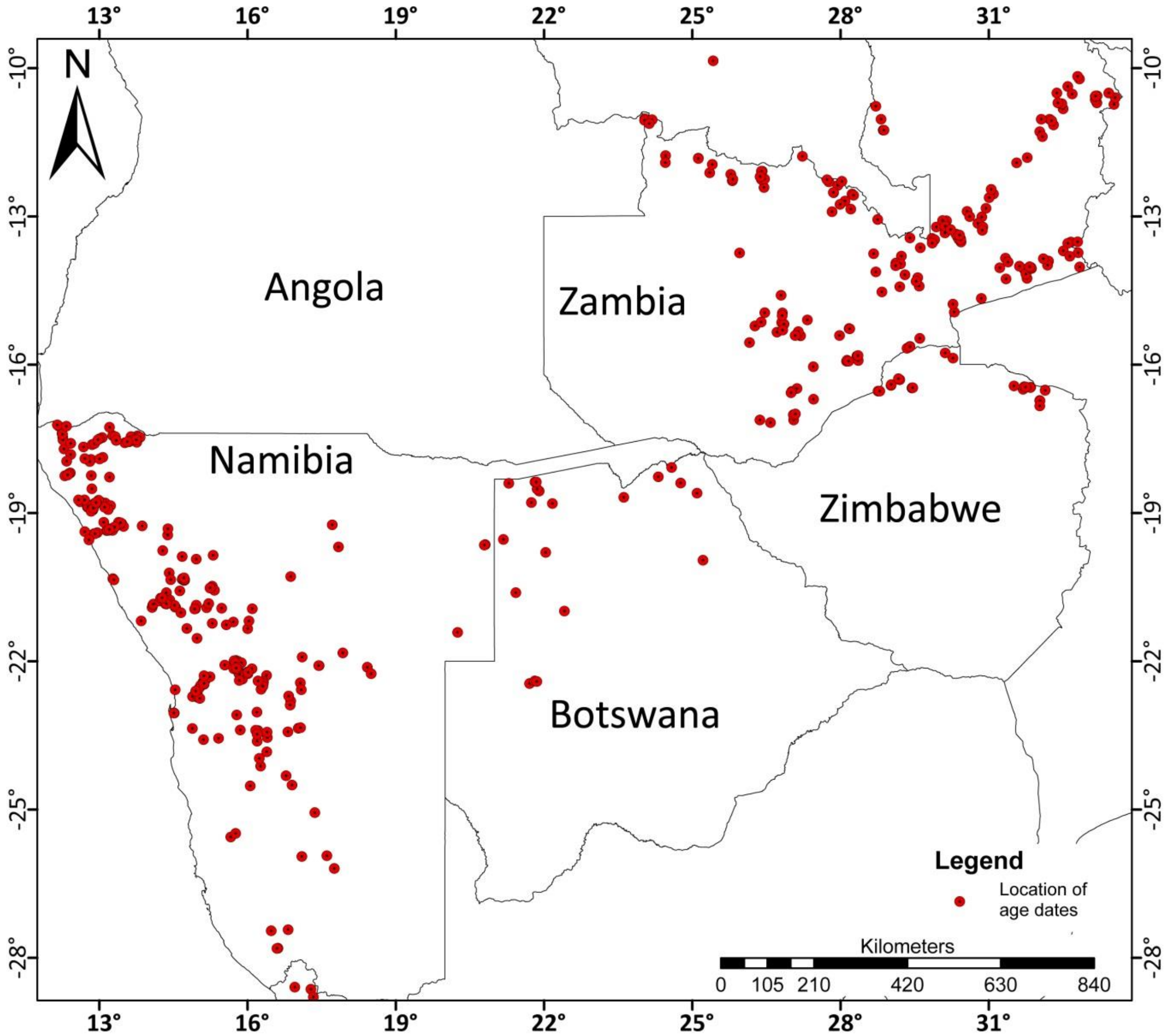

Figure 3.9: Location of age dates in the GIS database for Namibia, Botswana and Zambia and northern Zimbabwe (compiled by Naydenov, 2013).

3.10. Summary

This chapter discussed the available potential field, MT and geochronology data used in this study. In addition, the discrepancies between the previous sub-Kalahari geological maps of Pryer *et al*. (1997) and Key and Ayres (2000) were discussed. The following chapter discusses the filters applied to the potential field data that are used in the interpretation of the sub-Kalahari geological map.

Chapter 4

Image processing

4.1. Geophysical background

Geophysical studies are the dominant technique used where the majority of the study area is covered by younger strata with a limited amount of research boreholes to provide insight into the subsurface geology. To interpret the geology beneath the cover, a number of filters are applied to the potential field data. To interpret shallow features, high pass filters such as the vertical derivative and analytic signal are used. The analytic signal is also used to determine edges of features along with the tilt angle. Deep-seated features, such as basement trends, are enhanced by low-pass filters such as upward continuation and band-pass filtering. The general geological trend observed in the study area is northeast-southwest and this is cross-cut by the northwest-southeast trending Okavango Dyke Swarm. Directional filters such as sunshading, directional cosine filters, and Butterworth directional filters are applied to the aeromagnetic data in an attempt to suppress the high amplitude magnetic signal of the dyke swarm. All these image processing techniques along with the others discussed below have been carried out in Oasis Montaj, Geosoft, hereafter referred to as Geosoft.

4.2. Stitching of grids

The potential field data for this project were supplied by Rio Tinto and consists of gridded data for Namibia, Botswana, Zimbabwe and Zambia at grid cell sizes ranging from 75 m to 750 m (refer to Table 3.1 in Chapter 3). Stitching of the various grids was a challenging process, as the grids of each country have different parameters and grid cell sizes. There are many available interpolation techniques; however, the two preferred techniques in this study are bi-directional and minimum curvature gridding. Minimum curvature is used for irregularly sampled data (gravity data), and for parallel line data (aeromagnetic data), bi-directional gridding is the preferred technique.

Wavelengths that are longer than twice the sampling interval are reliably recorded. This spatial frequency is known as the Nyquist frequency. Frequencies in the sampled field that is greater than the Nyquist frequency cannot be reliably recorded. In frequencies that are lower than the Nyquist, errors will be introduced by a process known an aliasing (Billings and Richards, 2000).

The minimum curvature gridding in Geosoft fits the smoothest possible surface to the data points as described by the method of Briggs (1974) and Swain (1976). The minimum curvature algorithm is an iterative process which initially extends the grid to a maximum of eight times the grid cell size calculating the grid points weighted to the nearest neighbour search pattern. Once an acceptable fit is achieved, the initial grid is divided by two and the same process is repeated using the coarse grid as the starting surface. This process is repeated until the minimum curvature surface is fit at the final grid cell size.

As minimum curvature does not impose a directional bias in the data, while bi-directional gridding enhances trends that are perpendicular to the direction of the survey lines. Before interpolating the grid lines to the final nodes of the grid, each individual line is initially interpolated to determine the data value at the intersection of the grid lines. The result is that even narrow features that continue from line to line are interpolated correctly. As line data is already ordered, a bi-directional gridding algorithm is computationally faster than the minimum curvature method. Bi-directional gridding assumes that the survey lines are perpendicular to the geological strike. If this assumption is not met, the gridding leads to unreliable interpolation perpendicular to the survey lines. The gridding algorithm allows for the gridding direction to be perpendicular to one, but only one, geological strike (Zhou, 1992). In this study, maps were normally gridded at a third of the station spacing (gravity) or line spacing (aeromagnetic).

When stitching the aeromagnetic grids, especially when the grids have different survey parameters, flight line noise was enhanced. Flight line noise manifests as corrugations, which occur parallel to the flight line directions, and can be caused by subtle levelling problems, such as tie line levelling, lag corrections, base level corrections, topography, etc., that were not correctly removed during initial data processing. This noise was removed by decorrugation filtering (Section 4.5.7). Stitching grids of different cell sizes, the grid with the smaller grid size was re-gridded to the larger grid size. This acts as a smoothing filter upon re-gridding and will reduce noise and speed up computation time. If the larger grid size was re-gridded to the smaller grid size, noise, artefacts and gaps in the data appear. Unfortunately, this results in a loss of detail in the higher resolution grid, but allows for the interpretation of a consistent grid.

4.3. Fourier transform

Filtering in Geosoft is carried out in the frequency domain. Detailed information on the Fourier transform is found in Bracewell (1986), Blakely (1995) and Billings and Richards (2000). The classic

Fourier transform assumes an infinite amount of data that has been continuously sampled. However, potential field data is both finite and discrete and these parameters have profound effects when applying the Fourier transform to 'real' data sets. Thus, the discrete Fourier transform is used for 'real' data sets. As the discrete Fourier transform is periodic with a period inversely proportional to the sample interval, both the shortest and longest wavelengths cannot be represented effectively (Blakely, 1995).

Consider data interpolated onto an *N* x *M* spatial grid with a grid cell size of Δx and Δy for the x- and y-axes, respectively. The discrete Fourier transform is calculated on an *N* x *M* frequency grid with grid cell sizes of $\Delta u = \frac{1}{N}\Delta x$ and $\Delta v = \frac{1}{M}\Delta y$. Through the transformation of the 2D discrete Fourier transform, data elements (f_{nm}) in the space domain for the nth and mth column are transformed into the frequency domain elements (F_{jk}) for the jth and kth column, given by;

$$F_{jk} = \Delta x \Delta y \sum_{n=\frac{N}{2}+1}^{\frac{N}{2}} \sum_{m=\frac{M}{2}+1}^{\frac{M}{2}} f_{nm} e^{-2\pi i\left(\frac{jn}{2}+\frac{km}{2}\right)} \tag{4.1}$$

Therefore, the inverse 2D discrete Fourier transform is;

$$f_{nm} = \Delta u \Delta v \sum_{j=\frac{N}{2}+1}^{\frac{N}{2}} \sum_{k=\frac{M}{2}+1}^{\frac{M}{2}} F_{jk} e^{2\pi i\left(\frac{jn}{N}+\frac{km}{M}\right)} \tag{4.2}$$

The Nyquist frequency, given by $u_{max} = \frac{1}{2\Delta x}$ and $v_{max} = \frac{1}{2\Delta y}$, determines the highest wavenumbers that can be sampled (Blakely, 1995). Wave numbers which are higher than those of the Nyquist frequency will fall back into the lower parts of the spectrum values.

In the space domain, application of linear filters is a simple multiplication of F_{jk} with the Fourier transform of the chosen filter. Equation 4.2 is then applied to transform the product back into the space domain. The simplicity of this technique makes it attractive, however, Billings and Richards (2000) discuss the problems associated with it. Certain filters, such as the horizontal derivative, produce better results in the space domain compared to the frequency domain, where the process involves a simple convolution of the gridded data.

4.4. Aeromagnetic processing

4.4.1. Reduction to the pole

Magnetic anomalies located anywhere, but at the Earth's magnetic poles are asymmetric even when the magnetic source distribution is symmetrical because of the dipolar nature of the geomagnetic field. This complicates the interpretation of the Total Magnetic Intensity (TMI) data sets. One of the first operators applied to the aeromagnetic data set was the reduction to pole (RTP) operator. The operator is applied to the TMI grid. RTP takes the magnetic anomaly measured at any latitude and longitude and transforms it to what it would look like if the body was situated at the magnetic poles i.e. the area where inclination is vertical and anomalies are symmetrical (Baranov, 1957).

The frequency domain algorithm used by Geosoft is;

$$L(\theta) = \frac{[\sin(l) - icos(l)cos(\varphi - \theta)]^2}{[sin^2(I_\alpha) + cos^2(I_\alpha)cos^2(\varphi - \theta)[sin^2(I) + cos^2(I)cos^2(\varphi - \theta)]}, if\ (|I_\alpha| < |I|), I_\alpha = I \quad (4.3)$$

where θ is the wavenumber, I and φ are the geomagnetic inclination and declination respectively and I_α is the inclination for amplitude correction, which is never less than 1, $\sin(l)$ is the magnitude component and $i\cos(l)\cos(\varphi - \theta)$ is the phase component.

RTP has three main limitations.

1. It assumes that there is no remanent magnetisation present, which is clearly not true for the study area. If the magnetic remanence is known, it can be corrected for (Cooper and Cowan, 2005). However, as the remanent magnetisation is unknown, grids were processed with and without RTP and the resultant responses were compared in an attempt to constrain the source of the remanent magnetisation.
2. The inclination and declination of the magnetic field cannot change over regions to which the RTP is being applied. This means for regional data sets, where the inclination and declination varies, only one inclination and declination value can be used. In an attempt to mitigate this, smaller data sets were processed for the RTP, in order to try and minimise the variation of the inclination and declination (Table 4.1).
3. RTP does not work well at low latitudes (less than 10° declination) where the magnetic field is almost horizontal and the vertical field is small.

Table 4.1: Central parameters of the aeromagnetic grids used to compute the RTP. The regional grid names are in bold.

Grid names	Date of survey (dd/mm/yyyy)	Latitude (°)	Longitude (°)	Inclination (°)	Declination (°)
Namibia	13/06/1980	-22.53	18.00	-62.14	-15.87
Caprivi	15/02/2009	-17.76	24.05	-57.39	-7.22
Erongo	02/03/1995	-21.00	14.50	-62.30	-14.37
Gam-Bushmanland	30/08/1994	-20.11	20.58	-61.37	-11.14
Grootfontein	20/01/2000	-20.20	17.76	-61.78	-11.51
Okahandja	20/06/2003	-21.89	17.30	-63.33	-12.67
Rietfontein	05/06/2001	-21.23	19.85	-62.45	-11.60
Aminuis	15/02/2002	-22.96	19.47	-63.78	-13.23
Hochfield	10/03/1995	-21.60	17.69	-62.86	-13.49
Rehoboth	20/04/1999	-23.49	17.14	-64.43	-14.95
Steinhausen	23/10/2001	-21.25	18.48	-62.65	-11.95
Hakos	30/03/1995	-22.89	17.42	-63.79	-14.68
Kalahari	27/05/2008	-23.52	17.95	-64.35	-13.99
Kuiseb	13/06/2005	-23.84	15.86	-64.73	-14.88
Ugab	07/10/2007	-20.94	14.14	-62.87	-12.70
Khorixas	21/07/1997	-20.52	15.26	-62.09	-13.43
Otavi	05/03/2008	-19.57	23.49	-60.13	-9.44
northern Botswana	23/09/1998	-20.18	24.22	-61.04	-10.30
Ghanzi	15/05/1994	-21.33	21.08	-62.36	-12.02
Western Ngamiland	05/09/1997	-19.26	22.48	-60.44	-9.94
Maun	10/05/1995	-19.75	23.72	-60.66	-10.17
Okavango survey	17/09/2003	-18.96	23.43	-59.69	-8.70
Chobe	02/05/2003	-18.36	24.60	-58.79	-8.10
Boleti	25/08/2001	-20.22	24.08	-60.76	-9.94
Deception Pan	17/09/2004	-21.24	23.21	-61.81	-10.78
western Zambia	15/06/1982	-14.46	25.03	-53.76	-7.40

The inclination and declination values are calculated in Geosoft using the year specific IGRF model (measured every 5 years).

The application of the RTP operator for Ngamiland, northwest Botswana is shown in Figure 4.1. The TMI data shows asymmetric anomalies (1) (Figure 4.1a), while in the RTP data the anomalies have a more symmetric response (Figure 4.1b). Remnance is suggested from the more symmetric response in Figure 4.1a to an asymmetric response in Figure 4.1b (2).

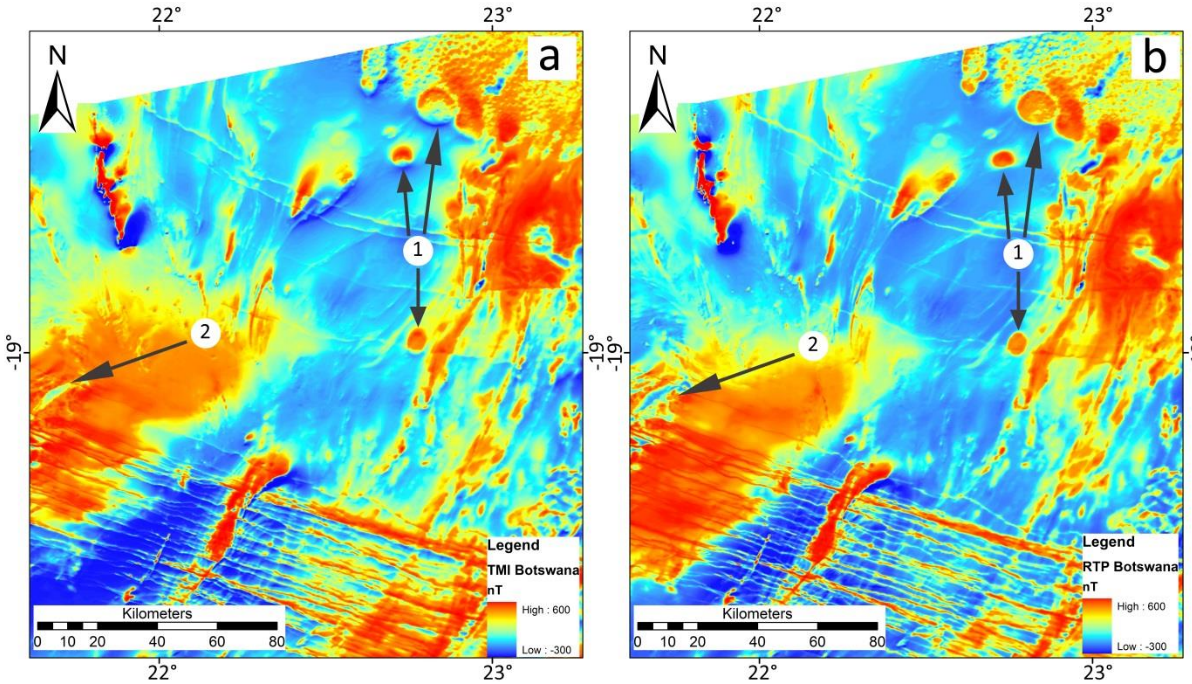

Figure 4.1: Aeromagnetic data of Ngamiland, northwest Botswana. a) Is the TMI image and b) is the applied RTP operator. The arrows associated with 1 show the transformation from asymmetric anomalies to symmetric anomalies while the arrow associated with 2 suggests the presence of remnant magnetisation in the data because of the transformation from a more symmetric anomaly to an asymmetric anomaly.

4.4.2. Vertical derivatives

The vertical derivative is one of the oldest methods used to enhance shallow features (short wavelengths, high frequencies) (Blakely, 1995). The filter accentuates shallow sources and removes deep-seated (long wavelength) features. Vertical derivatives narrow the width of the magnetic anomaly, locating the source bodies more accurately compared to interpreting the RTP and TMI images. The higher the order of the derivate used, the more pronounced the effect, but noise is similarly enhanced with increase of order of derivative (Cooper and Cowan, 2004). For this reason the highest vertical derivative used in this study is the second order.

The second order vertical derivative is derived from Laplace's equation and grids are calculated in Geosoft in the frequency domain. Assuming that *z* is positive downwards, the formula is given by;

$$F\left(\frac{\partial^n f}{\partial z^n}\right) = k^n . F(f) \tag{4.4}$$

where $k^n = \sqrt[n]{k_x + k_y}$, *F* is the Fourier representation of the field and *n* is the order of the vertical derivative (Cooper and Cowan, 2004). Equation 4.4 allows for the calculation of non-integer values. This allows for fractional vertical derivatives to be calculated that have an intermediate frequency content compared to integer order derivatives. This is useful for enhancing high frequencies in poor data sets (i.e. Zambia), where the first vertical derivative produces a poor signal to noise ratio compared to the 0.5 vertical derivative, which enhances more of the geology than the noise (Figure 4.2).

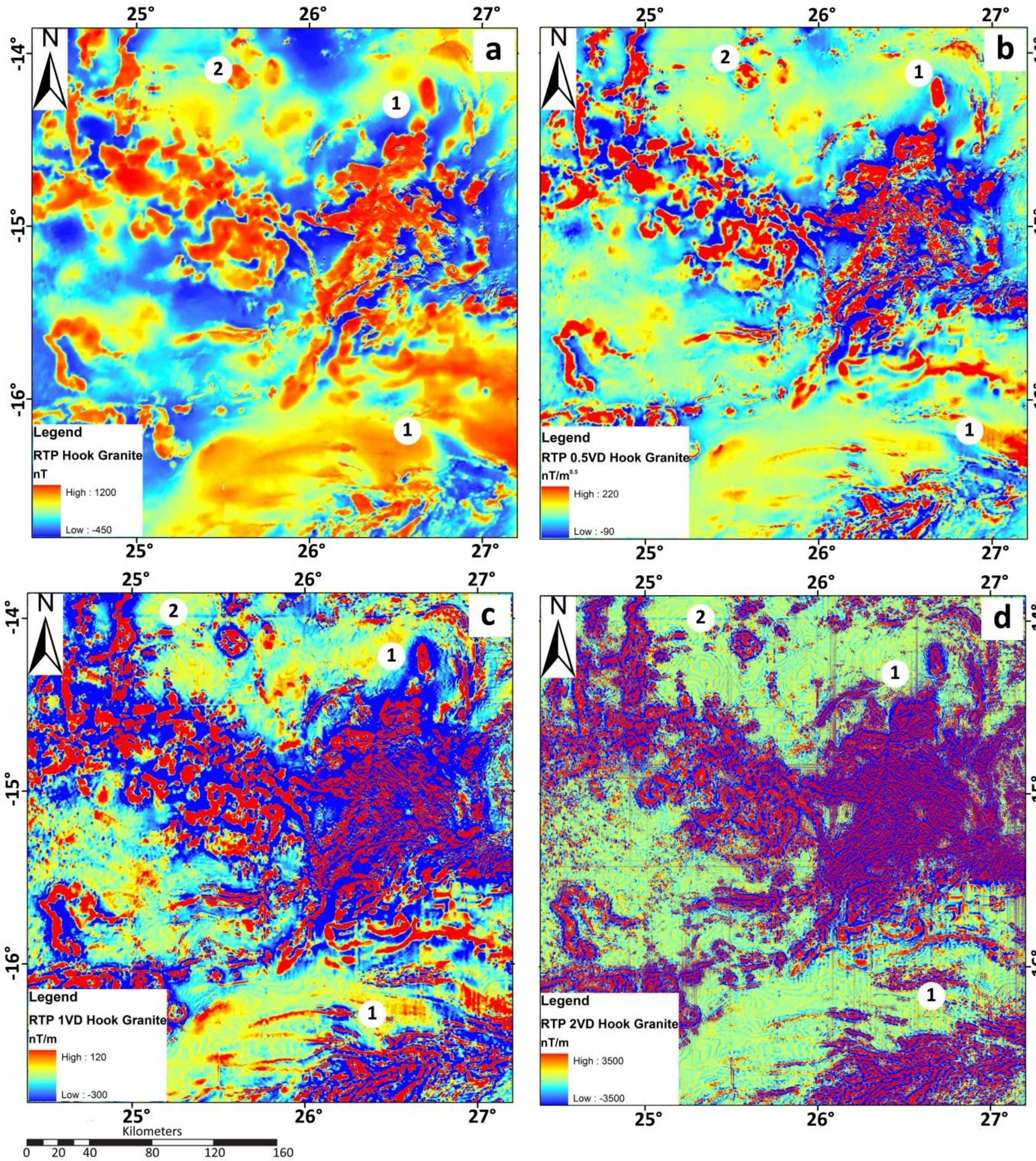

Figure 4.2: Aeromagnetic data of the Hook Batholith and surrounding area. a) RTP filtered data. b) 0.5 VD filtered data of Figure 4.2a. c) 1VD filtered data of Figure 4.2a. d) 2VD filtered data of Figure 4.2a. Notice how the noise increases with the higher order vertical derivative filters (1VD and 2VD) compared to the 0.5VD filtered data. Noise from the flight direction and stitching of aeromagnetic grids is visible in the RTP 1VD and 2VD images in the southern portion while in the RTP 0.5VD the data is not affected by the flight direction, which allows for the geology to be better defined.

In the 1VD and 2VD images north-south (labelled 1) and east-west (labelled 2) noise is enhanced, which is not clearly visible in the RTP and 0.5VD images (Figure 4.2). The north-south noise is suggested to resemble the flight lines while the east-west noise resembles the stitching of two aeromagnetic surveys.

4.4.3. Analytic signal

In the study area there are regional bodies of unknown remanent magnetisation and as discussed in Section 4.4.1 the RTP operator cannot resolve remanent magnetisation or when the data is at low magnetic latitudes. The analytic signal has been used to estimate magnetic source depth from the simple bell-shaped anomaly produced over the edges of the vertical source (Roest *et al*., 1992) and remanent magnetisation (Roest and Pilkington, 1993) for a 2D vertical-magnetic contact. However, the rocks of Namibia and Botswana are heavily deformed and cannot be assumed to be vertically dipping. Using a prism model, Zhang (2001) shows that the analytic signal is accurately estimates the magnetic source depth for a vertical contact model. Using a cube model Li (2006) demonstrates that the amplitude of the 3D analytic signal is dependent on the same parameters as the TMI data, which depends on the direction of the Earth's inducing field, the direction of magnetisation, the dip angle of the source, and the depth to the top and bottom of the source. However, Li (2006) states that the amplitude of the 3D analytic signal can be used to complement the RTP data and other edge detection techniques, especially when the top of the magnetic sources are shallow or very regional, the magnetic latitude is low, and remanent magnetisation is significant, yet its parameters are unknown.

Therefore, the analytic signal is used in regions were remanent magnetisation is significant e.g. northern Namibia (Figure 4.3) to simplify the interpretation of the TMI data, and as an edge detector for broad, regional magnetic features (Figure 4.4).

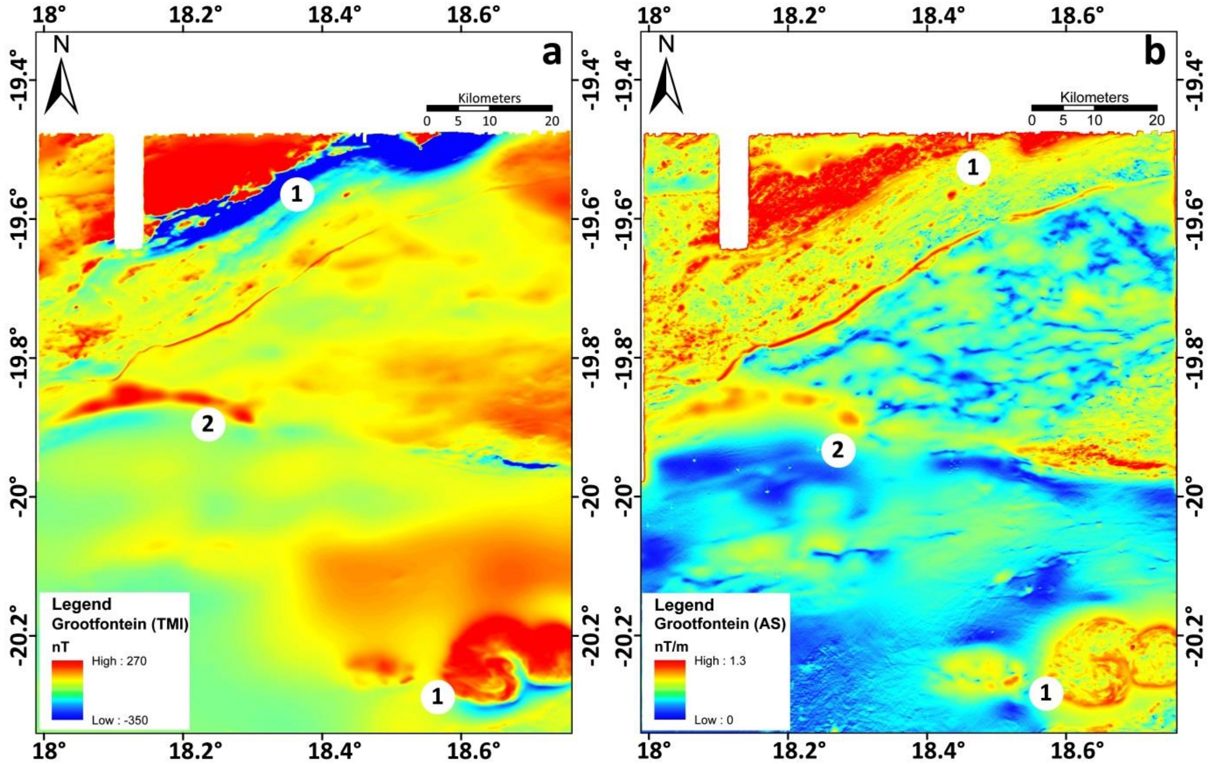

Figure 4.3: Aeromagnetic data of the Grootfontein area, northern Namibia. a) The TMI image, notice the asymmetric aeromagnetic anomalies (1). b) The analytic signal of the TMI data, notice that the previous asymmetric aeromagnetic anomalies are now symmetric (1). However (2) is more asymmetric in b) suggesting the presence of remnance and a dipping contact.

The concept of the analytic signal can be dated back to 1948 (Li, 2006). It was initially applied to a 2D potential field source that was aligned parallel to the y-axis and measured along the x-axis at a constant observation height (*z*) (Nabighian 1972, 1974). The analytic signal of the potential field is written as;

$$AS = \frac{\partial f}{\partial x} - i\,\frac{\partial f}{\partial z}, \tag{4.5}$$

where the horizontal derivative ($\frac{\partial f}{\partial x}$) and vertical derivative ($\frac{\partial f}{\partial z}$) are a Hilbert transform pair. The amplitude of the 2D analytic signal of the potential field data can be expressed as;

$$AS(x) = \sqrt{\left(\frac{\partial f}{\partial x}\right)^2 + \left(\frac{\partial f}{\partial z}\right)^2}\,. \tag{4.6}$$

From this 2D assumption it can be shown that the analytic signal is independent of the inclination and declination of the magnetic field. This allows the analytic signal to be a practical alternative to RTP to simplify the interpretation of magnetic anomalies (Blakely, 1995) and is particularly useful near the magnetic equator.

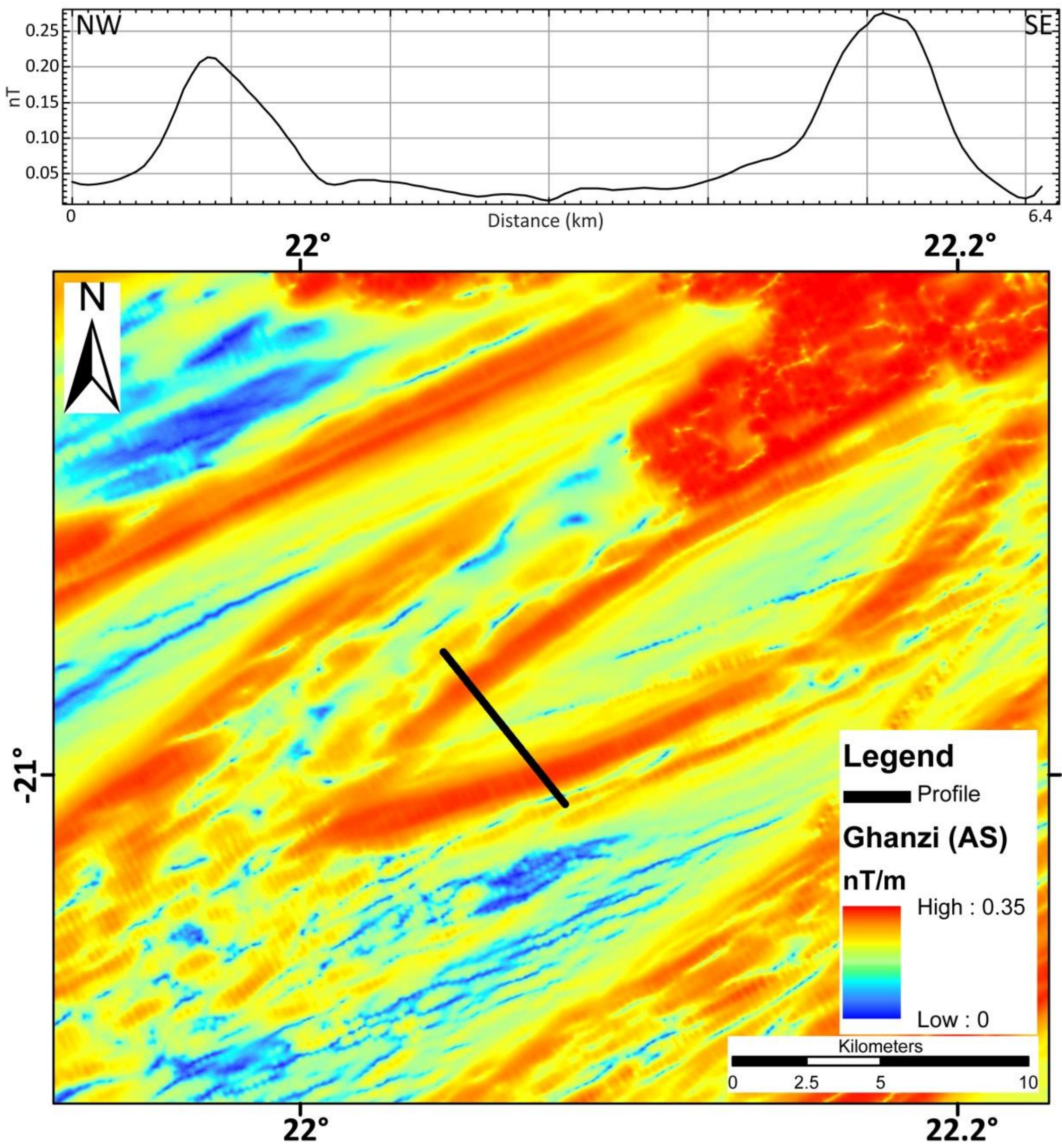

Figure 4.4: The aeromagnetic profile (top) of the analytic signal of the Ghanzi TMI data (bottom). The bell-shaped peaks in the profile correlate well with the edges in the map data.

A generalisation of the analytic signal and Hilbert transform allowed Nabighian (1984) to transform the analytic signal from 2D to 3D. The amplitude of the 3D analytic signal is the combination of the horizontal (*x*, *y*) and vertical (*z*) gradients of the magnetic anomaly;

$$AS(x,y) = \sqrt{\left(\frac{\partial f}{\partial x}\right)^2 + \left(\frac{\partial f}{\partial y}\right)^2 + \left(\frac{\partial f}{\partial z}\right)^2} \quad (4.7)$$

where $AS(x,y)$ is the amplitude of the analytic signal and f is the observed magnetic field (Roest *et al*. 1992).

4.4.4. Tilt derivative

As the amplitude of the 3D analytic signal (Section 4.4.3) is proportional to $\frac{1}{R^4}$, where R is the distance between the top of the source and observation, two closely spaced sources will produce a single anomaly (Figure 4.5a). To address this problem, a higher order vertical derivative can be applied to the analytic signal, however, this must be done with care as the analytic signal is already a high pass filter, which means noise is already enhanced (Blakely, 1995). In addition, shallow sources produce large amplitudes in the vertical and horizontal gradients, which present a problem in displaying the data. To resolve closely spaced magnetic sources, without filtering to the second order derivate, and to enhance the display of the data, the tilt derivate is utilised (Figure 4.5b).

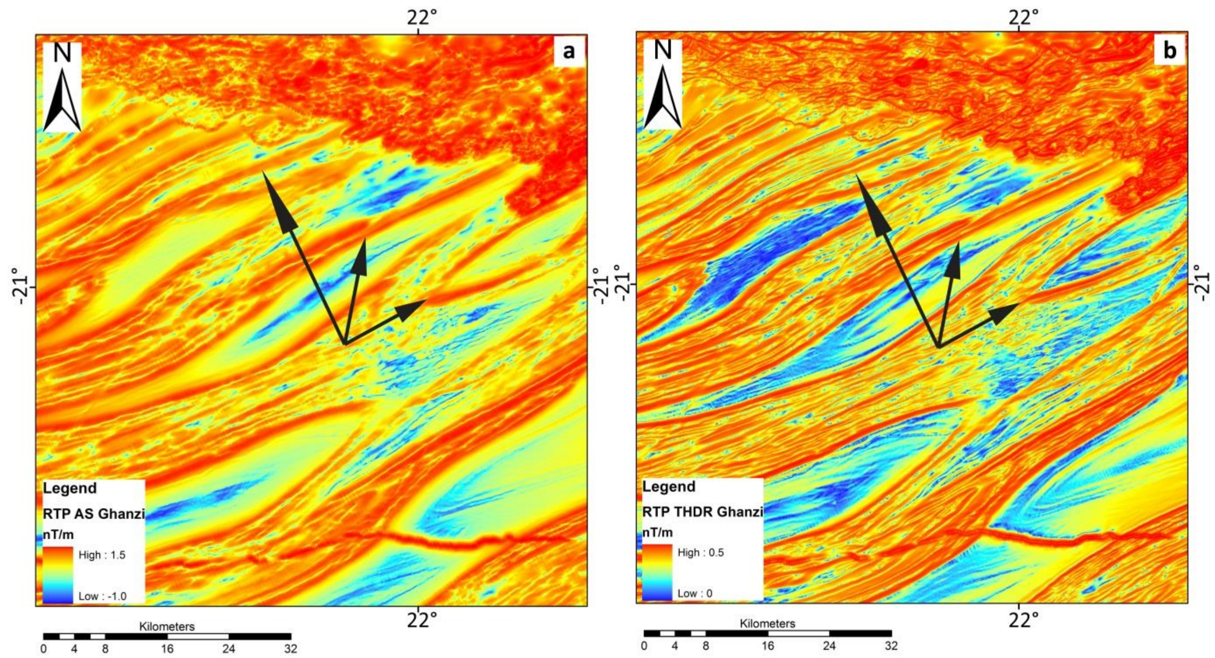

Figure 4.5: Aeromagnetic data of the Ghanzi-Chobe Belt. a) The application of the analytic signal. The edges of the folds are seen as a single "blurry" body compared to (b) the total horizontal derivative which clearly delineates a north-western and south-eastern boundary.

The tilt angle (TA) is the ratio of the vertical derivative (VDR) with the absolute amplitude of the horizontal derivative (HDR) defined by;

$$TA = tan^{-1} = \left(\frac{VDR}{HDR}\right), -\frac{\pi}{2} \leq TA \leq \frac{\pi}{2} \quad (4.8)$$

where $VDR = \frac{df}{dz}$ and $HDR = \sqrt{\left(\frac{\partial f}{\partial x}\right)^2 + \left(\frac{\partial f}{\partial y}\right)^2}$ and f is the total potential field intensity (Miller and Singh, 1994).

Since the TA is a ratio of the vertical and horizontal gradients it is positive over a source and negative elsewhere and enhances the edges of both shallow and deep-seated potential field sources equally well (Miller and Singh, 1994; Blakely, 1995).

Verduzco *et al*. (2004) uses the derivative of the tilt angle (DTA) (Equation 4.9) to map shallow basement structures (less than 400 m depth) and mineral exploration targets.

$$DTA\_HDR = \sqrt{\left(\frac{\partial TDR}{\partial x}\right)^2 + \left(\frac{\partial TDR}{\partial y}\right)^2}. \tag{4.9}$$

Verduzco *et al*. (2004) state, that the horizontal derivative of the TA is independent of the direction of magnetisation (only true for magnetic profiles) and that maximum values are generated over the edges of the bodies. The TDA is dependent on the direction of magnetisation, through the same arguments of Li (2006) for the amplitude of the 3D analytic signal (Cooper, *pers. comm.*, 2013). As this technique takes the derivative of a derivative it is sensitive to noise. For this reason, the DTA is only used in conjugation with the TA for delineating near-surface structures.

4.4.5. Upward continuation

The high amplitude magnetic signal of near-surface geological features such as the Okavango Dyke Swarm and *Karoo* volcanics obscure the potential field mapping of deeper features. Estimating the continuation of these deeper sources is easier when the high amplitude signal is removed. In this study upward continuation was used to remove these near-surface sources.

Upward continuation is a low-pass filter that smoothes the high frequency noise at the cost of detail to the image by calculating the potential field at a horizontal surface further from the source (Ivan, 1986). The further the data is upward continued above the source, the smoother the potential field becomes (Figure 4.6). Upward continuation is now commonly calculated in the frequency domain (Equation 4.10) (Hansen and Miyazaki, 1984);

$$\Phi\left(F_{z_0 - \Delta z}\right) = \Phi(F_{z_0})e^{-\Delta z|f|} \tag{4.10}$$

where ϕ is the Fourier transform operator, *F* is the potential field, *f* is the frequency and Δz is the vertical distance above the point of measurement and is positive upwards.

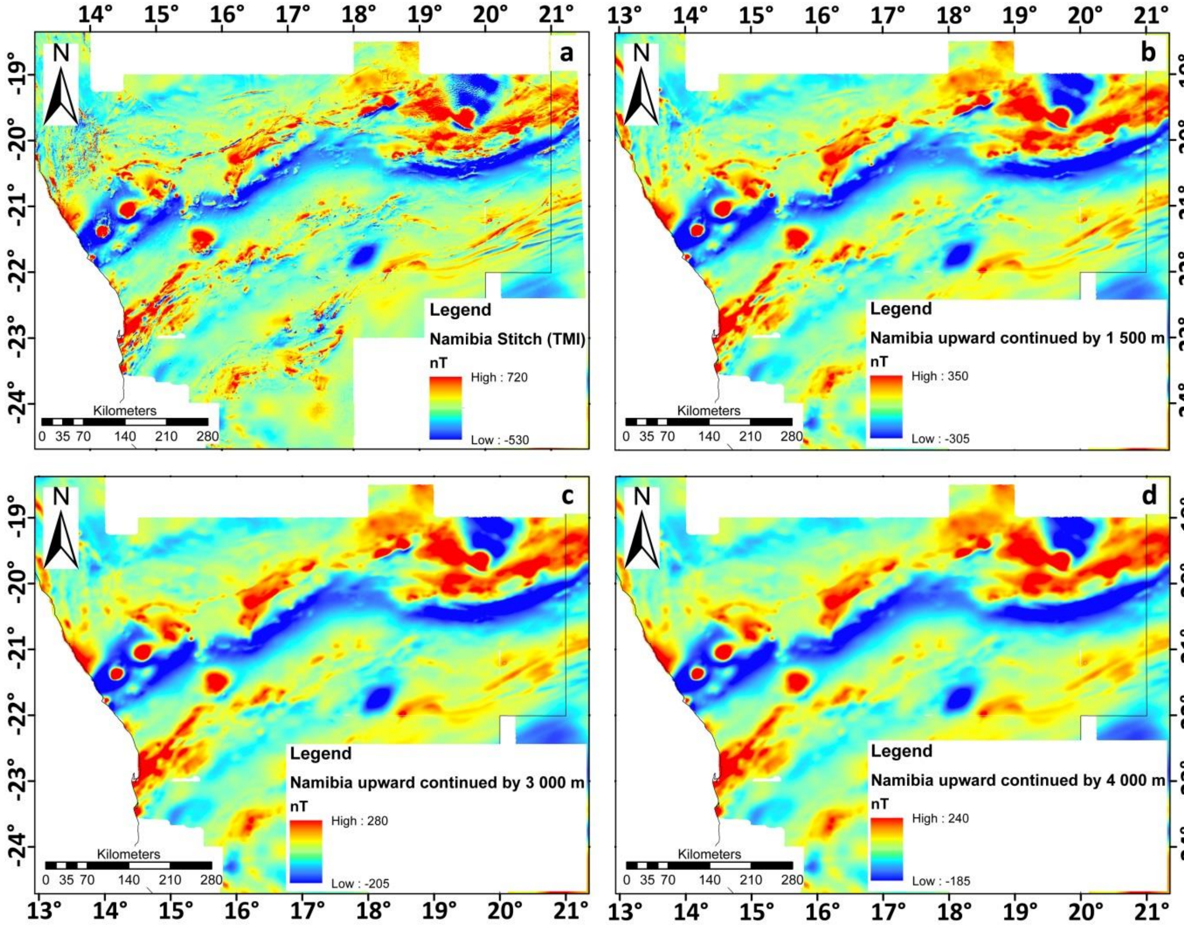

Figure 4.6: Application of upward continuing TMI aeromagnetic data of Namibia by various heights. a) The TMI data shows detail of the shallow magnetic sources. b) The TMI data upward continued by 1 500 m. c) The TMI data upward continued by 3 000 m. d) The TMI data upward continued by 4 000 m. Notice how the TMI data is smoothed with respect to the amount of upward continuation.

Upward continuation was used to delineate regional (long wavelength), deeper aeromagnetic trends that are suppressed by shorter wavelength, near-surface magnetic features.

4.4.6. Sunshading

Sunshading is a directional filter that enhances features in a particular orientation and suppresses features perpendicular to that direction. The filter is used to either enhance features of interest or to suppress problematic features such as dykes (Figure 4.7). The data are treated like topography, i.e. high anomalies are considered to be mountains and low anomalies valleys. A “sun” is placed at a chosen azimuth and elevation and the reflectance is calculated at each point on the surface.

The sunshading algorithm uses two horizontal gradients, which can be calculated independently to the position of the sun. This is done initially, and then each succeeding change of the sun's position requires a short recalculation. There are various reflectance models, but the most commonly used model is the Lambertian reflector (Cooper, 2003). This reflects the light equally in all directions and is given by;

$$R = \frac{1+p.p_o+q.q_o}{\sqrt{(1+p^2+q^2)+\sqrt{(1+p_o^2+q_o^2)}}} \tag{4.11}$$

where p and q are the east-west and north-south gradients of the data, $p_o = -\cos\emptyset tan\theta$, $q_o = -sin\theta tan\emptyset$; $\emptyset$ is the sun's azimuth, which is measured anticlockwise from east and θ is the elevation, which is measured from the vertical (Cooper, 2003).

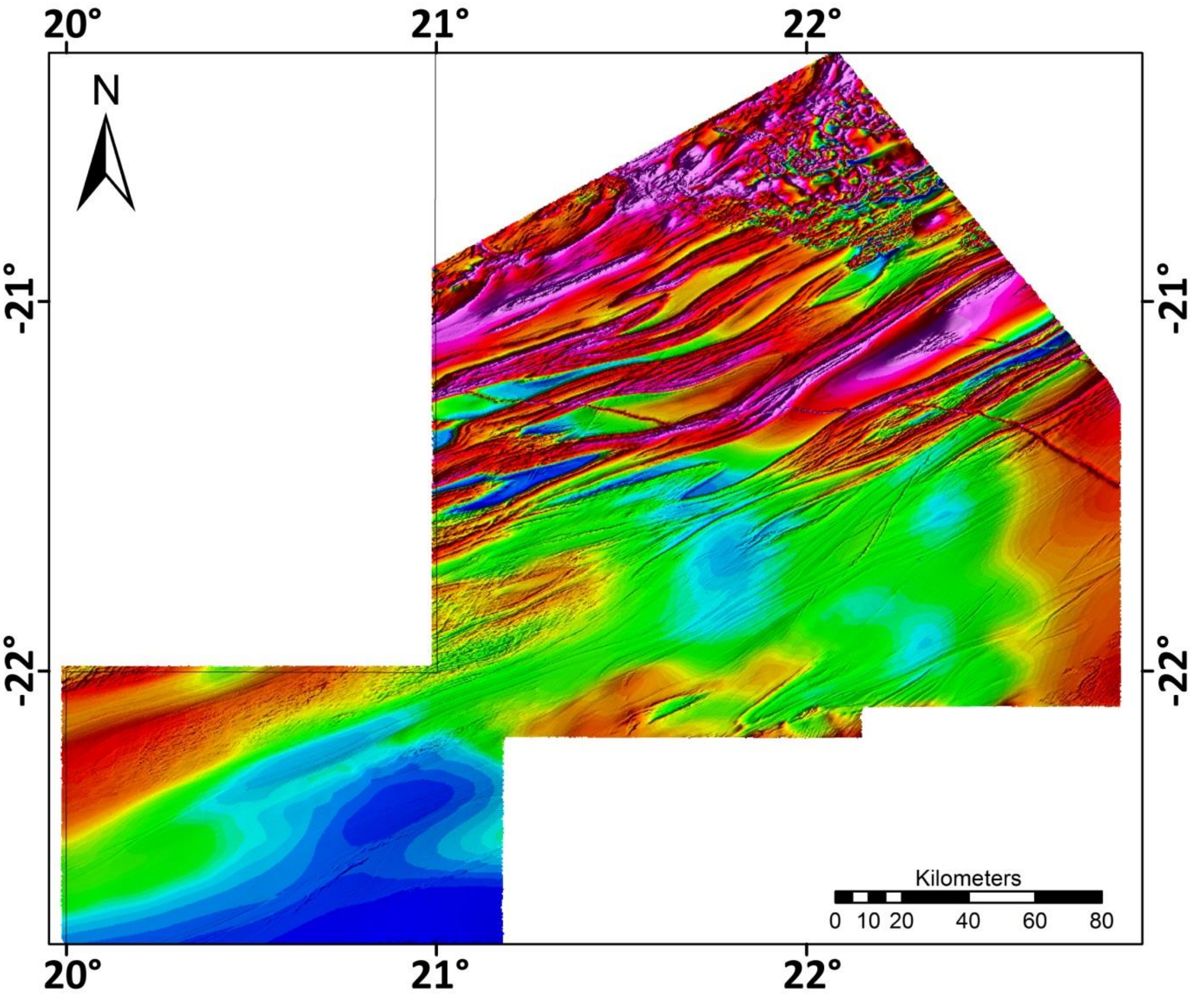

Figure 4.7: TMI Ghanzi aeromagnetic grid sunshaded at an inclination of 20° and declination of 100° enhancing the fold pattern of the Ghanzi-Chobe in the southern parts of the grid.

4.4.7. Combination of Butterworth and directional cosine filters (decorrugation)

Flight line noise occurs in the aeromagnetic grids as corrugated noise, mainly parallel to the flight and tie line directions. Levelling the flight lines with the tie lines is subject to noise due to poor flight path recovery, magnetometer noise, and poor altitude and diurnal corrections (Minty, 1991). These residual levelling errors often have a low amplitude but the application of high-pass filtering enhances their presence (Minty, 1991).

To suppress the high amplitude magnetic signal of the Okavango Dyke Swarm in northern Botswana (Figure 4.8a) and correct for subtle flight line noise in the high-pass aeromagnetic data sets, a decorrugation filter was applied (Figure 4.9a). Decorrugation is a two-step procedure, which involves first a Butterworth filter and secondly, a directional cosine filter. However, care must be taken when applying these filters as geological information of similar frequency, which is oriented parallel to the angle of the filter, will also be suppressed.

The Butterworth filter applied to the gridded aeromagnetic data, acts as a low-pass filter, which rejects a range of aeromagnetic frequencies and shows a uniform sensitivity for the remaining frequencies.

$$L(k) = \frac{1}{\left[1+\left(\frac{f}{f_o}\right)^N\right]} \tag{4.12}$$

where f is the frequency and f_o is the cut-off frequency or central frequency which the amplitudes will be filtered and N is the degree of the Butterworth function. Increasing the degree of the Butterworth filter will result in a faster fall-off rate for the frequency.

The directional cosine filter smoothes the image, so directional ringing (noise) problems do not usually occur. This filter can be narrowed or widened by setting the degree of the cosine function so that highly directional features can be isolated. The algorithm for the directional cosine filter for the rejection of features is;

$$L(\theta) = \left|cos^n\left(\alpha - \theta + \frac{\pi}{2}\right)\right| \tag{4.13}$$

where α is the direction of the filter in degrees from north and n is the degree of the cosine function used.

The Okavango Dyke Swarm strikes at ~110° east of north with a mean magnetic amplitude of ~350 nT and obscures the continuation of the underlying features (Figure 4.8a). To enhance these underlying features and suppress the dykes, decorrugation was applied to the data at an orientation of 290° (180° ambiguity, so 110° = 290°) with an amplitude of 350 nT (Figure 4.8b).

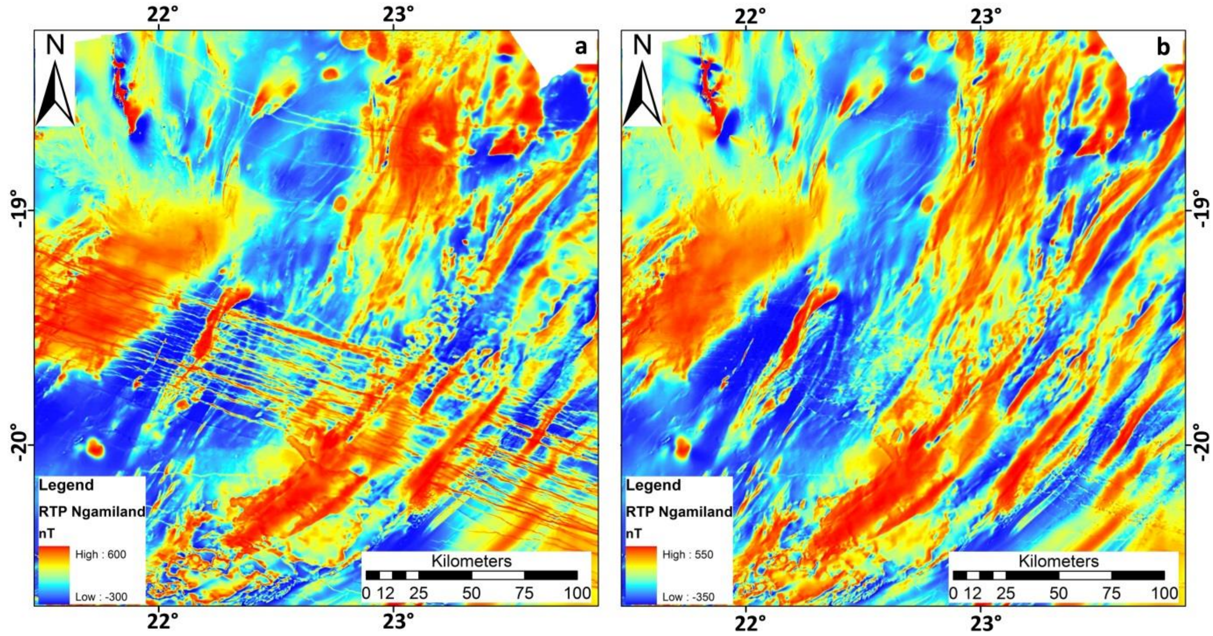

Figure 4.8: Aeromagnetic data of the Ngamiland area, northwest Botswana. a) RTP image with the prominent aeromagnetic northwest-southeast trending Okavango Dyke Swarm. b) Decorrugated aeromagnetic data with the high amplitude aeromagnetic signal of the northwest-southeast trending Okavango Dyke Swarm suppressed. The parameters of the Butterworth filter are; cut-off wavelength = 350 nT, selected for the amplitude of the aeromagnetic signal that needs to be suppressed, filter order = 4 and low-pass filter. The parameters of the directional cosine filter are; centre direction in space domain = 290° i.e. the direction in which the signal must be suppressed, degree of cosine function = 1 and rejection of the aeromagnetic signal that falls in the range of the above listed parameters.

The RTP 1VD filtered aeromagnetic image has subtle north-south trending lines which disrupts the interpretation of the northeast-southwest geological units (Figure 4.9a). To suppress these subtle features, the data was decorrugated at an orientation of 180° at an amplitude of 0.0044 nT (Figure 4.9b). The resultant image is a smoother image where the continuation of the geological units is easier to determine and the visual display is enhanced (Figure 4.9b).

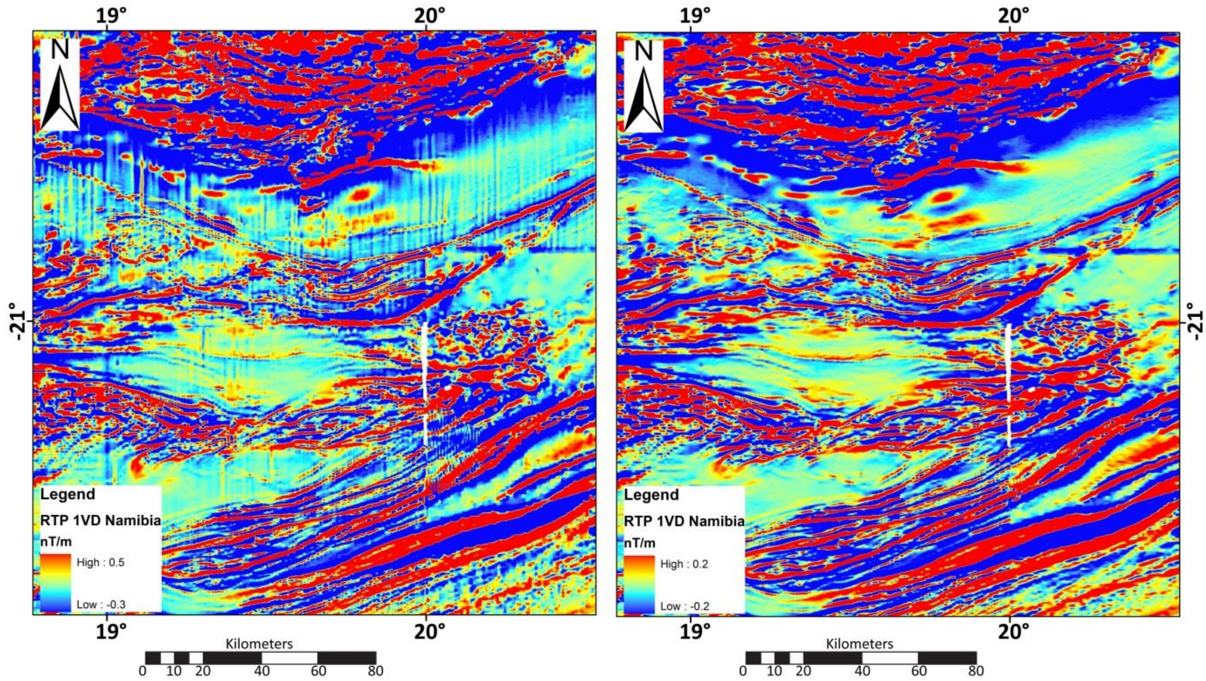

Figure 4.9: Aeromagnetic data of northeast Namibia. a) RTP 1VD image displaying the north-south orientation of the flight paths, appearing as flight line noise. b) Decorrugated aeromagnetic image. The north-south flight lines have been suppressed. The parameters of the Butterworth filter are; cut-off wavelength = 0.044 nT, selected for the amplitude of the aeromagnetic signal that needs to be suppressed, filter order = 4 and low-pass filter. The parameters of the directional cosine filter are; centre direction in space domain = 180° i.e. the direction in which the signal must be suppressed, degree of cosine function = 1 and rejection of the aeromagnetic signal that falls in the range of the above listed parameters.

4.4.8. Overlaying grids

To enhance and/or compare features, various grids were draped over each other. For example, to enhance shallow structural features, a colour scale 2VD grid, with a 55% transparency, was overlain on a grey scale RTP or 1VD grid (Figure 4.10).

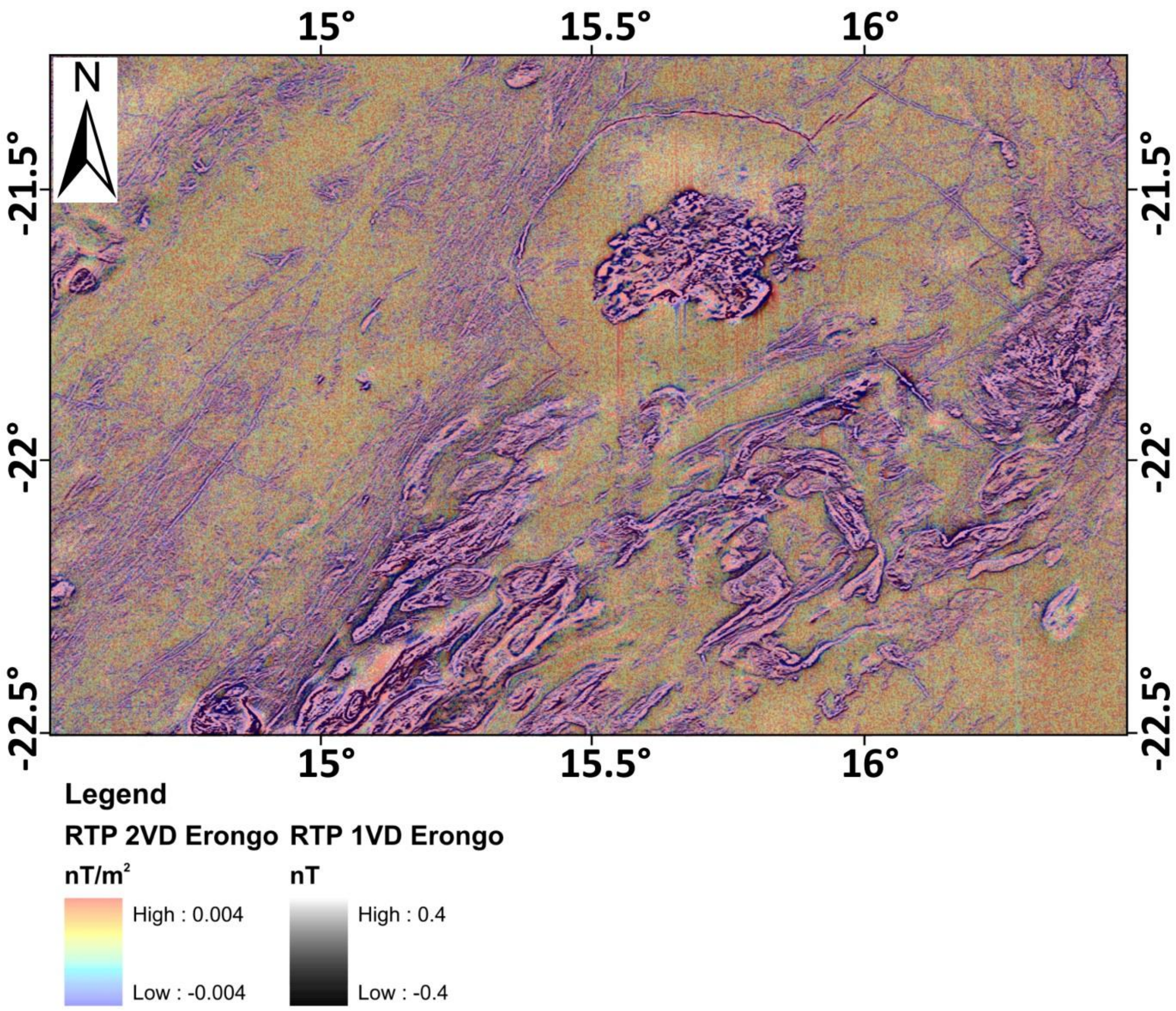

Figure 4.10: Colour scale RTP 2VD filtered aeromagnetic data overlain on 55% transparent greyscale RTP 1VD filtered aeromagnetic data of the Erongo area, western Namibia.

Another way to enhance shallow features is to drape the analytic signal over the HDR (Figure 4.11). The reason for this is that whilst the amplitude of the analytic signal enhances the edges of bodies, it cannot distinguish between two closely spaced bodies, (Section 4.4.3), whereas the HDR will be able to enhance this detail.

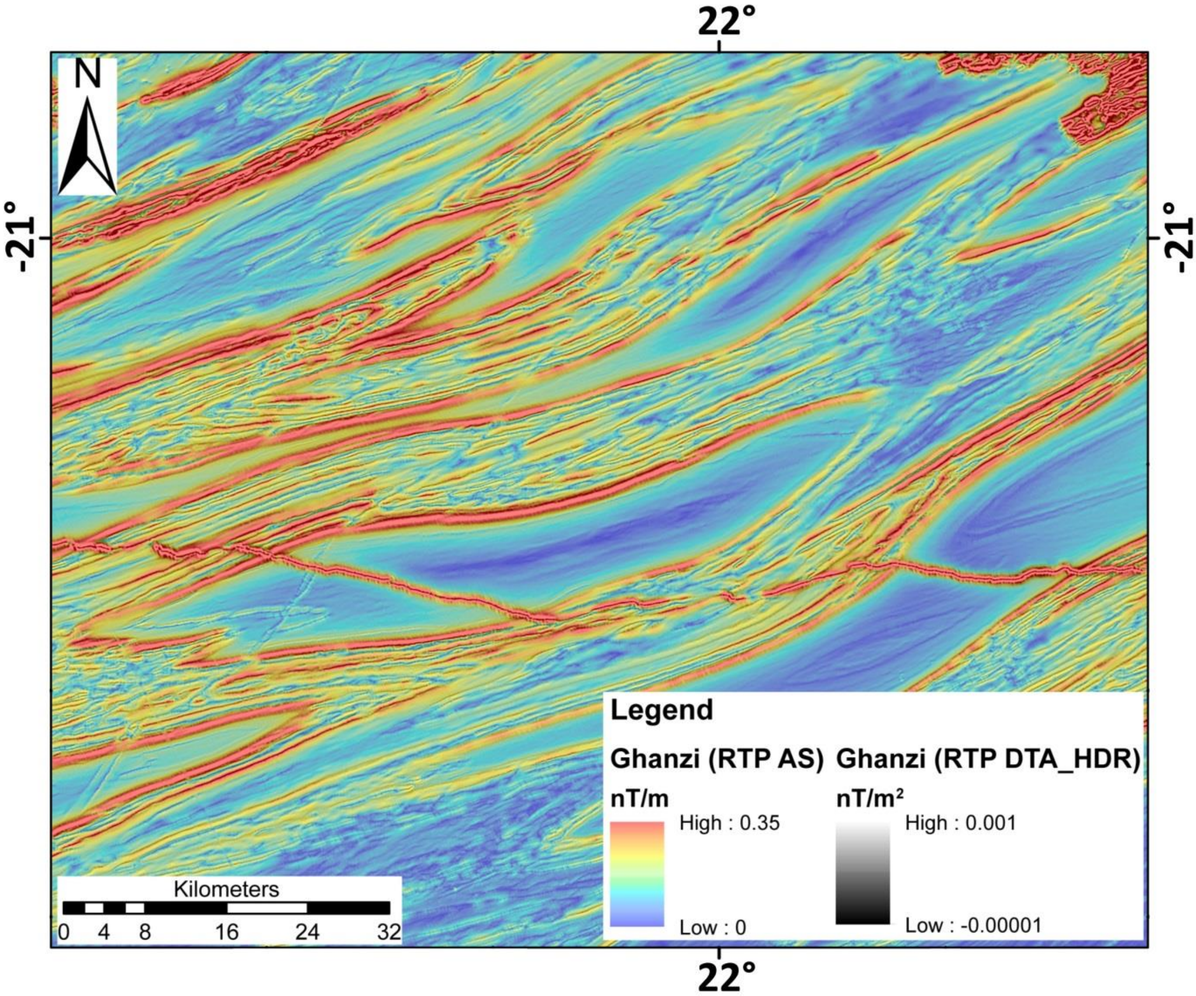

Figure 4.11: Colour scale RTP analytic signal filtered aeromagnetic image overlain on 50% transparent greyscale RTP DTA_HDR filtered aeromagnetic image of the Ghanzi grid.

4.5. Histogram modification

The processed images were loaded into ArcGIS v 9.3.1, where subtle details in an image were enhanced by modifying the histogram. A histogram is a graphical representation of the distribution of data i.e. an image histogram displays how many pixels in the image have a given shade of grey or colour and controls the brightness and contrast of the image. Histograms contain no information about the spatial extent of these pixels. As the data is real i.e. non-integer values, each data point will have a different value from another data point, and the histogram will be flat with all values equal to one. Instead, the data values are grouped together, such that the number of points with a value greater than the lower limit and less than the upper limit is counted. The process is known as binning and the bin size affects the results. Two commonly used histograms in this study are the standard deviation, with degree *n* between 0.2 to 2, and histogram equalisation (Figure 4.12).

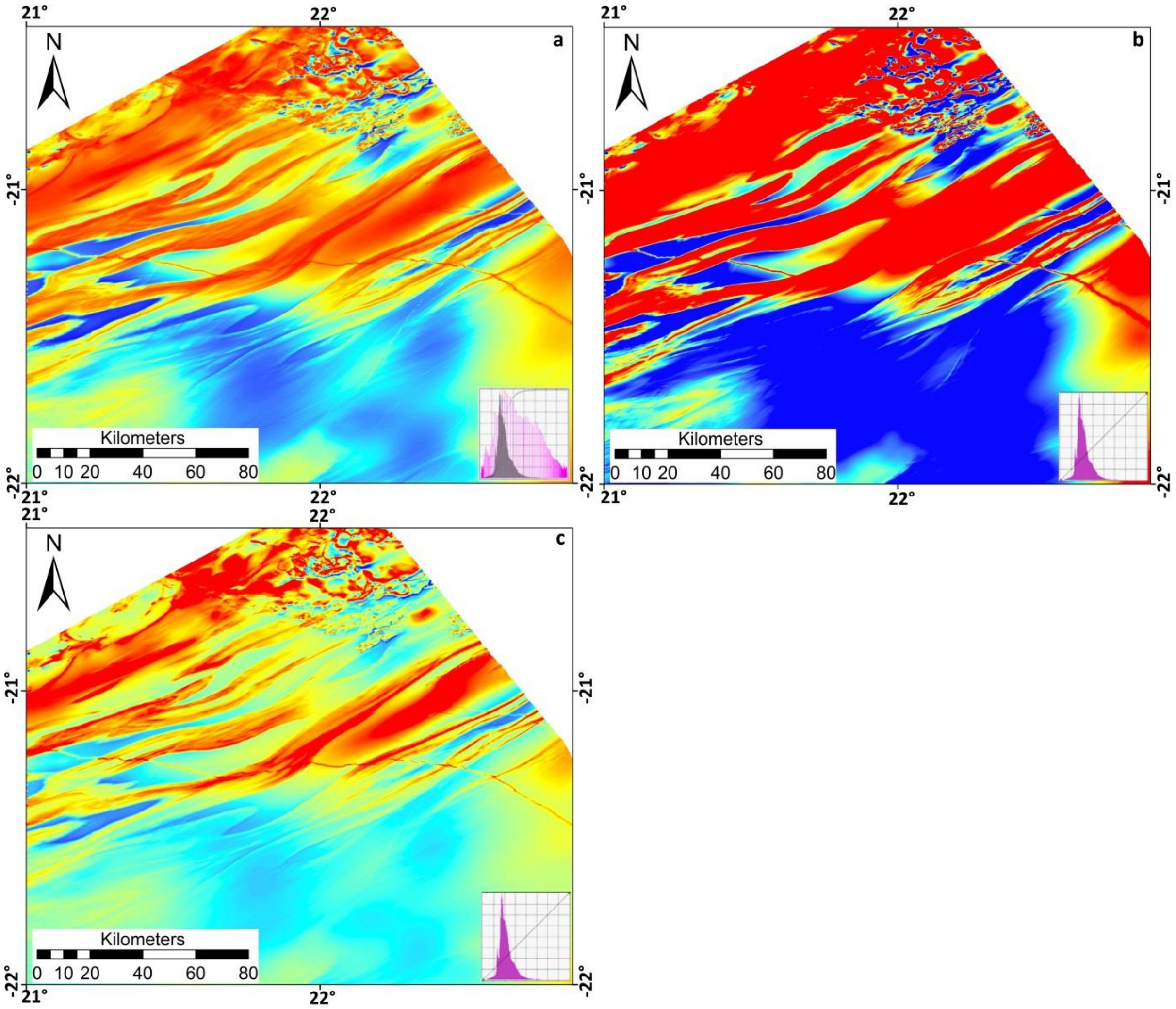

Figure 4.12: Application of some of the histogram modifications applied on RTP data of the Ghanzi aeromagnetic grid, Botswana. The respective histogram of each stretch is shown in the bottom right of the image. a) Histogram equalisation modification. b) Standard deviation of degree *n* = 0.2. c) Standard deviation of degree *n* = 2.

Histogram equalisation spreads the most common frequencies over the length of the histogram resulting in frequencies that were initially closed spaced being stretched. The histogram equalisation algorithm (Equation 4.14) determines the ideal number of times a frequency appears in an image by dividing the total number of pixels in the image by the total number of possible frequencies in the image (L).

$$p_n = \frac{number\ of\ pixels\ with\ frequency\ n}{total\ number\ of\ pixels} \qquad n = 0, 1, 2\ , \dots \dots , L - 1, \qquad (4.14)$$

where p is the normalised histogram.

The algorithm counts the frequencies from 0 to L – 1 (L = 256) and shifts the appropriate pixel frequencies into that position as long as this number of pixels is less than or equal to a certain delimiter that increases linearly to the frequency. The pixel frequency is shifted to the right along the horizontal axis of the histogram until an appropriate bin is determined.

Standard deviation (Equation 4.15) controls the brightness of the image. Decreasing the threshold will saturate the image as the frequencies used in the image will be in a smaller band i.e. the histogram does not change.

$$\sigma = \sqrt{\frac{1}{n-1}\sum_{i=1}^{n}(x_i - \bar{x})^2} \tag{4.15}$$

where n is the total number of data points, x_i are observation points and $\bar{x}$ is the mean of the data.

4.6. Gravity

The gravity data was supplied as free-air and Bouguer gravity grids (Figure 4.13). From the literature (e.g. Gordon-Welsh *et al*., 1986; Corner, 1982; Hutchins and Reeves, 1980; Yawsangratt, 2002) the gravity data has undergone the standard corrections of instrumental drift, latitude correction, free-air correction, and Bouguer correction.

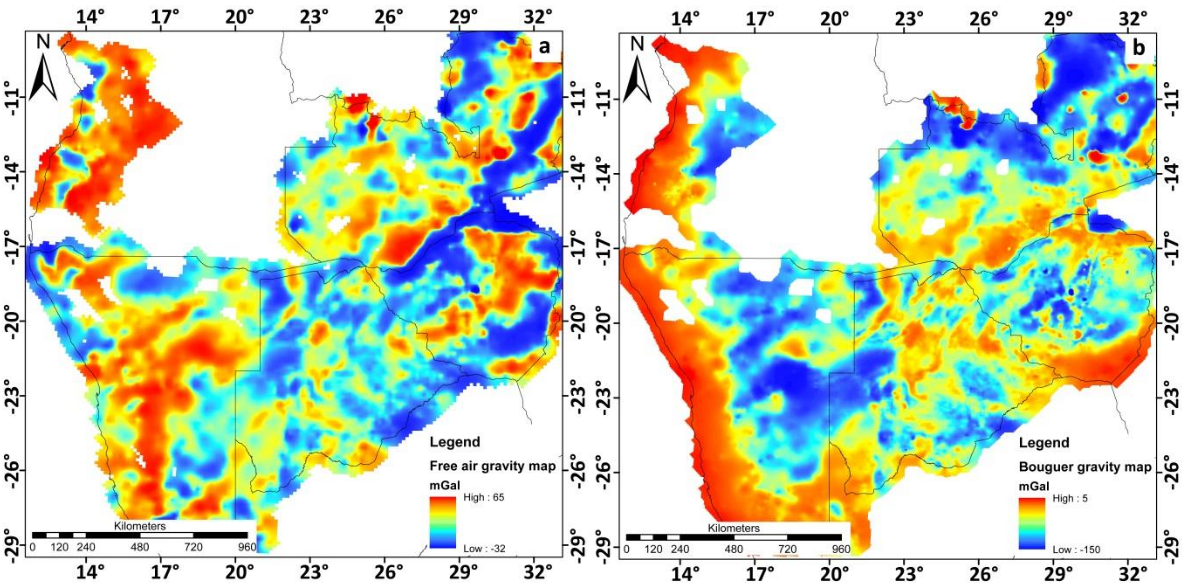

Figure 4.13: The two gravity grids provided by Rio Tinto for this study a) free-air gravity and b) Bouguer gravity map.

Instrumental drift was removed by directly subtracting the interpolated readings between repeated observation times. The observed gravity (g_{obs}) was converted to an absolute gravity value (g_{abs}) and a latitude correction (ϕ) was applied. Latitude corrections are applied to the data as the gravity field varies with latitude, if the profile is moving towards the equator the latitude correction is added and if the profile is moving towards the poles it is subtracted. The effects of latitude for Namibia and Botswana were calculated using the 1967 International Gravity Formula (IGF67) (Gordon-Welsh *et al*., 1986; Yawsangratt, 2002).

Country	Latitude correction
Botswana (GRS67)	g_ϕ = 978 031.846(1+0.005 278 895sin^2 ϕ-0.000 023 462sin^4 ϕ)
Namibia (IGF67)	g_ϕ = 978 031.8(1+0.005 3024sin^2 ϕ-0.000 005 8sin^2(2ϕ))

Furthermore, free-air and Bouguer corrections were applied to the absolute gravity data. The free-air correction (FAC) refers to the difference between the gravity that is measured at sea-level and at a certain elevation with no rock in between. It is computed as,

$$FAC = 0.3086 \times h \tag{4.16}$$

where, h is the elevation above the datum in metres. If the station is above the datum, the FAC is added and if the station is below the datum, the FAC is subtracted. Applying both the latitude and FAC to the absolute gravity data, yields the free-air anomaly (FA);

$$FA = g_{obs} - \ g_{\phi} + FAC \tag{4.17}$$

The free-air anomaly is commonly used to image the corrected gravity data for topography. In contrast, the Bouguer correction (BC) accounts for rock mass by assuming an infinity long, uniform flat slab between sea-level and the gravity station. It is generally calculated as;

$$BC = \ FA - 0.04192\rho h \tag{4.18}$$

where FA is the free-air anomaly, ρ is the average density (Gordon-Welsh *et al*. (1986) and Yawsangratt (2002) used 2.67 g/cm^3) and h is elevation above sea-level in meters. If the station is above the datum, the Bouguer correction is subtracted and if the datum is below the gravity station the Bouguer correction is added.

As the topography is fairly flat, terrain and isostatic corrections were not applied to the gravity data (Gordon-Welsh *et al*., 1986; Yawsangratt, 2002). However, the Damara Orogeny is associated with continental collision between the Congo and Kalahari Cratons during the Neoproterozoic. Kgotlhang *et al*. (submitted) suggests that isostatic correction should have been carried out. Relics of these mountains that formed during the collision are the Aha, Tsodilo, Kihabe and Koanaka Hills (Figure 2.19) (Kgotlhang *et al*., submitted). Failure to correct for these ancient mountain roots leads to an anti-correction between the Bouguer gravity map and DTM at the location of the mountains (negative Bouguer anomaly) because of the excess of mass deficiently (Figure 4.14). Geiger and Cook (2001) have shown from work in the Canadian Shield that band-pass filtered gravity images resemble isostatically corrected images.

This study does not claim to have applied isostatic correction but applying a band-pass filter of between 5 km and 100 km wavelengths (i.e. retaining Bouguer gravity signals at depths of between 1.25 km and 25 km for a 2D body) has corrected for this negative Bouguer anomaly in north-western Botswana (Figure 4.15). In addition, this study uses band-pass filtering to map regional deep-seated gravity trends.

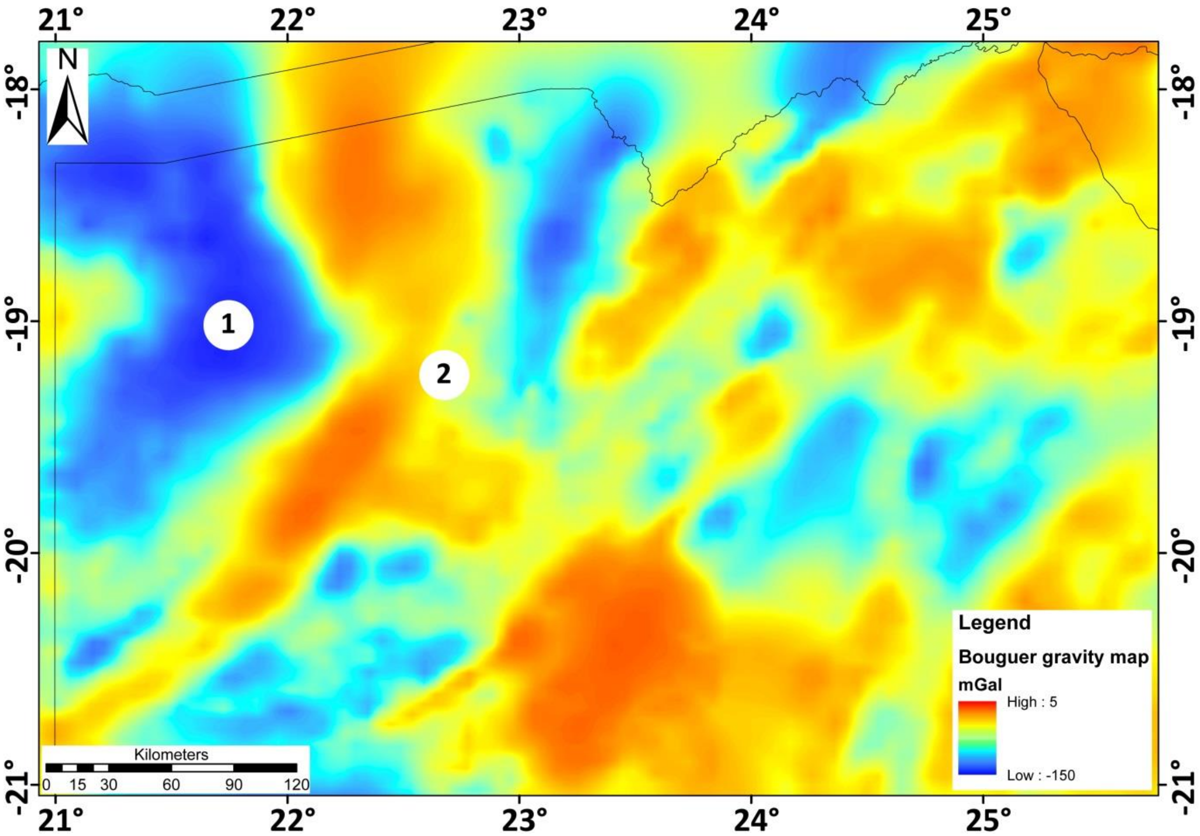

Figure 4.14: Bouguer gravity map of northwest Botswana. Note the negative Bouguer gravity anomaly in the north-western corner of the map (1) and the trend of the elongated positive gravity anomaly (2).

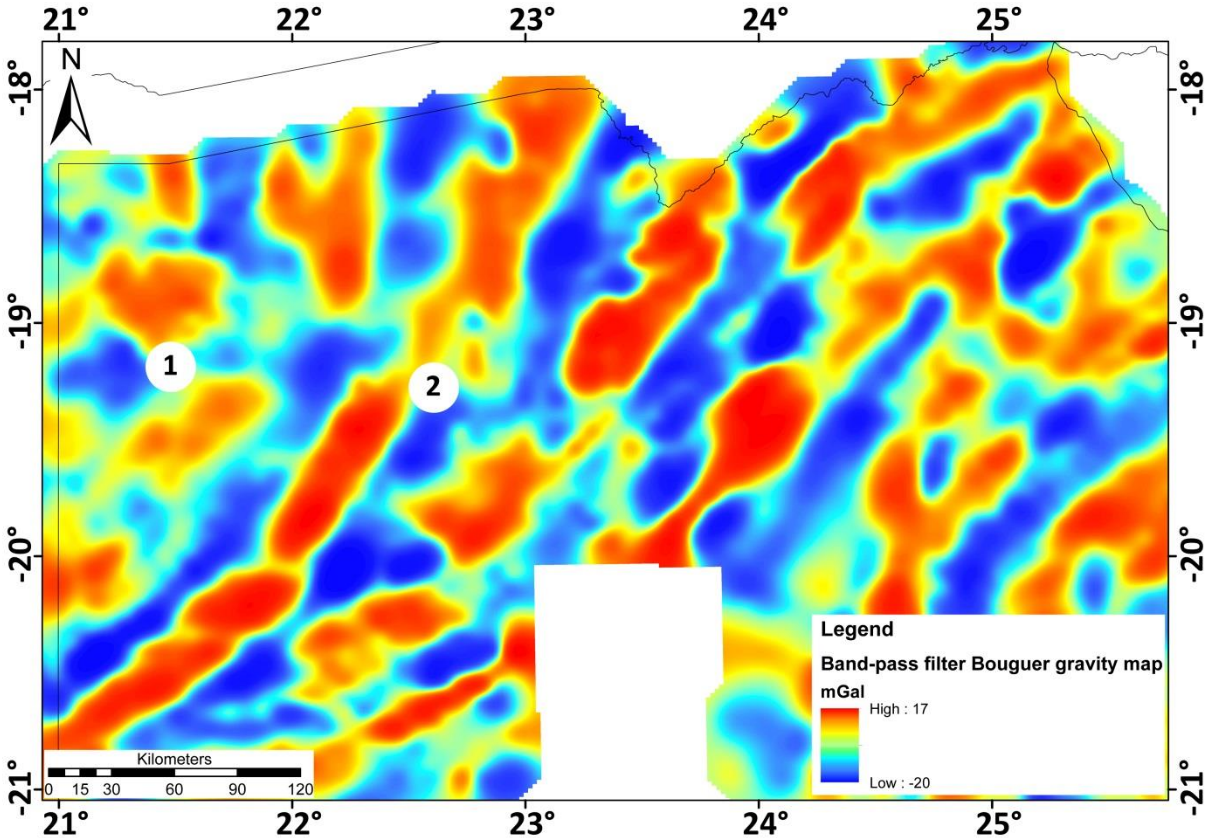

Figure 4.15: Bouguer gravity map of northwest Botswana band-pass filtered between 5 km and 100 km wavelengths. Note that the northwest corner (1) now consists of positive and negative gravity anomalies and the possible continuation of the elongated positive gravity anomaly (2).

In the northwest corner of Botswana is a negative Bouguer gravity anomaly of ~-150 mGal (Figure 4.14), which cannot be associated with a sedimentary basin because rocks of Congo Craton affinity have been intersected in Tsodilo Resources Ltd. boreholes at depths of less than 200 m whereas the sedimentary basin will need to be ~1 km thick to produce the observed Bouguer gravity anomaly. In the band-pass filtered image, the negative Bouguer gravity anomaly is replaced by discrete Bouguer gravity anomalies of between ~6 mGal to 9 mGal (Figure 4.15).

4.7. Summary

This chapter discussed the image processing techniques used to enhance aeromagnetic and gravity features in the data sets. These processed geophysical data sets were used in conjugation with the new physical property measurements (Chapter 5) and published geological and geophysical data to propose new geological cross-border correlations between Namibia and Botswana (Chapter 6).

Chapter 5

Physical properties

5.1. Introduction

The magnetic susceptibility and specific density of a lithology is controlled by its mineral assemblage. These mineral assemblages can be later altered through metamorphism and metasomatism either locally (i.e. shear and fault zones and/or contact aureoles), or regionally, such as gradual densification associated with burial. Lithologies may be remanently magnetised caused by either metamorphism, metasomatism or cooling.

Lithologies of the Southern Margin and Southern Zones are dominated by high pressure, low temperature (~600°C at ~10 kbar) (Kasch, 1983) kyanite facies minerals (Figure 5.1), while the lithologies of the Central Zone consist of low pressure, high temperature (~750°C at ~5 kbar to 6 kbar) (Jung *et al*., 2000) cordierite-sillimanite facies minerals (Figure 5.1). The Central Zone is associated with syn- to post-tectonic intrusions, predominately of granitic composition, indicating that the Damara Belt is a paired metamorphic belt (Goscombe *et al*., 2004).

The relationship (or lack thereof) between the magnetic susceptibility and density of mineral assemblages within different lithologies provides valuable information about the cause of their potential field anomalies. For example, iron formation is associated with a high density and magnetic susceptibility while hematite is associated with a lower magnetic susceptibility but a similar density.

In this study, magnetic susceptibility and specific density were measured to 1) characterise the lithologies and associated intrusions of the Damara and Ghanzi-Chobe Belts that may be responsible for the observed aeromagnetic anomalies. Unfortunately, the large grid size of 2.2 km for the Bouguer gravity map prohibits a direct correlation with the density measurements. 2) To investigate if an increase in magnetic susceptibility and density is associated with higher grades of metamorphism.

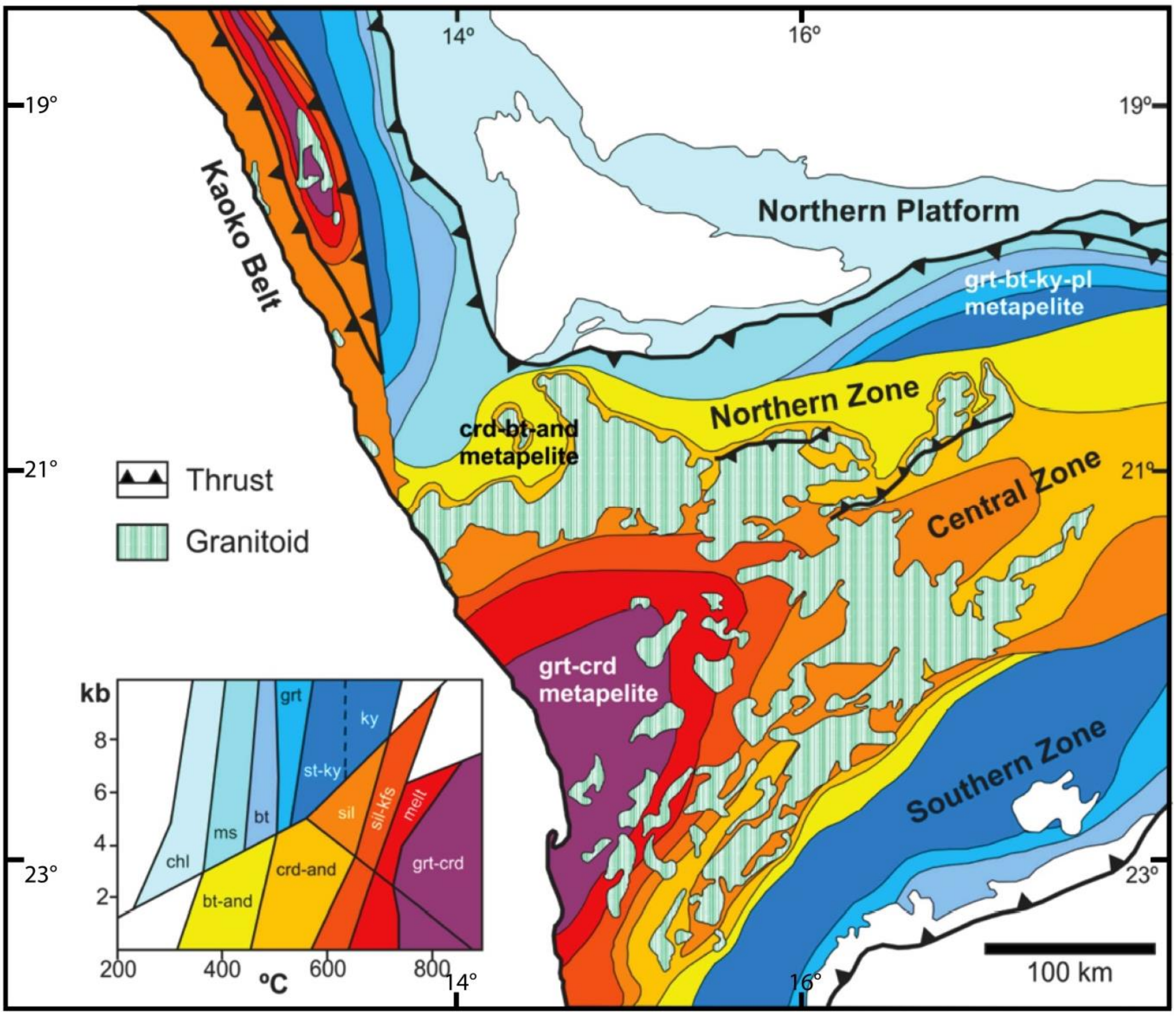

Figure 5.1: Simplified metamorphic map of peak metamorphic conditions in the Damara orogen (after Goscombe *et al*., 2004).

5.2. Collection of physical property measurements

Prior to fieldwork, satellite imagery from Google Earth was examined to determine outcrop localities where physical property measurements could be recorded. Field mapping was conducted with essential tools including a compass clinometer, to measure dip and strike of the outcrop, and a handheld Global Positioning System (GPS) to record the co-ordinates of the station points, using the Universal Mercator Projection (UTM) grid system (Namibia was measured in UTM zone 33S, Botswana in UTM zone 34S and Zambia in UTM zone 35S). Field notebooks were used to record the description of the lithologies encountered at each outcrop and the magnetic susceptibility measured.

Two field seasons (March 2012 (Namibia) and in May 2012 (Botswana and Zambia)) focused on geological mapping, magnetic susceptibility measurements and sampling for specific density measurements.

The UTM projected co-ordinates of the station locations were converted to Albers Equal Area Conic projection centred on a Meridian of 20°E with standard parallel 1 of -20°S and standard parallel 2 of -25°S co-ordinate system in ArcCatalog and imported into ArcGIS 9.3.1. This projection was chosen as it covers the complete study area with minimum distortion (which occurs in western Namibia and eastern Botswana when the World Geodetic System 1984 (WGS84) reference ellipsoid is used). In ArcGIS the physical property measurements were overlain on the aeromagnetic (Figure 5.2) and gravity data sets (Figure 5.3) to compare the relationship between the measured physical properties and the potential field anomalies.

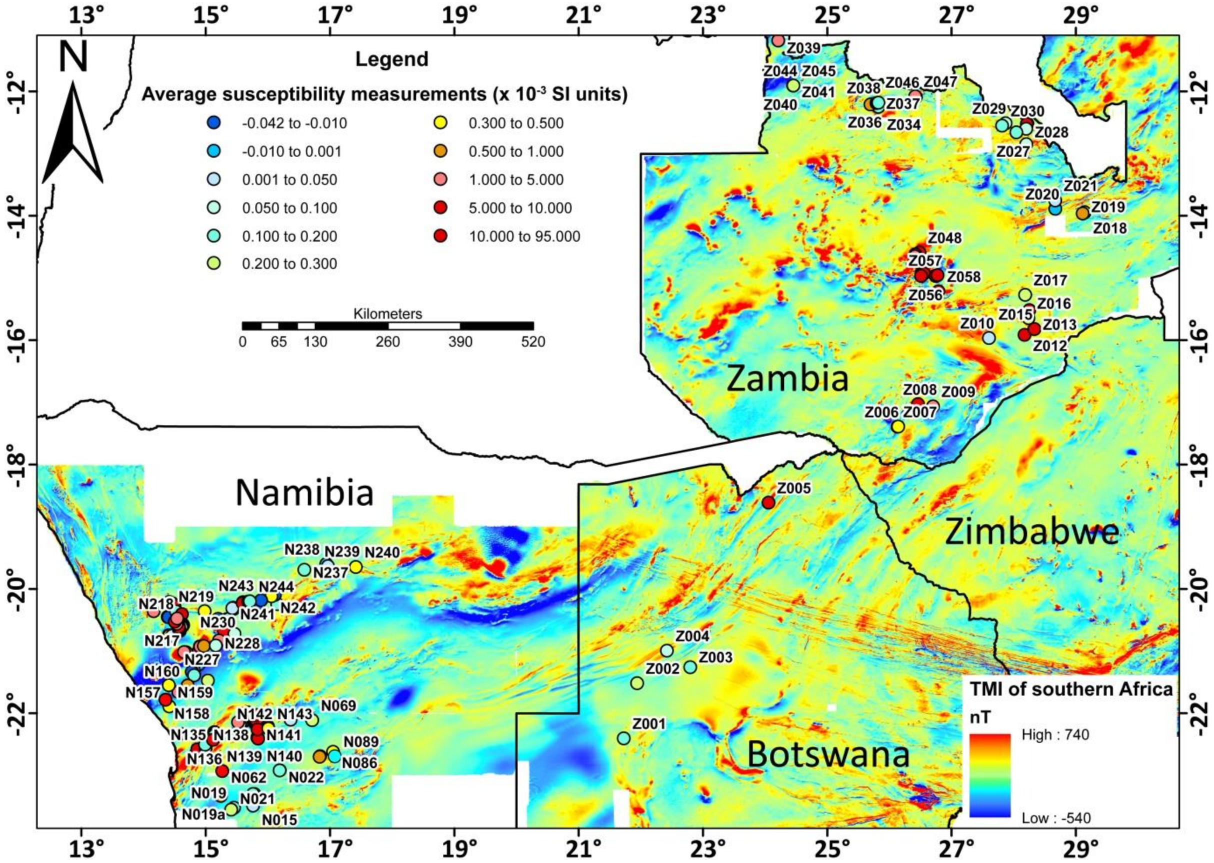

Figure 5.2: Location of average magnetic susceptibility measurements overlain on the TMI map of Namibia, Botswana, Zambia and Zimbabwe stitched at a grid cell size of 250 m.

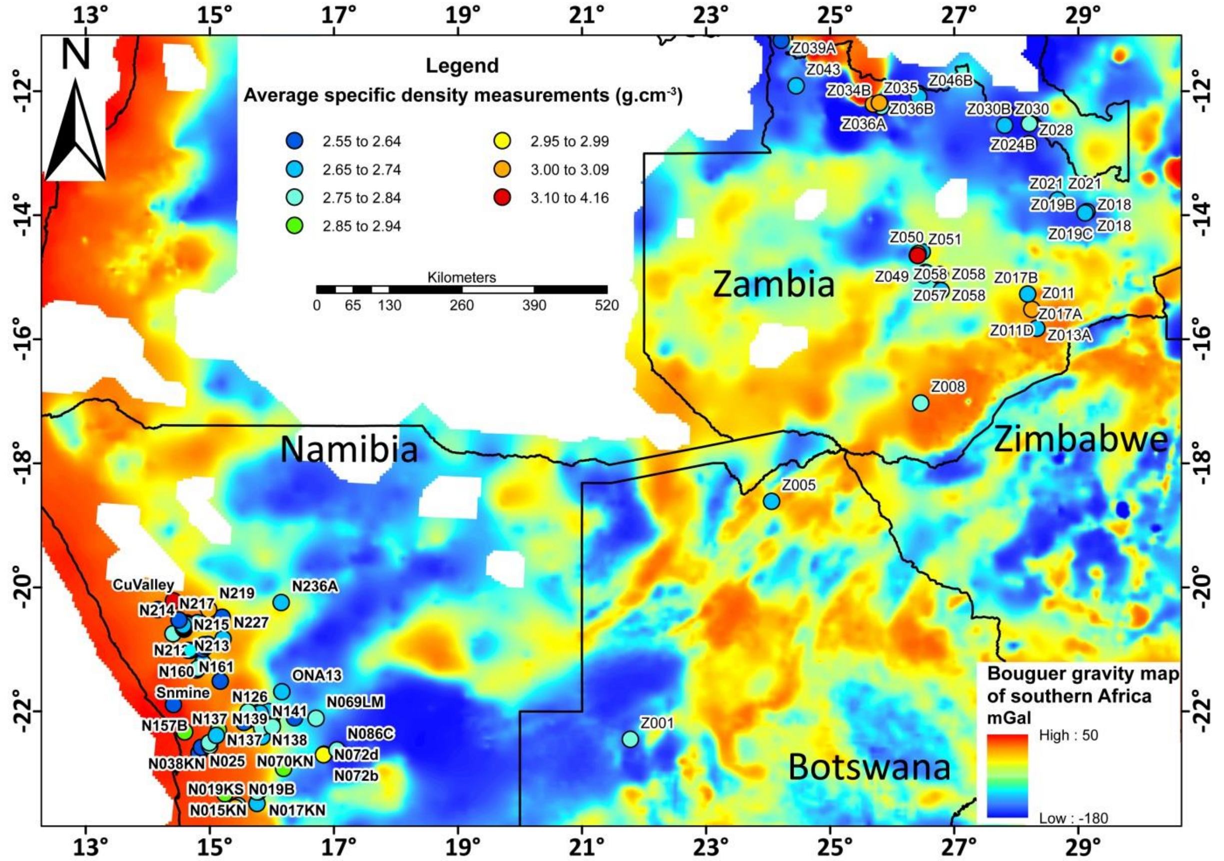

Figure 5.3: Location of density measurements overlain on the Bouguer gravity map of Namibia, Botswana, Zambia and Zimbabwe stitched at a grid cell size of 2.2 km.

5.2.1. Specific density data

The density of a lithology is controlled by its mineral composition, silica content, and porosity. Density increases with pressure because of mineral reactions resulting in a change in mineral assemblages from plagioclase-bearing, garnet-free to garnet-bearing and plagioclase-free (Sobolev *et al*., 1993).

Density measurements were collected on 174 samples using a top pan Sartorius scale (0.01 – 5500.00 g) 1507 MP balance with an accuracy of 0.01 g. Each sample was weighed three times in air (w_A) and then saturated in water for at least 24 hours before being weighed three times in water (w_w). Archimedes Principle was used to calculate the density of the sample and is given by;

$$\rho = \frac{w_A}{(w_A - w_w)} \tag{5.1}$$

where ρ is the density, w_A is the weight in air and w_w is the weight in water.

Standard deviation assumes a Gaussian distribution of the data and calculates the spread from the mean. Because of the small number of measurements the distribution of the data is not Gaussian. Therefore, to estimate errors associated with the calculated density, a simple Taylor series expansion is applied: consider a function f at a certain point $x + \Delta x$ in terms of its value and derivative in a neighbouring point x;

$$\Delta f = \frac{\partial f}{\partial x} \Delta x \tag{5.2}$$

When f is a function of more than one term (i.e. $x, y, z, \ldots$), the total error is the square root of the sum of the individual squared terms,

$$\Delta f(x, y) = \sqrt{\left(\frac{\partial f}{\partial x} \Delta x\right)^2 + \left(\frac{\partial f}{\partial y} \Delta y\right)^2} \tag{5.3}$$

Applying Equation 5.3 to Equation 5.1, the following equation has been derived to estimate the error associated with measuring the specific density measurements;

$$\Delta \rho = \rho \times \left(\sqrt{\left(\frac{w_A}{(w_A - w_W)^2} \Delta w_W\right)^2 + \left(\frac{w_W}{(w_A - w_W)^2} \Delta w_A\right)^2}\right) \tag{5.4}$$

where $\Delta \rho$ is the error in density, Δw_A and Δw_W are the errors in weight in air and water respectively. To calculate the error for an average of results;

$$\Delta \rho_{ave} = \frac{\sum \Delta \rho_n}{\sqrt{n}} \tag{5.5}$$

where $\Delta \rho_n$ is the error for a single density calculation and *n* is the number of recorded measurements.

The calculated density range and average densities of the lithologies of the Damara Supergroup and Ghanzi Group are listed in Table 5.1 with the density range and average densities of the intrusive units listed in Table 5.2. The location of each sample and the measured values in air and water and the Zambian lithologies are in Appendix 4.

Table 5.1: Average and range of density measurements for the lithological units of the Damara and Ghanzi-Chobe Belts. For simplicity the Okahandja and Southern Zones are grouped into the Southern Zone whilst the Granite only, Northern Zone Ais Dome and Northern Zone are grouped into the Northern Zone.

Tectonostratigraphic zone	Group	Formation/ Member	Simplified lithology	Density range ($g.cm^{-3}$)	Average density ($g.cm^{-3}$)	Uncertainty ($g.cm^{-3}$)	Number of samples	Total number of measurements
Southern Kaoko or Ugab Zone	Zerrissene	Amis	Quartzite	2.76 - 2.81	2.79	9.10×10^{-4}	2	6
			Mica schist	2.69 - 2.77	2.72	1.99×10^{-3}	5	15
Northern Zone	Swakop	Kuiseb	Schist	2.72 - 2.73	2.73	1.40×10^{-4}	1	3
		Karibib	Dolostone	2.70 - 2.71	2.71	1.65×10^{-4}	1	3
	Nosib	Naauwpoort	Rhyolite	2.58 - 2.59	2.58	6.30×10^{-5}	1	3
southern Central Zone	Swakop	Kuiseb	Mica schist	2.75 - 2.80	2.77	5.97×10^{-3}	2	6
		Karibib	Marble	2.70 - 2.86	2.78	1.55×10^{-3}	2	6
		Arandis	Marble	2.86 - 2.87	2.87	2.37×10^{-4}	1	3
	Nosib	Khan	Amphibolite	2.89 - 2.90	2.90	3.15×10^{-4}	1	3
			Gneiss	2.62 - 2.80	2.71	2.42×10^{-4}	2	6
Southern Zone	Swakop	Kuiseb	Gneiss	2.75	2.75	1.52×10^{-4}	1	3
			Amphibolite	2.83 - 2.84	2.84	7.79×10^{-4}	1	3
			Mica schist	2.67 - 3.37	2.95	1.26×10^{-3}	6	18
		Matchless	Amphibolite	3.00 - 3.01	3.00	1.66×10^{-3}	1	3
			Mica schist	2.83 - 3.03	2.91	1.84×10^{-3}	3	9
Southern Margin Zone	Swakop	Kuiseb	Metapsammite	2.61 - 2.62	2.62	1.11×10^{-4}	1	3
			Amphibolite	2.79 - 2.80	2.80	9.39×10^{-4}	1	3
			Gneiss	2.73 - 2.74	2.74	1.31×10^{-3}	1	3
	Hakos	Noas	Mica schist	2.68 - 2.70	2.69	2.00×10^{-3}	1	3

Table 5.2: Average and range of density measurements of the metamorphic and igneous complexes associated with the Damara and Ghanzi-Chobe Belts. For simplicity the Okahandja and Southern Zones are grouped into the Southern Zone whilst the Granite only, Northern Zone Ais Dome and Northern Zone are grouped into the Northern Zone.

Tectonostratigraphic zone	**Suite/Complex**	**Simplified lithology**	**Density range ($g.cm^{-3}$)**	**Average density ($g.cm^{-3}$)**	**Uncertainty ($g.cm^{-3}$)**	**Number of samples**	**Total number of measurements**
Kamanjab Inlier	Huab	Mica schist	3.14 - 3.79	3.32	3.20×10^{-4}	1	3
Southern Kaoko or Ugab Zone	Namibian gabbro	Gabbro	2.83 - 2.84	2.84	1.65×10^{-4}	1	3
		Pegmatite	2.55 - 2.68	2.64	9.50×10^{-4}	3	9
Northern Zone	Khorixas	Gabbro	2.99 - 3.00	3.00	1.96×10^{-4}	1	3
	Sorris Sorris	Granite	2.57 - 2.72	2.62	3.17×10^{-3}	16	48
	Omangambo	Granite	2.65 - 2.68	2.66	1.04×10^{-3}	7	21
northern Central Zone		Pegmatite	2.64	2.64	2.10×10^{-4}	1	3
southern Central Zone		Pegmatite	2.55 - 2.56	2.56	4.75×10^{-4}	1	3
	Red Granite	Granite	2.60 - 2.61	2.61	4.84×10^{-4}	1	3
	Salem	Granite	2.61 - 2.70	2.67	2.03×10^{-3}	8	24
	Abbabis	Pyroxenite	3.00 - 3.01	3.01	1.78×10^{-4}	1	3
		Mica schist	2.63 - 2.64	2.64	3.29×10^{-4}	1	3
		Gneiss	2.64 - 2.87	2.79	5.66×10^{-4}	3	9
		Granite	2.73 - 2.81	2.77	2.48×10^{-4}	2	6
	Goas	Granodiorite	2.65 - 2.75	2.71	5.92×10^{-4}	5	15
		Diorite	2.60 - 2.82	2.73	2.65×10^{-3}	17	51
		Gabbro	2.92 - 3.05	2.96	2.58×10^{-3}	12	36
		Granite	2.62 - 2.63	2.62	9.53×10^{-4}	1	3
		Amphibolite	3.25 - 3.26	3.25	7.42×10^{-4}	1	3
Ghanzi-Chobe Zone	Goha Hills	Dacite	2.68 - 2.69	2.68	8.88×10^{-4}	1	3
	Okwa	Granite	2.70 - 2.71	2.70	8.60×10^{-4}	1	3

5.2.2. Magnetic susceptibility data

The magnetic susceptibility of lithologies is controlled by the type and abundance of magnetic minerals in the sample. It can be controlled by paramagnetic minerals such as mafic silicates (olivine, pyroxene, tourmaline, garnet and micas); however, it is more often controlled by the ferromagnetic minerals such as magnetite and pyrrhotite. The ferromagnetic minerals are often accessory minerals, which can provide useful information on the geological process of the sample. Therefore, the measured magnetic susceptibility depends on the geochemical or mineralogical composition of the sample and on later metamorphic and alteration process.

Magnetic susceptibility measurements were recorded on 303 samples using a SM 30 handheld magnetic susceptibility meter, accurate to 1×10^{-7} SI units. In general, five measurements were recorded on each sample; however, when the magnetic susceptibility varied by more than 10% up to fifteen measurements were recorded on the sample. Measurements were taken parallel and perpendicular to foliation of the sample. Care was taken when measuring the magnetic susceptibility (i.e. measurements were carried out on fresh, flat and broad surfaces of the outcrop/sample), as surface roughness, weathering, and outcrop size can lower the apparent magnetic susceptibility relative to the true bulk magnetic susceptibility.

Magnetic susceptibility measures the ability of a material to be magnetised in the presence of an external magnetic field. In magnetically isotropic material, it is defined as;

$$J = \chi H, \tag{5.6}$$

where J is the intensity of magnetisation related to the strength of the magnetic field H, through the magnetic susceptibility χ (dimensionless scalar).

Magnetic susceptibility can have either positive or negative values. If the measurement is positive, it implies that the induced magnetisation is in the same direction as the inducing field, H, and negative values imply that the induced magnetisation is in the opposite direction to the inducing field, H (Irving, 1964). It can be measured in either SI units or the cgs system where the basic conversion is given by;

$$\chi_{SI} = 4\pi\chi_{cgs}. \tag{5.7}$$

The error for the magnetic susceptibility was calculated using;

$$\Delta J_m = \frac{1\times 10^{-7}}{J_m} \tag{5.8}$$

where J_m is the measured magnetic susceptibility and ΔJ_m the associated error in a single measurement. The average magnetic susceptibility error was calculated by summing the individual errors and dividing by the total number of measurements;

$$\Delta J_{ave} = \frac{\sum \Delta J_m}{\sqrt{n}} \tag{5.9}$$

where ΔJ_{ave} is the average magnetic susceptibility error and n is the number of measurements.

The range and average of the magnetic susceptibility measurements for the lithologies of the Damara Supergroup and Ghanzi Group are summarised in Table 5.3 and intrusive units in Table 5.4. The full table (including Zambia) is in Appendix 5.

Table 5.3: Average and range of the magnetic susceptibility measurements for lithological units of the Damara and Ghanzi-Chobe Belts. For simplicity the Okahandja and Southern Zones are grouped into the Southern Zone whilst the Granite only, Northern Zone Ais Dome and Northern Zone are grouped into the Northern Zone.

Tectonostratigraphic zone	Group	Formation/ Member	Simplified lithology	Magnetic susceptibility range (x 10^{-3} SI units)	Average magnetic susceptibility (x 10^{-3} SI units)	Uncertainty (SI units)	Number of samples	Total number of measurements
Northern Platform	Otavi	Elandshoek	Marble	-0.017 - 0.006	-0.006	5.20 x 10^{-2}	1	10
		Auros	Dolostone	0.005 - 0.482	0.133	1.14 x 10^{-2}	1	12
Northern Margin Zone	Mulden	Gaseneirob	Conglomerate	0.092 - 0.451	0.189	1.68 X 10^{-3}	1	5
	Otavi	Maieberg	Marble	-0.469 - 1.69	0.411	1.13 x 10^{-2}	1	13
		Gauss	Marble	-0.128 - 0.280	0.030	2.15 x 10^{-2}	1	10
Southern Kaoko or Ugab Zone	Nosib	Tsaun	Granite	0.115 - 11.4	4.18	5.04 x 10^{-4}	2	22
			Gneiss	0.011 - 2.05	0.385	4.84 x 10^{-3}	1	10
	Zerrissene	Amis	Schist	0.004 - 0.424	0.196	8.33 x 10^{-3}	3	27
			Mica schist	0.151 - 0.317	0.217	1.10 x 10^{-3}	1	5
			Quartzite	0.07 - 0.207	0.102	3.68 x 10^{-3}	2	12
			Sandstone	0.076 - 1.13	0.389	1.82 x 10^{-3}	1	10
			Metapelites	0.013 - 5.700	0.901	8.94 x 10^{-3}	4	20
		Gemsbok River	Marble	-0.009 - 0.152	0.041	4.85 x 10^{-2}	2	10
			Slate	0.104 - 1.93	0.361	1.66 x 10^{-3}	1	10
Northern Zone	Swakop	Kuiseb	Slate	0.058 - 1.4	0.356	1.85 x 10^{-3}	2	10
			Quartzite	-0.181 - 0.351	0.023	3.29 x 10^{-2}	3	17
			Sandstone	-0.025 - 0.501	0.137	2.37 x 10^{-3}	2	18
			Schist	0.068 - 10.6	3.27	1.09 x 10^{-3}	3	13
		Karibib	Schist	0.01 - 0.611	0.322	5.07 x 10^{-3}	1	5
			Dolostone	-0.073 - 0.432	0.160	3.71 x 10^{-3}	1	8
			Marble	-0.299 - 0.997	0.053	3.20 x 10^{-2}	12	97
		Chuos	Ironstone	66.2 - 114	92.0	2.54 x 10^{-6}	1	5
		Okatjize	Dolostone	0.037 - 0.558	0.260	2.20 x 10^{-3}	2	15
	Nosib	Naauwpoort	Rhyolite	-0.024 - -0.02	-0.024	1.36 x 10^{-2}	1	5
			Conglomerate	6.580 - 23.601	15.2	2.55 x 10^{-5}	2	11

Table 5.3: Continued.

Tectonostratigraphic zone	Group	Formation/ Member	Simplified lithology	Magnetic susceptibility range (x 10^{-3} SI units)	Average magnetic susceptibility (x 10^{-3} SI units)	Uncertainty (SI units)	Number of samples	Total number of measurements
northern Central Zone	Swakop	Kuiseb	Mica schist	0.268 - 0.303	0.283	7.91 x 10^{-4}	1	5
		Karibib	Marble	-0.011 - 0.133	0.010	1.22 x 10^{-1}	7	35
		Arandis	Mica schist	0.122 - 3.640	0.880	8.22 x 10^{-4}	1	10
southern Central Zone	Swakop	Kuiseb	Marble	0.008 - 0.089	0.029	1.48 x 10^{-2}	1	5
			Gneiss	0.111 - 0.607	0.277	1.13 x 10^{-3}	1	5
			Mica schist	0.023 - 0.34	0.177	4.75 x 10^{-3}	4	20
		Karibib	Marble	-0.021 - 0.357	0.057	5.73 x 10^{-2}	6	31
		Arandis	Mica schist	0.124 - 0.223	0.169	1.98 x 10^{-3}	2	10
			Quartzite	0.15 - 0.289	0.204	2.00 x 10^{-3}	3	15
			Marble	-0.021 - 0.657	0.183	1.23 x 10^{-2}	6	30
		Chuos	Quartzite	0.045 - 0.149	0.081	4.35 x 10^{-3}	2	10
			Ironstone	0.09 - 13	3.34	7.48 x 10^{-4}	1	5
			Diamictite	4.04 - 11.8	7.68	3.34 x 10^{-5}	1	5
		Rössing	Schist	0.043 - 6.49	1.87	2.82 x 10^{-3}	4	25
			Granite	4.99 - 40.6	15.7	3.00 x 10^{-5}	1	8
	Nosib	Khan	Gneiss	0.068 - 0.52	0.173	2.85 x 10^{-3}	3	16
			Amphibolite	0.703 - 1.1	0.945	2.43 x 10^{-4}	1	5
		Etusis	Quartzite	0.065 - 0.149	0.108	2.24 x 10^{-3}	1	5
			Marble	0.011 - 0.53	0.242	5.17 x 10^{-3}	1	10
			Slate	0.167 - 0.281	0.231	1.01 x 10^{-3}	1	5
			Gneiss	15 - 49.5	36.5	1.07 x 10^{-5}	2	13
Southern Zone	Swakop	Kuiseb	Mica schist	0.038 - 0.798	0.338	2.24 x 10^{-3}	5	25
			Amphibolite	0.106 - 0.202	0.167	1.43 x 10^{-3}	1	5
			Gneiss	0.251 - 0.284	0.268	8.35 x 10^{-4}	1	5
		Matchless	Mica schist	0.133 - 41.5	6.41	1.80 x 10^{-3}	5	30
			Amphibolite	0.298 - 0.383	0.351	6.43 x 10^{-4}	1	5

Table 5.3: Continued.

Tectonostratigraphic zone	Group	Formation/Member	Simplified lithology	Magnetic susceptibility range (x 10^{-3} SI units)	Average magnetic susceptibility (x 10^{-3} SI units)	Uncertainty (SI units)	Number of samples	Total number of measurements
Southern Margin Zone	Swakop	Kuiseb	Gneiss	0.272 - 0.414	0.342	6.72 x 10^{-4}	1	5
	Hakos	Noas	Mica schist	0.019 - 0.043	0.0491	9.42 x 10^{-3}	2	10
Ghanzi-Chobe Zone	Ghanzi	D'Kar	Sandstone	0.016 - 0.616	0.181	4.54 x 10^{-4}	2	21

Table 5.4: Average and range of the magnetic susceptibility measurements of the metamorphic and igneous complexes associated with the Damara and Ghanzi-Chobe Belts. For simplicity the Okahandja and Southern Zones are grouped into the Southern Zone whilst the Granite only, Northern Zone Ais Dome and Northern Zone are grouped into the Northern Zone.

Tectonostratigraphic zone	Suite/Complex	Simplified lithology	Magnetic susceptibility range (x 10^{-3} SI units)	Average magnetic susceptibility (x 10^{-3} SI units)	Uncertainty (SI units)	Number of samples	Total number of measurements
Kamanjab Inlier	Huab	Mica schist	0.037 - 0.676	0.200	3.64 x 10^{-3}	1	10
		Quartzite	-0.006 - 0.496	0.119	1.22 x 10^{-2}	1	12
		Gneiss	3.04 - 6.87	5.05	5.43 x 10^{-5}	1	6
		Granite	0.466 - 1.02	0.758	3.18 x 10^{-4}	1	5
		Gabbro	0.028 - 1.18	0.227	4.30 x 10^{-3}	1	8
Northern Margin Zone	Huab	Gneiss	1.99 - 10.5	6.12	5.04 x 10^{-5}	1	5
Southern Kaoko or Ugab Zone		Pegmatite	-0.034 - 0.821	0.109	3.76 x 10^{-2}	6	37
	Namibian gabbro	Gabbro	0.187 - 1.12	0.566	8.58 x 10^{-4}	2	15
Northern Zone	Khorixas	Gabbro	0.121 - 0.855	0.406	8.13 x 10^{-4}	1	5
	Omangambo	Granite	0.065 - 16.7	6.81	1.14 x 10^{-3}	8	42
	Salem	Granite	1.1 - 8.84	4.16	1.27 x 10^{-4}	2	10
	Sorris Sorris	Granite	-0.34 - 11.2	2.38	6.55 x 10^{-3}	16	99
northern Central Zone		Pegmatite	-0.014 - 0.024	0.001	9.85 x 10^{-2}	2	10
	Abbabis	Granite	1.05 - 1.24	1.16	1.93 x 10^{-4}	1	5

Table 5.4: Continued

Tectonostratigraphic zone	Suite/Complex	Simplified lithology	Magnetic susceptibility range (x 10^{-3} SI units)	Average magnetic susceptibility (x 10^{-3} SI units)	Uncertainty (SI units)	Number of samples	Total number of measurements
southern Central Zone		Pegmatite	-0.12 - 0.79	0.0685	1.13×10^{-1}	9	50
	Abbabis	Sandstone	0.102 - 0.666	0.356	9.23×10^{-4}	1	5
		Quartzite	0.002 - 0.031	0.0125	3.85×10^{-2}	1	5
		Mica schist	0.121 - 7.94	4.39	3.50×10^{-4}	1	9
		Meta-tuff	4.98 - 7.84	6.47	3.55×10^{-5}	1	5
		Amphibolite	0.343 - 0.701	0.512	4.63×10^{-4}	1	5
		Pyroxenite	3.44 - 9.2	5.96	4.15×10^{-5}	1	5
		Granite	0.002 - 9.14	2.52	2.22×10^{-2}	2	16
		Gneiss	0.249 - 7.47	1.72	5.11×10^{-4}	3	16
	Goas	Gneiss	0.079 - 0.462	0.222	2.08×10^{-3}	1	7
		Granite	0.044 - 0.456	0.168	2.63×10^{-3}	1	5
		Granodiorite	0.178 - 19.1	6.58	6.12×10^{-4}	3	17
		Diorite	0.393 - 60.8	11.6	2.55×10^{-4}	12	83
		Gabbro	0.075 - 47.8	3.41	2.00×10^{-3}	6	39
	Kobus	Granite	0.458 - 0.891	0.732	3.24×10^{-4}	1	5
	Red granite	Granite	7.43 - 21.8	11.3	2.30×10^{-5}	1	5
southern Central Zone	Salem	Granite	-0.02 - 11.7	1.12	2.72×10^{-2}	8	50
Ghanzi-Chobe Zone	Goha Hills	Dacite	8.12 - 12.8	10.7	2.14×10^{-5}	1	5
	Kgwebe	Rhyolite	0.041 - 0.74	0.057	$5.69 \text{ X } 10^{-3}$	1	10
	Okwa	Granite	0.079 - 0.152	0.199	$2.04 \text{ X } 10^{-3}$	1	5

5.3. Results and discussion

5.3.1. Specific density

Ghanzi Group and Damara Supergroup lithologies

The amphibolites have the highest average density of 2.80 ± 9.39 x 10^{-4} g.cm^{-3} to 3.00 ± 1.66 x 10^{-3} g.cm^{-3}. Generally, the increase in density follows the increase in metamorphic grade, from the greenschist facies of the Southern Margin Zone (Behr *et al*., 1983; Frimmel and Miller, 2009) to the amphibolite/granulite facies of the Central Zone (Goscombe *et al*., 2004). This observation is explained by the decrease in pore spaces associated with compaction during metamorphism. An exception to this is sample N019B, an amphibolite sample from the Matchless Member, whose increased density is associated with disseminated copper mineralisation. Rhyolite and augen gneiss have an average density of between 2.58 ± 6.30 x 10^{-4} g.cm^{-3} to 2.75 ± 1.52 x 10^{-4} g.cm^{-3} attributed to their dominantly felsic composition.

The cap carbonate of the Chuos Formation (i.e. Arandis Formation) has a higher average density of 2.87 ± 2.37 x 10^{-4} g.cm^{-3} compared to the cap carbonate of the Ghaub Formation (i.e. Karibib Formation) of ~2.75 ± 1.55 x 10^{-3} g.cm^{-3}. The higher density values for the Arandis Formation marble compared to the Karibib Formation marble is because of its decrease in silica contents and iron oxide impurities derived from the underlying Chuos Formation.

The schists/mica schists have the widest average density range from 2.69 ± 2.00 x 10^{-3} g.cm^{-3} to 2.95 ± 1.26 x 10^{-3} g.cm^{-3}. The schists/mica schists associated with the lower density values of 2.69 ± 2.00 x 10^{-3} g.cm^{-3} to 2.73 ± 1.40 x 10^{-4} g.cm^{-3} are of sedimentary origin located in the lower metamorphic domains of the Damara Orogen. This is observed in the average density contrast of ~0.04 g.cm^{-3} between the Kuiseb schists/mica schists of the Northern and southern Central Zones (Table 5.1). The mica schists of the Kuiseb Formation in the southern Central Zone have an average density of 2.77 ± 5.97 x 10^{-3} g.cm^{-3} compared to an average density of 2.73 ± 1.40 x 10^{-4} g.cm^{-3} for the schists of Kuiseb Formation in the Northern Zone. The higher metamorphic grades have resulted in greater compaction (decrease in porosity) and metamorphic minerals such as biotite and muscovite. The schist/mica schist with the highest average densities of 2.91 ± 1.84 x 10^{-3} g.cm^{-3} to 2.95 ± 1.26 x 10^{-3} g.cm^{-3} are associated with copper mineralisation and high-grade metamorphic minerals such as garnet, amphibole and kyanite.

Intrusive lithologies

The silica-rich pegmatites have the lowest average density of between 2.56 ± 4.75 x 10^{-4} g.cm^{-3} to 2.64 ± 2.10 x 10^{-4} g.cm^{-3} (Table 5.2). The granitic suites associated with the Damara Orogen have an average density of 2.61 ± 4.84 x 10^{-4} g.cm^{-3} to 2.77 ± 2.48 x 10^{-4} g.cm^{-3} (Table 5.2). The higher density values of 2.70 ± 8.60 x 10^{-4} g.cm^{-3} and 2.77 ± 2.48 x 10^{-4} g.cm^{-3} are associated with the older Okwa and Abbabis Complexes respectively, of ~2.0 Ga (Rainaud *et al*., 2005a; Mapeo *et al*., 2006; Longridge, 2012). Lower density values are associated with the granitic syn-to post tectonic Sorris-Sorris, Omangambo, Red Granite and Salem granitic intrusions. The Red Granite and Sorris-Sorris have the lowest average density of 2.61 ± 4.84 x 10^{-4} g.cm^{-3} and 2.62 ± 3.17 x 10^{-3} g.cm^{-3} respectively. The Red Granite and Sorris-Sorris are characterised by abundant quartz and large (~1 cm) K-feldspar grains with minor biotite and magnetite. The granites of the Salem and Omangambo Suites have a very similar average density of 2.67 ± 2.03 x 10^{-3} g.cm^{-3} and 2.66 ± 1.04 x 10^{-3} g.cm^{-3}, respectively (Table 5.2). The Salem and Omangambo Suites are characterised by megacrystic K-feldspars with minor hornblende, biotite and magnetite.

The mafic lithologies such as gabbro, amphibolite and pyroxenite are characterised by higher average density values of 3.00 ± 1.96 x 10^{-4} g.cm^{-3}, 3.25 ± 7.42 x 10^{-3} g.cm^{-4}, and 3.01 ± 1.78 x 10^{-4} g.cm^{-3}, respectively (Table 5.2). The densities of these volcanics are controlled by their silica contents. Samples with a lower silica content have a higher average density.

5.3.2. Magnetic susceptibility

Ghanzi Group and Damara Supergroup lithologies

The lithologies measured have a large range of magnetic susceptibilities, even for a particular sample, and a wide overlap between different samples, which is a common trend. The ironstones of the Chuos Formation have the highest average and range of magnetic susceptibility values of 3.34 x 10^{-3} ± 7.48 x 10^{-4} SI units to 92.0 x 10^{-3} ± 2.54 x 10^{-6} SI units (Table 5.3). The magnetic susceptibility of 92.0 x 10^{-3} ± 2.54 x 10^{-6} SI units is associated with a “pure” ironstone (sample N230) while the lower magnetic susceptibility is associated with localised ironstone horizons in a schistose matrix (sample N136.9).

Generally, the cap carbonate of the Chuos Formation (Arandis Formation) has a higher average magnetic susceptibility (0.183 x 10^{-3} ± 1.23 x 10^{-2} SI units) compared to the cap carbonate of the Ghaub Formation (Karibib Formation) (0.053 x 10^{-3} ± 3.20 x 10^{-2} SI units) (Table 5.3). The difference in magnetic susceptibility can possibly be associated with material derived from the underlying glaciogenic lithologies (i.e. the Chuos Formation is associated with iron formation, and the Ghaub Formation is not). An exception is the Maieberg Formation, in the Northern Margin Zone, (sample N240), that has an average magnetic susceptibility of $0.411 \times 10^{-3} \pm 1.13 \times 10^{-2}$ SI units. The sample contains small disseminated sulphide grains that previous studies have identified as pyrite and pyrrhotite (Hurtgen *et al*., 2006; Kamona and Günzel, 2007). Therefore, from the increase in magnetic susceptibility of sample N240 by an order of magnitude compared to the other marble samples, is caused by disseminated pyrrhotite.

The dolostone of the Okatjize and Karibib Formations have an average magnetic susceptibility of $0.260 \times 10^{-3} \pm 2.20 \times 10^{-3}$ SI units and $0.160 \times 10^{-3} \pm 3.71 \times 10^{-3}$ SI units respectively, compared to the average magnetic susceptibility of $0.133 \times 10^{-3} \pm 1.14 \times 10^{-2}$ SI units for dolostone of the Auros Formation (Table 5.3). As the higher average magnetic susceptibility values are associated with samples that are located in the higher metamorphic domains, it suggests that the samples contain larger amounts of dolomite compared to calcite. In a study on the physical properties of carbonate marbles, Kivekäs (1999) showed that the magnetic susceptibility of dolomite is greater than the magnetic susceptibility of calcite.

The Naauwpoort conglomerate has an average magnetic susceptibility of $15.2 \times 10^{-3} \pm 2.55 \times 10^{-5}$ SI units compared to an average magnetic susceptibility of $0.189 \times 10^{-3} \pm 1.68 \times 10^{-3}$ SI units for the Gaseneirob conglomerate (Table 5.3). From field observations the higher magnetic susceptibility of the Naauwpoort conglomerate is associated with mafic and granitic clasts compared to the carbonate clasts of the Gaseneirob conglomerate.

Gneisses have an average magnetic susceptibility of $0.173 \times 10^{-3} \pm 2.85 \times 10^{-3}$ SI units to $36.5 \times 10^{-3} \pm 1.07 \times 10^{-5}$ SI units (Table 5.3). The lower average magnetic susceptibility of $0.173 \times 10^{-3} \pm 2.85 \times 10^{-3}$ SI units is associated with gneisses of the Khan Formation (Table 5.3) which, from field observations, is either a deformed granite (sample N025.1KS) or contains weakly magnetic minerals such as muscovite (two-mica gneiss, sample N038KN) and a bluish-grey diopside (sample N135) (Appendix 5). The intermediate average magnetic susceptibility values of $0.268 \times 10^{-3} \pm 8.35 \times 10^{-4}$ SI units to $0.385 \times 10^{-3} \pm 4.84 \times 10^{-3}$ SI units are associated with the Kuiseb and Tsaun Formations (samples N070, N086KNa, N133.4, and N1555) (Appendix 5). The gneisses have a weak foliation and contain magnetic minerals such as garnet and biotite. The high average magnetic susceptibility of $36.5 \times 10^{-3} \pm 1.07 \times 10^{-5}$ SI units for the Etusis Formation (sample 052JLa and b) is associated a strong foliation of biotite and sillimanite minerals (Appendix 5). The magnetic susceptibility of these gneisses being dependant on the amount and alignment of biotite is supported by studies of Naba *et al*. (2004) and Vegas *et al*. (2008), who reported biotite as the main contributor of magnetic susceptibility in granites of eastern Burkina Faso.

The granites of the Rössing and Tsaun Formations have average magnetic susceptibilities of 15.7 x 10^{-3} ± 3.00 x 10^{-5} SI units and 4.18 x 10^{-3} ± 5.04 x 10^{-4} SI units, respectively (Table 5.3). The high magnetic susceptibility of the Rössing granites is associated with enclaves (oval shape ~5 cm long and 3 cm wide) of magnetite, while the Tsaun granites contain disseminated, small (~2 mm), black cubic minerals, suggested to be magnetite from field observations.

The mica schists of the Matchless Member have the highest average magnetic susceptibility of 6.41 x 10^{-3} ± 1.80 x 10^{-3} SI units compared to the schists/mica schist of the other formations, which are between 0.0491 x 10^{-3} ± 9.42 x 10^{-3} SI units to 3.27 x 10^{-3} ± 1.09 x 10^{-3} SI units (Table 5.3). The high average magnetic susceptibility of the Matchless Member mica schists is controlled by sample N072a, which hosts disseminated pyrrhotite and pyrite grains and has an average magnetic susceptibility of 18.7 x 10^{-3} ± 3.45 x 10^{-6} SI units (Appendix 5). The lowest average magnetic susceptibilities are associated with the weakly foliated biotite schists of the Noas Formation (Table 5.3). The difference in magnetic susceptibility between the Kuiseb schists of the southern Central Zone and the Northern Zone is because of sample N222, which contains oxidised pyrite and pyrrhotite grains. The remainder of the schists/mica schists either contain biotite, garnet, cordierite, muscovite, kyanite and/or sericite or a combination of these minerals (Appendix 5), with an average magnetic susceptibility of 0.196 x 10^{-3} ± 8.33 x 10^{-3} SI units to 0.338 x 10^{-3} ± 2.24 x 10^{-3} SI units (Table 5.3).

In a traverse across the Autseib Fault, a magnetic susceptibility change occurs between the marbles of the Karibib Formation (0.010 x 10^{-3} ± 1.22 x 10^{-1} SI units) and metapelites of the Amis Formation (0.901 x 10^{-3} ± 8.94 x 10^{-3} SI units) (Table 5.3). Generally, the metapelites are an order of magnitude greater than the marble with sample N153.9 having a magnetic susceptibility range of 0.351 x 10^{-3} SI units to 5.700 x 10^{-3} SI units (Appendix 5). Field observations describe the sample as being heavily fractured with disseminated magnetite grains.

The sandstones of the Abbabis Complex and Amis Formation have a higher average magnetic susceptibility of 0.356 x 10^{-3} ± 9.23 x 10^{-4} SI units and 0.389 x 10^{-3} ± 1.82 x 10^{-3} SI units respectively, compared to the average magnetic susceptibilities of the sandstone of the Kuiseb Formation (0.137 x 10^{-3} ± 2.37 x 10^{-3} SI units) and D'Kar Formation (0.181 x 10^{-3} ± 4.54 x 10^{-4} SI units) (Table 5.3 and 5.4). The Amis sandstone contains garnet and amphibolite and the Abbabis sandstone is arkosic compared to the greywackes of the Kuiseb Formation and the “pure” sandstones of the D’Kar Formation (Appendix 5).

Intrusive lithologies

The felsic-rich pegmatite and rhyolite samples have the lowest average magnetic susceptibility values ranging from 0.001 x 10^{-3} ± 9.85 x 10^{-2} SI units to 0.109 x 10^{-3} ± 3.76 x 10^{-2} SI units (Table 5.4). However, there are single magnetic susceptibility measurements as high as 0.790 x 10^{-3} SI units and 0.821 x 10^{-3} SI units for samples N91.2 and N157, respectively (Appendix 5). Sample N92.2 contains black tourmaline grains of ~2 cm long and 1 cm wide while sample N157 contains garnet and biotite.

The granites have an average magnetic susceptibility range of between 0.199 x 10^{-3} ± 2.04 x 10^{-3} SI units (Okwa Complex) and 11.3 x 10^{-3} ± 2.30 x 10^{-5} SI units (Red Granite) (Table 5.4). The higher average susceptibility values of between 2.38 x 10^{-3} ± 6.55 x 10^{-3} SI units to 11.3 x 10^{-3} ± 2.30 x 10^{-5} SI units are associated with the magnetite-bearing Omangambo, Salem, Sorris-Sorris and Red Granites. In addition, the Red Granites have a strong alignment of biotite and sillimanite.

The mafic lithologies have the highest average magnetic susceptibility, ranging between 0.566 x 10^{-3} ± 8.58 x 10^{-4} SI units to 11.6 x 10^{-3} ± 2.55 x 10^{-4} SI units (Table 5.4). The complexes/suites with the higher average magnetic susceptibility values are located within the southern Central Zone. This suggests that the variation in magnetic susceptibility may reflect alteration effects on accessory magnetic minerals such as magnetite.

The gneisses of the southern Central Zone have a lower average magnetic susceptibility (0.222 x 10^{-3} ± 2.08 x 10^{-3} SI units and 1.72 x 10^{-3} ± 5.11 x 10^{-4} SI units) compared to the gneisses of the Kamanjab Inlier (5.05 x 10^{-3} ± 5.43 x 10^{-5} SI units) and Northern Margin Zone (6.12 x 10^{-3} ± 5.04 x 10^{-5} SI units) (Table 5.4). The gneiss of the Huab Metamorphic Complex, within the Kamanjab Inlier, is interbanded with amphibolite layers while the gneiss within the Northern Margin Zone is in contact with overlying metasedimentary lithologies. The gneisses of the Abbabis Complex are augen gneisses and the gneiss of the Goas Suite is a granitic gneiss rich in K-feldspar. The opposite is observed in the magnetic susceptibility of the mica schist units of the Abbabis and Huab Complexes. The mica schist of the Abbabis Complex has an average magnetic susceptibility of 4.39 x 10^{-3} ± 3.50 x 10^{-4} SI units compared to an average susceptibility of 0.200 x 10^{-3} ± 3.64 x 10^{-3} SI units for the mica schist of the Huab Complex (Table 5.4). The mica schist of the Huab Complex contains muscovite while the schist of the Abbabis Complex contains veins of magnetite.

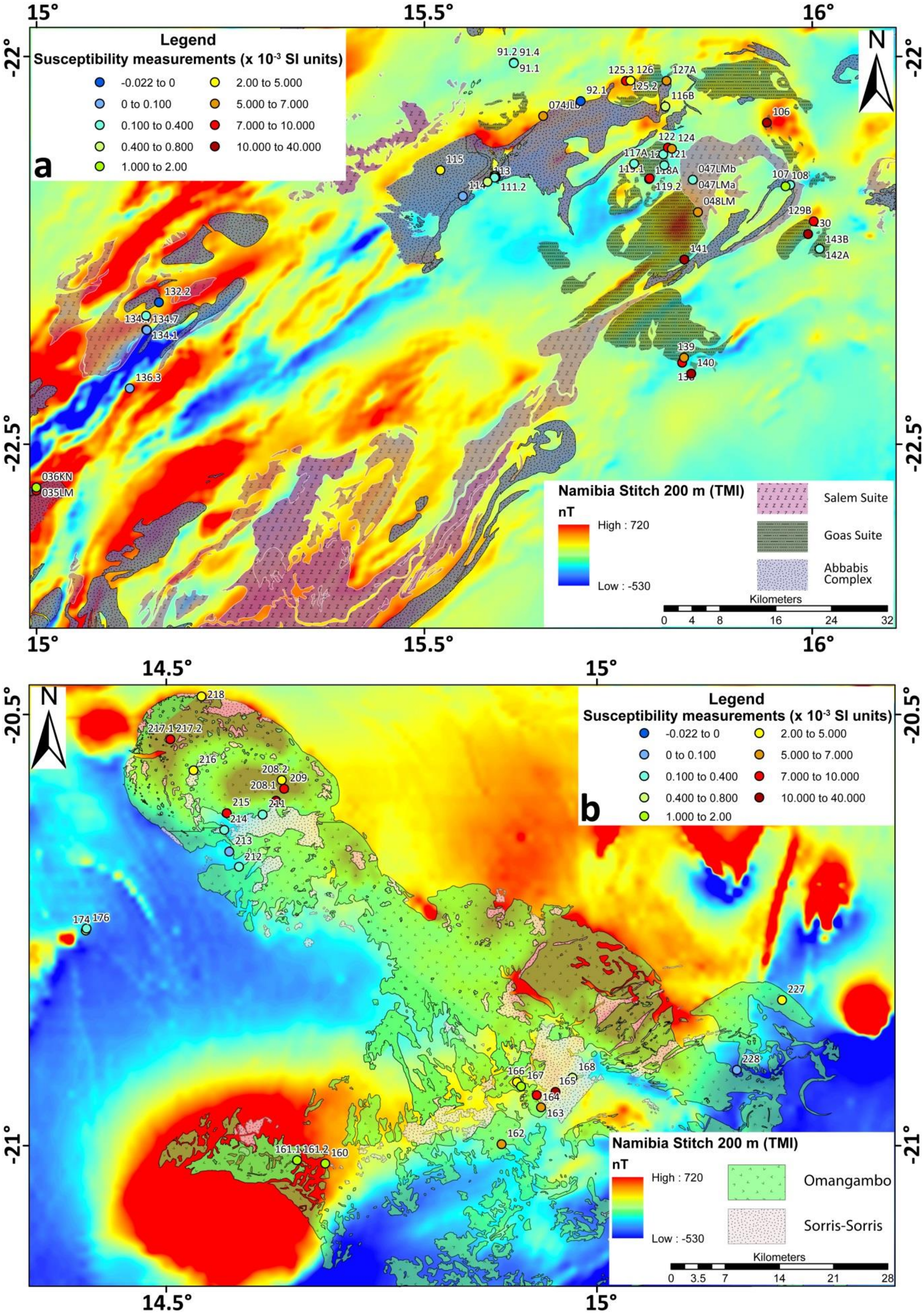

Figure 5.4: Comparison of the measured magnetic susceptibility and aeromagnetic signal of exposed igneous intrusions. a) Comparison of the Salem, Goas and Abbabis Complex. b) Comparison of the Omangambo and Sorris-Sorris Suites.

The difference in the magnetic susceptibility values of the Abbabis, Salem, Omangambo, Goas and Sorris-Sorris intrusions permits their differentiation based on their physical properties and aeromagnetic signal (Figure 5.4). The mafic dominant (diorite and gabbro) Goas Suite has the highest average magnetic susceptibility, while the high magnetic susceptibility of the Omangambo intrusion is because of the strong alignment of biotite and minor amounts of magnetite. The felsic dominant Salem, Abbabis and Sorris-Sorris Suites have low average magnetic susceptibility values because of their compositions, weak foliation, and very minor, if any magnetite.

There is a correlation between the physical property measurements and the metamorphic grades. The Central Zone has high magnetic susceptibility and density values whereas the outer zones have lower magnetic susceptibility and density values (Table 5.5). The reason for the Southern Zone having a higher than expected magnetic susceptibility and density is because the majority of the samples analysed are metamorphic lithologies associated with mineralisation from the Matchless Member.

The Northern and southern Central Zones are characterised by a high aeromagnetic signal because of the diamictite and iron formation of the Chuos Formation, pre-Damaran basement, high-grade metamorphic lithologies of the Etusis Formation and the granitic intrusions (Eberle *et al*., 1996; Corner, 2008). The lithologies listed above have at least one sample that has a magnetic susceptibility of greater than 5.00×10^{-3} SI units (Table 5.3 and 5.4), which correlates well with the aeromagnetic signal (Figure 5.5).

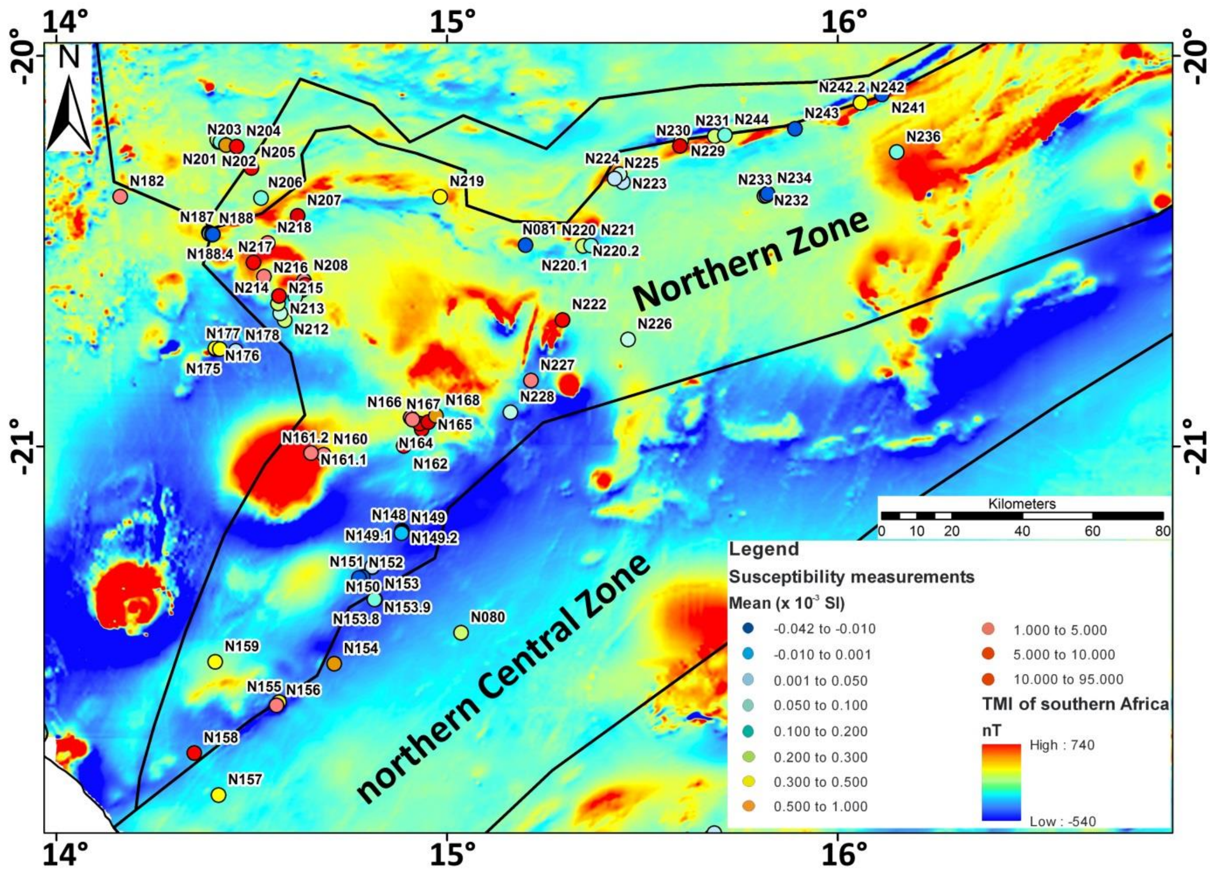

Figure 5.5: Correlation between measured magnetic susceptibility (circles) overlain on the TMI aeromagnetic response of the northern Central Zone and Northern Zone of the Damara Belt (tectonostratigraphic zones after Miller, 2008).

Table 5.5: Summary of the average and range of the magnetic susceptibility and density measurement of the tectonostratigraphic zones of the Damara and Ghanzi-Chobe Belts. For simplicity the Okahandja and Southern Zones are grouped into the Southern Zone whilst the Granite only, Northern Zone Ais Dome and Northern Zone are grouped into the Northern Zone.

Tectonostratigraphic zone	Density range ($g.cm^{-3}$)	Average density ($g.cm^{-3}$)	Uncertainty in density ($g.cm^{-3}$)	Number of samples	Total number of measurements	Magnetic susceptibility range ($x 10^{-3}$ SI units)	Average magnetic susceptibility ($x 10^{-3}$ SI units)	Uncertainty in magnetic susceptibility (SI units)	Number of samples	Total number of measurements
Kamanjab Inlier	3.14 - 3.79	3.32	3.20×10^{-4}	1	3	N/A	N/A	N/A	N/A	N/A
Northern Platform	N/A	N/A	N/A	N/A	N/A	-0.017 - 0.482	0.0700	2.26×10^{-2}	2	22
Northern Margin Zone	N/A	N/A	N/A	N/A	N/A	-0.468 - 10.5	1.127	1.96×10^{-2}	4	33
Northern Zone	2.57 - 3.00	2.65	3.08×10^{-3}	27	71	-0.299 - 114	3.421	1.34×10^{-2}	57	359
Southern Kaoko or Ugab Zone	2.55 - 2.84	2.72	1.78×10^{-3}	11	33	-0.034 - 11.4	0.761	3.81×10^{-2}	22	163
Central Zone	2.56 - 3.25	2.78	5.21×10^{-3}	62	186	-0.120 - 60.8	3.562	1.11×10^{-1}	110	636
Southern Zone	2.67 - 3.37	2.92	2.56×10^{-3}	12	36	0.038 - 41.5	2.925	3.30×10^{-3}	13	70
Southern Margin Zone	2.62 - 2.80	2.71	1.59×10^{-3}	4	12	0.019 - 0.414	0.134	9.81×10^{-3}	3	15
Ghanzi-Chobe Zone	2.68 - 2.71	2.69	1.24×10^{-3}	2	6	0.016 - 12.8	1.427	8.22×10^{-3}	5	41

5.4. Conclusion

The collected samples of this study are mainly restricted to western Namibian with four from northern Botswana because of the limited exposure. As a result, the limited number of measurements recorded is relatively insufficient for general conclusions of the physical parameters of this region. However, these measurements are recorded over the widest range of lithologies for Namibia and Botswana (and Zambia).

The measurements generally correlate with other physical property measurements (e.g. Sharma, 1987; McMullan *et al.*, 1995; Walker *et al.*, 2010; Lehmann *et al.*, submitted). The magnetic mineralogy of any of the lithologies studied is at present not known. However, field observations suggest that the mafic-rich igneous lithologies (gabbro, diorite, dacite and pyroxenite) have the highest magnetic susceptibility and density values. The more felsic-rich lithologies (pegmatite, rhyolite and granite) have lower values (Table 5.1 to 5.4). Lithologies with highest magnetic susceptibilities are the Red Granites, iron formation and diamictite of the Chuos Formation, Naauwpoort conglomerate and granite and gneiss of the Rössing and Etusis Formations, respectively. These high magnetic susceptibility values are associated with a strong alignment of biotite and/or sillimanite grains, the presence of ferromagnetic minerals, a low silica content and low porosity. Metamorphic lithologies have a wide range of magnetic susceptibility values from -0.299 x 10^{-3} SI units to 49.5 x 10^{-3} SI units and a density range of 2.61 g.cm^{-3} to 3.37 g.cm^{-3} (Table 5.1 to 5.4). The lower values are associated with low-grade metamorphism (greenschist facies) of sedimentary origin (marble, quartzite, slate, metapelite and metapsammite) while the higher values are associated with higher grade metamorphism (amphibolite facies) of an igneous origin (amphibolite, gneiss and mica schist). However, the highest density values (3.14 g.cm^{-3} to 3.37 g.cm^{-3}) are attributed to schists hosting disseminated ores. Excluding the sedimentary lithologies mentioned above, the range in average magnetic susceptibility of the sedimentary units is small, ranging from 0.133 x 10^{-3} SI units to 0.389 x 10^{-3} SI units. No conclusions are drawn on the density of sedimentary units, as only one sample was analysed.

5.5. Summary

Through the results and interpretation of the magnetic susceptibility and density measurements collected from two months spent in the field, this chapter has clarified which geological units in western Namibia are the most likely to be associated with magnetic high and low signals. This was obtained by overlying the collected magnetic susceptibility values over the aeromagnetic data and observing a strong correlation between them. A correlation between magnetic susceptibility and density was also determined for lithology types. The correlations are used to constrain the interpretation of the sub-Kalahari geological map by working from the known (areas of outcrop) to the unknown (areas beneath Phanerozoic cover).

Chapter 6

Sub-Kalahari geological map interpreted from potential field data

6.1. Introduction

The lack of cross-border correlation of Proterozoic rocks between Namibia and Botswana (Figure 1.4) is because of three factors 1) limited outcrops and pre-Karoo scientific boreholes in eastern Namibia and northwestern Botswana, 2) lack of geological and geophysical cross-border studies and 3) no sub-Kalahari geological map of western Namibia.

To contribute to the knowledge of the cross-border correlation, a new sub-Kalahari geological map was designed for this study (Figure 6.1). The sub-Kalahari geological map is based on the reinterpretation of available geological data from literature, direct new observations, physical property measurements in places where pre-Karoo rocks are exposed and interpretation of aeromagnetic and gravity data sets.

Currently the higher resolution digital geological maps of Namibia and Botswana terminate either at the border of the respective countries or short of the border. The available geological maps based on both geological and geophysical interpretations, aided with limited pre-Karoo boreholes are; Botswana 1:1 000 000 regional map (Key and Ayres, 2000) and 1:250 000 for northwest Botswana (Ngamiland, Pryer *et al*., 1997) and a Namibian regional 1:250 000 local map (compiled by the Geological Survey of Namibia from various geological maps). Currently the cross-border geological correlation between Namibia and Botswana relies on the 1:2 500 000 sub-Kalahari geological map of Haddon (2001). The purpose of the sub-Kalahari geological map determined in this study is to constrain the lateral extents of the Ghanzi-Chobe and Damara Belts contributing to the geological cross-border correlation of Meso- to Neoproterozoic lithologies between Namibia and Botswana, as currently this is very limited.

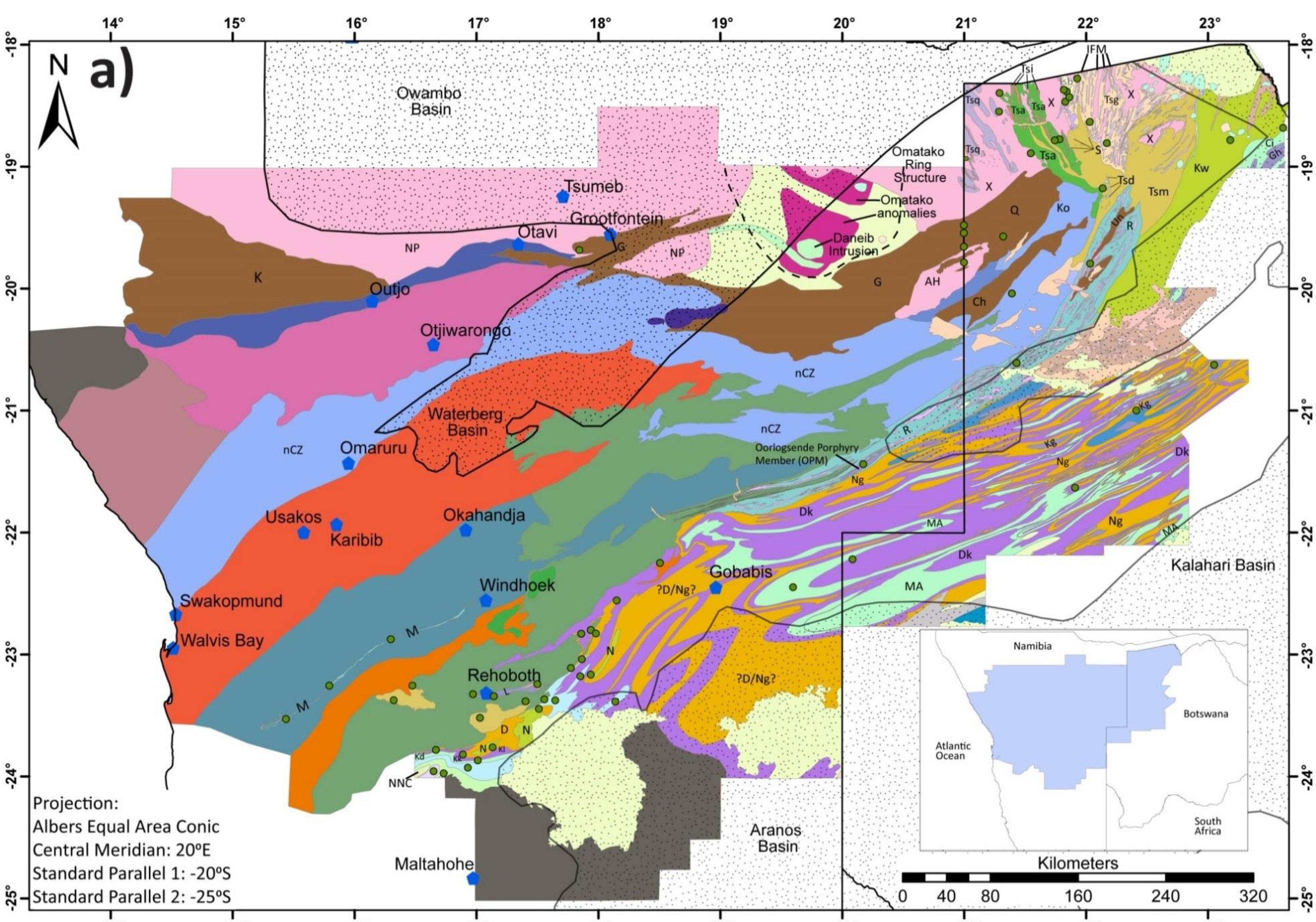

a)
N
Owambo Basin
Tsumeb
Grootfontein
Otavi
Outjo
Otjiwarongo
Omaruru
Waterberg Basin
Usakos
Karibib
Okahandja
Swakopmund
Walvis Bay
Windhoek
Rehoboth
Gobabis
Maltahohe
Aranos Basin
Kalahari Basin
Omatako Ring Structure
Omatako anomalies
Daneib Intrusion
Oorlogsende Porphyry Member (OPM)
IFM
NNC
nCZ
NP
K
G
AH
Ch
Q
Ko
X
Tsq
Tsa
Tsg
Tsd
Tsm
Kw
Un
R
S
Ci
Gh
Kg
Ng
Dk
MA
?D/Ng?
M
N
D
L
Kd
Kl
Namibia
Botswana
Atlantic Ocean
South Africa
Kilometers
0 40 80 160 240 320
Projection:
Albers Equal Area Conic
Central Meridian: 20ºE
Standard Parallel 1: -20ºS
Standard Parallel 2: -25ºS

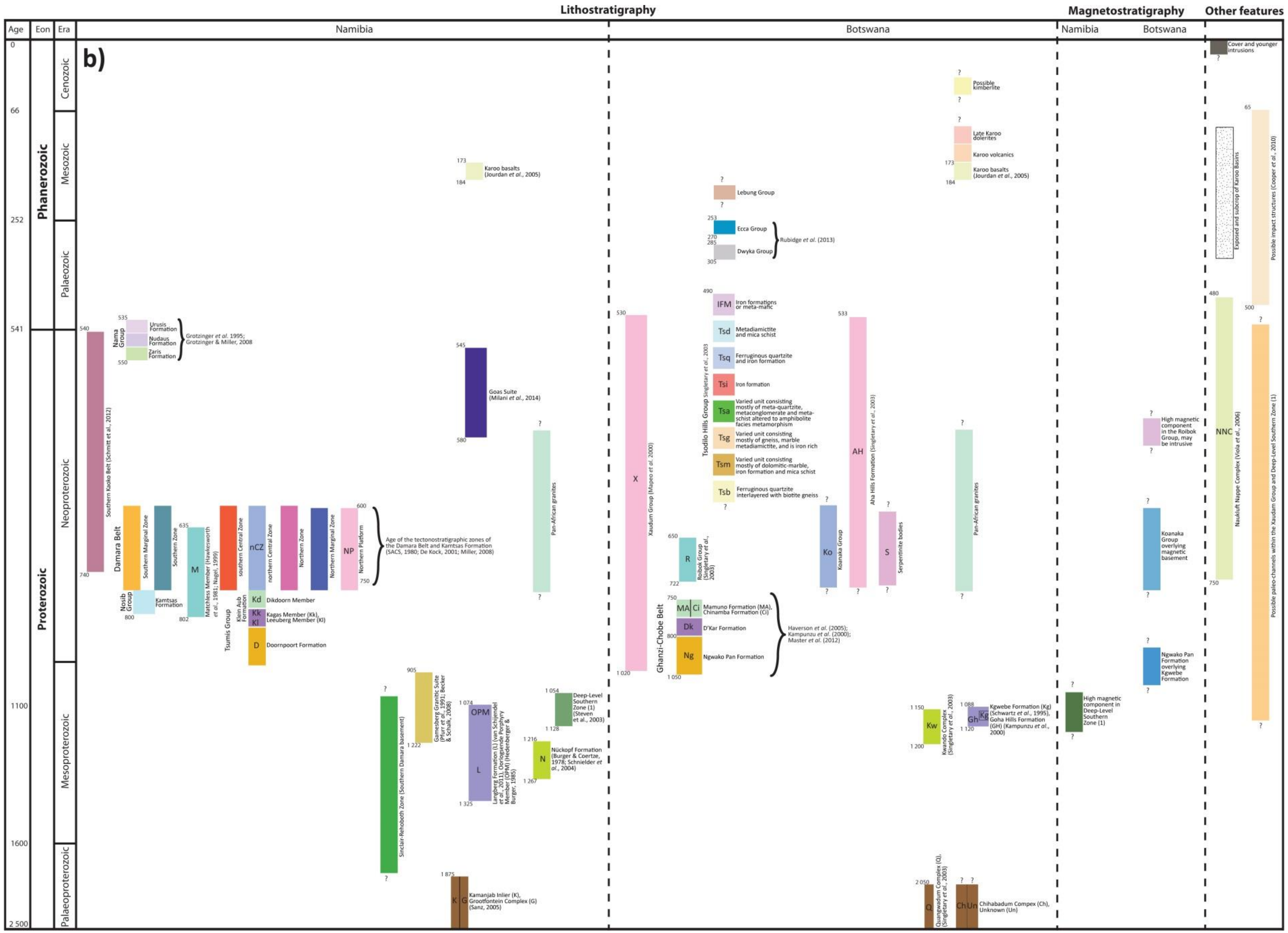

Lithostratigraphy
Magnetostratigraphy
Other features
Age
Eon
Era
Namibia
Botswana
Namibia
Botswana
b)
Phanerozoic
Proterozoic
Cenozoic
Mesozoic
Palaeozoic
Neoproterozoic
Mesoproterozoic
Palaeoproterozoic
0
66
252
541
1100
1600
2 500
Southern Kaoko Belt (Schmitt et al., 2012)
Nama Group
Urusis Formation
Nudaus Formation
Zaris Formation
Grotzinger et al. 1995; Grotzinger & Miller, 2008
Damara Belt
Southern Marginal Zone
Southern Zone
Matchless Member (Hawkesworth et al., 1981; Nagel, 1999)
southern Central Zone
northern Central Zone
Northern Zone
Northern Marginal Zone
Northern Platform
Age of the tectonostratigraphic zones of the Damara Belt and Kamtsas Formation (SACS, 1980; De Kock, 2001; Miller, 2008)
Nosib Group
Kamtsas Formation
Tsumis Group
Klein Aub Formation
Kd Dikdoorn Member
Kk Kagas Member (Kk)
Kl Leeuberg Member (Kl)
D Doornpoort Formation
Karoo basalts (Jourdan et al., 2005)
Goas Suite (Milani et al., 2014)
Pan-African granites
Sinclair-Rehoboth Zone (Southern Damara basement)
Gamsberg Granitic Suite (Pfurr et al., 1991; Becker & Schalk, 2008)
Langberg Formation (L) (van Schijndel et al., 2011), Oorlogsende Porphyry Member (OPM) (Hoffmann et al., 1985)
Deep-Level Southern Zone (1) (Steven et al., 2003)
Nückopf Formation (Burger & Coertze, 1978; Schneider et al., 2004)
Kamanjab Inlier (K), Grootfontein Complex (G) (Sanz, 2005)
Xaudum Group (Mapeo et al. 2000)
Lebung Group
Ecca Group
Dwyka Group
Rubidge et al. (2013)
Tsodilo Hills Group (Singletary et al., 2003)
IFM Iron formations or meta-mafic
Tsd Metadiamictite and mica schist
Tsq Ferruginous quartzite and iron formation
Tsi Iron formation
Tsa Varied unit consisting mostly of meta-quartzite, metaconglomerate and meta-schist altered to amphibolite facies metamorphism
Tsg Varied unit consisting mostly of gneiss, marble metadiamictite, and is iron rich
Tsm Varied unit consisting mostly of dolomitic-marble, iron formation and mica schist
Tsb Ferruginous quartzite interlayered with biotite gneiss
Ricbok Group (Singletary et al., 2003)
Ghanzi-Chobe Belt
Mamuno Formation (MA), Chinamba Formation (Ci)
D'Kar Formation
Ngwako Pan Formation
Haverson et al. (2005); Kampunzu et al. (2000); Master et al. (2012)
Koanaka Group
Aha Hills Formation (Singletary et al., 2003)
Serpentinite bodies
Possible kimberlite
Late Karoo dolerites
Karoo volcanics
Karoo basalts (Jourdan et al., 2005)
Kwando Complex (Singletary et al., 2003)
Kgwebe Formation (Kg) (Schwartz et al., 1995), Goha Hills Formation (GH) (Kampunzu et al., 2000)
Quangwadum Complex (Q), (Singletary et al., 2003)
Chihabadum Compex (Ch), Unknown (Un)
High magnetic component in Deep-Level Southern Zone (1)
High magnetic component in the Roibok Group, may be intrusive
Koanaka Group overlying magnetic basement
Ngwako Pan Formation overlying Kgwebe Formation
Cover and younger intrusions
Exposed and subcrop of Karoo Basins
Possible impact structures (Cooper et al., 2010)
Naukluft Nappe Complex (Viola et al., 2006)
Possible paleo-channels within the Xaudum Group and Deep-Level Southern Zone (1)

Figure 6.1 (previous pages)**:** a) Sub-Kalahari geological map of Namibia and Botswana based on the interpretation of potential field data constrained by outcrop geology (Figure 2.17) and pre-Karoo and Tsodilo Resources Ltd. boreholes (green circles). b) Legend/stratigraphic table for the sub-Kalahari geological map of Namibia and Botswana. The age ranges are the maximum and minimum age dates. The dating techniques are discussed in the text and Chapter 2 (see Appendix 6 for fold out).

The interpretation of the sub-Kalahari geological map is based on potential field signatures of exposed geological units and lithologies observed by Carney *et al*. (1994), Key and Ayres (2000) and Singletary *et al*. (2003) in the pre-Karoo boreholes, and new direct observations of the available Tsodilo Resources Ltd. boreholes. These are used to extrapolate geological interpretations beneath the Kalahari and Karoo cover. To confirm the interpretation of the sub-Kalahari geological units the digital geological maps are used. However, as discussed in Section 3.8., there are important discrepancies between the sub-Kalahari geological maps of Pryer *et al*. (1997) and Key and Ayres (2000) in northwest Botswana. The discrepancies are resolved by reviewing the new observations of the Tsodilo Resources Ltd. boreholes with the limited detailed studies published in the literature.

The sub-Kalahari geological map constructed in this study comprises over 23 000 magnetic lineaments (1 dimensional magnetic anomaly in map view) and 1 150 geophysical polygons (2 dimensional geophysical anomalies in map view). The geophysical and geological properties, of the magnetic lineaments and geophysical polygons are available in both digital (ArcGIS feature class) and hard copy format.

6.2. Constructing the sub-Kalahari geological map through geophysical interpretations

The first step in constructing the sub-Kalahari geological map was to know what data was available in order to constrain the potential field interpretation. The geophysical signatures of the sub-Kalahari were constrained by observing the geophysical signatures of known exposures of pre-Kalahari units and extrapolating the geophysical signal to covered areas (Figure 2.17) (summarised in Table 6.1). As ~80% of Botswana is covered by Kalahari sediments geological observations of the NG and CKP pre-Karoo boreholes by Carney *et al*. (1994), Key and Ayres (2000) and Singletary *et al*. (2003) were used to constrain the geology at three localities in Botswana (Figure 6.2). In addition to these boreholes, Tsodilo Resources Ltd. has drilled numerous boreholes in the Ngamiland area, some of which were made available for this study

(Figure 6.2). For geological domains in Botswana where there are no boreholes or outcrops the 1:1 000 000 sub-Kalahari geological map of Keys and Ayres (2000), and the 1:250 000 sub-Kalahari map of Pryer *et al*. (1997) were used for nomenclature.

The second step was to re-project the potential field grids from their UTM co-ordinate system to the Albers Equal Area Conic projection for reason as discussed in Chapter 5.

Table 6.1: RTP 1VD aeromagnetic signal of the geological units of Namibia and Botswana. The geological units are grouped according to geographic location.

Geological domain	Lithology	Aeromagnetic response in RTP and/or RTP 1VD	RTP 1VD aeromagnetic image
Karoo Supergroup			
Late Karoo dolerites	Dolerite sheet and stocks	Smaller, closer spaced sub-linear to linear, higher amplitude anomalies than the Karoo volcanics	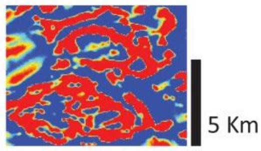
Karoo volcanics	Undifferentiated intrusive and/or Karoo dolerite/basalt	Large continuous linear to sub-linear, high amplitude anomalies	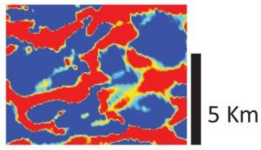
Karoo Basalts	Flood basalts with variable amygdales with minor siliclastic sedimentary interbeds and lenses	Mottled texture produced by the sub-linear alternating magnetic responses	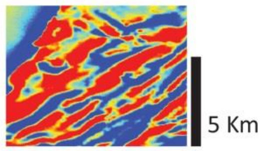
Damara Belt			
Matchless Member	Amphibolite sheets associated with ferruginous quartzite markers	Outer margins are characterised by linear to sub-linear, alternating positive and negative magnetic amplitudes, while within these margins the response ranges from low to high amplitudes, noisy, mottled texture	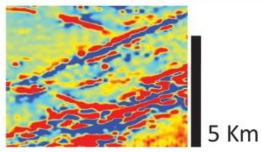
Kamtsas Formation (Nosib Group)	Feldspathic quartzite, shale and conglomerate	Sub-linear texture formed by NE magnetic features, moderate to low amplitude. Alternating internal high and low frequency, positive and negative anomalies	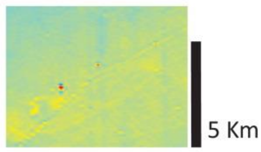
Abbabis Complex	Metapelite, augen gneiss, meta-arkose, marble, meta-conglomerate, amphibolite, quartzite, calc-silicate, schist, syenite and metavolcanics	Linear NE trending, positive high amplitude, low frequency anomalies that show signs of folding	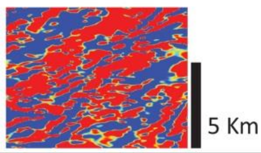
Eastern Namibia region			
Oorlogsende Porphyry Member	Porphyritic rhyolite, quartz porphyry, and tuffaceous ignimbrites	Noisy, pitted texture, internal roughness sub-parallel to oblique to external margin. Positive high amplitude, high frequency anomaly	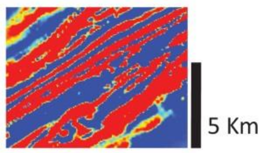
Grootfontein Complex	Gneiss, amphibolite, gabbro and granite with metasediments	Sub-linear to linear, high amplitude, variable frequency	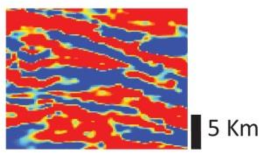

Table 6.1: continued.

Geological domain	Lithology	Aeromagnetic response in RTP and/or RTP 1VD	RTP 1VD aeromagnetic image
Rehoboth Subprovince			
Klein Aub Formation (Tsumis Group)	Calcareous quartzite, slate, limestone and conglomerate	Linear, positive high amplitude, medium to high frequency anomaly. High amplitudes are restricted to the margins	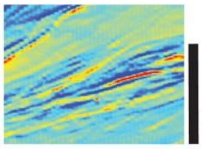 5 Km
Eskadron Formation (Tsumis Group)	Red quartzite, marble and shale	Sub-linear, moderate to high amplitude, low to moderate frequency	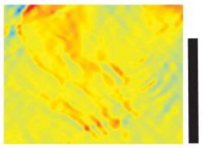 5 Km
Doornpoort Formation (Tsumis Group)	Conglomerate and quartzite intercalated with slate	Smooth, negative amplitude, medium to low frequency	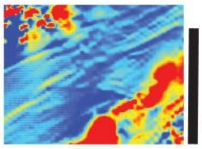 5 Km
Gamsberg Granitic Suite	Monogranite to granodiorite	Magnetic fabric bends around, smooth, moderate to low amplitude with localised higher amplitude sub-linear anomalies that follow the stronger, more pronounced magnetic fabric of the surrounding units	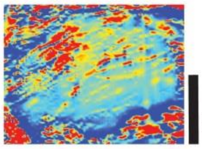 5 Km
Opdam Formation (Nauzerus Group)	Basalt, quartzite and conglomerate	Linear, high amplitude, high frequency	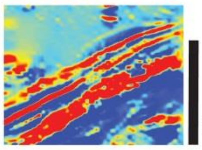 5 Km
Langberg Formation (Nauzerus Group)	Conglomerate and felsic volcanics interbedded with immature arenite	Outer margins are characterised by linear to sublinear, positive, high magnetic amplitudes, while within these margins the response is smooth, low to moderate amplitude	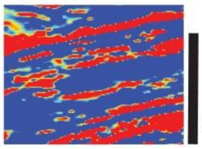 5 Km
Grauwater Formation (Nauzerus Group)	Quartzite, conglomerate and shale	Flat, negative amplitude with slightly higher localised linear amplitudes giving a magnetic fabric. Moderate frequencies	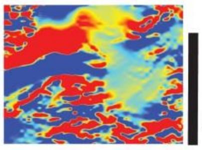 5 Km
Nückopf Formation (Nauzerus Group)	Rhyolitic pyroclastic/tuffite, quartzite and conglomerate	Inner smooth, low to moderate amplitude with outer margins defined by linear to sub-linear, variable amplitude and frequency anomalies	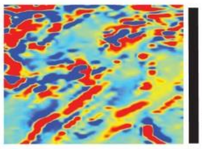 5 Km
Uncertain regions in Botswana			
Roibok Group	Amphibolite, magnetite-schist and felsic gneiss	Smooth, low to moderate amplitude with sub-linear high, northeast trending magnetic anomalies.	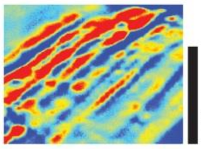 5 Km
Kwando Complex	Granitic gneiss interlayered with amphibolite and metagabbro to diorite	Southern portion is smooth, low amplitude with localised higher amplitude anomalies while the northern portion is noisy, pitted, high amplitude, high frequency anomalies	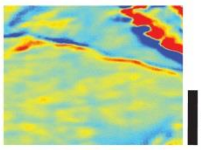 5 Km

Table 6.1: continued.

Geological domain	Lithology	Aeromagnetic response in RTP and/or RTP 1VD	RTP 1VD aeromagnetic image
Northwest Botswana			
Tsodilo Hills Group	Ferruginous quartzite interlayered with biotite gneiss	Noisy, alternating high and low amplitudes, short wavelength	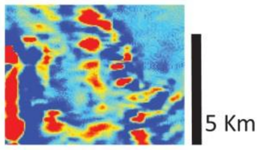
Tsodilo Hills Group	Varied unit consisting mainly of gneiss, marble, and metadiamictite and is iron-rich	Mottled, moderate to high amplitude, high frequency	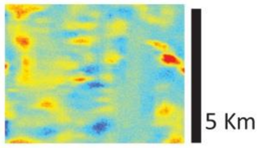
Tsodilo Hills Group	Ferruginous quartzite and iron formations	Sub-linear texture formed by NW trending magnetic folds. Alternating internal high frequency positive and negative anomalies	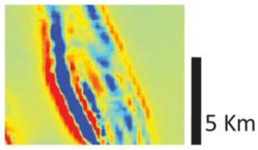
Tsodilo Hills Group	Varied unit consisting mainly of dolomitic-marble, iron formation and mica schist	Smooth magnetic domain overprinted by higher amplitude, high frequency anomalies that have a random orientation	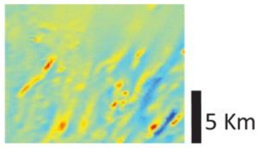
Tsodilo Hills Group	Iron formation	Linear, positive high amplitude, high frequency anomalies	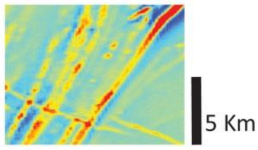
Tsodilo Hills Group	Varied unit consisting mainly of meta-quartzite and mica schist altered to amphibolite facies	Sub-linear texture, alternating positive and negative amplitudes, high frequency	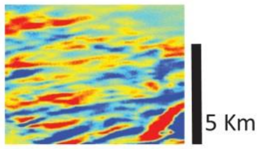
Xaudum Group	Assorted low grade meta-sediments (siliciclastic and calcareous carbonate)	Very smooth, uniform, low to moderate amplitude and broad wavelength	
Aha Hills Formation	Chert-rich limestone and dolomite	Smooth, higher than expect amplitude because of the underlying basement rocks	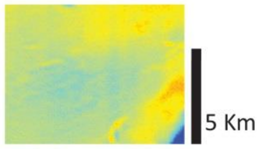
Koanaka Group	Dolomite, chert, metapelite and possible paragneiss	Smooth, low to moderate amplitude with sub-linear, higher amplitude magnetic anomalies producing a NE trend	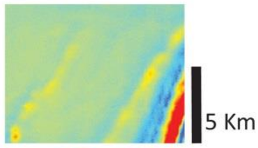
Chihabadum Complex	Igneous and meta-igneous rocks?	Sub-linear to linear, variable amplitude, high frequency northeast-southwest striking anomalies	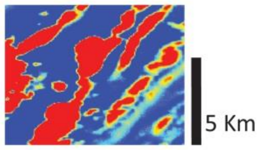
Quangwadum Complex	Porphyritic granite, augen gneiss and talc-biotite schist	Sharp sub-linear magnetic highs that define the magnetic orientation of the complex	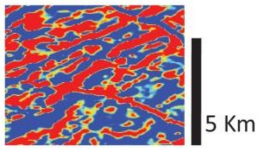

Table 6.1: continued.

Geological domain	Lithology	Aeromagnetic response in RTP and/or RTP 1VD	RTP 1VD aeromagnetic image
Goha and Chinamba Hills region			
Chinamba Formation	Carbonate-bearing siliciclastic rock	Smooth, low amplitude, negative anomaly. Broad wavelength.	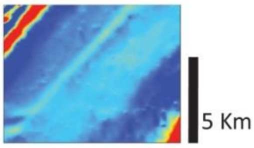
Goha Hills Formation	Meta-felsic volcanic rock, volcaniclastic rock and chert	Similar features but lower amplitudes than the Kgwebe Formation	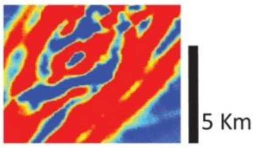
Ghanzi Ridge region			
Mamuno Formation	Arkosic sandstone interbedded with siltstone, mudstone and limestone	Sub-linear texture formed by NE trending magnetic features. Lower magnetic amplitude than the D'Kar Formation. Alternating internal high frequency positive and negative anomalies	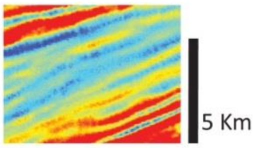
D'Kar Formation	Reduced facies. Siltstone and mudstone interbedded with sandstone and limestone. Pyrrhotite at the base and within the unit	Sub-linear, positive high amplitude and medium to high frequency anomaly. Highly magnetic basal contact	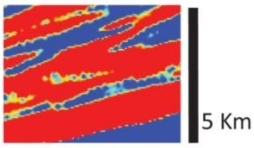
Ngwako Pan Formation	Oxidised facies. Sandstone and mudstone	Smooth, broad, negative amplitude, medium to low frequency anomaly	
Kgwebe Formation	Bimodal volcanic rock containing magnetite and volcaniclastic rock	Noisy, pitted texture, internal roughness sub-parallel to oblique to external margin. Positive high amplitude, high frequency anomaly	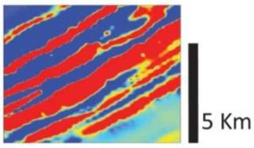

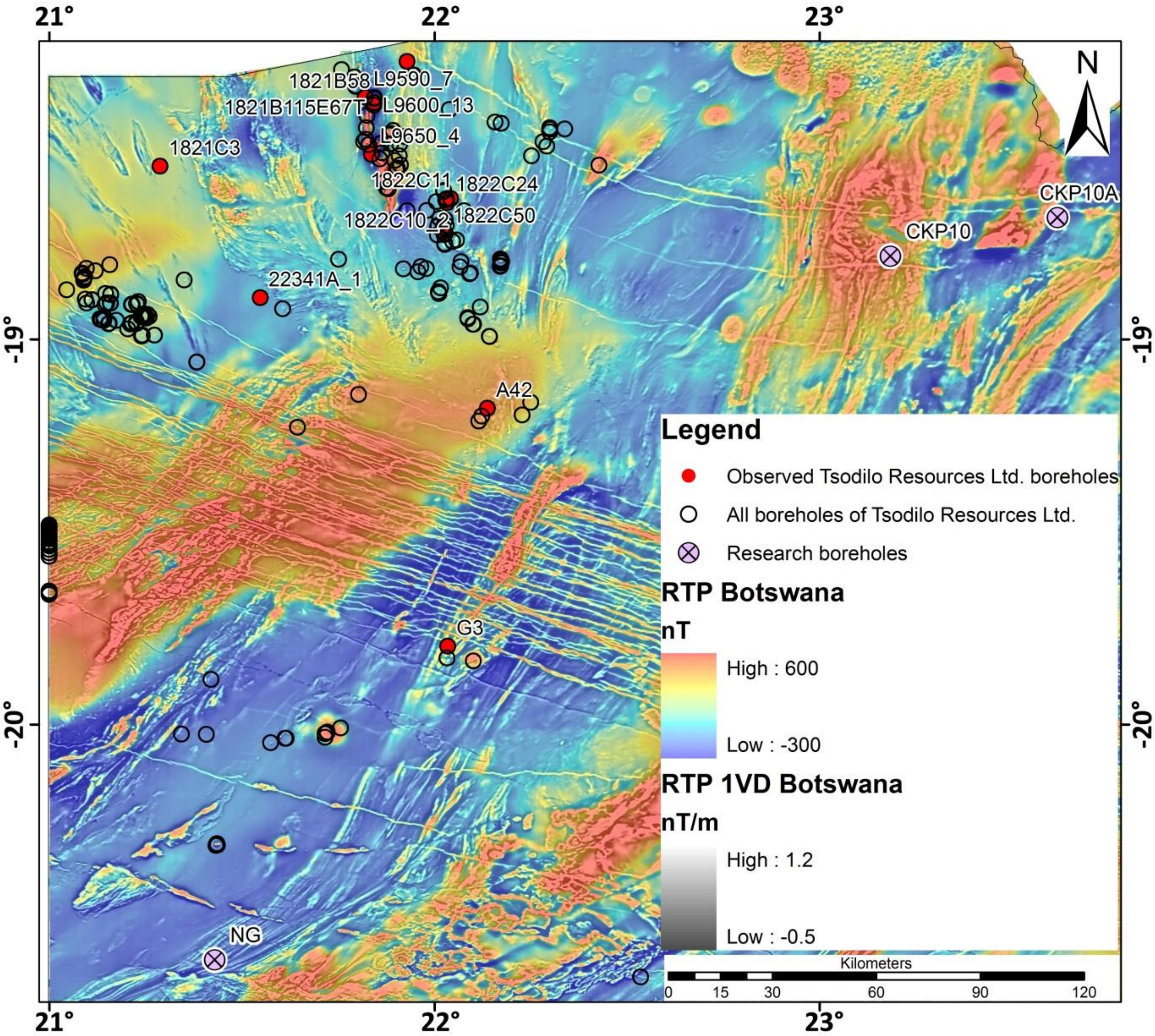

Figure 6.2: Location of the pre-Karoo research boreholes (purple circles with cross), all the boreholes drilled by Tsodilo Resources Ltd. (open black circles) and the boreholes of Tsodilo Resources Ltd. that were studied (solid red dots). Background image is a 50% transparent colour scale RTP image overlain on a 30% transparent greyscale RTP 1VD image of Botswana.

The third step was to create an attribute table to assign to the magnetic lineaments. This was prepared in ArcCatalog with the following table headers; geophysical description, primary interpretation, comments, and source. The magnetic amplitude of the anomaly (i.e. low, moderate or high or a combination thereof) trace is discussed under the geophysical description heading. The primary description is the geological interpretation of the magnetic lineament, which included the following descriptions, bedding, dyke, normal fault, reverse fault, strike-slip fault, shear zone, undetermined fault type, discordant intrusive contact (with angular unconformity), discordant intrusive contact (without angular unconformity), fold axis – anticline, fold axis – syncline, fold axis – unknown, joint, magmatic fabric, metamorphic fabric, unconformity, lithological contact unknown, not known, ring structure unknown, impact contact and small anomalies in volcanic bodies. Comments were used to describe the displacement of magnetic markers in order to determine the sense of movement. The potential field data set used to trace the magnetic lineament i.e. RTP 1VD, analytic signal etc., was listed under the source heading.

The magnetic lineaments that have amplitudes greater than 0.004 nT/m and extents greater than ~1.5 km (not always visible in the RTP and TMI data sets) were traced in ArcMap v. 9.3.1. On completion of tracing the magnetic lineaments, they were assigned their respective attributes. The attributes were assigned based on the magnetic amplitude, texture and their relation to known geological domains.

The fourth step was to create an attribute table for the geophysical polygon map (sub-Kalahari geological map) which consists of the following headings; geological description, lithology, the Formations, Groups and Supergroups of Namibia and Botswana, age, age error, reference for the age dates, exposure, source, and if the polygon (geological domain) has been ground checked. In the geophysical description the following parameters were used to describe the geological domain; amplitude, frequency or wavelength (low, medium or high or a combination of thereof) and texture i.e. flat (smooth), undulating, mottled, linear and sub-linear. The lithology, Formation, Group and Supergroup were determined from the digital and geological maps of Namibia and Botswana. The age and age error of the formation (when available) was extracted from the literature. The exposure of the geological domain was determined by the digital map of Figure 2.17. Ground checked domains involve both borehole and outcrops of geological units.

6.2.1. Magnetic lineaments

Seafloor magnetic anomalies provide a mechanism for developing geotectonic reconstructions that enable the comparison of matching continental counterparts. The continental magnetic anomalies can also provide useful information on lithologies, folding, intrusions, orientation of faults and lineaments in deformed areas (Stettler *et al.*, 1989). Aeromagnetic data are ideal for mapping magnetic geophysical lineaments, as it is sensitive to near surface magnetic rocks. Geophysical lineaments can be used in estimating different lithological terranes and crustal stress patterns in both space and time, which can aid in the reconstruction of continental blocks. The main aim of geophysical lineament interpretation, in this study, is to define lithological boundaries and the orientation of the lithological units that can lead to a reinterpretation of the evolution of the Congo and Kalahari Cratons and Damara and Ghanzi-Chobe belts.

Magnetic lineament mapping is a subjective but integral part of aeromagnetic interpretation. Lineaments are mostly, with the exception of the Okavango Dyke Swarm, subtle features indicated by indirect expressions i.e. lateral offsets of magnetic anomalies along strike, changes in the separation of magnetic highs and lows, and sudden changes in strike direction. These signatures were enhanced by high-pass filters such as the vertical derivatives (first, second and integral i.e. 0.5), analytic signal, tilt angle, total horizontal derivative and directional filters such as sunshading and combination of Butterworth and directional cosine filters. This is one of, if not the first, cross political border magnetic lineament and detailed lithology interpretation maps of Namibia, northern Botswana and southwestern Zambia (Figure 6.3). The study area is subdivided into several domains based on the orientation and amplitude of the magnetic lineaments.

The majority of the magnetic lineaments are not revealed in the geological maps as the study area is covered by Kalahari and Karoo Supergroup lithologies. Some geologically mapped features have no magnetic response either due to the flight line directions of the aeromagnetic surveys being parallel to their strike, they are too small to produce an observable aeromagnetic signal at the flight height of the survey, or contain no magnetic minerals. This may lead to arguments that the various domains defined by the orientation of the magnetic lineaments do not reflect true geological orientations. In some cases the lineaments will be at depth and are often represented by the magnetic trends in similar lithologies. However, comparing the dominant magnetic lineament domains in Namibia with the tectonostratigraphic domains of Miller (2008) and the domains in Botswana with the various geological maps and sub-surface Precambrian map of Singletary *et al*. (2003), there is a strong correlation between the magnetic lineament domains and geological domains.

The northwest-southeast trending Karoo-aged (~180 Ma) Okavango Dyke Swarm, has been excluded from this magnetic lineament map for visual clarity of the underlying pre-Karoo geology (Figure 6.3). The Okavango Dyke Swarm is associated with a magnetic amplitude of ~215 nT to 300 nT that is superimposed on the pre-Karoo geology. The length of the magnetic lineaments ranges from a few tens of metres to tens of kilometres. The dyke swarm is ~55 km wide and is represented by linear magnetic anomalies which can be traced into northern Namibia, where their signal weakens since the grid cell size in Namibia is four times larger than in Botswana. Locally, the dykes are offset by younger faults associated with the Okavango Rift Zone (Section 6.2.2.).

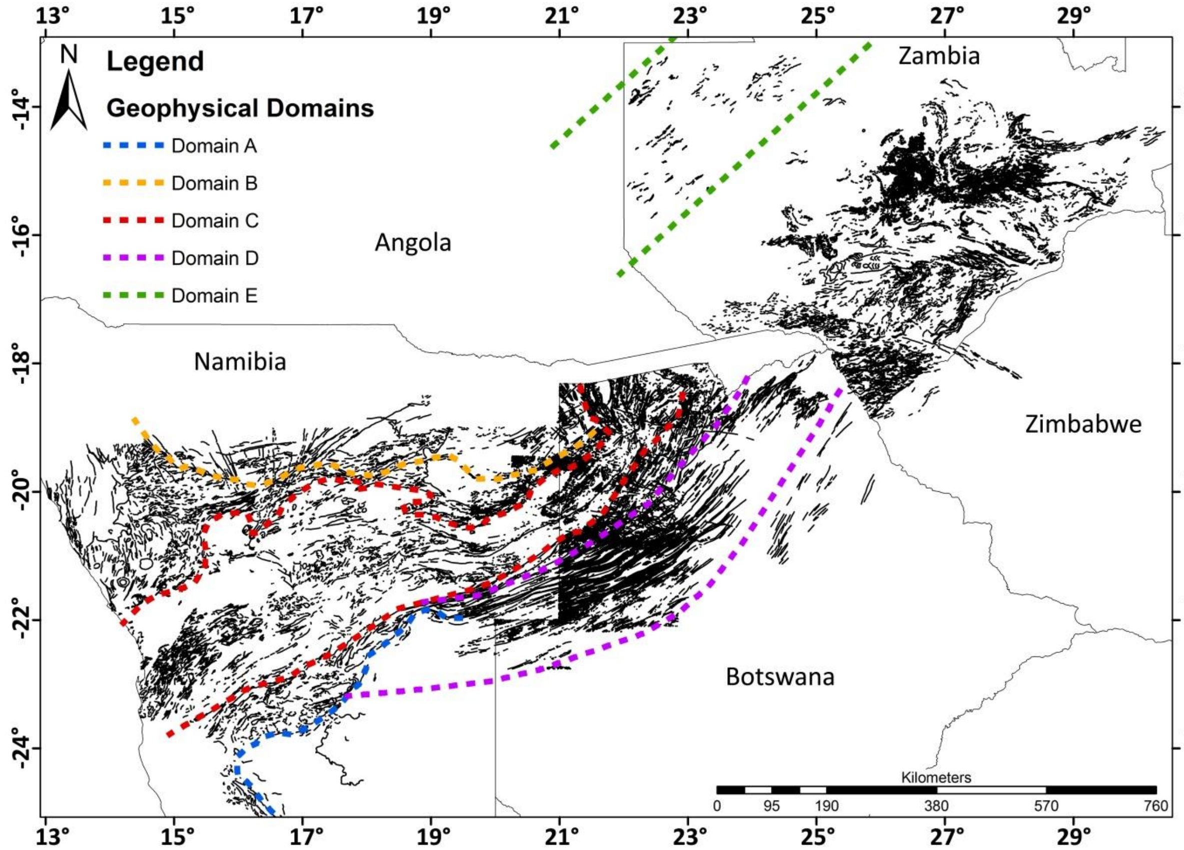

Figure 6.3: Aeromagnetic lineaments of Namibia, Botswana and Zambia as derived from RTP 1VD data with the various interpretations of the magnetic domains. Domain A is the northern extension of the Kalahari Craton, domain B is the southern extension of the Congo Craton, domain C is the northeast-southwest magnetic trend of the Damara Belt, domain D is the magnetically visible Ghanzi-Chobe Belt, and domain E is a northeast magnetic trend in western Zambia.

There are various theories on the emplacement of the dyke swarm such as; 1) along continental rift margins, where the dykes intrude continental crust rather than oceanic crust (Stettler *et al*., 1989), 2) failed arm of a triple-rift junction above a juvenile mantle plume, which led to the break-up of Gondwana (Reeves, 1978b), 3) associated with magmatism emplacement along a Cretaceous continental transverse fracture (Reeves, 2000), 4) Proterozoic-aged dykes in the Okavango Dyke Swarm and in southern Africa, suggest that the Karoo-aged dykes were emplaced along pre-existing zones of weakness in the lithosphere (Jourdan *et al*., 2004; Le Gall *et al*., 2005). In all of these scenarios the dykes are considered to be intrusions that occur in a specific geological era.

Domains A and B

Domains A (Kalahari Craton) and B (Congo Craton) show a decrease in the number of magnetic lineaments compared to the curvilinear northeast-southwest striking domain C (extent of the

Damara Belt) (Figure 6.3). The boundaries of this decrease in the number of magnetic lineaments are interpreted as the southern extent of the Congo Craton in the north and the northern extent of the Kalahari Craton in the south by Corner (2008). The magnetic lineaments on these cratons have a random orientation. According to Eberle *et al*. (1996), as the magnetic lineaments can be traced from domain C into domains A and B, it suggests that they have been irregularly active throughout geological time.

Domain C

The approximate northeast-southwest curvilinear magnetic trend of the Damara Belt is defined as domain C. It is traced from the Namibian coast into Botswana where it bends in a north-northeast direction into the Caprivi Strip (Figure 6.3). The domain is characterised by magnetically inert southern and northern margins and magnetic lineaments ranging in amplitude from -100 nT to 1 000 nT. The granite dominated northern part of the southern Central Zone can be seen by the heavily dense, short (~1 km long), randomly oriented magnetic lineaments (Figure 6.3), which are interpreted to represent the magnetic fabric in the granites and magnetic units. In Botswana, the magnetic lineaments are ~1 km in length with amplitudes of ~0.3 nT/m in the RTP 1VD data and have a north-northeast magnetic trend. The magnetic lineaments are interpreted as magmatic fabric in the igneous to meta-igneous bodies of the Chihabadum Complex (Key and Ayres, 2000). In Botswana, the northern margin of Domain C is interpreted to wrap around the Quangwadum Complex before entering the Caprivi Strip where there is no available data (Figure 6.3).

Domain D

The folds of the Ghanzi-Chobe Belt, in domain D (Figure 6.3), are delineated by the contrast in magnetic signatures between the magnetic high anomalies of the D'Kar Formation, ~170 nT, and the magnetic low anomalies of the Ngwako Pan Formation of ~-50 nT. The Mamuno Formation was identified by magnetic signatures with amplitudes in the range of -20 nT to 15 nT that have sub-linear orientations. At the base of the Ghanzi Group are volcanics of the Kgwebe Formation, which are defined by their high magnetic signal of ~600 nT, which preserves pre-folding internal layering. In the aeromagnetic data the magnetic amplitude and deformation of folding decreases to the southeast. This can be because of an increase in sedimentation or a decrease in the concentration of pyrrhotite at the contact between the Ngwako Pan and D'Kar Formations.

Domain D is traced northeastwards from within Namibia to the Botswana-Zimbabwe and Zambian border (Figure 6.3).

Domain E

This domain is situated in northwest Zambia (Figure 6.3) and consists of a northeast-southwest magnetic trend which is associated with magnetic amplitudes of ~0.006 nT/m to 0.1 nT/m observed in the RTP 1VD data. These anomalies are not clearly visible in the TMI and RTP data sets. The reason for the sparseness of magnetic lineaments in this area is because of an increase in thickness of non-magnetic cover and a grid cell size of 250 m.

In northwesternmost Botswana, three sub-domains are characterised by the abundance and strike of the magnetic lineaments observed in the aeromagnetic data (Figure 6.4). These are labelled, from west to east, as sub-domains 1 to 3.

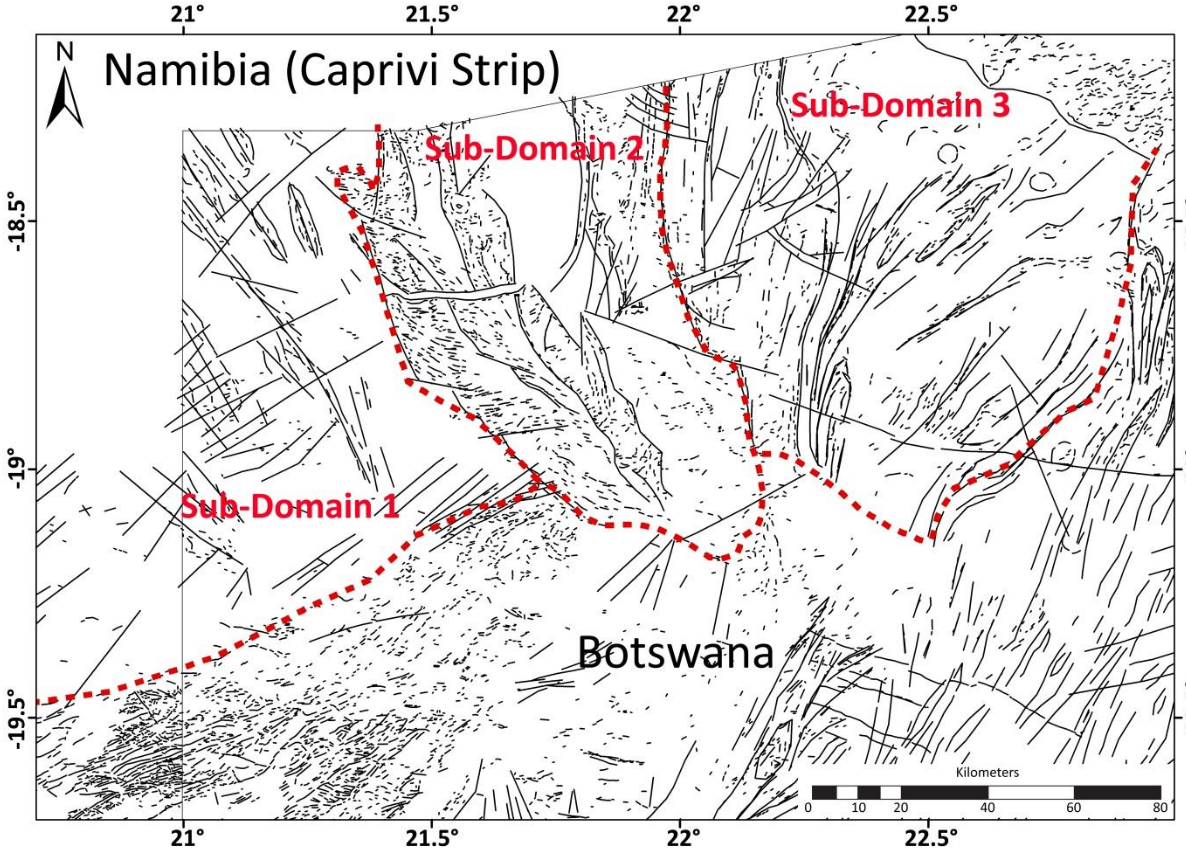

Figure 6.4: Aeromagnetic RTP 1VD lineament map of the three domains in northwest Botswana and northeast Namibia with the Okavango Dyke Swarm removed. The solid north-south line represents the political border between Namibia (west) and Botswana (east).

Sub-domain 1

Sub-domain 1 is characterised by a lack of numerous magnetic lineaments (Figure 6.4). The magnetic lineaments are separated into two groups; the generally shorter, northwest striking lineaments that are associated with magnetic foliation of the rocks defining northwest trending folds, and the longer, northeast striking lineaments that are associated with structural features. The longer northwest striking magnetic lineaments are associated with fold axes while the longer magnetic lineaments striking northeast are associated with faults. The shorter lineaments have a magnetic amplitude of ~ -85 nT to 95 nT and range in length from ~1 km to 5 km. The folds range in length and width from ~17 km to 75 km and 3 km to 4.5 km, respectively.

The longer, northeast striking magnetic lineaments were defined by the sudden termination of a series of folds along a continuous line, or locally in the south of the domain, by the displacement of dykes of the Okavango Dyke Swarm. Therefore, they are defined by indirect observations and range in length from ~6 km to 45 km.

Sub-domain 2

This sub-domain is characterised by an increase in magnetic lineaments that have a north to northwest strike (Figure 6.4). The majority of the lineaments range in magnetic amplitude from ~80 nT to 250 nT and are short in length from ~500 m to 4 km. They are associated with magnetic foliation in the metasediments. The longer lineaments, ranging from ~9.5 km to 55 km are randomly oriented and are associated with structural features. The longer lineaments are defined by indirect techniques i.e. mainly by the displacement of both the shorter and longer lineaments and are suggested to be a combination of thrust and strike-slip faults.

Sub-domain 1 and 2 are separated by a distinctive magnetic feature, which is best described as a fern-like pattern. This feature is defined by a series of north-south striking thrust faults (Wendorff, 2005; discussed later in greater detail). The western part of this feature has a northwest trend while the eastern part has a northeast trend. These trends are seen by the shorter lineaments and is suggested to be a caused by ductile deformation of the metasediments. The thrust faults associated with this structure are interpreted by a repetition in the magnetic signal of higher magnetic amplitudes (directly to the east of the thrust) followed by lower magnetic amplitudes (further to the east), seen in the RTP 1VD aeromagnetic data of Botswana.

Sub-domain 3

Sub-domain 3 is associated with a decrease in the occurrences of magnetic lineaments (compared to sub-domain 2) with the majority of the lineaments producing a north-northeast to northeast strike (Figure 6.4). The lineaments in this domain are generally longer in length than in the previous domains ranging from ~590 m to 70 km. Once again the shorter lineaments are associated with magnetic foliation in the metasediments while the longer lineaments are associated with structural features. The shorter lineaments are associated with a magnetic amplitude of ~20 nT to 240 nT. The higher amplitude lineaments tend to characterise fold hinges where various layers can be seen to fold along the same location. The folds are ~4.5 km to 50 km wide and some are suggested to be fold closures by Key and Ayres (2000) (Figure 6.4).

In the northern part of this domain there are a number of circular to semi-circular features which Key and Ayres (2000) have interpreted as post-tectonic granites. The features range in diameter from ~3.5 km to 6 km and have a magnetic amplitude of ~10 nT to 240 nT.

6.2.2. Okavango Rift Zone

As mentioned above, the longer magnetic lineaments observed are generally associated with structural features. These structural features are not necessarily associated with a magnetic signal but are interpreted from the displacement and/or sudden termination or change in the magnetic signal. In map view these linear features can show typical extensional fault patterns such as anastomosing and en échelon segments. According to Kinabo *et al*. (2008), linear anomalies associated with faults generally have a magnetic amplitude in the range of 200 nT to 600 nT with anomaly widths of 150 m to 200 m.

In northern Botswana, the Okavango Rift Zone is defined by several northeast–southwest striking lineaments that range in strike length from ~45 km to 280 km. The lineaments are interpreted by the alignment of magnetic anomalies of ~300 nT to 600 nT and by the displacement of older magnetic units. The Okavango Rift Zone has been suggested to be the southern continuation of the southern branch of the East African Rift System (EARS) (Figure 6.5) (Kinabo *et al*., 2008).

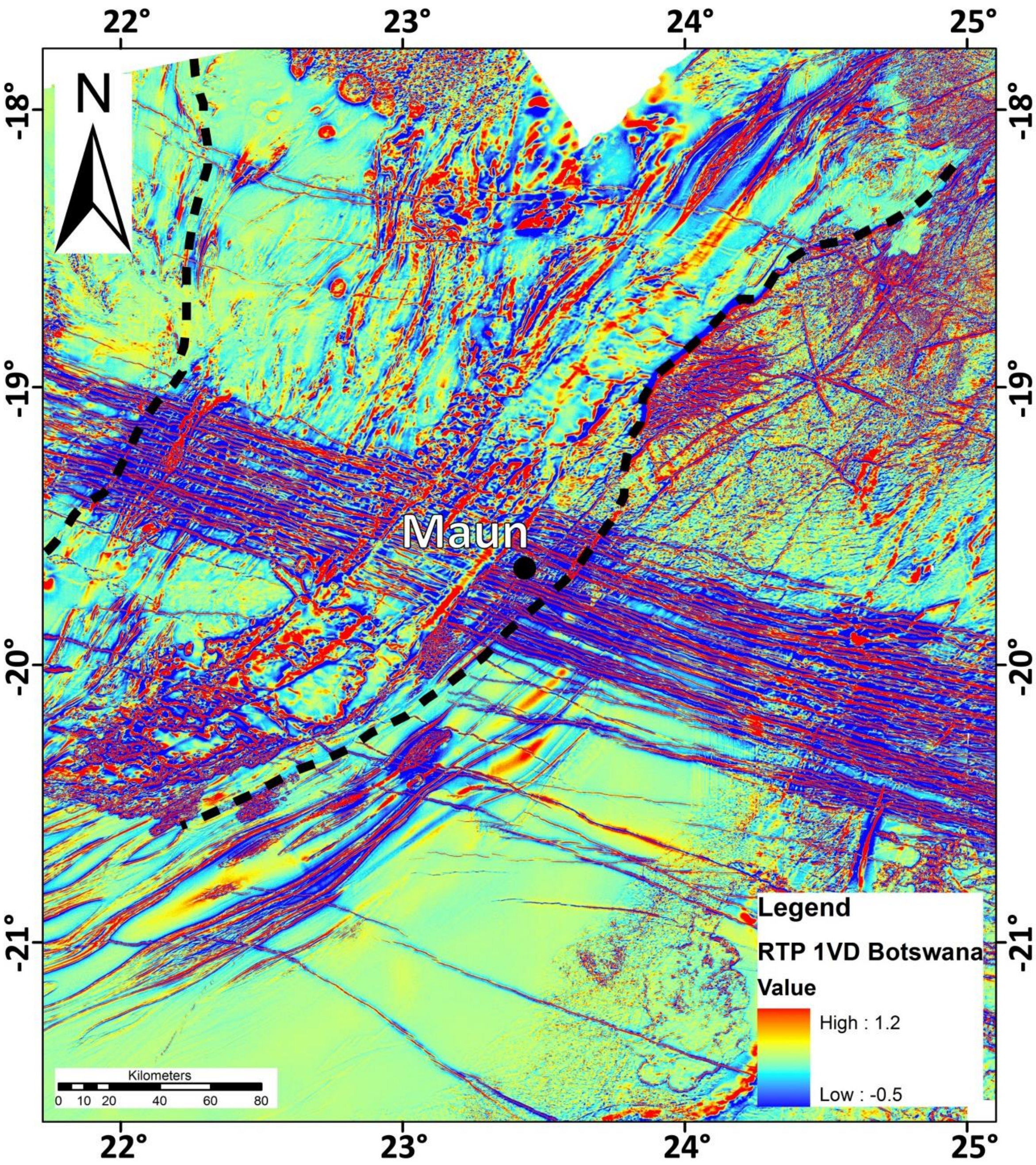

Figure 6.5: RTP 1VD anomaly map of northwest Botswana with the width of the Okavango Rift Zone (black dashed lines) defined by the Gumare Fault in the northwest and Nare Fault in the southeast (after Modisi *et al*., 2000; Kinabo *et al*., 2007; Kgotlhang *et al*., submitted). The black dot represents the location of the town of Maun.

Present in the basement fabric, which is covered by ~200 m to 300 m of Kalahari Group sediments except for a few inliers, are relicts of Meso- to Neoproterozoic-aged northeast trends that define the Northwest Botswana Rift (Modisi *et al*., 2000; Kinabo *et al*., 2008). The Northwest Botswana Rift is ~600 km long, 250 km wide and forms the northwest margin of the Kalahari Craton that is composed of the Palaeoproterozoic Magondi Belt (2.05 Ga to 1.8 Ga orogenic belt) (Key and Ayres, 2000; Singletary *et al*., 2003). Initial rifting began in the Mesoproterozoic, with the later main phase of rifting occurring during the Neoproterozoic (Kinabo *et al*., 2008). The original northwestern boundary of the Northwest Botswana Rift has been destroyed by Damara tectonics and is now interpreted as the Roibok Group (Key and Ayres, 2000). The southeastern boundary of the Northwest Botswana Rift is defined by the present-day Kalahari Suture Zone (Key and Mapeo, 1999). The Kalahari Suture Zone was initially a thrust fault during the Palaeoproterozoic that was reactivated during the Mesoproterozoic and Neoproterozoic as a major (bounding) rift fault that was down-thrown to the northwest (Key and Mapeo, 1999; Kinabo *et al*., 2008). The Okavango Rift Zone is currently forming within the boundaries of the older Northwest Botswana Rift which greatly influences the development of the faults associated with the Okavango Rift (Kinabo *et al*., 2008). The rifts associated with the Okavango Rift Zone from northwest to southeast include, the Gumare, Linyanti, Tsau, Lecah, Kunyere, Thamalakane, Phuti and Nare rifts (Figure 6.6) (Modisi *et al*., 2000; Kinabo *et al*., 2007; Kinabo *et al*., 2008). These rifts define a northeast trending rift zone that is ~400 km long and 150 km wide (Kinabo *et al*., 2008).

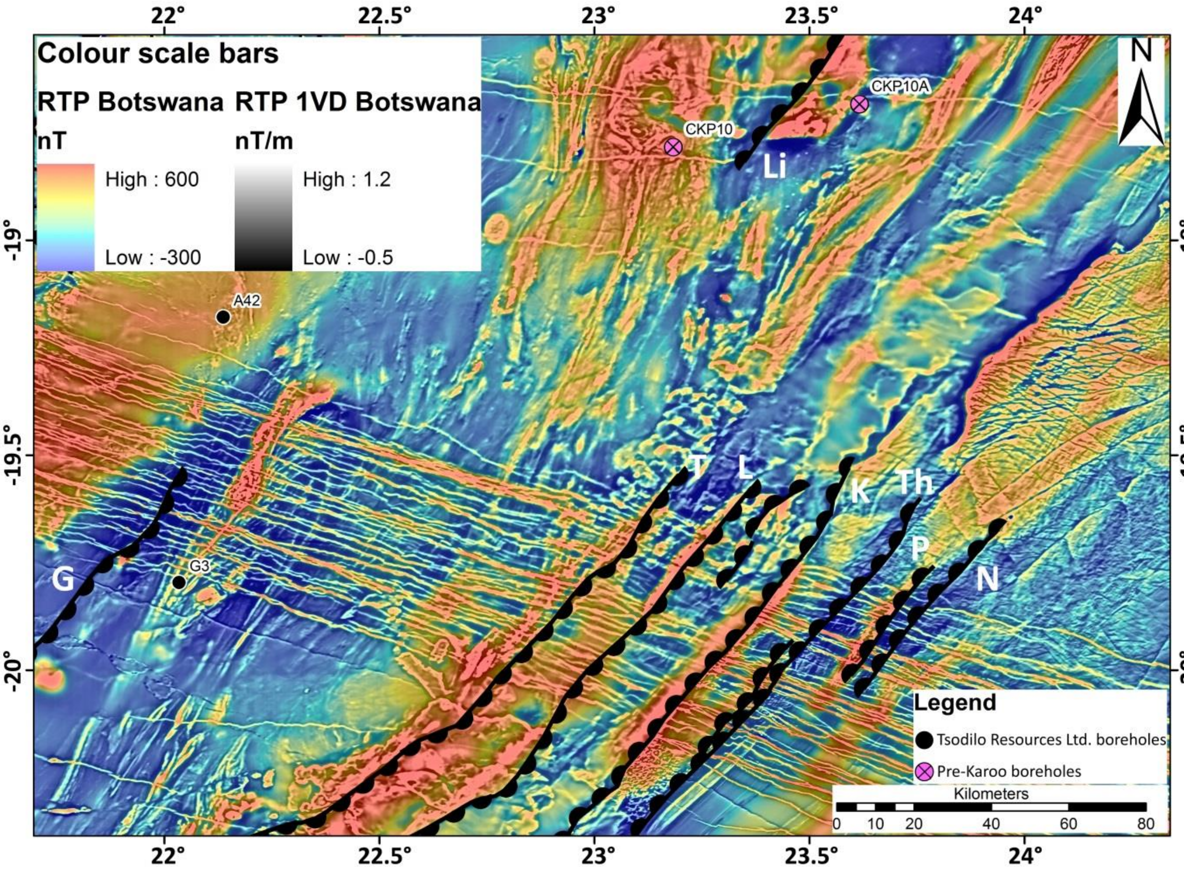

Figure 6.6: Aeromagnetic interpretation of the major northwest-southeast trending rift faults associated with the Okavango Rift Zone. Background is a 50% transparent colour scale RTP image of Botswana overlain on a greyscale RTP 1VD image of Botswana. G = Gumare, Li = Linyanti, T = Tsau, L = Lecha, K = Kunyere, Th = Thamalakane, P = Phuti and N = Nare faults (after Modisi *et al*., 2000; Kinabo *et al*., 2007, 2008).

In northwest Botswana the northern limit of the Gumare Fault is defined by the lack of displacement of the dykes (Figure 6.6). In the southern part of the Okavango Dyke Swarm the dykes are displaced by a sinistral movement. A magnetic anomaly of ~250 nT to 610 nT and a width of 500 m to 780 m, correlates well with the northern limit of the Gumare Fault, as defined by the displacement of the dykes. Tracing a series of magnetic anomalies southwards, the Gumare Fault can be traced across the political border into Namibia. The magnetic anomalies traced are associated with the alignment of Karoo volcanics in Botswana and defines the boundary between pre-Damaran lithologies of the Deep-Level Southern Zone to the north, and the Damaran sediments of Southern Zone to the south (defined in this study). According to Kinabo *et al*. (2007) and Bufford *et al*. (2012) the Gumare Fault is a normal fault that dips to the southeast with a throw range of ~17 m (Kinabo *et al*., 2007).

The Linyanti Fault is ~50 km long and is located in northern Botswana, in the vicinity of the Caprivi Strip. It is characterised by the dextral displacement of dykes and en échelon segments. The fault is situated on the boundary between the Kgwebe Formation (Goha Hills Formation) to the east and the Kwando Complex to the west (Figure 6.6). The Linyanti Fault is a normal fault that is dipping to the northwest (Kinabo *et al*., 2007).

The Tsau Fault occurs towards the interior of the rift basin with a throw range of ~43 m to 130 m to the southeast (Figure 6.6) (Kinabo *et al*., 2008). It is easily identified in the aeromagnetic data as an ~220 km long feature. The southern part of the fault is associated with dextral displacement of Karoo volcanics while the central part is associated with the alignment of these volcanics. This suggests that the southern part has been reactivated more recently than the central part. The northern part of the fault is the most easily recognised. It is associated with a graben that has resulted in the dykes being down thrown to the southeast, thus, suppressing the magnetic signal of the dykes due to the cover of recent sediments. The dykes to the northwest of the Tsau Fault have an average magnetic amplitude of 300 nT compared to an amplitude of 210 nT for the southeastern dykes. The magnetic anomaly that defines the location of the Tsau Fault is ~800 m in length and has a large magnetic amplitude range of ~80 nT to 430 nT. The Tsau Fault is also characterised by a localised high conductivity anomaly (Bufford *et al*., 2012).

The Lecha Fault, immediately to the southeast of the Tsau Fault, is ~210 km long (Figure 6.6). It is a southeast dipping normal fault that has a vertical throw of ~56 m to 163 m (Kinabo *et al*., 2007, 2008). The southern and central parts of this fault are characterised by the same parameters as the Tsau Fault discussed above. The northern part is associated with a magnetic anomaly of ~230 nT to 500 nT and is 900 m wide. There is no noticeable displacement of the dykes suggesting that the northern part of the Lecha Fault is characterised by the older basement fabric. According to Bufford *et al*. (2012) the Lecha Fault is associated with a localised high conductivity anomaly.

The southeastern margin of the graben is defined by the Kunyere Fault (Figure 6.6). It is an ~240 km long northwest dipping normal fault that has a fault throw of ~334 m in the south and ~286 m in the north (Kinabo *et al*., 2007). The southern and central parts of the fault are associated with the alignment of the magnetic fabric in the Karoo volcanics and locally define the south-southeast margin of Karoo volcanics, separating them from the metasediments of the Ghanzi Group. The northern part is characterised by the downthrow of the dykes to the northwest resulting in a sudden change in the aeromagnetic signal, as discussed above in the Tsau Fault. Modisi *et al*. (2000) determined that the average depth to pre-Kalahari basement to the northeast of the Kunyere Fault is 250 m, whereas to the southwest, depths of 500 m to 550 m were determined. The magnetic anomaly that defines the location of the Kunyere Fault is ~700 m wide and has a magnetic amplitude of ~310 nT to 580 nT. There is no conductive anomaly associated with the Kunyere Fault (Bufford *et al*., 2012).

The Kunyere and Thamalakane Faults are considered to be boundary faults, defining the south eastern margin of the Okavango Rift Zone (Modisi *et al*., 2000; Hall, 2013; Bufford *et al*., 2012). The Thamalakane Fault is an ~230 km long, northwest dipping normal fault that has a fault throw of ~80 m (Kinabo *et al*., 2007, 2008). The southern part of the Thamalakane Fault is characterised by the alignment of Karoo volcanics while the central part by displacement and termination of dykes and the alignment of magnetic foliation in the metasediments of the Ghanzi Group. It is seen by a magnetic amplitude of ~85 nT and is 450 m wide. The northern part is associated with dextral displacement of the dykes of ~800 m (in map view) and a magnetic amplitude of 130 nT and 500 m wide. According to Bufford *et al*. (2012), this border fault is associated with a localised high conductivity anomaly.

To the southeast of the Thamalakane Fault are the Phuti and Nare Faults (Figure 6.6). They are northwest dipping normal faults that have a fault throw of ~18 m and 70 m, respectively (Kinabo *et al*., 2007, 2008). In the aeromagnetic data there are no noticeable lateral offsets of the dykes. This suggests that the dykes are near vertical and the Phuti and Nare Faults cross-cut them perpendicularly. The Phuti Fault is associated with an ~35 km long magnetic signal of ~430 nT to 690 nT and is 850 m wide. The Nare Fault is associated with an ~50 km long and 600 m wide magnetic anomaly of 120 nT. There appears to be no displacement of the dykes suggesting that the magnetic signal is produced by the basement fabric. These faults only displace dykes in the northern part of the Okavango Dyke Swarm and the southeastern continuation of these faults, into the southern part of the Okavango Dyke Swarm, intersects dykes without any displacement (Modisi *et al*., 2000). These relationships suggest that the faults are pre-dyke emplacement and that the northern part of these faults have been reactivated during the rifting of the Okavango Rift Zone in the Cenozoic (Modisi *et al*., 2000).

The Tsau, Lecha, Kunyere and Thamalakane Faults terminate against the Proterozoic Sekaka Shear Zone marking the southeastern limit of these faults (Figure 6.7) (Modisi *et al*., 2000). From map view, the Sekaka Shear Zone is interpreted as a northwest-southeast striking apparent dextral shear zone, suggested by the right lateral displacement of the linear high magnetic amplitude anomalies present in the Roibok Group and the alignment of Karoo basalts. The shear zone also marks the boundary between Karoo basalts and the Ghanzi-Chobe Belt. There is no evidence of neotectonic activity south of this shear zone (Modisi *et al*., 2000). In the gravity data the Sekaka Shear Zone is not visible because of the large station spacing.

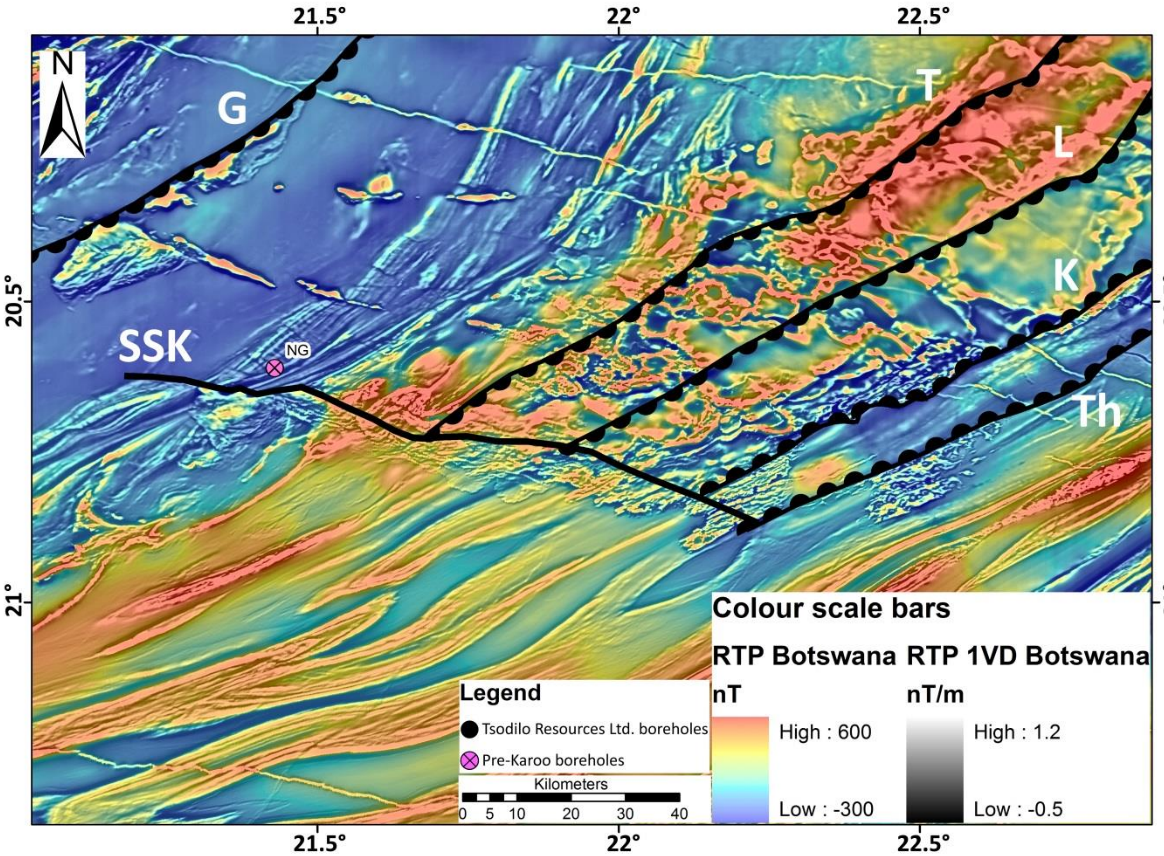

Figure 6.7: Aeromagnetic interpretation of the termination of the rift faults associated with the Okavango Rift Zone against the apparent dextral west-northwest trending Sekaka Shear Zone (SSK). Background is a 50% transparent colour scale RTP image of Botswana overlain on a greyscale RTP 1VD image of Botswana. G = Gumare, T = Tsau, L = Lecha, K = Kunyere and Th = Thamalakane faults (after Modisi *et al*., 2000; Kinabo *et al*., 2007, 2008).

The width of the Okavango Rift Zone between the Gumare Fault, to the west, and the Nare Fault, to the east, is ~170 km (Figure 6.5). The southern limit of the rift zone is determined by the Sekaka Shear Zone while the basement trends of the Tsau, Lecha, Kunyere and Thamalakane Faults north the rift zone can be traced to the Caprivi. Igneous activity within the margins of this initial rift zone occurred at ~1.1 Ga with the emplacement of mafic intrusions into the Kwando Complex (U-Pb zircon age of 1 107 ± 0.8 Ma) (Singletary *et al*., 2003), rhyolites of the Goha Hills Formation (U-Pb zircon age of 1 107 ± 0.5 Ma) and the Kavimba granite (U-Pb zircon age of 1 107 ± 2.1 Ma) (Singletary *et al*., 2003).

Overlying the faults of the Okavango Rift Zone, on the band-pass filter Bouguer gravity map of northern Botswana between wavelengths 5 km and 100 km, a correlation between these near-surface features and basement trends can be noted (Figure 6.8). The faults follow the high Bouguer anomaly trends of ~11 mGal to 15 mGal implying that they were reactivated in previous zones of weakness.

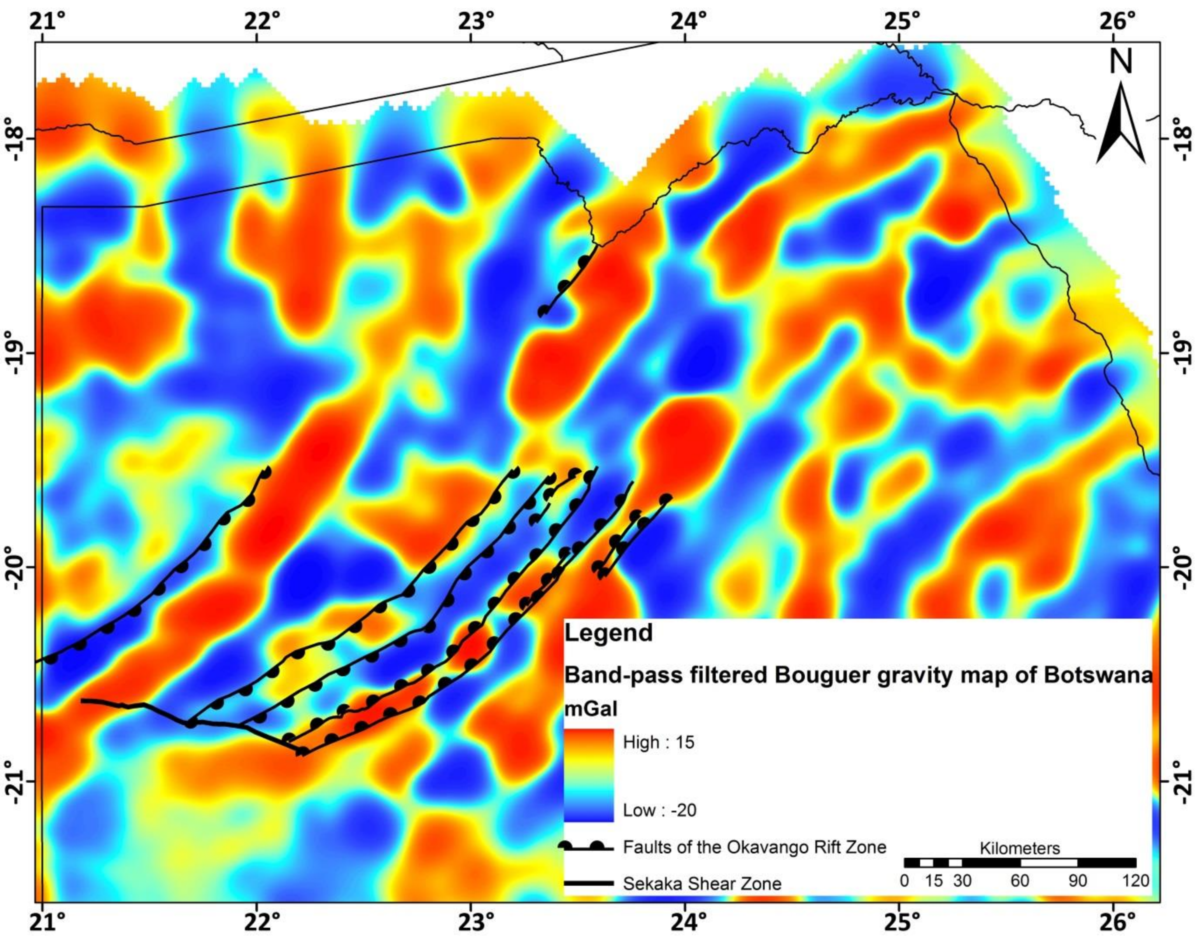

Figure 6.8: Band-pass filtered Bouguer gravity map of northwest Botswana, between wavelengths of 5 km and 100 km, retaining gravity signals of 2D features in a depth range of 1.25 km and 25 km. Notice the correlation between the faults interpreted from high-pass aeromagnetic data sets and the basement trends.

6.3. Results and interpretation of the geophysical polygons

The interpretation of the geophysical polygons situated in Namibia is a challenging task, as there are no sub-surface geological maps for eastern Namibia near the Namibia - Botswana border. Tentative interpretations are made based on the aeromagnetic signals and from the closest mapped Damaran lithology from the 1:250 000 geological map of Namibia.

6.3.1. The Ghanzi-Chobe Belt and correlatives in Namibia

The Oorlogsende Porphyry Member, in eastern Namibia, has been correlated with the Kgwebe Formation by Modie (2000) based on similar U-Pb zircon age dates of 1 094 $^{+18}/_{-20}$ Ma (Hegenberger and Burger, 1985) and 1 106 ± 2 Ma (Schwartz *et al*., 1995), respectively, and similar volcanic assemblages. In addition, the Oorlogsende Porphyry Member has been correlated with the Nückopf Formation, in the Rehoboth Subprovince, near Klein Aub, based on U-Pb radiometric age ranges between 1 010 Ma to 1 172 Ma and similar volcanic assemblages (Hegenberger and Burger, 1985; Schwartz *et al*., 1995). As the majority of the Ghanzi-Chobe Belt (in Botswana and eastern Namibia) is covered by younger sediments (Figure 2.19), the aeromagnetic signal of the Oorlogsende Porphyry Member and mapped volcanic exposures in the Ghanzi Ridge (Modie, 1996; Kampunzu *et al*., 1998; Modie, 2000; Singletary *et al*., 2003) are used to define the magnetic response of the Kgwebe Formation. The magnetic response of the individual metasedimentary formations of the Ghanzi Group was determined from the geological map of south Ngamiland (Thomas, 1969, 1973).

This study defines the north-south extent of the Ghanzi-Chobe Belt by a series of northeast–southwest trending folds. The folds were interpreted by their alternating magnetic high amplitudes of ~340 nT of the D'Kar Formation and low magnetic amplitudes of ~-40 nT of the Ngwako Pan Formation (Table 6.1, Figure 6.9). The underlying Kgwebe volcanics display high magnetic amplitudes of ~600 nT (Figure 6.9). According to Kahle (2012) both the Kuke and Ngwako Pan Formations are characterised by a smooth, low magnetic amplitude. This study has not been able to differentiate between the two. In addition, the Kuke Formation has not been mapped in the geological maps of either Pryer *et al*. (1997) or Key and Ayres (2000). The high magnetic response of the D'Kar Formation is believed to be associated with very fine-grained pyrrhotite mineralisation which formed along the redox boundary with the underlying Ngwako Pan Formation (Hendjala, 2011) and Hall (2013) believes the magnetic response of the Kgwebe Formation is associated with disseminated magnetite.

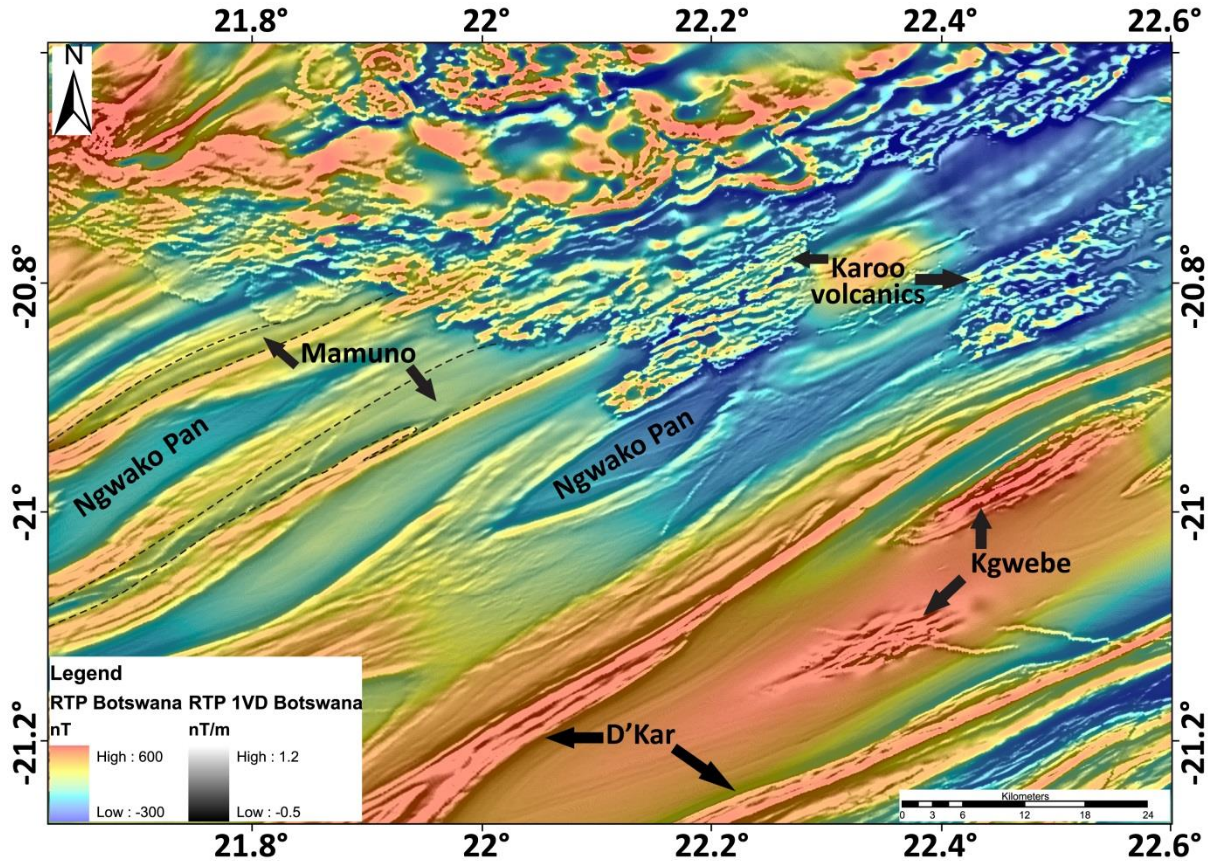

Figure 6.9: Interpretation of the Kgwebe Formation, Ghanzi Group and Karoo basalts of central Botswana based on their aeromagnetic signature. Background image is a 50% transparent colour scale RTP image of Botswana overlain on the RTP 1VD greyscale image of Botswana.

Anticline and syncline axial surfaces of the Ghanzi-Chobe Belt can be traced over 10 km to 50 km with traces spaced 2 km to 8 km apart (Hall, 2013). As the majority of the belt is beneath Kalahari and Karoo cover, to verify the fold pattern, a north-northwest geological cross-section mapped by Modie (2000) across the Ghanzi Ridge (Figure 6.10), was magnetically 2D forward modelled in GM-SYS, an extension in Geosoft. The profile was extracted from the TMI aeromagnetic data of Botswana with elevation extracted from the STRM data (Section 3.6). The profile was modelled with the following parameters;

- declination: -11°
- inclination: -62°
- magnetic field intensity: 30 025 nT
- flight height: 80 m

The geological cross-section of Modie (2000) suggests that the folds are open to tight with fold amplitudes of ~4 km to 6 km and with the Kgwebe Formation forming the cores of the anticlines and the Mamuno Formation forming the cores of the synclines (Figure 6.10b). Fold limbs range in dip from vertical (southeastern fold between the Kgwebe and Kuke Formations) to ~45° (northwestern fold between the metasediments of the Ghanzi Group; Figure 6.10b). The D'Kar Formation (northwestern fold) is suggested to have a thickened hinge and thinning limbs away from the hinge (Figure 6.10c).

To determine the reliability of the geological mapping and descriptions the geological cross-section of Modie (2000) was magnetically 2D forward modelled (Figure 6.10c). The magnetic susceptibility values are based on physical property measurements (Chapter 5) and published values (Poseidon Geophysics, 1995; Hendjala, 2011; Bauer *et al.*, 2003; Lehmann *et al.*, submitted). However, as the magnetic model was modelled to a depth of ~3 km to correlate with the geological cross-section of Modie (2000) (Figure 6.10) some of the magnetic susceptibility values had to be increased to compensate for this shallow model depth. As the margins of the profile are covered by Kalahari sediments, Modie (2000) was unable to assign a rock unit to depth (Figure 6.10b). The magnetic susceptibility of 3.78×10^{-3} SI units and the aeromagnetic signal suggests that underlying the Kalahari sediments in the northwest are volcanics of the Karoo Supergroup, while in the southeast, with a magnetic susceptibility of 2.53×10^{-3} SI units, is Ngwako Pan Formation overlying Kgwebe Formation. The inverse in the calculated and observed magnetic responses, in the centre of the profile, suggests that the contact between the Ngwako Pan, D'Kar and Mamuno Formations should be shifted to the northwest (Figure 6.10b, c).

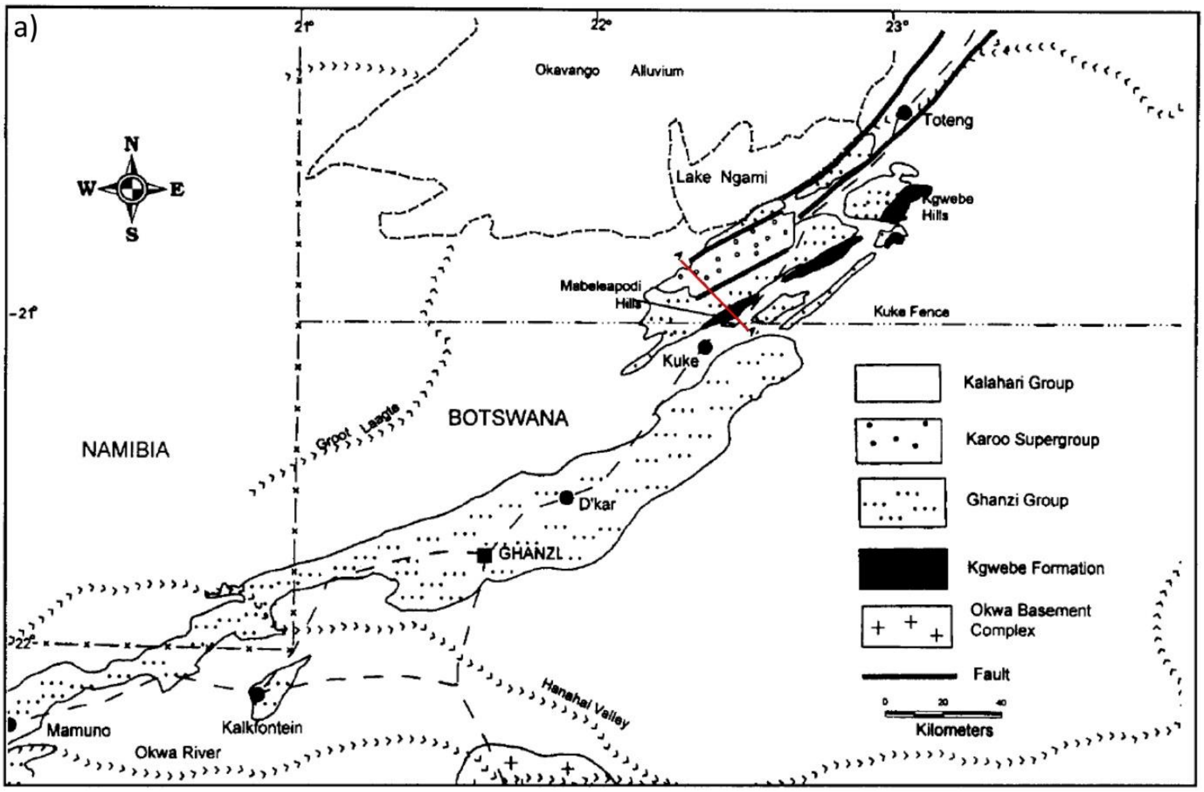

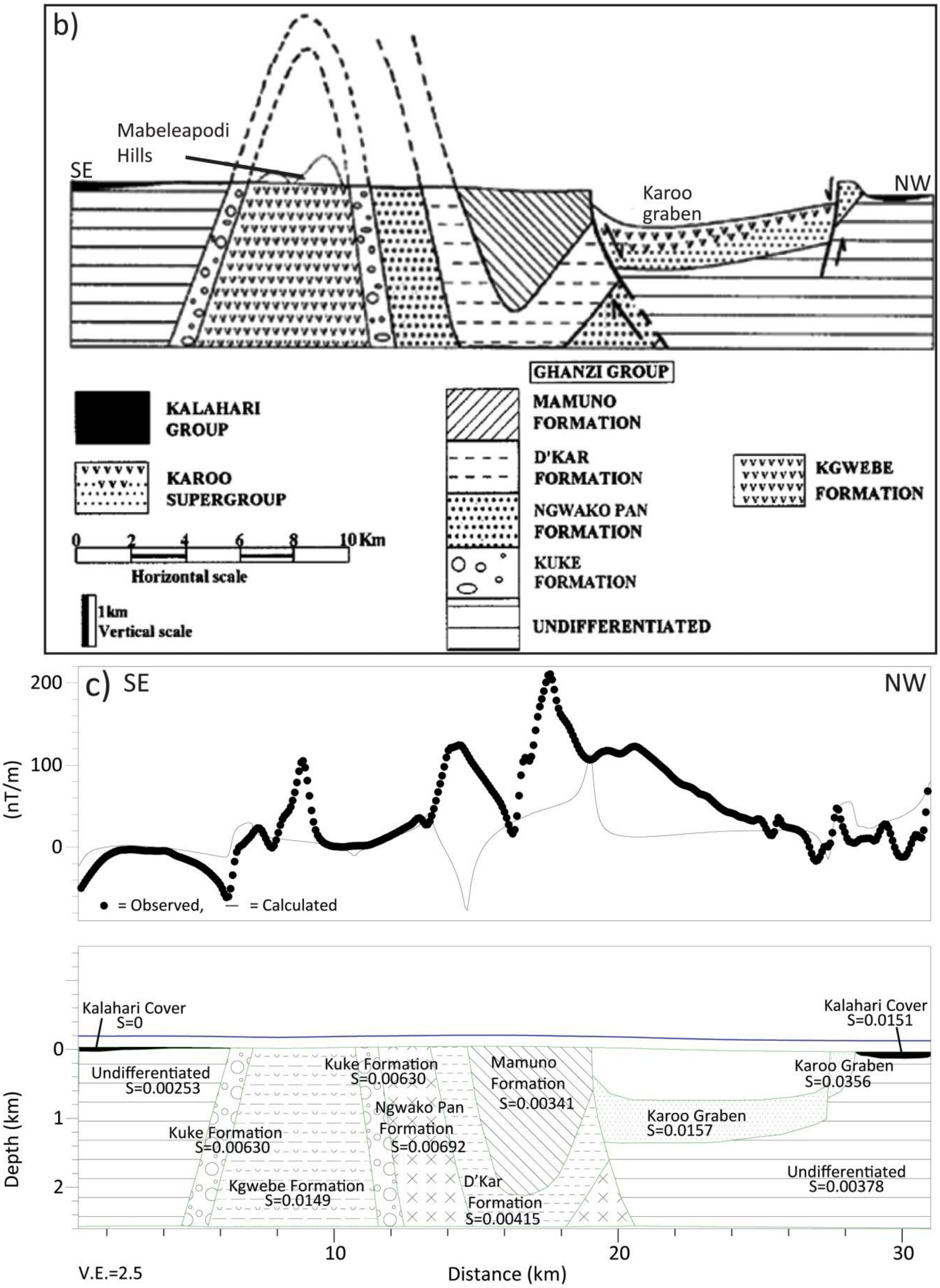

Figure 6.10: Comparison between the geological cross-section and 2D magnetic forward model across the Ghanzi Ridge. a) Geological outcrop map with the location (red line) of modelled profile (after Modie, 2000). b) Geological cross section (Modie, 2000). C) 2D magnetic forward model. The blue line represents the flight height of 80 m above the topography determined from STRM data. The dotted and solid curves are observed and calculated magnetic responses respectively.

Northeastwards of the Ghanzi Ridge, in the Goha, Gubatsha and Chinamba Hills (Figure 2.19), the Kgwebe Formation and Ghanzi Group have been correlated with exposed rhyolites of the informally termed Goha Hills Formation which is surrounded by Neoproterozoic low-grade carbonate rocks of the Chinamba Formation (Kampunzu *et al*., 2000; Modie, 2000; Key and Ayres, 2000; Singletary *et al*., 2003). The Goha Hills Formation is defined by a similar magnetic texture but lower amplitude (~580 nT) than the Kgwebe Formation. The Chinamba Formation has a smooth, low magnetic amplitude, ~-20 nT, and similar lithological composition (meta-carbonate) to the Mamuno Formation (Table 6.1).

In Namibia, the northern boundary of the Ghanzi-Chobe Belt is defined by the noisy, pitted texture, positive high amplitude of 245 nT to 330 nT Oorlogsende Porphyry Member (Figure 2.19). Tracing the aeromagnetic signal of the northern boundary of the Oorlogsende Porphyry Member westwards, the western boundary of the Ghanzi-Chobe Belt is defined by the heavily deformed, high amplitude magnetic signal of the Rehoboth Subprovince. At ~19.10°E, -22.00°S, the folds of the belt bend in a southwest direction. The folds decrease in magnetic amplitude to between -70 nT and 20 nT and increase in size to the south. This is suggested to be as a result of the increase in sedimentation related to the Aranos and Kalahari Basins.

The Oorlogsende Porphyry Member, Dordabis, Klein Aub and Sinclair basins are associated with elongated Bouguer gravity high anomalies flanked by negative anomalies while the Witvlei Basin is associated with a negative Bouguer anomaly (Borg, 1987). The Bouguer gravity data, interpreted in this study, associates the Oorlogsende Porphyry Member, Dordabis, Klein Aub and Sinclair basins with Bouguer gravity anomalies of -95 mGal to -125 mGal flanked by -150 mGal to -170 mGal. In Botswana, the Kgwebe Formation and Ghanzi Group are associated with Bouguer gravity anomalies of -140 mGal compared to -100 mGal of the Goha Hills and Chinamba Formations. The possible cause of this gravity contrast is the thicker sedimentary sequence of the Ghazi Group and Kalahari sediments compared to the Goha Hills and Chinamba Formations and/or as the gravity data has a grid cell size of 2.2 km the deeper features are being seen, compared to shallower features or the shallower, shorter wavelength features have been aliased into longer wavelength features which appear to be deeper, which can be interpreted from the 50 m aeromagnetic data.

The Ghanzi-Chobe Belt is therefore traced northeast from the Rehoboth Subprovince, in Namibia, through Botswana to the Zimbabwe/Zambia border (Figure 6.1). In this region the aeromagnetic signal of the Ghanzi-Chobe Belt is suppressed by the near surface, mottled, high amplitude magnetic signal of ~150 nT associated with the overlying Karoo volcanics. The folding of the

Ghanzi-Chobe Belt in Namibia is not as pronounced as in central Botswana (Figure 6.1). This could be related to an increase in sedimentary cover of the Aranos Basin, which is ~1 km thick (Catuneanu *et al*., 2005). The Oorlogsende Porphyry Member is used to define the northern boundary of the Ghanzi-Chobe Belt while the southern boundary is interpreted by the last visible fold in the aeromagnetic data and is reinforced by the MT 1D inversion models (Chapter 7).

6.3.2. Roibok Group

The Roibok Group is an unexposed geological domain that has been intersected by the NG boreholes (Figure 6.11). It separates the Ghanzi-Chobe Belt in the southeast from magmatic and migmatitic rocks, which are locally overlain by carbonates and sediments in the northwest (Figure 6.1) (Key and Ayres, 2000). The Roibok Group is interpreted as north-northeast striking, characterised by linear high magnetic anomalies of 80 nT to 100 nT a relative to smooth, lower magnetic amplitude signal of -70 nT to -50 nT (Table 6.1). The high amplitude, linear magnetic anomalies are suggested to be associated with the amphibolite intersected in the drill core while the schists and paragneisses are suggested to be the cause of the smoother, lower magnetic response. Approximately 30 km within Botswana, from the border with Namibia, the Roibok Group is cross-cut by the Sekaka Shear Zone (Figure 6.6; for a local view of the SSK; Figure 6.11 for a regional position of the SSK).

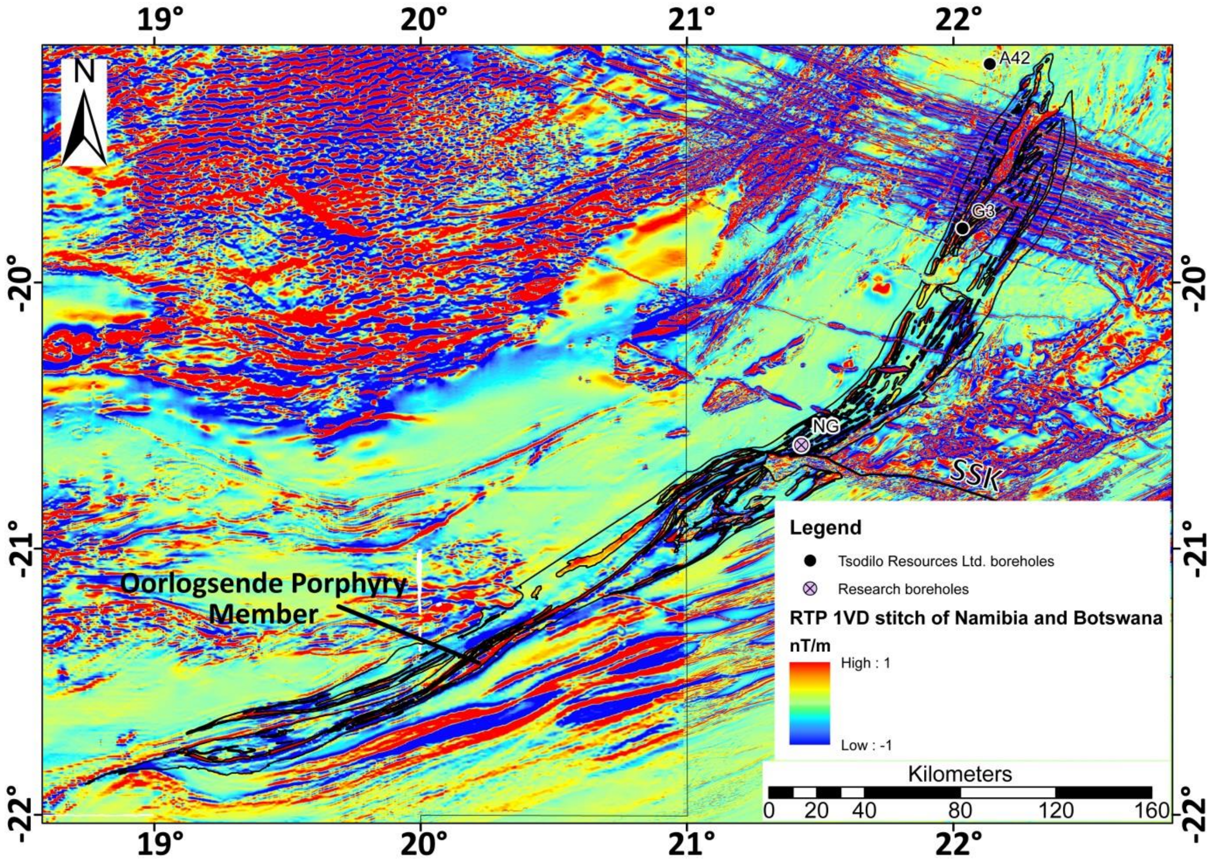

Figure 6.11: The proposed continuation of the Roibok Group from northwest Botswana into central Namibia from the aeromagnetic interpretation. The Oorlogsende Porphyry Member is used to determine the southern margin of the Roibok Group. The location of the Sekaka Shear Zone (SSK) is shown (solid black line). The solid north-south line represents the political border between Namibia (west) and Botswana (east).

The high amplitude, near surface aeromagnetic signal of the Okavango Dyke Swarm and lack of boreholes has led to difficulty in constraining the northeastern extent of the Roibok Group. Both Pryer *et al*. (1997) and Key and Ayres (2000) map the Roibok Group to the Caprivi (Figure 3.8). To suppress the aeromagnetic signal of the dykes, a directional filter was applied (Butterworth and directional cosine filters) to the RTP data set (Figure 6.12). Various orientations and wavelengths were processed with the best result obtained from an orientation of 110° at a wavelength of 350 m. To completely suppress the aeromagnetic signal of the dyke swarm and enhance north-south structures, the filtered image was upward continued by 500 m and sunshaded at an inclination of 30° and declination of 150° (Figure 6.12). From the interpretation of the filtered aeromagnetic image, the Roibok Group is proposed to terminate in a fold closure at ~22.40°E, -19.37°S. In the vicinity, there are elongated sub-linear northeast striking high amplitude magnetic anomalies of 550 nT to 700 nT (Figure 6.12). These magnetic high anomalies have been mapped as either Kgwebe Formation (Key and Ayres, 2000) or Kwando Complex (Pryer *et al*., 1997) (Figure 3.8).

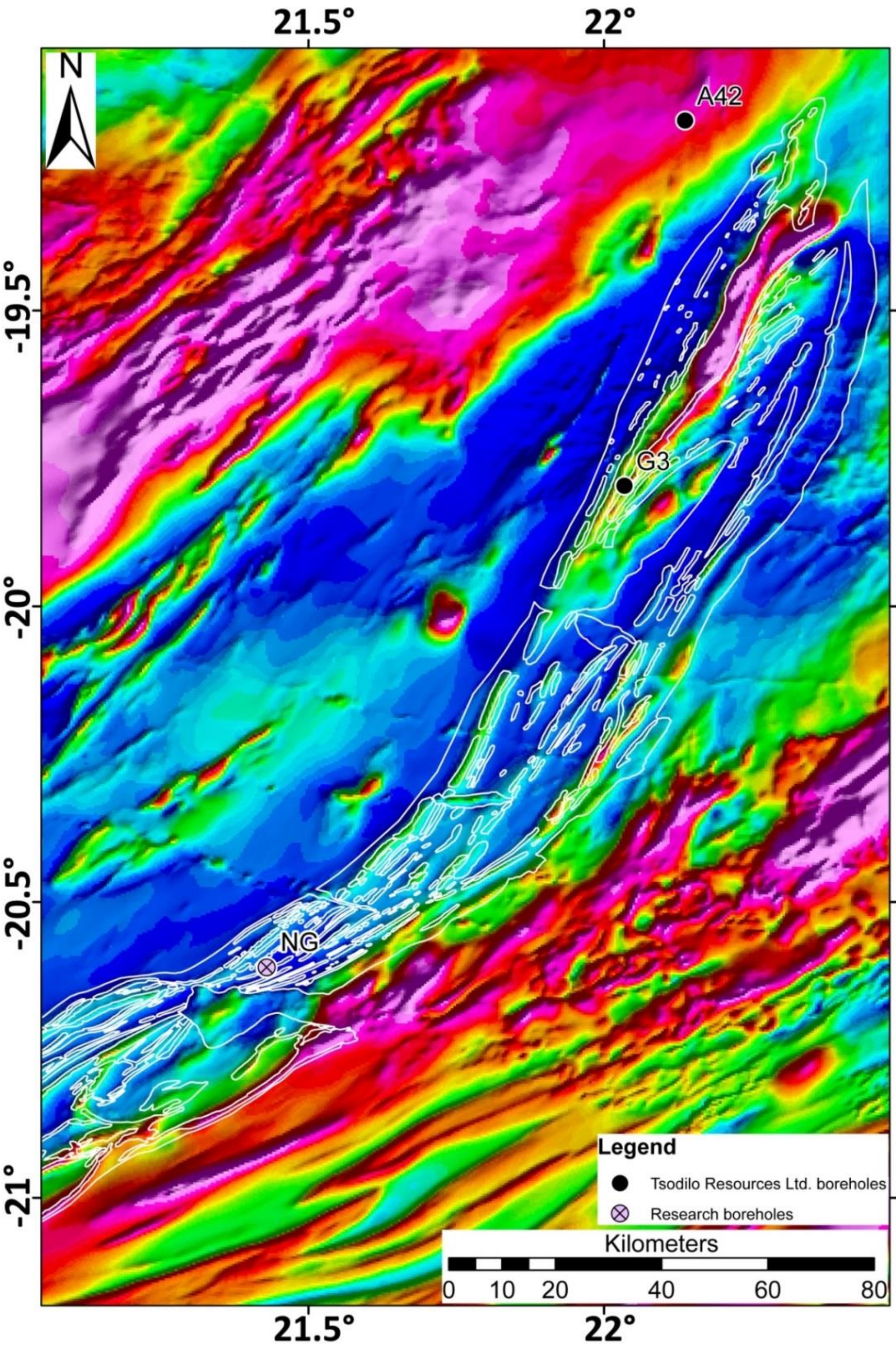

Figure 6.12: Aeromagnetic sunshaded image of northwest Botswana (inclination = 30°, declination = 150°) with the aeromagnetic signal of the northwest striking Okavango Dyke Swarm being suppressed by first decorrugation filtering with the Butterworth filter having the following parameters; cut-off wavelength = 350 m, selected for the intensity of the aeromagnetic signal that needs to be suppressed, filter order = 4 and low pass filter. The parameters of the directional cosine filter are; centre direction in space domain = 290° i.e. the direction in which the signal must be suppressed, degree of cosine function = 1 and reject the aeromagnetic signal that falls in the range of the above listed parameters. Secondly, the filtered data was upward continued by 500 m to fully remove the aeromagnetic signal of the dykes. To enhance the edges of the Roibok Group (outlined in white) the image was sunshaded (parameters listed above). The location of the pre-Karoo and Tsodilo Resources Ltd. boreholes are shown.

Tsodilo Resources Ltd., based in Maun, have drilled borehole G3 into the southern part of one of these magnetic high anomalies; less than 900 m from the Roibok Group (Figure 6.12). The core of G3 is typically migmatitic gneiss intercalated with garnet-bearing amphibolite (Figure 6.13) (Gaisford, 2010). CL images suggest that the zircons are of primary magmatic origin (Gaisford, 2010). Weighted mean ^{207}Pb-^{206}Pb zircon dating on a pink granite yielded an age of 1 979 ± 92 Ma for nine of the twelve concordant zircons (Gaisford, 2010). This age has affinities to both the Congo and Kalahari Cratons. In the Rehoboth Subprovince the Kalahari Craton has a Palaeoproterozoic zircon population of between 2.1 Ga to 1.8 Ga (Jacobs *et al*., 2008; van Schijndel *et al*., 2011, 2013). The age also falls within error of the SHRIMP zircon age from the Magondi Belt (Gweta Borehole) (Figure 1.4 and 2.19) of 2 027 ± 8 Ma (Mapeo *et al*., 2001). The Congo Craton, to the northwest has a zircon population of 2.0 Ga to 1.7 Ga (van Schijndel *et al*., 2013), and the Abbabis Complex, in the Central Zone of the Damara Belt, has a zircon population of 2.1 Ga to 2.0 Ga and is of Congo Craton affinity (Miller, 2008; Longridge, 2012).

Figure 6.13: Photograph of the typical gneiss intersected in borehole G3. Location of the borehole is shown in Figure 6.12.

The Roibok Group can be traced southwestwards into Namibia by following the linear, high amplitude anomalies. The Roibok Group is traced around the Oorlogsende Porphyry Member and interfingers with pre-Damaran rocks of the Deep-Level Southern Zone (Figure 6.1). The southern margin of the Roibok Group is in contact with the Ngwako Pan Formation and the northwestern margin of the Roibok Group was determined by the heavily deformed, high amplitude signal of the pre-Damaran rocks.

In Botswana, the Roibok Group is associated with a Bouguer gravity anomaly of -70 mGal to -100 mGal. This gravity trend is traced into Namibia, where the amplitude of the gravity signal decreases slightly, possibly due to the larger station spacing of the gravity stations and/or thicker sedimentary cover. The Bouguer gravity anomaly correlates well with the aeromagnetic spatial extent of the Roibok Group (Figure 6.14). The Bouguer anomaly map was band-passed filtered between wavelengths of 5 km to 100 km to enhance 2D bodies between depths of 1.25 km and 25 km. To enhance basement features, the band-passed image was then sunshaded at various inclinations and declinations to enhance features perpendicular to the selected inclination. The sunshaded, band-passed Bouguer gravity anomaly map suggests that the Roibok Group is associated with a northeast-southwest basement trend (Figure 6.15).

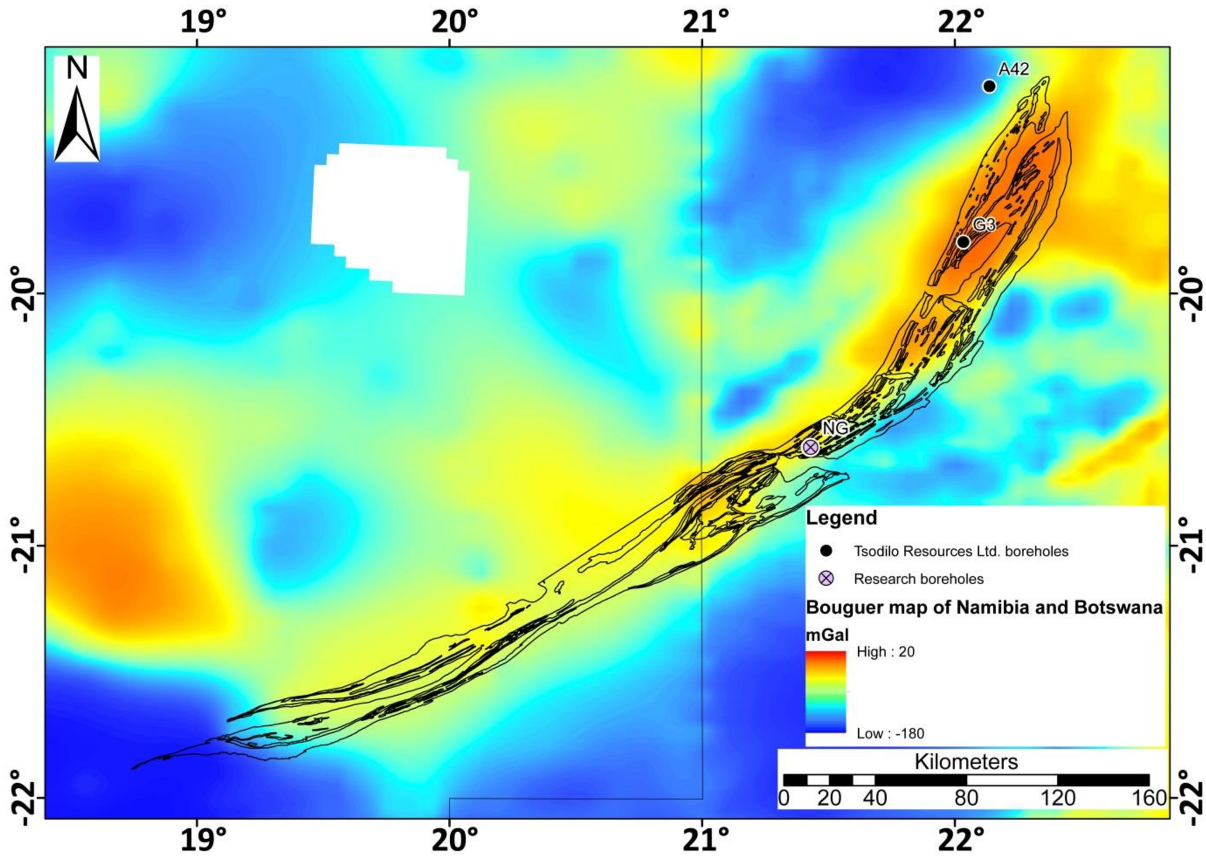

Figure 6.14: The aeromagnetic proposed continuation of the Roibok Group (black outline) overlain on the Bouguer gravity anomaly map of Namibia and Botswana. Notice the correlation between the aeromagnetic interpretation and the higher Bouguer gravity anomaly (northeast striking red anomaly). The location of the pre-Karoo and Tsodilo Resources Ltd. boreholes are shown. The solid line represents the political border between Namibia (west) and Botswana (east).

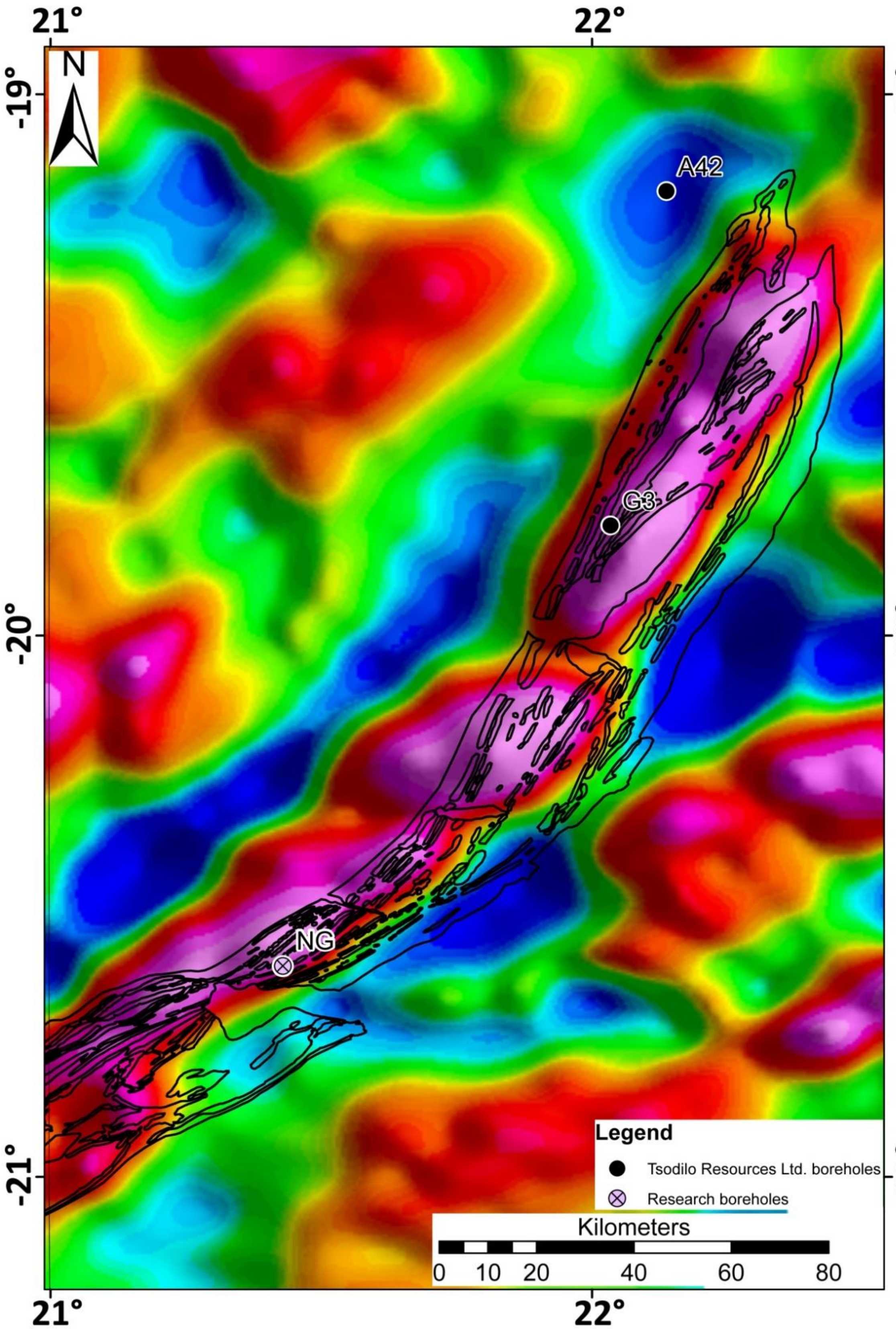

Figure 6.15: Sunshaded (inclination = 35°, declination = 65°) band-pass Bouguer anomaly map of Botswana between wavelengths of 5 km and 100 km, retaining gravity signals of 2D features in a depth range of 1.25 km and 25 km with the outline of the Roibok Group (black), as interpreted from aeromagnetic data. The location of the pre-Karoo and Tsodilo Resources Ltd. boreholes are shown.

6.3.3. Kwando Complex

The term Kwando Complex was first introduced by Carney *et al*. (1994) for a geophysically distinct subsurface terrane located northwest of the Ghanzi-Chobe Belt and east-southeast of the northern extent of the Roibok Group (Figure 6.1). The Kwando Complex is a northeast-southwest striking, unexposed complex with geological information obtained from borehole CKP-10, which intersects granitic gneiss with amphibolite layers. Borehole CKP-10A intersected weakly metamorphosed gabbro to diorite (Carney *et al*., 1994; Singletary *et al*., 2003). Age dating by Singletary *et al*. (2003) suggests that granite emplacement occurred between 1.20 to 1.15 Ga while the metagabbro (borehole CKP-10A) yielded an age of 1 107 ± 0.8 Ma, suggesting a later emplacement event. The age of the metagabbro falls within age error obtained by Schwartz *et al*. (1995) of 1 106 ± 2 Ma for the Kgwebe Formation in the Mabeleapodi Hills and the U-Pb age of 1 104 ± 16 Ma of Kampunzu *et al*. (2000) for its northeastern extension in the Goha Hills (Figure 2.19). In addition, borehole CKP-10A plots in a magnetic low, which this study interprets as the Mamuno Formation. Therefore, the lithologies intersected in borehole CKP-10A are suggested to be part of the Ghanzi-Chobe Belt based on zircon ages and geophysical signatures.

The Kwando Complex has two distinct aeromagnetic signals, which are separated by the Okavango Dyke Swarm (Figure 6.16). The southern part of the complex has smooth, low magnetic amplitude in the range of -60 nT to -10 nT. The northern part of the complex is associated with noisier, curvilinear to linear, north-northeast striking moderate to high magnetic amplitudes of 65 nT to 480 nT. Both the southern and northern margins of the Kwando Complex are in contact with Karoo volcanics (Figure 6.16).

The curvilinear to linear magnetic features are interpreted to represent the metagabbro-diorite, as gabbro and diorite have average susceptibilities of 70 x 10^{-3} SI and 85 x 10^{-3} SI, respectively, while the highest susceptibility value of granite is 50 x 10^{-3} SI (Telford *et al*., 1990). The discrepancy in aeromagnetic signal between the southern and northern parts of the complex may be because of the southern extent of the complex being beneath a thicker sedimentary cover, as it is in the vicinity of the Passarge Basin, and/or the intrusion of the metagabbro to dolerite is restricted to the northern part of the complex.

The Kwando Complex is characterised by a negative Bouguer gravity signal of ~120 mGal. The first vertical derivative of the Bouguer gravity signal correlates well with the V-shaped wedge in the northern part of the complex, as interpreted in the aeromagnetic data (Figure 6.17). In the Bouguer gravity data the complex is cross-cut by a northwest-southeast trending, higher gravity anomaly of ~-90 mGal of the Okavango Dyke Swarm (Figure 6.17). To remove the shallow gravity signal of the dykes and enhance the deeper, longer wavelength signal of the Kwando Complex, a band-pass filtered image was investigated (Figure 6.18). In the band-pass image the continuation of the Kwando Complex is visible by a low Bouguer gravity anomaly. This low Bouguer gravity anomaly is traced to the Caprivi Strip while the southern extent is difficult to determine because of the overlying metasediments of the Ghanzi Group, which are associated with a low Bouguer gravity signal.

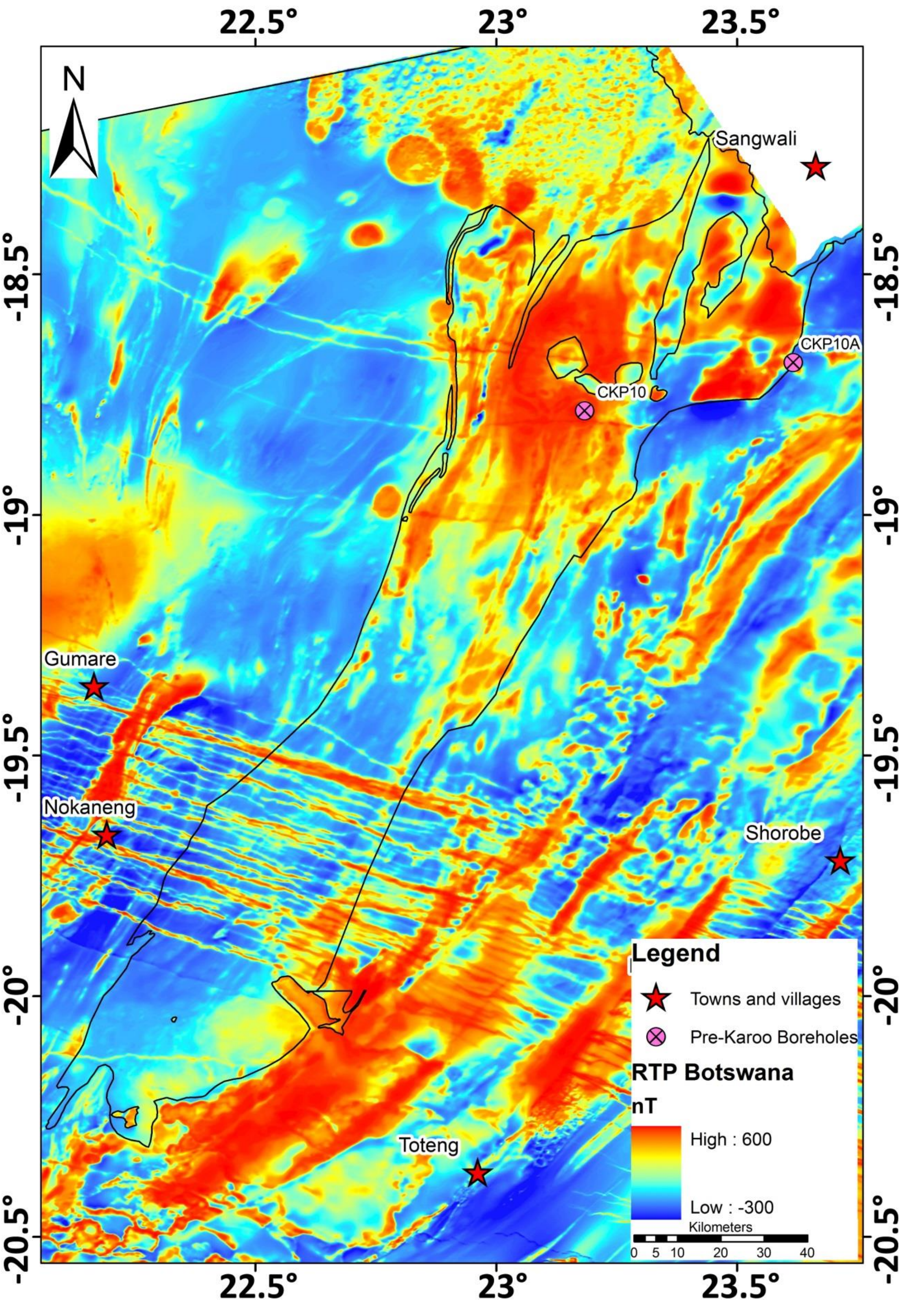

Figure 6.16: RTP image of northern Botswana with the outline of the Kwando Complex interpreted from high-pass data sets. The location of the pre-Karoo boreholes, towns and villages are shown.

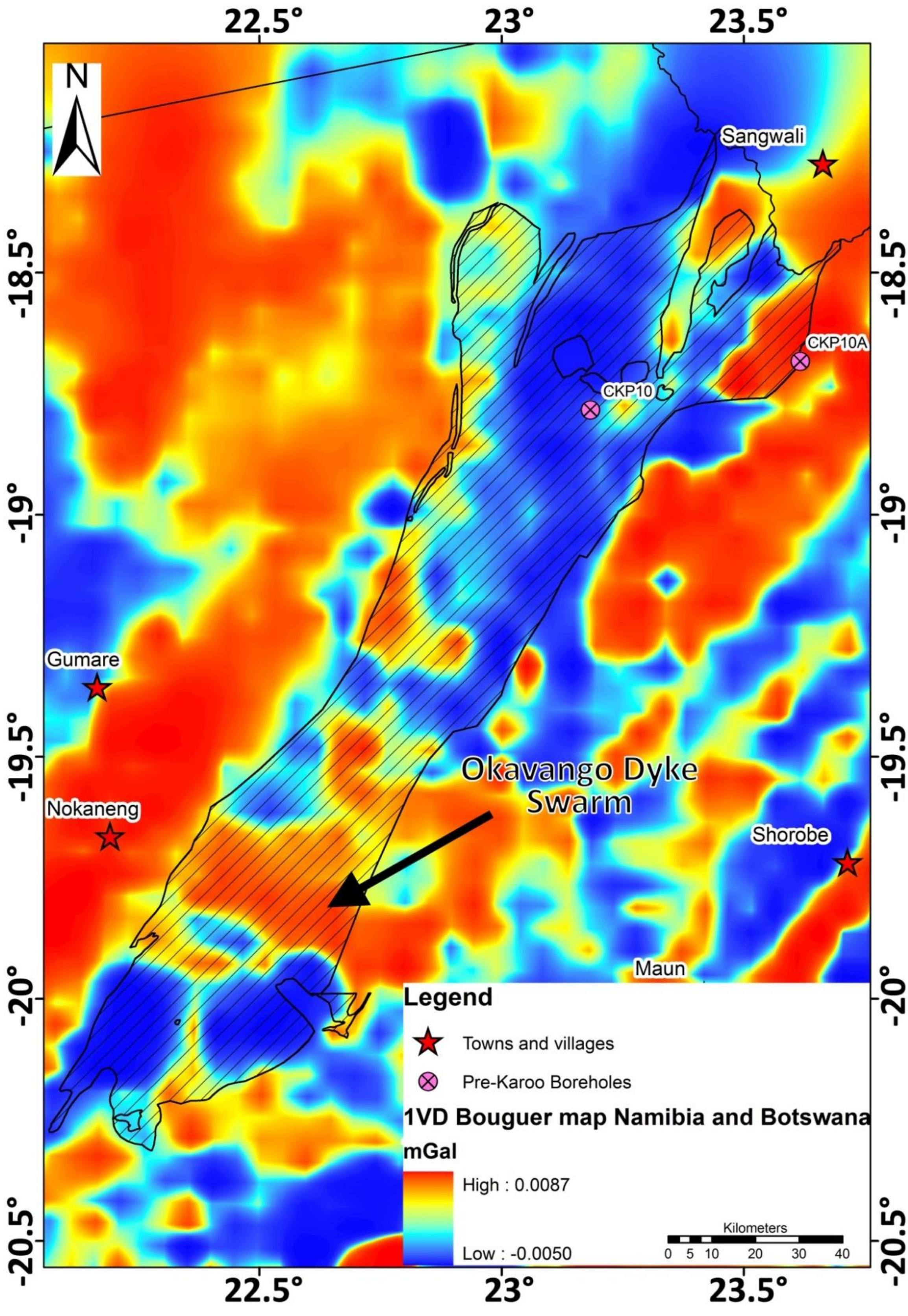

Figure 6.17: First vertical derivative of the Bouguer gravity map overlain by the aeromagnetic interpretation of the Kwando Complex. Note the correlation of the V-shaped northern margin of the complex and the northwest striking higher Bouguer anomaly that is associated with the Okavango Dyke Swarm. Location of the pre-Karoo boreholes, towns and villages are shown.

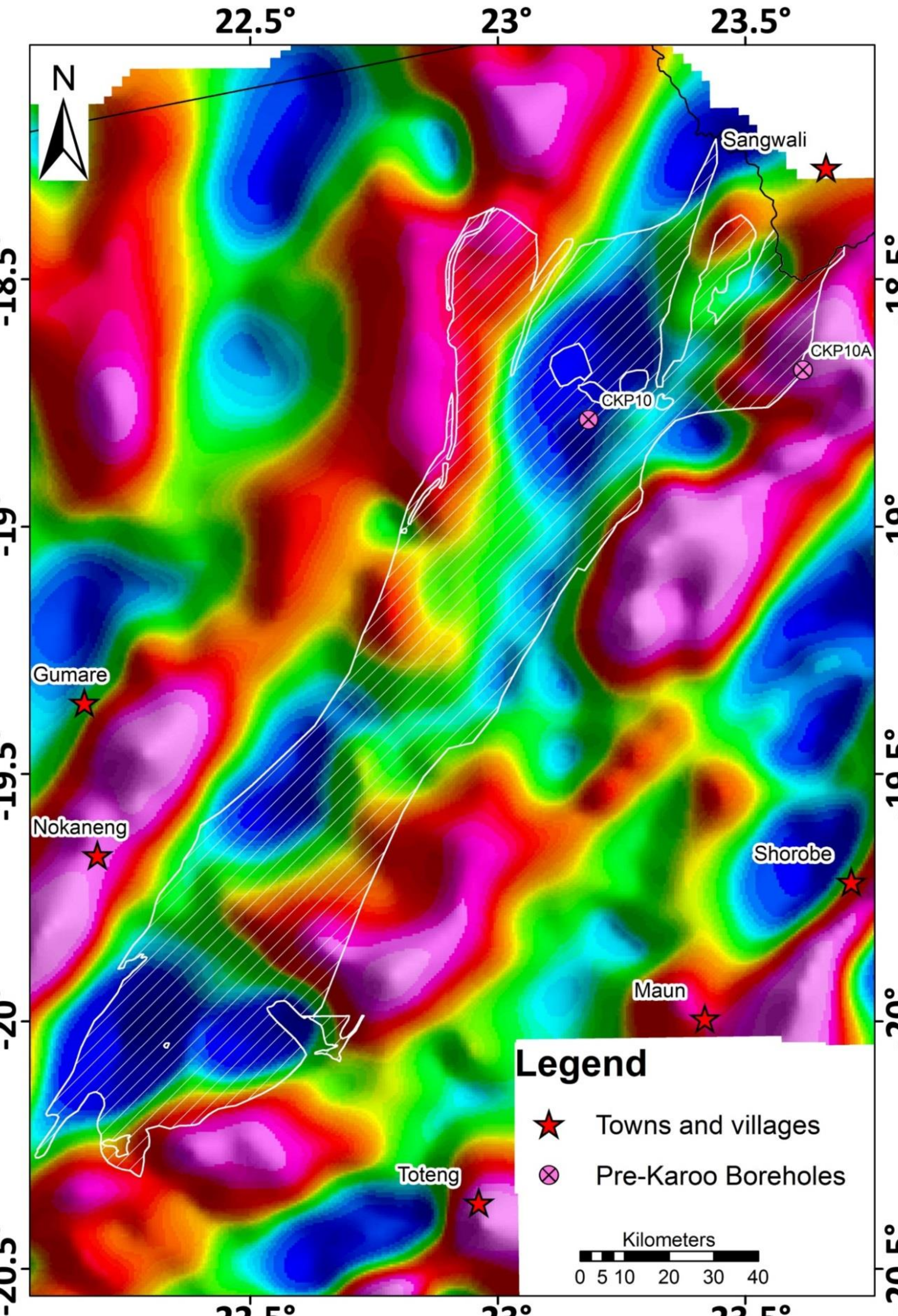

Figure 6.18: Bouguer anomaly map band-pass filtered between wavelengths of 5 km to 100 km overlain by the outline of the Kwando Complex, as interpreted from aeromagnetic data. Note the continuation of the Bouguer gravity signal with the removal of the northwest-southeast striking Okavango Dyke Swarm. Location of the pre-Karoo boreholes, towns and villages are shown.

6.3.4. Koanaka Group

In Botswana, immediately to the northwest of the Roibok Group, Lebung Group (Karoo Supergroup) sediments have been previously demarcated in the 1:250 000 (Pryer *et al*., 1997) and 1:1 000 000 (Key and Ayres, 2000) geological maps. The aeromagnetic signal of this area is characterised by smooth, low amplitudes of -120 nT to -80 nT with northeast-southwest striking higher magnetic amplitude anomalies -20 nT to 20 nT. The aeromagnetic signal is traced southwards into Namibia to ~18.68°E, -21.15°S where it terminates against a heavily deformed terrane. The heavily deformed terrane is associated with randomly orientated and deformed (possibly folded), high magnetic amplitudes of 150 nT to 210 nT. Corner (2000; 2008) interprets this terrane as the Deep-Level Southern Zone of the Damara Belt which consists of pre-Damara rocks. The 1:250 000 Namibian geological map does not extend this far east. The nearest mapped lithological group of Damaran age that lies along strike to the Deep-Level Southern Zone is the Swakop Group of the Southern Zone, which consists of marbles and mica schists with minor amounts of quartzite, greywacke, limestone, dolostone and glaciogenic diamictite.

To the northwest of this zone, lies the Koanaka and Kihabe Hills (Figure 2.19) exposing deformed, greenschist-facies dolomitic marbles of the Koanaka Group (Carney *et al*., 1994; Key and Ayres, 2000; Singletary *et al*., 2003). The 1:125 000 (Pryer *et al*., 1997) and 1:1 000 000 (Key and Ayres, 2000) geological maps interpret the area as consisting of dolomitic marble and poorly exposed granitic gneiss of the Koanaka Group. The Koanaka Group is characterised by a smooth, low magnetic amplitude of -105 nT to -65 nT with subtle northeast-southwest trends associated with slightly higher magnetic amplitude anomalies of -40 nT to -20 nT. As the aeromagnetic signal of the Koanaka Group is very similar to the area immediately to the northwest of the Roibok Group and since the only recorded outcrops are in the vicinity of the Kihabe and Koanaka Hills this report tentatively suggests that this is a single unit consisting dominantly of meta-carbonates of the Koanaka Group. This implies that the Koanaka Group is ~40 km wider than previously mapped by Pryer *et al*. (1997) and Key and Ayres (2000).

The Koanaka Group is divided into a southeastern and northwestern limb by the high magnetic signal associated with the Chihabadum Complex (Figure 6.1 and 6.19). The contact between the younger Koanaka Group and older Chihabadum Complex is structurally controlled, resulting in the Chihabadum Complex being juxtaposed to the Koanaka Group (Key and Ayres, 2000). The southeastern limb has a smooth, low magnetic amplitude of -105 nT to -65 nT compared to the northwestern limb which has a mottled, higher magnetic signal of -50 nT to -20 nT. The higher magnetic amplitude is suggested to be caused by the underlying magnetic basement of either the

Chihabadum or Quangwadum Complexes (Figure 6.19). The northeastern boundary of the Koanaka Group is in contact with the magnetic units of the Tsodilo Hills Group.

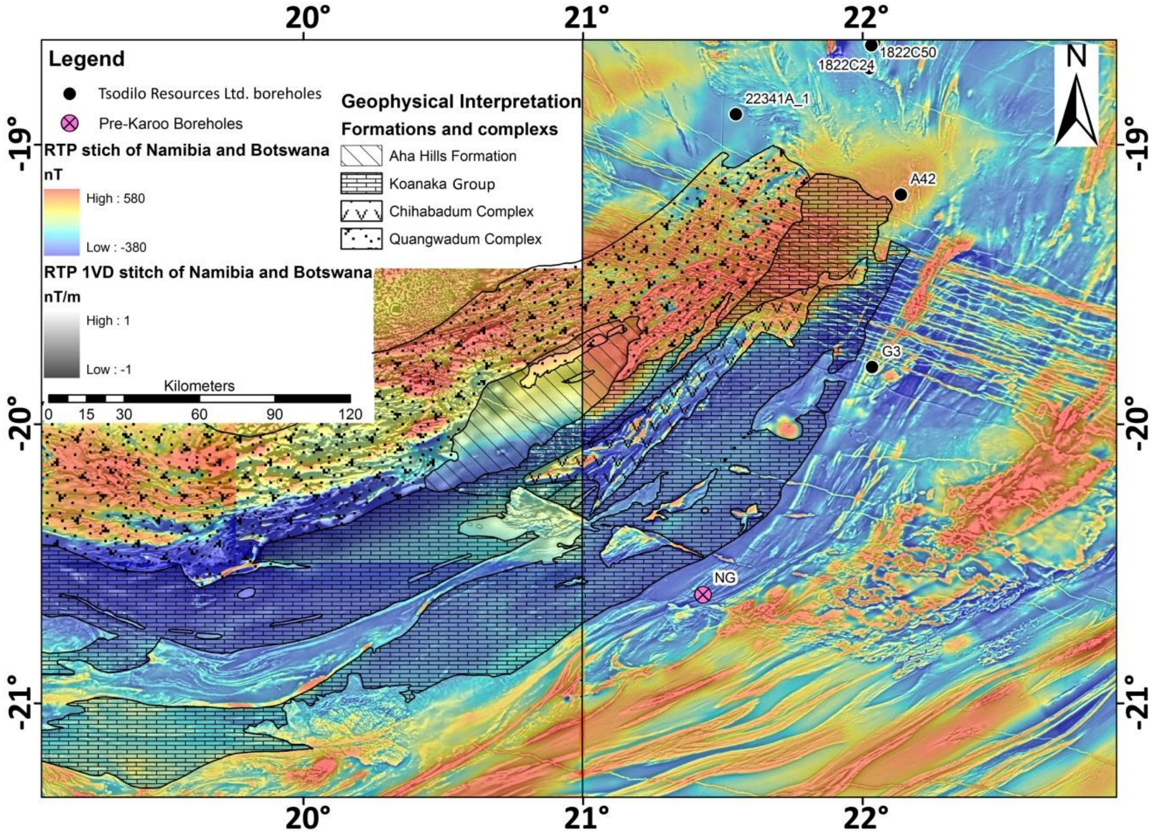

Figure 6.19: Aeromagnetic interpretation, from south to north, of the Koanaka Group, Chihabadum Complex, Aha Hills Formation and Quangwadum Complex. Background is a 50% transparent colour scale RTP image overlain on a 30% transparent greyscale RTP 1VD image of Namibia and Botswana. Location of the pre-Karoo and observed Tsodilo Resources Ltd. boreholes, towns and villages are shown. The solid line represents the political border between Namibia (west) and Botswana (east).

The southeastern limb of the Koanaka Group has a Bouguer gravity signal of ~-115 mGal compared to the ~-130 mGal for the northeastern limb. Even though the difference is only 15 mGal, the paragneisses, which were interpreted by Key and Ayres (2000), are expected to have a similar specific density to the metacarbonates of the Koanaka Group. Possible explanations for the difference in the Bouguer gravity signal are 1) the metacarbonates of the Koanaka Group are shallowly underlain by the meta-igneous to igneous rocks of the Chihabadum Complex, and/or 2) during the uplift of the Chihabadum Complex the dolostones of the Koanaka Group were metamorphosed to marble in the southeast. This metamorphism would lead to an increase in specific density from 2.71 $g.cm^{-3}$ to 2.82 $g.cm^{-3}$.

6.3.5. Chihabadum Complex

The Chihabadum Complex is associated with a low magnetic amplitude of ~-110 nT, consisting of elongated northeast-southwest striking, high magnetic amplitude anomalies reaching 515 nT, which Pryer *et al*. (1997) suggest are younger intrusions (Figure 6.1 and 6.19). According to Key and Ayres (2000), the aeromagnetic signal of the Chihabadum Complex suggests that it comprises igneous to meta-igneous rocks. There are, however, no drill-core samples which intersect the complex to substantiate this interpretation (Singletary *et al*., 2003). The Chihabadum Complex is an elongated northeast–southwest striking complex with the southwestern boundary of the Chihabadum Complex being concaved to the northeast. The northwestern limb extends ~20 km into Namibia while the southeastern limb does not cross the Namibia - Botswana border (Figure 6.19). In the vicinity of the Namibia – Botswana border, the Chihabadum Complex is ~20 km wide and thins northwards to ~8 km beneath the Okavango Dyke Swarm where the aeromagnetic signal is obscured by the higher magnetic amplitudes of the dykes. This results in difficulty in defining the northeastern extension of the complex. Hence, the northern limit of the Chihabadum Complex was determined by the interpretation of the directional filtered image where the complex extends to ~22.00°E, -19.40°S.

The southwestern extension of the complex has a higher Bouguer gravity signal of ~-100 mGal compared to the northeastern extension of ~-120 mGal. This gravity contrast can possibly be caused by the presence of younger intrusions, as suggested by the 1:125 000 geological map (Pryer *et al*., 1997), and/or be caused by the Okavango Dyke Swarm.

6.3.6. Quangwadum Complex

The Quangwadum Complex is characterised by a high magnetic amplitude of 200 nT to 620 nT with well-defined sub-linear northeast-southwest trends (Figure 6.19). Similar to the Chihabadum Complex, a part of the Quangwadum Complex forms a concave contact with the Aha Hills Formation in the southwest, which creates a northwestern and southeastern limb. The northern extent of the Quangwadum Complex is abruptly terminated by a structurally controlled contact with the northwest-southeast striking pronounced aeromagnetic signal of the Tsodilo Hills Group (Figure 6.1). The pronounced aeromagnetic signal of the southeastern limb of the Quangwadum Complex is absent ~15 km away from the political border with Namibia. The northwestern limb of the Quangwadum Complex is traced into Namibia where it correlates with the sub-linear, northeast-southwest striking high magnetic amplitude (500 nT to 720 nT) trends of the

Grootfontein Complex. The complex is associated with a fairly uniform, negative Bouguer anomaly of -150 mGal to-135 mGal which is also traced westwards into Namibia.

In the TMI data of northern Namibia, the northern boundary of the Quangwadum Complex is overlain by a mottled, semi-circular magnetic anomaly (diameter of ~160 km) with two magnetically low zones of -630 nT to -300 nT within its centre (Omatako anomalies), which Corner (2000) terms the Omatako Ring Structure. While in Botswana, the northern boundary is identified by the contrast in the aeromagnetic signal with the Xaudum Group. The Omatako Ring Structure occurs on the intersection of the Kudu, Waterberg Fault/Omaruru Lineament (WF/OL), Khoisan, and Gam Lineaments and the Okavango Dyke Swarm (Corner, 2008). The Omatako anomalies are best evident in the TMI data whereas, the overall structure is best evident in the upward continued data to a height of 1 500 m, which implies that it is a deep-seated anomaly. The Omatako anomalies have been modelled in two ways (models are not provided) by Corner (2008) with identical TMI responses. The first model involves remanent magnetised intrusions and the second involves magnetically inert zones encompassed by lithologies of relatively high magnetic susceptibilities (remanent magnetisation and magnetic susceptibility values used are not provided). As the source of the Omatako anomalies are overlain by extensive Karoo basalts, and the fact that magnetic reversals were common during the Karoo, Corner (2008) favours the former model and that the remanent magnetisations are associated with the Karoo-age intrusions.

On the southern margin of the Omatako Ring Structure, at ~19.70°E, -19.70°S, there is the normally magnetised Daneib Intrusion (Figure 6.1) (Corner, 2008). Through the interpretation of high-pass filtered aeromagnetic images, this study suggests that this intrusion consists of two features 1) a small circular feature (diameter of ~18 km) of magnetic amplitude of 665 nT to 850 nT and 2) an elongated north-northwest striking feature of magnetic amplitude 550 nT to 820 nT (Figure 6.1).

The circular feature lies on the intersection of the Kudu and Khoisan Lineaments (Corner, 2008) (see Table 2.1 for the properties of these geophysical lineaments) and predates the basalts in the area, which are seen to overlie the circular feature (e.g. in the TMI and second vertical derivate). To the southwest, along strike of the circular feature, lies the Early Cretaceous-aged Erongo Complex determined from weighted mean U-Pb zircon age of 135 ± 3.2 Ma for the Ombu Ash Flow Tuff (Piranjo *et al*., 2000). The Erongo Complex lies on the intersection of the Erongo and Welwitschia Lineaments and is also capped by basalts, suggesting that this circular feature is also Cretaceous in age (Corner, 2008).

The elongated feature lies on strike with the Gam Lineament which can be traced southeast into Botswana (Corner, 2008) (Table 2.1 for the properties of this geophysical lineament). From the interpretation of the tilt angle, sunshaded and vertical derivative images, this study suggests the northern part of this elongated feature bends westwards and is traced northwestward to an area where Corner (2008) has interpreted Palaeoproterozoic intrusions including the Grootfontein Complex. This study suggests that this elongated feature marks a near-surface part of the Grootfontein Complex based on the alignment of strike with previously mapped Grootfontein Complex by Corner (2008). This is supported by Grootfontein basement being intersected in water boreholes drilled into the “Danieb Intrusion” (Figure 6.1) (Corner, 2008). To the south of this elongated feature, the Damara Belt suddenly narrows and bends to the south. According to Eberle *et al*. (1996) and Singletary *et al*. (2003) there needs to be an exposed cratonic margin in this region to cause this sudden narrowing and bending. Therefore, this study tentatively suggests that this elongated feature marks the promontory required to cause the Damara Belt to bend.

6.3.7. Aha Hills Formation

The Aha Hills Formation consists of dolostones and chert-rich limestones that are exposed in the Aha Hills (Figure 2.19) (Singletary *et al*., 2003). This study characterises the Aha Hills Formation by a smooth, low to moderate magnetic signal with amplitudes of -20 nT to 320 nT and by Bouguer gravity anomalies of -120 mGal to -130 mGal. The Aha Hills Formation forms an oval shaped feature striking northeast–southwest from Botswana into Namibia (Figure 6.19). The northern boundary of the Aha Hills Formation is in contact with the Quangwadum Complex and the southeastern boundary is in contact with the Koanaka Group (Figure 6.1). The high magnetic anomalies within the Aha Hills Formation are mapped as Quangwadum Complex (Pryer *et al*., 1997; Key and Ayres, 2000).

6.3.8. Northwestern Botswana

Northwest Botswana is divided into three sub-domains (Figure 6.20) based on the radial aeromagnetic signal and difference in metamorphic grade determined from drill core observations of Tsodilo Resources Ltd. boreholes.

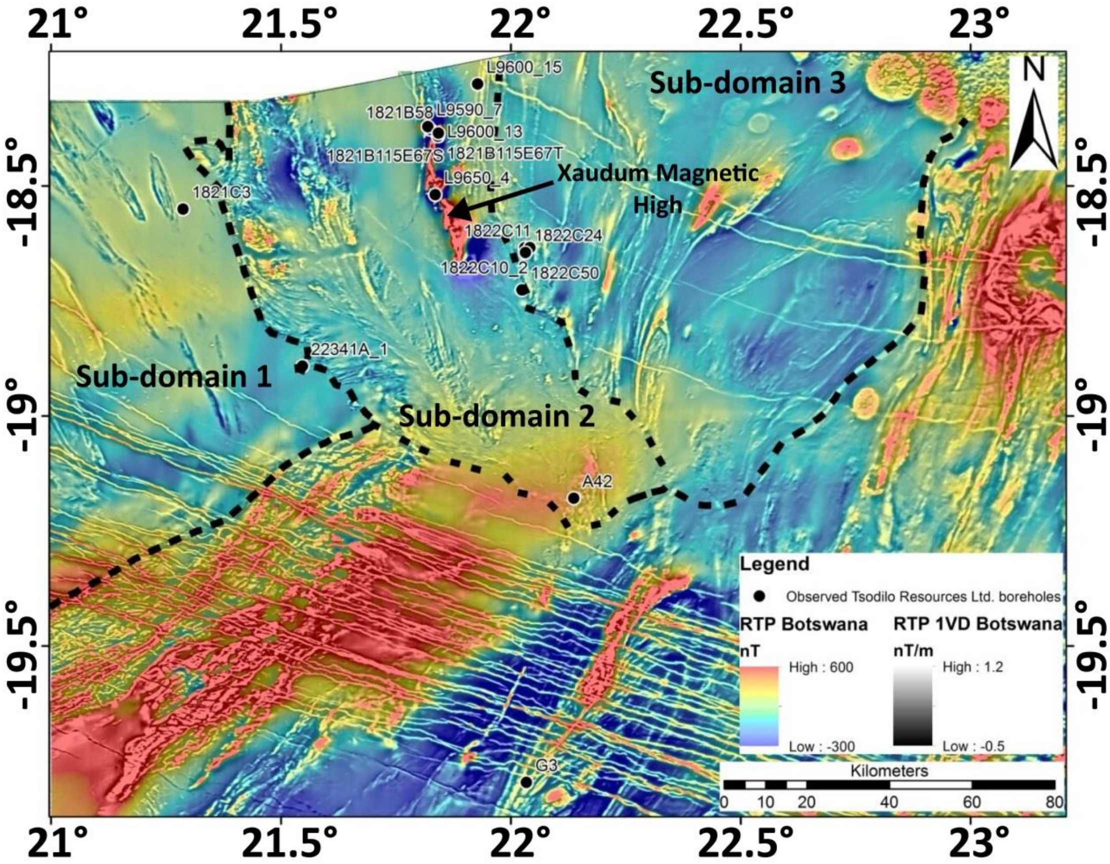

Figure 6.20: Location of studied Tsodilo Resources Ltd. boreholes (black circles with a white halo) and the Xaudum Magnetic High, indicated by the black arrow. Sub-domain 1, 2 and 3 refer to magnetically and metamorphically different domains which are discussed below. Background image is a 50% transparent colour scale RTP image of Botswana overlain on a RTP 1VD greyscale image of Botswana.

Sub-domain 1

Sub-domain 1 corresponds to a smooth, low to moderate magnetic amplitude of -75 nT to 15 nT with minor aeromagnetic foliation produced by localised mottled, alternating magnetic high and low amplitudes of -50 nT to 95 nT (Figure 6.20). The contact with the Quangwadum Complex appears to be transitional (Figure 6.20). The alternating magnetic high and low aeromagnetic amplitudes are interpreted as northwest-southeast trending folds (Key and Ayres, 2000). The low magnetic amplitudes are associated with carbonate units while the high magnetic amplitudes are sandstones or quartzites Kgotlhang *et al*. (submitted). These magnetic folds are also observed in Google Earth images. The sub-domain is characterised by a Bouguer gravity signal that ranges between -105 mGal to -150 mGal.

Geological information of this sub-domain is provided from rock exposures located along the Nxau Nxau and Quangwadum Valleys and borehole 1821C3 (Figure 2.19 and 6.20), which was drilled into a small (~400 m wide and 600 m long), low magnetic anomaly. The borehole intersected shales and carbonates (slatey dolomitic marble) with overturned bedding affected by low-grade greenschist facies metamorphism (Figure 6.21) (Lehmann, *pers. comm*., 2013).

To the southwest of borehole 1821C3, in the Nxau Nxau and Quangwadum Valleys (Figure 2.19) Carney *et al*. (1994), Mapeo *et al*. (2000) and Singletary *et al*. (2003) describe a variety of low-grade carbonates and siliciclastics and iron formations (see Chapter 2 for the descriptions). The smooth, low to moderate aeromagnetic signal is correlated with the carbonates and sandstones of the Xaudum Group while the folded, alternating low and high amplitudes are correlated with ferruginous quartzites and iron formations of the Tsodilo Hills Group (Figure 6.1 and 6.22).

Figure 6.21: Photograph of the low-grade greenschist metamorphism overprinted on shale intersected in borehole 1821C3. Figure 6.22 shows the location of the borehole.

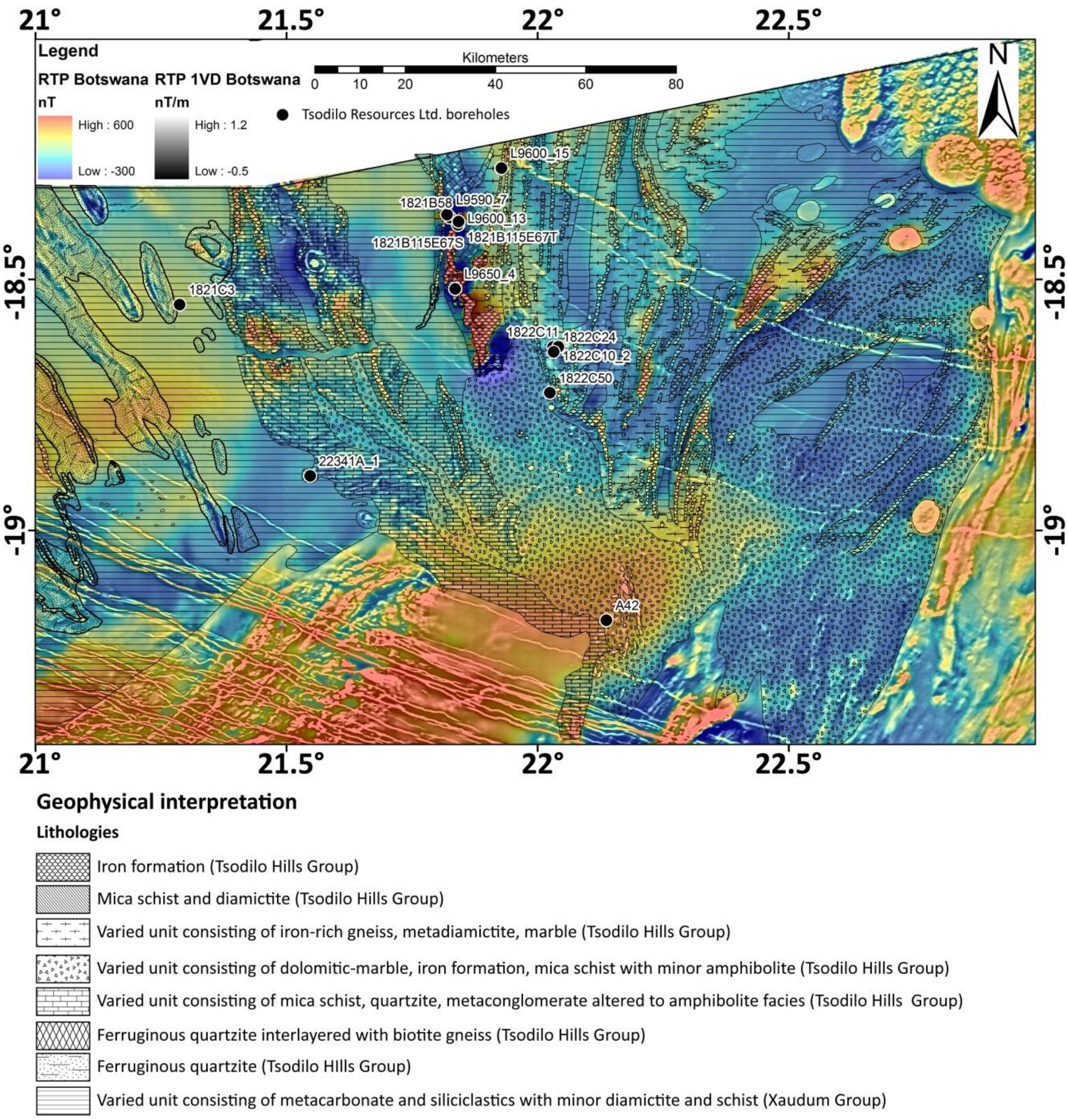

Figure 6.22: Aeromagnetic interpretation of the Xaudum and Tsodilo Hills Groups. Background is a 50% transparent colour scale RTP image overlain on a 30% transparent greyscale RTP 1VD image of Namibia and Botswana. Location of the pre-Karoo and observed Tsodilo Resources Ltd. boreholes and towns and villages are shown.

The 500 m upward continued, sunshaded (inclination = 30°, declination = 150°) image of the northwesternmost part of Botswana displays a prominent north-northeast trending magnetic high anomaly in the range of 80 nT to 110 nT (Figure 6.23a). In the RTP 1VD image the prominent northwest magnetic trend is revealed by the folded units (Figure 6.23b). The low-pass filter enhances deeper magnetic sources compared to the high-pass filter that enhances near-surface magnetic sources. This implies that the northwest trends in the RTP 1VD image is caused by near surface sources which are underlain by the north-northeast trend in the low-passed filter image.

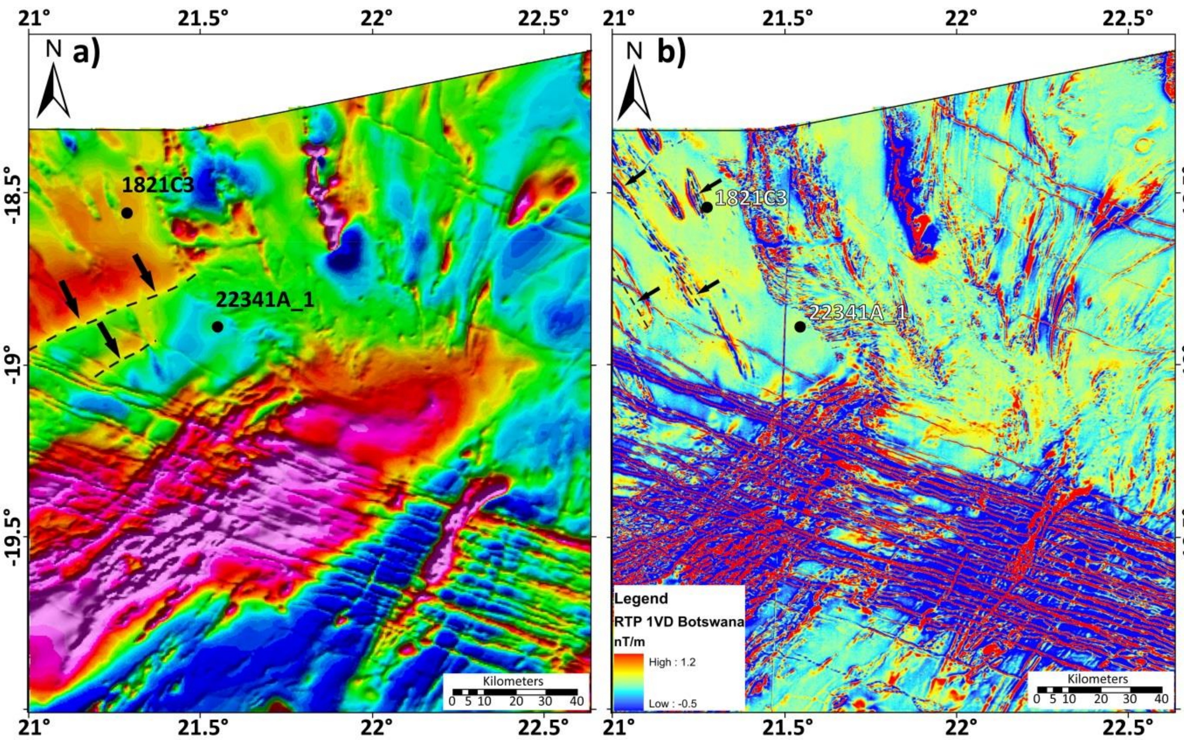

Figure 6.23: Filtered aeromagnetic data of the northwest corner of Botswana. a) RTP 500 m upward continued, sunshaded (inclination = 30° and declination = 150°). b) RTP 1VD. Notice the north-northeast magnetic trend in a) compared to the northwest magnetic trend in b).

The deeper north-northeast striking features are traced into Namibia where the aeromagnetic signal is suppressed by the mottled, negative magnetic amplitude of the central Omatako anomalies (Figure 6.24). The fold intensity of the north-northwest striking folds is greatest above these deeper trends and decreases southwards and to the northeast (Figure 6.23b).

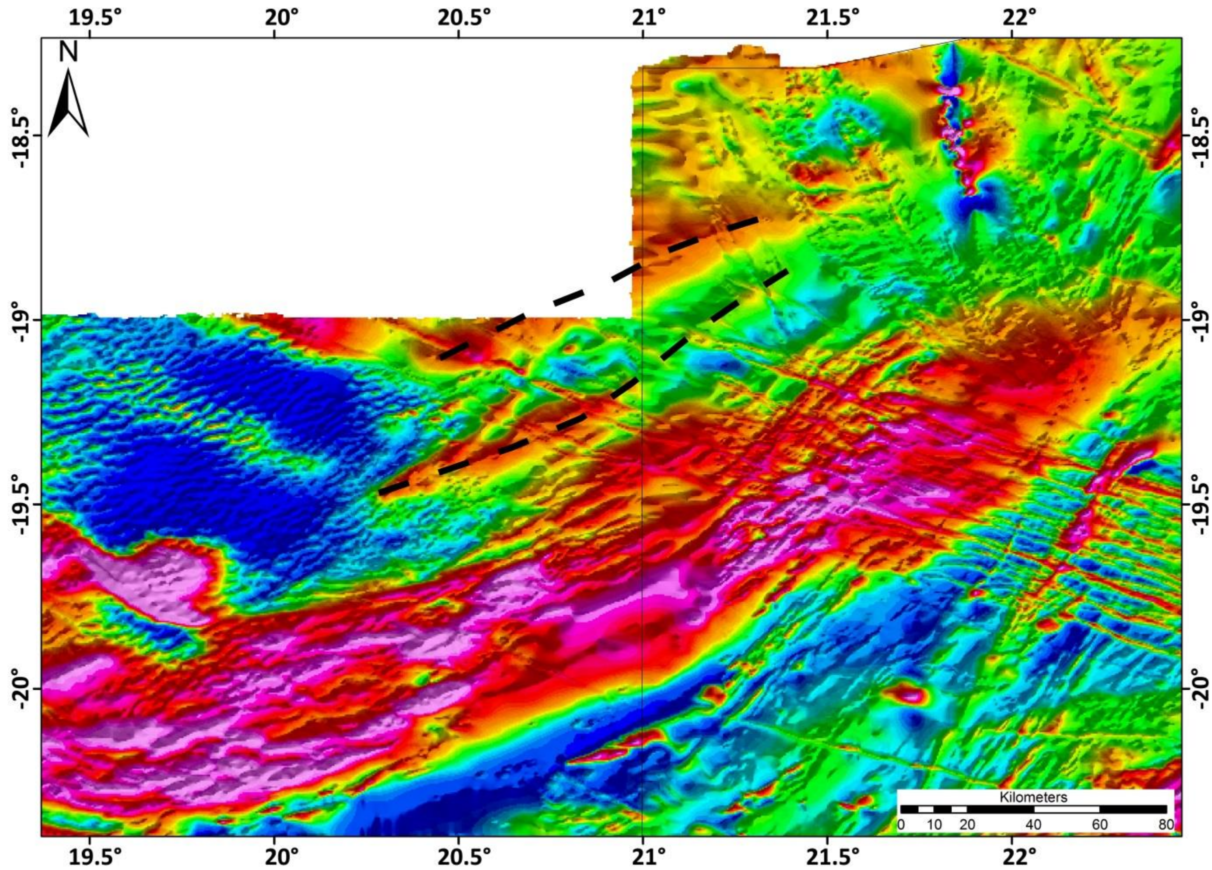

Figure 6.24: RTP sunshaded (inclination = 30° and declination = 150°) image of northeastern Namibia and northwestern Botswana showing the continuation of the north-northeast trending magnetic basement (shown by the dashed black lines). Decorrugation was applied to remove north-south flight lines at the following parameters; the Butterworth filter; cut-off wavelength (in ground units) = 0.02, selected for the intensity of the aeromagnetic signal that needs to be suppressed, filter order = 2 and low pass filter. The parameters of the directional cosine filter are; centre direction in space domain = 180° i.e. the direction in which the signal must be suppressed, degree of cosine function = 1 and rejection of the aeromagnetic signal that falls in the range of the above listed parameters. The solid line represents the political border between Namibia (west) and Botswana (east).

Sub-domain 2

Sub-domain 2 is separated from sub-domain 1 by a north-northwest striking zone with a distinct aeromagnetic signal, which can be described as a “fern-like” pattern (northeast of borehole 22341A_1 on Figure 6.23 and 6.25). The geology of this “fern-like” pattern is determined from outcrops in the Tsodilo Hills, in the vicinity of Shakawe Village and borehole 22341A_1 drilled into the southwestern part of this distinctive aeromagnetic pattern (Figure 6.25).

This is a high-grade metamorphic domain deformed to possibly amphibolite facies with kyanite and garnet as the typical metamorphic index minerals. This sub-domain is characterised by an intercalation of magnetically smooth, inert and noisier, higher magnetic anomalies with a dominant north-south to northeast-southwest strike (Figure 6.25). The general aeromagnetic amplitude of this sub-domain, with the exception of the Xaudum Magnetic High, is ~-175 nT to -375 nT. The Xaudum Magnetic High, as termed in mining literature, is a pronounced north-south striking aeromagnetic feature that has a magnetic amplitude of ~225 nT to 2 500 nT (Figure 6.25) and a Bouguer gravity signal between ~-145 mGal to -105 mGal.

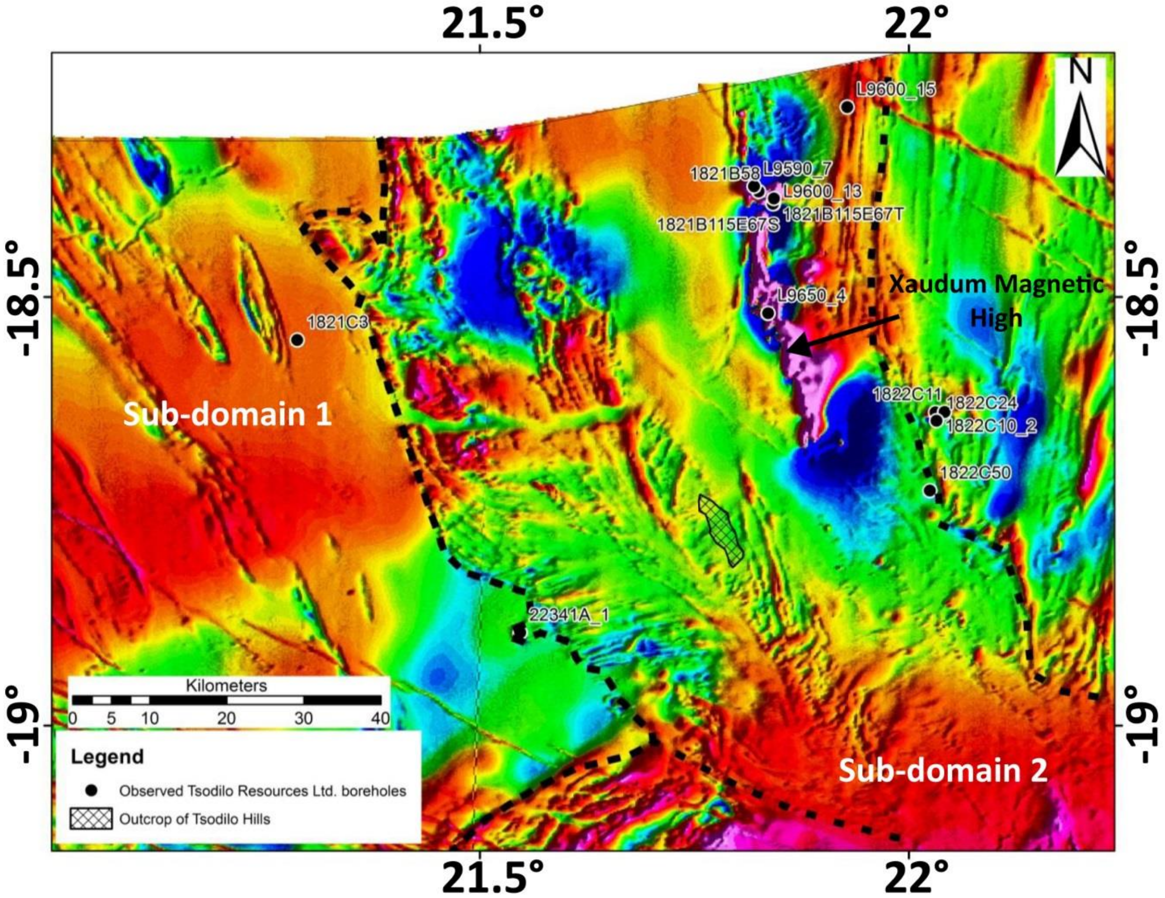

Figure 6.25: Aeromagnetic sunshaded map (inclination = 20°, declination = 110°) of the contact between sub-domain 1 and sub-domain 2. Location of observed boreholes drilled by Tsodilo Resources Ltd. (black circle with a white halo) and the Xaudum Magnetic High. Clearly visible is the “fern-like” pattern in the vicinity of the Tsodilo Hills (hashed area). Note the radial structure trend, from northwest trending in the west to northeast trending in the east.

The Tsodilo Hills, located near the eastern margin of the aeromagnetic “fern-like” pattern comprise Tsodilo Hills Group schists and meta-silicates and iron formations metamorphosed to kyanite-grade facies (Figure 6.25) (Carney *et al*., 1994; Key and Ayres, 2000; Singletary *et al*., 2003; Wendorff, 2005). Rock exposures in the vicinity of Shakawe Village include biotite gneisses and ferruginous quartzites that are tightly folded (Key and Ayres, 2000).

In addition to borehole 22341A_1, another borehole, to the southeast of the “fern-like” pattern, drilled into a sub-linear magnetic high anomaly, is borehole A42 (Figure 6.22). Borehole 22341A_1 is ~90 m deep and intersected, from bottom to top, glaciogenic metadiamictite overlain by a metacarbonate with an interleaving contact. The metadiamictite and metacarbonates contain clasts of biotite-schist that are locally isoclinally folded (Figure 6.26). Borehole A42 intersected mica schist containing mostly white micas with minor bluish mica, which could not be confidently identified, and garnet porphyroblasts which is interpreted as a glaciogenic metadiamictite containing only quartz clasts.

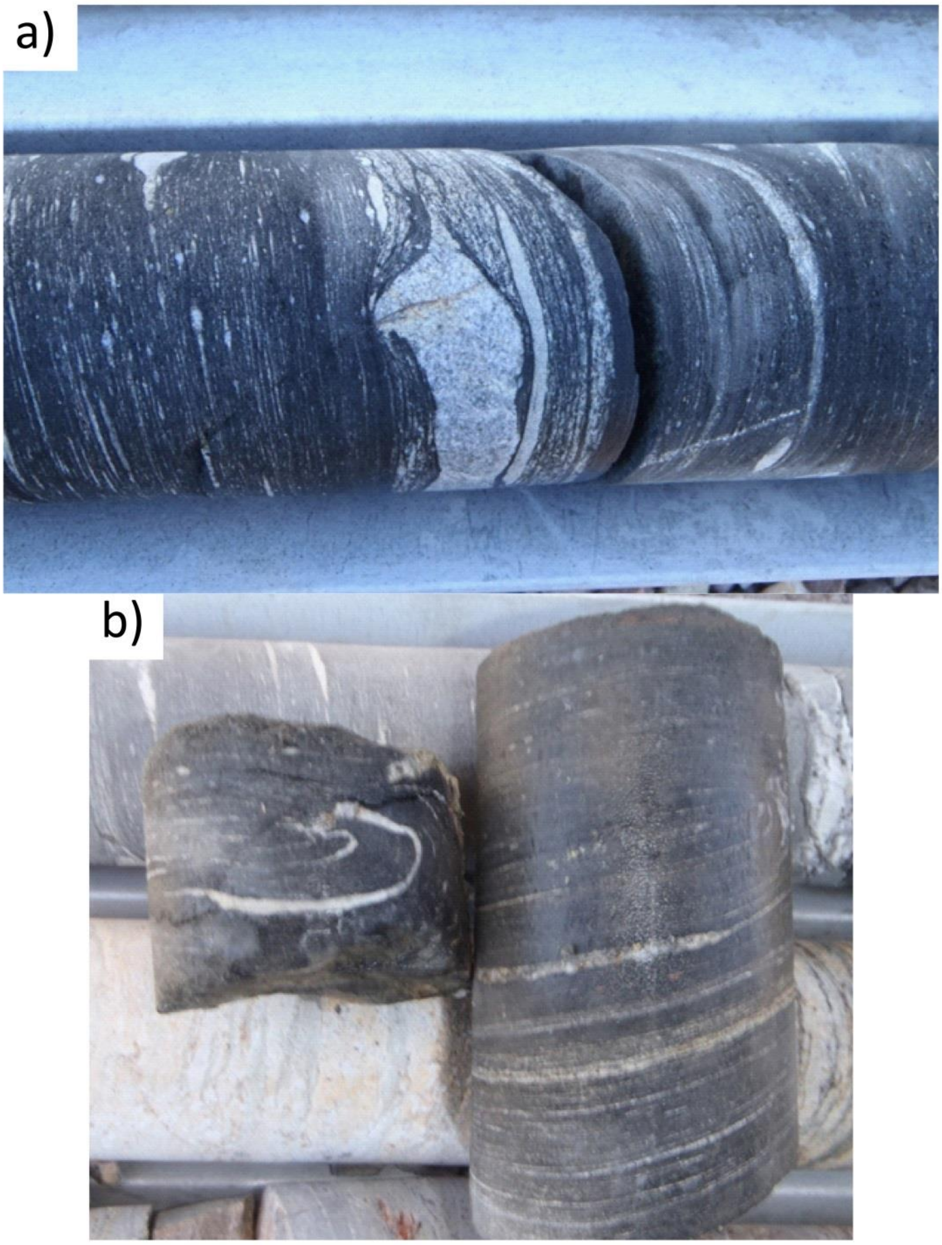

Figure 6.26: Drill core from borehole 22341A_1. (a) Meta-diamictite with clasts of biotite schist in a fine-grained matrix. (b) Isoclinal folding in the biotite schist. Location of borehole is shown in Figure 6.25.

The western and eastern margins of the "fern-like" pattern have a similar aeromagnetic signature. Both Pryer *et al*. (1997) and Key and Ayres (2000) have mapped the western side as Karoo volcanics while the eastern side has been mapped as Xaudum Group consisting of ferruginous quartzite and ironstone by Pryer *et al*. (1997) and Tsodilo Hills Group by Key and Ayres (2000). The aeromagnetic signature suggests that these are near-surface occurrences of magnetic-bearing metamorphic and/or igneous rocks that are strongly deformed. However, as there are no recorded major deformation events post-Karoo it is unlikely that the Karoo volcanics would be this heavily deformed and hence, the cause of the magnetic signal.

The core from ten boreholes, which were drilled on the eastern margin of this sub-domain, was provided for analysis by Tsodilo Resources Ltd. (Figure 6.22 and 6.25). Nine of these boreholes were drilled into and around the Xaudum Magnetic High with a single borehole 1822C50 to the south-southeast (Figure 6.25). The boreholes in the vicinity of the Xaudum Magnetic High mainly intersected heavily folded metacarbonates, iron-rich rocks and metadiamictite with clasts of carbonate, granitoid and mica schist with minor garnet-amphibolite, gneiss and garnet-rich mica schist. Borehole 1822C50 intersected amphibolite locally containing garnets, and minor amounts of micaceous quartzite, magnetite-bearing metacarbonate, mica schist and metadiamictite and granitic gneiss. The amphibolites that do not contain garnets can be very coarse-grained and can possibly be termed metagabbro.

Magnetic susceptibility measurements recorded from borehole L9 590_7, which contains garnet-bearing glaciogenic metadiamictites yielded an average susceptibility of 1.46×10^{-3} SI units. Assuming that the susceptibility of the glaciogenic metadiamictites in borehole L9 590_7 and A42 (Figure 6.22) are similar, the high aeromagnetic signal in the vicinity of borehole A42 are assigned as glaciogenic metadiamictites of the Tsodilo Hills Group and the low amplitudes, of ~-20 nT, as a varied unit consisting mostly of dolomitic-marble, mica schist and iron formation with minor amphibolite of the Tsodilo Hills Group (Figure 6.1 and 6.22). Therefore, this study associates the western and eastern margins of the "fern-like" pattern as varied lithologies consisting mainly of quartzite, meta-conglomerate and mica schist altered to amphibolite facies of the Tsodilo Hills Group while the smoother aeromagnetic signal of the centre of the "fern-like" pattern and eastern margin of the sub-domain as a varied unit consisting mainly of dolomitic-marble, mica schist and iron formation with minor amphibolite. The localised, linear, high magnetic amplitudes are assigned as iron formations of the Tsodilo Hills Group (Figure 6.1 and 6.22). The moderate to low aeromagnetic amplitudes with randomly oriented high magnetic amplitudes in the Shakawe Village area are associated with the ferruginous quartzite and biotite schist.

^{207}Pb-^{206}Pb dating on five zircon grains sampled from a basement granite-gneiss from borehole L9660_5 yielded a weighted mean age of 2 596 ± 110 Ma (Gaisford, 2010). The borehole log of borehole L9660_5 suggests that the granite-gneiss overlies a metapelite with foliation derived during the Pan-African Orogeny (Gaisford, 2010). This suggests that the granite-gneiss has been thrust over the younger Pan-African metasediments.

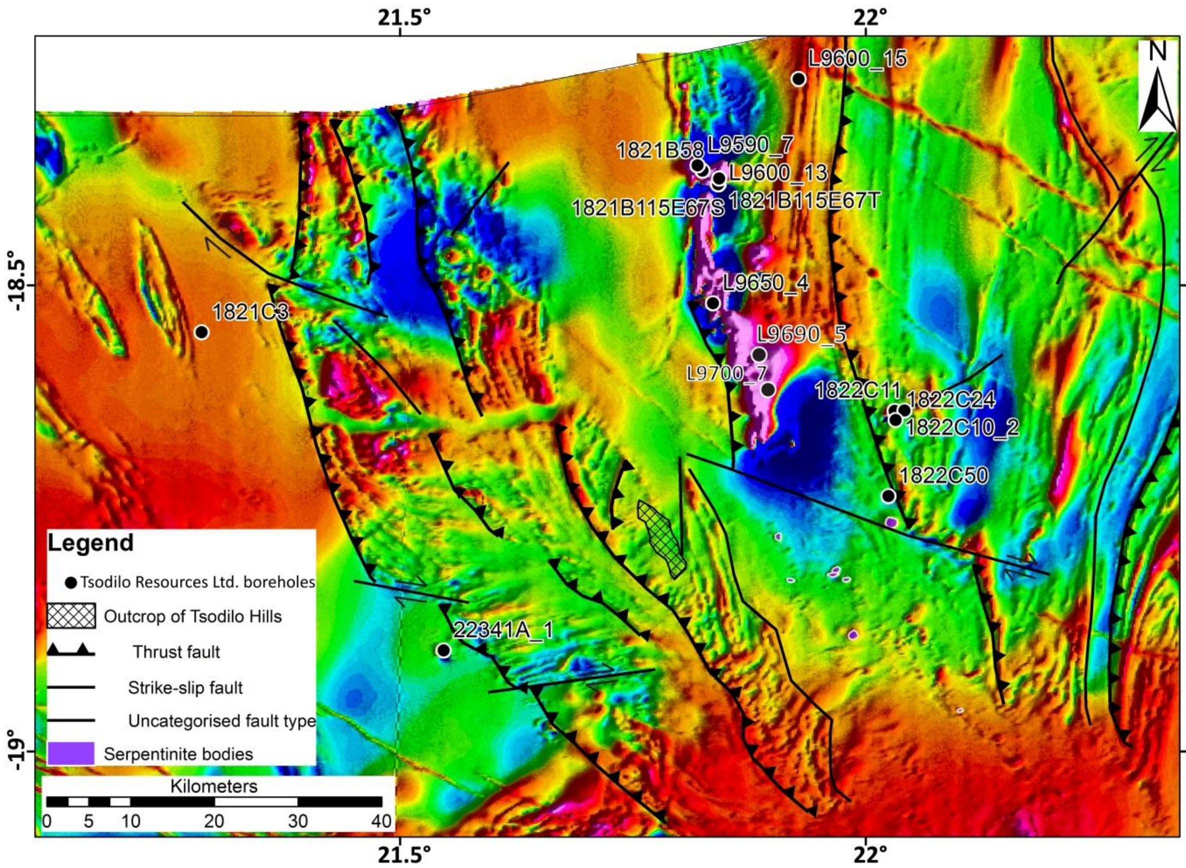

Figure 6.27: RTP Aeromagnetic sunshaded image (inclination = 20° and declination = 110°) of the Tsodilo Hills area, northwest Botswana. Major structural features are interpreted predominantly from the RTP 1VD and sunshaded data sets (modified after Kgotlhang, 2008).

In borehole L9700_7, the amphibolite-gneiss basement is overlying a graphitic schist. This suggests that the amphibolite-gneiss was thrust across the graphitic schist into its current position during tectonic stacking subsequent to amphibolite-facies metamorphism. This is supported by airborne time-domain electromagnetic data that shows a dipping conductive zone (blue in Figure 6.28) (Kgotlhang, 2008). According to Miller (2008), the soft nature of the graphitic shale is often exploited as thrust planes. In the Tsodilo Hills, to the southwest of these boreholes (Figure 6.27), Wendorff (2005) mapped numerous shear zones, a small amount of small-scale reverse faults and a major thrust fault that resulted in the strata being displaced to the southwest.

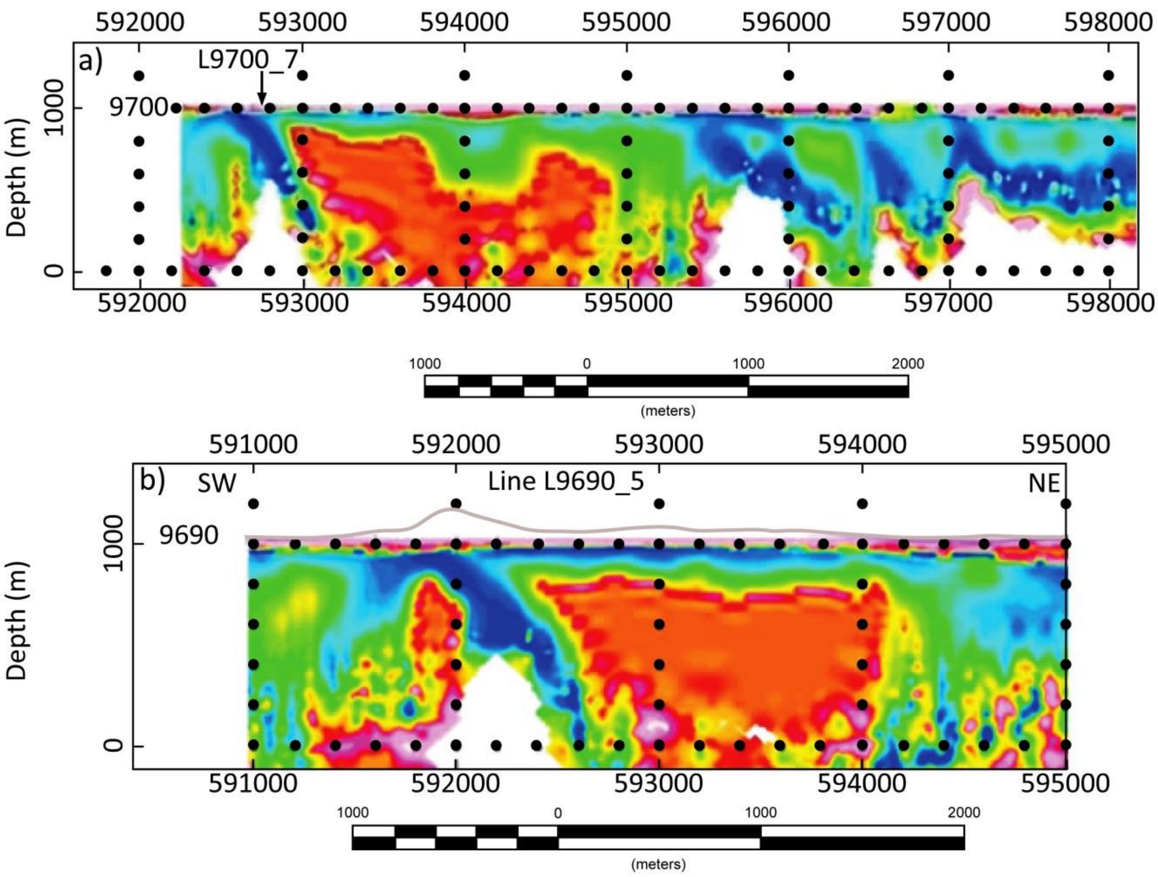

Figure 6.28: Airborne time domain electromagnetic profiles (after Kgotlhang, 2008). Conductive zones are represented by the blue colours and resistive zones by red colours. Drilling into the conductive zones has intersected either graphitic shale or mineralised metapelites. The black dots represent a spacing of 200 m. a) Profile across borehole L9700_7. b) Profile across borehole L9690_5. Locations of boreholes are displayed in Figure 6.27.

Therefore, from the interpretation of the aeromagnetic data and the above mentioned studies, a number of thrust, strike-slip and unknown faults are suggested in sub-domain 2 (Figure 6.27). The thrust faults are associated with repetitive higher magnetic amplitudes (directly to the east of the thrust) followed by lower magnetic amplitudes (further to the east), as seen from the RTP 1VD aeromagnetic data of Botswana. The strike-slip faults were determined by the displacement of the thrust faults and dykes. The unknown faults are characterised by a non-unique magnetic signal (e.g. a sudden change in the magnetic signal). As a result, any structural feature interpreted on the eastern boundary of the fern-like feature, with a magnetic signal that does not follow the magnetic signal described for thrust or strike-slip faulting, is assigned as an unknown fault.

To the east of the lower part of the "fern-like" pattern and south of the Xaudum Magnetic High, Tsodilo Resources Ltd. has drilled boreholes into serpentinite-composed small semi-circular to circular (~1 km in diameter) magnetic high anomalies of 35 nT to 170 nT during kimberlite exploration (Figure 6.27). In the vicinity of these known serpentinite bodies are other circular magnetic high anomalies that are yet to be drilled by Tsodilo Resources Ltd. but are assumed to also be serpentinite bodies by Kgotlhang (2008). These magnetic anomalies are aligned to the southeast of the thrust faults defined by Kgotlhang (2008) (Figure 6.27).

A combination of the structural interpretations of sub-domain 1 and 2 have shown that an easterly amphibolite facies is juxtaposed to the east with low-grade greenschist facies rocks to the west along structures orientated northwest-southeast (Figure 6.27). These structures are the observed folds, sheared folds verging to the southeast in the Tsodilo Hills (Wendorff, 2005) as well as the thrust faults (Kgotlhang, 2008) (Figure 6.28). The association of an eastward inverted metamorphic sequence with a style of folding-thrusting that has allowed exhumation of amphibolite facies and Archaean basement rocks on top of greenschist facies rocks, is suggested by a west to southwest directed ductile thrusting of an (in this case "thick-skinned") orogenic core over an external orogenic area.

The problem with mutual relationships between sub-domain 1 and 2 with respect to the northeast strike of the Damara Orogen is addressed by Kgotlhang (2008). The geophysical signature suggests that these structures do not continue south of 19.5°S, 22.0°E (Kgotlhang, 2008). In map view these structures seem to follow a radial distribution with a rotation axis centred on 19.5°S, 22.0°E (i.e. the northeastern extension of the Quangwadum Complex), from northwest-striking in the west to northeast-striking in the east. The low-pass filtered aeromagnetic data suggest that the main crustal structural grain is northeast striking (Figure 6.23b). The radial structural grain is only visible in the high-pass filtered aeromagnetic data sets (Figure 6.23a). This may illustrate the indentation of a rigid block represented by sub-domain 1, during east-west to southwest-northeast shortening forming at the indenter front the exhumation of deep-seated rocks and farther from the indenter, to the east, a smooth rotation of the Damara trend from the original northeast to north-northeast strike. Even if the indenter is not well identified in the geophysics, it appears that the Quangwadum Complex is a good candidate, providing that the complex continues below the overlain metasediments of sub-domain 1. This would assume that the westward directed fold-shearing postdates the typical northwest-southeast Damara shortening which is suggested to be reflected in the diachronous cooling ages at ~530 Ma in the northeast striking belt versus ~490 Ma in the north-south striking area (age dates of Singletary *et al*., 2003).

Sub-domain 3

Sub-domain 3 is characterised by an intercalation of magnetically smooth, inert and noisier, high aeromagnetic anomalies with a dominant north-northeast to northeast strike produced by the sub-linear, high magnetic amplitude anomalies (Figure 6.20). The general aeromagnetic amplitude for the high amplitude anomalies is 180 nT to 330 nT while the magnetically inert regions have amplitudes between -100 nT to -20 nT. The Bouguer gravity signal of sub-domain 3 is between -105 mGal to -75 mGal. Sub-domain 3 is separated from sub-domain 2 by a thrust fault that is interpreted by the sudden termination of the high amplitude magnetic anomalies.

The metamorphic grade of this sub-domain cannot be easily determined as there are no exposed outcrops but is estimated as being at amphibolite facies because of the indicator minerals (kyanite and garnet) intersected in the boreholes. Borehole data is provided from four boreholes located near the western margin of sub-domain 3 (Figure 6.20). Pryer *et al*. (1997) suggest that the magnetically inert amplitudes are a combination of the Xaudum Group consisting of carbonates, shales and sandstones, and Karoo sediments while the magnetic high anomalies are Xaudum Group consisting of ferruginous quartzite and ironstone (Chuos equivalent). Key and Ayres (2000) assign the western margin of this sub-domain as Tsodilo Hills Group consisting of ferruginous and micaceous quartzite, quartz-mica schist, metamorphosed conglomerate, minor shale, phyllite, sandstone and ironstone and the eastern margin as Karoo volcanics and sediments and Roibok Group consisting of amphibolite, magnetite-schist and granitic gneiss.

Borehole L9600_15 was drilled into a sub-linear north-northeast striking magnetic high lineament and intersected oxidised, iron-rich graphitic schist that locally contains massive pyrite and pyrrhotite mineralisation, overlying a biotite schist. Metamorphic grade can be estimated from the presence of garnet and kyanite. Borehole 1822C11 was drilled into a small semi-circular magnetic high anomaly and intersected a schist containing a coarse-grained bluish mineral (kyanite?) underlain by a possible meta-tuff. Boreholes 1822C24 and 1822C10_2 were drilled into the lower magnetic anomaly and intersected meta-carbonates and glaciogenic metadiamictites with minor iron formation (Figure 6.20 and 6.27). Approximately 23 km to the southeast of this group of boreholes, is borehole 1822C26_1 which was drilled into a magnetic anomaly of ~100 nT. It intersected a meta-mafic rock that yielded a ^{207}Pb-^{206}Pb weighted mean age of 541 ± 14 Ma from six concordant zircons (Gaisford, 2010).

Therefore, from the aeromagnetic signal and borehole data, the western margin of sub-domain 3 is suggested to dominantly comprise glaciogenic metadiamictite, gneiss and meta-carbonate of the Tsodilo Hills Group. The sub-linear, high magnetic amplitudes are interpreted as either iron formation of the Tsodilo Hills Group or possibly a meta-mafic rock (Figure 6.22). As the aeromagnetic signal of the eastern margin of sub-domain 3 is similar to the aeromagnetic signal of sub-domain 2, and there are no available boreholes or outcrops, it is suggested to be dominantly dolomitic-marble, mica schist and iron formation with minor amphibolite of the Tsodilo Hills Group (Figure 6.22).

6.3.9. Karoo Supergroup and circular features

From the interpretation of the sub-Kalahari geological map, a number of Karoo-aged igneous lithologies are identified from the different aeromagnetic signals and orientation of the magnetic fabric (Table 6.1). These were termed Karoo basalts, Karoo volcanics or Late Karoo dolerites from the nomenclature of the 1:1 000 000 geological map of Key and Ayres (2000). In addition, there are a number of circular to semi-circular features that have either a positive or negative magnetic amplitude; these have been previously interpreted as either Neoproterozoic granites or Pan-African intrusions. As there is no additional information on these features the nomenclature of Key and Ayres (2000) is followed. Previously unidentified circular to semi-circular features, however, are termed according to the closest circular to semi-circular feature. There are a number of small, ~500 m wide, high amplitude, ~120 nT, semi-circular to circular features, which have been suggested as possible kimberlite or serpentinite bodies in northwest Botswana through the boreholes of Tsodilo Resources Ltd.

6.4. Discussion

The cross-border correlation process between Namibia and Botswana involves characterising the nature and amplitude of the potential field signal of the various lithotectonic domains (Table 6.1). Magnetic markers are traced to define these domains where these lithotectonic domains are traced across the political border. Correlations are proposed based on the cratonic affinity of the Proterozoic basement. To constrain the cratonic affinity of the magnetic events, the Umkondo intraplate magnetic event is referred to. The Umkondo intraplate magmatic event (1 112 Ma to 1 106 Ma) (Hanson *et al*., 1998, 2004) is a Large Igneous Province that is restricted to the Kalahari Craton (Hanson *et al*., 1998; Powell *et al*., 2001). However, there is an overlap with early ages of the Irumide Orogeny (Congo Craton affinity), Zambia, which can reach 1 100 Ma but typically is between 1. 09 Ga to 1.02 Ga (Johnson *et al*., 2006). The next line of evidence used is the Bitter Spring carbon excursion (Halverson *et al*., 2005, 2010). According to Halverson *et al*. (2005) the Bitter Spring carbon excursion occurred between 802 ± 10 Ma and 777 ± 7 Ma. This carbon anomaly is used to constrain the time of deposition of the metasedimentary sequences of the Ghanzi Group. However, it is not known if the isotope signature is a primary signal or if it has been altered from the later deformation events. The worldwide Sturtian glaciation (Halverson *et al*., 2005, 2010) led to the deposition of glaciogenic diamictites that occurred in both inverted passive margins of the Khomas Ocean and northwest Botswana. In the Damara Orogen, Sturtian glaciation is regarded as being represented by the Chuos diamictites (Killick, 1986; Bühn *et al*., 1992; Hoffman and Prave, 1996; Hoffman *et al*., 1996; Halverson *et al*., 2005; Miller, 2008; Miller *et al*., 2009a) dated at ~745 Ma (Hoffman *et al*., 1996). According to Bühn *et al*. (1992) and Singletary *et al*. (2003) there is no evidence for glacial deposits in northwest Botswana. However, glaciogenic diamictites are interpreted in the borehole core of Tsodilo Resources Ltd. The diamictites are associated with iron-rich strata which has a pronounced aeromagnetic signal that is used in the correlation of the tectonostratigraphic zones. A second glacial diamictite horizon related to the Marinoan glaciation is only dated in the Central Zone of the Damara Belt at 635.5 ± 1.2 Ma (Hoffmann *et al*., 2004). This was used to constrain the deposition of higher stratigraphic sequences within the Neoproterozoic rocks.

In Botswana, where the post-Ghanzi Group sediments are less than ~1 600 m thick (as in the Aranos-Nosop Basins, accumulated thicknesses are determined from Kalahari Group (up to 270 m, Haddon, 2001), Karoo Supergroup (between 641 m to 785 m, Nxumalo, 2013) and Nama Group (> 1 000 m, Key and Ayres, 2000), the typical aeromagnetic signal of the rocks of the Ghanzi-Chobe Belt can be depicted on the aeromagnetic images as northeast trending folds extending from the Goha and Chinamba Hills to the Namibia – Botswana border (Figure 2.19, Table 6.1). The geophysical continuation of these folds into Namibia is challenging because of the increase in sedimentary cover in the Aranos and Nosop Basins where the folds of the Ghanzi-Chobe Belt are suppressed by the overlying lithologies (Figure 6.1). Even though the folds can be traced across the political border into Namibia in the aeromagnetic data, this is does not provide a confident link between the rocks of the Ghanzi-Chobe Belt and their correlatives in Namibia.

The Kgwebe Formation is correlated with the Oorlogsende Porphyry Member, in eastern Namibia, based on similar U-Pb zircon age dates and rhyolitic composition (Figure 6.29 and 6.30) (Schwartz *et al*., 1995; Modie, 1996). The Oorlogsende Porphyry Member has been correlated with the Nückopf Formation, in the Rehoboth Subprovince, near Klein Aub, by Hegenberger and Burger

(1985) as single samples from the Nückopf Formation yielded U-Pb zircon ages in the range of 1 010 Ma to 1 172 Ma and has a similar volcanic assemblages (Figure 6.29). This led Borg (1987) and Borg and Maiden (1989) to correlate the Kgwebe Formation with the Nückopf Formation. However, ages of ~1.2 Ga has been determined for the Nückopf Formation by Burger and Coertze (1978), Schneider *et al*. (2004) and Becker and Schalk (2008). From the stratigraphic review in Chapter 2, this study favours a correlation between the Kgwebe Formation and the Langberg Formation (Sinclair Supergroup) (Figure 6.29 and 6.30). This correlation is based on both of these volcanic units being dated at ~1.1 Ga, both are dominantly felsic with metasedimentary layers and have been metamorphosed to lower greenschist facies. Geochemical analyses and field observations of the Kgwebe Formation suggest that the sequence was emplaced in a continental rift basin, which was initiated by extensional tectonics associated with a continental collision along the Namaqua-Natal Belt (Kampunzu *et al*., 1998; Modie, 2000). Unfortunately, to date there is no geochemical analysis of the Oorlogsende Porphyry Member in order to determine its emplacement environment.

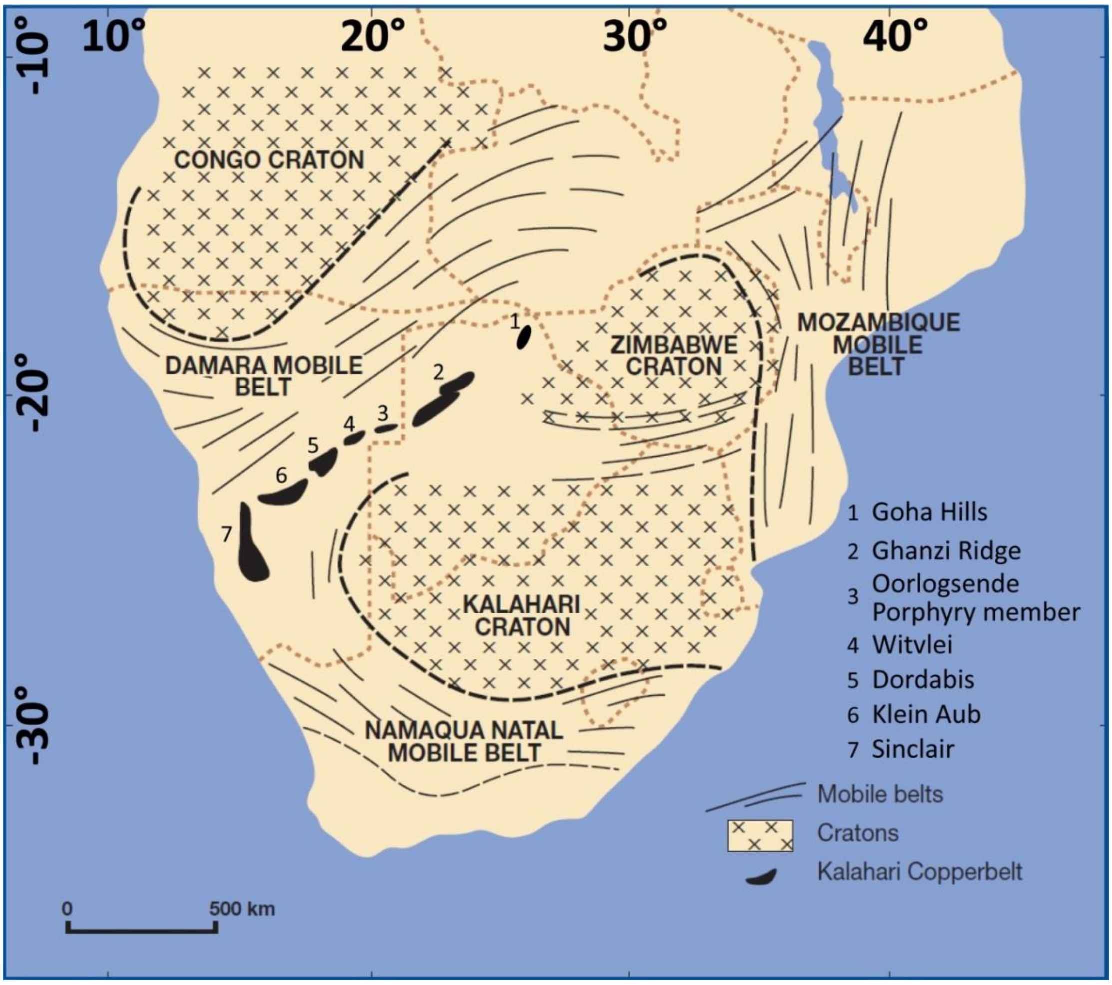

Figure 6.29: Location and tectonic map of southern Africa showing the position of the Ghanzi-Chobe Belt (black polygons) (modified after Borg, 1987, 1988; Modie, 2000; Maiden and Borg, 2011).

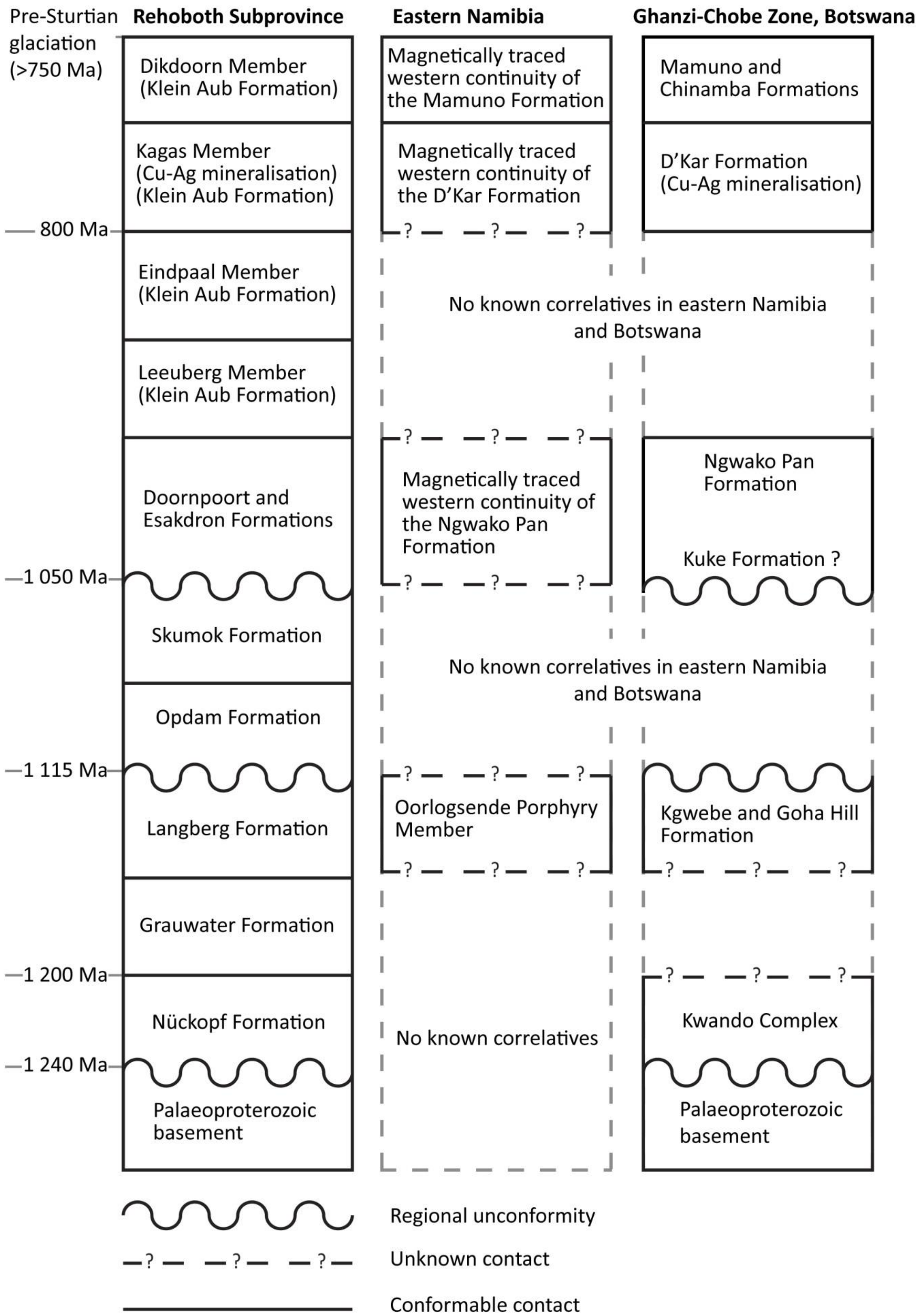

Figure 6.30: Tectonostratigraphic cross-border correlations of the Kalahari Copper Belt based on geophysical and geological evidence.

The correlation of the unconformably overlying metasedimentary rocks is more challenging because of the lack of datable volcanic rocks within the metasediments in both Namibia and Botswana. The deposition of the Ghanzi Group is bracketed between 1 047 ± 24 Ma (youngest detrital zircons) (Kampunzu *et al*., 2000) and ~750 Ma (U-Pb zircon age for felsic rocks from the Ghanzi-Chobe Belt) (Ramokate *et al*., 2000). The approximate depositional date of the Ghanzi Group is further defined at the base of the D'Kar Formation by the Bitter Springs carbon excursion, which occurred at ~800 Ma to 780 Ma (Halverson *et al*., 2005, 2010). This permitted Master *et al*. (2012) to bracket the Kuke and Ngwako Pan Formations between ~1 050 Ma and 800 Ma, and the upper part of the D'Kar and overlying Mamuno Formations to ~780 Ma and 750 Ma, respectively. Carbon isotope work by Walraven and Borg (1992) on a limestone sample from the Kagas Member (Klein Aub Formation) yielded a $\delta^{13}C$ anomaly of -0.77 and -0.46 ‰ V-PDB, which may resemble the Bitter Springs anomaly. In the Rehoboth Subprovince and Ghanzi-Chobe Belt copper mineralisation occurs discontinuously for ~800 km (Borg and Maiden, 1989). In the Ghanzi-Chobe Belt this mineralisation occurs at the redox boundary between the Ngwako Pan and D'Kar Formations (Modie, 2000), while in the Rehoboth Subprovince the mineralisation occurs in the Kagas Member (Borg and Maiden, 1989).

The metasediments are correlated on similar stratigraphic position, lithologies and aeromagnetic signal because of the lack of age data. This study correlates the lower part of the Doornpoort Formation with the Kuke Formation based on the basal conglomerate unit hosting clasts of the respective basement rocks which is overlain by quartzite intercalated with red-bed sedimentary rocks (Figure 6.30). This correlation is reinforced by the correlation of the Ngwako Pan Formation with the upper part of the Doornpoort Formation, both consisting of a thick package of clastic rocks (Figure 6.30). In addition, both the Ngwako Pan and Doornpoort Formations are characterised by smooth, negative amplitude, medium to low frequency magnetic anomalies (Table 6.1). The correlation of the lower part of the Ghanzi Group with the Doornpoort Formation is in agreement with sedimentological correlations of Borg and Maiden (1989) and Modie (1996).

The copper-silver mineralised Klein Aub Formation is correlated with the mineralised D'Kar Formation (Figure 6.30). The mineralisation is localised within and immediately below the reduced horizons which formed in the deepest environments where rocks in both countries record the Bitter Spring carbon excursion, implying that deposition occurred at ~800 Ma to 780 Ma. This correlation is also based on similar lithological units such as siltstones and mudstones interbedded with fine-grained sandstones and limestone units. In addition, both units are defined by sub-linear to linear, positive, high magnetic amplitudes (Table 6.1).

Chemostratigraphy suggests that the Mamuno Formation was deposited pre-750 Ma. In Namibia, trace fossils *Treptichnus* and *Planolites ichnogenera* found in the lower parts of the Kamtsas Formation suggest an age less than 750 Ma (Schwartz *et al*., 1995). This age was interpreted as being the minimum age of the Ghanzi and Nosib Groups, and was reinforced by a U-Pb zircon age of 756 ± 2 Ma for a syenite that intruded the Lower Nosib Group (Hoffman *et al*., 1996) as well as felsic lavas, which occur at the top of the Nosib Group, with ages of 728 ± 40 Ma, 746 ± 2 Ma and 750 ± 65 Ma (Hoffman *et al*., 1996). The lowermost formation of the Witvlei Group (overlying the Nosib Group), is the Blaubeker Formation. The Blaubeker Formation consists of diamictite and paraconformably overlies the Kamtsas Formation. According to Schwartz *et al*. (1995) the pebble beds at the top of the Mamuno Formation are either diamictite equivalents to the Blaubeker Formation or else a younger lithological unit. However, the above correlations do not include the regional unconformity noted by Miller (1983a, 2008) at the base of the Kamtsas Formation. There has been no noted unconformity within the Ghanzi Group (Modie, 1996, 2000). This led Modie (1996) to correlate the Mamuno Formation with the upper formations of the Klein Aub Formation. Therefore, even though both the Kamtsas and Mamuno Formations are associated with variable internal frequencies, moderate to low amplitude, northeast trending, sub-linear magnetic textures (Table 6.1), this is not enough to confidently correlate the two formations. Therefore, this study suggests that the Mamuno Formation is correlated with the Dikdoorn Member (top of the Klein Aub Formation) based on lithological similarities and stratigraphic position (Figure 6.30). However, another scenario is that the Mamuno Formation pinches out immediately after crossing into Namibia or that its equivalent is not exposed in Namibia.

There are two known amphibolite occurrences in the study area, the Matchless Member (Namibia) and Roibok Group (Botswana) (Figure 6.1). Reeves (1978a) was one of the first to propose a link between the Matchless Member and the Roibok Group based on their alignment of strike in the aeromagnetic data. The correlation of these two units is supported by their similar MORB-like and within-plate compositions (Miller, 1983a; Breitkopf and Maiden, 1988; Lüdkte *et al*., 1986, in Carney *et al*. 1994). However, correlating the Roibok Group with the Matchless Member, which is in contact with schists of the Kuiseb Formation, presents two lines of evidence suggesting that there was a lateral change in thermal and structural history in the Damara Belt in the vicinity of the Namibia – Botswana border (Carney *et al*., 1994). The first would relate to the occurrence of migmatitic and gneissic layers present in the Roibok Group and not in the Matchless Member, which suggests a southeast displacement of Pan-African geotherms in Botswana relative to Windhoek (Carney *et al*., 1994). The second relates to the tectonic position of the Roibok Group being in contact with the Ghanzi-Chobe Belt; this contact indicates that the equivalent lithologies of the Southern Margin Zone of the Damara Belt do not occur in Botswana (Carney *et al*., 1994). An alternative view proposed by Carney *et al*. (1994), is that the Roibok Group correlates with pre-Damaran lithologies and that the resemblance with the Matchless Member is a coincidence. Corner (2008) states that the Matchless Member cannot be geophysically or geologically mapped east of 18.15°E, -21.85°S where it is cross-cut by the Kudu Lineament, which is associated with uplift to the east resulting in the Matchless Member not being geologically or geophysically mapped to the east of the lineament.

There are no reliable age dates for the Matchless Member with a minimum Rb-Sr emplacement age of 765 ± 37 Ma (Hawkesworth *et al*., 1981) and an Sm-Nd isochron age of 711 ± 35 Ma (Nagel, 1999). The Roibok Group has a ^{207}Pb-^{206}Pb zircon crystallisation age of 716.8 ± 2.2 Ma (Singletary *et al*., 2003). As the Matchless Member is in contact with the Kuiseb schist, constraining its maximum emplacement age is to ~635 Ma, corresponding to the Marinoan glaciation (Ghaub Formation), which predates the latest formations of the Swakop Group. In addition, the minimum age of spreading in the Damara Belt is constrained by the emplacement of the syn-tectonic granites (Salem-type Granites) at ~600 Ma (Marlow, 1983; Miller *et al*., 2009a; Frimmel *et al*., 2011). The Roibok Group is in contact with the carbonates of the Koanaka Group, which this study suggests is younger than ~635 Ma based on its correlatives in Namibia (discussed later).

In the high resolution aeromagnetic data, the outer margins of the Matchless Member are characterised by linear to sub-linear, positive, high magnetic amplitudes, while within these margins the magnetic response ranges from a relatively moderate amplitude to a high amplitude, noisy, mottled magnetic texture (Table 6.1). Approximately 20 km west-southwest of Windhoek, this signal can be up to 6 km wide, while to the east of Windhoek the signal thins drastically before being lost within the Steinhausen anomaly. The Roibok Group is characterised by linear, high amplitude anomalies relative to a smooth, lower amplitude background anomaly (Table 6.1). The alignment of the linear, high magnetic amplitude markers suggests that the Roibok Group formed in a high strain domain. In the Bouguer gravity map the Roibok Group is associated with an elongated, northeast-southwest striking gravity low of ~-70 mGal to -100 mGal while, because of the thin size of the Matchless Member and the coarse grid spacing of the gravity data, no confident gravity signal can be assigned to the Matchless Member.

This study suggests that the Matchless Member and Roibok Group were emplaced in a similar setting, most likely during the rifting of the Khomas Ocean, however a clear correlation between these two units cannot be confidently made with the limited age dates, of both the Matchless Member and Roibok Group, and limited exposure of the Roibok Group.

The Kwando Complex is an unexposed terrane estimated to have been emplaced between 1.20 Ga to 1.15 Ga (Singletary *et al*., 2003). It is impossible to directly trace the northeast continuation of the Kwando Complex because of the near-surface, high amplitude magnetic signal of the Karoo volcanics which obscures the aeromagnetic signal of the Kwando Complex. The southwest continuation of the Kwando Complex further into Botswana is, however, obscured by Karoo volcanics and thick Neoproterozoic and younger cover in the Nosop Basin and Northwest Botswana Rift (Reeves, 1978a; Key and Mapeo, 1999; Singletary *et al*., 2003). The Nauzerus Group (Sinclair Supergroup), further along strike to the southwest, has been affected by similar dated tectonothermal events. These rocks record regional metamorphism, ductile deformation and pre- to synorogenic magnetism at ~1.23 Ga to 1.10 Ga (Burger and Coertze, 1978; Schneider *et al*., 2004; Becker and Schalk, 2008). Other Mesoproterozoic events are recorded in the Abbabis Complex of 1.33 Ga to 1.03 Ga (Kröner *et al*., 1991) and in the Gamsberg Granitic Suite of 1.22 Ga to 1.04 Ga (Burger and Coertze, 1975; Pfurr *et al*., 1991; Nagel, 1999).

The Bouguer anomaly signal of the Nauzerus Group and Abbabis Complex could not be determined because they form small, discontinuous inliers. Comparison of the aeromagnetic signals rules out a possible correlation between the Kwando Complex and Abbabis Complex (Table 6.1). The aeromagnetic signal of the Kwando Complex, Nauzerus Group (Nückopf Formation) and Gamsberg Granitic Suite are similar i.e. smooth, low to moderate amplitude with higher magnetic amplitudes defining a magnetic trend (Table 6.1). The main zircon population of ~1.1 Ga for the Gamsberg Granitic Suite suggests that it is part of a younger volcanic event compared to the Nückopf Formation and Kwando Complex as the Nückopf Formation and Kwando Complex have their main zircon population between ~1.20 Ga to 1.15 Ga. Both the Nückopf Formation and Kwando Complex consist of a bimodal volcanic composition and have been intruded by younger intrusions at ~1.1 Ga (the Nückopf Formation by the Gamsberg Granitic Suite and the Kwando Complex by the Goha Hills Formation). Therefore, the Kwando Complex is tentatively suggested to have formed in a similar setting to the Nückopf Formation, which is either within-plate or volcanic arc (Becker *et al*., 2008) (Figure 6.30).

Carney *et al*. (1994) and Kgotlhang *et al*. (submitted) suggest that the Central Zone pinches out within Namibia, which results in the merging of the Northern and Southern Zones to form a single zone that continues into Botswana (Figure 2.30). This resulted in the Koanaka Group being correlated with the Noas or Karibib Formations (Vaalgras Subgroup), Southern Margin Zone by Carney *et al*. (1994) or a more general correlation by Kgotlhang *et al*. (submitted) with the Swakop Group of the Southern Zone. The correlation of Carney *et al*. (1994) was based on dolostones and calc-silicate rocks forming a minor component of the Kuiseb Formation and is better represented in the Vaalgras Subgroup and mapping of Miller and Schalk (1980), which correlates the Koanaka Group with the Vaalgras Subgroup. There are no age dates for the Koanaka Group, Noas and Karibib Formations. The Noas Formation is speculated as being equivalent to the Ghaub Formation in the north (Miller, 2008), which suggests an age of ~635 Ma (Hoffmann *et al*., 2004).

Interpretation of the aeromagnetic data, suggests that the smooth, low with a minor magnetic foliation of the Koanaka Group can be divided into a northern and southern limb (Figure 6.1). The northern limb correlates both spatially and geophysically (smooth, low to moderate magnetic amplitude with minor foliation) with the eastern continuation of the northern Central Zone, while the southern limb correlates spatially and geophysically with the eastern continuation of the Southern Zone below cover as identified by Corner (2008) and Miller (2008) (Figure 2.4). Corner (2008) associates the low magnetic amplitude of the northern Central Zone to the Karibib marble and schist, calc-silicate and marble of the Usakos Subgroup, while the low magnetic amplitude of the Southern Zone is caused by the Kuiseb schist. On the northern edge of the Southern Zone and southern edge of the southern Central Zone is the Tinkas Formation, the lateral equivalent of the Karibib Formation, north of the Okahandja Lineament (Miller *et al*., 2009a). Therefore, this study suggests that the Koanaka Group is correlated with the Karibib Formation and its lateral equivalent, the Tinkas Formation, based on similar lithologies and aeromagnetic signal.

To the north of the Koanaka Group is the Aha Hills Formation (Figure 6.19). The carbonates of the Aha Hills Formation appear different from the carbonates of the Koanaka Group and crop out in a more deformed part of the orogen (Carney *et al*., 1994). One of the earliest cross-border correlations of the Aha Hills Formation was with either the Northern Platform or Northern Zone, based on similar northwest verging fold structures (Loxton Hunting and Associates, 1981; in Carney *et al*., 1994). Later studies suggested that the Aha Hills Formation is better correlated with the Otavi Group of the Northern Platform (Carney *et al*., 1994; Key and Ayres, 2000; Singletary *et al*., 2003). Carney *et al*. (1994) based his interpretation on the works of Wright (1957), who recognised that the chert-dolostones of the Aha Hills Formation are similar to those in the Otavi Group of the Northern Platform, and Stalker (1983), who tentatively suggested that the Aha Hills Formation and Abenab Subgroup (Otavi Group) share similar styles of Pb-Zn mineralisation.

The Aha Hills Formation may possibly represent the cap carbonate sequence of either the Chuos (Rastof/Berg Aukas Formations) or Ghaub (Maieberg Formation) Formations. This study favours a correlation with the Keilberg Member (base of the Maieberg Formation) based on (1) the lack of iron-rich lithologies in the Aha Hills Formation and (2) the Ghaub Formation being pyritic and lacking primary iron oxides in an upper sandstone and shale succession (Figure 6.31). The presence of pyrite and low iron contents is typical of carbonate-hosted lead-zinc deposits, which Stalker (1983; in Carney *et al*., 1994) notes for the Aha Hills Formation. There are no direct age dates for either the Aha Hills Formation or Keilberg Member to constrain this correlation. Singletary *et al*. (2003) dated one of the shear zones between the Aha Hills Formation and Quangwadum Complex at 533.3 ± 2.9 Ma. This provides a maximum depositional age for the Aha Hills Formation as pre-535 Ma. The maximum age of deposition of the Keilberg Member is constrained by the maximum age of deposition of the Maieberg Formation, from $\delta^{13}C$ values of between -5 to -3 ‰ V-PDB (Hoffman and Schrag, 2002), which suggests an age of ~636 Ma to 620 Ma (Figure 6.32). In addition, the top of the Tsumeb Subgroup can be constrained at ~600 Ma because of the positive carbon isotope excursion of ~8 ‰ V-PDB in the lower Hüttenberg Formation (Figure 6.32) (Halverson, 2002; Hoffman and Halverson, 2008).

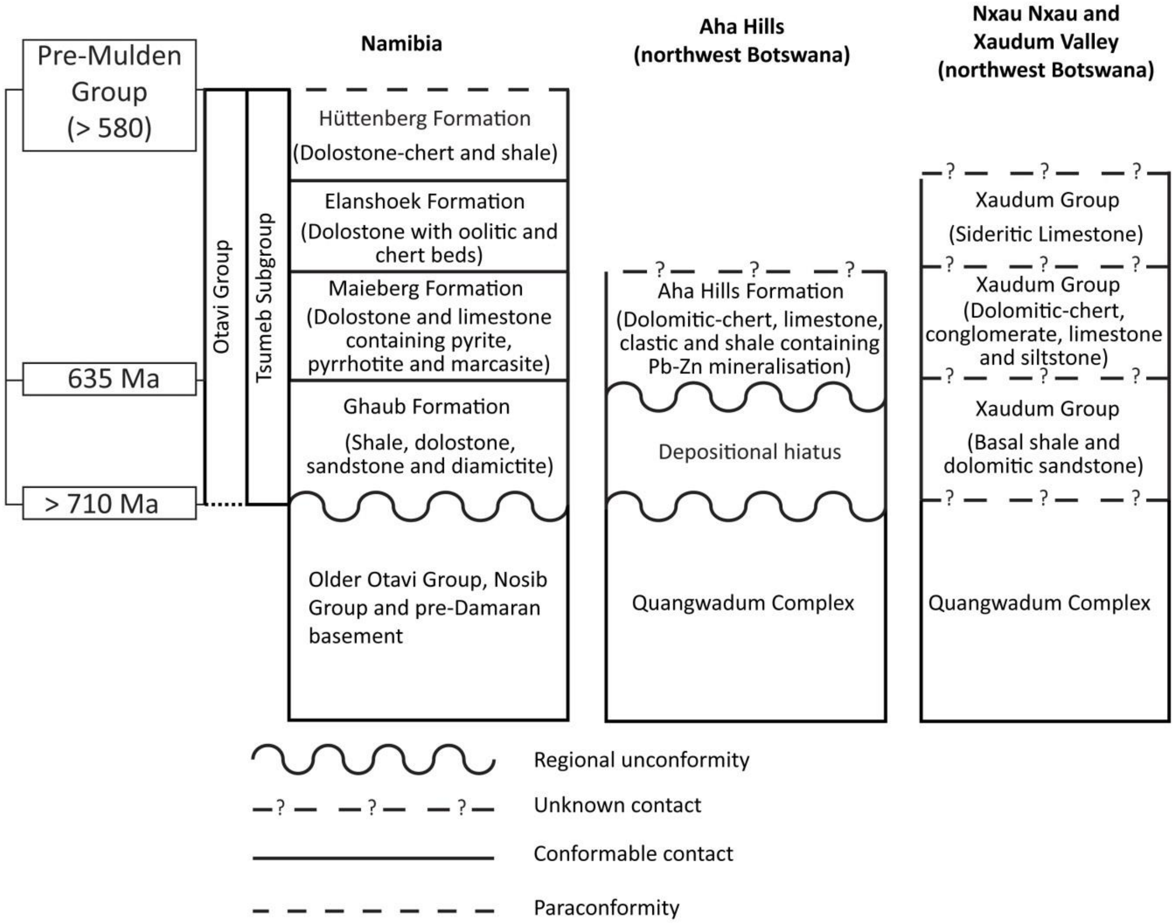

Figure 6.31: Tectonostratigraphic cross-border correlations of the Aha Hills Formation and Xaudum Group based on geological and aeromagnetic evidence with the Northern Platform, Damara Belt.

The Quangwadum Complex is a Paleoproterozoic basement of Congo Craton affinity. The aeromagnetic signal of the Quangwadum Complex can be easily traced across the border into Namibia, where it is correlated with the Grootfontein Complex (Figure 6.1, Table 6.1). Both these complexes comprise an older granitic gneiss suite of ~2.0 Ga (Hoal *et al*., 2000; Singletary *et al*., 2003) and a younger finer-grained granite suite.

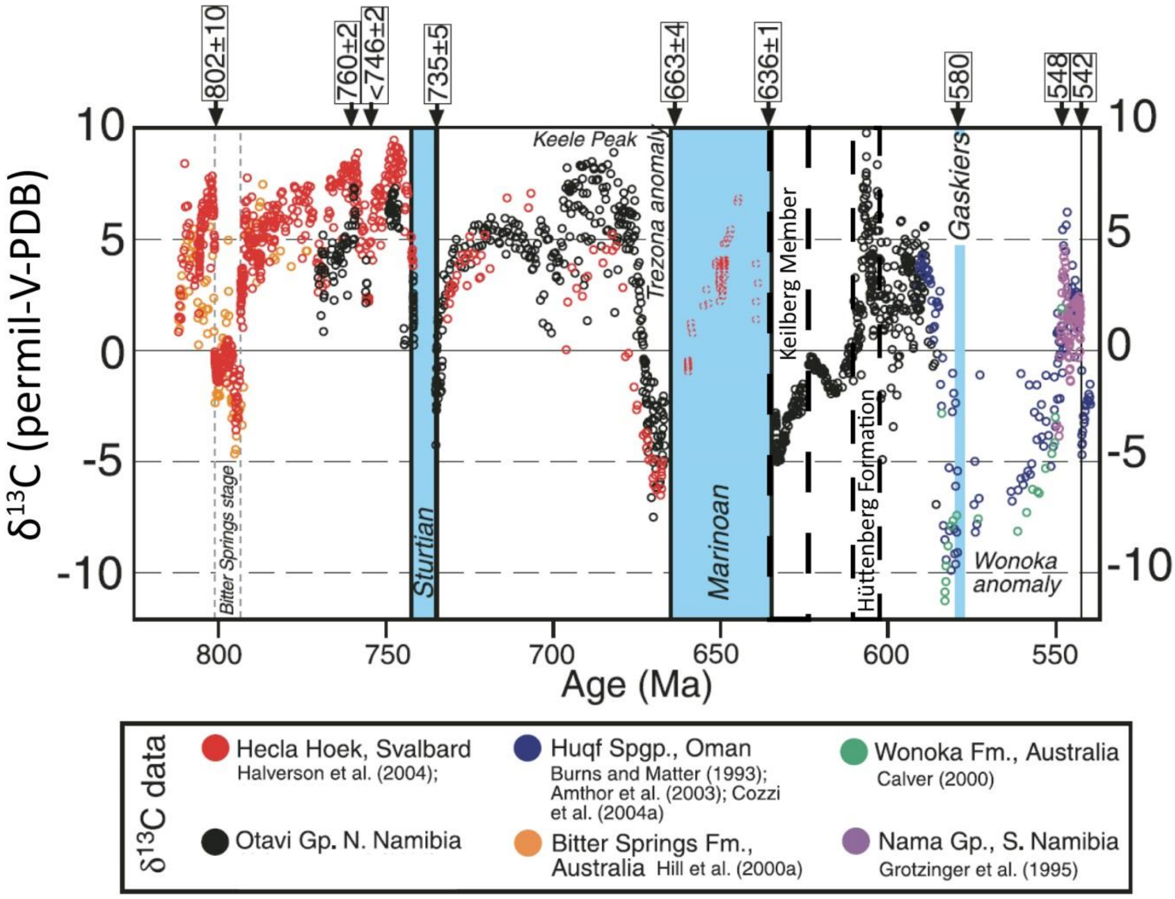

Figure 6.32: Age estimates based on $\delta^{13}C$ (permil-V-PDB) signatures for Neoproterozoic marine carbonates (modified after Halverson, 2002; Halverson *et al*., 2005; Hoffman and Halverson, 2008).

In Botswana, to the southeast of the Quangwadum Complex, is the unexposed and undrilled Chihabadum Complex (Figure 6.19). Key and Ayres (2000) poorly describe the complex as consisting of igneous to meta-igneous rocks. Pryer *et al*. (1997) suggests that the higher magnetic amplitudes are caused by younger intrusions. These pronounced sub-linear to linear, northeast-southwest trending high magnetic anomalies of the Chihabadum Complex suggest that it was emplaced pre- to syn-Damara Orogen. The southwestern margin of the Chihabadum Complex is truncated by northwest trending Karoo volcanics and the aeromagnetic pattern of the northeastern part is suppressed by the Okavango Dyke Swarm (Figure 6.19). For a confident correlation between these units there is no other option but to drill the Chihabadum Complex.

North of the Nxau Nxau and Quangwadum Valleys, sub-domain 1 wraps around the northeastern margin of the Quangwadum Complex (Figure 2.19 and 6.20). This sub-domain consists of low to moderate magnetic lithologies. In high-pass filtered images (e.g. first vertical derivative, analytic signal and tilt angle) northwest trending moderate to high magnetic lenses, typical of plunging folds are enhanced. The low magnetic lithologies are interpreted as carbonate of the Xaudum Group and the higher amplitudes as ferruginous quartzite and iron formation of the Tsodilo Hills Group.

The Xaudum Group has been previously correlated with the Otavi Group of the Northern Platform based on similar lithologies (Carney *et al*., 1994), while Miller and Schalk (1980) have mapped Nosib Group rocks immediately to the west of the Xaudum Valley. Singletary *et al*. (2003) correlates the Xaudum Group with the Nosib Group, based on similar lithologies, whose characteristics were not stated. A more recent geophysical study of northwest Botswana by Kgotlhang *et al*. (submitted) correlates the Xaudum Group with the Otavi Group based on similar contacts with the underlying basement and magnetic outline of the Damara Belt.

The deposition of the Xaudum Group is constrained between 1 020 Ma to 530 Ma (Mapeo *et al*., 2000). This large time span includes the deposition of the Sturtian and Marinoan glacial events. The depositional age of the Otavi Group is constrained by the Sturtian (746 ± 2 Ma) (Hoffmann *et al*., 1996) and Marinoan (635.5 ± 1.2 Ma) (Hoffmann *et al*., 2004) glacial events and an age of ~780 Ma for the Ombombo Subgroup (Halverson *et al*., 2005). The Otavi Group, situated on the southern margin of the Northern Platform, is paraconformably overlain by Kuiseb schist (Hoffman and Halverson, 2008), which further constrains the depositional age of the Otavi Group to pre-635 Ma (maximum depositional age of the Kuiseb Formation). The low to moderate magnetic amplitude signal of the southern margin of the Northern Platform spatially correlates with the aeromagnetic signal in the vicinity of the Xaudum Valley where Lemaire (1971; in Carney *et al*., 1994) observed schists.

The lack of observed iron-rich lithologies in the Xaudum Group (Carney *et al*., 1994; Mapeo *et al*., 2000) suggests that deposition of the Xaudum Group was either pre- or post-Sturtian glaciation. The characteristic roll-up structures of the Rasthof/Berg Aukas Formations (cap carbonates of the Chuos Formation) have not been noted in the carbonates of northwest Botswana. Carney *et al*. (1994) notes the similarities of the dolomitic-chert units of the Xaudum Group and the Aha Hills Formation. The correlation of the Aha Hills Formation with the Maieberg Formation and the similarities between the Aha Hills Formation and dolomitic-chert units of the Xaudum Group observed by Carney *et al*. (1994) suggests that the Xaudum Group correlates with the Tsumeb

Subgroup (Figure 6.31). The structural base of the Xaudum Group is interpreted to be shales and sandstones (Carney *et al*., 1994 and references within). This basal sequence is tentatively correlated with the Ghaub Formation based on lithological similarities, even though there are no observed diamictites present in the Xaudum Group (Figure 6.31). The dolomitic-chert unit of the Xaudum Group is capped by a sideritic limestone unit (Carney *et al*., 1994), which is correlated with the Elanshoek Formation based on lithological similarities and the correlation of the lower two units of the Xaudum Group (Figure 6.31).

The iron-rich strata of the Tsodilo Hills Group of sub-domain 2 and 3 have strong lithological affinities with the Chuos Formation of the southern Central Zone, which in places contains an iron formation associated with ferruginous quartzite (Miller, 1983a; Breitkopf, 1988; Hoffman, 1989; Bühn *et al*., 1992). Kgotlhang *et al*. (submitted) agrees with the correlation of the iron formations with the Chuos Formation but favours a correlation with the Kuiseb Formation (Southern Zone) for the dolostone, schist and quartzite units, based on their correlation of the Roibok Group with the Matchless Member.

One of the geological correlations between the Damara Supergroup and the Katangan Supergroup is the presence of two glaciomarine diamictites that formed during the Sturtian and Marinoan global glaciation events. In Namibia, the Sturtian glaciation is represented by the Chuos Formation and the Marinoan glaciation by the Ghaub Formation (Hoffman *et al*., 1996, 2004). In Zambia, the Sturtian glaciation is represented by the Grand Conglomérat and the Marinoan glaciation by the Petit Conglomérat (Kampunzu *et al*., 2009). Until recent drilling by Tsodilo Resources Ltd. in the Shakawe area (Figure 6.33), there were no recorded glacial-type deposits in northwest Botswana. These glaciomarine diamictites have been intersected in boreholes L9690_8, L9700_7, L9590_7, and 1822C10 (Witbooi, 2011), L9600_10 and L9600_11 (Gerner, 2011) (Figure 6.33) and have a close association with iron-rich lithologies. Other lithologies include, biotite-garnet-amphibole schist, mylonitised granitic gneiss, meta-conglomerate, iron formation, mica-schist, ferruginous quartzite, and carbonate (Gerner, 2011; Witbooi, 2011).

The diamictite yielded ^{207}Pb-^{206}Pb weighted mean detrital zircon ages of 743 ± 62 Ma and 1 056 ± 42 Ma (L9690_8) (Figure 6.33) (Witbooi, 2011). Gerner (2011) obtained ^{207}Pb-^{206}Pb weighted mean detrital zircon ages of 2 747 ± 21 Ma, 2 656 ± 25 Ma, 2 052 ± 42 Ma and 1 029 ± 14 Ma (L9600_10) (Figure 6.33) for a metadiamictite and 2 619 ± 6 Ma, 2 620 ± 9 Ma, 2 746 ± 8 Ma and 1 994 ± 82 Ma for a quartzite-quartz-mica-carbonate schist. In addition to these ages, ^{207}Pb-^{206}Pb weighted mean Archaean ages were determined for a granitic gneiss of 2 645 ± 14 Ma (L9590_7)

(Figure 6.33) (Witbooi, 2011), 2 548 ± 65 Ma (L9660_5) (Gaisford, 2010), and a younger age of 541 ± 14 Ma for a meta-mafic rock (1822C26_1) (Figure 6.33) (Gaisford, 2010).

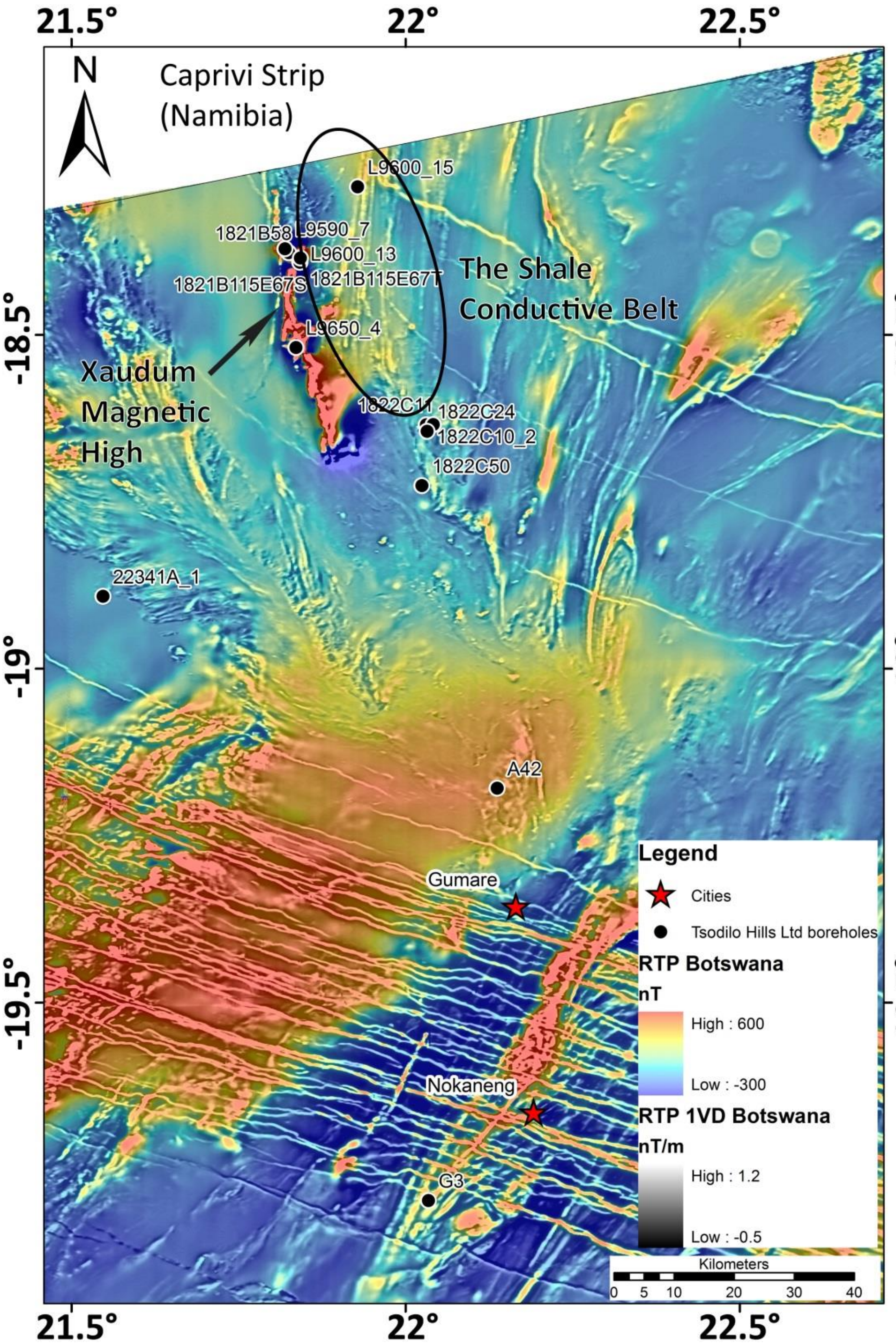

Figure 6.33: Location of the Xaudum Magnetic High and The Shale Conductive Belt relative to towns in Botswana (red stars) and the boreholes of Tsodilo Resources Ltd. (black circles). Background image is a 50% transparent colour scale RTP image of Botswana overlain on the RTP 1VD greyscale image of Botswana.

The ~2.5 Ga age of the granitic gneiss strongly suggests Congo Craton affinity, while the detrital zircons extracted from the metadiamictite and schist suggest that the clasts were derived from both an Archaean and Proterozoic source. The possible presence of a shallow basement is reinforced by the north-south trending, 20 nT to 55 nT magnetic feature immediately to the west of the Xaudum Magnetic High, in the 500 m upward continued data (Figure 6.23a).

A confident correlation between northwest Botswana and the Katangan Supergroup strata is still missing as the carbonaceous black shale in Zambia is not present in either outcrop or boreholes in northwest Botswana (exploration in the Papa Falls area) (Figure 2.33) (Master, *pers. comm*., 2013). In addition, the Tsodilo Hills Group quartzites do not correlate with the stratigraphy of the Zambian Copperbelt. Tsodilo Resources Ltd. has conducted airborne magnetics and time-domain electromagnetic surveys in northwest Botswana. These surveys led to the discovery of a mineralised carbonaceous black shale, to the east of the Xaudum Magnetic High, (Figure 6.33). The existence of this shale, termed The Shale Conductive Belt by Tsodilo Resources Ltd., was confirmed in boreholes, L9600_14, L9670_7, L9690_9, L9700_7 and 1822C10 (Figure 6.33) (Mojaki, 2009; Gaisford, 2010; Gerner, 2011; Witbooi, 2011). The shales and diamictites are mineralised in pyrite and pyrrhotite with minor amounts of chalcopyrite (Witbooi, 2011). These carbonaceous shales may correlate with the carbonaceous shales of the Kafubu Formation of the Mwashya Subgroup in the Katangan Supergroup (Gerner, 2011).

A number of spatially separate serpentinite bodies have been mapped along thrusts, to the south of the Xaudum Magnetic High (Figure 6.27), similar to that observed in the vicinity and south of the Matchless Member by Barnes (1982). Barnes and Sawyer (1980) interpreted that the serpentinite bodies were emplaced into a variety of country rocks, including pre-Damaran basement. The Matchless Member comprises amphibolite sheets hosted in Kuiseb schists. Corner (2008) associates magnetic (ferruginous) quartzite markers with the Matchless Member. These lithological correlations would suggest that the Tsodilo Hills Group correlates with Damara stratigraphy of the Southern Zone. However, the Neoproterozoic age of 743 ± 62 Ma for the diamictite (Witbooi, 2011) falls within the age error of 746 ± 2 Ma for the Chuos diamictite dated by Hoffmann *et al*. (1996). These overlapping age dates suggest a correlation with the Chuos diamictites of the southern Central Zone. Miller (2008) has suggested that the Abbabis Complex, in the southern Central Zone, is of Congo Craton affinity from age dates of ~2.0 Ga (see Section 2.2.3 for exact dates). Therefore, there is a possibility that the Tsodilo Hills Group and pre-Damaran basement in northern Botswana correlate with the Usakos Subgroup and pre-Damaran basement of the southern Central Zone. However, the southern Central Zone does not continue into Botswana (Figure 6.1). Additionally, the linear, high amplitude magnetic signals of sub-domain 2 and 3 do not continue south of ~19.5°S, 22.0°E and the high amplitude magnetic anomalies of the southern Central Zone do not correlate with the general moderate to low, smooth magnetic anomalies of northern Botswana.

The age of 541 ± 14 Ma for the meta-mafic sample (Gerner, 2011) and the northeast trend of the high aeromagnetic signal that borehole 1822C26_1 is drilled into, suggests emplacement occurred during the time of subduction of oceanic crust beneath the Congo Craton. This is in agreement with the age of closure of the Khomas Ocean and doming in the southern Central Zone and Southern Margin Zone, which is estimated at ~542 Ma (Frimmel *et al*., 2011). In the Southern Margin Zone, diamictite, iron formation, amphibolite, schist and serpentinite bodies (same source as the serpentinite in the Southern Zone) are present in the Noas Formation (Hoffmann, 1983; Breitkopf, 1988; Miller, 2008) whilst the overlying Kudis Subgroup contains glaciogenic diamictite, conglomerate, graphitic schist, dolomitic and calcitic marble and black shale (Miller, 2008). The Kuiseb Formation consists of metagreywacke, metasiltstone, metapelite, graphitic schist, calc-silicate and marble unit (Miller, 2008). In addition, from borehole observations sub-domain 2 is a high-grade metamorphic domain characterised by kyanite and garnet. Both the Southern and Southern Margin Zone are dominated by high pressure, low temperature kyanite facies metamorphic minerals (Kasch, 1983), while the Central Zone is a low pressure, high temperature zone containing cordierite-sillimanite facies minerals (Kasch, 1983; Jung *et al*., 2000).

Sub-domain 2 cannot be confidently correlated with a single tectonostratigraphic zone of the Damara Belt. The Southern Zone and sub-domain 2 have similar metamorphic grades, aeromagnetic signal, contain serpentinite bodies, and the Kuiseb Formation, shares lithological similarities with sub-domain 2. However, sub-domain 2 is abundant in iron formations and diamictites. The only recorded diamictites in the Southern Zone are associated with the Ghaub Formation, which is not associated with iron formations (Miller, 2008). The Southern Margin Zone has a similar metamorphic grade to sub-domain 2 and contains the Kudis and Vaalgras Subgroups (see Section 2.4.2 for detailed lithologies), which lithologically correlates with sub-domain 2. However, the aeromagnetic signal of sub-domain 2 and the Southern Margin Zone are completely different. The high amplitude aeromagnetic fabric of the Southern Margin Zone is controlled by Chuos Formation while the Nosib Group is characterised by lower levels of magnetisation (Corner, 2008). Correlating the Southern Margin Zone with sub-domain 2 will have a space problem as the Koanaka Group (immediately south of sub-domain 2) (Figure 6.1) is correlated with the Southern Zone. Therefore, without age dates and drill core on the Namibian side of the Namibia – Botswana border, no correlation can be confidently determined for sub-domain 2.

From the limited boreholes in sub-domain 3, the intersected lithologies can be correlated with either the Southern Margin Zone or the southern Central Zone whereas, the aeromagnetic signal of sub-domain 3 is smooth with sub-linear to linear high aeromagnetic features defining a northeast trend compared to the noisy, randomly oriented aeromagnetic signal of the Southern Margin and southern Central Zones. In addition, the Southern Margin Zone is abundant in pre-Damaran granitoids and the southern Central Zone contains extensive syn-to post tectonic granite intrusions. Therefore, in order to correlate sub-domain 3 with a tectonostratigraphic zone in Namibia boreholes will need to be drilled in this sub-domain to determine an abundant lithological unit.

6.5. Conclusion

The previous geological cross-border correlations between Namibia and Botswana have been on a broad scale (Carney *et al*., 1994; Haddon, 2001; Kgotlhang *et al*., submitted) or restricted to certain tectonostratigraphic zones e.g. Borg and Maiden (1987), Borg (1987, 1988), Modie (1996) and Maiden and Borg (2011) correlate the Ghanzi-Chobe Belt with lithologies in the Rehoboth Subprovince. Another favoured and extensively studied correlation is the Matchless Member with the Roibok Group (Reeves, 1978a; Miller, 1983b; Breitkopf and Maiden, 1988; Lüdkte *et al*., 1986, in Carney *et al*., 1994).

The previous correlations have been based on either geological or geophysical similarities with no in-depth correlations based on a combination of these. This is the first cross-border correlation study that incorporates both geophysical (aeromagnetic and gravity) and geological (lithological, geochronology, chemostratigraphy, structural and mineralisation styles) data to determine the most likely correlations. However, as the majority of the study area is covered by Karoo and Kalahari lithologies these correlations are tentative and will only be confirmed by new borehole data.

This chapter clarifies the differences in the geological maps of Pryer *et al*. (1997) and Key and Ayres (2000) (discussed in Section 3.7), by defining a specific aeromagnetic signal for lithologies intersected in boreholes and observed exposures (Table 6.1) which is used to interpret the sub-surface geology.

The interpretation of potential field data complimented with lithological, geochronology and chemostratigraphy have shown that the metasediments of the Ghanzi-Chobe Belt are pre-

Damaran in age and hence, not the northwest continuation of the Damara Belt. The Ghanzi-Chobe Belt can be traced from central Namibia through Botswana to Caprivi (Figure 6.1). This study correlates the Ghanzi-Chobe Belt with the Sinclair Supergroup in the Rehoboth Subprovince from the folds depicted in the aeromagnetic images, basal meta-volcanics dated at ~1.1 Ga (Langberg Formation, in Namibia and Goha and Kgwebe Formations, in Botswana), lithological similarities bracketed by chemostratigraphy (Botswana), and datable volcanic units in Namibia (Figure 6.34).

Historically, the Matchless Member has been correlated with the Roibok Group based on the alignment of strike and similar geochemical composition (Reeves, 1978a; Miller, 1983b; Breitkopf and Maiden, 1988; Lüdkte *et al*., 1986, in Carney *et al*., 1994). Both units were emplaced at ~710 Ma with their upper limit constrained to ~635 Ma based on lithological contacts. If the Matchless Member and Roibok Group are connected it suggests that the Kuiseb Formation is not present in Botswana. This led Carney *et al*. (1994) and Corner (2008) to suggest that these units are not connected. Therefore, with the current available data, this study favours the suggestion of Carney *et al*. (1994) and Corner (2008), which is the Matchless Member and Roibok Group are not connected but were emplaced in a similar tectonic setting, most likely during the rifting forming the Khomas Ocean.

The Kwando Complex represents a Mesoproterozoic massif separating the Ghanzi-Chobe Belt from the higher grade metamorphic rocks of the Damara Belt. From the interpretation of aeromagnetic imagery, similar felsic assemblages and geochronology, this study correlates the Kwando Complex with the Nückopf Formation, which is situated north of the interpreted aeromagnetic folds in the Rehoboth Subprovince. The Kwando Complex has been previously placed in the Okavango Zone (Figure 2.15) (Carney *et al*., 1994) however, from the age dates of Singletary *et al*. (2003), and the possible correlation with the Nückopf Formation, this study suggests that Kwando Complex should be placed in the Ghanzi-Chobe Zone (Figure 2.15). This will lead to the zone containing only pre-Damaran lithologies and on a regional correlation can be traced along the northern margin of the Rehoboth Subprovince.

Figure 6.34 (following page)**:** Tectonostratigraphic cross-border correlations of the Rehoboth Subprovince and Damara Belt with geological domains in northwestern Botswana based on geological and aeromagnetic evidence.

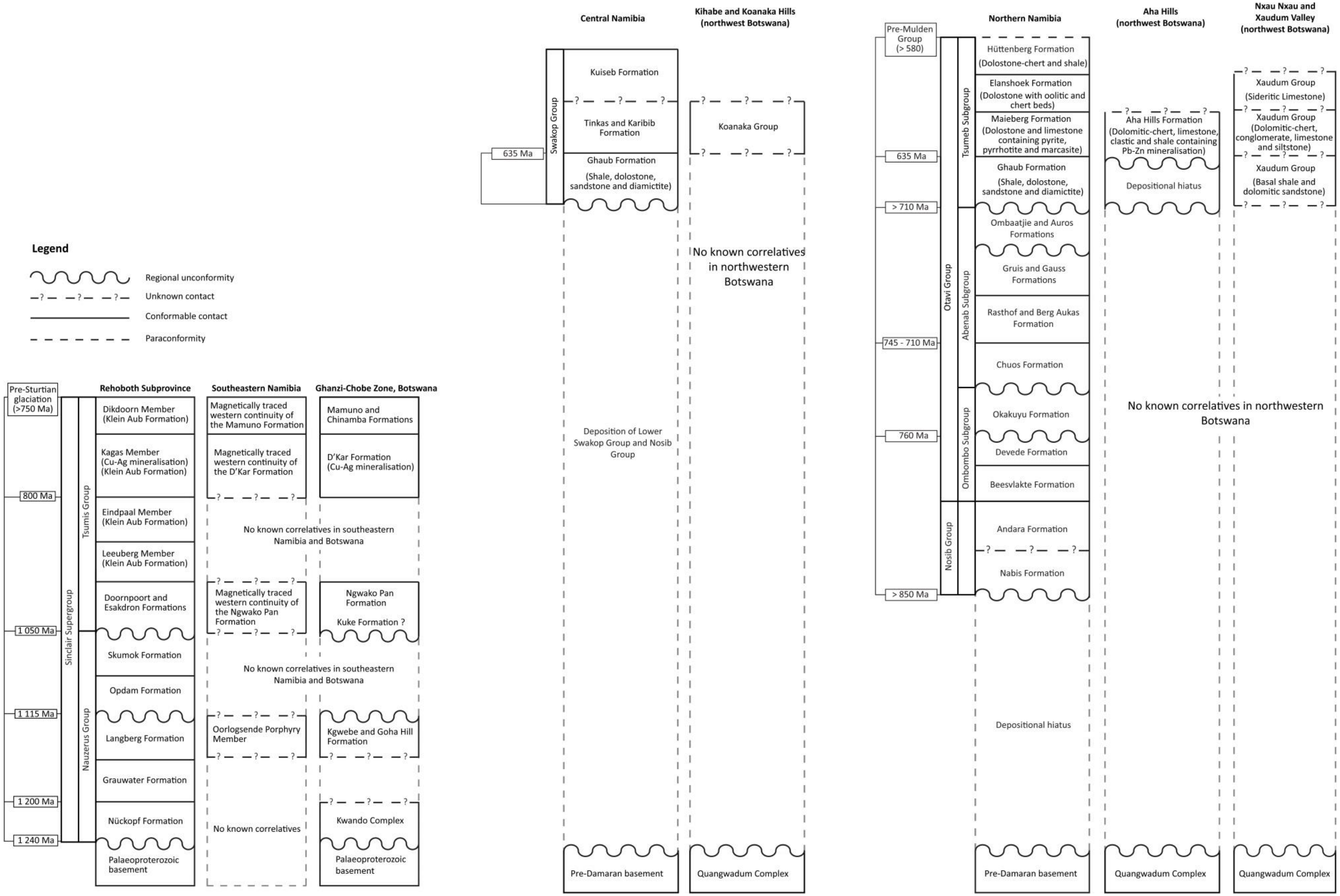

Legend
Regional unconformity
Unknown contact
Conformable contact
Paraconformity
Pre-Sturtian glaciation (>750 Ma)
Rehoboth Subprovince
Southeastern Namibia
Ghanzi-Chobe Zone, Botswana
Sinclair Supergroup
Tsumis Group
Nauzerus Group
800 Ma
1 050 Ma
1 115 Ma
1 200 Ma
1 240 Ma
Dikdoorn Member (Klein Aub Formation)
Kagas Member (Cu-Ag mineralisation) (Klein Aub Formation)
Eindpaal Member (Klein Aub Formation)
Leeuberg Member (Klein Aub Formation)
Doornpoort and Esakdron Formations
Skumok Formation
Opdam Formation
Langberg Formation
Grauwater Formation
Nückopf Formation
Palaeoproterozoic basement
Magnetically traced western continuity of the Mamuno Formation
Magnetically traced western continuity of the D'Kar Formation
No known correlatives in southeastern Namibia and Botswana
Magnetically traced western continuity of the Ngwako Pan Formation
No known correlatives in southeastern Namibia and Botswana
Oorlogsende Porphyry Member
No known correlatives
Mamuno and Chinamba Formations
D'Kar Formation (Cu-Ag mineralisation)
Ngwako Pan Formation
Kuke Formation ?
Kgwebe and Goha Hill Formation
Kwando Complex
Palaeoproterozoic basement
Central Namibia
Kihabe and Koanaka Hills (northwest Botswana)
635 Ma
Swakop Group
Kuiseb Formation
Tinkas and Karibib Formation
Ghaub Formation (Shale, dolostone, sandstone and diamictite)
Deposition of Lower Swakop Group and Nosib Group
Pre-Damaran basement
Koanaka Group
No known correlatives in northwestern Botswana
Quangwadum Complex
Pre-Mulden Group (> 580)
635 Ma
> 710 Ma
745 - 710 Ma
760 Ma
> 850 Ma
Otavi Group
Tsumeb Subgroup
Abenab Subgroup
Ombombo Subgroup
Nosib Group
Northern Namibia
Hüttenberg Formation (Dolostone-chert and shale)
Elanshoek Formation (Dolostone with oolitic and chert beds)
Maieberg Formation (Dolostone and limestone containing pyrite, pyrrhotite and marcasite)
Ghaub Formation (Shale, dolostone, sandstone and diamictite)
Ombaatjie and Auros Formations
Gruis and Gauss Formations
Rasthof and Berg Aukas Formation
Chuos Formation
Okakuyu Formation
Devede Formation
Beesvlakte Formation
Andara Formation
Nabis Formation
Depositional hiatus
Pre-Damaran basement
Aha Hills (northwest Botswana)
Aha Hills Formation (Dolomitic-chert, limestone, clastic and shale containing Pb-Zn mineralisation)
Depositional hiatus
Quangwadum Complex
Nxau Nxau and Xaudum Valley (northwest Botswana)
Xaudum Group (Sideritic Limestone)
Xaudum Group (Dolomitic-chert, conglomerate, limestone and siltstone)
Xaudum Group (Basal shale and dolomitic sandstone)
No known correlatives in northwestern Botswana
Quangwadum Complex

Immediately to the northwest of the Roibok Group is the Koanaka Group. The Koanaka Group is suggested to correlate with the cap carbonate units (Karibib and Tinkas Formations) of the Ghaub Formation (Figure 6.34). This correlation is based on exposures of greenschist-facies dolomitic marbles in the Kihabe and Koanaka Hills (Figure 2.19) and Corner's (2008) lithological cause of the inert magnetic signal of the Southern and northern Central Zones of the Damara belt. Correlating the Koanaka Group with the Southern Zone and northern Central Zone suggests that the southern Central Zone pinches out before entering Botswana (Figure 6.1). In Namibia, the Southern and northern Central Zone are separated by pre-Damaran lithologies (Deep-Level Southern Zone) while in Botswana the northern and southern limbs of the Koanaka Group is separated by the Chihabadum Complex (Figure 6.1). The Gumare Fault, which forms the northwestern boundary marker of the Okavango Rift Zone, is interpreted to be the southern boundary of the Deep-Level Southern Zone.

The Aha Hills Formation has a higher than expected aeromagnetic signal suggested to be caused by the underlying Quangwadum Complex. This study correlates the Aha Hills Formation with the Keilberg Member (base of the Maieberg Formation, of the Tsumeb Subgroup of the Northern Platform) (Figure 2.14) based on similar lithologies and pyrite mineralisation in both units (Figure 6.34). This and the above correlation suggests that the Northern Zone pinches out before entering Namibia, which is in agreement with regional aeromagnetic and geological interpretation of the tectonostratigraphic zones of the Damara Belt (Figure 2.4) (Corner, 2008; Miller, 2008).

The aeromagnetic signal of the Quangwadum Complex is easily traced across the Namibia – Botswana border, where it is correlated with the Grootfontein Complex based on similar lithologies, aeromagnetic signals (Table 6.1) and age dates of ~2.0 Ga.

The Xaudum Group, in sub-domain 1 of northwest Botswana, is correlated with the upper formations of the Abenab Subgroup (Otavi Group) of the Northern Platform based on similar low-grade metamorphic carbonate sequences and aeromagnetic signal (Figure 6.34). In the Northern Platform, the iron formation is associated with the Chuos Formation, however, there have been no documented ferruginous quartzites in the Northern Platform. Therefore, there is no confident correlation for the northwest-southeast trending folds in sub-domain 1 with Damaran lithologies of the Northern Platform.

Sub-domains 2 and 3 cannot be confidently correlated with a single tectonostratigraphic zone in the Damara Belt with the available data sets. Sub-domain 2 can possibly correlate with either the

Southern Zone or Southern Margin Zone while sub-domain 3 can possibly correlate with either the Southern Zone or the southern Central Zone.

6.6. Summary

This chapter resolved the discrepancies in the previous sub-Kalahari geological maps of Pryer *et al*. (1997) and Key and Ayres (2000) substantiated by new borehole data of Tsodilo Resources Ltd. and 50 m resolution aeromagnetic data. This re-interpretation of the sub-surface geology has resulted in a new sub-Kalahari map between Namibia and Botswana. In addition, one of the first lineament maps for Namibia, Botswana and Zambia has been interpreted from processed aeromagnetic images. The interpretation of potential field data is a non-unique technique and to thus verify the boundaries of the Ghanzi-Chobe and Damara Belt and Kalahari and Congo Cratons, three magnetotelluric profiles (DMD, NEN and OKA-CAM) from the Southern African MagnetoTelluric EXperiment were 1D inversed modelled and discussed in the following chapter.

Chapter 7

Magnetotelluric data and interpretations

7.1. Introduction

One month was spent at the Dublin Institute of Advanced Studies (DIAS), Ireland, processing three roughly north-south magnetotelluric (MT) profiles within the vicinity of the Namibia – Botswana border (Figure 7.1). The DMB, NEN and OKA-CAM profiles (Figure 7.1) are part of the 780 MT stations of the South African MagnetoTelluric EXperiment (SAMTEX). The MT data was interpreted to constrain the extent of the mobile belts and cratons and to verify the regional conductor first discovered by de Beer *et al*. (1975) (discussed in Section 2.6.3).

The westernmost profile, the DMB profile, is ~680 km long and consists of 35 broad-band MT (BBMT) stations (Figure 7.1). These stations were deployed at ~20 km intervals along the profile. The central NEN profile is ~440 km long and composed of 23 BBMT stations (Figure 7.1). These stations were deployed at ~20 km intervals along the profile. The ~260 km long, OKA-CAM profile is the easternmost profile (Figure 7.1). In 2006, BBMT data were acquired from a total of 15 locations with a station spacing of ~20 km along the OKA profile (Figure 7.1). In 2009, additional stations of the CAM profile were interspersed with the OKA profile, improving the station spacing on the OKA-CAM profile to ~5 km (Figure 7.1).

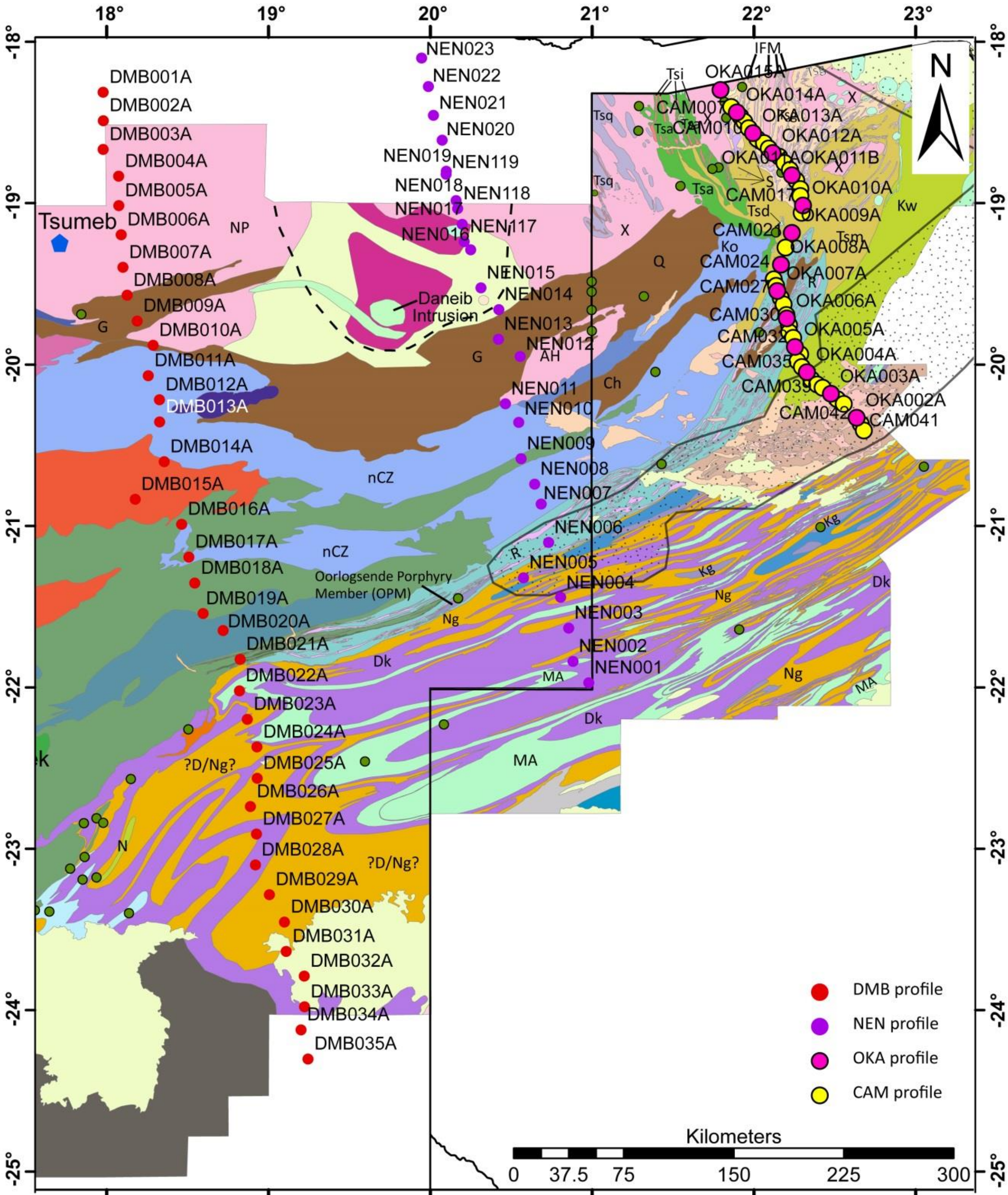

Figure 7.1: Location of the DMB, NEN and OKA-CAM MT profiles overlain on this studies sub-Kalahari geological map. See Figure 6.1 and fold out for legend to the sub-Kalahari geology.

7.2. Magnetotelluric theory

The magnetotelluric (MT) technique is a passive-source electromagnetic (EM) sounding technique that utilises naturally occurring geomagnetic variations as its source to measure resistivity changes in the subsurface from a few metres to hundreds of kilometres (Chave and Jones, 2012; Khoza *et al*., 2013). MT is based on several assumptions (Section 7.2.3) and the fundamental equations of EM theory (Maxwell's equations) that describe the relationship between the electrical and magnetic fields (Section 7.2.4).

7.2.1. Magnetotelluric sources

The naturally occurring electromagnetic signals used in the MT technique originate from lightning strikes and interactions between the atmosphere, ionosphere and magnetosphere (Tikhonov, 1986; Cagniard, 1953). The ionosphere is the boundary between the atmosphere and the magnetosphere and hosts a number of gases, such as oxygen and nitrogen, which ionize from ultraviolet and other solar radiation. The ionosphere and magnetosphere are constantly battered by solar winds (a plasma containing energetic ions, of electrons and protons), emitted from the sun (Vozoff, 1991). The different processes described above, are dominantly long-wavelength in nature (less than 1Hz) and so penetrate deep into the Earth (Bedrosian, 2007). Short period signals (greater than 1 Hz) originate from lightning strikes which generate EM fields (sferics) that propagate over great distances in the waveguide bounded by the ionosphere and the Earth's surface (Garcia and Jones, 2002). Sferics propagate as either transverse electric, transverse magnetic or transverse electric and magnetic waves, and are amplified or attenuated depending on frequency. If they are in phase after surrounding the Earth, the signal is amplified by constructive interference; otherwise the signal is destroyed by destructive interferences.

At the transition zone between lightning and solar winds, causing a region of signals at frequencies of ~1 Hz. This interaction causes a reduction of data quality and is known as the dead-band (Simpson and Bahr, 2005).

7.2.2. Electrical properties of Earth minerals

Electrical properties of rocks and minerals

The conductivity (σ), and its inverse, resistivity (ρ), and electrical permittivity (ε) describe the electrical properties of a material (Telford *et al*., 1990).

Electrical conductivity

Electrical conductivity (σ) measures a material's ability to conduct an electrical current. For different rocks and minerals, this parameter can vary by several orders of magnitude (Figure 7.2), creating large conductivity contrasts that can be imaged by the MT method in order to investigate geological and structural changes in the crust (Khoza *et al*., 2013). Conductive anomalies can be caused in a number of ways including mineral phases (such as graphite and sulphides), the physical condition of the rock (Kariya and Shankland, 1983), partial melting of the crust (Unsworth *et al*., 2004; Le Pape *et al*., 2012), and the presence of fluids (Karato, 1990).

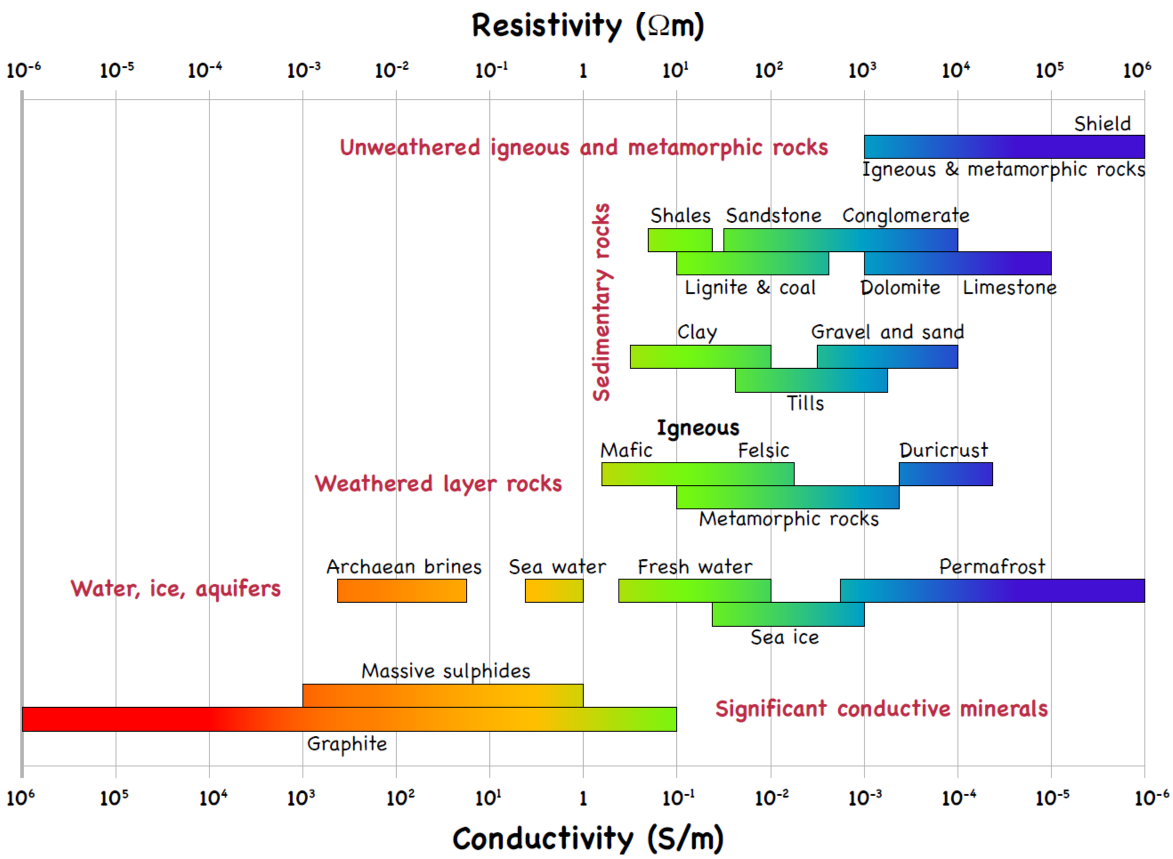

Figure 7.2: Ranges of electrical conductivity/resistivity of some common Earth materials (after Miensopust, 2010). Red colours indicate conductive material, whilst blue colours indicate resistive material.

The electric current density ($\boldsymbol{j}$) is directly related to the electric field ($\boldsymbol{E}$) by a constant factor called conductivity (σ). This is Ohm's Law, expressed as;

$$\boldsymbol{j} = \sigma \boldsymbol{B}. \tag{7.1}$$

As both the current density and electric field are vectors, the conductivity is a tensor. If the rock or mineral is isotropic (uniform in all directions) the three principle values of the conductivity are the same and the conductivity can be treated as a scalar.

Electrical permittivity

Electrical permittivity (ε) characterises how an electrical field affects, and is affected by, a dielectric medium. It measures a material's ability to become polarised by the external electrical field and in doing so reduces the total electrical field present inside the material i.e. the nature in which the material transmits or permits an electric field.

The equation that relates the electric field ($\boldsymbol{E}$) to the electrical displacement ($\boldsymbol{D}$) is expressed as;

$$\boldsymbol{D} = \varepsilon \boldsymbol{E}, \tag{7.2}$$

where ε is the dielectric permittivity of free-space, which is given by the combination of the electrical permittivity in a vacuum (ε_0 = 8.85x10^{-12} $^{f}/_{m}$) and the relative electrical permittivity (ε_r), which is unitless and specific to the material;

$$\varepsilon = \varepsilon_0 \varepsilon_r. \tag{7.3}$$

ε_r varies from 1, inside a vacuum, to 80.36 for water at 20°C (Telford *et al.*, 1990).

Magnetic properties of rocks and minerals

Magnetic permeability (μ) is the degree of magnetisation of a material in response to an applied magnetic field. Permeability is a scalar when the medium is isotropic and for an anisotropic linear medium the permeability is a second rank tensor.

The relationship between magnetic induction ($\boldsymbol{B}$), magnetic intensity ($\boldsymbol{H}$) and magnetic permeability can be expressed as;

$$\boldsymbol{B} = \mu \boldsymbol{H}. \tag{7.4}$$

where μ is the product of the magnetic permeability in a vacuum (μ_0 = 4πx10^{-7} $^{H}/_{m}$) and the relative permeability (μ_r), which is unitless and specific to the material;

$$\mu = \mu_0 \mu_r. \tag{7.5}$$

Commonly, the permeability of Earth's materials is close to the vacuum (free-space) value however, if there is a large concentration of iron (magnetic minerals) then the permeability will be higher.

7.2.3. Assumptions of the MT method

MT applies a number of simplifying assumptions when considering EM induction in the Earth. There are a number of papers that discuss these assumptions (Cagniard, 1953; Price, 1973; Vozoff, 1991 and Simpson and Bahr, 2005) which are briefly discussed below (modified from Simpson and Bahr, 2005).

I. Maxwell's four equations are obeyed.

II. The Earth does not produce EM energy, but only absorbs or dissipates it.

III. Away from their source, all fields can be treated as conservative and analytic.

IV. The natural EM fields used by the MT method may be treated as being uniform, plane-polarised EM waves, which are produced by a source far from the Earth's surface, and have a near-vertical incident angle at the Earth's surface. This assumption may not hold at polar and equatorial regions on the Earth.

V. In a 1D layered Earth, the accumulation of free charges is non-continuous. In a 2D or 3D layered Earth, charges accumulate along discontinuities causing static shift.

VI. The Earth behaves as an Ohmic conductor and charge is conserved, obeying the following equation, $\boldsymbol{j} = \sigma \boldsymbol{B}$.

VII. For MT sounding periods (~10^{-5} s to 10^{5} s) the electrical field is quasi-static. The time-vary currents ($\frac{\partial D}{\partial t}$ in Equation 7.7) are small compared to the time-varying conduction currents ($\boldsymbol{j}_f$ in Equation 7.7) and can be neglected (Section 7.2.4).

VIII. Any variations in the magnetic and electrical permeability of rocks and minerals are insignificant compared to variations in the bulk rock conductivity.

7.2.4. The fundamental equations of the MT technique

The theory of the EM technique is governed by Maxwell's equations, which describe the behaviour of both the electric and magnetic fields and their interactions. At any frequency the physical principles of the MT method are based on the following four equations;

1. Faraday's Law: Time variations in the magnetic field (***B***) induce a proportional electrical field (***E***) perpendicular to the direction of the inducing field (Figure 7.3),

$$\nabla \times \boldsymbol{E} = -\frac{\partial \boldsymbol{B}}{\partial t}. \tag{7.6}$$

2. Ampere's Law: Current flow or time varying electric fields induce a proportional magnetic field perpendicular to the direction of the electric field (Figure 7.4),

$$\nabla \times \boldsymbol{H} = \frac{\partial \boldsymbol{D}}{\partial t} + \underline{j}_{\mathrm{f}} \qquad (7.7)$$

3. Gauss' Law: Divergence of the electric field in a certain volume is equal to the total charge density inside the volume,

$$\nabla \cdot \boldsymbol{D} = q_c \qquad (7.8)$$

4. Unnamed equation: The divergence of the magnetic field in a certain volume is zero, meaning that positive and negative magnetic poles always exist in pairs (i.e. no monopoles),

$$\nabla \cdot \boldsymbol{B} = 0 \qquad (7.9)$$

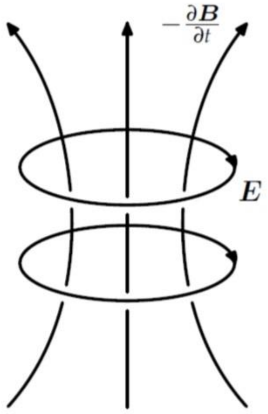

Figure 7.3: Sketch depicting an induced magnetic field created from a time-varying magnetic field i.e. Faraday's Law.

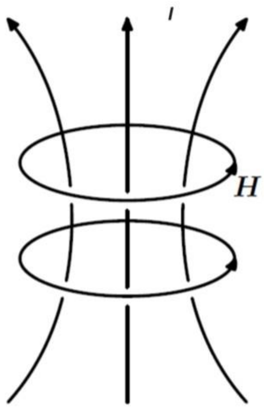

Figure 7.4: Sketch depicting a changing electric field inducing a magnetic field i.e. Ampere's Law.

Taking the curl of Equation 7.6 and 7.7 and applying the vector calculus identities (Equation 7.10 and 7.11), a diffusion equation can be derived for the electric and magnetic fields.

$$\nabla \times (\nabla \times \mathrm{A}) = \nabla(\nabla \cdot \mathrm{A}) - \nabla^2 \mathrm{A}, \text{ and} \qquad (7.10)$$

$$\nabla \times (\psi \mathrm{A}) = \psi \nabla \times \mathrm{A} - \mathrm{A} \times \nabla \psi \qquad (7.11)$$

where A is a vector and ψ is a scalar field.

The diffusion equation of the electric field is given by

$$\nabla \times (\nabla \times \boldsymbol{E}) = \nabla \times (-i\omega \boldsymbol{B})$$

$$\Rightarrow \nabla \cdot \nabla \cdot \boldsymbol{E} - \nabla^2 \boldsymbol{E} = -i\omega \nabla \times \boldsymbol{B}$$

$$\Rightarrow \nabla^2 \boldsymbol{E} = i\omega \mu_0 \sigma \boldsymbol{E} - \nabla(\boldsymbol{E} \nabla \ln \sigma) \qquad (7.12)$$

where μ_0 is the magnetic permeability (in freespace: $\mu_0 = 1.2566 \times 10^{-6}\ Hm^{-1}$) and ω is the angular frequency ($\omega = 2\pi f$, with f being frequency). Similarly, it applies to the magnetic field ***B***.

Assuming an isotropic and homogeneous space, the conductivity σ is constant ($\nabla\sigma = 0$), therefore, the diffusion equation 7.12 simplifies to

$$\nabla^2 \boldsymbol{E} = i\omega\mu_0\sigma\boldsymbol{E} \tag{7.13}$$

and

$$\nabla^2 \boldsymbol{B} = i\omega\mu_0\sigma\boldsymbol{B} \tag{7.14}$$

Equation 7.13 and 7.14 are second order differential equations with solutions valid for a vertical external source field and of the form

$$\boldsymbol{E} = \boldsymbol{E}_1 e^{i\omega t - qz} + \boldsymbol{E}_2 e^{i\omega t + qz} \quad \text{and} \quad \boldsymbol{B} = \boldsymbol{B}_1 e^{i\omega t - qz} + \boldsymbol{B}_2 e^{i\omega t + qz} \qquad 7.15)$$

where t is time and q is defined below. The second term on the right-hand side increases with depth z because the Earth does not generate EM fields but absorbs or dissipates them (assumption (II) in Section 7.2.3), within the Earth arbitrary large amplitudes cannot be support and $\boldsymbol{E}_2$ and $\boldsymbol{B}_2$ should be set to zero (Simpson and Bahr, 2005). Applying the solutions of Equation 7.15 and assuming a vertical incidence such that $\frac{\partial \boldsymbol{E}}{\partial x} = \frac{\partial \boldsymbol{B}}{\partial x} = 0$ to the left-hand side of Equation 7.13, yields;

$$\nabla^2 \boldsymbol{E} = \frac{\partial^2 \boldsymbol{E}}{\partial^2 z} = q^2 \boldsymbol{E}_1 e^{i\omega t - qz} = q^2 \boldsymbol{E}, \tag{7.16}$$

and therefore, Equation 7.13 becomes

$$q^2 \boldsymbol{E} = i\omega\mu_0\sigma\boldsymbol{E} \Rightarrow q^2 = i\omega\mu_0\sigma. \tag{7.17}$$

Solving for q yields

$$q = \sqrt{i\omega\mu_0\sigma} = \pm\left(\sqrt{\frac{\omega\mu_0\sigma}{2}} + i\sqrt{\frac{\omega\mu_0\sigma}{2}}\right). \tag{7.18}$$

The inverse of q is known as the Schmucker-Weidelt transfer function (Weidelt, 1972; Schmucker, 1973) and can be expressed as a relation between the EM field components;

$$C = \frac{1}{q} = \frac{\boldsymbol{E}_x}{i\omega \boldsymbol{B}_y} = -\frac{\boldsymbol{E}_y}{i\omega \boldsymbol{B}_x}. \tag{7.19}$$

Combining Equation 7.19 with Equation 7.18 yields the definition for the resistivity ρ in a homogeneous half-space;

$$\rho = \frac{1}{\sigma} = \frac{1}{|q|^2}\,\omega\mu_0 = |C|^2\omega\mu_0. \tag{7.20}$$

Since C is complex, an impedance phase ϕ can be derived and expressed as;

$$\phi = tan^{-1}\left(\frac{ImC}{ReC}\right). \tag{7.21}$$

Equation 7.20 and 7.21 for the resistivity and phase are the most important MT parameters and are normally plotted as a function of period T (Simpson and Bahr, 2005).

7.2.5. The impedance tensor

Signal processing investigates the response of a linear and time-invariant system to an artificial input signal. In the MT technique, the linear system can be thought of having two inputs, the horizontal components of the time-varying magnetic field $(b_x(t))$ and $(b_y(t))$, and two independent outputs, the horizontal components of the time-varying electric field $(e_x(t))$ and $(e_y(t))$ (Jones *et al.*, 1989). In the time-domain, and neglecting the noise components, these fields are connected by convolution to four weighting functions, $z_{xx}(t)$, $z_{xy}(t)$, $z_{yx}(t)$ and $z_{yy}(t)$, which describe how the input $(b_x(t))$ and $(b_y(t))$ is modelled to produce the outputs $(e_x(t))$ and $(e_y(t))$. Their Fourier transform equivalent in the frequency-domain is the Z-transform or impedance tensor (Jones *et al.*, 1989). The function that relates the input and output signals using a transformation operator is termed a transfer function. The impedance tensor for MT was first defined by Berdichevesky (1960) and Tikhonov and Berdichevesky (1966), and is usually expressed as a 2 X 2 complex transfer function

$$\begin{pmatrix} E_x \\ E_y \end{pmatrix} = \begin{pmatrix} 0 & Z_{xy} \\ Z_{yx} & 0 \end{pmatrix} \begin{pmatrix} \frac{B_x}{\mu_0} \\ \frac{B_y}{\mu_0} \end{pmatrix} \quad \text{or} \quad \mathbf{E} = \frac{\underline{\underline{\mathbf{Z}}}\mathbf{B}}{\mu_0}, \tag{7.22}$$

where **E**, **B** and $\underline{\underline{Z}}$ are in S.I. units (Vm^{-1}, T = $\frac{Vs}{m^2}$ and $\Omega = \frac{V}{A}$). Applying the relation of $\boldsymbol{B} = \mu_0 \boldsymbol{H}$ (Equation 7.4), results in the following equivalent equation;

$$\begin{pmatrix} E_x \\ E_y \end{pmatrix} = \begin{pmatrix} 0 & Z_{xy} \\ Z_{yx} & 0 \end{pmatrix} \begin{pmatrix} H_x \\ H_y \end{pmatrix} \quad \text{or} \quad \mathbf{E} = \underline{\underline{\mathbf{Z}}}\mathbf{H} \tag{7.23}$$

Each component of the impedance tensor defines two mutually perpendicular horizontal components of **E** and **B** measured in the field. For example in the 1D Earth, the component $Z_{xy} = \frac{E_x}{\mathbf{H_y}}$, defines the impedance given by the electric field in the x-direction and the magnetic field in the y-direction. Another transfer function commonly used in the MT technique is the geomagnetic transfer function, which relates the horizontal and vertical components of the magnetic field. The complex induction arrows or tipper pointers, initially introduced by Parkinson (1959), are used to represent the presence, or absence of lateral variations of conductivity, that generate vertical magnetic fields (Simpson and Bahr, 2005).

$$\boldsymbol{H}_z = \left(T_x, T_y\right)\begin{pmatrix}H_x \\ H_y\end{pmatrix}. \tag{7.24}$$

These pointers are termed tipper pointers or misleadingly tipper vectors because they transform or tip the horizontal magnetic fields into the vertical plane. They are diagnostic of lateral conductivity variations (Simpson and Bahr, 2005).

7.2.6. The 1D Earth

In the simplest case of a 1D isotropic layered Earth, the conductivity only changes with depth, the diagonal components (Z_{xx} and Z_{yy}) of the impedance tensor, which are related to the parallel electric and magnetic fields are reduced to zero. As there is no lateral conductivity change, the off-diagonal elements (Z_{xy} and Z_{yx}) have the same amplitude. However, to preserve the right-hand rule, they must have a different sign (Simpson and Bahr, 2005). Therefore, the transfer function for a 1D Earth can be written as;

$$\begin{pmatrix}E_x \\ E_y\end{pmatrix} = \begin{pmatrix}0 & Z_{xy} \\ -Z_{yx} & 0\end{pmatrix}\begin{pmatrix}\frac{B_x}{\mu_0} \\ \frac{B_y}{\mu_0}\end{pmatrix} \qquad \text{or} \qquad \boldsymbol{E} = \underline{\underline{Z}}_{1D}\,\frac{\boldsymbol{B}}{\mu_0}. \tag{7.25}$$

Decomposing the transfer function into its components and solving for Z_{yx} yields;

$$Z_{xy} = \mu_0 \frac{E_x}{B_y} = -\mu_0 \frac{E_y}{B_x}. \tag{7.26}$$

Equation 7.26 is comparable to the Schmucker-Weidelt transfer function (Equation 7.19) and can also be derived from Maxwell's Equations for the 1D case. The only difference is in the definition of the transfer function where $C = {}^{1}/_{q}$ for the Schmucker-Weidelt function and $Z = {}^{i\omega\mu_0}/_{q}$ for the impedance tensor and these transfer functions can be related by $Z = i\omega\mu_0 C$. Therefore, an apparent resistivity and phase for a 1D layered Earth is given by;

$$\rho_a = \frac{1}{\sigma} = \frac{1}{|q|^2}\mu_0\omega = \frac{|Z|^2}{\mu_0\omega} \tag{7.27}$$

$$\phi = tan^{-1}\left(\frac{ImZ}{ReZ}\right) \tag{7.28}$$

these equations (Equation 7.27 and 7.28) are similar to Equations 7.20 and 7.21 however, apparent resistivity in their case is defined as the average resistivity of a homogenous half-space.

7.2.7. The 2D Earth

For a 2D Earth, conductivity varies with depth and along a single lateral dimension (Figure 7.5). When one of the incorporating fields, either the **E** or **B** field, is parallel to the strike direction, the diagonal impedance components are zero (Z_{xy} and Z_{yx}), as an electric field parallel to strike induces a magnetic field perpendicular to strike and vice versa. The off-diagonals now differ from each other, and the transfer function is represented as;

$$\begin{pmatrix} E_x \\ E_y \end{pmatrix} = \begin{pmatrix} 0 & Z_{xy} \\ Z_{yx} & 0 \end{pmatrix} \begin{pmatrix} \frac{B_x}{\mu_0} \\ \frac{B_y}{\mu_0} \end{pmatrix} \qquad \text{or} \qquad \boldsymbol{E} = \underline{\underline{Z}}_{2D} \frac{\boldsymbol{B}}{\mu_0}. \tag{7.29}$$

Equation (7.29) represents the along strike case, where the x-axis is defined parallel to the strike direction. Therefore, the off-diagonal elements of the impedance tensor represent two polarisation modes, defined as the transverse electric (TE) and transverse magnetic (TM) modes.

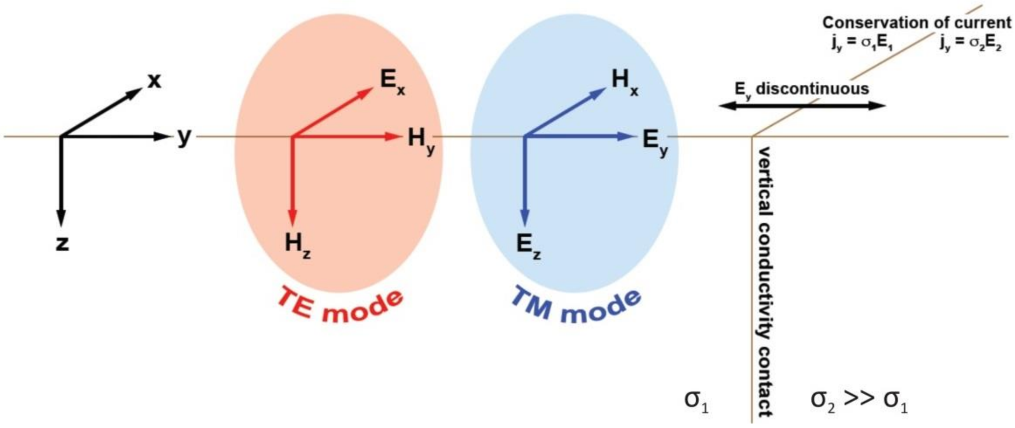

Figure 7.5: A simplistic 2D model with a planar boundary separating two quarter-spaces with different conductivities (σ_1 and σ_2; modified after Simpson and Bahr, 2005). The y-component of the electric field (E_y) is discontinuous across the vertical boundary because of the conservation of current across a vertical discontinuity. For an ideal 2D case, the EM fields can be decoupled into the two independent modes i.e. the TE and TM modes.

The TE mode is composed of E_x, B_y and B_z and can be expressed as (Simpson and Bahr, 2005);

$$\left.\begin{aligned} \frac{\partial E_x}{\partial y} &= i\omega B_z \\ \frac{\partial E_x}{\partial z} &= -i\omega B_y \\ \frac{\partial B_z}{\partial y} - \frac{\partial B_y}{\partial z} &= \mu\sigma E_x \end{aligned}\right\} TE\ mode, \tag{7.30}$$

while the TM mode is composed of E_y, B_x and E_z and can be expresses as (Simpson and Bahr, 2005);

$$\left.\begin{aligned} \frac{\partial B_x}{\partial y} &= \mu_0\sigma E_z \\ -\frac{\partial B_x}{\partial z} &= \mu_0\sigma E_y \\ \frac{\partial E_z}{\partial y} - \frac{\partial E_y}{\partial z} &= i\omega B_x \end{aligned}\right\} TM\ mode. \tag{7.31}$$

According to Ohm's Law, the current density j_y across a vertical boundary must be conserved (Figure 7.5), causing discontinuity in the electric field E_y. Impedance tensors associated with E_y (Z_{yx}, since Z_{yy} is zero for an ideal case) are also discontinuous across the boundary with the discontinuity having a magnitude of σ_2/σ_1, and from Equation 7.27 the apparent resistivity perpendicular to the strike direction (ρ_{yx}) will have a magnitude discontinuity of $(\sigma_2/\sigma_1)^2$. As a result of the discontinuous behaviour of ρ_{yx} across the vertical boundary, the TM mode resolves lateral conductivity changes better than the TE mode resistivities (Figure 7.5). Since the geomagnetic transfer function is sensitive to lateral conductivity changes, the TE mode can also be used to identify lateral conductivity changes.

The transfer function for the 2D Earth is based on the assumption that the induction of the electric fields is parallel or perpendicular to the geoelectric strike direction. However, this is rarely the case for MT soundings, since the strike direction is often not known precisely at the time of the survey (Vozoff, 1991). As a result, the diagonal components of the impedance tensor will not be zero and the off-diagonal components will be mixed within the impedance tensor. In the case of an ideal 2D structure with no noise in the data, it is possible to rotate the impedance tensor around a vertical axis until the diagonal components are zero and the 2D impedance tensor is in the strike coordinates. However, this is only possible when assuming an ideal 2D structure and that there is no noise in the data. The ideal 2D impedance tensor can be calculated using the Cartesian rotation matrix $\underline{\underline{R_\theta}}$ with a rotation angle θ as;

$$\underline{\underline{Z_{2D}}} = \underline{\underline{R_\theta}}\,\underline{\underline{Z_{Obs}}}\,\underline{\underline{R_\theta^T}}\text{ , where} \tag{7.32}$$

$$\underline{\underline{R_\theta}} = \begin{pmatrix} cos\,\theta & sin\,\theta \\ -sin\,\theta & cos\,\theta \end{pmatrix} \text{ and } \underline{\underline{R_\theta^T}} = \begin{pmatrix} cos\,\theta & -sin\,\theta \\ sin\,\theta & cos\,\theta \end{pmatrix} \tag{7.33}$$

where $\underline{\underline{R_\theta}}$ is the rotation matrix and its transposed $\underline{\underline{R_\theta^T}} \cdot \underline{\underline{Z_{Obs}}}$ is the observed impedance tensor of the measured data. In principle, it is possible to find the rotation angle between the measured direction and strike by simply rotating the 2D impedance tensor in increments of the rotation angle and plotting the off-diagonal impedances on a polar diagram to examine the best angle from the plots. In the presence of noise, however, an appropriate rotation angle cannot be determined and techniques that rely solely on the analytic rotational properties of the MT impedance tensor can yield erroneous results (Jones and Groom, 1993).

7.2.8. Depth and resistivity approximations

It is often useful to determine a first-order approximation of the investigation depth. These approximations are all based on the homogenous half-space approach. One of these depth estimates is based on the inverse of the real part of q (Equation 7.18) and is known as the skin depth δ, expressed as;

$$\delta(T) = \sqrt{\frac{2}{\mu_0 \sigma(T) \omega(T)}} = \sqrt{\frac{T}{\mu_0 \sigma(T) \omega(T)}}, \tag{7.34}$$

with $T = \frac{2\pi}{\omega}$. Equation 4.30 states that for each chosen depth δ(T), the amplitude of the penetrating fields are attenuated to $\frac{1}{e}$ in a homogenous half-space of the resistivity equal to the apparent resistivity measured at the chosen period. Replacing the average conductivity σ of the half-space by its inverse, the apparent resistivity $\rho_a$an approximation for the penetration depth (in metres) is determined;

$$\delta(T) \approx 503\sqrt{\rho_a(T)T} \tag{7.36}$$

where $\rho_a = \frac{1}{\sigma}$ is the apparent resistivity at a period $T = \frac{1}{f}$ with $\omega = 2\pi f$.

Different penetration depth estimates which apply an attenuation factor of approximately $\frac{1}{2}$ at each period were in dependently developed by Niblett and Sayn-Wittgenstein (1960) and Bostick (1977). These two depth estimates have been shown to be equivalent and was termed the Niblett-Bostick depth approximation by Jones (1983a). The approximation depth for the Niblett-Bostick approximation (δ_{NB}) is given by;

$$\delta_{NB} = \sqrt{\frac{\rho_a(T)T}{2\pi\mu_0}} \tag{4.37}$$

The Niblett-Bostick resistivity at the depth δ_{NB} is estimated as

$$\rho_{NB}(\delta_{NB}) = \rho_a(T)\frac{1+m(T)}{1-m(T)} \tag{4.38}$$

where on a log-log scale, $m(T)$ is the gradient of the apparent resistivity curve and can be expressed as;

$$m(T) = \frac{\partial \, log(\rho_a(T))}{\partial \, log(T)} = \frac{T}{\rho_a(T)}\frac{\partial \rho_a(T)}{\partial T}, \tag{4.39}$$

where ρ_a is the apparent resistivity, T is the period and μ_0 is the magnetic permeability.

7.2.9. Distortion effects

Distortion effects are caused by small-scale, near-surface conductivity heterogeneities and topography that cannot be resolved within the conductivity model of the subsurface. Distortion effects can be classified into two major classes, galvanic and inductive effects. Galvanic effects are caused by the primary electric fields generating electrical charges where variations in conductivity occur (i.e. at distinct boundaries or continuous transitions), leading to distortion in the primary electric field from the excess electrical charges in the secondary electric field that adds vectorially to the primary field. Inductive effects are related to time-varying magnetic fields inducing currents flow in closed loops, which produce a secondary magnetic field that adds vectorially to the primary field (Jiracek, 1990).

Galvanic distortion affects both the electric and magnetic fields and whilst not completely separate, these effects are often considered as different and are termed galvanic electric distortion and galvanic magnetic distortion (Chave and Smith, 1994; Chave and Jones, 1997; Garcia and Jones, 2002). A conductive inclusion generates boundary charges that cause a secondary field anti-parallel to the primary field along the sides and over the conductive body, reducing the total field. The total field is however, locally enhanced off the ends of the conductive body. The effects are reversed for a resistive inclusion, with the total field locally enhanced along the sides and over the resistive body and reduced off the end of the body (Figure 7.6) (Jiracek, 1990). According to Smith (1997), galvanic electric fields channel the current around resistive heterogeneities and through conductive heterogeneities. The apparent resistivity recorded in an MT sounding directly above a resistive body, are shifted upwards compared to directly over a conductive body which is shifted downwards. This upwards and downwards shift is asymptotically a constant on the MT log-log graph of apparent resistivity versus period. These shifts (effects) are known as static shifts. No distortion occurs in the impedance phase.

Jiracek (1990) showed that these galvanic effects can also be caused by 2D topography, termed galvanic topographic effect. This effect occurs when the primary electric field is perpendicular to the trend of the topography, and is associated with the TM mode. At the top of a hill or bottom of a valley, there are no surface charges whilst, where the topography is steepest there is a maximum charge concentration. Beneath the surface, the total electric field generates a current flow tangential to the topography reducing the electric fields at the top of the hill and increasing those in a valley. The apparent resistivity values are lowest on topographic peaks and highest in topographic lows. The galvanic topographic effects do not require a conductivity inhomogeneity to be present unlike the "normal" galvanic effects (Jiracek, 1990).

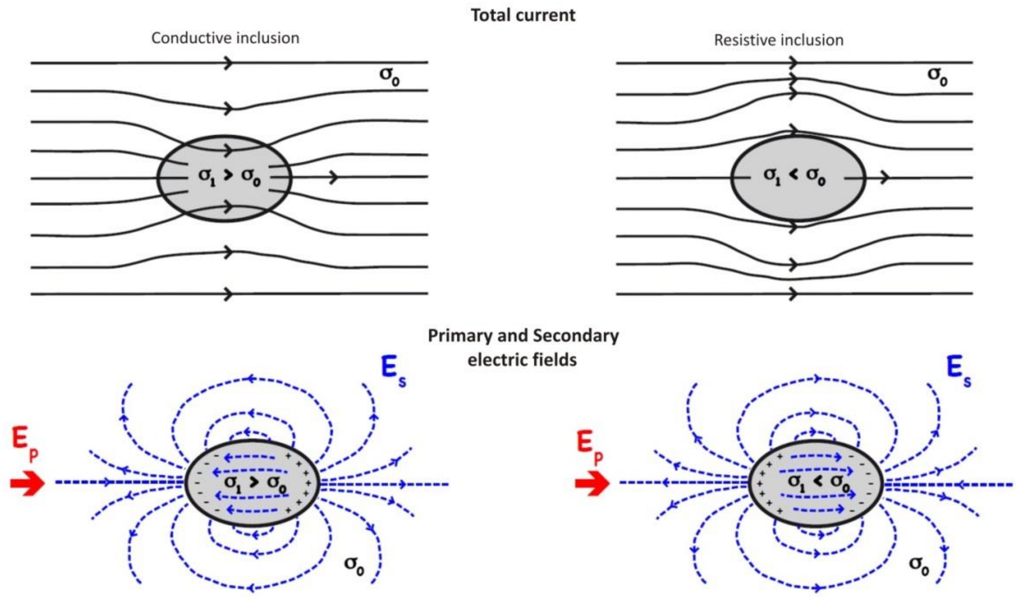

Figure 7.6: Galvanic effects for a conductive (left) and resistive (right) inclusion (after Jiracek, 1990). Charge build-up on the surface of the inclusion causes the secondary electric field ($\underline{E}_s$) that is vectorially added to the primary electric field ($\underline{E}_p$) (bottom) resulting in current channelling (top left) and current deflection (top right).

Inductive effects are dependent on the frequency, electrical properties and geometry of the subsurface. The phase of the secondary magnetic field for the inductive effects varies between 0 (resistive limit) and $\frac{\pi}{2}$ (inductive limit) relative to the primary magnetic field compared to galvanic effects where the secondary electric field is in phase with the causative primary electric field. The main difference between galvanic and inductive effects is that the latter increases to saturation as frequency increases and the magnetic field has the leading role, while the electric field is more important in the former, which increases to saturation with decreasing frequency (Jiracek, 1990).

For the quasi-stationary approximation ($\sigma = \frac{\varepsilon}{T}$; assumption VII) inductive effects can be ignored (Berdichevsky and Dmitriev, 1976). For the mathematical description of the galvanic distortion, the reader is referred to Chave and Smith (1994) and Smith (1997).

Several distortion correction approaches (statistically, mathematically or physically based) have been proposed to deal with or remove the unwanted galvanic effects due to near-surface heterogeneities and topography (see Jiracek, 1990; Groom and Bahr, 1992 for more details). To correct for static shifts in the MT response, Pellerin and Hohmann (1990) and Sternberg (1993) use the Transient ElectroMagnetic (TEM) data, either by joint inversion allowing vertical shifts in the MT apparent resistivity curves, or by a correction scheme that is based on the 1D inversion of the TEM soundings. A synthetic MT response is computed for short periods (≤ 1 s) from the estimated 1D structure. Static shift is then removed by shifting the observed MT curves to match the computed curves. The different approaches to accomplish this are described by de Groot-Hedlin (1991, 1995). To find the smoothest model, de Groot-Hedlin (1991) inverts for the static shift while de Groot-Hedlin (1995) inverts for the full electric galvanic matrix and resistivities in 2D simultaneously.

One of the most commonly used decomposition techniques to obtain the regional 2D strike direction, a measure of the anisotropy and galvanic distortion effects from distorted measured data, is by Groom and Bailey (1989) (discussed below). There are however, several other techniques available, such as Swift (1967), Bahr (1988) and Martí *et al*. (2005), which are not discussed in this dissertation.

Groom-Bailey decomposition

A distortion tensor decomposition based on a physical model of distortion for a 2D regional impedance was first proposed by Bailey and Groom (1987), Groom (1988) and Groom and Bailey (1989). Their model was based on Larsen's (1977) decomposition model comprising a local, small-scale 3D anomaly over a layered Earth. The galvanic distortion is neglected and only the real and frequency independent electric galvanic distortion matrix is dealt with. The Groom-Bailey decomposition aims to factorise the measured impedance ($\underline{\underline{Z}}_{obs}$) (in Equation 7.32) into a rotation matrix ($\underline{\underline{R}}$), distortion matrix ($\underline{\underline{C}}$) and a scaled regional 2D impedance tensor ($\underline{\underline{Z}}_{2D}$), thus separating the local 3D distortion from the regional 1D or 2D response.

$$\underline{\underline{Z}}_{2D} = \begin{pmatrix} 0 & Z_{xy} \\ Z_{xy} & 0 \end{pmatrix} \quad \text{and} \quad \underline{\underline{C}} = \begin{pmatrix} C_{xx} & C_{xy} \\ C_{xy} & C_{yy} \end{pmatrix} \tag{7.49}$$

A parameterisation of the distortion matrix, which has a physical meaning, but also separates determinable and indeterminable parts, was used by Groom (1988) and Groom and Bailey (1989). $\underline{\underline{C}}$ is a product of a scaling factor (g) and three tensors; local anisotropy ($\underline{\underline{A}}$), shear ($\underline{\underline{S}}$) and twist ($\underline{\underline{T}}$) and can be expresses as;

$$\underline{\underline{Z}}_{2D} = \underline{\underline{R}}_{\theta}\underline{\underline{C}}\underline{\underline{Z}}_{2D}\underline{\underline{R}}_{\theta}^{T}, \text{ where } \underline{\underline{C}} = g\underline{\underline{T}}\,\underline{\underline{S}}\,\underline{\underline{A}}. \tag{7.50}$$

The idealised physical model comprises an elongated swamp (ellipse), representing a highly conductive region surrounded by a moderately conductive region. In turn, the moderately conductive region is encompassed by an insulating region, in 360° spatial arrangement. MT data that are collected at the centre of the ellipse will be rotated in the direction of the major axis of the ellipse (towards local strike). The rotational component of the telluric vector can be stored in the twist tensor $\underline{\underline{T}}$ (Equation 7.51). Since the elongation of the ellipse also leads to anisotropy, perpendicular/parallel to the major axis, distortion-related to stretching of the telluric currents can be stored in the anisotropy tensor $\underline{\underline{A}}$ (Equation 7.51). The shear tensor $\underline{\underline{S}}$ develops anisotropy on axes which bisects the regional inductive principle axes (Groom and Bailey, 1989). In contrast to $\underline{\underline{A}}$ which does not change the direction of the telluric vectors, $\underline{\underline{S}}$ rotates a vector on the x-axis clockwise and a vector on the y-axis anti-clockwise by an angle of $tan^{-1}\, e$ (the axes are non-orthogonal). For a shear angle of ± 45° the electric field becomes polarised, and information about the subsurface is obtained in the direction of the polarised electric field (which may not be the regional strike direction) (McNeice and Jones, 2001). The gain (g) performs an overall scaling of the electric field. The unit vector operators twist $\underline{\underline{T}}$, shear $\underline{\underline{S}}$ and $\underline{\underline{A}}$ are expressed in terms of the real values *t*, *e*, and s, respectively as;

$$\underline{\underline{T}} = \frac{1}{\sqrt{1+t^2}}\begin{pmatrix} 1 & -t \\ t & 1 \end{pmatrix}, \quad \underline{\underline{S}} = \frac{1}{\sqrt{1+e^2}}\begin{pmatrix} 1 & e \\ e & 1 \end{pmatrix}, \quad \underline{\underline{A}} = \frac{1}{\sqrt{1+s^2}}\begin{pmatrix} 1+s & 0 \\ 0 & 1-s \end{pmatrix} \tag{7.51}$$

Equation 7.50 does not have a unique solution however, since the gain g and anisotropy tensor $\underline{\underline{A}}$ cannot be determined separately from $\underline{\underline{Z}}_{2D}$ i.e. $\underline{\underline{Z}}'_{2D} = g\underline{\underline{A}}\,\underline{\underline{Z}}_{2D}$, a unique solution exists.

In general, two solutions exist but only one is practical (Groom and Bailey, 1989). One solution is when $|e| \leq 1$ and the other is $|e| \geq 1$ (Groom and Bailey, 1989). Considering the shear operator (Equation 7.51), a shear angle larger than 45° is not practical, as it implies a reversal of the current flow direction. Therefore, a practical physical solution is provided by $|e| \leq 1$.

If both noise and local galvanic distortion is present in the MT data then care must be taken when determining the geoelectric strike (Jones and Groom, 1993). According to Jones and Groom (1993), twist and shear are more stable over a wide period band compared to the regional strike direction. This occurs as distortion caused by charge effects being dominant over induction caused by currents. The choice of distortion parameters impose a coordinate system on the MT data, which leads to erroneous strike determination (Jones and Groom, 1993). To minimise this error, Jones and Groom (1993) iterated between constraining the strike and distortion parameters until a reliable result was obtained. Strong distortion is characterised by high twist and shear. Jones and Groom (1993) state that when shear is unity, the local current channelling is so severe that the MT data will only contain information from a single electric field direction, and no technique will ever be able to extract the regional impedance from both modes.

7.3. Magnetotelluric processing

This section illustrates the analysis and primary approaches applied prior to modelling the MT data. These approaches involve strike analysis using the Groom-Bailey decomposition (Section 7.2.9) and editing of the data to identify and deactivate outliers in the data. To support the selection and deactivation of data points, which have large error bars and scatter D^+ and ρ^+ were analysed (Section 7.3.2). This section establishes the MT modelling procedure and selected results. The 1D models 'guessed' from the smooth Occam inversion (Constable *et al*., 1987) form the starting models for the 1D sharp boundary models for each station.

7.3.1. Strike analysis and decomposition

Sections 7.2.5 and 7.2.7 establish the advantage of decomposing the measured impedance tensor $\underline{\underline{Z}}_{Obs}$, when dealing with 2D subsurface in the presence of telluric distortion. In general, the dimensionality of the problem is unknown and MT measurements are not conducted parallel or perpendicular to the geological strike. The decomposition approach of Groom and Bailey (1989) calculates the regional 2D strike direction and yields measurements of the distortion effect by separating the observed impedance data into a distortion matrix and recalculated impedance matrix (Equation 7.32). A rotational framework around these matrices attempts to recalculate the impedance matrix in away, that the new matrix $\underline{\underline{Z}}_{2D}$ describes a 2D tensor (along strike case, where the diagonal elements are zero, Equation 7.29). The angle θ, used in the rotation matrix, Equation 7.33, is referred to as the strike angle. These calculations have to be carried out independently on a frequency-by-frequency and site-by-site basis (Groom and Baily, 1989). The accuracy of the galvanic distortion and dimensionality assumption is statistically analysed yielding a Root Mean Squared (RMS) misfit between the observed impedance tensor $\underline{\underline{Z}}_{Obs}$ and the calculated decomposition factors (rand-hand side of Equation 7.32). A less time-consuming approach is proposed by of McNeice and Jones (2001), in which a global minimum is required to determine the most appropriate geoelectric strike direction and electromagnetic distortion parameters for a range of frequencies and stations (i.e. multi-frequency, multi-site analysis). This multi-frequency, multi-site analysis is useful in determining the approximate geoelectric strike direction for the whole MT profile or segments of it at various frequency bandwidths (a maximum and minimum frequency). McNeice and Jones developed a computer code based on the Groom and Bailey decomposition (Groom and Bailey, 1989; Groom *et al*., 1993) called *strike*. This study uses the latest version (version 6.0) of *strike*, which allows for user defined frequency bandwidth by defining the maximum and minimum depth ranges based on the Niblett-Bostick depth approximation (Equation 4.38) for the strike analysis of the DMB, NEN and OKA-CAM profiles.

Note, that decomposition to strike is not the same as a simple rotation of the data in that direction. When applying decomposition, the impedance elements are recalculated and the majority of the distortion effects are removed with only static shifts remaining. The maximum phase difference in decomposed data has been used as an indication of data dimensionality (Spratt *et al*., 2009). Decomposed data that has a maximum phase difference of below 10° over a broad period band is considered as 1D (Spratt *et al*., 2009).

Geoelectric strike angle analysis

Before the strike analysis (single or multi-strike) is conducted the quality of the data beneath each station is analysed. The accuracy of the strike analysis beneath each station or profile is determined by examining the Root Mean Squared (RMS) misfit. The RMS is computed after the strike analysis and is the difference of the data and modelled values. If the RMS is greater than three, the data is considered poor and the station is neglected from the strike analysis. The blank (white) stations occur because the station has a shallower depth penetration compared to the selected depths. The RMS plots also show how sensitive the data are to the geoelectric strike angle, with lower RMS values indicating stations that are insensitive to, or compatible with, the geoelectric strike direction of the geology beneath the station.

Error analysis (RMS plots)

The colour beneath each station represents the average RMS misfit of the distortion model to the data. Green colours indicate a good data fit while red colours indicate a bad data fit. The dimensionality of each station cannot be estimated by the RMS misfit plots, as a high RMS misfit can be caused by a distortion or higher dimensionality, or both.

Figure 7.7 shows the sensitivity of each station on the DMB profile to the geoelectric strike. For the depths of 1 – 5 km and 1 – 35 km, all stations, except station DMB013, are relatively insensitive to the geoelectric strike with an RMS value of less than 1.5 (Figure 7.7a and c). For the depth of 1 – 15 km a geoelectric strike of ~30° to 60° is preferred with an RMS value of 0.6 inside this range and 1.2 outside the this range (Figure 7.7b). Station DMB013 is sensitive to a geoelectric strike angle between ~10° to 35° for the depths of 1 – 5 km and 1 – 35 km (Figure 7.7a and b) and between 75° to 90° for the depth of 1 – 15 km (Figure 7.7b). There is no noticeable change in the preferred geoelectric strike angle between the Damara Belt and the conductive zone (van Zijl and de Beer, 1983) with the surrounding geology.

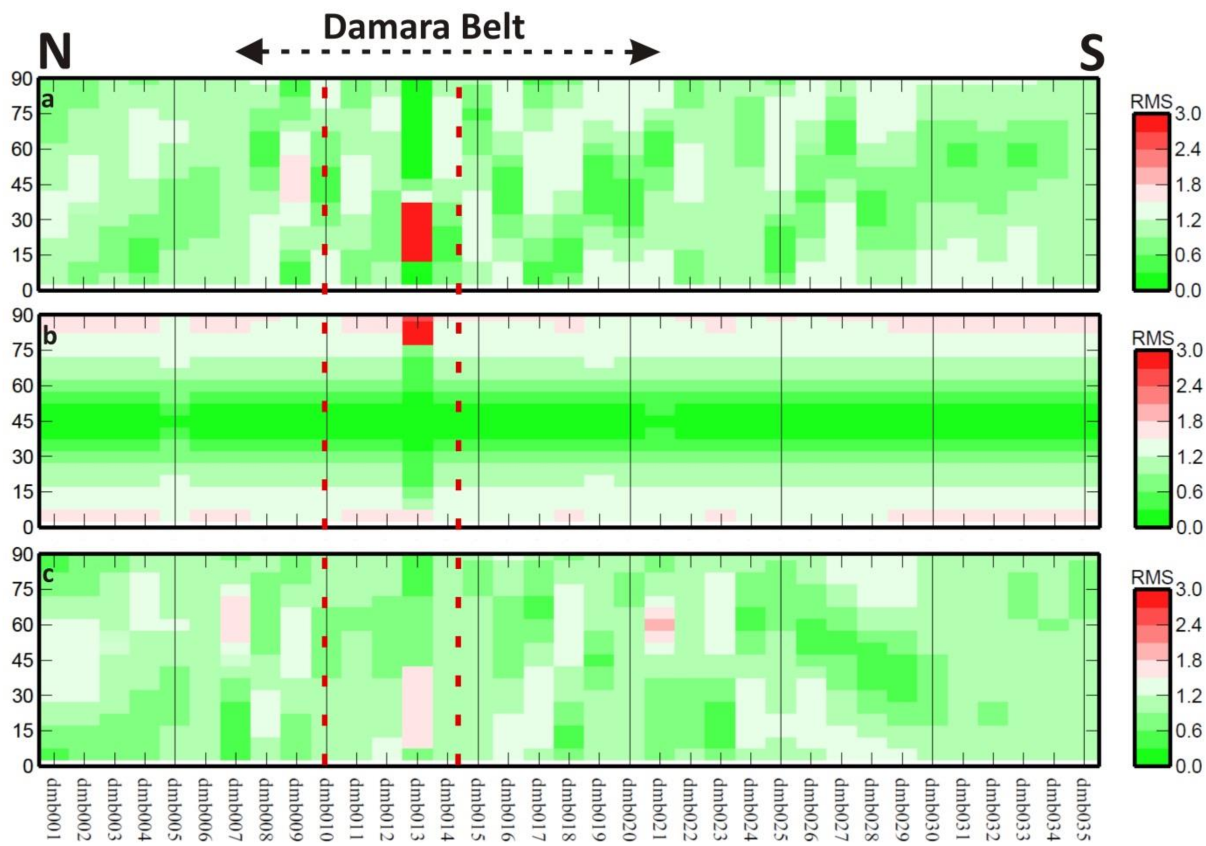

Figure 7.7: Single strike RMS plot for the DMB profile for depths of a) 1 – 5 km, b) 1 – 15 km and c) 1 – 35 km. The red dashed lines represent the surface outline of the conductive zone as defined by van Zijl and de Beer (1983). The aeromagnetic interpreted extent of the Damara Belt in relation to the MT stations is shown by the dashed arrow along the top of profile a).

The following NEN stations have a shallow depth penetration, NEN018, NEN019 and NEN118, seen by the blank (white) RMS plots beneath the respective stations (Figure 7.8a, b and c). The data of these stations were masked to depths of between 2.5 km and 3.5 km, as one if not both modes (TE and TM modes) plotted out of phase (> 90°), where geoelectric strike information was obtained. At a depth of 1 – 5 km, an RMS value of ~2 is seen beneath stations NEN003 and NEN004, for a geoelectric angle of ~40° - 50° and beneath stations NEN012 and NEN014 at geoelectric angles of ~15° and 30°, respectively (Figure 7.8a). The deeper depths have RMS values of ~2 for high geoelectric strike angles of ~90° beneath station NEN012 for depths of 1 – 15 km and 1 – 135 km and beneath station NEN006 at a depth of 1 – 35 km (Figure 7.8b and c). The conductive zone of van Zijl and de Beer (1983) has a smooth geoelectric strike RMS of less than one compared to the other zones that have various RMS value ranges (Figure 7.8).

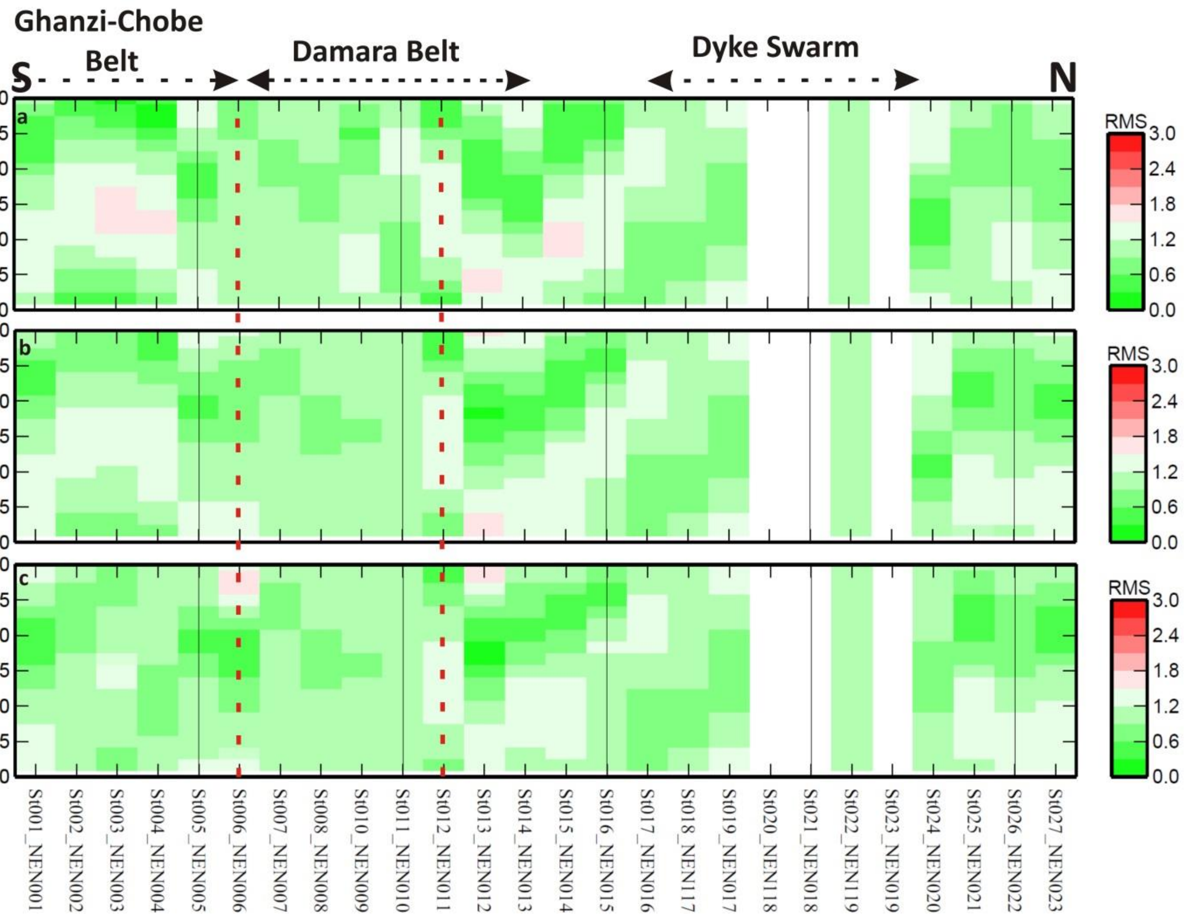

Figure 7.8: Single strike RMS plot for the NEN profile for depths of a) 1 – 5 km, b) 1 – 15 km and c) 1 – 35 km. The red dashed lines represent the surface outline of the conductive zone as defined by van Zijl and de Beer (1983). The aeromagnetic interpreted extent of the Damara Belt, Ghanzi-Chobe Belt and Dyke Swarm in relation to the MT stations is shown by the dashed arrows along the top of profile a).

The sensitivity of each station on the OKA-CAM profile to the geoelectric strike is shown in Figure 7.9. Stations CAM043 to CAM048 were excluded from this study as they are located off the main OKA-CAM profile while stations CAM018 to CAM020, CAM022 and CAM023 were excluded because of their shallow penetration depths and/or poor data quality on the resistivity and phase curves. Beneath the inferred aeromagnetic extent of the Ghanzi-Chobe Belt, the MT stations are more sensitive to geoelectric strike angles between 15° to 45°, seen by the RMS value of greater than 1.2 (Figure 7.9). The stations above the Okavango Dyke Swarm generally have an RMS value of less than 1.2, with stations CAM026 and CAM027 having an RMS of greater than two for a geoelectrical strike angle of ~45° and 60°, respectively for a depth interval of 1 – 5 km (Figure 7.9a). The stations above the Damara Belt for the all depth intervals are sensitive to geoelectric strike angles of between 15° to 60°, seen by the RMS values of ~2 beneath stations CAM006 to OKA013, CAM010, CAM014, CAM017 and OKA019 (Figure 7.9).

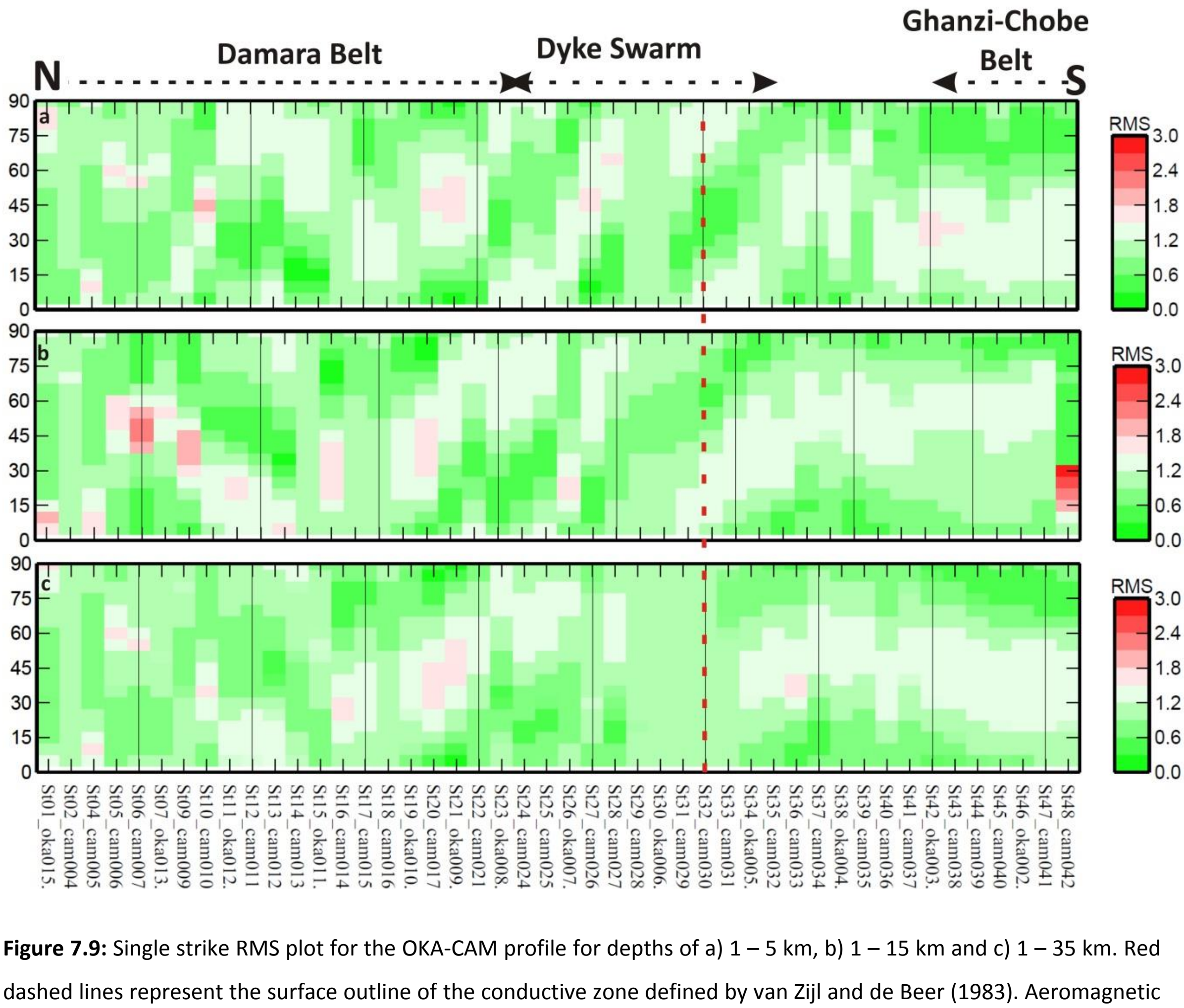

Figure 7.9: Single strike RMS plot for the OKA-CAM profile for depths of a) 1 – 5 km, b) 1 – 15 km and c) 1 – 35 km. Red dashed lines represent the surface outline of the conductive zone defined by van Zijl and de Beer (1983). Aeromagnetic interpreted extent of the Damara and Ghanzi-Chobe Belts and Dyke Swarm in relation to the MT stations is shown by the dashed arrows along the top of profile a).

Single-strike analysis

To determine if the geoelectric strike varies with respect to depth, single strike analyses were applied to each station along the profile.

Single station geoelectric strike angles were calculated for a depth interval of 1 – 15 km on the DMB profile (Table 7.1). Table 7.1 is divided into three parts based on the location of the stations in relation to the inferred extent of the Damara Belt. The northern stations are north of the northern boundary of the Damara Belt. The central part comprises stations that lie within the boundaries of the Damara Belt and the southern part comprises stations that lie to the south of the southern boundary of the Damara Belt. The RMS-error value for the DMB profile is generally less than 2, except for five stations (DMB005, DMB011, DMB012, DMB013 and DMB028) which have an RMS value of two or greater. In general, these higher RMS values are located in the vicinity of the northern boundary of the Damara Belt. There is a strong correlation between the extent of the Damara Belt, as interpreted from aeromagnetic data and a sudden change in the geoelectric strike. The northern boundary of the Damara Belt is inferred to be in the vicinity of station DMB008, which has a geoelectric strike of 55.13° E of north compared to the geoelectric strike of station DMB007, which is 16.96° E of north (or its 90° ambiguity). The southern boundary is inferred to be in the vicinity of station DMB021 that has a geoelectric strike of 50.18° E of north compared to station DMB022, which has a geoelectric strike of 19.19° E of north (Table 7.1).

Table 7.1: Single strike analysis for the DMB profile for a depth interval of 1 – 15 km indicating the preferred geoelectric strike with the smallest resultant misfit (RMS) and the preferred strike range. The profile is divided into northern, central and southern parts from the interpreted aeromagnetic extent of the Damara Belt.

Section	Site	1 - 15 km		
		Strike (°)	Range (°)	RMS
Northern	dmb001	86.80	86.95 - 86.45	1.13
	dmb002	88.90	88.80 - 89.01	1.14
	dmb003	17.67	17.24 - 18.10	1.54
	dmb004	18.40	18.35 - 18.4	1.56
	dmb005	36.40	36.28 - 36.53	2.00
	dmb006	43.12	42.98 - 43.26	1.53
	dmb007	16.96	16.96 - 17.06	0.70
Central	dmb008	55.13	54.97 - 55.28	0.23
	dmb009	87.00	86.76 - 87.25	0.37
	dmb010	53.01	52.74 - 53.29	1.98
	dmb011	72.10	72.01 - 72.19	3.30
	dmb012	59.33	59.26 - 59.41	2.59
	dmb013	84.00	83.92 - 84.08	2.17
	dmb014	80.39	80.06 - 80.72	1.07
	dmb015	80.00	79.96 - 80.04	0.91
	dmb016	45.15	45.04 - 45.25	0.77
	dmb017	74.59	74.11 - 75.07	0.44
	dmb018	8.29	8.12 - 8.47	0.49
	dmb019	49.49	49.44 - 49.54	1.03
	dmb020	46.86	46.19 - 47.52	1.68
	dmb021	50.18	50.59 - 50.77	0.76
Southern	dmb022	19.19	18.81 - 19.58	0.77
	dmb023	21.67	21.44 - 21.91	0.48
	dmb024	65.57	65.41 - 65.72	0.52
	dmb025	6.27	6.18 - 6.35	1.47
	dmb026	54.90	54.82 - 54.98	1.34
	dmb027	80.00	80.00 - 80.00	1.86
	dmb028	80.00	80.00 - 80.00	2.56
	dmb029	37.39	35.23 - 37.39	0.85
	dmb030	52.88	52.00 - 53.77	1.15
	dmb031	68.20	67.85 - 68.56	0.81
	dmb032	75.56	67.85 - 68.56	0.58
	dmb033	80.00	80.00 - 80.00	0.82
	dmb034	57.78	53.37 - 58.19	0.53
	dmb035	80.00	80.00 - 80.00	0.71

The geoelectric strike angle was calculated for depth intervals of 1 – 5 km and 1 – 15 km on the NEN profile (Table 7.2). The stations on the NEN profile are also divided into southern, central and northern parts (Table 7.2). The RMS value for both depth intervals is low with station NEN007 having a RMS value greater than two. The geoelectric strike of the two depth ranges correlates well with six stations (NEN006, NEN007, NEN009, NEN010, NEN014 and NEN022) having a geoelectric strike difference of 5° (Table 7.2). In general, the depth interval of 1 – 5 km is associated with higher geoelectric strike angles (Table 7.2). Stations NEN012 to NEN014 lie above the Quangwadum Complex. These stations are associated with a difference in geoelectric strike angle of ~5°. This difference in geoelectric strike suggests that the Quangwadum Complex is either underlain by a different geological terrain or it varies in geoelectric strike with depth. The stations (NEN017, NEN118, NEN018, NEN119 and NEN019) that lie above the Okavango Dyke Swarm have the same geoelectric strike angle and in general the same RMS value.

The northern boundary of the Damara Belt is inferred to be in the vicinity of station NEN015 that has a geoelectric strike angle of 80.27°E of north compared to the station NEN016, immediately to the north, which has a geoelectric strike of 19.23°E of north. The inferred southern boundary of the Damara Belt is in the vicinity of station NEN007 which has a geoelectric strike angle of 63.86° E of north compared to the station NEN006 to the south, which has a geoelectric strike of 81.65° E of north (Table 7.2). The central part of the NEN profile has an average geoelectric strike angle of 62.16°.

On the OKA-CAM profile, single station geoelectric strike angles analysis were calculated for depth ranges of 1 – 15 km and 1 – 35 km (Table 7.3). The OKA-CAM profile is divided into a southern and central part. The majority of the stations, for both depth ranges, have a RMS value of approximately one, with the exception of stations CAM004 and CAM009 which both have a RMS value of greater than three for both depth intervals. Comparing the geoelectric strike of the two depth intervals there are a large number of stations that have a geoelectric strike angle difference of greater than 5° (Table 7.3). The majority of these stations are situated in the central part of the OKA-CAM profile. The inferred southern boundary of the Damara Belt is in the vicinity of station CAM025 which has a geoelectric strike angle of 30.02°E of north compared to station CAM024, immediately to the north, which has a geoelectric strike of 20.65°E of north (Table 7.3) at a depth range of 1 -15 km. A difference in geoelectric strike angle of greater than 5° is also observed for the depth interval of 1 – 35 km.

Table 7.2: Single strike analysis for the NEN profile for depth intervals of 1 – 5 km and 1 – 15 km indicating the preferred geoelectric strike producing the smallest resultant misfit (RMS) and the preferred strike range. The profile is divided into northern, central and southern parts from the interpreted aeromagnetic extent of the Damara Belt.

Section	Site	1 - 5 km			1 - 15 km		
		Strike (°)	Range (°)	RMS	Strike (°)	Range (°)	RMS
Southern	NEN001	73.52	73.24 - 73.81	0.29	69.09	69.28 - 68.90	0.35
	NEN002	88.40	88.14 - 88.65	0.36	83.84	83.64 - 84.05	0.87
	NEN003	88.83	88.70 - 88.96	0.27	88.56	88.43 - 88.69	1.15
	NEN004	83.35	83.18 - 83.53	0.23	83.05	82.88 - 83.21	0.38
	NEN005	55.50	55.25 - 55.75	0.34	57.56	57.40 - 57.72	0.46
	NEN006	81.65	80.90 - 82.40	0.51	63.71	63.43 - 63.98	0.58
Central	NEN007	63.86	63.74 - 63.97	2.88	70.89	70.89 - 71.00	2.93
	NEN008	50.15	50.04 - 50.25	1.35	50.15	50.04 - 50.26	1.35
	NEN009	74.67	74.51 - 74.85	0.73	39.84	39.73 - 39.94	2.52
	NEN010	19.01	18.25 - 19.77	0.32	5.08	4.86 - 5.31	1.20
	NEN011	87.96	88.09 - 87.83	0.34	86.66	86.58 - 86.74	0.53
	NEN012	60.09	59.89 - 60.28	0.50	55.70	55.63 - 55.78	0.43
	NEN013	49.51	49.10 - 49.28	0.59	54.60	54.54 - 54.65	1.16
	NEN014	73.96	73.85 - 74.07	0.56	67.73	67.68 - 67.77	1.09
	NEN015	80.27	80.20 - 80.34	0.93	77.28	77.23 - 77.33	1.11
Northern	NEN016	19.23	18.72 - 19.75	0.40	19.23	18.73 - 19.74	0.40
	NEN117	25.39	24.09 - 26.68	0.61	25.39	24.08 - 26.69	0.61
	NEN017	80.00	80.20 - 80.34	1.66	80.00	78.32 - 81.68	1.66
	NEN118	7.71	7.48 - 7.95	0.51	7.71	7.45 - 7.97	0.51
	NEN018	3.07	2.58 - 3.56	0.26	3.07	2.65 - 3.50	0.26
	NEN119	11.97	10.16 - 13.77	0.79	11.97	10.25 - 13.68	0.79
	NEN019	12.89	12.25 - 13.53	0.27	12.89	12.25 - 12.35	0.27
	NEN020	37.41	37.30 - 37.52	0.88	34.77	34.70 - 34.83	1.27
	NEN021	63.56	62.94 - 64.17	0.70	65.52	65.34 - 65.70	0.82
	NEN022	71.65	71.31 - 71.98	0.63	63.71	63.47 - 63.95	0.61
	NEN023	80.00	79.18 - 80.82	0.63	80.00	80.00 - 80.00	0.87

Aeromagnetic interpretation suggests that the Okavango Dyke Swarm lies beneath stations CAM032 (south) and CAM021 (north). To the north and south of these stations there is a change in the geoelectric strike angle. The majority of the stations that have a difference in geoelectric strike angle of greater of 5°E of north are located between stations CAM032 and CAM021. Therefore, it is suggested that the dykes have a maximum depth of ~15 km or that the geoelectric strike of the dykes change with depth.

Table 7.3: Single strike analysis for the OKA-CAM profile for the depth intervals of 1 – 15 km and 1 – 35 km indicating the preferred geoelectric strike producing the smallest resultant misfit (RMS) and the preferred geoelectric strike range. The profile is divided into a northern and central part from the interpreted aeromagnetic extent of the Damara Belt.

Section	Site	1 - 15 km			1 -35 km		
		Strike (°)	Range (°)	RMS	Strike (°)	Range (°)	RMS
Central	OKA015	30.31	29.65 - 30.66	0.39	28.88	28.55 - 29.22	0.42
	CAM004A	65.19	64.99 - 65.39	3.78	65.19	64.99 - 65.39	3.78
	CAM005	41.44	41.10 - 41.78	0.86	41.44	41.10 - 41.78	0.86
	CAM006A	11.28	11.15 - 11.41	1.27	11.28	11.15 - 11.41	1.27
	CAM007A	26.85	26.77 - 26.93	0.95	26.85	26.77 - 26.93	0.95
	OKA013	27.43	27.37 - 27.49	1.68	27.13	27.06 - 27.21	1.63
	CAM009A	50.42	50.38 - 50.47	3.46	50.42	50.38 - 50.47	3.46
	CAM010	83.39	83.77 - 84.00	0.74	78.16	78.06 - 78.26	1.40
	OKA012	42.53	42.48 - 42.58	2.41	49.42	49.39 - 49.46	2.77
	CAM011	39.81	39.71 - 39.9	1.31	49.95	49.88 - 50.02	1.56
	CAM012	41.08	41.01 - 41.15	0.91	47.76	47.71 - 47.82	1.40
	CAM013	23.22	23.12 - 23.31	0.63	32.11	31.97 - 32.26	1.16
	OKA011	14.96	14.83 - 15.08	0.53	11.45	11.31 - 11.59	0.77
	CAM014	67.91	67.75 - 68.07	0.97	73.06	72.98 - 73.14	0.98
	CAM015	76.16	76.07 - 76.24	0.84	76.29	76.20 - 76.38	1.00
	CAM016A	69.27	69.17 - 69.36	1.52	67.51	67.43 - 67.59	1.82
	OKA010	82.48	82.13 - 82.83	0.90	82.40	82.21 - 82.59	0.74
	CAM017A	87.18	86.96 - 87.39	0.19	84.23	84.12 - 84.34	0.27
	OKA009	2.79	2.22 - 3.36	0.13	2.79	2.22 - 3.36	0.13
	CAM021	14.57	14.28 - 14.85	0.44	9.41	9.25 - 9.57	0.83
	OKA008	37.97	37.76 - 38.18	0.41	30.35	30.21 - 30.50	0.72
	CAM024	20.65	20.15 - 21.14	0.59	18.40	18.27 - 18.53	0.67
Southern	CAM025	30.02	29.90 - 30.14	1.00	22.90	22.83 - 22.97	1.31
	OKA007	46.38	46.10 - 46.66	1.25	28.13	28.02 - 28.23	1.56
	CAM026A	98.14	8.01 - 8.26	0.64	83.58	83.32 - 83.84	1.45
	CAM027A	19.22	19.12 - 19.36	0.52	18.13	18.04 - 18.21	0.91
	CAM028A	80.00	78.37 - 82.00	0.80	101.91	11.51 - 12.30	1.04
	OKA006	80.00	80.00 - 80.00	1.01	93.42	3.19 - 3.66	1.60
	CAM029A	80.00	78.37 - 81.63	0.92	100.46	10.27 - 10.65	1.51
	CAM030A	50.12	48.66 - 51.57	0.72	87.72	87.46 - 87.99	1.82
	CAM031A	80.00	80.00 - 80.00	1.52	83.22	83.05 - 83.39	1.77
	OKA005	80.00	80.00 - 80.00	1.06	89.59	89.69 - 89.50	1.53
	CAM032	85.63	85.49 - 85.78	0.82	91.70	1.63 - 1.78	1.42
	CAM033A	6.63	6.57 - 6.70	1.28	4.24	4.19 - 4.30	1.39
	CAM034A	14.32	14.24 - 14.40	1.26	13.70	13.65 - 13.75	1.79
	OKA004	4.95	4.86 - 5.04	1.40	7.30	7.23 - 7.37	1.79
	CAM035A	8.78	8.64 - 8.91	1.05	9.90	9.85 - 9.95	2.25
	CAM036A	85.33	85.16 - 85.49	1.02	85.33	85.20 - 85.46	1.02
	CAM037A	91.84	87.25 - 87.50	1.84	97.48	7.41 - 7.54	2.05
	OKA003	86.84	86.77 - 86.90	1.47	89.83	89.78 - 89.89	1.54
	CAM038A	85.21	85.15 - 85.27	1.17	87.91	87.87 - 87.91	1.26
	CAM039A	80.22	80.17 - 80.28	0.95	82.70	82.65 - 82.76	1.06
	OKA002	79.40	79.35 - 79.45	1.01	80.93	80.89 - 80.98	1.01
	CAM041	102.97	76.84 - 77.03	1.00	76.63	76.84 - 77.02	1.00
	CAM042A	75.75	75.70 - 75.80	1.00	75.96	75.91 - 76.01	1.03

Multi-strike analysis

Multi-site, multi-frequency strike analysis (*multi-strike*) was run on the three MT profiles for the various depths and sub-divisions, north, central and south, based on the inferred boundary of the Damara Belt. This was done to determine a regional geoelectric strike angle of each MT profile.

Table 7.4 shows the multi-strike results for DMB profile for a range of 1 – 15 km. The various divisions of the profile exhibited different strike directions. There is a clear difference between the geoelectric strike angle for the Damara Belt and the terranes to the north and south. A complete profile *multi-strike* analysis was undertaken, which yielded a geoelectric strike angle of 46.60°E of north. For simplicity the DMB profile was decomposed to a single geoelectric strike angle of 45°E of north. Since the major interest in this study is the continuation of the Damara Belt, this geoelectric strike angle was firstly chosen since it is consistent with the structural trends in the aeromagnetic images and mapped geology of the belt. Secondly, Khoza *et al*. (2013) determined a crustal geoelectric strike angle of 50°E of north for the ETO-KIM profile and thirdly, the data set has an ~20 km station spacing and is under sampled for detailed crustal images.

Table 7.4: *Multi-strike* analysis for the divisions of the DMB profile for a depth range of 1 – 15 km.

Multi-strike Results (°)					
Line	Depth	Northern	Central	Southern	Complete Line
DMB	1 - 15 km	44.90	60.80	52.50	46.60

Multi-strike analysis was run for the three divisions of the NEN profile (Table 7.5). The three divisions of the NEN profile produced similar geoelectric strike angles for the complete profile. Similar geoelectric strike angles were also obtained for the various depth ranges (1 – 5 km and 1 – 15 km) (Table 7.5). Therefore, from the similar geoelectric strike angles and structural trends observed in the aeromagnetic data the data set was decomposed to a geoelectric strike angle of 65°E of north.

Table 7.5: *Multi-strike* analysis for the divisions of the NEN profile for a depth range of 1 – 5 km and 1 – 15 km with an overall multi-strike for a depth range of 1 -35 km.

Multi-strike Results (°)					
Line	Depth	Northern	Central	Southern	Complete Line
NEN	1 - 5 km	68.90	67.20	69.30	68.40
	1 - 15 km	64.20	64.00	65.50	64.10
	1 - 35 km				63.80

As *multi-strike* can analyse a maximum of 35 stations at a time, the OKA stations were analysed initially followed by the CAM stations and then finally a complete multi-strike analysis for the complete data set for the central and southern parts was analysed. A complete *multi-strike* analysis for the whole OKA-CAM data set was not processed as there are more than 35 stations on the profile, exceeding the limit of the *multi-strike* programmed used. The northern and central parts of the data set have a geoelectric strike angle difference of ~10° for the various depths ranges (1 – 15 km and 1 – 35 km) (Table 7.6). Comparing the northern and central parts, a large difference in the geoelectric strike angle of ~50°E of north is observed. *Multi-strike* analysis for the complete OKA profile for the depth range of 1 – 15 km produced a geoelectric strike angle of 31.00°E of north (Table 7.6). This geoelectric strike angle is ~50° less than the geoelectric strike angle for the depth range of 1 – 35 km for the OKA profile and both depth ranges for the CAM profile (Table 7.6). The difference in geoelectric strike is because of the limited amount of stations (seven) at a station spacing of 20 km, which has led to under sampling for crustal images. Therefore, the single geoelectric strike angle chosen for the decomposition of the data set is 85°E of north.

Table 7.6: *Multi-strike* analysis for the divisions of the OKA and OKA-CAM profiles, for a depth range of 1 – 15 km and 1 – 35 km with an overall *multi-strike* for a depth range of 1 -35 km for the CAM and OKA profiles.

Multi-strike Results (°)				
Depth	Central	Southern	Complete Line	Line
1 - 15 km	84.60	41.00		oka and CAM
1 - 35 km	89.20	51.00		
1 - 15 km	83.00	37.00	31.00	oka
1 - 35 km	89.70	45.80	87.10	
1 - 15 km			82.50	CAM
1 - 35 km			87.50	

7.3.2. D$^+$ and ρ$^+$

The *D*$^+$ method is based on arbitrarily matching discrete MT response functions of any 1D conductivity profile with a finite number of frequencies by the response of a finite system of delta functions. Parker (1980, 1982) performed 1D modelling of the admittance *c*. The ρ^+ is a development on the *D*$^+$ method and uses the logarithm of admittance, $\log(c)$, instead of the admittance itself (Parker and Brooker, 1996). The admittance is related to the apparent resistivity (ρ_a) and the impedance phase (φ) by;

$$\rho_a = \mu_0 \omega |c|^2 \quad (4.42)$$

and

$$c = |c|e^{i\left(\phi - \frac{\pi}{2}\right)}. \tag{4.43}$$

Therefore, the 1D model can be calculated from apparent resistivity, phase, or both (Parker and Brooker, 1996). This is used to check the reliability of the measured data and gives information for the selection, or rejection of apparent resistivity and/or phase values at a given frequency. Spratt *et al*. (2005) provides an example of this.

7.3.3. Data editing

Prior to the strike analysis and to obtain a first order idea of the quality of the data (Figure 7.10, Appendix 7 to 9 for all original responses), the MT data was loaded into WinGLink, which provides editing and analysis tools. As this study focuses on specific depth ranges (1 – 5 km, 1 – 15 km and 1 – 35 km), a Matlab code was supplied by DIAS, based on the Niblett-Bostick approach, to calculate the apparent resistivity values for the TE and TM modes associated with an estimated depth value. The two modes were then masked in WinGLink to the respective depths associated with the apparent resistivity values.

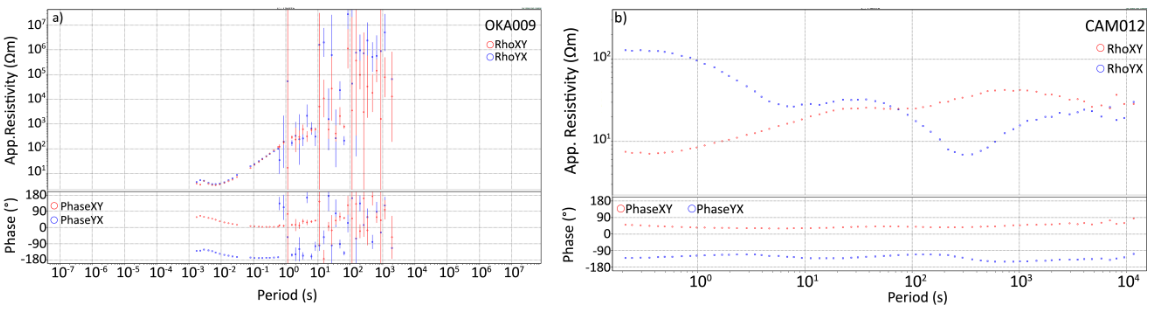

Figure 7.10: MT sounding curve showing apparent resistivity (ρ) and phase (ϕ) against period. Red dots denote the TE mode (ρ_{xy}) and blue dots denote the TM mode (ρ_{yx}). a) Poor quality data seen by the large error bars and the poor signal to noise ratio at greater than 10^0 s and the phase is has a greater than 90° tolerance b) Good quality data seen by the small error bars and obeys the 45° rule for amplitude and 90° for phase.

Strike analysis was carried out on the masked data and after decomposing the MT soundings to their respective geoelectric strike angle, they were reloaded into WinGLink for editing of single (bad) data points (Figure 7.11, Appendix 10 to 12 to see the decomposed data for a depth interval of 1 – 15 km). The quality of the data was determined by examining the size of the error bars, if the phase lies within a 90° tolerance, and the smoothed D^+ curves, which relates apparent resistivity and phase of the same component (xy or yx) through a D^+ function (Section 7.3.2) and attempts to find the 1D Earth that best fits both parameters simultaneously (resistivity and phase) (WinGLink, 2005).

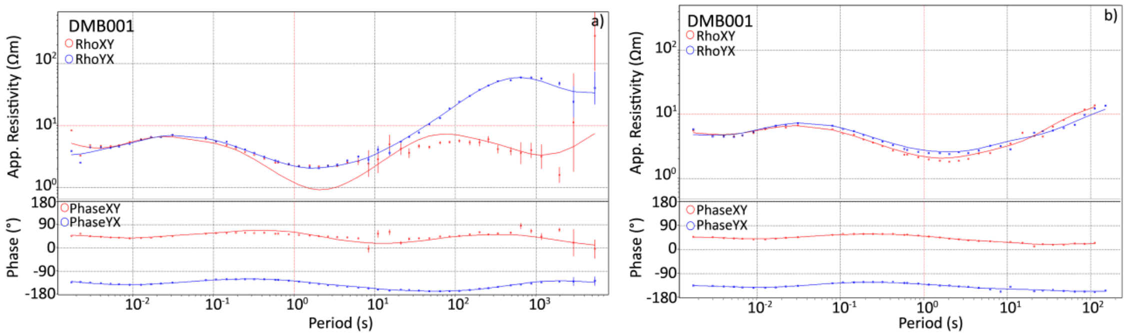

Figure 7.11: DMB001 MT sounding curve showing apparent resistivity (ρ) and phase (ϕ) against period. Red dots denote the TE mode (ρ_{xy}) and blue dots denote the TM mode (ρ_{yx}). The smoothed D^+ curves relate apparent resistivity and phase of the same component (xy or yx) through a D^+ function. a) is the unedited data and b) is the decomposed (45°E of north), masked data to a depth of 15 km with the single (bad) data points deactivated.

7.3.4. Pseudo-sections

To gain an initial impression of the resistivity and phase values of the frequency-dependant data, pseudo-sections are plotted for each profile at the various depths.

Pseudo-sections are contoured images of apparent resistivity or phase values against the period. Figure 7.12 shows the apparent resistivity and phase pseudo-sections for both the TE and TM modes for the OKA-CAM profile for the depth of 1 – 15 km. The blue colours represent high resistivity values while the red colours represent low resistivity values (conductors). Phase angles smaller than 45° represent increasing resistivity values, displayed by blue colours, while red colours represent phase angles larger than 45° and are shown in red colours (increasing conductivity). Station locations are labelled and represented as inverted black triangles. The geometries presented in these images are distorted by plotting period instead of true depth. However, some major features can still be recognised. In both modes there are large conductive bodies, one small moderate conductive body and two resistive bodies. In the TE mode the southern conductor (C_1) is located beneath stations CAM014 and extends southwards to past the limit of the profile (Figure 7.12a) while in the TM mode C_1 extends from the southern limit of the profile to the northern limit (Figure 7.12b). This suggests that C_1 is connected to C_2 in the TE mode (Figure 7.12a). Both modes have a shallow conductive body (C_3) (less than 0.01 s) beneath stations CAM016/OKA010 to CAM026/CAM027 (Figure 7.12). In the TM mode, there is another shallow conductive body (less than 0.1 s) (C_4) beneath stations CAM004 to OKA012, which is not present in the TE mode (Figure 7.12).

In both modes there is a resistive body (R_1), at depths of 1 s to 10 s beneath stations OKA012/CAM011 to CAM028/OKA006 (Figure 7.12). In the TE mode R_1 has an apparent southward dip whilst in the TM mode it is horizontal. In the TE mode, the second resistive body (R_2) is situated beneath stations CAM006/CAM007 to past the southern extent of the profile while in the TM mode, R_2 is more resistive and is situated beneath CAM004 to past the southern extent of the profile (Figure 7.12).

The phase plots of both modes suggest that R_1 and R_2 are connected by the continuous seen by the continuous phase of less than 20° (Figure 7.12). The phase plot of the TM mode shows an increase of conductivity beneath stations CAM006 to CAM010/OKA012, suggesting that C4 is connected to C_1 (Figure 7.12).

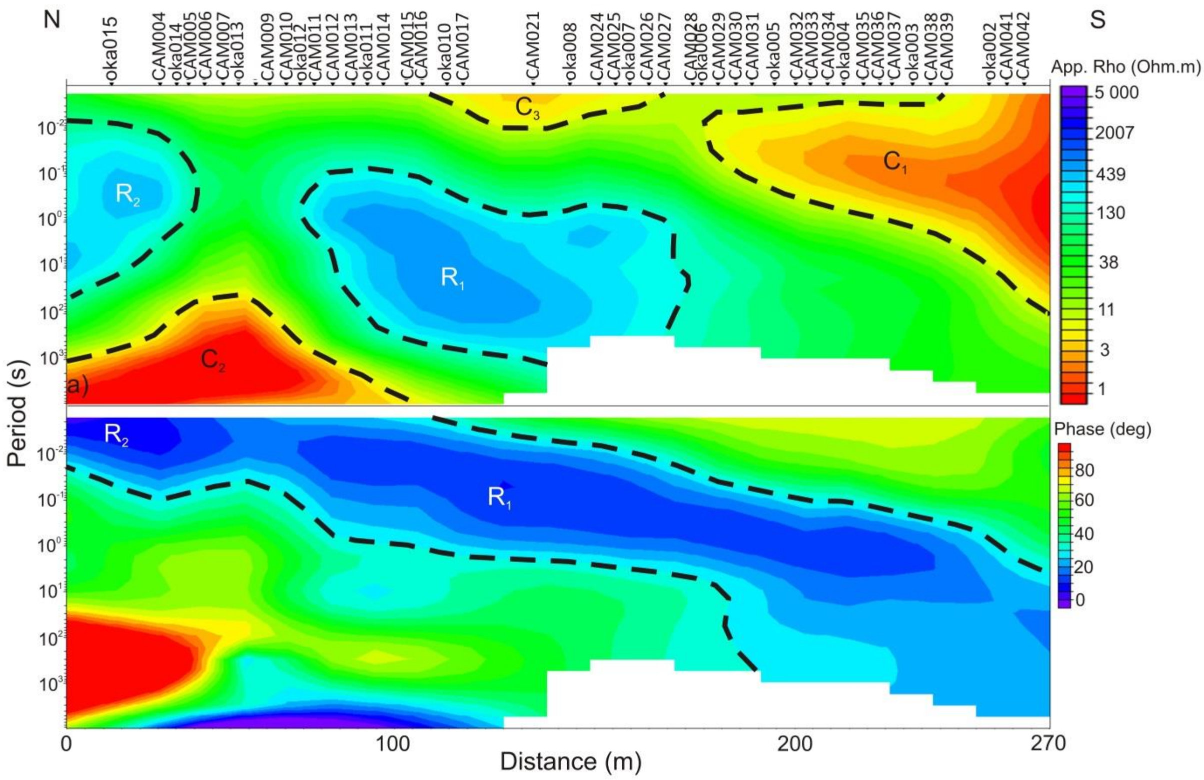

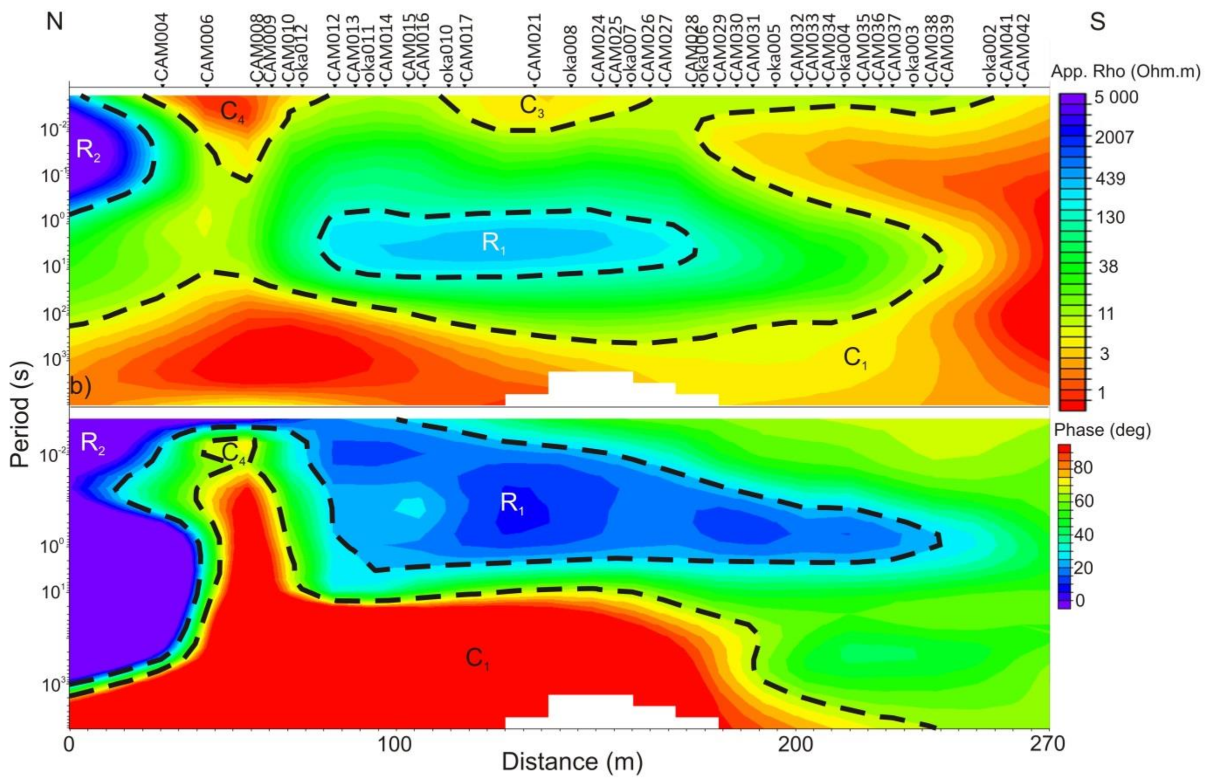

Figure 7.12: Pseudo-sections for the depth range of 1 -15 km for the OKA-CAM profile for a) TE mode data and b) TM mode data. The top image is the apparent resistivity and the bottom image is the phase versus period.

7.3.5. 1D inversion modelling

WinGLink offers two types of smoothing models that can be calculated from the data: the Bostick model and the Occam model. One of the benefits of smooth modelling is the decrease of non-essential features which can lead to misrepresentation and misinterpretation of the data (Constable *et al*., 1987). The Bostick inversion generates a continuous or near-continuous resistivity distribution versus depth (Bostick, 1977) while the 1D Occam inversion generates stepped resistivity distribution versus depth (Constable *et al*., 1987). This study uses the 1D Occam inversion algorithm applied to each MT sounding curve to produce smooth models. To minimise the risk of over-interpreting the data or to eliminate arbitrary discontinuities in simple layered models, Constable *et al*. (1987) suggests that the model should be as smooth as possible. For each edited MT sounding curve the TE and TM modes were calculated for an inversion model. For each station the Occam inversion was run with 10 iterations using the maximum number of layers (43) to produce the smoothest model. To produce a layered model from the smooth Occam model, a “sharp-boundary” layered model inversion was run with 10 iterations with an acceptable RMS-error value of 5%. Layer thickness and resistivity values were manually edited and fixed and run again to increase the fit with the Occam inversion models. Unfortunately, WinGLink constrains the maximum layers for the "sharp-boundary" models to eight.

It is well known that the resistivity structures obtained by the TE and TM modes will be different because of the different sensitivities of the two modes (Figure 7.13) (Unsworth *et al*., 1999; Ritter *et al*., 2003). Thus, before observations of the two modes are discussed the work of Berdichevsky *et al*. (1998) on the advantages and disadvantages of the TM and TE modes needs to be discussed. Berdichevsky *et al*. (1998) discovered from synthetic tests that the TM mode is more sensitive to near-surface structures, whereas the TE mode is more sensitive to deeper structures. The one exception is for strong anisotropic conductors where the TM mode becomes "arrested" in the conductor, while in the TE mode the conductor can be invisible (Jones, 2006). Another observation by Berdichevsky *et al*. (1998) was that the TM mode is more accurate if a 3D structure is interpreted by a 2D approximation, while for a 3D resistive body the TE mode is more accurate. It was shown by Hamilton *et al*. (2006) and later by Miensopust *et al*. (2011) that on the resistive side of a fault or terrane boundary the TE mode is more conductive than the TM mode, while on the conductive side of a fault the TM mode is more conductive than the TE mode.

Therefore, the TE mode can provide details of sedimentary units and the evaluation of the outlines of deep-seated conductive faults, whereas the TM mode can help detect conductive zones in deep layers of the lithosphere and asthenosphere (Berdichevsky *et al*., 1998). The TE mode will be used to show the lateral extent of conductive zones while the TM mode is used to estimate the edges of features, such as craton and mobile belt boundaries.

The depth of penetration below each station is approximated by the length of the 1D inversion plot (Figure 7.13). If a station is not present for one of the modes at a certain depth interval on the cross-section it implies that there is no 1D inversion model available for that mode at that depth interval. This is because of poor data quality observed on the resistivity and phase curves and/or the penetration depth is too shallow. The depth and lateral extent of an anomaly is constrained by the 1D inversion plots and so if a body extends beyond the limits of the 1D inversion plots, uncertainty must be considered when interpreting it. In this study, for simplicity, the interpolated cross-section is described in the observation and interpretation, unless otherwise stated.

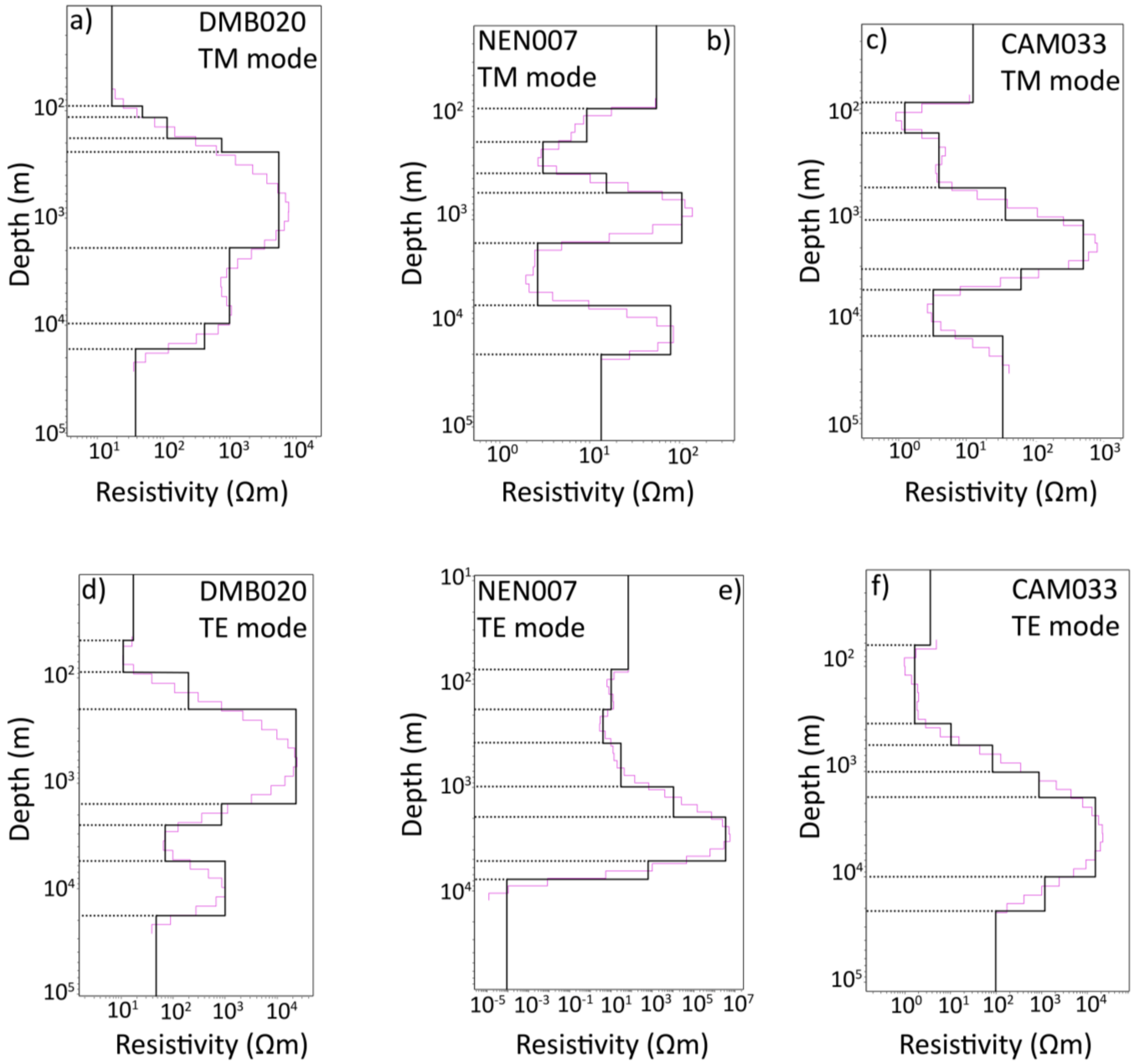

Figure 7.13: Occam 1D inversion and sharp boundary models plotted with log resistivity against log depth. The pink line represents the 1D Occam model and the black line represents the sharp boundary model. The depths are real modelled depths to a depth of 15 km. Notice the different responses between the three TE mode 1D models (a, b and c) and their respective TM mode 1D models (d, e and f).

There is a clear difference in the resistivity response beneath station NEN007 at a depth of ~2 km to 5 km, where the TM mode has a resistivity of ~3 Ωm compared to 1 000 000 Ωm of the TE mode (Figure 7.13b and e). A similar difference, where the TM mode is more conductive than the TE mode, is noted beneath station CAM033 (Figure 7.13c and f). Beneath station CAM033, the TM mode, at a depth of ~5 km to 12 km has a resistivity of ~2 Ωm compared to the TE mode with a resistivity response of ~1 000 Ωm (Figure 7.13c and f).

7.4. Results of the 1D inversion MT cross-sections

The 1D inversion cross-sections are contoured images that have been interpolated for resistivity against period. As period increases the depth increases downwards. The blue colours represent high resistivity values while the red colours represent low resistivity values i.e. conductors. Beneath each station is a resistivity plot based on the Occam inversion (Constable *et al*., 1987), showing the constrained resistivity values beneath each station. The background resistivity values are interpolations of the resistivity between stations based on Occam's inversion (Constable *et al*., 1987). As this is a regional study, the interpolated anomalies are interpreted to understand the broader setting. However, as the Occam inversion is a non-unique process caution is taken in the interpretation. Also reference to the resistivity plots beneath each station is made to determine the constrained resistivity, depth and width of the anomaly. In addition, the large station spacing of ~20 km and the distance between the MT profiles of ~215 km results in a low confidence of the location and depth of a body, unless it lies directly beneath one of the stations.

The interpolated cross-sections of the TE and TM modes are divided into horizontal layers, resistive, and conductive bodies. These various domains are assigned as either H (horizontal layer), C (conductive body), or R (resistive body) with a prefix depicting the first letter respective to the profile.

7.4.1. DMB profile

In the TE and TM modes of the DMB profile at a depth interval of 1 – 5 km, multiple horizontal layers can be identified according to the changes in resistivity values. DH_1 is an undulating layer that stretches from beyond the northern limit of the profile to stations DMB014/DMB016 (Figure 7.14). On the resistivity plots, DH_1 is associated with resistivity values of ~1 Ωm to 50 Ωm and has a maximum thickness of ~900 m beneath stations DMB010 and DMB011. In the southern part of the profile, beneath stations DMB026/DMB027 to beyond the southern limit of the profile, DH_2 is associated with a resistivity value of ~5 Ωm to 80 Ωm (Figure 7.14). DH_2 has an apparent southward dip, reaching a maximum thickness of ~300 m beneath station DMB035. In both modes, DH_2 is underlain by a more resistive semi-horizontal feature beneath stations DMB026/DMB027 denoted DH_3 (Figure 7.14 and 7.15). DH_3 has an apparent southward dip and is associated with resistivity values of ~30 Ωm to 130 Ωm. The layer extends from near-surface beneath stations DMB026/DMB027 to depths of ~300 m to 3.5 km beneath station DMB035 in the TE mode (Figure 7.14). While in the TM mode, beneath station DMB035, DH_3 is at a depth of

~500 m to 2.1 km (Figure 7.14). Underlying DH_3 is a more resistive layer, DH_4 (Figure 7.14 and 7.15). DH_4 is characterised by a resistivity value of ~230 Ωm to 1 800 Ωm with an apparent southward dip for its upper surface (Figure 7.14 and 7.15). In the TE mode, the upper surface of DH_4 is at a depth of ~3.5 km while the lower surface forms an arc-shape at a depth of ~9.5 km beneath station DMB031 (Figure 7.14 and 7.15). In the TM mode, DH_4 is fairly flat extending from a depth of ~2.2 km to 8.7 km (Figure 7.14 and 7.15).

In the TE and TM modes of the depth interval 1 – 5 km there is a conductive body of ~1 Ωm to 10 Ωm (DC_1) situated beneath station DMB003, extending beyond the northernmost station (DMB001; Figure 7.14). The inclusion of this conductive body is very speculative as there are no stations to the north to emphasize it and the penetration depths of stations DMB001, DMB002 and DMB003 are very shallow in relation to the extent of the body. In both modes beneath stations DMB001 and DMB002 and in the TE mode beneath station DMB003 there is a thin (~300 m thick) conductive band of ~1 Ωm to 3 Ωm at a depth of 180 m. In the depth interval of 1 – 15 km, DC_1 is only present in the TM mode with a depth extent of ~8.5 km (Figure 7.15).

In the depth interval of 1 – 15 km the first resistor (DR_1) of ~1 200 Ωm to greater than 5 000 Ωm is observed (Figure 7.15). In the TE mode DR_1 is situated beneath stations DMB006/DMB007 to DMB010/DMB011 while in the TM mode DR_1 is as far north as stations DMB003/DMB004 (Figure 7.15). DR_1 starts at a depth of ~500 m and extends to a depth of greater than 15 km. However, DR_1 cannot be observed in the depth interval of 1 – 5 km (Figure 7.14).

In both modes at a depth interval of 1 – 15 km there is a conductive zone (DC_2) to the south of DR_1 (Figure 7.15). In the TE mode the northern boundary of DC_2 is sub-vertical and beneath stations DMB010/DMB011 while the southern boundary has an apparent southward dip from beneath DMB016/DMB015 to DMB015 (Figure 7.15). DC_2 is at a depth of ~3.5 km to 8 km observed from the station plots of DMB011 and DMB013 and has a resistivity value of ~1 Ωm to 3 Ωm with a background resistivity value of ~10 Ωm to 70 Ωm to (Figure 7.15). While in the TM mode of the depth interval 1 – 15 km, DC_2 has an apparent southward dip with its northern boundary beneath stations DMB009/DMB010 to DMB010/DMB011 and its southern boundary beneath stations DMB011/DMB012 to DMB014/DMB016. In the TM mode DC_2 is shallower than in the TE mode starting at a depth of ~2.5 km and extending to ~6.5 km (beneath station DMB013; Figure 7.15). Background resistivity values suggest that DC_2 may extend further to depths of ~12.5 km. These depths should be observed with caution as the resistivity plot beneath station DMB013 extends to a depth of only 6.5 km (Figure 7.15). In the TM mode the background resistivity values are slightly lower than in the TE mode (i.e. they are more conductive, ~1 Ωm to

70 Ωm). In the TE and TM modes of the depth interval of 1 – 5 km DC_2 has a similar spatial extent as the depth interval of 1 – 15 km. In the TE mode of the depth interval 1 – 5 km, there are inferred highly conductive bands of ~1 Ωm beneath stations DMB011 and DMB013 at a depth of ~3.5 km to greater than 5 km (Figure 7.14). In the TM mode of the depth interval 1 – 5 km, DC_2 is observed at a depth of ~2.5 km to greater than 5 km with a background resistivity value of ~300 Ωm (Figure 7.14).

In both modes and depth intervals the most prominent feature on the DMB profile is DR_2 (Figure 7.14 and 7.15). DR_2 is a highly resistive body characterised by a resistivity value of ~2 800 Ωm to greater than 5 000 Ωm which has a depth extent from 500 m to greater than 15 km. In the TE modes for both depth intervals, DR_2 is located beneath stations DMB011/DMB012 to DMB023/DMB024 (Figure 7.14 and 7.15). The shape of DR_2 can be determined from the depth interval of 1 – 15 km where it is observed as a cone-shape structure. At a depth of just under 15 km DR_2 is located between stations DMB016/DMB017 and DMB018 (Figure 7.15). While in the TM mode for both depth intervals DR_2 is located beneath stations DMB009/DMB010 to DMB027/DMB028 (Figure 7.14 and 7.15). For the depth interval of 1 – 15 km the southern boundary of DR_2 has an apparent southward dip to beneath stations DMB014/DMB016 while the northern boundary is sub-vertical (Figure 7.15).

Underlying DR_2 at a depth of ~2.5 km in the depth range of 1 – 15 km is a moderate resistive body (DR_3) which is not observed in either mode in the depth range of 1 – 5 km (Figure 7.14 and 7.15). In the TE mode DR_3 is characterised by resistivity value of ~20 Ωm to 1 000 Ωm located beneath stations DMB018/DMB019 to DMB021/DMB022. While in the TM mode DR_3 is characterised by resistivity values of ~300 Ωm to 800 Ωm and is situated beneath stations DMB019/DMB020 and DMB020/DMB021 (Figure 7.15).

DR_4 is only observed in the TE mode of the depth interval 1 – 15 km (Figure 7.15). DR_4 is located beneath stations DMB020/DMB021 to DMB025/DMB027 at a depth of ~3 km to greater than 15 km, from the resistivity plots. DR_4 comprises two semi-circular to circular resistive bodies associated with a resistivity value of ~2 800 Ωm to greater than 5 000 Ωm (Figure 7.15).

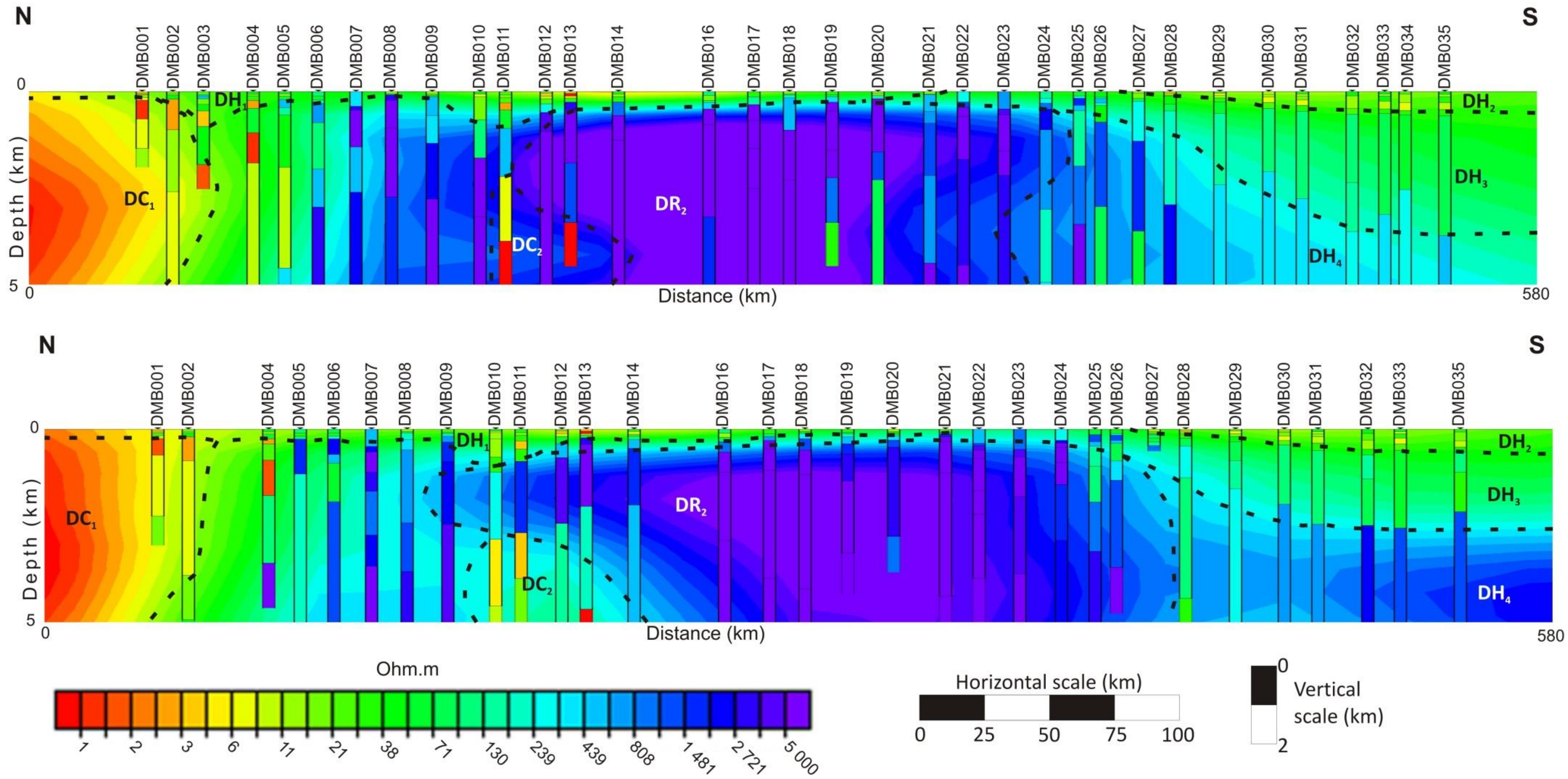

Figure 7.14: 1D inversion models for the DMB profile at a depth interval of 1 – 5 km. The top image is the TE mode and bottom image is the TM mode. The various horizontal layers (DH), conductive bodies (DC) and resistive bodies (DR) are discussed in the text.

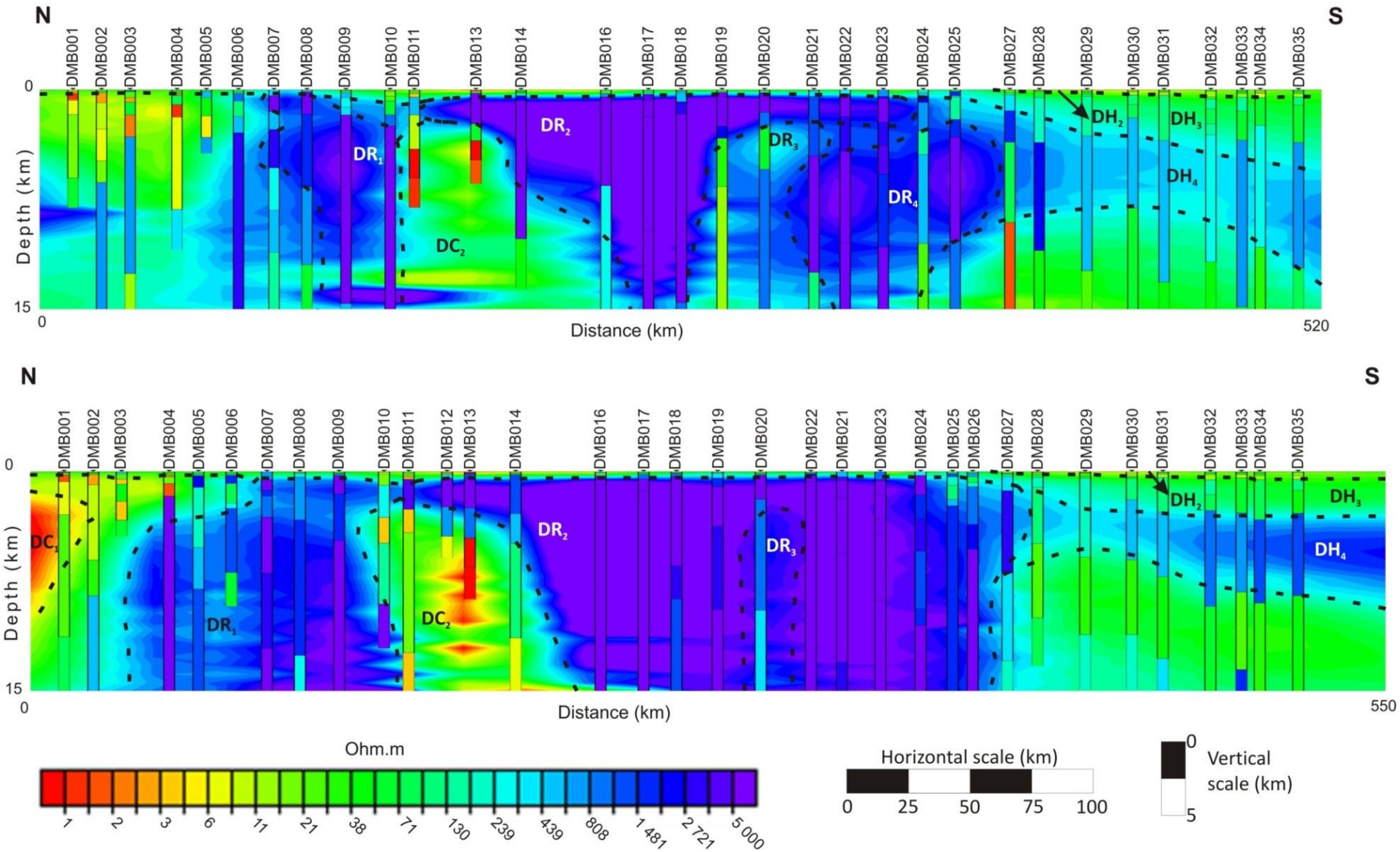

Figure 7.15: 1D inversion models for the DMB profile at a depth interval of 1 – 15 km. The top image is the TE mode and bottom image is the TM mode. The various horizontal layers (DH), conductive bodies (DC) and resistive bodies (DR) are discussed in the text.

7.4.2. NEN profile

In the northern part of the NEN profile, in both modes, the first horizontal layer (NH_1) undulates and stretches from beyond the northern limit of the profile to beneath station NEN014/NEN013 (Figure 7.16). NH_1 is associated with a moderate resistive upper layer of ~20 Ωm to 70 Ωm and a more conductive lower layer of ~2 Ωm to 5 Ωm (Figure 7.16). NH_1 extends from surface to a depth of ~650 m beneath NEN021. Beneath stations NEN009/NEN008 and NEN007/NEN005, there is a similar resistivity pattern that has a basin- shape. This feature has a maximum depth of ~550 m and is assigned as NH_2 (Figure 7.16). NH_3 is situated in the southern part of the TE profile beneath stations NEN007/NEN005 to beyond the southern limit of the profile and in the TM mode, beneath stations NEN004/NEN003 to beyond the southern limit (Figure 7.16). In the TE mode, NH_3 is associated with resistivity values of ~20 Ωm to 140 Ωm with a maximum thickness of ~800 m beyond the southern limit of the profile. In the TM mode, NH_3 is associated with higher resistivity values of ~100 Ωm to 1 000 Ωm with a maximum depth of ~700 m beyond the southern limit of the profile (Figure 7.16). As there are no stations to the south of NEN001 the apparent southward dip and maximum depth of NH_3 must be treated with caution.

In both modes, at both depth intervals, there is a resistive body (NR_1) ranging from ~2 500 Ωm to greater than 5 000 Ωm (Figure 7.16 and 7.17). In the TE mode of both depth intervals, NR_1 extends laterally from beyond the northern limit of the profile to beneath station NEN023/NEN022 (Figure 7.16 and 7.17) and is at a depth of ~2.5 km to 12.5 km. In the TM mode, however, at a depth interval of 1 – 5 km, NR_1 extends from beyond the northern extent of the profile to beneath station NEN022/NEN021 and at a depth interval of 1 – 15 km to beneath station NEN020/NEN019 (Figure 7.16 and 7.17) NR_1 starts at a depth of ~2.5 km and extends to depths greater than 15 km (Figure 7.17). As there are no stations to the north of NEN023 the continuation of NR_1 to the north is speculative.

In both modes at both depth intervals, the resistivity plots suggest that NR_1 is overlain by a conductive body (NC_1) of ~2 Ωm to 6 Ωm (Figure 7.16 and 7.17). At the depth interval of 1 – 5 km, NC_1 is located beneath stations NEN023 to NEN020 (Figure 7.16) while for a depth range of 1 – 15 km, NC_1 is located beneath stations NEN023 to NEN021 (Figure 7.17) and occurs in both modes at a depth of ~400 m to 1.6 km.

To the south of NC_1 is another conductive body (NC_2) of ~1 Ωm to 6 Ωm (Figure 7.16 and 7.17). NC_2 is more prominent in the TE modes beneath stations NEN019 to NEN014/NEN013, at a depth of ~1.8 km to 11 km i.e. NC_2 is observed in both the cross-section and the resistivity plots for the shallower depths in the TE mode (Figure 7.16 and 7.17). In the TM modes, NC_2 is inferred on the resistivity plots beneath station NEN118 for a depth interval of 1 – 5 km (Figure 7.16) and beneath stations NEN019, NEN118 and NEN017 for the depth interval of 1 – 15 km (Figure 7.17) and is situated at a depth of ~1.8 km to 5.8 km (Figure 1 – 15 km). However, as there are no 'true' resistivity plots for the maximum depth of NC_2 in either mode, this conductor can only be constrained to depths of approximately less than 8 km in the TE mode for the depth interval of 1 – 15 km beneath station NEN014 (Figure 7.17).

Overlying NC_2 is a more resistive body (NR_2) of ~220 Ωm to 750 Ωm (on the cross-section) however, on the resistivity plots it reaches resistivity values of ~3 000 Ωm to greater than 5 000 Ωm (Figure 7.16 and 7.17). In the TM mode for both depth intervals NR_2 is located between stations NEN019 to NEN016 at a depth of ~500 m to 1.8 km (Figure 7.16 and 7.17). In the TE mode for a depth interval of 1 – 5 km, NR_2 is located at stations NEN018 and NEN017, while for a depth interval of 1 – 15 km beneath stations NEN019 to NEN017. For both depth intervals, in the TE mode, NR_2 is at a depth of ~700 m to 2 km (Figure 7.16 and 7.17).

In the TM modes for both depth intervals there is a resistive body (NR_3) of ~2 000 Ωm to greater than 5 000 Ωm (Figure 7.16 and 7.17). In the depth interval 1 – 5 km, NR_3 has an apparent northward dip being deeper than 5 km beneath station NEN016/NEN015 and shallowing to ~300 m beneath station NEN009/NEN008 (Figure 7.16). In the depth interval of 1 – 15 km, NR_3 extends as far north as station NEN117 and reaches depths greater than 15 km (Figure 7.17). NR_3, however, is not present in either of the TE modes for both depth intervals (Figure 7.16 and 7.17).

Immediately south of NR_3, for both depth intervals, is an apparent northward dipping conductive body (NC_3) of ~1 Ωm to 5 Ωm. Beneath stations NEN008 and NEN007, NC_3 is at a depth of ~1 km while beneath stations NEN010 to NEN009 it is as deep as 11.5 km (Figure 7.16 and 7.17). In the TE mode of the resistivity plots, NC_3 is located beneath stations NEN011/NEN010 to NEN007/NEN006 at a depth of ~3.5 km to 11.5 km. On the interpolated cross-section this body extends to a depth of ~14 km (Figure 7.16 and 7.17). Therefore, the deeper limits of NC_3 can only be tentatively determined. In the TE mode of the depth range of 1 – 15 km the lower depths of NC_3 are ~6.5 km beneath station NEN008 while in the TM mode is ~3 km (Figure 7.16 and 7.17).

In both modes and depth intervals, NR_4 is a resistive body of ~2 000 Ωm to greater than 5 000 Ωm (Figure 7.16 and 7.17). In the TE mode, for both depth intervals, NR_4 is located beneath stations NEN009/NEN008 and extends beyond the southern limits of the profile at a depth of ~400 m. NR_4 forms an arc-shape around NC_3 and can possibly be separated into two bodies (Figure 7.17). The first body is a thin, shallow (~1.2 km to 2.2 km depth) lens-shaped feature that is located beneath stations NEN009/NEN008 to NEN005/NEN004 (Figure 7.16). The second body is a deeper feature, at a depth of ~5 km to greater than 15 km, situated beneath station NEN005 passed the southern limit of the profile (Figure 7.16). Whereas in the TM mode NR_4 is observed as a single, solid feature with an apparent northward dip beneath stations NEN007/NEN005 (Figure 7.16 and 7.17). In this mode NR_4, also extends to depths greater than 15 km and beyond the southern limit of the profile. Therefore, as there are no resistivity plots to the south of station NEN001, the southern continuation NR_4 cannot be certain.

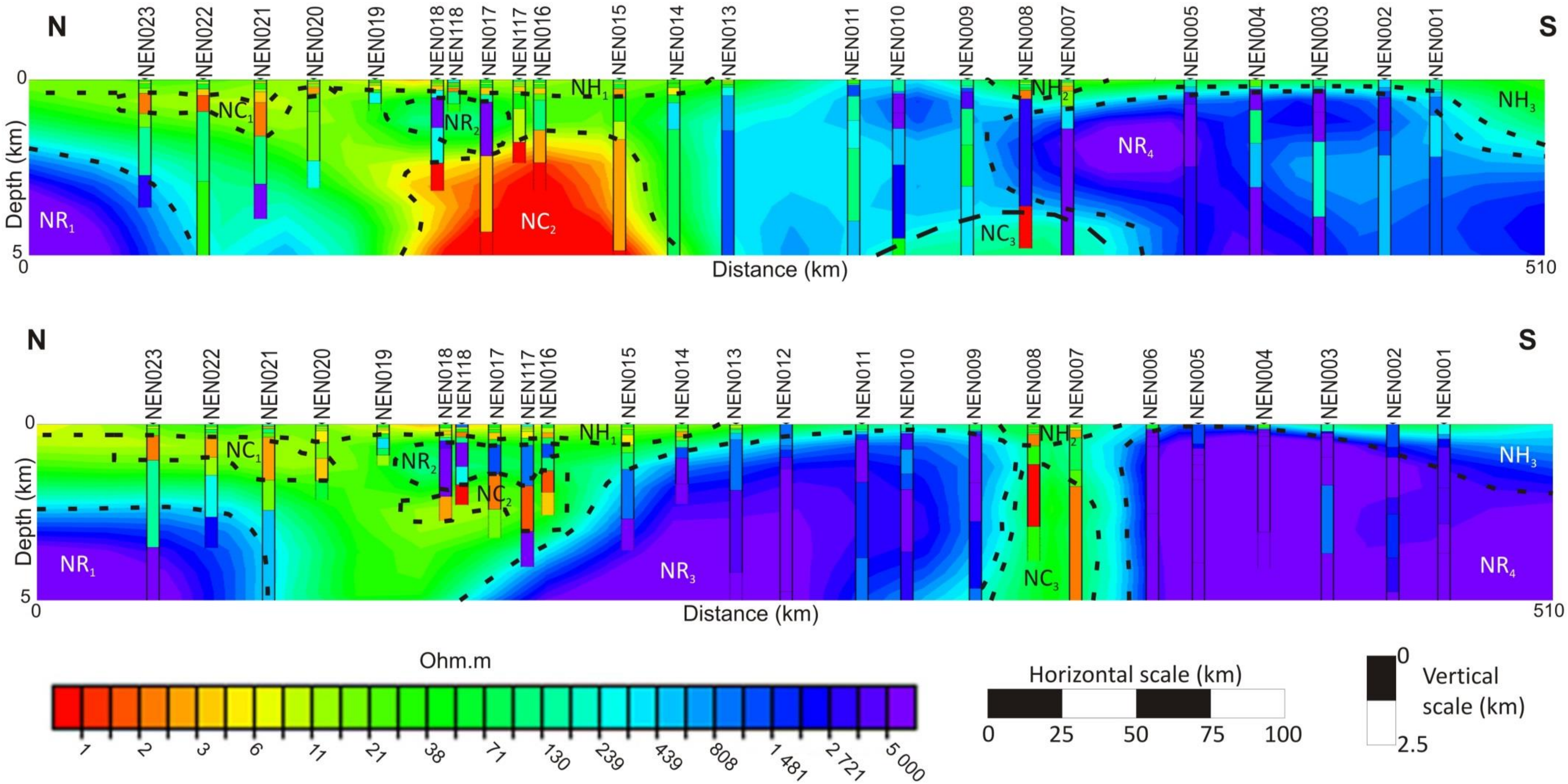

Figure 7.16: 1D inversion models for the NEN profile at a depth interval of 1 – 5 km. The top image is the TE mode and bottom image is the TM mode. The various horizontal layers (NH), conductive bodies (NC) and resistive bodies (NR) are discussed in the text.

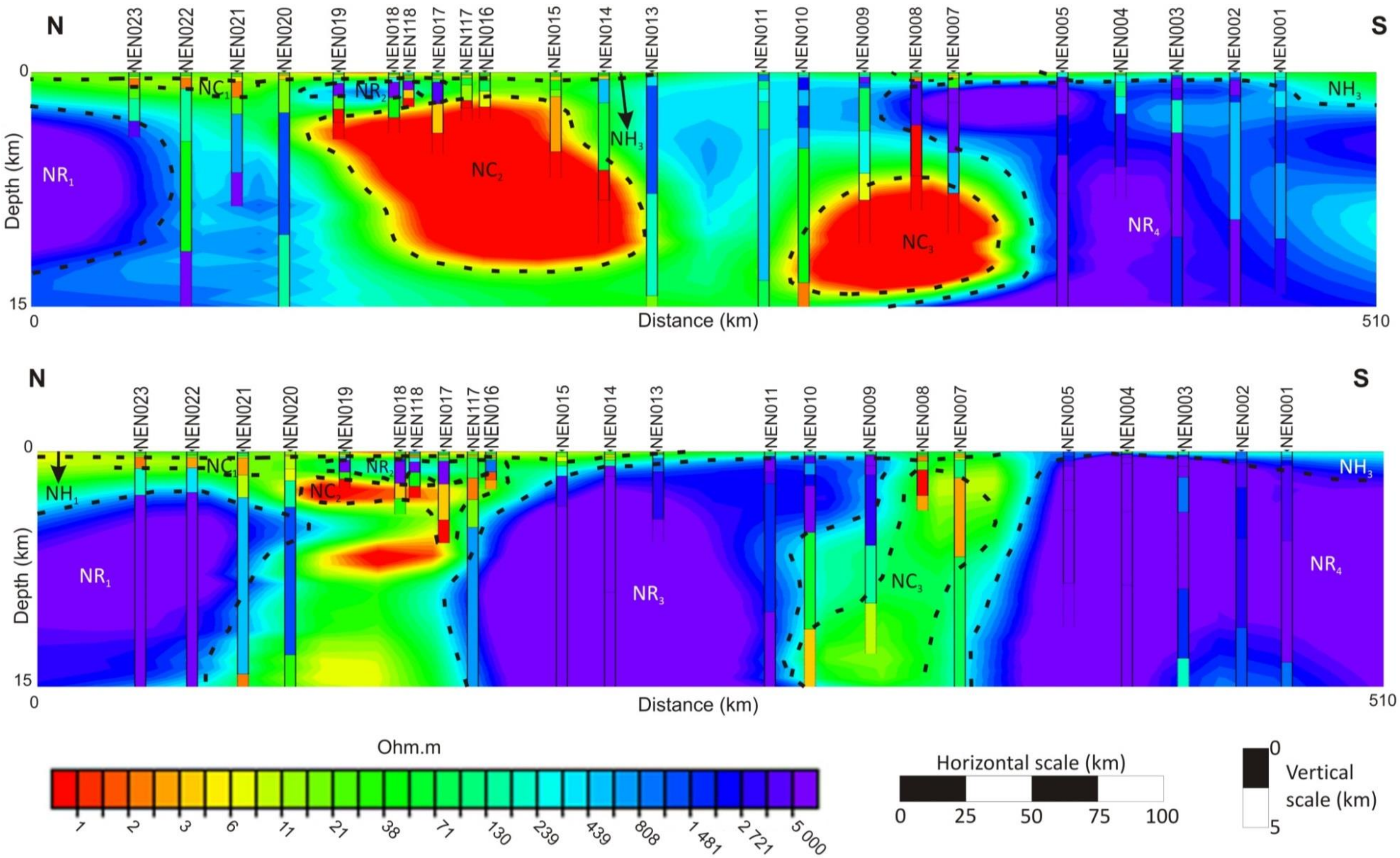

Figure 7.17: 1D inversion cross-sections of the TE (top) and TM (bottom) modes of the NEN profile at a depth interval of 1 – 15 km. The various horizontal layers (NH), conductive bodies (NC) and resistive bodies (NR) are discussed in the text.

7.4.3. OKA-CAM profile

For the depth interval of 1 – 5 km on the OKA-CAM profile, the first horizontal layer (OCH_1) is defined by a resistivity value of ~5 Ωm to 80 Ωm with the lower resistive values being at its base (Figure 7.18). In both modes, OCH_1 stretches from beyond the northern extent of the profile to beyond the southern extent of the profile at a depth generally shallower than 150 m (Figure 7.18). In the south, on the OKA-CAM profile, in both modes at all depth intervals there is a conductive horizontal layer (OCH_2) of ~1 Ωm to 6 Ωm (Figure 7.18 - 7.20). OCH_2 is situated beneath CAM033/CAM034 to beyond the southern limit of the profile. OCH_2 thickens from a few metres beneath stations CAM033/CAM034 to ~300 m beneath station CAM042 (Figure 7.18).

In both modes, at all depth intervals, there is a shallow resistive body (OCR_1) of ~2 500 Ωm to greater than 5 000 Ωm (Figure 7.18 - 7.20). In the TE mode OCR_1 stretches from beneath the northern limit of the profile to stations CAM006/CAM007 while in the TM mode OCR_1 to stations CAM004/OKA014 (Figure 7.18 - 7.20). In the TE mode OCR_1 extends from surface to ~2.4 km while in the TM mode OCR_1 has a maximum depth of ~1.8 km (Figure 7.18). As there are no stations to the north of OKA015, the northern extent of OCR_1 needs to be considered with care.

Overlying OCR_1, in the TM mode, at a depth interval of 1 – 5 km and 1 – 15 km is a conductive body (OCC_1) of ~1 Ωm to 5 Ωm (Figure 7.18 and 7.19). OCC_1 extends from beyond the northern limit of the profile to stations CAM007/CAM009 in the depth interval of 1 – 5 km (Figure 7.18) and stations CAM008/CAM009 in the depth interval of 1 – 15 km (Figure 7.19). From the resistivity plots, for the depth interval of 1 – 15 km, OCC_1 is suggested to be as shallow as a kilometre beneath station CAM008 while beneath CAM006, OCC_1 has a maximum depth of ~8.2 km (Figure 7.19). However, OCC_1 is interpolated to extend to depths of greater than 15 km and as OCC_1 is not present in the depth interval of 1 – 35 km and no resistivity plots show a conductive body at these depths the continuation of OCC_1 must be treated with care.

At all depth intervals the resistivity plots in the TE mode and in the TM mode for a depth interval of 1 – 35 km, there is a suggested conductive body (OCC_2) of ~1 Ωm to 10 Ωm beneath stations OKA014/CAM005 to CAM010/OKA012 (Figure 7.18 - 7.20). In the TE mode OCC_2 at depths of ~1 km to 19.5 km (Figure 7.18 and 7.20) however, in the depth interval of 1 – 35 km OCC_2 is interpolated to depths greater than 35 km (Figure 7.20). In the TM mode, however, OCC_2 is constrained to a depth of ~1 km to 11 km (Figure 7.20). Therefore, from the resistivity plots, OCC_2 is suggested to be at a depth of 1 km to 19.5 km with greater depths being tentatively suggested as these are most likely due to the gridding algorithm.

To the south of OCC_2, in both modes, at all depth intervals, is a large resistive body of ~1 500 Ωm to greater than 5 000 Ωm (Figure 7.18 - 7.20). This may be a singular body extending from beneath stations CAM010/OKA012 to CAM039/OKA002 or it may be two separate bodies (preferred for this study termed OCR_2 and OCR_3).

In the TE mode, for all depth intervals, OCR_2 is beneath stations CAM010/OKA012 to CAM017/CAM021 while in the TM mode, OCR_2 continues as far south as OKA007CAM026 (Figure 7.18 - 7.20). In the TE mode, OCR_2 is at a depth of ~150 m to greater than 35 km while in the TM mode OCR_2 is slightly deeper, ranging from ~200 m to greater than 35 km (Figure 7.18 and 7.20).

In the TE mode, for all depth intervals, OCR_3 is situated beneath stations CAM011/OKA008 to CAM039/OKA002 while in the TM mode OCR_3 stretches from CAM025/OKA007 to CAM038/CAM039 (Figure 7.18 - 7.20). In the TE mode OCR_3 is at a depth of ~800 m to greater than 35 km compared to the TM mode where OCR_3 is at a depth of ~500 m to 9 km (Figure 7.18 - 7.20).

In the TE mode for a depth interval of 1 – 15 km and 1 – 35 km, there is a semi-circular to circular, moderately conductive body (OCC_3) of ~20 Ωm to 130 Ωm located beneath stations CAM027/CAM028 to OKA004/CAM035 at a depth of ~8 km to 32 km (Figure 7.19 and 7.20). While in the TM mode, for depth intervals of 1 – 15 km and 1 – 35 km beneath stations OKA006/CAM029 to CAM039/OKA002, OCC_3 is more conductive with a resistivity value of ~2 Ωm to 130 Ωm (Figure 7.19 and 7.20). In the TM mode, OCC_3 is at shallower depths of ~5 km to 25 km and is lens-shaped in comparison to OCC_3 in the TE mode (Figure 7.19 and 7.20).

In the TM mode, at all depth intervals, there is a highly conductive body (OCC_4) of ~1 Ωm to 10 Ωm beneath stations CAM037/OKA003 to beyond the southern extent of the profile (Figure 7.18 - 7.20). OCC_4 is a lens shaped body at a depth of ~1 km to 11 km (Figure 7.18 - 7.20).

Underlying OCC_4 in the TM mode, of the depth interval 1 – 35 km, at a depth of ~15 km to 34 km is another lens-shaped conductive body (OCC_5) of ~1 Ωm to 10 Ωm (Figure 7.20). OCC_5 is located beneath stations CAM035/CAM036 extending beyond the southern limit of the profile (Figure 7.20). Both OCC_4 and OCC_5 are not observed in the TE mode at any depth interval (Figure 7.18 – 7.20). As there are no stations to the south of CAM042 the southern continuation of OCC_4 and OCC_5 cannot be constrained.

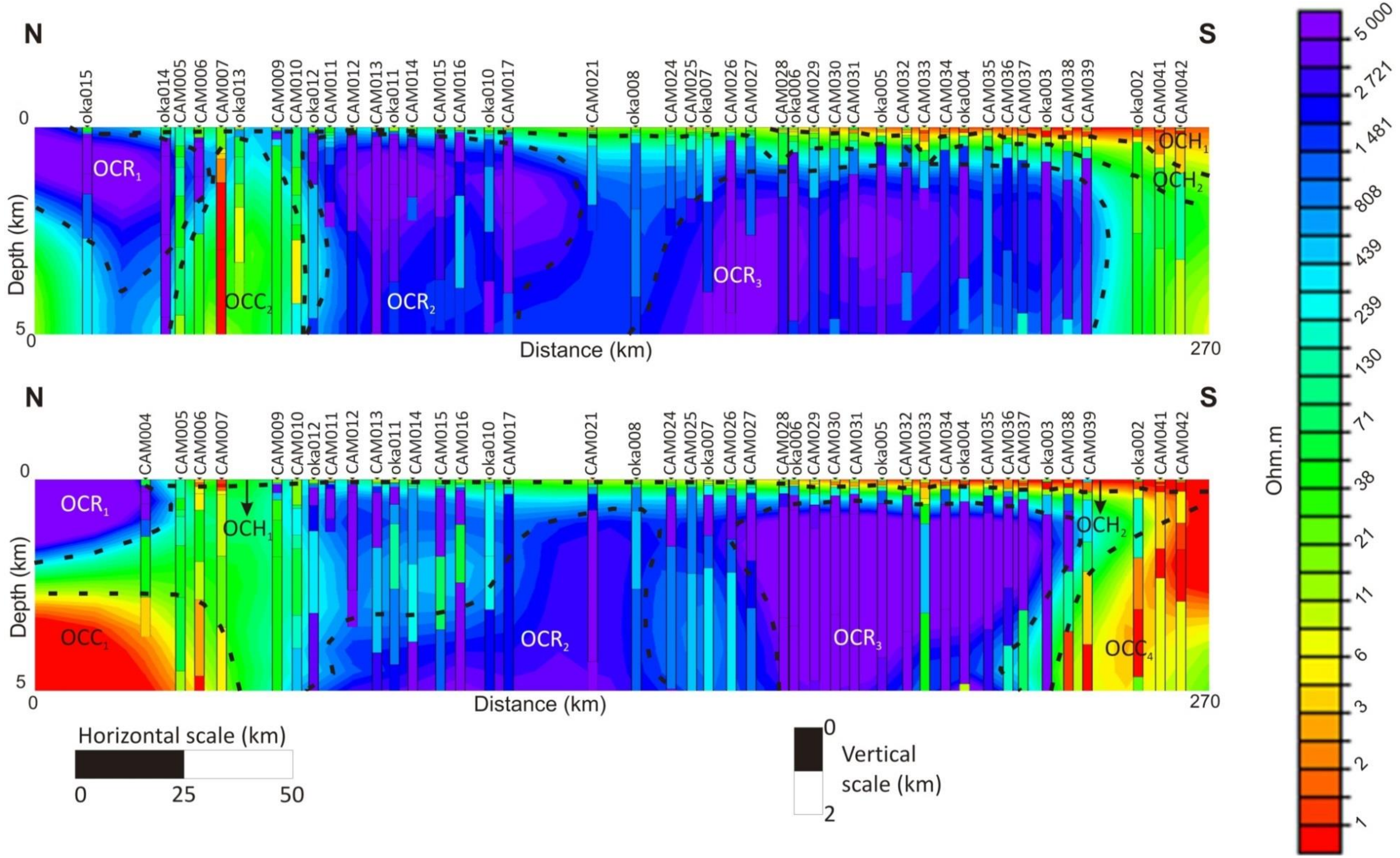

Figure 7.18: 1D inversion models for the OKA-CAM profile at a depth interval of 1 – 5 km. The top image is the TE mode and bottom image is the TM mode. The various horizontal layers (OCH), conductive bodies (OCC) and resistive bodies (OCR) are discussed in the text.

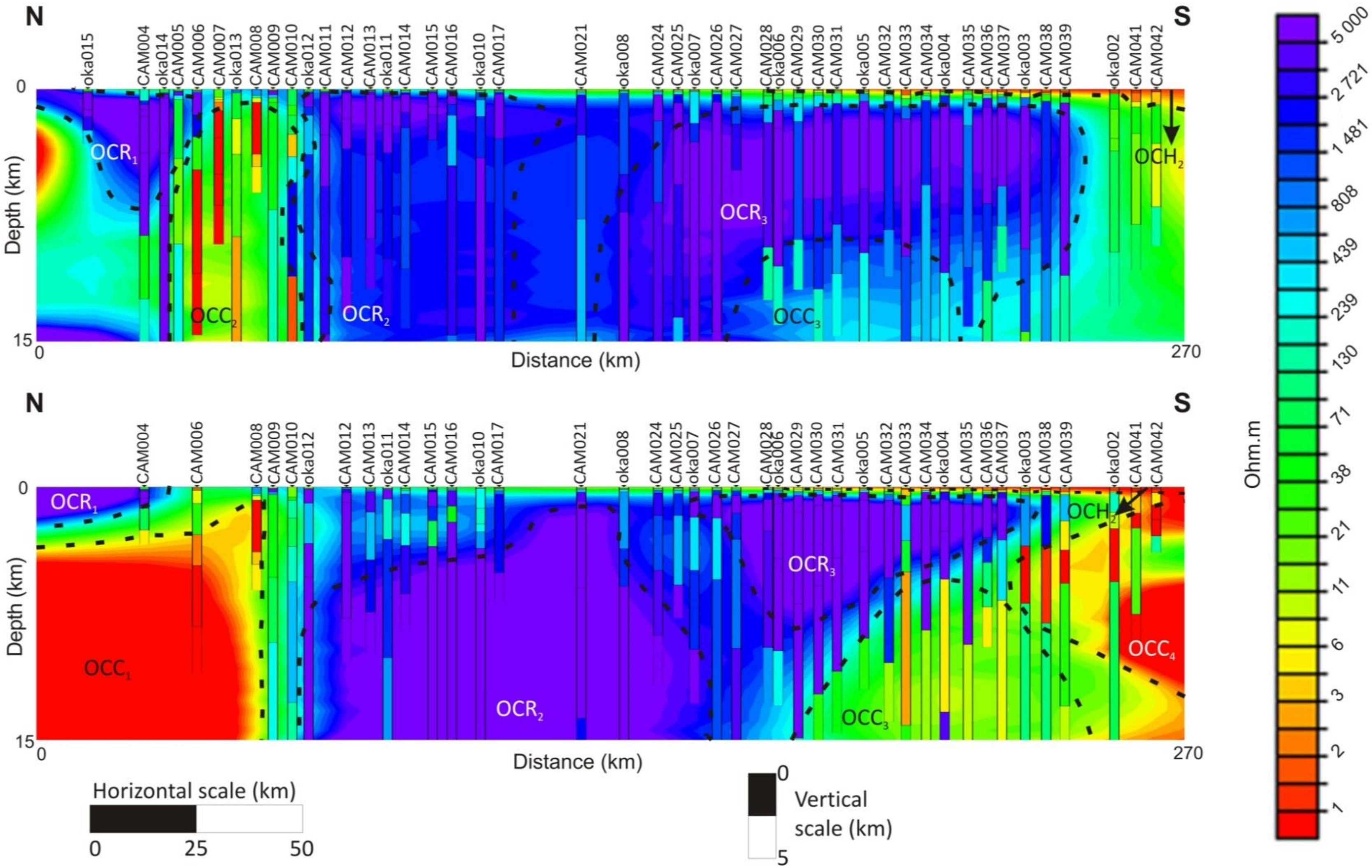

Figure 7.19: 1D inversion models for the OKA-CAM profile at a depth interval of 1 – 15 km. The top image is the TE mode and bottom image is the TM mode. The various horizontal layers (OCH), conductive bodies (OCC) and resistive bodies (OCR) are discussed in the text.

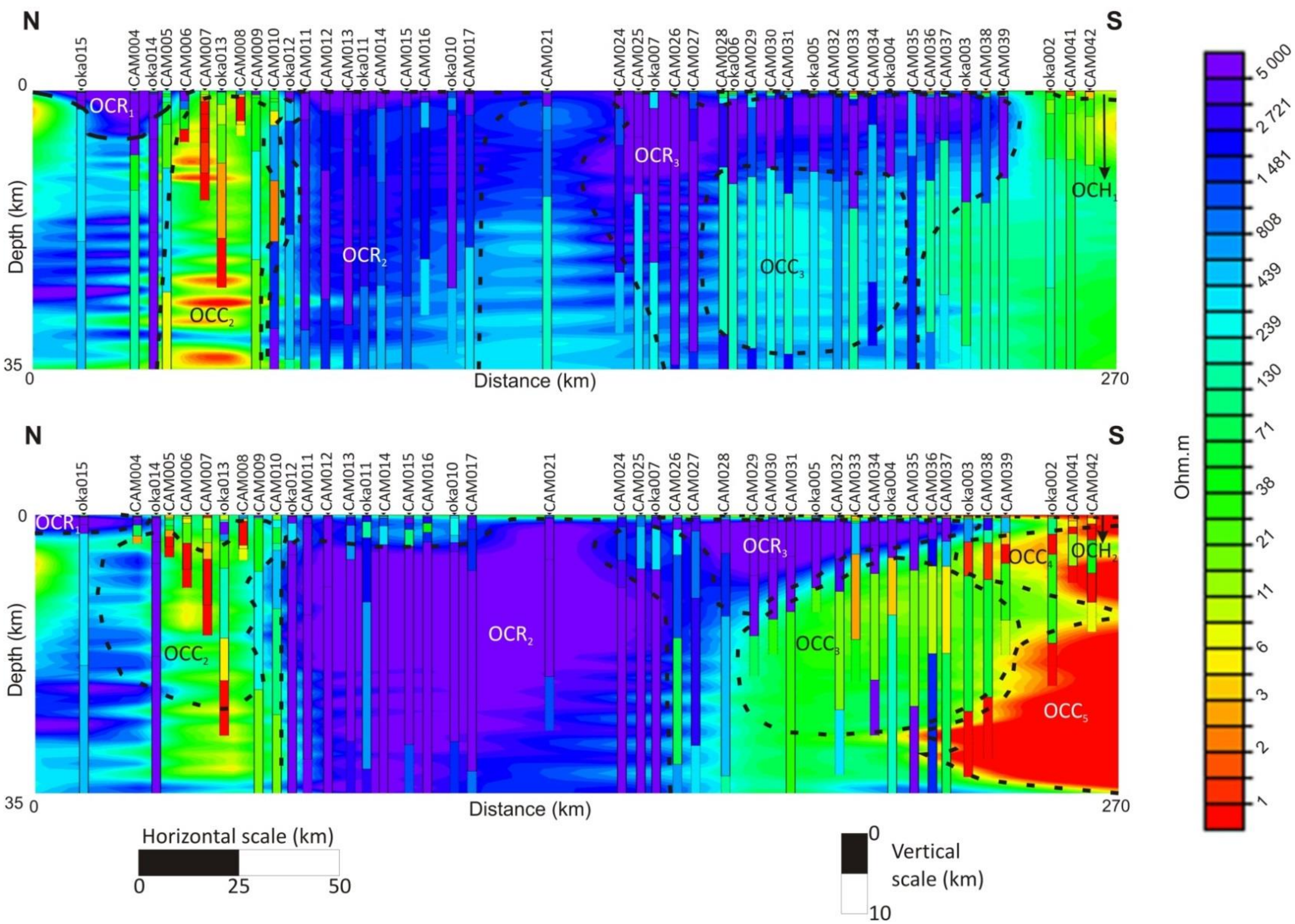

Figure 7.20: 1D inversion models for the OKA-CAM profile at a depth interval of 1 – 35 km. The top image is the TE mode and bottom image is the TM mode. The various horizontal layers (OCH), conductive bodies (OCC) and resistive bodies (OCR) are discussed in the text.

7.5. Interpretation

An along-strike crustal conductor extending from Namibia into Botswana has been mapped since the late 1970s to early 1980s by magnetovariational and Schlumberger sounding surveys of de Beer *et al*. (1975, 1976, 1982) and van Zijl and de Beer (1983). The interpretations as to the cause of this conductor have changed several times over the years. Ritter *et al*. (2003) detected a conductive body beneath the Waterberg Fault/Omaruru Lineament, which the authors suggested was caused by the alignment of graphite in deep-seated shear zones. This became the favoured theory for the cause of conductivity. In addition, Ritter *et al*. (2003) discovered another sub-vertical conductor associated with the Autseib Lineament. Khoza *et al*. (2013) detected a mid-crustal conductive body trending east – west, through the Central Zone of the Damara Orogen. Khoza *et al*. (2013) interpreted that the conductivity was caused by sulphides in the upper crust underlain by graphite in deep-seated shear zones. The following sections discuss the possible causes of conductivity in an attempt to verify the continuity or lack of continuity of the conductive zone of de Beer *et al*. (1975, 1976, 1982) and van Zijl and de Beer (1983), and the possible southern and northern continuation of the Congo and Kalahari Cratons, respectively.

7.5.1. Horizontal layering

In all the MT models, a semi-conductive horizontal layer is observed. In the northern and central parts of the profiles, the horizontal layer is generally less than 200 m thick (Figure 7.14 to 7.20). The layer thickens towards the south to ~300 m (Figure 7.14, 7.16 and 7.18). However, on the DMB profile from stations DMB026/DMB027 southwards there is a moderate resistive feature denoted DH_3 (Figure 7.14 and 7.15). Studies of the distribution of Karoo Basins of southern Africa by Johnson *et al*. (1996) and Catuneanu *et al*. (2005) have outlined the northern margin of the Aranos Basin to lie between stations DMB026/DMB027 (Figure 7.21). From the interpretation of the DMB profile by Muller (*pers. comm*., 2013), DH_3 is correlated with the third layer of Muller (*pers. comm*., 2013) i.e. upper Karoo sediments (Figure 2.29).

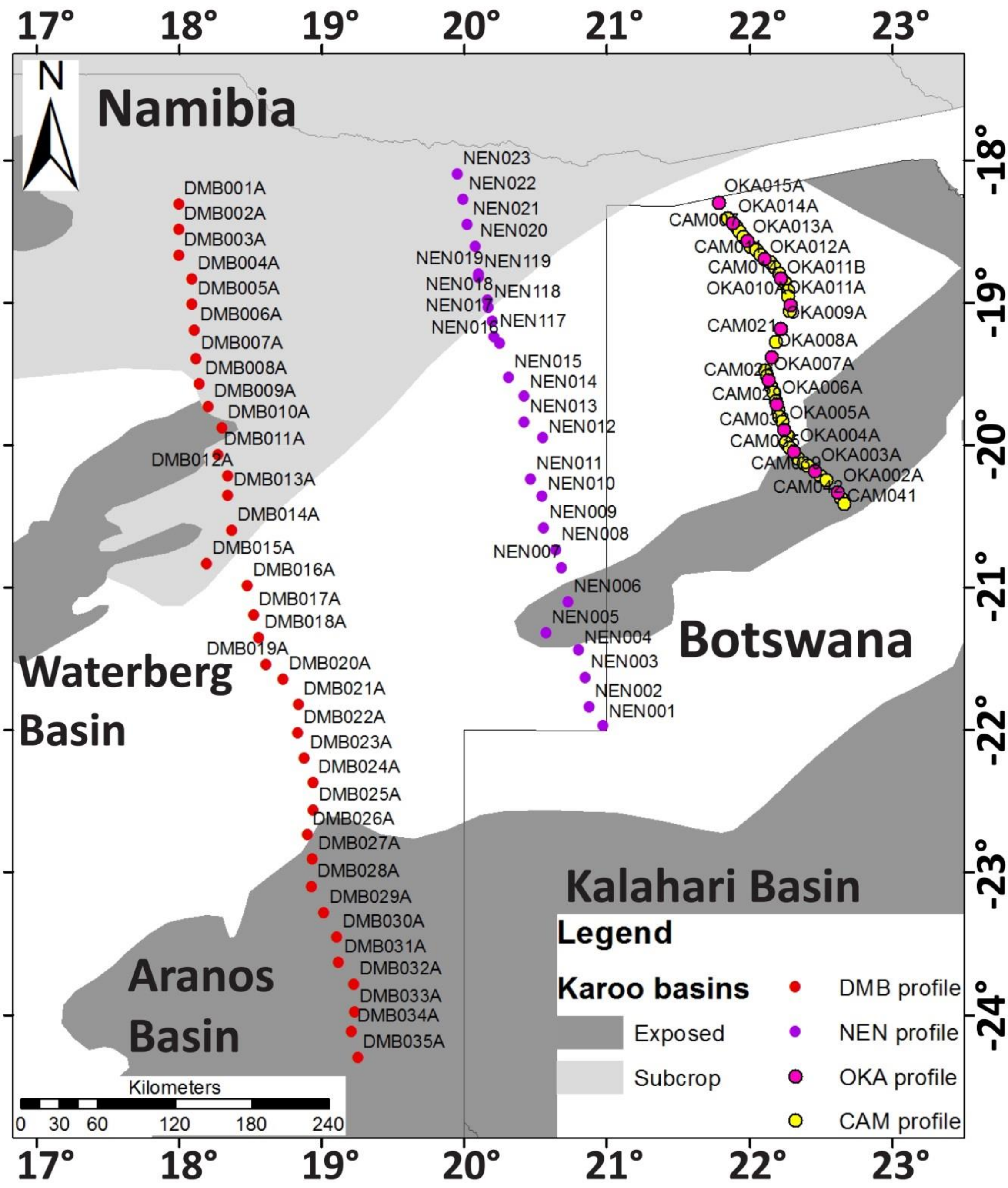

Figure 7.21: The spatial distribution of the Karoo Basins in Namibia and Botswana (after Johnson *et al*., 1996; Catuneanu *et al*., 2005) overlain by the three MT profiles.

From the interpretation of the 1D inversion models of the DMB profile and the work of Muller (*pers. comm*., 2013), DH_2 is interpreted as being associated with the Kalahari Group with a basal conductive layer at a depth of ~200 m which overlies Karoo sediments of DH_3. The contact between DH_2 and DH_3 marks the transition from the Kalahari Group to Karoo Supergroup and the northern limit of the Aranos Basin. Johnson *et al*. (1996) and Catuneanu *et al*. (2005) estimate that the Aranos Basin is ~500 m thick from the stratigraphic logs of Heath (1972). Heath (1972) studied the southwestern part of the Aranos Basin between 17°40′ E; 18°13′ E and 25°30′ S; 24°30′ S and determined that the palaeocurrents are in a south-southeast direction. However, from the TM mode of the depth interval 1 – 5 km for the DMB profile (Figure 7.14), as it is more sensitive to shallow structures (Berdichevsky *et al*., 1998), the northern limit of the Aranos Basin lies between stations DMB026/DMB027 with an increased thickness of sedimentary lithologies to the south with an estimated maximum thickness of 1.6 km at a depth range of ~500 m to 2.1 km beneath station DMB033 (Figure 7.14).

The resistivity plots of DH_1, NH_1 and NH_2 have two cycles of resistivity values ranging from a moderately resistive upper part of ~20 Ωm to 70 Ωm to a more conductive 2 Ωm to 5 Ωm lower part underlain by a similar sequence of resistivity values. From the interpretation of Muller (*pers. comm*., 2013), the first sequence is suggested to be the Kalahari Group i.e. the conductive layer marks the base of the Group, which is underlain by the resistive lithologies of the upper Karoo Supergroup. Therefore, the Kalahari Group is suggested to be the upper 100 m to 150 m with the lower cycle being Karoo Supergroup. The estimated thickness of the Kalahari Group is similar to that determined by Haddon (2001) of ~80 m to 150 m.

Interpretation of the MT profiles suggest that there is Karoo subcrop, extending from north of the DMB and NEN profiles to beneath stations DMB014/DMB016 and NEN014/NEN013 and a localised basin feature beneath stations NEN009/NEN008 to NEN007/NEN005. The extent of Karoo subcrop is similar to that suggested by Johnson *et al*. (1996) and Catuneanu *et al*. (2005), which extends from the north of the DMB and NEN profiles to beneath stations DMB015/ DMB016 and NEN118/NEN017 (Figure 7.21). Johnson *et al*. (1996) and Catuneanu *et al*. (2005) have mapped exposed Karoo rocks beneath stations NEN007/NEN006 to NEN005/NEN004 with no Karoo subcrops in the vicinity (Figure 7.21) which is in agreement with the resistivity plots (Figure 7.16).

OCH_1 is suggested to be Kalahari Group. Johnson *et al*. (1996) and Catuneanu *et al*. (2005) have mapped the northern limit of the Kalahari Basin to lie beneath stations CAM034/OKA004 (Figure 7.21). Therefore, OCH_2 is interpreted as the Karoo Supergroup with the upper more resistive values being the upper Karoo sediments and the more conductive resistivity values being the lower Karoo sediments.

7.5.2. Cratonic regions

Electrical and seismic studies conducted over Precambrian regions of the world have divided the continental crust into distinct layers based on changes in resistivity values and seismic wave velocities (e.g. Jones, 1983b; Corner, 1998). Direct observations of these stratigraphic divisions are provided by the ultra-deep borehole drilled in the Kola Peninsula (Kozlovsky, 1984). A three layer model for ancient cratons was first proposed by Pavlenkova in 1979 from deep seismic studies in the former USSR. Jones (1981) used seismic, geoelectric and heat flow results from a variety of studies over stable cratonic regions around the world to verify Pavlenkova (1979) interpretation of a three layer model. The three layer model has been proposed for the Namibian and Botswana crust from magnetovariation and electrical studies by van Zijl and de Beer (1983) (Figure 2.25). However, Gough (1986) divides the crust beneath western Europe and North America into a two layer model with the upper crust (10 km to 15 km) having resistivity values of 1 000 Ωm to 100 000 Ωm compared to resistivity values of 1 Ωm to 50 Ωm for the lower crust. Corner (1998) suggests that the three layer model applies to the Kaapvaal Craton based on seismic and geoelectric studies.

Therefore, from the above studies a generalised model for the continental crust can be determined with the upper crust being characterised by resistive material of greater than 5 000 Ωm underlain by less resistive material of ~50 Ωm to 1 000 Ωm with a very conductive lower crust of ~1 Ωm to 50 Ωm. The depth to the top and thickness of these layers vary depending on the location of the survey.

Geomagnetic deep sounding (GDS) studies have revealed numerous subsurface conductive anomalies in stable cratonic regions (summarised in Table 7.7). Multiple geophysical techniques (e.g. electrical methods, seismics and heat flow) have been used to infer the depth of the conductive layer. In each case study there is a remarkable correlation between the different geophysical techniques in constraining this layer. The low resistivity values in continental crustal lithologies are generally accepted as being associated with free water or occurrences of carbon, serpentine (or other hydrated minerals), sulphides, sulphur and magnetic oxides (Jones, 1982; Gough, 1983; Haak and Hutton, 1986; Corner, 1998). At lower-crustal depths, where rock-melts occur, considerably lower resistivity values are expected, as discussed by Schwartz *et al*. (1984) in their study of the Andes in northern Chile. This is in agreement with the study by Shankland and Ander (1983), which inferred that resistivity values in tectonically active regions (with the exception of regions of partial melting) are due to the same conductivity mechanism as in stable regions and that resistivity values are generally lower in tectonically active regions. Shankland and

Ander (1983) concluded that the low resistivity values are controlled by porosity and fluid content and is not associated with lithological compositions. Therefore, according to Haak and Hutton (1986), one can argue that there is more graphite in tectonically active regions compared to cratonic regions for which there is no petrological evidence. Corner (1998) attributes the conductivity values at mid-crustal depths (~5 km) to microfracturing and saturation of the rocks by fluids. Direct evidence for microfracturing and fluids at these depths is provided by the Kola Peninsula borehole (Kozlovsky, 1984), which intersected hydraulic disaggregation of metamorphic lithologies and large amounts of highly mineralised water at a depth of ~4.5 km (Kozlovsky, 1984). Continental crustal studies by Gough (1986) characterise mid-crustal depths at ~10 km to 15 km, with conductivity values in the range of 1 Ωm to 50 Ωm. The conductivity values can be associated with metal sulphides or carbon (i.e. graphite). Gough (1986) however, prefers saline fluids trapped in fractures and pores throughout the upper crust to be the cause of the conductivity. The presence of water-filled fractured metamorphic lithologies have also been suggested in Zone 2 of the crustal interpretation of van Zijl and de Beer (1983) where resistivity values drop from greater than 10 000 Ωm to a range of 2 000 Ωm to 10 000 Ωm. Therefore, it is suggested that there are various amounts of water at different crustal depths based on the resistivity values at the different depths (Table 7.7).

There have been numerous studies on how water can be contained at mid-crustal levels, as according to Walther and Orville (1982), free water has the tendency to rise to the Earth's surface either by diffusion or by advection thus leaving the lower crust. Theoretical studies by Klever (1984) have shown that convective flow of fluids can exist in impermeable crustal lithologies and that the pattern of anisotropy of permeability strongly influences the start and geometry of the convention flow. Therefore, the low resistivity structures may represent the pattern of such fluid flow influenced by the anisotropic permeability. A possible explanation for fluids being contained in the lower crust was proposed by Etheridge and Wall (1983). They proposed the existence of an impermeable layer at mid-crustal levels, which is created by the precipitation of the fluid mineral content. Ringwood (1975) proposes that the source of free water is derived from dehydration reactions reaching temperatures of ~400°C. Studies from the Kola Peninsula borehole revealed that temperature gradients increase 1°C every 100 m for the first 3 km and then rise to 2.5°C every 100 m (Kozlovsky, 1984). Another possible explanation for water in the crust is the adsorption of water molecules within the crystal lattice or "inner surface" of rocks. This would result in a decrease in resistivity because of the surface-conduction-mechanism with resistivity values being dependant on the inner surface area, grain size and amount of time that the crustal rocks have been exposed to volatiles and fluids rising from the mantle (Haak and Hutton, 1986).

Continuous recharge of water is suggested to be derived from the upper mantle, adsorption of water molecules to the grain surface and the existence of an impermeable middle crust, which are all possible solutions for retaining water in the crust (Haak and Hutton, 1986). However, Jones *et al*. (2012 and references within) have shown that with ascent there is a decrease in the amount of water molecules in olivine and pyroxene grains. Therefore, water molecules within a crystal lattice or "inner rock surface" may be possible for low resistivity values at the mantle transition zone; however, it is unlikely to be the case at mid-crustal levels.

Table 7.7: Summary of previous case studies of low resistive (high conductive) anomalies in the crust. GDS is Geomagnetic Deep Sounding studies and HSG is Horizontal Spatial Gradient technique.

Site	Method	Inversion	Depth range (km)	Resistivity (Ωm)	Reference
Europe/Asia					
Scotland	MT	1D and 2D	20 - 50	≈ 50	Jones and Hutton (1979) Sule and Hutton (1986)
West Germany	MT	2D	15 - 30	≈ 10	Jödicke *et al*. (1983)
Fennoscandian Shield (Sau)	MT/HG	1D	20 to undetermined	≈ 25	Jones (1983b)
Central Sweden and Finland	MT	1D	10 to 20	≈ 1	Zhang *et al*. (1984)
North America					
Canadian Shield	MT/GDS	1D and 2D	24 - 35	≈ 20	Kurtz (1982)
(Grenville Province)	MT/GDS	1D	9 - 14	80	Kurtz (1982)
Superior Province	EM	1D	> 20	≈ 270	Duncan *et al*. (1980)
Canada (Atlantic)	MT/GDS	2D	20 - 60	2 - 20	Cochrane and Hyndman (1974)
Wisconsin	MT	1D	12 - 40	≈ 20	Dowling (1970)
North American Central Plains	MT	2D	9 to undetermined	≈ 60	Jones (1993)
Jalisco Block	MT	2D	< 10	< 50	Corbo-Camargo *et al*. (2013)
Africa					
southern Africa (craton)	D.C. Schlumberger	1D	12 - 30	50	van Zijl (1977)
Damara Belt	D.C. Schlumberger	1D	4 - 20	10	de Beer *et al*. (1982)
central Africa (mobile Belt)	MT	2D	30 - 40	100 - 300	Ritz (1983)

Therefore, the preferred theory of conductivity in mid-to- lower layers of Precambrian crust, in areas where there is no partial melting, is an abundance of free water in microfractures, however, the other causes of conductivity (e.g. structural controls (shear zone and faults), graphite (free carbon), hydrated minerals, sulphides, sulphur, and magnetic oxides) cannot be ruled out without direct evidence.

Elongated conductive features are associated with Proterozoic plate boundaries and subduction zones (Giese *et al*., 1983; Haak and Hutton, 1986; Jones *et al*., 1993). This was determined by a MT study by Zhdanov *et al*. (1986) on the Carpathian anomaly, which is a prominent elongated conductive anomaly with a surface exposure marking a known plate boundary. There are a number of other unexposed elongated conductive anomalies that are suggested to resemble plate boundaries and subduction zones. One such anomaly, which is suggested to mark a subduction zone, is the Proterozoic North American Central Plain anomaly (Camfield and Gough, 1977; Jones, 1993). The anomaly has conductive values of less than 5 Ωm at a depth of 9 km (Jones, 1993). Jones and Craven (1990) discuss various possible causes of conductivity but came to no satisfactory conclusions. MT studies by Jones *et al*. (1993) on ancient subduction-collisional zones showed that some of these zones are associated with conductive anomalies, such as the Fennoscandian, Trans-Hudson, Iapetus, and Southern Cape suture zones whereas others such as Wopmay (Canada) and Penokean (North America) lack a conductive signal. Haak and Hutton (1986) state that these elongated conductive anomalies represent ancient subduction zones and Proterozoic plate boundaries but probably only applies to conductive anomalies in inactive continental regions. Another theory on the cause of this conductive layer is that it represents the actual shear zones generated during the crustal thickening by stacking (Giese *et al*., 1983).

Congo Craton

Interpretation of aeromagnetic data suggests that the Archaean southern margin of the Congo Craton is beneath stations DMB006, NEN022/NEN021 and beyond the northern limit of the OKA-CAM profile (Figure 7.22) (Corner, 2008). Miller (2008) interprets from age dates of granitic rocks that the Abbabis Complex in the southern Central Zone of the Damara Belt is of Congo Craton affinity. Kukla (1992) and Miller (2008) suggest that the Okahandja Lineament marks the southern margin of the Congo Craton, suggesting that the Congo Craton extends as far south as stations DMB015/DMB016 (Figure 7.22). In Botswana, Key and Ayres (2000) and Singletary *et al*. (2003) infer the southern margin of the Congo Craton as the northern margin of the Quangwadum

Complex. This places the Congo Craton to the north of station NEN014 (Figure 7.22). In the vicinity of stations OKA015/CAM004, Tsodilo Resources Ltd. intersected a metagranite in boreholes L9600, L9660/5 and L950/7, which has been dated at ~2.0 Ga (Figure 7.22). This metagranite is proposed to be of Congo Craton affinity (Gaisford, 2010; Gerner, 2011; Witbooi, 2011). Hence, the southern margin of the Congo Craton is suggested to be further south of these stations. From interpretation of 2D MT profiles extracted from a 3D MT inversion model, Khoza *et al*. (2013) images the Congo Craton as a highly resistive feature underlying a crustal conductor (Autseib Lineament) both of which are steeply dipping to the south. The authors conclude that the southern extent of the Congo Craton can be mapped at a depth of ~150 km beneath the Autseib Lineament i.e. the southern margin of the Congo Craton lies beneath stations ETO009/ETO010 and NEN118.

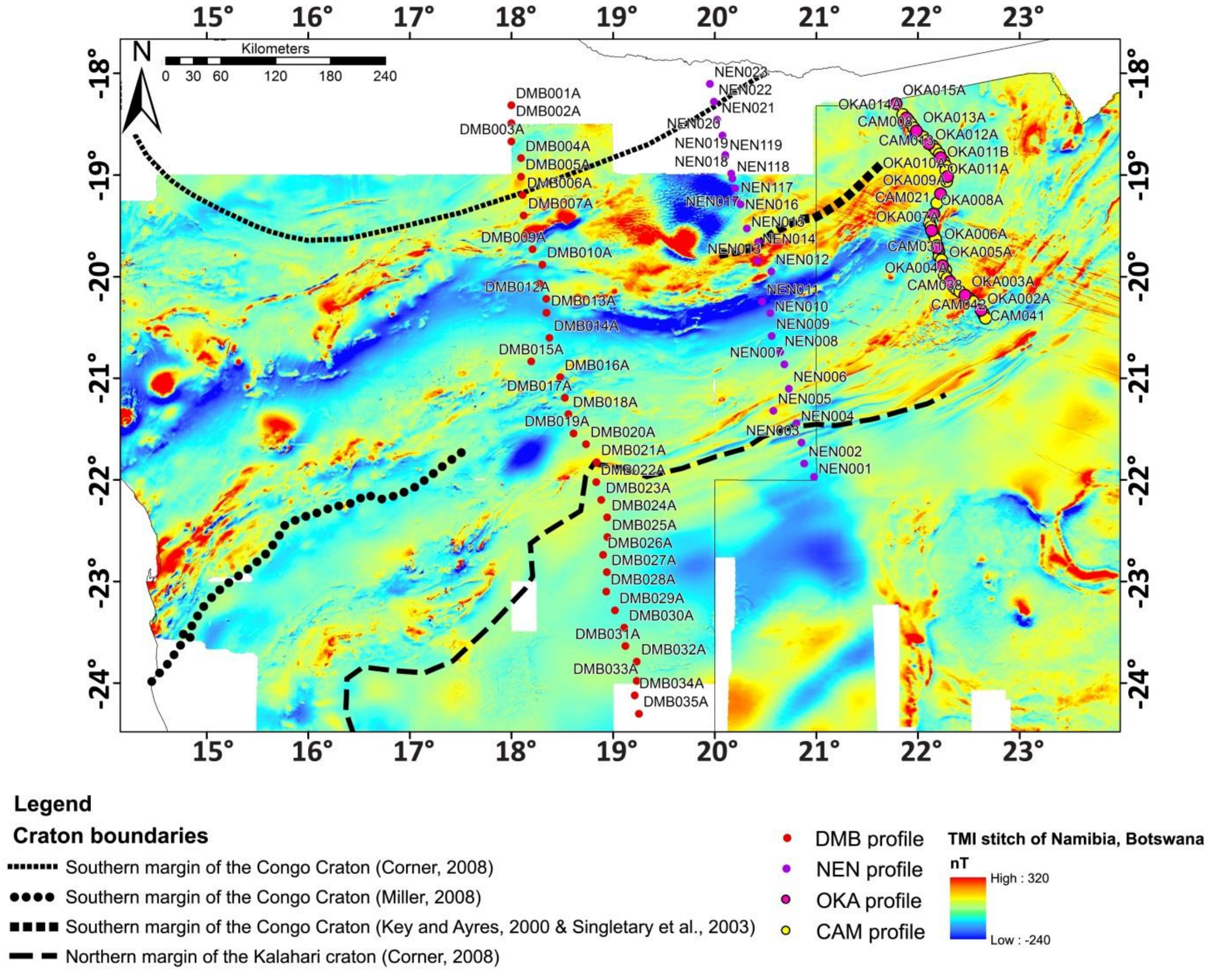

Figure 7.22: The near-surface southern extent of the Congo Craton by Corner (2008), Key and Ayres (2000) and Singletary *et al*. (2003) and Miller (2008) and the northern limit of the Kalahari Craton by Corner (2008) overlain on the TMI stitched aeromagnetic grid of Namibia and Botswana.

This study suggests a promontory exists in northwest Botswana associated with the Congo Craton. This is reinforced by DR_1, which extends to depths greater than 15 km (Figure 7.15), NR_1

and NR_2, and OCR_1. In the TM mode these bodies extend to a depth of ~2.5 km while in the TE mode they extend to ~5 km (Figure 7.17 and 7.19). This study favours the depth of 5 km, as the TE mode is more sensitive to deeper structures from synthetic tests of Berdichevsky *et al*. (1998).

Corner (2008), from aeromagnetic interpretation, marks the extent of Palaeoproterozoic rocks of the Grootfontein Complex beneath stations DMB006 to DMB009. The gneisses and granites of the Grootfontein Complex are associated with the high resistivity values of DR_1 beneath these stations. The resistivity values of OCR_1 can be correlated with the metagranite drilled immediately to the west of these stations by Tsodilo Resources Ltd. However, lithological units in the area are metasediments of the Xaudum Group and gneiss, marble, metadiamictite, and mica schist of the Tsodilo Hills Group. Therefore, the resistivity of OCR_1 can be associated with either the Congo Craton or the Xaudum and/or Tsodilo Hills Groups. Interpretation of aeromagnetic data sets, suggest that beneath stations NEN118/NEN017 to NEN014 are Karoo basalts and beneath NEN014 to NEN011 is the Quangwadum Complex. Both of these units are characterised by high resistivity values, which are illustrated in the TM mode (NR_3) but not in the TE mode of the NEN profile, which has the southern part of a conductor, NC_2 (beneath stations NEN015 and NEN014; Figure 7.16 and 7.17). According to Hamilton *et al*. (2006) and Miensopust *et al*. (2011) the TE mode will be more conductive than the TM mode on the resistive side of a fault or terrane boundary. Therefore, it is suggest that there is a terrane boundary beneath station NEN014 with the more resistive terrane to the north.

Separating NR_1 from NR_2 is a conductive body, NC_2. NC_2 correlates with the Omatako Ring Structure (ORS) of Corner (2000; 2008). The ORS occurs at the intersection of a number of geophysical lineaments, namely, the Kudu, Waterberg Fault/Omaruru Lineament (WF/OL), Khoisan, and Gam Lineaments and the Okavango Dyke Swarm (Figure 2.20) (Corner, 2008). From the two negative magnetic marks in the centre of the ORS and extensive Karoo basalts in the vicinity, Corner (2008) suggests that the ORS has been intruded by Karoo basalts, which overlie the source of the Omatako anomaly. The conductivity in the southern part of NC_2, beneath stations NEN015 and NEN016 has already been associated with the electrical properties of the TE and TM modes. From the numerous geophysical lineaments and the emplacement of Karoo basalts, the conductivity of NC_2 can be caused by a number of scenarios. For instance, high heat flow is associated with crustal conductors in the Trans-Hudson Orogen (Jones *et al*., 1993) and Wopmay Orogen (Wu *et al*., 2005). The emplacement of the Karoo basalts would generate hydrothermal fluids, however according to Thompson and Connolly (1990) fluids have a relatively short residence time in the crust of ~70 Ma or longer depending on crustal temperatures (Bailey, 1990). The Kudu, Khoisan, and Gam Lineaments (Figure 2.20) are associated with fractured rocks, either by being defined as fault zones or emplacement of dolerite dykes (Table 2.1) (Corner, 2008). Therefore, because of the lack of available field evidence, it is suggested that the conductivity of NC_2 is caused by fractures in the rocks as a result of one, or a combination of geophysical lineaments. The depth of NC_2 is unresolved because of the inductive nature of the MT method and limited penetration ability of EM fields beneath a conductor. Therefore, from the poor depth penetration of the resistivity logs beneath stations NEN019 to NEN016, it is tentatively suggested that NR_1 and NR_2 is a single body at depths greater than 5 km.

The WF/OL has been traced by aeromagnetic interpretation to beneath stations DMB009, NEN021 and beyond the northern limit of the OKA-CAM profile by Corner (2008). Ritter *et al*. (2003) associate the WF/OL with a crustal conductor dipping at 65° south of north. While Weckmann *et al*. (2003) interpret the WF/OL as a 10 km wide and 14 km deep fault zone with enhanced conductivity parallel to the fault.

Approximately 40 km to the south of the WF/OL is DC_2. Previous electrical studies have associated crustal conductive zones with zones of crustal weakness (de Beer *et al*. 1982), serpentinised lower crust (van Zijl and de Beer, 1983), fractured rocks i.e. increase in porosity (Corner, 1998) and the saturation of saline fluids, and/or the presence of conductive minerals such as graphite and sulphides (Ritter *et al*., 2003). Khoza *et al*. (2013) determines a mid-crustal conductive layer (top of the conductor is at a depth of 20 km) in the Central Zone, which is traced from the west coast of Namibia to the Namibia-Botswana border. The authors attribute the conductivity to a combination of sulphide in the upper crust and graphite in the mid- to lower crust. From the interpretation of aeromagnetic data, DC_2 is situated in a magnetically inert part of the aeromagnetic data. From geophysical evidence, however, Corner (2008) interprets a north-northwest striking fault, cross-cutting stations DMB013 to DMB011, and the Khorixas-Gaseneirob Lineament and a thrust fault beneath station DMB010. Fault gouges can contribute to the conductive values. However, immediately to the east of these stations Corner (2008) has interpreted a number of early-stage magmatic intrusions (Goas Suite). According to Gray *et al*. (2007) the granites of the Central Zone formed from dehydration melting at a mid-crustal source. McDermott *et al*. (2000) suggests that the post-tectonic granites of the Central Zone, which is characterised by a high thermal gradient of $30°C.km^{-1}$ to $50°C.km^{-1}$, high-temperature and moderate-pressure metamorphic conditions, were generated by mid to lower crustal low-pressure melting. These elevated gradients can be associated with the conductivity observed in the Central Zone on the MT profiles (Khoza *et al*., 2013). Milani *et al*. (2014) suggests, from geochemical and age dating, that the Goas Suite is influenced by a major Paleoproterozoic crustal source and minor, if any, juvenile crust from the Pan-African period. This correlates with experimental data of Roberts and Clemens (1993), which indicated that dehydration melting of basaltic material within the lower crust, can generate large volumes of mafic melts. Therefore, from the resistivity contrast beneath station DMB009/DMB010 and the interpretation of Corner (2008) of a major geophysical lineament beneath the station, this study suggests that there is a terrane boundary beneath station DMB010 with older resistive, Congo Craton lithologies to the north and conductively enhance Palaeoproterozoic rocks with an apparent southward dip, south of station DMB009/ DMB010 (Figure 7.15).

In the TE mode of the NEN profile, there is a less resistive zone beneath stations NEN013 to NEN011 (Figure 7.17) (NEN012 has been excluded from the MT cross-section because of poor data quality) where NEN011 correlates with the aeromagnetic southern boundary of the Grootfontein Complex. As this less resistive zone is illustrated in the upper resistivity part of the TE mode compared to the TM mode, it suggests that the upper terrane is more resistive compared to a lower terrane at a depth of ~3.5 km. In the TMI data, this less resistive zone lies within the regional, east-west trending, deep-negative magnetic feature, which Eberle *et al*. (1996) describe as a possible failed rift or subduction zone beneath the Congo Craton. The long wavelengths of this negative magnetic feature and the decrease in resistivity with depth on the resistivity plots would suggest that there is a conductive terrane of ~10 Ωm to 130 Ωm associated with the magnetic signal. Therefore, it is suggested that the upper resistivity values are associated with dolomitic-marbles and schists of the northern Central Zone while the lithology of the less resistive layer is not known.

In the vicinity of OCC_2, Tsodilo Resources Ltd. has intersected possible conductive lithologies such as graphitic shale, mineralised metapelites containing pyrite, pyrrhotite and minor chalcopyrite, an iron formation and serpentine bodies in a number of boreholes (Figure 7.23). In addition, from geophysical lineament mapping, a number of faults are interpreted in the region. The serpentine bodies are located to the south of these faults which lie on either side of OCC_2 (Figure 7.23). Therefore, OCC_2 could be associated with the remobilisation of serpentine along these faults. Approximately 10 km to the west of OCC_2 is the Xaudum Magnetic High. Observations from core from Tsodilo Resources Ltd. (e.g. L9600_13, L9650_4, L9600_11, and L9600_15) by Lehmann and Master (*pers. comm*., 2013) suggest that the Xaudum Magnetic High is highly folded. To the southwest of the Xaudum Magnetic High are the Tsodilo Hills, which Wendorff (2005) determined have a southward dip. Therefore, assuming that the Xaudum Magnetic High has a similar dip angle as the lithologies of the Tsodilo Hills, it could be a possible cause of the OCC_2. From the interpretation of the aeromagnetic data a number of linear features were defined. These linear features were suggested to be either iron formations or metamafic rocks. If the conductivity of OCC_2 is associated with these aeromagnetic lineations, then they are probably iron formations. Time-domain electromagnetic surveys carried out in a northwest-southeast direction across the Xaudum Magnetic High revealed a northeast dipping conductive body immediately to the east of the Xaudum Magnetic High and another ~6 km further east (Figure 6.12) (Kgotlhang, 2011). Drilling of these dipping conductors by Tsodilo Resources Ltd. intersected basement granite thrust over graphitic schist (Gerner, 2011; Kgotlhang, 2011). Kgotlhang *et al*. (2011) associates the cause of conductivity to be either the graphitic shale or mineralised metapelite. However, laboratory experiments by Duba *et al*. (1989) and thin section observations by Stanley *et al*. (1990) have revealed that high-grade metashales will have minor amounts of carbon, especially in continuous form. Therefore, for graphite to be conductive, it would have had to have formed in a low-grade metamorphic region (Stanley *et al*., 1990). Observations of borehole L9600_15 (to the north-northwest of OCC_3) and 1822C11 (~1 km southwest of station CAM009) intersected kyanite-garnet bearing rocks and garnet amphibolites suggesting that this region has undergone amphibolite facies metamorphism (Lehmann, *pers. comm*., 2013). As amphibolite metamorphism is associated with temperatures greater than 500°C, the graphite will be oxidised and the grain boundaries unconnected resulting in resistive graphite, similar to a highly resistive graphitic pelite observed in northern Canada by Camfield *et al*. (1989). Assuming conductivity is associated with mineralisation is also dangerous, as according to Jones (1993), if the sulphides formed during diagenesis of the sediments, they would not enhance the conductivity as they remain in unconnected nodules. Therefore, for the upper part of OCC_3, enhanced conductivity may be associated with either serpentinite and/or iron formation and/or mineralisation (depending on their connectivity).

OCC_2 extends to depths of ~32 km, at these depths, the favoured causes of conductivity are saturation of water formed by dehydration escaping into pore spaces (Hyndman and Hyndman, 1968), hydrous serpentinite or an edge effect of the craton (Jones, 1981).

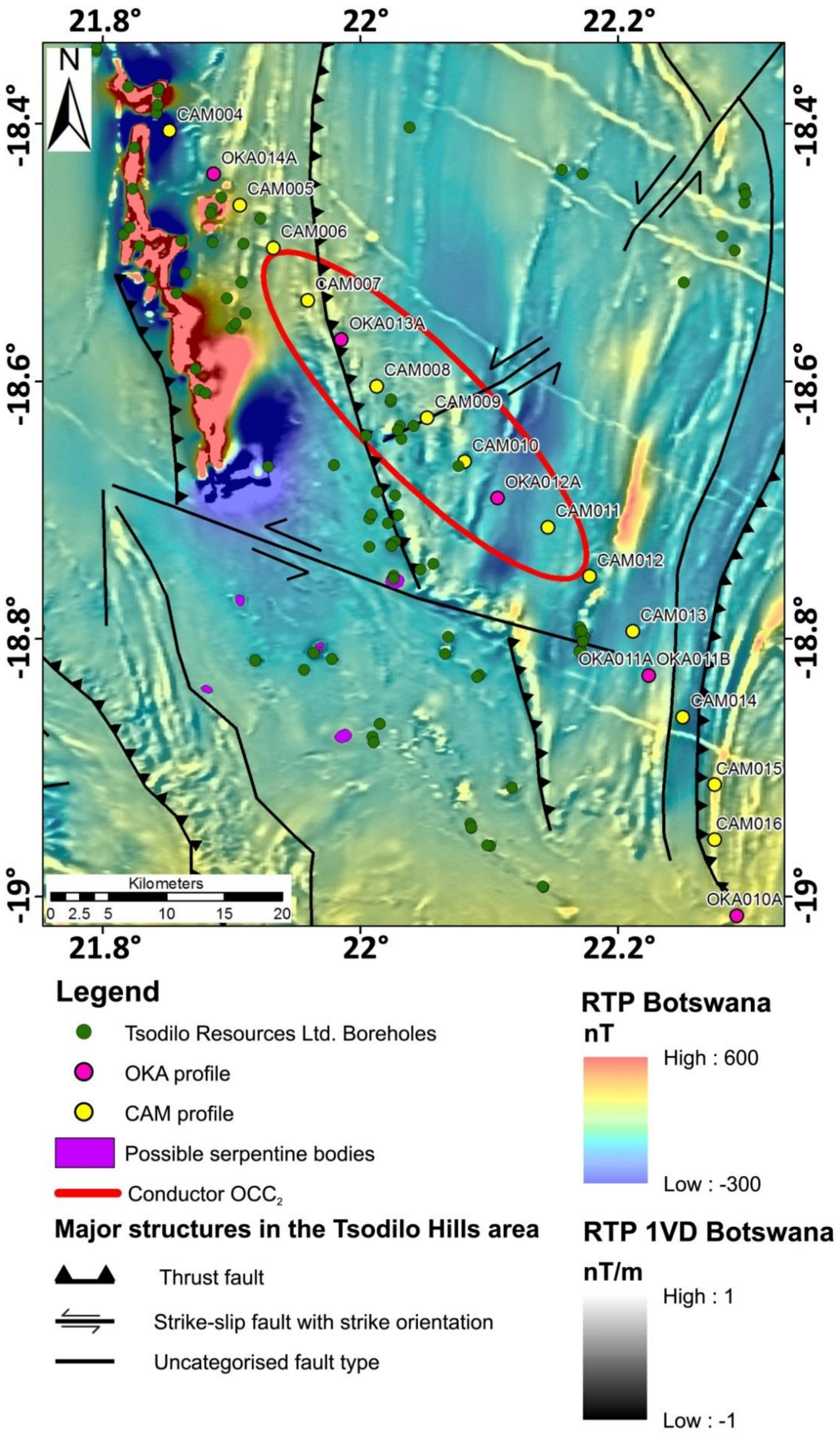

Figure 7.23: RTP with 50% transparency colour scale draped on the RTP 1VD greyscale aeromagnetic data of Botswana showing the conductive body on the OKA-CAM profile (outline in red ellipsoid) in relation to the thrust faults and serpentinite bodies (purple circles) in the Tsodilo Hills area. The green circles represent the boreholes of Tsodilo Resources Ltd.

Kalahari Craton

The aeromagnetic interpretation by Corner (2008), maps the northern margin of the Kalahari Craton beneath stations DMB021/DMB022, NEN004/NEN003 and beyond the southern limit of the OKA-CAM profile (Figure 7.22). Muller *et al*. (2009) characterises the Rehoboth Subprovince with a resistivity value of ~1 000 Ωm and the Damara/Ghanzi-Chobe Belt with a resistivity value of ~500 Ωm. Rocks of Kalahari Craton affinity have been mapped as far north as station DMB017/DMB018 by Miller (2008).

DR_4 and DH_4, in the TE mode and the southern part of DR_2 in the TM mode of the DMB profile (Figure 7.14 and 7.15), are associated with the Kalahari Craton. DR_4 and DR_2 are associated with the Kalahari Craton based on spatial correlation with the northern extent of the craton from aeromagnetic data and resistivity values of greater than 5 000 Ωm. DH_4 is associated with the Kalahari Craton, as it is suggested to be the resistive upper 5 km of the craton, which is underlain by a less resistive middle crust, as suggested by Jones (1981), Gough (1983), and Corner (1998). Direct observations of a layered crust are observed in the Kola Peninsula borehole (Kozlovsky, 1984).

Beneath the NEN profile, NR_4 (Figure 7.16 and 7.17) is suggested to represent the northern extension of the Kalahari Craton. The possible reason why NR_4 extends to depths greater than 15 km is because of the thick metasediments of the Ghanzi Group and metavolcanics of the Kgwebe Formation of ~7.5 km (Modie, 2000) and the increased sedimentary thickness in the Nama Basin beneath stations NEN002 to beyond the southern limit of the profile, which can be associated with the decrease in resistivity values in the TM mode south of station NEN005. However, in the TE mode, beneath stations NEN008 and NEN007, the northern extent of NR_4, is represented by a shallow resistive body while in the TM mode there is a conductor (NC_3) beneath these stations (Figure 7.16). From the interpretation of aeromagnetic data, the Gumare Fault is suggested to continue into Namibia by the contact of the Deep-Level Southern Zone, to the north, and Koanaka Group, to the south, i.e. beneath station NEN009 (Figure 7.24). Therefore, the resistivity contrast between the TE and TM modes agrees with a terrane/fault boundary with the Deep-Level Southern Zone being more resistive than the Koanaka Group. The MT models suggest that the Koanaka Group beneath stations NEN008 and NEN007 is at a depth of ~500 m to 3 km. From the lower resistivity values of ~550 Ωm to 800 Ωm it is suggested that the Kalahari Craton is beneath stations NEN007/NEN005 at a depth of ~2 km to 9 km overlain by the Ghanzi-Chobe Belt (Figure 7.17).

The eastern continuation of the Gomab River Line, a thrust fault, has been traced by Corner (2008) and Miller (2008) to lie beneath stations DMB020/DMB021 and NEN007. In addition, the Roibok Group has been proposed to be the continuation of the Matchless Member by Reeves (1978a), Miller (1983b), Breitkopf and Maiden (1988) and Lüdkte *et al*. (1986, in Singletary *et al*., 2003). This implies that the Matchless Member will cross-cut stations DMB020 and NEN008/ NEN007 correlating with DR_3 and NC_3 (Figure 7.15 and 7.16). Tracing this aeromagnetic trend into Botswana, it can be correlated with a resistive body of ~400 Ω m beneath stations OKA008 to CAM027 on the OKA-CAM profile (Figure 7.19).

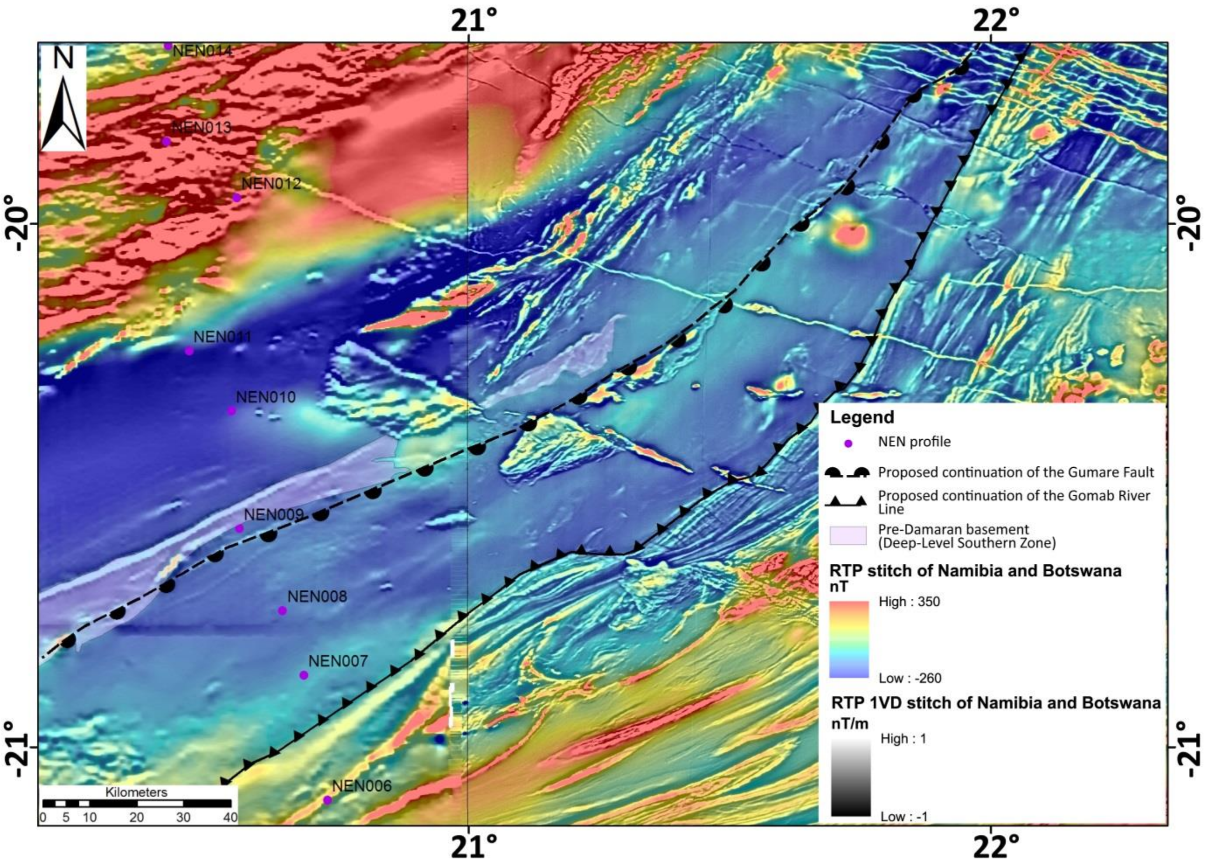

Figure 7.24: The proposed southwest continuation of the Gumare Fault into Namibia and the northeast continuation of the Gomab River Line into Botswana in relation to the Deep-Level Southern Zone (defined in this study) and the NEN profile. Background image is a 50% transparent RTP colour scale aeromagnetic map of Namibia and Botswana overlain on a greyscale RTP 1VD stitched grid of Namibia and Botswana.

According to the 1:250 000 geological map of Namibia, the dominant lithological units in the vicinity of DR_3 are the Kuiseb Formation, consisting of mica schist, metagreywacke and migmatite with minor amounts of calc-silicates, graphitic schist, carbonate rocks and amphibolite. Therefore, the decrease in resistivity values can be characteristic of graphite situated in the fault zone. This was similarly illustrated by Ritter *et al*. (2003) for the proposed conductivity of the WF/OL.

The Matchless Member is associated with sulphide mineralisation (Breitkopf and Maiden, 1988; Häussinger *et al*., 1993; Killick, 1983, 2000) and ancient oceanic crust (Barnes and Sawyer, 1980). This led Khoza *et al*. (2013) to propose that mineralisation may have been placed in the crust of the Damara Belt as in a similar manner as the North American Central Plains conductor during subduction. In addition, from MT 2D inversion modelling, Corbo-Camargo *et al*. (2013) determined the oceanic-continental interface by a diffuse conductive body. Corbo-Camargo *et al*. (2013) suggested that this represents the top of the subducting slab at a depth of less than 10 km with cause of conductivity being attributed to fractures saturated with mineralised fluids. According to Khoza *et al*. (2013) if the Matchless Member does represent oceanic crust, the formation of graphite should be expected. However, Camfield and Gough (1977) noted that the southern margin of the Wyoming Orogen, which is generally resistive, correlates spatially with a major fault zone known to contain graphite. Camfield *et al*. (1989) illustrated that graphite is not always conductive. Ballhaus and Stumpfl (1985) observed that graphite has many forms, hence caution must be taken when suggesting graphite is the cause of enhanced conductivity.

Barnes and Sawyer (1980) mapped numerous serpentine-bearing bodies in the vicinity and to the south of the Matchless Member derived from mantle harzburgites. As van Zijl and de Beer (1983) associate the cause of their conductive zone to a serpentinised lower crust, serpentine cannot be ruled out as a possible cause of conductivity. As the Gomab River Line is a thrust fault, and fluids move along pre-existing zones of weakness, the Gomab River Line can provide the transport mechanism for the serpentinite. However, to form serpentine, 10 – 15 per cent by weight of water and temperatures in the range of 100°C - 300°C are needed (van Zijl and de Beer, 1983). The water can be derived from two sources, either percolation from the surface, or from degassing of the mantle from later igneous events (van Zijl and de Beer, 1983). Laboratory observation by Olhoeft (1981) on hydrated minerals have shown that they are intrinsically resistive i.e. water released during dehydration reactions cause the lithologies to have low resistivity values.

Beneath the OKA-CAM profile, there is OCR_3, which is underlain by OCC_3 (Figure 7.19 and 7.20). The resistive values associated with OCR_3 can be caused by a number of geological features mapped from aeromagnetic data sets i.e. Roibok Group, Kwando Complex and Okavango Dyke Swarm. Following the three layer model of Corner (1998) for the Kaapvaal Craton, and since OCR_3 is underlain by OCC_3, it is suggested that the resistivity of OCR_3 is associated with a combination of geological features including the Roibok Group, Kwando Complex and Okavango Dyke Swarm (discussed in their respective sections in Section 7.5.4), comprising the upper part of OCR_3 and the lower part of OCR_3 comprising the upper resistive layer of the Kalahari Craton.

In the TM mode, the underlying conductor, OCC_3, can be divided into an upper and lower part based on resistivity values (Figure 7. 19). The upper part (5 km to 14 km) is more conductive than the lower part (14 km to 32 km) with a conductivity of ~5 Ωm to 100 Ωm compared to ~70 Ωm to 1 000 Ωm (Figure 7.19 and 7.20). From previous studies of mid-crustal conductors and direct observations provided by the Kola Peninsula borehole (Kozlovsky, 1984), the most likely cause of conductivity for the upper part of OCC_3 are microfractured metamorphic lithologies hydrated in water.

To verify the continuity of the conductive zone the properties of the conductors beneath each profile are compared. Table 7.8 lists the electrical and spatial proprieties of the three conductive anomalies in the southern part of the MT profiles. It is clear from Table 7.8 that all three conductors have similar geophysical and geometrical characteristics, which leads to the possibility that they formed in the same tectonic process. The assumption that these conductive zones are connected is strengthened by the regional conductor observed in the early electrical studies of de Beer *et al*. (1976), the MT study of Khoza *et al*. (2013), and by Jones (1993) correlating conductive terranes with non-conductive terranes in the Trans-Hudson Orogeny. This study suggests that these southern conductors represent a palaeo-subduction zone between the Kalahari and Congo Cratons. This is based on the studies by Jones (1993), Jones *et al*. (1993), Jones *et al*. (2005) and Corbo-Camargo *et al*. (2013) which determined that subduction zones can be marked by a conductive front. In addition to the conductivity observed beneath these stations, these stations correlate with a Bouguer gravity anomaly of ~-100 mGal (Figure 7.25). In a study of the Cascadia convergence, Blakely *et al*. (2005) illustrated that a subduction zone is associated with a low Bouguer gravity anomaly over the subducting plate (Figure 2 in Blakely *et al*., 2005). Both the Matchless Member and Roibok Group are Neoproterozoic in age (Singletary *et al*., 2003) and have a similar geochemical composition representing MORB-like and within-plate metabasalts (Miller, 1983b; Lüdtke *et al*., 1986; Breitkopf and Maiden, 1988). From the interpretation of potential field data this southern conductive zone lies immediately to the north of the Roibok Group (Figure 7.25). The folds of both the Ghanzi-Chobe Belt and Hureb Formation of the Southern Zone are southeast verging, with the Hureb Formation being characterised by a forearc-trench sequence containing minor amounts of graphite (Kukla and Stanistreet, 1991; Kukla, 1992). To the north of these conductive features, Miller (2008) determined from geochemistry that the metabasalts of the Lievental Member (Ghaub Formation) have a continental within-plate, alkaline to tholeiitic composition.

Table 7.8: Geoelectric and spatial comparison of DR_3, NC_3 and the less resistive zone beneath stations OKA008 to CAM027 on the OKA-CAM profile.

Conductor	Resistivity (Ωm)	Approximate depth to top (km)	Lateral extent (km)
DR_3	20 - 300	2.5	20
NC_3	1 - 70	3.5	33
Less resistive zone on the OKA-CAM profile	230 - 300	2	27

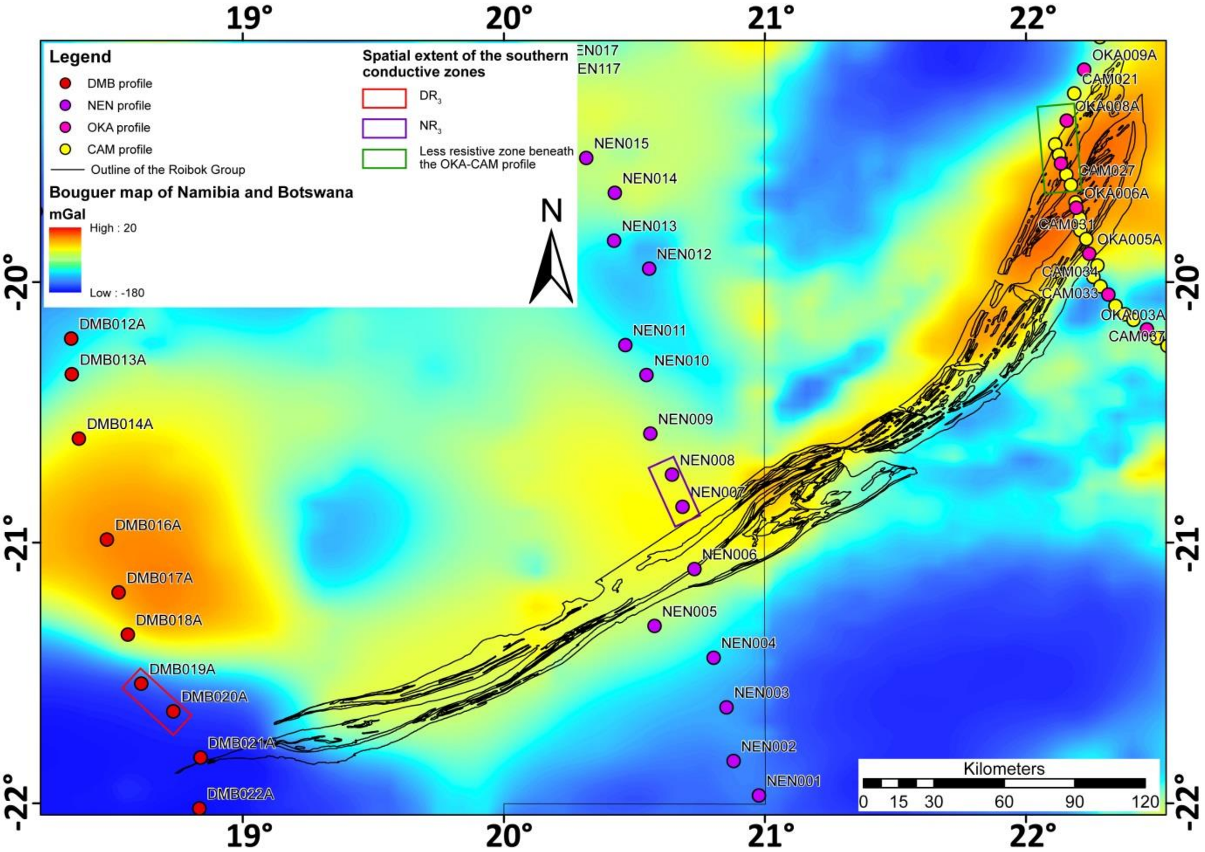

Figure 7.25: The spatial extent of the Roibok Group in relation to the three MT profiles and the conductive zones (coloured squares) overlain on the Bouguer gravity map of Namibia and Botswana.

Assigning a single cause of conductivity to these anomalies is a challenging task, as they have a strike length of ~470 km (Figure 7.25). The previous theories of conductivity ranged from weakened lithospheric crust, extension of the East African Rift System, serpentine, and a combination of sulphide and graphite mineralisation. The favoured theories for enhanced conductivity at shallow depths for an oceanic subducting plate are hydrated minerals (Green *et al.*, 1985), and fractures saturated in mineralised fluids (Corbo-Camargo *et al.*, 2013). As previously mentioned, using sulphide and graphite mineralisation and hydrated minerals as the cause of conductivity needs to be treated with care as it depends on their interconnectivity and inherent amount of water. The fluids are generated by the dehydration of the subducting plate, or from the compression of the subducting sediments (Peacock, 1990). According to Jones (1993) fluids can only cause enhanced conductivity in subduction zones younger than 100 Ma because of their short residence time in the crust. Thus, it is unlikely that Proterozoic subduction zones will still contain fluids (Jones, 1993). If fluids are excluded as a possible cause of enhanced conductivity, to generate a conductive anomaly of less than 5 Ωm, the porosity of the rocks would have to increase to 12% to 20% (Jones, 1993). The probability of serpentine being the cause of conductivity is unlikely because of the large amount of water that would be needed and the natural resistive behaviour of serpentine. In addition, graphite (carbon) can be ruled out as the sole continuous cause of conductivity based on the Roibok Group being interpreted, by both potential field and MT data, to lie immediately to the south of the conductive zone. The Roibok Group consists of amphibolite and at depth of ~100 m to 130 m, cm-sized, euhedral garnets are present (Carney *et al*., 1994). Jones *et al*. (1993) propose that the conductivity of the North American Central Plain's conductive anomaly is associated with sulphide mineralisation. Even though both the Matchless Member and Ghanzi-Chobe Belt are associated with known copper deposits, the interconnection of the mineralisation is not known. NC_3, the conductive values of DR_3 and the less resistive zone on the OKA-CAM profile lie on strike with the Gomab River Line and the mylonitic texture of the Roibok Group, respectively. These features would lead to an increase in porosity and hence, possible enhanced conductivity.

Therefore, if these conductive features do mark the palaeo-subduction zone between the Congo and Kalahari Cratons, it would imply that the northern extent of the Kalahari Craton immediately to the west of the border between Namibia and Botswana needs to be moved ~60 km north, while in Botswana this is the first time (to the authors knowledge) that the northern margin of the Kalahari Craton has been defined without cross-cutting either geological or geophysical domains (defined by aeromagnetic data). All these conductive zones are steeply dipping to the north, which is in agreement with the simplified cross-section of Gray *et al*. (2006, 2007) depicting the Khomas Ocean dipping to the north beneath the Congo Craton. To verify these conductive features as a palaeo-subduction zone further geophysical investigations, such as reflection seismic surveys should be carried out to determine reflective layers of the subducting slab. In addition, comparative studies of known Proterozoic subduction zones could be compiled in order to find similar characteristics. A simpler scenario is that the conductivity is associated with the Gomab River Line, and depending on when this thrust was last active, fluids could have an effect on the conductivity values.

7.5.3. Mobile belts

Mobile belts are regarded as moderately resistive Fractured Terranes which are weak zones in the crust compared to the older, strong, stable cratons, which are seen as Massive Terranes with higher resistivity values in the crust (van Zijl, 1977; van Zijl and de Beer, 1983). Van Zijl (1977) states that the average resistivity of mobile belts is ~5 000 Ωm and that they extend to depths of 25 km to 30 km.

Damara Belt

The interpreted aeromagnetic extent of the Damara Belt is beneath stations DMB006/ DMB007 to DMB020/DMB021; NEN118/NEN017 to NEN006/NEN005 and extrapolating the Damara Belt into Botswana based on aeromagnetic images, lies past the northern limit of the OKA-CAM profile to beneath stations OKA005/CAM032 (Figure 7.26). Resistive bodies that fall within these stations are DR_1, to DR_4, NR_3, NR_4, OCR_1 and OCR_2.

The granite dominated Central Zone and pre-Damaran Deep-Level Southern Zone are situated beneath stations DMB010 to DMB019 and NEN009 i.e. DR_2 and southernmost part of NR_3. Khoza *et al*. (2013) interprets the Central Zone as being associated with an upper crustal resistive feature because of the extensive granites. Therefore, DR_2 is interpreted as being caused by the post-tectonic and syn-tectonic granites of the Central Zone, beneath stations DMB010 to DMB015/ DMB016, and pre-Damaran basement consisting of rhyolite, amphibolite and gneiss of the Deep-Level Southern Zone beneath stations DMB015/ DMB016 to DMB019 and NEN009. The resistivity of NR_3, beneath NEN011 to NEN010, is suggested to be caused by the Kuiseb schists of the northern Central Zone. On the OKA-CAM profile, both OCR_1 and OCR_2 are suggested to be caused by gneisses, metadiamictites and marbles of the Tsodilo Hills Group and to a lesser extent the metacarbonates, shale and sandstone of the Xaudum Group. However, OCR_1 may possibly resemble the southern continuation of the Congo Craton, which is discussed in Section 7.5.2. Therefore, the aeromagnetic extent of the Damara Belt correlates well with resistive features on the MT 1D inversion plots.

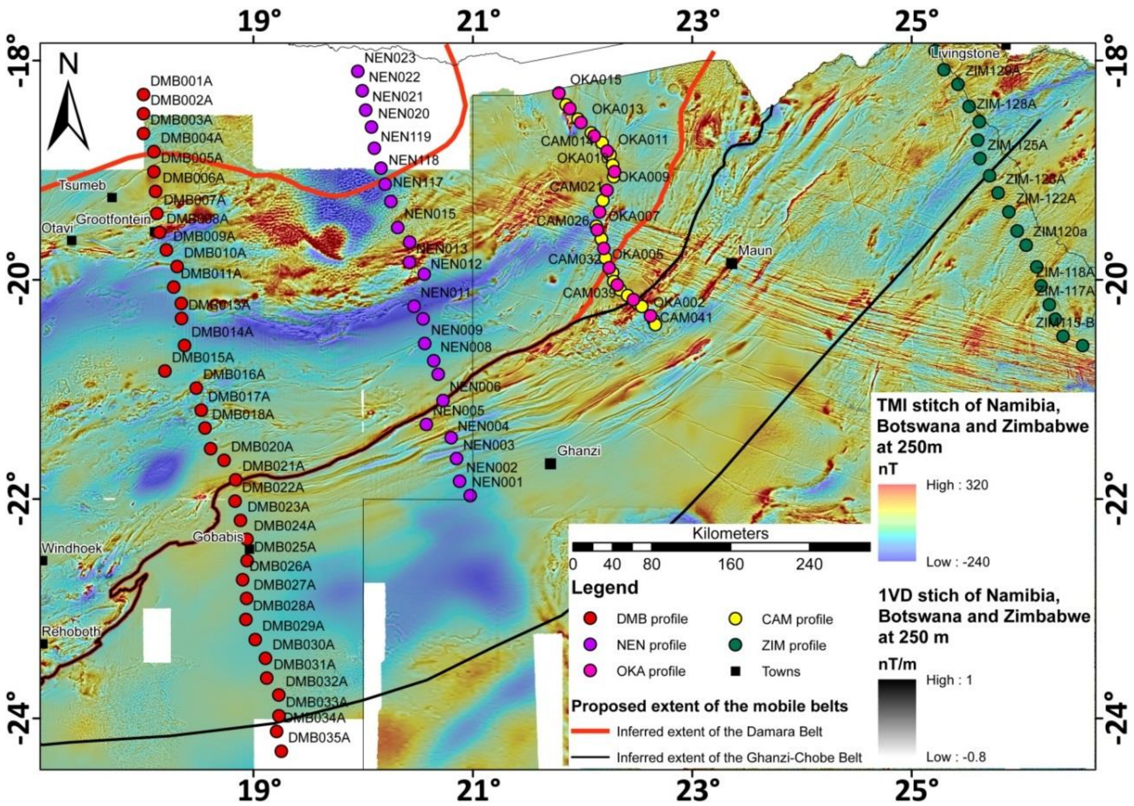

Figure 7.26: The proposed spatial extent of the Damara Belt (red line) and Ghanzi-Chobe Belt (black line) constrained by aeromagnetic and MT data in relation to the DMB profile (red circles), NEN profile (purple circles), OKA profile (pink circles), CAM profile (yellow circles) and ZIM profile (green circles; Miensopust *et al*., 2011). In the southwest the southern margin of the Ghanzi-Chobe Belt is defined by the southernmost fold visible in high-pass filtered aeromagnetic images while in the northeast by the MT interpretation of the ZIM profile (Miensopust *et al*., 2011). Background image is a 50% transparent colour scale TMI aeromagnetic map of Namibia, Botswana, and Zimbabwe gridded at 250 m overlain by a greyscale RTP 1VD stitched grid of Namibia, Botswana and Zimbabwe.

Ghanzi-Chobe Belt

This study, through the interpretation of potential field data sets, suggests that the Ghanzi-Chobe Belt extends from Botswana into Namibia beneath stations DMB021/DMB022 to DMB033/DMB034, NEN006/NEN005 to beyond the southern extent of the NEN profile and is not present beneath the OKA-CAM profile (Figure 7.26). From 2D inversion modelling of the ZIM profile, Miensopust *et al*. (2011) states that the Ghanzi-Chobe Belt is a highly resistive feature with its southern contact with the Magondi Belt dipping and increasing in thickness northwards beneath stations ZIM124/ ZIM125 to ZIM128/ZIM129 (Figure 7.26). In the TE mode of the DMB profile for a depth range of 1 – 15 km there are two resistive bodies (DR_4 and DH_4) while in the TM mode, the southern limit of DR_2 is situated beneath stations DMB020/DMB021 to DMB027/DMB028 and DH_4 is beneath the above listed stations (Figure 7.15). In the TM mode for the NEN profile, at a depth range of 1 – 15 km, NR_4 is a well-defined resistive body beneath station NEN007/NEN005 to beyond the southern limit of the profile (Figure 7.17).

The resistivity values of the Ghanzi-Chobe Belt are associated with the metavolcanics and metasediments of the Kgwebe Formation and metasediments of the Ghanzi Group. Carney *et al*. (1994) suggest that the structural style of the Ghanzi-Chobe Belt is similar to the Southern Foreland, of the Damara Belt, with open to tight folds that are southeast verging. As the folds of the Ghanzi-Chobe Belt are southeast verging, this would imply the folds are dipping in a northwest direction. This verifies the interpretation that DH_4 is associated with the Kalahari Craton, as DH_4 has an apparent northward dip. This is a similar scenario to that of NR_4 beneath the NEN profile. This study, from the interpretation of the MT 1D inversion models and aeromagnetic data, suggests that the Ghanzi-Chobe Belt is overlying the Proterozoic part of the Kalahari Craton, clearly visible beneath stations DMB021/DMB022 to DMB025/ DMB027 in the TE mode, however, because of the colour scale of the MT inversion models, a clear lower layer of the mobile belts cannot be defined from the upper layer of the craton.

7.5.4. Continental geological domains

Roibok Group and Kwando Complex

From the interpretation of potential field data sets the Roibok Group is suggested to lie beneath stations DMB021, NEN006/NEN007 and OKA005 to CAM024/OKA008 and the Kwando Complex beneath OKA005/CAM032 to CAM037/OKA003. As both these geological units are igneous events, they cannot be distinguished from each other or neighbouring mobile belts in the MT profiles without the aid of other geophysical methods. As their spatial extent is constrained by potential field data, resistive features beneath the listed stations are suggested to be associated with the Roibok Group and Kwando Complex. Therefore, from the OKA-CAM profile, the Kwando Complex is buried beneath ~100 m of cover and is associated with an apparent northward dipping southern boundary. The Kwando Complex is suggested to be in contact with the Roibok Group beneath stations OKA005/CAM032. In the TM mode, the Roibok Group is suggested to be cone-shape (Figure 7.20). The northern boundary of the Roibok Group is defined by the resistivity value contrast in the TE and TM modes, in the depth interval of 1 – 35 km, where the TM mode is slightly less resistive than the TE mode, suggesting that the dolomitic marbles of the Koanaka Group, which has an apparent southward dip, is more conductive than the amphibolites, gneisses and magnetite-schists of the Roibok Group. As station NEN006 is rejected, because of poor data quality, the Roibok Group cannot be determined beneath the NEN profile. In the TE mode of the DMB profile, beneath station DMB021, the Roibok Group is suggested to be ~4 km thick at a depth of 500 m to 4.5 km, seen by the resistivity plot of ~1 500 Ωm to 2 500 Ωm (Figure 7.15).

Okavango Dyke Swarm

Geophysical lineament mapping from aeromagnetic data suggests that the Okavango Dyke Swarm extends beneath stations NEN118/NEN017 to NEN020/NEN019 and CAM021/ OKA008 to OKA005/CAM032. The Okavango Dyke Swarm consists mainly of dolerite dykes that vary in thickness from 0.2 m to 67 m (Miensopust *et al*., 2011). From MT 2D inversion modelling, Miensopust *et al*. (2011) states that the dykes are anisotropic with resistivity values of greater than 5 000 Ωm. Beneath both the NEN and OKA-CAM profiles there are resistive bodies NR_2 and OCR_3, respectively (Figure 7.17, 7.19 and 7.20). NR_2 can possibly represent the continuation of the Okavango Dyke Swarm at a depth of ~600 m to 1.8 km. On the OKA-CAM profile the Okavango Dyke Swarm cross cuts the Kwando Complex and Roibok Group, which have similar resistivity values to the dykes. This prohibits the distinction of the dykes from these igneous intrusions.

Okavango Rift Zone

Caution needs to be taken when interpreting the possible cause of conductivity of OCC_4 since it is present in the TM mode but not in the TE mode (i.e. resistivity contrast) and is situated in the Okavango Rift Zone. The Okavango Rift Zone is associated with conductive values to depths of ~300 m because of the enrichment of saline and brackish water contained in the sediments derived from the Okavango Delta and active faults (Bufford *et al*., 2012). The estimated depths of the faults associated with the Okavango Rift Zone has been modelled to an average depth of 900 m by Kinabo *et al*. (2007) using a 3D Euler deconvolution solution to determine the top of the magnetic basement. Therefore, the faults and conductive fluids of the Okavango Delta may account for conductivity in the upper one kilometre of the crust (probably contributing to the conductivity of OCH_2), but is unlikely the cause for OCC_4.

The eastward extension of the conductive anomaly of de Beer *et al*. (1975) lies in the vicinity of OCC_4. De Beer *et al*. (1975) argue that the conductive anomaly is associated with pre-existing zones of weakness in the crust. Haak and Hutton (1986) however, propose that the conductivity at these depths is most probably caused by saline fluids circulating in an incipiently fractured zone of crustal weakness. The southward extension of the East African Rift System into northwest Botswana has been proposed by geophysical studies such as persistent seismicity (Reeves, 1972), magnetic and gravity forward modelling (Kinabo *et al*., 2007), and anomalous heat flow (Chapman and Pollock, 1977). However, as the faults of the Okavango Dyke Swarm have been reactivated across Mesoproterozoic zones of weakness and are still active (Modisi *et al*., 2000), high temperatures effects and partial melting needs to be considered as a possible cause of conductivity.

At the depth of OCC_5, conductivity can be associated with partial melting, edge effects of a cratonic block, or fractures saturated with fluids. However, the resistivity plots defining OCC_5 are inferred by the cross-section, suggesting that this conductive body is an artefact.

7.6. Discussion

Previous seismic and electrical studies focused on defining deeper structures such as the depth to Moho and lithospheric characteristics of the Congo and Kalahari Cratons. This is one of the first MT studies that focuses on near-surface crustal features in an attempt to constrain Kalahari and Karoo thickness and a geological cross-border correlation between Namibia and Botswana. The station spacing of 20 km on the DMB and NEN profiles and 5 km on the OKA-CAM profile results in imaging of structures at depths of 10 km and 2.5 km respectively, and deeper. Therefore, care was taken in interpreting structures shallower than these depths. The interpretations discussed above are non-unique and a number of other scenarios can result in the conductivity and resistivity values observed beneath the 1D inversion models. The interpretations of the MT profiles are simplified idealistic cases based on limited geological studies and potential field data (Chapter 6), which constrain the extent of the geological terranes. To verify the interpretations, multidisciplinary geophysical studies, mainly shallow seismic and MT studies, drilling and geochronology studies will be needed to constrain the sub-surface geology.

7.6.1. Horizontal layering

The sediments of the Kalahari Group are generally marked by a basal conductive layer, defined as a Kalahari aquifer (Muller, *pers. comm*., 2013). In the MT profiles, this basal conductive layer is discontinuous and is generally at a depth of less than 200 m in the northern and central parts of the profiles. The Kalahari sediments increase in thickness in a southern direction to ~300 m. The isopach map by Haddon (2001) suggests that the Kalahari sediments are ~150 m to 270 m thick beneath the northern part of the DMB profile and shallow to ~30 m to 100 m in the central part of the profile before thickening again in the Aranos Basin area to ~180 m to 210 m. The isopach map of Haddon (2001) also shows an increase in thickness of sedimentary lithologies towards the south in the vicinity of the NEN and OKA-CAM profiles, from ~30 m to 60 m to 90 m to 120 m. The disagreement in depth extents is suggested to be caused by the Occam inversion creating the simplest eight layer model.

The extent of the Karoo Supergroup interpreted from the MT profiles correlates well with mapped Karoo Basins (Johnson *et al*., 1996; Catuneanu *et al*., 2005). The 1D inversion models of the DMB and NEN profile suggest that there is Karoo subcrop north of stations DMB014/DMB016 and NEN014/NEN013, as interpreted by Johnson *et al*. (1996) and Catuneanu *et al*. (2005). Heath (1972) determined, from a borehole in the southwestern part of the Aranos Basin that the basin is ~500 m thick with a south-southeast palaeocurrent. As the palaeocurrent is in a south-southeast direction, the north-northwestern part of the basin should be thicker than the southeastern part of the basin. This is seen in the 1D inversion model of the DMB profile, which suggests that the basin is 1.6 km thick.

7.6.2. Crustal setting

The extent of the Congo and Kalahari Cratons and the suture zone between these cratons has not been confidently mapped, with Barnes and Sawyer (1980) proposing that the Matchless Member may mark the suture zone. Previous multidisciplinary geophysical studies and direct observations from the ultra-deep borehole have divided stable cratonic blocks into three layers. These observations were used in conjugation with the MT 1D inversion models to infer the margins of the Congo and Kalahari Cratons. In addition, MT studies by Jones (1993); Jones *et al*. (1993) and Corbo-Camargo *et al*. (2013) have associated enhanced conductivity with subduction zones. These studies and geological observations by Kukla and Stanistreet (1991); Kukla (1992) and Miller (2008) are used to propose a palaeo-subduction between the Congo and Kalahari Cratons.

In general, the MT models suggest that the Archaean crust of the Congo Craton extends southward to the Khorixas-Gaseneirob Lineament where Proterozoic rocks of the Quangwadum Complex have been thrust over the Archaean crust. The Proterozoic rocks of the Congo Craton extend further southwards to beneath the Central Zone of the Damara Belt. These Proterozoic rocks are observed in the MT profiles by the decrease in resistivity values and correlate with the studies of Haak and Hutton (1986) and Jones (1993), which infer Proterozoic plate margins with low resistivity values. The MT profiles also suggest that the northern extent of the Kalahari Craton should be moved northwards incorporating the Southern Zone of the Damara Belt, Ghanzi-Chobe Belt, Roibok Group and Kwando Complex.

Evidence for the southward extension of the Congo Craton is provided by drill core of Tsodilo Resources Ltd., which intersected a basement granite dated at ~2.0 Ga. ^{207}Pb-^{206}Pb detrital zircon dating of immature sandstones of the Xaudum Group by Mapeo *et al*. (2000) yielded ages of 2 055 ± 14 Ma and 2 043 ± 16 Ma, which suggests a Paleoproterozoic source rock. The Damara Orogen is a doubly vergent orogen with northwest vergent folds thrust onto the southern margin of the Congo Craton (e.g. Goscombe *et al*., 2004). In addition, age dates from the Abbabis Complex and sedimentological evidence, from the Karibib Formation, led Miller (2008) to suggest that the Okahandja Lineaments marks the southern margin of the Congo Craton. Evidence for the northward extension of the Kalahari Craton is provided by age dates of the Oorlogsende Porphyry Member (Hegenberger and Burger, 1985), Kgwebe Formation (Schwartz *et al*., 1995) and Kwando Complex (Singletary *et al*., 2003), which all yield ages of ~1.1 Ga. This, correlates with the Umkondo intraplate magmatic event of Hanson *et al*. (2004) and the folds of both the Southern Zone and Ghanzi-Chobe Belt which have a southeast vergence. In the MT models, the Damara Belt, Ghanzi-Chobe Belt, Roibok Group and Kwando Complex appear to be over-thrust onto their respective Proterozoic crusts. This and opposing verging folding supports a doubly vergent orogen, as observed by Goscombe *et al*. (2004) and Gray *et al*. (2007).

Geoelectrical studies by van Zijl and de Beer (1983) detected a regional conductor that follows the basic gravity trend, however the conductor could not be associated with either a positive or negative gravity trend (Figure 7.27). The regional conductor cross-cuts the tectonostratigraphic zones of the Damara Belt, as defined by Corner (2008) and Miller (2008), which should not occur if this conductor is syn- to post-Damara Orogen. The surface outline of the conductive feature described by van Zijl and de Beer (1983) cross-cuts stations DMB009/DMB010 to DMB014 and NEN011 to NEN006, which correlates with DC_2 and NC_3 (Figure 7.27). As van Zijl and de Beer (1983) were only considering features of 20 Ωm or less as conductive, they neglected DR_3, which lies on a positive Bouguer gravity high with NC_3. In addition, this study has already suggested that DR_3 and NC_3 are a single conductive anomaly, while DC_2 is a localised conductive anomaly.

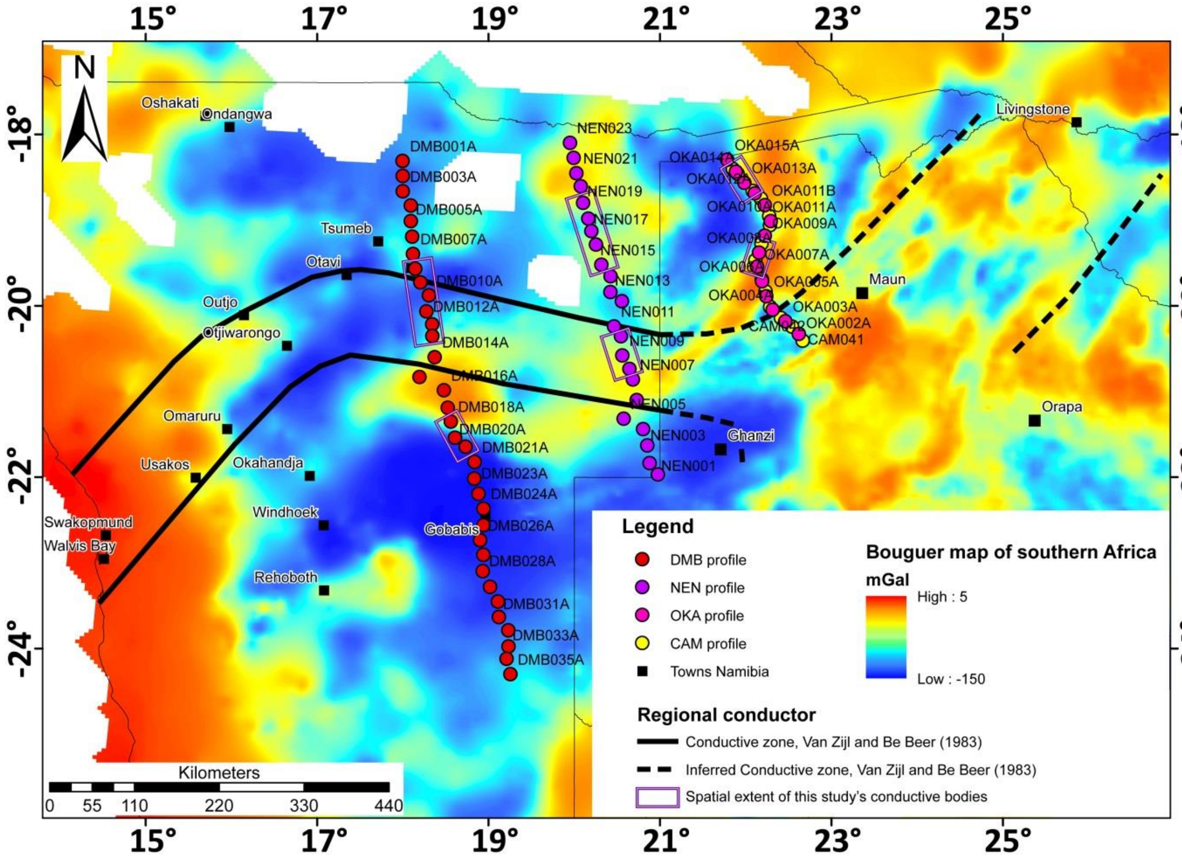

Figure 7.27: Bouguer gravity map of southern Africa with the surface outline of the regional conductive zone of van Zijl and de Beer (1983) in relation to the MT profiles and the observed conductive zones of this study.

Barnes and Sawyer (1980) and de Kock (1991) have proposed that the orogen formed as a result of continent-continent collision between the Congo and Kalahari Cratons. Becker *et al*. (2006) suggest that subduction was in a northeast direction based on magmatic and metamorphic units of the Sinclair Supergroup. Jones (1993) showed how the MT method was effective at imaging anomalies of enhanced conductivity associated with Early Proterozoic subduction zones at various locations on the Earth. Where seismic reflection data is available, enhanced reflectivity correlates spatially with the conductive anomalies (Jones, 1993). Therefore, this study suggests that DR_3, NC_3, and the less resistive zone beneath OKA008 to CAM027 represent a palaeo-subduction zone between the Congo and Kalahari Cratons (Figure 7.28). This is based on the following observations (1) the conductive bodies share similar properties (Table 7.8), they lie on the tectonostratigraphic strike of geological domains, seen in the aeromagnetic data i.e. they do not cross-cut tectonostratigraphic domains, unlike previous interpretations of the conductive zone observed in the Damara Orogen. (2) They lie on the geological strike of the Matchless Member, which has been proposed to represent oceanic crust between the Congo and Kalahari Cratons (Figure 7.28) (Barnes and Sawyer, 1980). (3) Both the Matchless Member (Namibia) and Roibok Group (Botswana) have a MORB-like and within-plate composition (Miller, 1983b; Lüdtke *et al*., 1986; in Singletary *et al*., 2003; Breitkopf and Maiden, 1988). (4) Volcanic units to the south southeast of the conductive zone, have ages of the Umkondo intraplate magmatic event (~1.1 Ga), which is a widespread post-accretion bimodal magmatic event restricted to the Kalahari Craton (Hanson *et al*., 2004) while volcanic units to the north of the conductive zone have ages of Congo Craton affinity (≥ 2.0 Ga) (Jacob *et al*., 1978; Hawkesworth and Marlow, 1983; Tack *et al*., 2002; Longridge, 2012). (5) The subducting slab is associated with a high Bouguer gravity anomaly (e.g. Romanyuk *et al*., 1998; Blakely *et al*., 2005). The three conductors lie on a Bouguer gravity anomaly of ~-100 mGal, which is high compared to the surrounding lithologies (Figure 7.28). (6) In general, folded geological units on the Kalahari Craton are southeast verging while on the Congo Craton they are northwest verging (Gray *et al*., 2007). (7) DR_4 in the TE mode of the DMB profile represents a thickened crust, suggested to be the indenter front of the Kalahari Craton, which formed as a result of the collision with the Congo Craton (Figure 7.15). (8) Proterozoic plate margins are associated with zones of enhanced conductivity, even though the cause of the conductivity values are still not fully understood (e.g. Haak and Hutton, 1986; Jones, 1993).

To verify this possible palaeo-subduction zone, further reflective seismic surveys are required in an attempt to determine the upper reflective surface of the subducting slab. In addition, near-surface (less than 15 km depth) reflection seismic surveys should be carried out in the area to determine if there is an increase in reflectivity, similar to that observed in other known palaeo-subduction zones (Jones, 1993). Thus, if this zone is marked by an enhanced conductivity and reflectivity, shear wave velocity studies should be carried out to determine Poisson's ratio. To determine the cause of enhanced conductivity, there may be no other choice but to drill boreholes. As NC_3, is the most conductive anomaly, along the proposed palaeo-subduction zone, and at a depth of ~3.5 km, drilling of this anomaly will most likely provide the best results for the possible cause(s) of conductivity.

In addition, to these possible scenarios for a palaeo-subduction zone, other lines of evidence for this are the granites of the Central Zone, which are suggested to represent dehydration of a subducting slab at mid-crustal depths (Gray *et al*., 2007). Geochemical studies of the Goas Suite, revealed that they are strongly influenced by a Proterozoic crust (Milani *et al*., 2014), which is suggested to be the subducting slab from the enhanced conductivity anomalies beneath the MT profiles.

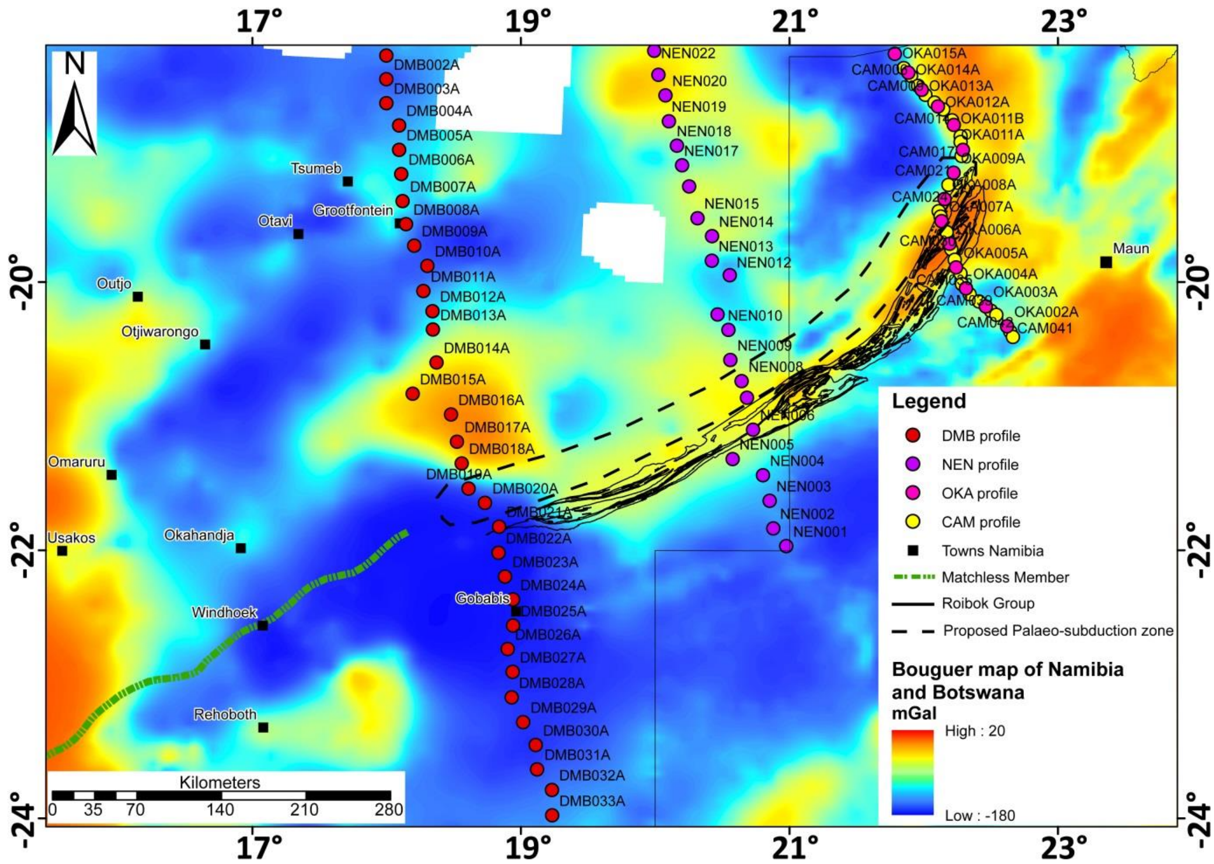

Figure 7.28: Bouguer gravity map of Namibia and Botswana with the surface outline of a possible palaeo-subduction zone defined by the less resistive zones, DR_3, NC_3 and beneath stations OKA008 to CAM027 relative to the Matchless Member and Roibok Group.

7.7. Conclusion

Therefore, from the interpretation of the DMB, NEN and OKA-CAM profiles, constrained spatially by potential field data sets, a palaeo-subduction zone is tentatively suggested to be beneath stations DMB020/DMB021, NEN008/NEN007 and OKA008 to CAM027 (Figure 7.28). Previous geoelectric studies have been proven to be robust in detecting and identifying Proterozoic subduction zones and plate margins. The most noteworthy and studied Proterozoic suture zone is the North American Central Plains conductivity anomaly, which is buried beneath a sedimentary cover (Camfield and Gough, 1977; Jones, 1993; Jones *et al*., 1993). Enhanced conductivity for recent subduction zones (younger than 100 Ma) can be explained by fractures statured with fluids (Corbo-Camargo *et al*., 2013), whereas for Proterozoic subduction zones it is more difficult to associate a cause of conductivity because of the lack of knowledge about various conditions during that time period (Jones, 1993). There are known Proterozoic suture zones which are not conductive (e.g. Wopmay and Penokean Orogens) (Jones, 1993).

7.8. Summary

This chapter covers MT theory, analysis, editing and 1D Occam inversion of the MT data. Two conductive zones, a northern and southern zone respectively, were observed beneath the three MT profiles. The northern zone is suggested to be associated with individual discrete conductive bodies, while the southern zone forms an elongated conductive zone. Geoelectric studies have associated elongated conductive zones with Palaeoproterozoic plate margins and subduction zones (e.g. Haak and Hutton, 1986; Jones, 1993; Corbo-Camargo *et al*., 2013). The palaeo-subduction zone is suggested to be northward dipping by Barnes and Sawyer (1980), Becker *et al*. (2006) and Foster *et al*. (2014). To verifying this, three approximately north-south trending magnetic profiles in the vicinity of the Namibia – Botswana border are 2D forward modelled and discussed in the following chapter.

Chapter 8

Magnetic forward modelling

8.1. Introduction

The Damara Belt formed during the collision between the Kalahari and Congo Cratons between ~560 Ma to 540 Ma (Goscombe *et al*., 2003; Gray *et al*., 2006, 2008; Frimmel *et al*., 2009; Miller *et al*., 2009a; Frimmel *et al*., 2011). The subduction of oceanic crust beneath the Congo Craton is still under debate (Kröner, 1982; Jung *et al*., 2002; Miller *et al*., 2009a) with previous geodynamic discussions on the evolution of the Damara Belt being concerned with whether or not oceanic crust formed during spreading prior to subduction and continental collision. Subduction models suggest the subduction of both oceanic crust and the Kalahari Plate beneath the Congo Craton (e.g. Barnes and Sawyer, 1980; Longridge *et al*., 2011; Frimmel *et al*., 2011), while other models suggest no clear evidence for a subduction environment and favour an intracontinental orogenic environment (Kröner, 1982; Jung *et al*., 2002).

An aulacogen model which initiates the development of the Damara Orogen with three symmetrical rift grabens induced by the cooling of asthenospheric material was proposed by Martin and Porada (1977) and Porada *et al*. (1983). The authors suggested that this was followed by a downwarping stage and a final post-geosynclinal stage. The delamination model of Kröner (1982) involves initial crustal stretching over a mantle plume located beneath the Southern Zone leading to the extrusion of the Matchless Member. Further processes in this model involve lithospheric delamination, continental subduction, crustal underthrusting and high-level thrusting. The location and geochemical signatures of the large volumes of granitoids within the Damara Orogen do not correspond with the structure of typical collisional belts (Jung *et al*., 2002 and references within), and the lack of high-grade metamorphism (i.e. eclogites) and exposure of oceanic crust provides scarce evidence for the existence of a palaeo-subduction setting.

Hartnady (1978), Kasch (1979) and Barnes and Sawyer (1980) favour an ocean-floor subduction model where several thousand kilometres-wide oceanic crust was subducted. The subduction of a narrow, Red Sea-type ocean was favoured by Miller (1983a) by interpreting the Matchless Member as a remanent of a spreading centre which was covered by clastic sediments. Downing and Coward (1981) and Coward (1983) proposed a small ocean-basin model associated with strike-slip movement involving the formation of pull-apart basins which are partly floored by oceanic crust in the Damara Belt. A limited ocean-basin model involving fault-related development of sub-basins in the Southern Zone on both continental and oceanic crust was suggested by Breitkopf and Maiden (1988). Kukla (1992) used mineral deposits associated with the Matchless Member, sedimentological, structural and metamorphic evolution to determine the size of the Khomas Ocean and position of the mid-ocean ridge relative to the continental margin. The amount of tectonic shortening calculated, indicated that the basin had a minimum width of hundreds of kilometres once spreading stopped (Kukla, 1992). Frimmel *et al*. (2011) estimated a maximum width of 1 200 km for the Khomas Ocean based on the Matchless Member being younger than 635 Ma and that spreading continued until 575 Ma (end of Ghaub glaciation).

Three approximately north-south, 340 km long 2D magnetic profiles were modelled in the vicinity of the Namibia – Botswana border (Figure 8.1) to verify the palaeo-subduction zone interpreted from the MT data (Chapter 7) and the geological cross-border correlations (Chapter 6). In addition, the fold structure of the Ghanzi-Chobe Belt was investigated and the possible cause of the roughly east-west striking negative magnetic feature in northern Namibia (Figure 8.1).

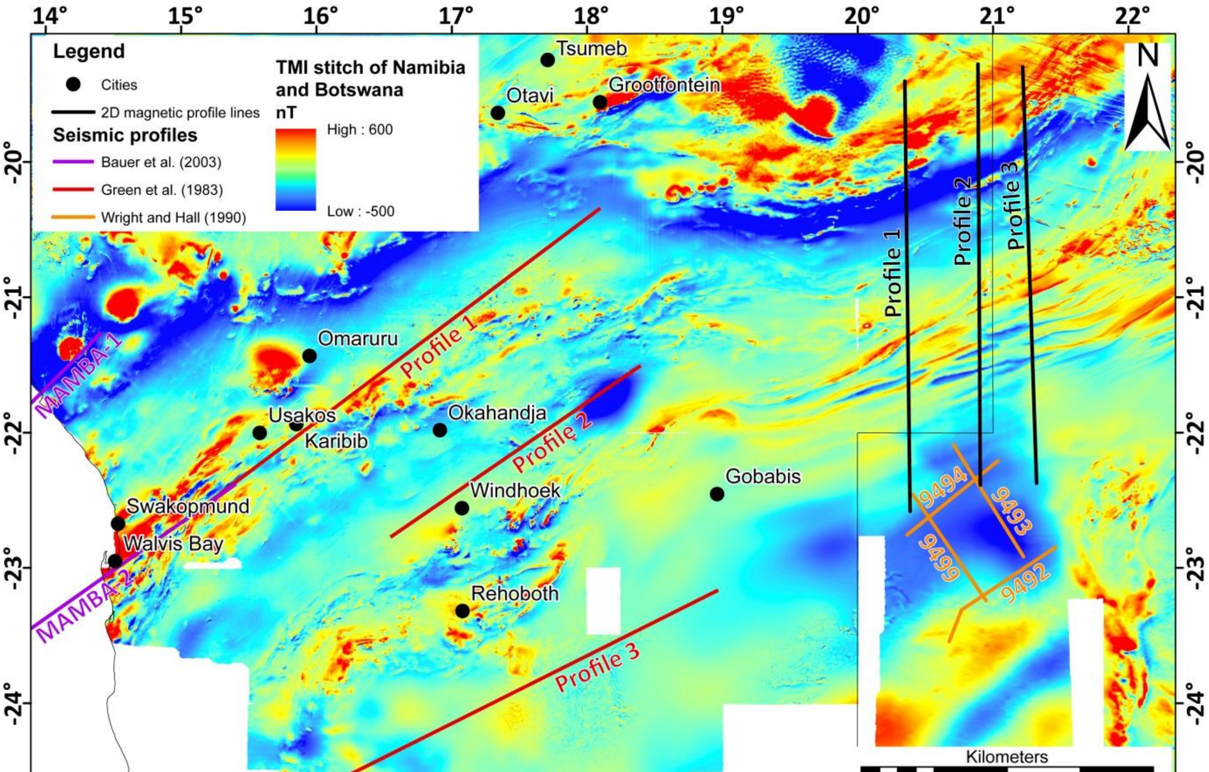

Figure 8.1: Location of the three 2D magnetic profiles (black lines), in relation to the four explosive seismic profiles of Wright and Hall (1990) in the Nosop Basin (orange lines), the three seismic refraction profiles in the Central Zone of Green (1983) (red lines) and the seismic reflection profiles of the MAMBA (Geophysical Measurements Across the Continental Margin of Namibia) project (Bauer *et al*. 2000, 2003) (purple lines). Background image is the TMI stitch at 250 m of Namibia and Botswana.

8.2. Forward modelling theory

Forward modelling involves creating a hypothetical geological model and calculating the expected geophysical response from the geological model. The techniques used to calculate the potential field response are based on the methods of Talwani *et al*. (1959), and Talwani and Heirtzler (1964) and make use of the algorithms described in Won and Bevis (1987).

For the calculations of the potential field sources, a 2D, flat-Earth model is used, which means that in the direction perpendicular to the profile each block extends to plus and minus infinity. The Earth is assumed to have topography but no curvature.

8.2.1. Euler deconvolution

Euler deconvolution is a semi-automatic interpretation technique used to estimate the location and depth of magnetic source bodies beneath the magnetic profiles. The technique was initially developed and applied to magnetic data along profiles by Thompson (1982). Reid *et al*. (1990) developed 3D Euler deconvolution that can be applied to both gridded and profile data sets. Euler deconvolution requires no a prior information about the direction of magnetisation of the source body other than the Structural Index (N), which leads to the technique not being affected by remanence (Oruç and Selim, 2011).

Theory of Euler deconvolution

Any function in the Cartesian plane having co-ordinates *x*, *y* and *z* is denoted by *f*(*x*, *y*, *z*) (Thompson, 1982). The plane *z* = 0 is taken as the plane of observation with z being positive downwards. Therefore, the x-axis is the north-south plane and the y-axis the east-west plane. The function *f*(*x*, *y*, *z*) is homogenous of degree *N* if;

$$f(tx, ty, tz) = t^N f(x, y, z), \tag{8.1}$$

where *t* is a scaling factor. Then Euler's equation is satisfied and is given by (Blakely, 1995);

$$\boldsymbol{r} \cdot \nabla f = -Nf. \tag{8.2}$$

Where $r = \sqrt{x^2 + y^2 + z^2}$ and N is the structural index, which measures the rate of change with respect to distance of the field i.e. the decay of amplitude of the field with distance. By considering (x_o, y_o, z_o) as the location of the magnetic source relative to the plane of measurement (x, y, z), Euler's equation can be written as;

$$(x - x_0)\frac{\partial f}{\partial x} + (y - y_0)\frac{\partial f}{\partial y} + (z - z_0)\frac{\partial f}{\partial z} = -Nf \tag{8.3}$$

where *f* is the total magnetic field anomaly and *N* is the structural index. Equation 8.3 is valid for the TMI data where the co-ordinates (x_0, y_0, z_0) are expressive for the derivative of the magnetic field in x and y directions. For profile data, the transverse gradient $(\frac{\partial f}{\partial y})$ in Equation 8.3 is assumed to equal zero. Therefore, for profile data Equation 8.3 simplifies to the expression;

$$(x - x_0)\frac{\partial f}{\partial x} + (z - z_0)\frac{\partial f}{\partial z} = -Nf \tag{8.4}$$

Application of Euler deconvolution

Euler deconvolution calculations were processed in Euler Deconvolution (freeware developed by Prof. Gordon Cooper of the University of the Witwatersrand) with the following steps taken;

1. A window of n grid cells is selected and run along the profile. A window size of 11 has been shown to produce reliable results reasonably quickly (Reid *et al*., 1990). The general convention in selecting a window size is based on the data response; normally the window size used is half the anomaly size (Ravat, 1996). If the window size is too large it may contain more than one source body, resulting in incorrect source locations. If the window size is too small then, two problems may occur; firstly, source bodies may not be sufficiently sampled, and secondly, as the number of data points decreases in the window the solutions become more sensitive to noise. However, a smaller window size can improve solution clustering and thus is preferable over a window size that is too large.
2. The window is moved and step (1) is repeated, until all possible window positions have been calculated.
3. A plot of the solutions is mapped. Each solution is plotted at a cross-sectional (*x*, *z*) position.

Choice of structural index (N)

Approximate structural index values for magnetic sources are provided in Table 8.1. If the structural index is chosen too strictly, reliable depth estimates are obtained but some structures are poorly defined because of a limitation in solutions being obtained. If the structural index is chosen too loosely, the structural contrast is surrounded by poorly defined solutions that obscure the better solutions. To determine the correct structural index, Euler deconvolution is applied several times with various structural indices. The correct index selected is the one that gives the tightest clustering and linear grouping of solutions for a certain model.

Table 8.1: Structural indices used to estimate the depth and extent of simplistic magnetic sources beneath the aeromagnetic profiles (after Reid *et al*., 1990; FitzGerald *et al*., 2004).

Structural index (N)	**Model features**
0	Contact
1	Fault
1	Dyke
2	Vertical pipe
3	Sphere

8.3. Construction of the forward models

The shape and amplitude of any magnetic anomaly is influenced by a combination of spatial, physical and magnetic parameters of the source body (Cole *et al*., 2013). Its location determines the magnetic intensity, inclination and declination of the inducing field. Physical parameters to consider are width, depth and dip of the magnetic source while magnetic parameters are magnetic susceptibility and remanent magnetisation (defined by the intensity, inclination and declination) (Cole *et al*., 2013).

The 2D magnetic models were modelled in GM-SYS, an extension in Geosoft, on the Total Magnetic Intensity (TMI) map of Namibia and Botswana at a grid resolution of 250 m (Figure 8.1). GM-SYS enables the computation of magnetic anomalies caused by 2D structures (i.e. infinite strike length) that are arbitrary in shape by representing a cross-section of the body by an irregular polygon. The horizontal, vertical and total-field intensity magnetic anomalies caused by a body are calculated by non-iterative, analytical expressions. GM-SYS can calculate induced, remanent or mixed magnetisation.

A STRM model at a spatial resolution of 90 m (from Seeker, Geosoft) was used to determine the topography along the profiles. It was assumed that the aeromagnetic survey was a draped survey at a flight height of 150 m above the topography. As the profiles are ~50 km apart and the Earth's magnetic field varies spatially, the centre of the profiles have the following parameters;

- Profile 1
  - declination: -14°
  - inclination: -61°
  - magnetic field intensity: 31 050 nT
- Profile 2
  - declination: -14°
  - inclination: -61°
  - magnetic field intensity: 31 085 nT
- Profile 3
  - declination: -13°
  - inclination: -61°
  - magnetic field intensity: 31 100 nT

The lack of outcrop in the vicinity of the magnetic profiles and the non-uniqueness associated with potential field modelling allows for multiple scenarios producing the same observed magnetic data. To constrain the models the thickness of the Kalahari sediments was determined by the isopach map of Haddon (2001) and the extent and depth of Karoo basins by the studies of Johnson *et al*. (1996), Haddon (2001), and Catuneanu *et al*. (2005) and the interpretation of aeromagnetic data (this study). The lateral extent of the geological units was constrained by overlying the magnetic profiles on the sub-Kalahari geological map and delineating the location of the geological units (Figure 8.2). The depth and lateral extent of magnetic sources was further constrained by Euler deconvolution with window sizes of either 11 or 22. To estimate the position of the deeper magnetic features Euler deconvolution was carried out on TMI Namibian data upward continued by 7.5 km and regridded to a resolution of 1 km. Euler deconvolution was calculated with the following parameters;

- declination: dependent on profile. Listed above
- inclination: dependent on profile. Listed above
- magnetic field intensity: dependent on profile. Listed above
- bearing (degrees positive from north): 0° (assumed north-south orientation)
- flight height: 150 m

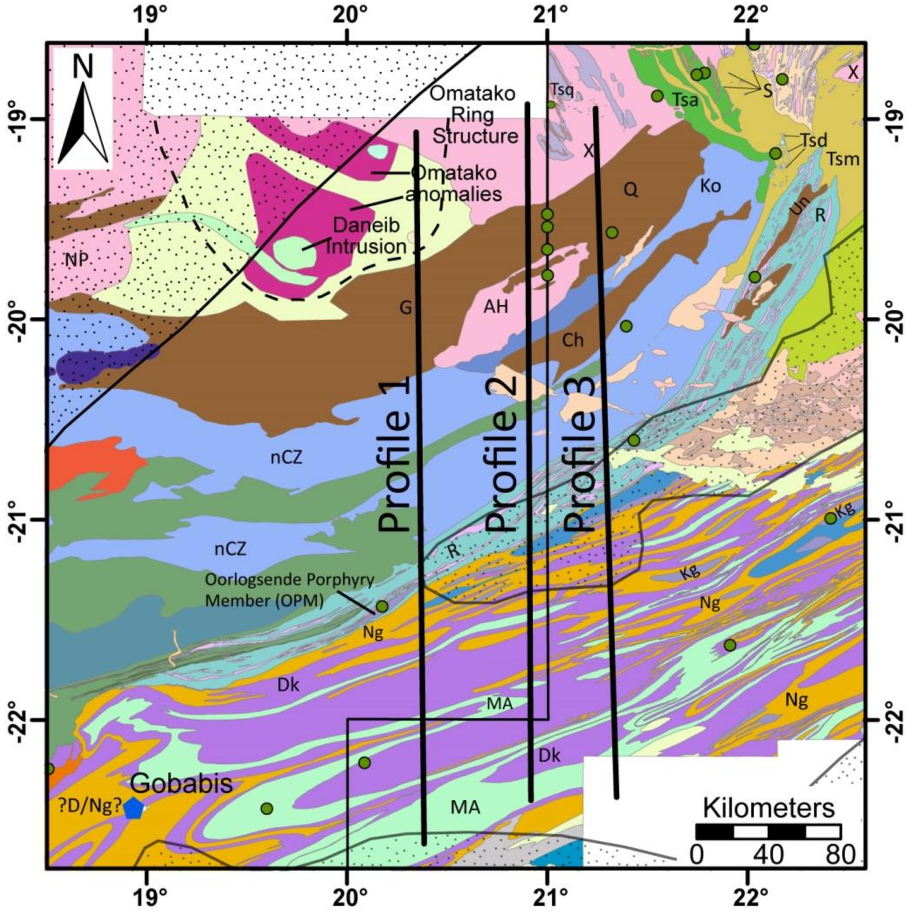

Figure 8.2: Location of the three 2D magnetic profiles (black lines), overlain on the sub-Kalahari geology interpreted by aeromagnetic data. See Figure 6.1 and fold out for legend to the sub-Kalahari geology.

8.3.1. Determination of depth to the top of the Moho

In 1975, three explosion-seismic refraction profiles were carried out in the Central Zone of the Damara Belt (Green *et al*., 1983; Baier *et al*., 1983). The results showed a dominantly felsic (v_p = 5.9 km.s^{-1} to 6.2 km.s^{-1}) upper crust to a depth of ~15 km. Beneath that depth the seismic velocity jumps to 6.4 km.s^{-1} and, according to Green (1983), the material extends down to the Moho at a depth of 40 km to 50 km. In contrast, Baier *et al*. (1983) suggested that the higher-velocity material (v_p = 7.8 km.s^{-1}) is present in the lower crust at a depth of 30 km to 50 km and indicates magmatic underplating. A crustal thickness of ~55 km was inferred by Green (1983) for the Central Zone based on gravity data. A later wide-angle reflection seismic profile (2.5 km station spacing), part of the MAMBA-1 (Geophysical Measurements Across the Continental Margin of Namibia) project, was carried out along profile 1 of Green (1983) (Bauer *et al*., 2000). The profile failed to detect a Moho reflection because of very thick sedimentary sequences (thickness of the sediments was not stated) (Bauer *et al*., 2000). In a 2D potential field model across the Messum

Igneous Complex, Bauer *et al*. (2003) inferred an inclined Moho at a depth of 37 km to 38 km from the MAMBA-1 data.

Four explosion-seismic reflection profiles were carried out across the Nosop Basin (Wright and Hall, 1990). The data revealed a depositional centre of the Nosop Basin with greater than 10 km of Palaeozoic and younger sediments. At ~14 s TWT (two-way travel time) a continuously reflective horizon is suggested to be the Moho (Wright and Hall, 1990). There is no systematic change in the depth to the Moho through the Nosop Basin. Wright and Hall (1990) do not provide a depth to the top of the Moho in terms of kilometres or seismic velocities of the individual layers. The only depth estimates provided is a depth of 12 km to 18 km for the first 6 – 7 s TWT (Wright and Hall, 1990). The depth to the top of the Moho is estimated at being between ~33 km to 42 km assuming an average velocity of 5 900 m.s^{-1} for the overlying basement at 7 – 8 s TWT.

8.3.2. Determination of the depth of the Curie point

The magnetic signal is detectable to a specific depth (Curie depth) determined from the Curie temperature of the mainly magnetite and to a lesser extent pyrrhotite of ~580°C and 320°C, respectively. The Curie temperature of magnetite varies with titanium content, adding a degree of uncertainty to depth estimates using the degree of magnetisation. Magnetic field observations can be divided into short crustal magnetic sources and longer, lower amplitude anomalies caused by the demagnetisation at the Curie depth. For simplicity, Bauer *et al*. (2003) assumed that the Curie depth is reached at a depth of ~20 km for a typical crustal geothermal gradient of 25°C km^{-1} to 30°C km^{-1}. In a heat flow review paper on southern Africa the Curie depth of magnetite was estimated at ~35 km beneath the mobile belts and 50 km beneath the cratons based on 2D numerical modelling of the lithosphere and P-T regimes obtained from kimberlite nodules (Jones, 1998). Thermal models of Cascadia, south Alaska, southwest Japan and Chile suggest that the Curie depth of magnetite at an active subduction zone is reached at a depth of ~50 km (Oleskevich *et al*., 1999).

8.3.3. Determination of physical properties of magnetic bodies

As the majority of the physical property measurements were collected in western Namibia and Zambia (Chapter 5), ~340 km away from the magnetic profiles, magnetic susceptibility values of

Sharma (1987), Sanger and Glenn (2003), Walker *et al*. (2010), and Lehmann *et al*. (submitted) have been used to substantiate the measured physical properties.

8.4. Geophysical observations

8.4.1 Fence plots

To simplify the magnetic interpretation of the three magnetic profiles, they were compared to each other to determine similar magnetic sources for the magnetic signal (Figure 8.3).

The magnetic profiles are divided into a long wavelength and three shorter wavelength domains (Figure 8.3). The first domain (D_1) is ~180 km wide (Figure 8.3) and is associated with geological units of the northern margin of the Kalahari Craton (i.e. Ghanzi-Chobe Belt and Roibok Group). The first 100 km of D_1 has a gradual increase in magnetic amplitude from ~-170 nT in the south to -50 nT in the north. The low magnetic amplitudes are caused by the Ghanzi-Chobe Belt formation being covered by Nama and Kalahari Group sediments within the Nosop (Botswana) and Aranos (Namibia) Basins. The next 80 km of D_1 is associated with magnetic amplitudes of ~-100 nT to 150 nT caused by near-surface Ghanzi-Chobe Belt formations. The magnetic peaks in this section can be correlated across the profiles by examining the sub-Kalahari geological map (GCB in Figure 8.2). The highest magnetic amplitude in D_1 of ~300 nT is caused by the Roibok Group (RBG in Figure 8.3). The difference of magnetic amplitude observed for the individual peaks can be caused by thickening of sedimentary cover and lateral variance in magnetic susceptibility.

The second domain (D_2) is ~90 km wide and characterised by a magnetic amplitude of ~0 nT in the south which decreases to ~-400 nT in the north (Figure 8.3). The shorter wavelengths are associated with the Deep-Level Southern Zone (defined by Corner, 2008) and the Chihabadum Complex (Key and Ayres, 2000) while the long wavelength is associated with the northward subduction of the Kalahari Plate beneath the Congo Craton and thick accretionary prism (Koanaka Group) (KG in Figure 8.3). The magnetic amplitude of the Deep-Level Southern Zone can be correlated across all three profiles (DLSZ in Figure 8.3) while the magnetic amplitude of the Chihabadum Complex can be correlated across profiles 2 and 3 (CC in Figure 8.3).

The final domain (D_3) is ~90 km wide and is characterised by an increase in magnetic amplitude from ~-400 nT to 400 nT (Figure 8.3). The increase in magnetic amplitude is associated with the Quangwadum Complex (QC in Figure 8.3) and the Okavango Dyke Swarm (ODS in Figure 8.3), which are correlated across profiles 2 and 3 (ODS in Figure 8.3).

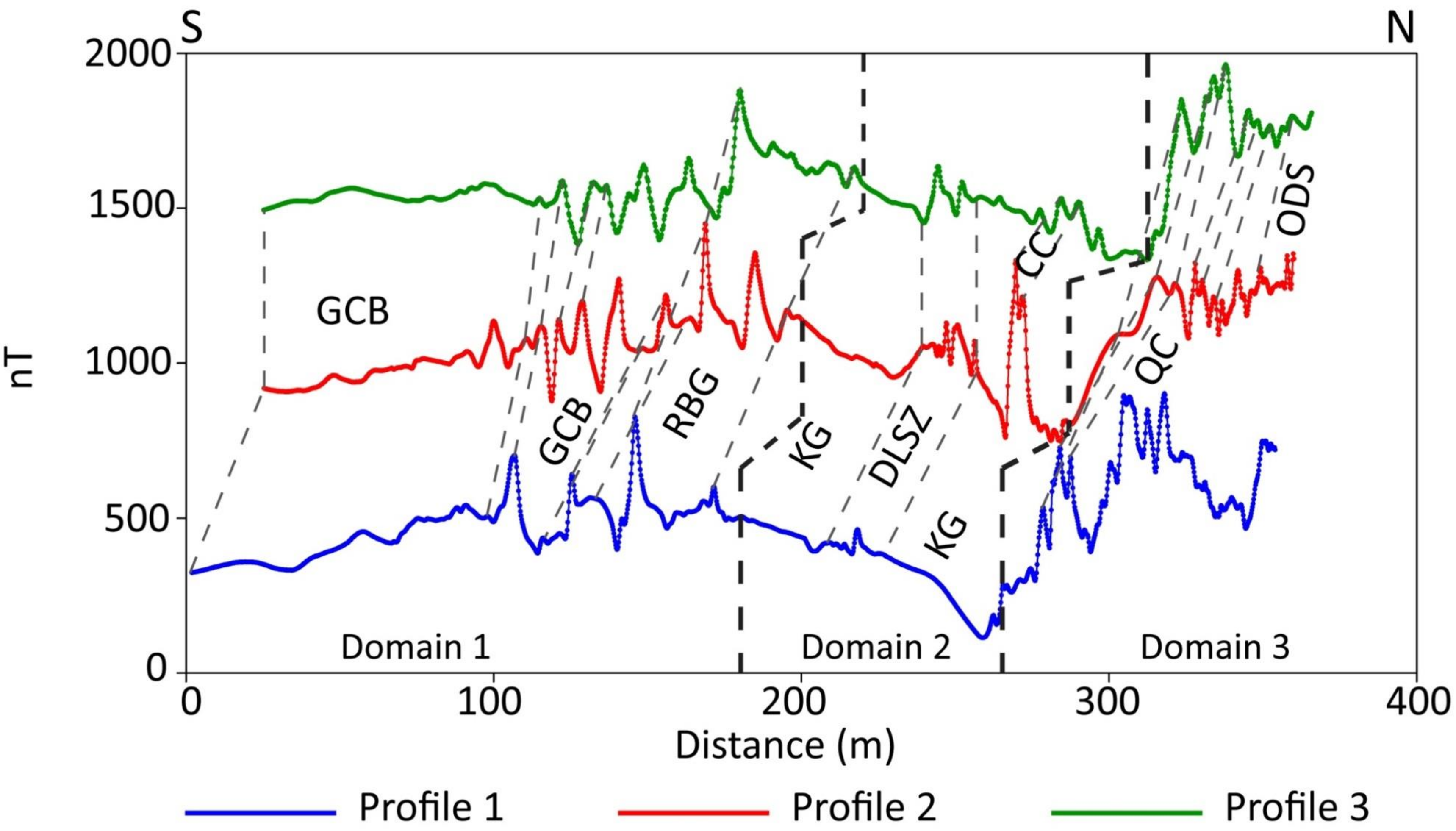

Figure 8.3: Fence plots of the three magnetic profiles. 500 nT was added to profile 1 (blue line), 1 100 nT was added to profile 2 (red line) and 1 600 nT was added to Profile 3 (green line). GCB is the Ghanzi-Chobe Belt, RBG is the Roibok Group, DLSZ is Deep-Level Southern Zone, KG is the Koanaka Group, CC is the Chihabadum Complex, QC is the Quangwadum Complex and ODS is the Okavango Dyke Swarm.

8.4.2. 2D magnetic forward models

The lack of seismic, borehole and outcrop data in the vicinity of the Namibia – Botswana has resulted in the models being unconstrained at both depth and near-surface. Therefore, a number of assumptions were taken in the development of the models.

The geological bodies and structures were assumed to be two dimensional (i.e. they have an infinite strike). The majority of the geological features are elongated and may be considered at a first approximation to be 2D. However, some of the smaller features such as folds within the Ghanzi-Chobe Belt, the Aha Hills Formation and southwestern part of the Chihabadum Complex, should not be considered two dimensional because of their limited strike.

Each of the magnetic models consists of ~65 bodies and two layers above a horizontal Moho at a depth of ~47 km. The upper of 10 km to 15 km consist of metasediments and metavolcanics representing the upper crust while the lower 15 km to 47 km represent the middle to lower crust of the cratons. The lithologies were assigned magnetic susceptibility values (Table 8.2) based on field measurements (Chapter 5) and compatible published magnetic susceptibility values (Poseidon Geophysics, 1995; Lehmann *et al*., submitted). The same magnetic susceptibilities were used for bodies that correlate across the profiles.

From the seismic data of Wright and Hall (1990), the Nosop Basin was modelled beneath the southern part of profiles 1 and 2 above the Ghanzi-Chobe Belt. The thicknesses of the Ghanzi Group and Kgwebe Formation were estimated from geological studies in the Mamuno and Ghanzi Ridge areas by Modie (1996, 2000) and Kampunzu *et al*. (1998, 2000). The Ghanzi-Chobe Belt was modelled with southwest verging folds based on the geological observations of Carney *et al*. (1994) and Hall (2013). The magnetic susceptibility of the Ghanzi-Chobe Belt lithologies was determined by field measurements (Figure 5.2) and borehole (HA 17D) measurements of Handjala (2011) from the Ghanzi Ridge.

Remnant magnetisation was not modelled because of the lack of palaeomagnetic data for northern Namibia and Botswana and Eberle *et al*. (2002) does not consider remnance in the northern part their regional magnetic profile of Namibia.

Table 8.2: Range and average magnetic susceptibility values from other studies and the magnetic susceptibility values used in the magnetic models. [#] is the magnetic susceptibility values of lithologies with similar geological affinity elsewhere. N/A is unexposed and undrilled geological domains.

Geological unit	Range of magnetic susceptibility (SI units)	Average magnetic susceptibility (SI units)	Reference	Magnetic susceptibility (SI units) used in the models
Kalahari Cover	-	0	Poseidon Geophysics, 1995; Bauer *et al*., 2003	0
Dyke	0.00425 - 0.0165	0.0126	Poseidon Geophysics, 1995; Walker *et al*., 2010	0.0163 - 0.0534
Karoo sediments		0.000125*	Poseidon Geophysics, 1995*	0.000653
Karoo volcanics	0.000628 - 0.0189	0.0126	Poseidon Geophysics, 1995	0.00504 - 0.0271
Nama Group	0 - 0.000666[#]	0.0100*	Poseidon Geophysics, 1995*; this study[#]	0.0101
Koanaka Group	0 - 0.000558[#]	0.000225[#]	This study[#]	0.000829
Aha Hills Formation	0 - 0.00570[#]	0.000236[#]	This study[#]	0.000567
Xaudum Group	0 - 0.00113[#]	0.000118[#]	This study[#]	0.000168
Roibok Group	0.000133 - 0.415[#]	0.0557[#]	This study[#]	0.00441 - 0.00253
Mamuno Formation	0 - 0.000646[#]	0.000183[#]	This study[#]	0.000181
D'Kar Formation	0.000014 - 0.00180	0.000232	Hendjala, 2011; Lehmann *et al*., submitted,	0.000251 - 0.00340
Ngwako Pan Formation	0.000006 - 0.000027	0.0000148	Hendjala, 2011; Lehmann *et al*., submitted,	0.000148
Kgwebe Formation	0.000057 - 0.0107	0.00361	This study	0.00505
Oorlogsende Porphyry Member	0.00041 - 0.0315[#]	0.00930[#]	This study[#]	0.0277
Deep-Level Southern Zone	0.0001 - 0.0478[#]	0.00169[#]	This study[#]	0.00630 - 0.0161
Chihabadum Complex	-	-	N/A	0.00944 - 0.0177
Kalahari Craton/Plate	0.100 – 2.80[#]	1.000[#]	Ferraccioli *et al*. 2001[#]	0.0317
Quangwadum/Grootfontein Complex	0.000352 – 0.0277[#]	0.0137[#]	Kadima *et al*. 2011[#]	0.0132 - 0.0500

8.5. Interpretation and discussion

8.5.1. The Ghanzi-Chobe Belt

The dominant structural features of the Ghanzi-Chobe Belt are isoclinal southeast verging folds (Carney *et al*., 1994; Schwartz *et al*., 1995; Hall, 2013). Within the Ghanzi Ridge area the major anticlinal and synclinal axial surfaces can be traced over distances of 10 km to 50 km. These traces are spaced 2 km to 8 km apart (Schwartz *et al*., 1995) with fold amplitudes of ~4 km to 6 km (Hall, 2013). Fold limbs have a dip angle of between 45° to 90° and the fold axial planes dip between 80° and 90° to the northwest (Hall, 2013). With the exemption of the area to the northeast of the town of Kuke, anticlines and synclines plunge at angles between 0° to 15° in a northeast and southwest direction, creating doubly plunging folds (Schwartz *et al*., 1995).

From the interpretation of aeromagnetic data, Hall (2013) suggests that the Ghanzi-Chobe Belt is dissected by several laterally extensive southwest-striking reverse faults with a sinistral displacement. A major structural element in the area is an ~15 km long northeast-striking dextral strike slip fault on the northwestern margin of the Ngunaekau Hills (Schwartz and Akanyang, 1994). Schwartz and Akanyang (1994) suggest that the fault is a regional feature associated with the dextral displacement of the Kaapvaal Craton with the respect to the Congo Craton.

The magnetic profiles modelled are located to the southwest of the Ghanzi Ridge (Figure 1.4) where the majority of the above observations were made based on outcrop geology. The magnetic response of the geological model of the Ghanzi-Chobe Belt fits the observed aeromagnetic data (Figure 8.4). The Ghanzi-Chobe Belt can be traced for a distance of ~145 km from northern Botswana into Namibia. In the south of profiles 1 and 2, within the Nosop Basin, the metasediments of the Ghanzi Group are modelled to a depth of ~10 km and lie directly on Proterozoic basement as proposed by Reeves (1978), Hutchins and Reeves (1980) and Wright and Hall (1990). The magnetic models suggest that the Kgwebe Formation increases in thickness to the north, which is the same as observed by Schwartz *et al*. (1995) in the Ghanzi Ridge. The Bouguer gravity data shows an increase in gravity signal from ~-140 mGal to -100 mGal north of -21.60°S. Therefore, a thick package of high-density, magnetic rocks associated with the metabasalts of the Kgwebe Formation are likely to be absent in the southern parts of the profiles (Figure 8.4).

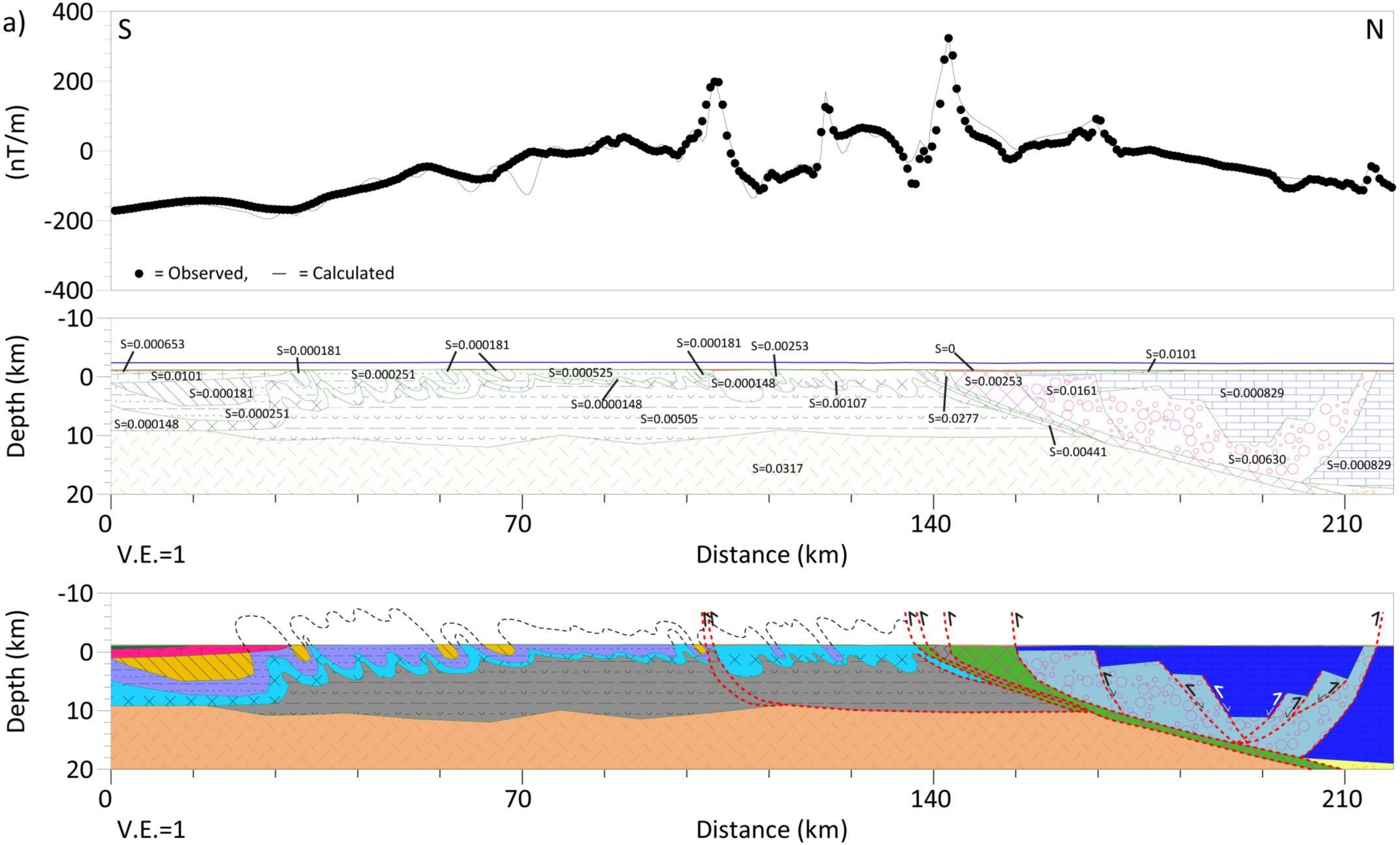
a)
S
N
400
200
0
-200
-400
(nT/m)
● = Observed, — = Calculated
-10
0
10
20
Depth (km)
S=0.000653
S=0.0101
S=0.000181
S=0.000251
S=0.000148
S=0.000525
S=0.0000148
S=0.00505
S=0.00253
S=0.00107
S=0
S=0.0277
S=0.0161
S=0.00441
S=0.000829
S=0.00630
S=0.0317
0
70
140
210
V.E.=1
Distance (km)

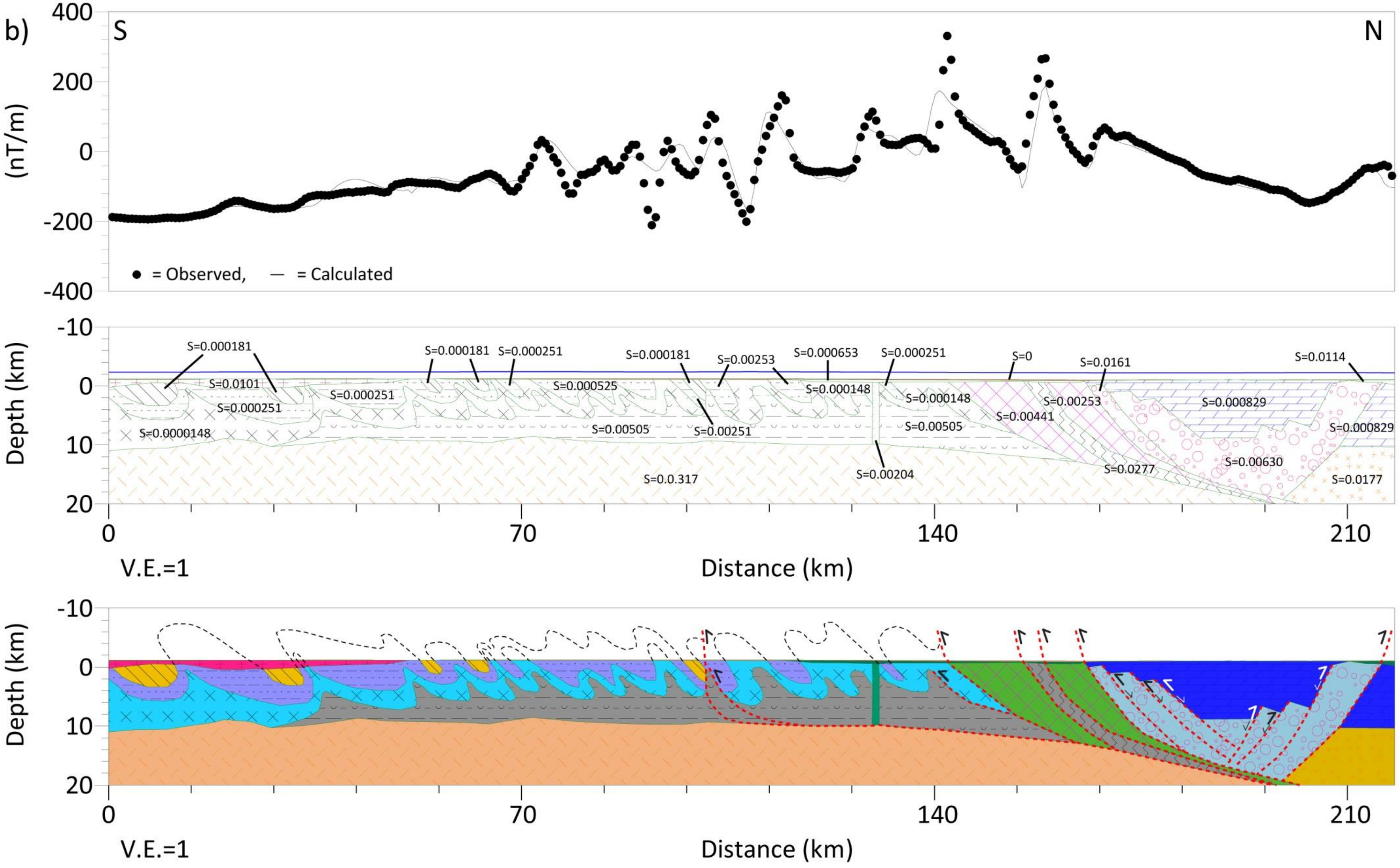
b)
S
N
(nT/m)
400
200
0
-200
-400
● = Observed, — = Calculated
Depth (km)
-10
0
10
20
S=0.000181
S=0.0101
S=0.000251
S=0.000251
S=0.0000148
S=0.000181
S=0.000251
S=0.000525
S=0.000181
S=0.00253
S=0.000653
S=0.000251
S=0.000148
S=0.000148
S=0.00505
S=0.00251
S=0.00505
S=0.0.317
S=0.00204
S=0
S=0.0161
S=0.00441
S=0.00253
S=0.000829
S=0.0114
S=0.000829
S=0.00630
S=0.0277
S=0.0177
0
70
140
210
V.E.=1
Distance (km)
Depth (km)
-10
0
10
20
0
70
140
210
V.E.=1
Distance (km)

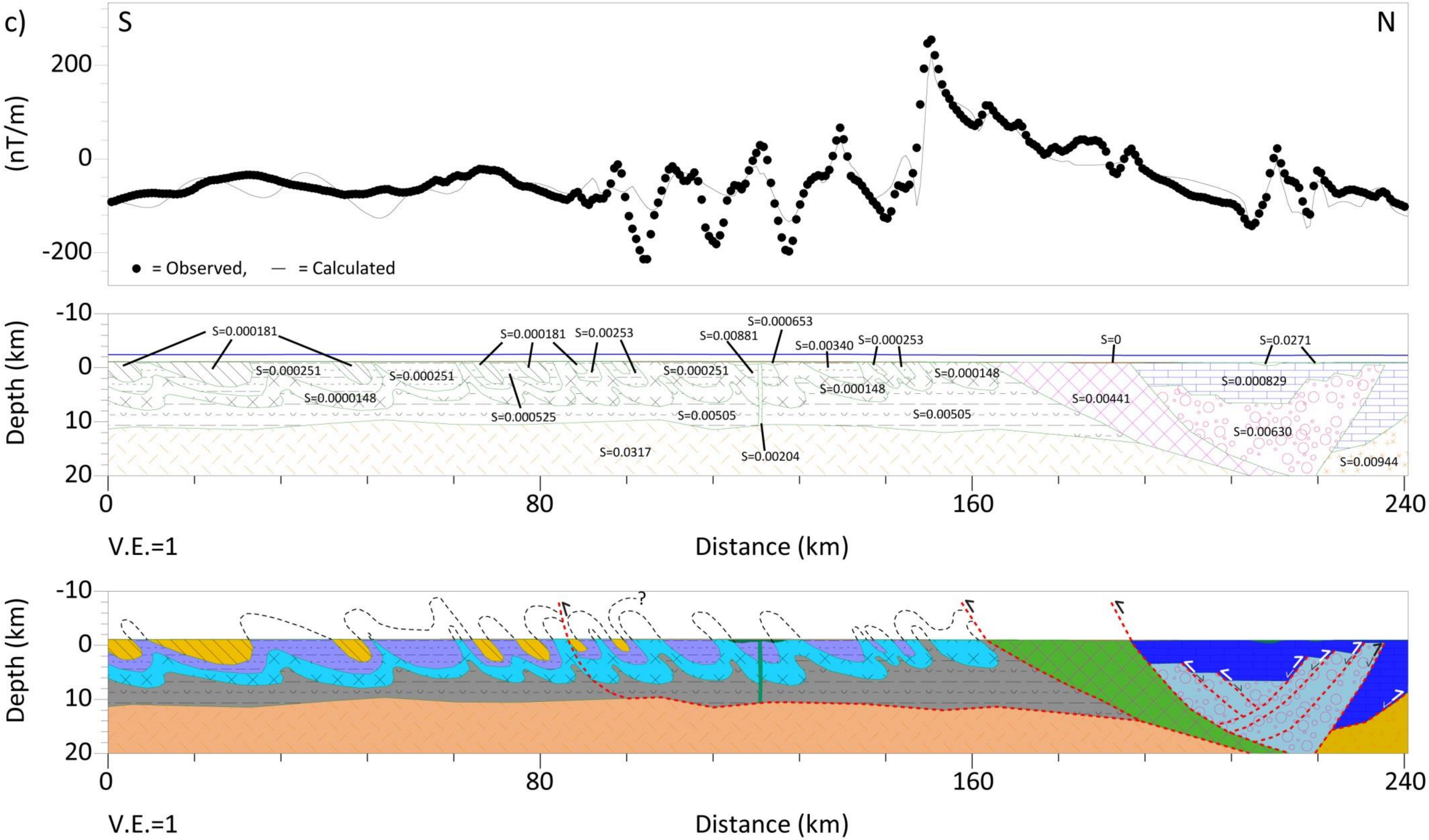
c)
S
N
200
0
-200
(nT/m)
● = Observed, — = Calculated
-10
0
10
20
Depth (km)
S=0.000181
S=0.000251
S=0.0000148
S=0.000181
S=0.00253
S=0.000251
S=0.000525
S=0.00881
S=0.000653
S=0.000251
S=0.00340
S=0.000253
S=0.000148
S=0.000148
S=0.00505
S=0.00505
S=0.0317
S=0.00204
S=0
S=0.0271
S=0.00441
S=0.000829
S=0.00630
S=0.00944
0
80
160
240
V.E.=1
Distance (km)
-10
0
10
20
Depth (km)
?
0
80
160
240
V.E.=1
Distance (km)

d)

Figure 8.4 (previous pages)**:** 2D magnetic and geological models of the Ghanzi-Chobe Belt with the interpretation of first order thrust faults. a) is profile 1, b) is profile 2, c) is profile 3 and d) is the legend for the profiles. The upper panel is the aeromagnetic response of the profile with the black dots representing the observed magnetic response and the solid black line the calculated magnetic response from the geological model. The middle panel is the 2D magnetic model with magnetic susceptibilities used in the model listed in Table 8.2. The blue line represents the flight height. The lower panel is a simplified geological interpretation of the 2D magnetic model. The locations of the profiles are shown in Figure 8.1.

The intensity of folding and thrusting increases to the north as noted by Key and Ayres (2000). The folds of the Ghanzi-Chobe Belt were modelled with fold amplitudes of ~4 km to 8 km with wavelengths of ~20 km in the south to 5 km in the north. Fold axial planes dip ~65° northwards in the south to near-vertical in the north with fold limbs dipping at ~35° to near-vertical (Figure 8.4). In the northern part of the Ghanzi-Chobe Belt a number of thick-skinned (décollement surface cuts through the basement) listric thrust faults are interpreted. These faults were interpreted on the basis that a thickened package of metasediments is needed to produce a magnetic anomaly and/or a disconformity between two formations e.g. the D'Kar Formation being in contact with the Kgwebe Formation and/or when a continuous folding pattern could no longer be determined (Figure 8.4). These thrusts dip northwards and merge into a common décollement on the northern margin of the Kalahari Craton. As the folds are displaced and cut by the thrusts it suggests that faulting occurred during prolonged compression.

The metasedimentary units of the Ghanzi Group within the vicinity of the faults have higher magnetic susceptibility values compared to the units to the south. This suggests that magnetic minerals such as ilmenite, magnetite and pyrrhotite are present. These minerals and other Cu-bearing minerals (e.g. chalcocite and bornite) have been identified by Hall (2013) within and at the base of the D'Kar Formation. Hall (2013) suggests that these minerals have moved in a northeast to southwest direction in hydrothermal fluids along northwest-southeast-trending normal faults, which have not been located to date.

Aeromagnetic interpretation (Chapter 6) and modelling suggests that the Mamuno Formation is absent to the north of the southernmost fault (Figure 8.4). This can be caused by either regional uplift and erosion associated with faulting or the formation was not deposited as far north, as Master (2010) interprets the palaeo-environment of the Mamuno Formation as foreshore. The Ghanzi-Chobe Belt terminates against the Roibok Group, which is suggested to be of oceanic crust affinity (Lüdkte *et al*., 1986; in Singletary *et al*., 2003). The Roibok Group has been aeromagnetically interpreted (Chapter 6) and modelled to be tectonically interleaved and thrust stacked with the Oorlogsende Porphyry Member (Figure 8.4). Similarly the Matchless Member has been noted to have been exposed along thrusts and is found in a variety of country lithologies, including pre-Damara basement (Barnes, 1982). The thrust faulting observed in both the Ghanzi-Chobe Belt and Roibok Group suggests a southwards movement onto the Kalahari Craton, which is observed for the southern parts of the Damara Belt (e.g. Barnes, 1982; Miller, 1983a, 2008; Kukla, 1992; Gray *et al*., 2008).

The continued subduction of oceanic crust led to the collision of the Kalahari and Congo Cratons. The Roibok Group and Ghanzi-Chobe Belt are compressed against the Deep-Level Southern Zone (Figure 8.4). The Deep-Level Southern Zone is suggested to be of Kalahari Craton affinity emplaced within the pro-wedge (Figure 8.4). According to Butler *et al*. (2011) exhumation to the pro-wedge occurs during collision where the retro-continent crust (Congo Craton) is initially as strong as the pro-continental crust (Kalahari Craton). The Deep-Level Southern Zone was detached from the subducting Kalahari Plate and the Congo Craton acts as a backstop emplacing the Deep-Level Southern Zone within the pro-wedge (Figure 8.5). The exhumation of the Deep-Level Southern Zone forces uplift, internal extension, and normal faulting (Jamieson and Beaumont, 2013). The final geometry of a pro-wedge is associated with a structural dome at its rear containing (ultra)-high-pressure pro-continent crust, flanked toward its toe by a molasse of marginal pro-continent sediment, oceanic suture zone material (Roibok Group), and retro-continent margin crust (Butler *et al*., 2011). This is similarly observed in the Tso Morari Complex, northwestern Himalaya (Beaumont *et al*., 2009), where subduction of the Indian plate beneath Asia led to rapid exhumation and metamorphism between 55 Ma to 45 Ma (e.g. de Sigoyer *et al*., 2004; Epard and Steck, 2008). Models predict that the exhuming material forms nappe stack and structural domes as it penetrates and destabilises the orogenic wedge, driving thrusting and internal extension in the overlying crust. These models are comparable with the geology, petrology, and structure of the Tso Morari Complex (Beaumont *et al*., 2009).

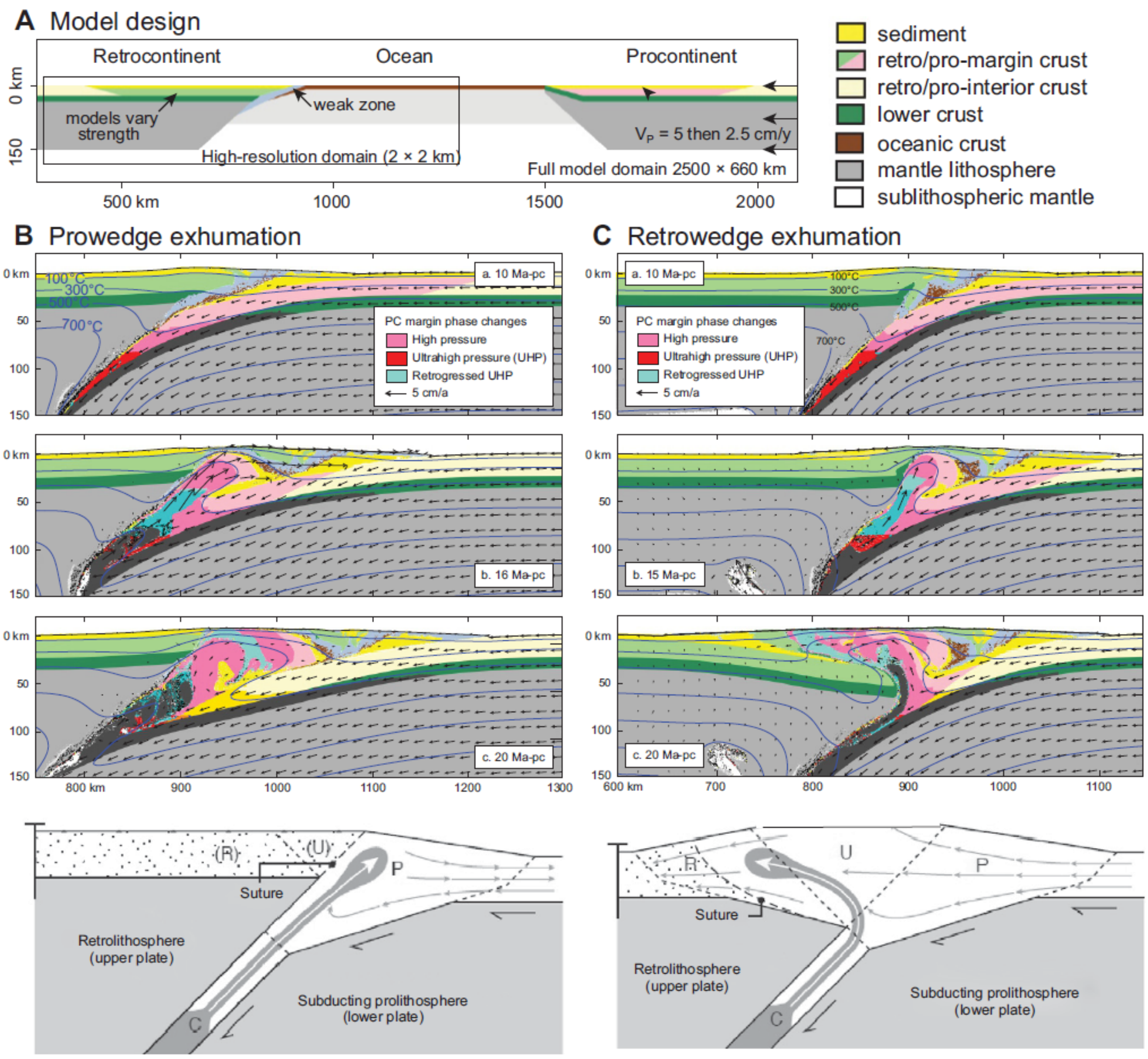

Figure 8.5: Model of exhumation of subducted material (after Butler *et al*., 2011; Jamison and Beaumont, 2013). A) 2D upper mantle scale model. For the details of the model see Butler *et al*. (2011). B) Pro-wedge exhumation model. The bottom panel shows the interpretation, typical style of exhumation from the subducting slab during early stages of collision. C is subducting slab, P is pro-wedge, U is uplifted plug, and R is retro-wedge (U, R inactive). C) Retro-wedge exhumation, which leads to the emplacement of (ultra)-high-pressure lithologies into the upper crust. The bottom panel is the same as B) with all compartments active.

8.5.2. Northeast Namibia and northwest Botswana

One of the most prominent magnetic features in the Namibian aeromagnetic data set is the strong magnetically negative zone, which extends across Namibia in an east-northeast direction from Cape Cross to the Gam area near the Botswana border. Within this zone are the majority of Mesozoic anorogenic intrusions such as Cape Cross, Messum, Brandberg and Erongo intrusions (Eberle *et al*., 1996, 2002). This zone is bounded to the north by a series of high magnetic amplitudes (~120 nT to 330 nT) associated with the Northern Zone (including the Goas Complex in Figure 6.1). Eberle *et al*. (1996) suggested that the magnetically negative zone could possibly represent a failed or former north-dipping subduction zone. Later magnetic modelling by Eberle *et al*. (2002) postulates that this zone is rift-related based on a system of ridges and half-grabens as proposed by Porada *et al*. (1983). An alternative model assumes thinning of the magnetic crust beneath the Northern Zone that will produce increased heat flow as occurring in the rift zone (Eberle *et al*., 2002). Both of these models place the top of the magnetic body at a depth of ~5 km to 10 km (Figure 6a and b in Eberle *et al*., 2002).

The Kalahari Plate and associated oceanic crust was modelled to be northward subducted beneath the Congo Craton following the geological observations of Barnes and Sawyer (1980) and Becker *et al*. (2006). From observation of early compressional stresses within metasediments of the Southern Zone, Kukla (1992) and Frimmel *et al*. (2011) suggest that they are characteristic of low-angle subduction (angle is not provided). Magnetic modelling suggests that this low-convergence angel can be as low as ~10° (Figure 8.6).

This study suggests that the Chihabadum Complex is of Kalahari Craton affinity emplaced within the retro-wedge (Figure 8.5). The Chihabadum Complex was attached to the subducting slab (Kalahari Plate) and was carried deep into the subduction zone where it was affected by (ultra)-high-pressure (~50 kbar, 800°C; Butler *et al*., 2011) metamorphism. Subsequent weakening and detachment of this continental material led to buoyancy-driven exhumation. According to Butler *et al*. (2011), if the exhuming plume disrupts and crosses the suture it will be hosted by retro-crust. This is observed beneath profile 2 and 3 (Figure 8.4 b and c) where the Chihabadum Complex is hosted in metasediments that were deposited on the southern margin of the Congo Craton. The rapid exhumation of the Chihabadum Complex from the subducting slab is accompanied by extension within the overlying wedge (Butler *et al*., 2013). Emplacement of (ultra)-high-pressure material is similarly observed in the Internal Crystalline Massif of the western Alps (Jamieson and Beaumont, 2013). Retro-wedge exhumation has also been interpreted to explain the presence of (ultra)-high-pressure lithologies within the upper Laurentian crust in east Greenland (Butler *et al*., 2011). However, as the Chihabadum Complex is an unexposed, undrilled domain this is all speculative. There have been no observations of high-grade metamorphic lithologies within the Damara Belt or northwest Botswana unlike in the Lufilian Arc where eclogites have been observed (John *et al*., 2003, 2004).

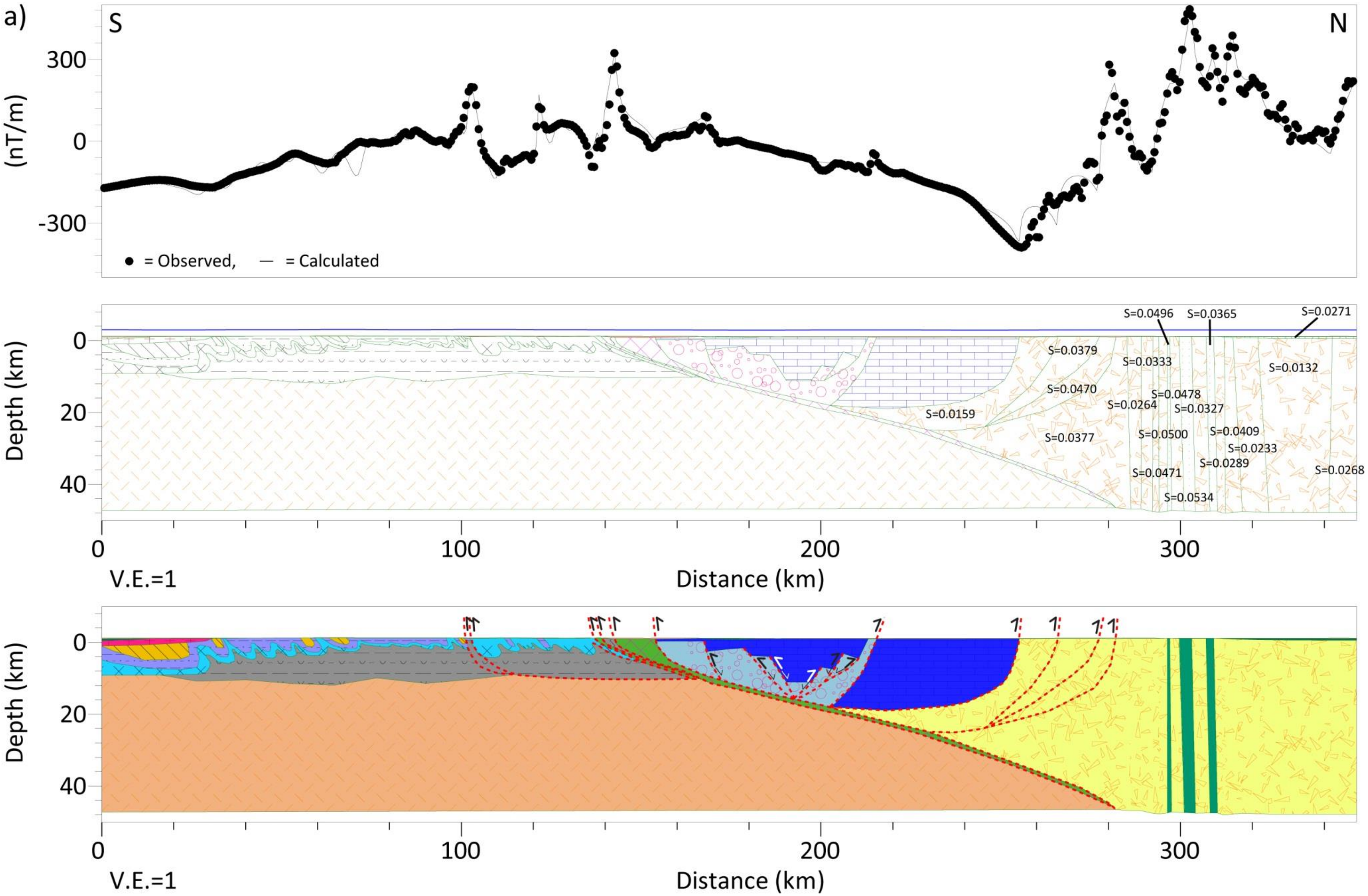
a)
S
N
300
0
-300
(nT/m)
● = Observed, — = Calculated
Depth (km)
0
20
40
S=0.0496
S=0.0365
S=0.0271
S=0.0379
S=0.0333
S=0.0132
S=0.0470
S=0.0478
S=0.0264
S=0.0327
S=0.0159
S=0.0377
S=0.0500
S=0.0409
S=0.0233
S=0.0289
S=0.0471
S=0.0268
S=0.0534
0
100
200
300
V.E.=1
Distance (km)
Depth (km)
0
20
40
0
100
200
300
V.E.=1
Distance (km)

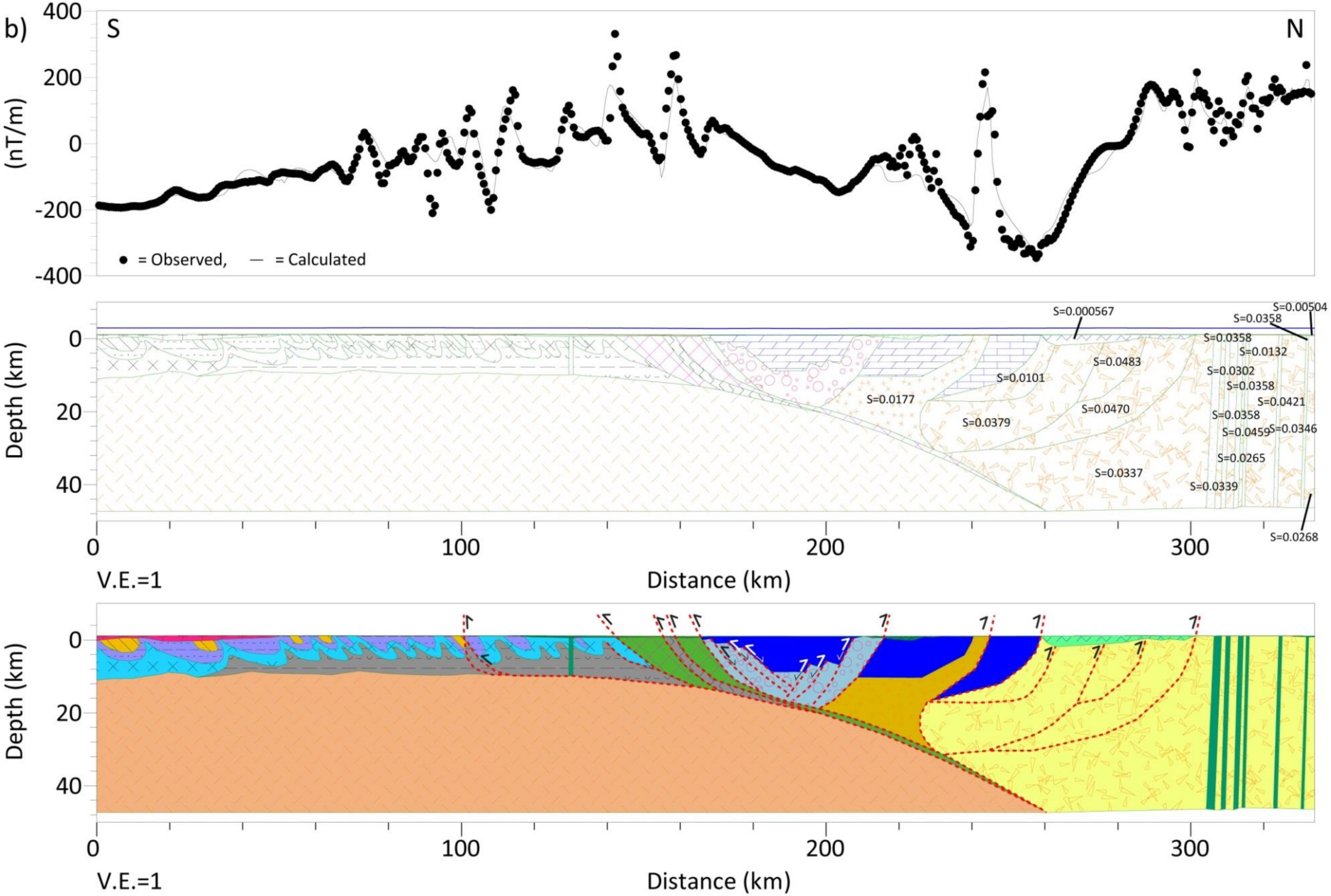
b)
S
N
400
200
0
-200
-400
(nT/m)
● = Observed, — = Calculated
S=0.000567
S=0.00504
S=0.0358
S=0.0358
S=0.0132
S=0.0483
S=0.0302
S=0.0358
S=0.0101
S=0.0421
S=0.0177
S=0.0470
S=0.0358
S=0.0379
S=0.0459
S=0.0346
S=0.0265
S=0.0337
S=0.0339
S=0.0268
Depth (km)
0
20
40
100
200
300
V.E.=1
Distance (km)
Depth (km)
0
20
40
100
200
300
V.E.=1
Distance (km)

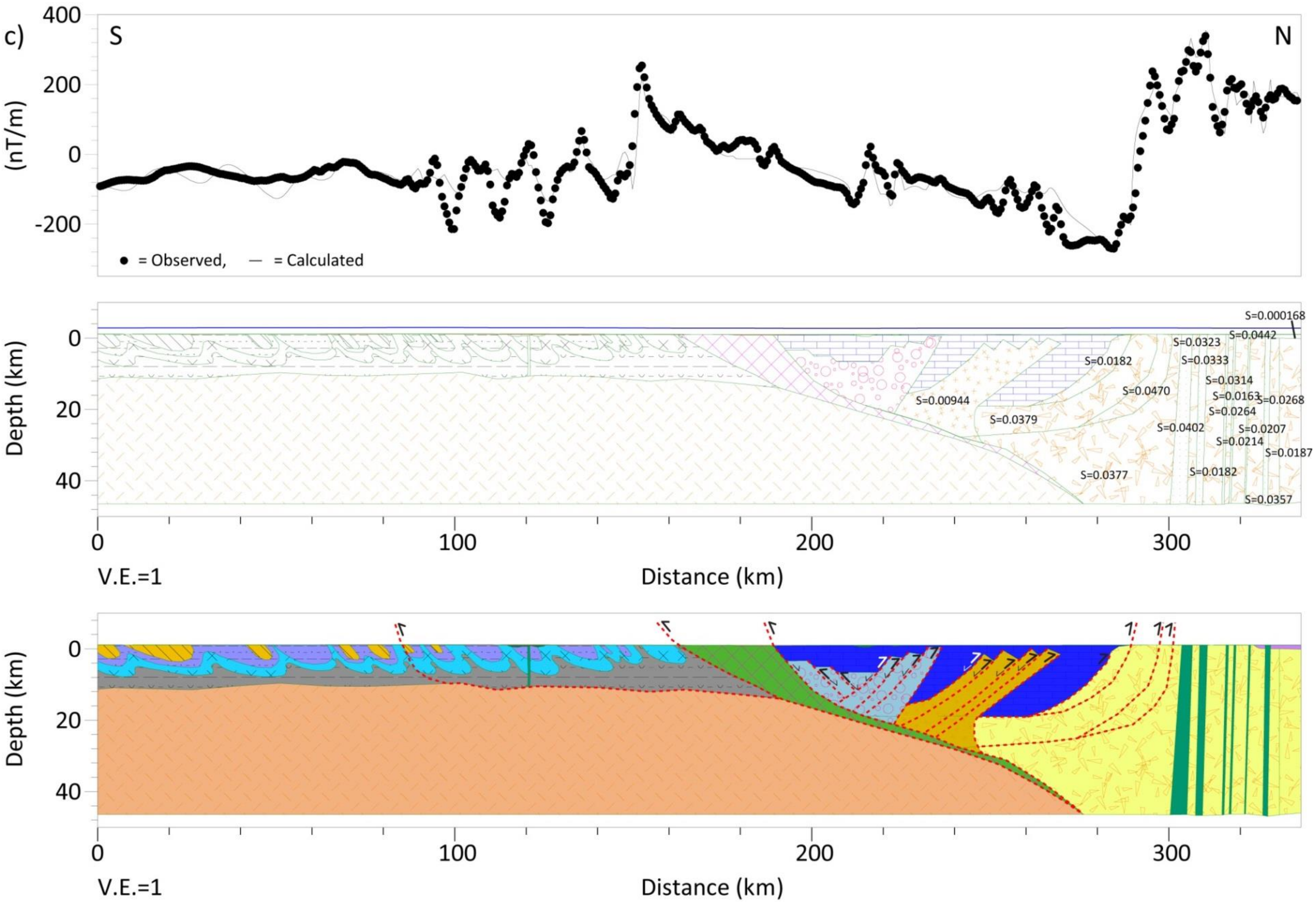

c)
S
N
400
200
0
-200
(nT/m)
● = Observed, — = Calculated
S=0.000168
S=0.0442
S=0.0323
S=0.0333
S=0.0182
S=0.0314
S=0.0163
S=0.0268
S=0.0470
S=0.00944
S=0.0264
S=0.0379
S=0.0402
S=0.0207
S=0.0214
S=0.0187
S=0.0377
S=0.0182
S=0.0357
Depth (km)
0
20
40
0
100
200
300
V.E.=1
Distance (km)
Depth (km)
0
20
40
0
100
200
300
V.E.=1
Distance (km)

d)

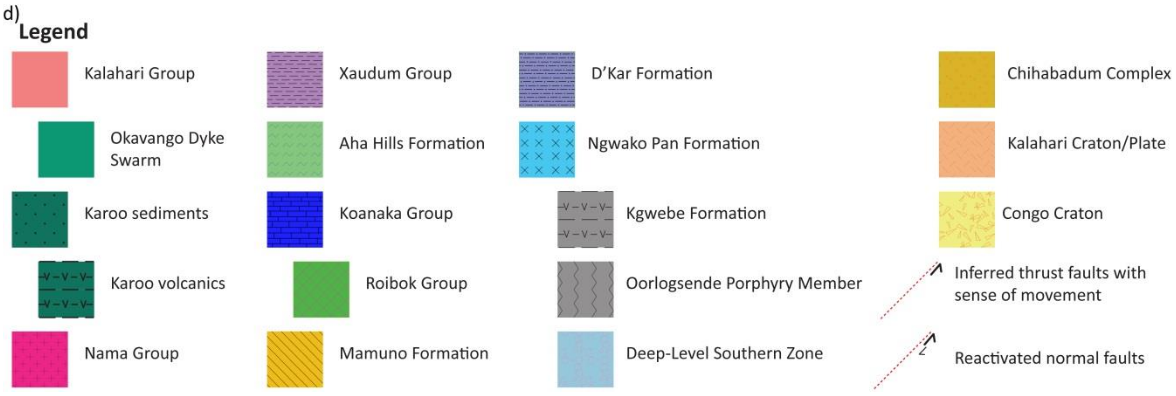

Figure 8.6 (previous pages)**:** 2D magnetic and geological models of the proposed northward subduction of the Kalahari Plate beneath the Congo Craton with the interpretation of first order thrust faults. a) is profile 1, b) is profile 2, c) is profile 3 and d) is the legend for the profiles. The upper panel is the aeromagnetic response of the profile with the black dots representing the observed magnetic response and the solid black line the calculated magnetic response from the geological model. The middle panel is the 2D magnetic model with magnetic susceptibilities used in the model listed in Table 8.2. The lower panel is a simplified geological interpretation of the 2D magnetic model. The locations of the profiles are shown in Figure 8.1.

The amplitude of the regional negative magnetic feature increases from ~-385 nT (beneath profile 1) to -280 nT (beneath profile 3) (Figure 8.6). To account for this regional negative magnetic feature the Koanaka Group was modelled to a depth of ~12 km to 20 km, shallowing to the northeast (Figure 8.6).

Examining the Bouguer gravity data in relation to the magnetic profiles (Figure 8.7), a similar Bouguer gravity signal is observed to other known subduction zones (e.g. Romanyuk *et al*., 1998; Blakely *et al*., 2005; Henrys *et al*., 2006). The increase in the Bouguer gravity signal to the north from ~-140 mGal to -120 mGal is associated with the Kgwebe Formation. At the deformation front the gravity signal decreases steadily to ~-125 mGal (Figure 8.7). The cause of this gravity low has varied from downwarping of oceanic crust that has allowed for sediment infill in the forearc basin (Henrys *et al*., 2006) to a serpentinite mantle wedge (Blakely *et al*., 2005). In a comparative study of Vancouver (southwest Canada) and Oregon (northwest United States of America), Romanyuk *et al*. (1998) attributes this gravity low to the bathymetry, depth to the top of the subducting plate and metamorphic grade and thickness of the sediments within the accretionary wedge. Blakely *et al*. (2005) suggests that the gravity low is caused by a 34 km thick accretionary wedge and a serpentinite mantle wedge at a depth of ~40 km. The gravity signal increases to ~-110 mGal in the north (Figure 8.7) associated with a thinning of the metasediments and a basement rise. This study suggests that the gravity low (Figure 8.7) is caused by a combination of metasediments (~12 km to 20 km thick) and a serpentinite mantle wedge. The serpentinite mantle wedge was not modelled in the magnetic forward models because it would be situated below the Curie geothermal gradient.

Therefore, this prominent negative magnetic feature fits either a rift model (Eberle *et al.*, 2002) or a palaeo-subduction zone (this study). To confirm the geological-related cause of this negative magnetic zone, north-south reflection seismic surveys need be carried out in the vicinity of the Namibia – Botswana border to detect the top of the Kalahari Craton and the top of the Moho.

The northern part of profile 1 has magnetic amplitudes of > 400 nT. These higher amplitudes (compared to profile 2 and 3) are associated with Karoo basalts overlying the Omatako Ring Structure (Corner, 2000, 2008). The source of the Omatako Ring Structure remains unknown but Corner (2000, 2008) suggests that it is a deep-seated pluton that is related to hydrothermal fluids and intrusions. Ring structures are associated with mineralising fluids, as extensively studied in Austria (e.g. O' Driscoll and Campbell, 1997). These mineralisation fluids have remagnetised the Grootfontein Complex, which has been intersected in water boreholes in the south of the Omatako Ring Structure (Corner, 2008). This has led to the Grootfontein Complex being separated into a number of sub-vertical pipe-like bodies with varying magnetic susceptibilities (Figure 8.6).

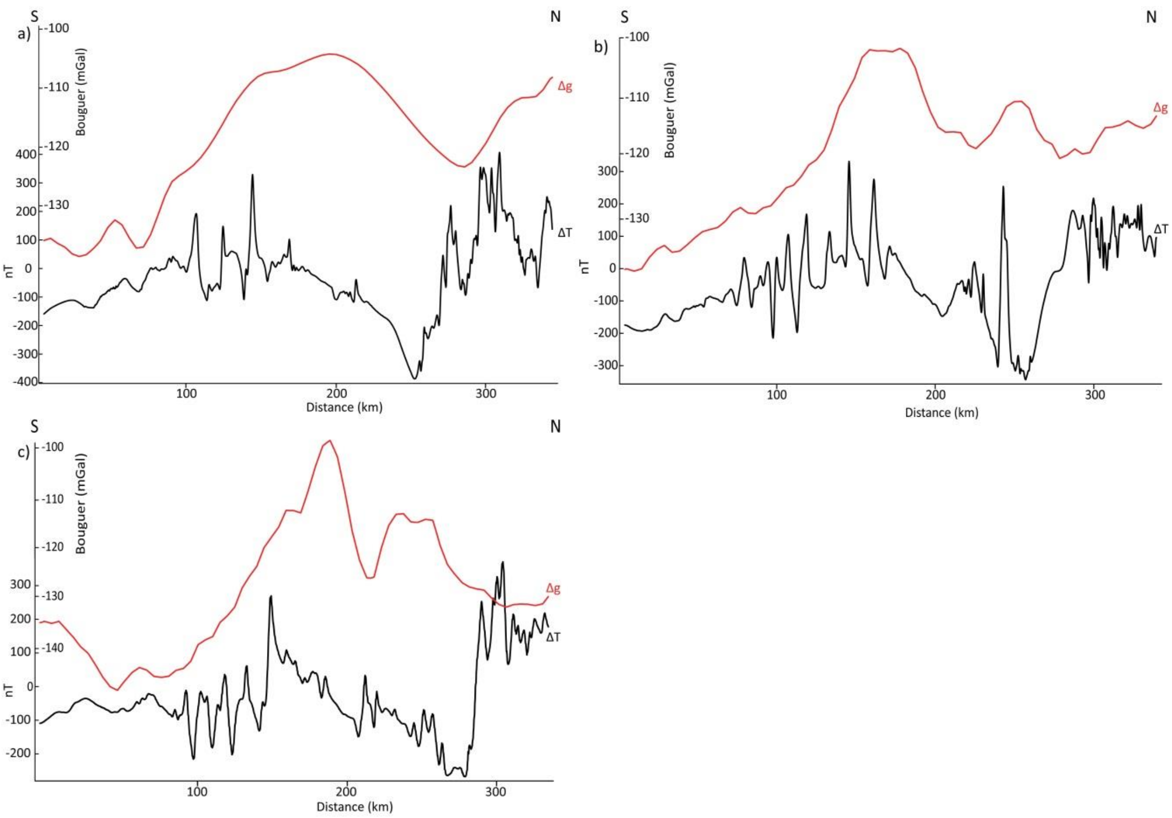

Figure 8.7: Comparison of TMI anomalies (ΔT) and Bouguer-corrected anomalies (Δg) along a) profile 1, b) profile 2, and c) profile 3.

8.6. Conclusion

This is the first time that the proposed palaeo-subduction zone between the Kalahari and Congo Cratons has been magnetically modelled. The models suggest the northward subduction of the Kalahari Plate beneath the Congo Craton as originally proposed by Barnes and Sawyer (1980). The low-angle of subduction of the Kalahari Plate, as interpreted from structural data within the Southern Zone of the Damara Belt, has been constrained to ~10° by the magnetic models.

Magnetic modelling and observation of Bouguer gravity data suggests that the regional, east-west trending negative magnetic anomaly in Namibia can be associated with a thick (12 km to 20 km) package of relatively non-magnetic sediments. These sediments were structurally emplaced during the subduction of the Kalahari Plate and adjacent oceanic crust beneath the Congo Craton.

The Deep-Level Southern Zone formed a buttress to the lithologies of the Ghanzi-Chobe Belt and Roibok Group resulting in greater deformation in the north. The folding pattern of the Ghanzi-Chobe Belt correlates with structural measurements observed to the northeast of the profiles in the Ghanzi Ridge area (Schwartz *et al*., 1995; Hall, 2013). The southeast verging folds are later cut by thrust-faults associated with increase compression during the subduction event.

8.7. Summary

The proposed northward subduction of the Khomas Ocean and adjacent Kalahari Plate beneath the Congo Craton and folding pattern of the Ghanzi-Chobe Belt has been magnetically 2D forward modelled and discussed in this chapter. The models were constrained by magnetic susceptibility measurements (collected and published), by estimating the depth of the Curie point from heat flow measurements of Jones (1998), and by constraining the near-surface extent of the geological bodies by overlying the profiles on the sub-Kalahari geological map. The Deep-Level Southern Zone (Corner, 2008) is suggested to be of Kalahari Craton affinity, which forms a buttress to the Ghanzi-Chobe Belt leading to an increase in deformation in the northern part of the belt.

The lack of high-grade metamorphic lithologies within Namibia and northwest Botswana has provided evidence for challenging the theory of northward subduction. This study suggests that the Chihabadum Complex may be the locus of these high-grade metamorphic lithologies. The complex is suggested to be of Kalahari Craton affinity that was emplaced into the retro-wedge (Congo Craton). Emplacement of high-grade metamorphic lithologies within the retro-wedge is similarly observed in the Internal Crystalline Massif in the western Alps (Butler *et al*., 2013).

Chapter 9

Discussion

9.1. Introduction

New cross-border correlations between the Meso- to Neoproterozoic lithologies of the Damara Belt and northwest Botswana based on the interpretation of potential field and MT data sets complimented with geological observations and published literature are presented in this study. The new proposed correlations have led to the development of a new sub-Kalahari geological map between the two countries, where the irregularities in the previous cross-border map of Haddon (2001) were resolved. The results of this study are summarised in conjunction with other studies, to redefine the tectonostratigraphic zones of the Damara Belt and northwest Botswana. The redefined tectonostratigraphic zones have led to an adjustment in the southern and northern margins of the Congo and Kalahari Cratons. The regional conductive anomaly of de Beer *et al*. (1975) has been redefined and interpreted to not cross-cut any of the tectonostratigraphic zones. The cause of this conductive anomaly has yet to be resolved and can only be speculated in this study.

9.2. Inferred correlations of the tectonostratigraphic zones of the Damara Belt and northwest Botswana

There are limited cross-border geological studies of the Damara Belt and northwest Botswana. The documented studies are focused on either geological (Carney *et al*., 1994; Haddon, 2001) or geophysical (Kgotlhang *et al*., submitted) interpretations and are seldom a combination of the two. Acquisition of new, high resolution aeromagnetic (50 m grid size), MT (SAMTEX project) and geochronological data and new interpretations of existing data reveals potential misinterpretations in these previous cross-border correlation studies.

These previous studies characterise the Damara Belt bending and narrowing suddenly before entering Botswana (Figure 2.30 and 2.31) (e.g. Carney *et al*., 1994; Singletary *et al*., 2003; Kgotlhang *et al*., submitted). The proposed causes of this interpretation include a promontory existing on the southern edge of the Congo Craton (Eberle *et al*., 1996; Singletary *et al*., 2003) or a sediment-filled meteorite impact crater (Kgotlhang *et al*., submitted). The impact crater spatially corresponds with the Omatako Ring Structure of Corner (2008) (Figure 6.1). The proposition of sudden narrowing of the Damara Belt would require pinching out of some of the tectonostratigraphic zones before entering Botswana. Carney *et al*. (1994) suggests pinching of the Central, Northern and Southern Margin Zones while Kgotlhang *et al*. (submitted) suggests only the Central Zone pinches out with mergence of the Northern and Southern Zones in the east. Neither of these authors discussed the nature of the Northern Margin Zone in this event. Subsequently, in contrast, Corner (2008) and Miller (2008) interpreted that the Okahandja Lineament, southern Central and Northern Zones pinch out before the Botswana border.

Studies within Botswana have largely focused on the potential relationship between the Ghanzi-Chobe Belt and Namibian correlatives. Regional interpretations based on geochronology, geophysical trends, sediment-hosted mineralisation and lithological similarities have correlated the lithologies of the Ghanzi-Chobe Belt with discrete individual basins in Namibia (Sinclair, Klein Aub, Witvlei and Dordabis Basins, Figure 6.30) (e.g. Borg and Maiden, 1987; Borg, 1988; Modie, 1996; Maiden and Borg, 2011). Another proposed correlation for the Ghanzi-Chobe Belt is with the Southern Foreland. This is based on similar southeast verging folds observed in both domains (Carney *et al*., 1994) and on the sub-Kalahari geological map of Haddon (2001).

The Kgwebe Formation is correlated with the Oorlogsende Porphyry Member and Langberg Formation (Figure 6.30 and 6.34) based on similar grades of metamorphism (greenschist), age dates of ~1.1 Ga, magmatic composition and aeromagnetic signal (Table 6.1). The Ngwako Pan and Kuke Formations are correlated with the Doornpoort Formation and the D'Kar and Mamuno Formations are correlated with the Klein Aub Formation (Figure 6.30 and 6.34). These correlations are based on lithological, mineralisation and aeromagnetic similarities (discussed in Section 6.4). Based on these correlations and the interpretation of low-pass, directionally filtered aeromagnetic data, the Ghanzi-Chobe Belt and its correlatives in Namibia appear to form a continuous belt stretching from the Rehoboth Subprovince, through Botswana to the Caprivi (Figure 9.1). The northern margin is defined by the sudden change in the aeromagnetic signal to a smooth, low amplitude signal and by the resistivity contrast beneath the MT profiles (discussed in Section 7.5.3). The southern margin is defined by the last visible fold in the high-pass aeromagnetic data i.e. to the south of the Aranos (Namibia) and Nosop (Botswana) Basins. The northern margin has been inferred by Miensopust *et al*. (2011) to lie beneath stations ZIM124/ ZIM125 on the ZIM profile (Figure 7.26).

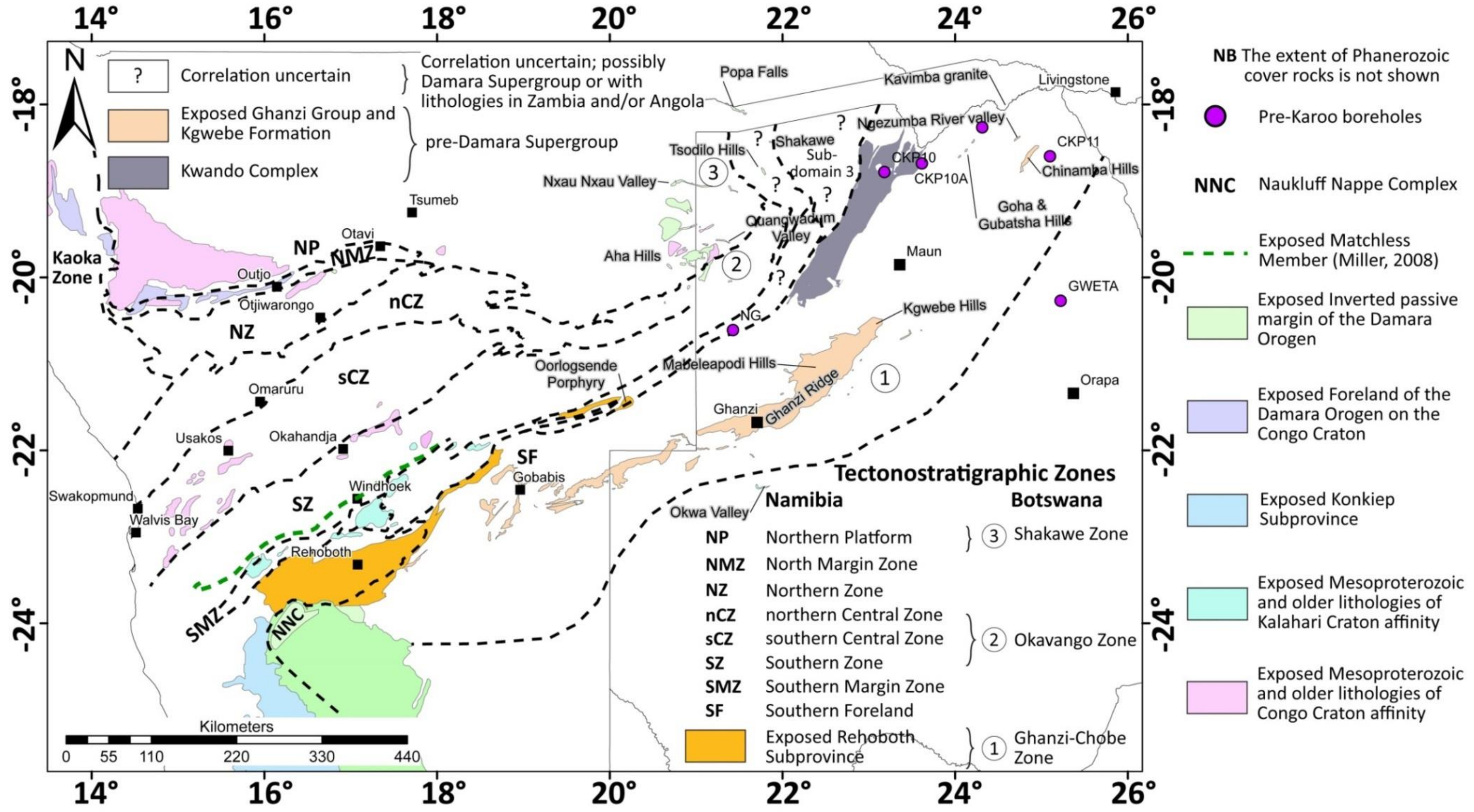

Figure 9.1: Proposed correlation between the tectonostratigraphic zones of Namibia (west) and Botswana (east) based on potential field, magnetotelluric, geological, geochronology and structural information. Geological exposures are after Miller (1983a, 2008), Hegenberger and Burger (1985), Carney *et al*. (1994), Haddon (2001). The numbers in circles correspond to the tectonostratigraphic of northwest Botswana.

Unconformably overlying the Ghanzi Group is the Okwa Group that was deposited in the Nama Foreland Basin, which formed on the Kalahari Craton during the closure of the Khomas Ocean (Ramokate *et al*., 2000). The depositional age of the Okwa Group is bracketed between 580 Ma and 530 Ma from a U-Pb detrital zircon ages and U-Pb zircon age for a cross-cutting intrusion (Ramokate *et al*., 2000). In Namibia, the depositional age of the Nama Group is bracketed between 550 Ma and 535 Ma (Grotzinger *et al*., 1995; Grotzinger and Miller, 2008). These similar depositional ages and lithologies allowed Ramokate *et al*. (2000) and Kampunzu *et al*. (2000) to correlate the Okwa Group with the Nama Group. The correlation of the Kgwebe Formation and Ghanzi Group with lithologies of the Sinclair Supergroup and the correlation between the Okwa and Nama Groups produce a hiatus of ~200 Ma within the Ghanzi-Chobe Belt (i.e. the correlatives of the Nosib and Witvlei Groups are missing within Botswana).

To the north of the Ghanzi-Chobe Belt is the Mesoproterozoic granitic massif Kwando Complex. It has been previously broadly correlated with the Sinclair Supergroup based on similar tectonothermal events recorded in both units and pre- to synorogenic magnetism at 1.20 Ga to 1.38 Ga (Burger and Coertze, 1978; Schneider *et al*., 2004; Becker and Schalk, 2008). This study tentatively correlates the Kwando Complex with the Nückopf Formation (Figure 6.30 and 6.34) based on similar lithological, aeromagnetic signatures (Table 6.1) and age dates.

The Kwando Complex was previously placed in the Okavango Zone (Figure 2.15) by Carney *et al*. (1994). However, from the age dates of Singletary *et al*. (2003), and the possible correlation with the Nückopf Formation, this study places the Kwando Complex in the Ghanzi-Chobe Zone (Figure 9.1). The northern margin of the Ghanzi-Chobe Zone is traced in the Bouguer gravity data by following a Bouguer gravity anomaly of ~-135 mGal to -120 mGal from northern Botswana southwestwards into Namibia.

The Roibok Group has been correlated with the Matchless Member because of their alignment of strike in both geological and geophysical mapping and MORB-like and within-plate geochemical compositions (Reeves, 1978a; Miller, 1983b; Breitkopf and Maiden, 1988; Lüdkte *et al*., 1986, in Singletary *et al*., 2003; Kgotlhang *et al*., submitted). The lack of reliable age constraints for the Roibok Group (twelve zircons with a range of ^{207}Pb-^{206}Pb dates from 659 Ma to 719 Ma, Singletary *et al*., 2003) and Matchless Member (Rb-Sr age of 765 ± 37 Ma, Hawkesworth *et al*., 1981 and Sm-Nd isochron age of 711 ± 35 Ma, Nagel, 1999) however, prevents a confident correlation between these two units. Corner (2008) suggests that the Matchless Member does not continue east of the Kudu Lineament while Carney *et al*. (1994) suggests that the resemblance between the Matchless Member and Roibok Group is coincidental. This coincidence is because of the absence of lithologies of the Southern Marginal Zone in Botswana and suggests that the Roibok Group may correlate with pre-Damaran basement. From the interpretation of the aeromagnetic data, lithological description in the literature (e.g. Breitkopf and Maiden, 1988; Carney *et al*., 1994; Singletary *et al*., 2003; Miller, 2008) and the limited age dates, this study suggests that the Roibok Group and Matchless Member do not form a continuous unit but were rather emplaced in a similar tectonic setting, most probably during the late stages of rifting between the Congo and Kalahari Cratons.

To the northwest of these igneous terranes are the metacarbonate successions of the Koanaka Group and Aha Hills Formation. The Koanaka Group and Aha Hills Formation have been previously correlated with the Swakop Group (Kgotlhang *et al*., submitted). Carney *et al*. (1994) on the other hand correlates the Koanaka Group in part with either the Karibib or Chuos Formations of the Southern and Okahandja Zones based on similar lithologies and alignment of strike. An alternative correlation for the Aha Hills Formation is with the Abenab Subgroup (Otavi Group) of the Northern Platform based on mineralisation, structures and lithological similarities (Carney *et al*., 1994 and references within). This study correlates the Koanaka Group with the cap carbonates (Karibib and Tinkas Formations) of the Ghaub Formation of the northern Central Zone and Southern Zone based on similar greenschist metamorphic facies of the dolomitic marbles, smooth, low aeromagnetic signals and the alignment along strike (Figure 6.1 and 6.34). The Aha Hills Formation is correlated with the cap carbonate (Keilberg Member, Maieberg Formation) of the Ghaub Formation of the Northern Platform based on similar mineralisation and lithologies (Figure 6.31 and 6.34).

The Quangwadum Complex is correlated with the Grootfontein Complex based on the alignment of strike, similar lithologies and aeromagnetic signal that is traced across the political border.

The Xaudum Group has been previously correlated with the Otavi Group based on similar lithologies, basement contact, and aeromagnetic signal (Kgotlhang *et al*., submitted). From the detrital zircon ages of Mapeo *et al*. (2000) (~1.02 Ga) and similar lithologies, Singletary *et al*. (2003) correlates the Xaudum Group with the Nosib Group. Carney *et al*. (1994 and references within) correlates the Xaudum Group with the Otavi Group of the Northern Platform based on similar lithologies and structures. This study correlates the Lower Xaudum Group, consisting of shales and dolomitic marble with the Ombombo Subgroup and the Upper Xaudum Group with the Gauss/Gruis Formation (Abenab Subgroup) of the Northern Platform (Figure 6.31 and 6.34).

The above correlations suggest that the Southern Zone and northern Central Zone are adjacent to each other before entering into Botswana (Figure 9.1). This interpretation results in the southern Central Zone and Northern Zone pinching out before the Namibia – Botswana border (Figure 9.1). The southern Central Zone is suggested to pinch-out at ~19°E, -21°S marked by the disappearance of the high amplitude aeromagnetic signal. The Northern Zone is interpreted to terminate against the Northern Marginal Zone (Figure 9.1). These interpretations are in agreement with geological and geophysical interpretations of Miller (2008) and Corner (2008) for the tectonostratigraphic zones of the Damara Belt.

The abundant iron formations and ferruginous quartzites of the Tsodilo Hills Group have been correlated with the iron-rich strata of the Chuos Formation of the Central Zone (Miller, 1983a; Breitkopf, 1988; Hoffman, 1989; Bühn *et al*., 1992). Kgotlhang *et al*. (submitted) correlates the iron formations of the Tsodilo Hills Group with the Chuos Formation but favours a correlation with the Kuiseb Formation (Southern Zone) for the dolostone, schist and quartzite units, based on their correlation of the Roibok Group with the Matchless Member. This is reinforced by observation of ferruginous quartzite markers associated with the Matchless Member in the Southern Zone (Corner, 2008). Congo Craton affinity has been documented in the Central Zone in the Abbabis Complex (Tack *et al*., 2002; Rainaud *et al*., 2005a; Miller, 2008; Longridge *et al*., 2012) from age dates of ~2.0 Ga. Similar age dates have been recorded in northwest Botswana from granites intersected in the boreholes of Tsodilo Resources Ltd. (Gaisford, 2010; Gerner, 2011; Witbooi, 2011). There are no reliable age dates for the Tsodilo Hills Group. Singletary *et al*. (2003) obtained a $^{40}Ar/^{39}Ar$ muscovite metamorphic age of 490 ± 2.3 Ma, which suggests that the Tsodilo Hills Group was deformed during the Damara Orogenesis. From the interpretation of potential field data, lithological observations from Tsodilo Resources Ltd. borehole core, and published literature and age dates, this study cannot confidently correlate the Tsodilo Hills Group with a single tectonostratigraphic zone of the Damara Belt. This study speculates that the Tsodilo Hills Group can be correlated with either the Southern Margin Zone or Southern Zone. Alternatively, the Tsodilo Hills Group may not correlate with any of the Damaran tectonostratigraphic zone and their correlatives may be in either Angola and/or Zambia. For these reasons sub-domains 2 and 3 are labelled with question marks for unknown tectonostratigraphic correlations on Figure 9.1.

9.3. Inferred margins of the Kalahari and Congo Cratons

The previous interpreted extents of the cratons have been discussed in Section 7.5.2. In addition to the data discussed below to constrain the inferred extents of the cratons, this study utilised upward continued aeromagnetic data at intervals of 3 000 m, 5 000 m, 8 000 m and 12 000 m to smooth the shallow (high-frequency) aeromagnetic signal and attenuate the long-wavelength (deep feature) associated with the cratons.

The Northern Platform, Northern Margin Zone and Northern Zone represent a shelf environment along the south-western passive margin of the Congo Craton with the Central Zone representing a magmatic arc (Miller, 1983a, 2008). The Southern Zone, Southern Margin Zone and Southern Foreland, each contain exposed Mesoproterozoic basement gneiss, formed on the passive margin of the Kalahari Craton. Detrital zircons from a metapsammite of the Kuiseb Formation (sample N86C) support a passive margin setting for the Southern Zone with a Kalahari basement gneiss-derived zircon population of ~1.1 Ga (white star in Figure 9.2) (Milani, *pers. comm*, 2013). The thick turbiditic sequences of the Southern Zone formed as submarine fans (Kukla, 1992) along the continental slope of the Kalahari Craton. Slices of oceanic crust (Matchless Member) were preserved as tectonic slivers within the imbricated succession.

The cratonic affinity of the Central Zone is ambiguous. Gneiss of the Abbabis Complex yielded Palaeoproterozoic ages of ~2.0 Ga (orange stars in Figure 9.2) (Hawkesworth and Marlow, 1983; Tack *et al*., 2002; Longridge, 2012), which correlates with Congo Craton basement (Rainaud *et al*., 2005a) whilst a concordant xenocrystic zircon from a Pan-African pegmatite in the Northern Zone yielded a LA-SF-ICP-MS age of 2 048 ± 12 Ma (sample N152; Milani, *pers. comm*, 2013) (yellow star in Figure 9.2). The Okahandja Lineament forms the present-day southern boundary of the southern Central Zone at surface and is suggested to represent the southern margin of the Congo Craton (Kukla, 1992; Frimmel *et al*., 2011). However, the actual suture coincides with the Gomab River Line (Corner, 2008; Miller, 2008) or Us Pass Lineament (Hoffmann, 1983) located along the northern margin of the Southern Margin Zone. This zone contains nappes of basement and ultramafic rocks and has been suggested to mark a suture zone between the two cratons (Hartnady, 1978; Hoffmann, 1983). The southward-directed thrust transport along this zone suggests that it dips northwards and possibly merges at depth with the contact zone of the Kalahari and Congo Cratons. The suggested northward subduction of the Khomas Ocean beneath the Congo Craton (Barnes and Sawyer, 1980) implies that the marine portion, adjacent to the Kalahari Plate, subducted beneath the Congo plate (Gray *et al*., 2007).

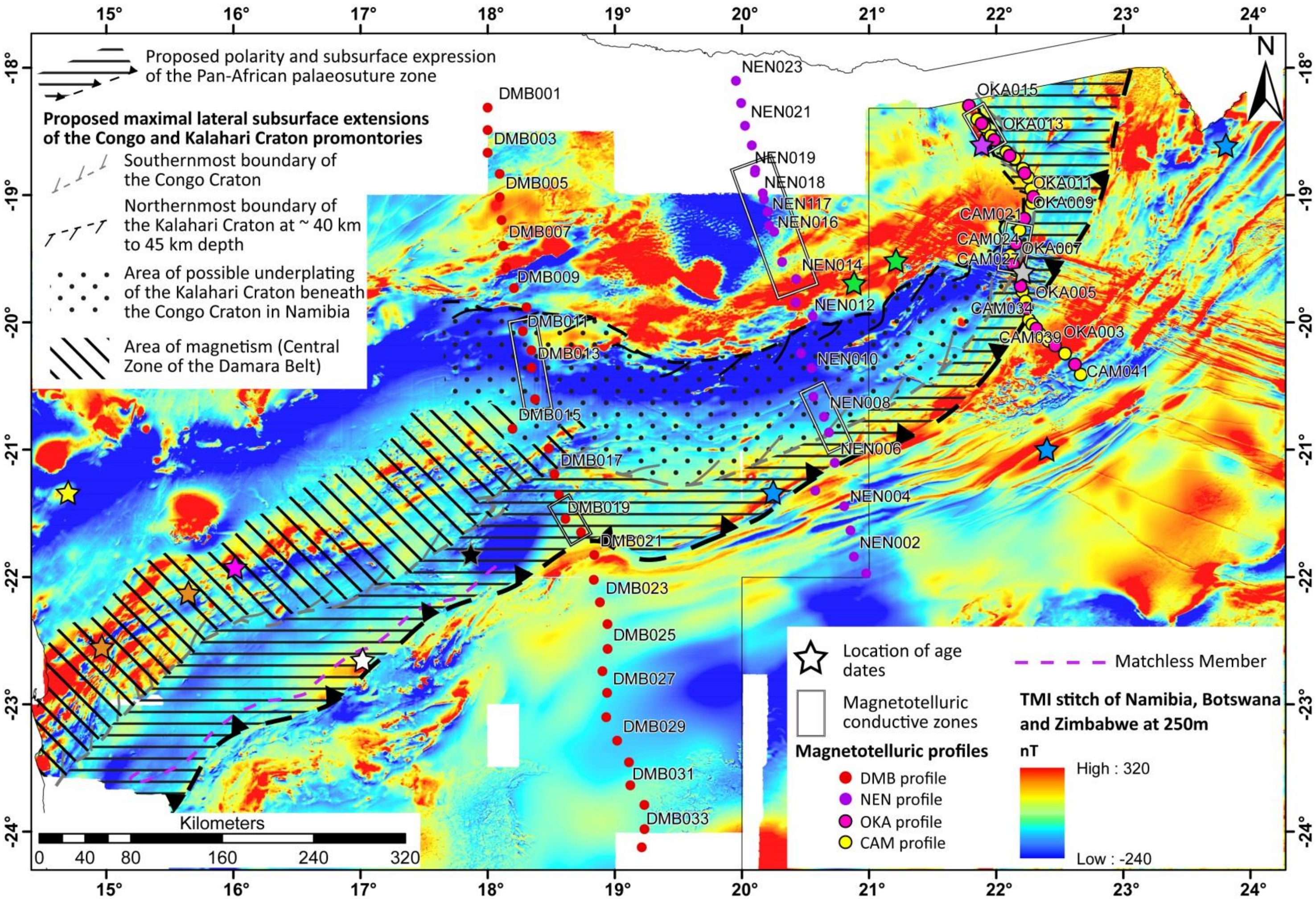

Figure 9.2: Inferred subsurface extension of the Kalahari Craton (to the south) and Congo Craton (to the north) and polarity and subsurface extension of the Pan-African palaeo-suture zone. The stars represent the location of age dates used for the inferred extent of the cratons. The location of the DMB (red circles), NEN (purple circles), OKA (pink circles) and CAM (yellow circles) profile stations are shown with the black rectangles defining conductive zones beneath the profiles. The geological extent of the Matchless Member (purple dashed line) is after Miller (2008).

The Rehoboth Subprovince forms a major component of the northwestern margin of the Kalahari Craton, which grew during prolonged crustal accretion during the Palaeo- and Mesoproterozoic (Jacobs *et al*., 2008; van Schijndel *et al*., 2013). In the Ekuja-Otjhangwe Nappe Complex (Figure 1.4), Cu-bearing metavolcanic lithologies yielded Umkondo magnetic event ages (1 130 Ma to 1 060 Ma, Steven *et al*., 2000, black star in Figure 9.2). Mesoproterozoic ages have been recorded in the Abbabis Complex (1.24 Ga to 1.04 Ga, Kröner *et al*., 1991, orange star in Figure 9.2) and the Pan-African Goas Suite (1.10 Ga to 1.07 Ga, Milani *et al*., 2014) (pink star in Figure 9.2), which suggests that fragments of the Kalahari Craton extend ~200 km north of the Rehoboth Subprovince. Foster *et al*. (2014) suggests that detrital zircons in the Damara Belt, with an age range of 1.35 Ga to 1.10 Ga, are sourced from the Kalahari Craton.

In eastern Namibia the Oorlogsende Porphyry Member (western blue star in Figure 9.2) has an Umkondo magnetic event age of ~1.1 Ga (Hegenberger and Burger, 1985). The Deep-Level Southern Zone (Figure 6.1) is suggested to be of Kalahari Craton affinity that, during collision, was detached from the subducted plate and thrust upwards. There are no age dates for the Deep-Level Southern Zone marking its emplacement and origin. It is only speculative at this stage and is based on aeromagnetic interpretations (Chapter 6) and modelling (Chapter 8).

The continuation of the Kalahari Craton into western Botswana is constrained by the Kgwebe and Goha Hills Formations, which both have ages of ~1.1 Ga (eastern blue star in Figure 9.2, Schwartz *et al*., 1995; Kampunzu *et al*., 2000) and are correlated with the Oorlogsende Porphyry Member, in eastern Namibia, and Langberg Formation in the Rehoboth Subprovince (Chapter 6). The overlying metasediments of the Ghanzi Group and its correlatives in Namibia (Figure 6.31) were deposited along the northwestern margin of the Kalahari Craton (Borg, 1988; Borg and Maiden, 1989; Modie, 1996, 2000).

To the north of the Ghanzi-Chobe Belt is the Roibok Group (Figure 6.1). Within the northern part of the Roibok Group are a series of magnetic high anomalies (between 550 nT to 700 nT), into which Tsodilo Resources Ltd. drilled borehole G3. This core intersected a pink granitic gneiss which was dated at 1 979 ± 92 Ma (Gaisford, 2010) (grey star in Figure 9.2). This age falls within error of the SHRIMP zircon age from the Magondi Belt (Gweta Borehole) (Figure 1.4 and 2.19) of 2 027 ± 8 Ma (Mapeo *et al*., 2001). This study suggests that the granite in borehole G3 resembles slivers of Kalahari Craton that have been thrust southeastwards and tectonically interleaved with the Roibok Group.

To the east of the Roibok Group is the Kwando Complex consisting of gneisses and granitoids emplaced at ~1.20 to 1.15 Ga (Singletary *et al*., 2003). There is no geochemical data for the Kwando Complex but it has been correlated with the Sinclair Supergroup based on similar tectonothermal events, recorded in both units, and pre- to synorogenic aged magnetism at 1.20 Ga to 1.38 Ga (Burger and Coertze, 1978; Schneider *et al*., 2004; Becker and Schalk, 2008). The Kwando Complex has been tentatively correlated with the Nückopf Formation suggesting that the Kwando Complex is part of the Umkondo magmatic event (Hanson *et al*., 1998).

In the low-pass filter, sunshaded aeromagnetic images of northwestern Botswana, north-northwest trending linear, high magnetic anomalies were interpreted as basement features (Figure 6.24a). These basement features are overprinted by northwest-southeast trending folds in the high-pass filtered aeromagnetic images (Figure 6.24b). Key and Ayres (2000) suggest that these metasedimentary structures cover the southern extent of the Congo Craton.

To the east of these features, Tsodilo Resources Ltd. has drilled a number of boreholes in the vicinity of the Xaudum Magnetic High. A granitic gneiss was intersected in the boreholes that was dated at 2 548 ± 65 Ma (Gaisford, 2010) and 2 645 ± 14 Ma (Witbooi, 2011) (purple star in Figure 9.2). Overlying the granite gneiss are metamorphosed glaciomarine diamictites with Archaean detrital zircon ages of between ~2.75 Ga to 2.05 Ga (Witbooi, 2011; Gerner, 2011). This suggests that the underlying basement is most likely the source of the detritus in the diamictite. However, the diamictites also have a Neoproterozoic age of 743 ± 62 Ma (Witbooi, 2011). This age falls within the age error of the Chuos diamictite of 746 ± 2 Ma (Hoffman *et al*., 1996), which is part of the Damara succession deposited on the Congo Craton, in Namibia. To the south of the Xaudum Magnetic High are a number of circular serpentinite bodies drilled by Tsodilo Resources Ltd. (Figure 7.23). Kgotlhang *et al*. (2011) suggests these bodies resemble oceanic crust that was serpentinised indicating a fully developed rift between the Congo and Kalahari Cratons.

The Grootfontein and Quangwadum Complexes are of Congo Craton affinity (e.g. Key and Ayres, 2000; Singletary *et al*., 2003) determined from age dates of ~2.0 Ga (green stars in Figure 9.2, Hoal *et al*., 2000; Singletary *et al*., 2003). To the south of the Quangwadum Complex, the Chihabadum Complex (Figure 6.1) is an unexposed and undrilled domain (Key and Ayres, 2000). This study tentatively suggests it is of Congo Craton affinity from aeromagnetic interpretation and forward modelling.

The inferred elongated conductor beneath the DMB (DR_3), NEN (NC_3) and OKA-CAM profiles (beneath stations OKA008 to CAM027) (Figure 7.14 to 7.20) is suggested to represent either the palaeo-subduction zone and/or the Proterozoic plate margin of the cratons. This is in agreement with previous geoelectrical studies that have associated elongated conductive zones with known recent and ancient subduction zones and Proterozoic plate margins around the world (Gough, 1983; Haak and Hutton, 1986; Kurtz *et al*., 1986; Jones, 1993; Jones *et al*. 1993, 2005; Selway *et al*. 2009; Padilha *et al*. 2013; Corbo-Camargo *et al*., 2013). Where reflection seismic data are available, the elongated conductor coincides spatially with a highly reflective dipping horizon (e.g. Kurtz *et al*., 1986; Jones, 1993).

Therefore, from these constraints and the forward modelling, the northern margin of the Kalahari Craton, at a depth of ~40 km to 45 km, is placed on the northern margin of the Northern Zone i.e. southern margin of the Grootfontein and Quangwadum Complexes (Figure 9.2). The southern margin of the Congo Craton is inferred to be the Okahandja Lineament (Kukla, 1992; Frimmel *et al*., 2011), which can be traced westwards following the northern margin of the Roibok Group. In northwestern Botswana the Congo Craton margin bends northwards where it is traced along the eastern margin of sub-domain 2 to the Caprivi Strip (Figure 9.2).

9.4. Subduction polarity and location of a possible palaeo-subduction zone

The evolution of the Damara-Zambezi-Lufilian Orogeny began during the Neoproterozoic rifting. Originally, the Damara Orogen was considered to be an intracratonic fold belt that formed in an ensialic aulacogen (Martin, 1965; Martin and Porada, 1977; Kröner, 1977, 1982). Early plate-tectonic classification of orogenic belts by Wilson (1966), and Dewey and Bird (1970), recognised that orogens can form fundamentally through subduction at continental margins, intra-oceanic subduction (i.e. oceanic island arcs), arc-continent accretion, ophiolite obduction, collision between continents and island arcs, or continent-continent collision. The first plate-tectonic model involving northward subduction of oceanic crust and later continent-continent collision was proposed by Barnes and Sawyer (1980). Other Early plate-tectonic models suggest either limited rifting (Porada, 1989) or a Red-Sea type proto-ocean rift basin (Hanson *et al*., 1994; Kampunzu and Cailteux, 1999) for the earliest phase of the Damara-Zambezi-Lufilian Orogen. These models conflict with the discovery of ~600 Ma subduction-related eclogites in the Zambezi Belt (John *et al*., 2003), substantial orogen-wide crustal thickening and high-pressure metamorphism at ~530 Ma, and associated white schist formation (John *et al*., 2004). Along the southern margin of the Congo Craton, an Andean-type margin developed with voluminous magmatism (Gray *et al*., 2007) facing a relatively large ocean, considering the low geothermal gradient reconstructed for the subduction-related eclogite metamorphism (John *et al*., 2003). Hence, the Damara-Zambezi-Lufilian Orogeny is associated with subduction and closure of an oceanic basin during convergence between the Kalahari and Congo Cratons. The location of the Pan-African palaeo-suture zone between the cratons and subduction polarity is conjectural.

A northwest-verging subduction sense is generally accepted for the closure of the Khomas Ocean (e.g. Barnes and Sawyer, 1980; Kukla, 1992; Becker *et al*., 2006) with the calcalkaline Goas Suite (Central Zone) representing the magmatic arc followed by collision-related extensive magmatism, i.e. the Kalahari Plate and associated oceanic crust were underthrusted beneath the Congo Craton. In tectonic orogens, suture zones mark the former plate boundaries and often contain slivers of oceanic crust relics in ophiolitic bodies and/or eclogites. Kröner (1982) and Jung *et al*. (2002) debate the presence of “true” oceanic crust because of the abundant granitoids in the orogen, which do not correspond with the structure of typical collisional belts. The lack of oceanic crust and high-grade metamorphism signatures (eclogite-facies) provides no support for the existence of a palaeo-subduction zone.

A regional conductor of less than 20 Ωm has been mapped across Namibia and Botswana since the mid-1970s (de Beer *et al*., 1975, 1976, 1982; van Zijl, 1977; van Zijl and de Beer, 1983; Khoza *et al*., 2013). In these studies the conductive zone cross-cuts the tectonostratigraphic zones of Namibia defined by Corner (2008) and Miller (1983a, 2008) and in Botswana defined by Carney *et al*. (1994). The suggestions on cause, size and depth of the conductor have changed with the increase of geoelectrical studies. The theories on the cause of this enhanced conductivity have ranged from rift related to serpentinised ultramafic rocks to a combination of sulphides and graphite. All of these proposed theories on the cause of enhanced conductivity have flaws, which have been discussed in Section 7.5.2. A possible cause of enhanced conductivity that has not been proposed is that it is associated with Palaeoproterozoic plate margins and/or an ancient subduction-collision zone. Elongated conductive anomalies in stable cratonic regions have been associated with ancient and modern subduction-collision zones around the world (e.g. Haak and Hutton, 1986; Jones, 1993; Soyer and Unsworth, 2006; Selway *et al*., 2009; Türkoğlu *et al*., 2009; Corbo-Camargo *et al*., 2013; Padilha *et al*., 2013).

Beneath the DMB, NEN and OKA-CAM profiles there are a number of conductive bodies (less than 230 Ωm) which can broadly correlate to a northern and southern conductive zone (Figure 7.16 to 7.21 and 8.2). The northern conductors are interpreted to be discontinuous with the possible causes of enhanced conductivity discussed in Chapter 7, while the southern conductors are interpreted to form a continuous elongated conductive zone associated with a palaeo-subduction zone between the Congo and Kalahari Cratons (Figure 9.2). Additional evidence for a palaeo-subduction zone is represented by several features. (1) The voluminous intrusions of the southern Central Zone which have been suggested to represent dehydration of a subducting slab at mid-crustal depths (Gray *et al*., 2007) and (2) the MORB-type and within-plate composition of the amphibolites and granites of the Matchless Member (Southern Zone) and Roibok Group (Okavango Zone) (Barnes and Sawyer, 1980; Miller, 1983a; Breitkopf and Maiden, 1988; Lüdkte *et al*., 1986 in Singletary *et al*., 2003) that lie on strike with the elongated conductor. (3) To the south of the proposed palaeo-subduction zone are the Kgwebe, Langberg and Oorlogsende Porphyry volcanics dated at ~1.1 Ga (Hegenberger and Burger, 1985; Schwartz *et al*., 1995; Singletary *et al*., 2003) representing the Umkondo magmatic event of Hanson *et al*. (1998, 2004). To the north of the elongated conductor the Abbabis Complex is dated at ~2.0 Ga resembling Congo Craton affinity (Jacob *et al*., 1978; Hawkesworth and Marlow, 1983; Tack *et al*., 2002; Longridge, 2012). (4) The elongated conductor correlates spatially with a Bouguer gravity anomaly of ~-100 mGal. (5) The 2D forward magnetic modelling suggests that a northward dipping, palaeo-subduction is possible (Figure 8.4). (6) The fold and deformation intensity of the Ghanzi-Chobe Belt increases towards the deformation front (Figure 8.3). (7) Finally, airborne time domain electromagnetic profiles conducted in the vicinity of the Xaudum Magnetic High suggest northeast subduction by the southwest thrusting of granitic-gneisses over metapelites with a Pan-African Orogeny foliation.

The Zambezi Belt and Lufilian Arc lie along strike to the Damara Belt and have shared a similar history since the breakup of Rodinia at ~750 Ma (Master, 2009). In the Damara Belt, syenites, granites and rhyolites are dated between ~747 Ma to 765 Ma (Hoffman *et al*., 1996; Konopásek *et al*., 2008; McGee *et al*., 2012), which is similar to ages of ~765 Ma to 730 Ma recorded from volcanics, syenites and granites from Zambia (Key *et al*., 2001; Sanz, 2005). These similar age dates suggest that rifting and spreading during the Damara-Zambezi-Lufilian Orogen was fairly uniform along the southern margin of the Congo Craton (Master, 2009). During the rifting phase, continental rupture is evident in the Khomas Ocean from the eruption of MORB-like amphibolites of the Matchless Member and Roibok Group (Barnes and Sawyer, 1980; Killick, 1983; Breitkopf and Maiden, 1986; Killick, 2000; Lüdkte *et al*., 1986 in Singletary *et al*., 2003) that were emplaced at ~715 Ma (Hawkesworth *et al*., 1981; Nagel, 1999; Singletary *et al*., 2003). The Damara-Zambezi-Lufilian Orogen also has similar ages of subduction and collision. In the Zambezi Belt, eclogite-facies metamorphism related to northward subduction beneath the Congo Craton is dated at 595 ± 10 Ma (John *et al*., 2003) or 592 ± 22 Ma (Rainaud *et al*., 2005b). In the Damara Belt, northwestward subduction beneath the Congo Craton is bracketed between 580 Ma to 545

Ma, from age dates of the mafic (diorite) Goas Suite and related volcanics (Milani *et al*., 2014). Continent-continent collision, granulite-facies metamorphism and magmatism in the Zambezi Belt (northern Zimbabwe) have been recorded between ~560 Ma to 510 Ma (Hanson *et al*., 1993; Rainaud *et al*., 2005b), which is similar to continent-continent collision, metamorphism and magmatism in the Damara Belt between 540 Ma to 510 Ma (Goscombe *et al*., 2000; Tack *et al*., 2002; Longridge *et al*., 2011; Frimmel *et al*., 2011). The final stages of collision between the Congo and Kalahari Cratons have been dated in the Zambezi Belt at ~530 Ma to 510 Ma (John *et al*., 2004; Rainaud *et al*., 2005b), which is the same as recorded for the Damara Belt (Goscombe *et al*., 2000; Singletary *et al*., 2003; Longridge *et al*., 2011).

There are currently very limited age dates for northwest Botswana to provide a confident correction for the age of the Damara-Zambezi-Lufilian Orogeny. An age date of a metamafic by Gaisford (2010), suggests westward subduction beneath the Congo Craton at ~540 Ma. In this area, direction of subduction can also be determined from the combination of structural and metamorphic grades of sub-domain 1 and 2 (Section 6.3.8). An amphibolite facies (sub-domain 2) is juxtaposed to the east with a low-grade greenschist facies to the west (sub-domain 1) along structures orientated northwest-southeast. The association of an eastward inverted metamorphic sequence with a style of folding-thrusting allowed for exhumation of amphibolite facies and Archaean basement rocks on top of greenschist facies rocks. The geophysical signature of the radial structural grains suggests that these structures do not continue south of 19.5°S, 22.0°E. In map view these structures seem to follow a radial distribution with a rotation axis centred on 19.5°S, 22.0°E (the northeastern extension of the Quangwadum Complex), from northwest-striking in the west to northeast-striking in the east. Low-pass filtered aeromagnetic images suggest that the main crustal structural grain is northeast striking. The radial structural grain, with a rotation axis centred along the northeastern extension of the Quangwadum Complex (i.e. Congo Craton), from northwest-striking in the west to northeast-striking in the east, is only visible in the high-pass filtered aeromagnetic images. This suggests that sub-domain 1 formed an indenter front for the exhumation of deep-seated lithologies of sub-domain 2.

This study brackets continent-continent collision and metamorphism in northwestern Botswana between ~550 Ma to 530 Ma from the age of metamorphism of the Roibok Group (Singletary *et al*., 2003) and $^{40}Ar/^{39}Ar$ muscovite age of a shear zone within the Quangwadum Complex (Singletary *et al*., 2003). The main orogenic movement terminated in the Central Zone at ~490 Ma to 460 Ma, interpreted by regional cooling through 350°C to 300°C (Gray *et al*., 2006), immediately after the emplacement of the post-tectonic A-type granites (McDermott *et al*., 2000). This is despite the distinct magma pulses that intruded the Central Zone at 570 Ma to 540 Ma, 535 Ma to 510 Ma, and 505 Ma to 485 Ma (Gray *et al*., 2006). In northwest Botswana cooling below 400°C to 350°C occurred at 490 ± 2.3 Ma in the Tsodilo Hills Group (Singletary *et al*., 2003). A number of circular magnetic anomalies suggested to be buried Pan-African granites (Figure 3.8a) have been interpreted to the east of these age dates (Pryer *et al*., 1997). To confirm these as Pan-African granites, drilling and dating of specimens will need to be carried out.

9.5. Type of orogen

The Damara Orogen formed as a result of continent-continent collision. What is not clear is what type of orogen the Damara Belt represents. Subduction of oceanic crust is favoured to have preceded this collision, however, the lack of high-grade metamorphic lithologies in the Damara Belt and northwest Botswana as well as no recorded occurrence of long-lived continental arc magmatism, suggesting that this period of subduction was relatively shorted lived.

In an understanding of how orogens develop, Jamieson and Beaumont (2013) proposed two types of orogens; (1) small-cold orogens and (2) more evolved large-hot orogens or transitional orogens. The Damara Orogeny shares characteristics of both of these orogen types.

Small-cold orogens are characterised by low-temperatures that develop above the subduction zone (Jamieson and Beaumont, 2013). This is observed in the low-temperature metamorphic grades of the outer zones of the Damara Belt (Goscombe *et al*., 2004; Miller, 2008) and the low-temperature, greenschist-facies of sub-domain 1 in northwest Botswana. Above the subduction zone, forearcs form in areas that are not directly affected by magmatism, and in the early stages of continent-continent collision precursor arc magmatism was either insignificant or terminated prior to the onset of collision (Jamieson and Beaumont, 2013). The deep-water metapelites and metagreywackes with minor graphitic mica schists of the Hureb Formation (Southern Zone) are interpreted as a forearc-trench sequence by Sawyer (1981), Kukla (1992), and Kukla and Stanistreet (1991). The schists of the Southern Zone are suggested to be an accretionary wedge or subduction-accretion complex (Kukla and Stanistreet, 1991). In the Southern Zone, large volumes of granite are absent even in the highest metamorphic grades (Jung *et al*., 2001). Another characteristic of a small-cold orogen is a doubly vergent crustal domain (Willett *et al*., 1993). In addition, the exhumation of the Deep-Level Southern Zone and Chihabadum Complex during collision with subduction of little or crustal material is typical of small-cold orogens (Jamieson and Beaumont, 2013).

The transition from small-cold orogens to large-hot orogens typically involves a change from the subduction of oceanic crust to terrane accretion or continental collision, and evolution from a system with doubly vergent wedge to an orogenic plateau. In the plate-tectonic models of the Damara Orogeny, continent-continent collision and subduction of both oceanic and continental crust are all involved (e.g. Barnes and Sawyer, 1980; Kukla, 1992, Gray *et al*., 2006, 2008; Miller, 2008; Frimmel *et al*., 2011; Foster *et al*., 2014). During this transition, from a small-cold orogen to a large-hot orogen, pro-continental crust can be detached from the subducting plate and exhumed, creating high-pressure metamorphic complexes that in many orogens are characteristic of early collisional zones (Jamieson and Beaumont, 2013). From the interpretation of the magnetic forward models, the Deep-Level Southern Zone and Chihabadum Complex are suggested to be the exhumation of the subducting slab. As the Chihabadum Complex is an unexposed and undrilled domain it may be the reason why no (ultra)-high-pressure metamorphic lithologies have been found in northwest Botswana to date. The emplacement of pro-continental material into the pro-wedge (Deep-Level Southern Zone) and retro-wedge (Chihabadum Complex) respectively is typical of small cold-orogens (Butler *et al*., 2011, 2013). Temperature increases during collision are associated with accretion and burial of radioactive crustal material that heats up, typically resulting in Barrovian metamorphism (Jamieson and Beaumont, 2013). This process may lead to a second transition, in which the back-to-back wedges evolve into a system with a central orogenic plateau flanked by external wedges. The metamorphic grade of the Northern Zone varies along strike with low pressure contact metamorphism with anticlockwise P-T paths in the west and higher pressure (Barrovian series) metamorphism with clockwise P-T paths in the east (Goscombe *et al*., 2005). The eastern part of the Northern Zone experienced peak metamorphic conditions of ~635°C and ~8.7 kbar, associated with deep burial, high pressure and moderate temperature Barrovian metamorphism (Goscombe *et al*., 2005). Similarly, the Southern Zone is characterised by Barrovian-type regional metamorphism that increases in metamorphic grade from south to north (Jung *et al*., 2001).

Based on numerical models (e.g. Jamieson *et al*., 2004, 2007; Beaumont *et al*., 2009; Sizova *et al*., 2012), the metamorphic grade of an orogen is shown to increase inwards to the centre of the orogen. In large-hot orogens, the orogenic flanks display inverted metamorphic sequences that pass upward into normal sequences (e.g. Jamieson *et al*., 2004), with the orogenic core generally underlain by granulite terranes (Jamieson *et al*., 2007; Jamieson and Beaumont, 2013). The metamorphic grade of the Damara Belt increases inwards (e.g. Kasch, 1983; Goscombe *et al*., 2004; Kinnaird and Nex, 2007) to the granulite-facies southern Central Zone (Longridge, 2012). The zone is flanked by the amphibolite-facies northern Central Zone and Southern Zone. The decrease in metamorphic grade from the southern Central Zone to the northern Central Zone represents a normal metamorphic sequence. The delay between continent-continent collision at ~540 Ma (Miller, 2008) and the 520 Ma onset of extension and exhumation of the southern Central Zone (Longridge, 2012) is consistent with the 20 Myr to 25 Myr incubation period required to raise temperatures to greater than 700°C in the lower crust. This increase is a result of thermal relaxation and radioactive heating in the thickened crust (Jamieson and Beaumont, 2013). The juxtaposition of granulite facies lithologies of the southern Central Zone with amphibolite facies lithologies of the Southern Zone appears to represent an inverted metamorphic sequence, which would only apply if the metamorphism in both zones was coeval. Granulite facies metamorphism in the Central Zone is dated at 520 Ma to 510 Ma (Longridge, 2012), whilst the Southern Zone and Southern Margin Zone are characterised by deformation and metamorphism at ~560 Ma and 550 Ma (Miller, 2008).

Therefore, the Damara Orogeny has characteristics of both a small-cold orogen and large-hot orogen. It can be confidently said that the Damara Orogeny has undergone continent-continent collision, which according to Jamieson and Beaumont (2013) typically represents the transition from a small-cold orogen to a large-hot orogen. However, there is no documented orogenic plateau associated with the Damara Orogen, which generally evolves in the large-hot orogens. The Alps Orogeny is an example of an orogen that passed through the subduction-collision transition but did not evolve into a large-hot orogen with an orogenic plateau. In addition, the Chihabadum Complex has similarities with the Internal Crystalline Massif in the western Alps. Therefore, this study suggests that the Damara Orogen formed in a similar manner to the Alps Orogeny.

Chapter 10

Conclusions and further work

A new sub-Kalahari geological map was created based on the interpretation of 50 m grid cell sized aeromagnetic grids of Namibia and Botswana complemented by gravity data at a grid cell size of 2.2 km. The geophysical interpretation was constrained by field observations (outcrops and boreholes) and published literature, including geological maps and mining reports. Cross-border correlations of Haddon (2001) have correlated the Ghanzi-Chobe Belt with Neoproterozoic lithologies of the Nosib Group (Kamtsas and Duruchaus Formations) or, in other studies, correlated with discrete individual basins (the Sinclair, Klein Aub, Dordabis, and Witvlei Basins) (e.g. Borg and Maiden, 1987; Borg, 1987, 1988; Modie, 1996). The correlation of the volcanic units (Goha Hills, Kgwebe, Langberg Formations and Oorlogsende Porphyry Member) and the Ngwako Pan Formation with the Doornpoort Formation, and the D'Kar, Mamuno and Chinamba Formations with the Klein Aub Formation, and the use of directional, low-pass filtered images suggest that the Ghanzi-Chobe Belt forms a continuous linear to curvilinear belt that can be traced from the Rehoboth Subprovince through Botswana to the Caprivi.

The new cross-border geological corrections have resulted in the tectonostratigraphic zones of the Damara Belt and northwest Botswana and the extents of the Congo and Kalahari Cratons being redefined. The Kwando Complex is now included in the Ghanzi-Chobe Zone based on age dates of ~1.20 Ga to 1.15 Ga and its tentative correlation with the Nückopf Formation. The Northern Margin Zone, Northern Zone, southern Central Zone and Southern Margin Zone pinch out eastwards before reaching the Namibia – Botswana border resulting in the northern Central Zone and Southern Zone merging before the border. Its Namibian correlative has been interpreted as being the Okavango Zone. The Northern Platform is correlated with the Shakawe Zone. There are no confident correlations for sub-domain 2 and 3, in northwest Botswana, with lithologies of the Damara Belt. These two sub-domains may correlate better with lithologies in southern Zambia or Angola.

The southern margin of the Congo Craton is placed as far south as the Okahandja Lineament (Miller, 2008) and is traced into Botswana based on geological and geophysical evidence where it bends around the southern margin of the Quangwadum Complex and continues to the Caprivi Strip. The cause of the Damara Belt and pinching out of tectonostratigraphic zones is most likely caused by the Congo Craton (Grootfontein and Quangwadum Complexes) that acted as an indenter front between sub-domain 1 and 2 in northwest Botswana. This study has shown that the northern margin of the Kalahari Craton at a depth of 40 km to 45 km extends as far north as the northern limit of the northern Central Zone as interpreted from the 2D magnetic forward models.

The DMB, NEN and OKA-CAM profiles of the SAMTEX project were 1D Occam inversed modelled at depth ranges of 1 – 5 km, 1 – 15 km and 1 – 35 km. The aim of the magnetotelluric data modelling was to investigate continuity in crustal structures and verify the presence of a regional conductive zone (de Beer *et al*., 1975, 1976, 1982; van Zijl, 1977; van Zijl and de Beer, 1983; Ritter *et al*., 2003; Khoza *et al*., 2013). The modelling of the TE and TM modes revealed two conductive zones, a northern and southern zone. The northern zone is interpreted as discrete individual conductors, while the southern conductive zone is suggested to form a northward dipping elongated zone of conductivity. Elongated conductive zones have been previously associated with Proterozoic plate margins and/or ancient subduction-collision zones (e.g. Geise *et al*., 1983; Haak and Hutton, 1986; Jones *et al*., 1993). The southern conductive zone is suggested to represent a palaeo-subduction between the Kalahari and Congo Cratons. Additional evidence is that this elongated conductive zone spatially correlates with the Matchless Member and Roibok Group, both of which have a MORB-like geochemical signature (Barnes and Sawyer, 1980; Miller, 1983a; Breitkopf and Maiden, 1988; Lüdkte *et al*., 1986 in Singletary *et al*., 2003). The Abbabis Complex of Congo affinity (Jacob *et al*., 1978; Hawkesworth and Marlow, 1983; Tack *et al*., 2002; Miller, 2008; Longridge, 2012) lies to the north of the conductive zone, while to the south are the Langberg Formation, Kgwebe Formation and Oorlogsende Porphyry Member all of which have an age of ~1.1 Ga, which is associated with the Umkondo magmatic event of Hansen *et al*. (1998, 2004).

Enhanced conductivity in recent and modern subduction zones (younger than 100 Ma) can be easily associated with a saturation of pore spaces with fluids (Jones, 1993; Corbo-Camargo, 2013). However, the cause of enhanced conductivity in ancient subduction zones is more difficult to determine because of the lack of knowledge of the various conditions at the time (Jones, 1993). The common causes of enhanced conductivity such as carbon, sulphides and hydrate minerals (e.g. serpentinite) should be treated with care and their orogenesis must be understood. Laboratory experiments by Duba *et al*. (1989) and thin section observations by Stanley *et al*. (1990) have revealed that high-grade metashales will have minor amounts of carbon, especially in continuous form. Illustrated in the experiments of Duba *et al*. (1989) was that temperatures of 417°C were high enough to oxidise the carbon and break the grain boundary interconnection.

Therefore, for graphite to be conductive, it would have had to have formed in a low-grade metamorphic region (Stanley *et al*., 1990). If the sulphide mineralisation formed during diagenesis of the sediments, they would not enhance the conductivity as they remain in unconnected nodules (Jones, 1993). Hydration minerals will be conductive provided that the water of hydration has not escaped (van Zijl, 1977). According to Thompson and Connolly (1990) fluids have a relatively short residence time in the crust of ~70 Ma or slightly longer depending on crustal temperatures (Bailey, 1990). The Damara Orogen formed as an orogenic collisional event and is associated with metamorphic grades of up to granulite-facies (Longridge, 2012). The high metamorphic grades will therefore, break down the carbon bonds making them non-conductive.

Therefore, the cause of enhanced conductivity of the southern conductive zone remains uncertain and can only be speculated. As the Ghanzi-Chobe Belt, and its correlatives in Namibia, and the Matchless Member are associated with known sulphide deposits, and the zone with the highest enhanced conductivity value is beneath the NEN profile (NC_3) where the Ghanzi-Chobe Belt is thickest and along strike of the Matchless Member, the enhanced conductivity can possibly be caused by sulphide mineralisation depending on the genesis of mineralisation. However, another possible cause of enhanced conductivity can be as a result of increased pore spaces, as the southern conductive zone follows the aeromagnetic interpreted trend of a thrust fault, the Gomab River Line.

This is the first study that does not cross-cut any of the tectonostratigraphic domains of the Damara Belt and northwestern Botswana but rather follows their general trend with the continuation of the Kalahari Craton and the regional conductor into Botswana.

Three approximately north-south trending magnetic profiles were 2D forward modelled to investigate the proposed northward subduction polarity (Barnes and Sawyer, 1980; Becker *et al*., 2006). The magnetic models demonstrate that the northward subduction of oceanic crust and subsequently the Kalahari Plate beneath the Congo Craton is a possible scenario. Beneath the northern part of the magnetic profiles, is a distinct roughly trending east-west aeromagnetically negative feature, which follows the general trend of the Rehoboth Subprovince. The suggested cause of this negative anomaly is a thick package, ~12 km to 20 km thick, of relatively non-magnetic metasediments overlying the collisional zone between the Kalahari and Congo Cratons. An alternative model proposed by Eberle *et al*. (2002) is that the negative magnetic feature is caused by rifting of the magnetic crust.

The Damara-Zambezi-Lufilian Orogeny is suggested to be an orogen that has passed through the subduction-collisional transition but did not evolve into a large-hot orogen. This is suggested because the Damara-Zambezi-Lufilian Orogeny has clearly gone through the transition of subduction of oceanic crust to terrane accretion (speculated to be represented by the Deep-Level Southern Zone and Chihabadum Complex) and continental collision. However, the doubly vergent wedges did not evolve into an orogenic plateau completing the transition from a small-cold orogen to a large-hot orogen. The Alps Orogeny is an example of an orogen that passed through the subduction-collision transition but did not evolve into a large-hot orogen with an orogenic plateau.

The correlations defined in this study are largely based on geophysical interpretations complemented with limited outcrops making them highly speculative. The correlations are largely based on the Ghanzi-Chobe Belt correlating with the Sinclair Supergroup within the Rehoboth Subprovince and a northward subduction sense of the Kalahari Plate beneath the Congo Craton.

There are no reliable crystallisation age dates for the Matchless Member and the only geochemical analysis for the Roibok Group has been carried out by Lüdkte *et al*., 1986, in Singletary *et al*. 2003. This study suggests that geochemical analysis should be carried out on the amphibolites of the Roibok Group and U-Pb zircon dating on the Matchless Member. To determine the sudden narrowing of the Damara Belt before entering into northwest Botswana, the origin and emplacement of the Omatako Ring Suture should be investigated.

To the author's knowledge, there is a lack, if any, of regional seismic profiles in the vicinity of the Namibia – Botswana border. To constrain the geological cause of the negative regional east-west trending aeromagnetic anomaly north-south trending reflection seismic lines should be shot. In particular, it is suggested that shear wave velocity studies be initiated to determine Poisson's ratio for depths associated with enhanced conductivity. However, to constrain the depth to the Moho in the vicinity of the Namibia – Botswana border, the seismic lines will need to have a northeast-southwest trend in order to suppress seismic reflections associated with the Damara Orogen.

To constrain the elongated conductive zone, the station spacing on the DMB and NEN profiles can be increased to ~5 km, similar to the OKA-CAM profile. This will increase the resolution of crustal features since the current station spacing is ~20 km, which are designed to image the lower crust and lithosphere. The TE and TM mode 1D Occam inversion models can be jointly 2D inversed modelled to obtain the most accurate location for the conductive bodies. The 2D models can then be 3D modelled to visually display the elongated conductor, which can incorporate topography into the inversion. The 2D and 3D inversion models could further improve the understanding of the Damara Orogen. Currently, the cause of the elongated conductive zone is unknown. There may be no alternative option but to drill one of the conductive bodies: the conductive body beneath the NEN profile is most probably the best target as it lies in the vicinity of the Roibok Group and where the Ghanzi-Chobe Belt is thickest.

To verify the 2D magnetic models, gravity modelling of the same profiles should be carried out to determine if the same geological scenario is valid for both methods. In addition, magnetic modelling is suitable for the upper 20 km, while gravity modelling is highly influenced by the depth of the Moho.

To determine the northward continuation of the Ghanzi-Chobe Belt into Zambia/Zimbabwe geochronology studies should be carried out on the Choma-Kaloma Block to determine cratonic affinity and emplacement history. As the majority of Pan-African lithologies in southern Zambia are covered, the best way in determining a link between the Damara Orogeny and Zambezi Orogeny would be to obtained higher resolution aeromagnetic data, as currently it is at 250 m grid cell size.

References

Alkmim, F.F., Marshak, S., Pedrosa-Soares, A.C., Peres, G.G., Cruz, S.C.P., and Whittington, A. 2006. Kinematic evolution of the Araçuaí-West Congo orogen in Brazil and Africa: Nutcracker tectonics during the Neoproterozoic assembly of Gondwana. *Precambrian Research*, **149**, 43 – 64.

Anderson, E.D., Hitzman, M.W., Monecke, T., Bedrosian, P.A., Shah, A.K., and Kelley, K.D. 2013. Geological analysis of aeromagnetic data from southwestern Alaska: Implications for exploration in the area of the pebble porphyry Cu-Au-Mo deposit. *Economic Geology*, **108**, 421 – 436.

Amthor, J.E., Grotzinger, J.P., Schröder, S., Bowring, S.A., Ramezani, J., Martin, M.W., and Matter, A. 2003, Extinction of Cloudina and Namacalathus at the Precambrian-Cambrian boundary in Oman. *Geology*, **31**, 431 – 434.

Badenhorst, F.P. 1992. The lithostratigraphy of area 2115 B and D in the central zone of the Damara orogen, Namibia: With emphasis on facies changes and regional correlation. *Unpublished MSc. Thesis*, University of Port Elizabeth, Port Elizabeth, South Africa, 124 pp.

Bahr, K. 1988. Interpretation of the magnetotelluric impedance tensor: regional induction and local telluric distortion. *Journal of Geophysics*, **62**, 119 – 127.

Baier, B., Berckhemer, H., Gajewski, D., Green, R.W., Grimsel, C., Prodehl, C., and Vees, R. 1983. Deep seismic sounding in the area of the Damara Orogen, Namibia, South West Africa. *In*: Martin, H., and Eder, F. (Eds.), *Intercontinental Fold Belts*, 885 - 900.

Bailey, R.C. 1990. Trapping of aqueous fluids in the deep crust. *Geophysical Research Letters*, **17**, 1 129 – 1 132.

Bailey, R.C., and Groom, R.W. 1987. Decomposition of the magnetotelluric impedance tensor which is useful in the presence of channelling. *In:* Expanded abstracts of the 57th annual international Society of Exploration Geophysics meeting and exposition, **57**, Tulsa, Oklahoma, 157 – 156.

Ballhaus, C.G. and Stumpfl, E.F. 1985. Occurrence and petrological significance of graphite in the Upper Critical Zone, western Bushveld Complex, South Africa. *Earth and Planetary Science Letter*, **74**, 58 - 68.

Baranov, V. 1957. A new method for interpretation of aeromagnetic maps: pseudo-gravimetric anomalies. *Geophysics*, **22**, 359 - 383.

Barnes, S.J. 1982. Serpentinites in central South West Africa/Namibia – a reconnaissance study. *Memoirs of the Geological Survey of South West Africa*, **8**, 90 pp.

Barnes, S.J., and Sawyer, E.W. 1980. An alternative model for the Damara Mobile Belt. Ocean crust subduction and continental convergence, *Precambrian Research*, **13**, 297 – 336.

Basson, I.J., and Greenway, G. 2004. The Rössing Uranium deposit: a product of late-kinematic localization of uraniferous granites in the Central Zone of the Damara Orogen, Namibia. *Journal of African Earth Sciences*, **38**, 413 – 435.

Bauer, K., Neben, S., Schreckenberger, B., Emmermann, R., Hinz, K., Fechner, N., Gohl, K., Schulze, A., Trumbull, R.B., and Weber, K. 2000. Deep structure of the Namibia continental margin as derived from integrated geophysical studies. *Journal of Geophysical Research*, **105** (B11), 25 829 – 25 853.

Bauer, K., Trumbull, R.B., and Vietor, T. 2003. Geophysical images and a crustal model of intrusive structures beneath the Messum ring complex, Namibia. *Earth and Planetary Science Letters*, **216**, 65 – 80.

Beaumont, C., Jamieson, R.A., Butler, J.P., and Warren, C.J. 2009, Crustal structure: A key constraint on the mechanism of ultra-high-pressure rock exhumation. *Earth and Planetary Science Letters*, **287**, 116 – 129.

Becker, T., and Schalk, K.E.L. 2008. The Sinclair Supergroup of the Rehoboth volcanic arc from the Sossusvlei-Gamsberg area to the Gobabis Region. *In:* Miller, R.McG. (Ed.), The Geology of Namibia: Archaean to Mesoproterozoic, *Ministry of Mines and Energy, Geological Survey of Namibia,* Windhoek, **1**, 8-68 – 8-102.

Becker, T., Garoeb, H., Ledru, P., and Milesi, J.P. 2005. The Mesoproterozoic event within the Rehoboth Basement Inlier of Namibia: review and new aspects of stratigraphy, geochemistry, structure and plate tectonic setting. *South African Journal of Geology*, **108**, 465 - 492.

Becker, T., Schriber, U., Kampunzu, A.B., and Armstrong, R. 2006. Mesoproterozoic rocks of Namibia and their plate tectonic setting. *Journal of African Earth Sciences*, **46**, 112 – 140.

Bedrosian, P., Pellerin, L., and Box, S. 2007. Fitting a round peg in a square hole: 3D inversion of complex MT profile data. *In: Proceeding of the 4th International Symposium in Three-Dimensional Electromagnetics*.

Behr, H.J., Aherendt, H., Porada, H., Röhrs, J., and Weber, K. 1983. Upper Proterozoic playa and Sabkha deposits in the Damara Orogen, SWA/Namibia. *Special Publication of the Geological Society of South Africa*, **11**, 1 – 20.

Berdichevsky, M.N., and Dmitriev, V.I. 1976. Basic principles of interpretation of magnetotelluric sounding curves. *In*: Adam, A. (Ed.), *Geoelectric and geothermal studies, KAPG Geophysical Monograph*, Akadémiai Kiadó, Budapest, 165 – 221 pp.

Berdichevsky, M.N., Dmitriev, V.I., and Pozdnjakova, E.E. 1998. On two-dimensional interpretation of magnetotelluric soundings. *Geophysical Journal International*, **133**, 585 – 606.

Billings, S., and Richards, D. 2000. Quality control of gridded aeromagnetic data. *Exploration Geophysics*, **31**, 611 – 616.

Blakely, R.J. 1995. Potential theory in gravity and magnetic application. Cambridge *University Press, Cambridge,* 441 pp.

Blakely, R.J., Brocher, T.M., and Wells, R.E. 2005. Subduction-zone magnetic anomalies and implications for hydrated forearc mantle. *Geology*, **33**, 445 – 448.

Blanco, G., Germs, G.J.B., Rajesh, H.M., Chemal Jr, F., Dussin, I.A., and Justino, D. 2011. Provence and paleogeography of the Nama Group (Ediacaran to early Palaeozoic, Namibia): petrography, geochemistry and U-Pb detrital zircon geochronology. *Precambrian Research*, **187**, 15 – 32.

Borg, G. 1987. Controls on stratabound copper mineralisation at Klein Aub Mine and similar deposits within the Kalahari Copperbelt of South West Africa/Namibia and Botswana. *Unpublished Ph.D. Thesis*, University of the Witwatersrand, Johannesburg, South Africa, 107 pp.

Borg, G. 1988. The Koras-Sinclair-Ghanzi rift in southern Africa. Volcanism, sedimentation, age relationships and geophysical signature of a late middle Proterozoic rift system. *Precambrian Research*, **38**, 75 – 90.

Borg, G., and Maiden, K.J. 1986. Stratabound copper-silver-gold mineralisation of Late Proterozoic age along the margin of the Kalahari Craton in SWA/Namibia and Botswana. Abstract, Symposium on sediment-hosted stratiform copper deposits, Ottawa, *Canadian Mineralogist* , **24**, 178 pp.

Borg, G., and Maiden, K.J. 1987. Basalt alteration and its relation to Middle Proterozoic stratabound copper-silver-gold deposits along the margin of the Kalahari Craton in SWA/Namibia and Botswana. *In:* Pharaoh, T.C., Beckinsale, R.D., and Richard, D.T. (Eds.), Geochemistry and mineralisation of Proterozoic volcanic suites. *Geological Society of London, Special publication,* **33**, 347 – 354.

Borg, G., and Maiden, K.J. 1989. The Middle Proterozoic Kalahari Copperbelt of Namibia and Botswana. *In*: Boyle, R.W., Brown, A.C., Jefferson, C.W., Jowett, E.C., Kirkham, R.V. (Eds.), Sediment-hosted stratiform copper deposits. *Geological Association Canada*, Special paper, **36**, 525 – 540.

Bostick, F.X. 1977. A simple almost exact method of MT analysis. Workshop on electrical Methods in Geothermal Exploration, US. Geological Survey. Contract number 14080001-8-359.

Bracewell, R.N. 1986. The Fourier transform and its applications. (2nd ed.), McGraw Hill Book Company, United States of America, 474 pp.

Brandt, R. 1987. A revised stratigraphy for the Abbabis Complex in the Abbabis Inlier, Namibia. *South African Journal of Geology*, **90**, 314 – 323.

Breitkopf, J. H., and Maiden, K. J. 1986. A volcanogenic exhalative iron formation in the Southern Margin Zone of the Damara Orogen. *Communications of the Geological Survey of South West Africa/Namibia*, **2**, 131 - 143.

Breitkopf, J.H. 1988. Iron formations related to mafic volcanism and ensialic rifting in the Southern Margin Zone of the Damara orogen, Namibia. *Precambrian Research*, **38**, 111 – 130.

Breitkopf, J.H., and Maiden, K.J. 1988. Tectonic setting of the Matchless Belt pytitic copper deposits, Namibia. *Economic Geology*, **83**, 710 – 723.

Briggs, I.C. 1974. Machine contouring using minimum curvature. *Geophysics*, **39**, 39 – 48.

Bufford, K.M., Atekwana, E.A., Abdelsalam, G., Shemang, E., Atekwana, E.A., Mickus, K., Moidaki, M., Modisi, M.P., Molwalefha, L. 2012. Geometry and faults tectonic activity of the Okavango Rift Zone, Botswana: Evidence from magnetotelluric and electrical resistivity tomography imaging. *Journal of African Earth Sciences*, **65**, 61 – 71.

Bühn, B., Stanistreet, I.G., Okrusch, M. 1992. Late Proterozoic outer shelf manganese and iron deposits at Ojosondu (Namibia) related to the Damaran oceanic opening. *Economic Geology and the bulletin of the Society of Economic Geologists*, **87** (5), 1 393 - 1 411.

Burger, A.J., and Coertze, F.J. 1975. Age determinations – April 1972 to March 1974. *Annual Report of the Geological Survey of South Africa*, **11**, 135 – 141.

Burger, A.J., and Coertze, F.J. 1978. Summary of age determinations carried out during the period April 1974 to March 1975. *Annals of the Geological Survey of South Africa*, **11**, 317 - 321.

Burns, S.J., and Matter, A. 1993. Carbon isotopic record of the latest Proterozoic from Oman. *Eclogae Geologicae Helviticae*, **86**, 595 – 607.

Butler, J.P., Beaumont, C., and Jamieson, R.A. 2011. Crustal emplacement of exhuming (ultra)high-pressure rocks: Will that be pro- or retro-side? *Geology* **39**, 635 – 638.

Butler, J.P., Beaumont, C., and Jamieson, R.A. 2013. The Alps 1: A working geodynamic model for burial and exhumation of (ultra)high-pressure rocks in Alpine type orogens. *Earth and Planetary Science Letters*, **377 – 378**, 114 - 131.

Cagniard, L. 1953. Basic theory of the magneto-telluric method of geophysical prospecting. *Geophysics*, **18**, 605 – 635.

Calver, C.R. 2000. Isotope stratigraphy of the Ediacarian (Neoproterozoic III) of the Adelaide Rift Complex, Australia, and the overprint of water column stratifi cation. *Precambrian Research*, **100**, 121 – 150.

Camfield, P.A, Gupta, J.C., Jones, A.G., Kurtz, R.D., Krentz, D.H., Ostrowski, J.A., and Craven, J.A. 1989. Electromagnetic sounding and crustal electrical conductivity structure in the region of the Wopmay Orogen, Northwest Territories, Canada. *Canadian Journal of Earth Sciences*, **26**, 2 385 - 2 395.

Camfield, P.A., and Gough, D.I. 1977. A possible Proterozoic plate boundary in North America, *Canadian Journal of Earth Science*, **14**, 1 229 – 1 238.

Carney, J.N., Aldiss, D.T., and Lock, N.P. 1994. The geology of Botswana. *Botswana Geological Survey,* Bulletin, **37**, 1 – 113.

Carruthers, R.M., and Reeves, C.V. 1974. Botswana gravity reference net. *Bulletin Gaeodésique*, **114**, 409 – 148.

Catuneanu, O., Wopfner, H., Eriksson, P.G., Cairncross, B., Rubidge, B.S., Smith, R.M.H., and Hancox, P.J. 2005. The Karoo basins of south-central Africa. *Journal of African Earth Sciences*, **43**, 211 – 253.

Chapman, S., and Pollack, N. 1977. Heat flow and heat production in Zambia: Evidence for lithospheric thinning in central Africa. *Tectonophysics*, **41**, 79 – 100.

Chave, A.D. and Jones, A.G. 1997. Electric and magnetic field galvanic distortion decomposition of BC87 data. *Journal of Geomagnetism and Geoelectricity*, **49**, 767 – 789.

Chave, A.D. and Smith, J.T. 1994. On electric and magnetic galvanic distortion tensor decompositions. *Journal of Geophysical Research (Solid Earth)*, **99** (B3), 4 669 – 4 682.

Chave, A.D., and Jones, A.G. 2012. The Magnetotelluric Method: Theory and practice. Cambridge University Press, New York, 1 – 570 pp.

Chetty, D., and Frimmel, H.E. 2000. The role of evaporates in the genesis of base metal sulphide mineralisation in the Northern Platform of the Pan-African Damara Belt, Namibia: geochemical and fluid inclusion evidence from carbonate wall rock alteration. *Mineralium Deposita*, **35**, 364 – 376.

Church, J., and Winker, F. 2013. Otjikoto Gold Mine: NW landfill and HFO power plant EIA, groundwater and surface water study. SLR environmental Consulting (Namibia) (Pty) Ltd., SLR Project number 733.01023.00007, 50 pp.

Clifford, T.N. 2008. The geology of the Neoproterozoic Swakop-Otavi transition zone of the Outjo district, northern Damara Orogen, Namibia. *South African Journal of Geology*, **111**, 117 – 140.

Cochrane, N.A., and Hyndman, R.D. 1974. Magnetotelluric and magnetovariational studies in Atlantic Canada. *Geophysical Journal of the Royal Astronomical Society*, **39** (2), 385 – 406.

Cole, J., Finn, C.A., and Webb, S.J. 2013. Overview of the magnetic signature of the Palaeoproterozoic Rustenburg Layered Suite, Bushveld Complex, South Africa. *Precambrian Research*, **236**, 193 – 213.

Constable, S.C., Parker, R.L., and Constable, C.G. 1987. Occam's inversion: A practical algorithm for generating smooth models from electromagnetic sounding data. *Geophysics*, **52** (3), 289 – 300.

Cooper, G.R.J. 2003. Feature detection using sun shading. *Computers and Geosciences*, **29**, 941 – 948.

Cooper, G.R.J. and Cowan, D.R. 2004. Filtering using variable order vertical derivatives. *Computers and Geosciences*, **30**, 455 – 459.

Cooper, G.R.J. and Cowan, D.R. 2005. Differential reduction to the pole. *Computers and Geosciences*, **31**, 989 – 999.

Cooper, G.R.J., Webb, S.J., Gibson, R.L., and Martinez, I. 2010. A possible new impact structure in the Okavango Delta, Botswana. *In*: Gibson, R.L., and Reimold, W.U. (Eds.), Large Meteorite Impacts and Planetary Evolution IV, *Geological Society of America*, *Special Paper 465*, 191 – 199.

Corbo-Camargo, F., Arzate-Floresm J.A., Álverez-Béjar, R., Aranda-Gómez, J.J., and Yutsis, V. 2013. Subduction of the Rivera plate beneath the Jalisco block as imaged by magnetotelluric data. *Revista Mexicana de Ciencias Geológicas,* **30** (2), 268 – 281.

Cordell, L., and Grauch, V.J.S. 1985. Mapping basement magnetisation zones from aeromagnetic data in the San Juan basin, New Mexico. *In*: Hinze, W.J. (Ed.), The utility of regional gravity and magnetic anomaly maps. *Society of Exploration Geophysicists*, 181 – 198.

Corner, B. 1977. A geophysical investigation of the area surrounding Dordabis in South West Africa. *Unpublished* MSc. *Thesis*, University of the Witwatersrand, Johannesburg, South Africa, 71 pp.

Corner, B. 1982. An interpretation of the aeromagnetic data covering portion of the Damara Orogenic Belt, with special reference to the occurrence of uraniferous granite. *Unpublished Ph.D. Thesis,* University of the Witwatersrand, Johannesburg, South Africa, 115 pp.

Corner, B. 1983. An interpretation of the aeromagnetic data covering the western portion of the Damara Orogen in South West Africa/Namibia. *In*: Miller, R.McG. (Ed.), *Evolution of the Damara Orogen of South West Africa/Namibia*, *Geological Society of South Africa, Special publication*, **11**, 339 – 354.

Corner, B. 1998. A geophysical perspective of the Kaapvaal Province. *In:* Durrheim, R.J., and Webb, S.J. (Eds.), *Southern African Geophysical Review, special issue: geophysical framework of the Kaapvaal Craton,* **2**, 19 – 28.

Corner, B. 2000. Crustal framework of Namibia derived from magnetic and gravity data. *In*: Miller, R.McG. (Ed.), *Henno* Martin Commemorative volume. *Communications of the Geological Survey of Namibia*, **12**, 13 – 19.

Corner, B. 2008. The crustal framework of Namibia derived from an integrated interpretation of geophysical and geological data. *In:* Miller, R. McG. (Ed.), *The Geology of Namibia*, **1**, *Archaean to Mesoproterozoic*, Ministry of Mines and Energy, Geological Survey of Namibia, Windhoek, 2-1 – 2-19.

Cowan, I. M., and Pollack, H.N. 1977. Gravity in Zambia. *Nature*, **266**, 615 – 617.

Coward, M.P. 1983. The tectonic history of the Damara Belt. *Special Publication of the Geological Society of South Africa*, **11**, 409 – 421.

Cozzi, A., Allen, P.A., and Grotzinger, J.P. 2004. Understanding carbonate ramp dynamics using $\delta^{13}C$ profiles: Examples from the Neoproterozoic Buah Formation of Oman. *Terra Nova*, **16**, 62 – 67.

Craig, H. 1953. The geochemistry of the stable carbon isotopes. *Geochimica et Cosmochimica Acta*, Pergamon Press Ltd, London, **3**, 53 – 92.

de Beer, J.H., Gough, D.I., and van Zijl, J.S.V. 1975. An electrical conductivity anomaly and rifting in southern Africa, *Nature*, **225**, 678 – 680.

de Beer, J.H., Huyssen, R.M.J., Joubert, S.J., and van Zijl, S.V.V. 1982. Magnetometer array studies and seep Schlumberger soundings in the Damara orogenic belt, South West Africa. *Geophysical Journal International*, **70** (1), 11 – 29.

de Beer, J.H., van Zijl, J.S.V., Huyssen, R.M.J., Hugo, P.L.V., Joubert, S.J., Meyer, R. 1976. A magnetometer array study in South-West Africa, Botswana and Rhodesia. *Geophysical Journal International*, **45**, 1 – 17.

de Groot-Hedlin, C. 1991. Short Note: Removal of static shift in two dimensions by regularized inversion. *Geophysics*, **56** (12), 2 102 – 2 106.

de Groot-Hedlin, C. 1995. Inversion for regional 2-D resistivity structure in the presence of galvanic scatters. *Geophysical Journal International*, **122**, 877 – 888.

de Kock, G.S. 1991. The mafic Audawib Suite in the Central Damara orogeny of Namibia: geochemical evidence for volcanic arc volcanism. *Journal of African Earth Science*, **12**, 593 - 599.

de Kock, G.S. 1992. Forearc basin evolution in the Pan-African Damara Belt, central Namibia: the Hureb Formation of the Khomas Zone. *Precambrian Research*, **57**, 169 – 194.

de Kock, G.S. 2001. A reappraisal of the Namibian Damara stratigraphy in part of the Southern Swakop Terrane and its implications to basin evolution. *South African Journal of Geology*, **104**, 115 - 136.

de Sigoyer, J., Guillot, S., and Dick, P. 2004. Exhumation of the ultrahigh-pressure Tso Morari Unit in eastern Ladakh (NW Himalaya); a case study. *Tectonics*, **23**,TC3003.

Dentith, M., and Mudge, S.T. 2014. Geophysics for the mineral exploration geoscientist. Cambridge University Press, United Kingdom. 516 pp.

Dewey, J.F., and Bird, J.M. 1970. Mountain belts and the new global tectonics. *Journal of Geophysical Research*, **75**, 2 625 – 2 647.

Dill, H.G., Pöllmann, H., Bosecker, K., Hahn, L., and Mwiya, S. 2002. Supergene mineralization in mining residues of the Matchless cupreous pyrite deposit (Namibia) –a clue to the origin of modern and fossil duricrusts in semiarid climates. *Journal of Geochemical Exploration*, **75**, 43 – 70.

Domack, E.W., and Hoffman, P.F. 2011. An ice grounding-line wedge from the Ghaub glaciation (635 Ma) on the distal foreslope of the Otavi carbonate platform, Namibia, and its bearing on the snowball Earth hypothesis. *Geological Society of America Bulletin*, **123** (7/8), 1448 – 1477.

Dowling, F. 1970. Magnetotelluric measurements across the Wisconsin Arch. *Journal of Geophysical Research*, **75** (14), 2 683 – 2 698.

Downing, K.N., and Coward, M.P. 1981. The Okahandja Lineament and its significance for the Damara tectonics in Namibia. *Geological Research*, **70**, 972 – 1 000.

Duba, A.G., Huenges, E., Nover, G., Will, G., and Jödicke, H. 1989.Impedance of black shale from Münsterland I borehole: an anomalous good conductor? *Journal of Geophysics*, **94**, 413 – 419.

Duncan, P.M., Hwang, A., Edwards, R.N., Bailey, R.C., and Garlands, G.D. 1980. The development and applications of a wide band electromagnetic sounding system using a pseudo-noise source. *Geophysics*, **45** (8), 1 276 – 1 296.

Dziggel, A., Wulf, K., Kolb, J., and Meyer, F.M. 2009. Processes of high-T fluid-rock interaction during gold mineralisation in carbonate-bearing metasediments: the Navachab gold deposit, Namibia. *Miner Deposita*, **44**, 665 – 687.

Eberle, D., Hutchins, D.G., Rebbeck, R.J., and Somerton, I. 1996. Compilation of the Namibian airborne magnetic surveys: procedures, problems and results. *Journal of African Sciences,* **22**, 191 – 205.

Eberle, D.G., Andritzky, G., Hutchins, D.G., and Wackerle, R. 2002. The regional magnetic data set of Namibia: Compilation, contributions to crustal studies and support to natural resource management. *South African Journal of Geology*, **105**, 361 – 380.

Epard, J.-L., and Steck, A. 2008. Structural development of the Tso Morari ultra-high pressure nappe of the Ladakh Himalaya. *Tectonophysics*, **451**, 242 – 264.

Etheridge, M.A., and Wall., V.J. 1983. The role of the fluid phase during regional metamorphism and deformation. *Journal of metamorphic geology*, **1**, 205 – 226.

Ferraccioli, F., Coren, F., Bozzo, E., Zanolla, C., Gandolfi, S., Tabacco, I., and Frezzotti, M. 2001. Rifted(?) crust at the East Antarctic Craton margin: gravity and magnetic interpretation along traverse across the Wilkes Subglacial Basin region. *Earth and Planetary Science Letters*, **192**, 407 – 421.

FitzGerald, D., Reid, A.B. and McInerney, P. 2004. New discrimination techniques for Euler deconvolution. *Computers and Geosciences,* **30**, 461 - 469.

Foster, D.A., Goscombe, B.D., Newstead, B., Mapani, B., Mueller, P.A., Gregory, L.C., and Muvangua, E. 2014. U–Pb age and Lu–Hf isotopic data of detrital zircons from the Neoproterozoic Damara Sequence: Implications for Congo and Kalahari before Gondwana. *Gondwana Research*, http://dx.doi.org/10.1016/j.gr.2014.04.011

Frimmel, H.E. 2010. On the reliability of stable carbon isotopes for Neoproterozoic chemostratigraphy correlation. *Precambrian Research*, **182**, 239 – 253.

Frimmel, H.E., and Miller, R. 2009. Continental rifting. Neoproterozoic to Early Palaeozoic evolution of southwestern Africa. *In*: Gaucher, C., Sial, A.N., and Frimmel, H.E. (Eds.), Neoproterozoic-Cambrian tectonics, global change and evolution: a focus on southwestern Gondwana. *Developments in Precambrian Geology*, **16**, 153 – 159.

Frimmel, H.E., Basei, M.S. and Gaucher, C. 2011. Neoproterozoic geodynamic evolution of SW-Gondwana: a southern African perspective. *International Journal of Earth Sciences*, **100**, 323 - 354.

Gaisford, J. 2010. Geochronology, petrography and tectonic implications of lithologies and base metal mineralisation encountered in NW Ngamiland, Botswana, *Unpublished Honours Thesis,* University of Cape Town, Cape Town, South Africa, 63 pp.

Garcia, X., and Jones, A.G. 2002. Atmospheric sources for audio-magnetotelluric (AMT) sounding. *Geophysics*, **67** (2), 448 – 458.

Geiger, H. D., and Cook, F. A. 2001. Analyses of crustal structure from bandpass and directionally filtered potential-field data: an example from western Canada, *Canadian Journal of Earth Science*, **38** (1), 953 – 961.

Geological Survey of Namibia. 1998. Ministry of Mines, annual report 1997: Earth Sciences for Namibia's sustainable development. *Geological Survey of Namibia, Windhoek*, 16 pp.

Geological Survey of Namibia. 2000. Ministry of Mines, annual report 1999: Earth Sciences for Namibia's sustainable development. *Geological Survey of Namibia, Windhoek*, 28 pp.

Geological Survey of Namibia. 2001. Ministry of Mines, annual report 2000: Earth Sciences for Namibia's sustainable development. *Geological Survey of Namibia, Windhoek*, 28 pp.

Geological Survey of Namibia. 2003a. Ministry of Mines, annual report 2002: Earth Sciences for Namibia's sustainable development. *Geological Survey of Namibia, Windhoek*, 28 pp.

Geological Survey of Namibia. 2003b. Ministry of Mines, annual report 2004: Earth Sciences for Namibia's sustainable development. *Geological Survey of Namibia, Windhoek*, 28 pp.

Germs, G.J.B. 1983. Implications of a sedimentary facies and depositional environmental analysis of the Nama Group in South West Africa/Namibia. *In*: Miller, R.McG. (Ed.), *Evolution of the Damara Orogen of South West Africa/Namibia*, *Geological Society of South Africa, Special publication*, **11**, 339 – 354.

Germs, G.J.B., Miller, R.McG., Frimmel, H.E., and Gaucher, C. 2009. Syn-to late-orogenic sedimentary basins of southwestern Africa. Neoproterozoic to Early Palaeozoic evolution of southwestern Africa. *In*: Gaucher, C., Sial, A.N., Halverson, G.P., and Frimmel, H.E. (Eds.), Neoproterozoic-Cambrian tectonics, global change and evolution; a focus on southwestern Gondwana. *Developments in Precambrian Geology*, **16**, 183 – 203.

Gerner, R. 2011. Geology and mineralisation in the Precambrian basement of northwest Botswana and their geological significance. *Unpublished Honours Thesis,* University of Cape Town, Cape Town, South Africa, 55 pp.

Giese, P., Jödicke, H., Prodehl, C., Weber, K. 1983. The crustal structure of the Hercynian mountain system--a model for crustal thickening by stacking. *In*: Martin, H., and Eder, F.W. (Eds.), *lntracontinental Fold Belts,* Springer Verlag, Berlin, 405 - 426.

Gordon-Welsh, J.F., Kleywegt, R.J., Venter, C.P., du Plessis, A., Beukes, J.H.T., and du Plessis, J.G. 1986. Regional gravity surveys by the Geological Survey – Data acquisition, reduction and presentation. *Annals of the Geological Survey of South Africa*, **20**, 59 – 68.

Goscombe, B., and Gray, D.R. 2008. Structure and strain variation at mid-crustal levels in a transpressional orogen: A review of Kaoko Belt structure and the character of West Gondwana amalgamation and dispersal. *Gondwana Research*, **13**, 45 – 85.

Goscombe, B., Armstrong, R., and Barton, J.M. 2000. Geology of the Chewore Inliers, Zimbabwe: constraining the Mesoproterozoic to Palaeoozoic evolution of the Zambezi Belt. *Journal of African Earth Sciences*, **30** (3), 589 – 627.

Goscombe, B., Gray, D., and Hand, M. 2005. Extrusional tectonics in the core of a transpressional orogen; the Kaoko Belt, Namibia. *Journal of Petrology*, **46** (6), 1 203 – 1 241.

Goscombe, B., Gray, D.R., and Hand, M. 2004. Variation in metamorphic style along the northern margin of the Damara orogen, Namibia. *Journal of Petrology*. **45**, 1 261 – 1 295.

Goscombe, B., Hand, M., Gray, D., and Mawbay, J. 2003. The metamorphic architecture of a transpressional orogen: the Kaoko Belt, Namibia. *Journal of Petrology*, **44**, 679 – 711.

Gough, D.I. 1983. Electromagnetic geophysics and global tectonics. *Journal of Geophysical Research*, **88**, 3 367 – 3 377.

Gough, D.I. 1986. Seismic reflectors, conductivity, water and stress in the continental crust. *Nature*, **323**, 143 – 144.

Grant, F.S. 1985. Aeromagnetics, geology and ore environments, I. Magnetite in igneous, sedimentary and metamorphic rocks. An overview. *Geoexploration*, **23**, 303 – 333.

Gray, D.R., Foster, D.A., Goscombe, B., Passchier, C.W., Trouw, R.A.J. 2006. $^{40}Ar/^{39}Ar$ thermochronology of the Pan-African Damara Orogen, Namibia, with implications for tectonothermal and geodynamic evolution. *Precambrian Research*, **150**, 49 – 72.

Gray, D.R., Foster, D.A., Maas, R., Spaggiari, C.V., Gregory, R.T., Goscombe, B., and Hoffmann, K.H. 2007. Continental growth and recycling by accretion of deformed turbidite fans and remnant ocean basins: Examples from Neoproterozoic and Phanerozoic orogens. *In:* Hatcher, R.D., Jr., Carlson, M.P., McBride, J.H., and Martínez Catalán, J.R., (Eds.), 4-D Framework of Continental Crust: *Geological Society of America Memoir 200*, 63 – 92.

Gray, D.R., Foster, D.A., Meert, J.G., Goscombe, B.D., Armstrong, R., Trouw, R.A.J., and Passchier, C.W. 2008. A Damara orogen perspective on the assembly of southwestern Gondwana. *In:* Pankhurst, R.J., Trouw, R.A.J., Brito Neves, B., De Wit, M.J. (Eds.), West Gondwana: Pre-Cenozoic correlations across the South Atlantic region. *Geological Society, London, Special Publications*, **294**, 257 – 278.

Green, A.G., Hajnal, Z., and Weber, W. 1985. An evolutionary model of the western Churchill Province and western margin of the Superior Province in Canada and the northcentral United States. *Tectonophysics*, **116**, 281 - 322.

Green, R. W. E. 1983. Seismic refraction observations in the Damara Orogen and flanking craton and their bearing on deep seated processes in the orogen. *In*: Miller, R.McG (Ed.), The Pan-African Damara Orogen of South West Africa Namibia. Special Publication of the Geological Society of South Africa, **11**, 355 - 367.

Groom, R. W., Kurtz, R.D. Jones, A.G., and Boerner, D.E. 1993. A quantitative methodology for determining the dimensionality of conductive structure from magnetotelluric data, *Geophysical Journal International*, ***115*,** 1 095 - 1 118.

Groom, R.W. 1988. The effects of inhomogeneities on magnetotellurics. *Unpublished Ph.D. Thesis*, University of Toronto, Ontario, Canada.

Groom, R.W., and Bahr, K. 1992. Corrections for near surface effects: Decomposition of the magnetotelluric impedance tensor and scaling corrections for regional resistivities: A tutorial. *Surveys of Geophysics*, **13** (4-5), 341 – 379.

Groom, R.W., and Bailey, R.C. 1989. Decomposition of magnetotelluric impedance tensors in the presence of the local three-dimensional galvanic distortion. *Journal of Geophysics Research*, **94**, 1 913 – 1925.

Grotzinger, J.P., and Miller, R.McG. 2008. Nama Group. *In*: Miller, R.McG. (Ed.), The geology of Namibia, **2**, Geological Survey of Namibia, Windhoek. Ministry of Mines and Energy, Geological Survey, **2**, 12-229 – 12-283.

Grotzinger, J.P., Bowring, S.A., Saylor, B.Z., and Kaufman, A.J. 1995. Biostratigraphy and geochronologic constraints on early animal evolution. *Science*, **270**, 598 – 604.

Haak, V., and Hutton, R. 1986. Electrical resistivity in continental lower crust. *Geological Society of London, Special Publications*, **24**, 35 – 49.

Haddon, I, G., and McCarthy, T.S. 2005. The Mesozoic-Cenozoic interior sag basins of Central Africa: The Late-Cretaceous-Cenozoic Kalahari and Okavango basins. *Journal of African Earth Science*, **43**, 316 – 333.

Haddon, I.G. 2001. Sub-Kalahari Geological Map. 1:2 500 000 scale. Council for Geoscience, South Africa.

Hall, M., Kaufman, A.J., Vickers-Rich, P., Ivanstov, A., Trusler, P., Linnemann, U., Hofmann, M., Elliot, D., Cui, H., Fedonkin, M., Hoffmann, K.-H., Wilson, S.A., Schneider, G., and Smith, J. 2013. Stratigraphy, palaeontology and geochemistry of the late Neoproterozoic Aar Member, southwest Namibia: Reflecting environmental controls on Ediacara fossil preservation during the terminal Proterozoic in African Gondwana. *Precambrian Research*, **238**, 214 – 232.

Hall, W.S. 2013. Geology and paragenesis of the Boseto Copper deposit, Kalahari Copperbelt, northwest Botswana. *Unpublished MSc. Thesis*, Colorado School of Mines, Colorado, United States of America, 157 pp.

Halverson, G.P. 2002. Towards a composite δ^{13}C reference section for the Neoproterozoic. Abstracts of the *American Geophysical Union, Fall Meeting 2002*,San Francisco, California, 6th to 10th December.

Halverson, G.P., Hoffman, P.F., Schrag, D.P., Maloof, A.C., and Rice, A.H.N. 2005. Toward a Neoproterozoic composite carbon-isotope record. *Geological Society of America Bulletin*, **117** (9-10), 1 181 – 1 207.

Halverson, G.P., Maloof, A.C., and Hoffman, P.F. 2004. The Marinoan glaciation (Neoproterozoic) in Svalbard. *Basin Research*, **16**, 297 – 324.

Halverson, G.P., Wade, B.P., Hurtgen, M.T., and Barovich, K.M. 2010. Neoproterozoic chemostratigraphy. *Precambrian Research*, **182**, 337 – 350.

Hamilton, M.P., Jones, A.G., Evans, R.L., Evans, S., Fourier, C.J.S., Carcia, X., Mountford, A., and Spratt, J.E. 2006. Electrical anisotropy of South African lithosphere compared with seismic anisotropy form shear-wave splitting analyses. *Physics of the Earth and Planetary Interiors*, **158**, 226 – 239.

Hansen, R.O. and Miyazaki, Y. 1984. Continuation of potential fields between arbitrary surfaces. *Geophysics*, **6**, 787 - 795.

Hanson, R. E., Crowley, J. L., Bowring, S. A., Ramezani, J., Gose, W. A., Dalziel, I. W. D., Pancake, J. A., Seidel, E. K., Blenkinsop, T. G. and Mukwakwami, J. 2004. Coeval Large-scale Magmatism in the Kalahari and Laurentian Cratons during Rodinia assembly. *Science*, **304**, 1 126 – 1 129.

Hanson, R.E., Martin, M.W., Bowring, S.A., and Munyanyiwa, H. 1998. U-Pb zircon age for the Umkondo dolerites, eastern Zimbabwe: 1.1 Ga large igneous province in southern Africa-East Antarctica and possible Rodinia correlations. *Geology*, **26**, 1 143 – 1 146.

Hanson, R.E., Wardlaw, M.S., Wilson, T.J., and Mwale, G. 1993. U-Pb zircon ages from the Hook granite massif and Mwembeshi dislocation: constraints on Pan-African deformation, plutonism, and transcurrent shearing in central Zambia. *Precambrian Research*, **63**, 189 – 209.

Hanson, R.E., Wilson, T.J., and Munyanyiwa, H. 1994. Geologic evolution of the Neoproterozoic Zambezi Orogenic Belt in Zambia. *Journal of African Earth Sciences*, **18** (2), 135 – 150.

Hartnady, C., Joubert, P., and Stowe, C. 1985. Proterozoic crustal evolution in southwestern Africa. *Episodes*, **8**, 236 – 244.

Hartnady, C.J. 1978. The stratigraphy and structure of the Naukluft Nappe Complex. *14th and 15th Annual Report, Precambrian Research Unit*, University of Cape Town, 163 – 170.

Häussinger, H., Okrusch, M., and Scheepers, D. 1993. Geochemistry of premetamorphic hydrothermal alteration of Metasedimentary rocks associated with the Gorob Massive Sulphide prospect, Damara orogen, Namibia. *Economic Geology*, **88**, 72 – 90.

Hawkesworth, C.J., and Marlow, A.G. 1983. Isotope evolution of the Damara orogenic belt. *Special publication of the Geological Society of South Africa*, **11**, 397 – 407.

Hawkesworth, C.J., Kramers, J.D., Miller, R., 1981. Old model Nd ages in Namibian Pan-African rocks. *Nature* **289**, 278 – 282.

Heath, D.C. 1972. Die geologie van die Sisteem Karoo in die gebied Mariental-Asab, Suidwes-Afrika. *Memoir of the Geological Survey of South Africa*, **61**, 44 pp.

Hegenberger, W. 1993. Stratigraphy and sedimentology of the Late Precambrian Witvlei and Nama Groups, east of Windhoek. *Geological Survey of Namibia, Memoir*, **17**, 82 pp.

Hegenberger, W., and Burger, A.J. 1985. The Oorlogsende Porphyry Member, South West Africa/Namibia: its age and regional setting. *Communications of Geological Survey of South West Africa/Namibia*, **1**, 23 – 29.

Hendjala, F. 2011. Petrography and chemostratigraphy of the Ghanzi-Chobe Supergroup, Kalahari Copper Belt, Botswana. *Unpublished Honours Thesis,* University of the Witwatersrand, Johannesburg, South Africa, 68 pp.

Henrys, S., Reyners, M., Pecher, I., Bannister, S., Nishimura, Y., and Maslen, G. 2006. Kinking of the subduction slab by escalator normal faulting beneath the North Island of New Zealand. *Geology*, **34**, 777 – 780.

Hoal, B.G. 1993. The Proterzoic Sinclair Sequence in southern Namibia: intracrantonic rift or active continental margin setting? *Precambrian Research*, **63**, 143 – 162.

Hoal, K.O., Hoal, B.G., Griffin, W.L., and Armstrong, R.A. 2000. Characterization of the age and nature of the lithosphere in the Tsumkwe region, Namibia. *In*: Miller, R.McG. (Ed.), *Special Issue: Henno Martin Commemorative Volume*. Communications of the Geological Survey of Namibia, **12**, 21 – 28.

Hoffman, K.H. 1989. New aspects of lithostratigraphic subdivision and correlation of Late Proterozoic to Early Cambrian rocks of the southern Damara belt and their correlation with the central and northern Damara belt and the Gariep belt. *In*: Hoal, B.G. (Ed.), *Communications of the Geological Survey of Namibia*, **5**, 59 – 67.

Hoffman, P.F. 2005. On Cryogenian (Neoproterozoic) ice-sheet dynamics and the limitations of the glacial sedimentary record. *South African Journal of Geology*, **108**, 557 – 577.

Hoffman, P.F. 2011. Glaciogenic and associated strata of the Otavi carbonate platform and foreslope, northern Namibia: evidence for large base-level and glacioeustatic changes. *In*: Arnaud, E., Halverson, G.P., and Shields-Zhou, G. (Eds.), The geological record of Neoproterozoic glaciations. *Geological Society, London, Memoirs*, **36**, 195 – 209.

Hoffman, P.F., and Halverson, G.P. 2008. Otavi Group of the western Northern Platform, the Eastern Kaoko Zone and the western Northern Margin Zone. *In*: Miller, R.McG. (Ed.), The geology of Namibia, *Geological Survey of Namibia*, Windhoek. Ministry of Mines and Energy, Geological Survey, **2**, 13-69 – 13-136.

Hoffman, P.F., and Schrag, D.P. 2002. The snowball Earth hypothesis: Testing the limits of global change. *Terra Nova*, **14**, 129 – 155.

Hoffman, P.F., Hawkins, D.P., Isachsen, C.E., and Bowring, S.A. 1996. Precise U-Pb zircon ages for early Damaran magmatism in the Summas Mountains and Welwitschia inlier; northern Damara belt, Namibia. *In*: Groenewald, P.B. (Ed.), *Geological Survey of Namibia Communications*, **11**, 47 – 52.

Hoffman, P.F., Kaufman, A.J., Halverson, G.P., and Schrag, D.P. 1998. A Neoproterozoic snowball earth. *Science*, **281**, 1 342 – 1 346.

Hoffman, P.F., Swart, R., Freyer, E.E. and Guowei, H. 1994. Damara Orogen of Northwest Namibia. *In*: Niall, M., McManus, C. (Eds.), Geological Excursion Guide of the international conference Proterozoic crustal and metallogenic evolution. *Geological Society and the Geological Survey of Namibia*, 55 pp.

Hoffmann, K.H. 1983. Lithostratigraphy and facies of the Swakop Group of the southern Damara Belt, SWA/Namibia. *In:* Miller, R.McG (Ed.), Evolution of the Damara orogen. *Geological Society of South Africa, Special publication*, **11**, 11 – 43.

Hoffmann, K.H. 1989. New aspects of lithostratigraphic subdivision and correlation of Late Proterozoic to Early Cambrian rocks of the southern Damara Belt and their correlation with the central and northern Damara Belt and the Gariep Belt. *Communications of the Geological Survey of Namibia*, Windhoek, **5**, 59 – 67.

Hoffmann, K.H., and Prave, A.R. 1996. A preliminary note on a revised subdivision and regional correlation of the Otavi Group based on glaciogenic diamictites and associated cap dolostones. *In*: Groenewald, P.B. (Ed.), *Communications of the Geological Society of Namibia*, **11**, 77 – 82.

Hoffmann, K.-H., Condon, D.J., Bowring, S.A. and Crowley, J.L. 2004. U-Pb zircon date from the Neoproterozoic Ghaub Formation, Namibia: Constraints on Marinoan glaciation. *Geology*, **32**, 817 - 820.

Hugo, P.J., and Schalk, K.E.L. 1974. The isotopic ages of certain granites and acid lavas in the Rehoboth and Maltahohe Districts, South West Afri*ca. Annals of the Geological Survey of South Africa*, **9**, 103 - 105.

Hurtgen, M.T., Arthur, M.A., Suits, N.S., and Kaufman, A.J. 2002. The sulfur isotopic composition of Neoproterozoic seawater sulphate: implications for a snowball Earth? *Earth and Planetary Science Letters*, **203**, 413 – 429.

Hurtgen, M.T., Halverson, G.P., Arthur, M.A., and Hoffman, P.F. 2006. Sulfur cycling in the aftermath of a 635-Ma snowball glaciation: Evidence for a syn-glacial deep ocean. *Earth and Planetary Science Letters*, **245**, 551 – 570.

Hutchins, D.G., and Reeves, C.V. 1980. Regional geophysical exploration of the Kalahari in Botswana. *Tectonophysics*, **69**, 201 – 220.

Hutchins, D.G., Hutton, L.G., Hutton, S.M., Jones, C.R., and Loenhert, E.P. 1976. A summary of the geology, seismicity, geomorphology and hydrogeology of the Okavango Delta. *Geological Survey Department, Bulletin Series,* **7**, 1 – 39.

Hyndman, R.D. and Hyndman, D.W. 1968. Water saturation and high electrical conductivity in the lower continental crust. *Earth and Planetary Science Letter,* **4**, 427 - 432.

Irving, E. 1964. Paleomagnetism and its application to geological and geophysical problems. John Wiley and Sons, Inc., United States of America, New York. 399 pp.

Isaacs, K.N., 1968. Interpretation report of an airborne geophysical survey in the Republic of Zambia for the Geological Survey of Zambia, *Unpublished Report,* Canadian Aero Services Ltd.

Ivan, M. 1986. On the upward continuation of potential field data between irregular surfaces. *Geophysical prospecting*, **34**, 735 - 742.

Jacob, R.E. 1974. Geology and metamorphic petrology of part of the Damara orogen along the Lower Swakop River, South West Africa. *Bulletin of the Precambrian Research Unit*, *University of Cape Town*, **17**, 185 pp.

Jacob, R.E., Kröner, A., and Burger, A.J. 1978. Areal extent and first U-Pb age of the pre-Damaran Abbabis Complex in the central Damara belt of South West Africa (Namibia). *Geologische Rundschau*, **67**, 706 – 718.

Jacobs, J., Pisarevsky, S., Thomas, R.J., and Becker, T. 2008. The Kalahari Craton during the assembly and dispersal of Rodinia. *Precambrian Research*, **160**, 142 – 158.

Jamieson, R.A., and Beaumont, C. 2013. On the origin of orogens. *Geological Society of America Bulletin*, *Invited Review*. doi: 10.1130/B30855.1

Jamieson, R.A., Beaumont, C., Medvedev, S., and Nguyen, M.H. 2004. Crustal channel flows: 2. Numerical models with implications for metamorphism in the Himalayan-Tibetan orogen. *Journal of Geophysical Research*, **109**, B06407.

Jamieson, R.A., Beaumont, C., Nguyen, M.H., and Culshaw, N.G. 2007. Synconvergent ductile flow in variable strength continental crust: Numerical models with application to the western Grenville orogen: *Tectonics*, **26**, TC5005.

Jasper, M.J., Stanistreet, I.G., and Charlesworth, E.G. 1995. Opening and closure of the Adamastor Ocean: The Gariep Belt (southern Namibia) as a late Proterozoic/early Palaeozoic example of a Wilson Cycle. *In*: Wendorff, M., and Tack, L. (Eds.), Late Proterozoic Belts in Central and Southwestern Africa, IGCP Project 302. Annalen-Geologische Wetenschappen, Koninklijk Museum voor Midden-Afrika, Tervuren, Belgium, **101**, 143 – 161.

Jiracek, G.R. 1990. Near-surface and topography distortion in electromagnetic induction. *Surveys in Geophysics*, **11**, 163 – 203.

Jödicke, H., Untiedt, J., Olgemann, W., Schulte, L., and Wagenitz, V. 1983. Electrical conductivity structure of the crust and upper mantle beneath the Rhenish Massif. *In*: Fuchs, K., von Gehlen, K., Mälzer, H., Murawski, H., and Semmel, A. (Eds.), Plateau Uplift, Springer Verlag, Berlin, Heidelberg, 288 – 362.

John, T., Schenk, V., Haase, K., Scherer, R., and Tembo, F. 2003. Evidence for a Neoproterozoic ocean in South-central Africa from mid-oceanic ridge- type geochemical signatures and pressure–temperature estimates of Zambian eclogites. *Geology*, **31**, 243 - 246.

John, T., Schenk, V., Mezger, K., and Tembo, F. 2004. Timing and PT evolution of whiteschist metamorphism in the Lufilian arc-Zambezi belt orogen (Zambia): implications for the assembly of Gondwana. *The Journal of Geology*, **112**, 71 - 90.

Johnson, M.R., Van Vuuren, C.J., Hegenberger, W.F., Key, R., and Shoko, U. 1996. Stratigraphy of the Karoo Supergroup in southern Africa: an overview. *Journal of African Sciences,* **23** (1), 3 – 15.

Johnson, S.P., De Waele, B., Liyungu and K.A. 2006. U-Pb sensitive high-resolution ion microprobe (SHRIMP) zircon geochronology of granitoid rocks in eastern Zambia: Terrane subdivision of the Mesoproterozoic Southern Irumide Belt, *Tectonics*, **25**, TC6004.

Jones, A.G. 1981. On a type classification of lower crustal layers under Precambrian regions. *Journal of Geophysics*, **49**, 226 – 233.

Jones, A.G. 1982. On the electrical crust-mantle structure in Fennoscandia: no Moho, and the asthenosphere revealed? *Geophysical Journal of the Royal Astronomical Society*, **68**, 371 – 388.

Jones, A.G. 1983a. On the equivalence of the “Niblett” and “Bostick” Transformation in the magnetotelluric method. *Journal of Geophysics, Letter to the Editor*, **53**, 72 – 73.

Jones, A.G. 1983b. The electrical structure of the lithosphere and asthenosphere beneath the Fennoscandian Shield. *Journal of Geomagnetism and Geoelectricity*, **35**, 811 – 827.

Jones, A.G. 1993. Electromagnetic images of modern and ancient subduction zones. *In:* Green, A.G., Kröner, A., Götze, H.-J., and Pavlenkova, N. (Eds.), Plate tectonic signatures in the continental lithosphere, *Tectonophysics*, **219**, 29 – 45.

Jones, A.G. 2006. Electromagnetic interrogation of the anisotropic Earth: Looking into the Earth with polarized spectacles. *Physics of the Earth and Planetary Interiors*, **158**, 281 – 291.

Jones, A.G., and Craven, J.A. 1990. The North American Central Plains conductivity anomaly and its correlation with gravity, magnetic, seismic, and heat flow data in Saskatchewan, Canada. *Physics of the Earth and Planetary Interiors*, **60**, 169 – 194.

Jones, A.G., and Groom, R.W. 1993. Strike angle determination from the magnetotelluric tensor in the presence of noise and local distortion: rotate at your peril! *Geophysical Journal International*, **113**, 524 – 534.

Jones, A.G., and Hutton, R. 1979. A multi-station magnetotelluric study in southern Scotland – I. Fieldwork, data analysis and results. *Geophysical Journal of the Royal Astronomical Society*, **56**, 329 – 349.

Jones, A.G., Chave, A.D., Egbert, G., Auld, D., and Bahr, K. 1989. A comparison of techniques for magnetotelluric response function estimation. *Journal of Geophysical Research: Solid Earth*, **94**, 14 201 – 14 213.

Jones, A.G., Craven, J.A., McNeice, G.A., Ferguson, I.J., Boyce, T., Farquharson, C., and Ellis, R.G. 1993. North American Central plains conductivity anomaly within the Trans-Hudson Orogen in northern Saskatchewan, Canada. *Geology*, **21**, 1 027 – 1 030.

Jones, A.G., Evans, R.L., Muller, M.R., Hamilton, M.P., Miensopust, M.P., Garcia, X., Cole, P., Ngwisanyi, T., Hutchins, D., Fourie, C.J.S., Jelsma, H., Evans, S., Aravanis, T., Pettit, W., Webb, S., Wasborg, J., and the SAMTEX Team. 2009. Area selection for diamonds using magnetotellurics: Example from South Africa. *Lithos*, **112s**, 83 – 92.

Jones, A.G., Fullea, J., Evans, R.L., and Muller, M.R. 2012. Water in cratonic lithosphere: Calibrating laboratory-determined models of electrical conductivity of mantle minerals using geophysical and petrological observations. *Geochemistry Geophysics Geosystems*, **13** (6), 1 – 27.

Jones, A.G., Ledo, J., and Ferguson, I.J. 2005. Electromagnetic images of the Trans-Hudson orogen: the Northern American Central Plains anomaly revealed. *Canadian Journal of Earth Science*, **42**, 457 – 478.

Jones, A.G., Muller, M.R., Miensopust, M.P., Hamilton, M.P., Spratt, J.E., Garcia, X., Evans, R.L., Evans, S.F., Mountford, A., Petit., W., Cole, P., Ngwisanyi, T., Hutchins, D., Fourie. C.J.S., and the SAMTEX Team. 2007. Southern African MagnetoTelluric EXperiment (SAMTEX): Project overview and regional results. *10th SAGA Biennial Technical Meeting and Exhibition*, short paper, 4 pp.

Jones, M.Q.W. 1998. A review of heat flow in southern Africa and the thermal structure of the lithosphere. *In*: Durrheim, R.J., and Webb, S.J. (Eds.), *Southern Africa Geophysical review, special issue: geophysical framework of the Kaapvaal Craton,* **2**, 115 - 122.

Jourdan, F., Féraud, G., Bertrand, H., Kampunzu, A.B., Tshoso, G., Le Gall, B. Tiercelin, J.J., and Capiez, P. 2004. The Karoo triple junction questioned: evidence from Jurassic and Proterozoic ^{40}Ar/^{39}Ar ages and geochemistry of the giant Okavango dyke swarm (Botswana), Earth *and Planetary Science Letters,* **222**, 989 – 1 006.

Jourdan, F., Féraud, G., Bertrand, H., Kampunzu, A.B., Tshoso, G., Watkeys, M.K., and Le Gall. 2005. Karoo large igneous province: Brevity origin, and relation to mass extinction questioned by new ^{40}Ar/^{39}Ar age data. *Geology*, **33** (9), 745 – 748.

Jung, S., Hoernes, S. and Mezger, K. 2000. Geochronology and petrogenesis of Pan-African, syn-tectonic, S-type and post-tectonic A-type granite (Namibia): products of melting of crustal sources, fractional crystallisation and wall rock entrainment. *Lithos*, **50**, 259 - 287.

Jung, S., Hoernes, S., Mezger, K., 2002. Synorogenic melting of mafic lower crust: constraints from geochronology, petrology and Sr, Nd and O isotope geochemistry of quartz diorites (Damara orogen, Namibia). *Contributions to Mineralogy and Petrology*, **143**, 551 – 566.

Jung, S., Mezger, K., Hoernes, S. 2001. Trace element and isotopic (Sr, Nd, Pb, O) arguments for a mid-crustal origin of Pan-African garnet-bearing S-type granites from the Damara orogen (Namibia). *Precambrian Research*, **110**, 325 – 355.

Kadima, E., Delvaux, D., Sebagenzi, S.N., Tack, L., and Kabeya, S.M. 2011. Structure and geological history of the Congo Basin: an integrated interpretation of gravity, magnetic and reflection seismic data. *Basin Research*, **23**, 499 – 527.

Kahle, B., van Coller, B., Naude, C., Corner, B. and Mackay, W. 2012. Integration of high-resolution heli-mag data with soil sampling to target mineralization in the Kalahari Copperbelt, Botswana. *The Geological Society of Namibia*, *Copper conference*.

Kamona, A.F., and Günzel, A. 2007. Stratigraphy and base metal mineralisation in the Otavi Mountain Land, Northern Namibia-–a review and regional interpretation. *Gondwana Research*, **11**, 396 – 413.

Kampunzu, A.B., Akanyang, P., Mapeo, R.B., Modie, B.N., and Wendorff, M. 1998. Geochemistry and tectonic significance of the Mesoproterozoic Kgwebe metavolcanic rocks in northwest Botswana: implications for the evolution of the Kibaran Namaqua-Natal Belt. *Geological Magazine*, Cambridge University Press, United Kingdom, **135** (5). 669 – 683.

Kampunzu, A.B., and Cailteux, J. 1999. Tectonic evolution of the Lufilian Arc (Central Africa Copper Belt) during Neoproterozoic Pan-African orogenesis. *Gondwana Research*, **2** (3), 401 – 421.

Kampunzu, A.B., Armstrong, R.A., Modisi, M.P., and Mapeo, R.B.M. 2000. Ion microprobe U-Pb ages on detrital zircon grains from the Ghanzi Group: implications for the identification of a Kibaran-age crust in northwest Botswana. *Journal of African Earth Sciences,* Pergamon, Great Britain, **30** (3), 579 – 587.

Kampunzu, A.B., Cailteux, J.L.H., Kamona, A.F., Intiomale, M.M., and Melcher, F. 2009. Sediment-hosted Zn-Pb-Cu deposits in the Central African Copperbelt. *Ore Geology Reviews*, **35**, 263 – 297.

Karato, S. 1990. The role of hydrogen in the electrical conductivity of the upper mantle. *Nature*, **347**, 272 – 273.

Kariya, K.A. and Shankland, T.J. 1983. Electrical conductivity of dry lower crustal rocks. *Geophysics*, **48** (1), 52 – 61.

Kasch, K.W. 1979. A continental collision model for the tectono-thermal evolution of the (southern) Damara Belt. *16th Annual Report, Precambrian Research unit,* University of Cape Town, 102 – 138.

Kasch, K.W. 1983. Regional P-T variations in the Damara Orogen with particular reference to early high-pressure metamorphism along the southern margin. *In*: Miller, R.McG. (Ed.), Evolution of the Damara Orogen of South West Africa/Namibia. *Geological Society of South Africa Special Publication* **11**, 243 - 253.

Kasch, K.W. 1988. Lithostratigraphy and structural geology of the upper Swakop River area east of Okahandja, S.W.A/Namibia. *Communications of the Geological Survey of South West Africa/Namibia*, **4**, 59 – 66.

Katongo, C., Koeberl, C., Reimold, W.U., and Mubu, S. 2002. Remote sensing, field studies, petrography, and geochemistry of rocks in central Zambia: no evidence of a meteorite impact in the area of the Lukanga Swamp. *Journal of African Earth Sciences*, Elsevier, **35**, 365 – 384.

Kaufman, A.J., Sial, A.N., Frimmel., H.E. and Misi, A. 2009. Neoproterozoic to Cambrian palaeoclimitic events in southwestern Gondwana. *In:* Gaucher, C., Sial, A.N., Halverson, G.P., Frimmel., H.E. (Eds.), Neoproterozoic-Cambrian tectonics, global change and evolution: a focus on southwestern Gondwana. *Developments in Precambrian Geology*, **16**, 369 - 388.

Kennedy, W.Q. 1964. The structural differentiation of Africa in the Pan-African (± 500 m.y.) tectonic episode. *8th Annual Report of the Research Institute of African Geology*, University of Leeds, 9 - 11.

Key R.M., Liyungu A.K., Njamu F.M., Somwe V., Banda J., Mosley P.N., and Armstrong R. A. 2001. The western arm of the Lufilian Arc in NW Zambia and its potential for copper mineralization. *Journal of African Earth Sciences*, **33**, 503 - 528.

Key, R.M. and Ayres, N. 2000. The 1998 edition of the National Geological Map of Botswana. 1:1 000 000 scale. *Journal African Earth Sciences*, **30** (3), 427- 451.

Key, R.M., and Mapeo, R.B.M. 1999. The Mesoproterozoic history of Botswana and the relationship of the NW Botswana Rift to Rodinia. *A report on the second annual meeting of IGCP 418 – The Kibaran of southwest Africa*, 118 – 122.

Key, R.M., and Rundle, C.C. 1981. The regional significance of the new isotropic ages from Precambrian windows through the Kalahari Beds in north-western Botswana. *Transactions Geological Society of South Africa*, **84**, 51 – 66.

Kgotlhang, L. 2011. Delineation of targets in the prospecting licences 386-395/2008 using geophysical data. *Unpublished Report for Tsodilo Resources Ltd.*, 28 pp.

Kgotlhang, L., Green, A., and Kinzelbach, W. submitted. Structural and geological mapping of basement below the Kalahari sands mantle using potential field methods, the Okavango Delta, Botswana. 20 pp.

Kgotlhang, L.P. 2008. Application of airborne geophysics in large scale hydrological mapping; Okavango Delta, Botswana. *Unpublished Ph.D. Thesis*, ETH Zurich, Switzerland, 138 pp.

Khoza, T.D., Jones, A.G., Muller, M.R., Evans, R.L., Miensopust, M.P., and Webb, S.J. 2013. Lithospheric structure of an Archean craton and adjacent mobile belt revealed from 2-D and 3-D inversion of magnetotelluric data: Example from southern Congo craton in northern Namibia. *Journal of Geophysical Research: Solid Earth*, **118**, 1 – 20.

Killick, A.M. 1983. Sulphide mineralisation at Gorob and its genetic relationship to the Matchless Member, Damara Sequence, SWA/Namibia. *In*: Miller, R.McG. (Ed.), *Evolution of the Damara Orogen of South West Africa/Namibia, Geological Society of South Africa, Special publication*, **11**, 381 – 384.

Killick, A.M. 1986. A review of the economic geology of northern South West Africa/Namibia. *In:* Anhaeusser, C.R. and Maske, S. (Eds.), *Mineral Deposits of Southern Africa* **2**, Geological Society of South Africa, Johannesburg, 1 709 – 1 717.

Killick, A.M. 2000. The Matchless Belt and associated sulphide mineral deposits, Damara Orogen, Namibia. *Communications of the Geological Survey of Namibia*, **12**, 73 – 80.

Kinabo, B.D., Atekwana, E.A., Hogan, J.P., Modisi, M.P., Wheaton, D.D., Kampunzu, A.B. 2007. Early structural development of the Okavango rift zone, NW Botswana. *Journal of African Earth Sciences*, **48**, 125 – 136.

Kinabo, B.D., Hogan, J.P., Atekwana, E.A., Abdelsalam, M.G., and Modisi, M.P. 2008. Fault growth and propagation during incipient continental rifting: Insights from a combined aeromagnetic and Shuttle Radar Topography Mission digital elevation model investigation of the Okavango Rift Zone, northwest Botswana. *Tectonics*, **27**, 1 – 16.

Kinnaird, J.A. and Nex, P.A.M. 2007. A review of geological controls on uranium mineralisation in sheeted leucogranites within the Damara Orogen, Namibia. *Applied Earth Science*, **116** (2), 68 - 85.

Kisters, A.F.M. 2005. Controls of gold-quartz vein formation during regional folding in amphibolite-facies, marble-dominated metasediments of the Navachab Gold Mine in the Pan-African Damara Belt, Namibia. *South African Journal of Geology*, **108**, 365 – 380.

Kivekäs, L. 1999. Physical properties of carbonate marble samples from the Kisko region, southern Finland. *Geological Survey of Finland, Special Paper*, **27**, 151 – 158.

Klein, J. 1980. The geology of area 2115A. *Unpublished Report and 100 000 map, Geological Survey of Namibia*, 69 pp.

Klever, N. 1984. Stationäre Konvektion in porösen Medien – Numerische Untersuchungen an unterschiedlichen Fragestellungen aus der Hydrothermik and der Schneemetamorphose. *Berliner geowissenschafliche Abhandlungen*, (B), **11**, Verlag von Dietrich Reimer, Berlin, 114 pp.

Knoll, A.H. 2000. Learning to tell Neoproterozoic time. *Precambrian Research*, **100,** 3–20.

Knoll, A.H., and Water, M.R. 1992. Latest Proterozoic stratigraphy and Earth history. *Nature*, **356**, 673 – 677.

Knoll, A.H., Hayes, J.M., Kaufman, A.J., Swett, K., and Lambert, I.B. 1986. Secular variation in carbon isotope ratios from Upper Proterozoic successions of Svalbard and East Greenland. *Nature*, **321**, 832 – 838.

Kozlovsky, Ye. A. 1984. The world's deepest well. *Scientific America*, **251** (6), 98 – 104.

Konopásek, J., Kosler, J., Tacmanová, L., Ulrich, S., and Kitt, S.L. 2008. Neoproterozoic igneous complex emplaced along major tectonic boundary in the Kaoko Belt (NW Namibia): ion probe and LA-ICP-MS dating of magmatic and metamorphic zircons. *Journal of the Geological Society of London*, **165**, 153 – 165.

Kröner, A. 1977. Precambrian mobile belts in southern and eastern Africa—ancient sutures or sites of ensialic mobility. A case for crustal evolution towards plate tectonics. *Tectonophysics*, **40**, 101 - 135.

Kröner, A., 1982. Rb/Sr geochronology and tectonic evolution of the Pan-African Damara belt of Namibia, southwestern Africa. *American Journal of Science*, **282**, 1 471 – 1 507.

Kröner, A., Retief, E.A., Compston, W., Jacob, R.E., and Burger, A.J. 1991. Single-grain and conventional zircon dating of remobilized basement gneisses in the central Damara Belt of Namibia. *South African Journal of Geology*, **94**, 379 – 387.

Kukla, C. 1993. Strontium isotope heterogeneities in amphibolite facies, banded metasediments-a case study from the Late Proterozoic Kuiseb Formation of the southern Damara orogen, central Namibia. *Communications of the Geological Survey of Namibia Memoir*, **15**, 139 pp.

Kukla, P.A. 1992. Tectonics and sedimentation of a Late Proterozoic Damaran convergent continental margin. *Khomas Hochland*. *Memoir of the Geological Survey of Namibia*, **12**, 95 pp.

Kukla, P.A., and Stanistreet, I.A. 1991. Record of the Damaran Khomas Hochland accretionary prism in central Namibia: Refutation of an "ensialic" origin of a Late Proterozoic orogenic belt. *Geology*, **19**, 473 - 476.

Kurtz, R.D. 1982. Magnetotelluric interpretation of crustal and mantle structure in the Grenville Province. *Geophysical Journal of the Royal Astronomical Society*, **70**, 373 – 397.

Kurtz, R.D., Delaurier, J.M., and Gupta, J.C. 1986. A magnetotelluric sounding across Vancouver Island detects the subducting Juan De Fuca plate. Nature, **321**, 596 - 599.

Larsen, J.C. 1977. Removal of local surface conductivity effects from low frequency mantle response curves. *Acta Geodaetica, Geophysica et Montanistica Hungarica*, **12**, 183 – 186.

Le Ber, E., Le Heron, D.P., Winterleitner, G., Bosence, D.W.J., Vinning, B.A., and Kamona, F. 2013. Microbialite recovery in the aftermath of the Sturtian glaciation: Insights from the Rastof Formation, Namibia. *Sedimentary Geology*, **294**, 1 – 12.

Le Gall, B., Tshoso, G., Dyment, J., Kampunzu, A.B., Jourdan, F., Féraud, G., Bertrand, H., Aubourg, C., and Vétel, W. 2005. The Okavango giant mafic dyke swarm (NE Botswana): its structural significance within the Karoo Large Igneous Province, *Journal of structural geology*, **27**, 2234 – 2255.

Le Heron, D.P., Busfield, M.E., and Kamona, F. 2013. An interglacial on snowball Earth? Dynamic ice behaviour revealed in the Chuos Formation, Namibia. *Journal of the International Association of Sedimentologists*, *Sedimentology*, **60**, 411 – 427.

Le Pape, F., Jones, A.G., Vozar, J., and Wenbo, W. 2012. Penetration of crustal melt beyond the Kunlun Fault into northern Tibet. *Nature geoscience*, **5**, 330 – 335.

Lehmann, J., Master, S., Rankin, W., Milani, L., Kinnaird, J.A., Naydenov, K.V., Saalmann, and Kumar, M. submitted. New correlations and tectonic setting of the Kalahari Copper Belt in Namibia and Botswana. *Ore Geology Reviews*.

Lehtonen, M.I., Mannien, T.E.T., and Schreiber, U.M. 1995. The geology of the area between the Khan River and the coast, and in the vicinity of Omdel Dam. Mapping report and geochemical study, Finnish-Namibian Geological mapping and maps project. Map 2215A.

Lemaire, J. 1971. Status of the exploration on special prospecting licence 12/70. *Botswana Report*. South Africa Vendome Company (Pty) Ltd.

Li, X. 2006. Understanding 3D analytic signal amplitude. *Geophysics*, **71**, 13 - 16.

Loxton Hunting and Associates. 1981. A photogeological study of the Aha Hills, northwestern Botswana. *Report G.3/81*, Hunting and Associates, Bramley, South Africa.

Longridge, L. 2012. Tectonothermal Evolution of the southwestern Central Zone, Damara Belt, Namibia. *Unpublished Ph.D. Thesis*, University of the Witwatersrand, Johannesburg, South Africa, 524 pp.

Longridge, L., Gibson, R.L., Kinnaird, J.A., and Armstrong, R.A. 2011. Constraining the timing of deformation in the southwestern Central Zone of the Damara Belt, Namibia. *In*: van Hinsbergen, D.J.J., Buiter, S.J.H., Torsvik, T.H., Gaina, C., and Webb, S.J. (Eds.), The formation and evolution of Africa: A synopsis of 3.8 Ga of Earth history. *Geological Society of London special publication*, **357**, 107 – 135.

Lucius, J.E., and von Frese, R.R.B. 1988. Aeromagnetic and gravity constraints on the crustal geology of Ohio. *Geological Society of America Bulletin*, **100**, 104 – 116.

Lüdtke, G., Eberle, D., Van Der Boom, G. 1986. Geophysical, geochemical and geological investigations in the Ngami and Kheis areas of Botswana, 1980 – 1983. *Final Report*. *Bulletin of the Geological Survey of Botswana*, **32**, 319 pp.

Macey, P., and Harris, C. 2006. Stable isotope and fluid inclusion evidence for the origin of the Brandberg West area Sn-W vein deposits, NW Namibia. *Mineralium Deposita*, **41**, 671 – 690.

Maiden, K. J. and Borg, G. 2011. The Kalahari Copperbelt in Central Namibia: Controls on Copper Mineralization. *SEG Newsletter*, **87**, 14 – 19.

Malone, S.J., Meert, J.G., Banerjee, D.M., Pandit, M.K., Tamrat, E., Kamenov, G.D., Pradhan, V.R., Sohl, L.E. 2008. Paleomagnetism and detrital zircon geochronology of the Upper Vindhyan Sequence, Son Valley and Rajasthan, India: A ca. 1000 Ma closure age for the Purana Basin? *Precambrian Research*, **164**, 137 - 159.

Maloof, A.C. 2000. Superposed folding at the junction of the inland and coastal belts, Damara orogen, Namibia. *In:* Miller, R. McG. (Ed.), *Henno* Martin Commemorative volume. *Communications of the Geological Survey of Namibia*, **12**, 89 – 98.

Mapani, B., Ellmies, R., Kamona, F., Kříbek, B., Majer, V., Knésl, I., Pašava, J., Mufenda, M., and Mbingeneeko, F. 2010. Potential human health risks associated with historic ore processing at Berg Aukas, Grootfontein area, Namibia. *Journal of African Earth Sciences*, **58**, 634 – 647.

Mapeo, R.B.M., Armstrong, R.A., and Kampunzu, A.B. 2001. SHRIMP U-Pb zircon geochronology of gneisses from the Gweta borehole, northeast Botswana: implications for the Palaeoproterozoic Magondi Belt in southern Africa. *Geological Magazine*, **138** (3), 299 – 308.

Mapeo, R.B.M., Kampunzu, A.B., and Armstrong, R.A. 2000. Ages of detrital zircon grains from Neoproterozoic siliciclastic rocks of the Shakawe area: implications for the evolution of the Proterozoic crust in northern Botswana. *South African Journal of Geology*, **103** (2), 156 – 161.

Mapeo, R.B.M., Ramokate, L.V., Corfu, F., Davis, D.W., and Kampunzu, A.B. 2006. The Okwa basement complex, western Botswana: U-Pb zircon geochronology and implications for Eburnean processes in southern Africa. *Journal of African Earth Sciences*, **46**, 253 – 262.

Mapeo, R.B.M., Wendorff, M., Ramokate, L.V., and Armstrong, R.A. 2008. SHRIMP U-Pb dating of single metamorphic zircon grains from granitoid gneisses and detrital zircons from the Tsodilo quartzites in the

Pan-African Damara Belt, western Botswana: Age constraints, provenance and tectonic evolution. *Abstract, 22nd Colloquium of African Geology, Hammamet, Tunisia*.

Maré, L.P., Oosthuizen, B.C., and Tabane, L.R. 2002. South African geophysical atlas. *Physical properties of South African rocks*, Council for Geoscience, Pretoria, **1**, 37 pp.

Marlow, A. 1983. Geology and Rb-Sr geochronology of mineralised and radioactive granites and alaskites, Namibia *In* Miller, R.McG. (Ed.), *Evolution of the Damara Orogen of South West Africa/Namibia*, *Special Publication of the Geological Society of South Africa*, **11**, 515 pp.

Martí, A., Queralt, P., Jones, A.G., and Ledo, J. 2005. Research note: Improving Bahr's invariant parameters using the WAL approach. *Geophysics Journal International*, **163** (1), 38 – 41.

Martin, H. 1965. The Precambrian geology of South West Africa and Namaqualand. Precambrian Research Unit, University of Cape Town, Cape Town. 159 pp.

Martin, H., and Porada, H. 1977. The intracratonic branch of the Damara orogen in South West Africa I. Discussion of geodynamic models. *Precambrian Research,* **5**, 311 – 338.

Masson Smith, D., and Andrew, E.M. 1962. Gravity meter primary station net in East and Central Africa. *Geophysical Journal of the Royal Astronomical Society*, **7**, 65 – 86.

Master, S. 2009. Neoproterozoic DARCs in the Damara-Lufilian-Zambezi and Ubendian belts and the Western Rift Rise- relics of Rodinia fragmentation at 750 ± 50 Ma. *Abstract Volume: Out of Africa Conference, Wits University of the Witwatersrand, Johannesburg, South Africa*.

Master, S. 2010. Geological report on the Hana Mining Ltd. Copper concessions in the Ghanzi-Chobe Belt of Ngamiland, Botswana. *Unpublished Report*. University of the Witwatersrand, Johannesburg, South Africa, 127 pp.

Master, S. 2013. Aeolian sandstones of the Andara Formation: a Neoproterozoic erg on the Congo Craton of Caprivi, Namibia, its regional correlations, and economic implications. *Abstract, CAG24, 24th Colloquium of African Geology*, *Addis Ababa, Ethiopia*.

Master, S., Hendjala, F., and Kasirye, S. 2012. Isotope chemostratigraphy and sedimentology of the Neoproterozoic Kalahari Copperbelt (Botswana and Namibia): implications for the ages of sedimentation and mineralisation. *Abstract, Namibia copper conference, Geological Society of Namibia*, Windhoek, 13-14 September, 2012.

McDermott, F., Harris, N.B.W., and Hawkesworth, C.J. 1989. Crustal reworking in southern Africa: Constraints from Sr-Nd isotope studies in Archaean to Pan-African terrains. *Tectonophysics*, **161**, 257 – 270.

McDermott, F., Harris, N.B.W., Hawkesworth, C.J., 2000. Geochemical constraints on the petrogenesis of Pan-African A-type granites in the Damara Belt, Namibia. *In*: Miller, R.McG. (Ed.), *Henno Martin Commemorative Volume*, **12**, Communications of the Geological Survey of Namibia, 139 – 148.

McGee, B., Halverson, G.P., and Collins, A.S. 2012. Cryogenian rift-related magmatism and sedimentation: South-western Congo Craton, Namibia. *Journal of African Earth Sciences*, **76**, 34 – 49.

McMullan, S.R., Campbell, C.J., and Koosimile, D.I. 1995. National gravity survey of Botswana – second edition. *In*: Blenkinsop, T.G., and Tromp, P.L. (Eds.), Sub-Saharan Economic Geology, *Geological Society of Zimbabwe*, *Special publication,* **3**, 133 – 140.

McNeice, G.W. and Jones, A.G. 2001. Multiscale, multifrequency tensor decomposition of magnetotelluric data. *Geophysics*, **66**, 158 - 173.

Meert, J.G., Hargraves, R.B., Van der Voo, R., Hall, C.M., and Halliday, A.N. 1994. Paleomagnetic and $^{40}Ar/^{39}Ar$ studies of Late Kibaran intrusives in Burundi, East Africa: Implications for Late Proterozoic Supercontinents. *Journal of Geology*, **102**, 621 – 637.

Miensopust, M.P. 2010. Multidimensional magnetotellurics: A case study and a 3D approach to simultaneously invert for resistivity structure and distortion parameters. *Unpublished Ph.D. Thesis, National University of Ireland, Galway, Ireland*, 377 pp.

Miensopust, M.P., Jones, A.G., Muller, M.R., Garcia, X., and Evans, R.L. 2011. Lithospheric structures and Precambrian terrane boundaries in northwest Botswana revealed through magnetotelluric profiling as part of the Southern African Magnetotelluric Experiment. *Journal of Geophysical Research*, **116**, 1 – 21.

Milani, L., Kinnaird, J.A., Lehmann, J., Naydenov, K.V., Saalmann, K., Frei, D., and Gerdes, A. 2014. Role of crustal contribution in the early stage of the Damara Orogen, Namibia: New constraints from combined U-Pb and Lu-Hf isotopes from the Goas Magmatic Complex. *Gondwana Research*, http://dx.doi.org/10.1016/j.gr.2014.08.007.

Miller, H.G. and Singh, V. 1994. Potential field tilt-a new concept for location of potential field sources. *Applied Geophysics*, **32**, 213 - 217.

Miller, R. McG., Frimmel, H.E., and Halverson, G.P. 2009a. Passive continental margin evolution. Neoproterozoic to Early Palaeozoic evolution of Southwestern Africa. *In:* Gaucher, C., Sial, A.N., Halverson, G.P., Frimmel, H.E. (Eds.), Neoproterozoic-Cambrian tectonics, global change and evolution: a focus on southwestern Gondwana. *Developments in Precambrian Geology*, **16**, 161 - 181.

Miller, R.M., Frimmel, H.E., and Will, T.M. 2009b. Geodynamic synthesis of the Damara Orogen sensu lato. Neoproterozoic to early Palaeozoic evolution of Southwestern Africa. *In*: Gaucher, C., Sial., A.N., and Halverson, G.P., and Frimmel, H.E. (Eds.), Neoproterozoic-Cambrian Tectonics, Global Change and Evolution: A Focus on Southwestern Gondwana. *Developments in Precambrian Geology*, **16**, 231 – 235.

Miller, R.McG. 1979. The Okahandja Lineament, a fundamental tectonic boundary in the Damara Orogen of South West Africa/Namibia. *Transactions of the Geological Society of South Africa*, **82**, 349 – 361.

Miller, R.McG. 1983a. The Pan-African Damara Orogen of South West Africa/Namibia. *In:* Miller, R.McG. (Ed.), Evolution of the Damara Orogen South West Africa/Namibia. *Geological Society of South Africa, Special publication*, **11**, 431 – 515.

Miller, R.McG. 1983b. Tectonic implication of the contrasting geochemistry of Damaran mafic volcanic rocks, Southwest Africa/Namibia. *In:* Miller, R.McG (Ed.), Evolution of the Damara Orogen of South West Africa/Namibia. *Geological Society of South Africa Special Publication*, **11**, 115 – 138.

Miller, R.McG. 2008. The Geology of Namibia, volume 2: Neoproterozoic and early Palaeozoic rocks of the Damara Orogen. *In:* Miller, R.McG. (Ed.), *The Geology of Namibia,* **2**, Ministry of Mines and Energy, Geological Survey, Windhoek, 13-1 - 13-410.

Miller, R.McG., and Schalk, K.E.L. 1980. South West Africa/Namibia. 1:1000000 Geological map. *Geological Survey of the Republic of South West Africa and Namibia.* Windhoek.

Minty, B.R.S. 1991. Simple micro-levelling for aeromagnetic data. *Exploration Geophysics,* **22**, 591 -592.

Modie, B.N. 2000. Geology and mineralisation in the Meso- to Neoproterozoic Ghanzi-Chobe Belt in northwest Botswana. *Journal of African Earth Sciences*, Pergamon, **30** (3), 467 – 474.

Modie, B.N.J. 1996. Depositional environments of the Meso- to Neoproterozoic Ghanzi-Chobe belt, northwest Botswana. *Journal of African Earth Sciences*, **22** (3), 255 – 268.

Modisi, M.P., Atekwana, E.A., Kampunzu, A.B., and Ngwisanyi, T.H. 2000. Rift kinematics during the incipient stages of continental extension: Evidence from the nascent Okavango rift basin, northwest Botswana. *Geology*, **28** (10), 939 – 942.

Mojaki, T. 2009. Mineral exploration in Tsodilo Hills NW Ngamiland, Botswana: Mineralogical characterization and tectonic analysis. *Unpublished Honours Thesis*, University of Cape Town, Cape Town, South Africa, 101 pp.

Muller, M.R., Jones, A.G., Evans, R.L., Grütter, H.S., Hatton, C., Garcia, X., Hamilton, M.P., Miensopust, M.P., Cole, P., Ngwisanyi, T., Hutchins, D., Fourie, C.J., Jelsma, H.A., Evans, S.F., Aravanis, T., Pettit, W., Webb, S.J., Wasborg, J., and The SAMTEX Team. 2009. Lithospheric structure, evolution and diamond prospectively of the Rehoboth Terrane and western Kaapvaal Craton, southern Africa: Constraints from broadband magnetotellurics. *Lithos,* **112s,** 93 – 105.

Naba, S., Lompo, M., Debat, P., Bouchez, J.L., and Béziat, D. 2004. Structure and emplacement model for late-orogenic Paleoproterozoic granitoids: the Tenkodogo-Yamba elongate pluton (Eastern Burkina Faso). *Journal of African Earth Sciences*, **38**, 41 – 57.

Nabighian, M.N. 1972. The analytic signal of two-dimensional magnetic bodies with polygonal cross-section – Its properties and use for automated interpretation. *Geophysics*, **37**, 507 - 517.

Nabighian, M.N. 1974. Additional comments on the analytic signal of two-dimensional magnetic bodies with polygonal cross-section. *Geophysics*, **39**, 85 - 92.

Nabighian, M.N. 1984. Toward a three-dimensional automatic interpretation of potential field data via generalized Hilbert transforms – Fundamental relations. *Geophysics*, **49**, 780 – 786.

Nagel, R. 1999. Eine Milliarde Jahre geologischer Entwicklung am NW-Rand des Kalahari Kratons. *Unpublished Ph.D. Thesis,* University of Göttingen*,* Germany, 192 pp.

Niblett, E.R., and Sayn-Wittgenstein, C. 1960. Variation of electrical conductivity with depth by the magneto-telluric method. *Geophysics*, **25**, 2 501 – 2 504.

Nxumalo, V. 2013. Stratigraphy and sedimentology of the Karoo Supergroup in the Gemsbok sub-basin (Botswana and Namibia). *Council for Geoscience South Africa*, Bulletin, **146,** 98 pp.

O' Driscoll, E.S.D., and Campbell, I.B. 1997. Mineral deposits related to Australian continental ring and rift structures with some terrestrial and planetary analogies. *Global Tectonics and Metallogenesis*, **6**, 83 – 93.

Oleskevich, D.A., Hyndman, R.D., and Wang, K. 1999. The updip and downdip limits to great subduction earthquakes: Thermal and structural models of Cascadia, south Alaska, SW Japan, and Chile. *Journal of Geophysical Research*, **104**, 965 – 991.

Olhoeft, G.R. 1981. Electrical properties of granite with implications for the lower crust. *Journal of Geophysical Research*, **86**, 931 - 936.

Oliver, G.J.H. 1994. Mid-crustal detachment and domes in the central zone of the Damaran orogen, Namibia. *Journal of African Earth Sciences*, **19** (4), 331 – 344.

Oruç, B. and Selim, H.H. 2011. Interpretation of magnetic data in the Sinop area of Mid Black Sea, Turkey, using tilt derivative, Euler deconvolution, and discrete wavelet transform. *Journal of Applied Geophysics*, **74**, 194 - 204.

Padilha, A.L., Vitorello, Í, Pádua, M.B., and Bologna, M.S. 2013. Electromagnetic constraints for subduction zones beneath the northwest Borborema province: Evidence for Neoproterozoic island arc-continent collision in northeast Brazil. *Geology*, doi:10.1130/G34747.1

Parker, R.L. 1980. The inverse problem of electromagnetic induction: existence and construction of solutions based on incomplete data. *Journal of Geophysical Research*, **85**, 4 421 – 4 425.

Parker, R.L. 1982. The existence of a region inaccessible to magnetotelluric sounding. *Geophysical Journal of the Royal Astronomical Society*, **68**, 165 – 170.

Parker, R.L., and Brooker, J.R. 1996. Optimal one-dimensional inversion and bounding of the magnetotelluric apparent resistivity and phase measurements. *Physics of the Earth and Planetary Interiors*, **98**, 269 – 282.

Parkinson, W.D. 1959. Directions of rapid geomagnetic fluctuations. *Geophysical Journal of the Royal Astronomical Society*, **2** (1), 1 – 14.

Pavlenkova, N.I. 1979. Generalized geophysical model and dynamic properties of the continental crust. *Tectonophysics*, **59**, 381 – 390.

Peacock, S.M. 1990. Fluid processes in subduction zones. *Science*, **248**, 329 - 337.

Pellerin, L., and Hohmann, G.W. 1990. Transient electromagnetic inversion: A remedy for magnetotelluric static shifts. *Geophysics*, **55** (9), 1 242 – 1 250.

Pfurr, N., Ahrendt, H., Hansen, B.T., and Weber, K. 1991. U-Pb and Rb-Sr isotropic study of granitic gneisses and associated metavolcanic rocks from the Rostock massifs, southern margin of the Damara Orogen: implications for lithostratigraphy of this crustal segment. *Communications of the Geological Survey of Namibia*, **7**, 35 – 48.

Piranjo, F., Phillips, D., and Armstrong, R.A. 2000. Volcanology and eruptive histories of the Erongo Volcanic Complex and the Paresis Igneous Complex, Namibia: implications for mineral deposit styles. *In*: Miller, R.McG., (Ed.), *Communications of the Geological Survey of Namibia, Special Issue: Henno Martin commemorative volume*, **12**, 301 – 312.

Porada, H. 1979. The Damara-Ribeiro Orogen of the Pan-African-Brasiliano cycle in Namibia (South West Africa) and Brazil as interpreted in terms of continental collision. *Tectonophysics*, **57**, 237 - 265.

Porada, H. 1989. Pan-African rifting and orogenesis in southern to Equatorial Africa and eastern Brazil. *Pre-Cambrian Research*, **44**, 103 – 136.

Porada, H., Ahrendt, H., Behr, J., Weber, K. 1983. The join of the coastal and intracontinental branches of the Damara orogen, Namibia, South West Africa. *In:* Martin, H., and Eder, F.W. (Eds.), Intracontinental fold belts, 901 – 912.

Porada, H., and Behr, H.J. 1988. Setting and sedimentary facies of late Proterozoic alkali lake Playa deposits in the southern Damara Belt of Namibia. *Sedimentary Geology*, **58**, 171 – 194.

Poseidon Geophysics (Pty) Limited. 1995. Regional aeromagnetic and gravity interpretation. Matsheng area groundwater investigation (TB 10/2/12/92-93). *Technical report T 5*, 59 pp.

Powell, C.McA., Jones, D.L., Pisarevsky, S., and Wingate, M.T.D. 2001. Palaeomagnetic constraints on the position of the Kalahari Craton in Rodinia. *Precambrian Research*, **110**, 33 – 46.

Prave, A.R. 1996. Tale of three cratons: Tectonostratigraphic anatomy of the Damara orogen in northwestern Namibia and the assembly of Gondwana. *Geology*, **24**, 1 115 – 1 118.

Prave, A.R., Hoffmann, K.-H., Hegenberger, W., and Fallick, A.E. 2011. The Witvlei Group of east-central Namibia. *In:* Arnaud, E., Halverson, G.P., and Shields-Zhou, G. (Eds.), The geological record of Neoproterozoic glaciations. *Geological Society of London*, **36**, 211 – 216.

Pretorius, A., and Park, V. 2011. Resource estimate update Hana Mining Ltd Ghanzi copper-silver project Ghanzi District, Botswana, *Technical Report*, 235 pp.

Price, A.T. 1973. The theory of geomagnetic induction. *Physics of the Earth and Planetary Interiors*, **7**, 227 – 233.

Pruss, S.B., Bosak, T., Macdonald, F.A., McLane, M., and Hoffman, P.F. 2010. Microbial facies in a Sturtian cap carbonate, the Rasthof Formation, Otavi Group, northern Namibia. *Precambrian Research*, **181**, 187 – 198.

Pryer, L., Windle, S., Etheridge, M., Farquar-Smith, D., Guillemot, D., Foss, C. and Prat, D. 1997. Geological Interpretation of the Aeromagnetic Survey of Western Ngamiland, Botswana. 1: 250 000 scale. Department of Geological Survey, Lobatse, Botswana.

Raab, M.J., Brown, R.W., Gallagher, K., Carter, A., and Weber, K. 2002. Late Cretaceous reactivation of major crustal shear zones in northern Namibia: constraints from apatite fission track analysis. *Tectonophysics*, **349**, 75 – 92.

Rainaud, C., Master, S., Armstrong, R.A., Phillips, D., and Robb, L.J. 2005b. Monazite U–Pb dating and ^{40}Ar–^{39}Ar thermochronology of metamorphic events in the Central African Copperbelt during the Pan-African Lufilian Orogeny. *Journal of African Earth Sciences*, **42**, 183 - 199.

Rainuad, C., Master, S., Armstrong, R.A., and Robb, L.J. 2005a. Geochronology and nature of the Palaeoproterozoic basement in the Central African Copperbelt (Zambia and the Democratic Republic of Congo), with regional implications. *Journal of African Earth Sciences*, **42**, 1 – 31.

Ramokate, L.V., Mapeo, R.B.M., Corfu, F., and Kampunzu, A.B. 2000. Proterozoic geology and regional correlation of the Ghanzi-Makunda area, western Botswana. *Journal of African Earth Science*, **30** (3), 453 – 466.

Ravat, D. 1996. Analysis of the Euler method and its applicability in environmental investigations. *Journal of Environmental and Engineering Geophysics*, **1**, 229 - 238.

Reeves, C.V. 1972. Rifting in the Kalahari? *Nature*, **237**, 95 – 96.

Reeves, C.V. 1978a. The reconnaissance aeromagnetic survey of Botswana, 1975 – 1977. Final interpretation report. *Geological Survey of Botswana*, Terra Surveys. 315 pp.

Reeves, C.V. 1978b. A failed Gondwana spreading axis in southern Africa, *Nature*, London, **273**, 222 – 223.

Reeves, C.V. 1985. The Kalahari Desert, central southern Africa; A case history of regional gravity and magnetic exploration. *In*: Hinze, W.J. (Ed.), The utility of regional gravity and magnetic anomaly maps. *Society Exploration Geophysics*, 144 - 153.

Reeves, C.V. 2000. The geophysical mapping of Mesozoic dyke swarms in southern Africa and their origin in the disruption of Gondwana. *Journal of African Earth Sciences*, **30**, 499 – 513.

Reeves, C.V., and Hutchins, D.G. 1975. Crustal structures in central southern Africa. *Nature*, **254**, 408 – 410.

Reeves, C.V., and Hutchins, D.G. 1976. National gravity survey of Botswana. *Bulletin of the Botswana Geological Survey*, **5**, 1 – 55 pp.

Reeves, C.V., and Hutchins, D.G. 1982. A progress report on the geophysical exploration of the Kalahari in Botswana. *Geoexploration*, **20**, 209 – 224.

Reid, A.B., Allsop, J.M., Granser, H., Millett, A.J. and Somerton, I.W. 1990. Magnetic interpretation in three dimensions using Euler deconvolution, *Geophysics*, **55**, 80 - 91.

Ringwood, A.E. 1975. Composition and petrology of the Earth's mantle. McGraw Hill, New York, 618 pp.

Ritter, O., Weckmann, U, Vietor, T., and Haak, V. 2003. A magnetotelluric study of the Damara Belt in Namibia 1. Regional scale conductivity anomalies, *Physics of the Earth and Planetary Interiors*, **138**, 71 – 90.

Ritz, M. 1983. Use of the magnetotelluric method for a better understanding of the West African Shield. *Journal of Geophysical Research*, **88** (10), 625 – 633.

Roberts, M.P., and Clemens, J.D. 1993. Origin of high-potassium, calcalkaline, I-type granitoids. *Geology*, **21**, 825 – 828.

Roest, W.R., and Pilkington, M. 1993. Identifying remanent magnetization effects in magnetic data. *Geophysics*, **58**, 116 – 659.

Roest, W.R., Verhoef, J. and Pilkington, M. 1992. Magnetic interpretation using 3-D analytic signal. *Geophysics*, **57**, 116-125.

Roger, J.J.W., and Santosh, M. 2003. Supercontinents in Earth History. *Gondwana Research*, **6** (3), 257 – 368.

Roger, J.J.W., Unrug, R., and Sultan, M. 1995. Tectonic assembly of Gondwana. *Journal of Geodynamic*, **19** (1), 1 – 34.

Romanyuk, T.V., Blakely, R., and Mooney, W.D. 1998. The Cascadia subduction zone: two contrasting models of lithospheric structure. *Physics and Chemistry of the Earth*, **23**, 297 – 301.

Rubidge, B.S., Erwin, D.H., Ramezani, J., Bowring, S.A., and de Klerk, W.J. 2013. High-precision temporal calibration of Late Permian vertebrate biostratigraphy: U-Pb zircon constraints from the Karoo Supergroup, South Africa. *Geology*, **41**, 363 – 366.

Sanger, E.A., and Glen, J.M.G. 2003. Density and magnetic susceptibility values for rocks in the Talkeetna Mountains and adjacent regions, south-central Alaska. *United States Geological Survey*, 44 pp.

Sanz, A.L.-G. 2005. *Pre- and post-Katangan granitoids of the Greater Lufilian Arc - geology, geochemistry, geochronology and metallogenic significance*. *Unpublished Ph.D. Thesis*, University of the Witwatersrand, Johannesburg, South Africa, 734 pp.

Saviaro, K., 1980. Preliminary analysis of airborne magnetic surveys in Zambia. *Occasional Paper of the Geological Survey of Zambia*, **98**, 8 pp

Sawyer, E.W. 1981. Damaran structural and metamorphic geology of an area south-east of Walvis Bay, South West/Namibia. *Memoirs of the Geological Survey of Namibia*, **7**, 94 pp.

Schmitt, R.S., Trouw, R.A.J., Passchier, C.W., Medeiros, S., and Armstrong, R. 2012. 530 Ma syntectonic syentines and granites in NW Namibia – Their relation with collision along the junction of the Damara and Kaoko belts. *Gondwana Research*, **21**, 362 – 377.

Schneider, G.I.C., and Seeger, K.G. 1992. Copper, the mineral Resources of Namibia. *Geological Survey of Namibia, Special publication*. **118.N**, 2.3-1 – 2.3.

Schneider, J., Boni, M., Laukamp, C., Bechstädt, T., and Petzel, V. 2008. Willemite (Zn_2SiO_4) as a possible Rb-Sr geochronometer for dating nonsulfide Zn-Pb mineralisation: Examples from the Otavi Mountainland (Namibia). *Ore Geology Reviews*, **33**, 152 – 167.

Schneider, T., Becker, T., Borg, G., Hilken, U., Hansen, B.T., and Weber, K. 2004. New U-Pb zircon ages of the Nückopf Formation and their significance for the Mesoproterozoic event in Namibia. *Communications of the Geological Survey*, Namibia, **13**, 63 – 74.

Schumcker, U. 1973. Regional induction studies: a review of methods and results. *Physics of the Earth and Planetary Interiors*, **7**, 365 – 378.

Schwartz, M.O., Akanyang, P., Trippler, K., and Ngwisanyi, T.H. 1995. The sediment-hosted Ngwako Pan copper deposit, Botswana. *Economic Geology*, **90**, 1 118 – 1 147.

Schwartz, M.O., and Akanyang, P. 1994. Ngwako Pan: Lobatse, Botswana Geological Survey, Geological Map Q.D.S. 2022D and part of 2023C, scale 1:125 000.

Schwartz, G., Haak, V., Martinez, E., and Bannister, J. 1984. The electrical conductivity of the Andean crust in northern Chile and southern Bolivia as inferred from magnetotelluric measurements. *Journal of Geophysics*, **55**, 169 – 178.

Selway, K., Hand, M., Heinson, G.S., and Payne, J.L. 2009. Magnetotelluric constraints on subduction polarity: Reversing reconstruction models for Proterozoic Australia. *Geology*, **37** (9), 799 – 802.

Shankland, T.J., and Ander, M.C. 1983. Electrical conductivity, temperature and fluids in the lower crust. *Journal of Geophysical Research*, **84**, 212 – 228.

Sharma, P.V. 1987. Magnetic method applied to mineral exploration. *Ore Geology*, **2**, 323 – 357.

Simpson, F., and Bahr, K. 2005. Practical magnetotellurics. Cambridge University Press, United Kingdom, 1 – 254 pp.

Singletary, S.J., Hanson, R.E., Martin, M.W., Crowley, J.L., Bowring, S.A., Key, R.M., Ramokate, L.V., Direng, B.B., and Krol, M.A. 2003. Geochronology of basement rocks in the Kalahari Desert, Botswana, and implications for regional Proterozoic tectonics. *Precambrian Research*, **121**, 47 – 71.

Sizova, E., Gerya, T., and Brown, M. 2012. Exhumation mechanisms of melt-bearing ultrahigh pressure crustal rocks during collision of spontaneously moving plates: Journal of Metamorphic *Geology*, **30**, 927 – 955.

Smith, D.A.M. 1965. The geology of the area around the Khan and Swakop Rivers in South West Africa. *Memoir of the Geological Survey of South Africa*, **3**, 113 pp.

Smith, J.T. 1997. Estimating galvanic-distortion magnetic fields in magnetotellurics. *Geophysical Journal International*, **130**, 65 - 72.

Sobolev, S.V., and Babeyko, A.Y. 1993. Modelling of mineralogical composition, density and elastic wave velocities in anhydrous magmatic rocks. *Surveys in Geophysics*, **15**, 515 – 544.

South African Committee for Stratigraphy (SACS). 1980. The Damara Sequence. *In:* Stratigraphy of Southern Africa. I. Lithostratigraphy of South Africa, South West Africa/Namibia and the Republics of Bophuthatswana, Transkei and Venda. *Handbook of the Geological Survey of South Africa* **8**, 415 - 423.

Soyer, W., and Unsworth, M. 2006. Deep electrical structure of the northern Cascadia (British Columbia, Canada) subduction zone: implications for the distribution of fluids. *Geology*, **34** (1), 53 – 56.

Spratt, J.E., Jones, A.G., Jackson, V.A., Collins, L., and Avdeeva, A. 2009. Lithospheric geometry of the Wopmay orogen from a Slave Craton to Bear Province magnetotelluric transect. *Journal of Geophysical Research: Solid Earth*, **114**, B01101.

Spratt, J.E., Jones, A.G., Nelson, K.D., Unsworth, M.J., and INDEPTH MT Team. 2005. Crustal structure of the India-Asia collision zone, southern Tibet, from INDEPTH MT investigations. *Physics of the Earth and Planetary Interiors*, **150**, 227 – 237.

Stalker, A.D. 1983. Aha Hills prospecting licence 39/80. *Final Report*. Billiton Botswana (Pty) Limited, 13 pp.

Stanistreet, I.G., Kukla, P.A. and Henry, G. 1991. Sedimentary basin responses to a late Precambrian Wilson Cycle: the Damara orogen and Nama foreland, Namibia. *Journal of African Earth Sciences*, **13**, 141 - 156.

Stanley, W.D., Labson, V.F., Nokleberg, W.J., Csejtey, B., and Fisher, M.A. 1990. The Denali fault system and Alaska Range of Alaska: evidence for underplated Mesozoic flysch from magnetotelluric surveys. *Geological Society of America*, Bulletin **102** (2), 160 – 173.

Sternberg, B.K. 1993. On: "Removal of static shift in two dimensions by regularized inversion" by Catherine de Groot-Hedlin (December 1991 Geophysics, p 2102-2106). *Geophysics*, **58**, 598 – 599.

Stettler, E.H., de Beer, J.H., and Blom, M.P. 1989. Crustal domains in the northern Kaapvaal craton as defined by magnetic lineaments. *Precambrian Research*, **45**, 263 – 276.

Steven, N.M., Armstrong, R.A., Smalley, T. and Moore, J.M. 2000. First geological description of a Late Proterozoic (Kibaran) metabasaltic andesite-hosted chalcocite deposit at Omitiomire, Namibia. *In:* Cluer, J.K., Price, J.G., Strusacher, E.M., Hardyman, R.F. and Morris, C.L. (Eds.), Geology and Ore Deposits 2000: The Great Basin and Beyond. *Reno: Geological Society of Nevada,* 711 - 734.

Sule, P., and Hutton, V.R.S. 1986. A broadband magnetotelluric study in S.E. Scotland – Data acquisition analysis and one-dimensional modelling, *Annales Geophysicae*, **4** (B2), 145 – 156.

Sun, H. 2002. Tourmalines in Neoproterozoic metaevaporitic deposit of Duruchaus Formation, Damara Belt, Central Namibia. *Unpublished Ph.D. Thesis*, Louisiana State University and Agricultural and Mechanical College, Lousisinia, United States of America, 200 pp.

Swain, C.J. 1976. A FOTRAN IV program for interpolating irregularly spaced data using the difference equations for minimum curvature. *Computer and Geosciences*, **1**, 231 – 240.

Swift, C.M. 1967. A magnetotelluric investigation of an electrical conductivity anomaly in the southwestern United States. *Unpublished Ph.D. Thesis*, Massachusetts Institute of Technology, Cambridge, United States of America, 223 pp.

Tack, L., Williams, I. and Bowden, P. 2002. SHRIMP constraints on early post-collisional granitoids of the Ida Dome, central Damara (Pan-African) Belt, western Namibia. Abstracts of the 11th IAGOD Quadrennial Symposium and Geocongress, Windhoek, Namibia. Geological Survey of Namibia. 22 – 26 July.

Talwani, M., and Heirtzler, J. R. 1964. Computation of magnetic anomalies caused by two dimensional bodies of arbitrary shape. *In*: Parks, G. A. (Ed.), Computers in the mineral industries, Part 1. *Stanford University Publication, Geological Sciences*, **9** (1), 464 - 480.

Talwani, M., Worzel, J. L., and Landisman, M. 1959. Rapid gravity computations for two dimensional bodies with application to the Mendocino submarine fracture zone. *Journal of Geophysical Research*, **64** (1), 49 - 59.

Telford, W.M., Geldart, L.P., and Sheriff, R.E. 1990. Applied geophysics. New York, Cambridge University Press, 2nd edition, 770 pp.

Thomas, C. M. 1969. A short description of the geology of South Ngamiland (covering Q.D.S. 2022C, 2022D and 2023C). *Unpublished Report No. CMT/4/69*, *Geological Survey of Botswana*, Lobatse, 13 pp.

Thomas, C. M. 1973. Brief explanation of the geology of South Ngamiland (covering Q.D.S. 2022D with parts of 2022C and 2023C), accompanying geological map (1: 125 000 scale). *Geological Survey of Botswana*.

Thompson, A.B., and Connolly, J.A.D. 1990. Metamoprphic fluids and anomalous porosity in the lower crust. *Tectonophysics*, **182**, 47 – 55.

Thompson, D.T. 1982. EULDPH – A new technique for making computer – assisted depth estimates from magnetic data. *Geophysics*, **47**, 31 - 37.

Tikhonov, A.N. 1986. On determining electrical characteristics of the deep layers of the Earth's crust. *In*: Vozoff, K. (Ed.), *Magnetotelluric Methods*, *Tulsa: Society of Exploration Geophysicists*, *Reprinted from Doklady*, **73** (2), 295 – 297.

Tikhonov, A.N., and Berdichevsky, M.N. 1966. Experience in the use of magnetotelluric methods to study the geological structure of sedimentary basins. *Izestiya, Russian Academy of Sciences, Physic of the Solid Earth*, **2**, 34 – 41.

Trumbull, R.B., Vietor, T., Hahne, K., Wackerle, R., and Ledru, P. 2004. Aeromagnetic mapping and reconnaissance geochemistry of the Early Cretaceous Henties Bay-Outjo dike swarm, Etendeka Igneous Province, Namibia. *Journal of African Earth Sciences*, **40**, 17 – 29.

Türkoğlu, E., Unsworth, M., and Pana, D. 2009. Deep electrical structure of northern Alberta (Canada): implications for diamond exploration. *Canadian Journal of Earth Science*, **46**, 139 – 154.

Unrug, R. 1996. The assembly of Gondwanaland. *Episodes*, **19**, 11 - 20.

Unsworth, M., Wenbo, M., Jones, A.G., Li, S., Bedrosian, P., Booker, J., Sheng, J., Ming, D., and Handong, T. 2004. Crustal and upper mantle structure of Northern Tibet imaged with magnetotelluric data. *Journal of Geophysical Research: Solid Earth*, **109**, B02403.

Unsworth, M.J., Egbert, G., and Booker, J. 1999. High-resolution electromagnetic imaging of the San Andreas fault in Central California. *Journal of Geophysical Research: Solid Earth*, **105** (B1), 1 131 – 1 150.

van Schijndel, V., Cornell, D.H., Frei, D., Simonsen, S.L., and Whitehouse, M.J. 2013. Crustal evolution of the Rehoboth Province from Archaean to Mesoproterozoic times: Insights from the Rehoboth Basement Inlier. *Precambrian Research*, http://dx.doi.org/10.1016/j.precamres.2013.10.014.

van Schijndel, V., Cornell, D.H., Hoffmann, K.-H., and Frei, D. 2011. Three episodes of crustal development in the Rehoboth Province, Namibia. *In:* Van Hinsbergen, D.J.J., Butter, S.J.H., Torsvik, T.H., Gaina, C., and Webb, S.J. (Eds.), *The Formation and Evolution of Africa: A synopsis of 3.8 Ga of Earth History*. Geological Society, London, Special Publications, **357**, 27 – 48.

van Zijl, J.S.V. 1977. Electrical studies of the deep crust in various tectonic provinces of southern Africa. *In:* Heacock, J.G. (Ed.), The Earth's Crust, *Geophysical Monograph Series*, **20**, AGU, Washington, 470 – 500.

van Zijl, J.S.V., and de Beer, J.H. 1983. Electrical structure of the Damara orogen and its tectonic significance. *In*: Miller, R.McG. (Ed.), Evolution of the Damara Orogen of South West Africa/Namibia, **11**, 369 – 379.

Vegas, N., Naba, S., Bouchez, J.L., and Jessell, M. 2008. Structure and emplacement of granite plutons in the Paleoproterozoic crust of Eastern Burkina Faso: rheological implications. *International Journal of Earth Sciences (Geol. Rundsch)*, **97**, 1 165 – 1 180.

Verduzco, B., Fairhead, J.D., Green, C.M. and MacKenzie, C. 2004. New insights into magnetic derivatives for structural mapping. *Leading Edge*, **23**, 116 - 119.

Vermaak, C F. 1962. Botswana Reserve, Geological Report. *Final Report for CG33*, Johannesburg Consolidated Investment Company Ltd, 96 pp.

Viola, G., Mancktelow, N.S., and Miller, J.A. 2006. Cyclic frictional-viscous slip oscillations along the base of an advancing nappe complex: Insights into brittle-ductile nappe emplacement mechanisms from the Naukluft Nappe Complex, central Namibia. *Tectonics*, **25**, TC3016, 1 – 20.

Vozoff, K. 1991. The magnetotelluric method. *In*: Nabighian, M.N. (Ed.), *Electromagnetic methods in applied geophysics*, Society of Exploration Geophysicists, **2**, 641 – 712.

Walker, A.S.D., Key, R.M., Pouliquen, G., Gunn, G., Sharrock, J., McGeorge, I., Koketso, M., and Farr, J. 2010. Geophysical modelling of the Molopo Farm Complex in southern Botswana: implications for its emplacement within the ~2 Ga Large Igneous Province of southern and central Africa. *South African Journal of Geology*, **113** (4), 381 – 400.

Walther, J.V., and Orville, P.M. 1982. Volatile production and transport in regional metamorphism. *Contributions to Mineralogy and Petrology*, **79**, 252 – 257.

Watters, B.R. 1977. The Sinclair Group: definition and regional correlation. *Transactions of the Geological Society South Africa*, **80**, 9 - 16.

Weckmann, U., Ritter, O., and Haak, V. 2003. A magnetotelluric study of the Damara Belt in Namibia 2. MT phases over 90° reveal the internal structure of the Waterberg Fault/Omaruru Lineament. *Physics of the Earth and Planetary Interiors,* **138**, 91 – 112.

Weidelt, P. 1972. The inverse problem of geomagnetic induction. *Zeitschrift für Geophysik*, **38**, 257 – 289.

Wendorff, M. 2005. Outline of lithostratigraphy, sedimentation and tectonics of the Tsodilo Hills Group, a Neoproterozoic-Lower Palaeozoic siliciclastic succession in NW Botswana. *Annales Societatis Geologorum Poloniae*, **75**, 17 – 25.

Wilson, J.T. 1966. Did the Atlantic close and then re-open? *Nature*, **211**, 676 – 681.

Wilson, T.J., Grunow, A.M., and Hanson, R.E. 1997. Gondwana assembly: The view from southern Africa and East Gondwana. *Journal of Geodynamic*, **23** (3/4), 263 – 286.

WinGLink manual. 2005. WinGlink user's guide. Geosystems SRL, Milan, Italy, 2.07.04 edition. (www.geosystems.net).

Winker, F. 2013. Groundwater model report – Dordabis iron ore mine project. SLR environmental Consulting (Namibia) (Pty) Ltd., SLR Project number 733.12017.00003, 63 pp.

Witbooi, E.H. 2011. Petrology, petrography, geochemistry and geochronology of base-metal mineralisation in the Lufilian Arc extension in the Tsodilo Hills Area, NW Botswana, *Unpublished Honours Thesis,* Nelson Mandela Metropolitan University, Port Elizabeth, South Africa, 121 pp.

Won, I. J., and Bevis, M. 1987. Computing the gravitational and magnetic anomalies due to a polygon: Algorithms and Fortran subroutines. *Geophysics*, **52**, 232 - 238.

Wright, E.P. 1957. Geology of the valley of the Schadum. *Unpublished Report*, *Geological Survey of Botswana,* EPW/19/57, 3 pp.

Wright, E.P. 1958b. Reconnaissance geology of western Ngamiland. *Unpublished Report*, *Geological Survey of Botswana,* EPW/21/58, 8 pp.

Wright, E.P. 1958e. Geology of the Kihabedum Valley and Kihabe Hills. *Unpublished Report*. *Geological Survey of Botswana,* EPW/20/58, 3 pp.

Wright, J.A., and Hall, J. 1990. Deep seismic profiling in the Nosop Basin, Botswana: cratons, mobile belts and sedimentary basins. *Tectonophysics*, **173**, 333 - 343.

Wu, X., Ferguson, I.J., and Jones, A.G. 2005. Geoelectric structure of the Proterozoic Wopmay Orogen and adjacent terranes, Northwest Territories. *Canadian Journal of Earth Science*, **42**, 955 – 981.

Yawsangratt, S. 2002. A gravity study of northern Botswana: a new perspective and its implication for regional geology. International institute for geo-information science and Earth observation, *Unpublished MSc. Thesis*, The Netherlands, Enschede, 69 pp.

Zhang, J. 2001. An analysis of the accuracy of magnetic source-body geometry determined from the 3D analytic signal: *Geophysics*, **66**, 579 – 581.

Zhang, P., Rasmussen, T., Korja, T., Hjelt, S.E., and Pedersen, L.B. 1984. Preliminary results of MT measurements across the Oulu anomaly in 1983. *Proceedings of the Baltic Shield Symposium*, Department of Geophysics, Finland, Report number **8**, 296 – 306.

Zhdanov, M.S., Golubev, N.G, Varentsov, I.M., Abramova, L.M., Shneer, V.S., Berdichevsky, M.N., Zhdanova, O.N., Gordienko, V.V., Kulik, S.N., and Bilinsky, A.I. 1986. 2-D Model Fitting of a Geomagnetic Anomaly in the Soviet Carpathians, *Annales Geophysicae*, **4** B3, 335 - 342.

Zhou, Y. 1992. Application of radon transforms to the processing of airborne geophysical data. *Unpublished Ph.D. Thesis*, International Institute for Aerospace Survey and Earth Science (ICT), The Netherlands, 240 pp.

Ziegler, U.R.F., and Stoessel, G.F.U. 1993. Age determinations in the Rehoboth Basement Inlier, Namibia. *Memoirs of the Geological Survey of Namibia*, **14**, 106 pp.

Appendix 1:

This appendix presents Naydenov, K.V., Lehmann, J., Saalman, K., Milani, L., Kinnaird, J.A., Charlesworth, G., Frei, D., and Rankin, W. (2014) in its published format. Consequently, the formatting, layout, figure and table numbering do not follow the layout of this dissertation.

Tectonophysics 637 (2014) 80–105

Contents lists available at ScienceDirect

Tectonophysics

journal homepage: www.elsevier.com/locate/tecto

New constraints on the Pan-African Orogeny in Central Zambia: A structural and geochronological study of the Hook Batholith and the Mwembeshi Zone

Kalin V. Naydenov [a,*], Jeremie Lehmann [a], Kerstin Saalmann [a,1], Lorenzo Milani [a], Judith A. Kinnaird [a], Guy Charlesworth [a], Dirk Frei [b], William Rankin [a]

[a] School of Geosciences, University of the Witwatersrand, Pvt Bag 3, Wits 2050, South Africa
[b] Department of Earth Sciences, Stellenbosch University, Pvt Bag X1, Matieland 7602, South Africa

ARTICLE INFO

Article history:
Received 8 April 2014
Received in revised form 20 September 2014
Accepted 26 September 2014
Available online 13 October 2014

Keywords:
Pan-African Orogeny
Central Zambia
Hook Batholith
Mwembeshi Zone
Orthogonal shortening events
Zircon geochronology

ABSTRACT

In Central Zambia, the Mwembeshi Zone (MwZ) separates two branches of the Pan-African Orogen: the Lufilian Arc and the Zambezi Belt. To the north of the MwZ, the Hook Batholith was emplaced within Neoproterozoic Katangan metasedimentary rocks. Field mapping and structural studies, microstructural observations, interpretation of airborne geophysical images and U–Pb zircon geochronology constrain a new model for the tectonic evolution of this poorly studied part of the orogen.

Two temporarily separated and highly oblique orogenic contraction events are defined. D1 is characterised by a regional low-metamorphic grade E–W shortening that produced strain partitioning between N–S trending pure-shear-dominated and NW trending sinistral simple-shear dominated domains. The emplacement of the batholith between ca. 550 and 533 Ma (U–Pb zircon ages) is syn-tectonic to D1. The D2 N–S shortening event was active after ca. 530, which is indicated by the age of the newly dated, deformed molasse of the Hook Batholith. During D2, the MwZ developed as an E- to ENE-striking zone of pure-shear dominated deformation that localised to the south and within the already exhumed Hook Batholith.

At the scale of the Pan-African Orogen in Southern Africa, the D1 is considered to be a far field expression of the E–W collision event in the Mozambique Belt. The following Early Cambrian D2 event corresponds to the high angle collision between the Congo and Kalahari Cratons and the stitching of the Lufilian and Zambezi belts along the MwZ. Therefore, in the Hook area, the MwZ cannot be regarded as a continental-scale wrench structure as widely discussed in the literature. The tectonic events in Central Zambia suggest that the amalgamation of Gondwana was accompanied by suturing along highly oblique orogenic belts during plate reorganization at around 530 Ma.

1. Introduction

The Pan-African Damara-Lufilian Orogen is part of a system of Neoproterozoic to Early Palaeozoic mobile belts that formed during the amalgamation of Gondwana (e.g. Frimmel et al., 2011; Gray et al., 2008; Meert, 2003; Porada, 1989). To the west, the Damara Orogen developed at the triple junction between the Congo, Kalahari, and Rio de la Plata Cratons (Prave, 1996) in response to the closure of two oceanic basins: the Adamastor Ocean between the Kalahari/Congo and Rio de la Plata Cratons (e.g. Basei et al., 2008, 2010; Frimmel et al., 2011; Saalmann et al., 2011), and the Khomas Ocean between the Kalahari and Congo Cratons (e.g. Miller, 2008 and references therein). To the east, the Lufilian Arc and the Zambezi Belt developed in response to the collision between the Congo and Kalahari plates (e.g., John et al., 2004a; Porada, 1989). Further east, a prolonged period of subduction and Andean-type orogeny followed by complicated collision between numerous continental fragments formed the approximately N–S trending Mozambique Belt (e.g. Grantham et al., 2003, 2008; Meert, 2003).

The Lufilian Arc is a northward-convex belt (Fig. 1) that consists predominantly of metasedimentary rocks of the Neoproterozoic Katanga Supergroup. It is bordered to the N and NW by the Archaean Kasai Shield (ca. 2.54–2.56 Ga, Key et al., 2001) and the Mesoproterozoic Kibaran Belt (ca. 1.38–1.37 Ga and ca. 1.07 Ga, Kokonyangi et al., 2004, 2006; Tack et al., 2010), to the NE by the Palaeoproterozoic Bangweulu Block (ca. 2.0–1.8 Ga, Andersen and Unrug, 1984; De Waele and Fitzsimons, 2007; Hanson, 2003), and to the SE by the Late Mesoproterozoic Irumide Belt (ca. 1.05–0.95 Ma, De Waele et al., 2006, 2009).

The Zambezi Belt is a SW- to SSW-vergent fold-and-thrust complex. In Southern Zambia it comprises a thick metasedimentary succession unconformably overlying or in tectonic contact with late Mesoproterozoic

* Corresponding author. Tel.: +27 117176551.
E-mail address: k.naidenov@gmail.com (K.V. Naydenov).
[1] Present address: Norges Geologiske Undersøkelse (NGU), Postboks 6315 Sluppen, 7491 Trondheim, Norway.

http://dx.doi.org/10.1016/j.tecto.2014.09.010
0040-1951/

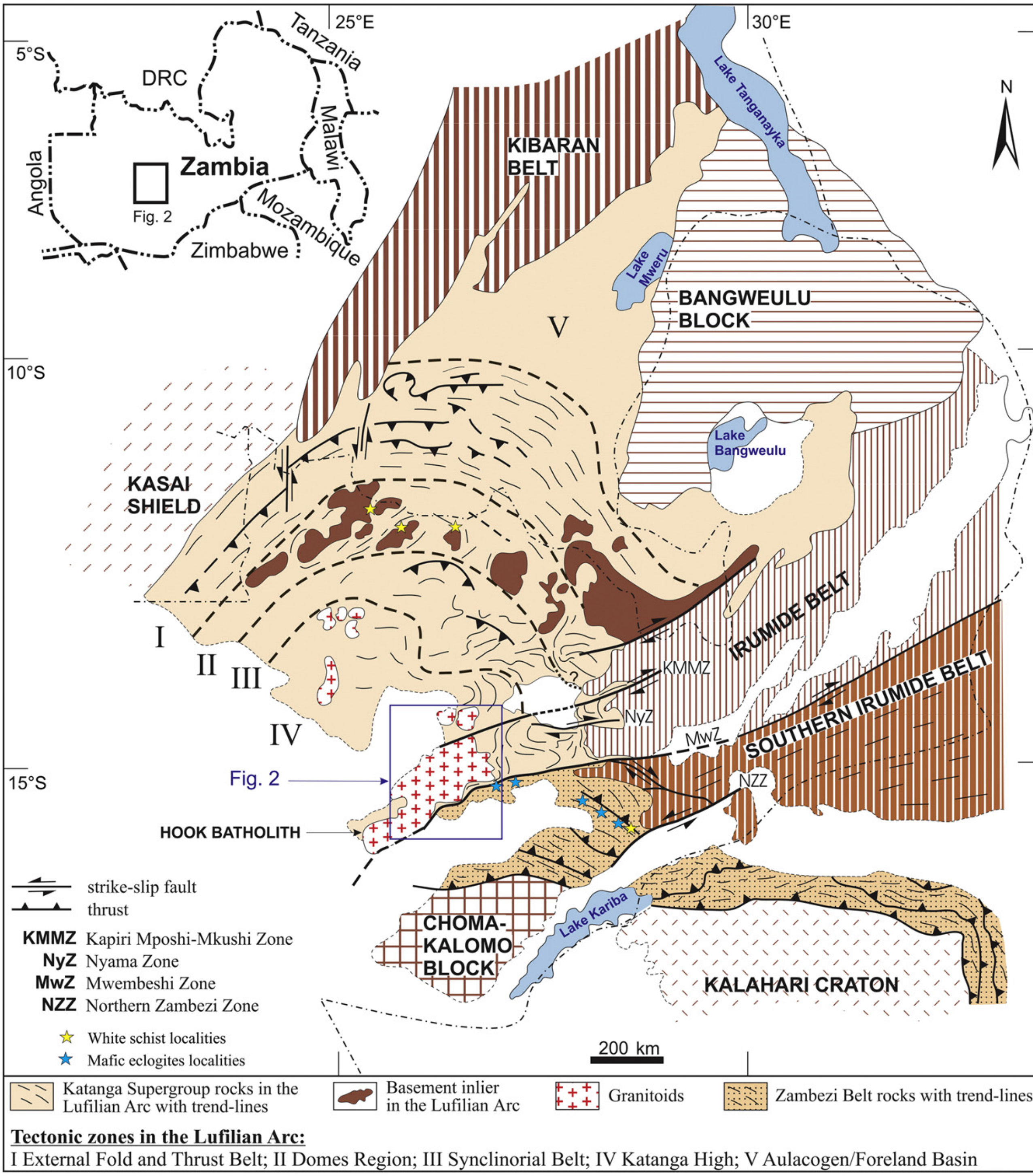

Fig. 1. Schematic tectonic map of the Lufilian Arc and the Zambezi Belt (modified after de Swardt et al., 1964, 1965; John et al., 2004a, 2004b; Johnson et al., 2005; Katongo et al., 2002; Porada, 1989; Selley et al., 2005) with the study area outlined.

basement gneisses and granites (Hanson et al., 1988, 1994; Johnson et al., 2007; Katongo et al., 2004). In Northern Zimbabwe, the Zambezi Belt is characterised by SW-directed thrusting and duplex formation in which slivers from the Kalahari Craton basement gneisses are tectonically intercalated with the supracrustal sequence (Dirks et al., 1999; Goscombe et al., 2000; Hargrove et al., 2003; Vinyu et al., 1999).

The boundary between the Lufilian Arc and the Zambezi Belt is marked by the Mwembeshi Zone (MwZ). This structure juxtaposes the low-metamorphic grade inner zones of the Lufilian Arc with the amphibolite and eclogite facies rocks of the Zambezi Belt (de Swardt et al., 1965; John et al., 2003, 2004a, 2004b; Vrána et al., 1975). The MwZ was described as a major sinistral wrench fault that accommodated horizontal displacement of ca. 200 km (de Swardt et al., 1964, 1965). North of it, in Central Zambia, the emplacement of one of the largest magmatic complexes in the orogen, the Hook Batholith, is considered to be syntectonic to the sinistral shearing (Hanson et al., 1993). To the west, across the Kalahari Desert deposits, correlations have been made with the Okahanja lineament or the Schlesien line in the Damara Belt in Namibia (Daly, 1986; Porada, 1989; Unrug, 1983). In all cases, the MwZ is interpreted as a major continental-scale shear zone and as a first order geological structure that is thought to have accommodated the convergence between the Kalahari and Congo Cratons. However, detailed modern structural investigation of this first order tectonic boundary in Central Zambia has never been undertaken.

The study area of this research is located at the poorly investigated junction between the innermost zone of the Lufilian Arc and the NW part of the Zambezi Belt along the MwZ in Central Zambia (Fig. 1). Therefore, this is a key area for the reconstruction of the Pan-African Orogen in Zambia. By studying the field relationships and structural characteristics of the MwZ, Hook Batholith and different sections of the Katangan stratigraphy, and including new U–Pb geochronology data and interpretation of aeromagnetic images, this work aims at (i) providing new tectonic constraints on the MwZ, (ii) studying the emplacement chronology and deformation history of the Hook Batholith (iii) characterising the deformation history of the Katangan metasedimentary rocks adjacent to the MwZ, and (iv) unravelling the role and significance of the zone in the Pan-African tectonics. At the end, a new tectonic model is proposed for the Pan-African Orogen evolution at the junction between the Lufilian Arc and the Zambezi Belt.

2. Geological setting

The Lufilian Arc is characterised by 5 tectonic zones (Fig. 1) defined by Porada (1989): i) The External Fold and Thrust Belt is a NW- to NE-vergent zone of thin-skin thrusting and related synmetamorphic folding under greenschist to locally lower amphibolite facies. ii) The Domes Region is characterised by numerous basement inliers deformed together with the Katangan cover-rocks along N-vergent thrusts. Metamorphic petrology studies of HP mafic rocks and talk-kyanite schists and microstructural analysis indicate a transitional upper amphibolite-eclogite facies overprint at ca. 650–750 °C and pressure of ca. 13 kbar (Cosi et al., 1992; John et al., 2004a). The associated synmetamorphic monazite grains determine an age range of ca. 530–523 Ma for the temperature peak of the metamorphic overprint (John et al., 2004a) and Eglinger et al. (2014) suggested longer period of synmetamorphic monazite growth starting at ca. 550 Ma. iii) The Synclinorial Belt and iv) the Katanga High are characterised by complicated folding, in which two generations of structures are interfered and by voluminous magmatism in the Katanga High (de Swardt et al., 1964; Porada, 1989; Porada and Berhorst, 2000). These two zones and their structural evolution are described in more details in the following subsection. v) The Katangan Aulacogen or "Golfe du Katanga" represents the foreland basin.

2.1. Structure of the inner zones of the Lufilian Arc

The Synclinorial Belt and the Katanga High (Fig. 1) represent the inner zones of the arcuate Lufilian Arc. The distinction between the two is based on the widespread magmatism in the Katanga High and on stratigraphic differences. In the Synclinorial Belt only Kundelungu Group sedimentary rocks crop out, whereas in the Katanga High also lower stratigraphic levels are exposed. The boundary between the two is unclear and Unrug (1988, 1989) grouped them in one tectonic unit. In contrast, Porada and Berhorst (2000) regarded the Katanga High as the northern margin of the overriding plate in a scenario where the Pan-African suture zone between Angola-Kalahari Craton and the Congo-Tanzania Craton separates the Katanga High to the S and SW from the strongly deformed passive margin sequence of the Synclinorial Belt to the N and NE. The northern boundary of the inner zones with the Domes Region is marked by several N-vergent thrusts (Porada, 1989; Unrug, 1988, 1989), and the southern boundary is the MwZ (de Swardt et al., 1964, 1965). The inner zones are characterised by folding of the low grade metasedimentary rocks (greenschist facies to incipient metamorphism — Katongo et al., 2002; Ramsay and Ridgway, 1977; Unrug, 1988; Vajner, 1998) along N–S trending close to isoclinal folds with steep to vertical axial planes, refolded by E- or ENE-trending structures in its northern part (de Swardt et al., 1964; Porada, 1989). De Swardt et al. (1965) argued that the structural evolution is controlled by major zones of transcurrent displacement, postdating the main phase of deformation in the Lufilian Arc. In their interpretation, the two main shear zones are the presumed sinistral MwZ and the composite Kapiri Mposhi-Mkushi zone (KMMZ on Fig. 1), with possible dextral kinematics and considerable, although not quantified, vertical displacement.

2.2. Mwembeshi Zone

The available interpretations for the evolution, kinematics and role of the MwZ in the Pan-African Orogeny are contradictory. Based on the geometry analysis of the foliation trends, it has been described as a structure of ca. 200 km sinistral displacement formed after the main tectono-metamorphic event in the Lufilian Arc (de Swardt et al., 1964, 1965). Unrug (1983) suggested that the MwZ developed as the southern sinistral boundary of a clockwise rotated mega-block, which, in its northern part, was responsible for the NE-directed thrusting in the Lufilian Arc, implying that the transcurrent shearing is contemporaneous to the thrusts and folds development in the outer zones of the Arc. According to Coward and Daly (1984) and Daly (1986, 1988), the MwZ represents a transform shear zone between the ENE-vergent structures in the eastern arm of the Lufilian Arc and the WSW-vergent thrusting in the Zambezi Belt. The authors reported both dextral and sinistral movements — an interpretation that agreed with the understanding of the kinematics of lateral ramps by Butler et al. (1986). Hanson et al. (1993) and Johnson et al. (2005) suggested that the sinistral kinematics correspond to oblique convergence between the Congo and Kalahari Cratons. In the area to the N and NW of Lusaka, dextral faults were interpreted to reflect lagging of tectonic slices in the sinistral strike-slip system (de Swardt et al., 1964). Further NE, along the supposed continuation of the MwZ in the Irumide Belt, Johns et al. (1989) described several contemporaneous dextral strike-slip zones of presumably Pan-African age. Although a correlation with the MwZ was suggested, the authors emphasized the uncertainty caused by the opposite kinematics of the structures. Further NE, to the area of Lake Malawi, the MwZ is again described as a dextral wrench zone (e.g. Bjerkgard et al., 2009; Ring et al., 2002). Ring et al. (2002) consider the shearing to be related to the E–W shortening tectonics in the Mozambique Belt at ca. 580–550 Ma. Porada and Berhorst (2000) suggested that the MwZ is a Palaeoproterozoic lineament that was repeatedly reactivated at Meso- and Neoproterozoic times. In their model, the Pan-African sinistral shearing reflects the difference in the amount of shortening in the Lufilian and Zambezi belts. However, the authors also suggest that the final convergence between East and West Gondwana could have triggered continental-scale dextral shearing along the same structure.

2.3. Hook Batholith

The Hook Batholith (Figs. 1, 2) is the largest known intrusion in the eastern section of the Damara-Lufilian branch of the Pan-African Orogen. Prior to Hanson et al. (1993), it was considered as a remobilised basement pluton (de Swardt et al., 1965; Unrug, 1983, 1988, 1989). In the regional interpretation of Unrug (1983), its Pan-African rejuvenation is triggered by the sinistral movements along the MwZ. Hanson et al. (1993) provided U–Pb zircon geochronology data and distinguished several granitoid phases which they described as syn- or post-tectonic based on the development (or lack) of solid state deformation structures. Fine- to medium-grained and megacrystic granites yielded upper intercept ages of 559 ± 18 and 566 ± 5 Ma, respectively. A rhyolite dyke sample, dated at 538 ± 1.5 Ma was interpreted as a member of a late syn-tectonic phase to which the authors assigned also numerous microgranites, biotite- and hornblende-bearing granites and leucogranites. An undeformed megacrystic granite, sampled in the central part of the batholith, was dated at 533 ± 3 Ma and interpreted as post-tectonic. A sample from a rhyolite dyke that crops out within the

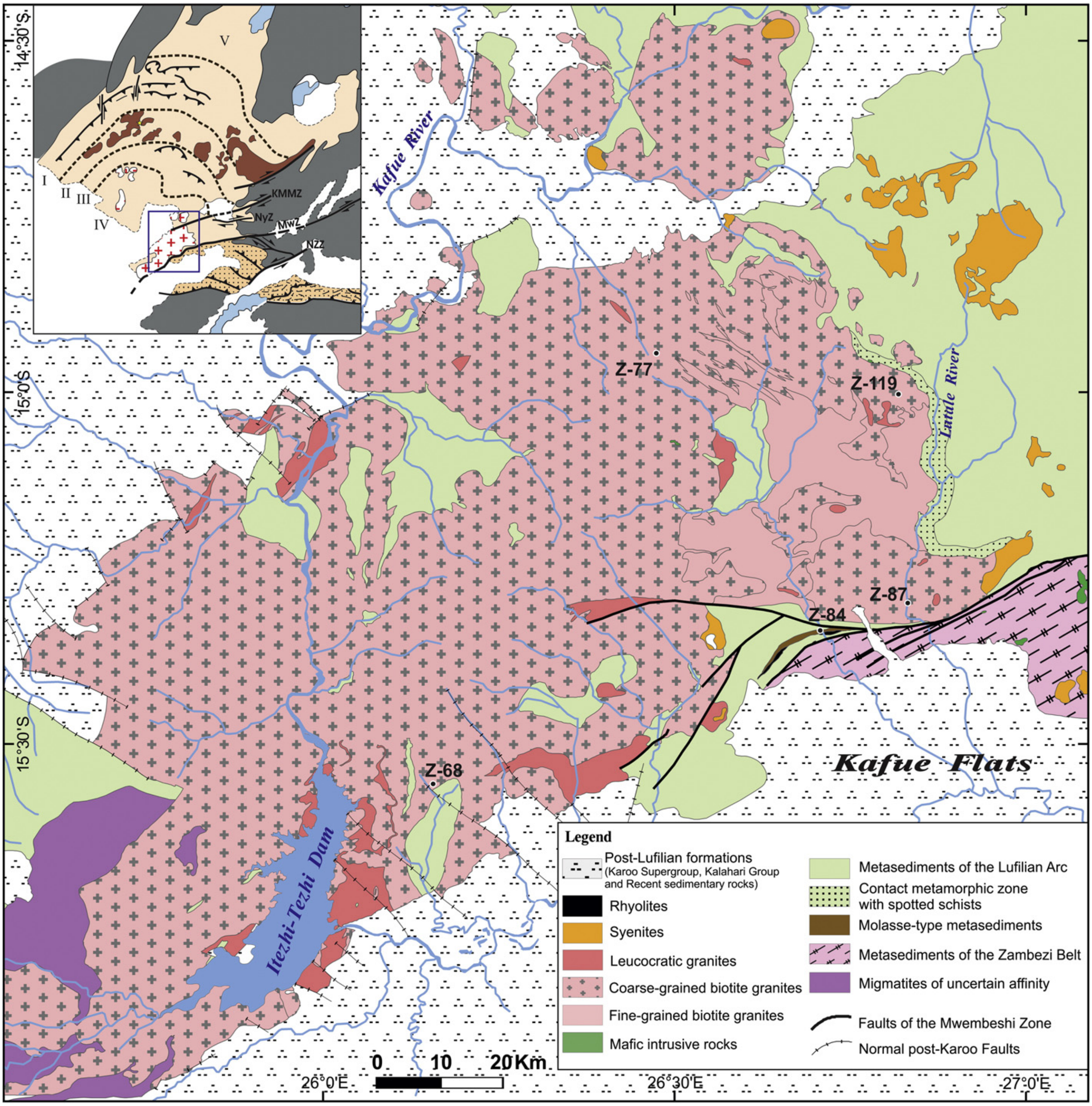

Fig. 2. Geological map of the Hook Batholith area, compiled by incorporating personal field and analytical data with published geological maps of the Zambian Geological Survey (Abell, 1970, 1976; Cikin, 1971; Griffiths, 1998; Page, 1974; Pippin, 1975; Seifert, 2000; Thieme and Johnson, 1981), with the localities for the U–Pb geochronology study. The inset shows the location of the presented map in a simplified version of Fig. 1.

MwZ gave an age of 551 ± 19 Ma and the authors suggested that it is syn-tectonic to the movements along the MwZ. Considering that the southern margin of the batholith is ductilely deformed by the MwZ, they further interpreted the Hook granitoids as emplaced during the sinistral transpression. Abell (1970), Cikin (1971) and Lobo-Guerrero Sanz (2005) described numerous but scattered and volumetrically minor gabbroic and gabbro-dioritic bodies within the granitoids of the batholith or in the adjacent metasedimentary rocks that remain so far undated. Undeformed, medium- to fine-grained and porphyritic syenites intrude the metasedimentary sequence east of the batholith (Abell, 1970; Cikin, 1971). A syenite and an alkali granite, within the Zambezi Belt south of the MwZ, were dated, respectively, at 550 ± 25 and 538 ± 3.3 Ma (SHRIMP U–Pb on zircons, Lobo-Guerrero Sanz, 2005). Snelling et al. (1972) reported K–Ar amphibole and mica cooling ages for the Hook granitoids and the results spread between 465 ± 16 and 450 ± 14 Ma. One pegmatite sample revealed an age of 440 ± 15 Ma. The ages were interpreted by the author as the time of final cooling after tectonic rejuvenation during the Lufilian Orogeny of pre-Pan-African basement gneisses.

Based on the geochemical signature, Lobo-Guerrero Sanz (2005) interpreted the batholith as an intraplate anorogenic complex intruded in rift environment. New data on the Hook geochemistry (unpublished personal data) and the results provided by Lobo-Guerrero Sanz (2005) indicate that the felsic rocks form a prevalent alkali-calcic suite that consists of quartz-monzonite, granodiorite and granite, plus an alkali suite with quartz-monzonite, syenite and alkali-granite. The granitoids are mostly metaluminous, show a high Fe/Mg and K/Na ratio and are compatible with a late- to post-orogenic setting. Either tholeiitic or alkaline affinities have been documented for the small, scattered mafic intrusions and, at least in part, testify the interaction between mantle and crustal components.

2.4. Stratigraphy of the Hook area

To the north of the MwZ, the metasedimentary rocks of the Katanga High in the Hook area consist of alternating fine-grained quartzites, quartz-schists and sericite schists overlain by a sequence of dolomites and marbles, calc-silicates, and schists, all metamorphosed under greenschist facies. The succession is broadly correlated with the Lower and Middle Kundelungu Group (Abell, 1970; Cikin, 1971; Phillips, 1958; Phillips and Newton, 1956; Vajner, 1998). Phillips (1958) and Cikin (1971) assigned the siliciclastic metasediments at the base of the succession to the Roan Group, but this was not accepted in later interpretations (e.g. Thieme, 1984; Vajner, 1998). The uppermost unit in the area, the Upper Kundelungu (de Swardt et al., 1964), unconformably overlies the described section (Abell, 1970; Phillips, 1958; Vajner, 1998) and consists of weakly metamorphosed argillaceous and arenaceous sedimentary rocks: shales, slates, siltstones, mudstones, occasionally with lenses of limestones, sandstones to arkoses and conglomerates. The conglomerates comprise pebbles from the underlying metasedimentary formations which indicate a major unconformity and deposition after the exhumation of the older units (de Swardt et al., 1964). Abell (1970) and Cikin (1971, 1972) described a large (up to 3 km wide) zone of contact metamorphism along the eastern margin of the Hook Batholith (Fig. 2) where metapelites developed into andalusite–cordierite mica schists. Chilled margins and contact metamorphic aureoles are also described for the small, composite granite-syenite satellite intrusions and for some of the gabbro bodies (de Swardt et al., 1964 and references therein).

South of the MwZ, the stratigraphy of the Zambezi Belt is represented by an alternation of muscovite schists, biotite schists (often affected by chloritisation) and coarse-grained, partly dolomitic marbles (Abell, 1970; Griffiths, 1998; Phillips, 1958). Mafic magmatic rocks crop out within the metasedimentary sequence in a WNW trending belt. Some of them show eclogite-facies mineral assemblages and N-MORB geochemical characteristics (John et al., 2003, 2004a, 2004b; Vrána et al., 1975). Sm–Nd and Lu–Hf garnet-whole rock isochrones gave ages of the high pressure (26–28 kbar) overprint between 659 ± 14 Ma and 595 ± 10 Ma (John et al., 2003, 2004b) and the eclogites were interpreted as exhumed remnants of the subducted oceanic crust that mark the suture zone between the Congo and Kalahari Cratons (John et al., 2003, 2004a, 2004b; Johnson et al., 2005; Vrána et al., 1975).

To the SW of the Hook Batholith, the granitoids are in contact with metatectic migmatites of uncertain origin and age (Griffiths, 1998). As the metamorphic grade is much higher than along the eastern margin of the granite, Hanson et al. (1993) suggested exposure of much deeper structural levels in this area. The lithologies observed by Griffiths (1998) include muscovite and two-mica gneisses, muscovite schists, quartzites and subordinate marbles.

3. Methodology

3.1. Aeromagnetic data set and processing

The digital aeromagnetic dataset used in this study is a compilation of various digitalised contour maps of the country-wide aeromagnetic surveys undertaken by the Geological Survey of Zambia between 1967 and 1982 (Katongo et al., 2002; Saviaro, 1980). The surveys were carried out at a line spacing of between 800 m and 2000 m at a mean flight height of 150 m. Manually contoured magnetic intensity maps, at a scale of 1:50,000, were produced from data obtained from these surveys (Isaacs, 1968). These contoured maps, along with data collected from later surveys, were digitalized, with the help of the Council of Geosciences of South Africa, and merged to produce the regional 250 m grid cell size digital map of Zambia (Katongo et al., 2002). Oasis Montaj software (Geosoft) version 8.0 was used to process the data. Reduction to pole (RTP) filter was applied to the Total Magnetic Intensity (TMI) grid using inclination of −54.37° and declination of −9.08°. To enhance the shallow, high-frequency magnetic fabrics of the granitoids, the first vertical derivative and analytic signal were processed. These filters were mainly interpreted individually but to visualise subtle features a colour scale vertical derivative was overlain on a greyscale analytic signal image. Histogram modifications were carried-out in ESRI ArcGIS software to produce the clearest images and further enhance subtle magnetic foliations.

3.2. U–Pb zircon geochronology

Zircon grains were extracted from whole rock samples by standard crushing, heavy liquid, and magnetic separation techniques and final handpicking. A characterization of the internal structure in the selected zircon grains was obtained by analysing cathodoluminescence (CL) images obtained by scanning electron microscopy. U–Pb isotopic analyses were carried out at the Central Analytical Facility at Stellenbosch University using a Thermo Finnigan Element2 magnetic sectorfield-inductively coupled plasma-mass spectrometer (SF-ICP-MS) coupled to two different laser ablation (LA) systems: a NewWave UP213 and a Resonetics M-50-LR Excimer. The diameters of the ablation craters ranged between 25 and 35 μm with a penetration depth of about 15–20 μm. The methods employed for analysis and data processing are described in detail by Gerdes and Zeh (2006) and Frei and Gerdes (2009). For quality control, the Plešovice (Sláma et al., 2008) and M127 (Mattinson, 2010; Nasdala et al., 2008) zircon reference materials were analysed, and our results were consistently in excellent agreement with the published ID-TIMS ages. GLITTER software package was used for the data reduction. Common lead correction was applied by combining the interference and background corrected ^{204}Pb signal with a model Pb composition (Stacey and Kramers, 1975).

4. Interpretation of airborne magnetic survey data in the Hook Batholith

In order to unravel the variation in the foliation trajectories, three different methods where employed: i) interpretation of airborne magnetic geophysical images, ii) analysis of the structural data in published geological maps and iii) structural fieldwork and mapping.

The studied granitoids are characterised by a high content of ferromagnetic minerals, mainly magnetite and in some places pyrrhotite. Field and thin-section studies of deformed granitoids revealed that these minerals are aligned in the foliation planes and in the shear bands, forming well-developed elongated domains. Magnetite aggregates constitute monomineralic ribbons or, more commonly, are in association with biotite (see the microstructural sections in the next two chapters). At the outcrop-scale, a concentration of magnetite was observed in centimetre to decimetre-wide mylonite–ultramylonite zones. Therefore, the specific structural position of the ferromagnetic minerals was used in the structural interpretation of the airborne magnetic data.

About 1800 linear (in map view) magnetic positive and negative anomalies were picked out in the exposed or sub-exposed part of the batholith (Fig. 3). The intensity of the magnetic response decreases rapidly when entering areas more deeply buried underneath the Kalahari and/or Karoo deposits and this data was not useful for the structural mapping.

In the NE and S parts of the batholith, the magnetic anomalies are characterised by parallelism with the trend of the solid-state planar

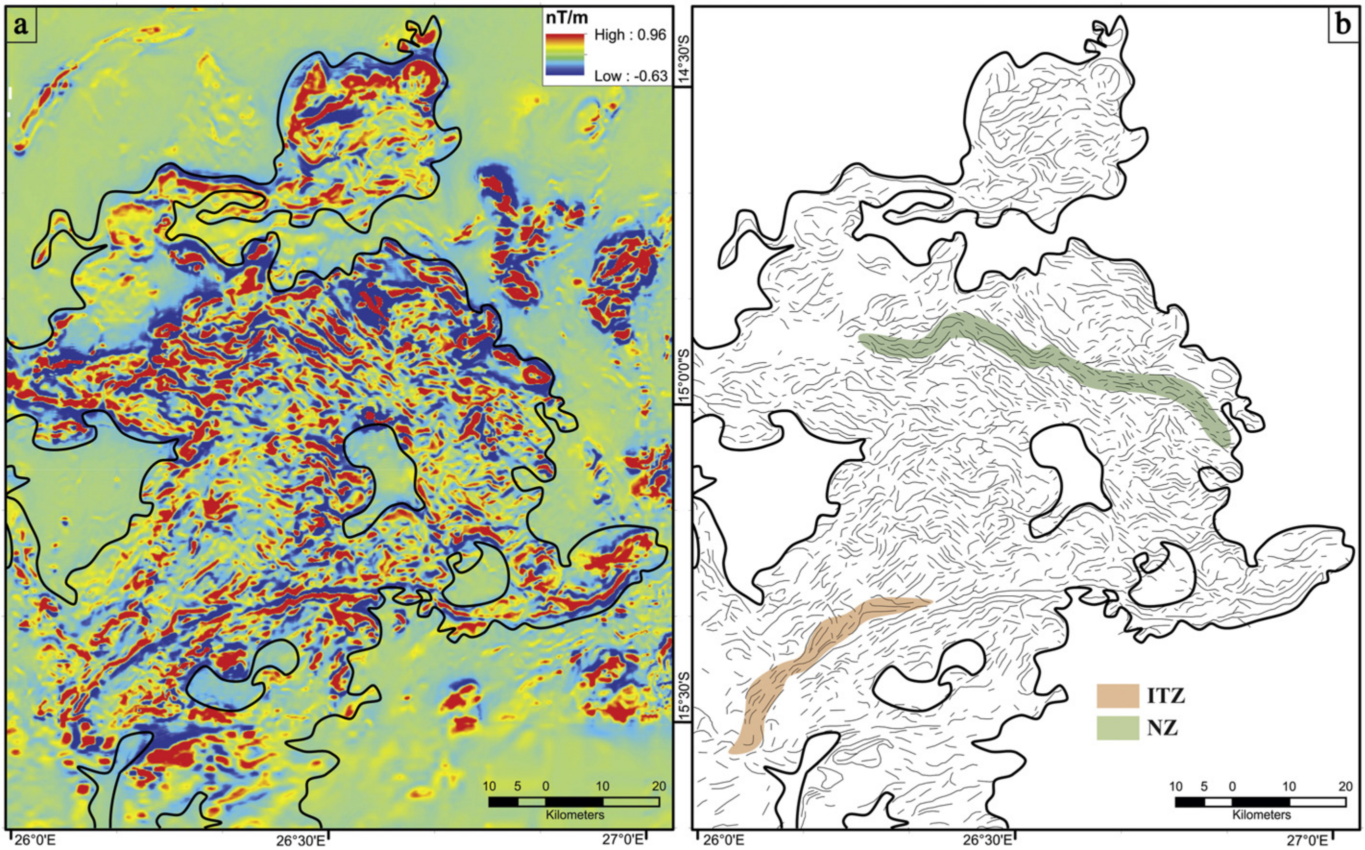

Fig. 3. Linear magnetic anomalies in the Hook Batholith. a) reduce to pole (RTP) first vertical derivative (1-VD) filtered total magnetic intensity (TMI) image of the study area with the outlines of the batholith as it is interpreted from the geophysics. The "quiet" low-intensity, low-frequency units within the granite broadly correspond to large metasedimentary pendants; b) map of the linear magnetic anomalies in the batholith. The coloured semi-transparent areas correspond to the Itezhi-Tezhi Zone (ITZ) and Nalusanga Zone (NZ).

fabrics in the deformed granitoid measured in the field. The central and the northernmost sectors of the batholith show magnetic anomalies with lower intensity, outlining much shorter and discontinuous magnetic anomalies often with an unstable trend. Limited field observations and correlation with the 1:100,000 scale geological maps allowed us to interpret this fabric as related to magmatic foliation.

Based on the interpretation of the magnetic survey, geometry of deformation fabrics at outcrop scale and metamorphic conditions of deformation, the study area has been divided into different structural domains. In the NE and SW part of the batholith, two kilometre-wide high-strain zones were documented — respectively, the Nalusanga Zone (NZ) and the Itezhi-Tezhi Zone (ITZ) (Fig. 4). Another area of detailed work is the SE part of the batholith and the adjacent metasedimentary rocks within the MwZ (area SP-3 in Fig. 4b). Structural studies in the Katangan rocks were also carried out along cross-sections east of the contact with the granites (area SP-5 in Fig. 4b). Where polyphase fabric development has been observed, a local chronology of fabric formation has been performed. Accordingly, two deformation events are recorded and described in the following sections and their significance for the regional tectonic evolution is addressed in the discussion part of this work.

5. Characteristics of the deformation in the Nalusanga Zone (NZ)

5.1. Macroscopic characteristics and geometry

The NZ is a ca. 3 km wide, steep SW- to SSW-dipping high-strain ductile shear zone located in the NE part of the Hook Batholith (Fig. 4). Structural field studies and sampling for microstructural characterisations were carried out along NE–SW sections across the zone (in key-area SP-4, Fig. 4b). To the SE, the zone marks the contact between the granites and the metasedimentary rocks. When approaching the eastern contact of the batholith, there is a swing of the NZ trend towards SE, but here the ductile deformation is weaker and less pronounced. The deformed rocks are fine- to medium-grained, equigranular to fine-porphyritic biotite granites and very coarse-grained to megacrystic biotite granites, both types with subordinate hornblende, sometimes garnet and accessory titanite, zircon, magnetite and sulphides. The porphyries are of K-feldspar (microcline) and less abundant plagioclase. The distinction between the two types is sometimes very difficult as they both grade smoothly towards medium-grained and moderately porphyritic granite. In addition, in high-strain domains, the mega-porphyroclastic type

Fig. 4. Structural map of the study area. a) Structural map with foliations presented as form lines with the inclinations added where data is available. F1 and F2 fold trends are shown in the metasedimentary host rocks east of the batholith. The localities sampled for U–Pb zircon isotope geochronology are indicated; b) main structural trends in the granite ITZ — Itezhi-Tezhi Zone, NZ — Nalusanga Zone, and MwZ — Mwembeshi Zone. The ellipses labelled Sp-1 to Sp-5 show the areas where data for the stereographic plots were collected: All stereographic plots are equal area (Schmidt) lower hemisphere projections. SP-1 — solid state planar fabrics in the ITZ (great circles) and associated mineral lineations (black points); SP-2 — orientation of the D2 shear zones (great circles) with associated mineral stretching lineation (three-sided stars) from the SW part of the batholith; SP-3 — contoured plot of poles to the S_{0-1}-rotated during D2 in the area south of the Hook Batholith, within the MwZ; SP-4 — contoured plot of poles to the S-planes (grey areas) and associated mineral lineations (black points) in the NZ; SP-5 — orientation of the foliation planes in the metasedimentary rocks east of the Hook Batholith (great circles).

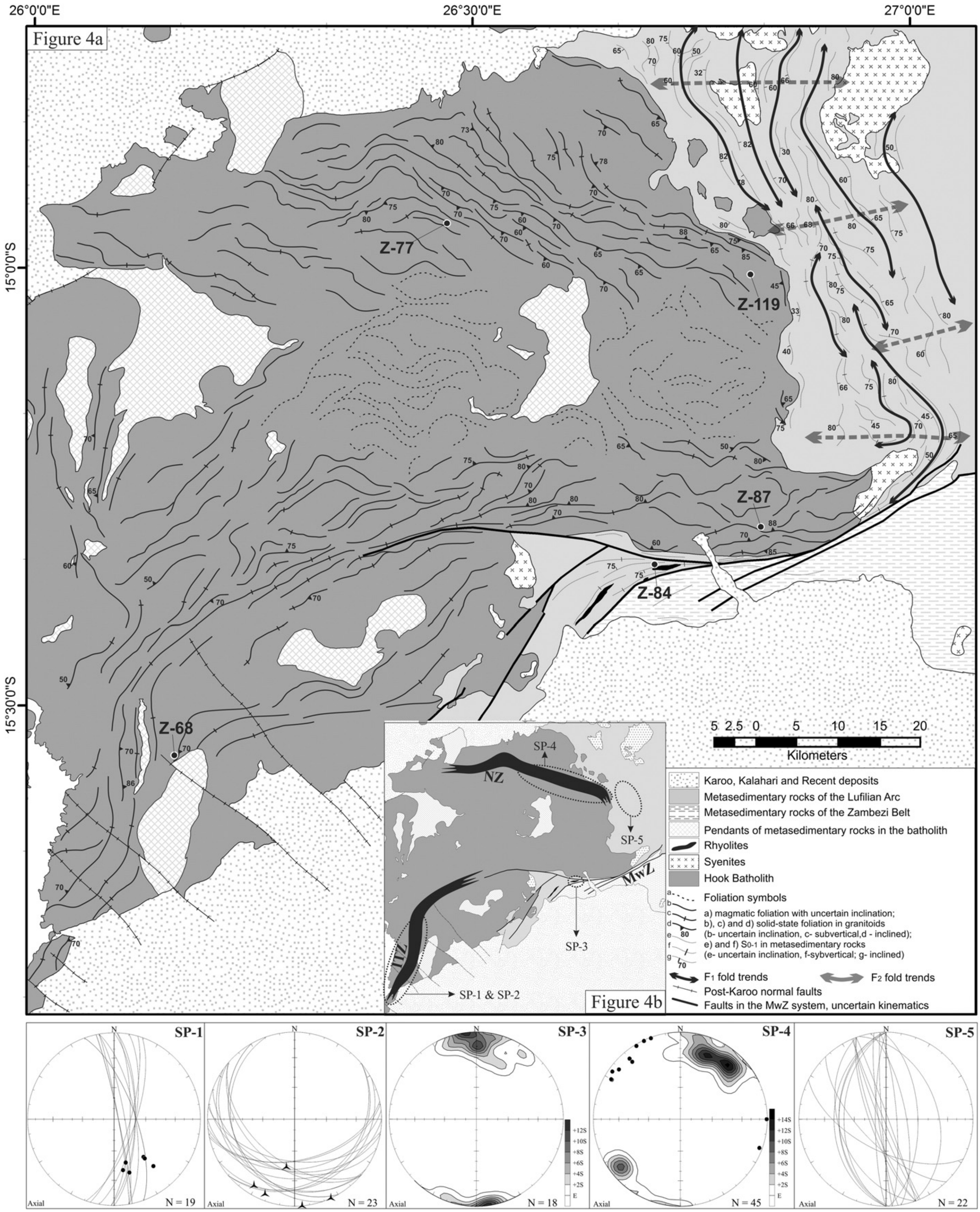

shows significant recrystallisation and grain-size reduction and primary relationships between the fine- and coarse-grained granites are obliterated by the progressive deformation. At map scale, they are in flame-shape interfingering relationships (Fig. 2) and the contacts are parallel to the solid-state foliations. Within the NZ, the granites show a smooth kilometre-scale transition from weakly-

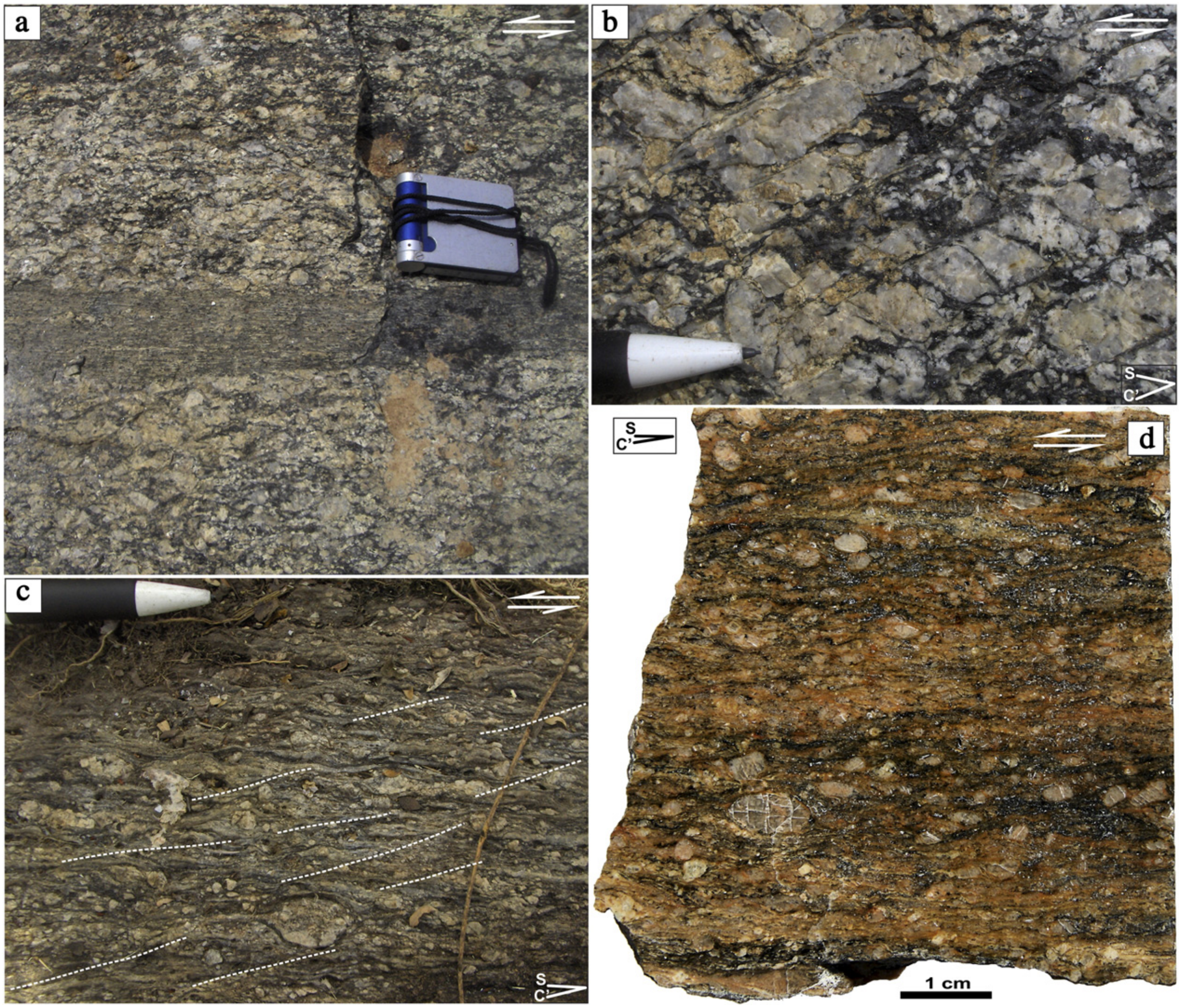

Fig. 5. Photographs of the deformed granites within the NZ. All sections are parallel to the stretching lineation and orthogonal to the foliation: a) ca. 10 cm wide ultra-mylonite zone with sharp boundaries in protomylonitic granite; b) detail of the protomylonite in Fig. 5a, that shows the relationships between the S-planes (left–right to right-sloping, undulating) and the C′ shear bands (left-sloping). Note the development of σ-porphyroclasts with short tails deflected by the shear bands. The acute angle between the S-planes and the shear bands is about 30°; c) mylonitic granite with few preserved large σ-porphyroclasts and developed augen-banded texture. The former mega-porphyroclasts are very small, rounded and with strongly elongated tails. The angle between the foliations and the shear bands is about 20° (shear bands, marked with dashed lines, trend upper right to lower left; S-planes anastomose from left-right to slightly right-sloping); d) polished slice showing left-right compositional banding and development of gneiss texture in fine-porphyroclastic granite. Low angle left-sloping C′ shear bands are visible in the upper left and central right hand side of the sample. Sinistral sense of shear is inferred from the fabrics geometry on images b), c) and d).

foliated rocks at the margins of the zone, to mylonites in its central part (in sections across the shear zone). Centimetre- to decimetre-wide ultramylonite bands with sharp contacts with protomylonitic granite developed in the central part of the NZ (Fig. 5a, b) but more often there is a smooth transition from protomylonites to mylonites. The deformed granites are characterised by well-developed foliation planes (S-planes) and C′ shear bands. The S and C′ foliations were observed in both weakly and strongly deformed rocks. The shear band cleavage and augen-gneiss texture are more common in the coarse-grained granites (Fig. 5a, b). With progressive deformation, the S-foliation becomes continuous and preserved large K-feldspar porphyroclasts are scarce (Fig. 5c). The fine porphyroclastic granites are characterised by better developed gneissic texture defined by the formation of feldspar- or quartz–feldspar-dominated bands and mica-rich domains (Fig. 5d).

The S-planes in protomylonites of the NZ are marked by the long axes of the porphyroclasts and by the incipient development of tails (Fig. 5b). In the mylonites, they are defined by the developed compositional

Fig. 6. Microphotographs of thin-sections from the deformed granitoids in the NZ. Orientation of the thin-sections is parallel to the stretching mineral lineation and orthogonal to the foliation: a) photo-stitch of 9 microphotographs illustrating sigma- (σ) and delta-type (δ) porphyroclasts. Recrystallised quartz and feldspar aggregates form strongly elongated ribbons (white and greyish, respectively). They are separated by dark domains constituted of biotite and opaques (mainly magnetite). Larger magnetite aggregates are visible in the strain shadows of the porphyroclasts. PPL; b) one large (centre) and several smaller (lower part) mantled K-feldspar porphyroclasts. The grains in the rims recrystallised mainly by subgrain rotation (sg). The large clast in the centre has strongly elongated tails where the recrystallised grains are much larger. It also shows incipient subgrain formation and strong undulose extinction (ue). Bulging recrystallisation (blg) is not common, visible mainly at the subgrain boundaries of the feldspars. Quartz is fully recrystallised mainly by grain boundary migration (gbm) and subgrain rotation, forming monomineralic microlithons and ribbons (white arrows). Red and green arrows point to feldspar-dominated and biotite-magnetite dominated domains respectively. CPL; c) relics of former large K-feldspar porphyroclasts (k) are surrounded by fine-grained recrystallised feldspars. Each fragment forms a small core and rim porphyroclast. The recrystallisation is by SGR. CPL; d) big K-feldspar porphyroclast (ca. 6 mm long) is fragmented along synthetic shear bands. Cryptocrystalline feldspar aggregates developed along the margins of the clast and along the micro fractures by bulging recrystallisation. The quartz grains from the matrix tend to form elongated monomineralic ribbons. CPL; e) large euhedral K-feldspar with undulose extinction in a fine-grained recrystallised polymineralic matrix. At the upper left and lower right part of the photograph, initial stage of sinistral sigma-tails formation and partial recrystallisation in the strain shadows is visible. CPL. All photographs show sinistral kinematics.

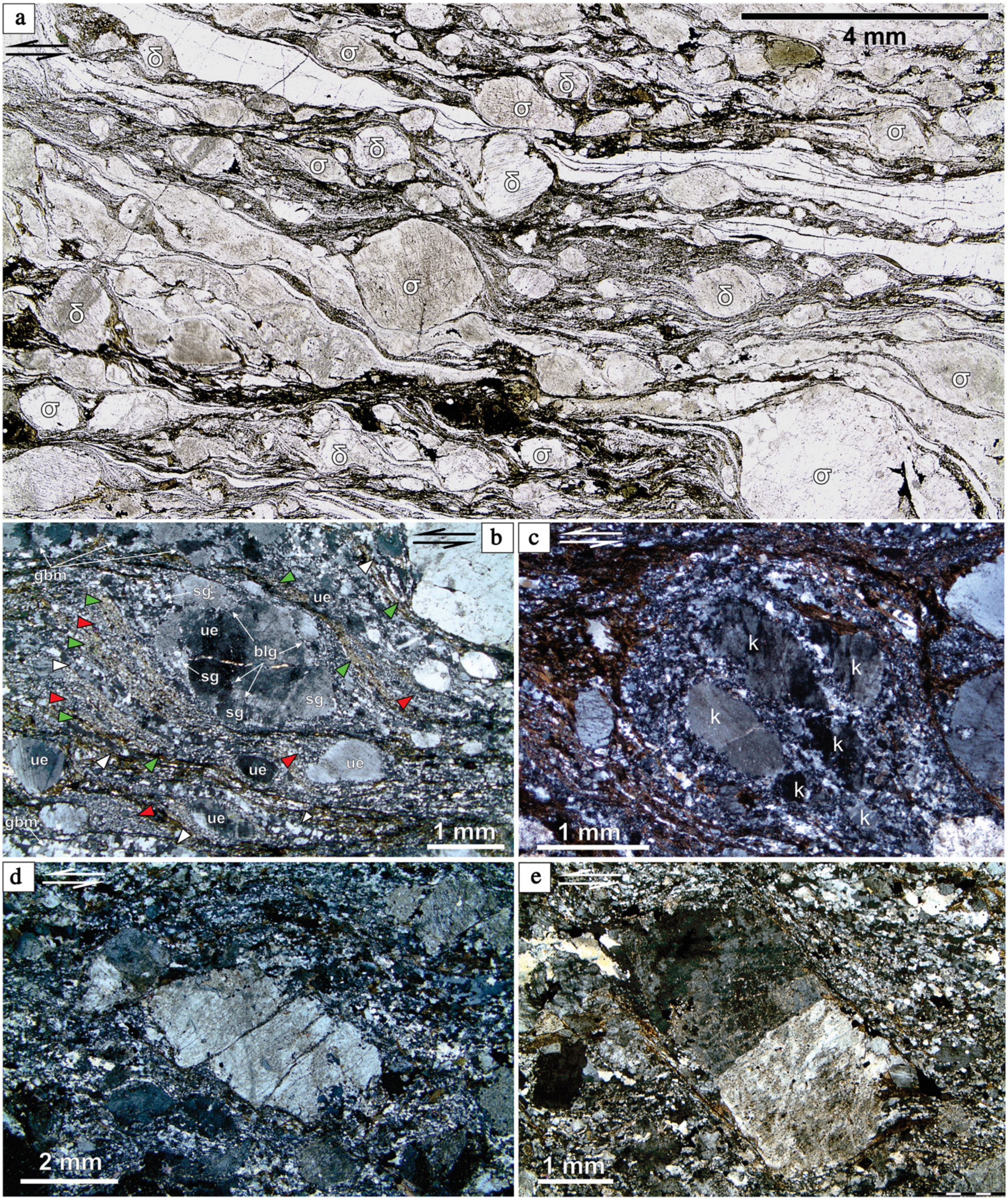

layering and by the strongly elongated tails of the porphyroclasts (Fig. 5c, d). The ultramylonite zones show continuous foliation marked by compositional layering and by grain shape preferred orientation. The C′-planes are characterised by a concentration of biotite in discrete micro-domains, often in association with cryptocrystalline felsic minerals and opaques. In the protomylonites, the spacing of the shear bands varies but averages ca. 2 cm (Fig. 5b). The acute angles between S- and C′ planes decrease with decreasing distance to the central, high-strain part of the NZ, ranging from 38° to 10° and the two structures are parallel in the ultramylonite bands. Stereographic plots of S-planes measured in the field show two very close maxima, respectively at about 220°/70° and 200°/70° (Fig. 4, SP4). The associated mineral lineations plunge gently towards WNW to NW or are subhorizontal (Fig. 4, SP4) and are defined by grain shape preferred orientation of biotite, elongated biotite aggregates and stretched quartz and feldspar aggregates. Subhorizontal stretching lineation is also carried by the shear bands where it is defined by elongated to needle-shape quartz grains, stretched feldspar grains and elongated felsic and biotite aggregates. The angular relationships between foliation planes and shear bands and the geometry and orientation of deformed minerals or aggregates (Figs. 5 and 6) define the NZ as a sinistral strike-slip structure.

5.2. Microstructural analysis

Samples from mylonitic granites from the central part of the NZ show that quartz and feldspar form strongly elongated ribbons (Fig. 6a, b). In the ribbons, quartz recrystallised by grain boundary migration (GBM). The recrystallised grains, between 100 and 200 μm in size and sometimes larger, often have a grain-shape preferred orientation parallel to the ribbons. Locally, grain boundary area reduction (GBAR) was observed with the dihedral angles between the annealed grains tending to ca. 120°. The feldspar ribbons show dominant recrystallisation by subgrain rotation (SGR) (Fig. 6b, c). The size of the neograins is in the range between 50 and 100 μm and larger in the strain shadows. The porphyroclasts, K-feldspar and subordinate plagioclase, are either rounded δ-clasts or very strongly elongated σ-clasts (Fig. 6a). Most of them show development of core-and-mantle structure by SGR recrystallisation (Fig. 6b, c). The width of the mantles is commonly about 100 μm but varies strongly. Deformation myrmekites developed at the high-strain sides of the K-feldspar clasts. The largest feldspar grains show very strong undulose extinction, development of deformation lamellae and incipient subgrain formation (Fig. 6b). Bulging (BLG) recrystallisation was observed sporadically at the boundaries between the subgrains. The biotite micas are fully recrystallised and constitute (together with opaques) well-defined domains that separate the felsic ribbons. Mica-magnetite aggregates are also abundant in the shear bands. High-strained biotite flakes, deformed along the shear bands and forming large mica fish with undulose extinction and tails of small, recrystallised biotites are still preserved in the rock. The opaque minerals (mainly magnetite) are abundant and although they are often in association with the biotite in the S- and C′-planes, they also were observed to constitute monomineralic layers in the S-planes. It was noted that completely recrystallised and sometimes annealed quartz grains in the microlithons show undulose extinction related to the later stages of the progressive deformation.

Towards the outer sections of the NZ, in protomylonites and further into areas with only weakly foliated granites, the size of the recrystallised felsic grains becomes progressively smaller. Monomineralic felsic ribbons become shorter or did not develop, corresponding to the formation of wider, polymineralic domains of small recrystallised grains. Quartz, sometimes clustered in lens-shape aggregates, recrystallised by SGR. In some places, grains with strong undulose extinction are deflected around the more resistant feldspar clasts. The feldspar porphyroclasts are larger, with undulose extinction and deformation lamellae, and commonly fragmented along synthetic and antithetic shear bands (Fig. 6d) or with preserved prismatic shape (Fig. 6e). The strain shadows are considerably smaller and recrystallised feldspar tails did not develop. BLG recrystallisation is common, and observed at the margins of the fractured feldspars (Fig. 6d). Further towards the undeformed granitic wall-rocks of the NZ, preserved magmatic textures were observed. The deformation here is only marked by undulose extinction in large quartz and biotite grains, the latter also showing weak bending of the (001) faces. Sporadically undulose extinction is visible in the feldspars.

The main strain-accommodating minerals in the central part of the NZ are quartz and micas and the feldspars have also important, although subordinate, contribution, whereas towards the outer section of the zone the role of feldspars for strain accommodation decreases significantly. The microstructural analysis confirmed the sinistral kinematics of the NZ observed on the field and in hand-samples (Fig. 6).

6. Characteristics of the deformation in the SW part of the Hook Batholith

Two deformation events can be distinguished in the SW part of the Hook Batholith.

6.1. D1 deformation in the Itezhi-Tezhi Zone (ITZ)

6.1.1. Macroscopic characteristics and geometry

The structural study across the N–S striking ITZ was focused on an approximately 30 km long section, NE of the Itezhi-Tezhi dam (Fig. 4b). The rocks deformed within the zone are coarse-grained, porphyroclastic, biotite granites and less abundant leucocratic quartz–feldspar granites. Within the middle, high-strain part of the ITZ, the biotite granites are characterised by a pronounced, yet heterogeneously developed at outcrop scale, penetrative solid-state foliation and development of an augen-gneiss texture (Fig. 7a). Some of the porphyroclasts have strongly elongated tails which together with the quartz and quartz–feldspar microlithons further contributed to the formation of a spaced gneissic foliation (Fig. 7b). Domains of biotite + opaques (magnetite and sulphides) often wrap around elongated porphyroclasts. At the margins of the ITZ, the foliation is outlined by the shape-preferred orientation of the micas and by alignment of preserved euhedral feldspars. In the leucocratic granites, the planar fabric reveals heterogeneous strain distribution (Fig. 7c). It is expressed by the formation of domains with discontinuous, anastomosing foliation defined by aligned quartz aggregates and domains where the quartz aggregates are arranged in up to 1 mm thick, fine-spaced layers. The foliations in the ITZ have an N- to NNE-trend and are steeply E-dipping to subvertical. Mineral lineations were observed in a few outcrops, marked by alignment of biotite with moderately (40–45°) S- to SSE-plunges (Fig. 4, SP-1).

6.1.2. Microstructural analysis

In thin-sections, the deformed rocks in the ITZ show similarities with the microstructural development in the NZ. From the central to the outer parts across the ITZ, a smooth transition in the microstructures is indicated by 1) change in the dominating recrystallisation mechanisms (Fig. 8a, b and c), 2) decrease in the recrystallised grain size, 3) decrease in the elongation of porphyroclast tails and in the size of the strain shadows, 4) decrease in the abundance and size of the deformation induced myrmekites, and 5) transition from core-and-mantle feldspar porphyroclasts to fractured grains with high internal strain and to preserved euhedral feldspars. An important difference with the NZ, is that in the middle part of the ITZ larger feldspar grains recrystallised by SGR and GBM in the matrix (red arrow in Fig. 8a) as well as in the elongated feldspar microlithons. There, the plagioclase grains often show polygonisation by GBAR and the size of the annealed grains exceeds 250–300 μm. Deformation myrmekites, here penetrating up to 1 mm into the K-feldspar grains, are much more abundant than in the NZ. Also, chessboard subgrain pattern formation in quartz grains was noted (Fig. 8b). The dominance of orthorhombic porphyroclast shape symmetry and the lack of stretching lineation and syn-kinematic shear-sense indicators suggest that ITZ developed as a pure-shear dominated high-strained zone.

6.2. D2 in the SW part of the batholith

Rocks with D1-related structures in the ITZ have been overprinted by a second deformation event. Its main expression is in the development of a system of discrete, 10 to 15 cm wide, ultra-mylonite zones (Fig. 9a, b) with very sharp shear zone boundaries. The sheared rocks are coarse-grained biotite and leucocratic granites. The shear zones

Fig. 7. Field photographs of the deformed granites within the ITZ. The foliation is N–S striking, subvertical to steep E-dipping. a) Subhorizontal section in pavement-outcrop showing mega-porphyroclastic granite with some of the K-feldspars exceeding 5 cm along their long axis; b) elongated tails of the porphyroclasts form the gneissic texture in the deformed granites (subhorizontal section); c) deformation style and strain partitioning in coarse-grained leucocratic granite. Note the fast transition from discontinuous to continuous foliation from left to right (vertical section).

are gently to moderately (25° to 50°) S- to SW-dipping and associated with down-dip stretching quartz aggregate lineations (Fig. 4, SP2). Kinematic indicators such as shear bands, mineral or aggregate fish, deflection of the D1 foliations and domino fractures in feldspars (Fig. 9a, b) define the zones as N-vergent thrusts. In thin-sections, the ultramylonite zones are characterised by a very fine-grained matrix of recrystallised K-feldspar, plagioclase and quartz and locally biotite. Large quartz grains recrystallised by grain boundary migration constitute ribbons ranging from 100 μm to 500 μm in width, sometimes up to 1 cm, which define the laminated mylonite texture. This feature is also visible at the scale of the samples (Fig. 9a, b). Some of the ribbons show polygonisation.

7. Structural characteristics of the SE part of the batholith, the adjacent metasedimentary rocks and the Mwembeshi Zone (MwZ)

In the eastern part of the Hook Batholith, south of the NZ and west of the Lutale River (Fig. 2), the granitoids are characterised by a weak and undulating magmatic foliation mainly outlined by the alignment of euhedral feldspars. Field studies, combined with interpretation of airborne geophysical images and the 1:100,000 geological map of the area (Abell, 1970), reveal a curved trend of steep to vertical magmatic fabrics (Fig. 4). To the east, the structures are parallel to the contacts with the metasedimentary host rocks. South of this domain, in the SE part of the batholith, the granitoids show a pronounced solid state foliation which is steep, undulating in map-view (Fig. 4) and strikes to the NE, E and NW. Along the southern margin of the batholith the foliations are subvertical E- to ENE-trending, parallel to the contact between the granite and its host rocks and parallel to the foliation within the MwZ. Mylonite zones did not develop and the mineral lineations are very weak, gently W-plunging on ENE-striking subvertical planes. Chessboard subgrain pattern in quartz was observed in thin-sections.

The E and NE contact of the granite is marked by a ca. 3 km wide zone of contact metamorphism (Abell, 1970; Cikin, 1971 and Fig. 2). To the NE of the NZ, the foliations in the host rocks are SSW- to SW-dipping, thus parallel to the solid-state fabrics in the sheared granites, and carry moderately WNW-plunging mineral lineations. To the E and SE, along the Lutale River, the conformity with the fabric in the granite is still present, although here, the granites display only weak foliations parallel to the contacts. Along the Lutale River and eastward, the batholith is hosted by argillaceous rocks intercalated with quartzite beds affected by very low-grade metamorphism. The structural record is defined by folding of the bedding associated with the formation of steep to vertical N- to NNW-striking axial-planar spaced cleavage (S_1). Sericite was observed along the bedding at the limbs of the folds and also in association with the cleavage planes. The folds are tight, upright, trending N to NNW and occasionally NW (Fig. 4, SP-5). The intersection lineation between the bedding and cleavage planes is predominantly horizontal.

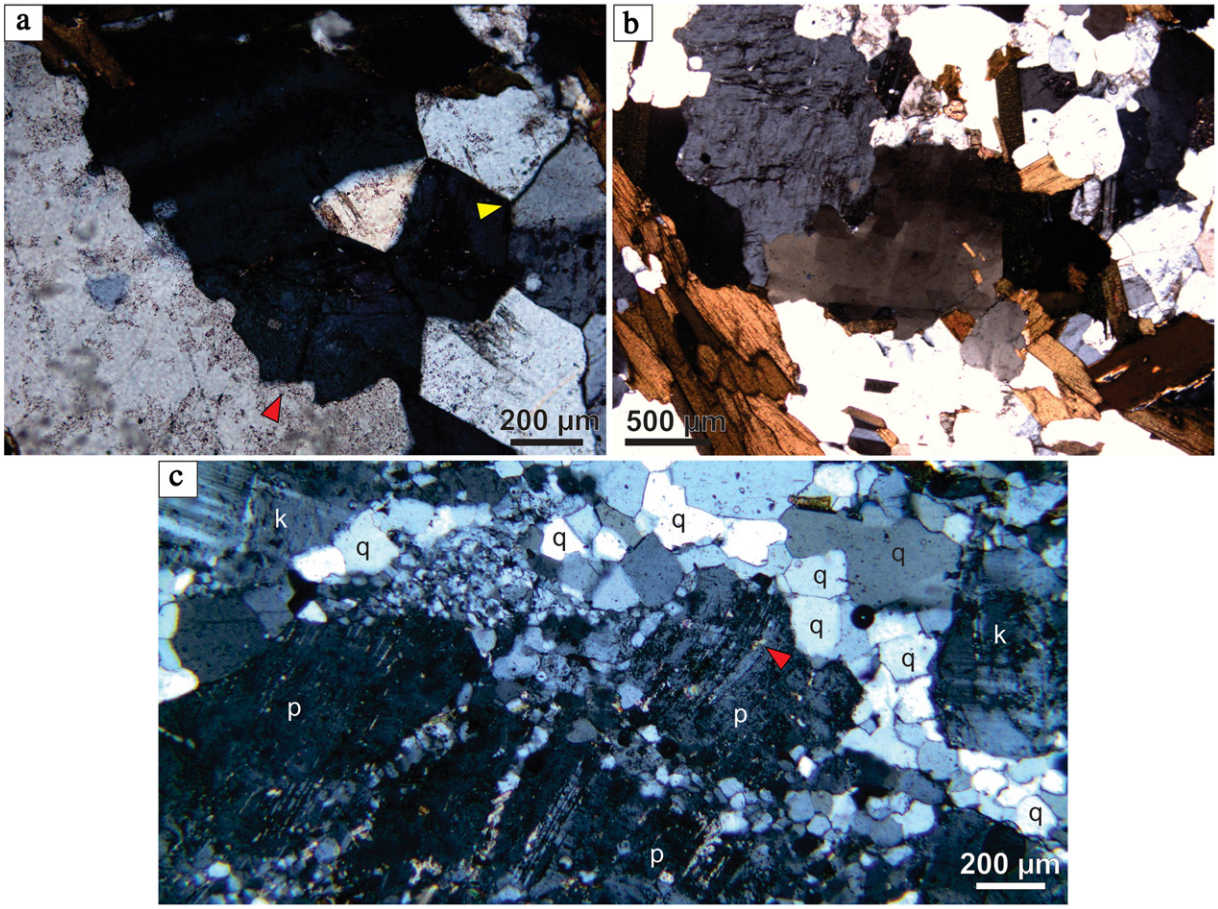

Fig. 8. Microphotographs from the biotite granite deformed in the central part of the ITZ showing high-temperature microstructures from the middle section of the zone (a and b) and low-temperature microstructures in the western margin (c). a) GBM recrystallisation in plagioclase (red arrow) and fully recrystallised and annealed large plagioclase grains (yellow arrow). CPL; b) close-up view of a 1.5 mm large quartz grain with chessboard subgrain pattern. CPL.; c) bulging recrystallisation along the margins and along micro fractures in large plagioclase grain (p) with undulose extinction. The grain in the centre of the photograph is completely detached from the parent porphyroclast and shows bending of the lamellae (red arrow). K-feldspar grains (k) show undulose extinction and incipient bulging recrystallisation (better seen in the grain at the upper left corner of the photograph). The quartz (q) is fully recrystallised and shows advanced annealing.

To the E and NE of the batholith, a second generation of folds developed. The E-striking, large amplitude F2 open folds (Fig. 4) are hardly detectable at outcrop scale and their geometry is deduced from the interference with the N–S trending F1 structures in map view (Fig. 4). Abell (1970) and Cikin (1971) describe an ENE- to E–W-trending and steeply S-dipping cleavage that is axial-planar to the F2 folds and also at high angle to the cleavage S_1. With decreasing distance to the MwZ the F2 folding becomes stronger and the D1 structures are refolded (type II of Ramsay, 1967) into parallelism with the zone (Fig. 4).

The metasedimentary succession within the MwZ (Fig. 4b, area SP3) comprises two different successions: i) an alternation of sericite schists with quartzite layers and ii) metagritstones and metaconglomerates.

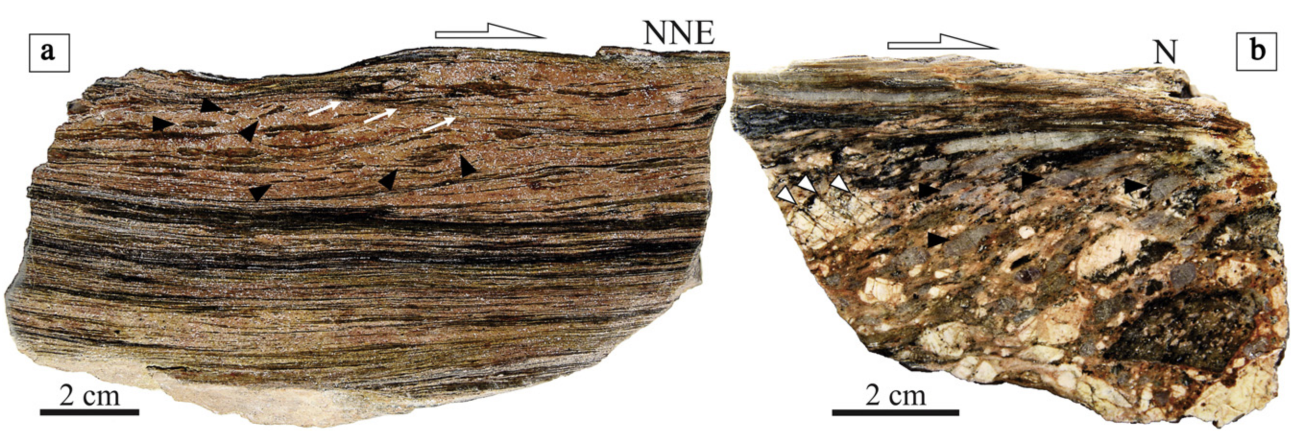

Fig. 9. D2 structures in the southern margin of the Hook Batholith. a)– Shearing in a leucogranite and b)– in a biotite granite. Mylonitic lamination is outlined by greyish ribbons of quartz. a) Shows C′ shear band development (white arrows) and quartz fish (black arrows) that define NNE directed thrust kinematics; b) shows N-vergent kinematics, marked by the asymptotically curved foliation planes, sigma- type quartz porphyroclasts (black arrows) and domino micro-fractures in feldspar (white arrows).

Both successions are metamorphosed under greenschist facies conditions but show different structural development. The schist–quartzite alternation is characterised by metamorphic foliation parallel to the bedding planes (S_{0-1}). F1 folds were not preserved within the MwZ and the section shows tight to isoclinal F2 folds with fold axis trending approximately E–W or ENE–WSW, parallel to the MwZ (Abell, 1970 and Fig. 4, SP3). This folding is associated with the formation of a closely spaced, pervasive S_2 cleavage that dips steeply towards SSE and occasionally, probably at hinge zones, angular relationships between S_{0-1} and S_2 have been observed (Fig. 10a). Thin-section observations of the schists show that the S_{0-1} bedding-parallel metamorphic foliation is folded by crenulation folds F2 whose axial planar cleavage (S_2) is defined by recrystallised fine-grained to cryptocrystalline synkinematic mica (Fig. 10b). Unlike the schists, the structural analysis revealed only one deformation event in the metaconglomerates and metagritstones. These rocks are polymictic, comprising schists and granite pebbles, although the quartz clasts dominate. The matrix is gritty with a poorly developed foliation. The pebbles in these rocks are oblate in shape, parallel to the S_2 foliation planes (Fig. 10c, d) with no preferred elongation or stretching direction recorded. In conglomerates with a coarse-grained matrix, the foliation (S_2) is marked only by the elongation of the lithoclasts and sometimes by the tails at the strain shadows of larger rounded pebbles (Fig. 10d). The structural features here show that the metaconglomerate-metagritstone alternation is affected only by the D2.

8. U–Pb isotope geochronology results

Six samples of the Hook granitoids were collected for U–Pb zircon geochronology dating. The sampling strategy aimed at obtaining new crystallisation ages for different parts of the batholith and time constraints on the deformation events. Intentionally, the dated samples were not collected from the high metamorphic grade central parts of the ITZ or NZ, in order to avoid any possible disturbance of the U–Pb isotope system during shearing and recrystallisation. Two localities showed cross-cutting relationships between foliated coarse-grained granites and undeformed granitic dykes (Fig. 11) and therefore presented an opportunity to constrain the time of the deformation.

Locality Z-68 is east of the high-strain central part of the ITZ (Figs. 2, 4). The sampled rock is a foliated, coarse-grained, porphyroclastic, biotite granite. The zircon population is of well-shaped short- and long-prismatic bipyramidal grains most of which display magmatic oscillatory zoning on the CL images. No evidence for inherited cores or xenocrystic zircons has been found. Some grains display large metamict zones and were not analysed. Four of the analyses are discordant and show post-crystallisation disturbance of the U–Pb isotope system. Two analyses were discarded due to anomalously high uranium content, probably linked to metamict zones. The 14 concordant analyses define a crystallisation age of 533 ± 3 Ma (Fig. 12a, Table 1).

At locality Z-77 (Figs. 2, 4), at the southern margin of the NZ, two samples were collected (Fig. 11a), one from a weakly deformed coarse-grained porphyroclastic biotite granite (Z-77A) and one from an undeformed aplitic vein (Z-77E). The morphology of the zircon grains in sample Z-77A is very similar to those in sample Z-68B. One zircon reveals an inherited core concordant at ca. 2.4 Ga. The other 22 analyses define a concordia crystallisation age of 549 ± 2 Ma (Fig. 10b, Table 1). The fine-grained aplitic vein (sample Z-77E) is characterised by similar zircon morphology and zoning but the strongly elongated to needle-shape grains are more abundant.

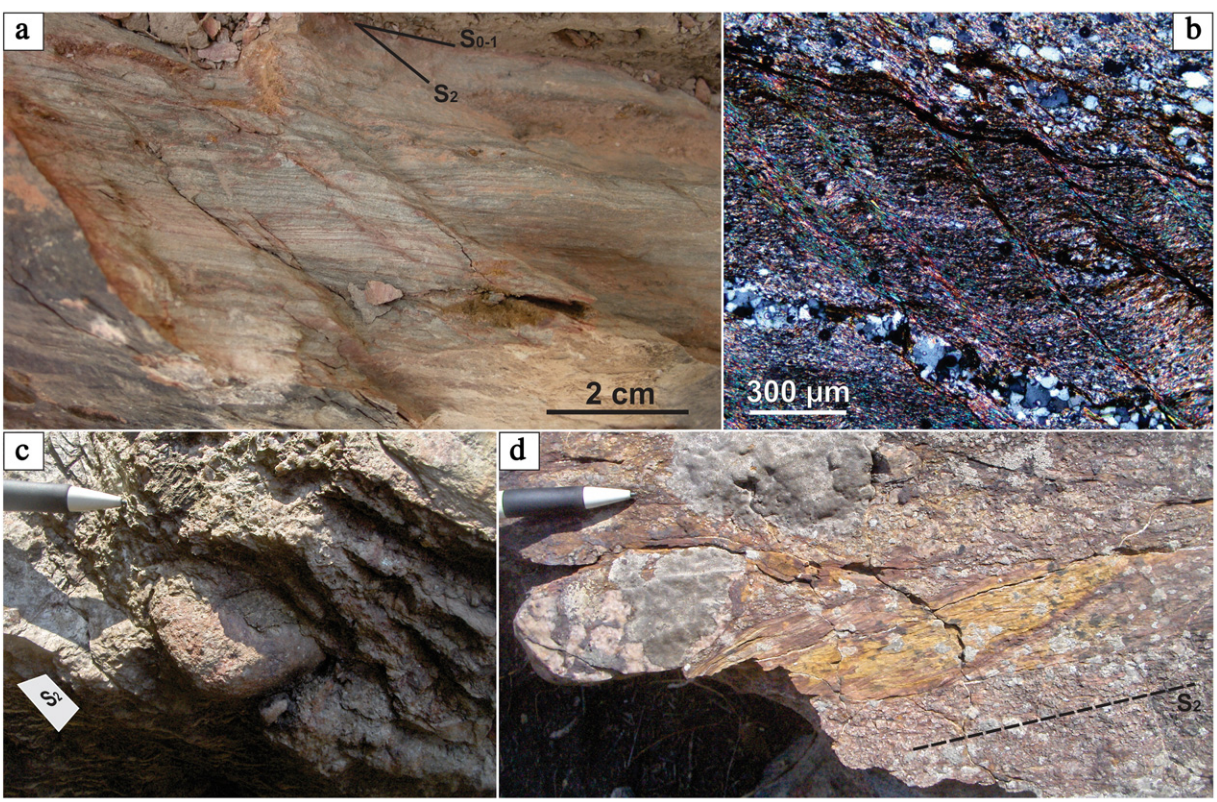

Fig. 10. Field and micro-photographs from the metasedimentary rocks within the MwZ south of the Hook Batholith (area SP3 on Fig. 4b). a) Low-grade schist with finely spaced S_2 cleavage that cuts at small angle the older metamorphic foliation which here is parallel to the bedding planes (S_{0-1}); b) microphotograph of the schists shown on a). The bedding planes (gently upper left to lower right sloping) are marked by alternating fine- and coarse-grained laminas and by metamorphic white mica and recrystallised elongated quartz grains which define the planes as S_{0-1}. The S_2 crenulation cleavage (steeply upper left to lower right sloping) is defined by reorientation of the white micas and subordinate recrystallisation of new syn-kinematic mica; c) conglomerate of the post D1 siliciclastic unit, affected only by the D2 with one large oblate-shape pebble laying parallel to the S_2 foliation planes; d) quartzite and schist pebbles in weakly foliated coarse-grained matrix from the same unit. The weak S_2 foliation is subvertical and the strike is marked on the photograph.

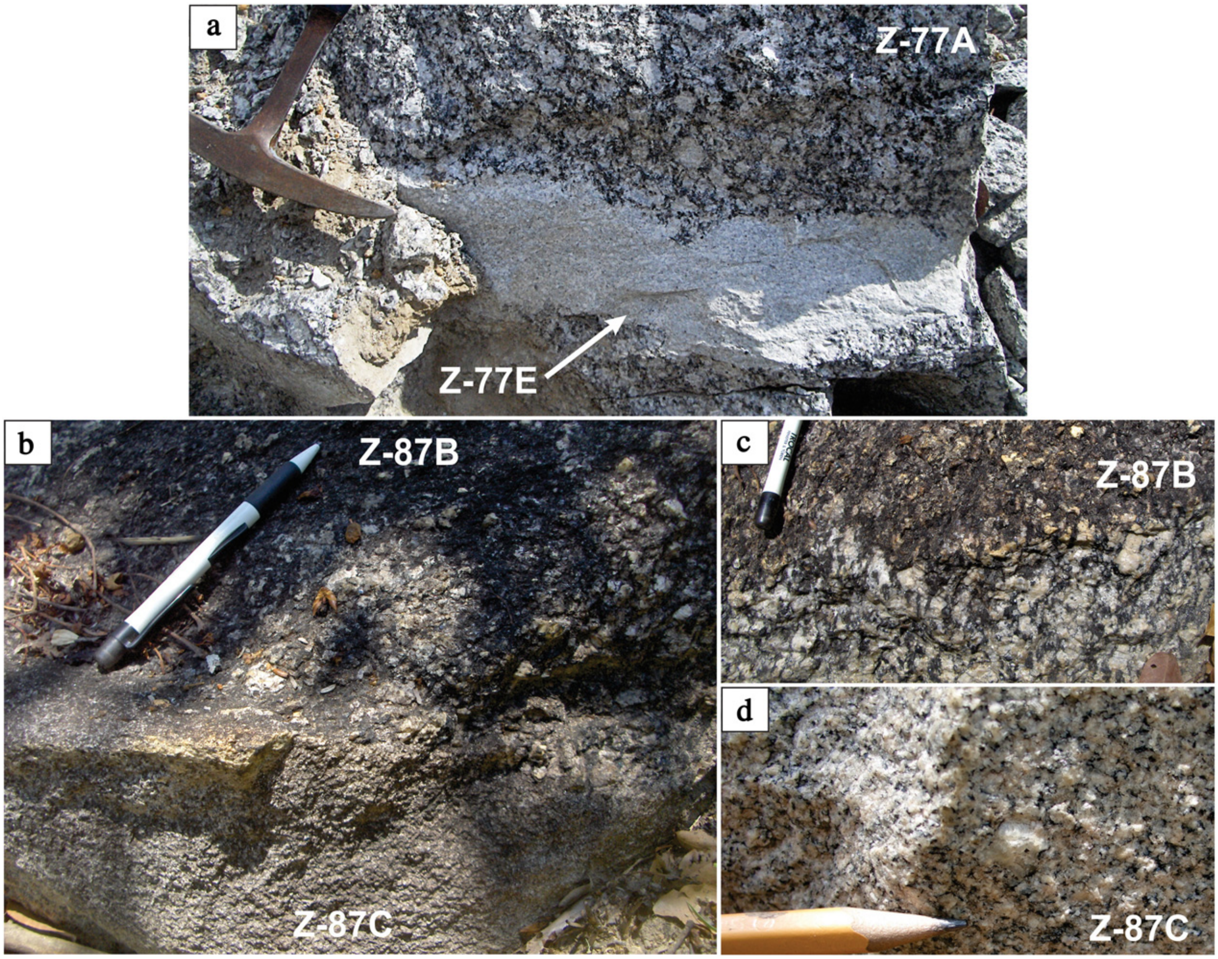

Fig. 11. Field photographs showing the relationships between the coarse grained foliated granites and cross-cutting dykes that have been sampled for geochronological study. a) Locality Z-77 with weakly foliated coarse-grained biotite granite (sample Z-77A) is intruded by undeformed aplite dyke (sample Z-77E); b) locality Z-87 showing deformed coarse-grained biotite granite (sample Z-87B) with foliation truncated by undeformed fine-grained granitic dyke (sample Z-87C). Pencil parallel to the foliation (S_1); c) and d) are close-up views illustrating the two sampled granites at locality Z-87.

The inherited core in one grain reveals a concordia age of ca. 1.1 Ga and 15 analyses are concordant at 541 ± 3 Ma, which is regarded as the crystallisation age (Fig. 12c, Table 1).

Locality Z-119 is in the eastern part of the NZ in undeformed fine- to medium-grained biotite granite (Figs. 2, 4). The granite was preserved from the deformation in a low-strain domain. The zircon population of the sample (Z-119A) is dominated by long-prismatic grains with clear oscillatory zoning. Twenty six analyses are concordant within ±2% giving a crystallisation age of 549 ± 2 Ma (Fig. 12d, Table 1).

In the SE part of the batholith, at locality Z-87 (Figs. 2, 4), a well-foliated coarse-grained biotite granite is intruded by a vein of undeformed fine- to medium-grained biotite (Fig. 11b, c, d). The foliated granite (sample Z-87B) is characterised by well-shaped long-prismatic zircon grains with oscillatory zoning. Even though no visible cores were observed in the CL images, one of the analyses gave a concordant age of ca. 1.1 Ga, interpreted as inherited from the source. Three analyses were discarded due to high common lead content or post-crystallisation lead-loss. Six results are variably discordant but 14 concordant analyses yielded a concordia age of 544 ± 2 Ma (Fig. 12e, Table 1) which is considered as crystallisation age. Two types of zircons, large (over 400 μm long) and small (between 150 and 250 μm) from the undeformed granitic vein (sample Z-87C) have been analysed. Both populations show long- and short-prismatic bipyramidal morphology and some grains display core-and-rim structure on the CL images. Some of the larger grains have uranium content in ppm an order of magnitude higher than the average for the sample (Table 1, sample Z-87C, analyses A_173, A_177, A_178, A_179). Two of the analysed cores give concordant ages at ca. 1.15 Ga and one is concordant at ca. 635 Ma. Four analyses were discarded because of their common lead content or lead-loss effect. Fourteen concordant analyses reveal an age of 543 ± 3 Ma considered to represent the crystallisation age (Fig. 12f, Table 1). When the common lead correction is solved graphically on the Tera-Wasserburg diagram, the calculated age is 542 ± 3 Ma.

At locality Z-84 (Figs. 2, 4), one sample from the metaconglomerate within the MwZ (Fig. 10c) was collected for detrital zircon geochronology, in order to define the maximum age of sedimentation of these rocks affected only by the D2. The detrital zircon population of sample Z-84 is characterised by a variety of morphologies. Long-, short-prismatic and sometimes rounded grains all show a fine magmatic oscillatory zoning. The grains have comparatively well-preserved crystal faces. One hundred and nine analyses have been performed; 42 are concordant at 95-105%, and 40 of these spread between 581 and 528 Ma (Fig. 13a, Table 2). The probability density plot of the concordant analyses shows a peak at about 547 Ma, with a secondary one at 575 Ma (Fig. 13b). The majority of the discordant analyses plot along a regression towards the origin of the chart, indicating that a recent event caused significant lead-loss. Using all 42 concordant analyses, the calculated age of the youngest zircon is 524.38 + 6.6/-10 Ma (Fig. 13c). The three youngest and most concordant analyses (99–101% conc.) give a mean age of 530.6 ± 6.5 Ma.

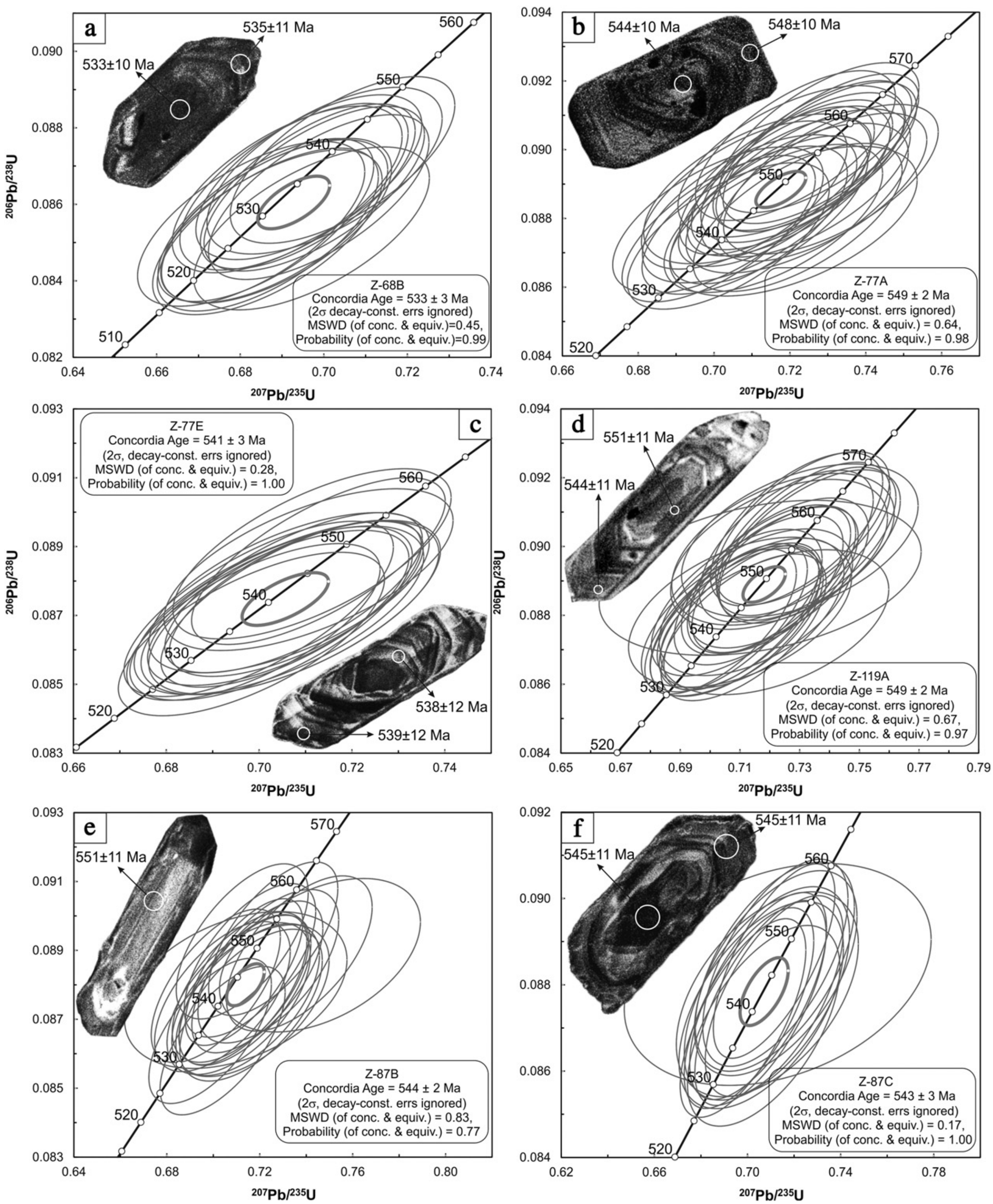

Fig. 12. Concordia diagrams for the U–Pb crystallisation age calculations for granitoid samples from the Hook Batholith. All data-point error ellipses are 2-sigma. The sample numbers and the exact age estimations, MSWD and probability numbers are plotted at the corner of each diagram. Representative CL microphotographs of selected zircon grains are shown for each sample with the position of the laser ablation craters (white circles) and the corresponding age estimates. The diameters of the craters are between 25 and 35 μm and the penetration depth is of ca. 15–20 μm. Data calculations and plots are made in Isoplot v. 3.70 of Ludwig (2008). For sample locations see Figs. 2 and 4. The geographic coordinates are given in Table 1.

9. Discussion

Detailed field structural analysis of critical domains in the Hook Batholith, its enveloping metasedimentary rocks and along the strike-extent of the MwZ suggest that two consecutive, highly oblique orogenic contractional events affected the area. U–Pb zircon dating of key magmatic and siliciclastic rocks constrains the timescales for activity of these two deformation events and led us to propose a new tectonic model for the evolution of the junction of the Lufilian and Zambezi belts (Fig. 14).

9.1. D1 deformation event

The structural study in the Katangan metasedimentary rocks to the E and NE of the batholith revealed the existence of a D1 deformation event associated with lower greenschist facies synmetamorphic folding

Table 1
Summary of the U–Pb LA-SF-ICP-MS analyses on zircons from granitoid samples from the Hook batholith.

					Isotopic ratios							Ages (Ma)						Conc.
Analysis	Comment	U [ppm][a]	Pb [ppm][a]	Th/U	$^{207}Pb/^{235}U$[b]	2 σ[c]	$^{206}Pb/^{238}U$[b]	2 σ[c]	Rho[d]	$^{207}Pb/^{206}Pb$[e]	2 σ[c]	$^{207}Pb/^{235}U$	2 σ	$^{206}Pb/^{238}U$	2 σ	$^{207}Pb/^{206}Pb$	2 σ	%[f]
Z-68B foliated coarse-grained biotite granite (Itezhi-Tezhi Zone), coordinates: 26°9′41.7″E/15°33′13.4″S																		
A_100		170	14	0.43	0.69	0.02	0.085	0.002	0.63	0.0584	0.0015	531	17	528	10	544	55	97
A_101		178	15	0.44	0.68	0.02	0.085	0.002	0.63	0.0579	0.0015	528	17	529	10	526	55	100
A_102		174	15	0.46	0.69	0.02	0.086	0.002	0.63	0.0580	0.0015	534	17	534	11	530	56	101
A_103		367	32	0.57	0.70	0.02	0.086	0.002	0.66	0.0588	0.0014	538	17	533	10	560	50	95
A_104		195	17	0.16	0.69	0.02	0.086	0.002	0.64	0.0581	0.0014	535	17	535	11	534	55	100
A_105		305	27	0.35	0.70	0.02	0.087	0.002	0.66	0.0586	0.0014	541	17	539	11	553	51	97
A_108		391	33	0.62	0.69	0.02	0.086	0.002	0.66	0.0581	0.0013	530	16	529	10	535	51	99
A_109		706	60	0.35	0.69	0.02	0.086	0.002	0.63	0.0583	0.0015	532	17	529	10	542	55	98
A_110		183	16	0.35	0.69	0.02	0.086	0.002	0.63	0.0584	0.0015	532	17	529	10	544	55	97
A_111		268	17	0.64	0.51	0.02	0.064	0.001	0.52	0.0583	0.0020	421	17	399	8	541	74	74
A_112		176	15	0.35	0.70	0.02	0.087	0.002	0.62	0.0585	0.0015	539	18	537	11	547	56	98
A_113		248	21	0.39	0.70	0.02	0.085	0.002	0.62	0.0592	0.0015	537	18	528	10	575	56	92
A_114		227	19	0.30	0.66	0.02	0.082	0.002	0.62	0.0585	0.0015	517	17	509	10	549	56	93
A_116		320	27	0.32	0.69	0.02	0.085	0.002	0.65	0.0584	0.0014	531	17	528	10	543	52	97
A_117		117	9	0.64	0.61	0.03	0.075	0.002	0.47	0.0583	0.0022	481	21	469	9	540	84	87
A_118		1044	90	0.31	0.70	0.02	0.086	0.002	0.67	0.0584	0.0013	536	16	535	10	544	48	98
A_119		299	26	0.35	0.70	0.02	0.087	0.002	0.64	0.0583	0.0014	537	17	536	11	539	54	100
A_120		412	33	0.49	0.65	0.02	0.080	0.002	0.61	0.0588	0.0016	508	17	497	10	558	57	89
A_122		580	50	0.33	0.70	0.02	0.086	0.002	0.66	0.0586	0.0014	537	17	534	10	551	50	97
Z-77A foliated coarse-grained biotite granite (Nalusanga Zone), coordinates: 26°28′4.7″E/14°56′55.7″S																		
A_040		575	51	1.32	0.72	0.02	0.089	0.002	0.67	0.0583	0.0013	549	16	550	10	542	49	102
A_041		297	26	0.53	0.72	0.02	0.089	0.002	0.66	0.0586	0.0013	550	17	550	11	552	50	100
A_042		515	45	0.58	0.70	0.02	0.088	0.002	0.67	0.0580	0.0013	540	16	542	10	529	49	102
A_043		1585	141	1.04	0.72	0.02	0.089	0.002	0.68	0.0585	0.0012	548	16	548	10	549	46	100
A_044		91	8	0.31	0.72	0.03	0.088	0.002	0.55	0.0595	0.0018	551	20	543	11	585	67	93
A_045		224	20	0.59	0.71	0.02	0.088	0.002	0.64	0.0584	0.0014	544	17	543	10	544	52	100
A_046		351	31	0.39	0.70	0.02	0.088	0.002	0.61	0.0578	0.0015	539	17	543	10	522	56	104
A_047	Inherited core	54	24	0.87	9.61	0.29	0.450	0.009	0.66	0.1548	0.0035	2399	73	2397	41	2400	39	100
A_048		524	46	0.47	0.71	0.02	0.088	0.002	0.67	0.0587	0.0013	547	16	545	10	557	48	98
A_049		344	31	0.88	0.72	0.02	0.089	0.002	0.66	0.0586	0.0013	553	17	553	11	553	49	100
A_050		379	34	0.51	0.72	0.02	0.089	0.002	0.66	0.0585	0.0013	551	17	551	10	550	49	100
A_051		1776	160	0.57	0.73	0.02	0.090	0.002	0.68	0.0587	0.0012	555	16	556	11	555	46	100
A_052		576	52	0.48	0.73	0.02	0.090	0.002	0.67	0.0584	0.0013	555	16	558	11	546	48	102
A_053		255	22	0.41	0.72	0.02	0.088	0.002	0.64	0.0595	0.0014	552	17	544	10	585	51	93
A_054		220	20	0.45	0.71	0.02	0.089	0.002	0.63	0.0579	0.0014	544	17	548	10	526	53	104
A_057		153	14	0.37	0.72	0.02	0.089	0.002	0.61	0.0591	0.0016	552	18	547	11	571	57	96
A_058		565	49	0.51	0.70	0.02	0.087	0.002	0.64	0.0583	0.0014	541	17	541	10	543	52	100
A_059		493	44	0.68	0.72	0.02	0.090	0.002	0.66	0.0581	0.0013	552	16	556	11	532	50	105
A_060		827	74	0.76	0.73	0.02	0.090	0.002	0.67	0.0587	0.0013	555	16	554	11	557	48	100
A_061		843	76	0.37	0.73	0.02	0.090	0.002	0.67	0.0586	0.0013	554	16	555	11	553	48	100
A_062		188	17	0.50	0.71	0.02	0.088	0.002	0.61	0.0583	0.0015	544	18	545	10	540	57	101
A_063		116	10	0.36	0.71	0.02	0.089	0.002	0.58	0.0581	0.0016	546	19	549	11	532	61	103
A_064		276	25	0.47	0.72	0.02	0.089	0.002	0.63	0.0590	0.0014	553	17	550	10	567	53	97
A_065		252	22	0.92	0.72	0.02	0.088	0.002	0.61	0.0590	0.0015	548	18	544	10	566	56	96
A_066		227	20	0.36	0.73	0.02	0.089	0.002	0.63	0.0595	0.0015	557	18	551	11	584	53	94
A_067		123	11	0.43	0.72	0.02	0.090	0.002	0.59	0.0583	0.0016	551	19	554	11	540	61	103
A_069		592	53	0.19	0.73	0.02	0.089	0.002	0.64	0.0594	0.0014	556	17	549	10	583	51	94
Z-119A undeformed fine- to medium-grained biotite granite (Nalusanga Zone, low-strain lens), coordinates: 26°49′7.3″E/15°0′26.7″S																		
A_004		188	17	0.33	0.72	0.02	0.089	0.002	0.63	0.0588	0.0014	551	17	550	10	558	52	99
A_005		146	13	0.31	0.72	0.03	0.088	0.002	0.53	0.0587	0.0018	548	20	546	10	556	68	98

(continued on next page)

Table 1 *(continued)*

Analysis	Comment	U [ppm][a]	Pb [ppm][a]	Th/U	Isotopic ratios							Ages (Ma)						Conc.
					$^{207}Pb/^{235}U$[b]	2 σ[c]	$^{206}Pb/^{238}U$[b]	2 σ[c]	Rho[d]	$^{207}Pb/^{206}Pb$[e]	2 σ[c]	$^{207}Pb/^{235}U$	2 σ	$^{206}Pb/^{238}U$	2 σ	$^{207}Pb/^{206}Pb$	2 σ	%[f]
A_006		143	13	0.37	0.72	0.02	0.089	0.002	0.60	0.0587	0.0015	551	18	550	10	558	56	99
A_007		132	12	0.35	0.73	0.02	0.090	0.002	0.61	0.0585	0.0015	554	18	556	11	547	57	102
A_008		338	30	0.42	0.71	0.02	0.088	0.002	0.66	0.0586	0.0013	545	16	543	10	552	49	98
A_009		151	13	0.39	0.72	0.03	0.088	0.002	0.45	0.0596	0.0023	552	24	543	10	589	82	92
A_010		174	15	0.47	0.71	0.02	0.088	0.002	0.62	0.0589	0.0015	545	17	542	10	562	54	96
A_011		59	5	0.45	0.71	0.03	0.088	0.002	0.47	0.0585	0.0022	545	23	544	11	547	82	100
A_012		123	11	0.44	0.72	0.03	0.090	0.002	0.48	0.0584	0.0021	552	23	554	11	546	77	102
A_013		433	38	0.34	0.70	0.02	0.088	0.002	0.66	0.0581	0.0013	541	16	543	10	533	49	102
A_016		65	6	0.41	0.72	0.03	0.090	0.002	0.48	0.0584	0.0022	553	23	555	11	546	80	102
A_017		102	9	0.50	0.72	0.02	0.089	0.002	0.59	0.0588	0.0016	552	19	551	11	558	59	99
A_018		82	7	0.35	0.71	0.03	0.088	0.002	0.56	0.0588	0.0017	547	20	544	11	559	64	97
A_019		173	15	0.46	0.71	0.02	0.088	0.002	0.60	0.0582	0.0015	544	18	546	10	536	59	102
A_020		73	7	0.46	0.73	0.03	0.090	0.002	0.45	0.0587	0.0023	557	25	557	11	557	85	100
A_021		149	13	0.41	0.71	0.02	0.088	0.002	0.61	0.0585	0.0015	544	18	543	10	549	56	99
A_022		91	8	0.37	0.71	0.02	0.088	0.002	0.58	0.0584	0.0017	543	19	543	11	545	62	100
A_023		166	15	0.31	0.72	0.02	0.089	0.002	0.62	0.0586	0.0015	550	18	550	11	551	55	100
A_024		222	20	0.42	0.71	0.02	0.088	0.002	0.63	0.0586	0.0014	545	17	544	10	550	52	99
A_025		161	14	0.40	0.72	0.02	0.089	0.002	0.62	0.0585	0.0015	548	18	548	10	550	54	100
A_028		163	15	0.24	0.73	0.02	0.091	0.002	0.62	0.0584	0.0015	556	18	559	11	546	55	102
A_029		154	14	0.36	0.73	0.02	0.091	0.002	0.62	0.0586	0.0015	557	18	559	11	551	55	101
A_030		146	13	0.37	0.73	0.02	0.090	0.002	0.62	0.0588	0.0015	557	18	557	11	559	55	100
A_031		54	5	0.52	0.72	0.04	0.089	0.002	0.34	0.0584	0.0034	549	34	550	11	543	124	101
A_032		124	11	0.41	0.73	0.02	0.090	0.002	0.61	0.0590	0.0016	558	19	556	11	566	57	98
A_033		112	10	0.55	0.73	0.02	0.090	0.002	0.60	0.0591	0.0016	559	19	556	11	571	59	97
A_034		370	32	0.46	0.71	0.02	0.088	0.002	0.66	0.0583	0.0013	542	17	543	10	539	51	101
Z-77E undeformed fine-grained leucocratic vein (Nalusanga Zone), coordinates: 26°28′4.7″E/14°56′55.7″S																		
A_004		267	23	0.37	0.70	0.02	0.087	0.002	0.70	0.0582	0.0014	539	18	539	12	538	54	100
A_005		307	27	0.33	0.71	0.03	0.087	0.002	0.64	0.0588	0.0017	543	20	539	12	558	62	97
A_006		187	16	0.35	0.70	0.02	0.087	0.002	0.67	0.0585	0.0015	540	19	538	12	550	57	98
A_007		259	23	0.31	0.71	0.03	0.087	0.002	0.65	0.0588	0.0016	543	20	539	12	561	59	96
A_008	Inherited	74	14	1.03	1.91	0.07	0.183	0.004	0.68	0.0758	0.0019	1085	38	1082	24	1091	51	99
A_016		219	19	0.74	0.71	0.02	0.089	0.002	0.66	0.0581	0.0015	546	19	548	12	534	57	103
A_017		104	9	0.32	0.70	0.03	0.087	0.002	0.63	0.0586	0.0016	541	20	539	12	553	60	97
A_018		320	28	0.30	0.71	0.02	0.087	0.002	0.70	0.0587	0.0014	543	18	540	12	556	50	97
A_019		241	21	0.41	0.70	0.02	0.086	0.002	0.67	0.0586	0.0015	538	18	535	12	552	54	97
A_020		1278	113	0.45	0.71	0.02	0.089	0.002	0.71	0.0584	0.0013	546	17	547	12	543	48	101
A_028		215	19	0.36	0.71	0.03	0.088	0.002	0.61	0.0584	0.0017	545	20	546	11	543	62	100
A_029		593	52	0.55	0.71	0.02	0.088	0.002	0.68	0.0585	0.0014	543	17	542	11	550	51	99
A_031		180	16	0.36	0.71	0.02	0.088	0.002	0.62	0.0585	0.0016	543	19	542	11	547	59	99
A_032		658	57	0.49	0.70	0.02	0.087	0.002	0.67	0.0584	0.0014	538	17	537	11	544	51	99
A_033	Disc.	113	10	0.51	0.76	0.03	0.087	0.002	0.54	0.0637	0.0023	574	25	536	12	731	76	73
A_034	Rev. disc.	4328	379	0.33	0.69	0.02	0.088	0.002	0.69	0.0569	0.0013	530	16	541	11	485	49	112
A_035		416	36	0.27	0.70	0.02	0.087	0.002	0.65	0.0586	0.0015	541	18	539	11	551	54	98
A_036		634	55	0.51	0.71	0.02	0.087	0.002	0.67	0.0587	0.0014	544	17	541	11	556	51	97
Z-87B foliated coarse-grained biotite granite (SE part of the Hook Batholith), coordinates: 26°49′49.1″E/15°17′52.5″S																		
A_074		1905	168	1.02	0.71	0.02	0.088	0.002	0.68	0.0585	0.0012	547	16	546	10	550	46	99
A_075		272	24	0.31	0.70	0.02	0.087	0.002	0.64	0.0585	0.0014	538	17	536	10	547	51	98
A_076		70	6	0.33	0.75	0.04	0.089	0.002	0.43	0.0609	0.0026	566	27	549	11	635	91	86
A_077	Inherited core	255	42	0.36	1.75	0.05	0.166	0.003	0.66	0.0766	0.0017	1027	31	988	18	1111	44	89
A_078		120	11	0.34	0.71	0.02	0.088	0.002	0.60	0.0587	0.0016	546	18	543	11	556	58	98
A_079		42	4	0.48	0.71	0.04	0.088	0.002	0.38	0.0586	0.0030	545	30	543	11	552	109	98
A_080		157	14	0.38	0.71	0.02	0.088	0.002	0.62	0.0589	0.0015	547	18	543	11	564	55	96
A_082		93	8	0.39	0.71	0.03	0.088	0.002	0.58	0.0592	0.0017	548	19	541	11	574	62	94
A_083		95	8	0.40	0.72	0.03	0.088	0.002	0.53	0.0593	0.0019	548	21	541	11	579	70	93

A_084		120	10	0.45	0.70	0.02	0.088	0.002	0.60	0.0582	0.0016	541	18	542	11	538	60	101
A_085		235	21	0.34	0.71	0.02	0.088	0.002	0.64	0.0588	0.0014	546	17	543	11	561	52	97
A_088		219	19	0.39	0.72	0.02	0.088	0.002	0.64	0.0591	0.0015	550	18	545	11	571	53	96
A_091		204	18	0.33	0.72	0.02	0.089	0.002	0.60	0.0593	0.0016	553	19	547	11	578	59	95
A_092		960	83	0.51	0.70	0.02	0.086	0.002	0.65	0.0591	0.0014	541	17	534	10	571	51	94
Z-87B foliated coarse-grained biotite granite (SE part of the Hook Batholith), coordinates: 26°49′49.1″E/15°17′52.5″S																		
A_093		200	18	0.32	0.72	0.02	0.089	0.002	0.64	0.0585	0.0015	548	18	548	11	549	54	100
A_094		319	29	0.33	0.73	0.02	0.089	0.002	0.65	0.0589	0.0014	554	17	552	11	564	52	98
A_095		158	14	0.29	0.71	0.03	0.088	0.002	0.58	0.0589	0.0017	545	19	541	11	562	63	96
A_096		148	13	0.29	0.72	0.03	0.087	0.002	0.59	0.0594	0.0017	548	19	540	11	583	60	93
A_097		153	14	0.43	0.74	0.03	0.089	0.002	0.60	0.0601	0.0017	561	19	549	11	608	60	90
A_098		219	19	0.29	0.70	0.02	0.088	0.002	0.64	0.0578	0.0014	539	17	544	11	522	55	104
A_099		248	22	0.28	0.71	0.02	0.089	0.002	0.63	0.0579	0.0015	546	18	551	11	526	56	105
Z-87C undeformed fine- to medium-grained biotite granite vain (SE part of the Hook Batholith), coordinates: 26°49′49.1″E/15°17′52.5″S																		
A_170	cPb-inherited	93	10	0.36	1.07	0.06	0.112	0.003	0.52	0.0689	0.0032	737	40	686	18	895	93	77
A_171	Disc.	252	22	0.69	0.83	0.03	0.088	0.002	0.64	0.0687	0.0017	614	20	541	11	891	51	61
A_173		1442	128	0.08	0.71	0.02	0.089	0.002	0.69	0.0583	0.0013	546	16	547	11	539	49	101
A_177	Disc.	3845	338	0.17	0.86	0.03	0.088	0.002	0.70	0.0709	0.0015	630	19	543	11	956	43	57
A_178	Disc.	2741	239	0.24	0.74	0.02	0.087	0.002	0.69	0.0617	0.0014	563	17	538	11	664	47	81
A_179	Disc.	1113	97	0.17	0.72	0.02	0.087	0.002	0.68	0.0605	0.0014	553	17	537	11	620	49	87
A_180	Disc.	244	21	0.38	0.76	0.02	0.088	0.002	0.65	0.0623	0.0016	572	19	544	11	685	53	79
A_044		199	17	0.31	0.71	0.03	0.087	0.002	0.58	0.0589	0.0018	543	21	538	11	564	66	95
A_045		136	12	0.38	0.71	0.03	0.088	0.002	0.55	0.0585	0.0020	546	22	545	11	549	72	99
A_046		229	20	0.31	0.71	0.02	0.088	0.002	0.64	0.0588	0.0015	546	19	542	11	560	56	97
A_047	Inherited	326	34	0.18	0.87	0.03	0.104	0.002	0.69	0.0610	0.0014	636	20	635	13	640	48	99
A_048		396	35	0.23	0.70	0.02	0.087	0.002	0.68	0.0580	0.0013	538	17	539	11	531	51	102
A_049		81	7	0.32	0.71	0.03	0.088	0.002	0.57	0.0584	0.0019	546	21	546	12	544	70	100
A_050	Disc.	90	8	0.51	0.72	0.03	0.088	0.002	0.62	0.0596	0.0017	552	20	543	12	590	61	92
A_051		121	11	0.31	0.71	0.03	0.089	0.002	0.62	0.0583	0.0016	546	20	547	12	543	61	101
A_052		84	7	0.40	0.71	0.03	0.088	0.002	0.49	0.0585	0.0023	544	25	542	12	550	86	99
A_053	Inherited	154	30	0.23	2.10	0.08	0.195	0.004	0.62	0.0781	0.0022	1150	42	1150	24	1150	57	100
A_054		457	40	0.08	0.70	0.02	0.087	0.002	0.67	0.0581	0.0014	539	17	541	11	533	53	101
A_062	Inherited	200	39	0.18	2.09	0.07	0.194	0.004	0.63	0.0780	0.0022	1146	41	1145	24	1148	54	100
A_063	Disc.	549	48	0.17	0.94	0.03	0.087	0.002	0.68	0.0780	0.0019	672	22	539	11	1147	47	47
A_065		228	20	0.26	0.70	0.02	0.088	0.002	0.66	0.0582	0.0015	542	18	542	12	538	57	101
A_066		452	40	0.53	0.71	0.02	0.088	0.002	0.68	0.0584	0.0014	542	18	541	12	546	52	99
A_067	Disc.	51	4	0.23	0.71	0.04	0.087	0.002	0.45	0.0592	0.0027	546	28	539	12	574	99	94
A_068		40	4	0.23	0.71	0.05	0.088	0.002	0.32	0.0586	0.0042	547	41	545	13	552	153	99
A_069		116	10	0.28	0.71	0.03	0.088	0.002	0.56	0.0585	0.0020	544	22	543	12	549	73	99
A_070	Disc.	1723	151	0.28	0.75	0.02	0.088	0.002	0.70	0.0621	0.0014	569	18	542	12	679	49	80
A_071		462	40	0.29	0.71	0.03	0.088	0.002	0.55	0.0585	0.0020	542	22	541	12	548	74	99

[a] U and Pb concentrations and Th/U ratios are calculated relative to GJ-1 reference zircon.

[b] Corrected for background and within-run Pb/U fractionation and normalized to reference zircon GJ-1 (ID-TIMS values/measured value); $^{207}Pb/^{235}U$ calculated using $(^{207}Pb/^{206}Pb)/(^{238}U/^{206}Pb \times 1/137.88)$.

[c] Quadratic addition of within-run errors (2 SD) and daily reproducibility of GJ-1 (2 SD).

[d] Rho is the error correlation defined as the quotient of the propagated errors of the $^{206}Pb/^{238}U$ and the $^{207}Pb/^{235}U$ ratio.

[e] Corrected for mass-bias by normalizing to GJ-1 reference zircon (*0.6 per atomic mass unit) and common Pb using the model Pb composition of Stacey and Kramers (1975).

[f] Degree of concordance = ($^{206}Pb/^{238}U$ age x 100/$^{207}Pb/^{206}U$ age).

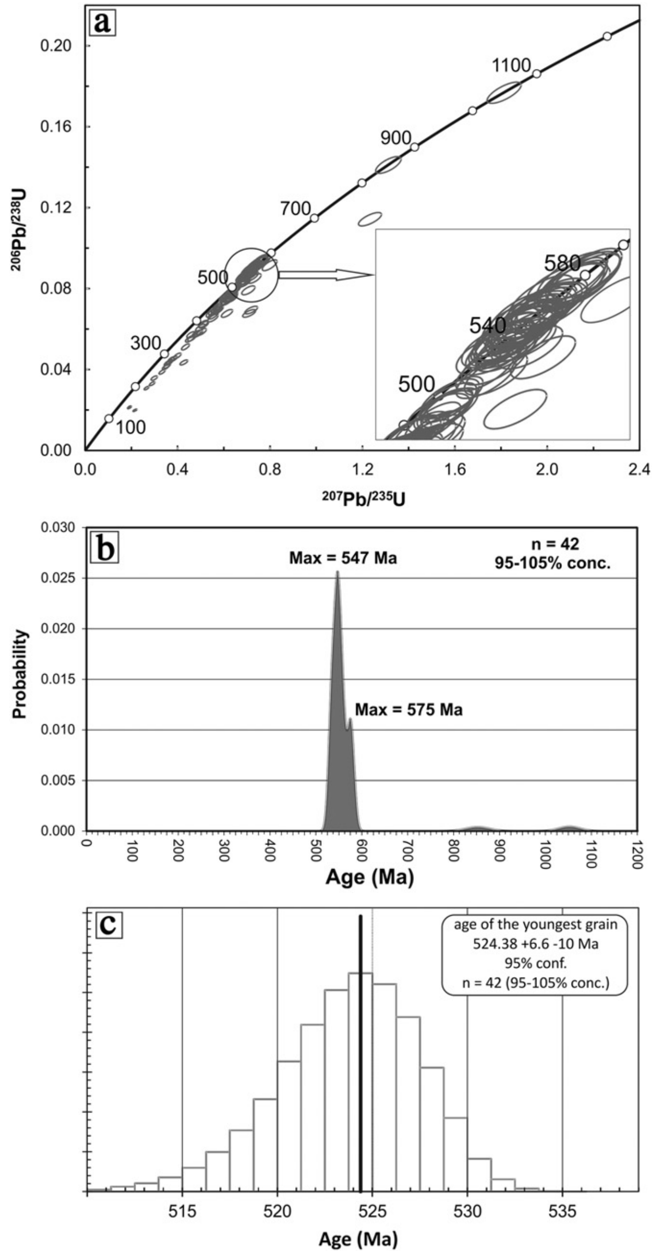

Fig. 13. U–Pb detrital zircon geochronology analyses for the metaconglomerate sample Z-84. a) Analyses plotted on the concordia diagram with close-up view on the cluster with the most concordant analyses; b) probability density plot for the 40 most concordant (95%–105%) analyses. c) Age of the youngest zircon calculated using 42 concordant (95%–105%) analyses. Data calculations and plots are made in Isoplot v. 3.70 of Ludwig (2008). For sample locations see Figs. 2 and 4. The geographic coordinates are given in Table 2.

along N- to NNW-trending upright folds and formation of an axial-planar cleavage that corresponds to regional E–W shortening (Fig. 14a). D1 heterogeneously affected large volumes of Hook granitoids and produced domains of pronounced penetrative solid-state deformation. In the NW-trending NZ, Cikin (1971, 1972) defined two ductile deformation events, related to the formation of two generations of planar structures, S_1 and S_2, separated by a stage of recrystallisation and porphyroblasts growth. We showed that the two planar structures in contrast correspond to the formation of S- and C′-planes and are related to a single deformation event (D1). The orientation of the structural elements, the sinistral strike-slip kinematics (e.g. Figs. 5, 6), and the rotation of the NZ foliations to parallelism with the east margin of the batholith are in agreement with the E–W bulk regional shortening depicted in the adjacent host rocks. Indeed, the fact that the NZ structures do not overprint the N–S-striking S_1 foliations in the host rocks supports their cogenetic relationships. On the other hand, the S_1 planes in the metasedimentary rocks are deflected around the granite and rotated to parallelism with the fabrics of the NZ. These features may indicate that the granite was emplaced in host rocks with already partially developed D1 structures. In the southern part of the batholith, the N–S trending, subvertical ITZ is interpreted as a high-strain pure-shear dominated zone. Its orientation and geometry are also consistent with an E–W shortening and therefore correlated here with D1 in the NE part of the study area (Fig. 14b, c). As described by de Swardt et al. (1964, 1965), Unrug (1988, 1989) and Porada (1989), the formation of tight to isoclinal N–S trending folds is characteristic for the first deformation event in the Synclinorial Belt and Katanga High zones of the Lufilian Arc and we consider it contemporaneous to and reflecting deformation in the same tectonic framework as the E–W shortening D1 deformation in the Hook area.

The microstructural analysis on rocks deformed within the ITZ and NZ allowed an approximate estimation of the metamorphic grade during the D1 deformation in the granitoids. The recrystallisation by grain-boundary migration (GBM) and subgrain rotation (SGR) in quartz, the size of the neograins and the development of fully recrystallised monomineralic ribbons, the formation of mantled feldspar porphyroclasts with rims that show SGR, and the development of deformation myrmekites, indicate deformation temperature probably at about 500 ° C or slightly higher in the central part of the NZ (Fig. 6a, b) (Passchier and Trouw, 2005; Stipp et al., 2002; Trouw et al., 2009; Tullis, 2002). In the central part of the ITZ, the larger size of feldspars recrystallised by SGR, the GBM recrystallisation in feldspar microlithons, and the chessboard subgrain pattern in quartz (Fig. 8a, b) indicate a higher temperature of the deformation than in the central part of the NZ. Comparison with studies on microstructures development in granitoid rocks, natural quartz and/or plagioclase aggregates and analogue materials under different metamorphic grade conditions, suggest that in the central part of the ITZ the D1 occurred above 650 ° C to subsolidus temperatures (e.g. Kruhl, 1996, 1998; Passchier and Trouw, 2005; Pryer, 1993; Rosenberg and Stünitz, 2003; Trouw et al., 2009; Tullis, 2002; Vernon et al., 2004). In order to allow the formation of the observed annealing in feldspars (Fig. 8a), the system probably stayed above ca. 600 °C at least shortly after the deformation ceased (Kruhl, 2001). As summarised in the review paper by Law (2014), the above temperature constraints should be taken only as imprecise gauges of the conditions of deformation, since factors like strain rate variation and water weakening have not been taken in consideration. Therefore, the microstructural analysis presented here does not give a quantitative estimation of the temperature of the deformation but, by combining different indicative microstructures, it broadly approximates its onset under amphibolite metamorphic facies conditions. Considering the lower greenschist facies regional metamorphism during D1 in the country-rocks, we can conclude that the medium (NZ) to high temperature (ITZ) D1 deformation has to be related to the heat derived from the granites intrusion. Both zones (ITZ and NZ) show a smooth transition to lower temperatures of the deformation towards their margins. This is marked by the transition from GBM and SGR recrystallisation mechanisms (Figs. 6b, c; 8a) to predominantly bulging (BLG) recrystallisation (Figs. 6d; 8c), to sections with only fractured or preserved euhedral feldspar grains (Fig. 6d, e), and, in the outermost parts of the zones, to preserved magmatic texture and undulose extinction only in quartz and biotite. The progressively lower grade of the deformation towards the margins of the zones can be interpreted as an effect of a widening of the deformation zones during cooling. Undulose extinction in fully recrystallised and annealed quartz microlithons from the inner part of the zones correspond to lower temperature overprinting at the end of the progressive ductile deformation. It is possible that the sinistral shearing in the NZ started at high-temperature conditions, but the progressive deformation

Table 2
Summary of the U-Pb LA-SF-ICP-MS analyses on zircons from sample Z-84 (metaconglomerate) south of the batholith within the Mwembeshi Zone.
Cooordinates: 26°42′31.9″E/15°20′27.9″S.

				Isotopic ratios							Ages (Ma)						Conc.				Conc.
Analysis	U [ppm][a]	Pb [ppm][a]	Th/U	^{207}Pb/^{235}U[b]	2 σ[c]	^{206}Pb/^{238}U[b]	2 σ[c]	Rho[d]	^{207}Pb/^{206}Pb[e]	2 σ[c]	^{207}Pb/^{235}U	2 σ	^{206}Pb/^{238}U	2 σ	^{207}Pb/^{206}Pb	2 σ	%[f]	^{206}Pb/^{238}U	1 σ	2σ	%[f]
A_004	192	18	0.54	0.77	0.03	0.094	0.002	0.71	0.0596	0.0015	579	20	577	14	587	54	98	577	7	14	98
A_005	215	20	0.34	0.76	0.03	0.094	0.002	0.71	0.0586	0.0014	573	20	579	14	551	53	105	579	7	14	105
A_006	360	34	0.38	0.76	0.03	0.093	0.002	0.73	0.0589	0.0014	573	19	575	14	564	50	102	575	7	14	102
A_007	181	14	0.80	0.63	0.02	0.076	0.002	0.68	0.0602	0.0016	497	18	473	11	610	57	78	473	6	11	78
A_008	431	29	0.68	0.55	0.02	0.068	0.002	0.72	0.0584	0.0014	443	15	424	10	544	51	78	424	5	10	78
A_009	509	34	0.45	0.55	0.02	0.067	0.002	0.73	0.0601	0.0014	448	15	418	10	609	49	69	418	5	10	69
A_010	334	29	0.47	0.70	0.03	0.087	0.002	0.65	0.0582	0.0017	539	21	539	13	537	64	101	539	6	13	101
A_011	245	23	0.37	0.77	0.03	0.094	0.002	0.69	0.0593	0.0015	579	21	579	14	578	56	100	579	7	14	100
A_012	432	30	0.69	0.56	0.02	0.069	0.002	0.69	0.0588	0.0015	451	16	430	10	559	55	77	430	5	10	77
A_013	286	25	0.32	0.71	0.03	0.088	0.002	0.69	0.0585	0.0015	545	19	544	13	548	55	99	544	6	13	99
A_016	534	31	0.79	0.49	0.02	0.058	0.001	0.73	0.0614	0.0014	404	14	362	9	653	49	55	362	4	9	55
A_017	380	27	1.04	0.57	0.02	0.070	0.002	0.70	0.0591	0.0015	458	16	436	10	569	55	77	436	5	10	77
A_018	595	36	0.41	0.50	0.02	0.061	0.001	0.72	0.0597	0.0014	411	14	379	9	593	50	64	379	5	9	64
A_019	784	34	0.76	0.36	0.01	0.043	0.001	0.73	0.0600	0.0014	310	10	272	7	602	49	45	272	3	7	45
A_020	273	24	0.30	0.71	0.03	0.088	0.002	0.70	0.0585	0.0015	544	19	544	13	547	55	99	544	6	13	99
A_021	1864	40	0.53	0.19	0.01	0.021	0.001	0.70	0.0655	0.0016	178	6	136	3	790	51	17	136	2	3	17
A_022	278	25	0.29	0.71	0.03	0.089	0.002	0.59	0.0583	0.0020	547	23	548	13	541	76	101	548	7	13	101
A_023	345	26	0.50	0.63	0.02	0.075	0.002	0.64	0.0606	0.0018	495	19	468	11	626	63	75	468	6	11	75
A_024	759	27	0.46	0.30	0.01	0.036	0.001	0.65	0.0607	0.0017	266	10	226	6	628	61	36	226	3	6	36
A_025	456	35	0.34	0.63	0.02	0.078	0.002	0.73	0.0589	0.0013	496	16	482	11	565	49	85	482	6	11	85
A_031	1622	32	1.28	0.22	0.01	0.020	0.000	0.73	0.0788	0.0018	198	7	127	3	1166	44	11	1166	22	44	11
A_032	265	21	1.48	0.64	0.02	0.079	0.002	0.71	0.0587	0.0014	503	17	491	11	557	52	88	491	6	11	88
A_033	199	19	0.41	0.77	0.03	0.094	0.002	0.70	0.0593	0.0015	580	20	581	14	577	54	101	581	7	14	101
A_034	292	52	0.57	1.81	0.06	0.177	0.004	0.73	0.0744	0.0017	1050	35	1049	23	1052	46	100	1052	23	46	100
A_035	220	16	0.98	0.61	0.02	0.074	0.002	0.69	0.0598	0.0015	486	17	462	11	598	55	77	462	5	11	77
A_036	87	8	0.38	0.72	0.03	0.090	0.002	0.61	0.0585	0.0019	553	22	554	13	548	69	101	554	7	13	101
A_037	435	38	0.33	0.71	0.02	0.088	0.002	0.73	0.0591	0.0013	547	18	541	13	569	49	95	541	6	13	95
A_042	870	45	0.92	0.43	0.01	0.051	0.001	0.73	0.0616	0.0014	366	12	322	8	660	47	49	322	4	8	49
A_043	498	29	1.00	0.50	0.02	0.059	0.001	0.72	0.0624	0.0014	415	14	367	9	689	49	53	367	4	9	53
A_044	356	33	0.45	0.76	0.03	0.093	0.002	0.72	0.0592	0.0014	574	19	574	13	574	50	100	574	7	13	100
A_045	422	36	0.30	0.69	0.02	0.087	0.002	0.69	0.0581	0.0015	535	19	535	12	534	55	100	535	6	12	100
A_046	1017	39	0.29	0.33	0.01	0.039	0.001	0.73	0.0622	0.0014	292	10	245	6	683	47	36	245	3	6	36
A_047	499	46	0.37	0.80	0.03	0.092	0.002	0.73	0.0633	0.0014	596	20	565	13	718	47	79	565	6	13	79
A_048	220	31	0.56	1.31	0.05	0.141	0.003	0.70	0.0675	0.0017	851	29	851	19	853	51	100	853	25	51	100
A_049	547	26	0.20	0.40	0.01	0.047	0.001	0.71	0.0619	0.0015	341	11	294	7	672	50	44	294	3	7	44
A_050	190	17	0.37	0.74	0.03	0.091	0.002	0.62	0.0589	0.0018	560	22	560	13	562	66	100	560	7	13	100
A_051	243	22	0.31	0.72	0.02	0.089	0.002	0.70	0.0587	0.0014	551	19	549	13	558	53	99	549	6	13	99
A_052	252	22	0.44	0.71	0.03	0.088	0.002	0.68	0.0585	0.0015	546	19	545	13	550	56	99	545	6	13	99
A_053	226	21	0.37	0.76	0.03	0.093	0.002	0.69	0.0591	0.0015	572	20	572	13	572	54	100	572	7	13	100
A_054	248	22	0.56	0.71	0.03	0.089	0.002	0.66	0.0585	0.0016	547	20	547	13	548	59	100	547	6	13	100
A_057	619	46	0.40	0.61	0.02	0.074	0.002	0.73	0.0603	0.0013	486	16	460	11	614	48	75	460	5	11	75
A_058	292	26	0.65	0.72	0.02	0.089	0.002	0.71	0.0584	0.0014	550	18	552	13	543	51	101	552	6	13	101
A_059	883	61	0.92	0.58	0.02	0.069	0.002	0.74	0.0602	0.0013	462	15	432	10	609	47	71	432	5	10	71
A_060	224	20	0.70	0.74	0.03	0.091	0.002	0.69	0.0589	0.0015	560	19	559	13	565	53	99	559	6	13	99
A_061	167	13	0.52	0.62	0.02	0.076	0.002	0.66	0.0598	0.0016	493	18	471	11	596	58	79	471	5	11	79
A_062	753	25	0.37	0.29	0.01	0.033	0.001	0.71	0.0637	0.0015	259	9	209	5	733	50	29	209	2	5	29
A_063	221	25	0.48	1.23	0.04	0.114	0.003	0.72	0.0783	0.0018	816	27	697	16	1154	45	60	1154	23	45	60
A_064	165	15	0.34	0.74	0.03	0.091	0.002	0.67	0.0589	0.0016	562	20	562	13	563	58	100	562	6	13	100
A_065	369	33	0.37	0.72	0.02	0.089	0.002	0.71	0.0585	0.0014	548	18	549	12	547	50	100	549	6	12	100
A_066	221	20	0.34	0.71	0.02	0.090	0.002	0.69	0.0576	0.0014	546	19	554	13	514	54	108	554	6	13	108
A_067	337	26	0.30	0.62	0.02	0.077	0.002	0.71	0.0586	0.0014	490	16	476	11	554	51	86	476	5	11	86
A_068	395	26	0.44	0.55	0.02	0.065	0.002	0.71	0.0613	0.0014	447	15	409	9	650	50	63	409	5	9	63
A_069	550	37	0.41	0.61	0.02	0.068	0.002	0.72	0.0658	0.0015	486	16	422	10	798	47	53	422	5	10	53
A_070	604	27	0.91	0.38	0.01	0.045	0.001	0.71	0.0613	0.0014	329	11	285	7	651	50	44	285	3	7	44
A_071	942	52	0.65	0.46	0.01	0.056	0.001	0.73	0.0603	0.0013	386	12	349	8	614	47	57	349	4	8	57
A_074	1075	47	0.20	0.37	0.01	0.044	0.001	0.73	0.0608	0.0013	316	10	275	6	633	47	43	275	3	6	43

(continued on next page)

Table 2 *(continued)*

				Isotopic ratios							Ages (Ma)						Conc.				Conc.
Analysis	U [ppm][a]	Pb [ppm][a]	Th/U	$^{207}Pb/^{235}U$[b]	2 σ[c]	$^{206}Pb/^{238}U$[b]	2 σ[c]	Rho[d]	$^{207}Pb/^{206}Pb$[e]	2 σ[c]	$^{207}Pb/^{235}U$	2 σ	$^{206}Pb/^{238}U$	2 σ	$^{207}Pb/^{206}Pb$	2 σ	%[f]	$^{206}Pb/^{238}U$	1 σ	2σ	%[f]
A_075	806	34	0.65	0.36	0.01	0.042	0.001	0.71	0.0616	0.0014	309	10	264	6	660	49	40	264	3	6	40
A_076	294	27	0.45	0.73	0.02	0.092	0.002	0.70	0.0578	0.0014	557	18	565	13	523	52	108	565	6	13	108
A_077	2160	46	0.35	0.19	0.01	0.021	0.001	0.73	0.0649	0.0014	178	6	136	3	770	47	18	136	2	3	18
A_078	318	26	0.37	0.68	0.02	0.083	0.002	0.70	0.0596	0.0014	527	17	512	11	589	50	87	512	6	11	87
A_079	220	18	0.37	0.69	0.02	0.083	0.002	0.68	0.0601	0.0015	532	18	514	12	608	53	85	514	6	12	85
A_080	594	42	0.22	0.57	0.02	0.071	0.002	0.72	0.0586	0.0013	461	15	443	10	551	49	80	443	5	10	80
A_081	728	42	0.24	0.48	0.02	0.058	0.001	0.71	0.0605	0.0014	399	13	362	8	623	49	58	362	4	8	58
A_082	459	19	0.41	0.35	0.01	0.041	0.001	0.69	0.0614	0.0015	304	10	260	6	655	53	40	260	3	6	40
A_083	267	24	0.50	0.73	0.02	0.090	0.002	0.69	0.0588	0.0014	557	19	557	12	560	53	99	557	6	12	99
A_084	148	12	0.37	0.69	0.02	0.084	0.002	0.66	0.0591	0.0016	531	19	522	12	571	58	91	522	6	12	91
A_086	300	26	0.34	0.73	0.02	0.085	0.002	0.70	0.0625	0.0015	558	18	526	12	691	50	76	526	6	12	76
A_087	454	25	0.80	0.45	0.02	0.055	0.001	0.70	0.0596	0.0014	379	13	346	8	589	51	59	346	4	8	59
A_088	242	22	0.41	0.73	0.02	0.091	0.002	0.69	0.0587	0.0014	558	19	559	12	555	52	101	559	6	12	101
A_091	388	29	0.35	0.60	0.02	0.076	0.002	0.70	0.0579	0.0014	480	16	471	10	525	51	90	471	5	10	90
A_092	747	34	0.65	0.37	0.01	0.045	0.001	0.71	0.0602	0.0014	322	10	284	6	611	49	46	284	3	6	46
A_093	260	23	0.48	0.71	0.02	0.088	0.002	0.68	0.0586	0.0014	547	18	546	12	551	53	99	546	6	12	99
A_094	316	29	0.33	0.72	0.02	0.090	0.002	0.69	0.0582	0.0014	553	18	557	12	536	53	104	557	6	12	104
A_095	890	39	2.08	0.43	0.01	0.043	0.001	0.72	0.0713	0.0016	361	12	274	6	965	45	28	965	23	45	28
A_099	301	27	0.31	0.71	0.02	0.089	0.002	0.69	0.0585	0.0014	547	18	547	12	547	53	100	547	6	12	100
A_100	398	25	0.54	0.51	0.02	0.063	0.001	0.69	0.0593	0.0014	419	14	391	9	577	51	68	391	4	9	68
A_101	192	17	0.30	0.71	0.03	0.089	0.002	0.63	0.0585	0.0017	547	20	548	12	547	62	100	548	6	12	100
A_102	527	37	0.82	0.57	0.02	0.070	0.002	0.71	0.0590	0.0013	458	15	437	10	566	49	77	437	5	10	77
A_103	57	5	0.43	0.71	0.03	0.087	0.002	0.56	0.0590	0.0021	543	23	537	12	567	76	95	537	6	12	95
A_104	326	26	0.42	0.65	0.02	0.079	0.002	0.70	0.0591	0.0014	506	17	492	11	571	51	86	492	5	11	86
A_105	160	14	0.46	0.70	0.02	0.088	0.002	0.66	0.0580	0.0015	538	19	541	12	528	58	103	541	6	12	103
A_108	360	24	0.73	0.71	0.02	0.068	0.002	0.70	0.0760	0.0018	545	18	422	9	1096	46	39	1096	23	46	39
A_109	246	19	0.36	0.64	0.02	0.079	0.002	0.63	0.0586	0.0017	500	18	488	11	553	62	88	488	5	11	88
A_110	259	20	0.27	0.61	0.02	0.076	0.002	0.68	0.0584	0.0014	485	16	473	10	544	54	87	473	5	10	87
A_111	253	22	0.52	0.70	0.02	0.086	0.002	0.68	0.0591	0.0014	538	18	530	12	571	53	93	530	6	12	93
A_112	448	37	0.44	0.68	0.02	0.084	0.002	0.70	0.0590	0.0014	526	17	517	11	565	50	91	517	6	11	91
A_113	293	23	0.30	0.64	0.02	0.080	0.002	0.68	0.0585	0.0014	505	17	495	11	550	52	90	495	5	11	90
A_114	178	15	0.30	0.70	0.02	0.087	0.002	0.66	0.0582	0.0015	536	19	536	12	535	58	100	536	6	12	100
A_115	220	19	0.37	0.72	0.02	0.086	0.002	0.68	0.0607	0.0015	551	19	532	12	628	53	85	532	6	12	85
A_116	287	23	0.48	0.71	0.02	0.079	0.002	0.69	0.0648	0.0016	543	18	491	11	766	51	64	491	5	11	64
A_117	291	27	0.36	0.75	0.03	0.093	0.002	0.57	0.0589	0.0020	571	24	573	13	564	73	101	573	6	13	101
A_118	474	41	0.44	0.70	0.02	0.086	0.002	0.69	0.0589	0.0014	538	18	533	12	562	51	95	533	6	12	95
A_119	209	17	0.31	0.65	0.02	0.080	0.002	0.67	0.0584	0.0015	506	17	498	11	545	55	91	498	5	11	91
A_120	1360	42	0.45	0.27	0.01	0.031	0.001	0.71	0.0626	0.0014	239	8	196	4	695	48	28	196	2	4	28
A_125	262	20	0.25	0.61	0.02	0.076	0.002	0.65	0.0584	0.0016	486	17	474	10	544	58	87	474	5	10	87
A_126	186	16	0.32	0.69	0.03	0.086	0.002	0.62	0.0579	0.0017	532	19	533	12	526	62	101	533	6	12	101
A_127	612	53	0.26	0.69	0.02	0.087	0.002	0.70	0.0580	0.0013	535	17	536	12	530	50	101	536	6	12	101
A_128	243	22	0.27	0.72	0.02	0.090	0.002	0.68	0.0585	0.0014	552	18	553	12	549	54	101	553	6	12	101
A_129	406	31	0.30	0.63	0.02	0.077	0.002	0.69	0.0598	0.0014	498	16	477	10	594	51	80	477	5	10	80
A_130	239	21	0.32	0.70	0.02	0.087	0.002	0.67	0.0584	0.0014	537	18	535	12	545	53	98	535	6	12	98
A_131	458	39	0.33	0.69	0.02	0.086	0.002	0.69	0.0582	0.0014	532	17	531	11	535	53	99	531	6	11	99
A_132	360	32	0.31	0.72	0.02	0.089	0.002	0.69	0.0586	0.0014	549	18	549	12	551	51	100	549	6	12	100
A_133	416	26	0.66	0.51	0.02	0.062	0.001	0.68	0.0600	0.0014	421	14	389	8	602	51	65	389	4	8	65
A_134	465	40	0.41	0.71	0.02	0.087	0.002	0.70	0.0595	0.0014	546	17	537	11	584	49	92	537	6	11	92
A_135	574	40	0.64	0.72	0.02	0.069	0.002	0.70	0.0751	0.0017	550	17	432	9	1072	45	40	1072	23	45	40
A_136	101	9	0.38	0.68	0.03	0.085	0.002	0.60	0.0581	0.0018	529	20	528	12	534	67	99	528	6	12	99
A_137	392	32	0.35	0.65	0.02	0.081	0.002	0.69	0.0586	0.0014	509	17	500	11	551	51	91	500	5	11	91
A_138	366	29	0.41	0.64	0.02	0.079	0.002	0.68	0.0589	0.0014	504	16	490	11	564	51	87	490	5	11	87
A_139	422	24	0.37	0.46	0.02	0.057	0.001	0.63	0.0584	0.0016	384	14	358	8	543	59	66	358	4	8	66

[a] U and Pb concentrations and Th/U ratios are calculated relative to GJ-1 reference zircon.
[b] Corrected for background and within-run Pb/U fractionation and normalized to reference zircon GJ-1 (ID-TIMS values/measured value); $^{207}Pb/^{235}U$ calculated using ($^{207}Pb/^{206}Pb$)/($^{238}U/^{206}Pb \times 1/137.88$).
[c] Quadratic addition of within-run errors (2 SD) and daily reproducibility of GJ-1 (2 SD).
[d] Rho is the error correlation defined as the quotient of the propagated errors of the $^{206}Pb/^{238}U$ and the $^{207}Pb/^{235}U$ ratio.
[e] Corrected for mass-bias by normalizing to GJ-1 reference zircon (*0.6 per atomic mass unit) and common Pb using the model Pb composition of Stacey and Kramers (1975).
[f] Degree of concordance = ($^{206}Pb/^{238}U$ age × 100 / $^{207}Pb/^{206}U$ age).

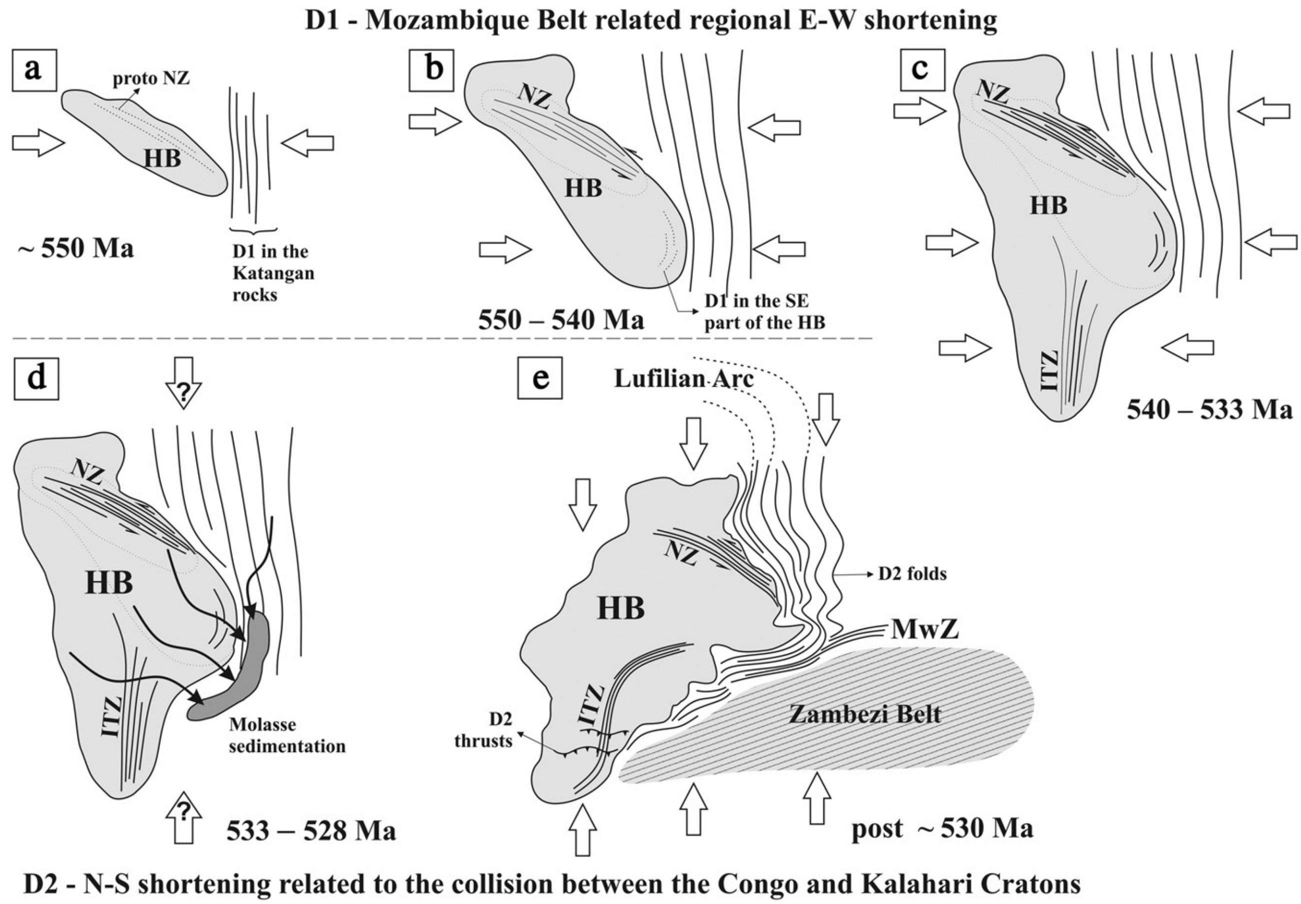

Fig. 14. Simplified tectonic model of the Pan-African evolution of the Hook Batholith area. a) At ca. 550 Ma the first portion of the Hook Batholith (HB) has been emplaced syn-tectonic to D1 of E–W shortening. Possible high-temperature deformation in the granite started along the proto Nalusanga Zone (NZ); b) between ca. 550 and 540 Ma in the same tectonic frame the sinistral NZ developed fully. Progressive deformation in the metasedimentary hosts continued to develop the F_1 structures which were also deflected along the NZ. The SE portion of the batholith has been emplaced and deformed under high temperature conditions; c) between ca. 540 and 530 Ma the central and southern portion of the batholith were emplaced and the pure-shear Itezhi-Tezhi Zone (ITZ) developed; d) at ca. 533–528 Ma probably during regional N–S shortening the granitoids and adjacent metasedimentary rocks were the source of the molasse type sedimentation; e) post 530 Ma during N-S shortening the D2 structures in the granitoids and its host rocks were formed in response to the stitching of the Lufilian and Zambezi belts along the Mwembeshi Zone (MwZ). For further details and explanation, refer to the text. Large arrows represent the regional shortening direction.

continued during cooling, thus resulting in full medium-temperature overprint of the microstructures. Higher strain-rates could also account for apparent lower-temperature deformation here (e.g. Tullis, 2002 and references therein).

The new isotope U–Pb geochronological data provide constraints on the emplacement and deformation history of the batholith. The two dominant lithologies, the deformed fine-grained and coarse-grained biotite granites, are probably co-magmatic since both granite varieties show concordia crystallisation ages of 549 ± 2 Ma in the NE part of the study area, which contrasts with Hanson et al. (1993) interpretation, based on field relationships, for an earlier emplacement of the fine-grained variety. At locality Z-77, the undeformed leucocratic veins that cross-cut the D1 fabrics in the coarse-grained biotite granite (Fig. 11a) have been dated at 541 ± 3 Ma. This age is therefore the younger limit for the activity of D1 in the NZ. In the SE part of the batholith (locality Z-87) the age of 544 ± 2 Ma for the foliated coarse-grained granite and of 543 ± 3 Ma for the fabric-truncating granitic vein (Fig. 11b) confirms deformation contemporaneous to the shearing in the NZ. These two overlapping ages and the high-temperature microstructures in the coarse-grained granite indicate crystallisation during the deformation. The crystallisation age of 533 ± 3 Ma obtained for sample Z-68B in the eastern margin of the ITZ indicates emplacement of the granitoids over a period of at least 15 Ma starting from the NE, then proceeding to the SE and finally to the central and SW parts of the batholith (Fig. 14a, b and c). On the other hand, this age attests to the prolonged character of the D1 deformation event that continued until at least ca. 533 Ma. To the north of the ITZ, Hanson et al. (1993) obtained an indistinguishable crystallisation age of 533 ± 3 Ma for an undeformed coarse-grained granite, which suggests that this undeformed portion of the batholith was not emplaced after the development of the S_1 solid-state fabric as previously thought (Hanson et al., 1993), but rather represents a low-strain domain at the centre of the batholith or was emplaced during the ceasing stage of D1.

Altogether the data suggest that the Hook Batholith is a syn-tectonic intrusion with respect to a regional D1 E–W shortening event that was active between ca. 550 and 533 Ma and probably for some time before this period. Our geochronological results improve and complement the age data of Hanson et al. (1993) for this large magmatic complex. This study, however, does not confirm the interpretation of Hanson et al. (1993) that the batholith is syn-tectonic to sinistral transpression along the MwZ but rather reveals that prolonged E–W shortening deformation accompanied the consecutive emplacement of different phases of the Hook granitoids at least between ca. 550 and 533 Ma.

9.2. D2 deformation event

The second deformation event, D2, formed during N–S regional shortening. To the SE of the batholith, the schists within the MwZ show steep to vertical E–W striking S_2 crenulation cleavage. Cross-cutting relationships with the S_1 foliations are sometimes preserved

(Fig. 10a, b). The metaconglomerates, which contain fragments from the underlying units that have been metamorphosed during D1, are characterised by the development of a single metamorphic S_2 foliation (Fig. 10c, d) parallel to the S_2 in the adjacent schists. To the NE of the batholith, the N-trending F1 folds are refolded along E–W trending open folds (Fig. 14e and Cikin, 1971, 1972). The F2 structures are associated with an axial planar cleavage S_2 that is orthogonal or at high angle to the S_1 foliation (Abell, 1970; Cikin, 1971, 1972). This indicates that the observed Type-II fold interference pattern (Ramsay, 1967) in the SE margin of the Hook Batholith (Fig. 4) is related to superimposition of two distinct sub-orthogonal deformation events. Further to the south, towards the MwZ, the F2-folds become progressively tighter, and within the MwZ the S_1 foliations are fully transposed to an E–W- to ENE-trend (Fig. 4) parallel to the steep S-dipping to vertical S_2 cleavage. Conversely, only open F2-folds and associated non-penetrative S_2 axial-planar cleavage developed north of the MwZ which indicates strong localisation of the N–S shortening south of the Hook granitoids. The batholith may have protected this low-D2-strain domain located at its NE margin, since further to the E and NE the Katangan rocks are again tightly folded into kilometre-scale structures (Vajner, 1998). Within the batholith, in its SW part, D2 is responsible for the formation of N-vergent thrust zones that overprint at high angle the D1 fabrics in the ITZ (Figs. 9, 14e). At a map scale, the N–S trending, subvertical ITZ is rotated towards NE- and ENE, thus trending approximately parallel to the southern contact of the batholith (Figs. 4, 14e). The curvature is smooth with no map-scale discontinuities, as depicted in the aeromagnetic images (Fig. 3) and supported by structural data documented by Abell (1970, 1976). The rotation of the D1 trend is not consistent with progressive E–W shortening deformation because of the lack of any observed or reported evidence for strong simple-shear dominated strike-slip deformation, as it would be expected along a NE- or ENE-trending subvertical zone during E–W compression.

For the first time since the interpretation of de Swardt et al. (1965), our study reports direct observations of the structures along the MwZ. Although being interpreted as a major, continental scale strike-slip shear zone (e.g. Coward and Daly, 1984; Daly, 1986, 1988; de Swardt et al., 1964, 1965; Hanson et al., 1993; Johnson et al., 2005; Porada and Berhorst, 2000; Unrug, 1983), in the area south of the Hook Batholith the MwZ has the characteristics of a pure-shear dominated zone that accommodated regional N–S shortening D2 event. This is a new view of the kinematics of this important structure and further studies of the timing of activity relative to the two shortening events and according kinematics in other key areas along the MwZ should be undertaken.

Relative time constraint on the activity of the D2 is deduced from the overprinting relationships with the solid-state D1 structures, which implies that this event was post-533 $\pm$ 3 Ma in the ITZ area. The timing of the D2 in the MwZ is given by the U–Pb isotope geochronology results from the detrital zircon population of sample Z-84 (metaconglomerate) that indicate deposition after ca. 530 Ma (mean age of the three youngest concordant zircon analyses) and consequently D2 was active after this time. The Hook Batholith is very likely one of the sources of the siliciclastic deposits, since the majority of the concordant analyses overlap with the ages obtained for the granitoids. In addition, the zircon population of grains with well-preserved crystal faces in Z-84 correspond to a proximal source and short transportation prior to deposition. This is further confirmed by the porphyritic granite pebbles found within the metaconglomerate (Abell, 1970). Therefore, these metasedimentary rocks are probably molasse-type deposits syn-tectonic to the exhumation of the batholith (Fig. 14d). A rhyolite dyke emplaced at the contact between the metaconglomerate and the schists in this area was dated by Hanson et al. (1993) at 551 $\pm$ 19 Ma and interpreted as a syn-tectonic intrusion in respect to the MwZ activity. Although we disagree with their interpretation for sinistral shearing, this result partially overlaps with the estimation of the onset of the D2 discussed above.

9.3. Regional implications

There is no agreement on the early Pan-African tectonic evolution of the Lufilian Arc. The N–S trending folds in the Katanga High and the Synclinorial Belt were described in numerous papers (e.g. de Swardt et al., 1964, 1965; Porada, 1989; Unrug, 1988, 1989) but, although regarded by the authors as a product of an early-Lufilian deformation, they had never been explained in respect to the regional Pan-African tectonic framework. Further north, in the Domes Region, Arthurs (1974), Porada (1989) and Barron (2003) reported a cryptic early deformation event that produced NE- to NNE-striking upright folds, compatible with bulk E–W shortening deformation, that were later overprinted during the N-vergent shearing and folding (e.g. Cosi et al., 1992; John et al., 2004a; Key et al., 2001). In the western part of the Lufilian Arc, Key et al. (2001) suggested that NW thrusting of Katangan metasedimentary rocks onto the Kibaran basement was facilitated by indentation of the Kalahari Craton during N–S collisional tectonics. Conversely, it is also possible that this NW-vergent thrusting event was triggered by bulk E–W crustal shortening in interaction with the NE–SW striking margin of the Kibaran Belt. Daly et al. (1984), Coward and Daly (1984) and Daly (1986, 1988) suggested that the Katangan sequence of the External Fold and Thrust Belt overthrusted the Irumide basement to the ENE to form several belts separated by lateral transcurrent ramps. Early low-angle ENE- to NE-vergent thrust complex, later overprinted by N-vergent thrusting are also described by Porada (1989) and Porada and Berhorst (2000). The polyphase tectonic evolution of this part of the orogen needs further investigations since Broughton et al. (2002) argued that early WNW–ESE folds were overprinted by N–S trending structures. At the apex of the Lufilian Arc in the DRC, the ENE-vergent thrusts were not observed (Kampunzu and Cailteux, 1999). South of the MwZ, Daly (1986) reported the existence of early WNW-verging thrusts in the Zambezi Belt. Although being documented at the regional scale, the early E–W shortening deformation event has not been dated so far and our study gives the first time constraints on its activity in the inner zones of the Lufilian Arc at ca. 560–550 Ma to ca. 533 Ma. Interestingly, this time frame overlaps partly with the latest stage of the evolution of the N–S striking Mozambique Belt, where collision between micro-continental blocks and the Tanzania–Congo Craton occurred after ca. 610 Ma (e.g. Kröner et al., 2001; Shackleton, 1993), with peak of the metamorphic overprint at amphibolite facies dated between ca. 580 and 550 Ma (Cutten et al., 2006; Hauzenberger et al., 2007; Ring, 1993; Ring et al., 1997, 1999, 2002; Rossetti et al., 2008) and developed in a bulk E–W or ESE–WNW horizontal crustal shortening (Ring et al., 1999, 2002). Although the geodynamic reconstruction for the colliding blocks and terranes during the Pan-African amalgamation between East and West Gondwana is rather unclear (e.g. Grantham et al., 2003, 2008; Kröner et al., 2001; Meert, 2003; Shackleton, 1993), these authors agree on the long-lasting bulk E–W shortening tectonics that controlled the evolution of the orogen. Therefore, it is suggested that the D1 deformation event in the Hook Batholith area and adjacent parts of the Lufilian Arc is a far field expression of the collision tectonics in the Mozambique Belt. The syn-tectonic emplacement of the Hook granitoids probably corresponds to the late stage of this convergence. It is noteworthy that a modern-day example of similar far-field tectonics with strike-slip zones and thrust-and-fold belts development at a distance greater than 1500 km from the thrust front can be seen in NE Tibet (e.g. Tapponnier et al., 2001).

The final amalgamation of Gondwana formed the Kuunga Orogen that is marked by general N–S collision with diachronous along-strike peak of the tectono-metamorphic overprint. The tectono-metamorphic evolution of the NE Mozambique part of the Kuunga Orogeny shows convergence tectonics and crustal thickening between ca. 570 and 535 Ma and cooling until ca. 490 Ma (e.g. Bingen et al., 2009; Viola et al., 2008). In Northern Malawi, the ca. 570–550 Ma E–W shortening was followed by development of NE- to

NNE-vergent shear zones along which eclogite-facies rocks have been exhumed between ca. 530 and 500 Ma (Ring et al., 2002). The main crustal thickening event in the Zambian part of the orogen occurred simultaneously in the Lufilian and Zambezi belts with early-synmetamorphic monazite growth at ca. 550–530 Ma (Eglinger et al., 2014) and temperature peak of the metamorphic overprint at ca. 530–520 Ma during N–S collision between the Congo and Kalahari Cratons (Goscombe et al., 2000; Hargrove et al., 2003; John et al., 2003, 2004a, 2004b; John and Schenk, 2003; Johnson and Oliver, 2004; Rainaud et al., 2005; Vinyu et al., 1999). Hence, we interpret the newly dated post ca. 533 Ma D2 event in the Hook Batholith area as being generated by this collision event and related to the same N–S shortening deformation.

The geodynamic significance of the ca. 660–595 Ma subduction related eclogite facies metamorphism of oceanic crust remnants in the Zambezi Belt (John et al., 2003, 2004b) is not clear as there is no described Pan-African subduction-related magmatism and no agreement in the literature on the geometry, polarity, position and number of subduction zones in Central Zambia. Porada and Berhorst (2000) suggested that the Katanga High is part of the overriding plate which is bounded to the N by an N-convex suture that abuts against the E–W to ESE-striking suture zone of the Zambezi Belt. Based on petrological investigations of the Lufilian Arc whiteschists and Zambian Belt eclogites, John et al. (2004a) refuted the model for a suture located within the Lufilian Arc and suggested southward subduction along the Zambezi zone. On the other hand, Rainaud et al. (2005) suggested northward subduction of the Kalahari beneath the Congo Craton. The A-type geochemistry of the Hook Batholith, while being so far interpreted as an indication for a rift-related ring complex (Lobo-Guerrero Sanz, 2005), can also be viewed as a result of heat advected from the mantle to the upper plate during northward subduction at ≥600 Ma combined with crustal heat controlled by radioactive heat-producing elements (U, Th, K).

The movements along the 3 km wide, NW-trending, sinistral Nalusanga strike-slip shear zone can be correlated with the activity along the NW-trending sinistral Mugesse shear zone formed in Malawi at ca. 570–550 Ma during regional E–W shortening (Ring et al., 1999, 2002). The Mugesse zone and a NE-trending dextral zone that has been correlated with the MwZ (Bjerkgard et al., 2009; Johns et al., 1989; Ring et al., 1999, 2002) are interpreted as contemporaneous conjugated lateral ramps (Ring et al., 2002). However, in the Hook area, the supposed crustal scale transcurrent MwZ (e.g. de Swardt et al., 1964, 1965; Hanson et al., 1993; Porada, 1989; Unrug, 1983) revealed an E–W to ENE-trending pure-shear dominated cleavage front that deformed the metasedimentary rocks south of the batholith. Even though an early Pan-African strike-slip shear zone cannot be excluded, the MwZ is better interpreted here as a highly oblique convergent feature that accommodated N–S shortening during the collision between the Congo and Kalahari Cratons and the stitching between the Lufilian and Zambezi belts after ca. 530 Ma (Fig. 14e).

10. Conclusions

Data from detailed structural field-studies, interpretation of aeromagnetic survey maps, microstructural observations and U–Pb dating of critical intrusive rocks and proximal siliciclastic sediments show that the Pan-African evolution of the Hook area is marked by two orthogonal tectono-metamorphic events. D1 corresponds to a regional E–W shortening and accounts for the development of N–S trending folds and associated subvertical axial-planar cleavage in the Katangan low-grade metasedimentary rocks. In the batholith, two high-strain zones developed — the N–S trending pure-shear Itezhi-Tezhi Zone and the NW-trending, simple-shear dominated sinistral Nalusanga Zone. The Hook granitoids are characterised as syn-tectonic to D1 and their emplacement span in the period between ca. 550 and 533 Ma ago. It is suggested that the D1 can be correlated to the early deformation event in the Katanga High and Synclinorial Belt of the Lufilian Arc. In terms of geometry and timing of deformation, the D1 in the Hook area can be linked to the E–W crustal shortening in the Mozambique Belt.

D2 in the Hook area is post ca. 533 Ma and occurred in tectonic settings of N–S shortening. It is defined by overprinting and rotation of the earlier D1-fabrics. The older time limit of the D2 is constrained by the relationships with dated D1 structures in the granitoids. The relative deposition age of the molasse-type rocks at the vicinity of the batholith, which recorded only one (D2) synmetamorphic deformation event, showed that D2 was active after ca. 530 Ma. D2 corresponds to the well-documented peak of the N–S shortening deformations in the Lufilian Arc and in the Zambezi Belt. It is therefore related to the collision between the Congo and Kalahari Cratons and the stitching of the two belts.

We have shown that the Mwembeshi Zone in the Hook area developed during the D2 as a structure accommodating pure-shear deformation, which marks the contact between the low metamorphic-grade inner zones of the Lufilian Arc and the high-grade rocks of the Zambezi Belt. Earlier, D1 movements along this zone, if existed in the Hook area, were either not recorded in sections underlain by younger than D1 Upper Kundelungu rocks or were fully overprinted during the D2 collision of the two cratons.

Acknowledgements

This paper forms part of the project “Geology, Tectonometamorphism, Magmatism and Mineralisation of the Damaran Orogen”, project of the EGRI (Economic Geology Research Institute), School of Geosciences, University of the Witwatersrand. The research was funded by Rio Tinto Exploration Ltd and by a THRIP (JKRT001/2 to Judith Kinnaird) grant. The authors are grateful to the technical staff at the School of Geosciences for the thin-sections and geochronology sample preparation. We would like to acknowledge K. Torremans and A. Eglinger who reviewed the manuscript and contributed significantly to the improvement of this paper.

Appendix A. Supplementary data

Supplementary data associated with this article can be found in the online version, at http://dx.doi.org/10.1016/j.tecto.2014.09.010. These data include Google map of the most important areas described in this article.

References

Abell, R., 1970. The geology of the Nansenga River area. Explanation of degree sheet 1526, NE quarter. Rep. Geol. Surv. Zambia 25 (62 pp.).
Abell, R., 1976. The geology of the Lukomezi River area. Explanation of degree sheet 1526, NW quarter. Rep. Geol. Surv. Zambia 33 (34 pp.).
Arthurs, J.W., 1974. The geology of the Solwezi area. Explanation of degree sheets 1226, NW quarter and 1126 SW part of SW quarter. Rep. Geol. Surv. Zambia 36 (48 pp.).
Andersen, L.S., Unrug, R., 1984. Geodynamic evolution of the Bangweulu Block, northern Zambia. Precambrian Res. 25, 187–212.
Barron, J.W., 2003. The stratigraphy, metamorphism, and tectonic history of the Solwezi area, Northwest Province, Zambia: integrating geological field observations and airborne geophysics in the interpretation of regional geology. Colorado School of Mines, (Ph.D. thesis, 233 pp.).
Basei, M.A.S., Frimmel, H.E., Nutman, A.P., Preciozzi, F., 2008. West Gondwana amalgamation based on detrital zircon ages from Neoproterozoic Ribeira and Dom Feliciano belts of South America and comparison with coeval sequences from SW Africa. In: Pankhurst, R.J., Trouw, R.A.J., Brito Neves, B.B., De Wit, M.J. (Eds.), West Gondwana: Pre-Cenozoic Correlations Across the South Atlantic Region. Geological Society of London, Special Publications 294, pp. 239–256.
Basei, M.A.S., Peel, E., Sánchez Bettucci, L., Preciozzi, F., Nutman, A.P., 2010. The basement of the Punta del Este Terrane (Uruguay): an African Mesoproterozoic fragment at the eastern border of the South American Río de La Plata Craton. Int. J. Earth Sci. 100, 289–304.
Bingen, B., Jacobs, J., Viola, G., Henderson, I.H.C., Skår, Ø., Boyd, R., Thomas, R.J., Solli, A., Key, R.M., Daudi, E.X.F., 2009. Geochronology of the Precambrian crust in the Mozambique belt in NE Mozambique, and implications for Gondwana assembly. Precambrian Res. 170, 231–255.
Bjerkgard, T., Stein, H., Bingen, B., Henderson, I., Sandstad, J., Moniz, A., 2009. The Niassa gold belt, northern Mozambique — a segment of a continental-scale Pan-African gold-bearing structure? J. Afr. Earth Sci. 53, 45–58.
Broughton, D.W., Hitzman, M.W., Stephens, A.J., 2002. Exploration history and geology of the Kansanshi Cu-(Au) deposit, Zambia. Soc. Econ. Geol., Spec. Publ. 9, 141–153.

Butler, R.W.H., Matthews, S.J., parish, M., 1986. The NW external Alpine Thrust Belt and its implications for the geometry of the Western Alpine Orogen. In: Coward, M.P., Ries, A.C. (Eds.), Collision Tectonics. Geological Society, London, Special Publications 19, pp. 245–260.
Cikin, M., 1971. The geology of the country north-west of Mumbwa (the Big Concession). Explanation of degree sheet 1426, SE quarter. Rep. Geol. Surv. Zambia 27 (72 pp.).
Cikin, M., 1972. Geology of the north-eastern margin of the Hook Granite Massif, Central Province. Rep. Geol. Surv. Zambia 12, 43–54.
Cosi, M., De Bonis, A., Gosso, G., Munziker, J., Martinotti, G., Moratto, S., Robert, J.P., Ruhlman, I., 1992. Late Proterozoic thrust tectonics, high-pressure metamorphism and uranium mineralization in the Domes Area, Lufilian Arc, northwestern Zambia. Precambrian Res. 58, 215–240.
Coward, M.P., Daly, M.C., 1984. Crustal lineaments and shear zones in Africa: their relationship to plate movements. Precambrian Res. 24, 27–45.
Cutten, H., Johnson, S.P., De Waele, B., 2006. Protolith ages and timing of the metasomatism related to the formation of whiteschists at Mautia Hill, Tanzania: implication for the assembly of Gondwana. J. Geol. 114, 683–698.
Daly, M.C., 1986. Crustal shear zones and thrust belts: their geometry and continuity in Central Africa. Philos. Trans. R. Soc. Lond. A317, 111–128.
Daly, M.C., 1988. Crustal shear zones in Central Africa: a kinematic approach to Proterozoic tectonics. Episodes 11 (1), 5–11.
Daly, M.C., Chakraborty, S.K., Kasolo, P., Musiwa, M., Mumba, P., Naidu, B., Namateba, C., Ngambi, O., Coward, M.P., 1984. The Lufilian Arc and the Irumide belt of Zambia: results of a geotraverse across their intersection. J. Afr. Earth Sci. 2, 311–318.
de Swardt, A.M.J., Drysdall, A.R., Garrard, P., 1964. Precambrian geology and structure in Central Northern Rhodesia. Mem. Geol. Surv. North. Rhod. 2, 82.
de Swardt, A.M.J., Gerrard, P., Simpson, J., 1965. Major zones of transcurrent dislocation and superposition of orogenic belts in part of Central Africa. Bull. Geol. Soc. Am. 76, 89–102.
De Waele, B., Fitzsimons, I.C.W., 2007. The nature and timing of Palaeoproterozoic sedimentation at the south-eastern margin of the Congo Craton; zircon U-Pb geochronology of plutonic, volcanic and clastic units in northern Zambia. Precambrian Res. 159, 95–116.
De Waele, B., Fitzsimons, I.C.W., Wingate, M.T.D., Tembo, F., Mapani, B., Belousova, E.A., 2009. The geochronological framework of the Irumide Belt: a prolonged crustal history along the margin of the Bangweulu Craton. Am. J. Sci. 309, 132–187.
De Waele, B., Kampunzu, A.B., Mapani, B.S.E., Tembo, F., 2006. The Mesoproterozoic Irumide belt of Zambia. J. Afr. Earth Sci. 46, 36–70.
Dirks, P.H.G.M., Kröner, A., Jelsma, H.A., Sithole, T.A., Vinyu, M.L., 1999. Structural relations and Pb-Pb zircon ages for the Makuti gneisses: evidence for a crustal-scale pan-African shear zone in the Zambezi belt, northwest Zimbabwe. J. Afr. Earth Sci. 28, 427–442.
Eglinger, A., Tarantola, A., Rurand, C., Ferraina, C., Vanderhaeghe, O., Andre'-Mayer, A.S., Paquette, J.-P., Deloule, E., 2014. Uranium mobilization by fluids associated with Ca–Na metasomatism: A P–T–t record of fluid-rock interactions during Pan-African metamorphism (Western Zambian Copperbelt). Chem. Geol. 386, 218–237.
Frei, D., Gerdes, A., 2009. Precise and accurate in situ U–Pb dating of zircon with high sample throughput by automated LA-SF-ICPMS. Chem. Geol. 261, 261–270.
Frimmel, H.E., Basei, M.S., Gaucher, C., 2011. Neoproterozoic geodynamic evolution of SW-Gondwana: a southern African perspective. Int. J. Earth Sci. 100, 323–354.
Gerdes, A., Zeh, A., 2006. Combined U–Pb and Hf isotope LA-(MC-)ICP-MS analyses of detrital zircons: comparison with SHRIMP and new constraints for the provenance and age of an Armorican metasediments in Central Germany. Earth Planet. Sci. Lett. 249 (1–2), 47–61.
Goscombe, B., Armstrong, R., Barton, J.M., 2000. Geology of the Chewore Inliers, Zimbabwe: constraining the Mesoproterozoic to Palaeozoic evolution of the Zambezi Belt. J. Afr. Earth Sci. 30, 589–627.
Grantham, G.H., Maboko, M., Eglington, B.M., 2003. A review of the evolution of the Mozambique Belt and implications for the amalgamation of Rodinia and Gondwana. In: Yoshida, M., Windley, B.F., Dasgupta, S. (Eds.), Proterozoic East Gondwana: Supercontinent Assembly and Breakup. Geological Society, London, Special Publications 206, pp. 401–426.
Grantham, G.H., Macey, P.H., Ingram, B.A., Poberts, M.P., Armstrong, R.A., Hokada, T., Shirashi, K., Jackson, C., Bisnath, A., Manhica, V., 2008. Terrane correlation between Antarctica, Mozambique and Sri Lanka; comparison of geochronology, lithology, structure and metamorphism and possible implications for the geology of southern Africa and Antarctica. In: Satish-Kumar, M., Motoyoshi, Y., Osanai, Y., Hiroi, Y., Shiraishi, K. (Eds.), Geodynamic Evolution of East Antarctica: A Key to the East–West Gondwana Connection. Geological Society, London, Special Publications 308, pp. 91–119.
Gray, D.R., Foster, D.A., Meert, J.G., Goscombe, B.D., Armstrong, A., Trouw, R.A.J., Passchier, C.W., 2008. A Damara orogen perspective on the assembly of southwestern Gondwana. In: Pankhurst, R.J., Trouw, R.A.J., Brito Neves, B.B., De Wit, M.J. (Eds.), West Gondwana: Pre-Cenozoic Correlations Across the South Atlantic Region. Geological Society, London, Special Publications 294, pp. 257–278.
Griffiths, C., 1998. Geology of the Namwala and Ngoma areas. Explanation of degree sheet 1525, SE quarter and 1526 SW quarter. Rep. Geol. Surv. Zambia 77 (66 pp.).
Hanson, R.E., 2003. Proterozoic geochronology and tectonic evolution of southern Africa. In: Yoshida, M., Windley, B.F., Dasgupta, S. (Eds.), Proterozoic East Gondwana: Supercontinent Assembly and Breakup. Geological Society of London, Special Publications 206, pp. 427–463.
Hanson, R.E., Wardlaw, M.S., Wilson, T.J., Mwale, G., 1993. U–Pb zircon ages from the Hook granite massif and Mwembeshi dislocation: constraints on pan-African deformation, plutonism, and transcurrent shearing in central Zambia. Precambrian Res. 63, 189–209.
Hanson, R.E., Wilson, T.J., Munyanyiwa, H., 1994. Geologic evolution of the Neoproterozoic Zambezi Orogenic Belt in Zambia. J. Afr. Earth Sci. 18, 135–150.
Hanson, R.E., Wilson, T.J., Wardlaw, M.S., 1988. Deformed batholiths in the Pan-African Zambezi belt, Zambia: age and implications for regional proterozoic tectonics. Geol. 16, 1134–1137.
Hauzenberger, C.A., Sommer, H., Fritz, H., Bauernhofer, A., Kröner, A., Hoinkes, G., Wallbrecher, E., Thöni, M., 2007. SHRIMP U–Pb and Sm–Nd garnet ages from the granulite-facies basement of SE Kenya: evidence for Neoproterozoic polycyclic assembly of the Mozambique Belt. J. Geol. Soc. Lond. 164, 189–201.
Hargrove, U.S., Hanson, R.E., Martin, M.W., Blenkinsop, T.G., Bowring, S.A., Walker, N., Munyanyiwa, H., 2003. Tectonic evolution of the Zambezi orogenic belt: geochronological, structural, and petrological constraints from northern Zimbabwe. Precambrian Res. 123, 159–186.
Isaacs, K.N., 1968. Interpretation Report of an Airborne Geophysical Survey in the Republic of Zambia for the Geological Survey of Zambia (Unpublished Report). Canadian Aero Services Ltd.
John, T., Schenk, V., 2003. Partial eclogitisation of gabbroic rocks in a late Precambrian subduction zone (Zambia): prograde metamorphism triggered by fluid infiltration. Contrib. Mineral. Petrol. 146, 174–191.
John, T., Schenk, V., Haase, K., Scherer, E., Tembo, F., 2003. Evidence for Neoproterozoic Ocean in south-central Africa from mid-oceanic-ridge-type geochemical signatures and pressure–temperature estimates of eclogites. Geology 31, 243–246.
John, T., Schenk, V., Mezger, K., Tembo, F., 2004a. Timing and PT evolution of whiteschist metamorphism in the Lufilian Arc-Zambezi Belt orogen (Zambia): implications for the assembly of Gondwana. J. Geol. 112, 71–90.
John, T., Scherer, E.E., Haase, K., Schenk, V., 2004b. Trace element fractionation during fluid-induced eclogitization in a subducting slab: trace element and Lu–Hf–Sm–Nd isotope systematics. Earth Planet. Sci. Lett. 227, 441–456.
Johns, C., Liyungu, K., Mabuku, S., Mwale, G., Sakungo, F., Tembo, D., Vallance, G., 1989. The stratigraphic and structural framework of Eastern Zambia: results of a geotraverse. J. Afr. Earth Sci. 9 (1), 123–136.
Johnson, S.P., Oliver, G.J.H., 2004. Tectonothermal history of the Kaourera Arc, northern Zimbabwe: implications for the tectonic evolution of the Irumide and Zambezi Bets of south central Africa. Precambrian Res. 130, 71–97.
Johnson, S.P., De Waele, B., Evans, D., Banda, W., Tembo, F., Milton, J.A., Tani, K., 2007. Geochronology of the Zambezi supracrustal sequence, southern Zambia: a record of Neoproterozoic divergent processes along the southern margin of the Congo Craton. J. Geol. 115, 355–374.
Johnson, S.P., Rivers, T., De Waele, B., 2005. A review of the Mesoproterozoic to early Palaeozoic magmatic and tectonothermal history of south-central Africa: implications for Rodinia and Gondwana. J. Geol. Soc. Lond. 162, 433–450.
Kampunzu, A.B., Cailteux, J.L.H., 1999. Tectonic evolution of the Lufilian Arc (Central Africa copper belt) during Neoproterozoic Pan African orogenesis. Gondwana Res. 2 (3), 401–421.
Katongo, C., Koeberl, C., Reimold, W.U., Mubu, S., 2002. Remote sensing, field studies, petrography, and geochemistry of rocks in central Zambia: no evidence of a meteoritic impact in the area of the Lukanga Swamp. J. Afr. Earth Sci. 35, 365–384.
Katongo, C., Koller, F., Kloetzli, U., Koeberl, C., Tembo, F., De Waele, B., 2004. Petrography, geochemistry, and geochronology of granitoid rocks in the Neoproterozoic-Paleozoic Lufilian–Zambezi belt, Zambia: implications for tectonic setting and regional correlation. J. Afr. Earth Sci. 40, 219–244.
Key, R.M., Liyungu, A.K., Njamu, F.M., Somwe, V., Banda, J., Mosley, P.N., Armstrong, R.A., 2001. The western arm of the Lufilian Arc in NW Zambia and its potential for copper mineralization. J. Afr. Earth Sci. 33, 503–528.
Kokonyangi, J.W., Armstrong, R., Kampunzu, A.B., Yoshida, M., Okudaria, T., 2004. U–Pb zircon geochronology and petrology of granitoids from Mitwaba (Katanga, Congo): implications for the evolution of the Mesoproterozoic Kibaran Belt. Precambrian Res. 132, 79–106.
Kokonyangi, J.W., Kampunzu, A.B., Armstrong, R., Yoshida, M., Okudaira, T., Arima, M., Ngulube, D.A., 2006. The Mesoproterozoic Kibaride belt (Katanga, SE D.R. Congo). J. Afr. Earth Sci. 46, 1–35.
Kröner, A., Wilner, A.P., Hegner, E., Jaeckel, P., Nemchin, A., 2001. Single zircon ages, PT evolution and Nd isotopic systematics of high-grade gneisses in southern Malawi and their bearing on the evolution of the Mozambique belt in southeastern Africa. Precambrian Res. 109, 257–291.
Kruhl, J.H., 1996. Prism- and basal-plane parallel subgrain boundaries in quartz: a microstructural geothermobarometer. J. Metamorph. Geol. 14, 581–589.
Kruhl, J.H., 1998. Reply: prism- and basal-plane parallel subgrain boundaries in quartz: a microstructural geothermobarometer. J. Metamorph. Geol. 16, 142–146.
Kruhl, J.H., 2001. Crystallographic control on the development of foam textures in quartz, plagioclase and analogue material. Int. J. Earth Sci. 90, 104–117.
Law, R.D., 2014. Deformation thermometry based on quartz c-axis fabrics and recrystallization microstructures: a review. J. Struct. Geol. 66, 129–161.
Lobo-Guerrero Sanz, A., 2005. Pre- and Post-Katangan Granitoids of the Greater Lufilian Arc: Geology, Geochemistry, Geochronology and Metallogenic Significance. University of the Witwatersrand, (Ph.D. thesis, 734 pp.).
Ludwig, K.R., 2008. User's manual for Isoplot 3.70. A geochronological toolkit for Microsoft Excel. Berkeley Geochronology Center. Special Publication 4, (74 pp.).
Mattinson, J.M., 2010. Analysis of the relative decay constants of ^{235}U and ^{238}U by multi-step CA-TIMS measurements of closed-system natural zircon samples. Chem. Geol. 275, 186–198.
Meert, J.G., 2003. A synopsis of events related to the assembly of eastern Gondwana. Tectonophysics 362, 1–40.
Miller, R.McG., 2008. The Geology of Namibia, Vol. 2 — Mesoproterozoic to Lower Palaeozoic. Ministry of Mines and Energy, Geological Survey, Windhoek (508 pp.).
Nasdala, L., Hofmeister, W., Norberg, N., Mattinson, J.M., Corfu, F., Dörr, W., Kamo, S.L., Kennedy, A.K., Kronz, A., Reiners, P.W., Frei, D., Košler, J., Wan, Y., Götze, J., Häger, T.,

Kröner, A., Valley, J.W., 2008. Zircon M257–a homogeneous natural reference material for the ion microprobe U-Pb analysis of zircon. Geostand. Geoanal. Res. 32, 247–265.
Page, T., 1974. Geology of the Lubungu and Lungu areas. Explanation of degree sheet 1426, NW quarter and 1426 SW quarter. Rep. Geol. Surv. Zambia 39 (23 pp.).
Passchier, C.W., Trouw, R.A.J., 2005. Microtectonics, Second, Revisited and Enlarged Edition. Springer-Verlag, Berlin Heidelberg (366 pp.).
Phillips, K.A., 1958. Geology of the Luiri Hill area. Explanation of degree sheet 1527, NW quarter. Rep. Geol. Surv. Zambia 4 (69 pp.).
Phillips, K.A., Newton, A.R., 1956. A summary of the Katanga succession in the Mumbwa area with a supplement on the igneous rocks of the area. Occas. Pap. Geol. Surv. North. Rhod. 10 (Supplement 4–5) (12 pp.).
Pippin, F., 1975. The geology of the Mutapanda River area. Explanation of degree sheet 1426, NE quarter. Rep. Geol. Surv. Zambia 31 (20 pp.).
Porada, H., 1989. Pan-African rifting and orogenesis in Southern to equatorial Africa and Eastern Brazil. Precambrian Res. 44, 103–136.
Porada, H., Berhorst, V., 2000. Towards a new understanding of the Neoproterozoic–Early Palaeozoic Lufilian and northern Zambezi Belts in Zambia and the Democratic Republic of Congo. J. Afr. Earth Sci. 30, 727–771.
Prave, A.R., 1996. Tale of three cratons: tectonostratigraphic anatomy of the Damara orogen in northwestern Namibia and the assembly of Gondwana. Geology 24, 1115–1118.
Pryer, L.L., 1993. Microstructures in feldspars from a major crustal thrust zone: the Grenville Front, Ontario, Canada. J. Struct. Geol. 15 (1), 21–36.
Rainaud, C., Master, S., Armstrong, R.A., Phillips, D., Robb, L.J., 2005. Monazite U–Pb dating and 40Ar–39Ar thermochronology of metamorphic events in the Central African Copperbelt during the Pan-African Lufilian Orogeny. J. Afr. Earth Sci. 42, 183–199.
Ramsay, J.G., 1967. Folding and Fracturing of Rocks. McGraw-Hill, New York (568 pp.).
Ramsay, C.R., Ridgway, J., 1977. Metamorphic patterns in Zambia and their bearing on problems of Zambian tectonic history. Precambrian Res. 4, 321–337.
Ring, U., 1993. Aspects of kinematic history and mechanisms of superposition of the Proterozoic mobile belts of eastern Central Africa (northern Malawi and southern Tanzania). Precambrian Res. 62, 207–226.
Ring, U., Kroner, A., Buchwald, R., Toulkeridis, T., Layer, P., 2002. Shear-zone patterns and eclogite-facies metamorphism in the Mozambique belt of northern Malawi, east-central Africa: implications for the assembly of Gondwana. Precambrian Res. 116, 19–56.
Ring, U., Kroner, A., Layer, P., Buchwald, R., Toulkeridis, T., 1999. Deformed A-type granites in northern Malawi, east-central Africa: pre- or syntectonic? J. Geol. Soc. Lond. 156, 695–714.
Ring, U., Kröner, A., Toulkeridis, T., 1997. Palaeoproterozoic granulite-facies metamorphism and granitoid intrusions in the Ubendian-Usagaran Orogen of northern Malawi, east-central Africa. Precambrian Res. 85, 27–51.
Rosenberg, C.L., Stünitz, H., 2003. Deformation and recrystallization of plagioclase along a temperature gradient: an example from the Bergell tonalite. J. Struct. Geol. 25, 389–408.
Rossetti, F., Cozzupoli, D., Phillips, D., 2008. Compressional reworking of East African Orogen in the Uluguru Mountains of eastern Tanzania at c. 550 Ma: implication for the final assembly of Gondwana. Terra Nova 1, 59–67.
Saalmann, K., Gerdes, A., Lahaye, Y., Hartmann, L.A., Remus, M.V.D., Läufer, A., 2011. Multiple accretion at the eastern margin of the Rio de la Plata craton: the prolonged Brasiliano orogeny in southernmost Brazil. Int. J. Earth Sci. 100, 355–378.
Saviaro, K., 1980. Preliminary analysis of airborne magnetic surveys in Zambia. Occas. Pap. Geol. Surv. Zambia 98, 8.
Selley, D., Broughton, D., Scott, R.J., Hitzman, M., Bull, S.W., Large, R.R., McGoldrick, P.J., Croaker, M., Pollington, N., 2005. A New Look at the Geology of the Zambian Copperbelt. Soc. Econ. Geol. Inc., 100th Anniversary Volume 965–1001.
Seifert, A.V., 2000. Geology of the Chunga area. Explanation of degree sheet 1525. NE quarter. Rep. Geol. Surv. Zambia 75, 23.
Sláma, J., Košler, J., Condon, D.J., Crowley, J.L., Gerdes, A., Hanchar, J.M., Horstwood, M.S.A., Morris, G.A., Nasdala, L., Norberg, N., Schaltegger, U., Schoene, B., Tubrett, M.N., Whitehouse, M.J., 2008. Plešovice zircon—a new natural reference material for U–Pb and Hf isotopic microanalysis. Chem. Geol. 249, 1–35.
Shackleton, R.M., 1993. Tectonics of the Mozambique Belt in East Africa. Geol. Soc. Lond., Spec. Publ. 76, 345–362.
Snelling, N.J., Johnson, R.L., Drysdall, A.R., 1972. The geochronology of Zambia. Rec. Geol. Surv. Zambia 12, 19–30.
Stacey, J.S., Kramers, J.D., 1975. Approximation of terrestrial lead isotope evolution by a two-stage model. Earth Planet. Sci. Lett. 26, 207–221.
Stipp, M., Stunitz, H., Heilbronner, R., Schmid, S., 2002. Dynamic recrystallization of quartz: correlation between natural and experimental conditions. Geol. Soc. Lond., Spec. Publ. 200, 171–190.
Tack, L., Wingate, M.T.D., De Waele, B., Meert, J., Belousova, E., Griffin, B., Tahon, A., Fernandez-Alonso, M., 2010. The 1375 Ma "Kibaran event" in central Africa: prominent emplacement of bimodal magmatism under extensional regime. Precambrian Res. 180, 63–84.
Tapponnier, P., Zhiqin, X., Roger, F., Meyer, B., Arnaud, N., Wittlinger, G., Jingsui, Y., 2001. Oblique stepwise rise and growth of the Tibet Plateau. Science 294, 1671–1677.
Thieme, J., 1984. Geological Map of Lusaka Area, 1:250,000, Sheet number SD-35-15. Directorate of Overseas Survey, Tolworth, Surbition, Surrey, England.
Thieme, J., Johnson, R., 1981. Geological map of Republic of Zambia, 1:1,000,000. Geological Survey of Zambia, Lusaka.
Trouw, A.J.R., Passchier, C.W., Wiersma, D.J., 2009. Atlas of Mylonites — and Related Microstructures. Springer-Verlag, Berlin Heidelberg (322 pp.).
Tullis, J., 2002. Deformation of granitic rocks: experimental studies and natural examples. Rev. Mineral. Geochem. 51, 51–95.
Unrug, R., 1983. The Lufilian Arc: a microplate in the Pan-African collision zone of the Congo and the Kalahari cratons. Precambrian Res. 21, 181–196.
Unrug, R., 1988. Mineralization controls and source of metals in the Lufilian Fold Belt, Shaba (Zaire), Zambia, and Angola. Econ. Geol. 83, 1247–1258.
Unrug, R., 1989. Landsat-based structural map of the Lufilian Fold Belt and the Kundelungu Aulacogen, Shaba (Zaire), Zambia, and Angola, and the regional position of Cu, Co, U, Au, Zn and Pb mineralization. In: Boyle, R.W., Broen, A.C., Jefferson, C.W., Kirkham, R.V. (Eds.), Sediment-hosted Stratiform Copper Deposits. Geological Association of Canada, Special Paper 36, pp. 519–524.
Vajner, V., 1998. Geology of the country north-east of Mumbwa. Explanation of degree sheet 1427, SW quarter. Rep. Geol. Surv. Zambia 29 (33 pp.).
Vernon, R.H., Johnson, S.E., Melis, E.A., 2004. Emplacement-related microstructures in the margin of a deformed pluton: the San Jose tonalite, Baja California, Mexico. J. Struct. Geol. 26, 1867–1884.
Vinyu, M.L., Hanson, R.E., Martin, M.W., Bowring, S.A., Jelsma, H.A., Krol, M.A., Dirks, P.H.G.M., 1999. U–Pb and $^{40}Ar/^{39}Ar$ geochronological constraints on the tectonic evolution of the easternmost part of the Zambezi orogenic belt, northeast Zimbabwe. Precambrian Res. 98, 67–82.
Viola, G., Henderson, I.H.C., Bingen, B., Thomas, R.J., Smethurst, M.A., de Azavedo, S., 2008. Growth and collapse of a deeply eroded orogen: insights from structural, geophysical, and geochronological constraints on the Pan-African evolution of NE Mozambique. Tectonics 27 (TC5009, 31 pp.).
Vrána, S., Prasad, R., Fediukova, E., 1975. Metamorphic kyanite eclogites in the Lufilian Arc of Zambia. Contrib. Mineral. Petrol. 51, 39–160.

Appendix 2:

This appendix presents Lehmann, J., Master, S., Rankin, W., Milani, L., Kinnaird, J.A., Naydenov, K.V., Saalmann, and Kumar, M. (submitted) in its submitted format to *Ore Geology Reviews*. Consequently, the formatting, layout, figure and table numbering do not follow the layout of this dissertation.

Regional aeromagnetic and stratigraphic correlations of the Kalahari Copperbelt in Namibia and Botswana

Jérémie Lehmann[1], Sharad Master[1], William Rankin[1], Lorenzo Milani[1], Judith A. Kinnaird[1], Kalin V. Naydenov[1,2], Kerstin Saalmann[1,3] and Manish Kumar[4]

[1] EGRI, School of Geosciences, University of the Witwatersrand, PVT Bag 3, Wits, 2050, South Africa

Corresponding author: Jérémie Lehmann - School of Geosciences, University of the Witwatersrand, PVT Bag 3, Wits, 2050, South Africa

[2] Geological Institute, BAS, 24 Acad. G. Bonchev str, 1113 Sofia, Bulgaria

[3] Norges Geologiske Undersøkelse (NGU), Postboks 6315 Sluppen, 7491 Trondheim, Norway

[4] Rio Tinto Mining and Exploration, 1 Harries Rod, Illovo, 2196, South Africa

Corresponding author: Jeremie Lehmann; tel.: +27 11 7176551. E-mail address: jerelehmann@gmail.com

Keywords: Kalahari Copperbelt, tectono-stratigraphy, sedimentary structures, aeromagnetic interpretation, mining exploration

Abstract

The late Mesoproterozoic to Neoproterozoic Kalahari Copperbelt (KCB) in Namibia and Botswana is widely covered by Kalahari sand, which precludes direct correlations between known stratabound sediment-hosted Cu-Ag districts. We use a combination of review of literature data, new sedimentological observations of key stratigraphic units from outcrops and drillcores, and newly processed and interpreted high-resolution aeromagnetic maps in both countries. Lithostratigraphic control on the aeromagnetic response allows detailed indirect mapping of the Kalahari Copperbelt lithotectonic domains below the sand cover. This enabled us to redefine the width and lateral extent of the KCB as two continuous magnetic domains (the Rehoboth and Ghanzi-Chobe domains) extending from central Namibia to northern Botswana, and helped in resolving problems of stratigraphic correlations across the international border.

The Rehoboth magnetic domain, in the western part of the KCB in Namibia, records continental arc magmatism at ~ 1200 Ma during orogenic events along the northwestern edge of the Kalahari Craton. This was followed at 1110-1090 Ma by widespread magmatism, identified within the entire KCB, related to the 1112-1006 Ma-old Umkondo Large Igneous Province. Following a period of erosion and peneplanation, a marine transgressive-regressive episode started with deposition of the basal parts of the Tsumis Group in Namibia and Ghanzi Group in Botswana. Subsequently, during a

second, pre-Sturtian transgressive-regressive episode, the host-rocks of the Cu-Ag deposits formed by the juxtaposition of deeper shelf offshore reduced facies shales and siltstones over underlying oxidised shallow-shelf sandstones. This regional interface, which is both a permeability barrier and redox boundary, played a critical role in the formation of the stratabound sediment-hosted Cu-Ag deposits of the Kalahari Copperbelt and can be followed through it because of the strong magnetic contrast across it. The overall KCB was affected by the Damara Orogeny which resulted in the formation of a NE-SW trending ~ 250 km-wide fold-and-thrust belt.

1. Introduction

The Kalahari Copperbelt, a 1000 km long by up to 250 km wide NE-trending Meso- to Neoproterozoic belt occurs discontinuously from western Namibia (Sinclair Supergroup) to northern Botswana (Kgwebe Formation and Ghanzi Group) along the NW edge of the Palaeoproterozoic Kalahari Craton (Fig. 1) (Borg and Maiden, 1989; Maiden and Borg, 2011). It is comprised of copper-silver deposits that are generally stratabound (i.e. restricted to a particular part of the stratigraphic column, Evans et al., 2006) and hosted in Meso- to Neoproterozoic metasedimentary rocks that have been folded, foliated and faulted and metamorphosed to greenschist facies during the Pan-African Damara Orogeny (Borg and Maiden, 1989).

Whereas the belt in western and central Namibia is relatively well-exposed, eastern Namibia and most of Botswana are covered by the late Carboniferous-middle Jurassic Karoo Supergroup and Cenozoic Kalahari sand and calcrete (Catuneanu et al., 2005; Haddon and McCarthy, 2005). In addition to the lack of exposure, the paucity in age constraints on the sedimentation precludes direct lateral correlations across the international border (Borg, 1988a; Kampunzu et al., 1998; Ramokate et al., 2000; Watters, 1976). In Botswana, the geology below the Kalahari cover had been extrapolated from a few inliers using aeromagnetic data interpretation and sparse drillholes which resulted in the publication of the 1:1 000 000 scale pre-Kalahari geological map of Botswana (Key and Ayres, 2000), subsequently integrated into the 1:2 500 000 scale sub-Kalahari geological map of southern Africa (Haddon, 2001). In Namibia however, such sub-cover mapping has not been edited and the correlations with the geology of Botswana rely on the 1:2 500 000 scale sub-Kalahari geological map (Haddon, 2001), and on geological inferences in the 1:1 000 000 scale Geological Map of Namibia (Miller and Schalk, 1980). In those maps, the Ghanzi Group is represented as the lateral equivalent of the Neoproterozoic Damara Supergroup, a well-dated sequence that is stratigraphically younger than the Sinclair Supergroup (Fig. 1). On the other hand, various correlative interpretations based on Rb-Sr ages, multigrain U-Pb zircon ages and sedimentological and chemical data have been published, including correlation of the Kgwebe Formation with volcanic rocks of the Sinclair Supergroup

(Kampunzu et al., 1998; Schwartz et al., 1996; Toens, 1975), and of the Ghanzi Group with either the lower part of the Damara Supergroup (Haddon, 2001; Kampunzu et al., 1998; Ramokate et al., 2000; Schwartz et al., 1996) or with the upper group of the Sinclair Supergroup (the Tsumis Group, Borg and Maiden, 1987). These different interpretations on cross-border correlations are presented in figure 2. The interest in the geology and spatial extent of the Kalahari Copperbelt has been renewed over the last 10 years since the development of the Boseto copper mine in Botswana (shown in Fig. 1), and the recent discovery of new high-grade occurrences which have been intersected in both Namibia and Botswana (e.g. 2.76 % Cu and 89 g/t Ag over 7 m, Enders, personal communication).

In this contribution, we present an integrated study in both countries based on an exhaustive compilation of published zircon ages of magmatic and sedimentary rocks and a summary of existing lithostratigraphic descriptions modified by new field observations of key sedimentological features. The spatial continuity of newly defined lithotectonic domains below cover and across the Namibia-Botswana border was inferred using processed 50 m resolution aeromagnetic maps. The important lithological control on the aeromagnetic signatures enabled detailed indirect mapping of the units constituting the Kalahari Copperbelt using total magnetic intensity (TMI), reduced-to-pole (RTP), first vertical derivative (1VD), total horizontal derivative (THDR) and analytical signal aeromagnetic maps. Together with the new palaeogeographic and chronological correlations, the continuity of these lithotectonic domains from Namibia to northern Botswana across the Namibia-Botswana border allows revision of existing tectonic models for the formation of the Meso- to Neoproterozoic rocks that host the Kalahari Copperbelt.

2. Lithostratigraphy of the Meso-to Neoproterozoic rocks in Central Namibia

Meso- to Neoproterozoic rocks in Central Namibia crop out in the Konkiep and Rehoboth subprovinces. Mesoproterozoic rocks are also locally found structurally below the Neoproterozoic rocks of the Damara Supergroup in the Damara Belt. In the Konkiep Subprovince, the rocks of the Sinclair Supergroup are unmetamorphosed and undeformed while the crust of the Rehoboth Subprovince has been highly deformed at greenschist facies during the Pan-African Orogeny with muscovite, and chlorite defining a slaty cleavage in metapelites in absence of biotite (Becker et al., 2006; Borg and Maiden, 1987).

2.1. Rocks of Pre-Sinclair Supergroup age

The basement of the oldest peri-Kalahari Craton Mesoproterozoic rocks in Central Namibia is of Palaeoproterozoic age (Becker et al., 2004; Van Schijndel et al., 2011). Pre-Sinclair Supergroup

Mesoproterozoic rocks are represented by the Kairab Formation and the Aunis Tonalite in the Konkiep Subprovince and the Billstein Formation in the Rehoboth Subprovince (Fig. 1). The Kairab Formation is composed of mafic and felsic volcanic rocks which are intruded by the Aunis Tonalite. Both units were metamorphosed in the amphibolite facies (Miller, 2008). Volcanic rocks from the Kairab Formation have yielded a poorly defined Pb/Pb isochron age of 1476 +201/-215 Ma (Hoal, 1990), the Aunis Tonalite was dated at 1376.5 ± 1.7 Ma (zircon U-Pb age, TIMS method, Hoal and Heamman, 1995), while a similar rock located 80 km north of the Aunis Tonalite, the Hammerstein Tonalite, was dated at 1380 ± 14 Ma (unpublished data in Becker et al., 2006). Geochemical data suggest that both units were produced within a continental arc setting (Hoal, 1990; Miller, 2008).

Conversely, the Billstein Formation is entirely sedimentary with basal cross-bedded quartzites that grade to meta-arenites interlayered with meta-conglomerates, which are in turn overlain by garnet- and hornblende-bearing metapelites (Van Schijndel et al., 2011). This formation may represent highly mature fluviatile and lacustrine sediments formed in an epicontinental setting (Becker et al., 2005). The age of sedimentation of the Billstein Formation is bracketed by the youngest detrital zircon dated at 1770 Ma (zircon U-Pb age, LA-ICP-MS method, Van Schijndel et al., 2011) and the age of cross-cutting 1210 ± 7 Ma porphyritic dykes (zircon U-Pb age, TIMS method, Ziegler and Stoessel, 1990). Accordingly, the Billstein Formation lacks the Palaeoproterozoic regional gneissic fabric (Becker and Schalk, 2008).

2.2. Metasedimentary and metavolcanic sequences of the Nauzerus Group (Sinclair Supergroup)

The basal clast-supported polymictic conglomerates of the Nückopf Formation overlie the Palaeoproterozoic basement and grade to cross-bedded sandstones interbedded with pelites (Fig. 3a) (Becker and Schalk, 2008). Intraformational felsic and mafic volcanic rocks (locally containing lithophysae), attest to pene-contemporaneous bimodal volcanic activity. Felsic volcanic rocks display A/CNK ratios suggesting an I-type origin with volcanic arc or a within-plate affinity according to the Rb-Nb-Y tectonic discrimination diagram (Becker and Schalk, 2008). The age of sedimentation of the Nückopf Formation is constrained by U-Pb crystallization ages on zircon from intraformational rhyolite samples of 1226 ± 10 Ma (ID-TIMS method, Schneider et al., 2004) and of 1226 ± 11 Ma (SHRIMP method, unpublished data in Becker and Schalk, 2008).

Higher in the stratigraphy, the Grauwater Formation mainly is comprised of siliciclastic rocks with minor basal felsic volcanic rocks. Basal conglomerates, interpreted as talus breccia (Becker et al., 2005) either interfinger with and overlay felsic volcanic rocks of the Nückopf Formation or transgress the Palaeoproterozoic basement. The overlaying thick sandstones and subordinate conglomerates and slate lenses show planar-bedding, cross-bedding and ripple marks. They are intercalated with a thick package (370 m) of felsic volcanic rocks, interpreted as ignimbrites, which are in turn interlayered with cross-bedded, pebbly sandstones containing lenses of conglomerates deposited in a fluviatile environment (Becker and Schalk, 2008).

The overlaying Langberg Formation outcrops in two distinct inliers (close to and to the SE of Rehoboth town, both labelled 2 in Fig. 3b). The first inlier shows a poorly sorted matrix-supported polymictic basal conglomerate with clasts of up to boulder size (Van Schijndel et al., 2011) resting in tectonic contact over the Billstein Formation (Becker and Schalk, 2008). A thick succession (several hundred metres) of felsic volcanic rocks occurs higher in the formation. It is interbedded with pebbly arenites, indicating contemporaneous volcanism and sedimentation, and is topped by quartzites and schists. The second inlier, the Langberg Formation, is represented by a basal conglomerate and a more than 700 m-thick conformable felsic volcanic sequence which contains interbedded pebbly sandstones and cross-bedded immature arenites. Felsic volcanic rocks of the Langberg Formation are mostly rhyolitic in composition and fall in the fields of volcanic arc, within plate and post-collisional affinities in the tectonic discrimination diagrams (Becker and Schalk, 2008). SHRIMP zircon U-Pb analyses from rhyolites, giving ages of 1100 ± 5 Ma (unpublished data in Becker and Schalk, 2008) and 1090 ± 15 Ma (Becker et al., 2005), confirm an earlier multigrain zircon U-Pb age of 1083 ± 30 Ma (Burger and Coertze, 1978). Detrital zircons from a quartzite sample, analysed by Van Schijndel et al. (2011) yielded a minor group of six grains with U-Pb ion probe ages from 2030 to 1750 Ma that reflects the major peak seen in the underlying Billstein Formation, while the other grains give ages spread from 1325 to 1080 Ma. Finally, the four youngest detrital grains have a mean Pb–Pb age of 1103 ± 24 Ma.

The Opdam Formation is either in unconformable or tectonic contact over the Langberg Formation or unconformably transgresses the Billstein Formation. The basal clastic sequence is made of sandstones, polymictic conglomerates with argillaceous matrix, and shales. It is conformably overlain by a thick basaltic package (at least 1800 m-thick) interbedded with cross-bedded to ripple-marked sandstones, locally magnetite-bearing, as well as conglomerates and phyllites. An intense hydrothermal event in the basaltic rocks is suggested by a pre-tectonic stockwork of epidote-chlorite-chalcocite alteration veins which invades the metabasalts and associated flow-top breccias (Becker and Schalk, 2008). Low-grade copper mineralisation occurs locally in phyllites. Upwards in the formation, a thin conglomerate layer is in paraconformable sedimentary contact over the above-mentioned metabasalts. No basaltic clasts have been found in the conglomerate (Becker and Schalk, 2008), which grades into quartzites, slates, conglomerates and subordinate basaltic lavas. Becker and Schalk (2008) interpret the sandstone to have been deposited in an aeolian environment based on local large-scale (10 m) cross-bedding. The formation ends with a succession of finely banded quartzites, slates, and calcareous phyllites, including lenses of marble, meta-conglomerates and subordinate metabasite lavas and feldspar porphyries. The basalts of the Opdam Formation are tholeiitic with a composition influenced by subduction-related mantle enrichment in their sources (Becker and Schalk, 2008 and references therein).

The youngest formation of the Nauzerus Group is the Skumok Formation, dominated by sandstones which are interbedded with felsic volcanic rocks in the upper part. The talus breccia at the base of the formation unconformably overlies rocks from the Opdam and Langberg formations. This formation attests to a limited reappearance of felsic volcanism at the end of the Nauzerus times.

2.3. Mesoproterozoic intrusive rocks

In the Rehoboth Subprovince, two magmatic suites are traditionally distinguished based on their mineralogy, geochemical composition and age. The older Gamsberg Granitic Suite is composed of granites to granodiorites and lacks the typical Palaeoproterozoic metamorphic foliation (Becker and Schalk, 2008). This suite is mostly peraluminous, high-K, alkali-calcic to calc-alkaline. Low Rb, Nb and Y suggest genesis in a volcanic arc setting while high Th/Ta and La/Nb vs. low Ce/Pb show the influence of subduction-generated mantle enrichment (Becker and Schalk, 2008). A granite sample was dated at 1102 ± 7 Ma and an older age of 1207 ± 15 Ma was obtained from a coarse-grained orthogneiss (U-Pb multigrain method, Pfurr et al., 1991). The Capricorn Granitic Suite forms small circular to sheeted bodies of mostly syenogranitic composition. The locally transitional contact of the Capricorn Suite with the Langberg Formation rhyolite suggests their cogenetic relationship which implies a granite emplacement age of about 1100 Ma (Becker and Schalk, 2008).

2.4. Metasedimentary sequences of the Tsumis Group (Sinclair Supergroup)

The Tsumis Group consists of the Doornpoort, Eskadron and Klein Aub formations that crop out within and to the south of the Rehoboth Subprovince (Fig. 3b). It postdates the regional-scale Mesoproterozoic igneous event. The Doornpoort Formation (4500 m-thick) is represented by a basal conglomerate which grades laterally into sedimentary breccia horizons with local amygdaloidal basalt intercalations. The conglomerate matrix is made of feldspar-rich sandstones while the clasts are commonly of quartz-feldspar porphyry and reddish granite. Becker and Schalk (2008) interpreted the deposition of the Doornpoort Formation to have been initiated on an uneven surface where breccias and conglomerates filled topographic depressions and with topographic highs made by granite hills. The rest of the formation consists of a several km-thick, monotonous succession of clastic rocks comprising well-bedded fine-grained sandstones with varying feldspar content intercalated with rare red-brown slates. Common sedimentary structures are wave ripple marks, swash marks, and dm- to m-thick planar crossbed sets. The ripples include flat-topped ripples, indicative of emergence and slack-water modification, and standing-wave “tadpole-nest” ripples produced by interference of two arcuate wave trains (Fig. 4a) (Master et al., 2014). Other structures found are primary current lineations, gypsum casts, and microbially-induced sedimentary structures such as sandcracks or polygonal petee ridges (Scheiber, 2004) (Fig. 4b), and wrinkle structures (Master et al., 2014). Rocks that resemble the Doornpoort Formation crop out north of Witvlei with the main differences being the occurrences of cupriferous shales and limestones at the base of the succession, which caused Hegenberger and Seeger (1980) to differentiate them under the name Eskadron Formation (Fig. 3b). Our new observations indicate that the conglomerates at Malachite Pan (Fig. 3b) are matrix-supported, with highly angular polymictic clasts (Figs. 4c and 4d), and interbedded with granulestones which show graded-bedding and swaley cross-stratification (SCS).

The Doornpoort Formation is overlain by a basal clast-supported conglomerate (up to 30 m-thick) of the Leeuberg Member of the Klein Aub Formation (Fig. 4e). The clasts consist of rounded pebbles of granite, vein quartz, porphyry and quartzite from the underlying Doornpoort Formation enclosed in a coarse sandy to arkosic matrix (Becker and Schalk, 2008). The Leeuberg Member grades upwards into a thick sequence (900 m) of quartzites with interbedded red slates increasing in feldspar content towards the top of the quartzitic package. It is followed by the Eindpaal Member conglomerate that is similar to the basal conglomerate, and which overlies the Leeuberg quartzitic rocks in the east and transgresses upon the Doornpoort Formation to the west where its thickness reaches 200 m. In the upper part of the member, the conglomerate alternates and interfingers with fine-grained sandstones marked locally by large-scale, low-angle cross-beds (Becker and Schalk, 2008). Above a distinct contact, the Kagas Member is composed of uniform reduced quartzite-laminated shale package that presents a considerable thickness variation. Slightly calcareous sandstones at the base grade to silty argillites containing up to 70 cm-thick beds of fine-grained sandstones, limestones and marls (Fig. 4f). These argillite-sandstone interbeds with siltstone and mudstone host the stratabound Cu-Ag deposit at Klein Aub (Fig. 2b) (Borg and Maiden, 1986). They are followed by fine-grained calcareous sandstones with shale interlayers. Sedimentary structures include flute casts, oscillation ripples, wave ripple cross-laminations, sandstone dykes and sills, and synaeresis cracks (Becker and Schalk, 2008) and hummocky cross-stratification (Fig. 4f). At the top of the Klein Aub Formation, the Dikdoorn Member of the Klein Aub Formation is made of slightly carbonaceous fine-grained finely laminated and thinly-bedded sandstones with scarce lenticular conglomeratic interbeds. Becker and Schalk (2008) pointed the conformable nature of the Dikdoorn Member and its lithological similarities with the underlying Doornpoort Formation.

2.5. Mesoproterozoic inliers within the Damara Belt

Three inliers within the Damara Belt contain igneous rocks which have crystallization ages that cluster around 1100 Ma. The first inlier, the Ekuja–Otjihangwe Nappe Complex located 120 km NE of Windhoek, is a tectonic window formed during the Damara Orogeny (Fig. 1). It exposes amphibolites, banded biotite paragneisses, amphibole schists, foliated tonalites (Kasch, 1986, 1987; Steven et al., 2000) for which SHRIMP crystallization ages are respectively 1115 ± 13 Ma, 1084 ± 7 Ma, 1081 ± 10 Ma and 1063 ± 9 Ma (Steven et al., 2000). The precursors of these gneisses are presumed to be basaltic andesite, dacite, rhyolite and tonalite (Steven et al., 2000). The Omitiomire copper deposit is hosted within this complex.

The second inlier, the Abbabis Metamorphic Complex, consists of isolated structural domes surrounded by rocks of the Damara Supergroup (Fig. 1). In the east of the complex, basal metapelites, gneisses, meta-arkoses, and subordinate marbles, calc-silicates and meta-conglomerates (Brandt, 1987), are overlain by metapelites and amphibolites, in turn covered by quartzites, marbles, calc-silicates and metavolcanic rocks. Granitoids intruded these supracrustal rocks and form the widespread augen gneisses of the Abbabis Metamorphic Complex. In the west, quartzo-feldspathic gneisses, quartzites, micaceous quartzites and cordierite schists constitute a lower metasedimentary sequence (Sawyer, 1981). Both the eastern and western sequences of the Abbabis Metamorphic Complex are overlain by an upper metasedimentary succession consisting of basal calc-silicates and marbles passing upwards into a sequence of gneisses, schists and glassy quartzites (Brandt, 1987). Typical augen gneisses and amphibolites occurring in the western part of the complex were respectively SHRIMP-dated at 2100-2000 Ma (Kröner et al., 1991; Longridge, 2012) and ~ 2027 Ma (Longridge et al., 2014). However, migmatitic orthogneisses from the same area yielded ion microprobe U-Pb ages of ~ 1.1 Ga (Tack and Bowden, 1999) while augen gneisses located some 25 km to the north gave SHRIMP ages between 1240 and 1040 Ma, both interpreted as the time of crystallization of the igneous protolith (Kröner et al., 1991).

The third inlier is the small Oorlogsende Member situated some 60 km west of the Botswana border in eastern Namibia (Figs. 1 and 3b). It comprises unmetamorphosed quartz-feldspar porphyry thought to be a tuffaceous ignimbrite (Fig. 3a) (Hegenberger and Burger, 1985). It displays a ubiquitous steeply dipping flow banding, in many places parallel to a steep to subvertical NE-SW striking intense fracture cleavage. A quartz-feldspar porphyry sample has been dated by TIMS on zircon at 1094 +18/-20 Ma (Hegenberger and Burger, 1985).

2.6. Post-Sinclair Supergroup rocks of the Damara Supergroup

The base of the Damara Supergroup in the Rehoboth Subprovince is marked by a regional unconformity at the bottom of the Kamtsas Formation. Clastic rocks rest either on the

Palaeoproterozoic basement or on the Doornpoort Formation and contain clasts of both (Miller, 2008 and references therein). The onset of the Damara Supergroup sedimentation is poorly constrained, the first clear chronostratigraphic marker being the diamictite that contains faceted and striated pebbles (Hofmann et al., in press; Figure 13.135b in Miller, 2008). This diamictite has been interpreted as correlating with the Sturtian glaciation (~ 750 to 710 Ma, Halverson et al., 2005; Macdonald et al., 2010).

3. Meso- to Neoproterozoic lithostratigraphy in Botswana

In Botswana, the studied Meso- to Neoproterozoic rocks formed the Ghanzi-Chobe Belt that extents from the Namibian border to the Goha and Chinamba Hills (Modie, 1996). These rocks are mostly exposed in the Ghanzi Ridge, and in the Goha and Chinamba Hills (Fig. 1). The oldest basement in this region occurs in the Okwa River valley just south of the Ghanzi Ridge, where Palaeoproterozoic, ~ 2.06 Ga granites, granitic gneisses and rhyolites of the Okwa Inlier are found (Mapeo et al., 2006). The contact between these basement rocks and the cover sequences of the Ghanzi Ridge is not exposed.

Only the lithostratigraphic succession of the Ghanzi Ridge has been described in detail in the literature and is reported in Figure 5a. Rocks of the Ghanzi Ridge have been metamorphosed to lower greenschist facies during the Damara orogenesis, as typified by the occurrence of muscovite, chlorite, actinolite, epidote, clinozoisite, calcite and rutile (e.g. Carney et al., 1994; Schwartz et al., 1996). Associated structures comprise upright to southeast verging open to tight folds, and a well-developed axial planar cleavage (Carney et al., 1994) with deformation intensity increasing to the northwest (Singletary et al., 2003). A sample from a protomylonitic shear zone within a granite located about 180 km north of the Ghanzi Ridge gave a $^{40}Ar/^{39}Ar$ white mica cooling age of 533.3 ± 2.3 Ma (Singletary et al., 2003). Geophysical investigations suggest that rocks of the Ghanzi-Chobe Belt can be extrapolated below cover as part of the northwest Botswana Rift (Key and Ayres, 2000) until they abut to the south onto the Okwa Inlier and to the southeast onto a putative and undercover high-angle normal faults that follows the older Magondi Belt NE-SW structural trend (Fig. 1). The northwest margin of the Ghanzi-Chobe Belt has been obscured by deformations related to the Damara Orogeny (Key and Mapeo, 1999). Using seismic reflection data, Wright and Hall (1990) extended the fold and thrust belt structures of the Ghanzi-Chobe Belt as far as 20°S latitude towards the SE.

3.1. Mesoproterozoic volcanic and sedimentary rocks of the Kgwebe Formation

In the Ghanzi Ridge (Fig. 5b), the lowest structural and stratigraphic unit is the Kgwebe Formation that cores NE-elongated anticlines flanked by outward-younging and steeply dipping beds of the

Ghanzi Group (Carney et al., 1994). The Kgwebe Formation consists of a volcanic succession some 2000 m thick, comprising magnetite-rich (in concentration of 1 to 10 volume %, Schwartz et al., 1995) porphyritic rhyolites and dacites, ignimbrites, pyroclastic flow deposits, minor pepperites, and subaerial basaltic lavas (vesicular to amygdaloidal with very rarely preserved pillow structures, Kampunzu et al., 1998), with subordinate flow breccias. These volcanic rocks are intercalated with minor epiclastic and tuffaceous sedimentary rocks and sandstones, grits, minor conglomerates containing clasts of porphyry and basalt (Modie, 1996; Thomas, 1973). The metasedimentary rocks are rich in magnetite (up to 5 % of total rock volume) and contain disseminated pyrite and pyrrhotite (Schwartz et al., 1995). Sedimentary structures in sandstones include wave ripples, mudstone intraclasts, desiccation marks and jointed sandstone-filled chert layers indicating sedimentation in shallow-water to emergent conditions (Modie, 1996). Decimetre-size xenoliths in the porphyry are composed of micaceous quartzite (Wright, 1958) and present an internal pervasive foliation marked by biotite which ends abruptly against the porphyry. Such a metamorphic foliation is absent in the sedimentary rocks of Ghanzi-Chobe Belt, suggesting that these xenoliths are samples of older metamorphic rocks brought to their present position by the extruding magma (Dietvorst and Gopolang, 1995).

The volcanic rocks of the Kgwebe Formation represent a bimodal suite of within-plate low Ti-P continental tholeiites and post-orogenic within-plate high-K rhyolites (Kampunzu et al., 1998). Chemical compositions of the mafic rocks suggest they may have originated in a mantle enriched during a previous subduction event (Kampunzu et al., 1998). The rhyolitic compositions cannot be produced by melting of sediments or subducting slab, but suggest partial melting of calcalkaline lower crust (Kampunzu et al., 1998). A porphyritic rhyolite has been dated by TIMS at 1106 ± 2 Ma (Schwartz et al., 1996). An ε_{Nd} value of -2.2 with a corresponding T_{dm} model age of 1845 Ma indicate that older crust was involved in the genesis of the rhyolite (Singletary et al., 2003).

In the Goha Hills, along strike with the Kgwebe Formation of the Ghanzi Ridge (Fig. 5b), there are outcrops in the cores of tight fold structures (Carney et al., 1994) of massive feldspar (± quartz) porphyry with subordinate pyroclastic flow deposits (Modie, 2000), lithologically similar to the felsic volcanic rocks of the Kgwebe Formation. They have been dated by ID-TIMS at 1106.2 ± 3.6 Ma and interpreted as a lateral equivalent of the Kgwebe Formation (Singletary et al., 2003). These rocks exhibit steep SW-NE striking metamorphic foliation of low metamorphic grade.

There are numerous mafic and felsic magmatic rocks with identical crystallization ages to the Kgwebe Formation in Botswana. Located in western Botswana about 150 km south of the Ghanzi Ridge, the unexposed Tshane, Xade and Tsetseng complexes and Rakops dykes (Fig. 1) have been dated at 1021-1109 Ma (Tshane Complex: Rb-Sr unpublished date at 1021 ± 86 Ma and $^{40}Ar/^{39}Ar$

dating of a borehole sample at 1071 ± 11 Ma, Key and Ayres, 2000; Xade Complex: ID-TIMS U-Pb date on zircon at 1109.0 ± 1.3 Ma, Hanson et al., 2004). The Tshane Complex is composed of gabbronorites and leucogabbronorites while the Xade Complex consists of tholeiitic dolerites and gabbronorites and mafic lavas (Pouliquen et al., 2008). Unfoliated gabbro to diorite of the Kwando Complex has been dated by ID-TIMS at 1107.0 ± 0.8 Ma (Singletary et al., 2003). Located in the vicinity of the Goha Hills, unfoliated granites gave ID-TIMS dates of 1107.4 ± 2.1 Ma and 1107.5 ± 0.5 Ma (Singletary et al., 2003).

3.2. The Ghanzi Group

The Ghanzi Group unconformably overlies the Kgwebe Formation (Fig. 5a). Its original stratigraphic nomenclature derives from the work of Thomas (1969), Borg and Maiden (1989) and Huch et al. (1992), who subdivided the Ghanzi Group into the Lower and Upper D'Kar formations, overlain by the Jakkalsputs Formation. This stratigraphic scheme has been modified by Modie et al. (1998) and Modie (2000), and now includes a basal Kuke Formation which unconformably overlies the Kgwebe Formation, followed successively by the Ngwako Pan (formerly Lower D'Kar), D'Kar (formerly Upper D'Kar) and Mamuno (formerly Jakkalsputs) formations.

The base of the Ghanzi Group is represented by a 500 m-thick cross-bedded, medium-grained quartz arenite with mudstone interclasts, and conglomerate, referred as the Kuke Formation in Modie (2000) and previously assigned either to the Kgwebe Formation (Modie, 1996; Kampunzu et al., 1998) or to the base of the Ngwako Pan Formation (Kampunzu et al., 2000). This unit lies unconformably upon and contains clasts of the Kgwebe Formation (Kampunzu et al., 2000; Modie, 2000).

The Kuke Formation is overlain by the Ngwako Pan Formation which varies from 2000 m-thick in the Ghanzi Ridge (Modie, 2000) to 3500 m below cover to the NE (Master, 2010). The basal part consists of wackes overlain by better-sorted red sandstones and arkoses that are locally interbedded with pebbly layers and granulestones. The upper part of the Ngwako Pan Formation is characterised by the predominance of parallel-laminated plane-bedded sandstones together with cm- to dm-scale ripple cross-laminated facies containing rip-up clasts of shale and associated graded beds of granulestones (Fig. 6a). Locally, these upper sandstones are red-beds (due to finely dispersed hematite, Schwartz et al., 1995), and often display diagenetic mottling. Some very thin shale drapes are found associated with hummocky cross-stratification; plane-laminated sandstones commonly have low-angle truncations and gently curving surfaces which resemble swaley cross-stratification (Fig. 6b) (Master, 2010). In contrast to the underlying Kgwebe Formation and the overlying D'Kar Formation, the Ngwako Pan Formation is devoid of copper minerals except for the uppermost 3 metres just below the contact with the D'Kar Formation (Schwartz et al., 1995).

The D'Kar Formation (also referred to as the Middle Ghanzi Formation in Schwartz et al., 1995) conformably overlies the Ngwako Pan Formation, is about 1500 m-thick, and is dominated by mainly parallel-laminated grey-green siltstones and mudstones with interbedded fine-grained sandstones (Fig. 7a) (Modie, 1996; 2000). Minor thin (1 to 3 m-thick) discontinuous limestone beds, locally oolitic, and marls occur near the base of the formation. The contact with the Ngwako Pan Formation is usually sharp, conformable but demonstrates topographic variation, representing a major regional transgressive flooding surface marking a sequence boundary. The rocks of this formation are reduced facies, locally characterised by an abundance of fine-grained pyrite, as well as organic-rich shales locally rich enough in carbon to be classified as black shales. The sedimentary structures are dominated by planar-parallel lamination that in the argillite units constitutes fining-upward pulses, indicating suspension deposition below wave base (Modie, 1996). Distinctive rhythmite units of fining-upward pale siltstones to dark shale beds result from cyclic sedimentation between traction currents and suspended sediment load (Modie, 1996). The sandstones are characterised by the presence of very thin interbeds of siltstone and shale, and by non-parallel curved layers and truncation surfaces, which are characteristic of hummocky cross-stratification (Figs. 7b and 7c) (HCS, Duke et al., 1991; Walker and Plint, 1992).

The uppermost unit of the Ghanzi Group, the Mamuno Formation, is composed of well-sorted, fine- to medium-grained arkosic sandstones, interbedded with siltstones, mudstones and limestones (Litherland, 1982; Modie, 1996). In NE Botswana, rocks of the Goha Hills Formation (i.e. lateral correlative of the Kgwebe Formation) are overlain by poorly exposed carbonate-bearing siliciclastic sedimentary rocks informally assigned to the Chinamba Hills Formation (Key and Ayres, 2000). These rocks consist of fine-grained, purple sandstones, which are lithologically similar to, and correlated with, the Mamuno Formation.

3.3. Post-Ghanzi Group rocks of the Okwa Group

Rocks of the Okwa Group (shown in green in Fig. 1) rest unconformably upon Palaeoproterozoic basement rocks and are characterised by several disconformities located below siliciclastic rocks which contain clasts from the underlying sequences (Ramokate et al., 2000). The basal Hanahai Formation, composed of rhyolite tuffs and plagioclase-phyric felsic rocks, is unconformably overlain by siltstones, shale-clast conglomerates, greywackes and dolerites that grade further up into limestones and dolomites. The inferred depositional settings of the rocks of the Okwa Group are lacustrine to fluvial. Only the basal part of the Okwa Group was affected by a NE-SW striking and steep cleavage, formed during greenschist metamorphism associated with the Pan-African Orogeny. Five detrital zircons analyses from a deformed basal siltstone yielded the ID-TIMS dates of 1887 ± 14 Ma, 1246 ± 4 Ma, 1054 ± 5 Ma, 627 ± 6 Ma and 579 ± 12 Ma (Ramokate et al., 2000). A maximum depositional age of 579 ± 12 Ma is compatible with palynological investigations indicating that the group is pre-Karoo in age (Ramokate et al., 2000).

4. Stratabound Cu-Ag deposits and prospects

4.1. Namibia

A number of stratabound sediment-hosted Cu or Cu-Ag deposits are known in the Klein Aub area (Fig. 3b), some of which have been mined in the past. The best known deposit is the Klein Aub Mine, which was mined from 1966 to 1987, during which time it produced 5.5 Mt of ore. The deposit contained 7.5 Mt ore at 2 % Cu and 50 ppm Ag (Schneider and Seeger, 1992). Mineralisation occurred in seven shale-siltstone beds of the Klein Aub Formation, adjacent to a regional strike-slip fault (Borg, 1988b). The main ore mineral is chalcocite and locally the Cu-Ag ores contain gold, zinc and molybdenum in trace amounts.

Another past-producing stratabound sediment-hosted copper deposit in Namibia that has been mined from 1971 to 1984 is the Oamites Mine (Fig. 3b). An ore reserve of 2 Mt at 1.58 % copper was outlined (Schneider and Seeger, 1992). The sulfides are disseminated, though concentrated along foliation planes within an allochthonous thrust sheet of metasedimentary rocks of the Billstein Formation (Miller and Schalk, 1980) formed during the Damara orogenesis (Schneider and Seeger, 1992).

In the Witvlei area (Fig. 3b), stratabound copper occurs in argillite, arenite and limestone beds averaging two metres in thickness in the Eskadron Formation. There are several prospects in this area, including Malachite Pan, Copper Causeway and Witvlei Pos. The Malachite Pan prospect was mined for a short while in 1974-1975. Two ore bodies have been detected, with widths and grades of 2 m @ 2 % Cu and 2.2 m @ 2.8 % Cu, respectively. The probable ore reserves are set at 2.98 Mt @ 2.1 % Cu over an average width of 2.36 m (Schneider and Seeger, 1992). Detailed studies of the Witvlei ores by Anhaeusser and Button (1973) showed that the mineralisation at Witvlei was produced by copper-rich fluids which successively replaced diagenetic pyrite with progressively more Cu-rich sulfides.

4.2. Botswana

Prospecting work in the Ghanzi Ridge in Botswana has shown that significant stratabound copper sulfides are present within basaltic flow breccias of the Kgwebe Formation (Siamisang, 1996; Modie, 2000). Estimated resources were calculated from two localities in the Ngwako Pan area (Siamisang, 1996). The first area yielded 27 Mt at 1.0 % Cu (0.2 % Cu cut-off grade), and 17 Mt at 1.5 % Cu (0.5 % Cu cut-off grade), while the second area yielded 95 Mt at 0.8 % Cu (0.2 % Cu cut-off grade), and 49

Mt at 1.4 % Cu (0.5 % Cu cut-off grade) (Siamisang, 1996; Modie, 2000). Copper-silver ores in the D'Kar Formation is being exploited at the Boseto Mine, the first mine in the Kalahari Copperbelt in Botswana, which started producing in 2011. There are also major resources delineated by Hana Mining (taken over by Cupric Resources in 2013), and by New Hana, and these exploration projects appear to be quite promising in terms of future mining activity (Catterall et al., 2012).

Stratabound copper-silver ores are found along the interface between the Ngwako Pan and D'Kar formations, which is both a regional redox boundary and a permeability barrier. The following styles of copper occurrences have been described in the Ngwako Pan Formation: 1) fine-grained copper sulfide (chalcopyrite) oxidised to chrysocolla rimming shale/siltstone clasts; 2) chalcocite and bornite in minor quartz-carbonate veins near the contact with the D'Kar Formation; and 3) significant but laterally discontinuous high-grade copper mineralisation occurring in sandstones just below the contact with the overlying mineralised D'Kar Formation (Master, 2010). Sandstone-hosted mineralisation with chalcocite and bornite occurs both in the D'Kar Formation and in the underlying Ngwako Pan Formation, and contains significant enrichment of molybdenum (in the form of molybdenite), and Re, which substitutes for Mo in molybdenite (Master, 2013).

However, copper is mainly found in the reduced shales and siltstones in the lowermost part of the D'Kar Formation. The mineralisation in the D'Kar Formation changes stratigraphically from Cu-Ag at the base through Pb-Zn to Fe-rich at the top, which is characterised by the mineralogical sequence chalcocite/(djurleite, digenite), bornite, chalcopyrite, galena, sphalerite and pyrite (Schwartz et al., 1995). The copper minerals are zoned in the sequence chalcocite – djurleite – digenite – bornite – chalcopyrite, reflecting a decreasing Cu/Fe ratio in the ore fluid with height in the mineralised zone. Two styles of mineralisation are found in the D'Kar Formation: (1) disseminated sulfides finely scattered through host sedimentary rocks, with a marked control by primary porosity and permeability; and (2) vein-hosted sulfides found in quartz and calcite veins (≤ 10 cm-thick) that are either concordant with bedding or, less frequently, cross-cutting (Sillitoe et al., 2010; Hall, 2012). In the upper fringes of the mineralised zones of the D'Kar Formation, where Pb and Zn are present, there is also a significant increase in the cadmium content, mostly as substitution for Zn in sphalerite. Recently, Pd and Ir have been discovered in veinlets cutting larger veins, in the form of Pd-Hg tellurides associated with molybdenite and Bi minerals (Letsholo et al., 2012). Significant concentrations of Re and Ir have also been found associated with bismuth oxides (Letsholo et al., 2012).

Shales, siltstones, and the fine-grained interbedded sandstones host to the copper zones of the D'Kar Formation contain pyrite that is either finely disseminated, or in numerous thin fractures as a paint-like film. This pyrite is regarded as diagenetic in origin, and is related to biogenic reduction of seawater sulphate by sulphate-reducing bacteria (fine-grained pyrite in shales), or due to sour gas (hydrogen sulfide) related to hydrocarbons derived from diagenesis of black shales (Master, 2010). A much coarser-grained euhedral pyrite occurs in the zonation sequence above the galena and sphalerite zones, sometimes intergrown with these minerals. This ore-stage coarse pyrite commonly shows chlorite-filled pressure shadows, indicating that it crystallized before regional deformation and metamorphism affected the host-rocks (Master, 2010).

5. Airborne magnetometry

5.1. Data

Aeromagnetic data are relatively cheap and quick to acquire compared to other geophysical data sets and allow mapping of magnetic anomalies even when the magnetic sources are sub-outcropping or covered. The Kalahari Copperbelt is covered by 18 different magnetic grids (Fig. 8) for which data acquisition parameters and specifications are reported in Appendix.

5.2. Enhancement of the magnetic signal

Magnetic anomalies are caused by remanent (permanent) and induced magnetization. The remanent magnetization is independent of the magnetizing field in which it is measured and will still be present even in the absence of magnetizing field. The induced magnetization, determined by the magnetic susceptibility of the rock, indicates the ability of the rock to become magnetized in the presence of a magnetic field.

Regional interpretations were based on the Total Magnetic Intensity (TMI) map and its filtered products calculated for each grid. Image processing was carried out in Oasis Montaj® (Geosoft®) version 8.0. Magnetic data from individual survey blocks were analytically transformed to enhance certain characteristics of the magnetic field. The RTP operator was applied to the individual survey blocks prior to merging because of the regional scale of the study. The high pass filters were applied to the individual grids as the computational time was faster. These filtered products include first vertical derivative (1VD), analytic signal, total horizontal derivative (THDR) and tilt angle (Miller and Singh, 1994; Cooper and Cowan, 2004; Verduzco et al., 2004). The 1VD filter was helpful for delineating boundaries of magnetic bodies while the THDR filter enhanced the edges as well as the internal texture of the magnetic bodies (Fig. 9). The enhanced images were calculated from reduced-to-pole data (Baranov and Naudy, 1964). As a general rule, boundaries are close to anomaly inflection points for sources with almost vertical sides. In addition, directional filtering was applied to enhance subtle features in a preferred orientation and suppress features perpendicular to such a direction (Cooper, 2003). Directional filtering consists of a combination of butterworth and cosine filters which are dependent on the magnetic intensity removed and strength of the filter. Low-pass filters such as the upward continuation were used in order to attenuate near-surface signals and accentuate anomalies from deeper magnetic sources (Blakely, 1995). Thus, the processing highlights longer spatial wave-length anomalies at the expense of shorter wave-length anomalies. Images are displayed with either an equalized or standard deviation colour table.

5.3. Impact of the post-Kalahari Copperbelt cover in the magnetic signal

The aeromagnetic data effectively map the geology beneath the Kalahari Supergroup because the relatively thin and non-magnetic cover material has minimal influence on the magnetic signal. However, the Karoo Supergroup and the normal faults associated with the Cenozoic Okavango Rift Zone strongly modify the aeromagnetic signal of the underlying rocks. The Karoo mafic lava flows form discordant crosscutting positive magnetic features with a mottled texture (arrow 1 in Fig. 10a and geological interpretation of Fig. 10b). Their tabular geometry is revealed by a typical dipolar anomaly visible at each end of the body (Cole et al., 2013) (domain 1 in Fig. 10c). The WNW-ESE striking Okavango dyke swarm in Botswana coincides with a 60 km-wide array of sub-parallel to slightly oblique strongly linear dipolar magnetic anomalies that are either positive or negative in their northern sides (typical values of ~ 200 nT, Fig. 8), indicating the presence of remanence and/or changes in dip of the dikes at depth. The results of 3-dimensional Euler deconvolution of aeromagnetic data over the faulted dykes indicate that the northeast-striking, 25-325 km-long faults have 17 to 334 m of normal throw; they were interpreted as reactivated Pan-African structures (Kinabo et al., 2008). These faults have amplitudes on the magnetic grids that commonly range from 200 to 600 nT, and indicated widths of 150-200 m (Kinabo et al., 2008) (Fig. 8).

5.4. Results: magnetic signatures of rock units of the Kalahari Copperbelt

At broad scale, the Kalahari Copperbelt contains two distinct magnetic domains – the Rehoboth domain in central Namibia and the Ghanzi-Chobe domain in eastern Namibia and Botswana (Fig. 8). The Rehoboth domain is marked by a complex magnetic pattern of juxtaposed multi-kilometre-scale high amplitude (~ 1600 nT) anomalies that result from the (sub-)surface juxtaposition of Palaeoproterozoic basement rocks, Nauzerus Group granitoids and volcanic and sedimentary rocks of the Sinclair Supergroup. Conversely, the Ghanzi-Chobe domain is magnetically defined by NE-SW alternating magnetic lows and highs with a typical wavelength of 10 to 20 km. These magnetic lineaments are parallel to the rock structural grain and folded structures described in the inliers of the Oorlogsende Member (Hegenberger and Burger, 1985), Ghanzi Ridge (Modie, 2000) and Chinamba and Goha Hills (Carney et al., 1994).

In more detail, the magnetic signature of the KCB in Botswana is partly obliterated east of the Ghanzi Ridge by a large area with a typical volcanic rocks signature that is, in turn, cross-cut by the

Okavango dyke swarm (Figs. 5b and 8). The very consistent orientation of the dykes makes them ideal features to be suppressed by using directional filtering at 290°. Figure 11 illustrates the result of such directional filtering which was combined with upward continuation by 500 m and subsequent sunshading from the SW on a RTP residual magnetic intensity grid. Accordingly, the linear anomalies of the KCB in the Ghanzi Ridge and Chinamba Hills appear to be continuous below the Karoo volcanics and Okavango dyke swarm.

Because the aeromagnetic response is influenced by both the induced and remanent magnetization, the causative link between lithology and regional magnetic anomaly can be difficult to establish (Nabighian et al., 2005). The distinguishing magnetic signature of individual rock units in the KCB was based on filtered magnetic data patterns over known outcrops. As a result, the rocks of the Kalahari Copperbelt in the Ghanzi-Chobe magnetic domain present four different geophysical signatures on the basis of variation in magnetic signal and discontinuity of structures (Fig. 9). A typical association of lithotectonic domains of distinct magnetic signatures in outcropping regions and their extrapolation below the Kalahari cover was then used to correlate the geology between the Ghanzi Ridge and Oorlogsende Member across the Botswana-Namibia border (Fig. 10b).

The Oorlogsende Member, Kgwebe and Goha Hills formations have similar magnetic signatures marked by a high frequency (≤ 1 km), high amplitude (~ 600 nT for the Kgwebe and Goha Hills Formation and 330 nT for the Oorlogsende Member), pitted texture that is typical for volcanic rocks (Dentith and Mudge, 2014) and often oblique to the outer envelopes of the magnetic units. The Ngwako Pan and Mamuno formations have comparable quiet and low magnetic signatures but can be distinguished from each other because the latter has a generally more pronounced internal high frequency alternation (≤ 0.5 km) of highs and lows. The Kuke Formation is also characterised by a smooth, low magnetic amplitude so that it cannot be magnetically differentiated from the Ngwako Pan Formation. In addition, the Kuke Formation has not been mapped by Pryer et al. (1997) or Key and Ayres (2000) and, as shown above, its stratigraphic significance is unclear. The Chinamba Formation has a smooth, low magnetic amplitude, approximately -20 nT, and similar lithological composition (meta-carbonate) to the Mamuno Formation.

The magnetic susceptibility values across the contact between the Ngwako Pan and D'Kar formations show a drastic break of one order of magnitude (Fig. 12) in the region of the Ghanzi Ridge. Typical susceptibility values for the uppermost 7 m of the Ngwako Pan sandstones are in the order of 0.01×10^{-3} SI while the basal 50 m of the D'Kar Formation are characterised by average values of 0.23×10^{-3} SI (range of 0.014 to 1.8×10^{-3} SI). This significantly higher magnetic susceptibility is because of the presence of disseminated monoclinic pyrrhotite and/or magnetite, observed within the magnetic fractions of 8 powered samples of the basal D'Kar Fm mineralised zones. The absence of observed ferromagnetic minerals under the microscope in reflected light is explained by the fact that a small volumetric content of 1 % of monoclinic pyrrhotite or 0.1 % of magnetite corresponds to a magnetic susceptibility value of 0.23×10^{-3} SI (Clark, 1997). In the aeromagnetic maps (e.g. Fig. 10a), the drastic jump at the foot-wall of the D'Kar Formation is an important regional marker that is evident in the aeromagnetic profiles (blue arrows in Fig. 10c), and can be traced through the entire Ghanzi-Chobe Belt and across the border into Namibia (Fig. 10b). Internally, the D'Kar Formation shows a rugose magnetic texture expressed by sublinear high frequency (≤ 1 km) alternation of high and lows that are subparallel to the magnetic grain of the belt.

Magnetic data were used to map structures. Discordant faults were inferred where magnetic anomalies of sedimentary layers were displaced, or where the amplitudes of anomalies suddenly changed. They were differentiated from chevron-type fold periclinal terminations, locally expressed as linear magnetic anomalies that form tight and sharp triangles, on the basis that faults have to truncate other magnetic units.

This study defines the Ghanzi-Chobe Belt and its extension in eastern Namibia and northernmost Botswana (i.e. the Ghanzi-Chobe magnetic domain) as a series of NE–SW trending folds highlighted by alternating magnetic high amplitudes of approximately ~ 340 nT of the D'Kar Formation and low magnetic amplitudes of approximately -40 nT of the Ngwako Pan Formation (Fig. 10). To the SE, fold wavelengths increase and the magnetic amplitude decreases to between -70 and 20 nT.

6. Discussion and conclusions

6.1. Reinterpretation of depositional palaeo-environmental settings

Early workers on the sedimentology of the Doornpoort, Eskadron and Klein Aub formations in Namibia (Ruxton, 1986; Ruxton and Clemmey, 1986; Borg and Maiden, 1986) and on the Ngwako Pan Formation in Botswana (Modie, 1996) regarded the deposits has having formed in continental, alluvial fan, fluvial and lacustrine environments. Our sedimentological observations have led us to propose a marginal marine to shelf depositional environment for these rocks. This is based on the absence of typical fluvial facies and the recognition of key sedimentary structures such as swaley and hummocky cross-stratifications and associated facies. On this basis we tentatively propose a new depositional facies model for the Ghanzi and Tsumis groups (Fig. 13).

6.1.1. The Tsumis Group

Ruxton (1986) and Ruxton and Clemmey (1986) interpreted the sedimentary rocks of the Eskadron Formation at the Malachite Pan copper occurrence area near Witvlei to have been deposited in alluvial fan, continental playa lake, aeolian dune and beach environments. According to Ruxton (1986), Ruxton and Clemmey (1986) and Borg and Maiden (1986), the Doornpoort Formation and the two oldest members of the Klein Aub Formation (Leeuberg and Eindpaal members, Fig. 3a) were deposited in small, fault-bounded intracontinental basins in braided stream and aeolian dune environments. The upper part of the Klein Aub Formation, i.e. the Kagas and Dikdoorn members, was previously interpreted as having been formed in a restricted, lacustrine basin or in a marine beach environment (Becker and Schalk, 2008) which deepened to the south or southeast (Kagas Member) continuing to still intracontinental sedimentation at the top (Dikdoorn Member, Borg and Maiden, 1986).

Alluvial fan conglomerates are usually clast-supported and interbedded with trough cross-bedded fluvial braided stream pebbly sandstones (Miall, 1977). None of these sedimentary features have been observed in the Eskadron Formation. Instead, the conglomerates at Malachite Pan are matrix-supported, with angular clasts which have not been rolled in a fluvial environment (Figs. 4c and 4d) and are interbedded with granulestones with graded-bedding and swaley cross-stratification. We interpret the Eskadron Formation to have been deposited in an upper shoreface environment in a shallow shelf. In this regard, they resemble the rudist-bearing Maastrichtian shelf conglomerates of the Qahlah Formation in Oman (Skelton et al., 1990; Master, 2002). New observations that include swash-marks, flat-topped and interference ripples (Fig. 4a) and petee structures (Fig. 4b) have led Master et al. (2014) to reinterpret the sandstones of the Doornpoort Formation as being deposited in a foreshore environment, while the conglomerates were deposited in the surf zone (Fig. 13).

At the base of the Klein Aub Formation, the Leeuberg and Eindpaal members, consisting of discontinuous clast-supported boulder conglomerates (Fig. 4e) interbedded with cross-bedded quartzites, represent continental alluvial fan and fluvial facies that have prograded over the marginal marine rocks of the underlying Doornpoort Formation. The Kagas siltstones (Fig. 4f), referred to as the “lacustrine facies” of Ruxton and Clemmey (1986), lack any evidence of shallow water sedimentation, such as flat-topped ripples or mudcracks and show hummocky cross-stratification (Fig. 4f). Hence, they are inferred to have formed in a deeper shelf environment compared to the underlying Doornpoort sandstones. Because the Dikdoorn Member is thought to be very similar to the Doornpoort Formation (Becker and Schalk, 2008), it is suggested that it has been deposited in similar beach or upper shore face environments (Fig. 13).

6.1.2. The Ghanzi Group

Modie (1996) regarded the Ghanzi Group as having formed during a period of continental rifting, of unknown age, sometimes after the deposition of the Kgwebe Formation. In his view, during initial rifting the basin filled with continental alluvial deposits of the Lower D’Kar (now Kuke and Ngwako

Pan) Formation followed by a period of thermal subsidence and basin expansion during the finer-grained sediments of the Upper D'Kar (now D'Kar) Formation were deposited. This was followed by period of compression, supposedly related to the Damara Orogeny, when the source regions were uplifted, and progradational shoreline sediments of the Jakkalsputs (now Mamuno) Formation were deposited. Modie's (1996) model for the development of the Ghanzi Group is problematic because if the Kuke and Ngwako Pan formations rocks were deposited in a continental fluvial depositional system, then one would expect to see typical facies associated with braided or meandering river systems, such as through-cross bedding, gravel bars with conglomerates, lateral accretion surfaces, basal conglomerates or gravel lags and overbank mudstones and many other indications of deposition in shallow-water with occasional periods of subaerial emergence. None of these features are present in the studied redbeds of the Ngwako Pan Formation. Furthermore, Modie's observations that the Mamuno Formation is fine-grained and conformable on the D'Kar Formation are incompatible with the Mamuno being a syn-orogenic unit.

The lower Ngwako Pan Formation, containing more immature wackes than the upper part, is interpreted to have been deposited in the lower shoreface. The upper Ngwako Pan Formation, containing better sorted sandstones and granulestones, is interpreted to have been deposited in the middle to upper shoreface environments, probably on longshore sand bars. This interpretation is supported by rip-up shale clasts in normally graded-bedded granulestones (Fig. 6a) and swaley cross-stratification in sandstones (Fig. 6b).

The limestones of the D'Kar Formation are regarded as having been deposited on a shallow shelf, in the upper offshore region, just below fair-weather wave base, farther out from the proximal foreshore siliciclastic shallow shelf represented by the Ngwako Pan Formation. However, the limestones were not totally cut off from sources of clastic sediment because they commonly grade into, and are interbedded with, marls and calcareous argillites. The thin and laterally extensive sandstone facies interbedded with rhythmites, and showing hummocky cross-stratification (Figs. 7b and c) are interpreted to have been deposited below fair-weather wave base but above storm wave based. The organic-rich black shales are regarded as having been deposited in the anoxic, deepest part of the shelf, below storm wave base. The interpreted depositional environment for the Mamuno Formation is a high energy, near shore environment regressively deposited over comparatively deeper water, shallow shelf sediments of the D'Kar Formation.

6.2. Aeromagnetic data

The rock units of the Kalahari Copperbelt have distinct magnetic signatures that can be traced beneath the Kalahari Supergroup from northernmost Botswana to central Namibia, where the Palaeoproterozoic basement of the Rehoboth Subprovince crops out. The two regional magnetic domains defined in this study – the Rehoboth domain in Central Namibia and the Ghanzi-Chobe domain in eastern Namibia and Botswana (Fig. 8) – correlate with known occurrences of Palaeoproterozoic basement and ~ 1.2 Ga magmatic rocks of the Nückopf Formation. Indeed, both the Palaeoproterozoic basement and the Nückopf Formation are reported in the Rehoboth Subprovince (Fig. 3) but are absent northeastward (Fig. 4), where they have not been identified in our magnetic study. In the Rehoboth domain, the complex small-scale juxtaposition of very different rock-types associated with the strong influence of the Palaeoproterozoic basement in the total magnetic signal did not allow identifying precisely the magnetic response of individual lithotectonic units of the Rehoboth Subprovince. In the Ghanzi-Chobe domain however, the rocks hosting the KCB are uniformly present and the covered domains display indistinguishable lithotectonic magnetic units from those of the discrete exposed inliers.

The new litho-structural map across the border between Namibia and Botswana (Fig. 8b) was constructed using literature data, including geological maps and reports from mining companies, field observations and airborne magnetic data. The map shows the SW continuity of the folded units mapped at the surface in the Ghanzi Ridge (Modie, 2000) and Goha-Chinamba Hills (Carney et al., 1994). Thus, the whole structural grain of the KCB in the Ghanzi-Chobe magnetic domain is defined by a NE-SW–striking fold train that slightly curves to the NNE-SSW in the region of the Goha Hills (Figs. 7 and 9). The folds are not cylindrical and form periclines (e.g. Price and Cosgrove, 1990), with the ratio of the maximum profile wave-length to the strike-length of the fold along the fold axis varying highly from approximately 1:3.5 to 1:40 (based on 13 measurements). The spatial arrangement of the periclines of different phase and wave-length produces oblique linking and folding bifurcation that, together with field observations, are compatible with a general NW-SE direction of orogenic contraction. The 30° strike variation in the KCB structural grain in the Goha and Chinamba Hills region might have been caused by E–directed indentation of a rigid Congo Craton–derived basement promontory located in NW Botswana (the Quangwadum Complex in Fig. 1). Such a scenario is supported by detailed gravity and aeromagnetic mapping of NNW-SSE-striking thrusts (Kgotlhang, 2008) that are exposed and WSW-vergent in the Tsodilo Hills (Wendorff, 2005).

A drawback of our methodology is that the 50 m airborne magnetic data do not allow resolution of stratigraphic versus structural contacts (i.e. faults, shear zones) that are parallel to lithological boundaries in fold and thrust belts. As a result, the mapping of Figure 8b provides only a minimum estimate of fault densities and lengths, and only few unambiguous major regional structural contacts have been depicted (e.g. arrow 1 in Fig. 8a).

From a lithological point of view, the volcanic rocks, sandstones, shales and carbonates can be well-differentiated using 50 m resolution aeromagnetic data and coincide well with occurrences in mapped outcropping areas. In particular, the sharp change in magnetic susceptibility at the base of the D'Kar Formation (Fig. 12) produces strong magnetic anomalies in aeromagnetic maps (Fig. 10a). This correlates with the principal potential target zone for Cu-Ag exploration which is therefore extremely well-defined magnetically and can be delineated even in areas with extensive cover. However, basic and felsic volcanic rocks as well as their intrusive counterparts were not distinguished as they yield similar magnetic texture, amplitude and frequency (e.g. Oorlogsende Member and Goha Hills Formation: mostly felsic, Kgwebe Formation: bimodal).

6.3. New correlations between Botswana and Namibia

New observations of sedimentary structures integrated with the interpretation of aeromagnetic data allow correlation of Meso- to Neoproterozoic stratigraphic units across the international border between Namibia and Botswana, below the Karoo and Kalahari cover at the NW margin of the Kalahari Craton (Fig. 14). The oldest correlative post-Palaeoproterozoic unit is represented by the Langberg Formation and Gamsberg Granitic Suite in the Rehoboth Subprovince, the Oorlogsende Member in Eastern Namibia and the Kgwebe and Goha Hills Formation in Botswana. Our review indicates that these units are dominated by bimodal within-plate volcanic and sub-volcanic products emplaced in between 1110 and 1090 Ma (Figs. 3a and 5a), and thus form part of the Umkondo Large Igneous Province that spreads across the entire Kalahari Craton and which is dated at ~ 1112-1106 Ma (Hanson et al., 2006; de Kock et al., 2014). The calc-alkaline character of some of the ~ 1.1 Ga magmatic rocks could be inherited, i.e. a product of remelting of juvenile crust, although not necessarily in an active arc setting (Kampunzu et al., 1998). The Opdam Formation although not dated is older than the Tsumis Group and younger than the Langberg Formation (Fig. 3a), and is therefore also considered to be an expression of the Umkondo LIP.

It is not clear if Umkondo-related rocks are continuous at the scale of our study, as they do not core many of the sub-outcropping anticlines of the Ghanzi-Chobe Belt in eastern Namibia and Botswana. Schwartz et al. (1995) interpreted the variation in gravimetric signal SW of the Ghanzi Ridge to reflect a heterogeneously developed Kgwebe Formation. Because the Kgwebe volcanic rocks contain gneiss xenoliths, this formation must overlay a basement that was already metamorphosed prior to the Umkondo event (Dietvorst and Gopolang, 1995).

The Doornpoort and Eskadron formations correlate with the Ngwako Pan Formation in Botswana and mark the onset of a marine transgression that is broadly constrained between 1090 Ma and the age of the Sturtian glaciation (~ 750 to 710 Ma, Halverson et al., 2005; Macdonald et al., 2010). The transgression is followed by a broad regressive cycle ending with the Leeuberg and Eindpaal members of the Klein Aub Formation. The Kagas Member (Klein Aub Formation) - the host-rocks of Cu-Ag stratabound deposits - is newly interpreted to have been deposited in a marine setting during a major transgression. The Kagas Member correlates with the D'Kar Formation in Botswana which was similarly deposited in a reduced environment. This country-scale correlation of transgressive rocks throughout the Kalahari Copperbelt may indicate a eustatic origin.

In Botswana, there are no documented lithostratigraphically correlative rocks of the Damara Supergroup which are pre-Nama in age (> 550 Ma; e.g. Miller, 2008) and deposited on the Kalahari Craton. The only unit which is post-D’Kar and pre-Nama in age is the Mamuno Formation which is diamictite-free. As this formation is described to lie conformably on the D'Kar Formation (Fig. 5a), it must have been formed before the global Sturtian glaciation (~ 750 to 710 Ma, Macdonald et al., 2010) unless the entire Ghanzi Group was deposited during an inter-diamictite event. Also, it is difficult to correlate the Mamuno Formation with the pre-Sturtian Nosib Group of the Rehoboth Subprovince in Namibia because the basal contact of the Nosib is marked by a regional unconformity expressed by clasts of the underlying units. Hence, the Mamuno Formation is better correlated with the Dikdoorn Member of the Klein Aub Formation as both units were deposited during regressive progradation.

Based on the correlation of the Kgwebe (Goha Hills, Langberg, Oorlogsende), Ngwako Pan (Doornpoort-Eskadron) and D’Kar (Klein Aub) formations and on the combination of directional filtering and up-ward continuation of aeromagnetic data (i.e. Fig. 11), the extent of the Kalahari Copperbelt is revised and significantly extended, to include the belt that runs SW of the Ghanzi-Chobe Belt in eastern Namibia (Fig. 1). Previously interpreted to be composed of the discrete individual basins of Klein Aub, Dorbabis/Witvlei, and Lake N’Gami (Borg and Maiden, 1987), the KCB now appears, to be an uninterrupted domain of about 100 000 km². The newly defined KCB is bordered to the NW by the sharp drop in magnetic amplitude that marks the NW limit of the Oorlogsende Member in eastern Namibia (labelled 2 in Fig. 10c) and which can be continued through Botswana. The extent of the KCB is essentially unchanged in the region of the Rehoboth Subprovince because of the complex nature of the magnetic signatures and good knowledge of the geology based on outcrop information. However, it is noteworthy that the Ekuja–Otjihangwe Nappe Complex contains Cu-bearing metavolcanic rocks of Umkondo-age (1120-1060 Ma, Steven et al., 2000). Mesoproterozoic ages have been recorded also in the Abbabis Metamorphic Complex (1240-1040 Ma, Kröner et al., 1991) and from xenocrysts in the Pan-African Goas magmatic suite in the Central Zone of the Damara Belt (1110-1100 Ma, Milani et al., in press) which might indicate that some fragments of the Kalahari Craton extend as far as 200 km NW of the Rehoboth Subprovince. Foster et al. (2014) suggest that detrital zircons of 1350-1100 Ma age in the Damara Belt point to a provenance from the Kalahari Craton. The southern boundary of the KCB in eastern Namibia and Botswana is interpreted to be the last visible lithotectonic domain in the aeromagnetic data. This boundary is slightly NW of the southern extent of the northwest Botswana Rift of Keys and Ayres (2000). Indeed, the undercover putative major rift faults marking the southern extent of the suggested northwest Botswana Rift have not been depicted in the aeromagnetic data. The smooth southeastward decrease in the aeromagnetic signal of the pre-Karoo rocks of the KCB is related to the increasing thickness of the Aranos and Kalahari Karoo basins to maximum depth of 700 m (Catuneanu et al., 2005). Using seismic reflection data, Wright and Hall (1990) revealed that fold and thrust structures of the Ghanzi-Chobe Belt extend ~ 80 km south of the limit inferred from interpretation of aeromagnetic data.

Stratabound sediment hosted copper-silver deposits are found in similar settings in the Rehoboth Subprovince and in the Ghanzi-Chobe Belt. Similarities include 1) the nature of the host-rocks (argillaceous sediments) with common occurrences of sedimentary pyrite; 2) a close spatial association with a major redox boundary (the Eindpaal/Kagas and Ngwako Pan/D'Kar contacts) which is here newly interpreted here as a regional marine transgressive surface; and 3) deformation at lower greenschist facies at Pan-African times during the Damara Orogeny.

6.4. Implications for the geodynamic settings of the Kalahari Copperbelt

Classically, it is inferred that two periods of continental arc magmatism at ~ 1400 Ma and ~ 1200 Ma mark the development of the Sinclair Supergroup in the Konkiep Subprovince (Fig. 1) (Hoal and Heaman, 1995; Miller, 2008). Miller (2008) suggests that the first event accreted the Konkiep Subprovince of supposed Palaeoproterozoic age to the Kalahari Palaeoproterozoic Craton along a putative SW-dipping suture (the Namaqua Front in Fig. 1) (Hoal and Heaman, 1995; Corner, 2000). Arc magmatism was associated with amphibolite facies metamorphism and formation of a regional NNW-striking metamorphic foliation (Miller, 2012). A second event is thought to have accreted the Palaeoproterozoic Gordonia Subprovince (2000-1700 Ma, Becker et al., 2006) to the SW of the Konkiep Subprovince at ~ 1200 Ma, during activity of a supposed NE-dipping subduction (Miller, 2012) (the Huchab-Excelsior-Lord Hill shear zone/lineament). Peripheral growth of the Kalahari Craton was consolidated by extensive granulite facies metamorphism and associated magmatism in the Gordonia Subprovince at ~ 1150-1000 Ma (e.g. Diener et al., 2013). The distinction of two accretionary subprovinces (the Konkiep and Gordonia) is supported by contrasting internal magnetic patterns that also differ from those of the Kalahari Craton to the east (Eberle et al., 2002).

The Sinclair Supergroup in the Rehoboth Subprovince shares similarities with rocks of the Konkiep Subprovince, including a magmatic event at ~ 1100 Ma and earlier continental arc evolution at ~ 1200 Ma (the Nückopf Formation). However, the separation of the Rehoboth Subprovince from the Konkiep Subprovince is supported by (1) the lack of typical ~ 1400 Ma arc-related magmatism in the Rehoboth Subprovince, and (2) the existence in the Rehoboth Subprovince of a post-1100 Ma and pre-Damara Supergroup thick sedimentary sequence (the Tsumis Group) which is weakly developed in the upper part of the Sinclair Supergroup in the Konkiep Subprovince (e.g. Borg, 1988a; Becker and Schalk, 2008; Miller, 2008).

This study reveals that there are no clear stratigraphic and magnetic indications of Mesoproterozoic orogenic activity in the eastern Namibian and Botswanan part (i.e. in the Ghanzi-Chobe magnetic domain) of the KCB. Evidence for Mesoproterozoic reworking in Botswana in general (Majaule et al., 1997; Majaule and Davis, 1998; Singletary et al., 2003) are (1) juvenile magmatism dated by U-Pb on zircons in between ~ 1250 and 1150 Ma in the contiguous Kwando Complex (Singletary et al., 2003); (2) K-Ar ages from Palaeoproterozoic basement gneisses that range from 1093 ± 36 to 1156 ± 28 Ma on biotite, and on hornblende of 1193 ± 35 Ma (Key and Rundle, 1981; Cahen et al., 1984), interpreted as a thermal event during low-grade metamorphism (Aldiss and Carney, 1992); (3) a Rb-Sr overprint of the Goha Hills volcanic rocks dated at 981 ± 43 Ma (Key and Rundle, 1981); and (4) U-Pb discordia upper intercept ages of 1020-1000 Ma obtained from the Quangwadum Complex (Fig. 1) (Singletary et al., 2003). However, the ages from the Quangwadum Complex cannot be used to evaluate the Mesoproterozoic tectonic evolution of the NW margin of the Kalahari Craton since this complex is interpreted to be a southern extension of the Congo Craton (Singletary et al., 2003) that is separated with the Kalahari Craton by the Pan-African continental suture. Based on age similarities and good continuity of NE-SW structural trends, Singletary et al. (2003) interpreted the Kwando Complex to be a sub-surface continuity of the NE-adjacent Choma-Kalomo block (Fig. 1 inset). The Choma-Kalomo block has yielded zircon ages of 1350-1200 Ma (multigrain analyses, Hanson et al., 1988), along with SHRIMP zircon dates with a similar age range (Bulambo et al., 2004, 2006). Our review of the geology of the Chinamba and Goha Hills and the processing of aeromagnetic data demonstrate that, in Botswana, the NE-SW structural trend is Pan-African in age, not Mesoproterozoic. Further work is required to constrain the tectonic significance of the Choma-Kalomo block and its geodynamic relationships with surrounding orogenic belts.

The apparent absence of peri-Kalahari Craton Mesoproterozoic orogenesis in Botswana, limited spatial extent of the Nückopf Formation in the Rehoboth Subprovince compared with its equivalent in the Konkiep Subprovince (Fig. 1), and discrete inliers dated at ~ 1100 Ma within the Damara Belt challenge suggestions of an ESE-dipping subduction zone located to the WNW of the Rehoboth Subprovince in Namibia and Botswana (Watters, 1976; Jacobs et al., 2008). Instead, the evidence is not in conflict with subduction occurring along the western margin of the Kalahari Craton (the Huchab-Excelsior-Lord Hill Lineament in Fig. 1).

The ≤ 340 Ma time span between the Umkondo event and the deposition of the basal rocks of the Damara Supergroup saw formation of the Tsumis and Ghanzi groups, both recording two regressive sequences starting with a basal marine transgression followed by progradation (Figs. 13 and 14). The first marine transgression at the base of the Tsumis and Ghanzi groups followed a long period (≥ 150 Ma) during the Mesoproterozoic of a continental to epicontinental environment in both Namibia and Botswana recorded in the Billstein, Kgwebe and Goha Hills formations, and the Nauzerus Group. This transgression indicates that the northwest Kalahari Craton was relatively peneplained, with subdued topography, and was submerged under a shallow shelf during a period of sea level highstands. Unlike underlying tectonostratigraphic sequences, the Tsumis and Ghanzi groups are marked by a general absence of volcanic and volcaniclastic components (Figs. 3 and 5) – ruling out formation in a peri-magmatic arc environment. Besides, fore-arc basins generally do not evolve from continental to oceanic environments through time. The second major marine transgressive-regressive sequence is probably also linked to eustatic sea-level changes because of its great regional extent over more than 1000 km coupled with a lack of evidence for tectonism and volcanism at this time. This second sequence juxtaposed deeper shelf offshore reduced facies shales and siltstones of the Kagas Member (Klein Aub Formation) and D'Kar Formation over oxidized shallow-shelf sandstones (Leeuberg and Eindpaal members, Klein Aub Formation and Ngwako Pan Formation) (Figs. 13 and 14). This regional interface, which is both a permeability barrier and redox boundary, seems to have played a critical role in the formation of the stratabound sediment-hosted Cu-Ag deposits of the Kalahari Copperbelt.

7. Acknowledgments

We thank Eric Anderson, Richard Hanson and an anonymous reviewer for detailed and constructive comments, and Jeffrey L. Mauk for editorial handling. This study is part of a two year research project involving the University of the Witwatersrand and Rio Tinto, in an effort to correlate the Damara Belt in Namibia with the Lufilian Arc and the Zambezi Belt in Zambia. The THRIP funding is acknowledged (grant JKRT001/2 to Judith Kinnaird). This research is (partially) funded by the DST-NRF Centre of Excellence for Integrated Mineral Resource Analysis (CIMERA) to which thanks is extended. Guy Charlesworth is thanked for his contribution to the understanding of the Namibian geology. We are grateful to Hana Mining for access to drillcore in Botswana. We thank Brian Ruzividzo (MSA) for measuring the magnetic susceptibility on Hana Mining drillcores. This study benefited also from the unpublished Wits Honours thesis of Frans Hendjala (2011).

Aldiss, D. T. and Carney, J. N. 1992. The geology and regional correlation of the Okwa Valley Inlier, western Botswana. Precambrian Research, 56, 255–274.

Anhaeusser, C. R. and Button, A. 1973. A petrographic and mineralogical study of the copper-bearing formations in the Witvlei area, South West Africa. Transactions of the Geological Society of South Africa, 76, 3, 279–299.

Baranov, V., and Naudy, H. 1964. Numerical calculation of the formula of reduction to the magnetic pole: Geophysics, 29, 67–79.

Becker, T., Wiegand, B., Hansen, B. T. and Weber, K. 2004. Sm-Nd, Rb-Sr and U-Pb data from the Rehoboth Basement Inlier, Namibia: Evidence of a Palaeoproterozoic magmatic arc. Communications of the Geological Survey, Namibia, 13, 75–84.

Becker, T., Garoeb, H., Ledru, P. and Milesi, J.P. 2005. The Mesoproterozoic event within the Rehoboth Basement Inlier of Namibia: review and new aspects of stratigraphy, geochemistry, structure and plate tectonic setting. South African Journal of Geology, 108, 465–492.

Becker, T., Schreiber, U., Kampunzu, A.B. and Armstrong, R. 2006. Mesoproterozoic rocks of Namibia and their plate tectonic setting. Journal of African Earth Sciences, 46, 112–140.

Becker, T. and Schalk, K. E. L. 2008. In: Miller, R. McG. (Ed.), The Geology of Namibia: Archaean to Mesoproterozoic, Volume 1. Ministry of Mines and Energy, Geological Survey of Namibia, Windhoek, 8-68–8-102.

Blakely, R.J. 1995. Potential theory in gravity and magnetic application. Cambridge University Press, Cambridge, 441 p.

Borg, G. 1988a. The Koras-Sinclair-Ghanzi Rift in southern Africa: Volcanism, Sedimentation, Age relationships and Geophysical signature of a late middle Proterozoic rift system. Precambrian Research, 38, 75–90.

Borg, G. 1988b. Controls on stratabound mineralisation at Klein Aub Mine and similar deposits within the Kalahari Copperbelt of South West Africa/ Namibia and Botswana. Unpublished Ph.D. thesis, University of the Witwatersrand, Johannesburg South Africa, 107 p.

Borg, G. and Maiden, K. 1986. Stratabound Copper-Silver-Gold Mineralisation of Late Proterozoic Age Along the Margin of the Kalahari Craton in SWA/Namibia and Botswana, Symposium on 'Sediment-hosted Stratiform Copper Deposits', Ottawa. Canadian Mineralogist, 24, 178 p.

Borg, G. and Maiden, K. J. 1987. Basalt alteration and its relation to Middle Proterozoic stratabound copper-silver-gold deposits along the margin of the Kalahari Craton in SWA/Namibia and Botswana. In: Pharaoh, T.C., Beckinsale, R.D. and Rickard, D.T. (Eds.), Geochemistry and Mineralisation of Proterozoic Volcanic Suites. Geological Society of London, Special Publication, 33, 347–354.

Borg, G. and Maiden, K. J. 1989. The Middle Proterozoic Kalahari Copperbelt of Namibia and Botswana. In: Boyle, R.W., Brown, A.C., Jefferson, C.W., Jowett, E.C. and Kirkham, R. V. (Eds.), Sediment-hosted Stratiform Copper Deposits. Geological Association of Canada, Special Paper, 36, 525–540.

Brandt, R. 1987. A revised stratigraphy for the Abbabis Complex in the Abbabis Inlier, Namibia. South African Journal of Geology, 90, 314–323.

Bulambo, M., De Waele, B. and Kampunzu, A.B. 2004. SHRIMP U-Pb zircon geochronology of the Choma-Kalomo Block (Zambia) and geological implications. Abstracts, 20th Colloquium of African Geology, Orleans, France, 96.

Bulambo, M., De Waele, B. and Kokonyangi, J. 2006. SHRIMP U-Pb zircon geochronology and geochemistry of the Choma-Kalomo Block granitoids (Zambia): geological implications. Abstracts, 21st Colloquium of African Geology, Maputo, Mozambique, 2 p.

Burger, A. J. and Coertze, F. J. 1978. Summary of age determinations carried out during the period April 1974 to March 1975. Annals of the Geological Survey of South Africa, 11, 317–321.

Briggs, I. C. 1974. Machine contouring using minimum curvature. Geophysics 39, 39–48.

Cahen, L., Snelling, N. J., Delhal, J., Vail, J. R., Bonhomme, M. and Ledent, D. 1984. Geochronology and Evolution of Africa. Clarendon, Oxford, 512 p.

Carney, J. N., Aldiss, D. T. and Lock, N.P. 1994. The geology of Botswana. Botswana Geological Survey Bulletin, 37, 113 p.

Caterall, D., Grant, J., Meister, S. N., Obiri-Yeboa, T., Cresswell, M. and Channon, W. 2012. Preliminary economic assessment – Ghanzi Copper-Silver Project, Ghanzi District, Botswana. NI 43-101 Technical Report Prepared for Hana Mining Ltd., 20-33.

Catuneanu, O., Wopfner, H., Eriksson, P. G., Cairncross, B., Rubidge, B. S., Smith, R. M. H. and Hancox, P. J. 2005. The Karoo basins of south-central Africa. Journal of African Earth Sciences, 43, 211–253.

Clark, D. A., 1997. Magnetic petrophysics and magnetic petrology: aids to geological interpretation of magnetic surveys. AGSO Journal of Australian Geology & Geophysics 17, 83–103.

Cole, J., Finn, C. A. and Webb, S. J. 2013. Overview of the magnetic signatures of the Palaeoproterozoic Rustenburg Layered Suite, Bushveld Complex, South Africa. Precambrian Research, 236, 193–213.

Cooper, G. R. J. 2003. Feature detection using sun shading. Computers & Geosciences, 29(8), 941–948.

Cooper, G. R. J. and Cowan, D. R. 2004. Filtering using variable order vertical derivatives. Computers & Geosciences, 30(5), 455–459.

Corner, B. 2000. Crustal framework of Namibia derived from magnetic and gravity data. Communications of the Geological Survey, Namibia, 12, 13–19.

de Kock, M. O., Ernst, R., Söderlund, U., Jourdan, F., Hofmann, A., Le Gall, B., Bertrand, H., Chisonga, B. C., Beukes, N., Rajesh, H. M., Moseki, L. M. and Fuchs, R. 2014. Dykes of the 1.11 Ga Umkondo LIP, Southern Africa: Clues to a complex plumbing system. Precambrian Research, 249, 129–143.

Dentith, M. and Mudge, S. T. 2014. Geophysics for the Mineral Exploration Geoscientist. Cambridge University Press, New York, United States of America. 516 p.

Diener, J. F. A., White, R. W., Link, K., Dreyer, T. S. and Moodley, A. 2013. Clockwise, low-metamorphism of the Aus granulite terrain, southern Namibia, during the Mesoproterozoic Namaqua Orogeny. Precambrian Research, 224, 629–652.

Dietvorst, E. J. L. and Gopolang, M. 1995. A tectonothermal model for Damaran folding, thrust faulting and metamorphism in the Kgwebe Hills, Botswana. In: Wendorf, M. and Tack, L. (Eds.), Late Proterozoic belts in central and southwestern Africa. Musée Royal de l'Afrique Centrale-Tervuren, Belgium, Sciences Geologiques, 101, 131–41.

Duke, W. L., Arnott, R. W. and Cheel, R. J. 1991. Shelf sandstones and hummocky cross-stratification: new insights on a stormy debate. Geology, 19, 625–628.

Eberle, D. G., Andritzky, G., Hutchins, D. G., and Wackerle, R. 2002. The regional magnetic data set of Namibia: Compilation, contributions to crustal studies and support to natural resource management. South African Journal of Geology, 105, 361–380.

Evans, A. M., and Moon, C. J. 2006. Mineral Deposit Geology and Models. In: Moon, C. J., Whateley, E. G., and Evans, A. M. (Eds.), Introduction to Mineral Exploration, second edition, Blackwell Publishing, 33–51.

Foster, D. A., Goscombe, B. D., Newstead, B., Mapani, B., Mueller, P. A., Gregory, L. C. and Muvangua, E. In press. U–Pb age and Lu–Hf isotopic data of detrital zircons from the Neoproterozoic Damara Sequence: Implications for Congo and Kalahari before Gondwana. Gondwana Research (0).

Haddon, I. G. 2001. Sub-Kalahari Geological Map. 1:2 500 000. Council for Geoscience, Pretoria, South Africa.

Haddon, I. G. and McCarthy, T. S. 2005. The Mesozoic–Cenozoic interior sag basins of Central Africa: The Late-Cretaceous–Cenozoic Kalahari and Okavango basins. Journal of African Earth Sciences, 43(1–3), 316–333.

Hall, W. 2012. Geology and paragenesis of the Boseto Copper Deposits, Kalahari Copperbelt, Northwest Botswana. M.Sc. thesis, Colorado School of Mines, Golden, CO, USA, 146 p.

Halverson, G. P., Hoffman, P. F., Schrag, D. P., Maloof, A. C. and Rice, A. H. N. 2005. Toward a Neoproterozoic composite carbon isotope record. Geological Society of America Bulletin, 117, 1181–1207.

Hanson, R. E., Wilson, T. J., Brueckner, H. K., Onstott, T. C., Wardlaw, M. S., Johns, C. C. and Hardcastle, K. C. 1988. Reconnaissance geochronology, tectonothermal evolution, and regional significance of the middle Proterozoic Choma-Kalomo block, southern Zambia. Precambrian Research, 42, 39–61.

Hanson, R. E., Crowley, J. L., Bowring, S. A., Ramezani, J., Gose, W. A., Dalziel, I. W. D., Pancake, J. A., Seidel, E. K., Blenkinsop, T. G. and Mukwakwami, J. 2004. Coeval Large-scale Magmatism in the Kalahari and Laurentian Cratons during Rodinia assembly. Science, 304, 1126–1129.

Hanson, R. E., Harmer, R. E., Blenkinsop, T. G., Bullen, D. S., Dalziel, I. W. D., Gose, W. A., Hall, R. P., Kampunzu, A. B., Key, R. M., Mukwakwami, J., Munyanyiwa, H., Pancake, J. A., Seidel, E. K., and Ward, S. E. 2006. Mesoproterozoic intraplate magmatism in the Kalahari Craton: A review. Journal of African Earth Sciences, 46, 141–167.

Hegenberger, W. and Burger, A. J. 1985. The Oorlogsende Porphyry Member, South West Africa/Namibia: Its age and regional setting. Communications of the Geological Survey, Namibia, 1, 23–29.

Hoal, B. G. 1990. The geology and geochemistry of the Proterozoic Awasib Mountain terrain southern Namibia. Memoir of the Geological Survey of Namibia, 11, 163 p.

Hoal, B. and Heaman, L. M. 1995. U–Pb age constraints from the Awasib Mountain area. In: Proterozoic Crustal and Metallogenic Evolution. Communications of the Geological Survey, Namibia, Special issue 10, 83–92.

Hofmann, M., Linnemann, U., Hoffmann, K.-H., Germs, G., Gerdes, A., Marko, L., Eckelmann, K., Gärtner, A. and Krause, R. In press. The four Neoproterozoic glaciations of southern Namibia and their detrital zircon record: The fingerprints of four crustal growth events during two supercontinent cycles. Precambrian Research (0).

Huch, K. M., Modie, B. N. J., Ratsoma, W. M. and Hannak, W. W. 1992. Mineral Prospecting in the Ghanzi-Chobe Belt of Botswana. Technical Report Phase 1 (1989–1991), Part 1. Geological Reconnaissance Mapping and Litho-Geochemical Investigations, BGR (Hannover)/ GSD (Lobatse), 154 p.

Jacobs, J., Pisarevsky, S., Thomas, R. J. and Becker, T. 2008. The Kalahari Craton during the assembly and dispersal of Rodinia. Precambrian Research, 160, 142–158.

Kampunzu, A. B., Akanyang, P., Mapeo, R. B. M., Modie, B. N. and Wendorff, M. 1998. Geochemistry and tectonic significance of the Mesoproterozoic Kgwebe metavolcanic rocks in northwest Botswana: implications for the evolution of the Kibaran Namaqua-Natal Belt. Geological Magazine, 135, 669–683.

Kampunzu, A. B., Tembo, F., Matheis, G., Kapenda, D. and Huntsman-Mapila, P. 2000. Geochemistry and tectonic setting of mafic igneous units in the Neoproterozoic Katangan basin, Central Africa: implications for Rodinia breakup. Gondwana Research, 3, 125—153.

Kasch, K. W. 1986. Tectonic subdivision, lithostratigraphy and structural geology of the Upper Black Nossob River area. Communications of the Geological Survey, Namibia, 2, 117–129.

Kasch, K. W. 1987. Metamorphism of pelites in the Upper Black Nossob River area of the Damara Orogen. Communications of the Geological Survey, Namibia, 3, 63–81.

Key, R. M. and Rundle, C. C. 1981. The regional significance of new isotope ages from Precambrian windows through the Kalahari Beds in north-western Botswana. Transactions Geological Society South Africa, 84, 51–66.

Key, R. M., Mapeo, R. 1999. The Mesoproterozoic history of Botswana and the relationship of the NW Botswana Rift of Rodinia. Episodes, 22, 118–122.

Key, R. M. and Ayres, N. 2000. The 1998 edition of the National Geological Map of Botswana. Journal of African Earth Sciences, 30, 427–451.

Kgotlhang, L. P. 2008. Application of airborne geophysics in large scale hydrological mapping; Okavango Delta, Botswana. PhD thesis, ETH Zurich, 138 p.

Kinabo, B. D., Hogan, J. P., Atekwana, E. A., Abdelsalam, M. G., and Modisi, M. P. 2008. Fault growth and propagation during incipient continental rifting: Insights from a combined aeromagnetic and Shuttle Radar Topography Mission digital elevation model investigation of the Okavango Rift Zone, northwest Botswana. Tectonics, 27, 1–16.

Kröner, A., Retief, E. A., Compston, W., Jacob, R. E. and Burger, A. J. 1991. Single-grain and conventional zircon dating of remobilized basement gneisses in the central Damara belt of Namibia. South African Journal of Geology, 94, 379–387.

Letsholo, A., Piestrzyński, A. and Wendorff, M. 2012. Mineralisation in the Neoproterozoic Ghanzi Group strata, the Boseto Exploration Area, NW Botswana and comparison with the Polish Kupferschiefer (Permian). Abstract, Namibia Copper Conference, Geological Society of Namibia, Windhoek, 13-14 September, 2012.

Litherland, M. 1982. The geology of the area around Mamuno and Kalkfontein, Ghanzi District, Botswana. Geological Survey of Botswana District Memoir, 4, 145 p.

Longridge, L. 2012. Tectonothermal evolution of the southwestern Central Zone, Damara Belt, Namibia. PhD thesis, University of the Witwatersrand, 522 p.

Longridge, L., Kinnaird, J. A., Gibson, R. L., and Armstrong, R. A. 2014. Amphibolites of the Central Zone: new SHRIMP U-Pb ages and implications for the evolution of the Damara Orogen, Namibia: South African Journal of Geology, 117, 1, 67—86, doi: 10.2113/gssajg.117.1.67.

Macdonald, F. A., Schmitz, M. D., Crowley, J. L., Roots, C. F., Jones, D. S., Maloof, A. C., Strauss, J. V., Cohen, P. A., Johnston, D. T. and Schrag, D. P. 2010. Calibrating the Cryogenian. Science, 327, 1241—1243.

Maiden, K. J. and Borg, G. 2011. The Kalahari Copperbelt in Central Namibia: Controls on Copper Mineralization. SEG Newsletter, 87, 14–19.

Majaule, T. & Davis, D. W. 1998. U-Pb zircon dating and geochemistry of granitoids in the Mosetse area, NE Botswana, and tectonic implications. Geol. Surv. Botswana, 50th Anniversary Intern. Conf., Abstract Volume, 46–48.

Majaule, T., Hall, R. P., Hughes, D. J. 1997. Geochemistry of mafic and ultramafic rocks of the Matsitama supra-crustal belt, northeastern Botswana — provenance implications. South African Journal Geology, 100, 169–179.

Mapeo, R. B. M., Romakate, L. V., Corfu, F., Davis, D. W. and Kampunzu, A.B. 2006. The Okwa basement complex, western Botswana: U-Pb zircon geochronology and implications for Eburnean processes in southern Africa. Journal of African Earth Sciences, 46, 253–262.

Master, S. 2002. Origin of angular elongate ultramafic pebbles in high-energy Maastrichtian conglomerates (Qahlah Formation) overlying the Semail Ophiolite, Northern Oman. Abstract, International Sedimentological Congress, International Association of Sedimentologists, Biennial Meeting, RAU, Johannesburg, 8–12 July 2002, CD-ROM.

Master, S. 2010. Geological report on the Hana Mining Ltd. copper concessions in the Ghanzi-Chobe Belt of Ngamiland, Botswana. Internal report for Hana Mining Ltd., Botswana, 148 p.

Master, S. 2013. Molybdenum and rhenium in the Hana Mining concession, Neoproterozoic Ghanzi copperbelt, Ngamiland, Botswana. Geocongress 2013, Biennial Congress of the Geological Society of South Africa, 3-5 July 2013, Turbine Hall, Johannesburg, South Africa.

Master, S., Hendjala, F. and Kasirye, S. 2012. Isotope chemostratigraphy and sedimentology of the Neoproterozoic Kalahari Copperbelt (Botswana and Namibia): implications for the ages of sedimentation and mineralisation. Abstract, Namibia Copper Conference, Geological Society of Namibia, Windhoek, 13-14 September, 2012.

Master, S., Kasirye, S. and Master, R. B. 2014. Microbially-induced sand cracks (polygonal petee ridges) in an early Neoproterozoic siliciclastic foreshore setting, Doornpoort Formation, Sinclair Supergroup (Rehoboth, Namibia). Abstract, Roy Miller Symposium, Geological Society of Namibia, Windhoek, Namibia, 18-20 August 2014.

Miall, A. D. 1977. A review of the braided-river depositional environment, Earth Science Reviews, 13(1), 1–62.

Milani, L., Kinnaird, J.A., Lehmann, J., Naydenov, K.V., Saalmann, K., Frei, D. and Gerdes, A. In press. Role of crustal contribution in the early stage of the Damara Orogen, Namibia: New constraints from combined U–Pb and Lu–Hf isotopes from the Goas Magmatic Complex. Gondwana Research (0).

Miller, H. G. and Singh, V. 1994. Potential field tilt — a new concept for location of potential field sources. Applied Geophysics, 32, 213—217.

Miller, R. McG. 2008. The Geology of Namibia, volume 1 – Archaean to Mesoproterozoic. Geological Survey of Namibia, Windhoek. Ministry of Mines and Energy, Geological Survey, Windhoek, 309 p.

Miller, R. McG. 2012. Review of Mesoproterozoic magmatism, sedimentation and terrane amalgamation in southwestern Africa. South African Journal of Geology, 115, 417–448.

Miller, R. McG. and Schalk, K. E. L. 1980, reprinted 1990. Geological Map of Namibia, 1:1 million. Geological Survey of Namibia.

Modie, B. N. 1996. Depositional environments of the Meso- to Neoproterozoic Ghanzi-Chobe belt, northwest Botswana. Journal of African Earth Sciences, 22(3), 255–268.

Modie, B. N., Akanyang, P. and Ramokate, L. V. 1998. Formalisation of the lithostratigraphy of the Kgwebe Formation and the Ghanzi Group, western Botswana. Geological Survey of Botswana Bulletin, Lobatse, 45, 32 p.

Modie, B. N. 2000. Geology and mineralisation in the Meso- to Neoproterozoic Ghanzi-Chobe Belt of northwest Botswana. Journal of African Earth Sciences, 30(3), 467–474.

Modisi, M. P., Atekwana, E. A., Kampunzu, A. B. and Ngwisanyi, T. H. 2000. Rift kinematics during the incipient stages of continental extension: Evidence from the nascent Okavango rift basin, northwest Botswana. Geology, 28(10), 939-942.

Nabighian, M., Grauch, V., Hansen, R., Lafehr, T., Li, Y., Peirce, J., Phillips, J. and Ruder, M. 2005. The historical development of the magnetic method in exploration. Geophysics, 70(6), 33ND–61ND.

Pfurr, N., Ahrendt, H., Hansen, B. T. and Weber, K. 1991. U-Pb and Rb-Sr isotopic study of granitic gneisses and associated metavolcanic rocks from the Rostock massifs, southern margin of the Damara Orogen: implications for lithostratigraphy of this crustal segment. Communications of the Geological Survey, Namibia, 7, 35–48.

Pouliquen, G., Key, R. M. and Walker, A. 2008. The internal structure and geotectonic setting of the Xade and Tsetseng complexes in the western most part of the Kaapvaal Craton. South African Journal of Geology, 111(4), 345–356.

Price, M. J. and Cosgrove J. W. 1990. Analysis of Geological Structures. Cambridge, Cambridge University Press. 502 p.

Pryer, L., Windle, S., Etheridge, M., Farquar-Smith, D., Guillemot, D., Foss, C. and Prat, D. 1997. Geological Interpretation of the aeromagnetic Survey of Western Ngamiland, Botswana. 1:250 000 scale. Department of Geological Survey, Lobatse, Botswana.

Ramokate, L.V., Mapeo, R.M.M., Corfu, F. and Kampunzu, A.B. 2000. Proterozoic geology and regional correlation of the Ghanzi-Makunda area, western Botswana. Journal of African Earth Sciences, 30, 453–466.

Ruxton, P. A. 1981. The sedimentology and diagenesis of copper-bearing rocks of the southern margin of the Damaran Orogenic Belt, Namibia and Botswana. Ph.D. thesis, University of Leeds, Leeds, UK, 241 p.

Ruxton, P. A. 1986. Sedimentology, isotopic signature and ore genesis of the Klein Aub Copper Mine, South West Africa/Namibia. In: Anhaeusser, C. R. and Maske, S. (Eds), Mineral Deposits of Southern Africa. South African Journal of Geology, Special Publication, II, 1725–1738

Ruxton, P.A. and Clemmey, H. 1986. Late Proterozoic Stratabound Red-Bed-Copper Deposits of the Witvlei area, South West Africa/Namibia. In: Anhaeusser, C. R. and Maske, S. (Eds), Mineral Deposits of Southern Africa. South African Journal of Geology, Special Publication, II, 1739–1754.

Sawyer, E.W. 1981. Damaran structural and metamorphic geology of an area south-east of Walvis Bay, South West / Namibia. Memoir of the Geological Survey of South West Afica., 7, 83 p.

Schieber, J. 2004. Microbial mats in the siliciclastic rock record: a summary of diagnostic features. In: Eriksson, P.G., Altermann, W., Nelson, D.R., Mueller, W.U., Catuneanu, O. (Eds.), The Precambrian Earth: tempos and events. Elsevier, Amsterdam, 663–673

Schneider, G. I. C. and Seeger, K. G. 1992. Copper. Mineral Resources of Namibia. Geological Survey of Namibia, 2.3-1–2.3-118.

Schneider, T., Becker, T., Borg, G., Hilken, U., Hansen, B.T., and Weber, K. 2004. New U-Pb zircon ages of the Nückopf Formation and their significance for the Mesoproterozoic event in Namibia. Communications of the Geological Survey, Namibia 13, 63–74.

Schwartz, M. O., Akanyang, P., Trippler, K., and Ngwisanyi, T. H. 1995. The sediment-hosted Ngwako Pan copper deposit, Botswana. Economic Geology, 90, 1118—1147.

Schwartz, M. O., Kwok, Y. Y., Davis, D. W. and Akanyang, P. 1996. Geology, geochronology and regional correlation of the Ghanzi Ridge, Botswana. South African Journal of Geology, 99, 245–250.

Siamisang, T. 1996. Resource evaluation of Ngwako Pan copper prospect. Unpublished Report, Geological Survey of Botswana, Lobatse.

Sillitoe, R. H., Perello, J., and Garcia, A. 2010. Sulfide-bearing veinlets throughout the stratiform mineralization of the Central African Copperblet: Temporal and genetic implications. Economic Geology, 105(8), 1361–1368.

Singletary, S. J., Hanson, R. E., Martin, M. W., Crowley, J. L., Bowring, S. A., Key, R. M., Ramokate, L. V., Direng, B. B. and Krol, M. A. 2003. Geochronology of basement rocks in the Kalahari Desert, Botswana, and implications for regional Proterozoic tectonics. Precambrian Research, 121, 47–71.

Skelton, P. W., Nolan, S. C. and Scott, R. W., 1990. The Maastrichtian transgression onto the northwestern flank of the Proto-Oman Mountains: sequences of rudist-bearing beach to open shelf facies. Geological Society, London, Special Publications, 49(1), 521–547.

Steven, N., Armstrong, R., Smalley, T., and Moore, J. 2000. First geological description of a Late Proterozoic (Kibaran) metabasaltic andesite-hosted chalcocite deposit at Omitiomire, Namibia. In: Clauer, J. K., Price, J. G., Struhsacker, E. M., Hardyman, R. F. and Morris, C .L. (Eds.) Geology and Ore Deposits

2000: The Great Basin and Beyond, Symposium Proceedings, Geological Society of Nevada, Reno, 2, 711–734.

Tack, L. and Bowden, P. 1999. Post-collisional granite magmatism in the central Damaran (Pan-African) Orogenic Belt, western Namibia. Journal of African Earth Sciences, 28, 653–674.

Thomas, C. M. 1969. A short description of the geology of South Ngamiland (covering Q.D.S. 2022C, 2022D and 2023C). Unpublished Report No. CMT/4/69, Geological Survey of Botswana, Lobatse, 13 p.

Thomas, C. M. 1973. Brief explanation of the geology of South Ngamiland (covering Q.D.S. 2022D with parts of 2022C and 2023C), accompanying geological map (1: 125 000 scale). Geological Survey of Botswana.

Toens, P. 1975. The geology of part of the Southern Foreland of the Damaran Orogenic Belt, South West Africa and Botswana. Geol. Runds., 64, 175–192.

Van Schijndel, V., Cornell, D. H., Hoffmann, K.-H. and Frei, D. 2011. Three episodes of crustal development in the Rehoboth Province, Namibia. In: Van Hinsbergen, D. J. J., Buiter, S. J. H., Torsvik, T. H., Gaina, C. and Webb, S. J. (Eds.) The Formation and Evolution of Africa: A Synopsis of 3.8 Ga of Earth History. Geological Society, London, Special Publications, 357, 27–47.

Verduzco, B., Fairhead, J. D., Green, C. M. and MacKenzie, C. 2004. New insights into magnetic derivatives for structural mapping. Leading Edge, 23, 116–119.

Walker, R. G. and Plint, A. G. 1992. Wave- and storm-dominated shallow marine systems. In: Walker, R. G. and James, N. P. (Eds.), Facies Models-Response to Sea Level Change. Geological Association of Canada, 219–238.

Watters, B. R. 1976. Possible late Precambrian subduction zone in South West Africa. Nature, 259, 471–472.

Wendorff, M. 2005. Outline of lithostratigraphy, sedimentation and tectonics of the Tsodilo Hills Group, a Neoproterozoic-Lower Palaeozoic siliciclastic succession in NW Botswana. Annales Societatis Geologorum Poloniae, 75, 17–25.

Wright, J. A. and Hall J. 1990. Deep seismic profiling in the Nosop Basin, Botswana: cratons, mobile belts and sedimentary basins, Tectonophysics, 173, 333–343.

Wright, E. P. 1958. Report on a visit to the Shinamba Hills. Unpublished Report No. EPW/22/58, Geological Survey of Botswana, Lobatse, 2 p.

Ziegler, U. R. F. and Stoessel, G. F. U. 1990. Isotope Geology and Geochemistry of the Rehoboth Basement Inlier, Namibia/S.W. Africa; a Multimethod Case History. Bull. Swiss Assoc. of Petroleum Geol. and Eng., 56, 13–33.

Figure 1: Simplified map of the exposed and sub-Kalahari Supergroup main geological domains of Namibia and Botswana (modified from Haddon, 2001; Key and Ayres, 2000; Miller, 2008). The extent of the Cenozoic Kalahari Supergroup cover is recorded as a semi-transparent stippled layer over pre-Cenozoic domains (Haddon, 2001). Note the interruption and lack of correlation between some geological domains between Namibia and Botswana. The letters A and B in the map refer to the Aunis Tonalite in the Konkiep Subprovince and the Boseto Copper Project to the NE of the Ghanzi Ridge. The southern extent of the northwest Botswana Rift, extent of the Okwa Inlier, Rakops dykes, Tshane, Tsetseng and Xade complexes are after Keys and Ayres (2000). Age span of the Kwando Complex in the legend is from Singletary et al. (2003). The revised extent of the Kalahari Copperbelt from this study is reported. Putative Mesoproterozoic arc magmatic rocks (Hoal and Heaman, 1995; Miller, 2008) and suture zones (Miller, 2008 and references therein) are also reported. The inset represents the major Precambrian tectonic domains of southern Africa (modified from Key and Ayres, 2000 with Choma-Kalomo block after Singletary et al., 2003) with the outline of Archaean and Palaeoproterozoic core of the Kalahari Craton after Jacobs et al. (2003).

Figure 2: The different published cross-border stratigraphic correlations of the Sinclair Supergroup in the Rehoboth Subprovince with the Kgwebe Formation and Ghanzi Group of western Botswana. Succession of stratigraphic units is according to our study.

Figure 3: **(a)** Simplified stratigraphic columns for the studied Meso- to Neoproterozoic sequences forming the Kalahari Copperbelt in Namibia (modified from Becker and Schalk, 2008). Circles enclosing letters refer to locations indicated in Fig. 3b. Sources of U-Pb ages and rock descriptions: (a) Becker and Schalk (2008), (b) Master et al. (2012), (c) Borg and Maiden (1986), (d) Schneider et al. (2004), (e) Becker et al. (2005), (f) Pfurr et al. (1991), (g) Hegenberger and Burger (1985) and (h) van Schijndel et al. (2011). **(b)** Simplified geological map of the Rehoboth Subprovince towards the Namibia/Botswana border (geological information form Namibian Geological Survey 1:250 000 scale geological maps based on 1:50 000 to 1:500 000 scale individual geological maps). The geology of the upper right corner is only published in the 1:1 000 000 scale Geological Map of Namibia (Miller and Schalk, 1980). Projection: Africa Albers Equal Area Conic, central meridian: 19° E, standard parallel 1: 21.5° S, standard parallel 2: 23.5° S.

Figure 4: Photographs of sedimentary structures in rocks of the Tsumis Group. **(a)** Photograph of a bedding plane, Doornpoort Formation, where the arrow shows “tadpoles-nest” type standing wave interference ripples formed by two simultaneous curves wave trains. **(b)** Polygonal sandcracks in the Doornpoort Formation: evidence for vanished siliciclastic algal mat, exposed, desiccated, and infilled with sand. **(c)** Drillcore and **(d)** outcrop from Malachite Pan conglomerate (Eskadron Formation) showing angular polymictic clasts in matrix-supported conglomerate. **(e)** Fluvial conglomerate overprinted by a strong steep Pan-African cleavage, Leeuberg member, Klein Aub Formation. **(f)** Hummocky cross-

stratified siltstone shale, Kagas Member, Klein Aub Formation. The arrow points to a cross-stratification at the base of a hummock.

Figure 5: **(a)** Simplified stratigraphic column of the studied rocks in Botswana. Legend is same as in Fig. 3a. Sources of U-Pb ages and rock descriptions: (a) Schwartz et al. (1996), (b) Modie (1996), (c) Kampunzu et al. (1998), (d) Kampunzu et al. (2000), (e) Modie (2000), (f) Master (2010) and (g) Singletary et al. (2003). **(b)** Simplified geological map of the Ghanzi-Chobe Belt in Botswana (modified from Key and Ayres, 2000) with a slightly opaque stippled layer representing the Kalahari Supergroup cover according to Haddon (2001). The location of drillcore HA17D and Boseto mine (B) are reported.

Figure 6: Photographs of sedimentary structures in rocks from drillcores of the Ngwako Pan Formation. **(a)** Tempestite- storm-generated shale rip-up clasts in a normally-graded granulestone layer. **(b)** Swaley cross-stratification. Note thin sandstone layers that pinch and swell between laminae, and some low-angle truncations of laminae.

Figure 7: Photographs of sedimentary structures in rocks of the D'Kar Formation (from drillcore HA17D, location in Fig. 5b). **(a)** Rhythmically graded siltstone-shale couplets. **(b)** Hummocky cross-stratification in sandstone interbedded with shale. **(c)** Thin light grey fine-grained sandstone interbedded with dark grey siltstone, and exhibiting curved, non-parallel contacts characteristic of hummocky cross-stratification.

Figure 8: Total Magnetic Intensity grid of the merged magnetic data sets (IGRF correction, equalized histogram) collected over the Kalahari Copperbelt. The slightly transparent colorscale map overlays a greyscale and sunshading grid with sun illumination from NW (315°) at 40° with vertical exaggeration of 2. The map is overlain by black dashed lines that outline the individual airborne surveys, for which specifications are reported in Table 1. Specifications and name(s) of survey block(s) located east of surveys A, B and E are missing. White lines are faults that are modified from Modisi et al. (2000) and Kinabo et al. (2008). Map projection is same as Fig. 1.

Figure 9: Summary diagram of lithologies and airborne magnetic characteristics for individual stratigraphic units of the Kalahari Copperbelt. Scale bar is 5 km. The Goha Hills, Oorlogsende and Kgwebe formations have very similar magnetic signatures, although the former displays a lower magnetic intensity than the two others. The Mamuno Formation displays a lower magnetic intensity than for the D'Kar Formation.

Figure 10: **(a)** Total Magnetic Intensity (TMI) grid in colorscale overlain by TMI grid in greyscale and sunshading with sun illumination from ENE (65°) at 45° across the political border between Namibia and Botswana. **(b)** Geological interpretation of the aeromagnetic data. The dated samples in the literature are reported as well as the location of drillcore HA17D. **(c)** Profiles of TMI data across important

stratigraphic units. Profiles reported in Figs. 10a and 10b. The colorcode of the map in **(b)** and profiles in **(c)** is identical to the Fig. 5b.

Figure 11: Processed magnetic map in NW Botswana. Directional filtering in the northwest direction (290°) of the RTP grid (D = 9.94°, I = -60.66°) to remove linear anomalies associated with the Okavango dyke swarm. The data have been upward-continued by 500 m and shaded with sun illumination from SW (210°) at 30° inclination. As a result, the characteristic structural grain of the KCB in Botswana can be followed continuously from the Ghanzi Ridge region to the Chinamba Hills. The extent of the Ghanzi Group, Kgwebe, Goha and Chinamba Hills Formations on the 1:1 000 000 scale pre-Kalahari geological map of Botswana (Key and Ayres, 2000) is also reported.

Figure 12: Variations in magnetic susceptibility across the contact between the D'Kar and Ngwako Pan Formations in the drillcore HA17D (location in Figs. 5b and 10b). The occurrences of ferromagnetic minerals observed in mineral separates from 8 samples are presented in the right column. Absence of ferromagnetic minerals in the separate is indicated by "n/o". Magnetic susceptibilities were measured using a hand-held Terraplus KT-10 Magnetic Susceptibility Meter. Measurements were taken on the convex portions of half or quarter-core samples, and were geometrically corrected for curvature of 4.7 cm diameter core. Because the depth penetration of the Susceptibility Meter is 4 cm, and it measures 92% of the information from the first 2 cm, measurement from half and quarter-cores are comparable. Repeat measurements on the same piece of core show repeatability of measurements to +/- 20%.

Figure 13: Cross-section summarizing the suggested depositional settings of the Tsumis and Ghanzi groups. See text for details.

Figure 14: Lithostratigraphic correlations across the Kalahari Copperbelt in Namibia and Botswana. See text for details.

Appendix: Flight data acquisition parameters and specifications of individual magnetic surveys. The individual survey blocks are reported in Fig. 8.

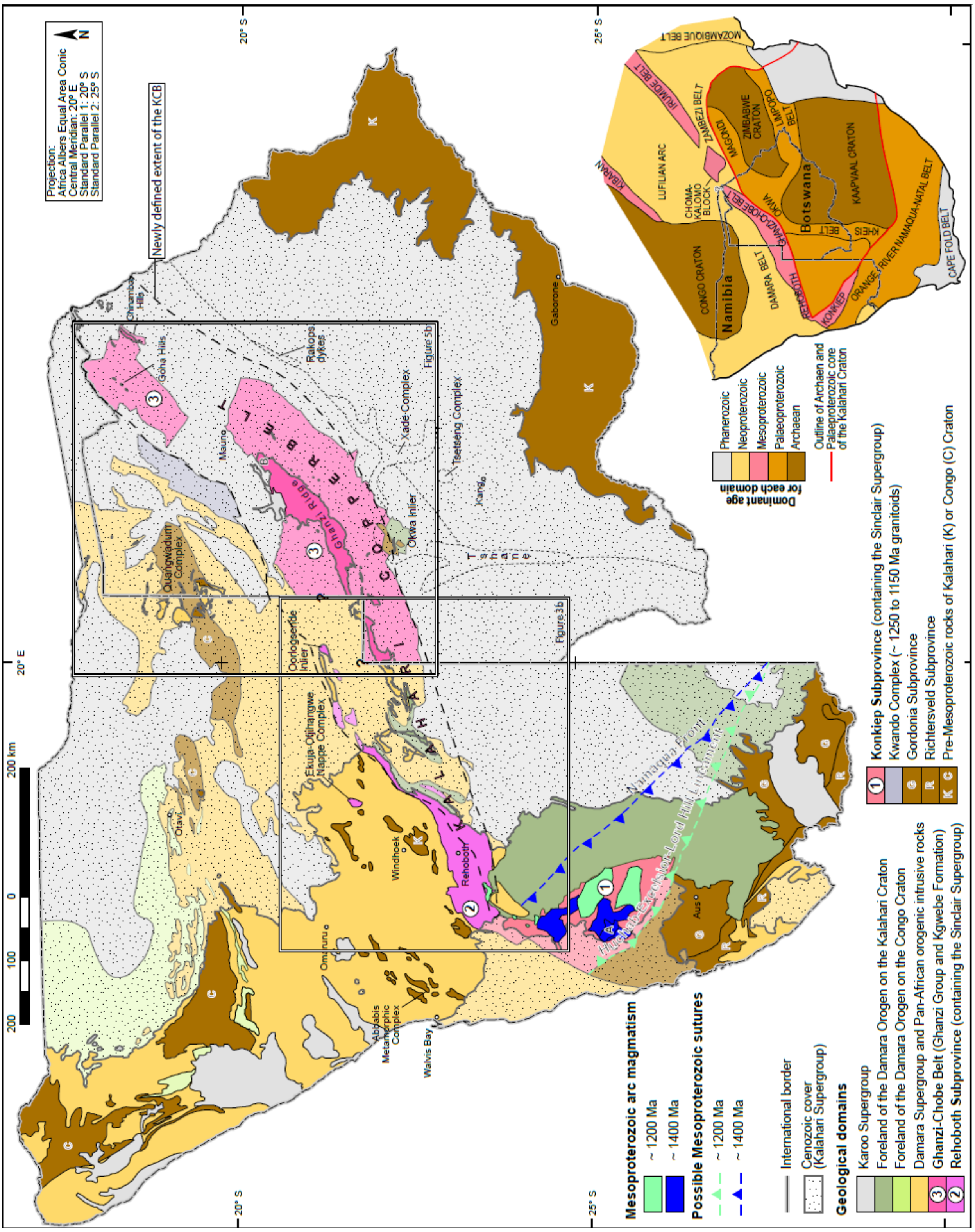
Projection:
Africa Albers Equal Area Conic
Central Meridian: 20° E
Standard Parallel 1: 20° S
Standard Parallel 2: 25° S
N
Newly defined extent of the KCB
200 km
200
100
0
20° S
25° S
20° E
Figure 5b
Figure 3b
Mesoproterozoic arc magmatism
~ 1200 Ma
~ 1400 Ma
Possible Mesoproterozoic sutures
~ 1200 Ma
~ 1400 Ma
International border
Cenozoic cover
(Kalahari Supergroup)
Geological domains
Karoo Supergroup
Foreland of the Damara Orogen on the Kalahari Craton
Foreland of the Damara Orogen on the Congo Craton
Damara Supergroup and Pan-African orogenic intrusive rocks
Ghanzi-Chobe Belt (Ghanzi Group and Kgwebe Formation)
Rehoboth Subprovince (containing the Sinclair Supergroup)
Konkiep Subprovince (containing the Sinclair Supergroup)
Kwando Complex (~ 1250 to 1150 Ma granitoids)
Gordonia Subprovince
Richtersveld Subprovince
Pre-Mesoproterozoic rocks of Kalahari (K) or Congo (C) Craton
Dominant age for each domain
Phanerozoic
Neoproterozoic
Mesoproterozoic
Palaeoproterozoic
Archaean
Outline of Archaean and Palaeoproterozoic core of the Kalahari Craton
Walvis Bay
Abbabis Metamorphic Complex
Omaruru
Windhoek
Rehoboth
Otavi
Ekuja-Otjinangwe Nappe Complex
Oorlogsende Inlier
Quangwadum Complex
Ghanzi Ridge
Mauno
Goha Hills
Chinamba Hills
Rakops dykes
Xade Complex
Okwa Inlier
Tsetseng Complex
Kang
Tshane
Gaborone
Aus
Namaqua Front
Hu-Gab-Excelsior-Lord Hill Lineament
KALAHARI COPPERBELT
CONGO CRATON
Namibia
Botswana
CHOMA-KALOMO BLOCK
LUFILIAN ARC
KIBARAN
IRUMIDE BELT
ZAMBEZI BELT
MOZAMBIQUE BELT
MAGONDI
ZIMBABWE CRATON
LIMPOPO BELT
KAAPVAAL CRATON
KHEIS BELT
OKWA
GHANZI-CHOBE BELT
DAMARA BELT
REHOBOTH
KONKIEP
ORANGE RIVER NAMAQUA-NATAL BELT
CAPE FOLD BELT

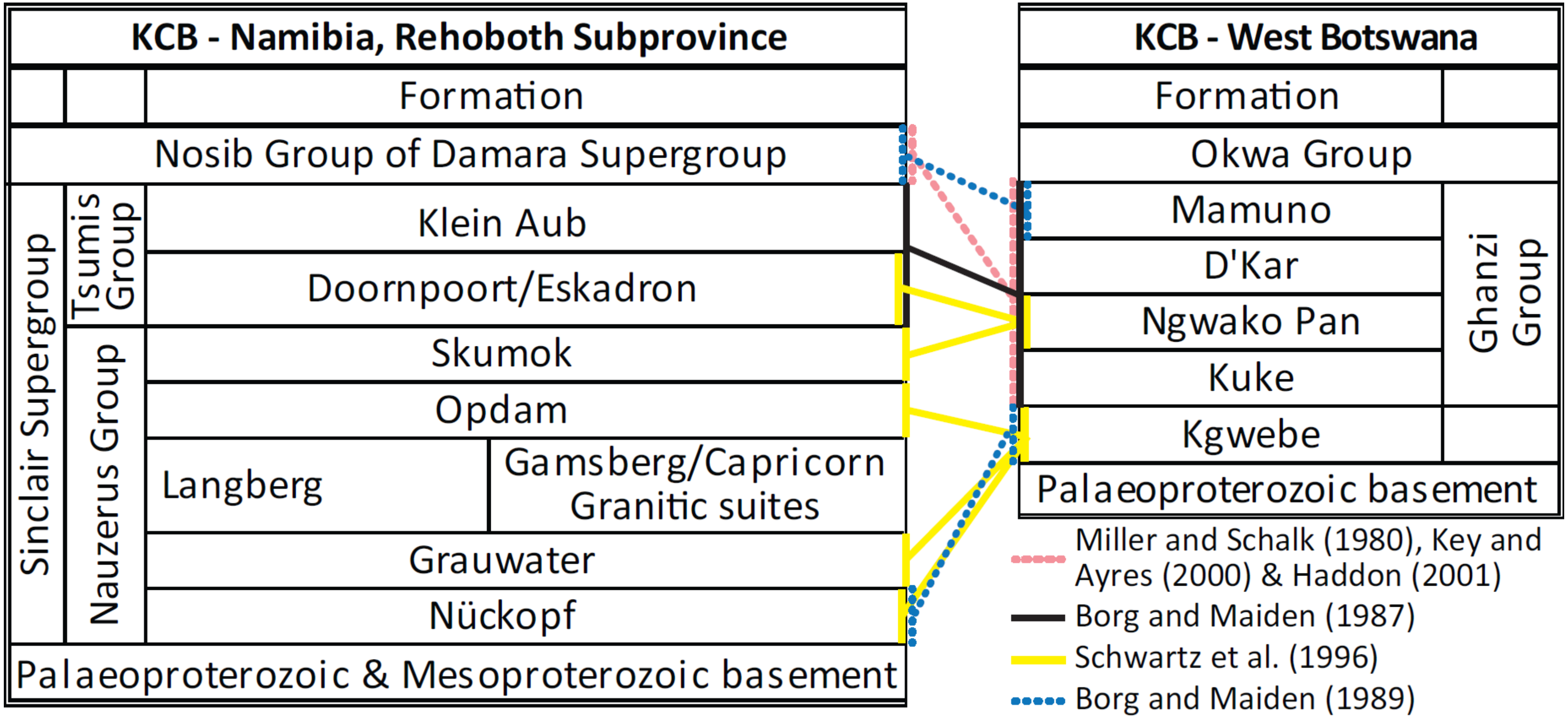
KCB - Namibia, Rehoboth Subprovince
Formation
Nosib Group of Damara Supergroup
Sinclair Supergroup
Tsumis Group
Nauzerus Group
Klein Aub
Doornpoort/Eskadron
Skumok
Opdam
Langberg
Gamsberg/Capricorn Granitic suites
Grauwater
Nückopf
Palaeoproterozoic & Mesoproterozoic basement
KCB - West Botswana
Formation
Okwa Group
Mamuno
D'Kar
Ngwako Pan
Kuke
Kgwebe
Ghanzi Group
Palaeoproterozoic basement
Miller and Schalk (1980), Key and Ayres (2000) & Haddon (2001)
Borg and Maiden (1987)
Schwartz et al. (1996)
Borg and Maiden (1989)

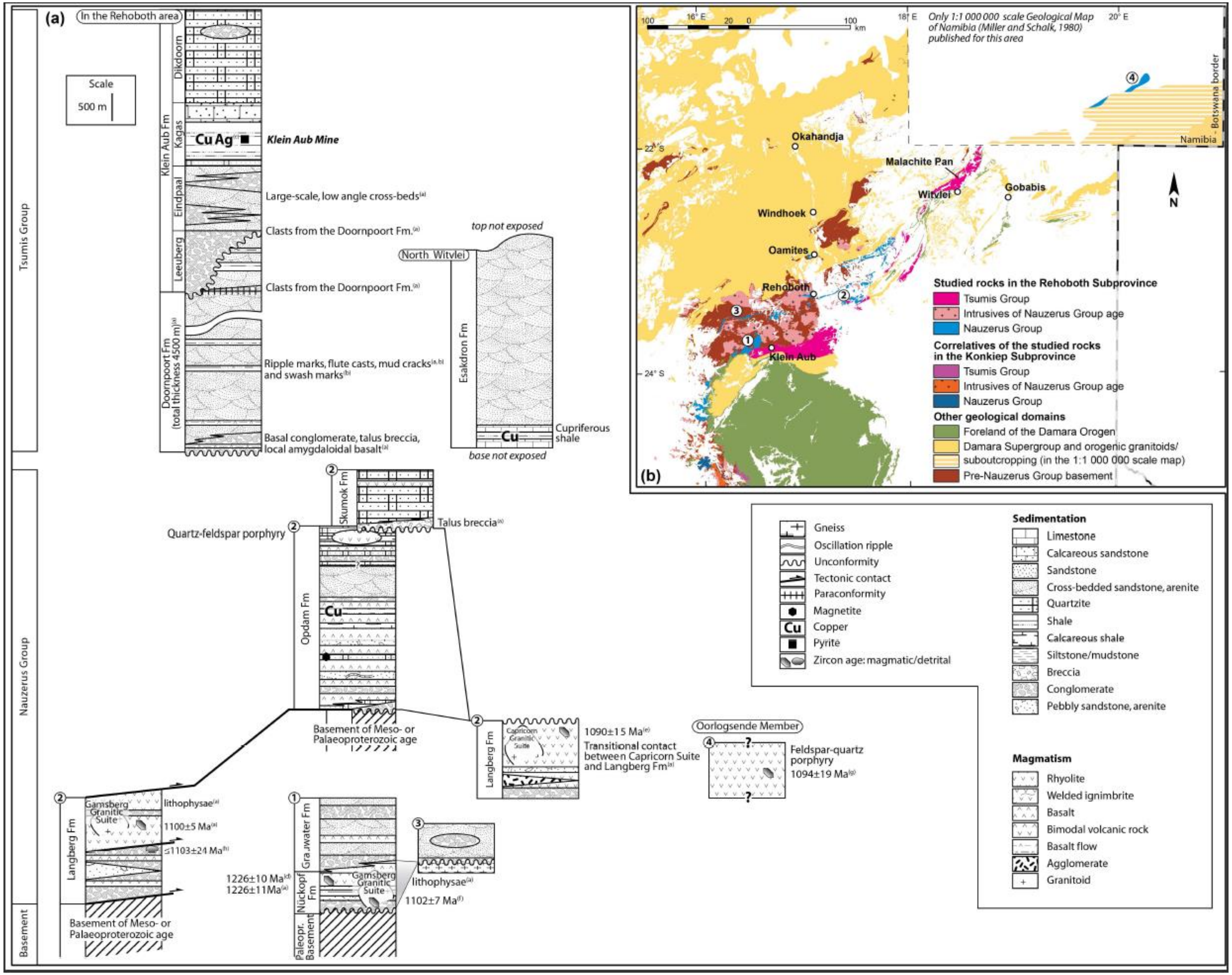

(a)
In the Rehoboth area
Scale
500 m
Tsumis Group
Nauzerus Group
Basement
Klein Aub Fm
Dikdoorn
Kagas
Eindpaal
Leeuberg
Doornpoort Fm (total thickness 4500 m)
Cu Ag
Klein Aub Mine
Large-scale, low angle cross-beds
Clasts from the Doornpoort Fm.
Clasts from the Doornpoort Fm.
Ripple marks, flute casts, mud cracks and swash marks
Basal conglomerate, talus breccia, local amygdaloidal basalt
North Witvlei
Esakdron Fm
top not exposed
Cu
Cupriferous shale
base not exposed
Skumok Fm
Talus breccia
Quartz-feldspar porphyry
Opdam Fm
Cu
Basement of Meso- or Palaeoproterozoic age
Langberg Fm
Capricorn Granitic Suite
1090±15 Ma
Transitional contact between Capricorn Suite and Langberg Fm
Oorlogsende Member
Feldspar-quartz porphyry
1094±19 Ma
Langberg Fm
Gamsberg Granitic Suite
lithophysae
1100±5 Ma
≤1103±24 Ma
Basement of Meso- or Palaeoproterozoic age
Gra.water Fm
Nückopf Fm
Paleopr. Basement
Gamsberg Granitic Suite
1226±10 Ma
1226±11Ma
lithophysae
1102±7 Ma
(b)
Only 1:1 000 000 scale Geological Map of Namibia (Miller and Schalk, 1980) published for this area
16° E
18° E
20° E
22° S
24° S
100 20 0 100 km
Okahandja
Windhoek
Oamites
Rehoboth
Klein Aub
Malachite Pan
Witvlei
Gobabis
Namibia
Botswana border
N
Studied rocks in the Rehoboth Subprovince
Tsumis Group
Intrusives of Nauzerus Group age
Nauzerus Group
Correlatives of the studied rocks in the Konkiep Subprovince
Tsumis Group
Intrusives of Nauzerus Group age
Nauzerus Group
Other geological domains
Foreland of the Damara Orogen
Damara Supergroup and orogenic granitoids/ suboutcropping (in the 1:1 000 000 scale map)
Pre-Nauzerus Group basement
Gneiss
Oscillation ripple
Unconformity
Tectonic contact
Paraconformity
Magnetite
Copper
Pyrite
Zircon age: magmatic/detrital
Sedimentation
Limestone
Calcareous sandstone
Sandstone
Cross-bedded sandstone, arenite
Quartzite
Shale
Calcareous shale
Siltstone/mudstone
Breccia
Conglomerate
Pebbly sandstone, arenite
Magmatism
Rhyolite
Welded ignimbrite
Basalt
Bimodal volcanic rock
Basalt flow
Agglomerate
Granitoid

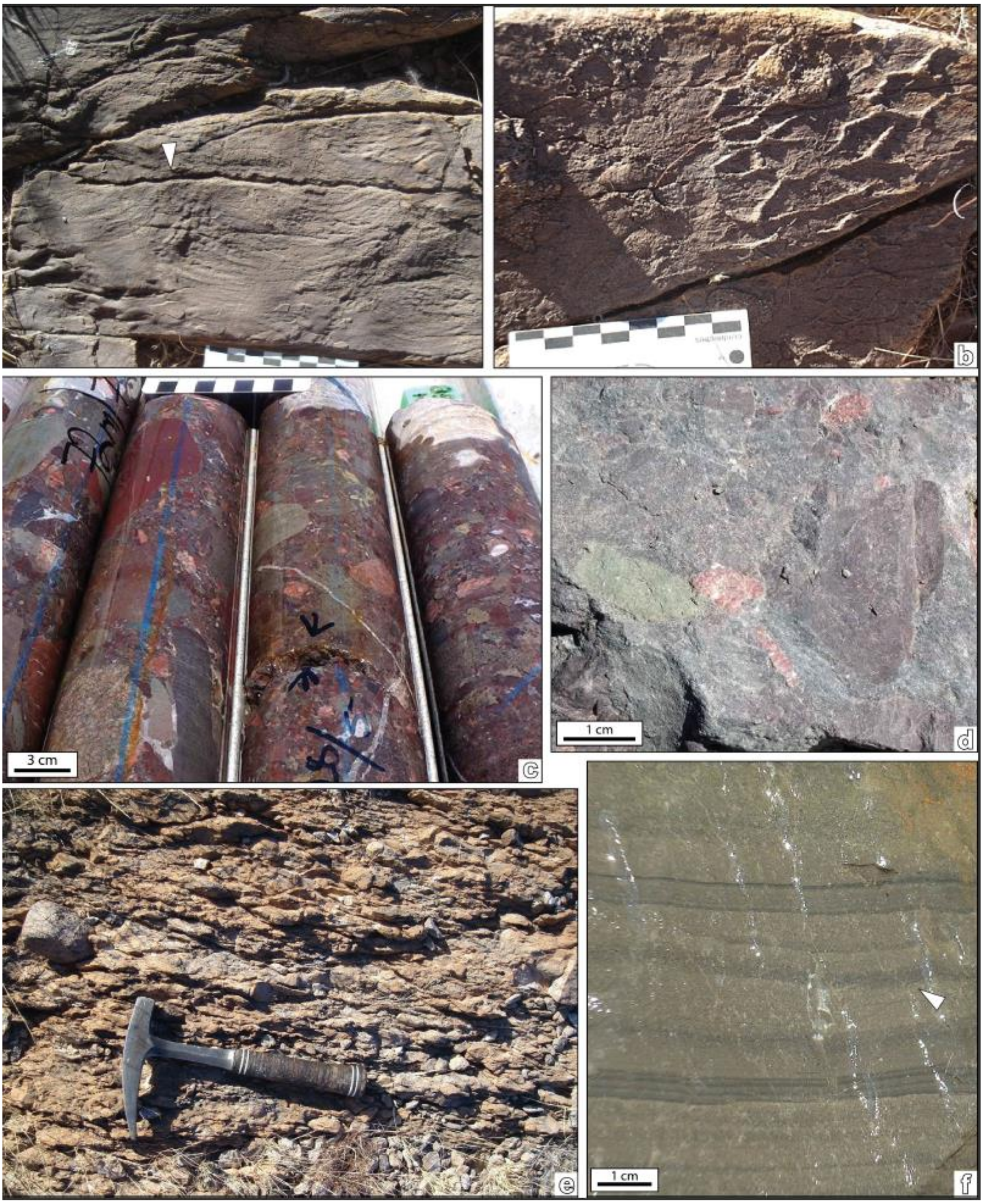
b
3 cm
c
1 cm
d
e
1 cm
f

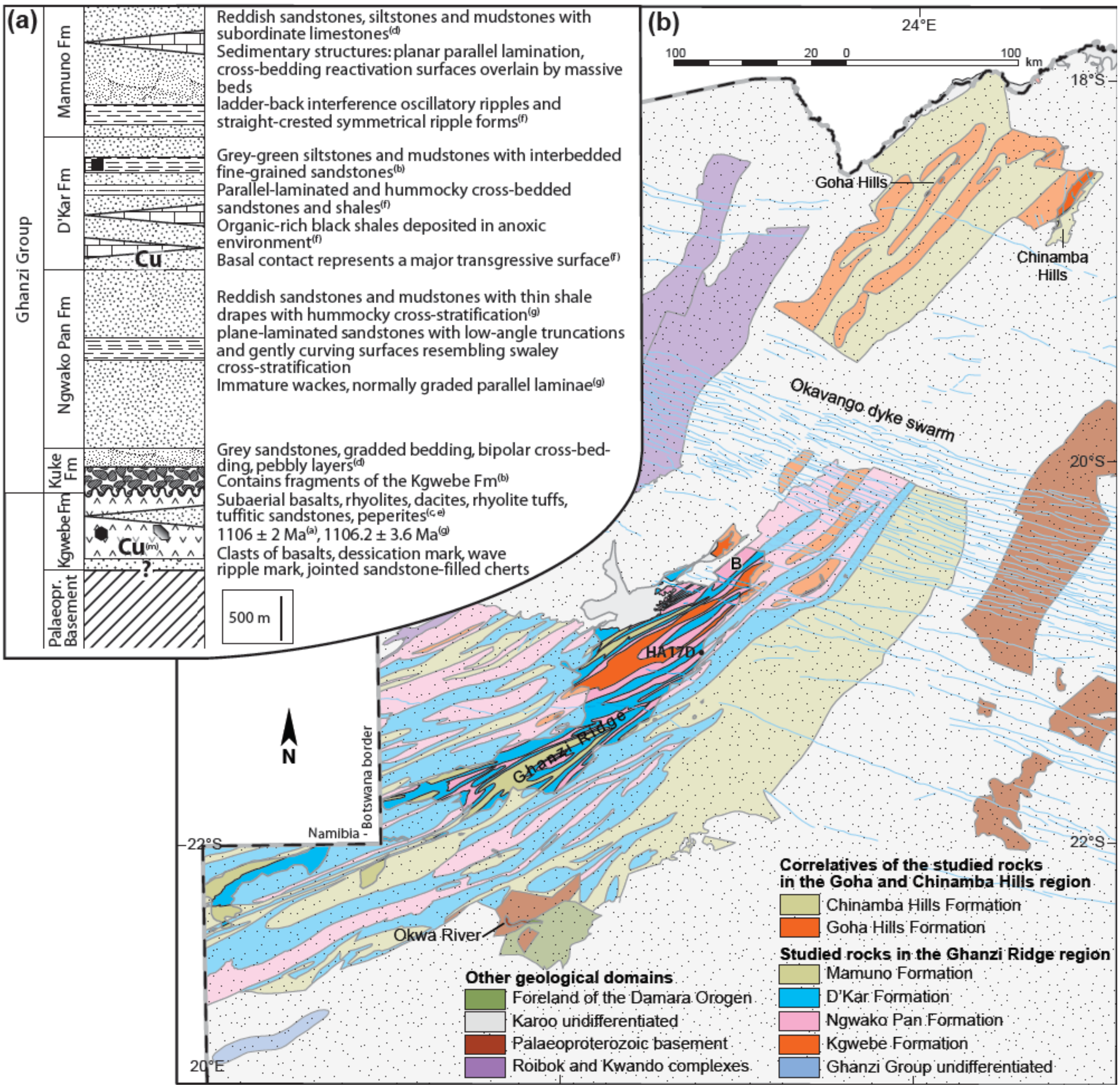

(a)
Ghanzi Group
Mamuno Fm
D'Kar Fm
Ngwako Pan Fm
Kuke Fm
Kgwebe Fm
Palaeopr. Basement
Cu
Cu(m)
?
Reddish sandstones, siltstones and mudstones with subordinate limestones(d)
Sedimentary structures: planar parallel lamination, cross-bedding reactivation surfaces overlain by massive beds
ladder-back interference oscillatory ripples and straight-crested symmetrical ripple forms(f)
Grey-green siltstones and mudstones with interbedded fine-grained sandstones(b)
Parallel-laminated and hummocky cross-bedded sandstones and shales(f)
Organic-rich black shales deposited in anoxic environment(f)
Basal contact represents a major transgressive surface(f)
Reddish sandstones and mudstones with thin shale drapes with hummocky cross-stratification(g)
plane-laminated sandstones with low-angle truncations and gently curving surfaces resembling swaley cross-stratification
Immature wackes, normally graded parallel laminae(g)
Grey sandstones, gradded bedding, bipolar cross-bedding, pebbly layers(d)
Contains fragments of the Kgwebe Fm(b)
Subaerial basalts, rhyolites, dacites, rhyolite tuffs, tuffitic sandstones, peperites(c,e)
1106 ± 2 Ma(a), 1106.2 ± 3.6 Ma(g)
Clasts of basalts, dessication mark, wave ripple mark, jointed sandstone-filled cherts
500 m
(b)
24°E
100 20 0 100 km
18°S
20°S
22°S
22°S
20°E
Goha Hills
Chinamba Hills
Okavango dyke swarm
B
HA17D
Ghanzi Ridge
Okwa River
N
Botswana border
Namibia
Correlatives of the studied rocks in the Goha and Chinamba Hills region
Chinamba Hills Formation
Goha Hills Formation
Studied rocks in the Ghanzi Ridge region
Mamuno Formation
D'Kar Formation
Ngwako Pan Formation
Kgwebe Formation
Ghanzi Group undifferentiated
Other geological domains
Foreland of the Damara Orogen
Karoo undifferentiated
Palaeoproterozoic basement
Roibok and Kwando complexes

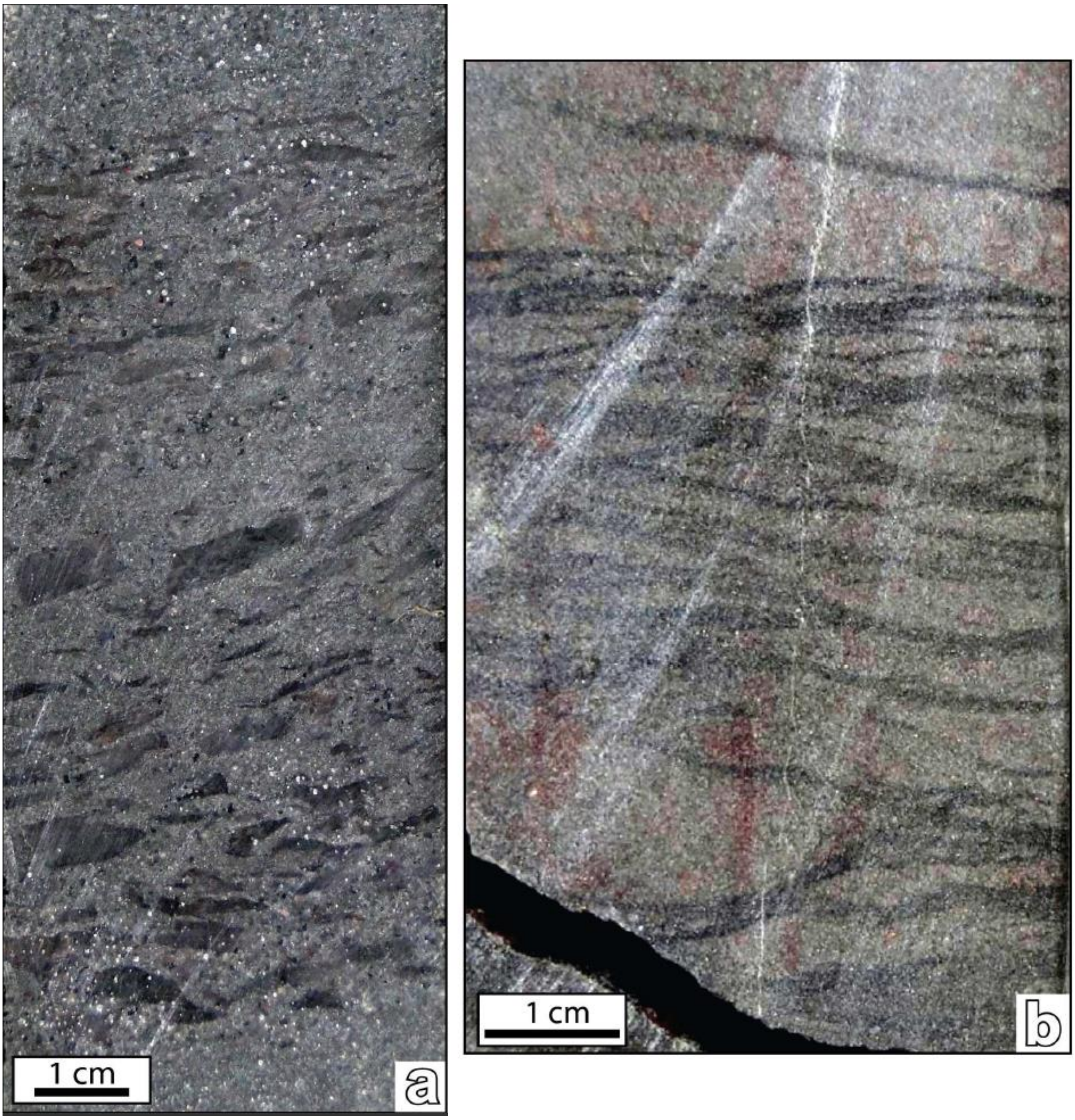
1 cm
a
1 cm
b


a
1 cm
b
1 cm
c
1 cm

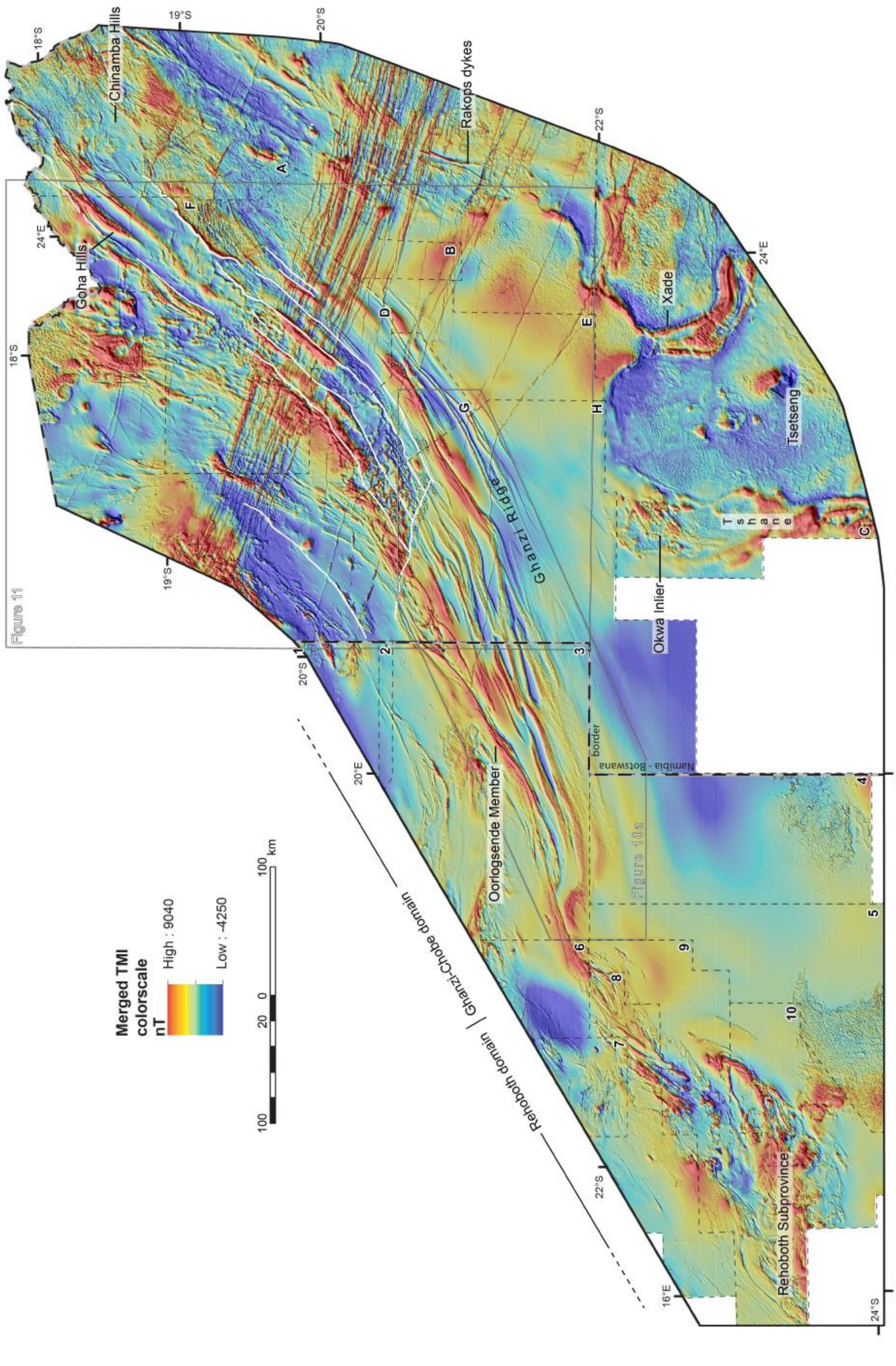

Merged TMI
colorscale
nT
High : 9040
Low : -4250
100
20
0
100 km
Chinamba Hills
Goha Hills
Rakops dykes
Ghanzi Ridge
Figure 11
Figure 10a
Oorlogsende Member
Namibia - Botswana
border
Okwa Inlier
Tshane
Xade
Tsetseng
Ghanzi-Chobe domain
Rehoboth domain
Rehoboth Subprovince
A
B
C
D
E
F
G
H
1
2
3
4
5
6
7
8
9
10
18°S
19°S
20°S
22°S
24°S
16°E
18°E
20°E
24°E

Lithostratigraphic unit	Lithology	Aiborne magnetic response in TMI, RTP 1VD and THDR	Magnetic image TMI	RTP 1VD	THDR
Chinamba and Goha Hills region					
Chinamba Hills	Carbonate-bearing siliciclastic rock	**TMI**: flat texture, low intensity, low frequency anomaly **RTP 1VD**: undulating texture, negative intensity, low frequency anomaly **THDR**: sublinear texture parallelel to margin of the magnetic body, medium to low intensity	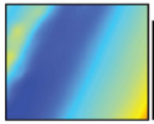	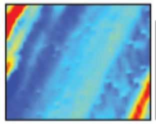	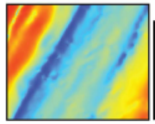
Goha Hills	Meta-felsic volcanic rock, volcaniclastic rock and chert	**TMI**: flat texture, high intensity, low frequency anomaly **RTP 1VD**: mottled texture, internal roughness sub-parallel to oblique to external margin. High intensity, high frequency anomaly **THDR**: mottled to sublinear texture, high intensity, high frequency anomaly	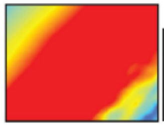	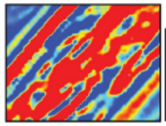	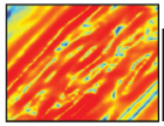
Ghanzi Ridge region					
Mamuno	Arkosic sandstone interbedded with siltstone, mudstone and limestone	**TMI**: flat texture, medium to low intensity, low frequency anomaly **RTP 1VD**: sublinear texture, relatively low intensity. Alternating internal high frequency positive and negative anomalies **THDR**: pronounced sublinear texture formed by alternating high frequency positive and negative anomalies . Relatively low magnetic intensity. Smooth transitions at magnetic body margins	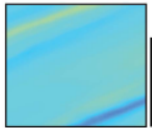	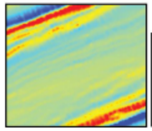	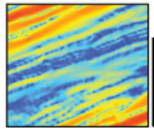
D'Kar	Reduced facies. Siltstone and mudstone interbedded with sandstone and limestone Monoclinic pyrrhotite and magnetite at the base and within the unit	**TMI**: elongate texture, high intensity, moderate to high frequency. Magnetic margins well-defined **RTP 1VD**: sublinear texture, positive high intensity & medium to high frequency anomaly. Highly magnetic basal contact **THDR**: sublinear texture, positive high intensity and high frequency anomaly.	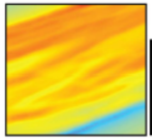	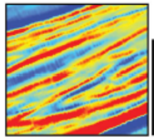	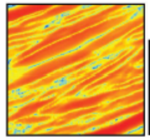
Ngwako Pan + Kuke?	Oxidised facies. Sandstone and mudstone	**TMI**: flat texture, low intensity, low frequency anomaly. Magnetic margins well-defined **RTP 1VD**: flat texture, low intensity, medium to low frequency anomaly. Magnetic margins well-defined **THDR**: sublinear texture, low intensity, medium to low frequency anomaly	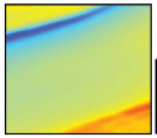	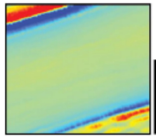	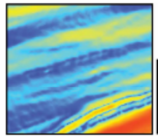
Kgwebe	Bimodal volcanic rock containing magnetite and volcaniclastic rock	**TMI**: undulose texture, high intensity, low frequency anomaly. Magnetic margins ill-defined **RTP 1VD**: mottled texture, internal roughness sub-parallel to oblique to external margin. Positive high intensity, high frequency anomaly **THDR**: undulose texture, high intensity, medium to high frequency anomaly		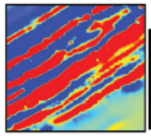	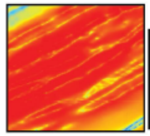
Eastern Namibia					
Oorlogsende Member	quartz-feldspar porphyry	**TMI**: elongate texture, medium to high intensity and medium to high frequency anomaly **RTP 1VD**: mottled texture, internal roughness sub-parallel to oblique to external margin. High intensity, high frequency anomaly **THDR**: mottled to sublinear texture, high intensity and high frequency anomaly	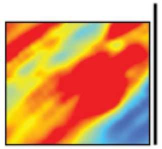	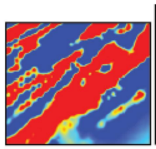	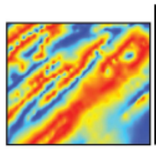

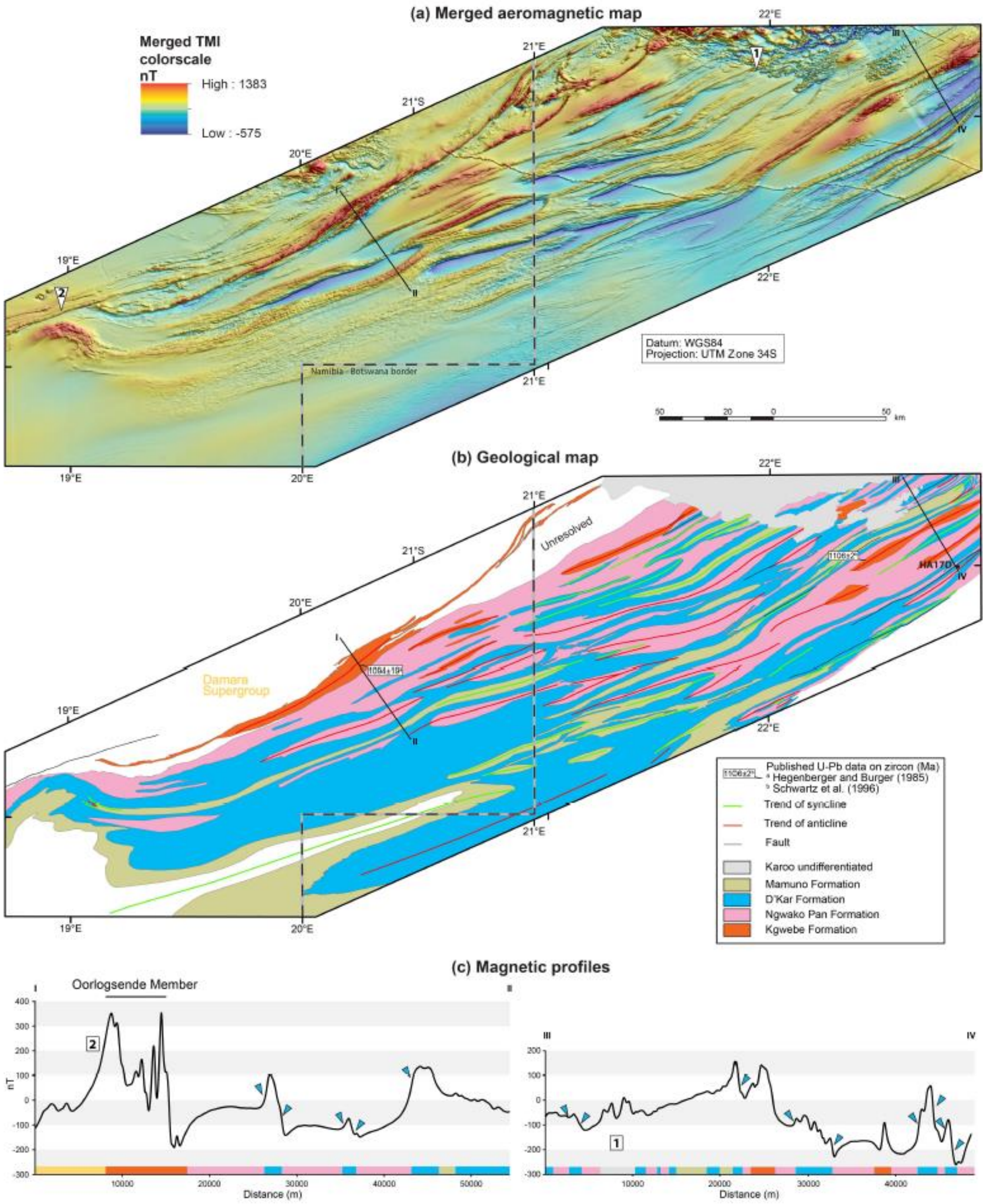
(a) Merged aeromagnetic map
Merged TMI
colorscale
nT
High : 1383
Low : -575
Datum: WGS84
Projection: UTM Zone 34S
Namibia - Botswana border
(b) Geological map
Unresolved
Damara
Supergroup
HA17D
Published U-Pb data on zircon (Ma)
a Hegenberger and Burger (1985)
b Schwartz et al. (1996)
Trend of syncline
Trend of anticline
Fault
Karoo undifferentiated
Mamuno Formation
D'Kar Formation
Ngwako Pan Formation
Kgwebe Formation
(c) Magnetic profiles
Oorlogsende Member
nT
Distance (m)
Distance (m)

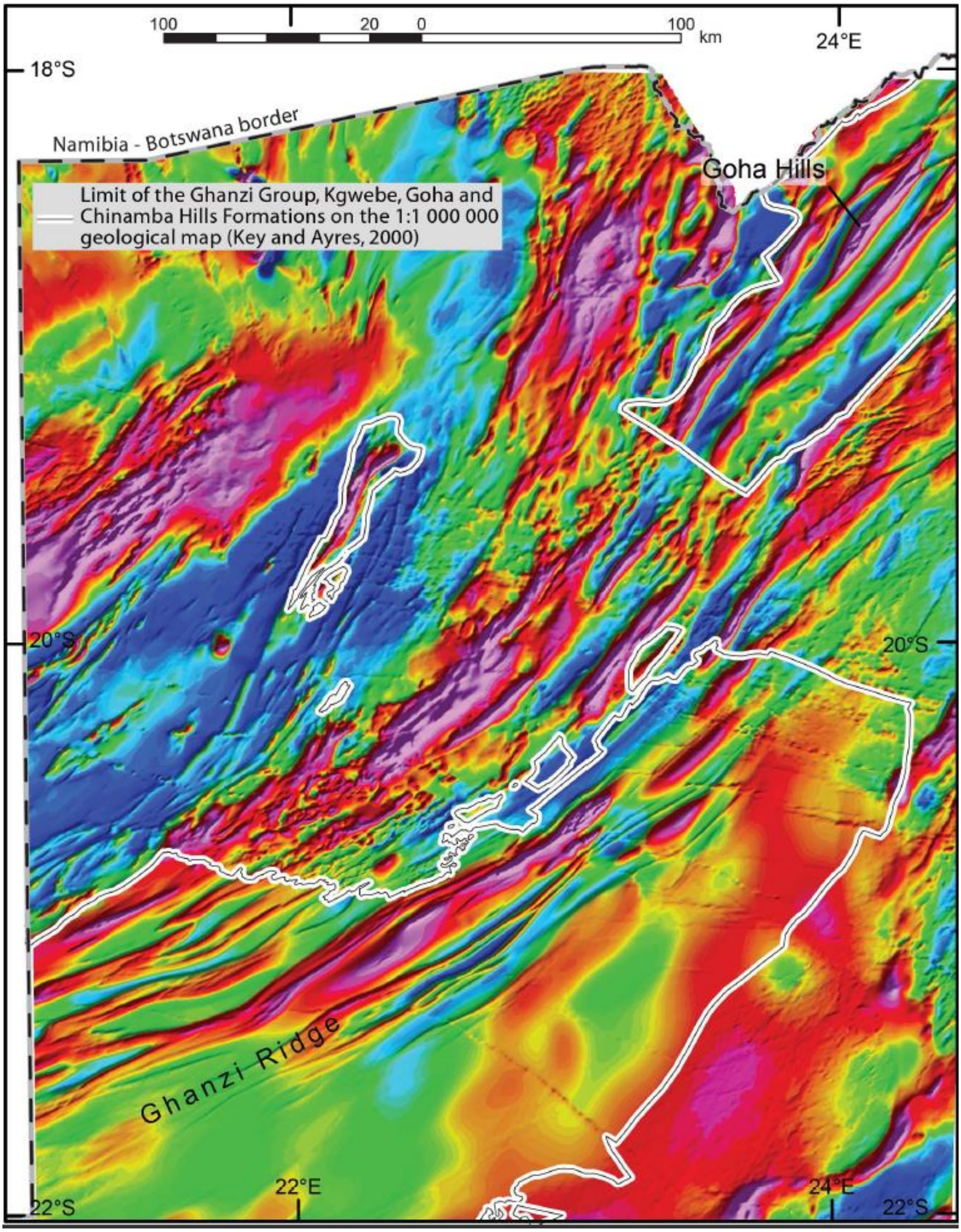

100
20
0
100
km
24°E
18°S
Namibia - Botswana border
Goha Hills
Limit of the Ghanzi Group, Kgwebe, Goha and Chinamba Hills Formations on the 1:1 000 000 geological map (Key and Ayres, 2000)
20°S
20°S
Ghanzi Ridge
22°E
24°E
22°S
22°S

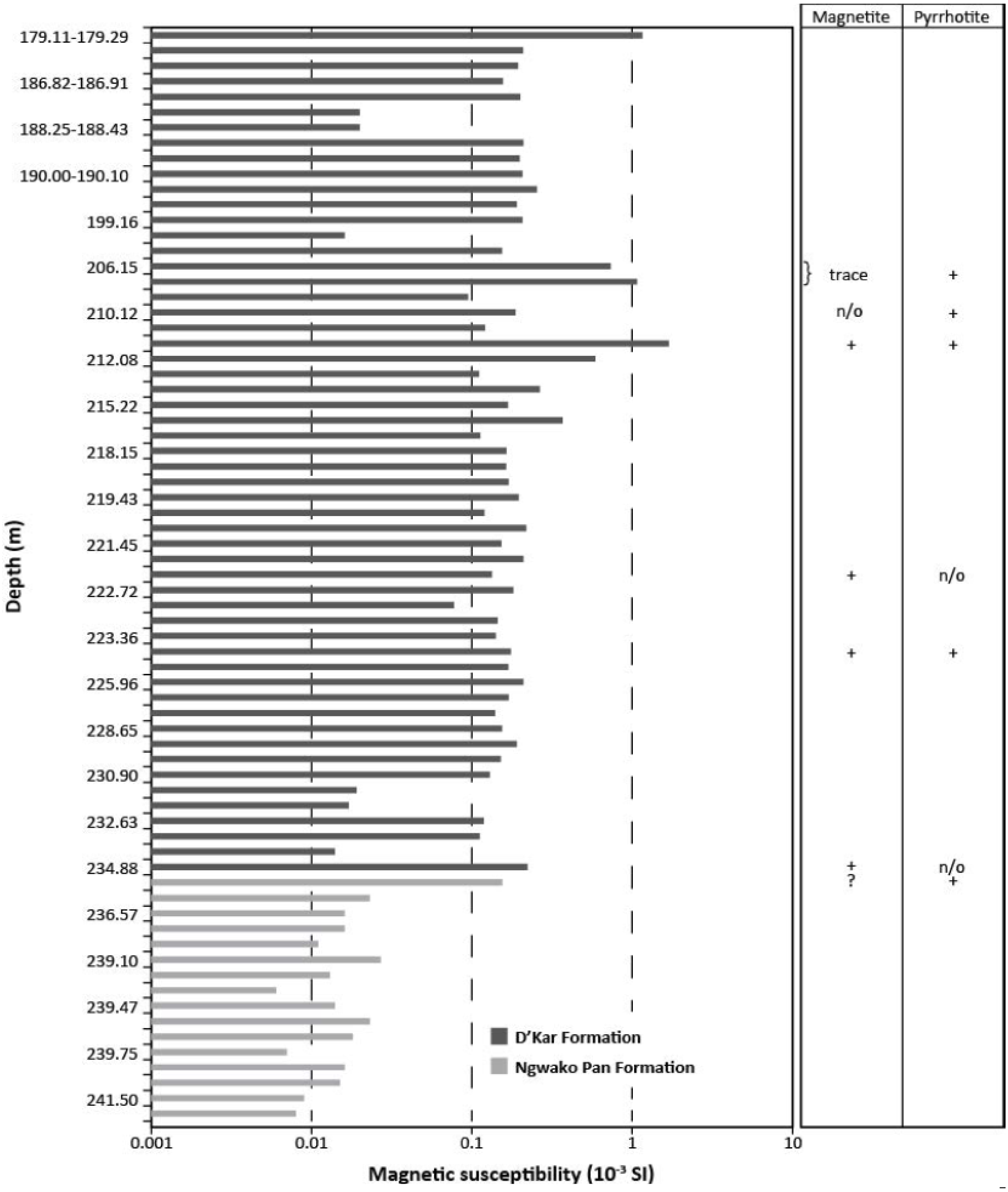
Magnetite
Pyrrhotite
179.11-179.29
186.82-186.91
188.25-188.43
190.00-190.10
199.16
206.15
210.12
212.08
215.22
218.15
219.43
221.45
222.72
223.36
225.96
228.65
230.90
232.63
234.88
236.57
239.10
239.47
239.75
241.50
Depth (m)
trace
n/o
+
?
0.001
0.01
0.1
1
10
Magnetic susceptibility (10⁻³ SI)
D'Kar Formation
Ngwako Pan Formation

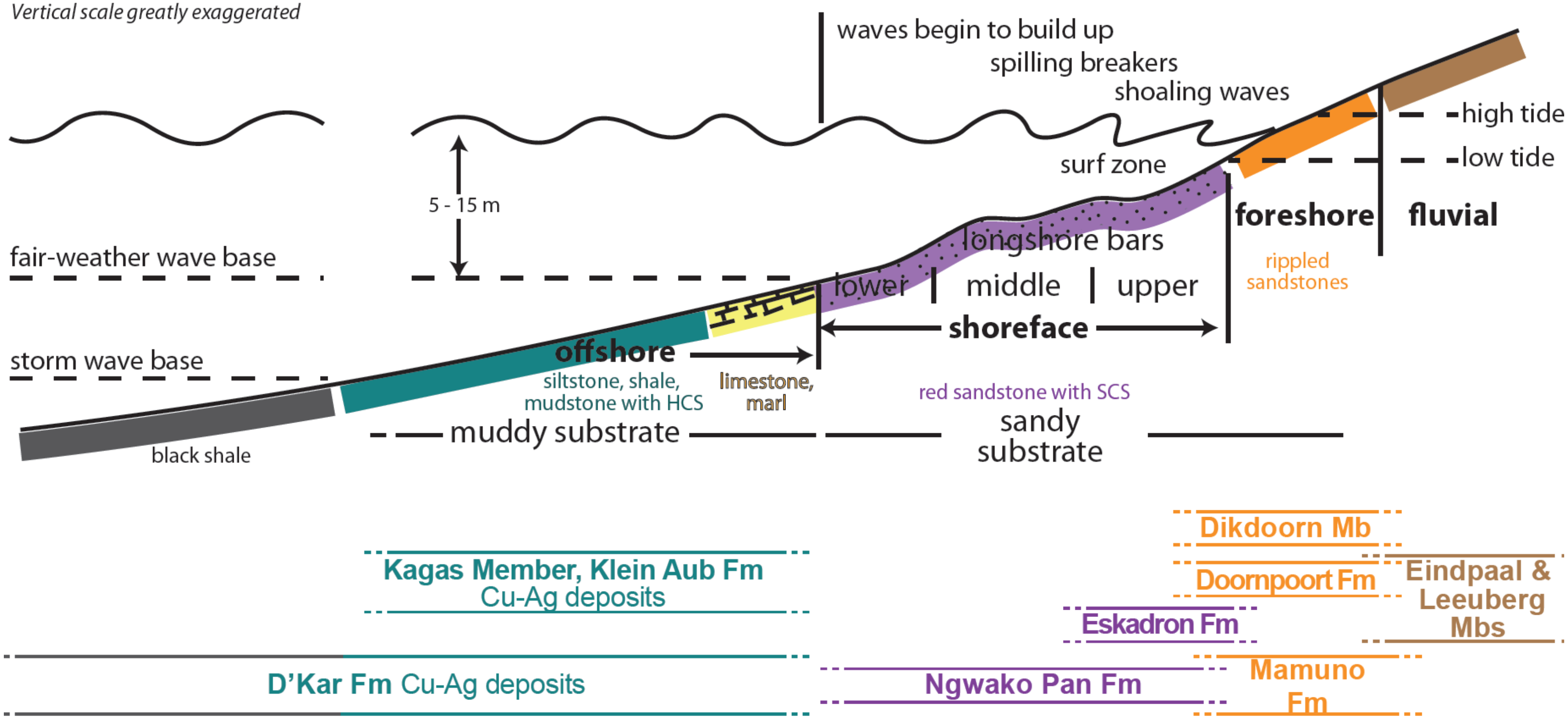
Vertical scale greatly exaggerated
waves begin to build up
spilling breakers
shoaling waves
surf zone
high tide
low tide
foreshore
fluvial
rippled sandstones
longshore bars
lower
middle
upper
shoreface
fair-weather wave base
5 - 15 m
storm wave base
offshore
siltstone, shale, mudstone with HCS
limestone, marl
red sandstone with SCS
black shale
muddy substrate
sandy substrate
Dikdoorn Mb
Kagas Member, Klein Aub Fm
Cu-Ag deposits
Doornpoort Fm
Eindpaal & Leeuberg Mbs
Eskadron Fm
D'Kar Fm Cu-Ag deposits
Ngwako Pan Fm
Mamuno Fm

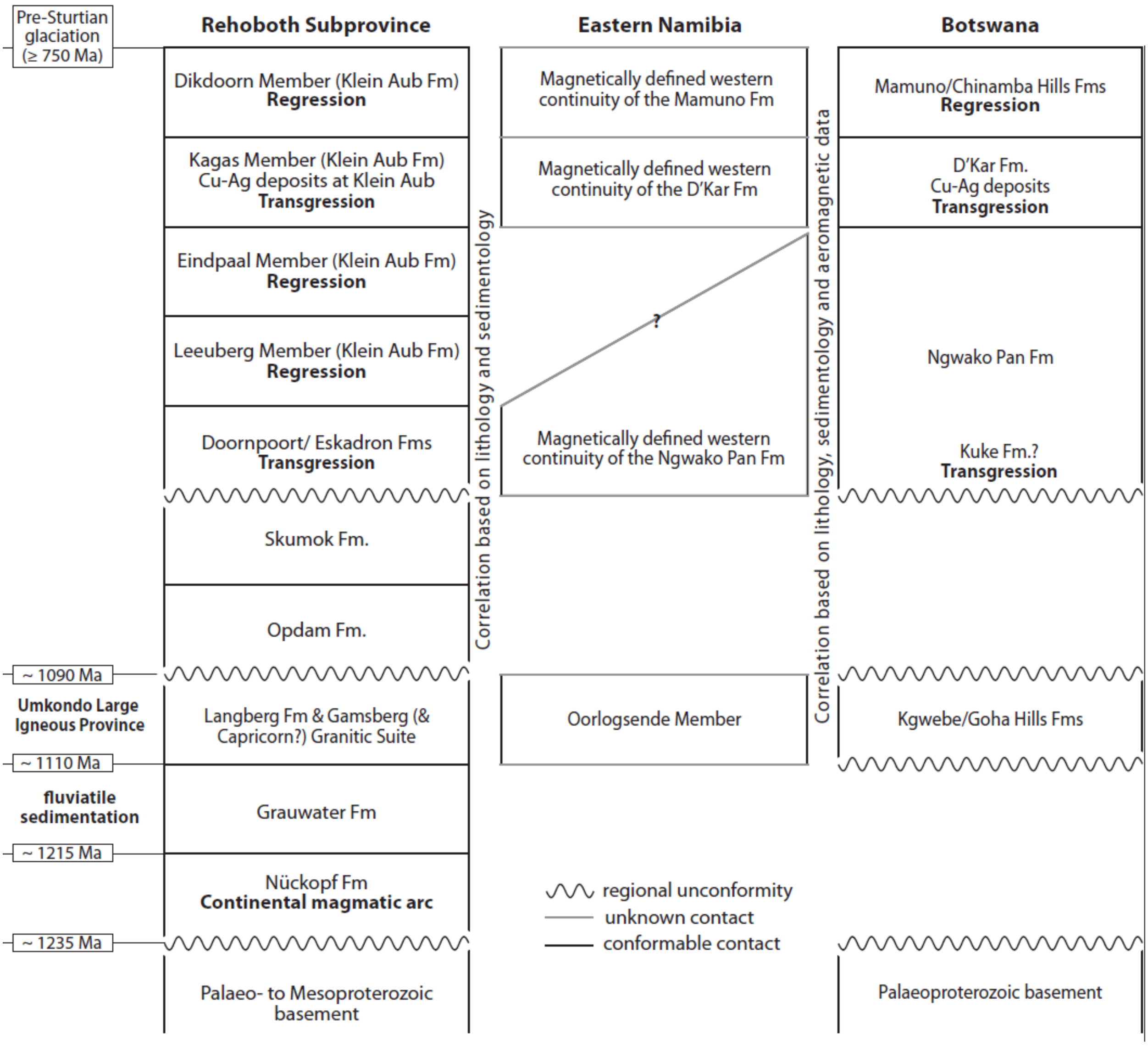
Pre-Sturtian glaciation (≥ 750 Ma)
Rehoboth Subprovince
Eastern Namibia
Botswana
Dikdoorn Member (Klein Aub Fm)
Regression
Kagas Member (Klein Aub Fm)
Cu-Ag deposits at Klein Aub
Transgression
Eindpaal Member (Klein Aub Fm)
Regression
Leeuberg Member (Klein Aub Fm)
Regression
Doornpoort/ Eskadron Fms
Transgression
Skumok Fm.
Opdam Fm.
Langberg Fm & Gamsberg (& Capricorn?) Granitic Suite
Grauwater Fm
Nückopf Fm
Continental magmatic arc
Palaeo- to Mesoproterozoic basement
Correlation based on lithology and sedimentology
Magnetically defined western continuity of the Mamuno Fm
Magnetically defined western continuity of the D'Kar Fm
?
Magnetically defined western continuity of the Ngwako Pan Fm
Oorlogsende Member
Correlation based on lithology, sedimentology and aeromagnetic data
Mamuno/Chinamba Hills Fms
Regression
D'Kar Fm.
Cu-Ag deposits
Transgression
Ngwako Pan Fm
Kuke Fm.?
Transgression
Kgwebe/Goha Hills Fms
Palaeoproterozoic basement
~ 1090 Ma
Umkondo Large Igneous Province
~ 1110 Ma
fluviatile sedimentation
~ 1215 Ma
~ 1235 Ma
regional unconformity
unknown contact
conformable contact

Appendix: Flight data acquisition parameters and specifications of individual magnetic surveys. The individual survey blocks are reported in Fig. 6.

In Namibia, high-resolution (200-250 m flight line spacing) aeromagnetic data collection started in 1994 and is still ongoing. All surveys were flown by consultant companies using fixed-wing aircrafts and Cesium-vapour magnetometers. The flight line spacing was 200 m (except for the Gam and Bushmanland surveys which were 250 m) with an average flight height of 80 m. Most of the surveys were flown in a north-south direction with a sampling rate of between 0.05 s to 0.1 s. Before merging the data the appropriate IGRF (International Geomagnetic Reference Field) was removed from each survey block by the contractor. The high-resolution survey blocks used in this study were supplied by the Geological Survey of Namibia.

Since 1993, the Geological Survey of Botswana contracted 15 high-resolution aeromagnetic surveys that cover approximately 90 % of Botswana. All surveys were flown with fixed-wing aircrafts at a flight line spacing of 250 m with and a nominal height of 80 m. A Scintrex CS-2 magnetometer was used with a sampling rate of 0.1 s. The surveys were flown perpendicular to the dominant structural trend. The IGRF (International Geomagnetic Reference Field) of each survey was removed prior to grid merging that was performed by the Geological Survey of Botswana.

The Namibian and Botswanan grids were gridded and levelled at a cell spacing of at 50 m using the minimum curvature algorithm (Briggs, 1974). The Gam and Bushmanland surveys were processed with the same method but at a cell spacing of 75 m, due to a grid resolution of 75 m. Then, the grid stitching was completed using the blending method in Oasis Montaj® (Geosoft®). The resulting stitched grid covers the entire KCB (Fig. 8). This method uses a blending function over the area of overlap so that the transition from one grid to the other is smooth. The blending function determines the weighting of one grid against the other inside the overlap region. It works by taking into account the relative proximity of the edges of the two grids to each position calculated; for instance, if a position is equidistant between both edges, its value is the average of the grid values found at that point. A "cosine" function is used which varies smoothly from 0 to 1, takes on a value of 0.5 at positions midway between two grids, and whose derivative approaches 0 at both ends. A static correction was applied where the grid overlap. The calculation was done using only the points which overlap with the other grid. The grids beyond the overlap regions remain unchanged.

Namibia

Survey block	Survey name	Line spacing (m)	Tie line spacing (m)	Orientation	Average flight height (m)	Magnetometer	Sampling interval (s)	Year of survey	Year of IGRF removal
1	Bushmanland	250	N/A*	15°	80	Cs vapour	0.1	1994	2005 Model
2	Gam	250	N/A	15°	80	Cs vapour	0.1	1994	1990 Model
3	Rietfontein	200	2500	N-S	80	Cs vapour	0.1	2001	2000 Model
4	Aminuis	200	2500	N-S	80	Cs vapour	0.1	2002	2000 Model
5	Steinhausen	200	2500	N-S	80	Cs vapour	0.1	2001	2000 Model
6	Kalahari	200	2500	N-S	80	Cs vapour	0.05	2007/2008	2000 Model
7	Hochfeld	200	2500	N-S	80	Cs vapour	0.1	1994/1995	1990 Model
8	Okahandja	200	2500	N-S	80	Cs vapour	0.1	2003	2000 Model
9	Hakos	200	2500	N-S	80	Cs vapour	0.1	1994/1995	1990 Model
10	Rehoboth	200	2500	N-S	80	Cs vapour	0.1	1999	1995 Model

Botswana

Survey block	Survey	Line spacing (m)	Tie line spacing (m)	Orientation	Average flight height (m)	Magnetometer	Sampling interval (s)	Year of survey	Year of IGRF removal
A	Chobe	250	2500	315°	80	Scintrex CS-2	0.1	2003	N/A
B	Boteti	250	N/A	N/A	80	N/A	N/A	2001	N/A
C	Kalahari	250	N/A	N/A	75	N/A	N/A	1996	N/A
D	Maun	250	N/A	N/A	80	N/A	N/A	1995	N/A
E	Deception Pan	250	2500	NE-SW	80	N/A	N/A	2004	N/A
F	Okavango	250	2500	345°	80	Scintrex CS-2	0.1	2003	N/A
G	Western Ngamiland	250	1250	330°	80	Scintrex CS-2	0.1	1996-1998	N/A
H	Ghanzi	250	1250	330°	80	N/A	N/A	1994	N/A

N/A* = not available

Appendix 3:

This appendix presents Rankin, W., Webb, S.J., Kiyan, D., Kinnaird, J.A., Jones, A.G., and Evans, R.L. (2013) in its published format. Consequently, the formatting, layout, figure and table numbering do not follow the layout of this dissertation.

Linking the Damara (Namibia) and Lufilian/Katangan (Zambia) Belts through Geophysical Interpretations

William Rankin[1], Susan J. Webb[1], Duygu Kiyan[2,3], Judith A. Kinnaird[1], Alan G.Jones[2], Rob L. Evans[4]

1. University of the Witwatersrand, South Africa
2. Dublin Institute for Advanced Studies, School of Cosmic Physics, Dublin, Ireland
3. National University of Ireland, Galway, Department of Earth and Ocean Science, Galway, Ireland
4. Woods Hole Oceanographic Institution, Woods Hole, MA, USA

ABSTRACT

The Damara Belt, (Namibia) and the Lufilian Arc/Katangan Belt, (Zambia) formed during the Pan-African orogeny (*ca*. 800 – 500 Ma) as a result of the collision of the composite Kalahari Craton, to the south, and the composite Congo Craton, to the north. Their connection is highly speculative due to Kalahari and Karoo cover and their extent holds both academic importance and economic interests as the Damara Belt is rich in Uranium (U) and the Lufilian Arc in Copper-cobalt (Cu-Co) mineralisation.

Due to limited outcrops on the border of Namibia and Botswana, geophysical techniques have become the main approach in constraining the possible extent of these belts. This study involves the interpretation of aeromagnetic and gravity datasets supplied by Rio Tinto complemented by regional-scale magnetotelluric (MT) data from the South African MagneTotelluric Experiment (SAMTEX) project. Three 400 km long potential field profiles are being modelled in Oasis Montaj using GM-SYS. These profiles intend to show the folding style of the Ghanzi-Chobe Belt, extent of the Matchless Amphibolite Belt (MAB) and contribute to the understanding of the strong remanent negative feature seen in northern Namibia. Potential field data as well as complementary MT data from SAMTEX were used, augmented by recent MT data acquired as part of the NSF Incipient Rifting project. Three roughly N-S MT profiles were analysed and modelled; DMB, NEN, OKA-CAM, listed west to east. The geoelectric strike analysis of the MT data shows different strike results for the upper 5 km of the crust compared to the strike results for 5 – 15 km of the crust. The strike angle increases from approximately 47° in the west to 85° in the east. These data will contribute to a better understanding of the tectonic evolution of these mobile belts and cratons by their incorporation into an interpretative sub-Kalahari geological map of the Kalahari Desert area.

Key words: Potential fields, Geophysical modelling, Damara, Lufilian, Pan-African

INTRODUCTION

The Damara Belt (Namibia), Ghanzi-Chobe Belt (Botswana) and the Katangan Belt\Lufilian Arc (referred to here as the Lufilian Arc; Zambia) constitute the focus of this study. They are Neoproterozoic mobile belts that formed during the tectonothermal Pan-African orogeny *ca*. 800 – 500 Ma (Miller, 1983; Porada, 1989; through the accretion of various cratons (Kennedy, 1964; Gray et al., 2008). The northern most of these belts is the Lufilian Arc. It is curvilinear in shape and is flanked by two additional north-south trending Neoproterozoic orogens; the Mozambique Belt to the east and the West Congo, Kaoko and Gariep Belts to the west (Kampunzu et al., 2009). These belts are thought to be linked by a third transcontinental orogen composed of the Damara Belt, Ghanzi-Chobe Belt and the Lufilian Arc and Zambezi Belt. The Lufilian Arc and Zambezi Belt are separated by the transcurrent Mwembeshi Dislocation Zone (MDZ) (Unrug, 1983). The Southern Zone of the Damara Belt contains the Matchless Amphibolite Belt (MAB). The MAB is a narrow belt comprising mid ocean ridge basalts (MORB) which are hosted in metasediments (Breitkopf and Maiden, 1998). The MAB is proposed to be part of the suture zone between the Kalahari and Congo cratons (Figure 1; Unrug, 1983).

Due to a lack of outcrop and research boreholes drilled in northern Botswana, direct observation in the field is limited (Singletary et al., 2003). Geophysical studies have become the main technique to constrain the direct connection between the belts. Early gravity data (Mazac, 1974) collected over Zambia suggested that the Lufilian Arc connects with the West Congo Belt, while more recent aeromagnetic studies by Eberle et al. (1995; 1996) and Corner (2008) indicated that the Lufilian Arc is probably connected with the north- east trending Damara Belt. In addition, the evolution and origin of these Neoproterozoic belts are not well defined.

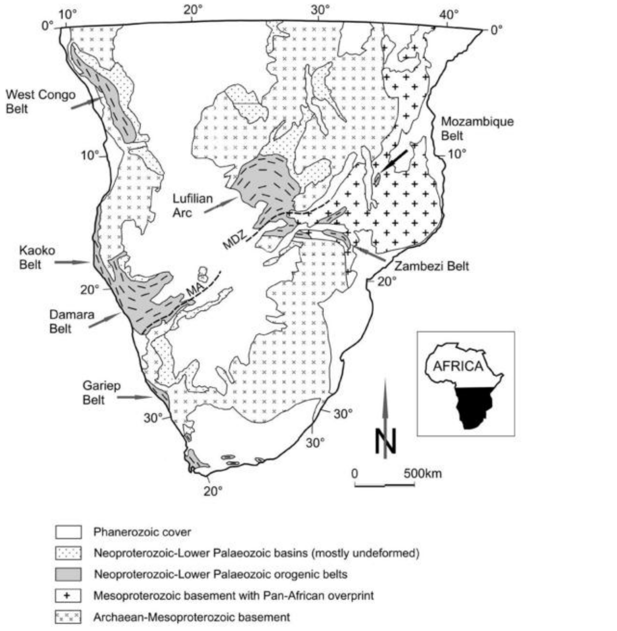

Figure 1: Basic geological map of southern Africa showing Archaean-Mesoproterozoic basement, Mesoproterozoic basement with Pan-African overprint, Neoproterozoic-Lower Palaeozoic orogenic belts and basins and Phanerozoic cover (Kampunzu et al., 2009). MA is the Matchless Amphibolite, MSZ is the Mwembeshi Shear Zone and GCB is the Ghanzi-Chobe Belt, which is covered by Kalahari sands.

Two contrasting models currently exist: the first favours the formation of an intracontinental setting (Daly, 1986; Hanson et al., 1994) and the second requires the development of an ocean basin (Barnes and Sawyer, 1980; Porada and Berhorst, 2000). These studies have also led to several proposed geodynamic models for the formation and connection of these mobile belts (Porada, 1989; Porada and Berhorst, 2000).

The aim of this study is to gain a better understanding of the sub-Kalahari geology and its tectonic evolution through the interpretation of potential field and magnetotelluric (MT) datasets of the South African MagneTotelluric Experiment (SAMTEX). Of particular interest are the cratonic boundaries (Kalahari and Congo), and the extent of the Ghanzi-Chobe Belt, Matchless Amphibolite Belt (MAB). In addition to this there is also a strong focus on a strong negative feature that Eberle et al. (1996) described as a remanent body that could possibly be a suture zone, failed rift or subduction zone beneath the Congo Craton. However, Corner (2008) interprets this magnetic low as the Autseib Lineament and in parts the Autseib thrust fault.

The area of interest straddles the border between Namibia and Botswana where potential field modelling is currently being performed on three roughly north-south trending profiles. Additionally, three MT profiles have also been modeled; DMB, NEN (situated in Namibia), and OKA-CAM (situated in Botswana). These profiles were selected to constrain the potential field models (Figure 2).

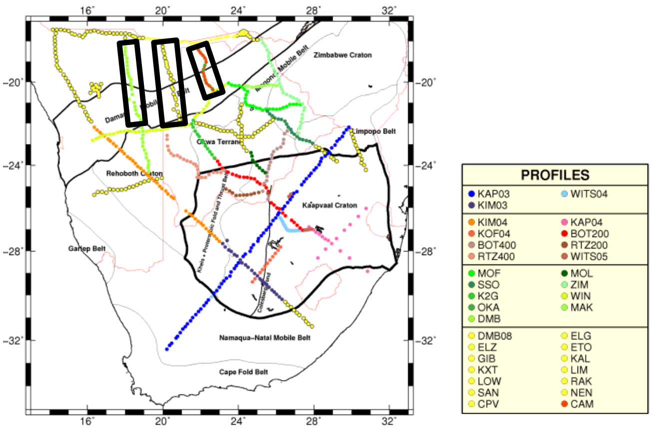

Figure 2: Location of the magnetotelluric stations for the SAMTEX project. The coloured circles represent the locations of stations in the various phases of the project, along with data donated by de Beers (Jones et al., 2009). The black circles are locations of teleseismic stations associated with the Southern Africa Seismic Experiment. The three MT profile lines used in the study are in the rectangles with the name of the respective profile.

METHOD AND RESULTS

The potential field datasets were supplied by Rio Tinto and consist of aeromagnetic data of Namibia, Caprivi, Botswana and Zambia at a grid cell size of 200 m, 50 m, 50 m, and 250 m respectively. The station spacing of the gravity data varies from country to country, with a complete Bouguer gravity map which is gridded at 2.2 km.

The steps currently being taken are: (i) picking of geological lineaments and polygon interpretation on the aeromagnetic data. From the interpretation of the magnetic signal of the various units (Table 1) and the trend of the lineaments, a geological sub Kalahari map is being built. (ii) Three N-S approximately 400 km long, forward models of the potential field data, which are being modelled using Oasis Montaj, GM-SYS extension. These models are used to examine the fold structures of the Ghazi-Chobe Belt and the possible extent of the MAB. They also attempt to evaluate to the possible cause of the strong negative feature.

The DMB profile is the western-most profile in this study. The profile runs in an approximately N-S direction and is approximately 660 km long. It consists of 35 broad-band MT (BBMT) stations. These stations were deployed at approximately 20 km along the DMB profile. The NEN profile is a 440 km long, approximately N-S profile that is composed of 23 BBMT stations. These stations were deployed at approximately 20 km intervals along the profile. The OKA-CAM profile is the most eastern profile in the study area. In 2006, BBMT data were acquired at a total of 15 locations with a station spacing of 20 km along the OKA profile. In 2009, the CAM data were collected along the OKA line with a station spacing of approximately 5 km. It comprises 32 BBMT sites.

An advanced version of the multi-site, multi-frequency McNeice and Jones (2001) distortion decomposition, based on the Groom and Bailey decomposition (Groom and Bailey, 1989; Groom et al., 1993), was applied to the MT responses to analyse the responses for galvanic distortions and to determine the most consistent geoelectric strike direction. We performed the latest version of the *strike* code of *McNeice and Jones (2001)*, which allows for a choice of data based on a depth-band selection, to the data set of three profiles for the crustal depth ranges (1 – 5 km, 5-15 km and 1-35 km). The analysis shows a best fitting strike angle of 47^o, 64^o and 85^o E of N for DMB, NEN and OKA-CAM lines, respectively.

The distortion removed and edited MT responses were modelled using both Occam (Constable et al., 1987) and layered 1-D modelling approaches, as implemented in WinGLink® software.

The next steps are (i) to model the resulting distortion-free responses using two-dimensional (2-D) smooth inversion method of Rodi and Mackie (2001), and (ii) to perform three-dimensional (3-D) inversion on the complete data set using the code of Egbert and Kelbert (2012).

CONCLUSIONS

Preliminary interpretations from the potential field data suggest a continuation of the Ghanzi-Chobe Belt into the Rehoboth Terrane, south of the Damara Belt. The possible continuation of the MAB can be seen by elongated strong magnetic and gravity highs signals. The forward models suggest that the Ghanzi-Chobe Belt is a series of isoclinal folds.
The geoelectric strike direction determined for the three MT profiles suggest that the upper 5 km of the crust has a similar strike to that seen in the magnetic data. For the depth range of 5 – 15 km, the strike angle changes, suggesting different geological units or a single geological unit that has varying strike with depth. The 1-D inversion models show a conductive body with a NE-SW trend that is most prominent in the NEN model between the stations NEN014 and NEN 018. The conductive anomaly has been interpreted to be the continuation of the Damara Belt into the Ghanzi-Chobe Belt by Khoza et al. (2012, (submitted)).

ACKNOWLEDGMENTS

We would like to acknowledge the University of the Witwatersrand for financial support, Rio Tinto for supplying the geophysical and geological data sets, and the Dublin Institute for Advanced Studies (DIAS) for the use of the SAMTEX data. Thank you to Oasis Montaj, Geosoft for extension of the various GX's.

REFERENCES

Barnes, S. –J., and Sawyer, E. W. (1980). An alternative model for the Damara Mobile Belt. Ocean crust subduction and continental convergence. *Precambrian Research*. **13,** pp. 297-336.

Breitkopf, J.H., and Maiden, K.J. (1988). Tectonic setting of the Matchless Belt pyritic copper deposits, Namibia. *Economic Geology.* **83,** pp. 710 – 723.

Corner, B. (2008). The crustal framework of Namibia derived from an integrated interpretation of geophysical and geological data. *In:* Miller, R. McG. (ed.) *The Geology of Namibia: Archaean to Mesoproterozoic.* **1.** Ministry of Mines and Energy, Geological Survey of Namibia, Windhoek. pp. 1 – 19.

Constable, S. C., R. L. Parker, and C. G. Constable (1987). Occam's inversion: A practical algorithm for generating smooth models from electromagnetic sounding data, *Geophysics*, ***52,*** pp. 289-300.

Daly, M.C. (1986a). The intracratonic Irumide belt of Zambia and its bearing on collision orogeny during the Proterozoic of Africa. *In:* Coward, M.P., and Ries, A.C. (eds.) Collision tectonics, *Geological Society of London Special Publication.* **19,** pp. 321 – 328.

de Wit, M. (2009). *Tsodilo Resources Ltd drills extension of Zambian copper belt-like mineralisation in Pan African Basement of northwest Botswsana.* [WWW]. http://www.tsodiloresources.com/i/pdf/2009-03-23_THDMPAB.pdf, (February 4th, 2012).

Eberle, D., Andritzky, G., and Wackerle, R. (1995). The new magnetic data set of Namibia: Its contributions to the understanding of crustal evolution and regional distribution of mineralisation. *Communications of the Geological Survey of Namibia.* **10,** pp. 141 – 150.

Eberle, D., Hutchins, D.G., Rebeck, R.J., and Somerton, I. (1996). Compilation of the Namibian airborne magnetic surveys: procedures, problems and results. *Journal of African Earth Sciences,* **22,** pp. 191 – 205.

Egbert, D. G., & Kelbert, A., 2012. Computational recipes for electromagnetic inverse problems. *Geophysical Journal International*, **189,** pp. 251-267.

Gray, D.R., Foster, D.A., Meert, J.G., Goscombe, B.D., Armstrong, R., Trouw, R.A.J., and Passchier, C.W. (2008). A Damara orogen perspective on the assembly of southwestern Gondwana. *Geological Society, special publications*, London. **294,** pp. 257 – 278.

Groom, R. W. and Bailey, R. C., 1989. Decomposition of magnetotelluric impedance tensors in the presence of local three dimensional galvanic distortion. Journal of Geophysical Research 94, pp. 1913-1925.

Groom, R. W., R. D. Kurtz, A. G. Jones, and D. E. Boerner (1993), A quantitative methodology for determining the dimensionality of conductive structure from magnetotelluric data, *Geophysical Journal International*, ***115,*** pp. 1095-1118.
Hanson, R.E., Wilson, T.J., and Munyanyiwa, H. (1994). Geologic evolution of the Neoproterozoic Zambezi orogenic belt in Zambia. *Journal of African Earth Sciences.* **18,** pp. 135 – 150.

Jones, A.G., Evans, R.L., Muller, M.R., Hamilton, M.P., Miensopust, M.P., Garcia, X., Cole, P., Ngwisanyi, T., Hutchins, D., Fourie, C.J.S., Jelsma, H., Evans, S., Aravanis, T., Pettit, W., Webb. S., Wasborg., and The SAMTEX Team. (2009). Area selection for diamonds using magnetotellurics: Example from southern Africa. *Lithos*, Elsevier. **112,** pp. 83 – 92.

Kampunzu, A.B., Cailteux, J.L.H., Kamona, A.F., Intiomale, M.M., and Melcher, F. (2009). Sediment-hosted Zn-Pb-Cu deposits in the Central African Copperbelt. *Ore Geology Reviews,* Elsevier. **35,** pp. 263 – 297.

Kennedy, W.Q. (1964). The structural differentiation of Africa in the Pan-African (± 500 m.y.) tectonic episode, 8th *Annual Report of the Research Institute of African Geology*, University of Leeds, pp. 9 – 11.

Khoza, T.D., Jones, A.G., Muller, M.R., Evans, R.L., Miensopust, M.P., Webb, S.J., and the SAMTEX Team (2012). Review of "Lithospheric structure of an Archean craton and adjacent mobile belt revealed from 2D and 3D inversion of magnetotelluric data: example from southern Congo craton in northern Namibia". (Submitted). Dublin Institute for Advanced Studies, Dublin, 64 pp.

Mazac, O. (1974). Reconnaissance gravity survey of Zambia. *Geological Survey of Zambia Technical Report.* **76,** 44 pp.
McNeice, G. W. and Jones, A. G., 2001. Multisite, multi-frequency tensor decomposition of magnetotelluric data. Geophysics **66,** pp. 158-173.
Miller, R. McG. (1983). The Pan – African Damara orogen of Namibia. *In:* Miller, R. McG. (ed.) *Evolution of the Damara orogen of south west Africa/ Namibia*. Geological Society of South African Special Publications. **11,** pp. 431 – 515.

Porada, H. (1989). Pan – African rifting and orogenesis in southern to Equatorial Africa and eastern Brazil. *PreCAMbrian Research.* **44,** pp. 103 – 136.

Porada, H., and Berhorst, V. (2000). Towards a new understanding of the Neoproterozoic – Early Palaeozoic Lufilian and northern Zambezi Belts in Zambia and the Democratic Republic of Congo. *Journal of African Earth Sciences,* Elsevier Science Ltd, Great Britain. **30,** pp. 727 – 771.

Rodi, W. and Mackie, R. L., 2001. Nonlinear conjugate gradients algorithm for 2-D magnetotelluric inversion. Geophysics **66**, pp. 174-187.

Singletary, S.J., Hanson, R.E., Martin, M.W., Crowley, J.L., Bowing, S.A., Key, R.M., RamOKAte, L.V., Direng, B.B., and Krol., M.A. (2003). Geochronology of basement rocks in the Kalahari Desert, Botswana, and implications for regional Proterozoic tectonics. *PreCAMbrian Research,* Elsevier. **121,** pp. 47 – 71.

Unrug, R. (1983). The Lufilian Arc: A microplate in the Pan-African collision zone of the Congo and the Kalahari cratons. *PreCAMbrian Research*, Elsevier Science, Amsterdam, The Netherlands. **21,** pp. 181 – 169.

Table 1: Lithological units with their respective magnetic signals present in the study area.

Supergroup	Group	Volcanics	Formation	Lithology	Magnetic Signal
Upper Karoo	Lebung		Unknown	Orange, red or white sandstone, locally calcareous with reddish siltstone	Intermediate smooth flat signal
		Karoo Volcanics		Dolerite/basalt	High amplitude, high frequency with a molted noisy texture
		Karoo Basalts		Flood basalts with variable amygdaloidal with minor siliclastic sedimentary interbeds and lenses	High amplitude, intermediate frequency with a smooth mottled texture. Generally a NE - SW trend can be seen in the signal
	Aha Hills		Unknown	Chert-rich limestone and dolomite	Intermediate to low smooth domains
	Roibok		Unknown	Amphibolite and mafic schist interleaved with felsic gneiss and pelitic schist	Defined by a narrow elongated belt of strong anomalies
	Tsodilo Hills		Unknown	Kyanite grade quartz-muscovite schists and ferruginous quartzites with laterally continuous units of ironstone	Ironstone units produce High frequency, high amplitude anomalies is a curvilinear trend
	Koanaka		Unknown	Metasedimentary rocks and possibly paragneiss ?	Low to intermediate smooth domains
		Chihabadum Complex		Inferred to comprise igneous and meta-igneous rocks	Noisy domain with elongated strong NE trending anomalies
		Quangwadum Complex		Augen gneiss and granite with metamorphosed sedimentary rocks	Noisy NE trending strong anomalies
	Xaudum		Unknown	Very low grade sandstone, siltstone, and chert-bearing carbonate rock	Low to moderate smooth domains
		kwando Complex		Granite gneiss, granite, amphibole-gneiss, migmatite and metadolerite	Domain is mainly quiet with pronounced NNE structural trends.
	Ghanzi		Mamuno	Red bed facies - Sandstone and mudstones	Generally low amplitudes that contain some high frequency units
			D'Kar	Dark grey-green facies - sandstone and mudstone	Sharp high amplitude, high frequency
			Ngwako Pan	Red bed facies - sandstone and mudstone.	low amplitudes with a smooth texture i.e. generally a quiet blue domain
	Sinclair	Kgwebe		Metavolcaincs and metasediments	High amplitude, high frequency. That generally displays pre-folded internal layers

Appendix 4:

Density measurements collected on lithologies from Namibia, northwestern Botswana and Zambia

Sample No.	UTM_X	UTM_Y	Zone	Suite	Supergroup
Cu Valley	438912.16	7764051.05	Kamanjab Inlier	Huab	
IHELA	605739	751564	southern Central Zone		Damara
IIKAR13	477626	7640783	Southern Kaoko or Ugab Zone		Damara
IIUIS11	487973	7653316	Southern Kaoko or Ugab Zone		Damara
IIUIS4	487868	7653543	Southern Kaoko or Ugab Zone		
IKAR15	480191	7643708	Southern Kaoko or Ugab Zone		Damara
IKAR16	480185	7643688	Southern Kaoko or Ugab Zone		Damara
IUIS11	487936	7653601	Southern Kaoko or Ugab Zone		Damara
IUIS9	488091	765344	Southern Kaoko or Ugab Zone		
N015KN	577826.19	7402353.15	Southern Margin Zone		Damara
N017KN	579989.38	7422966.53	Southern Zone		Damara
N018LMB	578009.27	7422869.59	Southern Zone		Damara
N019B	546509.69	7398697.60	Southern Zone		Damara
N019KS	546509.69	7398697.60	Southern Zone		Damara
N021JLA	524924.11	7419809.39	Southern Zone		Damara
N021JLB	542021.34	7395281.68	Southern Zone		Damara
N021LMA	542021.34	7395281.68	Okahandja Lineament Zone		Damara
N022JL2	622044.67	7464653.37	Southern Zone		Damara
N022LM	622086.27	7464723.89	Southern Zone		Damara
N025.2KS	482199.26	7492571.99	southern Central Zone		Damara
N025.1KS	482199.26	7492571.99	southern Central Zone		Damara
N028LM	486191.31	7502712.08	southern Central Zone	Red Granite	
N035LM	499996.57	7505190.45	southern Central Zone	Abbabis	
N036JL	499989.72	7505627.69	southern Central Zone	Abbabis	
N036KN	458393.47	7530347.34	southern Central Zone	Abbabis	
N036LM	499989.72	7505627.69	southern Central Zone	Abbabis	
N038KN	498997.22	7511022.11	southern Central Zone		Damara
N047LMA	587234.70	7549334.75	southern Central Zone	Salem	
N047LMB	587234.70	7549334.75	southern Central Zone	Salem	
N048LM	587903.22	7544695.90	southern Central Zone	Goas	
N052JL	514412.00	7533305.00	southern Central Zone	Abbabis	

Sample No.	Group	Formation	Lithology	Simplified lithology
Cu Valley			Quartz-mica schist	Mica schist
IHELA	Swakop	Karibib	Marble	Marble
IIKAR13	Zerrissene	Amis	Mica schist	Mica schist
IIUIS11	Zerrissene	Amis	Mica schist	Mica schist
IIUIS4			Pegmatite	Pegmatite
IKAR15	Zerrissene	Amis	Mica schist	Mica schist
IKAR16	Zerrissene	Amis	Mica schist	Mica schist
IUIS11	Zerrissene	Amis	Mica schist	Mica schist
IUIS9			Pegmatite	Pegmatite
N015KN	Hakos	Noas	Biotite - sericite schist	Mica schist
N017KN	Swakop	Kuiseb	Biotie - garnet gneiss-schist	Mica schist
N018LMB	Swakop	Kuiseb	Qtz-plag-amph-grt-vein in Kuseib	Amphibolite
N019B	Swakop	Matchless Member	Amphibolite	Amphibolite
N019KS	Swakop	Matchless Member	Amphibolite grt Hbl schist	Mica schist
N021JLA	Swakop	Kuiseb	Kyanite - garnet micaschist	Mica schist
N021JLB	Swakop	Kuiseb	Kyanite vein in micaschist	Mica schist
N021LMA	Swakop	Matchless Member	Amphibolite-epidote micaschist	Mica schist
N022JL2	Swakop	Kuiseb	Mica schist	Mica schist
N022LM	Swakop	Matchless Member	Micaschist	Mica Schist
N025.2KS	Nosib	Khan	Metavolcanic	Amphibolite
N025.1KS	Nosib	Khan	Banded Gneiss	Gneiss
N028LM			Granite	Granite
N035LM			Granite	Granite
N036JL			Granitic gneiss	Gneiss
N036KN			Sillimanite gneiss	Gneiss
N036LM			Granite	Granite
N038KN	Nosib	Khan	Two-mica gneiss	Gneiss
N047LMA			Granite	Granite
N047LMB			Granite	Granite
N048LM			Calcalkaline diorite	Diorite
N052JL			Sillimanite gneiss	Gneiss

Sample No.	Mass in Air (g)			Ave. In Air (g)	Mass in Water (g)			Ave. In Water (g)	Density (g.cm^{-3})	Error analysis
	1	2	3		1	2	4			
Cu Valley	1211.96	1121.97	1211.96	1181.96	826.36	826.32	826.40	826.36	3.32	0.009733
IHELA	163.19	163.21	163.20	163.20	106.07	106.06	106.10	106.08	2.86	0.022689
IIKAR13	302.30	302.30	302.30	302.30	189.86	189.89	189.92	189.89	2.69	0.015618
IIUIS11	580.76	580.75	580.75	580.75	370.81	370.83	370.84	370.83	2.77	0.011564
IIUIS4	1373.70	1373.70	1373.70	1373.70	861.40	861.42	861.45	861.42	2.68	0.007268
IKAR15	282.72	282.69	282.71	282.71	178.71	178.74	176.65	178.03	2.70	0.016226
IKAR16	392.29	392.30	392.30	392.30	246.40	246.31	246.36	246.36	2.69	0.013687
IUIS11	534.05	534.04	534.06	534.05	340.47	340.38	340.36	340.40	2.76	0.012025
IUIS9	1015.46	1015.45	1015.46	1015.46	636.52	636.43	636.46	636.47	2.68	0.008453
N015KN	119.93	119.94	119.92	119.93	75.11	75.34	75.51	75.32	2.69	0.024927
N017KN	1025.03	1025.04	1025.03	1025.03	641.02	641.09	640.90	641.00	2.67	0.00838
N018LMB	321.94	321.95	321.95	321.95	208.54	208.56	208.60	208.57	2.84	0.015988
N019B	189.71	189.71	189.71	189.71	126.47	126.53	126.66	126.55	3.00	0.022126
N019KS	218.28	218.28	218.28	218.28	141.03	141.07	141.29	141.13	2.83	0.019387
N021JLA	815.57	815.57	815.54	815.56	534.55	534.27	535.87	534.90	2.91	0.010243
N021JLB	1606.71	1606.70	1606.70	1606.70	1068.00	1068.50	1068.85	1068.45	2.99	0.007484
N021LMA	197.65	197.59	197.62	197.62	132.44	132.51	132.55	132.50	3.03	0.0219
N022JL2	430.01	430.01	430.01	430.01	275.60	275.61	275.59	275.60	2.78	0.013545
N022LM	665.90	665.91	665.89	665.90	433.41	433.39	433.43	433.41	2.86	0.01118
N025.2KS	805.59	805.59	805.59	805.59	527.72	528.05	528.04	527.94	2.90	0.010291
N025.1KS	879.95	879.95	879.96	879.95	543.53	543.55	543.61	543.56	2.62	0.008866
N028LM	395.22	395.23	395.21	395.22	243.68	243.83	243.93	243.81	2.61	0.013237
N035LM	1429.93	1429.94	1429.93	1429.93	906.68	906.69	906.70	906.69	2.73	0.00726
N036JL	440.96	440.95	440.93	440.95	274.03	274.04	274.10	274.06	2.64	0.012681
N036KN	839.16	839.16	839.16	839.16	546.12	546.27	546.32	546.24	2.86	0.009953
N036LM	1119.95	1119.96	1119.95	1119.95	721.92	721.89	721.87	721.89	2.81	0.008453
N038KN	1711.85	1711.85	1711.84	1711.85	1101.49	1101.37	1101.38	1101.41	2.80	0.006807
N047LMA	313.95	313.95	313.93	313.94	195.88	195.87	195.89	195.88	2.66	0.015148
N047LMB	907.78	907.78	907.79	907.78	572.38	572.50	571.64	572.17	2.70	0.009028
N048LM	219.13	219.13	219.13	219.13	139.98	139.96	140.03	139.99	2.77	0.018928
N052JL	273.37	273.39	273.37	273.38	177.78	178.11	178.23	178.04	2.87	0.017539

Sample No.	UTM_X	UTM_Y	Zone	Suite	Supergroup
N067	640911.47	7554793.71	southern Central Zone	Salem	
N067LM	640911.47	7554793.71	southern Central Zone	Salem	
N069LM	676681.48	7553557.56	southern Central Zone		Damara
N070KN	689132.28	7489292.59	Southern Zone		Damara
N072b	688345.59	7488379.04	Southern Zone		Damara
N072d	688345.59	7488379.04	Southern Zone		Damara
N081	520944.12	7734920.42	Northern Zone		Damara
N086C	710791.63	7496649.19	Southern Margin Zone		Damara
N086KNA	710791.63	7496649.19	Southern Margin Zone		Damara
N086KNB	710791.63	7496649.19	Southern Margin Zone		Damara
N100	570609.22	7568122.08	southern Central Zone		Damara
N105	597343.95	7566522.12	southern Central Zone	Salem	
N105	597343.95	7566522.12	southern Central Zone	Salem	
N111A	561066.00	7549801.00	southern Central Zone	Abbabis	
N114A	556674.40	7547119.47	southern Central Zone		
N114B	556674.40	7547119.47	southern Central Zone	Abbabis	
N116B	583641.18	7559801.52	southern Central Zone	Goas	
N116B	583641.18	7559801.52	southern Central Zone	Goas	
N117A	579458.94	7551665.02	southern Central Zone	Goas	
N117A	579458.94	7551665.02	southern Central Zone	Goas	
N117B	579458.94	7551665.02	southern Central Zone	Goas	
N117C	579458.94	7551665.02	southern Central Zone	Goas	
N118A	581425.72	7549459.55	southern Central Zone	Goas	
N118B	581425.72	7549459.55	southern Central Zone	Goas	
N118C	581425.72	7549459.55	southern Central Zone	Goas	
N119A	581511.00	7549549.00	southern Central Zone	Goas	
N120	583458.61	7551407.01	southern Central Zone	Goas	
N121	583335.34	7552973.72	southern Central Zone	Goas	
N122	583964.21	7553941.97	southern Central Zone	Goas	
N122	583964.21	7553941.97	southern Central Zone	Goas	
N123	584028.98	7553690.89	southern Central Zone	Goas	

Sample No.	Group	Formation	Lithology	Simplified lithology
N067			Granite	Granite
N067LM			Granite	Granite
N069LM	Swakop	Kuiseb	Muscovite biotite schist	Mica Schist
N070KN	Swakop	Kuiseb	Biotite gneiss	Gneiss
N072b	Swakop	Kuiseb	Disseminated ore in mica schist	Mica schist
N072d	Swakop	Kuiseb	Disseminated ore in mica schist	Mica schist
N081	Nosib	Naauwpoort	Felsic volcanic	Rhyolite
N086C	Swakop	Kusieb	Metapsammite	Metapsammite
N086KNA	Swakop	Kusieb	Biotite - garnet gneiss	Gneiss
N086KNB	Swakop	Kusieb	Amphibolite	Amphibolite
N100	Swakop	Arandis	Marble	Marble
N105			Deformed granite	Granite
N105			Deformed granite	Granite
N111A		Noab	Pyroxenite	Pyroxenite
N114A			Syntectonic pegmatite	Pegmatite
N114B			Biotite-silliminate schist	Mica schist
N116B			Granodiorite	Granodiorite
N116B			Granodiorite	Granodiorite
N117A			Gabbro	Gabbro
N117A			Gabbro	Gabbro
N117B			Gabbro	Gabbro
N117C			Gabbro	Gabbro
N118A			Porphyritic gabbro	Gabbro
N118B			Porphyritic gabbro	Gabbro
N118C			Porphyritic gabbro	Gabbro
N119A			Lighter granite	Granite
N120			Porphyritic gabbro	Gabbro
N121			Porphyritic gabbro	Gabbro
N122			Diorite	Diorite
N122			Diorite	Diorite
N123			Diorite	Diorite

Sample No.	Mass in Air (g)			Ave. In Air (g)	Mass in Water (g)			Ave. In Water (g)	Density ($g.cm^{-3}$)	Error analysis
	1	2	3		1	2	4			
N067	1364.96	1364.96	1364.97	1364.96	844.08	844.06	843.91	844.02	2.62	0.007123
N067LM	171.45	171.45	171.44	171.45	105.73	105.76	105.76	105.75	2.61	0.020176
N069LM	1168.15	1168.16	1168.13	1168.15	748.41	751.43	751.17	750.34	2.80	0.008223
N070KN	1399.72	1399.72	1399.71	1399.72	890.59	890.56	890.60	890.58	2.75	0.007383
N072b	1252.10	1252.09	1252.09	1252.09	880.88	880.84	880.85	880.86	3.37	0.009596
N072d	192.77	192.75	192.76	192.76	127.61	127.61	127.58	127.60	2.96	0.021608
N081	2780.03	2780.04	2780.02	2780.03	1703.56	1703.68	1703.64	1703.63	2.58	0.004913
N086C	1646.16	1649.18	1646.16	1647.17	1018.63	1018.61	1018.51	1018.58	2.62	0.006482
N086KNA	1605.28	1605.28	1605.27	1605.28	1019.04	1019.77	1019.86	1019.56	2.74	0.00687
N086KNB	261.02	261.03	261.02	261.02	167.79	167.82	167.82	167.81	2.80	0.017526
N100	1031.42	1031.43	1031.43	1031.43	672.47	672.57	672.59	672.54	2.87	0.009001
N105	2113.32	2113.31	2113.31	2113.31	1324.37	1324.29	1324.18	1324.28	2.68	0.005847
N105	1424.80	1424.81	1424.80	1424.80	890.69	890.70	890.82	890.74	2.67	0.007099
N111A	1553.39	1553.36	1553.36	1553.37	1036.44	1036.46	1036.47	1036.46	3.01	0.007663
N114A	378.94	378.91	378.90	378.92	230.69	230.64	230.61	230.65	2.56	0.013234
N114B	587.71	587.49	587.47	587.56	364.81	364.88	364.93	364.87	2.64	0.010959
N116B	505.74	505.73	505.73	505.73	322.04	322.10	322.09	322.08	2.75	0.01234
N116B	700.06	700.05	700.06	700.06	445.42	445.70	445.74	445.62	2.75	0.010468
N117A	157.20	157.20	157.20	157.20	104.99	104.90	105.09	104.99	3.01	0.024401
N117A	587.10	587.12	587.12	587.11	392.04	392.02	392.06	392.04	3.01	0.012524
N117B	1836.10	1836.11	1836.11	1836.11	1214.84	1214.82	1214.85	1214.84	2.96	0.006929
N117C	511.47	511.48	511.47	511.47	337.68	337.67	337.68	337.68	2.94	0.013125
N118A	949.91	949.90	949.90	949.90	626.08	626.05	626.12	626.08	2.93	0.009577
N118B	986.21	986.21	986.21	986.21	637.52	637.57	637.72	637.60	2.83	0.009061
N118C	2325.49	2325.50	2352.49	2334.49	1554.95	1555.05	1555.11	1555.04	3.00	0.006224
N119A	214.57	214.56	214.56	214.56	132.67	132.71	132.75	132.71	2.62	0.018093
N120	612.16	612.14	612.15	612.15	404.96	405.01	404.95	404.97	2.95	0.012037
N121	690.27	690.26	690.26	690.26	454.47	454.43	454.49	454.46	2.93	0.011224
N122	470.75	470.76	470.74	470.75	296.30	296.28	296.27	296.28	2.70	0.012533
N122	593.78	593.77	593.78	593.78	373.44	373.42	373.40	373.42	2.69	0.011135
N123	2258.51	2258.52	2258.51	2258.51	1418.83	1418.81	1418.88	1418.84	2.69	0.00568

Sample No.	UTM_X	UTM_Y	Zone	Suite	Supergroup
N124	584489.93	7553766.79	southern Central Zone	Goas	
N125A	578428.00	7563487.00	southern Central Zone	Goas	
N125B	578428.00	7563487.00	southern Central Zone	Goas	
N125C	578428.00	7563487.00	southern Central Zone	Goas	
N126	579041.61	7563533.30	southern Central Zone	Goas	
N127A	583836.29	7563482.18	southern Central Zone	Goas	
N127B	583836.29	7563482.18	southern Central Zone	Goas	
N129A	603266.70	7543296.77	southern Central Zone	Goas	
N129B	603266.70	7543296.77	southern Central Zone	Goas	
N129C	603266.70	7543296.77	southern Central Zone	Goas	
N130	602503.75	7541470.28	southern Central Zone	Goas	
N137	510889.99	7524079.02	southern Central Zone	Salem	
N137	510889.99	7524079.02	southern Central Zone	Salem	
N138	585686.00	7523211.00	southern Central Zone	Goas	
N139	585944.97	7523933.66	southern Central Zone	Goas	
N140A	586878.85	7521646.41	southern Central Zone	Goas	
N140B	586878.85	7521646.41	southern Central Zone	Goas	
N141	586053.87	7537946.74	southern Central Zone	Goas	
N142A	604043.68	7539361.43	southern Central Zone	Goas	
N142B	604043.68	7539361.43	southern Central Zone	Goas	
N143B	604039.00	7539359.00	southern Central Zone	Goas	
N143D	604039.00	7539359.00	southern Central Zone	Goas	
N150A	480155.00	7643739.00	Southern Kaoko or Ugab Zone		Damara
N150B	480155.00	7643739.00	Southern Kaoko or Ugab Zone		Damara
N157B	439595.15	7578984.44	Southern Kaoko or Ugab Zone		
N160	467231.00	7675508.00	Granite only	Sorris Sorris	
N161	463839.00	7675939.00	Granite only	Sorris Sorris	
N162A	488506.00	7678026.00	Granite only	Sorris Sorris	
N162A	488506.00	7678026.00	Granite only	Sorris Sorris	
N162B	488506.00	7678026.00	Granite only	Sorris Sorris	
N163A	493268.00	7682763.00	Northern Zone Ais Dome	Sorris Sorris	

Sample No.	Group	Formation	Lithology	Simplified lithology
N124			Darker granitoid	Diorite
N125A			Diorite with inclaves	Diorite
N125B			Diorite	Diorite
N125C			Diorite	Diorite
N126			Granodiorite	Granodiorite
N127A			Diorite	Diorite
N127B			Diorite	Diorite
N129A			Granodiorite	Granodiorite
N129B			Diorite (Tonolite?)	Diorite
N129C			Granodiorite	Granodiorite
N130			Diorite	Diorite
N137			Granite	Granite
N137			Granite	Granite
N138			Diorite	Diorite
N139			Diorite	Diorite
N140A			Palmental Horneblendite	Amphibolite
N140B			Hornblende diorite	Diorite
N141			Granite to granodiorite	Diorite
N142A			Meta-gabbro	Gabbro
N142B			Meta-gabbro	Gabbro
N143B			Gabbro	Gabbro
N143D			Audawib diorite	Diorite
N150A	Zerrissene	Amis	Garnet amphibole quartzite	Quartzite
N150B	Zerrissene	Amis	Garnet amphibole quartzite	Quartzite
N157B			Syntectonic pegmatite	Pegmatite
N160			Granite	Granite
N161			Two fsp granite	Granite
N162A			Granite	Granite
N162A			Granite	Granite
N162B			Granite	Granite
N163A			Granite	Granite

Sample No.	Mass in Air (g)			Ave. In Air (g)	Mass in Water (g)			Ave. In Water (g)	Density ($g.cm^{-3}$)	Error analysis
	1	2	3		1	2	4			
N124	238.24	238.22	238.25	238.24	149.20	149.22	149.21	149.21	2.68	0.017526
N125A	165.83	165.80	165.80	165.81	104.24	103.94	103.76	103.98	2.68	0.021098
N125B	755.12	755.12	755.11	755.12	480.06	480.12	480.14	480.11	2.75	0.010056
N125C	892.66	892.65	892.65	892.65	566.30	566.26	566.25	566.27	2.73	0.009207
N126	542.73	542.75	542.73	542.74	343.80	343.72	343.72	343.75	2.73	0.011794
N127A	626.61	626.61	626.60	626.61	404.57	404.70	404.61	404.63	2.82	0.011359
N127B	1439.31	1439.32	1439.30	1439.31	906.99	907.08	907.35	907.14	2.70	0.007161
N129A	2066.81	2066.81	2066.81	2066.81	1289.46	1289.43	1289.44	1289.44	2.66	0.00587
N129B	594.61	594.60	594.60	594.60	366.04	366.05	366.03	366.04	2.60	0.010739
N129C	2148.01	2148.00	2148.00	2148.00	1336.93	1337.08	1337.15	1337.05	2.65	0.005735
N130	1167.38	1167.38	1167.36	1167.37	739.99	740.43	740.48	740.30	2.73	0.008041
N137	625.49	625.45	625.45	625.46	393.99	394.06	393.89	393.98	2.70	0.010877
N137	2480.50	2480.60	2480.56	2480.55	1559.43	1560.56	1558.80	1559.60	2.69	0.005426
N138	1477.47	1477.49	1477.48	1477.48	947.92	948.05	948.22	948.06	2.79	0.007294
N139	99.27	99.26	99.26	99.26	63.29	63.21	63.28	63.26	2.76	0.028161
N140A	495.73	495.74	495.73	495.73	343.41	343.38	343.47	343.42	3.25	0.014766
N140B	944.37	944.39	944.36	944.37	600.33	600.27	600.30	600.30	2.74	0.008982
N141	149.33	149.33	149.33	149.33	96.15	96.13	96.08	96.12	2.81	0.023305
N142A	121.66	121.67	121.65	121.66	80.02	80.08	79.99	80.03	2.92	0.026957
N142B	786.34	786.33	786.34	786.34	528.15	528.11	528.13	528.13	3.05	0.010939
N143B	241.21	241.21	241.20	241.21	161.98	162.00	161.97	161.98	3.04	0.019862
N143D	745.67	745.66	745.67	745.67	479.24	479.17	479.21	479.21	2.80	0.010316
N150A	292.55	292.54	292.54	292.54	188.46	188.48	188.51	188.48	2.81	0.016611
N150B	498.44	498.44	498.45	498.44	317.86	317.87	317.87	317.87	2.76	0.012461
N157B	150.01	150.00	149.85	149.95	91.15	91.11	91.04	91.10	2.55	0.02107
N160	2057.03	2057.02	2057.01	2057.02	1265.10	1265.01	1265.14	1265.08	2.60	0.005747
N161	235.45	235.44	235.45	235.45	146.34	146.40	146.41	146.38	2.64	0.017413
N162A	1081.43	1081.43	1081.42	1081.43	680.05	680.01	679.94	680.00	2.69	0.008234
N162A	53.97	54.00	53.99	53.99	33.88	33.95	33.98	33.94	2.69	0.03749
N162B	824.75	824.74	824.74	824.74	512.18	512.03	512.14	512.12	2.64	0.009239
N163A	2963.30	2963.39	2963.33	2963.34	1872.82	1872.85	1872.75	1872.81	2.72	0.005007

Sample No.	UTM_X	UTM_Y	Zone	Suite	Supergroup
N164B	492744.00	7684329.00	Northern Zone Ais Dome	Sorris Sorris	
N165A	495003.00	7684737.00	Northern Zone Ais Dome	Omangambo	
N165B	495003.00	7684737.00	Northern Zone Ais Dome	Omangambo	
N166	490350.00	7686022.00	Northern Zone Ais Dome	Sorris Sorris	
N168	497050.00	7686559.00	Northern Zone Ais Dome	Sorris Sorris	
N174	438226.87	7705343.95	Southern Kaoko or Ugab Zone	Namibian gabbro	
N182	412716.17	7748454.10	Northern Zone	Sorris Sorris	
N197A	479239.21	7725216.50	Northern Zone		Damara
N208A	461868.00	7724724.00	Granite only	Sorris Sorris	
N208B	461868.00	7724724.00	Granite only	Sorris Sorris	
N208C	461868.00	7724724.00	Granite only	Omangambo	
N209	462161.37	7723607.36	Granite only	Omangambo	
N210A	461179.64	7722072.03	Granite only	Omangambo	
N212	456733.00	7713581.56	Granite only	Sorris Sorris	
N213	455549.17	7715527.63	Granite only	Sorris Sorris	
N214	454940.30	7718314.61	Granite only	Sorris Sorris	
N215	455230.08	7720465.93	Granite only	Omangambo	
N217	448376.00	7729925.00	Northern Zone	Sorris Sorris	
N219	498186.97	7748628.72	Northern Zone	Khorixas	
N227	522372.05	7696518.59	Granite only	Omangambo	
N236A	620236.57	7760853.35	Northern Zone		Damara
ONA13	620098	7601631	southern Central Zone		Damara
Sn mine	517483.29	7620902.30	northern Central Zone		
USK22	563499	7566127	southern Central Zone		Damara
Z001	575004.00	7521963.00	Ghanzi-Chobe Belt	Okwa Complex	
Z005	189504.00	7939211.00	Ghanzi-Chobe Belt	Ghanzi	
Z008	442868.00	8116980.00	Choma-Kalomo Block	Choma-Kalomo Batholith	
Z011	634604.00	8283895.00	Zambezi Belt		
Z011A	634604.00	8283895.00	Zambezi Belt		
Z011B	634604.00	8283895.00	Zambezi Belt		
Z011D	634604.00	8283895.00	Zambezi Belt		

Sample No.	Group	Formation	Lithology	Simplified lithology
N164B			Granite	Granite
N165A			Granite	Granite
N165B			Granite	Granite
N166			Granite (fine-grained)	Granite
N168			Granite (post - tectonic)	Granite
N174			Meta-gabbro	Gabbro
N182			Granite (post - tectonic)	Granite
N197A	Swakop	Kuiseb	Phyllite	Schist
N208A			Granite (medium-grained)	Granite
N208B			Megacrystic granite	Granite
N208C			Granite	Granite
N209			Megacrystic granite	Granite
N210A			Megacrystic granite	Granite
N212			Granite (coarse-grained)	Granite
N213			Granite (fine-grained) intruded by pegmatite	Granite
N214			Megacrystic granite	Granite
N215			Granite (coarse-grained)	Granite
N217			Granite	Granite
N219			Gabbro	Gabbro
N227			Granite (Syn - tectonic)	Granite
N236A	Swakop	Karibib	Dolostone	Dolostone
ONA13	Swakop	Karibib	Marble	Marble
Sn mine			Pegmatite	Pegmatite
USK22	Swakop	Kuiseb	Mica schist	Mica schist
Z001			Granite gneiss	Granite
Z005		Goha Hills	Poryritic Diacite	Dacite
Z008			Granodiorite	Granodiorite
Z011		Upper Roan	Eclogite	Eclogite
Z011A		Upper Roan	Eclogite	Eclogite
Z011B		Upper Roan	Fine-grained amphibolite	Amphibolite
Z011D		Upper Roan	Amphibolite	Amphibolite

Sample No.	Mass in Air (g)			Ave. In Air (g)	Mass in Water (g)			Ave. In Water (g)	Density ($g.cm^{-3}$)	Error analysis
	1	2	3		1	2	4			
N164B	712.81	712.80	712.79	712.80	440.35	440.34	440.40	440.36	2.62	0.009859
N165A	989.30	989.31	989.32	989.31	617.34	617.23	617.27	617.28	2.66	0.008499
N165B	260.60	260.60	260.61	260.60	162.54	162.36	162.93	162.61	2.66	0.016643
N166	2766.52	2766.53	2766.51	2766.52	1708.82	1708.88	1708.85	1708.85	2.62	0.004988
N168	2457.82	2457.70	2457.70	2457.74	1513.50	1513.77	1513.88	1513.72	2.60	0.005269
N174	1415.19	1415.19	1415.17	1415.18	916.42	916.49	916.38	916.43	2.84	0.007579
N182	1521.50	1521.48	1520.99	1521.32	929.40	929.47	929.27	929.38	2.57	0.006616
N197A	1476.13	1476.11	1476.11	1476.12	934.92	934.91	934.87	934.90	2.73	0.007131
N208A	124.28	124.28	124.28	124.28	76.37	76.36	76.33	76.35	2.59	0.023593
N208B	491.72	491.73	491.71	491.72	300.90	300.91	300.90	300.90	2.58	0.011704
N208C	1352.58	1353.55	1353.56	1353.23	845.72	845.63	845.65	845.67	2.67	0.00728
N209	840.40	840.39	840.40	840.40	522.65	522.72	522.80	522.72	2.65	0.009177
N210A	638.61	638.61	638.62	638.61	398.58	398.58	398.63	398.60	2.66	0.010598
N212	139.11	139.08	139.09	139.09	85.93	85.94	85.87	85.91	2.62	0.022481
N213	413.80	413.81	413.81	413.81	254.08	254.10	253.98	254.05	2.59	0.012833
N214	175.81	175.82	175.82	175.82	108.12	107.99	108.30	108.14	2.60	0.019828
N215	432.95	432.97	432.96	432.96	271.21	271.23	271.20	271.21	2.68	0.012968
N217	1241.58	1241.58	1241.57	1241.58	765.19	765.22	765.14	765.18	2.61	0.00743
N219	1403.56	1403.57	1403.58	1403.57	935.26	935.17	935.28	935.24	3.00	0.008042
N227	335.55	335.56	335.56	335.56	208.84	208.85	208.84	208.84	2.65	0.014586
N236A	1236.88	1236.86	1236.87	1236.87	780.39	780.40	780.42	780.40	2.71	0.007742
ONA13	421.36	421.36	421.34	421.35	265.41	265.43	265.42	265.42	2.70	0.013273
Sn mine	906.84	906.84	906.84	906.84	563.48	563.51	563.54	563.51	2.64	0.008819
USK22	40.58	40.57	40.55	40.57	25.85	25.83	25.82	25.83	2.75	0.04442
Z001	248.71	248.71	248.71	248.71	156.65	156.67	156.66	156.66	2.70	0.017317
Z005	250.62	250.61	250.61	250.61	157.12	157.16	157.17	157.15	2.68	0.017118
Z008	621.70	621.70	621.69	621.70	396.93	396.92	396.94	396.93	2.77	0.011172
Z011	299.05	299.06	299.06	299.06	204.08	204.01	203.96	204.02	3.15	0.018422
Z011A	1085.18	1085.18	1085.18	1085.18	734.54	734.67	734.59	734.60	3.10	0.009456
Z011B	2199.04	2199.03	2199.04	2199.04	1474.64	1474.59	1474.52	1474.58	3.04	0.006501
Z011D	1050.14	1050.14	1050.16	1050.15	706.70	706.68	706.70	706.69	3.06	0.009495

Sample No.	UTM_X	UTM_Y	Zone	Suite	Supergroup
Z013A	642892.00	8249991.00	Zambezi Belt	Zambezi Supracrustal Sequence	
Z017A	627417.00	8311191.00	(Northern) Zambezi Belt	Lusaka Granite	Lusaka
Z017A	627417.00	8311191.00	Zambezi Belt	Zambezi Supracrustal Sequence	
Z017B	627417.00	8311191.00	Zambezi Belt	Zambezi Supracrustal Sequence	
Z018	731593.00	8457390.00	Irumide Belt	Mkushi Metamorphic Complex	
Z018	731593.00	8457390.00	Irumide Belt	Mkushi Metamorphic Complex	
Z019B	728268.00	8455139.00	Irumide Belt	Mkushi Metamorphic Complex	
Z019C	728268.00	8455139.00	Irumide Belt	Mkushi Metamorphic Complex	
Z021	680661.00	8478704.00	Irumide Belt	Kampoyo Granite	
Z021	680661.00	8478704.00	Irumide Belt	Kampoyo Granite	
Z023A	632284.00	8615952.00	Kafue Anticline	Basement	
Z023B	632284.00	8615952.00	Kafue Anticline		
Z024B	631841.00	8615078.00	Kafue Anticline	Basement	
Z028	630821.00	8579083.00	Lufilian Arc / Kafue Anticline		Katanga
Z030	588719.00	8612344.00	Lufilian Arc / Kafue Anticline	Basement	
Z030B	588719.00	8612344.00	Lufilian Arc / Kafue Anticline	Basement	
Z031B	370932.00	8648080.00	Lufilian Arc/ Domes Region		Katanga?
Z031D	370932.00	8648080.00	Lufilian Arc/ Domes Region	Basement	
Z032B	371610.00	8645647.00	Lufilian Arc/ Domes Region		Katanga?
Z033A	371865.00	8645592.00	Lufilian Arc/ Domes Region	Basement??	
Z033B	371865.00	8645592.00	Lufilian Arc/ Domes Region	Basement??	
Z033C	371865.00	8645592.00	Lufilian Arc/ Domes Region	Basement??	
Z033C	371865.00	8645592.00	Lufilian Arc/ Domes Region	Basement??	
Z034A	372263.00	8645678.00	Lufilian Arc/ Domes Region		Katanga?
Z034B	372263.00	8645678.00	Lufilian Arc/ Domes Region		Katanga?
Z035	358183.00	8649861.00	Lufilian Arc/ Domes Region		Katanga?
Z036A	368976.00	8652214.00	Lufilian Arc/ Domes Region		Katanga?
Z036B	368976.00	8652214.00	Lufilian Arc/ Domes Region		Katanga?
Z039A	195684.00	8762428.00	Lufilian Arc/ Domes Region	Basement??	
Z043	222523.00	8681622.00	Lufilian Arc		
Z046B	437846.00	8663184.00	Lufilian Arc/ north of Solwezi Dome		Katanga

Sample No.	Group	Formation	Lithology	Simplified lithology
Z013A		Kafue	Meta-rhyolite	Rhyolite
Z017A			Granite	Granite
Z017A			Granite	Granite
Z017B			Granite	Granite
Z018			Augen Gneiss	Gneiss
Z018			Augen Gneiss	Gneiss
Z019B			Granite	Granite
Z019C			Granite	Granite
Z021			Foliated biotite gneiss	Gneiss
Z021			Granite	Granite
Z023A			Granodiorite	Granodiorite
Z023B	Muva		Quartzite	Quartzite
Z024B			Granodiorite	Granodiorite
Z028	Lower Roan	Ore Shale	Slate	Slate
Z030			Mica schist	Mica schist
Z030B			Granite	Granite
Z031B	Lower Roan?		Muscovite biotite schist	Mica schist
Z031D			Biotite schist	Mica schist
Z032B	Lower Roan?		Muscovite schist	Mica schist
Z033A			Granite	Granite
Z033B			Gneiss	Gneiss
Z033C			Granite	Granite
Z033C			Granite	Granite
Z034A	Lower Roan?		Muscovite biotite schist	Mica schist
Z034B	Lower Roan?		Muscovite biotite schist	Mica schist
Z035	Lower Roan?	Mosa Hills	Quartz-mica schist	Mica schist
Z036A	Upper Roan or Mwashya Subgroup		Basalt	Basalt
Z036B	Upper Roan or Mwashya Subgroup		Basalt	Basalt
Z039A			Granite	Granite
Z043			Meta-volcanic?	Tuff
Z046B	Nguba Group/Mwashya Subgroup?	Knotted schist	Mottled schist	Mica schist

Sample No.	Mass in Air (g)			Ave. In Air (g)	Mass in Water (g)			Ave. In Water (g)	Density ($g.cm^{-3}$)	Error analysis
	1	2	3		1	2	4			
Z013A	831.01	831.01	831.01	831.01	523.88	523.87	523.85	523.87	2.71	0.009441
Z017A	1083.35	1083.33	1083.34	1083.34	675.32	675.32	675.26	675.30	2.65	0.008107
Z017A	272.66	272.66	272.66	272.66	169.87	170.00	169.97	169.95	2.65	0.016237
Z017B	462.86	462.86	462.86	462.86	288.63	288.69	288.71	288.68	2.66	0.012447
Z018	270.21	270.22	270.21	270.21	171.44	171.49	171.50	171.48	2.74	0.016824
Z018	525.22	525.21	525.20	525.21	328.64	328.57	328.63	328.61	2.67	0.011742
Z019B	430.39	430.40	430.39	430.39	267.32	267.29	267.29	267.30	2.64	0.012821
Z019C	173.69	173.69	173.69	173.69	108.15	108.12	108.14	108.14	2.65	0.020356
Z021	1729.91	1729.90	1729.90	1729.90	1085.45	1085.46	1085.40	1085.44	2.68	0.00648
Z021	523.82	523.79	523.80	523.80	327.46	327.47	327.40	327.44	2.67	0.01174
Z023A	1445.90	1445.91	1445.91	1445.91	935.33	935.30	935.59	935.41	2.83	0.007484
Z023B	1717.54	1717.54	1717.53	1717.54	1087.18	1087.08	1087.09	1087.12	2.72	0.006601
Z024B	604.78	604.78	604.77	604.78	388.46	388.45	388.36	388.42	2.80	0.01145
Z028	473.06	473.06	473.05	473.06	296.26	296.29	296.28	296.28	2.68	0.012398
Z030	720.12	720.11	720.11	720.11	464.06	463.99	463.96	464.00	2.81	0.010549
Z030B	403.13	403.13	403.13	403.13	251.42	251.44	251.46	251.44	2.66	0.013346
Z031B	286.20	286.19	286.19	286.19	182.08	182.11	182.16	182.12	2.75	0.016423
Z031D	789.94	789.94	789.94	789.94	506.34	506.4	506.4	506.38	2.79	0.009975
Z032B	873.89	873.86	873.85	873.87	568.17	568.16	568.12	568.15	2.86	0.00973
Z033A	601.22	601.22	601.21	601.22	375.44	375.48	375.48	375.47	2.66	0.010935
Z033B	1242.49	1242.49	1242.48	1242.49	777.71	777.69	777.68	777.69	2.67	0.00762
Z033C	261.33	261.33	261.33	261.33	164.32	164.30	164.35	164.32	2.69	0.016839
Z033C	727.92	727.92	727.91	727.92	457.32	457.38	457.39	457.36	2.69	0.010035
Z034A	460.19	460.19	460.20	460.19	290.79	290.81	290.76	290.79	2.72	0.012764
Z034B	1590.57	1590.56	1590.57	1590.57	1024.76	1024.73	1024.68	1024.72	2.81	0.00708
Z035	985.75	985.75	985.76	985.75	665.67	665.74	665.77	665.73	3.08	0.009876
Z036A	2339.22	2339.21	2339.22	2339.22	1577.48	1577.45	1577.46	1577.46	3.07	0.006376
Z036B	404.25	404.23	404.24	404.24	271.30	271.31	271.35	271.32	3.04	0.01528
Z039A	985.16	985.18	985.16	985.17	612.40	612.32	612.46	612.39	2.64	0.008464
Z043	1006.45	1006.43	1006.44	1006.44	632.52	632.51	632.51	632.51	2.69	0.008529
Z046B	1556.61	1556.59	1556.60	1556.60	984.91	984.87	984.87	984.88	2.72	0.006931

Sample No.	UTM_X	UTM_Y	Zone	Suite	Lithology	Simplified lithology
Z048	444643.00	8386744.00	Lufilian Arc/Katanga High	Hook Batholith	Potassium feldspar porphyritic granite	Granite
Z048	444643.00	8386744.00	Lufilian Arc/Katanga High	Hook Batholith	Potassium feldspar porphyritic granite	Granite
Z049	436118.00	8380304.00	Lufilian Arc/Katanga High	Hook Batholith	Mineralised granite	Granite (Mineralised)
Z050	437787.00	8383682.00	Lufilian Arc/Katanga High	Hook Batholith	Hematite silicified breccai with flourite	Ironstone
Z051	436928.00	8379993.00	Lufilian Arc/Katanga High	Hook Batholith	Hematite breccai with flourite	Ironstone
Z053A	450486.00	8350019.00	Lufilian Arc/Katanga High	Hook Batholith	Coarse grained granitic mylonite	Granite
Z053B	450486.00	8350019.00	Lufilian Arc/Katanga High	Hook Batholith	Granitic mylonite (less porphyritic)	Granite
Z054	452202.00	8349417.00	Lufilian Arc/Katanga High	Hook Batholith	Granitic mylonite (less porphyritic)	Granite
Z054	452202.00	8349417.00	Lufilian Arc/Katanga High	Hook Batholith	Granitic mylonite (less porphyritic)	Granite
Z055	447710.00	8345121.00	Lufilian Arc/Katanga High	Hook Batholith	Fine grained porphyritic granite	Granite
Z055	447710.00	8345121.00	Lufilian Arc/Katanga High	Hook Batholith	Fine grained porphyritic granite	Granite
Z056A	472746.00	8345199.00	Lufilian Arc/Katanga High	Hook Batholith	Granodiorite	Granodiorite
Z056B	472746.00	8345199.00	Lufilian Arc/Katanga High	Hook Batholith	Granitic gneiss	Gneiss
Z056B	472746.00	8345199.00	Lufilian Arc/Katanga High	Hook Batholith	Granitic gneiss	Gneiss
Z057	476034.00	8346426.00	Lufilian Arc/Katanga High	Hook Batholith	Micro - Gabbro	Gabbro
Z058	477654.00	8317661.00	Lufilian Arc/Katanga High	Hook Batholith	Very coarse grained granite	Granite
Z058	477654.00	8317661.00	Lufilian Arc/Katanga High	Hook Batholith	Very coarse grained granite	Granite
Z058	477654.00	8317661.00	Lufilian Arc/Katanga High	Hook Batholith	Very coarse grained granite	Granite

Sample No.	Mass in Air (g)			Ave. In Air (g)	Mass in Water (g)			Ave. In Water (g)	Density ($g.cm^{-3}$)	Error analysis
	1	2	3		1	2	4			
Z048	878.72	878.71	878.71	878.71	550.51	550.52	550.48	550.50	2.68	0.009083
Z048	460.19	460.20	460.20	460.20	286.56	286.58	286.57	286.57	2.65	0.01245
Z049	775.92	775.89	775.91	775.91	508.11	508.15	508.15	508.14	2.90	0.010473
Z050	1965.06	1965.05	1965.06	1965.06	1294.88	1294.79	1294.75	1294.81	2.93	0.006643
Z051	651.13	651.13	651.13	651.13	494.49	494.55	494.56	494.53	4.16	0.016497
Z053A	1215.59	1215.60	1215.59	1215.59	758.76	758.78	758.73	758.76	2.66	0.007668
Z053B	1369.82	1369.82	1369.82	1369.82	855.24	855.37	855.40	855.34	2.66	0.007226
Z054	711.92	711.91	711.91	711.91	446.14	446.21	446.24	446.20	2.68	0.010105
Z054	474.14	474.14	474.15	474.14	297.09	297.12	297.11	297.11	2.68	0.012394
Z055	1603.67	1603.68	1603.68	1603.68	1001.85	1001.88	1001.78	1001.84	2.66	0.006682
Z055	496.68	496.69	496.69	496.69	309.03	309.10	309.06	309.06	2.65	0.011966
Z056A	766.63	766.62	766.62	766.62	487.61	487.58	487.60	487.60	2.75	0.009986
Z056B	546.67	546.66	546.66	546.66	353.16	353.20	353.18	353.18	2.83	0.012179
Z056B	2127.24	2127.23	2127.23	2127.23	1371.49	1371.45	1371.43	1371.46	2.81	0.006127
Z057	2048.27	2048.26	2048.26	2048.26	1379.40	1379.42	1379.33	1379.38	3.06	0.006797
Z058	947.47	947.47	947.47	947.47	591.23	591.23	591.32	591.26	2.66	0.008688
Z058	1821.35	1821.34	1821.33	1821.34	1135.50	1135.61	1135.66	1135.59	2.66	0.006248
Z058	1407.43	1407.42	1407.42	1407.42	875.57	875.59	875.62	875.59	2.65	0.007085

Appendix 5:

Magnetic susceptibility measurements collected on lithologies from Namibia, northwestern Botswana and Zambia

IDENT	Locality	UTM_X	UTM_Y	Zone	Suite
015KN	N015KN	577826.1941	7402353.146	Southern Margin Zone	
017KN	N017KN	579989.3812	7422966.534	Southern Zone	
018LMb	N018LMb	578009.2657	7422869.593	Southern Zone	
019a	N019a	546509.6902	7398697.599	Southern Zone	
019KS	N019KS	546509.6902	7398697.599	Southern Zone	
021LMa	N021LMa	524924.109	7419809.39	Okahandja Lineament Zone	
021.1JLa	N021.1JLa	542021.3355	7395281.676	Southern Zone	
021.2JLa	N021.2JLa	542021.3355	7395281.676	Southern Zone	
021JLb	N021LJb	542021.3355	7395281.676	Southern Zone	
022JL	N022JL	622044.672	7464653.368	Southern Zone	
022LM	N022LM	622086.268	7464723.894	Southern Zone	
025.1KS	N025.1KS	482199.264	7492571.986	southern Central Zone	
025.2KS	N025.2KS	482199.264	7492571.986	southern Central Zone	
028LM	N028LM	486191.312	7502712.077	southern Central Zone	Red granite
035LM	N035LM	499996.573	7505190.454	southern Central Zone	Abbabis
036KN	N036KN	499989.719	7505627.693	southern Central Zone	Abbabis
036JL	N036JL	458393.469	7530347.335	southern Central Zone	Abbabis
036LM	N036JL	499989.719	7505627.693	southern Central Zone	
038KN	N038KN	498997.215	7511022.11	southern Central Zone	
047LMa	N047LMa	587234.7027	7549334.748	southern Central Zone	Salem
047LMa	N047LMa	587234.7027	7549334.748	southern Central Zone	Salem
047LMb	N047LMb	587234.7027	7549334.748	southern Central Zone	Salem
048LM	N048LM	587903.2238	7544695.901	southern Central Zone	Goas
052JLa	N052JL	514412	7533305	southern Central Zone	
052JLb	N052JL	514412	7533305	southern Central Zone	
062LM	N062LM	527407.517	7463995.494	southern Central Zone	Salem
067LM	N067LM	640911.4747	7554793.713	southern Central Zone	Salem
069LM	N069LM	676681.4795	7553557.559	southern Central Zone	
070KN	N070KN	689132.2762	7489292.591	Southern Zone	
072a	N072a	688345.585	7488379.036	Southern Zone	
072b	N072b	688345.585	7488379.036	Southern Zone	

IDENT	Supergroup	Group	Formation	Lithology	Simplified Lithology
015KN	Damara	Hakos	Naos	Biotite - sericite schist	Mica schist
017KN	Damara	Swakop	Kuiseb	Biotite - garnet schist	Mica schist
018LMb	Damara	Swakop	Kuiseb	Qtz-plag-amph-grt-vein in Kuseib	Amphibolite
019a	Damara	Swakop	Matchless Member	Amphibolite	Amphibolite
019KS	Damara	Swakop	Matchless Member	Amphibolite grt Hbl schist	Mica schist
021LMa	Damara	Swakop	Matchless Member	Amphibolite-epidote micaschist	Mica schist
021.1JLa	Damara	Swakop	Kuiseb	Kyanite - garnet mica schist	Mica schist
021.2JLa	Damara	Swakop	Kuiseb	Kyanite - garnet mica schist	Mica schist
021JLb	Damara	Swakop	Kuiseb	Kyanite vein in mica schist	Mica schist
022JL	Damara	Swakop	Matchless Member	Mica schist	Mica schist
022LM	Damara	Swakop	Matchless Member	Mica schist	Mica schist
025.1KS	Damara	Nosib	Khan	Granitic banded Gneiss	Gneiss
025.2KS	Damara	Nosib	Khan	Metavolcanic rock	Amphibolite
028LM				Granite	Granite
035LM				Granite	Granite
036KN				Sillimanite gneiss	Gneiss
036JL				Granitic gneiss	Granite
036LM	Damara	Swakop	Kuiseb	Mica schist	Mica schist
038KN	Damara	Nosib	Khan	Two-mica gneiss	Gneiss
047LMa				Granite	Granite
047LMa				Granite	Granite
047LMb				Granite	Granite
048LM				Calcalkaline diorite	Diorite
052JLa	Damara	Nosib	Etusis	Silliminite - biotite gneiss	Gneiss
052JLb	Damara	Nosib	Etusis	Silliminite - biotite gneiss	Gneiss
062LM				Granite	Granite
067LM				Granite	Granite
069LM	Damara	Swakop	Kuiseb	Muscovite biotite schist	Mica schist
070KN	Damara	Swakop	Kuiseb	Biotite-garnet gneiss	Gneiss
072a	Damara	Swakop	Matchless Member	Disseminated ore in mica schist	Mica schist
072b	Damara	Swakop	Kuiseb	Disseminated ore in mica schist	Mica schist

IDENT	Individual magnetic susceptibility measurements (x10^{-3} SI units)																		Mean (x 10^{-3} SI units)
	1	2	3	4	5	6	7	8	9	10	11	12	13	14	15	16	17	18	
015KN	0.019	0.031	0.043	0.034	0.035														0.032
017KN	0.233	0.249	0.34	0.217	0.231														0.254
018LMb	0.106	0.19	0.138	0.202	0.2														0.167
019a	0.383	0.362	0.374	0.298	0.337														0.351
019KS	0.174	0.167	0.19	0.199	0.17														0.180
021LMa	0.495	0.388	1.07	1.05	0.255														0.652
021.1JLa	0.19	0.038	0.294	0.129	0.159														0.162
021.2JLa	0.281	0.502	0.288	0.561	0.416														0.410
021JLb	0.186	0.321	0.544	0.163	0.276														0.298
022JL	0.192	0.179	0.209	0.216	0.147														0.189
022LM	0.153	0.144	0.185	0.167	0.133														0.156
025.1KS	0.52	0.153	0.068	0.13	0.075	0.085													0.172
025.2KS	0.932	0.703	1.05	1.1	0.938														0.945
028LM	7.43	10.5	8.15	8.58	21.8														11.292
035LM	7.03	9.14	8.74	7.51	7.26														7.936
036KN	1.51	1.8	2.24	1.97	1.58														1.820
036JL	1.05	1.07	1.24	1.21	1.24														1.162
036LM	0.023	0.056	0.024	0.056	0.054														0.043
038KN	0.178	0.176	0.18	0.156	0.161														0.170
047LMa	0.133	0.105	0.098	0.111	0.13														0.115
047LMa	0.239	0.165	0.09	0.18	0.14														0.163
047LMb	0.179	0.346	0.166	0.175	0.29														0.231
048LM	6.75	8.02	4.7	6.85	8.39														6.942
052JLa	29.8	43.1	34.3	36.8	15	42.4	39.6	39.7											35.088
052JLb	31.7	33.3	35.9	49.5	43.6														38.800
062LM	7.52	4.42	6.45	11.7	9.77	9.54													8.233
067LM	0.039	0.043	0.027	0.032	0.032	0.03	0.023	0.023											0.031
069LM	0.34	0.219	0.261	0.111	0.249														0.236
070KN	0.281	0.284	0.251	0.265	0.261														0.268
072a	4.13	23.8	32.4	15.7	27.6	23.4	41.5	10.1	4.01	3.85									18.649
072b	0.798	0.477	0.408	0.42	0.727														0.566

IDENT	Locality	UTM_X	UTM_Y	Zone	Suite
074JLb	N074JLb	567400.9252	7558524.802	southern Central Zone	Abbabis
80	N080	503768.8958	7625080.625	Northern Central Zone	
81	N081	520944.1241	7734920.419	Northern Zone	
086KNa	N086KNa	710791.6294	7496649.191	Southern Margin Zone	
89	N089	713320.6552	7488924.376	Southern Margin Zone	
91.1	N091.1	563521	7566164	southern Central Zone	
91.2	N091.2	563521	7566164	southern Central Zone	
91.3	N091.3	563521	7566164	southern Central Zone	
91.4	N091.4	563522	7566094	southern Central Zone	
92.1	N092.1	572392	7560630	southern Central Zone	
94	N094	569216.5056	7561973.744	southern Central Zone	
95	N095	568724.5782	7562061.997	southern Central Zone	
96.1	N096.1	567589.0695	7561977.901	southern Central Zone	
96.2	N096.2	567589.0695	7561977.901	southern Central Zone	
97	N097	568320.6839	7564112.04	southern Central Zone	
98	N098	569254.5553	7565248.844	southern Central Zone	
99	N099	569882.072	7567104.774	southern Central Zone	
100	N100	570609.2218	7568122.08	southern Central Zone	
102	N102	569290.035	7561486.731	southern Central Zone	
106	N106	597142	7557428	southern Central Zone	Goas
107	N107	600186	7548502	southern Central Zone	Salem
108	N108	599567	7548313	southern Central Zone	Abbabis
110.1	N110.1	560881	7549974	southern Central Zone	
110.2	N110.2	560894	7549996	southern Central Zone	Abbabis
110.3	N110.3	560885	7550034	southern Central Zone	Abbabis
110.4	N110.4	561002	7550031	southern Central Zone	Abbabis
111.1	N111.1	561066	7549801	southern Central Zone	Abbabis
111.2	N111.2	560903	7549763	southern Central Zone	Abbabis
112	N112	560780.4611	7549772.892	southern Central Zone	
113	N113	559952.8826	7549154.757	southern Central Zone	Kobus intrusion (suite unknown)
114	N114	556674.3991	7547119.469	southern Central Zone	Abbabis

IDENT	Supergroup	Group	Formation	Lithology	Simplified Lithology
074JLb				Meta? felsic foliated tuff	Meta-tuff
80	Damara	Swakop	Kuiseb	Mica schist	Mica schist
81	Damara	Nosib	Naauwpoort	Felsic volcanic	Rhyolite
086KNa	Damara	Swakop	Kuiseb	Biotite - garnet gneiss	Gneiss
89	Damara	Hakos	Naos	Biotite schist	Mica schist
91.1				Pegmatite	Pegmatite
91.2				Tourmaline pegmatite	Pegmatite
91.3	Damara	Swakop	Kuiseb	Mica schist	Mica schist
91.4				Quartz vein with Tourmaline	Pegmatite
92.1				Pegmatite	Pegmatite
94	Damara	Swakop	Arandis	Bt-cord schist	Mica schist
95	Damara	Swakop	Arandis	Marble	Marble
96.1	Damara	Swakop	Arandis	Marble (Impure)	Marble
96.2	Damara	Swakop	Arandis	Quartzite	Quartzite
97	Damara	Swakop	Arandis	Mica schist	Mica schist
98	Damara	Swakop	Arandis	Quartzite	Quartzite
99	Damara	Swakop	Arandis	Quartzite	Quartzite
100	Damara	Swakop	Arandis	Marble	Marble
102	Damara	Swakop	Arandis	Calcschist and marble	Marble
106				Granodiorite	Granodiorite
107				Granite	Granite
108				Augen gneiss	Gneiss
110.1				Pegmatite	Pegmatite
110.2			Noab	Quartzite	Quartzite
110.3			Noab	Schist with magnetite vein	Mica Schist
110.4			Noab	Amphibolitic schist	Amphibolite
111.1			Noab	Pyroxenite	Pyroxenite
111.2			Noab	Arkose	Sandstone
112	Damara	Swakop	Karibib	Marble interlayered with dolomite	Marble
113				Biotite granite	Granite
114			Noab	Deformed granite	Granite

IDENT	Individual magnetic susceptibility measurements (x10^{-3} SI units)																		Mean (x 10^{-3} SI units)
	1	2	3	4	5	6	7	8	9	10	11	12	13	14	15	16	17	18	
074JLb	7.33	4.98	5.88	7.84	6.33														6.472
80	0.291	0.275	0.268	0.303	0.279														0.283
81	-0.02	-0.009	-0.053	-0.012	-0.024														-0.024
086KNa	0.272	0.407	0.414	0.308	0.31														0.342
89	0.032	0.023	0.027	0.029	0.019														0.026
91.1	-0.12	0.003	0.005	0.001	-0.001														-0.022
91.2	0.52	0.44	0.79	0.24	0.52														0.502
91.3	0.181	0.249	0.276	0.208	0.224														0.228
91.4	0.188	0.13	0.203	0.126	0.087	0.12													0.142
92.1	-0.006	0.005	0.006	0.005	-0.012	-0.011													-0.002
94	0.14	0.142	0.124	0.127	0.144														0.135
95	0.167	0.149	0.179	0.228	0.157														0.176
96.1	0.459	0.51	0.657	0.527	0.466														0.524
96.2	0.175	0.199	0.197	0.162	0.162														0.179
97	0.207	0.216	0.222	0.141	0.223														0.202
98	0.165	0.156	0.172	0.188	0.15														0.166
99	0.27	0.247	0.289	0.266	0.259														0.266
100	0.048	0.042	0.011	0.048	0.034														0.037
102	0.016	0.022	0.015	0.023	0.024														0.020
106	17.4	16.9	19.1	16.3	14.1														16.760
107	0.482	0.246	0.455	0.208	0.234														0.325
108	0.921	1.2	1.12	1.19	1.23														1.132
110.1	-0.002	0.01	0.004	0.036	0.007	0.009	0.015												0.011
110.2	0.015	0.009	0.002	0.031	0.007	0.011													0.013
110.3	5.77	7.94	7.78	2.95	3.68	7.27	2.5	1.51	0.121										4.391
110.4	0.569	0.343	0.701	0.517	0.432														0.512
111.1	9.2	6.4	5.24	3.44	5.54														5.964
111.2	0.102	0.254	0.439	0.666	0.317														0.356
112	0.021	0.039	0.013	0.036	0.006														0.023
113	0.458	0.672	0.867	0.773	0.891														0.732
114	0.109	0.094	0.113	0.102	0.097	0.024	0.009	0.007	0.107	0.002	0.031								0.063

IDENT	Locality	UTM_X	UTM_Y	Zone	Suite
115	N115	553694.7661	7550848.15	southern Central Zone	Abbabis
116B	N116	583641.1847	7559801.521	southern Central Zone	Goas
117A	N117	579458.9353	7551665.018	southern Central Zone	Goas
118A	N118	581425.7162	7549459.553	southern Central Zone	Goas
119.1	N119.1	581511	7549549	southern Central Zone	Goas
119.2	N119.2	581511	7549549	southern Central Zone	Goas
120	N120	583458.6083	7551407.008	southern Central Zone	Goas
121	N121	583335.3408	7552973.721	southern Central Zone	Goas
122	N122	583964.2071	7553941.971	southern Central Zone	Goas
124	N124	584489.9281	7553766.792	southern Central Zone	Goas
125.1	N125.1	578428	7563487	southern Central Zone	
125.2	N125.2	578428	7563487	southern Central Zone	Goas
125.3	N125.3	578428	7563487	southern Central Zone	Goas
126	N126	579041.6123	7563533.3	southern Central Zone	Goas
127A	N127	583836.2924	7563482.181	southern Central Zone	Goas
129B	N129	603266.6991	7543296.773	southern Central Zone	Goas
130	N130	602503.7549	7541470.283	southern Central Zone	Goas
132.1	N132.1	516255	7532054	southern Central Zone	
132.2	N132.2	516255	7532054	southern Central Zone	
132.3	N132.3	516255	7532054	southern Central Zone	
132.4	N132.4	516255	7532054	southern Central Zone	
133.1	N133.1	514561	7530143	southern Central Zone	Salem
133.2	N133.2	514561	7530143	southern Central Zone	
133.3	N133.3	514561	7530143	southern Central Zone	
133.4	N133.4	514561	7530143	southern Central Zone	
134.1	N134.1	514570	7528167	southern Central Zone	Salem
134.2	N134.2	514582	7528153	southern Central Zone	
134.3	N134.3	514584	7528158	southern Central Zone	
134.4	N134.4	514597	7528148	southern Central Zone	
134.5	N134.5	514632	7528122	southern Central Zone	
134.6	N134.6	514640	7528118	southern Central Zone	

IDENT	Supergroup	Group	Formation	Lithology	Simplified Lithology
115				Augen gneiss	Gneiss
116B				Granodiorite	Granodiorite
117A				Gabbro	Gabbro
118A				Porphyritic gabbro	Gabbro
119.1				Lighter granitoid	Granite
119.2				Darker granitoid	Diorite
120				Porphyritic gabbro	Gabbro
121				Porphyritic gabbro	Gabbro
122				Darker granitoid	Diorite
124				Darker granitoid	Diorite
125.1	Damara	Swakop	Karibib	Marble	Marble
125.2				Gneiss	Gneiss
125.3				Diorite with inclaves	Diorite
126				Granodiorite	Granodiorite
127A				Diorite	Diorite
129B				Diorite (Tonolite?)	Diorite
130				Diorite	Diorite
132.1	Damara	Nosib	Etusis	Marble	Marble
132.2				Pegmatite	Pegmatite
132.3	Damara	Nosib	Etusis	Pelitic schist	Slate
132.4	Damara	Nosib	Etusis	Quartzite	Quartzite
133.1				Biotite granite	Granite
133.2	Damara	Swakop	Kuiseb	Marble	Marble
133.3	Damara	Swakop	Kuiseb	Mica schist	Mica schist
133.4	Damara	Swakop	Kuiseb	Biotite - garnet gneiss	Gneiss
134.1				Biotite granite	Granite
134.2	Damara	Swakop	Karibib	Calc-silicate	Marble
134.3	Damara	Swakop	Karibib	Marble	Marble
134.4				Pegmatite	Pegmatite
134.5	Damara	Swakop	Karibib	Marble	Marble
134.6	Damara	Swakop	Karibib	Marble	Marble

IDENT	Individual magnetic susceptibility measurements (x10^{-3} SI units)																		Mean (x 10^{-3} SI units)
	1	2	3	4	5	6	7	8	9	10	11	12	13	14	15	16	17	18	
115	0.363	0.397	4.1	7.47	0.287	0.249													2.144
116B	0.217	0.196	0.178	0.287	1.81	0.362	0.593												0.520
117A	0.279	0.303	0.262	0.366	0.319	0.316	0.259	0.339	0.075	0.128	0.128								0.252
118A	0.428	0.338	0.48	0.386	0.444	0.522													0.433
119.1	0.456	0.094	0.044	0.056	0.188														0.168
119.2	6.63	4.99	13.3	8.84	11.8	10.9													9.410
120	0.213	0.339	0.251	0.261	0.304														0.274
121	0.319	0.324	0.232	0.367	0.251														0.299
122	11.7	10	5.85	10.8	8.08														9.286
124	6.4	5.99	8.59	4.97	3.78														5.946
125.1	0.003	0.003	0.027	0.011	0.125														0.034
125.2	0.079	0.089	0.091	0.079	0.396	0.355	0.462												0.222
125.3	10.3	8.71	1.36	10.9	13.5	9.38													9.025
126	6.63	3.53	4.96	3.23	6.02														4.874
127A	0.414	0.56	0.393	0.512	0.406	9.78	11.3	3.16	15.5	8.44	7.8								5.297
129B	9.92	7.15	8.96	4.93	7.06	7.71	7.61	6.76	6.93										7.448
130	15.3	16.1	24.1	14.6	11.8														16.380
132.1	0.338	0.384	0.218	0.101	0.371	0.011	0.038	0.053	0.38	0.53									0.242
132.2	-0.01	-0.014	-0.011	-0.008	-0.014														-0.011
132.3	0.267	0.263	0.281	0.167	0.179														0.231
132.4	0.098	0.065	0.097	0.133	0.149														0.108
133.1	0.25	0.187	0.057	0.048	0.062	0.112	0.112	0.847	0.54										0.246
133.2	0.012	0.008	0.017	0.089	0.019														0.029
133.3	0.202	0.194	0.214	0.275	0.127														0.202
133.4	0.202	0.152	0.111	0.607	0.314														0.277
134.1	0.029	-0.02	-0.001	0.019	0.018	0.006	-0.011												0.006
134.2	0.158	0.263	0.168	0.357	0.091	0.252													0.215
134.3	0.007	0.03	0.003	0.073	0.015														0.026
134.4	-0.016	0.001	-0.01	-0.004	-0.021	-0.026													-0.013
134.5	0.034	0.007	0.002	0.015	0.021														0.016
134.6	-0.021	0.003	-0.016	-0.008	0.015														-0.005

IDENT	Locality	UTM_X	UTM_Y	Zone	Suite
134.7	N134.7	514645	7528110	southern Central Zone	
134.8	N134.8	514629	7528083	southern Central Zone	
134.9	N134.9	514642	7528023	southern Central Zone	
135	N135	514709	7527658	southern Central Zone	
136	N136	512255	7519627	southern Central Zone	
136.1	N136.1	512445	7519864	southern Central Zone	
136.2	N136.2	512407	7519830	southern Central Zone	
136.3	N136.3	512375	7519794	southern Central Zone	
136.4	N136.4	512347	7519763	southern Central Zone	
136.5	N136.5	512327	7519731	southern Central Zone	
136.6	N136.6	512304	7519708	southern Central Zone	
136.7	N136.7	512293	7519690	southern Central Zone	
136.8	N136.8	512284	7519667	southern Central Zone	
136.9	N136.9	512283	7519636	southern Central Zone	
138	N138	585686	7523211	southern Central Zone	Goas
139	N139	585944.9733	7523933.66	southern Central Zone	Goas
140	N140	586878.8464	7521646.407	southern Central Zone	Goas
141	N141	586053.8699	7537946.739	southern Central Zone	Goas
142A	N142	604043.6756	7539361.43	southern Central Zone	Goas
143B	N143	604039	7539359	southern Central Zone	Goas
148.1	N148.1	488045	7654009	Southern Kaoko or Ugab Zone	
148.2	N148.2	488086	7653554	Southern Kaoko or Ugab Zone	
149.1	N149.1	487899	7653297	Southern Kaoko or Ugab Zone	
149.2	N149.2	487899	7653297	Southern Kaoko or Ugab Zone	
150.1	N150.1	480155	7643739	Southern Kaoko or Ugab Zone	
150.2	N150.2	480155	7643739	Southern Kaoko or Ugab Zone	
151.1	N151.1	477641	7640800	Southern Kaoko or Ugab Zone	
151.2	N151.2	477641	7640800	Southern Kaoko or Ugab Zone	
151.3	N151.3	477641	7640800	Southern Kaoko or Ugab Zone	
152.1	N152.1	476664	7640569	Southern Kaoko or Ugab Zone	
152.2	N152.2	476664	7640569	Southern Kaoko or Ugab Zone	

IDENT	Supergroup	Group	Formation	Lithology	Simplified Lithology
134.7				Pegmatite	Pegmatite
134.8	Damara	Swakop	Arandis	Calc-silicate	Marble
134.9	Damara	Swakop	Arandis	Calc-silicate	Marble
135	Damara	Nosib	Khan	Bluish-grey diopside-biotite gneiss	Gneiss
136	Damara	Swakop	Chuos	Diamictite with granitic clasts and magnetite	Diamictite
136.1	Damara	Swakop	Chuos	Quartzite	Quartzite
136.2	Damara	Swakop	Chuos	Quartzite	Quartzite
136.3				Pegmatite	Pegmatite
136.4	Damara	Swakop	Rössing	Schist	Schist
136.5	Damara	Swakop	Rössing	Schist	Schist
136.6	Damara	Swakop	Rössing	Leuco-granite	Granite
136.7	Damara	Swakop	Rössing	Schist	Schist
136.8	Damara	Swakop	Rössing	Schist	Schist
136.9	Damara	Swakop	Chuos	Ironstone	Ironstone
138				Diorite	Diorite
139				Diorite	Diorite
140				Hornblende diorite	Diorite
141				Granite to granodiorite	Diorite
142A				Meta-gabbro	Gabbro
143B				Gabbro	Gabbro
148.1	Damara	Zerrissene	Amis	Cordierite schist	Schist
148.2				Pegmatite	Pegmatite
149.1	Damara	Zerrissene	Amis	Cordierite schist	Schist
149.2				Pegmatite	Pegmatite
150.1	Damara	Zerrissene	Amis	Quartzite	Quartzite
150.2				Pegmatite	Pegmatite
151.1	Damara	Zerrissene	Amis	Biotite schist	Mica schist
151.2	Damara	Zerrissene	Amis	Quartzite	Quartzite
151.3				Pegmatite (mica-rich)	Pegmatite
152.1	Damara	Zerrissene	Amis	Interbandded layers of quartzite and schist intruded by pegmatite	Schist
152.2				Pegmatite	Pegmatite

IDENT	Individual magnetic susceptibility measurements (x10^{-3} SI units)																		Mean (x 10^{-3} SI units)
	1	2	3	4	5	6	7	8	9	10	11	12	13	14	15	16	17	18	
134.7	-0.003	0.007	0.006	0.012	-0.006														0.003
134.8	0.125	-0.021	-0.01	0.196	0.154														0.089
134.9	0.301	0.19	0.275	0.22	0.257														0.249
135	0.185	0.199	0.164	0.193	0.142														0.177
136	5.93	4.04	9.64	7.01	11.8														7.684
136.1	0.065	0.049	0.075	0.088	0.045														0.064
136.2	0.064	0.089	0.096	0.149	0.093														0.098
136.3	0.066	0.094	0.076	-0.007	-0.004														0.045
136.4	0.051	0.112	0.082	0.058	0.043														0.069
136.5	2.79	3.42	4.99	4.43	6.49														4.424
136.6	8.21	10.6	12.9	7.93	4.99	5.9	40.6	34.2											15.666
136.7	0.548	0.046	0.432	0.123	0.16	3.37	4.01	0.108	0.483	0.647									0.993
136.8	5.53	1.66	1.37	0.323	5.42														2.861
136.9	0.233	13	0.09	1.35	2														3.335
138	8.24	12.3	5.24	12.1	0.561	7.79	5.39	8.95	7.46	4.77	7.56	6.82							7.265
139	5.94	1.99	8.14	2.32	10.4														5.758
140	34.8	43	13	36.2	43.6	23.3	58.5	60.8	46.6										39.978
141	13.8	4.72	4.88	18.9	11.7														10.800
142A	0.913	47.8	1.5	24.3	47.3	0.582	0.511												17.558
143B	0.349	0.307	0.422	0.438	0.445														0.392
148.1	0.244	0.291	0.167	0.291	0.132	0.423	0.332	0.188	0.271	0.19									0.253
148.2	-0.011	-0.011	-0.007	-0.015	-0.011														-0.011
149.1	0.108	0.093	0.234	0.231	0.151														0.163
149.2	-0.013	-0.004	-0.009	-0.006	-0.007														-0.008
150.1	0.1	0.123	0.1	0.09	0.076	0.1	0.093												0.097
150.2	-0.014	-0.023	-0.013	-0.013	-0.02														-0.017
151.1	0.249	0.151	0.195	0.174	0.317														0.217
151.2	0.207	0.07	0.073	0.087	0.099														0.107
151.3	-0.016	-0.01	-0.034	-0.024	-0.018														-0.020
152.1	0.004	0.144	0.166	0.196	0.122	0.424	0.239	0.024	0.105	0.252	0.136	0.122							0.161
152.2	-0.006	-0.028	-0.028	-0.008	-0.024														-0.019

IDENT	Locality	UTM_X	UTM_Y	Zone	Suite
153.1	N153.1	480938	7634538	Northern Central Zone	
153.2	N153.2	480930	7634512	Northern Central Zone	
153.3	N153.3	480904	7634511	Northern Central Zone	
153.4	N153.4	480888	7634511	Northern Central Zone	
153.5	N153.5	480866	7634512	Northern Central Zone	
153.6	N153.6	480856	7634508	Northern Central Zone	
153.7	N153.7	480840	7634511	Northern Central Zone	
153.8	N153.8	480825	7634510	Northern Central Zone	
153.9	N153.9	480816	7634508	Northern Central Zone	
153.1	N153.10	480806	7634513	Northern Central Zone	
153.1	N153.10	480806	7634513	Northern Central Zone	
153.11	N153.11	480792	7634511	Northern Central Zone	
153.12	N153.12	480767	7634504	Northern Central Zone	
154	N154	470113.206	7616257.866	Northern Central Zone	
155	N155	455548.6108	7605342.9	Southern Kaoko or Ugab Zone	
156	N156	454836.213	7604420.681	Southern Kaoko or Ugab Zone	
157	N157	439595.1521	7578984.444	Southern Kaoko or Ugab Zone	
158	N158	433159	7590825	Southern Kaoko or Ugab Zone	
159	N159	438560.3714	7616711.987	Southern Kaoko or Ugab Zone	
160	N160	467231	7675508	Granite only	Sorris Sorris
161.1	N161.1	463839	7675939	Granite only	Sorris Sorris
161.2	N161.2	463839	7675939	Granite only	Sorris Sorris
162	N162	488506	7678026	Granite only	Salem
163	N163	493268	7682763	Northern Zone Ais Dome	Sorris Sorris
164	N164	492744	7684329	Northern Zone Ais Dome	Sorris Sorris
165	N165	495003	7684737	Northern Zone Ais Dome	Omangambo
166	N166	490350	7686022	Northern Zone Ais Dome	Sorris Sorris
167	N167	490855	7685446	Northern Zone Ais Dome	Salem
168	N168	497050	7686559	Northern Zone Ais Dome	Sorris Sorris
174	N174	438226.871	7705343.945	Southern Kaoko or Ugab Zone	Namibian gabbro
175	N175	438785.6764	7705325.18	Southern Kaoko or Ugab Zone	

IDENT	Supergroup	Group	Formation	Lithology	Simplified Lithology
153.1	Damara	Swakop	Karibib	Marble with dolostone	Marble
153.2	Damara	Swakop	Karibib	Marble	Marble
153.3	Damara	Swakop	Karibib	Marble	Marble
153.4	Damara	Swakop	Karibib	Marble	Marble
153.5	Damara	Swakop	Karibib	Marble	Marble
153.6	Damara	Swakop	Karibib	Marble	Marble
153.7	Damara	Swakop	Karibib	Marble	Marble
153.8	Damara	Zerrissene	Amis	Metapelites	Metapelites
153.9	Damara	Zerrissene	Amis	Metapelites	Metapelites
153.1	Damara	Zerrissene	Amis	Metapelites	Metapelites
153.1				Pegmatite	Pegmatite
153.11				Pegmatite	Pegmatite
153.12	Damara	Zerrissene	Amis	Metapelites	Metapelites
154	Damara	Swakop	Arandis	Interbanded layers of biotite schist and quartzite	Mica schist
155	Damara	Nosib	Tsaun	Biotite gneiss	Gneiss
156	Damara	Nosib	Tsaun	Granite (fine grained)	Granite
157				Syntectonic pegmatite	Pegmatite
158	Damara	Nosib	Tsaun	Granite	Granite
159	Damara	Zerrissene	Amis	Garnet-amphibolite metasammite	Sandstone
160				Granite	Granite
161.1				Two fsp granite	Granite
161.2				Granite cut by dyke	Granite
162				Granite	Granite
163				Granite	Granite
164				Granite	Granite
165				Granite (post - tectonic) intruded by pegmatite	Granite
166				Granite (fine-grained)	Granite
167				Granite	Granite
168				Granite (post - tectonic)	Granite
174				Meta-gabbro	Gabbro
175	Damara	Zerrissene	Gemsbok River	Marble	Marble

IDENT	Individual magnetic susceptibility measurements ($x10^{-3}$ SI units)																		Mean ($x 10^{-3}$ SI units)
	1	2	3	4	5	6	7	8	9	10	11	12	13	14	15	16	17	18	
153.1	-0.002	0.006	0.031	0.113	0.014														0.032
153.2	0.004	0.022	0.006	-0.002	0.024														0.011
153.3	0.006	0.011	0.008	0.013	0.021														0.012
153.4	0.028	-0.001	0.01	0.019	0.029														0.017
153.5	-0.004	0.015	-0.001	-0.002	-0.009														0.000
153.6	-0.006	-0.002	0.026	0.008	0.011														0.007
153.7	-0.011	-0.004	-0.007	-0.004	-0.009														-0.007
153.8	0.135	0.014	0.024	0.051	0.099														0.065
153.9	5.65	0.362	0.351	5.7	4.83														3.379
153.1	0.014	0.046	0.08	0.013	0.09														0.049
153.1	0.007	-0.005	-0.004	0.013	0.024														0.007
153.11	-0.004	0.001	-0.014	-0.012	0.001														-0.006
153.12	0.13	0.092	0.069	0.17	0.092														0.111
154	0.159	0.552	0.816	0.669	0.883	0.122	3.640	0.326	0.956	0.68									0.880
155	0.073	0.057	2.05	0.166	0.323	0.208	0.091	0.011	0.619	0.249									0.385
156	0.745	7.05	1.16	2.54	2.41	10.8	5.92	0.222	0.649	0.515	2.86	0.115							2.916
157	0.277	0.178	0.199	0.239	0.821	0.406	0.212	0.628	0.735	0.267	0.185	0.255							0.367
158	8.06	2.56	7.46	3.95	5.74	3.77	0.765	11.4	10.3	2.88									5.689
159	0.089	0.076	0.365	0.646	0.128	0.572	0.095	1.13	0.161	0.629									0.389
160	2.46	5.48	0.182	0.277	0.734	5.44	1.85	0.834	0.732	0.883									1.887
161.1	5.1	3.38	4.37	6.11	8.9	5.75													5.602
161.2	0.49	2.19	2.11	1.42	0.522														1.346
162	8.84	8.15	3.75	5.95	6.19														6.576
163	2.69	5.03	6.62	6.71	5.44														5.298
164	4.88	8.28	10.1	11.2	4.95	3.41	7.7	5.59											7.014
165	16.7	14.6	6.93	11.7	4.9	8.65													10.580
166	4.02	2.87	4.72	3.26	4.38														3.850
167	1.55	2.07	1.1	1.28	2.7														1.740
168	0.094	0.333	0.772	0.492	0.911														0.520
174	0.509	0.683	1.02	1.12	0.419	0.329	0.59	0.43	0.504	1.11									0.671
175	0.017	0.058	0.152	0.084	0.074														0.077

IDENT	Locality	UTM_X	UTM_Y	Zone	Suite
176	N176	438316.7007	7705603.477	Southern Kaoko or Ugab Zone	Namibian gabbro
177	N177	439468.7791	7705365.169	Southern Kaoko or Ugab Zone	
178	N178	443711.7645	7704911.737	Southern Kaoko or Ugab Zone	
182	N182	412716.1719	7748454.102	Northern Zone	Sorris Sorris
187	N187	436424.4451	7738365.208	Northern Zone	
188a	N188a	436623.3086	7737985.787	Northern Zone	
188.1	N188.1	437254	7737956	Northern Zone	
188.2	N188.2	437289	7737783	Northern Zone	
188.3	N188.3	437402	7737787	Northern Zone	
188.4	N188.4	437529	7737819	Northern Zone	
200	N200	438912.1633	7764051.05	Kamanjab Inlier	Huab Complex
201	N201	438569.653	7764690.831	Kamanjab Inlier	Huab Complex
202	N202	439434.394	7764107.112	Kamanjab Inlier	Huab Complex
203	N203	440933.6853	7763153.462	Kamanjab Inlier	Huab Complex
204	N204	443795.4774	7762752.413	Kamanjab Inlier	Huab Complex
205	N205	447725.784	7756722.95	Northern Margin Zone	Huab Complex
206	N206	450309.2528	7748167.431	Northern Margin Zone	
207	N207	460135.752	7743153.137	Northern Zone	
208.1	N208.1	461868	7724724	Granite only	Sorris Sorris
208.2	N208.2	461868	7724724	Granite only	Sorris Sorris
209	N209	462161.3727	7723607.36	Granite only	Omangambo
210	N210	461179.6379	7722072.035	Granite only	Omangambo
211	N211	459571.3191	7720284.496	Granite only	Sorris Sorris
212	N212	456732.9974	7713581.557	Granite only	Sorris Sorris
213	N213	455549.1727	7715527.632	Granite only	Sorris Sorris
214	N214	454940.3003	7718314.607	Granite only	Sorris Sorris
215	N215	455230.0807	7720465.934	Granite only	Omangambo
216	N216	451187.2062	7725955.135	Granite only	Omangambo
217.1	N217.1	448376	7729925	Northern Zone	Sorris Sorris
217.2	N217.2	448376	7729925	Northern Zone	Omangambo
218	N218	452134.2903	7735440.268	Northern Zone	Sorris Sorris

IDENT	Supergroup	Group	Formation	Lithology	Simplified Lithology
176				Gabbro	Gabbro
177	Damara	Zerrissene	Gemsbok River	Phyllite and metapelites	Slate
178	Damara	Zerrissene	Gemsbok River	Marble	Marble
182				Granite (post tectonic)	Granite
187	Damara	Swakop	Kuiseb	Schist (Slatey)	Slate
188a	Damara	Swakop	Kuiseb	Pelitic schist	Slate
188.1	Damara	Swakop	Karibib	Breccia carbonate	Marble
188.2	Damara	Swakop	Kuiseb	Quartz vein with puk marks	Quartzite
188.3	Damara	Swakop	Kuiseb	Quartzite	Quartzite
188.4	Damara	Swakop	Kuiseb	Quartzite	Quartzite
200				Muscovite schist	Mica Schist
201				Meta-gabbro	Gabbro
202				Quartzite	Quartzite
203				Interlayers of leuco granite and metagabbro	Granite
204				meta-granite with amphibolite layers	Gneiss
205				Contact between basement and quartzitic and argullious metasediments	Gneiss
206	Damara	Mulden	Gaseneirob	Conglomerate	Conglomerate
207	Damara	Nosib	Naauwpoort	Conglomerate	Conglomerate
208.1				Granite (medium-grained)	Granite
208.2				Megacrystic granite	Granite
209				Megacrystic granite	Granite
210				Megacrystic granite	Granite
211				Granite	Granite
212				Granite (coarse-grained)	Granite
213				Granite (fine-grained) intruded by pegmatite	Granite
214				Megacrystic granite	Granite
215				Granite (coarse-grained)	Granite
216				Granite (coarse-grained)	Granite
217.1				Granite	Granite
217.2				Megacrystic granite	Granite
218				Granite	Granite

IDENT	Individual magnetic susceptibility measurements (x10^{-3} SI units)																		Mean (x 10^{-3} SI units)
	1	2	3	4	5	6	7	8	9	10	11	12	13	14	15	16	17	18	
176	0.373	0.187	0.344	0.505	0.372														0.356
177	0.178	0.178	0.15	0.149	0.104	0.207	1.93	0.222	0.257	0.23									0.361
178	-0.009	-0.006	0.045	-0.001	-0.008														0.004
182	2.31	1.53	3.58	1.63	0.425														1.895
187	0.065	0.252	0.373	1.4	0.211														0.460
188a	0.224	0.323	0.337	0.316	0.058														0.252
188.1	0.027	0.057	0.075	0.298	0.997	0.104													0.260
188.2	-0.017	-0.027	-0.013	0.212	0.037	0.005	0.351												0.078
188.3	-0.009	0.006	-0.007	-0.037	-0.047														-0.019
188.4	-0.003	0.01	-0.029	-0.181	0.135														-0.014
200	0.047	0.33	0.192	0.676	0.311	0.037	0.187	0.042	0.074	0.09									0.199
201	0.055	0.25	1.18	0.028	0.042	0.099	0.051	0.108											0.227
202	0.09	0.008	0.033	-0.006	0.05	0.352	0.089	0.496	0.052	0.064	0.102	0.102							0.119
203	0.701	0.466	0.669	1.02	0.935														0.758
204	5.4	3.05	3.04	6.73	6.87	5.19													5.047
205	8.27	10.5	5.17	4.67	1.99														6.120
206	0.105	0.102	0.092	0.193	0.451														0.189
207	12.3	12.9	9.41	23.6	12.7	21.7	12.1	11.7	6.58	19.4									14.239
208.1	0.773	0.488	1.04	0.594	0.407														0.660
208.2	5.46	6.27	2.96	0.57	5.69	6.1													4.508
209	8.97	9.71	9.01	8.97	7.31														8.794
210	15.8	11	12.6	11.3	6.13	10.2													11.172
211	0.04	0.042	0.298	0.461	0.083	0.108	0.128	0.069	0.044	0.032									0.131
212	0.274	0.323	0.112	0.341	0.16														0.242
213	-0.006	-0.117	-0.34	-0.006	0.338	0.14	0.129	0.236	0.119										0.055
214	0.534	0.135	0.093	0.349	0.326														0.287
215	9.6	10	5.8	6.87	8.72														8.198
216	3.01	2.63	1.91	2.94	2.44														2.586
217.1	0.319	1.5	0.257	3.55	0.194														1.164
217.2	9.26	9.95	7.54	8.27	6.58														8.320
218	4.29	4.12	4.43	2.13	6.43														4.280

IDENT	Locality	UTM_X	UTM_Y	Zone	Suite
219	N219	498186.9703	7748628.723	Northern Zone	Khorixas
220.1	N220.1	536344	7734639	Northern Zone	
220.2	N220.2	536344	7734639	Northern Zone	
221	N221	538476.7149	7734762.918	Northern Zone	
222	N222	530815.343	7713656.325	Northern Zone	
223	N223	546981.9251	7752677.016	Northern Zone	
224	N224	546136.684	7754949.75	Northern Zone	
225	N225	544802.7884	7753706.826	Northern Zone	
226	N226	548254.4378	7708123.296	Northern Zone	
227	N227	522372.0485	7696518.586	Granite only	Omangambo
228	N228	516897.166	7687565.032	Granite only	Omangambo
229	N229	562638.3971	7764395.224	Northern Zone	
230	N230	562268.8655	7762875.967	Northern Zone	
231	N231	571602.7326	7765595.788	Northern Zone	
232	N232	584824.6243	7748645.046	Northern Zone	
233	N233	585307.6319	7748803.357	Northern Zone	
234	N234	585657.103	7749287.818	Northern Zone	
236	N236	620236.5653	7760853.352	Northern Zone	
237	N237	666521.9822	7821407.974	Northern Platform	
238	N238	703634.6061	7831425.489	Northern Platform	
239	N239	706365.3778	7827672.894	Northern Margin Zone	
240	N240	753228.2038	7825406.659	Northern Margin Zone	
241	N241	616354.0982	7777189.633	Northern Zone	
242.1	N242.1	610632	7774865	Northern Zone	
242.2	N242.2	610632	7774865	Northern Zone	
243	N243	593105.5188	7767616.585	Northern Zone	
244	N244	574329.9988	7765939.891	Northern Zone	
001	Z001	21.72871883	-22.40680041	Ghanzi-Chobe Belt	Okwa Complex
002	Z002	21.94390890	-21.51969610	Ghanzi-Chobe Belt	
003	Z003	22.79775859	-21.26091795	Ghanzi-Chobe Belt	
004	Z004	22.42257046	-20.99637274	Ghanzi-Chobe Belt	Ghanzi

IDENT	Supergroup	Group	Formation	Lithology	Simplified Lithology
219				Gabbro	Gabbro
220.1	Damara	Swakop	Karibib	Marbles with dolostone	Marble
220.2	Damara	Swakop	Kuiseb	Green schist	Schist
221	Damara	Swakop	Kuiseb	Compositional bedding between greywacke and schist	Sandstone
222	Damara	Swakop	Kuiseb	Sandy schist containing mineralisation interbedded with carbonate layers	Schist
223	Damara	Swakop	Karibib	Marble interbedded with dolostone	Marble
224	Damara	Swakop	Karibib	Marble interbedded with ironstone	Marble
225	Damara	Swakop	Karibib	Marble	Marble
226	Damara	Swakop	Kuiseb	Metagreywacke	Sandstone
227				Granite (Syn - tectonic)	Granite
228				Megacrystic granite	Granite
229	Damara	Swakop	Okatjize	Dolostone	Dolostone
230	Damara	Swakop	Chuos	Ironstone	Ironstone
231	Damara	Swakop	Okatjize	Dolostone	Dolostone
232	Damara	Swakop	Karibib	Marble	Marble
233	Damara	Swakop	Karibib	Marble	Marble
234	Damara	Swakop	Karibib	Marble	Marble
236	Damara	Swakop	Karibib	Dolostone	Dolostone
237	Damara	Otavi	Auros	Laminated siltstone, shale and carbonate	Dolostone
238	Damara	Otavi	Elandshoek	Marble	Marble
239	Damara	Otavi	Gauss	Marble	Marble
240	Damara	Otavi	Maieberg	Impure marble	Marble
241	Damara	Swakop	Karibib	Marble	Marble
242.1	Damara	Swakop	Karibib	Marble	Marble
242.2	Damara	Swakop	Karibib	Schist	Schist
243	Damara	Swakop	Karibib	Marble	Marble
244	Damara	Swakop	Karibib	Marble	Marble
001				Granite gneiss	Granite
002	Ghanzi-Chobe	Ghanzi	D'Kar	Sandstone	Sandstone
003	Ghanzi-Chobe	Ghanzi	D'Kar	Sandstone	Sandstone
004	Ghanzi-Chobe		Kgwebe	Felspathic porphyry rhyolite	Rhyolite

IDENT	Individual magnetic susceptibility measurements (x10^{-3} SI units)																		Mean (x 10^{-3} SI units)
	1	2	3	4	5	6	7	8	9	10	11	12	13	14	15	16	17	18	
219	0.279	0.414	0.121	0.363	0.855														0.406
220.1	-0.019	-0.299	-0.113	0.669	-0.015	-0.022	-0.024	-0.05	0.07										0.022
220.2	0.068	0.107	0.286	0.352	0.267														0.216
221	0.053	0.151	0.443	0.021	0.501	0.205	0.04	0.096	0.098	0.259									0.187
222	3.55	10.5	3.21	10.6	0.52	9.76	2.74	0.486											5.171
223	-0.007	-0.021	0.01	-0.02	-0.011	0.044	0.045												0.006
224	-0.014	0.048	0.206	-0.024	0.034	0.297													0.091
225	0.053	-0.004	-0.006	-0.014	0.055	0.013	0.009	-0.002	0										0.012
226	0.073	0.108	0.066	0.077	0.128	0.189	-0.018	-0.025											0.075
227	3.07	2.69	2.81	3.66	3.43														3.132
228	0.068	0.113	0.072	0.068	0.065														0.077
229	0.037	0.207	0.24	0.518	0.236	0.258	0.341	0.558	0.149	0.324									0.287
230	106	74	100	66.2	114														92.040
231	0.248	0.17	0.202	0.186	0.225														0.206
232	-0.022	-0.003	-0.023	0.531	0.057	-0.108	0.061	0.004	-0.008	-0.014	-0.021	-0.029	-0.018						0.031
233	-0.016	0.274	0.157	-0.001	-0.022	-0.013	-0.018	-0.012	-0.021	-0.022	-0.011	-0.003							0.024
234	-0.01	-0.004	-0.015	-0.024	-0.013														-0.013
236	-0.017	0.217	0.242	0.143	-0.073	0.098	0.432	0.239											0.160
237	0.059	0.037	0.024	0.109	0.017	0.482	0.259	0.272	0.08	0.084	0.005	0.168							0.133
238	-0.013	-0.004	-0.011	0.002	0.006	0	-0.006	-0.004	-0.017	-0.012									-0.006
239	-0.03	-0.027	0.079	-0.128	0.28	0.173	-0.004	-0.027	0.004	-0.023									0.030
240	-0.019	0.41	0.136	0.356	0.062	0.135	0.661	0.016	-0.469	1.07	1.3	1.69	-0.004						0.411
241	-0.011	-0.002	-0.008	-0.028	-0.015														-0.013
242.1	-0.034	0.623	-0.012	-0.01	-0.006	0.141	0.208	0.223	-0.028	-0.009									0.110
242.2	0.01	0.183	0.58	0.224	0.611														0.322
243	-0.027	-0.032	-0.011	-0.033	-0.016														-0.024
244	-0.007	0.056	0.523	0.364	0.02	0.016	0.021	0.041	0.028	0.043									0.111
001	0.142	0.082	0.079	0.139	0.152														0.119
002	0.156	0.223	0.181	0.210	0.230	0.256													0.209
003	0.066	0.182	0.363	0.617	0.016	0.025	0.132	0.163	0.200	0.598	0.048	0.034	0.030	0.053	0.048				0.172
004	0.048	0.059	0.041	0.047	0.067	0.071	0.054	0.074	0.057	0.056									0.057

IDENT	Locality	UTM_X	UTM_Y	Zone	Suite
005	Z005	24.05765438	-18.61512264	Ghanzi-Chobe Belt	Ghanzi
006	Z006	26.13403647	-17.39417227	Choma-Kalomo Block	
007	Z007	26.14355328	-17.39224297	Choma-Kalomo Block	Choma-Kalomo Batholith
008	Z008	26.46318254	-17.03061307	Choma-Kalomo Block	Choma-Kalomo Batholith
009	Z009	26.70339857	-17.06756126	Choma-Kalomo Block	Choma-Kalomo Batholith
010	Z010	27.60431080	-15.96634080		Zambezi Supracrustal Sequence
011	Z011	28.25503408	-15.51881471	Zambezi Belt	
011C	Z011	28.25503408	-15.51881471	Zambezi Belt	
012.1	Z012	28.17725410	-15.91654360		Basement??
012.2	Z012	28.17725410	-15.91654360		Basement??
013	Z013	28.33428448	-15.82479403	Zambezi Belt	Zambezi Supracrustal Sequence
015	Z015	28.33828054	-15.82339558	Zambezi Belt	Zambezi Supracrustal Sequence
016	Z016	28.24039155	-15.64679835	Zambezi Belt	Zambezi Supracrustal Sequence
017A	Z017	28.18663449	-15.27245791	(Northern) Zambezi Belt	Lusaka Granite
018.1a	Z018	29.14263333	-13.94881667	Irumide Belt	Mkushi Metamorphic Complex
018.1b	Z018	29.14263333	-13.94881667	Irumide Belt	Mkushi Metamorphic Complex
018.2	Z018	29.14268333	-13.94840000	Irumide Belt	Mkushi Metamorphic Complex
018.3	Z018	29.14273333	-13.94791667	Irumide Belt	Mkushi Metamorphic Complex
018.4	Z018	29.14293333	-13.94740000	Irumide Belt	Mkushi Metamorphic Complex
018.5a	Z018	29.14306667	-13.94683333	Irumide Belt	Mkushi Metamorphic Complex
018.5b	Z018	29.14306667	-13.94683333	Irumide Belt	Mkushi Metamorphic Complex
018.5c	Z018	29.14306667	-13.94683333	Irumide Belt	Mkushi Metamorphic Complex
018.6a	Z018	29.14265000	-13.94653333	Irumide Belt	Mkushi Metamorphic Complex
018.6b	Z018	29.14265000	-13.94653333	Irumide Belt	Mkushi Metamorphic Complex
018.6c	Z018	29.14265000	-13.94653333	Irumide Belt	Mkushi Metamorphic Complex
018.7	Z018	29.14316667	-13.94560000	Irumide Belt	Mkushi Metamorphic Complex
018.8a	Z018	29.14350000	-13.94396667	Irumide Belt	Mkushi Metamorphic Complex
018.8b	Z018	29.14350000	-13.94396667	Irumide Belt	Mkushi Metamorphic Complex
019B	Z019	29.11302657	-13.96490403	Irumide Belt	Mkushi Metamorphic Complex
020	Z020	28.67225493	-13.88939388	Irumide Belt	
021	Z021	28.67096555	-13.75534975	Irumide Belt	Kampoyo Granite

IDENT	Supergroup	Group	Formation	Lithology	Simplified Lithology
005	Ghanzi-Chobe		Goha Hills	Poryritic Diacite	Diacite
006			Choma ?	Micaschist	Schist
007				Chlorite - Actinolite schist	Schist
008				Granodiorite	Granodiorite
009			Choma ?	Muscovite shcist	Schist
010			Muzuma	Marble (Impure)	Marble
011				Eclogite	Eclogite
011C				Pyroxenite	Pyroxenite
012.1				Porphyritic biotite granite	Granite
012.2				Biotite rich strain zone	Gneiss
013			Kafue Rhyolite	Meta-rhyolite	Rhyolite
015				Scapolite schist	Schist
016	Lusaka		Cheta	Scapolite Marble	Marble
017A	Lusaka			Biotite granite	Granite
018.1a				Augen gneiss (quartz - biotite)	Gneiss
018.1b				Pegmatite	Pegmatite
018.2				High grade Cu ore	Shale
018.3				Augen gneiss	Gneiss
018.4				Amphibolite	Amphibolite
018.5a				Augen gneiss	Gneiss
018.5b				Pegmatite (coarse)	Pegmatite
018.5c				Pegmatite (fine)	Pegmatite
018.6a				Highly oxidised zone (Aplite)	Granite
018.6b				Augen gneiss	Gneiss
018.6c				Amphibolite	Amphibolite
018.7				Augen gneiss	Gneiss
018.8a				Aplites	Granite
018.8b				Augen gneiss	Gneiss
019B				Mtuga granite	Granite
020		Muva		Irumide quartzite	Quartzite
021				Foliated biotite gneiss	Gneiss

IDENT	Individual magnetic susceptibility measurements (x10^{-3} SI units)																		Mean (x 10^{-3} SI units)
	1	2	3	4	5	6	7	8	9	10	11	12	13	14	15	16	17	18	
005	12.800	10.000	8.120	12.000	10.600														10.704
006	0.146	5.340	3.860	0.423	0.205	1.050	1.470												1.785
007	0.405	0.486	0.297	0.619	0.355														0.432
008	6.500	3.760	5.100	6.650	13.300	9.160													7.412
009	1.970	0.372	2.260	1.090	0.447	1.200	0.806												1.164
010	0.030	0.021	0.032	0.012	0.042														0.027
011	1.040	1.840	0.854	8.380	0.745	1.200	1.300	1.260	1.200										1.980
011C	23.300	29.400	29.800	27.500	28.600	13.900													25.417
012.1	4.430	15.000	20.600	0.977	0.820	0.398	0.731	0.182											2.781
012.2	0.067	0.068	0.233	0.250	0.163	0.241													0.170
013	25.400	6.360	5.760	22.300	8.210	13.500	19.700	31.500	25.300	20.300									17.833
015	2.590	21.700	23.600	2.250	4.110	1.980	3.850	7.380	6.130	6.070	10.900								8.233
016	-0.009	-0.016	-0.008	-0.007	-0.085	-1.120	-0.021	0.174	0.501	3.060	0.307	0.606	-0.336	0.286	0.455				0.252
017A	0.350	0.258	0.305	0.275	0.269														0.291
018.1a	3.180	7.560	4.160	3.980	5.080														4.792
018.1b	0.472	2.270	1.010	1.100	0.508														1.072
018.2	-0.021	-0.022	-0.151	-0.009	-0.007														-0.042
018.3	3.360	8.360	2.740	5.060	4.900														4.884
018.4	0.299	0.117	0.411	0.409	0.797														0.407
018.5a	8.810	6.110	0.080	0.637	1.520														3.431
018.5b	1.250	0.110	0.224	0.106	0.066														0.351
018.5c	7.750	4.850	2.450	6.860	3.340														5.050
018.6a	0.009	0.010	0.012	0.039	-0.004														0.013
018.6b	0.090	0.179	0.126	0.259	0.217	0.223													0.182
018.6c	0.593	0.591	0.322	0.447	0.384														0.467
018.7	1.800	0.487	1.530	1.230	8.770														2.763
018.8a	0.100	0.082	0.079	0.053	0.380														0.139
018.8b	0.619	0.225	0.014	0.629	0.097														0.317
019B	0.818	1.210	0.838	0.009	0.235	0.102	0.317	1.420	1.240	3.630	0.752								0.961
020	-0.002	-0.010	-0.002	-0.004	-0.016														-0.007
021	0.033	0.030	0.081	0.022	0.024	0.068													0.043

IDENT	Locality	UTM_X	UTM_Y	Zone	Suite
022	Z022	28.22372654	-12.52232231	Kafue Anticline	
024a	Z024	28.21343285	-12.52509939	Kafue Anticline	Basement
025	Z025	28.20245583	-12.60266796	Kafue Anticline	
027.1	Z027	28.04460686	-12.65893723	Lufilian Arc / Kafue Anticline	
027.2	Z027	28.04460686	-12.65893723	Lufilian Arc / Kafue Anticline	
027.3	Z027	28.04460686	-12.65893723	Lufilian Arc / Kafue Anticline	
027.4	Z027	28.04460686	-12.65893723	Lufilian Arc / Kafue Anticline	
028.1	Z028	28.20557752	-12.85056950	Lufilian Arc / Kafue Anticline	
028.2	Z028	28.20557752	-12.85056950	Lufilian Arc / Kafue Anticline	
028.3	Z028	28.20557752	-12.85056950	Lufilian Arc / Kafue Anticline	
028.4	Z028	28.20557752	-12.85056950	Lufilian Arc / Kafue Anticline	
028.5	Z028	28.20557752	-12.85056950	Lufilian Arc / Kafue Anticline	
029.1	Z029	27.87286166	-12.51248688	Lufilian Arc / Kafue Anticline	
029.2	Z029	27.87286166	-12.51248688	Lufilian Arc / Kafue Anticline	
029.3	Z029	27.87286166	-12.51248688	Lufilian Arc / Kafue Anticline	
029.4	Z029	27.87286166	-12.51248688	Lufilian Arc / Kafue Anticline	
029.5	Z029	27.87286166	-12.51248688	Lufilian Arc / Kafue Anticline	
029.6	Z029	27.87286166	-12.51248688	Lufilian Arc / Kafue Anticline	Nchanga basement granite
029.7	Z029	27.87286166	-12.51248688	Lufilian Arc / Kafue Anticline	
030.1	Z030	27.81666138	-12.55131868	Lufilian Arc / Kafue Anticline	Basement
030.2	Z030	27.81666138	-12.55131868	Lufilian Arc / Kafue Anticline	
030.3	Z030	27.81666138	-12.55131868	Lufilian Arc / Kafue Anticline	
031.1	Z031	25.81343347	-12.22683609	Lufilian Arc/ Domes Region	Basement
031.2	Z031	25.81343347	-12.22683609	Lufilian Arc/ Domes Region	
032	Z032	25.81956795	-12.24886039	Lufilian Arc/ Domes Region	
033	Z033	25.82190989	-12.24936773	Lufilian Arc/ Domes Region	Basement??
034.1	Z034	25.82557206	-12.24860585	Lufilian Arc/ Domes Region	
034.2	Z034	25.82557206	-12.24860585	Lufilian Arc/ Domes Region	Basement??
035	Z035	25.69632668	-12.21020368	Lufilian Arc/ Domes Region	
036A	Z036	25.79562299	-12.18938143	Lufilian Arc/ Domes Region	
037	Z037	25.81435401	-12.18314259	Lufilian Arc/ Domes Region	

IDENT	Supergroup	Group	Formation	Lithology	Simplified Lithology
022	Katanga	Lower Roan		Argillite quartzite	Quartzite
024a				Grey granite	Granite
025		Muva		Quartzite	Quartzite
027.1	Katanga	Lower Roan	Chimfusi	Conglomerate (F/W)	Conglomerate
027.2	Katanga	Lower Roan	Ore Shale	Ore shale	Slate
027.3	Katanga	Lower Roan		Schist	Schist
027.4	Katanga	Lower Roan		Quartz vein with mylonitic layers	
028.1	Katanga	Lower Roan	Pelito-arkosic	Interbedded sandstones and slatey scists	Sandstone
028.2	Katanga	Lower Roan	Ore Shale	Ore shale	Slate
028.3	Katanga	Lower Roan	Pelito-arkosic	Interbedded sandstones and slatey scists (to the SW of GPS pt)	Sandstone
028.4	Katanga	Lower Roan		Alteration zone (white)	
028.5	Katanga	Lower Roan	Ore Shale	Ore shale (western side)	Slate
029.1	Katanga	Lower Roan	Chimfusi	Gritty conglomerate	Conglomerate
029.2	Katanga	Lower Roan	Ore Shale	Shale marker	Shale
029.3	Katanga	Lower Roan	Kafufya	Pink quartzite	Quartzite
029.4	Katanga	Lower Roan	Pelito-arkosic	Banded upper sandstone	Sandstone
029.5	Katanga	Lower Roan	Pelito-arkosic	Felspathic quartzite	Quartzite
029.6				Granite	Granite
029.7	Katanga	Lower Roan	Ore Shale	Lower banded shale	Shale
030.1				Schist	Schist
030.2	Katanga	Lower Roan	Pelito-arkosic	Arkose	Sandstone
030.3	Katanga	Lower Roan	Ore Shale	Lower banded shale	Slate
031.1				Biotite schist	Schist
031.2	Katanga?	Lower Roan?		Quartz - muscovite schist (ore body)	Schist
032	Katanga?	Lower Roan?		Two mica shist (H/W)	Schist
033				Migmatitic gneiss	Gneiss
034.1	Katanga?	Lower Roan?		Two mica shist (bt + musc)	Schist
034.2				Augen gneiss	Gneiss
035	Katanga?	Lower Roan?	Mosa Hill	Quartz - muscovite schist	Schist
036A	Katanga?	Upper Roan or Mwashya Subgroup		Basalt	Basalt
037	Katanga?	Lower Roan?		White micaschist	Schist

IDENT	Individual magnetic susceptibility measurements ($x10^{-3}$ SI units)																		Mean ($x 10^{-3}$ SI units)
	1	2	3	4	5	6	7	8	9	10	11	12	13	14	15	16	17	18	
022	0.089	0.132	0.069	0.039	0.075														0.081
024a	16.000	3.800	3.240	4.560	0.720														5.664
025	0.057	0.078	0.090	0.086	0.095														0.081
027.1	0.030	0.102	0.017	0.012	0.030														0.038
027.2	0.614	0.467	0.344	0.400	0.160	0.275	0.141	0.108	0.142										0.295
027.3	0.178	0.146	0.158	0.223	0.216														0.184
027.4	0.013	-0.018	0.011	0.064	-0.015	-0.011													0.007
028.1	0.087	0.386	0.357	0.073	0.186	0.004	-0.011	-0.001	-0.006	-0.001									0.107
028.2	0.178	0.005	0.005	0.025	0.113														0.065
028.3	0.093	0.048	0.010	0.103	0.036	0.006	-0.010	-0.004	-0.011	-0.018	-0.021								0.021
028.4	-0.004	-0.011	-0.009	0.022	-0.011														-0.003
028.5	0.112	0.176	0.133	0.121	0.157														0.140
029.1	0.022	0.022	0.012	0.038	0.023	0.170	0.125	0.161											0.072
029.2	0.044	0.050	0.031	0.049	0.051														0.045
029.3	0.022	0.018	0.002	0.009	0.001														0.010
029.4	0.011	-0.001	0.002	0.005	0.002	0.002													0.004
029.5	0.003	0.007	-0.008	0.004	0.007														0.003
029.6	0.256	0.471	0.337	0.213	0.324														0.320
029.7	0.011	0.056	0.052	0.046	0.044														0.042
030.1	0.136	0.163	0.374	0.119	0.145	0.188													0.188
030.2	0.029	0.043	0.011	0.007	0.004														0.019
030.3	0.102	0.182	0.364	0.256	0.098														0.200
031.1	0.182	0.194	0.116	0.109	0.097	0.135	0.143	0.120	0.168	0.042	1.620	0.742							0.306
031.2	0.098	0.078	0.112	0.109	0.194	0.341	0.308	0.052	0.048	0.031									0.137
032	0.299	0.101	0.090	0.182	0.043	0.044	0.056												0.116
033	0.037	0.072	0.431	0.074	0.045	0.661													0.220
034.1	0.043	0.053	0.112	0.184	0.215	0.251													0.143
034.2	0.074	0.057	0.059	0.074	0.063														0.065
035	0.183	0.372	0.439	0.198	0.768	0.727	0.619	0.403	1.110	1.470	0.411	0.479	0.712	0.642	0.566				0.607
036A	0.336	0.199	0.246	0.322	0.289	0.349	0.368	0.320	0.372	0.330									0.313
037	0.782	0.784	0.181	1.010	0.170	0.727	1.430	0.136	1.140	0.659	0.876								0.718

IDENT	Locality	UTM_X	UTM_Y	Zone	Suite
038	Z038	25.82471204	-12.18310553	Lufilian Arc/ Domes Region	
039	Z039	24.21363813	-11.18229630	Lufilian Arc/ Domes Region	Basement??
040.1	Z040	24.45310522	-11.90649624	Lufilian Arc	
040.2	Z040	24.45310522	-11.90649624	Lufilian Arc	
041	Z041	24.45573100	-11.90774500	Lufilian Arc	
044	Z044	24.45776247	-11.90687260	Lufilian Arc	
045	Z045	24.45650740	-11.90667153	Lufilian Arc	
046.1	Z046	26.42885551	-12.09221933	Lufilian Arc/ north of Solwezi Dome	
046.2	Z046	26.42885551	-12.09221933	Lufilian Arc/ north of Solwezi Dome	
046.3	Z046	26.42885551	-12.09221933	Lufilian Arc/ north of Solwezi Dome	
047	Z047	26.41709430	-12.07921835	Lufilian Arc/ north of Solwezi Dome	
048	Z048	26.48605468	-14.59193911	Lufilian Arc/Katanga High	Hook Batholith
049	Z049	26.40675345	-14.64997580	Lufilian Arc/Katanga High	Hook Batholith
050	Z050	26.42233213	-14.61947413	Lufilian Arc/Katanga High	Hook Batholith
051	Z051	26.41426785	-14.65280662	Lufilian Arc/Katanga High	Hook Batholith
052	Z052	26.52018643	-14.92082904	Lufilian Arc/Katanga High	Hook Batholith
053	Z053	26.53960300	-14.92408754	Lufilian Arc/Katanga High	Hook Batholith
054	Z054	26.55554738	-14.92956178	Lufilian Arc/Katanga High	Hook Batholith
055	Z055	26.51369181	-14.96831668	Lufilian Arc/Katanga High	Hook Batholith
056	Z056	26.74653042	-14.96798891	Lufilian Arc/Katanga High	Hook Batholith
057	Z057	26.77712100	-14.95692729	Lufilian Arc/Katanga High	Hook Batholith
058	Z058	26.79193375	-15.21700872	Lufilian Arc/Katanga High	Hook Batholith

IDENT	Supergroup	Group	Formation	Lithology	Simplified Lithology
038	Katanga?	Lower Roan?		Quartzite	Quartzite
039				Granite	Granite
040.1	Katanga	Nguba Group/Mwashya Subgroup?		Marl stone	Marlstone
040.2	Katanga	Nguba Group/Mwashya Subgroup?		Grey Ruk breccai	Breccai
041	Katanga	Nguba Group/Mwashya Subgroup?		Hematite	Ironstone
044	Katanga	Nguba	Mwale/Grand Conglomerate	Grand Conglomerate (diamictite)	Diamictite
045	Katanga	Nguba	Mwale/Grand Conglomerate	Grand Conglomerate (diamictite)	Diamictite
046.1	Katanga	Nguba Group/Mwashya Subgroup?	Dipeta Mwashya	Carbonaceous shale	Shale
046.2	Katanga	Nguba Group/Mwashya Subgroup?	Knotted shist	Mottled shist	Schist
046.3	Katanga			Quartz vein	Quartz vein
047	Katanga		Knotted shist	Mineralised mottled schist	Schist
048				Potassium feldspar porphyritic granite	Granite
049				Hippo Mine dumps	Granite
050				Hematite silicified breccai with flourite	Ironstone
051				Hematite breccai with flourite	Ironstone
052				Granitic mylonite	Granite
053				Coarse grained granitic mylonite	Granite
054				Granitic mylonite (less porphyritic)	Granite
055				Fine grained porphyritic granite	Granite
056				Granodiorite	Granodiorite
057				Micro - Gabbro	Gabbro
058				Very coarse grained granite	Granite

IDENT	Individual magnetic susceptibility measurements ($x10^{-3}$ SI units)																		Mean ($x 10^{-3}$ SI units)
	1	2	3	4	5	6	7	8	9	10	11	12	13	14	15	16	17	18	
038	0.011	0.592	0.044	0.098	0.022														0.153
039	1.070	5.370	4.210	2.160	2.370	4.920	5.230	5.150	2.030	2.790	11.200	10.800	2.530	0.645	3.830	7.120	0.492	7.040	4.387
040.1	0.108	0.102	0.046	0.038	0.041	0.058	0.086	0.063	0.011	0.030									0.058
040.2	0.080	0.063	0.095	0.275	0.061	0.143	0.030												0.107
041	5.820	2.900	2.980	5.390	3.280														4.074
044	0.614	0.141	0.142	0.301	0.342														0.308
045	0.876	0.176	0.126	0.147	0.065														0.278
046.1	-0.012	-0.011	0.023	0.036	0.010	-0.004	0.003												0.006
046.2	0.255	0.208	0.214	0.220	0.288														0.237
046.3	-0.010	-0.023	-0.020	-0.006	-0.010														-0.014
047	1.790	1.840	0.136	0.978	1.320	2.090	1.350	1.300	0.641	1.250									1.270
048	19.300	14.100	14.200	7.400	9.730	11.800													12.755
049	0.596	0.396	0.105	0.171	0.037	0.175	0.155	0.157	0.303	0.245									0.234
050	34.300	46.500	87.500	65.400	4.110	16.500	7.900	3.250	4.250										29.968
051	1.310	0.655	1.340	1.560	1.100	0.752	0.600												1.045
052	11.600	15.100	12.300	11.500	16.400	3.860	2.490	1.770	6.710	6.230									8.796
053	26.900	15.900	28.200	27.400	13.300	25.600	23.200	15.800	24.900	23.200	22.500	30.000							23.075
054	25.100	32.100	18.600	26.900	31.300	12.600													24.433
055	24.100	18.400	9.920	10.000	28.300	16.400	6.990	20.000	26.800										17.879
056	25.100	36.400	51.000	17.600	38.100	14.500	11.500	23.200	12.500	15.500									24.540
057	21.200	20.500	13.900	15.200	10.600														16.280
058	43.600	20.000	21.700	28.300	14.200	3.780	14.600	14.900	7.230	8.100									17.641

Appendix 6:

a) Sub-Kalahari geological map of Namibia and northwestern Botswana based on the interpretation of potential field data constrained by outcrop geology and pre-Karoo and Tsodilo Resources Ltd. boreholes (green circles).

b) Legend and lithostratigraphic table for the sub-Kalahari geological map.

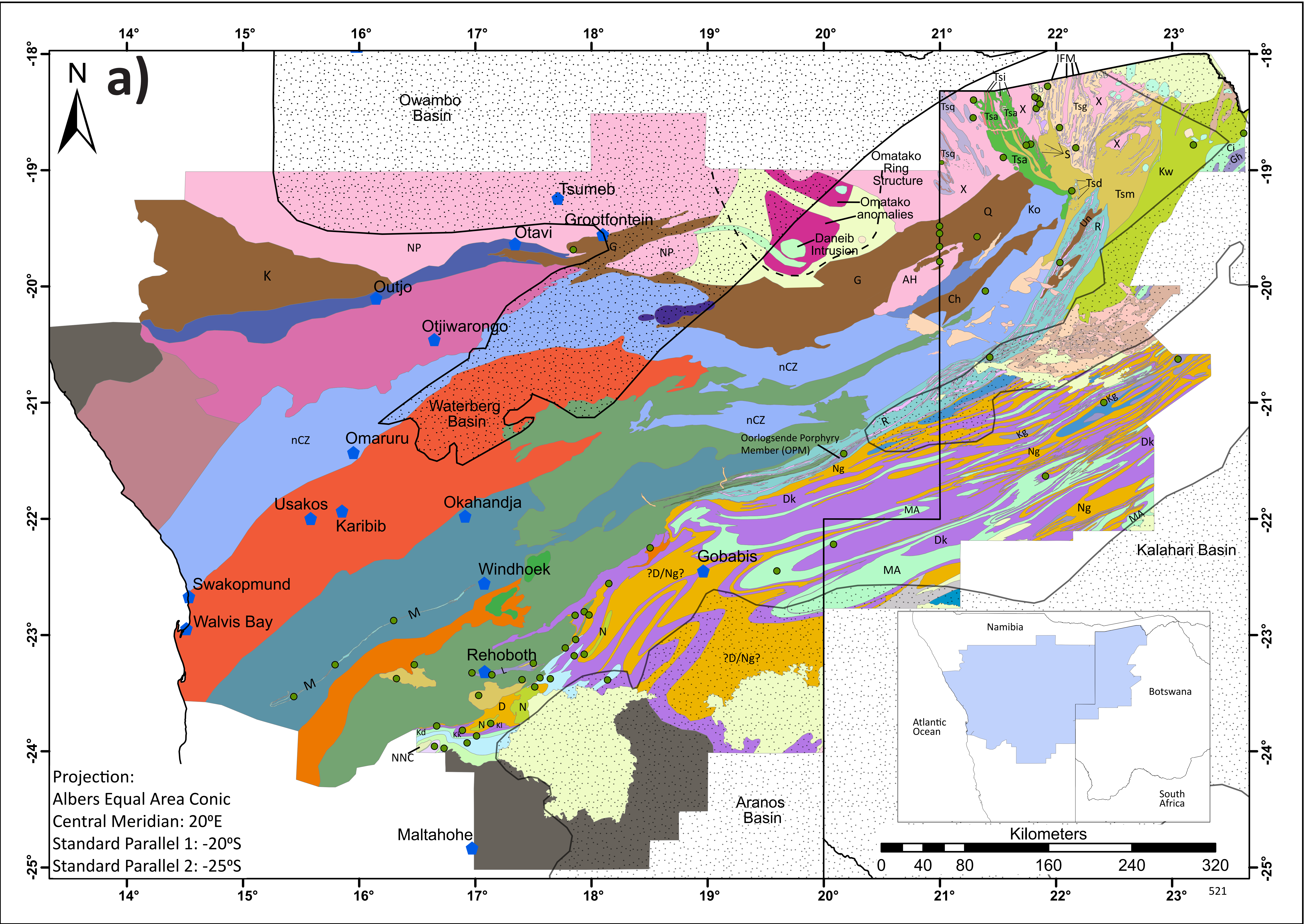

a)
N
Owambo Basin
Tsumeb
Grootfontein
Otavi
Outjo
Otjiwarongo
Omaruru
Usakos
Karibib
Okahandja
Windhoek
Swakopmund
Walvis Bay
Rehoboth
Maltahohe
Gobabis
Waterberg Basin
Omatako Ring Structure
Omatako anomalies
Daneib Intrusion
Oorlogsende Porphyry Member (OPM)
Kalahari Basin
Aranos Basin
Namibia
Botswana
Atlantic Ocean
South Africa
Kilometers
0 40 80 160 240 320
Projection:
Albers Equal Area Conic
Central Meridian: 20ºE
Standard Parallel 1: -20ºS
Standard Parallel 2: -25ºS
14° 15° 16° 17° 18° 19° 20° 21° 22° 23°
-18° -19° -20° -21° -22° -23° -24° -25°

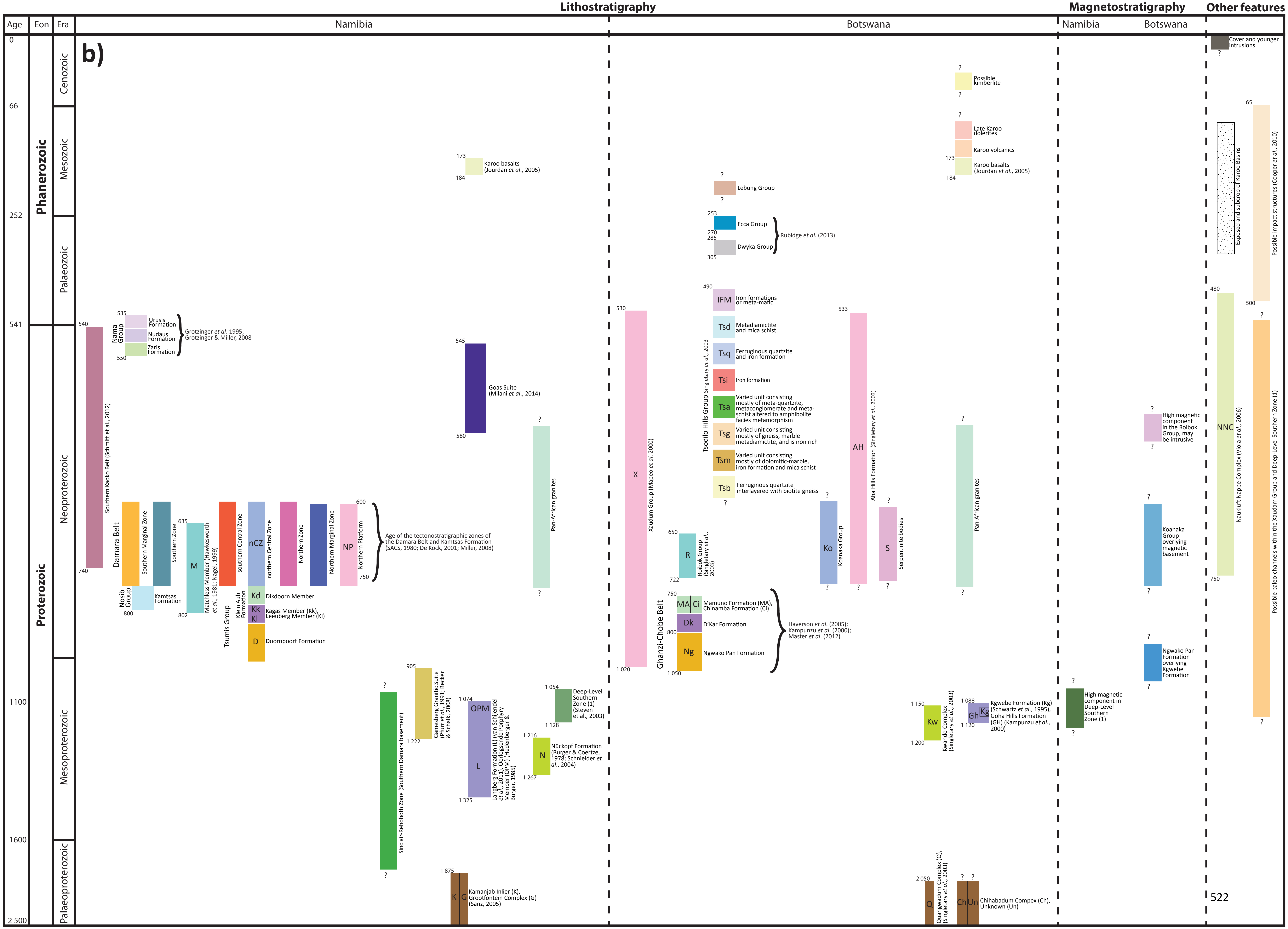
Lithostratigraphy
Magnetostratigraphy
Other features
Age
Eon
Era
Namibia
Botswana
Namibia
Botswana
b)
Phanerozoic
Proterozoic
Cenozoic
Mesozoic
Palaeozoic
Neoproterozoic
Mesoproterozoic
Palaeoproterozoic
0
66
252
541
1100
1600
2 500
Cover and younger intrusions
Possible kimberlite
Late Karoo dolerites
Karoo volcanics
Karoo basalts (Jourdan et al., 2005)
Lebung Group
Ecca Group
Dwyka Group
Rubidge et al. (2013)
Iron formations or meta-mafic
Metadiamictite and mica schist
Ferruginous quartzite and iron formation
Iron formation
Varied unit consisting mostly of meta-quartzite, metaconglomerate and meta-schist altered to amphibolite facies metamorphism
Varied unit consisting mostly of gneiss, marble metadiamictite, and is iron rich
Varied unit consisting mostly of dolomitic-marble, iron formation and mica schist
Ferruginous quartzite interlayered with biotite gneiss
Tsodilo Hills Group Singletary et al., 2003
Southern Kaoko Belt (Schmitt et al., 2012)
Nama Group
Urusis Formation
Nudaus Formation
Zaris Formation
Grotzinger et al. 1995; Grotzinger & Miller, 2008
Goas Suite (Milani et al., 2014)
Pan-African granites
Damara Belt
Southern Marginal Zone
Southern Zone
Matchless Member (Hawkesworth et al., 1981; Nagel, 1999)
southern Central Zone
northern Central Zone
Northern Zone
Northern Marginal Zone
Northern Platform
Age of the tectonostratigraphic zones of the Damara Belt and Kamtsas Formation (SACS, 1980; De Kock, 2001; Miller, 2008)
Nosib Group
Kamtsas Formation
Tsumis Group
Klein Aub Formation
Dikdoorn Member
Kagas Member (Kk), Leeuberg Member (Kl)
Doornpoort Formation
Xaudum Group (Mapeo et al. 2000)
Roibok Group (Singletary et al., 2003)
Ghanzi-Chobe Belt
Mamuno Formation (MA), Chinamba Formation (Ci)
D'Kar Formation
Ngwako Pan Formation
Haverson et al. (2005); Kampunzu et al. (2000); Master et al. (2012)
Koanaka Group
Aha Hills Formation (Singletary et al., 2003)
Serpentinite bodies
High magnetic component in the Roibok Group, may be intrusive
Koanaka Group overlying magnetic basement
Ngwako Pan Formation overlying Kgwebe Formation
Exposed and subcrop of Karoo Basins
Possible impact structures (Cooper et al., 2010)
Naukluft Nappe Complex (Viola et al., 2006)
Possible paleo-channels within the Xaudum Group and Deep-Level Southern Zone (1)
Sinclair-Rehoboth Zone (Southern Damara basement)
Gamsberg Granitic Suite (Pfurr et al., 1991; Becker & Schalk, 2008)
Langberg Formation (L) (van Schijendel et al., 2011), Oorlogsende Porphyry Member (OPM) (Hedenberger & Burger, 1985)
Deep-Level Southern Zone (1) (Steven et al., 2003)
Nückopf Formation (Burger & Coertze, 1978; Schnielder et al., 2004)
Kwando Complex (Singletary et al., 2003)
Kgwebe Formation (Kg) (Schwartz et al., 1995), Goha Hills Formation (GH) (Kampunzu et al., 2000)
High magnetic component in Deep-Level Southern Zone (1)
Kamanjab Inlier (K), Grootfontein Complex (G) (Sanz, 2005)
Quangwadum Complex (Q) (Singletary et al., 2003)
Chihabadum Compex (Ch), Unknown (Un)

Appendix 7:

Magnetotelluric responses of the DMB profile, demonstrating the quality range of the data. Apparent resistivity and phase are plotted against period. Red dots represent the TE mode (ρ_{xy}; electrical currents flowing parallel to strike) and the blue dots represent the TM mode (ρ_{yx}; electrical currents flowing perpendicular to the geological strike).

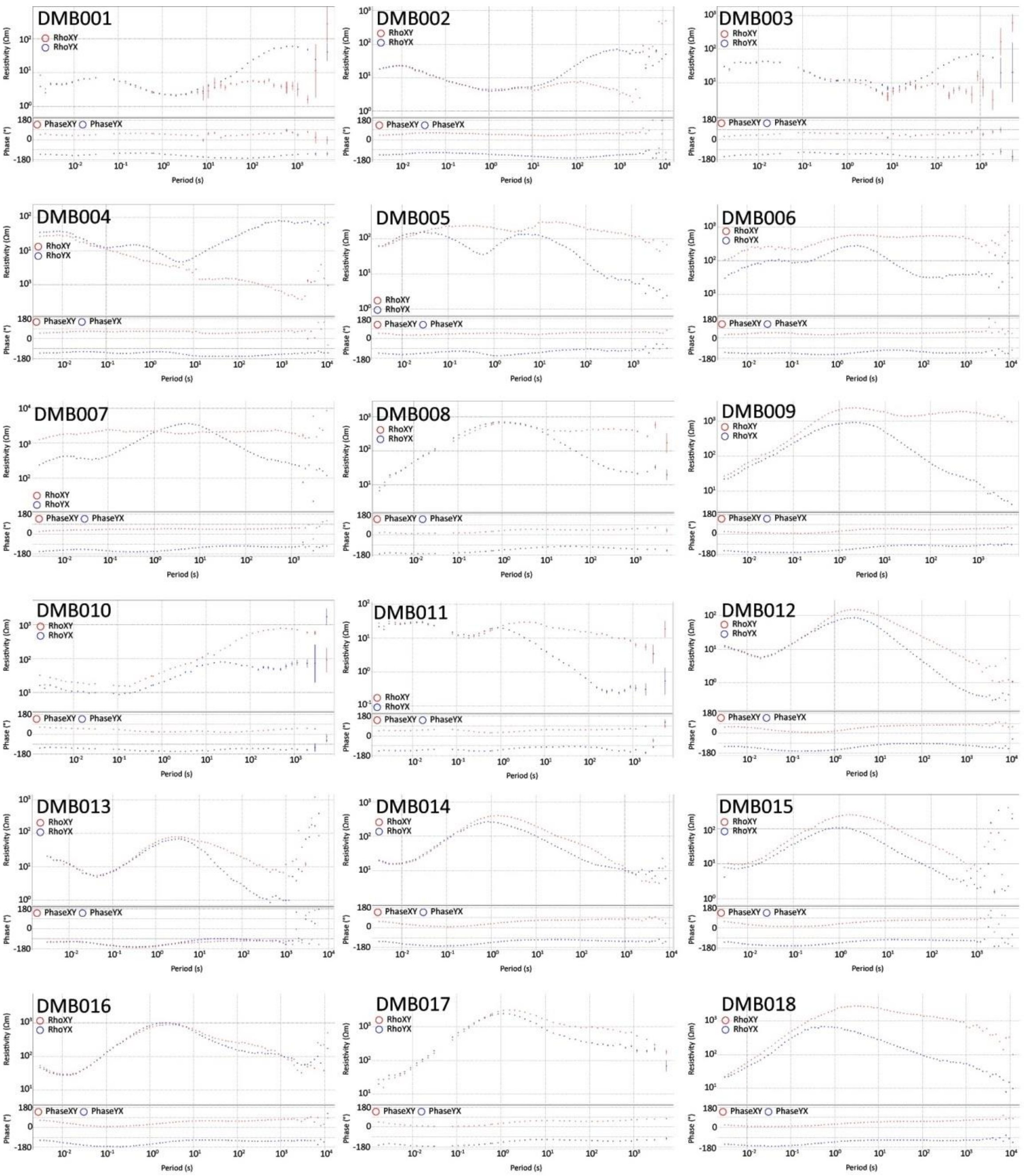
DMB001
DMB002
DMB003
DMB004
DMB005
DMB006
DMB007
DMB008
DMB009
DMB010
DMB011
DMB012
DMB013
DMB014
DMB015
DMB016
DMB017
DMB018
RhoXY
RhoYX
PhaseXY
PhaseYX
Resistivity (Ωm)
Phase (°)
Period (s)

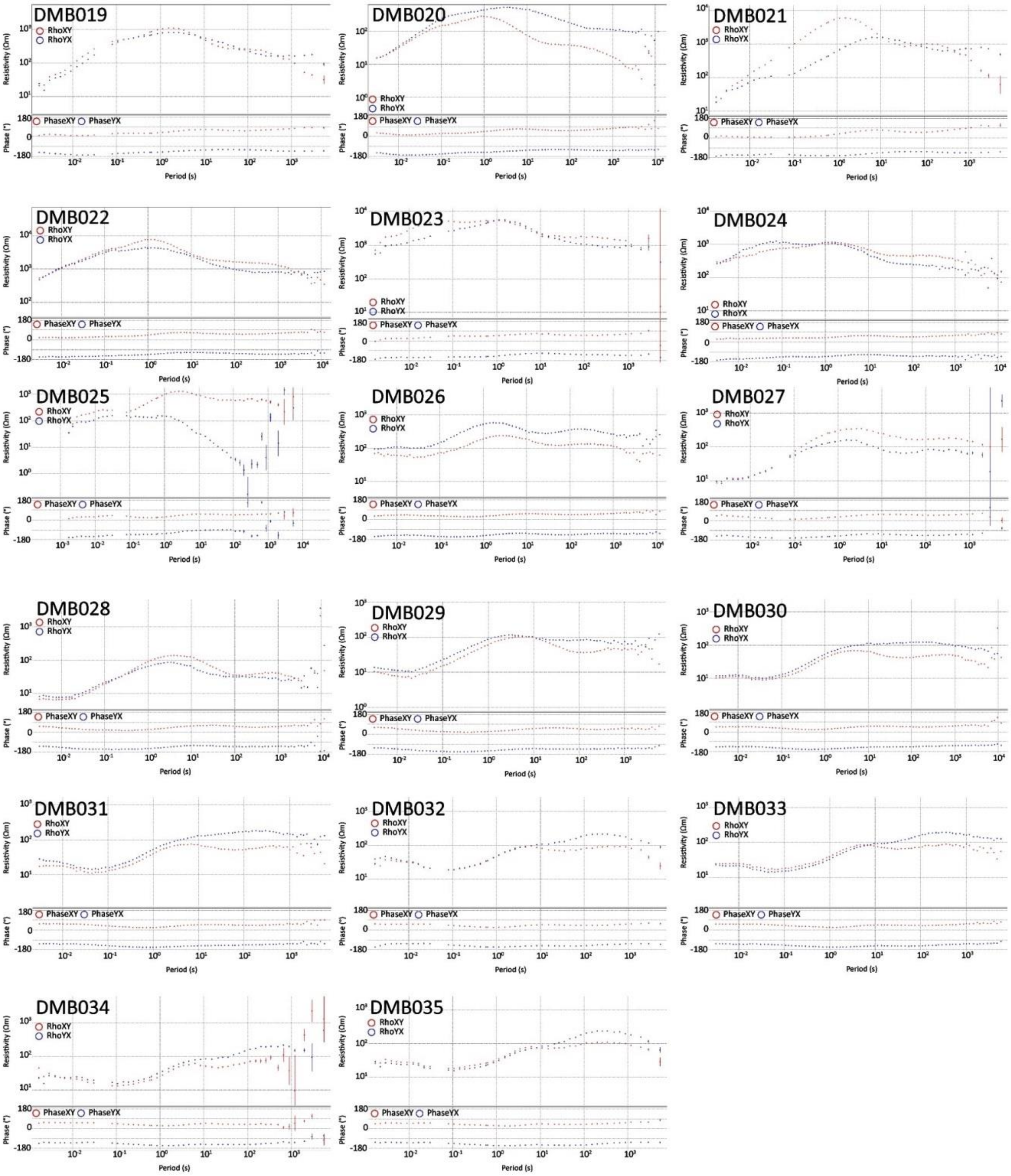
DMB019
DMB020
DMB021
DMB022
DMB023
DMB024
DMB025
DMB026
DMB027
DMB028
DMB029
DMB030
DMB031
DMB032
DMB033
DMB034
DMB035
RhoXY
RhoYX
PhaseXY
PhaseYX
Resistivity (Ωm)
Phase (°)
Period (s)

Appendix 8:

Magnetotelluric responses of the NEN profile, demonstrating the quality range of the data. Apparent resistivity and phase are plotted against period. Red dots represent the TE mode (ρ_{xy}; electrical currents flowing parallel to strike) and the blue dots represent the TM mode (ρ_{yx}; electrical currents flowing perpendicular to the geological strike).

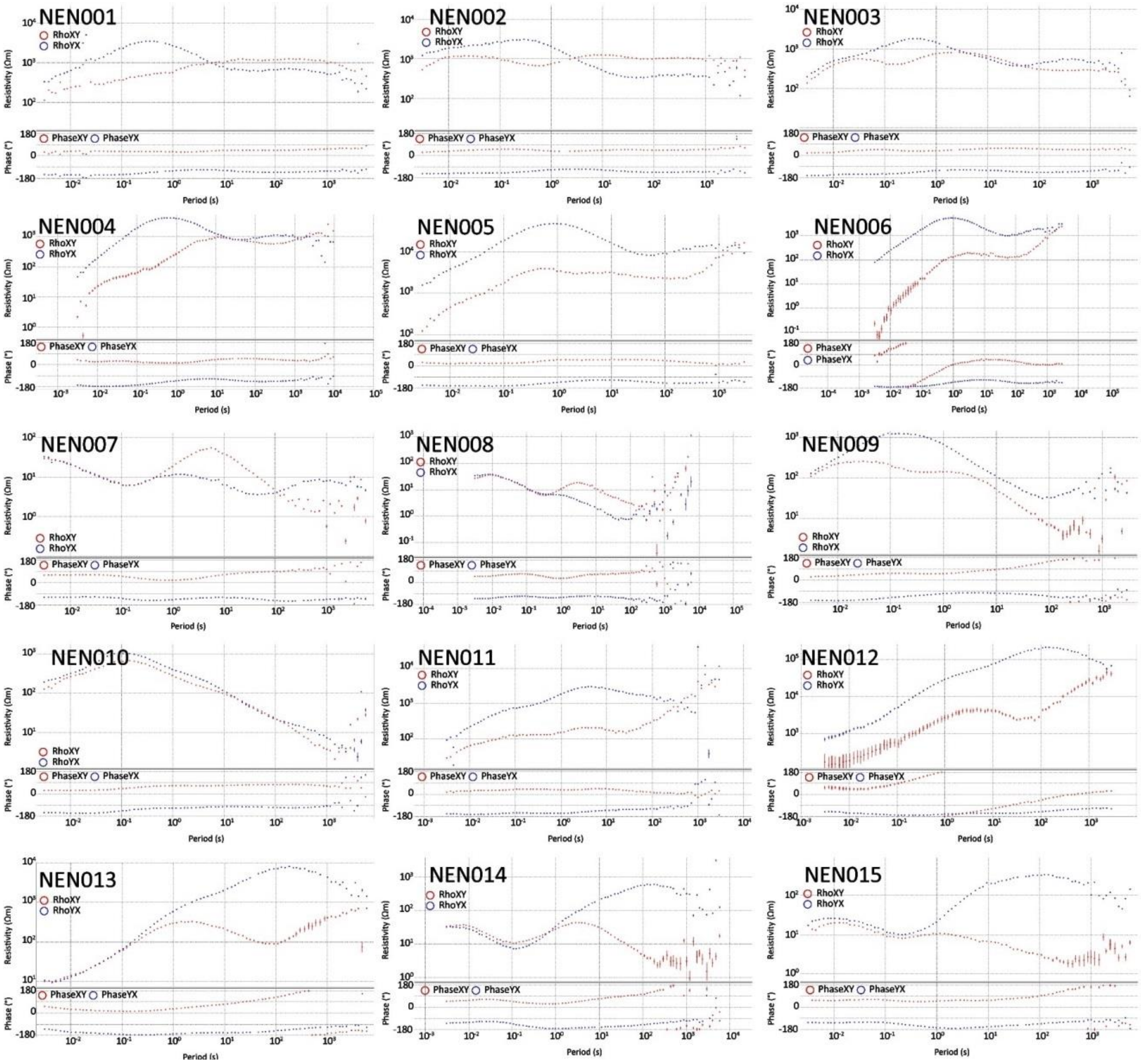
NEN001
NEN002
NEN003
NEN004
NEN005
NEN006
NEN007
NEN008
NEN009
NEN010
NEN011
NEN012
NEN013
NEN014
NEN015
RhoXY
RhoYX
PhaseXY
PhaseYX
Resistivity (Ωm)
Phase (°)
Period (s)

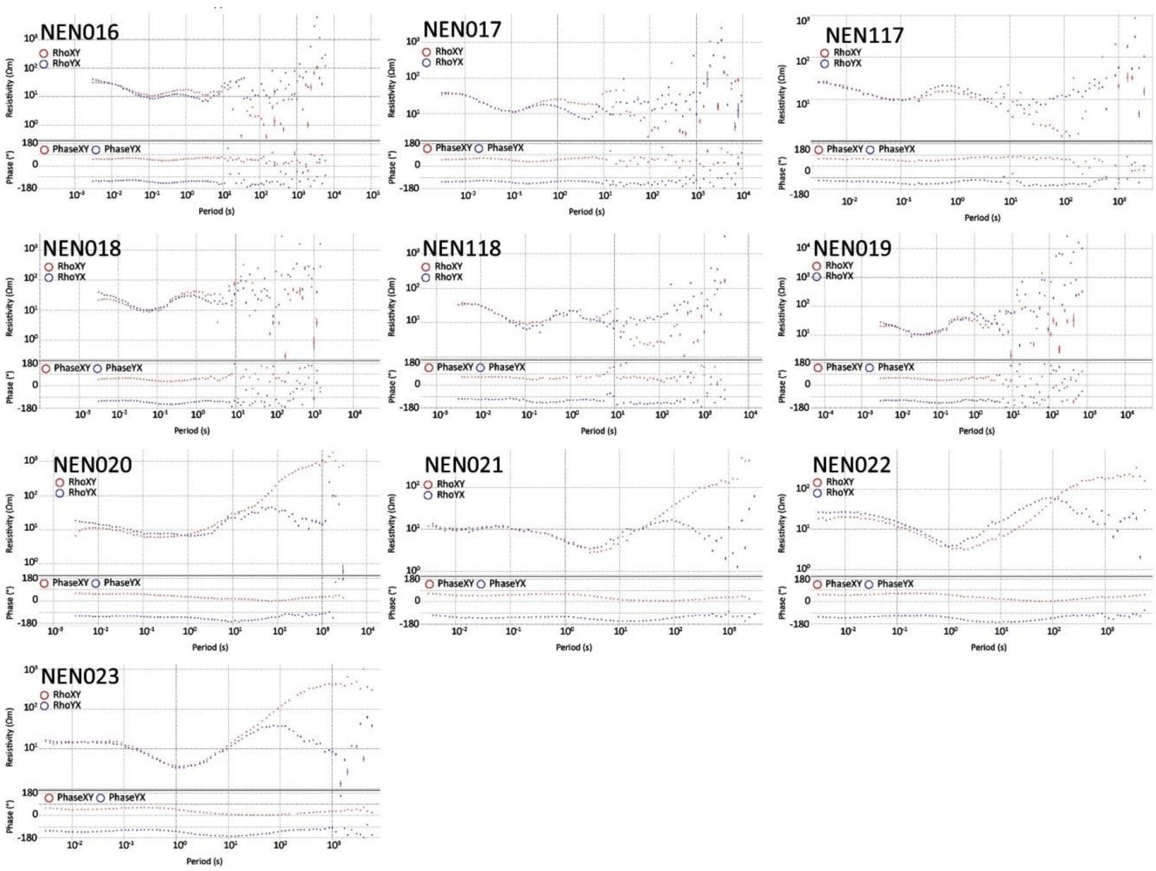
NEN016
NEN017
NEN117
NEN018
NEN118
NEN019
NEN020
NEN021
NEN022
NEN023
RhoXY
RhoYX
PhaseXY
PhaseYX
Resistivity (Ωm)
Phase (°)
Period (s)

Appendix 9:

Magnetotelluric responses of the OKA-CAM profile, demonstrating the quality range of the data. Apparent resistivity and phase are plotted against period. Red dots represent the TE mode (ρ_{xy}; electrical currents flowing parallel to strike) and the blue dots represent the TM mode (ρ_{yx}; electrical currents flowing perpendicular to the geological strike).

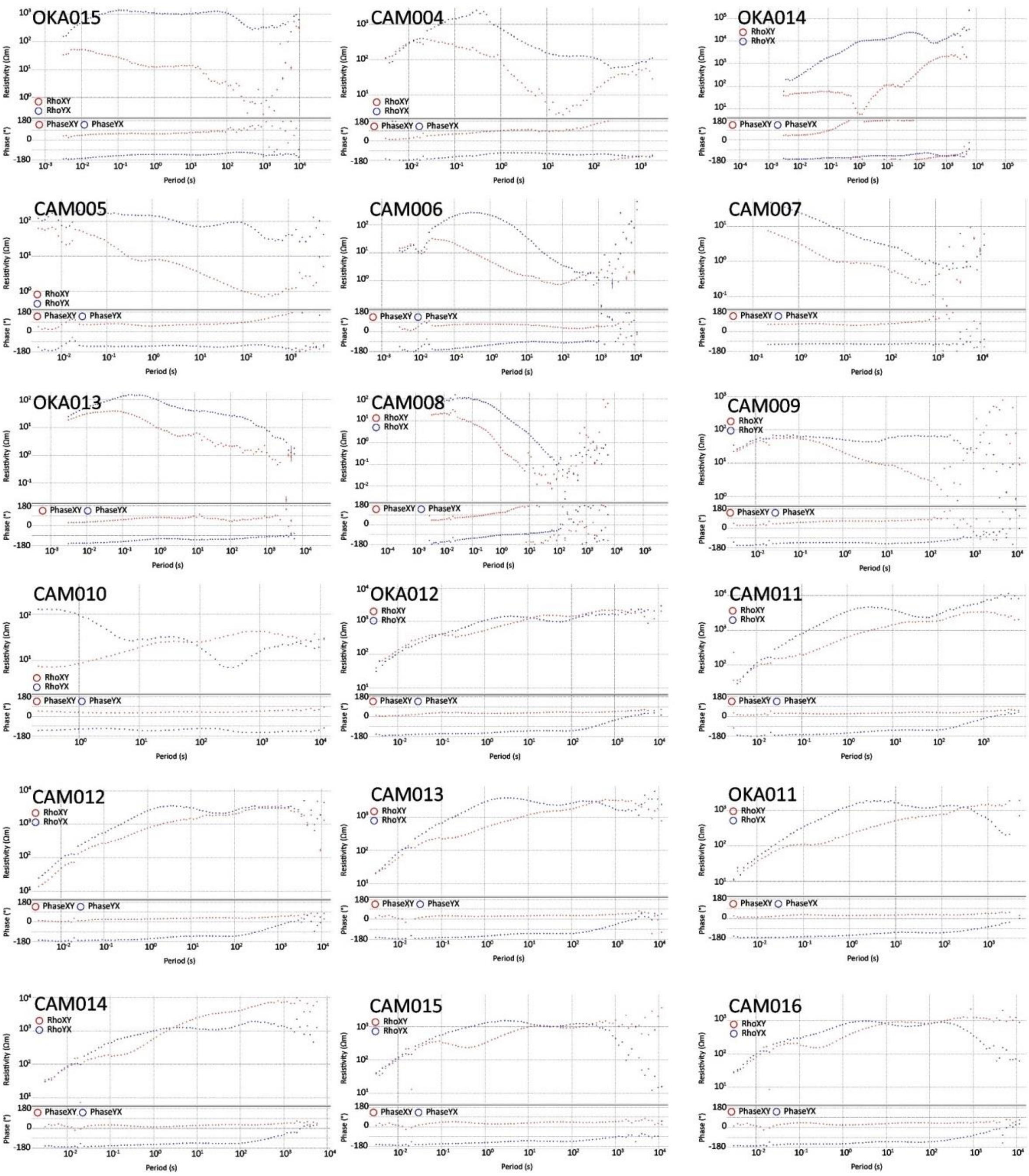
OKA015
CAM004
OKA014
CAM005
CAM006
CAM007
OKA013
CAM008
CAM009
CAM010
OKA012
CAM011
CAM012
CAM013
OKA011
CAM014
CAM015
CAM016
RhoXY
RhoYX
PhaseXY
PhaseYX
Resistivity (Ωm)
Phase (°)
Period (s)

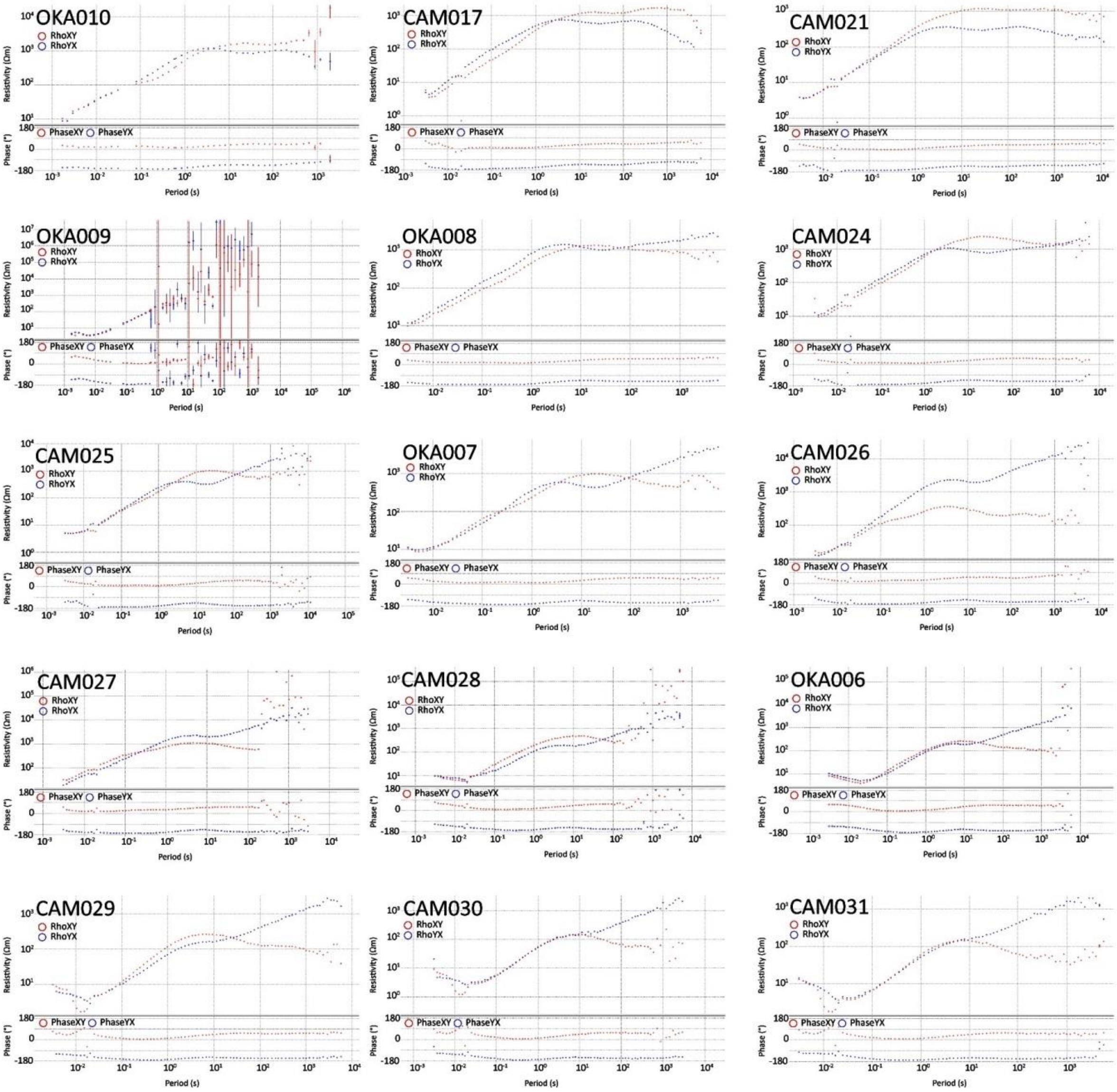
OKA010
CAM017
CAM021
OKA009
OKA008
CAM024
CAM025
OKA007
CAM026
CAM027
CAM028
OKA006
CAM029
CAM030
CAM031
RhoXY
RhoYX
PhaseXY
PhaseYX
Resistivity (Ωm)
Phase (°)
Period (s)

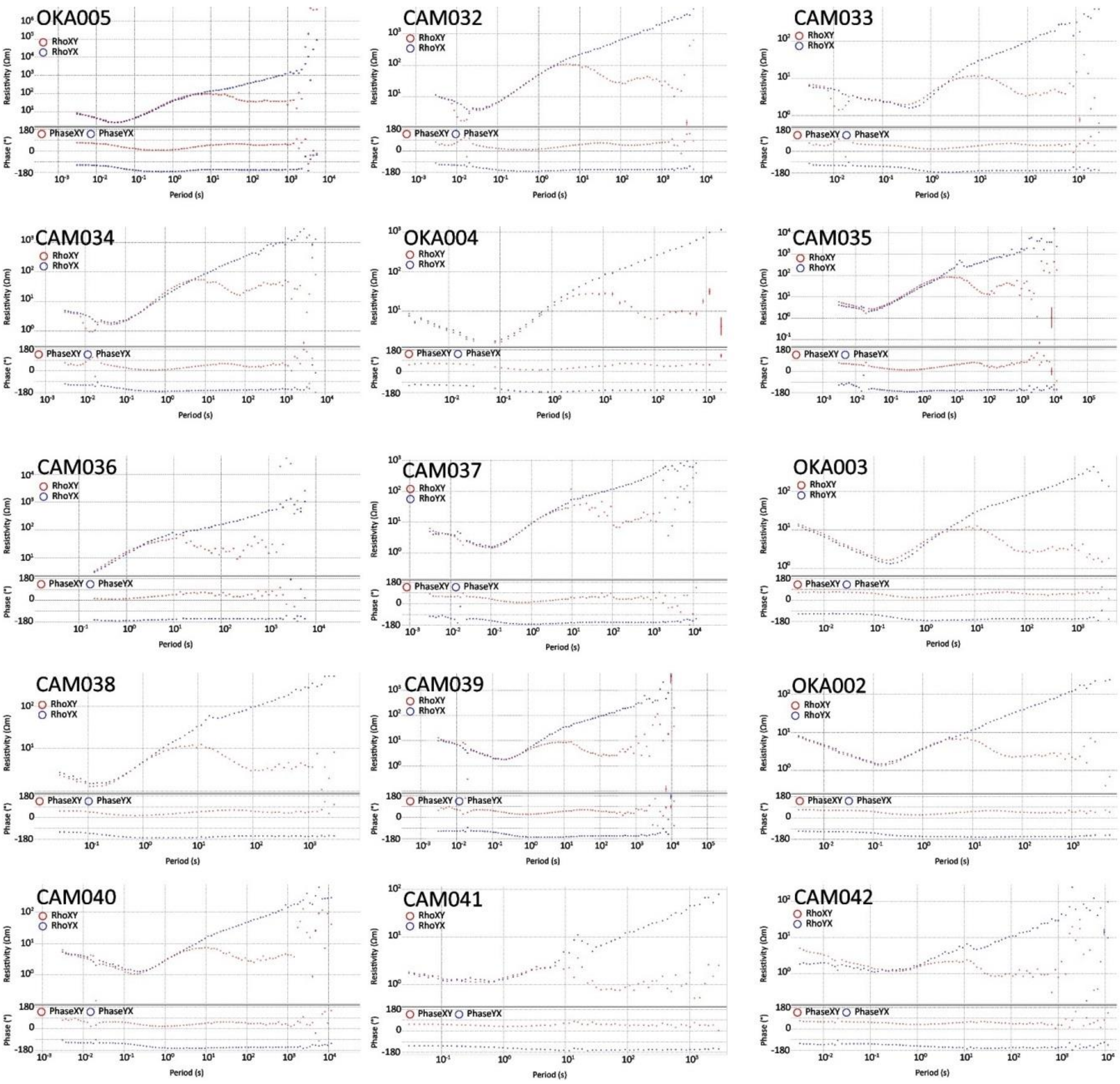
OKA005
CAM032
CAM033
CAM034
OKA004
CAM035
CAM036
CAM037
OKA003
CAM038
CAM039
OKA002
CAM040
CAM041
CAM042
RhoXY
RhoYX
PhaseXY
PhaseYX
Resistivity (Ωm)
Phase (°)
Period (s)

Appendix 10:

Magnetotelluric responses of the DMB profile masked for the depth interval of 1 – 15 km. The data are decomposed to a geoelectric strike angle of 45° E of north. Apparent resistivity and phase are plotted against period. Red dots represent the TE mode (ρ_{xy}; electrical currents flowing parallel to strike) and the blue dots represent the TM mode (ρ_{yx}; electrical currents flowing perpendicular to the geological strike). The smoothed D^+ curves relate apparent resistivity and phase of the same component (xy or yx) through a D^+ function (solid coloured line).

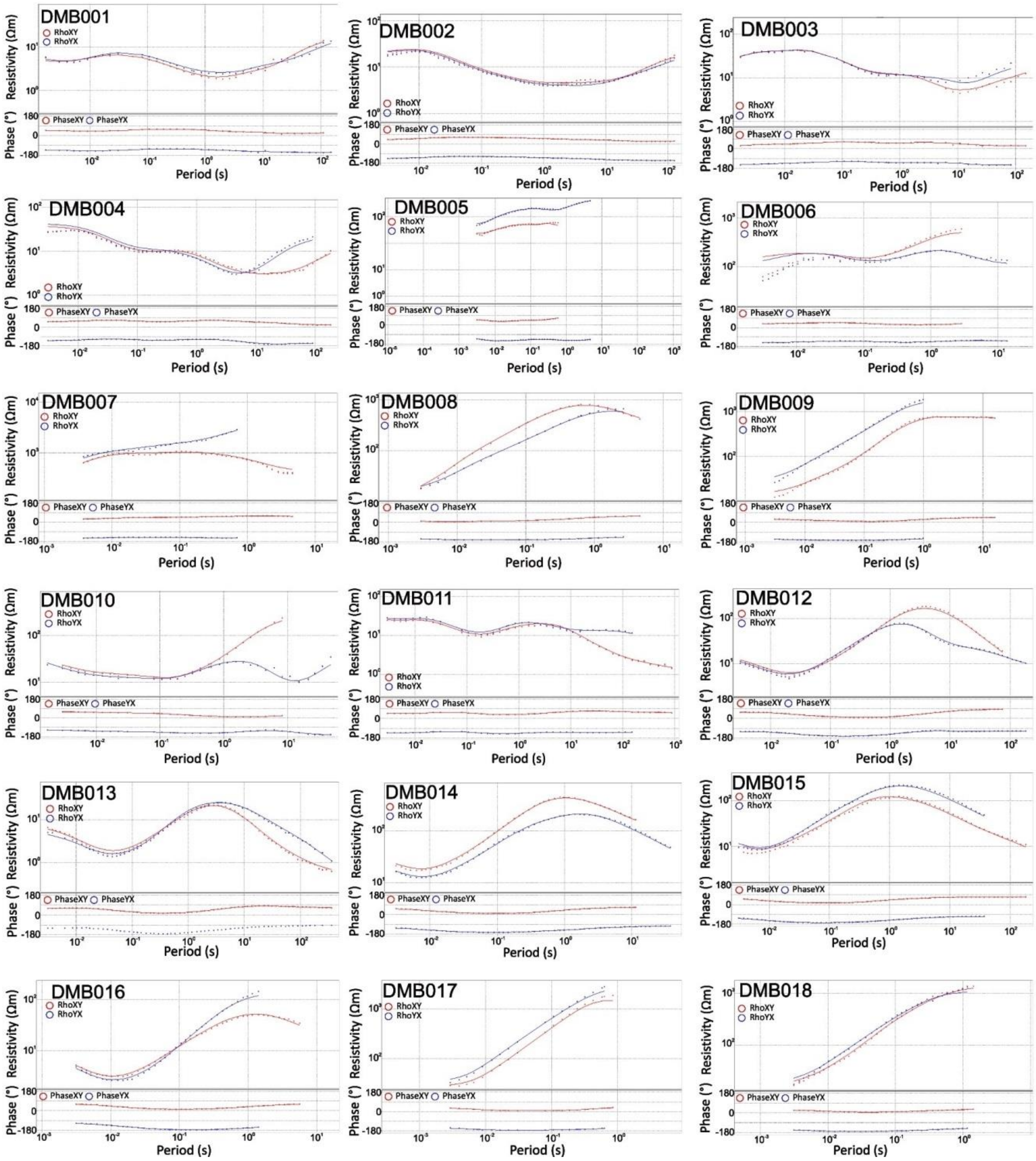
DMB001
DMB002
DMB003
DMB004
DMB005
DMB006
DMB007
DMB008
DMB009
DMB010
DMB011
DMB012
DMB013
DMB014
DMB015
DMB016
DMB017
DMB018
RhoXY
RhoYX
PhaseXY
PhaseYX
Resistivity (Ωm)
Phase (°)
Period (s)

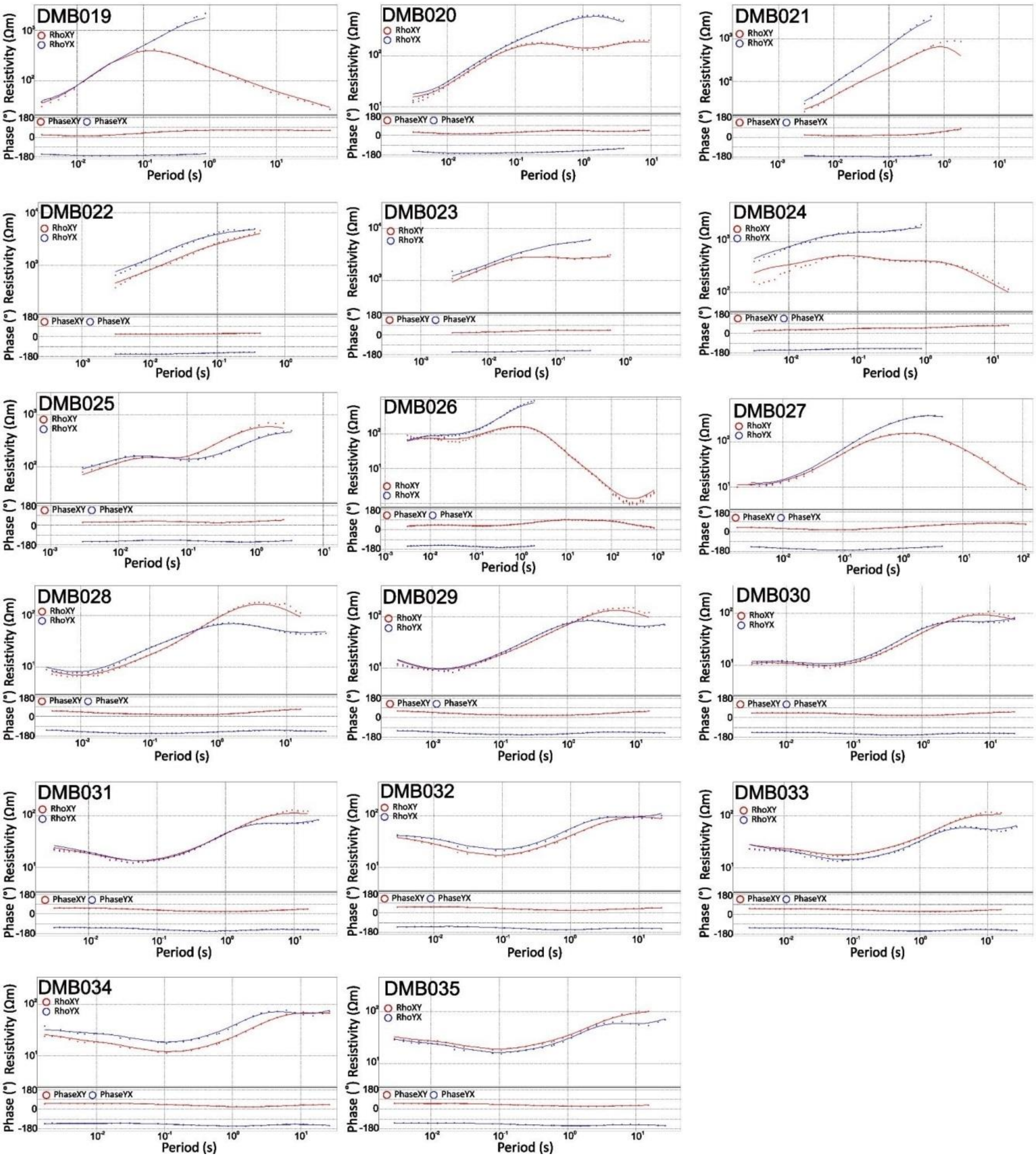
DMB019
DMB020
DMB021
DMB022
DMB023
DMB024
DMB025
DMB026
DMB027
DMB028
DMB029
DMB030
DMB031
DMB032
DMB033
DMB034
DMB035
RhoXY
RhoYX
PhaseXY
PhaseYX
Resistivity (Ωm)
Phase (°)
Period (s)

Appendix 11:

Magnetotelluric responses of the NEN profile masked for the depth interval of 1 – 15 km. The data are decomposed to a geoelectric strike angle of 65° E of north. Apparent resistivity and phase are plotted against period. Red dots represent the TE mode (ρ_{xy}; electrical currents flowing parallel to strike) and the blue dots represent the TM mode (ρ_{yx}; electrical currents flowing perpendicular to the geological strike). The smoothed D^+ curves relate apparent resistivity and phase of the same component (xy or yx) through a D^+ function (solid coloured line).

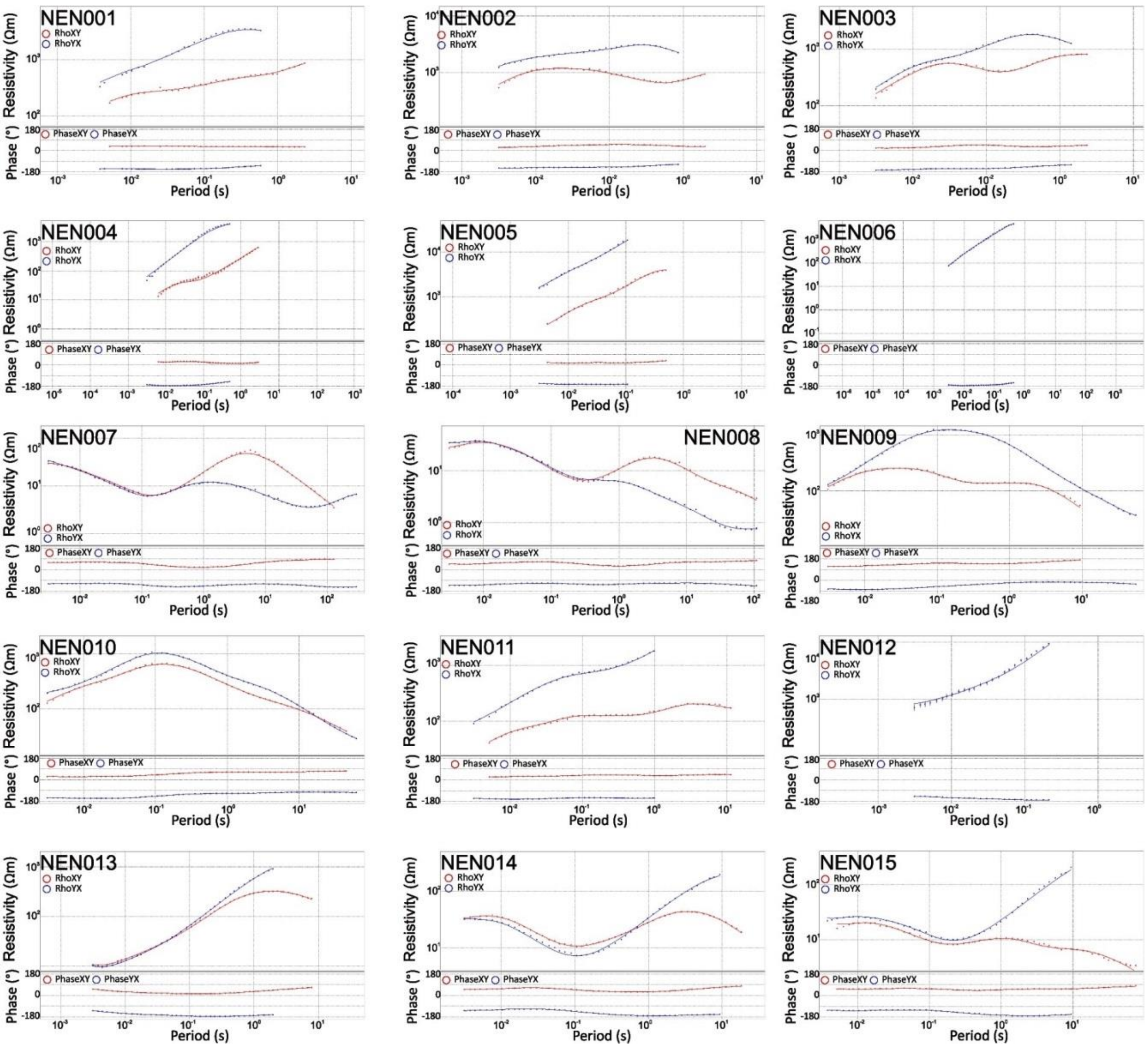
NEN001
NEN002
NEN003
NEN004
NEN005
NEN006
NEN007
NEN008
NEN009
NEN010
NEN011
NEN012
NEN013
NEN014
NEN015
RhoXY
RhoYX
PhaseXY
PhaseYX
Resistivity (Ωm)
Phase (°)
Period (s)

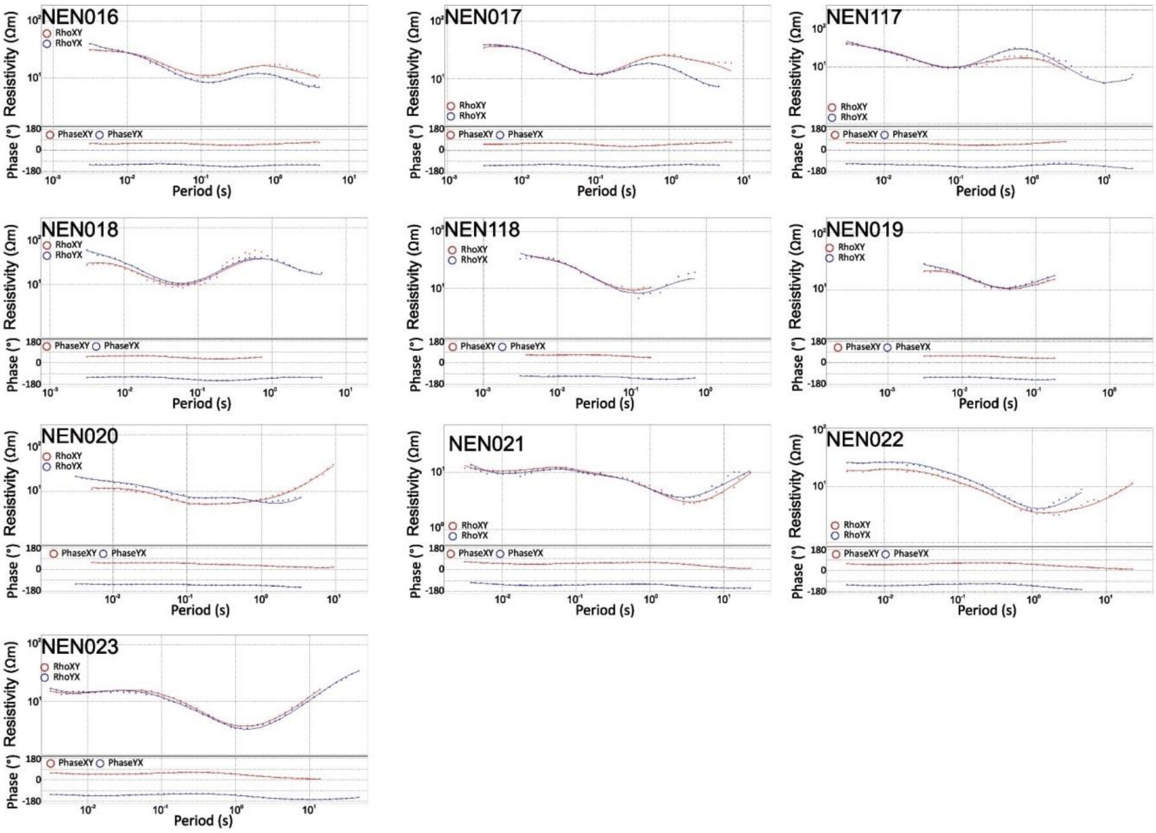
NEN016
NEN017
NEN117
NEN018
NEN118
NEN019
NEN020
NEN021
NEN022
NEN023
RhoXY
RhoYX
PhaseXY
PhaseYX
Resistivity (Ωm)
Phase (°)
Period (s)

Appendix 12:

Magnetotelluric responses of the OKA-CAM profile masked for the depth interval of 1 – 15 km. The data are decomposed to a geoelectric strike angle of 85° E of north. Apparent resistivity and phase are plotted against period. Red dots represent the TE mode (ρ_{xy}; electrical currents flowing parallel to strike) and the blue dots represent the TM mode (ρ_{yx}; electrical currents flowing perpendicular to the geological strike). The smoothed D^+ curves relate apparent resistivity and phase of the same component (xy or yx) through a D^+ function (solid coloured line).

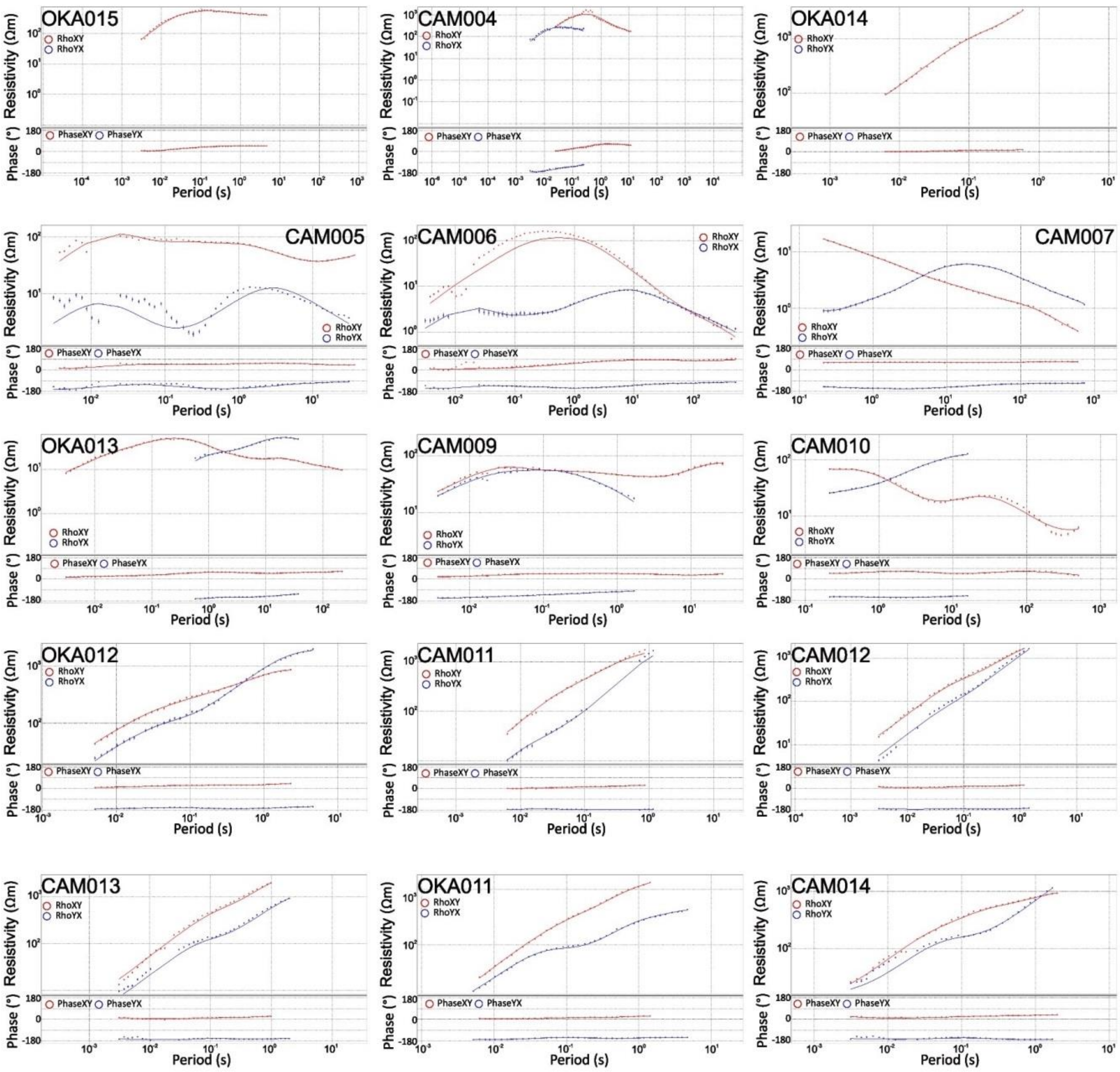
OKA015
CAM004
OKA014
CAM005
CAM006
CAM007
OKA013
CAM009
CAM010
OKA012
CAM011
CAM012
CAM013
OKA011
CAM014
Resistivity (Ωm)
Phase (°)
Period (s)
RhoXY
RhoYX
PhaseXY
PhaseYX

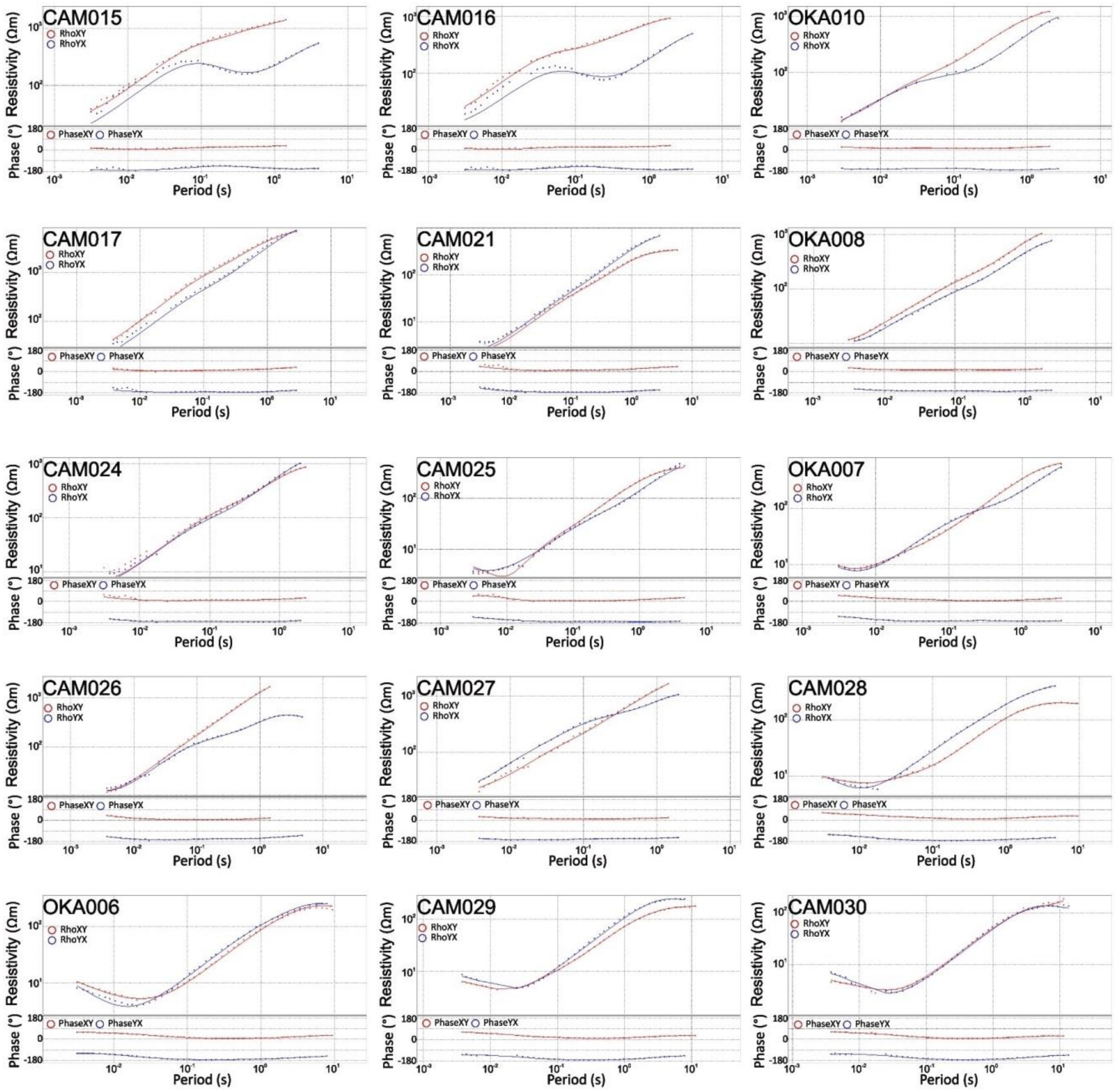
CAM015
CAM016
OKA010
CAM017
CAM021
OKA008
CAM024
CAM025
OKA007
CAM026
CAM027
CAM028
OKA006
CAM029
CAM030
RhoXY
RhoYX
PhaseXY
PhaseYX
Resistivity (Ωm)
Phase (°)
Period (s)

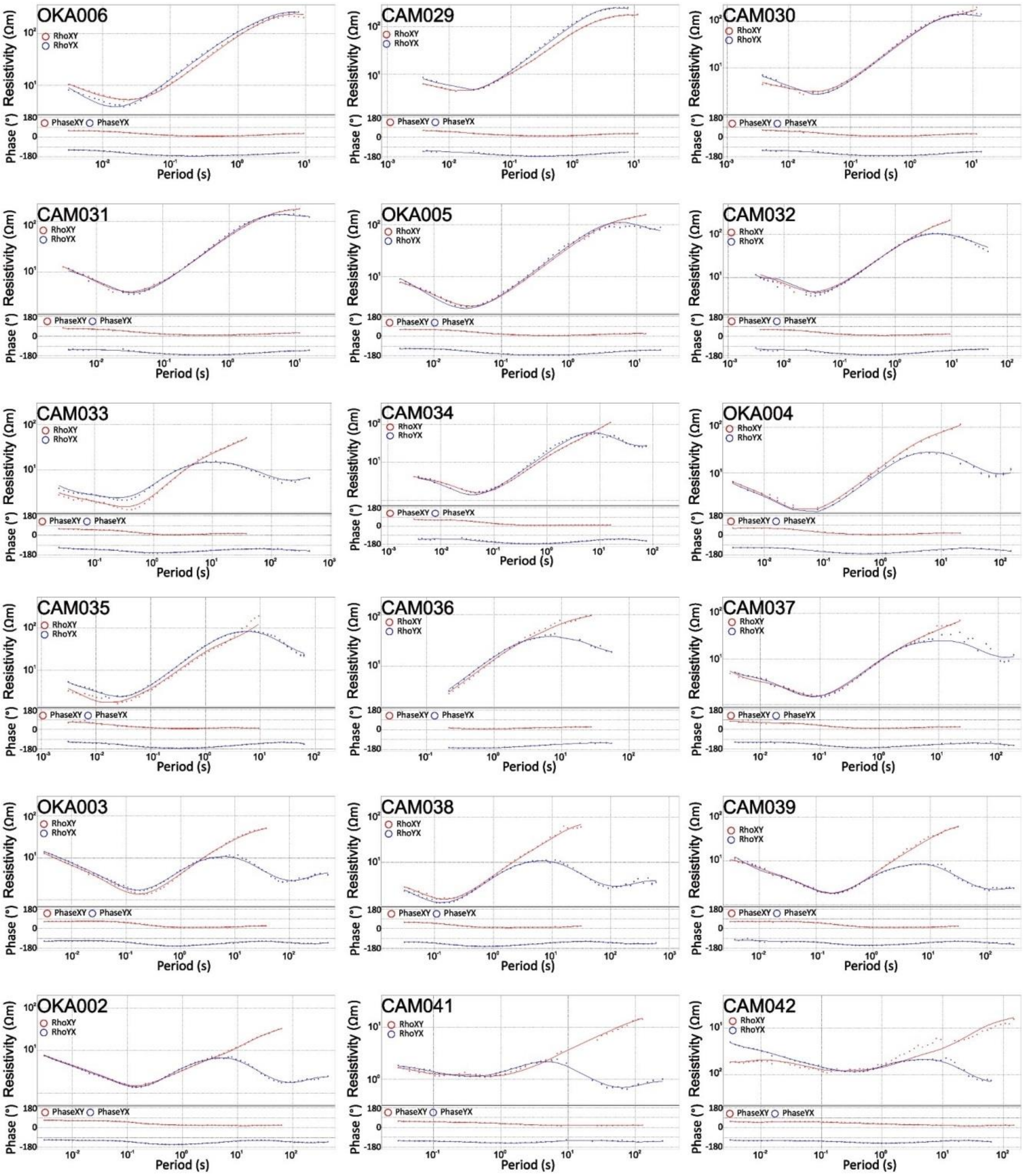
OKA006
CAM029
CAM030
CAM031
OKA005
CAM032
CAM033
CAM034
OKA004
CAM035
CAM036
CAM037
OKA003
CAM038
CAM039
OKA002
CAM041
CAM042
Resistivity (Ωm)
RhoXY
RhoYX
Phase (°)
PhaseXY
PhaseYX
Period (s)